

**Fifth Edition**

# COMPUTER VISION

**Principles  
Algorithms  
Applications  
Learning**

**E.R. Davies**



# Computer Vision

This page intentionally left blank

# Computer Vision

## Principles, Algorithms, Applications, Learning

**Fifth Edition**

**E.R. Davies**

*Royal Holloway, University of London, United Kingdom*



**ACADEMIC PRESS**

An imprint of Elsevier

Academic Press is an imprint of Elsevier  
125 London Wall, London EC2Y 5AS, United Kingdom  
525 B Street, Suite 1800, San Diego, CA 92101-4495, United States  
50 Hampshire Street, 5th Floor, Cambridge, MA 02139, United States  
The Boulevard, Langford Lane, Kidlington, Oxford OX5 1GB, United Kingdom

Copyright © 2018 Elsevier Inc. All rights reserved.

No part of this publication may be reproduced or transmitted in any form or by any means, electronic or mechanical, including photocopying, recording, or any information storage and retrieval system, without permission in writing from the publisher. Details on how to seek permission, further information about the Publisher's permissions policies and our arrangements with organizations such as the Copyright Clearance Center and the Copyright Licensing Agency, can be found at our website: [www.elsevier.com/permissions](http://www.elsevier.com/permissions).

This book and the individual contributions contained in it are protected under copyright by the Publisher (other than as may be noted herein).

#### Notices

Knowledge and best practice in this field are constantly changing. As new research and experience broaden our understanding, changes in research methods, professional practices, or medical treatment may become necessary.

Practitioners and researchers must always rely on their own experience and knowledge in evaluating and using any information, methods, compounds, or experiments described herein. In using such information or methods they should be mindful of their own safety and the safety of others, including parties for whom they have a professional responsibility.

To the fullest extent of the law, neither the Publisher nor the authors, contributors, or editors, assume any liability for any injury and/or damage to persons or property as a matter of products liability, negligence or otherwise, or from any use or operation of any methods, products, instructions, or ideas contained in the material herein.

#### British Library Cataloguing-in-Publication Data

A catalogue record for this book is available from the British Library

#### Library of Congress Cataloging-in-Publication Data

A catalog record for this book is available from the Library of Congress

ISBN: 978-0-12-809284-2

For Information on all Academic Press publications  
visit our website at <https://www.elsevier.com/books-and-journals>



Working together  
to grow libraries in  
developing countries

[www.elsevier.com](http://www.elsevier.com) • [www.bookaid.org](http://www.bookaid.org)

*Publisher:* Mara Conner  
*Acquisition Editor:* Tim Pitts  
*Editorial Project Manager:* Charlotte Kent  
*Production Project Manager:* Sruthi Satheesh  
*Cover Designer:* Greg Harris

Typeset by MPS Limited, Chennai, India

*This book is dedicated to my family.*

*To my late mother, Mary Davies, to record her never-failing love  
and devotion.*

*To my late father, Arthur Granville Davies, who passed on to me  
his appreciation of the beauties of mathematics and science.*

*To my wife, Joan, for love, patience, support, and inspiration.*

*To my children, Elizabeth, Sarah, and Marion, the music in my life.*

*To my grandchildren, Jasper, Jerome, Eva, and Tara, for constantly  
reminding me of the carefree joys of youth!*

This page intentionally left blank

# Contents

About the Author .....	xxi
Foreword .....	xxiii
Preface to the Fifth Edition .....	xxv
Preface to the First Edition .....	xxvii
Acknowledgments .....	xxxii
Topics Covered in Application Case Studies .....	xxxv
Glossary of Acronyms and Abbreviations .....	xxxix

<b>CHAPTER 1 Vision, the challenge .....</b>	<b>1</b>
<b>1.1 Introduction—Man and His Senses .....</b>	<b>1</b>
<b>1.2 The Nature of Vision .....</b>	<b>2</b>
1.2.1 The Process of Recognition .....	2
1.2.2 Tackling the Recognition Problem .....	4
1.2.3 Object Location .....	6
1.2.4 Scene Analysis .....	9
1.2.5 Vision as Inverse Graphics .....	9
<b>1.3 From Automated Visual Inspection to Surveillance .....</b>	<b>10</b>
<b>1.4 What This Book Is About .....</b>	<b>12</b>
<b>1.5 The Part Played by Machine Learning .....</b>	<b>13</b>
<b>1.6 The Following Chapters .....</b>	<b>14</b>
<b>1.7 Bibliographical Notes .....</b>	<b>15</b>

## **PART 1 LOW-LEVEL VISION**

---

<b>CHAPTER 2 Images and imaging operations .....</b>	<b>19</b>
<b>2.1 Introduction .....</b>	<b>19</b>
2.1.1 Gray Scale Versus Color .....	21
<b>2.2 Image Processing Operations .....</b>	<b>24</b>
2.2.1 Some Basic Operations on Grayscale Images .....	25
2.2.2 Basic Operations on Binary Images .....	29
<b>2.3 Convolutions and Point Spread Functions .....</b>	<b>33</b>
<b>2.4 Sequential Versus Parallel Operations .....</b>	<b>35</b>
<b>2.5 Concluding Remarks .....</b>	<b>36</b>
<b>2.6 Bibliographical and Historical Notes .....</b>	<b>37</b>
<b>2.7 Problems .....</b>	<b>37</b>



<b>CHAPTER 3</b>	<b>Image filtering and morphology</b>	<b>39</b>
3.1	Introduction	40
3.2	Noise Suppression by Gaussian Smoothing	42
3.3	Median Filters	44
3.4	Mode Filters	46
3.5	Rank Order Filters	53
3.6	Sharp–Unsharp Masking	54
3.7	Shifts Introduced by Median Filters	56
3.7.1	Continuum Model of Median Shifts	57
3.7.2	Generalization to Grayscale Images	58
3.7.3	Discrete Model of Median Shifts	60
3.8	Shifts Introduced by Rank Order Filters	61
3.8.1	Shifts in Rectangular Neighborhoods	62
3.9	The Role of Filters in Industrial Applications of Vision	66
3.10	Color in Image Filtering	68
3.11	Dilation and Erosion in Binary Images	69
3.11.1	Dilation and Erosion	69
3.11.2	Cancellation Effects	69
3.11.3	Modified Dilation and Erosion Operators	70
3.12	Mathematical Morphology	70
3.12.1	Generalized Morphological Dilation	70
3.12.2	Generalized Morphological Erosion	72
3.12.3	Duality Between Dilation and Erosion	72
3.12.4	Properties of Dilation and Erosion Operators	73
3.12.5	Closing and Opening	76
3.12.6	Summary of Basic Morphological Operations	78
3.13	Morphological Grouping	79
3.14	Morphology in Grayscale Images	84
3.15	Concluding Remarks	86
3.16	Bibliographical and Historical Notes	87
3.16.1	More Recent Developments	89
3.17	Problems	90
<b>CHAPTER 4</b>	<b>The role of thresholding</b>	<b>93</b>
4.1	Introduction	93
4.2	Region-Growing Methods	94
4.3	Thresholding	95
4.3.1	Finding a Suitable Threshold	95
4.3.2	Tackling the Problem of Bias in Threshold Selection	97

4.4	Adaptive Thresholding .....	97
4.4.1	Local Thresholding Methods .....	98
4.5	More Thoroughgoing Approaches to Threshold Selection .....	101
4.5.1	Variance-Based Thresholding .....	101
4.5.2	Entropy-Based Thresholding .....	104
4.5.3	Maximum Likelihood Thresholding .....	105
4.6	The Global Valley Approach to Thresholding .....	106
4.7	Practical Results Obtained Using the Global Valley Method .....	108
4.8	Histogram Concavity Analysis .....	113
4.9	Concluding Remarks .....	115
4.10	Bibliographical and Historical Notes .....	116
4.10.1	More Recent Developments .....	117
4.11	Problems .....	118
<b>CHAPTER 5</b>	<b>Edge detection .....</b>	<b>119</b>
5.1	Introduction .....	119
5.2	Basic Theory of Edge Detection .....	120
5.3	The Template Matching Approach .....	123
5.4	Theory of $3 \times 3$ Template Operators .....	123
5.5	The Design of Differential Gradient Operators .....	125
5.6	The Concept of a Circular Operator .....	126
5.7	Detailed Implementation of Circular Operators .....	127
5.8	The Systematic Design of Differential Edge Operators .....	130
5.9	Problems with the Above Approach—Some Alternative Schemes .....	130
5.10	Hysteresis Thresholding .....	134
5.11	The Canny Operator .....	136
5.12	The Laplacian Operator .....	139
5.13	Concluding Remarks .....	143
5.14	Bibliographical and Historical Notes .....	144
5.14.1	More Recent Developments .....	145
5.15	Problems .....	145
<b>CHAPTER 6</b>	<b>Corner, interest point, and invariant feature detection .....</b>	<b>147</b>
6.1	Introduction .....	147
6.2	Template Matching .....	148
6.3	Second-Order Derivative Schemes .....	149

<b>6.4</b>	A Median Filter–based Corner Detector .....	151
6.4.1	Analyzing the Operation of the Median Detector.....	152
6.4.2	Practical Results .....	154
<b>6.5</b>	The Harris Interest Point Operator .....	156
6.5.1	Corner Signals and Shifts for Various Geometric Configurations .....	159
6.5.2	Performance with Crossing Points and T-junctions .....	160
6.5.3	Different Forms of the Harris Operator.....	163
<b>6.6</b>	Corner Orientation.....	164
<b>6.7</b>	Local Invariant Feature Detectors and Descriptors.....	166
6.7.1	Geometric Transformations and Feature Normalization.....	167
6.7.2	Harris Scale and Affine Invariant Detectors and Descriptors .....	169
6.7.3	Hessian Scale and Affine Invariant Detectors and Descriptors .....	171
6.7.4	The Scale Invariant Feature Transforms Operator.....	171
6.7.5	The Speeded-Up Robust Features Operator.....	172
6.7.6	Maximally Stable Extremal Regions.....	174
6.7.7	Comparison of the Various Invariant Feature Detectors.....	175
6.7.8	Histograms of Oriented Gradients.....	177
<b>6.8</b>	Concluding Remarks .....	179
<b>6.9</b>	Bibliographical and Historical Notes.....	180
6.9.1	More Recent Developments.....	182
<b>6.10</b>	Problems .....	183
<b>CHAPTER 7</b>	<b>Texture analysis.....</b>	<b>185</b>
7.1	Introduction .....	185
7.2	Some Basic Approaches to Texture Analysis .....	188
7.3	Graylevel Co-occurrence Matrices .....	190
7.4	Laws’ Texture Energy Approach.....	193
7.5	Ade’s Eigenfilter Approach .....	195
7.6	Appraisal of the Laws and Ade Approaches.....	197
7.7	Concluding Remarks .....	198
7.8	Bibliographical and Historical Notes.....	199
7.8.1	More Recent Developments.....	200

## **PART 2 INTERMEDIATE-LEVEL VISION**

---

<b>CHAPTER 8</b>	<b>Binary shape analysis.....</b>	<b>203</b>
8.1	Introduction .....	203
8.2	Connectedness in Binary Images.....	204
8.3	Object Labeling and Counting.....	205
8.3.1	Solving the Labeling Problem in a More Complex Case .....	209
8.4	Size Filtering .....	212
8.5	Distance Functions and Their Uses .....	214
8.5.1	Local Maxima and Data Compression.....	216
8.6	Skeletons and Thinning.....	218
8.6.1	Crossing Number .....	219
8.6.2	Parallel and Sequential Implementations of Thinning.....	221
8.6.3	Guided Thinning .....	224
8.6.4	A Comment on the Nature of the Skeleton.....	224
8.6.5	Skeleton Node Analysis.....	225
8.6.6	Application of Skeletons for Shape Recognition.....	227
8.7	Other Measures for Shape Recognition.....	227
8.8	Boundary Tracking Procedures.....	230
8.9	Concluding Remarks.....	231
8.10	Bibliographical and Historical Notes.....	232
8.10.1	More Recent Developments.....	233
8.11	Problems .....	234
<b>CHAPTER 9</b>	<b>Boundary pattern analysis.....</b>	<b>239</b>
9.1	Introduction .....	239
9.2	Boundary Tracking Procedures.....	242
9.3	Centroidal Profiles.....	242
9.4	Problems with the Centroidal Profile Approach .....	243
9.4.1	Some Solutions .....	245
9.5	The $(s, \psi)$ Plot .....	247
9.6	Tackling the Problems of Occlusion .....	249
9.7	Accuracy of Boundary Length Measures .....	252
9.8	Concluding Remarks.....	253
9.9	Bibliographical and Historical Notes.....	254
9.9.1	More Recent Developments.....	255
9.10	Problems .....	256

<b>CHAPTER 10</b>	<b>Line, circle, and ellipse detection</b>	<b>259</b>
10.1	Introduction	259
10.2	Application of the Hough Transform to Line Detection	261
10.2.1	Longitudinal Line Localization	264
10.3	The Foot-of-Normal Method	265
10.3.1	Application of the Foot-of-Normal Method	266
10.4	Using RANSAC for Straight Line Detection	267
10.5	Location of Laparoscopic Tools	272
10.6	Hough-Based Schemes for Circular Object Detection	273
10.7	The Problem of Unknown Circle Radius	278
10.7.1	Practical Results	279
10.8	Overcoming the Speed Problem	279
10.8.1	Practical Results	281
10.9	Ellipse Detection	284
10.9.1	The Diameter Bisection Method	284
10.9.2	The Chord–Tangent Method	286
10.9.3	Finding the Remaining Ellipse Parameters	287
10.10	Human Iris Location	289
10.11	Concluding Remarks	290
10.12	Bibliographical and Historical Notes	292
10.12.1	More Recent Developments	294
10.13	Problems	295
<b>CHAPTER 11</b>	<b>The generalized Hough transform</b>	<b>299</b>
11.1	Introduction	299
11.2	The Generalized Hough Transform	300
11.3	The Relevance of Spatial Matched Filtering	302
11.4	Gradient Weighting Versus Uniform Weighting	304
11.4.1	Calculation of Sensitivity and Computational Load	306
11.4.2	Summary	307
11.5	Use of the GHT for Ellipse Detection	308
11.5.1	Practical Details	310
11.6	Comparing the Various Methods for Ellipse Detection	312
11.7	A Graph-Theoretic Approach to Object Location	314
11.7.1	A Practical Example—Locating Cream Biscuits	318
11.8	Possibilities for Saving Computation	319
11.9	Using the GHT for Feature Collation	323
11.9.1	Computational Load	325
11.10	Generalizing the Maximal Clique and Other Approaches	326
11.11	Search	327

11.12 Concluding Remarks .....328

11.13 Bibliographical and Historical Notes.....329

    11.13.1 More Recent Developments..... 333

11.14 Problems .....334

**CHAPTER 12 Object segmentation and shape models ..... 341**

    12.1 Introduction .....341

    12.2 Active Contours.....342

    12.3 Practical Results Obtained Using Active Contours.....344

    12.4 The Level-Set Approach to Object Segmentation.....346

    12.5 Shape Models .....348

        12.5.1 Locating Objects Using Shape Models ..... 353

    12.6 Concluding Remarks .....359

    12.7 Bibliographical and Historical Notes.....360

**PART 3 MACHINE LEARNING AND DEEP LEARNING NETWORKS**

---

**CHAPTER 13 Basic classification concepts ..... 365**

    13.1 Introduction .....365

    13.2 The Nearest Neighbor Algorithm .....367

    13.3 Bayes’ Decision Theory.....369

        13.3.1 The Naïve Bayes’ Classifier ..... 371

    13.4 Relation of the Nearest Neighbor and Bayes’ Approaches .....372

        13.4.1 Mathematical Statement of the Problem ..... 372

        13.4.2 The Importance of the Nearest Neighbor Algorithm ..... 374

    13.5 The Optimum Number of Features.....375

    13.6 Cost Functions and Error–Reject Tradeoff.....376

    13.7 Supervised and Unsupervised Learning .....377

    13.8 Cluster Analysis .....379

    13.9 The Support Vector Machine.....381

    13.10 Artificial Neural Networks.....383

    13.11 The Back-Propagation Algorithm.....388

    13.12 Multilayer Perceptron Architectures.....391

    13.13 Overfitting to the Training Data .....392

    13.14 Concluding Remarks .....395

    13.15 Bibliographical and Historical Notes.....396

        13.15.1 More Recent Developments..... 398

    13.16 Problems .....398

<b>CHAPTER 14 Machine learning: probabilistic methods</b> .....	<b>399</b>
14.1 Introduction .....	399
14.2 Mixtures of Gaussians and the EM Algorithm.....	402
14.2.1 Details of the Expectation Maximization Algorithm .....	405
14.3 A More General View of the EM Algorithm.....	408
14.4 Some Practical Examples.....	411
14.5 Principal Components Analysis.....	419
14.6 Multiple Classifiers .....	422
14.7 The Boosting Approach .....	425
14.8 Modeling AdaBoost .....	428
14.8.1 Real AdaBoost .....	430
14.9 Loss Functions for Boosting .....	431
14.10 The LogitBoost Algorithm.....	435
14.11 The Effectiveness of Boosting.....	438
14.12 Boosting with Multiple Classes .....	438
14.13 The Receiver Operating Characteristic.....	443
14.13.1 Performance Measures Relating to Error Rates .....	446
14.14 Concluding Remarks .....	447
14.15 Bibliographical and Historical Notes.....	448
14.16 Problems .....	451
 <b>CHAPTER 15 Deep-learning networks</b> .....	 <b>453</b>
15.1 Introduction .....	453
15.2 Convolutional Neural Networks .....	456
15.3 Parameters for Defining CNN Architectures.....	459
15.4 LeCun <i>et al.</i> 's LeNet Architecture .....	463
15.5 Krizhevsky <i>et al.</i> 's AlexNet Architecture .....	468
15.6 Zeiler and Fergus's Work on CNN Architectures.....	474
15.7 Zeiler and Fergus's Visualization Experiments .....	477
15.8 Simonyan and Zisserman's VGGNet Architecture .....	479
15.9 Noh <i>et al.</i> 's DeconvNet Architecture .....	481
15.10 Badrinarayanan <i>et al.</i> 's SegNet Architecture .....	484
15.11 Recurrent Neural Networks .....	487
15.12 Concluding Remarks .....	490
15.13 Bibliographical and Historical Notes.....	492

## **PART 4 3D VISION AND MOTION**

---

<b>CHAPTER 16</b>	<b>The three-dimensional world</b>	<b>497</b>
16.1	Introduction	497
16.2	Three-Dimensional Vision—The Variety of Methods	498
16.3	Projection Schemes for Three-Dimensional Vision	500
16.3.1	Binocular Images	502
16.3.2	The Correspondence Problem	504
16.4	Shape from Shading	506
16.5	Photometric Stereo	511
16.6	The Assumption of Surface Smoothness	514
16.7	Shape from Texture	515
16.8	Use of Structured Lighting	516
16.9	Three-Dimensional Object Recognition Schemes	518
16.10	Horaud’s Junction Orientation Technique	519
16.11	An Important Paradigm—Location of Industrial Parts	523
16.12	Concluding Remarks	525
16.13	Bibliographical and Historical Notes	526
16.13.1	More Recent Developments	528
16.14	Problems	529
<b>CHAPTER 17</b>	<b>Tackling the perspective <math>n</math>-point problem</b>	<b>533</b>
17.1	Introduction	533
17.2	The Phenomenon of Perspective Inversion	534
17.3	Ambiguity of Pose Under Weak Perspective Projection	535
17.4	Obtaining Unique Solutions to the Pose Problem	538
17.4.1	Solution of the Three-Point Problem	542
17.4.2	Using Symmetric Trapezia for Estimating Pose	543
17.5	Concluding Remarks	544
17.6	Bibliographical and Historical Notes	545
17.6.1	More Recent Developments	546
17.7	Problems	547
<b>CHAPTER 18</b>	<b>Invariants and perspective</b>	<b>549</b>
18.1	Introduction	549
18.2	Cross Ratios: The “Ratio of Ratios” Concept	551
18.3	Invariants for Noncollinear Points	555
18.3.1	Further Remarks About the 5-Point Configuration	558
18.4	Invariants for Points on Conics	559



18.5	Differential and Semidifferential Invariants .....	561
18.6	Symmetric Cross-Ratio Functions .....	564
18.7	Vanishing Point Detection .....	565
18.8	More on Vanishing Points .....	568
18.9	Apparent Centers of Circles and Ellipses .....	569
18.10	Perspective Effects in Art and Photography .....	572
18.11	Concluding Remarks .....	579
18.12	Bibliographical and Historical Notes .....	581
	18.12.1 More Recent Developments .....	582
18.13	Problems .....	583
<b>CHAPTER 19</b>	<b>Image transformations and camera calibration .....</b>	<b>585</b>
19.1	Introduction .....	585
19.2	Image Transformations .....	586
19.3	Camera Calibration .....	590
19.4	Intrinsic and Extrinsic Parameters .....	592
19.5	Correcting for Radial Distortions .....	595
19.6	Multiple View Vision .....	597
19.7	Generalized Epipolar Geometry .....	598
19.8	The Essential Matrix .....	599
19.9	The Fundamental Matrix .....	601
19.10	Properties of the Essential and Fundamental Matrices .....	602
19.11	Estimating the Fundamental Matrix .....	603
19.12	An Update on the Eight-Point Algorithm .....	603
19.13	Image Rectification .....	604
19.14	3-D Reconstruction .....	605
19.15	Concluding Remarks .....	608
19.16	Bibliographical and Historical Notes .....	608
	19.16.1 More Recent Developments .....	609
19.17	Problems .....	610
<b>CHAPTER 20</b>	<b>Motion .....</b>	<b>611</b>
20.1	Introduction .....	611
20.2	Optical Flow .....	612
20.3	Interpretation of Optical Flow Fields .....	615
20.4	Using Focus of Expansion to Avoid Collision .....	617
20.5	Time-to-Adjacency Analysis .....	618
20.6	Basic Difficulties with the Optical Flow Model .....	620
20.7	Stereo from Motion .....	621

20.8	The Kalman Filter .....	623
20.9	Wide Baseline Matching.....	625
20.10	Concluding Remarks .....	627
20.11	Bibliographical and Historical Notes.....	627
20.12	Problem.....	628

## **PART 5 PUTTING COMPUTER VISION TO WORK**

---

### **CHAPTER 21 Face detection and recognition: the impact of deep learning..... 631**

21.1	Introduction .....	631
21.2	A Simple Approach to Face Detection.....	632
21.3	Facial Feature Detection .....	634
21.4	The Viola–Jones Approach to Rapid Face Detection .....	636
21.5	The Eigenface Approach to Face Recognition.....	640
21.6	More on the Difficulties of Face Recognition.....	643
21.7	Frontalization.....	645
21.8	The Sun <i>et al.</i> DeepID Face Representation System .....	649
21.9	Fast Face Detection Revisited.....	654
	21.9.1 Even More Powerful Object Detection Schemes.....	656
21.10	The Face as Part of a 3-D Object .....	657
21.11	Concluding Remarks .....	659
21.12	Bibliographical and Historical Notes.....	661

### **CHAPTER 22 Surveillance .....** **663**

22.1	Introduction .....	664
22.2	Surveillance—The Basic Geometry .....	665
22.3	Foreground–Background Separation .....	669
	22.3.1 Background Modeling.....	669
	22.3.2 Practical Examples of Background Modeling.....	675
	22.3.3 Direct Detection of the Foreground.....	677
22.4	Particle Filters .....	678
22.5	Use of Color Histograms for Tracking .....	684
22.6	Implementation of Particle Filters .....	688
22.7	Chamfer Matching, Tracking, and Occlusion .....	691
22.8	Combining Views from Multiple Cameras .....	693
	22.8.1 The Case of Nonoverlapping Fields of View.....	697

<b>22.9</b>	Applications to the Monitoring of Traffic Flow .....	698
22.9.1	The System of Bascle <i>et al.</i> .....	698
22.9.2	The System of Koller <i>et al.</i> .....	700
<b>22.10</b>	License Plate Location .....	702
<b>22.11</b>	Occlusion Classification for Tracking .....	705
<b>22.12</b>	Distinguishing Pedestrians by Their Gait .....	708
<b>22.13</b>	Human Gait Analysis .....	711
<b>22.14</b>	Model-based Tracking of Animals .....	713
<b>22.15</b>	Concluding Remarks .....	716
<b>22.16</b>	Bibliographical and Historical Notes.....	717
22.16.1	More Recent Developments.....	719
<b>22.17</b>	Problem.....	720

**CHAPTER 23 In-vehicle vision systems ..... 721**

<b>23.1</b>	Introduction .....	721
<b>23.2</b>	Locating the Roadway .....	723
<b>23.3</b>	Location of Road Markings .....	725
<b>23.4</b>	Location of Road Signs.....	726
<b>23.5</b>	Location of Vehicles .....	728
<b>23.6</b>	Information Obtained by Viewing License Plates and Other Structural Features .....	731
<b>23.7</b>	Locating Pedestrians .....	734
<b>23.8</b>	Guidance and Egomotion.....	739
23.8.1	A Simple Path-Planning Algorithm.....	742
<b>23.9</b>	Vehicle Guidance in Agriculture .....	742
23.9.1	3-D Aspects of the Task .....	746
23.9.2	Real-Time Implementation .....	747
<b>23.10</b>	Concluding Remarks .....	747
<b>23.11</b>	More Detailed Developments and Bibliographies Relating to Advanced Driver Assistance Systems .....	749
23.11.1	Developments in Vehicle Detection .....	750
23.11.2	Developments in Pedestrian Detection.....	752
23.11.3	Developments in Road and Lane Detection.....	754
23.11.4	Developments in Road Sign Detection .....	755
23.11.5	Developments in Path Planning, Navigation, and Egomotion .....	757
<b>23.12</b>	Problem.....	757

**CHAPTER 24 Epilogue—Perspectives in vision** ..... 759

- 24.1** Introduction .....759
- 24.2** Parameters of Importance in Machine Vision .....760
- 24.3** Tradeoffs.....762
  - 24.3.1 Some Important Tradeoffs ..... 762
  - 24.3.2 Tradeoffs for Two-Stage Template Matching..... 763
- 24.4** Moore’s Law in Action.....764
- 24.5** Hardware, Algorithms, and Processes .....765
- 24.6** The Importance of Choice of Representation.....766
- 24.7** Past, Present, and Future .....767
- 24.8** The Deep Learning Explosion .....768
- 24.9** Bibliographical and Historical Notes.....769

Appendix A: Robust statistics .....771

Appendix B: The sampling theorem .....789

Appendix C: The representation of color .....793

Appendix D: Sampling from distributions.....797

References.....801

Index .....847

This page intentionally left blank

# About the Author

**Roy Davies** is Emeritus Professor of Machine Vision at Royal Holloway, University of London, United Kingdom. He has worked on many aspects of vision, from feature detection and noise suppression to robust pattern matching and real-time implementations of practical vision tasks. His interests include automated visual inspection, surveillance, vehicle guidance, and crime detection. He has published more than 200 papers and three books—*Machine Vision: Theory, Algorithms, Practicalities* (1990), *Electronics, Noise and Signal Recovery* (1993), and *Image Processing for the Food Industry* (2000); the first of these has been widely used internationally for more than 25 years, and is now out in this much enhanced fifth edition. Roy is a fellow of the IoP and the IET, and a senior member of the IEEE. He is on the Editorial Boards of *Pattern Recognition Letters*, *Real-Time Image Processing*, *Imaging Science*, and *IET Image Processing*. He holds a DSc from the University of London, he was awarded *BMVA Distinguished Fellow* in 2005, and *Fellow of the International Association of Pattern Recognition* in 2008.



This page intentionally left blank

# Foreword

It is an honor to write a foreword for Roy Davies' new edition of *Computer and Machine Vision*, now entitled *Computer Vision: Principles, Algorithms, Applications, Learning*. This is one of the major books in Computer Vision and not just for its longevity, having now reached its Fifth Edition. It is actually a splendid achievement to reach this status and it reflects not only on the tenacity and commitment of its author, but also on the achievements of the book itself.

Computer Vision has shown awesome progress in its short history. This is part due to technology: computers are much faster and memory is now much cheaper than they were in the early days when Roy started his research. There have been many achievements and many developments. All of this can affect the evolution of a textbook. There have been excellent textbooks in the past, which were neither continued nor maintained. That has been avoided here as the textbook has continued to mature with the field and its many developments.

We can look forward to a future where automated computer vision systems will make our lives easier while enriching them too. There are already many applications of Computer Vision in the food industry and robotic cars that will be with us very soon. Then there are continuing advancements in medical image analysis, where Computer Vision techniques can be used to aid in diagnosis and therapy by automated means. Even accessing a mobile phone is considerably more convenient when using a fingerprint and access by face recognition continues to improve. These have all come about due to advancements in computers, Computer Vision, and applied artificial intelligence.

Adherents of Computer Vision will know it to be an exciting field indeed. It manages to cover many aspects of technology from human vision to machine learning requiring electronic hardware, computer implementations, and a lot of computer software. Roy continues to cover these in excellent detail.

I remember the First Edition when it was first published in 1990 with its unique and pragmatic blend of theory, implementation, and algorithms. I am pleased to see that the Fifth Edition maintains this unique approach, much appreciated by students in previous editions who wanted an accessible introduction to Computer Vision. It has certainly increased in size with age, and that is often the way with books. It is most certainly the way with Computer Vision since many of its researchers continue to improve, refine, and develop new techniques.

A major change here is the inclusion of Deep Learning. Indeed, this has been a major change in the field of Computer Vision and Pattern Recognition. One implication of the increase in computing power and the reduction of memory cost is that techniques can become considerably more complex, and that complexity lends itself to application in the analysis of "big data." One cannot ignore the performance of deep learning and convolutional neural networks: one only has to peruse the program of top international conferences to perceive their revolutionary effect on research direction. Naturally, it is early days but it is good to have



guidance as we have here. The nature of performance is always in question in any system in artificial intelligence and part of the way to answer those questions is to consider more deeply the architectures and their basis. That again is the function of a textbook for it is the distillation of research and practice in a ratiocinated exposition. It is a brave move to include Deep Learning in this edition, but a necessary one.

And what of Roy Davies himself? Following his DPhil in Solid State Physics at Oxford, he later developed a new sensitive method in Nuclear Resonance called “Davies-ENDOR” (Electron and Nuclear Double Resonance) which avoided the blind spots of its predecessor “Mims-ENDOR.” In 1970 he was appointed as a lecturer at Royal Holloway and a long series of publications in pattern recognition and its applications led to the award of his Personal Chair, his DSc and then the Distinguished Fellow of the British Machine Vision Association (BMVA), 2005. He has served the BMVA in many ways, latterly editing its Newsletter. Clearly the level of his work and his many contacts and papers have contributed much to the material that is found herein.

I look forward to having this Fifth Edition sitting proudly in my shelf, replacing the Fourth that will in turn pass to one of my student’s shelves. It will not stop there for long for it is one of the textbooks I often turn to for the information I need. Unlike the snapshots to be found on the Web, in a textbook I find it placed in context and in sequence and with extension to other material. That is the function of a textbook and it will be well served by this Fifth Edition.

**Mark S. Nixon**

University of Southampton, Southampton, United Kingdom  
July 2017

# Preface to the Fifth Edition

The first edition of this book came out in 1990, and was welcomed by many researchers and practitioners. However, in the subsequent two decades the subject moved on at a rapidly accelerating rate, and many topics that hardly deserved a mention in the first edition had to be solidly incorporated into subsequent editions. For example, it seemed particularly important to bring in significant amounts of new material on feature detection, mathematical morphology, texture analysis, inspection, artificial neural networks, 3D vision, invariance, motion analysis, object tracking, and robust statistics. And in the fourth edition, cognizance had to be taken of the widening range of applications of the subject: in particular, two chapters had to be added on surveillance and in-vehicle vision systems. Since then, the subject has not stood still. In fact, the past four or five years have seen the onset of an explosive growth in research on deep neural networks, and the practical achievements resulting from this have been little short of staggering. It soon became abundantly clear that the fifth edition would have to reflect this radical departure—both in fundamental explanation and in practical coverage. Indeed, it necessitated a new part in the book—Part 3, *Machine Learning and Deep Learning Networks*—a heading which affirms that the new content reflects not only “Deep Learning” (a huge enhancement over the older “Artificial Neural Networks”) but also an approach to pattern recognition that is based on rigorous probabilistic methodology.

All this is not achieved without presentation problems: for probabilistic methodology can only be managed properly within a rather severe mathematical environment. Too little maths, and the subject could be so watered down as to be virtually content-free: too much maths, and many readers might not be able to follow the explanations. Clearly, one should not protect readers from the (mathematical) reality of the situation. Hence, Chapter 14 had to be written in such a way as to demonstrate in full what type of methodology is involved, while providing paths that would take readers past some of the mathematical complexities—at least, on first encounter. Once past the relatively taxing Chapter 14, Chapters 15 and 21 take the reader through two accounts consisting largely of case studies, the former through a crucial development period (2012–2015) for deep learning networks, and the latter through a similar period (2013–2016) during which deep learning was targeted strongly at face detection and recognition, enabling remarkable advances to be made. It should not go unnoticed that these additions have so influenced the content of the book that the title had to be modified to reflect them. Interestingly, the organization of the book was further modified by collecting three applications chapters into the new Part 5, *Putting Computer Vision to Work*.

It is worth remarking that, at this point in time, computer vision has attained a level of maturity that has made it substantially more rigorous, reliable, generic, and—in the light of the improved hardware facilities now available for its

implementation (in particular, extremely powerful GPUs)—capable of real-time performance. This means that workers are more than ever before using it in serious applications, and with fewer practical difficulties. It is intended that this edition of the book will reflect this radically new and exciting state of affairs at a fundamental level.

A typical final-year undergraduate course on vision for Electronic Engineering and Computer Science students might include much of the work of Chapters 1–13 and Chapter 16, plus a selection of sections from other chapters, according to requirements. For MSc or PhD research students, a suitable lecture course might go on to cover Parts 3 or 4 in depth, and several of the chapters in Part 5, with many practical exercises being undertaken on image analysis systems. (The importance of the appendix on robust statistics should not be underestimated once one gets onto serious work, though this will probably be outside the restrictive environment of an undergraduate syllabus.) Here much will depend on the research programme being undertaken by each individual student. At this stage the text may have to be used more as a handbook for research, and indeed, one of the prime aims of the volume is to act as a handbook for the researcher and practitioner in this important area.

As mentioned in the original Preface, this book leans heavily on experience I have gained from working with postgraduate students: in particular, I would like to express my gratitude to Mark Edmonds, Simon Barker, Daniel Celano, Darrel Greenhill, Derek Charles, Mark Sugrue, and Georgios Mastorakis, all of whom have in their own ways helped to shape my view of the subject. In addition, it is a pleasure to recall very many rewarding discussions with my colleagues Barry Cook, Zahid Hussain, Ian Hannah, Dev Patel, David Mason, Mark Bateman, Tieying Lu, Adrian Johnstone, and Piers Plummer, the last two of whom were particularly prolific in generating hardware systems for implementing my research group's vision algorithms. Next, I would like to record my thanks to my British Machine Vision Association colleagues for many wide-ranging discussions on the nature of the subject: in particular, I am hugely grateful to Majid Mirmehdi, Adrian Clark, Neil Thacker, and Mark Nixon, who, over time, have strongly influenced the development of the book and left a permanent mark on it. Next, I would like to thank the anonymous reviewers for making insightful comments and what have turned out to be extremely valuable suggestions. Finally, I am indebted to Tim Pitts of Elsevier Science for his help and encouragement, without which this fifth edition might never have been completed.

*Supporting materials:*

Elsevier's website for the book contains programming and other resources to help readers and students using this text. Please check the publisher's website for further information: <https://www.elsevier.com/books-and-journals/book-companion/9780128092842>.

**Roy Davies**

*Royal Holloway, University of London, United Kingdom*

# Preface to the First Edition

Over the past 30 years or so, machine vision has evolved into a mature subject embracing many topics and applications: these range from automatic (robot) assembly to automatic vehicle guidance, from automatic interpretation of documents to verification of signatures, and from analysis of remotely sensed images to checking of fingerprints and human blood cells; currently, automated visual inspection is undergoing very substantial growth, necessary improvements in quality, safety, and cost-effectiveness being the stimulating factors. With so much ongoing activity, it has become a difficult business for the professional to keep up with the subject and with relevant methodologies: in particular, it is difficult for them to distinguish accidental developments from genuine advances. It is the purpose of this book to provide background in this area.

The book was shaped over a period of 10–12 years, through material I have given on undergraduate and postgraduate courses at London University, and contributions to various industrial courses and seminars. At the same time, my own investigations coupled with experience gained while supervising PhD and post-doctoral researchers helped to form the state of mind and knowledge that is now set out here. Certainly it is true to say that if I had had this book 8, 6, 4, or even 2 years ago, it would have been of inestimable value to myself for solving practical problems in machine vision. It is therefore my hope that it will now be of use to others in the same way. Of course, it has tended to follow an emphasis that is my own—and in particular one view of one path towards solving automated visual inspection and other problems associated with the application of vision in industry. At the same time, although there is a specialism here, great care has been taken to bring out general principles—including many applying throughout the field of image analysis. The reader will note the universality of topics such as noise suppression, edge detection, principles of illumination, feature recognition, Bayes' theory, and (nowadays) Hough transforms. However, the generalities lie deeper than this. The book has aimed to make some general observations and messages about the limitations, constraints, and tradeoffs to which vision algorithms are subject. Thus there are themes about the effects of noise, occlusion, distortion, and the need for built-in forms of robustness (as distinct from less successful ad hoc varieties and those added on as an afterthought); there are also themes about accuracy, systematic design, and the matching of algorithms and architectures. Finally, there are the problems of setting up lighting schemes which must be addressed in complete systems, yet which receive scant attention in most books on image processing and analysis. These remarks will indicate that the text is intended to be read at various levels—a factor that should make it of more lasting value than might initially be supposed from a quick perusal of the contents.

Of course, writing a text such as this presents a great difficulty in that it is necessary to be highly selective: space simply does not allow everything in a subject of this nature and maturity to be dealt with adequately between two covers. One solution might be to dash rapidly through the whole area mentioning everything that comes to mind, but leaving the reader unable to understand anything in detail or to *achieve* anything having read the book. However, in a practical subject of this nature this seemed to me a rather worthless extreme. It is just possible that the emphasis has now veered too much in the opposite direction, by coming down to practicalities (detailed algorithms, details of lighting schemes, and so on): individual readers will have to judge this for themselves. On the other hand, an author has to be true to himself and my view is that it is better for a reader or student to have mastered a coherent series of topics than to have a mishmash of information that he is later unable to recall with any accuracy. This, then, is my justification for presenting this particular material in this particular way and for reluctantly omitting from detailed discussion such important topics as texture analysis, relaxation methods, motion, and optical flow.

As for the organization of the material, I have tried to make the early part of the book lead into the subject gently, giving enough detailed algorithms (especially in [Chapter 2](#): Images and imaging operations and [Chapter 6](#): Corner, interest point, and invariant feature detection) to provide a sound feel for the subject—including especially vital, and in their own way quite intricate, topics such as connectedness in binary images. Hence Part I provides the lead-in, although it is not always trivial material and indeed some of the latest research ideas have been brought in (e.g., on thresholding techniques and edge detection). Part II gives much of the meat of the book. Indeed, the (book) literature of the subject currently has a significant gap in the area of intermediate-level vision; while high-level vision (AI) topics have long caught the researcher's imagination, intermediate-level vision has its own difficulties which are currently being solved with great success (note that the Hough transform, originally developed in 1962, and by many thought to be a very specialist topic of rather esoteric interest, is arguably only now coming into its own). Part II and the early chapters of Part III aim to make this clear, while Part IV gives reasons why this particular transform has become so useful. As a whole, Part III aims to demonstrate some of the practical applications of the basic work covered earlier in the book, and to discuss some of the principles underlying implementation: it is here that chapters on lighting and hardware systems will be found. As there is a limit to what can be covered in the space available, there is a corresponding emphasis on the theory underpinning practicalities. Probably this is a vital feature, since there are many applications of vision both in industry and elsewhere, yet listing them and their intricacies risks dwelling on interminable detail, which some might find insipid; furthermore, detail has a tendency to date rather rapidly. Although the book could not cover 3D vision in full (this topic would easily consume a whole volume in its own right), a careful overview of this complex mathematical and highly important subject seemed vital. It is therefore no accident that [Chapter 16](#), The three-

dimensional world, is the longest in the book. Finally, Part IV asks questions about the limitations and constraints of vision algorithms and answers them by drawing on information and experience from earlier chapters. It is tempting to call the last chapter the Conclusion. However, in such a dynamic subject area any such temptation has to be resisted, although it has still been possible to draw a good number of lessons on the nature and current state of the subject. Clearly, this chapter presents a personal view but I hope it is one that readers will find interesting and useful.

This page intentionally left blank

# Acknowledgments

The author would like to credit the following sources for permission to reproduce tables, figures, and extracts of text from earlier publications:

## **Elsevier**

For permission to reprint portions of the following papers from *Image and Vision Computing* as text in [Chapter 5](#); as [Tables 5.1–5.5](#); and as [Figs. 3.31, 5.2](#):

Davies (1984b, 1987b)

For permission to reprint portions of the following paper from *Pattern Recognition* as text in [Chapter 8](#); and as [Fig. 8.11](#):

Davies and Plummer (1981)

For permission to reprint portions of the following papers from *Pattern Recognition Letters* as text in [Chapters 3, 5, 10, 11, 13](#); as [Tables 3.2; 10.4; 11.1](#); and as [Figs. 3.6, 3.8, 3.10; 5.1, 5.3; 10.1, 10.10, 10.11, 10.12, 10.13; 11.1, 11.3–11.11](#):

Davies (1986, 1987a,c,d, 1988b,c,e, 1989a)

For permission to reprint portions of the following paper from *Signal Processing* as text in [Chapter 3](#); and as [Figs. 3.15, 3.17–3.20](#):

Davies (1989b)

For permission to reprint portions of the following paper from *Advances in Imaging and Electron Physics* as text in [Chapter 13](#):

Davies (2003c)

For permission to reprint portions of the following article from *Encyclopedia of Physical Science and Technology* as [Figs. 8.9, 8.12, 9.1, 9.4](#):

Davies, E.R., 1987. Visual inspection, automatic (robotics). In: Meyers, R.A. (Ed.) *Encyclopedia of Physical Science and Technology*, vol. 14. Academic Press, San Diego, pp. 360–377.

## **IEEE**

For permission to reprint portions of the following paper as text in [Chapter 3](#); and as [Figs. 3.4, 3.5, 3.7, 3.11](#):

Davies (1984a)

## **IET**

For permission to reprint portions of the following papers from the *IET Proceedings and Colloquium Digests* as text in [Chapters 3, 4, 6, 13, 21, 22, 23](#); as



Tables 3.3, 4.2; and as Figs. 3.21, 3.28, 3.29; 4.6–4.10; 6.5–6.9, 6.12; 11.20; 14.16, 14.17, 22.16–22.18; 23.1, 23.3, 23.4:

Davies (1988a, 1999c, 2000a, 2005, 2008)  
Sugrue and Davies (2007)  
Mastorakis and Davies (2011)  
Davies et al. (1998)  
Davies et al. (2003)

***IFS Publications Ltd***

For permission to reprint portions of the following paper as text in Chapters 12, 20; and as Figs. 10.7, 10.8:

Davies (1984c)

***The Royal Photographic Society***

For permission to reprint portions of the following papers (see also the Maney website: [www.maney.co.uk/journals/ims](http://www.maney.co.uk/journals/ims)) as text in Chapter 3; and as Figs. 3.12, 3.13, 3.22–3.24:

Davies (2000c)  
Charles and Davies (2004)

***Springer-Verlag***

For permission to reprint portions of the following papers as text in Chapter 6; and as Figs. 6.2, 6.4:

Davies (1988d), Figs. 1–3

***World Scientific***

For permission to reprint portions of the following book as text in Chapters 7, 22, 23; and as Figs. 3.25–3.27; 5.4; 22.20; 23.15, 23.16:

Davies, 2000. Image Processing for the Food Industry. World Scientific, Singapore.

***The Committee of the Alvey Vision Club***

To acknowledge that extracts of text in Chapter 11 and Figs. 11.12, 11.13, 11.17 were first published in the *Proceedings of the 4th Alvey Vision Conference*:

Davies, E.R., 1988. An alternative to graph matching for locating objects from their salient features. In: *Proceedings of 4th Alvey Vision Conference*, Manchester, 31 August–2 September, pp. 281–286.

***F.H. Sumner***

For permission to reprint portions of the following article from *State of the Art Report: Supercomputer Systems Technology* as text in Chapter 8; and as Fig. 8.4:

Davies, E.R., 1982. Image processing. In: Sumner, F.H. (Ed.), *State of the Art Report: Supercomputer Systems Technology*. Pergamon Infotech, Maidenhead, pp. 223–244.

***Royal Holloway, University of London***

For permission to reprint extracts from the following examination questions, originally written by E.R. Davies:

EL385/97/2; EL333/98/2; EL333/99/2, 3, 5, 6; EL333/01/2, 4–6;  
PH5330/98/3, 5; PH5330/03/1–5; PH4760/04/1–5.

***University of London***

For permission to reprint extracts from the following examination questions, originally written by E.R. Davies:

PH385/92/2, 3; PH385/93/1–3; PH385/94/1–4; PH385/95/4; PH385/96/3, 6;  
PH433/94/3, 5; PH433/96/2, 5.

**Collectors of publicly available image databases and utilities**

To acknowledge use of the following image databases and utilities for generating a number of images presented in [Chapters 15 and 21](#):

***The Cambridge semantic segmentation online demo***

The images in [Fig. 15.14](#) were processed using the online demo available from the University of Cambridge, UK (see Badrinarayanan et al., 2015) at

<http://mi.eng.cam.ac.uk/projects/segnet/> (website accessed 07.10.16).

***The CMU image dataset***

The “newsradio” image used to obtain [Fig. 21.6](#) was taken from Test Set C—collected at CMU by Rowley, H.A., Baluja, S., and Kanade, T.—and is described in their paper:

Rowley, H.A., Baluja, S., Kanade, T., 1998. Neural network-based face detection. *IEEE Trans. Pattern Anal. Mach. Intell.* 20(1), 23–38.

It may be downloaded from the website:

[http://vasc.ri.cmu.edu/idb/html/face/frontal\\_images/](http://vasc.ri.cmu.edu/idb/html/face/frontal_images/) (website accessed 20.04.17).

***The Bush LFW dataset***

The images of George W. Bush used in [Chapter 21](#) were taken from the set collected at the University of Massachusetts:

Huang, G.B., Ramesh, M., Berg, T., Learned-Miller, E., 2007. Labeled Faces in the Wild: A Database for Studying Face Recognition in Unconstrained Environments. University of Massachusetts, Amherst, Technical Report 07-49, October.

The database may be downloaded from the website:

<http://vis-www.cs.umass.edu/lfw/> (website accessed 20.04.17).

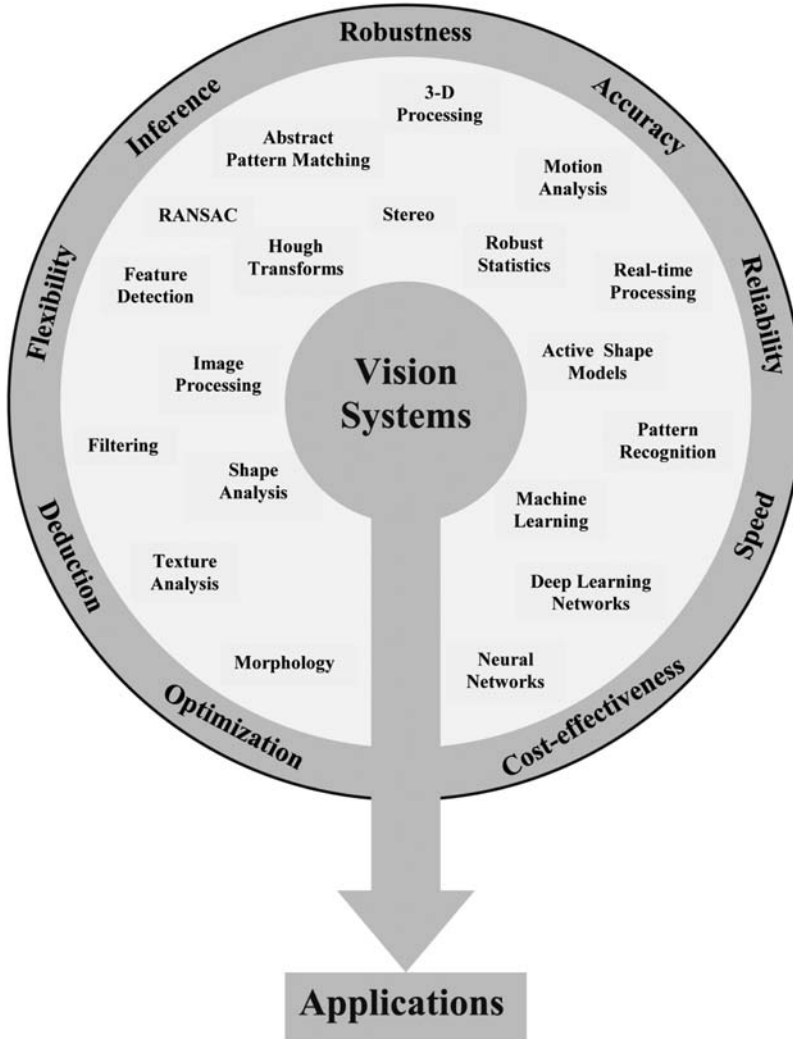
This page intentionally left blank

# Topics Covered in Application Case Studies

	Tracking Laparoscopic Tools	Hand Detection and Tracking	Locating Human Eyes and Irises	Face Detection and Recognition	Art, Photography, Image Stitching	Locating Contaminants in Cereals	Surveillance	Monitoring of Traffic Flow	Model-Based Tracking of Animals	Driver Assistance Systems	Road, Lane and Sign Detection	Locating Vehicles and Pedestrians	Vehicle Guidance in Agriculture
Affine motion models							✓	✓		✓			
Belief networks							✓	✓					
Boosting				✓									
Chamfer matching													
Circle and ellipse detection			✓								✓		
Decoupling shape and intensity									✓				
Deep learning			✓	✓							✓		
EM algorithm							✓				✓		
Hough transform			✓										
Hysteresis thresholding													✓
Kalman filter							✓	✓		✓			
Median-filter based analysis						✓							
Morphological processing	✓					✓							
Occlusion reasoning							✓	✓		✓			
Pattern recognition					✓	✓				✓			
Perspective and vanishing points	✓				✓	✓				✓			
Principal components analysis		✓		✓					✓				



## INFLUENCES IMPINGING UPON INTEGRATED VISION SYSTEM DESIGN



This page intentionally left blank

# Glossary of Acronyms and Abbreviations

<b>1-D</b>	one dimension/one-dimensional
<b>2-D</b>	two dimensions/two-dimensional
<b>3-D</b>	three dimensions/three-dimensional
<b>AAM</b>	active appearance model
<b>ACM</b>	Association for Computing Machinery (USA)
<b>ADAS</b>	advanced driver assistance system
<b>AFW</b>	annotated faces in the wild
<b>AI</b>	artificial intelligence
<b>ANN</b>	artificial neural network
<b>AP</b>	average precision
<b>APF</b>	auxiliary particle filter
<b>ASCII</b>	American Standard Code for Information Interchange
<b>ASIC</b>	application specific integrated circuit
<b>ASM</b>	active shape model
<b>ATM</b>	automated teller machine
<b>AUC</b>	area under curve
<b>AVI</b>	audio video interleave
<b>BCVM</b>	between-class variance method
<b>BDRF</b>	bidirectional reflectance distribution function
<b>BetaSAC</b>	beta [distribution] sampling consensus
<b>BMVA</b>	British Machine Vision Association
<b>BPTT</b>	backpropagation through time
<b>CAD</b>	computer-aided design
<b>CAM</b>	computer-aided manufacture
<b>CCTV</b>	closed-circuit television
<b>CDF</b>	cumulative distribution function
<b>CLIP</b>	cellular logic image processor
<b>CNN</b>	convolutional neural network
<b>CPU</b>	central processor unit
<b>CRF</b>	conditional random field
<b>DCSM</b>	distinct class based splitting measure
<b>DET</b>	Beaudet determinant operator
<b>DG</b>	differential gradient
<b>DN</b>	Dreschler–Nagel corner detector
<b>DNN</b>	deconvolution network
<b>DoF</b>	degree of freedom
<b>DoG</b>	difference of Gaussians
<b>DPM</b>	deformable parts models
<b>EM</b>	expectation maximization
<b>EURASIP</b>	European Association for Signal Processing
<b>f.c.</b>	fully connected
<b>FAR</b>	frontalization for alignment and recognition



<b>FAST</b>	features from accelerated segment test
<b>FCN</b>	fully convolutional network
<b>FDDB</b>	face detection data set and benchmark
<b>FDR</b>	face detection and recognition
<b>FFT</b>	fast Fourier transform
<b>FN</b>	false negative
<i>f<sub>nr</sub></i>	false negative rate
<b>FoE</b>	focus of expansion
<b>FoV</b>	field of view
<b>FP</b>	false positive
<b>FPGA</b>	field programmable gate array
<b>FPP</b>	full perspective projection
<i>f<sub>pr</sub></i>	false positive rate
<b>GHT</b>	generalized Hough transform
<b>GLOH</b>	gradient location and orientation histogram
<b>GMM</b>	Gaussian mixture model
<b>GPS</b>	global positioning system
<b>GPU</b>	graphics processing unit
<b>GroupSAC</b>	group sampling consensus
<b>GVM</b>	global valley method
<b>HOG</b>	histogram of orientated gradients
<b>HSI</b>	hue, saturation, intensity
<b>HT</b>	Hough transform
<b>IBR</b>	intensity extrema-based region detector
<b>IDD</b>	integrated directional derivative
<b>IEE</b>	Institution of Electrical Engineers (UK)
<b>IEEE</b>	Institute of Electrical and Electronics Engineers (USA)
<b>IET</b>	Institution of Engineering and Technology (UK)
<b>ILSVRC</b>	ImageNet large-scale visual recognition object challenge
<b>ILW</b>	iterated likelihood weighting
<b>IMPSAC</b>	importance sampling consensus
<b>IoP</b>	Institute of Physics (UK)
<b>IRLFOD</b>	image-restricted, label-free outside data
<b>ISODATA</b>	iterative self-organizing data analysis
<b>JPEG/JPG</b>	Joint Photographic Experts Group
<i>k</i> -NN	<i>k</i> -nearest neighbor
<b>KL</b>	Kullback–Leibler
<b>KR</b>	Kitchen–Rosenfeld corner detector
<b>LED</b>	light emitting diode
<b>LFF</b>	local-feature-focus method
<b>LFPW</b>	labeled face parts in the wild
<b>LFW</b>	labeled faces in the wild
<b>LIDAR</b>	light detection and ranging
<b>LMedS</b>	least median of squares
<b>LoG</b>	Laplacian of Gaussian
<b>LRN</b>	local response normalization
<b>LS</b>	least squares
<b>LSTM</b>	long short-term memory

<b>LUT</b>	lookup table
<b>MAP</b>	maximum a posteriori
<b>MDL</b>	minimum description length
<b>ML</b>	machine learning
<b>MLP</b>	multi-layer perceptron
<b>MoG</b>	mixture of Gaussians
<b>MP</b>	microprocessor
<b>MSER</b>	maximally stable extremal region
<b>NAPSAC</b>	$n$ adjacent points sample consensus
<b>NIR</b>	near infra-red
<b>NN</b>	nearest neighbor
<b>OCR</b>	optical character recognition
<b>OVR</b>	one versus the rest
<b>PASCAL</b>	Network of Excellence on pattern analysis, statistical modeling and computational learning
<b>PC</b>	personal computer
<b>PCA</b>	principal components analysis
<b>PE</b>	processing element
<b>P<sub>n</sub>P</b>	perspective $n$ -point
<b>PPR</b>	probabilistic pattern recognition
<b>PR</b>	pattern recognition
<b>PROSAC</b>	progressive sample consensus
<b>PSF</b>	point spread function
<b>R-CNN</b>	regions with CNN features
<b>RAM</b>	random access memory
<b>RANSAC</b>	random sample consensus
<b>RBF</b>	radial basis function [classifier]
<b>RELU</b>	rectified linear unit
<b>RGB</b>	red, green, blue
<b>RHT</b>	randomized Hough transform
<b>RKHS</b>	reproducible kernel Hilbert space
<b>RMS</b>	root mean square
<b>RNN</b>	recurrent neural network
<b>ROC</b>	receiver–operator characteristic
<b>RoI</b>	region of interest
<b>RPS</b>	Royal Photographic Society (UK)
<b>s.d.</b>	standard deviation
<b>SFC</b>	Facebook social face classification
<b>SFOP</b>	scale-invariant feature operator
<b>SIFT</b>	scale invariant feature transform
<b>SIMD</b>	single instruction stream, multiple data stream
<b>Sir</b>	sampling importance resampling
<b>SIS</b>	sequential importance sampling
<b>SISD</b>	single instruction stream, single data stream
<b>SOC</b>	sorting optimization curve
<b>SOM</b>	self-organizing map
<b>SPIE</b>	Society of Photo-optical Instrumentation Engineers
<b>SPR</b>	statistical pattern recognition

<b>STA</b>	spatiotemporal attention [neural network]
<b>SURF</b>	speeded-up robust features
<b>SUSAN</b>	smallest univalue segment assimilating nucleus
<b>SVM</b>	support vector machine
<b>TM</b>	template matching
<b>TMF</b>	truncated median filter
<b>TN</b>	true negative
<i>tnr</i>	true negative rate
<b>TP</b>	true positive
<i>tpr</i>	true positive rate
<b>TV</b>	television
<b>USEF</b>	unit step edge function
<b>VGG</b>	Visual Geometry Group (Oxford)
<b>VJ</b>	Viola–Jones
<b>VLSI</b>	very large scale integration
<b>VMF</b>	vector median filter
<b>VOC</b>	visual object classes
<b>VP</b>	vanishing point
<b>WPP</b>	weak perspective projection
<b>YOLO</b>	you only look once
<b>YTF</b>	YouTube faces
<b>ZH</b>	Zuniga–Haralick corner detector

# Vision, the challenge

# 1

## 1.1 INTRODUCTION—MAN AND HIS SENSES

Of the five senses—vision, hearing, smell, taste, and touch—vision is undoubtedly the one that man has come to depend upon above all others, and indeed the one that provides most of the data he receives. Not only do the input pathways from the eyes provide megabits of information at each glance but also the data rates for continuous viewing probably exceed 10 Mbps. However, much of this information is redundant and is compressed by the various layers of the visual cortex, so that the higher centers of the brain have to interpret abstractly only a small fraction of the data. Nonetheless, the amount of information the higher centers receive from the eyes must be at least two orders of magnitude greater than all the information they obtain from the other senses.

Another feature of the human visual system is the ease with which interpretation is carried out. We see a scene as it is—trees in a landscape, books on a desk, widgets in a factory. No obvious deductions are needed and no overt effort is required to interpret each scene; in addition, answers are effectively immediate and are normally available within a tenth of a second. Just now and again some doubt arises—e.g., a wire cube might be “seen” correctly or inside out. This and a host of other optical illusions are well known, although for the most part we can regard them as curiosities—irrelevant freaks of nature. Somewhat surprisingly, illusions are quite important, since they reflect hidden assumptions that the brain is making in its struggle with the huge amounts of complex visual data it is receiving. We have to pass by this story here (although it resurfaces now and again in various parts of this book). However, the important point is that we are for the most part unaware of the complexities of vision. Seeing is not a simple process: it is just that vision has evolved over millions of years, and there was no particular advantage in evolution giving us any indication of the difficulties of the task (if anything, to have done so would have cluttered our minds with irrelevant information and slowed our reaction times).

In the present-day and age, man is trying to get machines to do much of his work for him. For simple mechanistic tasks this is not particularly difficult, but

for more complex tasks the machine must be given the sense of vision. Efforts have been made to achieve this, sometimes in modest ways, for well over 40 years. At first, schemes were devised for reading, for interpreting chromosome images, and so on; but when such schemes were confronted with rigorous practical tests, the problems often turned out to be more difficult. Generally, researchers react to finding that apparent “trivia” are getting in the way by intensifying their efforts and applying great ingenuity, and this was certainly so with early efforts at vision algorithm design. However, it soon became plain that the task really is a complex one, in which numerous fundamental problems confront the researcher, and the ease with which the eye can interpret scenes turned out to be highly deceptive.

Of course, one of the ways in which the human visual system gains over the machine is that the brain possesses more than  $10^{10}$  cells (or neurons), some of which have well over 10,000 contacts (or synapses) with other neurons. If each neuron acts as a type of microprocessor, then we have an immense computer in which all the processing elements can operate concurrently. Taking the largest single man-made computer to contain several hundred million rather modest processing elements, the majority of the visual and mental processing tasks that the eye–brain system can perform in a flash have no chance of being performed by present-day man-made systems. Added to these problems of scale, there is the problem of how to organize such a large processing system and also how to program it. Clearly, the eye–brain system is partly hard-wired by evolution but there is also an interesting capability to program it dynamically by training during active use. This need for a large parallel processing system with the attendant complex control problems shows that computer vision must indeed be one of the most difficult intellectual problems to tackle.

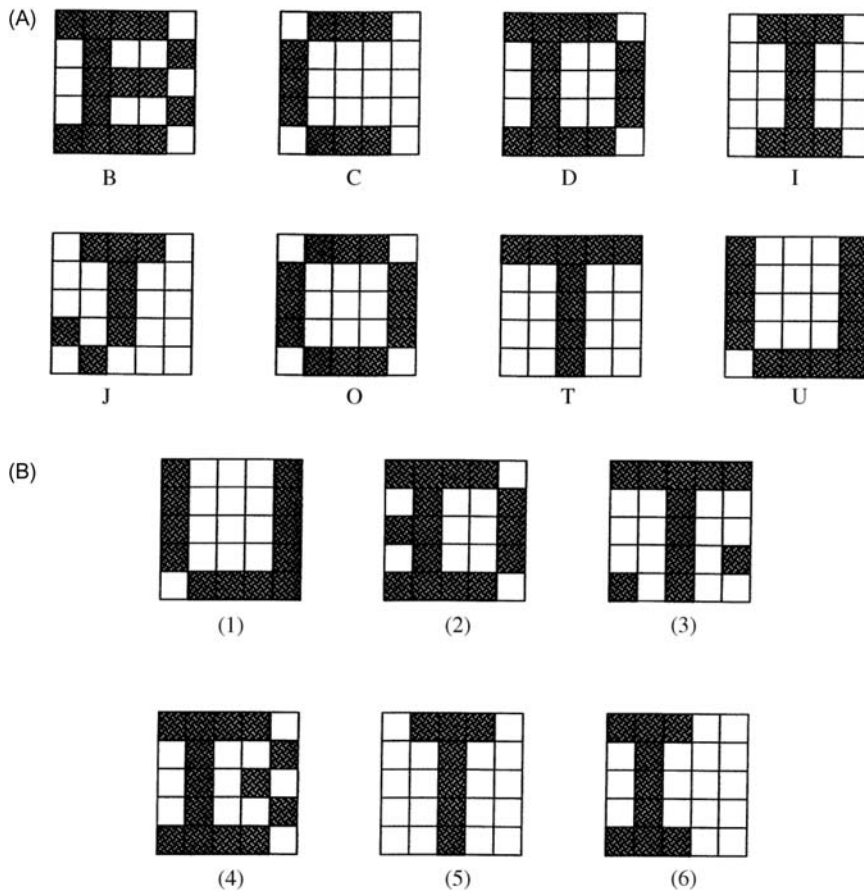
So what are the problems involved in vision that make it apparently so easy for the eye, yet so difficult for the machine? In the next few sections an attempt is made to answer this question.

---

## 1.2 THE NATURE OF VISION

### 1.2.1 THE PROCESS OF RECOGNITION

This section illustrates the intrinsic difficulties of implementing computer vision, starting with an extremely simple example—that of character recognition. Consider the set of patterns shown in [Fig. 1.1A](#). Each pattern can be considered as a set of 25 bits of information, together with an associated class indicating its interpretation. In each case imagine a computer learning the patterns and their classes by rote. Then any new pattern may be classified (or “recognized”) by comparing it with this previously learnt “training set,” and assigning it to the class of the nearest pattern in the training set. Clearly, test pattern (1) ([Fig. 1.1B](#)) will be allotted to class U on this basis. [Chapter 13](#), Basic Classification Concepts,

**FIGURE 1.1**

Some simple 25-bit patterns and their recognition classes used to illustrate some of the basic problems of recognition: (A) training set patterns (for which the known classes are indicated); (B) test patterns.

shows that this method is a simple form of the nearest neighbor approach to pattern recognition.

The scheme outlined above seems straightforward and is indeed highly effective, even being able to cope with situations where distortions of the test patterns occur or where noise is present: this is illustrated by test patterns (2) and (3). However, this approach is not always foolproof. First, there are situations where distortions or noise is excessive, so errors of interpretation arise. Second, there are situations where patterns are not badly distorted or subject to obvious noise, yet are misinterpreted: this seems much more serious, since it indicates an unexpected limitation of the technique rather than a reasonable result of noise or

distortion. In particular, these problems arise where the test pattern is displaced or misorientated relative to the appropriate training set pattern, as with test pattern (6).

As will be seen in [Chapter 13](#), Basic Classification Concepts, there is a powerful principle that indicates why the unlikely limitation given above can arise: it is simply that there are *insufficient training set patterns*, and that those that are present are *insufficiently representative* of what will arise in practical situations. Unfortunately, this presents a major difficulty, since providing enough training set patterns incurs a serious storage problem and an even more serious search problem when patterns are tested. Furthermore, it is easy to see that these problems are exacerbated as patterns become larger and more real (obviously, the examples of [Fig. 1.1](#) are far from having enough resolution even to display normal type-faces). In fact, a “combinatorial explosion” takes place: this is normally taken to mean that one or more parameters produce fast-varying (often exponential) effects, which “explode” as the parameters increase by modest amounts. Forgetting for the moment that the patterns of [Fig. 1.1](#) have familiar shapes, let us temporarily regard them as random bit patterns. Now the number of bits in these  $N \times N$  patterns is  $N^2$ , and the number of possible patterns of this size is  $2^{N^2}$ : even in a case where  $N = 20$ , remembering all these patterns and their interpretations would be impossible on any practical machine, and searching systematically through them would take impracticably long (involving times of the order of the age of the universe). Thus it is not only impracticable to consider such brute force means of solving the recognition problem, but is also effectively impossible theoretically. These considerations show that other means are required to tackle the problem.

### 1.2.2 TACKLING THE RECOGNITION PROBLEM

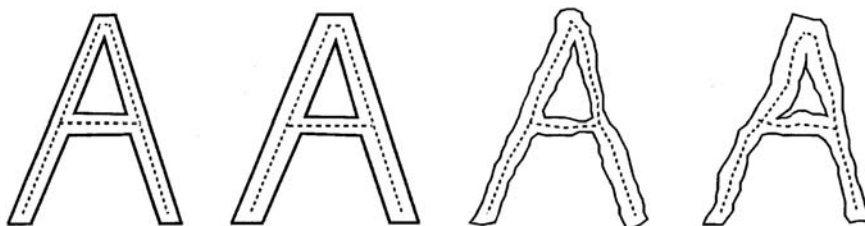
An obvious means of tackling the recognition problem is to standardize the images in some way. Clearly, normalizing the position and orientation of any 2D picture object would help considerably: indeed this would reduce the number of degrees of freedom by three. Methods for achieving this involve centralizing the objects—arranging that their centroids are at the center of the normalized image—and making their major axes (e.g., deduced by moment calculations) vertical or horizontal. Next, we can make use of the order that is known to be present in the image—and here it may be noted that very few patterns of real interest are indistinguishable from random dot patterns. This approach can be taken further: if patterns are to be nonrandom, isolated noise points may be eliminated. Ultimately, all these methods help by making the test pattern closer to a restricted set of training set patterns (although care must also be taken to process the training set patterns initially so that they are representative of the processed test patterns).

It is useful to consider character recognition further. Here we can make additional use of what is known about the structure of characters—namely, that they

consist of limbs of roughly constant width. In that case the width carries no useful information, so the patterns can be thinned to stick figures (called skeletons—see [Chapter 8: Binary Shape Analysis](#)); then, hopefully, there is an even greater chance that the test patterns will be similar to appropriate training set patterns ([Fig. 1.2](#)). This process can be regarded as another instance of reducing the number of degrees of freedom in the image, and hence of helping to minimize the combinatorial explosion—or, from a practical point of view, to minimize the size of the training set necessary for effective recognition.

Next, consider a rather different way of looking at the problem. Recognition is necessarily a problem of discrimination—i.e., of discriminating between patterns of different classes. However, in practice, considering the natural variation of patterns, including the effects of noise and distortions (or even the effects of breakages or occlusions), there is also a problem of generalizing over patterns of the same class. In practical problems there is a tension between the need to discriminate and the need to generalize. Nor is this a fixed situation. Even for the character recognition task, some classes are so close to others (*n*'s and *h*'s will be similar) that less generalization is possible than in other cases. On the other hand, extreme forms of generalization arise when, for example, an *A* is to be recognized as an *A* whether it is a capital or small letter, or in italic, bold, suffix, or other form of font—even if it is handwritten. The variability is determined largely by the training set initially provided. What we emphasize here, however, is that generalization is as necessary a prerequisite to successful recognition as is discrimination.

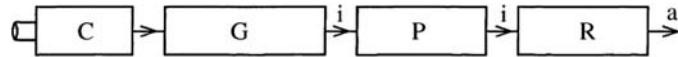
At this point it is worth considering more carefully the means whereby generalization was achieved in the examples cited above. First, objects were positioned and orientated appropriately; second, they were cleaned of noise spots; and third, they were thinned to skeleton figures (although the latter process is relevant only for certain tasks such as character recognition). In the last case, we are generalizing over characters drawn with all possible limb widths, width being an irrelevant degree of freedom for this type of recognition task. Note that we could have



**FIGURE 1.2**

Use of thinning to regularize character shapes. Here character shapes of different limb widths—or even varying limb widths—are reduced to stick figures or skeletons. Thus irrelevant information is removed and at the same time recognition is facilitated.



**FIGURE 1.3**

The two-stage recognition paradigm: C, input from camera; G, grab image (digitize and store); P, preprocess; R, recognize (i, image data; a, abstract data). The classical paradigm for object recognition is that of (1) preprocessing (image processing) to suppress noise or other artefacts and to regularize the image data and (2) applying a process of abstract (often statistical) pattern recognition to extract the very few bits required to classify the object.

generalized the characters further by normalizing their size and saving another degree of freedom. The common feature of all these processes is that they aim to give the characters a high level of standardization against known types of variability before finally attempting to recognize them.

The standardization (or generalization) processes outlined above are all realized by image processing, i.e., the conversion of one image into another by suitable means. The result is a two-stage recognition scheme: first, images are converted into more amenable forms containing the same numbers of bits of data; and second, they are classified with the result that their data content is reduced to very few bits (Fig. 1.3). In fact, recognition is a process of data abstraction, the final data being abstract and totally unlike the original data. Thus we must imagine a letter *A* starting as an array of perhaps  $20 \times 20$  bits arranged in the form of an *A*, and then ending as the 7 bits in an ASCII representation of an *A*, namely 1000001 (which is essentially a random bit pattern bearing no resemblance to an *A*).

The last paragraph reflects to a large extent the history of image analysis. Early on, a good proportion of the image analysis problems being tackled were envisaged as consisting of an image “preprocessing” task carried out by image processing techniques, followed by a recognition task undertaken by pure pattern recognition methods (see Chapter 13: Basic Classification Concepts). These two topics—image processing and pattern recognition—consumed much research effort and effectively dominated the subject of image analysis, while “intermediate-level” approaches such as the Hough transform were, for a time, slower to develop. One of the aims of this book is to ensure that such intermediate-level processing techniques are given due emphasis, and indeed that the best range of techniques is applied to any computer vision task.

### 1.2.3 OBJECT LOCATION

The problem that was tackled above—that of character recognition—is a highly constrained one. In a great many practical applications it is necessary to search pictures for objects of various types, rather than just interpreting a small area of a picture.

Search is a task that can involve prodigious amounts of computation and is also subject to a combinatorial explosion. Imagine the task of searching for a letter  $E$  in a page of text. An obvious way of achieving this is to move a suitable “template” of size  $n \times n$  over the whole image, of size  $N \times N$ , and to find where a match occurs (Fig. 1.4). A match can be defined as a position where there is exact agreement between the template and the local portion of the image but, in keeping with the ideas of Section 1.2.1, it will evidently be more relevant to look for a best local match (i.e., a position where the match is locally better than in adjacent regions) and where the match is also good in some more absolute sense, indicating that an  $E$  is present.

One of the most natural ways of checking for a match is to measure the Hamming distance between the template and the local  $n \times n$  region of the image, i.e., to sum the number of differences between corresponding bits. This is essentially the process described in Section 1.2.1. Then places with a low Hamming distance are places where the match is good. These template-matching ideas can be extended to cases where the corresponding bit positions in the template and the image do not just have binary values but may have intensity values over a range 0–255. In that case the sums obtained are no longer Hamming distances but may be generalized to the form:

$$\mathcal{D} = \sum_t |I_t - I_i| \quad (1.1)$$

$I_t$  being the local template value,  $I_i$  being the local image value, and the sum being taken over the area of the template. This makes template matching practicable in many situations: the possibilities are examined in more detail in subsequent chapters.

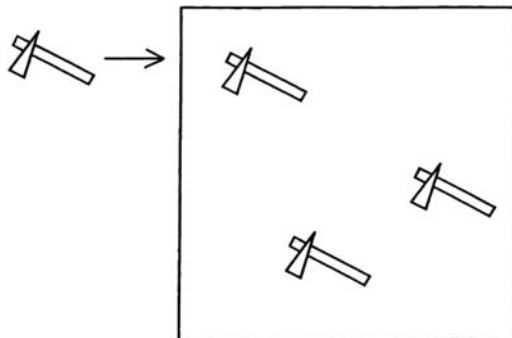


**FIGURE 1.4**

Template matching, the process of moving a suitable template over an image to determine the precise positions at which a match occurs, hence revealing the presence of objects of a particular type.

We referred above to a combinatorial explosion in this search problem too. The reason this arises is as follows. First, when a  $5 \times 5$  template is moved over an  $N \times N$  image in order to look for a match, the number of operations required is of the order of  $5^2 N^2$ , totaling some 1 million operations for a  $256 \times 256$  image. The problem is that when larger objects are being sought in an image, the number of operations increases as the square of the size of the object, the total number of operations being  $N^2 n^2$  when an  $n \times n$  template is used. For a  $30 \times 30$  template and a  $256 \times 256$  image, the number of operations required rises to  $\sim 60$  million. Note that, in general, a template will be larger than the object it is used to search for, because some background will have to be included to help demarcate the object.

Next, recall that in general, objects may appear in many orientations in an image ( $E$ 's on a printed page are exceptional). If we imagine a possible 360 orientations (i.e., one per degree of rotation), then a corresponding number of templates will in principle have to be applied in order to locate the object. This additional degree of freedom pushes the search effort and time to enormous levels, so far away from the possibility of real-time implementation that new approaches must be found for tackling the task. ["Real-time" is a commonly used phrase meaning that the information has to be processed as it becomes available: this contrasts with the many situations (such as the processing of images from space probes) where the information may be stored and processed at leisure.] Fortunately, many researchers have applied their minds to this problem and there are a many good ideas for tackling it. Perhaps the most important general means for saving effort on this sort of scale is that of two-stage (or multistage) template matching. The principle is to search for objects via their features. For example, we might consider searching for  $E$ 's by looking for characters that have horizontal line segments within them. Similarly, we might search for hinges on a manufacturer's conveyor by looking first for the screw holes they possess. In general it is useful to look for small features, since they require smaller templates and hence involve significantly less computation, as demonstrated above. This means that it may be better to search for  $E$ 's by looking for corners instead of horizontal line segments.

Unfortunately, noise and distortions give rise to problems if we search for objects via small features—there is a risk of missing the object altogether. Hence it is necessary to collate the information from a number of such features. This is the point where the many available methods start to differ from each other. How many features should be collated? Is it better to take a few larger features than many smaller ones? And so on. Also, we have not answered in full the question of what types of feature are the best to employ. These and other questions are considered in the subsequent chapters.

Indeed, in a sense, these questions are the subject of this book. Search is one of the fundamental problems of vision, yet the details and the application of the basic idea of two-stage template matching give the subject much of its richness: to solve the recognition problem, the data set needs to be explored carefully. Clearly, any answers will tend to be data-dependent but it is worth exploring to what extent there are generalized solutions to the problem.

### 1.2.4 SCENE ANALYSIS

The last subsection considered what is involved in searching an image for objects of a certain type: the result of such a search is likely to be a list of centroid coordinates for these objects, although an accompanying list of orientations might also be obtained. This subsection considers what is involved in scene analysis—the activity we are continually engaged in as we walk around, negotiating obstacles, finding food, and so on. Scenes contain a multitude of objects, and it is their interrelationships and relative positions that matter as much as identifying what they are. It may seem that there is no need for a search *per se* and that we could passively take in what is in the scene. However, there is much evidence (e.g., from analysis of eye movements) that the eye–brain system interprets scenes by continually asking questions about what is there. For example, we might ask the following questions: Is this a lamppost? How far away is it? Do I know this person? Is it safe to cross the road? And so on. It is not the purpose here to dwell on these human activities or introspection about them but merely to observe that scene analysis involves enormous amounts of input data, complex relationships between objects within scenes and, ultimately, descriptions of these complex relationships. The latter no longer take the form of simple classification labels, or lists of object coordinates, but have a much richer information content: indeed, a scene will, to a first approximation, be better described in English than as a list of numbers. It seems likely that a much greater combinatorial explosion is involved in determining relationships between objects than in merely identifying and locating them. Hence, all sorts of props must be used to aid visual interpretation: there is considerable evidence of this in the human visual system, where contextual information and the availability of immense databases of possibilities clearly help the eye to a considerable degree.

Note also that scene descriptions may initially be at the level of factual content but will eventually be at a deeper level—that of meaning, significance, and relevance. However, we shall not be able to delve further into these areas in this book.

### 1.2.5 VISION AS INVERSE GRAPHICS

It has often been said that vision is “merely” inverse graphics. There is a certain amount of truth in this. Computer graphics is the generation of images by computer, starting from abstract descriptions of scenes and knowledge of the laws of image formation. Also, it is difficult to quarrel with the idea that vision is the process of obtaining descriptions of sets of objects, starting from sets of images and a knowledge of the laws of image formation (indeed, it is good to see a definition that explicitly brings in the need to know the laws of image formation, since it is all too easy to forget that this is a prerequisite when building descriptions incorporating heuristics that aid interpretation).

However, this similarity in formulation of the two processes hides some fundamental points. First, graphics is a “feedforward” activity, i.e., images can be

produced straightforwardly once sufficient specification about the viewpoint and the objects, and knowledge of the laws of image formation, have been obtained. True, considerable computation may be required but the process is entirely determined and predictable. The situation is not so straightforward for vision because search is involved and there is an accompanying combinatorial explosion. Indeed, some vision packages incorporate graphics (or CAD) packages (Tabandeh and Fallside, 1986), which are inserted into feedback loops for interpretation: the graphics package is then guided iteratively until it produces an acceptable approximation to the input image, when its input parameters embody the correct interpretation (there is a close parallel here with the problem of designing analog-to-digital converters by making use of digital-to-analog converters). Hence, it seems inescapable that vision is intrinsically more complex than graphics.

We can clarify the situation somewhat by noting that, as a scene is observed, a 3-D environment is compressed into a 2-D image and a considerable amount of depth and other information is lost. This can lead to ambiguity of interpretation of the image (both a helix viewed end-on and a circle project into a circle), so the 3-D to 2-D transformation is many-to-one. Conversely, the interpretation must be one-to-many, meaning that there are many possible interpretations, yet we know that only one can be correct: vision involves not merely providing a list of all possible interpretations but providing the most likely one. Hence, some additional rules or constraints must be involved in order to determine the single most likely interpretation. Graphics, in contrast, does not have these problems, as the above ideas show it to be a many-to-one process.

---

### 1.3 FROM AUTOMATED VISUAL INSPECTION TO SURVEILLANCE

So far we have considered the nature of vision but not what man-made vision systems may be used for. There is in fact a great variety of applications for artificial vision systems—including, of course, all of those for which man employs his visual senses. Of particular interest in this book are surveillance, automated inspection, robot assembly, vehicle guidance, traffic monitoring and control, biometric measurement, and analysis of remotely sensed images. By way of example, fingerprint analysis and recognition have long been important applications of computer vision, as have the counting of red blood cells, signature verification and character recognition, and aeroplane identification (both from aerial silhouettes and from ground surveillance pictures taken from satellites). Face recognition and even iris recognition have become practical possibilities and vehicle guidance by vision will in principle soon be sufficiently reliable for urban use. Whether the public will accept this, with all its legal implications, is another matter, but note that radar blind-landing aids for aircraft have been in wide use for some years. In fact, last-minute automatic action to prevent accidents is a good

compromise (see [Chapter 24: Epilogue—Perspectives in Vision](#), for a related discussion on driver assistance schemes).

Among the applications of vision considered in this book are those of manufacturing industry—particularly, automated visual inspection and vision for automated assembly. In these cases, much of the same manufactured components are viewed by cameras: the difference lies in how the resulting information is used. In assembly, components must be located and orientated so that a robot can pick them up and assemble them. For example, the various parts of a motor or brake system need to be taken in turn and put into the correct positions, or a coil may have to be mounted on a television tube, an integrated circuit placed on a printed circuit board, or a chocolate placed into a box. In inspection, objects may pass the inspection station on a moving conveyor at rates typically between 10 and 30 items per second, and it has to be ascertained whether they have any defects. If any defects are detected, the offending parts will usually have to be rejected: that is the feedforward solution. In addition, a feedback solution may be instigated—i.e., some parameter may have to be adjusted to control plant further back down the production line (this is especially true for parameters that control dimensional characteristics such as product diameter). Inspection also has the potential for amassing a wealth of information that is useful for management, on the state of the parts coming down the line: the total number of products per day, the number of defective products per day, the distribution of sizes of products, and so on. The important feature of artificial vision is that it is tireless and that *all* products can be scrutinized and measured: thus quality control can be maintained to a very high standard. In automated assembly too, a considerable amount of on-the-spot inspection can be performed and this may help to avoid the problem of complex assemblies being rejected or having to be subjected to expensive repairs, because (for example) a proportion of screws were threadless and could not be inserted properly.

An important feature of most industrial tasks is that they take place in real time: if it is used, vision must be able to keep up with the manufacturing process. For assembly, this may not be too exacting a problem, since a robot may not be able to pick up and place more than one item per second—leaving the vision system a similar time to do its processing. For inspection, this supposition is rarely valid: even a single automated line (e.g., one for stoppering bottles) is able to keep up a rate of 10 items per second (and, of course, parallel lines are able to keep up much higher rates). Hence, visual inspection tends to press computer hardware very hard, so care needs to be taken in the design of hardware accelerators for such applications.

Finally, we return to the starting discussion about the huge variety of applications of vision, and it is interesting to consider surveillance tasks as the outdoor analogs of automated inspection (indeed, it is amusing to imagine that cars speeding along a road are just as subject to inspection as products speeding along a product line!). In fact, they have recently been acquiring close to exponentially increasing application. Thus the techniques used for inspection have acquired an

injection of vitality, and many more techniques have been developed. Naturally, this has meant the introduction of whole tranches of new subject matter, such as motion analysis and perspective invariants (see Part 4, 3-D Vision and Motion). It is also interesting that such techniques add richness to topics as face recognition (see [Chapter 21](#): Face Detection and Recognition: the Impact of Deep Learning).

---

## 1.4 WHAT THIS BOOK IS ABOUT

The foregoing sections have examined something of the nature of computer vision and have briefly considered its applications and implementation. It is already clear that implementing computer vision involves considerable practical difficulties but, more important, these practical difficulties embody substantial fundamental problems: these include various factors giving rise to excessive processing load and time. Practical problems may be overcome by ingenuity and care: however, by definition, truly fundamental limitations cannot be overcome by *any* means—the best that we can hope for is that we will be able to minimize their effects following a complete understanding of their nature.

Understanding is thus a cornerstone for success in computer vision. It is often difficult to achieve, since the data set (i.e., all pictures that could reasonably be expected to arise) is highly variegated. Indeed, much investigation is required to determine the nature of a given data set, including not only the objects being observed but also the noise levels, degrees of occlusion, breakage, defect, and distortion that are to be expected, and the quality and nature of the lighting. Ultimately, sufficient knowledge might be obtained in a useful set of cases so that a good understanding of the milieu can be attained. Then it remains to compare and contrast the various methods of image analysis that are available. Some methods will turn out to be quite unsatisfactory for reasons of robustness, accuracy or cost of implementation, or other relevant variables: and who is to say in advance what a relevant set of variables is? This, too, needs to be ascertained and defined. Finally, among the methods that could reasonably be used, there will be competition: tradeoffs between parameters such as accuracy, speed, robustness, and cost will have to be worked out first theoretically and then in numerical detail to find an optimal solution. This is a complex and long process in a situation where workers have in the past aimed to find solutions for their own particular (often short-term) needs. Clearly, there is a need to ensure that practical computer vision advances from an art to a science. Fortunately this process has been developing for some years, and one of the aims of this book is to throw additional light on the problem.

Before proceeding further, there are one or two more pieces to fit into the jigsaw. First, there is an important guiding principle: *if the eye can do it, so can the machine*. Thus, if an object is fairly well hidden in an image, yet the eye can see it and track it, then it should be possible to devise a vision algorithm that can do

the same. Next, although we can expect to meet this challenge, should we set our sights even higher and aim to devise algorithms that can beat the eye? There seems no reason to suppose that the eye is the ultimate vision machine: it has been built through the vagaries of evolution, so it may be well adapted for finding berries or nuts, or for recognizing faces, but ill-suited for certain other tasks. One such task is that of measurement. The eye probably does not need to measure the sizes of objects, at a glance, to better than a few percent accuracy. However, it could be distinctly useful if the robot eye could achieve remote size measurement, at a glance, and with an accuracy of say 0.001%. Clearly, the robot eye could acquire capabilities superior to those of biological systems. Again, this book aims to point out such possibilities where they exist.

Finally, it will be useful to clarify the terms *Machine Vision* and *Computer Vision*. In fact, these arose a good many years ago when the situation was quite different from what it is today. Over time, computer technology has advanced hugely and at the same time knowledge about the whole area of vision has been radically developed. In the early days, *Computer Vision* meant the study of the science of vision and the *possible* design of the software—and to a lesser extent with what goes into an integrated vision system, whereas *Machine Vision* meant the study not only of the software but also of the hardware environment and of the image acquisition techniques needed for real applications—so it was a much more engineering-orientated subject. At this point in time, computer technology has advanced so far that a sizeable proportion of real-world and real-time applications can be realized on unaided PCs. This and the many developments in knowledge in this area have led to significant convergence between the terms, with the result that they are often used more or less interchangeably, although in this book we aim to unify the subject under the name *Computer Vision*.

---

## 1.5 THE PART PLAYED BY MACHINE LEARNING

During the whole period that computer vision was developing in the way described above, the subject of pattern recognition was also progressing. Basic ideas on pattern recognition that started with Bayes theory and the nearest neighbor approach gradually changed with the advent of artificial neural networks, which were designed to emulate the neuron networks known to exist in the human brain. In addition, other methods such as support vector machines and boosting arrived on the scene: then, during the last decade or so, “deep learning” came into prominence. All these techniques led to a new subject called Machine Learning, which embodies pure pattern recognition but emphasizes not only minimization of error rates but also systematic inclusion of probability and mathematical optimization. The impact of this subject on computer vision has been increasingly dramatic over the past decade and particularly during the past 4–5 years. This book aims to include this development



as an integral part of its coverage: [Chapters 2](#), Images and Imaging Operations and [Chapter 13](#), Basic Classification Concepts, introduce in turn the imaging side of computer vision and the machine learning side, while [Chapter 15](#), Deep Learning Networks, leads the reader into the newer area of deep learning.

*Broadly, the modern subject of Computer Vision embodies both the earlier methods of computer and machine vision and also a range of machine learning techniques: the latter are based on earlier pattern recognition methods including standard artificial neural networks, the latest “deep learning” networks and a range of rigorous techniques involving probabilistic optimization.*

---

## 1.6 THE FOLLOWING CHAPTERS

[Chapters 2 and 13](#) form the introductions to the two main branches of the subject—image processing and machine learning. [Chapters 2–7](#) follow the image-processing theme, covering low-level vision and various widely used segmentation techniques, ranging from thresholding, through edge and feature detection to texture analysis. [Chapters 8–12](#) move on to intermediate-level processing, which has developed significantly in the past two decades and is important for the inference of complex objects: to this end, key model-based vision techniques such as the Hough transform and RANSAC are covered in detail ([Chapters 10 and 11](#)). Active shape models ([Chapter 12](#)) are also important for many practical applications. However, the latter require knowledge of PCA and other machine learning concepts: these are covered in [Chapter 14](#). [Chapters 16–19](#) develop the subject of 3-D vision, while [Chapter 20](#) introduces motion. [Chapters 21–23](#) attend to three key application areas—face detection and recognition; surveillance; and in-vehicle vision systems. [Chapter 24](#) reiterates and highlights some of the lessons and topics dealt with in the book; [Appendix A](#) develops the subject of Robust Statistics, which relates to a large proportion of the methods that are covered here; and [Appendix B](#) covers a topic that is essential background to a subject such as vision—namely the sampling theorem. [Appendix C](#) discusses the representation of color, while [Appendix D](#) is relevant to machine learning and contains important material on sampling from distributions.

To help the reader by giving more perspective on the later chapters, the main text is divided into five parts:

- Part 1 ([Chapters 2–7](#)) Low-Level Vision
- Part 2 ([Chapters 8–12](#)) Intermediate-Level Vision
- Part 3 ([Chapters 13–15](#)) Machine Learning and Deep Learning Networks
- Part 4 ([Chapters 16–20](#)) 3-D Vision and Motion
- Part 5 ([Chapters 21–23](#)) Putting Computer Vision to Work.

This last heading is used to emphasize real-world applications with high data flow rates and the need to integrate all the necessary recognition processes into reliable working systems.

Although the sequence of chapters follows the somewhat logical order just described, the ideas outlined in [Section 1.4](#)—understanding of the visual process, constraints imposed by realities such as noise and occlusion, tradeoffs between relevant parameters, and so on—are mixed into the text at relevant junctures, as they reflect all-pervasive issues.

Finally, there are many topics that could not be included in the book for reasons of space. The chapter bibliographies, the main list of references, and the indexes are intended to make good this limitation.

---

## 1.7 BIBLIOGRAPHICAL NOTES

The purpose of this chapter has been to introduce the reader to some of the problems of machine vision, showing the intrinsic difficulties but not at this stage getting into details. For detailed references the reader should consult the subsequent chapters. Meanwhile, further background on the world of machine learning can be obtained from Bishop (2006), Prince (2012), and Theodoridis (2015). In addition, some insight into human vision can be obtained from the fascinating monograph by Hubel (1995).

This page intentionally left blank

# Low-level vision

# 1

*This part of the book introduces images and image processing, and then proceeds to show how image processing may be developed in order to start the process of image analysis. By the end of [Chapter 7](#), Texture analysis, image analysis has been taken, via this “traditional” route, far enough to achieve a good many useful practical aims. The main topics to be developed are noise suppression, feature detection, object segmentation, and region analysis with the aid of morphology—itsself a development of basic procedures defined and elaborated in the first two chapters of Part 1.*

This page intentionally left blank

# Images and imaging operations

# 2

Images are at the core of vision, and there are many ways—from simple to sophisticated—for processing and analyzing them. This chapter concentrates on simple algorithms, which nevertheless need to be treated carefully as there are important subtleties to be learnt. Above all, it aims to show that quite a lot can be achieved with such algorithms, which can readily be programmed and tested by the reader.

Look out for:

- the different types of image—binary, gray scale, and color
- a compact notation for presenting image processing operations
- basic pixel operations—clearing, copying, inverting, and thresholding
- basic window operations—shifting, shrinking, and expanding
- grayscale brightening and contrast-stretching operations
- binary edge location and noise removal operations
- multiimage and convolution operations
- the distinction between sequential and parallel operations, and complications that can arise in the sequential case
- problems that arise around the edge of the image.

Although elementary, this chapter actually provides basic methodology for the whole of Part 1 and much of Part 2 of the book, and its importance should neither be underestimated nor the subtleties be ignored. Full understanding at this stage will save many complications later, when programming more sophisticated algorithms.

*pīx'ēllātēd*, a. picture broken into a regular tiling

*pīx'ītātēd*, a. pixie-like, crazy, deranged

## 2.1 INTRODUCTION

This chapter is concerned with images and simple image processing operations. It is intended to lead on to more advanced image analysis operations that are of use for machine vision in an industrial environment. Perhaps the main purpose of this

chapter is to introduce the reader to some basic techniques and notation that will be of use throughout the book. However, the image processing algorithms introduced here are of value in their own right in disciplines ranging from remote sensing to medicine and from forensic to military and scientific applications.

This chapter deals with images that have already been obtained from suitable sensors: the latter are covered in a later chapter. Typical of such images is that shown in Fig. 2.1A. This is a gray-tone image that at first sight appears to be a normal “black and white” photograph. However, closer inspection shows that it is composed of a large number of individual picture cells or “pixels.” In fact, the image is a  $128 \times 128$  array of pixels. To get a better feel for the limitations

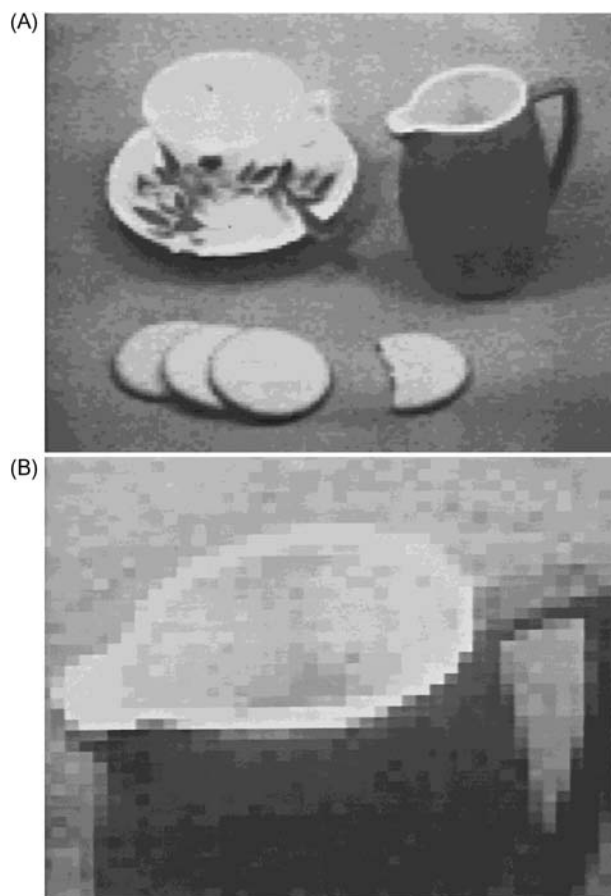


**FIGURE 2.1**

Typical grayscale image: (A) grayscale image digitized into a  $128 \times 128$  array of pixels; (B) section of image shown in (A) subjected to 3-fold linear magnification: the individual pixels are now clearly visible.

of such a digitized image, Fig. 2.1B shows a  $42 \times 42$  section that has been subjected to a 3-fold magnification so that the pixels can be examined individually.

It is not easy to see that these gray-tone images are digitized into a gray scale containing just 64 gray levels. To some extent, high spatial resolution compensates for lack of grayscale resolution, and as a result it is difficult to see the difference between an individual shade of gray and the shade it would have had in an ideal picture. In addition, when we look at the magnified section of image in Fig. 2.1B, it is difficult to understand the significance of the individual pixel intensities—the whole is becoming lost in a mass of small parts. Early television cameras typically gave a grayscale resolution that was accurate only to about one part in 50, corresponding to about 6 bits of useful information per pixel. Modern solid-state cameras commonly give less noise and may allow 8 or even 9 bits of information per pixel. However, there are many occasions when it is not worthwhile to aim for such high grayscale resolutions, particularly when the result will not be visible to the human eye or when there is an enormous amount of other data that a robot can use to locate objects within the field of view. Note that if the human eye can see an object in a digitized image of particular spatial and grayscale resolution, it is in principle possible to devise a computer algorithm to do the same thing.

Nevertheless, there is a range of applications for which it is valuable to retain a good grayscale resolution, so that highly accurate measurements can be made from a digital image. This is the case in many robotic applications, where high-accuracy checking of components is critical. More details will be shared about this later. In addition, it will be seen in Part 2 that certain techniques for locating components efficiently require local edge orientation to be estimated to better than  $1^\circ$ , and this can be achieved only if at least 6 bits of grayscale information are available per pixel.

### 2.1.1 GRAY SCALE VERSUS COLOR

Returning now to the image of Fig. 2.1A, we might reasonably ask whether it would be better to replace the gray scale with color, using an RGB color camera and three digitizers for the three main colors. There are two aspects of color that are important for the present discussion. One is the *intrinsic value* of color in machine vision: the other is the *additional storage and processing penalty* it might bring. It is tempting to say that the latter aspect is of no great importance given the cheapness of modern computers that have both high storage and high speed. On the other hand, high-resolution images can arrive from a collection of CCTV cameras at huge data rates, and it will be many years before it will be possible to analyze *all* the data arriving from such sources as they come in. Hence if color adds substantially to the storage and processing load, this will need to be justified.

Against this, the *potential* of color for helping with many aspects of inspection, surveillance, control, and a wide variety of other applications including medicine (color playing a crucial role in images taken during surgery) is enormous. This is illustrated with regard to robot navigation and driving in Figs. 2.2 and 2.3;





**FIGURE 2.2**

Value of color for segmentation and recognition. In natural outdoor scenes such as this, color helps with segmentation and with recognition. While it may have been important to the early human when discerning sources of food in the wild, robot drones may benefit by using color to aid navigation.



**FIGURE 2.3**

Value of color in the built environment. Color plays an important role for the human in managing the built environment. In a vehicle, a plethora of bright lights, road signs, and markings (such as yellow lines) are coded to help the driver; they may likewise help a robot to drive more safely by the provision of crucial information.



**FIGURE 2.4**

Value of color for food inspection. Much food is brightly colored, as with this Japanese meal. While this may be attractive to the human, it could also help the robot to check quickly for foreign bodies or toxic substances.

and for food inspection in [Figs. 2.4 and 2.5](#); for color filtering, see [Figs. 3.12 and 3.13](#). Notice that some of these images almost have color for color's sake (especially in [Figs. 2.4 and 2.5](#)), although none of them are artificially generated. In others the color is more subdued ([Fig. 2.3](#)), and in [Fig. 2.5](#) (excluding the tomatoes) it is quite subtle. The point to be made here is that for color to be useful it need not be garish, but can be subtle as long as it brings the right sort of information to bear on the task in hand. Suffice it to say that in some of the simpler inspection applications, where mechanical components are scrutinized on a conveyor or workbench, it is quite likely to be the shape that is in question rather than the color of the object or its parts. On the other hand, if an automatic fruit picker is to be devised, it will probably be more crucial to check color than specific shape. We leave it to the reader to imagine when and where color is particularly useful or merely an unnecessary luxury.

Next, it is useful to consider the processing aspect of color. In many cases good color discrimination is required to separate and segment two types of object from each other. Typically this will mean not using one or other specific color channel, but subtracting two or combining three in such a way as to foster discrimination. [We use the term "channel" not just to refer to the red, green, or blue channel, but any derived channel obtained by combining the colors into a single color dimension.] In the worst case of combining three color channels by simple

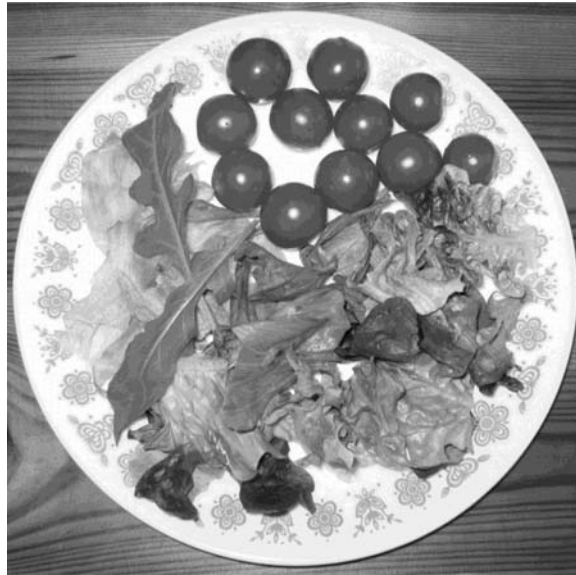


**FIGURE 2.5**

Subtle shades of color in food inspection. While much food is brightly colored, as for the tomatoes in this picture, green salad leaves show much more subtle combinations of color, and may indeed provide the only reliable means of identification. This could be important for inspection both of the raw product and its state when it reaches the warehouse or the supermarket.

arithmetic processing in which each pixel is treated identically, the processing load will be very light. In contrast, the amount of processing required to *determine* the optimal means of combining the data from the color channels and to carry out different operations dynamically on different parts of the image may be far from negligible, and some care will be needed in the analysis. These problems arise because color signals are inhomogeneous: this contrasts with the situation for grayscale images, where the bits representing the gray scale are of the same type and take the form of a number representing the pixel intensity: they can thus be processed as a single entity on a digital computer.

---

## 2.2 IMAGE PROCESSING OPERATIONS

In what follows the images of [Figs. 2.1A and 2.7A](#) are considered in some detail, examining some of the many image processing operations that can be performed

on them. The resolution of these images reveals a considerable amount of detail and at the same time shows how it relates to the more “meaningful” global information. This should help to make it clear how simple imaging operations contribute to image interpretation.

When performing image processing operations, we start with an image in one storage area and generate a new processed image in another storage area. In practice these storage areas may either be in a special hardware unit called a frame store that is interfaced to the computer or they may be in the main memory of the computer or on one of its discs. In the past a special frame store was required to store images, since each image contains a good fraction of a megabyte of information and this amount of space was not available for normal users in the computer main memory. Nowadays this is less of a problem, but for image acquisition and display a frame store is still required. However, we shall not worry about such details here. Instead it will be assumed that all images are inherently visible and that they are stored in various image “spaces” P, Q, R, etc. Thus we might start with an image in space P and copy it to space Q, for example.

### 2.2.1 SOME BASIC OPERATIONS ON GRAYSCALE IMAGES

In the following sections we assume a certain degree of familiarity with a language such as C++: readers who are unfamiliar with C++, or Java, which is similar at the required level of programming, should refer to books such as Stroustrup (1991) and Schildt (1995).

Perhaps the simplest of imaging operations is that of clearing an image or setting the contents of a given image space to a constant level. We need some way of arranging this, and accordingly the following C++ routine may be written for implementing it:

```
for (j = 0; j <= 127; j++)  
  for (i = 0; i <= 127; i++)  
    P[j][i] = alpha; (2.1)
```

In this routine the local pixel intensity value is expressed as  $P[j][i]$ , since P-space is taken to be a 2-D array of intensity values (Table 2.1). In what follows it will be advantageous to rewrite such routines in the more succinct form:

```
for all pixels in image do {P0 = alpha; } (2.2)
```

as this will aid understanding by removing irrelevant programming detail. The reason for calling the pixel intensity P0 will become clear later.

Another simple imaging operation is to copy an image from one space to another. This is achieved, without changing the contents of the original space P, by the routine:

```
for all pixels in image do {Q0 = P0; } (2.3)
```

Table 2.1 C++ Notation.

Notation	Meaning
++	Increment the preceding variable
[ ]	Add array index after a variable
[ ][ ]	Add two array indices after a variable: the last is the faster running index
(int)	Changes the following variable to integer type
(float)	Changes the following variable to floating point
{ }	Encloses a sequence of instructions
if ( ) { };	Basic conditional statement: ( ) encloses the condition; { } encloses the instructions to be executed
if ( ) { } ; else if ( ) { } ; ... ; else { } ;	The most general type of conditional statement
while ( ) { }	Common type of iterated loop
do { } while ( ) ;	Another common type of iterated loop
do { } until ( ) ;	“until” means the same as “while not.” This is often a convenient notation, although it is not strict C++.
for ( ; ; ) { } ;	Here the conditional statement ( ) has three arguments separated by semicolons: they are the initial condition; the terminating condition; and the incrementation operation, respectively
=	Forces equality (literally: “takes the value”)
==	Tests for equality in a conditional expression
<=	≤
>=	≥
!=	≠
!	Logical NOT
&&	Logical AND
	Logical OR
//	Indicates that the remainder of the line is a comment
/* ... */	Brackets enclosing a comment
A0...A8 } B0...B8 } C0...C8 }	Bit image variables in 3 × 3 window <sup>a</sup>
P0...P8 } Q0...Q8 } R0...R8 }	Byte image variables in 3 × 3 window <sup>a</sup>
P[0], ...	Equivalent to P0, ...

*The purpose of this table is to show what is meant by the various C++ commands and instructions used in this book. It is not intended to be comprehensive: The aim is merely to be helpful to the reader. In general, only notation that differs between C++ and other commonly used languages such as Pascal is included, in order to eliminate possible ambiguity or confusion.*

<sup>a</sup>These predefined variables denote special syntax not available in C++, but useful for simplifying the image processing algorithms presented in Chapter 2 et seq.

A more interesting operation is that of inverting the image, as in the process of converting a photographic negative to a positive. This process is represented as follows:

$$\text{for all pixels in image do } \{Q_0 = 255 - P_0; \} \quad (2.4)$$

In this case it is assumed that pixel intensity values lie within the range 0–255, as is commonly true for frame stores that represent each pixel as one byte of information. Note that such intensity values are commonly unsigned and this is assumed generally in what follows.

There are many operations of these types. Some other simple operations are those that shift the image left, right, up, down, or diagonally. They are easy to implement if the new local intensity is made identical to that at a neighboring location in the original image. It is evident how this would be expressed in the double suffix notation used in the original C++ routine. In the new shortened notation, it is necessary to name neighboring pixels in some convenient way, and we here employ the following simple scheme:

P4	P3	P2
P5	P0	P1
P6	P7	P8

with a similar scheme for other image spaces. With this notation, it is easy to express a left shift of an image as follows:

$$\text{for all pixels in image do } \{Q_0 = P_1; \} \quad (2.5)$$

Similarly, a shift down to the bottom right is expressed as:

$$\text{for all pixels in image do } \{Q_0 = P_4; \} \quad (2.6)$$

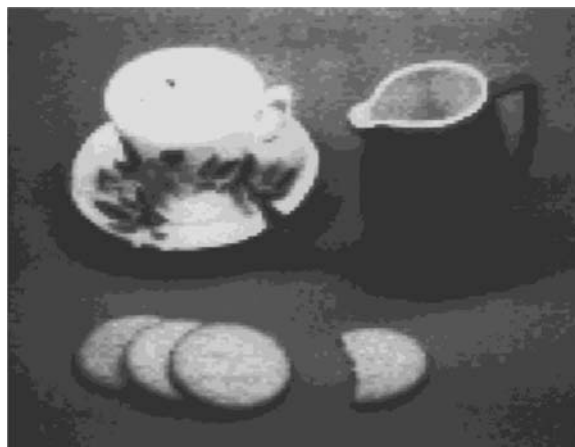
It will now be clear why  $P_0$  and  $Q_0$  were chosen for the basic notation of pixel intensity: the “0” denotes the central pixel in the “neighborhood” or “window,” and corresponds to zero shift when copying from one space to another. However, the type of window operation presented above is much more powerful than single pixel operations, and we shall see many examples of it in what follows. Meanwhile, note that it can give rise to difficulties around the boundaries of the image: we shall return to this point in [Section 2.4](#).

There is a whole range of possible operations associated with modifying images in such a way as to match them to the requirements of a human viewer. For example, adding a constant intensity makes the image brighter:

$$\text{for all pixels in image do } \{Q_0 = P_0 + \text{beta}; \} \quad (2.7)$$

and the image can be made darker in the same way. A more interesting operation is to stretch the contrast of a dull image:

$$\text{for all pixels in image do } \{Q_0 = P_0 * \text{gamma} + \text{beta}; \} \quad (2.8)$$

**FIGURE 2.6**

Contrast stretching: Effect of increasing the contrast in the image of Fig. 2.1A by a factor of two and adjusting the mean intensity level appropriately. The interior of the jug can now be seen more easily. Note, however, that there is no additional information in the new image.

where  $\gamma > 1$ . In practice (as for Fig. 2.6), it is necessary to ensure that intensities do not result that are outside the normal range, e.g., by using an operation of the form:

```

for all pixels in image do {
  QQ = P0*gamma + beta;
  if (QQ < 0) Q0 = 0;
  else if (QQ > 255) Q0 = 255;
  else Q0 = QQ;
}

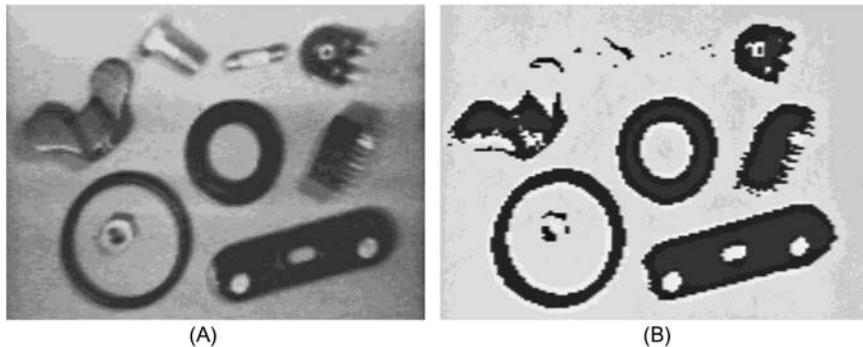
```

(2.9)

Most practical situations demand more sophisticated transfer functions—either nonlinear or piecewise linear—but such complexities are ignored here.

In what follows we clarify the discussion by adopting a simple set of notations: the first few letters of the alphabet (A, B, C, . . .) are used consistently to denote binary image spaces, and later letters (P, Q, R, . . .) to denote grayscale images (Table 2.1). In software these variables are assumed to be predeclared, and in hardware (e.g., frame store) terms they are taken to refer to dedicated memory spaces containing only the necessary 1 or 8 bits per pixel. The intricacies of data transfer between variables of different types are important considerations, which are not addressed in detail here: it is sufficient to assume that both  $A0 = P0$  and  $P0 = A0$  correspond to a single-bit transfer, except that in the latter case the top 7 bits are assigned the value 0.

The next operation we shall consider is that of thresholding grayscale images to convert them to binary images. This topic is covered in more detail later, since it is widely used to detect objects in images. However, our purpose here is to

**FIGURE 2.7**

Thresholding of grayscale images: (A)  $128 \times 128$  pixel grayscale image of a collection of parts; (B) effect of thresholding the image.

look on it as another basic imaging operation. It can be implemented using the routine

```

for all pixels in image do {
  if ( $P_0 > \text{thresh}$ )  $A_0 = 1$ ; else  $A_0 = 0$ ;
}

```

(2.10)

If, as very often happens, objects appear as dark objects on a light background, it is easier to visualize the subsequent binary processing operations by inverting the thresholded image using a routine such as:

```

for all pixels in image do { $A_0 = 1 - A_0$ ; }

```

(2.11)

However, it would be more usual to combine the two operations into a single routine of the form:

```

for all pixels in image do {
  if ( $P_0 > \text{thresh}$ )  $A_0 = 0$ ; else  $A_0 = 1$ ;
}

```

(2.12)

To display the resulting image in a form as close as possible to the original, it can be reinverted and given the full range of intensity values (intensity values 0 and 1 being scarcely visible):

```

for all pixels in image do { $R_0 = 255 * (1 - A_0)$ ; }

```

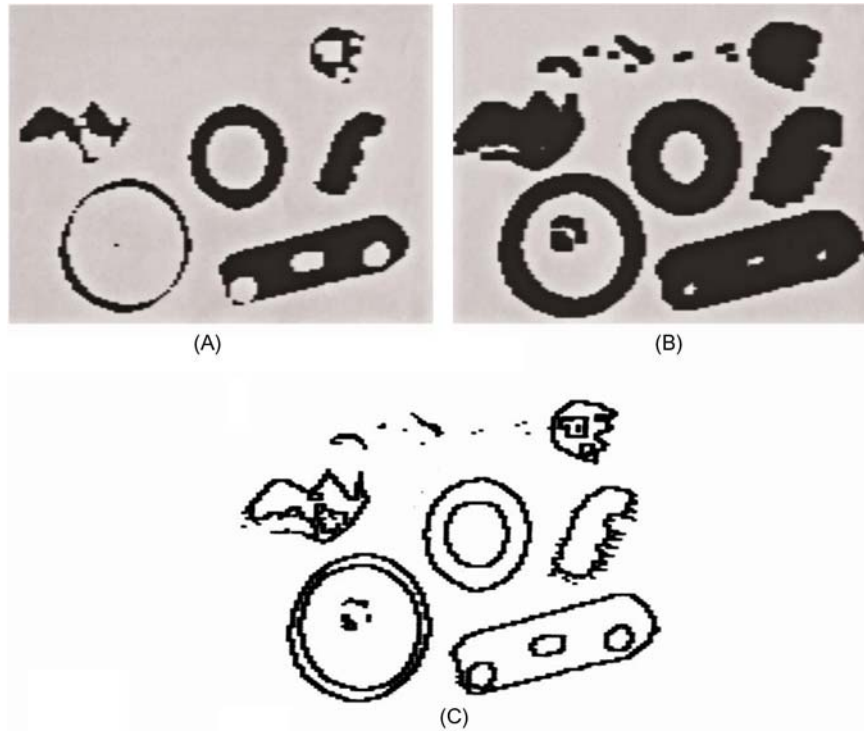
(2.13)

Fig. 2.7 shows the effect of these two operations.

### 2.2.2 BASIC OPERATIONS ON BINARY IMAGES

Once the image has been thresholded, a wide range of binary imaging operations become possible. Only a few such operations are covered here, with the aim of



**FIGURE 2.8**

Simple operations applied to binary images: (A) effect of shrinking the dark-thresholded objects appearing in Fig. 2.7B; (B) effect of expanding these dark objects; (C) result of applying an edge location routine. Note that the shrink, expand, and edge routines are applied to the *dark* objects: this implies that the intensities are initially inverted as part of the thresholding operation and then reinverted as part of the display operation (see text).

being instructive rather than comprehensive. With this in mind, a routine may be written for shrinking dark thresholded objects (Fig. 2.8A), which is here represented by a set of 1s in a background of 0s:

```

for all pixels in image do {
  sigma = A1 + A2 + A3 + A4 + A5 + A6 + A7 + A8;
  if (A0 == 0) B0 = 0;
  else if (sigma < 8) B0 = 0;
  else B0 = 1;
}

```

(2.14)

In fact, the logic of this routine can be simplified to give the following more compact version:

```

for all pixels in image do {
  sigma = A1 + A2 + A3 + A4 + A5 + A6 + A7 + A8;
  if (sigma < 8) B0 = 0; else B0 = A0;
}

```

(2.15)

Note that the process of shrinking dark objects also expands light objects, including the light background. It also expands holes in dark objects. The opposite process, that of expanding dark objects (or shrinking light ones), is achieved (Fig. 2.8B) with the routine:

```

for all pixels in image do {
  sigma = A1 + A2 + A3 + A4 + A5 + A6 + A7 + A8;
  if (sigma > 0) B0 = 1; else B0 = A0;
}

```

(2.16)

The processes of shrinking and expanding are also widely known by the respective terms “erosion” and “dilation” (see also Chapter 7: Texture Analysis). Each of the above routines using them employs the same technique for interrogating neighboring pixels in the original image: as will be apparent on numerous occasions in this book, the sigma value is a useful and powerful descriptor for  $3 \times 3$  pixel neighborhoods. Thus “if (sigma > 0)” can be taken to mean “if next to a dark object” and the consequence can be read as “then expand it.” Similarly, “if (sigma < 8)” can be taken to mean “if next to a light object” or “if next to light background,” and the consequence can be read as “then expand the light background into the dark object.”

The process of finding the edge of a binary object has several possible interpretations. Clearly, it can be assumed that an edge point has a sigma value in the range 1–7 inclusive. However, it may be defined as being within the object, within the background, or in either position. Taking the definition that the edge of an object has to lie within the object (Fig. 2.8C), the following edge-finding routine for binary images results:

```

for all pixels in image do {
  sigma = A1 + A2 + A3 + A4 + A5 + A6 + A7 + A8;
  if (sigma == 8) B0 = 0; else B0 = A0;
}

```

(2.17)

This strategy amounts to canceling out object pixels that are not on the edge. For this and a number of other algorithms (including the shrink and expand algorithms already encountered), a thorough analysis of exactly which pixels should be set to 1 and 0 (or which should be retained and which eliminated), involves drawing up tables of the form:

		Sigma	
		0 to 7	8
A0	0	0	0
	1	1	0

This reflects the fact that algorithm specification includes a recognition phase and an action phase, i.e., it is necessary first to locate situations within an image where (for example) edges are to be marked or noise eliminated, and then action must be taken to implement the change.

Another function that can usefully be performed on binary images is the removal of “salt and pepper” noise, i.e., noise that appears as a light spot on a dark background or a dark spot on a light background. The first problem to be solved is that of recognizing such noise spots; the second is the simpler one of correcting the intensity value. For the first of these tasks the sigma value is again useful. To remove salt noise (which has binary value 0 in our convention), we arrive at the following routine:

```
for all pixels in image do {
  sigma = A1 + A2 + A3 + A4 + A5 + A6 + A7 + A8;
  if (sigma == 8) B0 = 1; else B0 = A0;
}
```

(2.18)

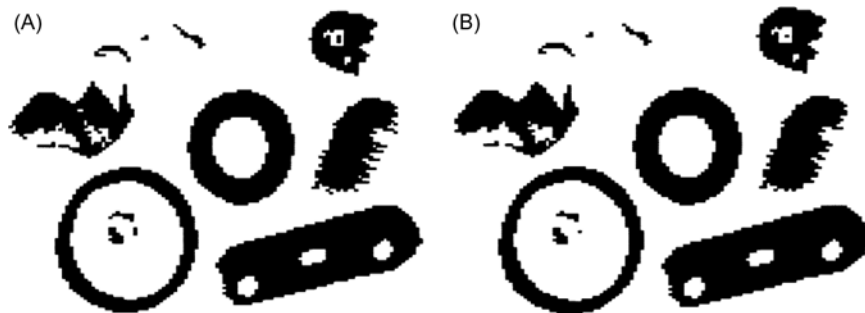
which can be read as leaving the pixel intensity unchanged unless it is proven to be a salt noise spot. The corresponding routine for removing pepper noise (binary value 1) is:

```
for all pixels in image do {
  sigma = A1 + A2 + A3 + A4 + A5 + A6 + A7 + A8;
  if (sigma == 0) B0 = 0; else B0 = A0;
}
```

(2.19)

Combining these two routines into one operation (Fig. 2.9A) gives:

```
for all pixels in image do {
  sigma = A1 + A2 + A3 + A4 + A5 + A6 + A7 + A8;
  if (sigma == 0) B0 = 0;
  else if (sigma == 8) B0 = 1;
  else B0 = A0;
}
```

(2.20)


**FIGURE 2.9**

Simple binary noise removal operations: (A) result of applying a “salt and pepper” noise removal operation to the thresholded image in Fig. 2.7B; (B) result of applying a less stringent noise removal routine: this is effective in cutting down the jagged spurs that appear on some of the objects.

The routine can be made less stringent in its specification of noise pixels, so that it removes spurs on objects and background: this is achieved (Fig. 2.9B) by a variant such as:

```

for all pixels in image do {
  sigma = A1 + A2 + A3 + A4 + A5 + A6 + A7 + A8;
  if (sigma < 2) B0 = 0;
  else if (sigma > 6) B0 = 1;
  else B0 = A0;
}

```

(2.21)

As before, if there is any doubt about the algorithm, its specification should be set up rigorously—as shown in the following table.

		Sigma		
		0 or 1	2 to 6	7 or 8
A0	0	0	0	1
	1	0	1	1

There are many other simple operations that can usefully be applied to binary images and some of them are dealt with in Chapter 8, Binary Shape Analysis.

## 2.3 CONVOLUTIONS AND POINT SPREAD FUNCTIONS

Convolution is a powerful and widely used technique in image processing and other areas of science. It appears in many applications throughout this book, and it is therefore useful to introduce it at an early stage. We start by defining the convolution of two functions  $f(x)$  and  $g(x)$  as the integral:

$$f(x) \otimes g(x) = \int_{-\infty}^{\infty} f(u)g(x-u)du \quad (2.22)$$

The action of this integral is normally described as the result of applying a point spread function (PSF)  $g(x)$  to all points of a function  $f(x)$  and accumulating the contributions at every point. It is significant that if the PSF is very narrow—ideally, a delta function—then the convolution is identical to the original function  $f(x)$ . This makes it natural to think of the function  $f(x)$  as having been spread out under the influence of  $g(x)$ . This argument may give the impression that convolution necessarily blurs the original function but this is not always so if, for example, the PSF has a distribution of positive and negative values.

When convolution is applied to digital images, the above formulation changes in two ways: (1) a double integral must be used in respect of the two dimensions and (2) integration must be changed into discrete summation. The new form of the convolution is:

$$F(x, y) = f(x, y) \otimes g(x, y) = \sum_i \sum_j f(i, j)g(x - i, y - j) \quad (2.23)$$

where  $g$  is now referred to as a spatial convolution mask. The fact that the mask has to be inverted before it is applied is inconvenient for visualizing the process of convolution—particularly when matching operations are involved, e.g., for corner location (see [Chapter 6: Corner, Interest Point, and Invariant Feature Detection](#)). In this book we therefore present only preinverted masks of the form:

$$h(x, y) = g(-x, -y) \quad (2.24)$$

Convolution can then be calculated using the more intuitive formula:

$$F(x, y) = \sum_i \sum_j f(x + i, y + j)h(i, j) \quad (2.25)$$

which involves multiplying corresponding values in the modified mask and the neighborhood under consideration. Reexpressing this result for a  $3 \times 3$  neighborhood and writing the mask coefficients in the form:

$$\begin{bmatrix} h4 & h3 & h2 \\ h5 & h0 & h1 \\ h6 & h7 & h8 \end{bmatrix}$$

the algorithm can be obtained in terms of our earlier notation:

$$\begin{aligned} &\text{for all pixels in image do } \{ \\ &\quad Q0 = P0*h0 + P1*h1 + P2*h2 + P3*h3 + P4*h4 \\ &\quad \quad + P5*h5 + P6*h6 + P7*h7 + P8*h8; \\ &\quad \} \end{aligned} \quad (2.26)$$

We are now in a position to apply convolution to a real situation. At this stage we attempt to suppress noise by averaging over nearby pixels. A simple way of achieving this is to use the convolution mask:

$$\frac{1}{9} \begin{bmatrix} 1 & 1 & 1 \\ 1 & 1 & 1 \\ 1 & 1 & 1 \end{bmatrix}$$

where the number in front of the mask weights all the coefficients in the mask and is inserted to ensure that applying the convolution does not alter the mean intensity in the image. As hinted above, this particular convolution has the effect of blurring the image as well as reducing the noise level ([Fig. 2.10](#)). More details will be shared about this in [Chapter 3, Image Filtering and Morphology](#).

The above discussion makes it clear that convolutions are linear operators. In fact, they are the most general spatially invariant linear operators that can be applied to a signal such as an image. Note that linearity is often of interest in that it permits mathematical analysis to be performed that would otherwise be intractable.

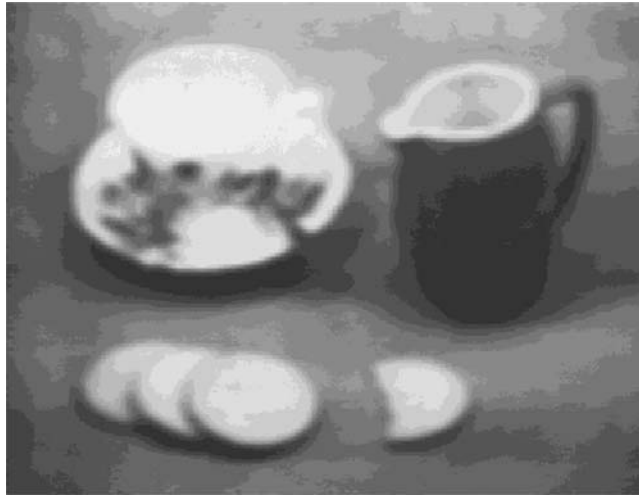


**FIGURE 2.10**

Noise suppression by neighborhood averaging achieved by convolving the original image of Fig. 2.1A with a uniform mask within a  $3 \times 3$  neighborhood. Note that noise is suppressed only at the expense of introducing significant blurring.

## 2.4 SEQUENTIAL VERSUS PARALLEL OPERATIONS

It will be noticed that most of the operations defined so far have started with an image in one space and finished with an image in a different space. Unfortunately, many of the operations will not work satisfactorily if we do not use separate input and output spaces in this way. This is because they are inherently “parallel processing” routines. This term is used, as these are the types of process that would be performed by a parallel computer possessing a number of processing elements equal to the number of pixels in the image, so that all the pixels are processed simultaneously. If a serial computer is to *simulate* the operation of a parallel computer, then it must have separate input and output image spaces and rigorously work in such a way that it uses the original image values to compute the output pixel values. This means that an operation such as the following cannot be an ideal parallel process:

```

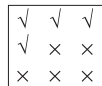
for all pixels in image do {
  sigma = A1 + A2 + A3 + A4 + A5 + A6 + A7 + A8;
  if (sigma < 8) A0 = 0; else A0 = A0;
}

```

(2.27)

This is so because, when the operation is half completed, the output pixel intensity will depend not only on some of the unprocessed pixel values but also on some that have already been processed. For example, if the computer makes a

normal (forward) TV raster scan through the image, the situation at a general point in the scan will be



where the ticked pixels have already been processed and the others have not. As a result, the above operation will shrink all objects to nothing!

A much simpler illustration of this is obtained by attempting to shift an image to the right using the following routine:

$$\text{for all pixels in image do } \{P_0 = P_5; \} \quad (2.28)$$

In fact, all this achieves is to fill up the image with values corresponding to those off its left edge, whatever they are assumed to be. Thus we have shown that the shifting process is inherently parallel. (Note that whenever the computer is performing a  $3 \times 3$  (or larger) window operation, it has to assume some value for off-image pixel intensities: usually whatever value is selected will be inaccurate, and so the final processed image will contain a border that is also inaccurate. This will be so whether the off-image pixel addresses are trapped in software or in specially designed circuitry in the frame store.)

It will be seen later that there are some processes that are inherently sequential—i.e., the processed pixel has to be returned immediately to the *original* image space. Meanwhile, note that not all of the routines described so far need to be restricted rigorously to parallel processing. In particular, all single-pixel routines (essentially, those that only refer to the single pixel in a  $1 \times 1$  neighborhood) can validly be performed as if they were sequential in nature. Such routines include the following intensity adjustment and thresholding operations:

$$\text{for all pixels in image do } \{P_0 = P_0 * \text{gamma} + \text{beta}; \} \quad (2.29)$$

$$\text{for all pixels in image do } \{ \text{if } (P_0 > \text{thresh}) P_0 = 1; \text{ else } P_0 = 0; \} \quad (2.30)$$

These remarks are intended to act as a warning. In general, it is safest to design algorithms that are exclusively parallel processes unless there is a definite need to make them sequential. It will be seen later how this need can arise.

---

## 2.5 CONCLUDING REMARKS

This chapter has introduced a compact notation for representing imaging operations and has demonstrated some basic parallel processing routines. [Chapter 3](#), Image Filtering and Morphology, extends this work to see how noise suppression can be achieved in grayscale images. This leads on to more advanced image analysis work that is directly relevant to machine vision applications. In particular,

Chapter 4, The Role of Thresholding, studies in more detail the thresholding of grayscale images, building on the work of Section 2.2.1, while Chapter 8, Binary Shape Analysis, studies object shape analysis in binary images.

*Pixel–pixel operations can be used to make radical changes in digital images. However, this chapter has shown that window–pixel operations are far more powerful, and capable of performing all manner of size- and-shape changing operations, as well as eliminating noise. But caveat emptor—sequential operations can have some odd effects if adventitiously applied.*

---

## 2.6 BIBLIOGRAPHICAL AND HISTORICAL NOTES

Since the aim of this chapter was not to cover the most recent material but to provide a succinct overview of basic techniques, it will not be surprising that most of the topics discussed were developed well over 20 years ago and have been used by a large number of workers in many areas. For example, thresholding of grayscale images was first reported at least as long ago as 1960, while shrinking and expanding of binary picture objects dates from a similar period. Discussion of the origins of other techniques is curtailed: for further details, the reader is referred to the texts by (for example) Gonzalez and Woods (2008), Nixon and Aguado (2008), Petrou and Petrou (2010), and Sonka et al. (2007). We also refer to two texts that cover programming aspects of image processing in some depth: Parker (1994) that covers C programming and Whelan and Molloy (2001) that covers Java programming. More specialized texts will be referred to in the subsequent chapters.

---

## 2.7 PROBLEMS

1. Derive an algorithm for finding the edges of binary picture objects by applying a shrink operation and combining the result with the original image. Is the result the same as that obtained using the edge-finding routine (2.17)? Prove your statement rigorously by drawing up suitable algorithm tables as in Section 2.2.2.
2. In a certain frame store, each off-image pixel can be taken to have either the value 0 or the intensity for the nearest image pixel. Which will give the more meaningful results for (1) shrinking, (2) expanding, and (3) a blurring convolution?
3. Suppose the noise elimination routines of Eqs. (2.20) and (2.21) were reimplemented as sequential algorithms. Show that the action of the first would be unchanged, whereas the second would produce very odd effects on some binary images.



This page intentionally left blank

# Image filtering and morphology

# 3

Image filtering involves the application of window operations that perform useful functions, such as noise removal and image enhancement. This chapter is concerned particularly with what can be achieved with quite basic filters, such as mean, median, and mode filters. Interestingly, these filters have significant effects on the shapes of objects; in fact, the study of shape took place over a long period of time and resulted in a highly variegated set of algorithms and methods, during which the overarching formalism of mathematical morphology was set up. This chapter steers an intuitive path between the many mathematical theorems, showing how they lead to practically useful techniques. The focus is on grayscale images, although some aspects of color processing are also covered.

*Look out for:*

- what can be achieved by low-pass filtering
- the problem of impulse noise and how it can be eliminated
- the value of median, mode, and rank order filters
- the shifts and distortions produced by median and rank order filters
- how “expanding” and “shrinking” are generalized to dilation and erosion
- how dilation and erosion may be combined to form more complex operations with predictable properties
- how “closing” and “opening” are defined, and how they are used to find defects in binary object shapes, via residue (“top hat”) operations
- how mathematical morphology is generalized to cover grayscale processing.

This chapter delves into the properties of a variety of common types of filter, aiming to understand both what they can achieve and their limitations. In fact, the edge shifts produced by most of these filters are small, predictable, and in principle correctable. The exception is the rank order filter, for which the shifts can be large—but this is the *advantage* of this type of filter, which is at the core of mathematical morphology. The theory in this chapter is especially valuable because of the way in which it integrates a range of topics, at the same time being of value in many applications.

### 3.1 INTRODUCTION

Chapter 2, Images and Imaging Operations, was concerned with simple imaging operations, including such problems as thresholding grayscale images and suppressing noise in binary images. In this chapter the discussion is extended to noise suppression and enhancement in grayscale images. Although in many applications these types of operation are unnecessary, it is useful to examine them in some depth because of their wide use in a number of other cases and because they set the scene for much of what follows.

It has already been seen that noise can arise in real images, and it is hence necessary to have sound techniques for suppressing it. Commonly, in electrical engineering applications, noise is removed by means of low-pass or other filters that operate in the frequency domain (Rosie, 1966). Applying these filters to 1-D time-varying analog signals is straightforward, since it is necessary only to place them at suitable stages in the sequence of black boxes through which the signals pass. For digital signals the situation is more complicated, since the frequency transform of the signal must first be computed, then the low-pass filter applied, and finally the signal obtained from the modified transform by converting back to the time domain. Thus two Fourier transforms have to be computed, although modifying the signal while it is in the frequency domain is a straightforward task (Fig. 3.1). In fact, the amount of processing involved in computing the discrete Fourier transform of a signal represented by  $N$  samples is of order  $N^2$  (we shall write this as  $O(N^2)$ ), although the amount of computation can be cut down to  $O(N \log_2 N)$  by employing the fast Fourier transform (FFT) (Gonzalez and Woods, 1992). This then becomes a practical approach for the elimination of noise.

When applying these ideas to images we first note that the signal is a spatial rather than a time-varying quantity and must be filtered in the spatial frequency

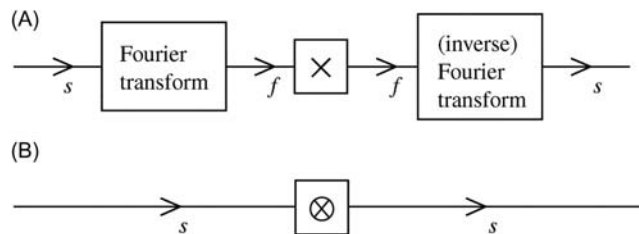


**FIGURE 3.1**

Low-pass filtering for noise suppression:  $s$ , spatial domain;  $f$ , spatial frequency domain;  $\times$ , multiplication by low-pass characteristic;  $\otimes$ , convolution with Fourier transform of low-pass characteristics. (A) Low-pass filtering achieved most simply, by a process of multiplication in the (spatial) frequency domain; (B) low-pass filtering achieved by a process of convolution. Note that (A) may require more computation overall, because of the two Fourier transforms that have to be performed.

domain. Mathematically this makes no real difference but there are nevertheless significant problems. First, there is no satisfactory analog shortcut and the whole process has to be carried out digitally (we here ignore optical processing methods despite their obvious power, speed, and high resolution, because they are by no means trivial to marry with digital computer technology). Second, for an  $N \times N$  pixel image, the number of operations required to compute a Fourier transform is  $O(N^3)$  and the FFT only reduces this to  $O(N^2 \log_2 N)$ , so the amount of computation is quite considerable (here it is assumed that the 2-D transforms are implemented by successive passes of 1-D transforms: see Gonzalez and Woods, 1992). Note also that two Fourier transforms are required for the purpose of noise suppression (Fig. 3.1). Nevertheless, in many imaging applications it is worth proceeding in this way, not only so that noise can be removed but also so that television scan lines and other artefacts can be filtered out. This situation applies particularly in remote sensing and space technology. However, in industrial applications the emphasis is always on real-time processing, so in many cases it is not practicable to remove noise by spatial frequency domain operations. A further problem is that low-pass filtering is suited to removing Gaussian noise but distorts the image if it is used to remove impulse noise.

In Chapter 2, Images and Imaging Operations, we met the operations of erosion and dilation: in Section 3.11 we apply them to the filtering of binary images and will show that with suitable combinations of these operators it is possible to eliminate certain types of object from images and also to locate other objects. These possibilities are not fortuitous but, on the contrary, reflect fundamental properties of shape, which are dealt with in the subject known as mathematical morphology. This subject has grown up over the past few decades and by now has become a mature subject. It is the purpose of this chapter to give some insight into this vital area of study. Note that mathematical morphology is especially important because it provides a backbone for the study of shape and is thus able to unify techniques as disparate as noise suppression, shape analysis, feature recognition, skeletonization, convex hull formation, and a host of other topics.

Section 3.2 discusses Gaussian smoothing, in both the spatial frequency and the spatial domains. The subsequent three sections introduce median filters, mode filters, and general rank order filters, and contrast their main properties and uses. Section 3.6 introduces the sharp–unsharp masking technique, which provides a rather simple although extremely widely used route to image enhancement. Section 3.7 examines the edge shifts produced by median filters, and Section 3.8 extends this work to cover the larger shifts produced by rank order filters: these are treated fairly fully because of their relevance to morphological operators that turn the shifts to advantage. Section 3.10 gives a brief discussion on the application of filters to color images. Section 3.11 starts the discussion of morphology by extending the concepts of expanding and shrinking first encountered in Section 2.2. Section 3.12 develops the theory, arriving at many important results—emphasis being placed less on mathematical rigor than on understanding

of concepts. [Section 3.13](#) examines morphological grouping operations. [Section 3.14](#) goes on to show how morphology can be generalized to cope with grayscale images.

---

## 3.2 NOISE SUPPRESSION BY GAUSSIAN SMOOTHING

Low-pass filtering is normally thought of as the elimination of signal components with high spatial frequencies, and it is therefore natural to carry it out in the spatial frequency domain. Nevertheless, it is possible to implement it directly in the spatial domain. This is possible due to the well-known fact (Rosie, 1966) that multiplying a signal by a function in the spatial frequency domain is equivalent to convolving it with the Fourier transform of the function in the spatial domain ([Fig. 3.1](#)). If the final convolving function in the spatial domain is sufficiently narrow, then the amount of computation involved will not be excessive: in this way a satisfactory implementation of the low-pass filter can be sought. It now remains to find a suitable convolving function.

If the low-pass filter is to have a sharp cutoff, then its transform in image space will be oscillatory: an extreme example of this is the sinc ( $\sin x/x$ ) function, which is the spatial transform of a low-pass filter of rectangular profile (Rosie, 1966). Oscillatory convolving functions are unsatisfactory since they can introduce halos around objects, hence distorting the image quite grossly. Marr and Hildreth (1980) suggested that the right types of filter to apply to images are those that are well behaved (nonoscillatory) both in the frequency and in the spatial domain. Gaussian filters are able to fulfill this criterion optimally: they have identical forms in the spatial and spatial frequency domains. In 1-D these forms are

$$f(x) = \frac{1}{(2\pi\sigma^2)^{1/2}} \exp\left(-\frac{x^2}{2\sigma^2}\right) \quad (3.1)$$

$$F(\omega) = \exp\left(-\frac{1}{2}\sigma^2\omega^2\right) \quad (3.2)$$

Thus the type of spatial convolving operator required for the purpose of noise suppression by low-pass filtering is the one that approximates to a Gaussian profile. Many such approximations appear in the literature: these vary with the size of the neighborhood chosen and in the precise values of the convolution mask coefficients.

One of the most common is the following mask, first introduced in [Chapter 2](#), [Images and Imaging Operations](#), which is used more for simplicity of computation than for its fidelity to a Gaussian profile:

$$\frac{1}{9} \begin{bmatrix} 1 & 1 & 1 \\ 1 & 1 & 1 \\ 1 & 1 & 1 \end{bmatrix}$$

Another commonly used mask, which approximates more closely to a Gaussian profile, is the following:

$$\frac{1}{16} \begin{bmatrix} 1 & 2 & 1 \\ 2 & 4 & 2 \\ 1 & 2 & 1 \end{bmatrix}$$

In both cases the coefficients that precede the mask are used to weight all the mask coefficients: as mentioned in [Section 2.3](#), these weights are chosen so that applying the convolution to an image does not affect the average image intensity. These two convolution masks probably account for over 80% of all discrete approximations to a Gaussian. Notice that as they operate within a  $3 \times 3$  neighborhood, they are reasonably narrow and hence incur a relatively small computational load.

Let us next study the properties of this type of operator, deferring for now consideration of Gaussian operators in larger neighborhoods. First, imagine such an operator applied to a noisy image whose intensity is inherently uniform. Then clearly noise is suppressed, as it is now averaged over nine pixels. This averaging model is obvious for the first of the two masks above but in fact applies equally to the second mask, once it is accepted that the averaging effect is differently distributed in accordance with the improved approximation to a Gaussian profile.

Although this example shows that noise is suppressed, it is clear that the signal will also be affected. This problem arises only where the signal is initially non-uniform: indeed, if the image intensity is constant or if the intensity map approximates to a plane, there is again no problem. However, if the signal is uniform over one part of a neighborhood and rises in another part of it, as is bound to occur adjacent to the edge of an object, then the object will make itself felt at the center of the neighborhood in the filtered image ([Fig. 3.2](#)). As a result, the edges of objects become somewhat blurred. Looking at the operator as a “mixing

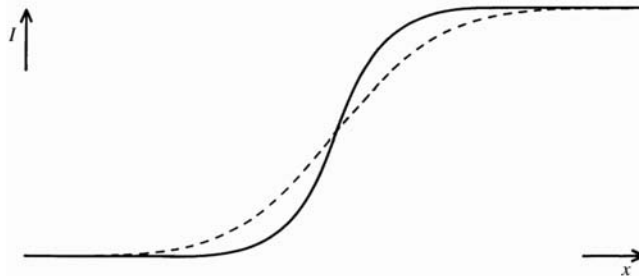


**FIGURE 3.2**

Blurring of object edges by simple Gaussian convolutions. The simple Gaussian convolution can be regarded as a grayscale neighborhood “mixing” operator, hence explaining why blurring arises.

operator,” which forms a new picture by mixing together the intensities of pixels fairly close to each other, it is intuitively obvious why blurring occurs.

It is also apparent from a spatial frequency viewpoint why blurring should occur. Basically, we are aiming to give the signal a sharp cutoff in the spatial frequency domain, and as a result it will become slightly blurred in the spatial domain. Clearly, the blurring effect can be reduced by using the narrowest possible approximation to a Gaussian convolution filter but at the same time the noise suppression properties of the filter are lessened. Assuming that the image was initially digitized at roughly the correct spatial resolution, it will not normally be appropriate to smooth it using convolution masks larger than  $3 \times 3$  or at most  $5 \times 5$  pixels (here we ignore methods of analyzing images that use a number of versions of the image with different spatial resolutions: see for example, Babaud et al., 1986).

Overall, low-pass filtering and Gaussian smoothing are not appropriate for the applications considered here, because of the blurring effects they introduce. Notice also that where interference occurs which can give rise to impulse or “spike” noise (corresponding to a number of individual pixels having totally the wrong intensities), merely averaging this noise over a larger neighborhood can make the situation worse, since the spikes will be smeared over a sizeable number of pixels and will distort the intensity values of all of them. This consideration is important as it leads naturally to the concepts of limit and median filtering.

---

### 3.3 MEDIAN FILTERS

The idea explored here is to locate those pixels in the image, which have extreme and therefore highly improbable intensities, and to ignore their actual intensities, replacing them with more suitable values. This is akin to drawing a graph through a set of plots and ignoring those plots that are evidently a long way from the best-fit curve. An obvious way of achieving this is to apply a “limit” filter that prevents any pixel having an intensity outside the intensity range of its neighbors:

```

for all pixels in image do {
  minP = min(P1, P2, P3, P4, P5, P6, P7, P8);
  maxP = max(P1, P2, P3, P4, P5, P6, P7, P8);
  if (P0 < minP) Q0 = minP;
  else if (P0 > maxP) Q0 = maxP;
  else Q0 = P0;
}

```

(3.3)

To develop this technique it is necessary to examine the local intensity distribution within a particular neighborhood. Points at the extremes of the distribution are quite likely to have arisen from impulse noise. So it is sensible not only to eliminate these points, as in the limit filter, but also to try taking the process further, removing equal areas at either end of the distribution and ending with the median. Thus we arrive at the median filter that takes all the local intensity



**FIGURE 3.3**

Effect of applying a  $3 \times 3$  median filter to the image of Fig. 2.1A. Note the slight loss of fine detail and the rather “softened” appearance of the whole image.

distributions and generates a new image corresponding to the set of median values. As the preceding argument indicates, the median filter is excellent at impulse noise suppression and this is amply confirmed in practice (Fig. 3.3).

In view of the blurring caused by Gaussian smoothing operators, it is pertinent to ask whether the median filter also induces blurring. In fact, Fig. 3.3 shows that any blurring is only marginal, although there is some slight loss of fine detail, which can give the resulting pictures a “softened” appearance. Theoretical discussion of this point is deferred for now; the lack of blur makes good the main deficiency of the Gaussian smoothing filter and results in the median filter being perhaps the most widely used filter in general image processing applications.

There are many ways of implementing the median filter: Table 3.1 reproduces only an obvious algorithm that essentially implements the above description. The notation of Chapter 2, Images and Imaging Operations, is used but is augmented in order to permit the nine pixels in a  $3 \times 3$  neighborhood to be accessed in turn with a running suffix (specifically, P0 to P8 are written as P[m] where  $m$  runs from 0 to 8).

The operation of the algorithm is as follows: first, the histogram array is cleared and the image is scanned, generating a new image in Q-space; then, for each neighborhood, the histogram of intensity values is constructed; then the median is found; and, finally, points in the histogram array that have been incremented are cleared. This last feature eliminates the need to clear the whole histogram and hence saves computation. Unlike the general situation in which the



**Table 3.1** An Implementation of the Median Filter

---

```

for (i = 0; i <= 255; i++) hist[i] = 0;
for all pixels in image do {
  for (m = 0; m <= 8; m++) hist[ P[m] ]++;
  i = 0; sum = 0;
  while (sum < 5) {
    sum = sum + hist[i];
    i = i + 1;
  }
  Q0 = i - 1;
  for (m = 0; m <= 8; m++) hist[ P[m] ] = 0;
}

```

---

median of a distribution is being located, only one (half) scan through the distribution is required, since the total area is known in advance (in this case it is nine).

As is clear from the above, methods of computing the median involve pixel intensity sorting operations. If a bubble sort (Gonnet, 1984) were used for this purpose, then up to  $O(n^4)$  operations would be required for an  $n \times n$  neighborhood, compared with some 256 operations for the histogram method described above. Thus sorting methods such as the bubble sort are faster for small neighborhoods where  $n$  is 3 or 4 but not for neighborhoods where  $n$  is greater than about 5, or where pixel intensity values are more restricted.

Much of the discussion of the median filter in the literature is concerned with saving computation (Narendra, 1978; Huang et al., 1979; Danielsson, 1981). In particular, it has been noticed that, on proceeding from one neighborhood to the next, relatively few new pixels are encountered: this means that the new median value can be found by updating the old value rather than starting from scratch (Huang et al., 1979).

---

### 3.4 MODE FILTERS

Having considered the mean and the median of the local intensity distribution as candidate intensity values for noise smoothing filters, it also seems relevant to consider the mode of the distribution. Indeed, we might imagine that this is, if anything, more important than the mean or the median, since the mode represents the most probable value of any distribution.

However, a tedious problem arises as soon as we attempt to apply this idea. The local intensity distribution is calculated from relatively few pixel intensity values (Fig. 3.4). This means that instead of a smooth intensity distribution whose mode is easily located, we are almost certain to have a multimodal distribution



**FIGURE 3.4**

The sparse nature of the local intensity histogram for a small neighborhood. This situation clearly causes significant problems for estimation of the mode. It also has definite implications for rigorous estimation of the underlying median, assuming that the observed intensities are only noisy samples of the ideal intensity pattern (see [Section 3.4](#)).

© IEEE 1984.

whose highest point does not indicate the position of the *underlying* mode. Clearly the distribution needs to be smoothed out considerably before the mode is computed. Another tedious problem is that the width of the distribution varies widely from neighborhood to neighborhood (e.g., from close to zero to close to 256), so that it is quite difficult to know how much to smooth the distribution in any instance. For these reasons, it is likely to be better to choose an indirect measure of the position of the mode rather than to attempt to measure it directly.

In fact, the position of the mode can be estimated with reasonable accuracy once the median has been located (Davies, 1984a, 1988c). To understand the technique, it is necessary to consider how local intensity distributions of various sorts arise in practical situations. At most positions in an image, variations in pixel intensity are generated by steady changes in background illumination, by steady variations in surface orientation, or by noise. Thus a symmetrical unimodal local intensity distribution is to be expected. It is well known that the mean, median, and mode are coincident in such cases. More problematic is what happens to the intensity variation near the edge of an object in the image. Here the local intensity distribution is unlikely to be symmetrical and, more important, it may not even be unimodal. In fact, near an edge the distribution is in general inherently *bimodal*, since the neighborhood contains pixels with intensities corresponding to the values they would have on either side of the edge ([Fig. 3.5](#)). Considering the image as a whole, this will be the most likely alternative to a symmetrical unimodal distribution, any further possibilities such as trimodal distributions being rare and of varied causes (e.g., odd glints on the edges of metal objects), which are outside the scope of the present discussion. (Here we are ignoring the effects of noise and just considering the underlying image signal.)

If the neighborhood straddles an edge and the local intensity distribution is bimodal, the larger peak position should clearly be selected as the most probable intensity value. A good strategy for finding the larger peak is to eliminate the smaller peak. If we knew the position of the mode, we could find where to truncate the smaller peak by first finding which extreme of the distribution was closer to the mode and then moving an equal distance to the opposite side of the mode

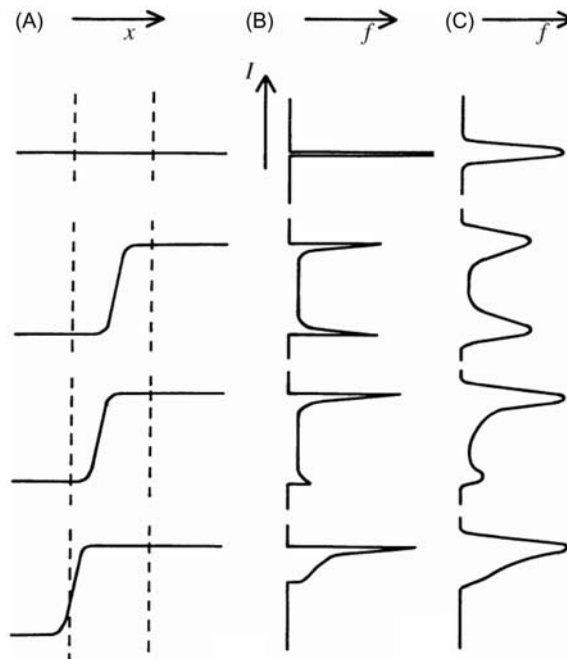


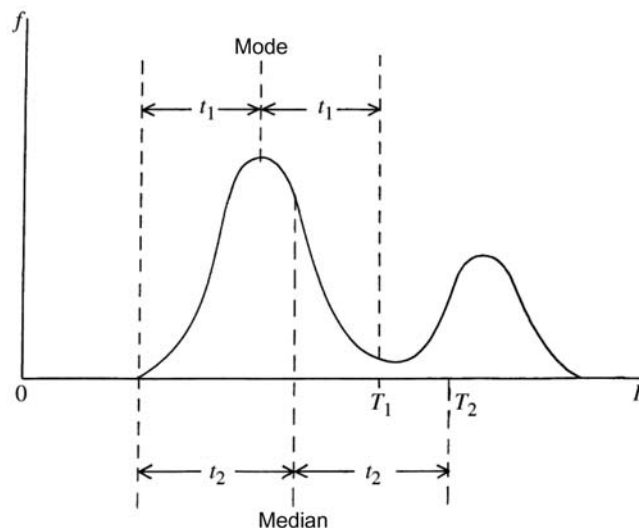
**FIGURE 3.5**

Local models of image data near the edge of an object: (A) cross-sections of an edge falling in the vicinity of a filter neighborhood; (B) corresponding local intensity distributions when very little image noise is present; (C) situation when the noise level is increased.

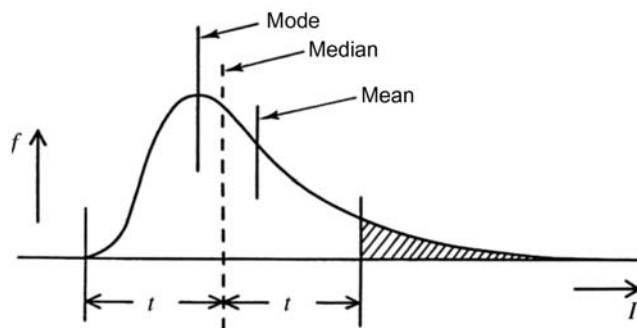
© IEEE 1984.

(Fig. 3.6). Since we start off *not* knowing the position of the mode, one option is to use the position of the median as an estimator of the position of the mode and then to use that position to find where to truncate the distribution. Since it invariably happens that the three means take the order mean, median, and mode (Fig. 3.7), except when distributions are badly behaved or multimodal, this method is cautious in the sense that it truncates less of the distribution than the required amount: this makes it a safe method to use. When we now find the median of the truncated distribution, the position is much closer to the mode than the original median was, a good proportion of the second peak having been removed (Fig. 3.8). Iteration could be used to find an even closer approximation to the position of the mode. However, the method gives a marked enhancement in the image even when this is not done (Fig. 3.9).

We next examine more closely the properties of the “truncated median filter” (TMF) described above. Whereas the median filter is highly successful at removing noise, the TMF not only removes noise but also enhances the image so that edges become sharper. Fig. 3.10 makes it clear why this should happen.

**FIGURE 3.6**

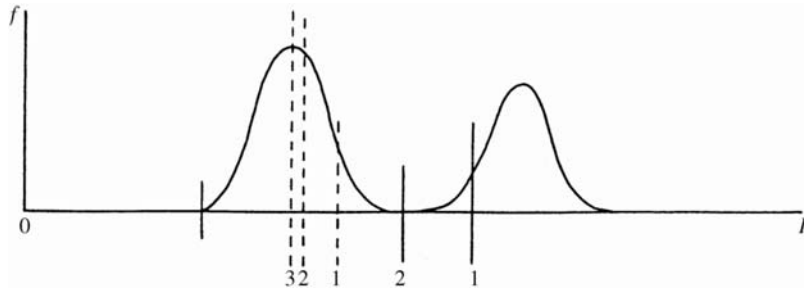
Rationale for the method of truncation. The obvious position at which to truncate the distribution is  $T_1$ . Since the position of the mode is not initially known, it is suboptimal but safe to truncate instead at  $T_2$ .

**FIGURE 3.7**

Relative positions of the mode, median and mean for a typical unimodal distribution. This ordering is unchanged for a bimodal distribution, as long as it can be approximated by two Gaussian distributions of similar width.

© IEEE 1984.

Basically, at a location even very slightly to one side of an edge, a majority of the pixel intensities contribute to the larger peak and the TMF ignores the pixel intensities contributing to the smaller peak. Thus the TMF makes an informed binary choice about which side of the edge it is on. At first this seems to mean

**FIGURE 3.8**

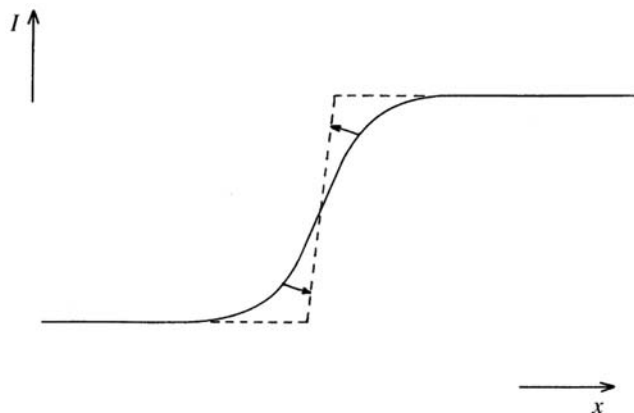
Iterative truncation of the local intensity distribution. Here the median converges on the mode within three iterations of the truncation procedure. This is possible since at each stage the mode of the new truncated distribution remains the same as that of the previous distribution.

**FIGURE 3.9**

Effect of a single application of  $3 \times 3$  truncated median filter to the image of Fig. 2.1A.

that it pushes a nearby edge further away. However, it must be remembered that it actually “pushes the edge away” from both sides, and the result is that its sides are made sharper and object outlines are crispened up. Particularly striking is the effect of applying the TMF to an image a number of times, when objects start to become segmented into regions of fairly uniform intensity (Fig. 3.11). The complete algorithm for achieving this is outlined in Table 3.2.

This problem has been dealt with at some length for a number of reasons. First, the mode filter has not hitherto received the attention it deserves. Second, the median filter seems to be used fairly universally, often without very much justification or thought. Third, all these filters show what markedly different characteristics are available merely by analyzing the contents of the



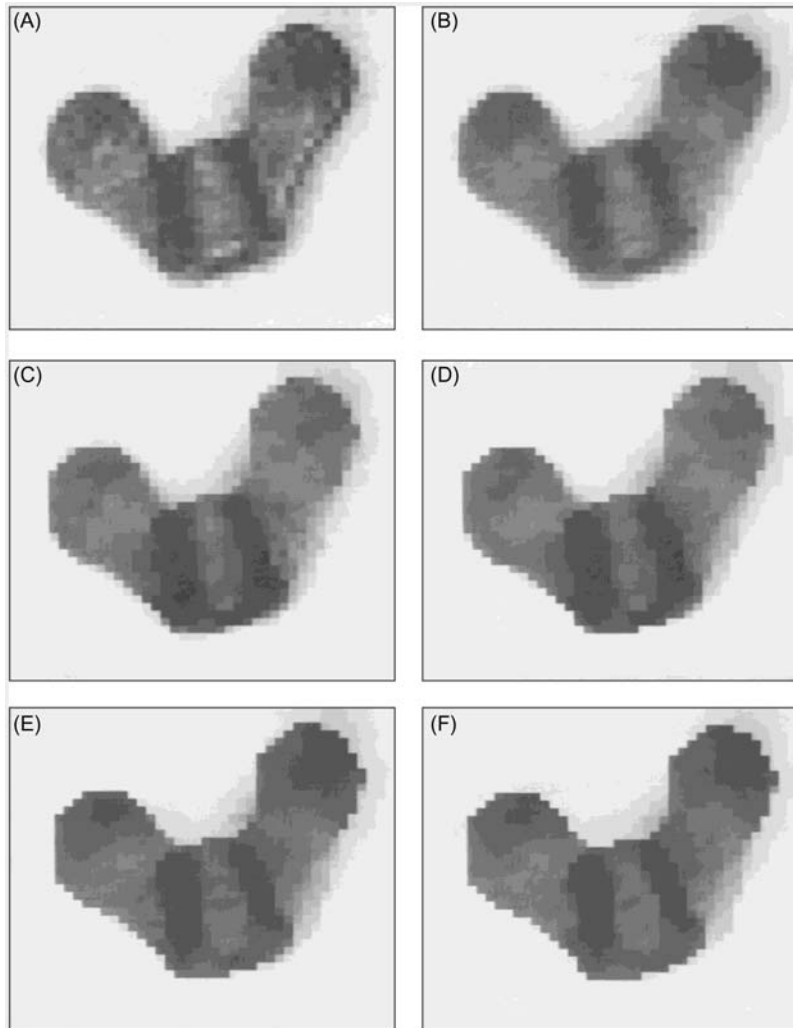
**FIGURE 3.10**

Image enhancement performed by the mode filter. Here the onset of the edge is pushed laterally by the action of the mode filter within one neighborhood; since the same happens from the other side within an adjacent neighborhood, the actual position of the edge is unchanged in first order. The overall effect is to sharpen the edge.

local intensity distribution, and ignoring totally where in the neighborhood the different intensities appear: it is perhaps remarkable that there is sufficient information in the local intensity distribution for this to be possible. All these show the danger of applying operators that have been derived in an ad hoc manner without first making a specification of what is required and then designing an operator with the required characteristics. In fact, the situation appears to be that if we want a filter that has maximum impulse noise suppression capability, then we should use a median filter; and if we want a filter that enhances images by sharpening edges, then we should use a mode filter or TMF (note that the TMF should be an improvement on the mode filter in that it is more cautious very close to an edge transition, where noise prevents an exact judgment being made as to which side of the edge a pixel is on: see Davies, 1984a, 1988c).

While considering enhancement, attention has been restricted to filters based on the local intensity distribution; there are many filters that enhance images without the aid of the local intensity distribution (Lev et al., 1977; Nagao and Matsuyama, 1979), but they are not within the scope of this chapter. Note that the method of “sharp–unsharp masking” (Section 3.6) performs an enhancement function, although its main purpose is to restore images that have inadvertently become blurred, e.g., by a hazy atmosphere or defocussed camera.

Finally, while this section has concentrated on the grayscale properties of mode filters, Charles and Davies (2003a, 2004) have shown how to devise versions of the TMF that operates on color images. Typical results are shown in



**FIGURE 3.11**

Results of repeated action of the truncated median filter: (A) the original, moderately noisy picture; (B) effect of a  $3 \times 3$  median filter; (C)–(F) effect of 1–4 passes of the basic truncated median filter, respectively.

© IEEE 1984.

**Fig. 3.12.** In addition, **Fig. 3.13** shows that the TMF has the useful property of being able to eliminate very large amounts of impulse noise from images—significantly more than a median filter—in spite of being designated as an image enhancement filter.

**Table 3.2** Outline of Algorithm for Implementing the Truncated Median Filter

---

```

do { // as many passes over image as necessary
  for all pixels in image do {
    compute local intensity distribution;
    do { // iterate to improve estimate of mode
      find minimum, median and maximum intensity values;
      decide from which end local intensity distribution should be
      truncated;
      deduce where local intensity distribution should be truncated;
      truncate local intensity distribution;
      find median of truncated local intensity distribution;
    } until median sufficiently close to mode of local distribution;
    transfer estimate of mode to output image space;
  }
} until sufficient enhancement of image;

```

---

*Comments:*

- (i) *The outermost and innermost loops can normally be omitted (i.e. they need to be executed once only).*
  - (ii) *The final estimate of the position of the mode can be performed by simple averaging instead of computing the median: this has been found to save computation with negligible loss of accuracy.*
  - (iii) *Instead of the minimum and maximum intensity values, the positions of the outermost octiles (for example) may be used to give more stable estimates of the extremes of the local intensity distribution.*
- 

## 3.5 RANK ORDER FILTERS

The principle employed in rank order filters is to take all the intensity values in a given neighborhood; to place these in order of increasing value; and finally to select the  $r$ th of the  $n$  values and return this value as the filter local output value. Clearly,  $n$  rank order filters can be specified in terms of the value  $r$  that is used, but these filters have the characteristic that they are intrinsically nonlinear, i.e., the output intensity cannot be expressed as a linear sum of the component intensities within the neighborhood. In particular, the median filter (for which  $r = (n + 1)/2$ , and which is only defined if  $n$  is odd) does not normally give the same output image as a mean filter; indeed, it is well known that the mean and median of a distribution are in general only coincident for symmetrical distributions. Note that minimum and maximum filters (corresponding to  $r = 1$  and  $r = n$ , respectively) are also often classed as morphological filters (see [Section 3.8.1](#)). Finally, for generality we point out that if  $n$  is even, it is usual to take the median as the mean of the central two values in the distribution.



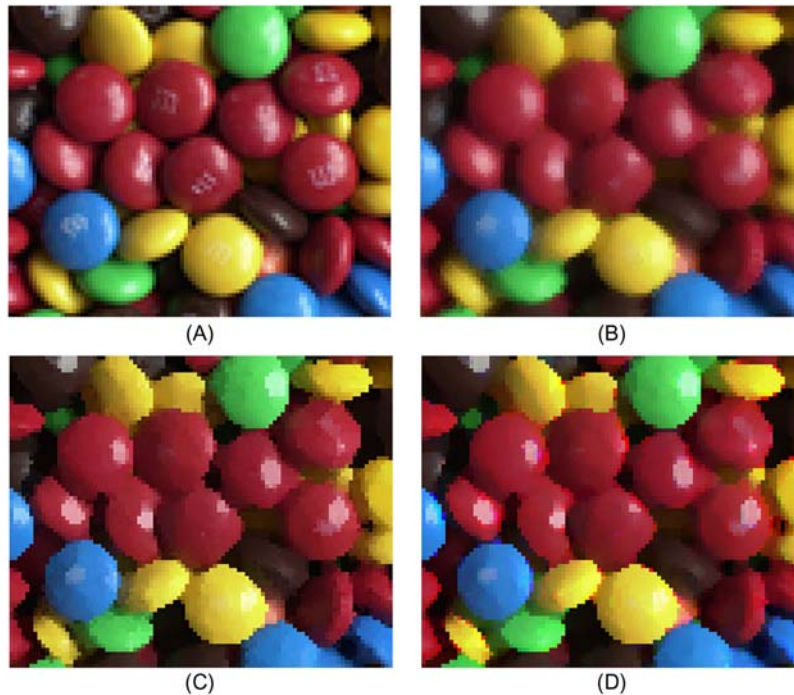


**FIGURE 3.12**

Color filtering of brightly colored objects. (A) Original color image of some sweets. (B) Vector median filtered version. (C) Vector mode filtered version. (D) Version to which a mode filter has been applied to each color channel separately. Note that (B) and (C) show no evidence of color bleeding, although it is strongly evident in (D). It is most noticeable as isolated pink pixels, plus a few green pixels, around the yellow sweets. For further details on color bleeding, see [Section 3.10](#).

© RPS 2004.

### 3.6 SHARP—UNSHARP MASKING

When images are blurred either before or as part of the process of acquisition, it is frequently possible to restore them to substantially their ideal state. Properly, this is achieved by making a model of the blurring process and applying an inverse transformation that is intended to cancel the blurring. This is a complex task to carry out rigorously but in some cases a rather simple method called sharp—unsharp masking is able to produce significant improvement (Gonzalez and Woods, 1992). As indicated in [Fig. 3.14](#), this technique involves first obtaining an even more blurred version of the image (e.g., with the aid of a Gaussian

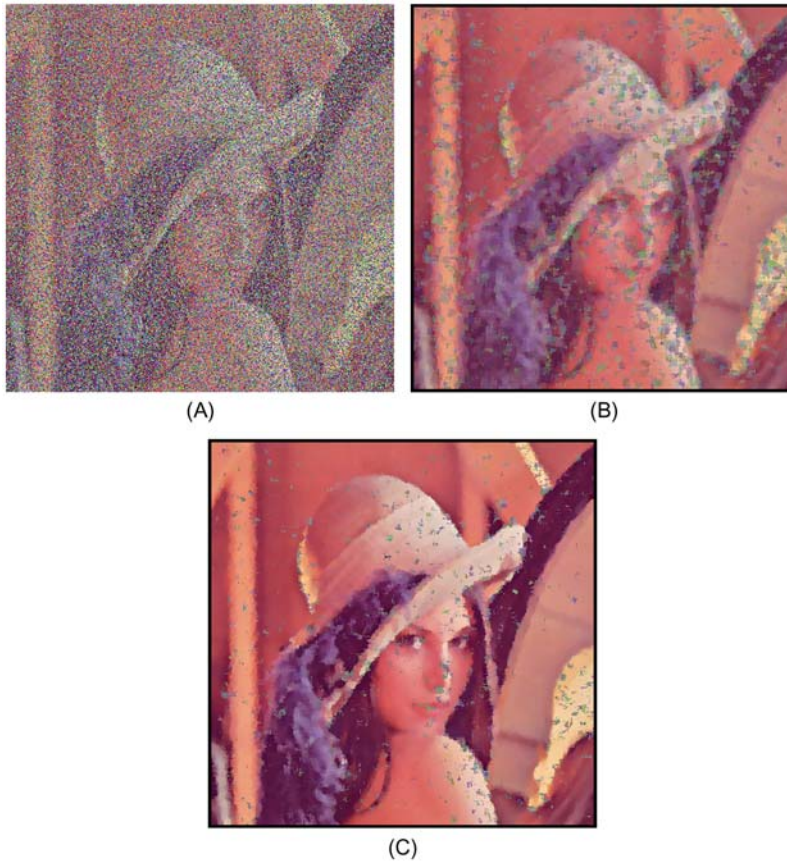


**FIGURE 3.13**

Color filtering of images containing substantial impulse noise. (A) Version of the Lena image containing 70% random color impulse noise. (B) Effect of applying a vector median filter, and (C) effect of applying a vector mode filter. While the mode filter is designed more for enhancement than for noise suppression, it has been found to perform remarkably well at this task when the noise level is very high.

© RPS 2004.

filter) and then subtracting this image from the original. Note that the amount of artificial blurring to apply and the proportion of the blurred image to subtract are rather arbitrary quantities that are normally adjusted by eye. Thus the method is better categorized under the heading “enhancement” than “restoration,” as it is not the precise mathematical technique normally understood by the latter term. Of such enhancement techniques, Hall (1979) states: “Much of the art of enhancement is knowing when to stop.”

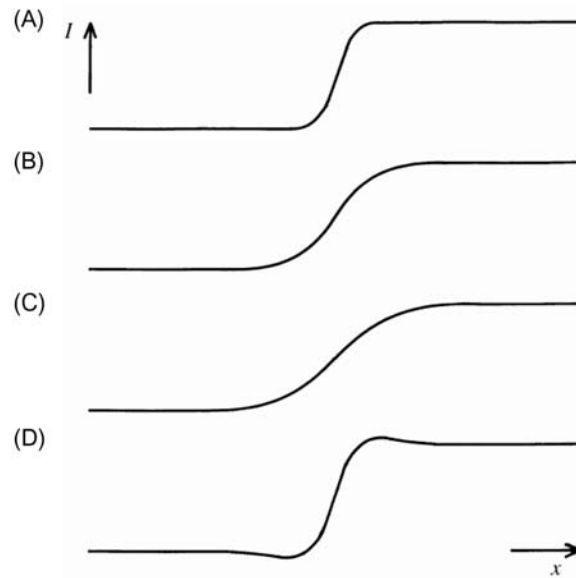


**FIGURE 3.14**

The principle of sharp–unsharp masking: (A) cross-section of an idealized edge; (B) observed edge; (C) artificially blurred version of (B); and (D) result of subtracting a proportion of (C) from (B).

### 3.7 SHIFTS INTRODUCED BY MEDIAN FILTERS

Despite knowing the main characteristics of the different types of filter, there are still some unknown factors. In particular, it is often important (e.g., when making precision measurements on manufactured components) to ensure that noise is removed in such a way that object locations and sizes are unchanged. However, at this point the following two problems arise.

First, it has been assumed that the intensity profile of an edge is symmetrical. If this is so, then the mean, median, and mode of the local intensity distribution will be coincident and there will clearly be no overall bias for any of them. However, when the edge profile is asymmetrical, it will not be obvious in the absence of a detailed model of the situation what the result will be for any of the filters. The situation becomes even more involved when significant noise is present, but then it becomes highly data-dependent and it is not profitable to analyze it further here.

The second problem concerns the situation for a curved edge. In this case there is again a variety of possibilities, and filters employing the different means will modify the edge position in ways that depend markedly on its shape. In vision applications the median filter is the one we are most likely to use, because its main purpose is to suppress noise without introducing blurring. Hence it is

worth considering in some detail the bias produced by this type of filter: this is done in the next subsection.

### 3.7.1 CONTINUUM MODEL OF MEDIAN SHIFTS

This section takes the case of a continuous image (i.e., a nondiscrete lattice), assuming that (1) the image is binary, (2) neighborhoods are exactly circular, and (3) images are noise-free. To proceed, we notice that binary edges have symmetrical cross-sections, while straight edges extend this symmetry into 2-D: hence applying a median filter in a (symmetrical) circular neighborhood cannot pull a straight edge to one side or the other.

Now consider what happens when the filter is applied to an edge that is not straight. If, for example, the edge is circular, the local intensity distribution will contain two peaks whose relative sizes will vary with the precise position of the neighborhood (Fig. 3.15). At some position the sizes of the two peaks will be identical. Clearly, this happens when the center of the neighborhood is situated at a point where the output of the median filter changes from dark to light (or vice versa). Thus the median filter produces an inward shift towards the center of a circular object (or the center of curvature), whether the object is dark on a light background or light on a dark background. To calculate the magnitude of this effect, we need to determine exactly where the area of a circular neighborhood is bisected by the object boundary.

We can obtain a good approximation to this by estimating the mean lateral displacement  $\bar{x}$  of the circular object within the neighborhood, which shows where the median of the area must be situated. First note from Fig. 3.16 that the object is a circle whose equation is:

$$(x-b)^2 + y^2 = b^2 \quad (3.4)$$

Hence

$$x = b - (b^2 - y^2)^{1/2} \approx \frac{y^2}{2b} \quad (3.5)$$

$$\therefore \bar{x} = \int_{-a}^a x dy / \int_{-a}^a dy \approx \frac{1}{2a} \int_{-a}^a \frac{y^2}{2b} dy = \frac{1}{2ab} \left[ \frac{y^3}{3} \right]_0^a = \frac{a^2}{6b} \quad (3.6)$$

Noting that the curvature of the object is  $\kappa = 1/b$ , we immediately deduce that the lateral shift is:

$$D = \frac{1}{6} \kappa a^2 \quad (3.7)$$

Note that this approximate calculation relies on the fact that for small curvatures the object boundary will pass through points on the neighborhood that are separated by a distance close to  $2a$ .

A full calculation (Davies 1989b) shows that, as might be expected, the median shift  $D \rightarrow 0$  as  $b \rightarrow \infty$  or as  $a \rightarrow 0$ . Conversely, the shift becomes very

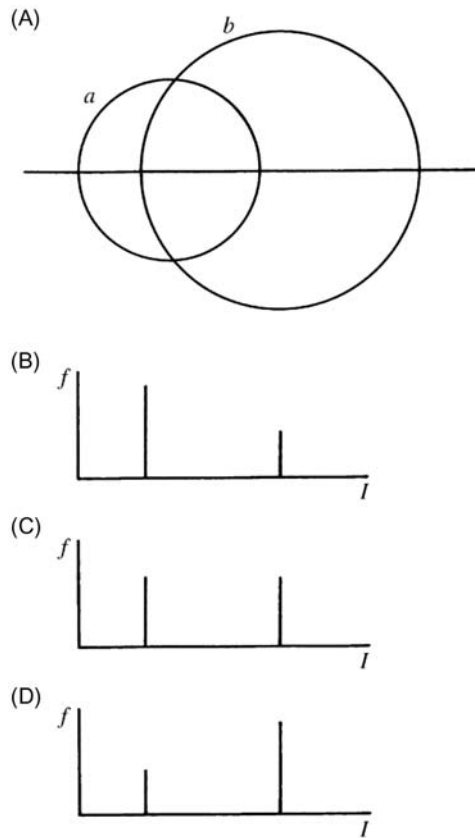


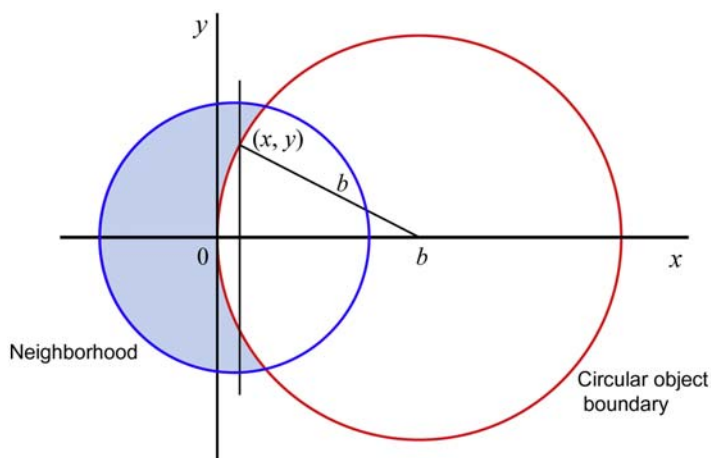
**FIGURE 3.15**

Variation in local intensity distribution with position of neighborhood: (A) neighborhood of radius  $a$  overlapping a dark circular object of radius  $b$ ; (B–D) intensity distributions  $f$  when the separations of the centers are, respectively, less than, equal to, or greater than the distance  $d$  for which the object bisects the area of the neighborhood.

large as  $a$  first approaches and then exceeds  $b$ . Note, however, that when  $a > \sqrt{2}b$ , the object is ignored, being small enough to be regarded as irrelevant noise by the filter: beyond this point it has no effect at all on the final image. The maximum edge shift before the object finally disappears is  $(2 - \sqrt{2})b \approx 0.586 b$ .

### 3.7.2 GENERALIZATION TO GRAYSCALE IMAGES

To extend these results to grayscale images, first consider the effect of applying a median filter near a smooth step edge in 1-D. Here the median filter gives zero shift, since for equal distances from the center to either end of the neighborhood

**FIGURE 3.16**

Geometry for calculating neighborhood and object overlap. The object is circular and has radius  $b$ ; the neighborhood is also circular and has radius  $a$ . The origin of the  $x$  and  $y$  axes is on the object boundary. The areas of the shaded and unshaded parts of the neighborhood are equal.

there are equal numbers of higher and lower intensity values and hence equal areas under the corresponding portions of the intensity histogram. Clearly, this is always valid where the intensity increases monotonically from one end of the neighborhood to the other.

Next, it is clear that for 2-D images, the situation is again unchanged in the vicinity of a straight edge, since the situation remains highly symmetrical. Hence the median filter gives zero shift, as in the binary case.

For curved boundaries, the situation has to be considered carefully for grayscale edges, which, unlike binary edges, have finite slope. When boundaries are roughly circular, contours of constant intensity often appear as in Fig. 3.17. To find how a median filter acts we merely need to identify the contour of median intensity (in 2-D the median intensity value labels a whole contour), which divides the area of the neighborhood into two equal parts. The geometry of the situation is identical to that already examined in Section 3.7.1: the main difference here is that for every position of the neighborhood, there is a corresponding median contour with its own particular value of shift depending on the curvature. Intriguingly, the formulae already deduced may immediately be applied for calculating the shift for each contour. Fig. 3.17 shows an idealized case in which the contours of constant intensity have similar curvature, so that they are all moved inwards by similar amounts. This means that to a first approximation, the edges of the object retain their cross-sectional profile as it becomes smaller.

For grayscale images the shifts predicted by this theory agree with experimental shifts within approximately 10% for a large range of circle sizes in a discrete lattice

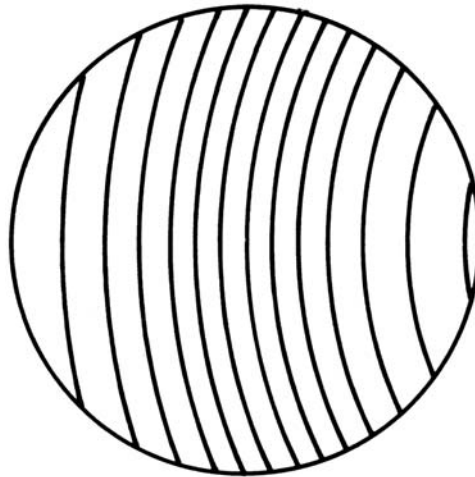


**FIGURE 3.17**

Contours of constant intensity on the edge of a large circular object, as seen within a small circular neighborhood.

(albeit with certain additional corrections but no approximations such as that made in Eq. (3.5): see Davies, 1989b) (Fig. 3.18). Figs. 3.19 and 3.20 give some indication of the magnitudes of these shifts in practical situations. Note that once image detail such as a small hole or screw thread has been eliminated by a filter, it is not possible to apply any edge shift correction formula to recover it, although for larger features such formulae are useful for deducing true edge positions.

Finally, we note that edge shifts are not avoided merely by choosing an alternative method of neighborhood averaging, but rather that they are intrinsic to the averaging process: in fact, they can be reduced by applying specially designed operators—see Nieminen et al. (1987), Greenhill and Davies (1994). In particular, mode and mean filters have been shown to produce shifts comparable in size to those generated by median filters—as shown in Table 3.3 (the fact that mean, median, and mode filters produce identical shifts for symmetrical step edges is obvious because the mean, median, and mode are coincident for symmetric distributions).

### 3.7.3 DISCRETE MODEL OF MEDIAN SHIFTS

It was noted in Section 3.7.2 that the median shifts predicted using the continuum model did not agree exactly with the experimental shifts, and for small values of  $b$  the discrepancies were quite substantial (Fig. 3.18). To eliminate this problem, investigation showed that a discrete model was required, with the positions of the pixels within the chosen neighborhood being explicitly defined (Davies, 1999c).

It is too tedious to recount the complete analysis of this approach here. Suffice it to say that it leads to essentially exact agreement between theory and

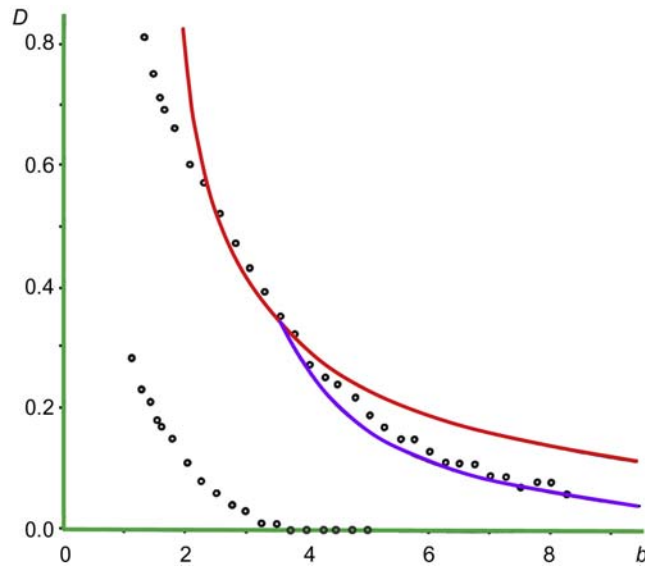


**FIGURE 3.18**

Edge shifts for  $5 \times 5$  median filter applied to a grayscale image. The upper set of plots represents the experimental results and the upper continuous curve is derived from the theory of Section 3.7.1. The lower continuous curve is derived from a more accurate model (Davies, 1989b). The lower set of plots represents the much reduced shifts obtained with the “detail-preserving” type of filter (see Section 3.16).

experiment over a wide range of values of  $\kappa$ , as shown in Fig. 3.21: the reason for the discrepancy for high values of  $\kappa$  is due to the limited intensity gradients that occur at edges in grayscale images.

Overall, the problem of median shifts is now well understood and is fully explained by using the discrete model. The continuum model turns out to be capable of giving accurate results only in the limiting case where  $a$  and  $b$  ( $= 1/\kappa$ ) are many pixels in size (i.e.,  $a, b \gg 1$ ).

### 3.8 SHIFTS INTRODUCED BY RANK ORDER FILTERS

This section is particularly concerned with rank order filters (Bovik et al., 1983), which form a whole family of filters that can be applied to digital images—often in combination with other filters of the family—in order to give a variety of effects (Goetcherian, 1980; Hodgson et al., 1985): other notable members of the family are max and min filters. Because rank order filters generalize the concept of the median filter, it is relevant to study the types of distortion they produce on straight and curved intensity contours. It should also be pointed out that these



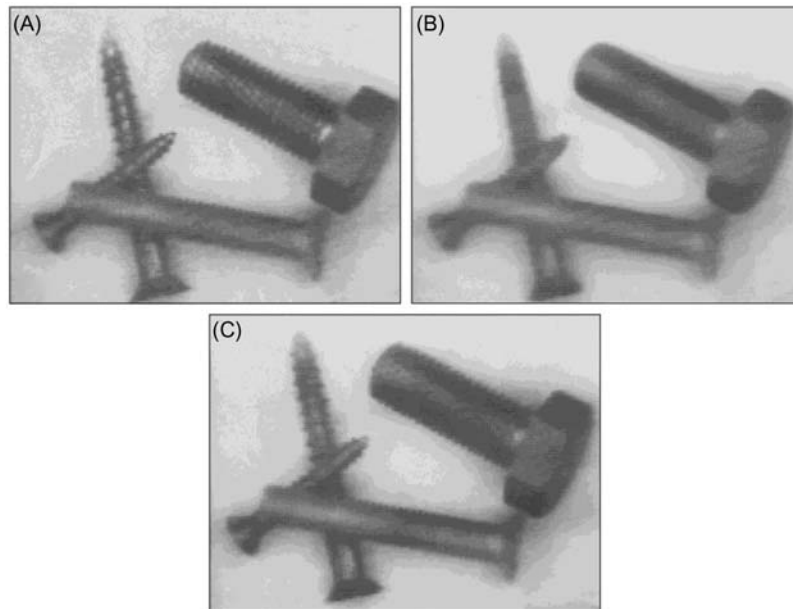


**FIGURE 3.19**

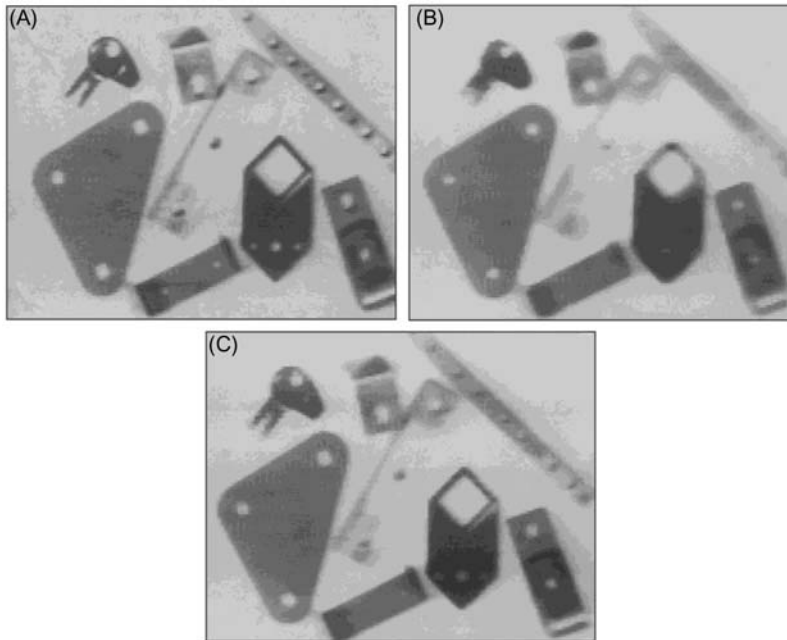
Edge smoothing property of the median filter. (A) Original image, (B) median filter smoothing of irregularities, in particular those around the boundaries (notice how the threads on the crews are virtually eliminated although detail larger in scale than half the filter area is preserved), using a 21-element filter operating within a  $5 \times 5$  neighborhood on a  $128 \times 128$  pixel image of 6-bit gray scale; (C) effect of the detail-preserving filter (see [Section 3.16](#)).

filters are of central importance in the design of filters for morphological image analysis and measurement. In addition, they have some advantages when used for this purpose in that they help to suppress noise (Harvey and Marshall, 1995), although the effect vanishes in the special cases of max and min filters.

[Section 3.8.1](#) examines the reasons underlying the shifts produced by rank order filters and indicates how their operation in rectangular neighborhoods can be calculated. It also examines the extent to which the theoretical predictions are borne out in practice by measurements of the shifts produced by  $5 \times 5$  rank order filters on circular discs of varying sizes.

### 3.8.1 SHIFTS IN RECTANGULAR NEIGHBORHOODS

In common with previous work on median shifts we here concentrate on the ideal noiseless case, in which the filter operates within a small neighborhood, over which the signal is basically a monotonically increasing intensity function in

**FIGURE 3.20**

Circular holes in metal objects before and after filtering: (A) original  $128 \times 128$  pixel image with 6-bit gray scale; (B)  $5 \times 5$  median-filtered image: the diminution in size of the hole is clearly visible and such distortions would have to be corrected for when taking measurement from real filtered images of this type; (C) result using a detail-preserving filter: some distortions are present although the overall result is much better than in (B).

**Table 3.3** Summary of Edge Shifts for Neighborhood Averaging Filters

Edge type	Mean	Filter	
		Median	Mode
Step	$\frac{1}{6}\kappa a^2$	$\frac{1}{6}\kappa a^2$	$\frac{1}{6}\kappa a^2$
Intermediate	$\sim \frac{1}{7}\kappa a^2$	$\frac{1}{6}\kappa a^2$	$\frac{1}{2}\kappa a^2$
Linear	$\frac{1}{8}\kappa a^2$	$\frac{1}{6}\kappa a^2$	$\frac{1}{2}\kappa a^2$

© IEE 1999.

some direction. The most complex intensity variation that will be considered is that in which the intensity contours have curvature  $\kappa$ . In spite of this simplification, valuable statements can still be made about the level of distortion likely to be produced in practice by rank order filters.

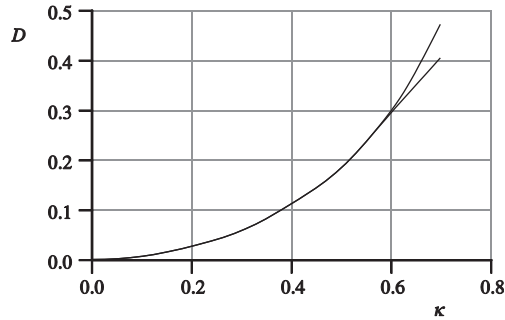


**FIGURE 3.21**

Comparisons of  $3 \times 3$  median shifts. The lower solid curve shows the non-approximated results of the discrete model (Davies, 1999f); the upper solid curve shows the results of experiments on grayscale circles.

© IEE 1999.

Because of the complexity of the calculations that arise in the case of rank order filters, which involve an additional parameter vis-à-vis the median filter, it is worth studying their properties first for the simple case of rectangular neighborhoods (Davies, 2000c). Let us presume that a rank order filter is being applied in a situation in which straight intensity contours are aligned parallel to the short sides of a rectangular neighborhood, which we initially take to be a  $1 \times n$  array of pixels (Fig. 3.22). In this case, we can assume without loss of generality that the successive pixels within the neighborhood will have *increasing* values of intensity. We next take the basic property of the rank order filter as being to take an intensity histogram of the local intensity distribution and return the value of the  $r$ th of the  $n$  intensity values within the neighborhood. This means that the rank order filter selects an intensity that has a separation  $B$  from the lowest intensity pixel of the neighborhood and  $C$  from the highest intensity pixel.

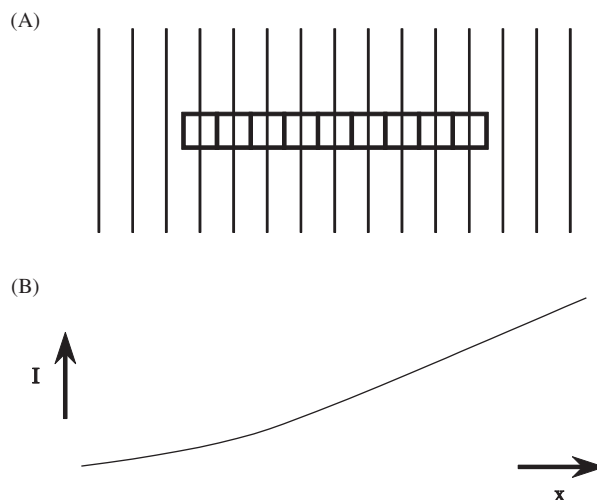
Starting with these considerations, Davies (2000c) developed the theory of the shifts for rank order filters. For clarity, in preference to  $r$ , he used a symmetric rank order parameter  $\eta$  varying smoothly from  $-1$  (for max filters) to  $+1$  (for min filters), with value 0 for median filters, where:

$$\eta = (n - 2r + 1)/(n - 1) \quad (3.8)$$

Proceeding to a continuum model and assuming a large number of pixels in any neighborhood (i.e.,  $n \rightarrow \infty$ ), the predicted shift is:

$$D = \eta a + \frac{1}{6} \kappa \tilde{a}^2 \quad (3.9)$$

where  $a$  and  $\tilde{a}$  are the half-length and half-width of the rectangular neighborhood, respectively. Rather than dwell on this formula, which only applies for

**FIGURE 3.22**

Basic situation for a rank-order filter in a rectangular neighborhood. This figure illustrates the problem of applying a rank-order filter within a rectangular neighborhood consisting of a  $1 \times n$  array of pixels. The intensity is taken to increase monotonically from left to right, as in (B); the intensity contours in (A) are taken to be parallel to the short sides of the neighborhood.

© RPS 2000.

low curvature contours in rectangular neighborhoods, we show graphically the result of refining the theory to cover the case of high curvature contours in circular neighborhoods (Fig. 3.23). Fig. 3.24 shows the actual shifts obtained in the particular case of a truncated  $5 \times 5$  neighborhood (Davies, 2000c): these are sufficiently similar to the theoretical graphs to demonstrate the conceptual validity of the theory, even when a more accurate discrete model is not employed.

It is important to note that these results are highly general and cover the special cases of max, min, and median filters. In particular, the median case arises when  $\eta = 0$  and is in agreement with the calculations of Section 3.7; and the max and min filters arise for  $\eta = -1$  and  $1$ , respectively. In the latter limiting cases, the shifts are  $D = -a$  and  $a$ , respectively, the results being independent of  $\kappa$ , all of which agrees with a priori notions of the meaning of max and min (intensity) in this context. Between the max and min filters, there is a continuous gradation of performance, with very significant but opposite shifts for the max and min filters, the two basic effects canceling out for median filters, although the cancellation is only exact for straight contours. The full situation is summarized in Fig. 3.23.

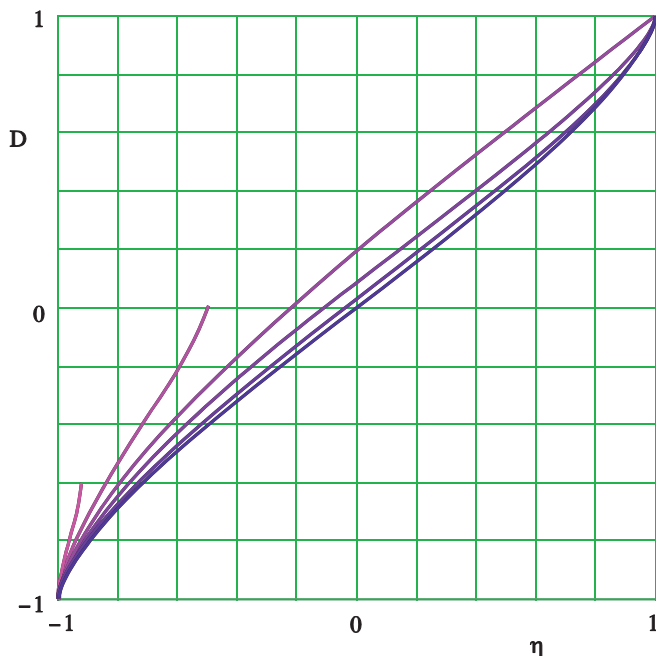


**FIGURE 3.23**

Graphs of shift  $D$  against rank-order parameter  $\eta$  for various  $\kappa$ . This diagram summarizes the operation of rank-order filters, with graphs, bottom to top, respectively, for  $\kappa = 0, 0.2/a, 0.5/a, 1/a, 2a, 5a$ . Note that graphs for which  $b < a$  ( $\kappa > 1/a$ ) apply for restricted ranges of  $\eta$  and  $D$  (see Section 3.8.1). A multiplier of  $a$  must be included in the  $D$ -values.

© RPS 2000.

### 3.9 THE ROLE OF FILTERS IN INDUSTRIAL APPLICATIONS OF VISION

It has been shown above how the median filter can successfully remove noise and artefacts such as spots and streaks from images. Unfortunately, many useful features such as fine lines and important points and holes are effectively indistinguishable from spots and streaks. In addition, it has been seen that the median filter “softens” pictures by removing fine detail. It is also found to clip corners of objects—another generally undesirable trait (but see Chapter 6: Corner, Interest Point, and Invariant Feature Detection). Finally, although it does not blur edges, it can still shift them slightly. In fact, shifting of curved edges seems likely to be a general characteristic of noise suppression filters.

Such distortions are quite alarming and mitigate against the indiscriminate use of filters. If applied in situations where accurate measurements are to be made on images, particular care must be taken to test whether the data are being biased in

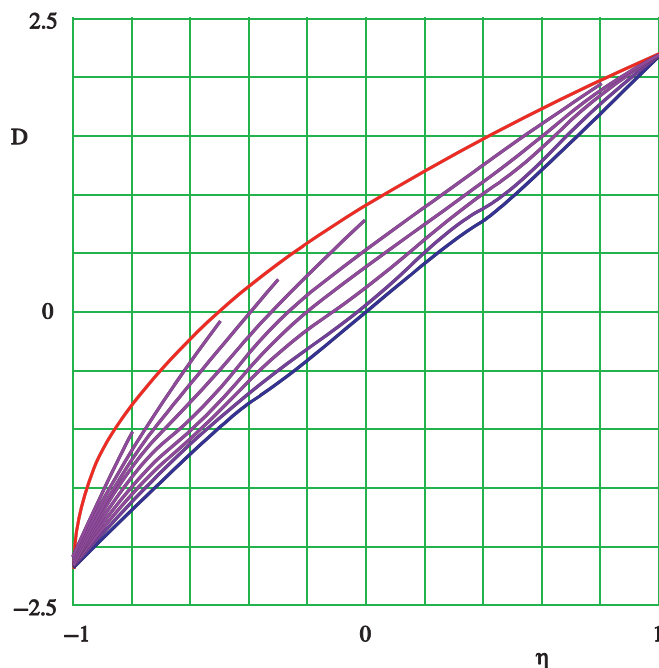


**FIGURE 3.24**

Shifts obtained for a typical discrete neighborhood. These shifts were obtained for rank-order filters operating within a truncated  $5 \times 5$  neighborhood when applied to eight discrete circular discs with radii ranging from 10.0 down to 1.25 pixels, the mean curvatures being 0.1–0.8 in steps of 0.1; the lowest curve was obtained by averaging the responses from circular discs of radius  $\pm 20.0$  pixels, with curvatures  $\pm 0.05$ , and to the given scale are indistinguishable from the result that would be obtained with zero curvature. The uppermost curve represents the theoretical limiting value. However, because of the directional effects that occur in the discrete case, the upper limit is actually lower than indicated by this curve (see text).

© RPS 2000.

any way. Although it is possible to make suitable corrections to the data, it seems a good general policy to employ noise removal filters only where they are absolutely essential for object visibility. The alternative is to employ edge detection and other operators that automatically suppress noise as an integral part of their function. This is the general approach taken in subsequent chapters: indeed, it is one of the principles underlined in this book that algorithms should be “robust” against noise or other artefacts that might upset measurements. There is quite significant scope for the design of robust algorithms, since images contain so much information that it is normally possible to arrange for erroneous information to be ignored.

### 3.10 COLOR IN IMAGE FILTERING

In Chapter 2, Images and Imaging Operations, it was indicated that color often adds to the complexity of image analysis algorithms and could also add to the associated computational costs. From these points of view color might, except for applications such as assessing the ripeness of a fruit, be regarded as an irrelevant luxury. Nevertheless, in the field of image processing and image filtering, where good quality images have to be presented to human operators, it is a vital concern. In fact, in recent years much effort has been devoted to the development of effective color filtering algorithms. Here we shall consider mainly median and related impulse noise filtering procedures.

Perhaps, the first point to note is that median filtering is defined in terms of sorting operations and is thus undefined in the color domain, which normally contains three dimensions. However, a simple solution is to apply a standard median filter to each of the color channels and then to reassemble the color image. Unfortunately, this approach leads to certain problems, the most obvious one being that of color “bleeding” (Fig. 3.12). This occurs when an impulse noise point appears in just one of the channels and is situated near an edge or other image feature. The case of an impulse noise point near an edge is hereby illustrated in simplified form:

```
Original:  0  0  0  0  1  0  1  1  1  1  1  1
Filtered:  ?  0  0  0  0  1  1  1  1  1  1  ?
```

We see that a three-element median filter eliminates the impulse noise point but at the same time moves the edge towards it. The end result for a color image is that the edge will be tinted with the color of the impulse noise point.

Fortunately, there is a standard solution to this problem. First, note that it is possible to express single-channel median filtering as the minimization of a distance metric, and this metric is trivially extendible to three-color channels (or indeed any number of channels). The relevant single channel metric is:

$$\text{median} = \arg \min_i \sum_j |d_{ij}| \quad (3.10)$$

where  $d_{ij}$  is the distance between sample points  $i$  and  $j$  in the single channel (gray scale) space; and “arg min” is a standard mathematical term that means the argument (here pixel intensity) corresponding to the index (here  $i$ ) giving rise to the minimum value of the following expression (here  $\sum_j |d_{ij}|$ ). In the three-color domain the metric is readily extended to:

$$\text{median} = \arg \min_i \sum_j |\tilde{d}_{ij}| \quad (3.11)$$

where  $\tilde{d}_{ij}$  is the generalized distance between sample points  $i$  and  $j$ , and we typically take the  $L_2$  norm to define the distance measure for three colors:

$$\tilde{d}_{ij} = \left[ \sum_{k=1}^3 (I_{i,k} - I_{j,k})^2 \right]^{1/2} \quad (3.12)$$

Here  $\mathbf{I}_i, \mathbf{I}_j$  are RGB vectors and  $I_{i,k}, I_{j,k}$  ( $k = 1, 2, 3$ ) are their color components.

While the resulting vector median filter (VMF) no longer treats the individual color components separately, it is by no means guaranteed to eliminate color bleeding completely. In fact, like the standard median, it replaces any noisy intensity  $\mathbf{I}_n$ , (including color) by the intensity  $\mathbf{I}_j$  of another pixel that exists in the same window—rather than by an ideal intensity  $\mathbf{I}$ . Hence color bleeding is only reduced but not eliminated. If indeed there is a confluence of colors at any one point in an image, even in the absence of any impulse noise, there is the possibility that these sorts of algorithms will become confused and inadvertently introduce small amounts of color bleeding: ultimately, the effect is due to the increased dimensionality of the data, which means that the algorithm has to contend with a greatly increased number of possible outcomes, in spite of being an ad hoc procedure which does not embody specific understanding of images.

Fig. 3.12 demonstrates the nature of color bleeding, albeit in the case of mode filtering. It shows vector median and vector mode filters to be remarkably free from color bleeding, but the same does not apply to scalar mode filters—for similar reasons to those indicated above for median filters.

---

## 3.11 DILATION AND EROSION IN BINARY IMAGES

### 3.11.1 DILATION AND EROSION

As we have seen in [Chapter 2, Images and Imaging Operations](#), dilation expands objects into the background and is able to eliminate “salt” noise within an object. It can also be used to remove cracks in objects, which are less than three pixels in width.

In contrast, erosion shrinks binary picture objects and has the effect of removing “pepper” noise. It also removes thin object “hairs” whose widths are less than three pixels.

As we shall see in more detail below, erosion is strongly related to dilation, in that a dilation acting on the inverted input image acts as an erosion, and vice versa.

### 3.11.2 CANCELLATION EFFECTS

An obvious question is whether erosions cancel out dilations, or vice versa. We can easily answer this question: for if a dilation has been carried out, salt noise and cracks will have been removed, and once they are gone, erosion cannot bring them back; hence exact cancellation will not in general occur. Thus, for the set  $S$  of object pixels in a general image  $I$ , we may write:

$$\text{erode}(\text{dilate}(S)) \neq S \quad (3.13)$$



equality only occurring for certain specific types of image (these will lack salt noise, cracks, and fine boundary detail). Similarly, pepper noise or hairs that are eliminated by erosion will not in general be restored by dilation:

$$\text{dilate}(\text{erode}(S)) \neq S \quad (3.14)$$

Overall, the most general statements that can be made are:

$$\text{erode}(\text{dilate}(S)) \supseteq S \quad (3.15)$$

$$\text{dilate}(\text{erode}(S)) \subseteq S \quad (3.16)$$

We may note, however, that large objects will be made one pixel larger all round by dilation and will be reduced by one pixel all round by erosion, so a considerable amount of cancellation will normally take place when the two operations are applied in sequence. This means that sequences of erosions and dilations provide a good basis for filtering noise and unwanted detail from images.

### 3.11.3 MODIFIED DILATION AND EROSION OPERATORS

It sometimes happens that images contain structures that are aligned more or less along the image axes directions, and in such cases it is useful to be able to process these structures differently. For example, it might be useful to eliminate fine vertical lines, without altering broad horizontal strips. In that case the following “vertical erosion” operator will be useful:

```
for all pixels in image do {
  sigma = A1 + A5;
  if (sigma < 2) B0 = 0; else B0 = A0;
}
```

(3.17)

although it will be necessary to follow it with a compensating dilation operator so that horizontal strips are not shortened:

```
for all pixels in image do {
  sigma = A1 + A5;
  if (sigma > 0) B0 = 1; else B0 = A0;
}
```

(3.18)

Here and elsewhere in this chapter, any operations required to restore the image to the original image space are not considered or included.

This example demonstrates some of the potential for constructing more powerful types of image filter. To realize these possibilities, we next develop a more general mathematical morphology formalism.

## 3.12 MATHEMATICAL MORPHOLOGY

### 3.12.1 GENERALIZED MORPHOLOGICAL DILATION

The basis of mathematical morphology is the application of set operations to images and their operators. We start by defining a generalized dilation mask as a

set of locations within a  $3 \times 3$  neighborhood. When referred to the center of the neighborhood as origin, each of these locations causes a shift of the image in the direction defined by the vector from the origin to the location. When several shifts are prescribed by a mask, the 1 locations in the various shifted images are combined by a set union operation.

The simplest example of this type is the identity operation that leaves the image unchanged:



(Notice that we leave the 0's out of this mask, as we are now focusing on the set of elements at the various locations, and set elements are either present or absent.)

The next operation to consider is:



which is a left shift, equivalent to the one discussed in [Section 2.2](#). Combining the two operations into a single mask:



leads to a horizontal thickening of all objects in the image, by combining it with a left-shifted version of itself. An isotropic thickening of all objects is achieved by the operator:



(clearly, this is equivalent to the dilation operator discussed in [Sections 2.2](#) and [3.11](#)), while a symmetrical horizontal thickening operation (see [Section 3.11.3](#)) is achieved by the mask:



A rule of such operations is that if we want to guarantee that all the original object pixels are included in the output image, then we must include a 1 at the center (origin) of the mask.

Finally, there is no compulsion for all masks to be  $3 \times 3$ . Indeed, all but one of those listed above are effectively smaller than  $3 \times 3$ , and in more complex cases larger masks could be used. To emphasize this point, and to allow for asymmetrical masks in which the full  $3 \times 3$  neighborhood is not given, we shall shade the origin, as shown in the above cases.

### 3.12.2 GENERALIZED MORPHOLOGICAL EROSION

We now move on to describe erosion in terms of set operations. The definition is somewhat peculiar in that it involves reverse shifts, but the reason for this will become clear as we proceed. Here the masks define directions as before, but in this case we shift the image in the reverse of each of these directions and perform intersection operations to combine the resulting images. For masks with a single element (as for the identity and shift left operators of [Section 3.12.1](#)), the intersection operation is improper and the final result is as for the corresponding dilation operator but with a reverse shift. For more complex cases the intersection operation results in objects being reduced in size. Thus the mask:

1	1	

has the effect of stripping away the left sides of objects (the object is moved right and ANDed with itself). Similarly, the mask:

1	1	1
1	1	1
1	1	1

results in an isotropic stripping operation and is hence identical to the erosion operation described in [Section 3.11.1](#).

### 3.12.3 DUALITY BETWEEN DILATION AND EROSION

We shall write the dilation and erosion operations formally as  $A \oplus B$  and  $A \ominus B$ , respectively, where  $A$  is an image and  $B$  is the mask of the relevant operation:

$$A \oplus B = \cup_{b \in B} A_b \quad (3.19)$$

$$A \ominus B = \cap_{b \in B} A_{-b} \quad (3.20)$$

In these equations,  $A_b$  indicates a basic shift operation in the direction of element  $b$  of  $B$  and  $A_{-b}$  indicates the reverse shift operation.

We next state two important theorems relating the dilation and erosion operations:

$$(A \ominus B)^c = A^c \oplus B^r \quad (3.21)$$

$$(A \oplus B)^c = A^c \ominus B^r \quad (3.22)$$

where  $A^c$  represents the complement of  $A$ , and  $B^r$  represents the reflection of  $B$  in its origin. Proofs of these theorems have been given by Haralick et al. (1987).

The fact that there are two such closely related theorems, following the related union and intersection definitions of dilation and erosion given above, indicates an important duality between the two operations. Indeed, as stated earlier, erosion of the objects in an image corresponds to dilation of the background, and vice versa. However, this relation is not absolutely trivial, on account of the reflections of the masks required in the two cases. It is perhaps curious that, in contrast with the case of the de Morgan rule for complementation of an intersection,

$$(P \cap Q)^c = P^c \cup Q^c \quad (3.23)$$

the effective complementation of the dilating or eroding mask is its reflection rather than its complement *per se*, while that for the operator is the alternate operator.

### 3.12.4 PROPERTIES OF DILATION AND EROSION OPERATORS

Dilation and erosion operators have some very important and useful properties. First, note that successive dilations are associative:

$$(A \oplus B) \oplus C = A \oplus (B \oplus C) \quad (3.24)$$

whereas successive erosions are not. In fact, the corresponding relation for erosions is:

$$(A \ominus B) \ominus C = A \ominus (B \oplus C) \quad (3.25)$$

Clearly, the apparent symmetry between the two operators is more subtle than their simple origins in expanding and shrinking might indicate.

Next, the property:

$$X \oplus Y = Y \oplus X \quad (3.26)$$

means that the order in which dilations of an image are carried out does not matter and the same applies to the order in which erosions are carried out:

$$(A \oplus B) \oplus C = (A \oplus C) \oplus B \quad (3.27)$$

$$(A \ominus B) \ominus C = (A \ominus C) \ominus B \quad (3.28)$$

In addition to the above relations, which use only the morphological operators  $\oplus$  and  $\ominus$ , there are many more relations that involve set operations. In the

examples that follow, great care must be exercised to note which particular distributive operations are actually valid:

$$A \oplus (B \cup C) = (A \oplus B) \cup (A \oplus C) \tag{3.29}$$

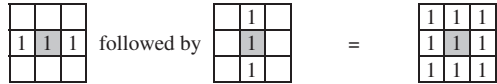
$$A \ominus (B \cup C) = (A \ominus B) \cap (A \ominus C) \tag{3.30}$$

$$(A \cap B) \ominus C = (A \ominus C) \cap (B \ominus C) \tag{3.31}$$

In certain other cases, where equality might a priori have been expected, the strongest statements that can be made are typified by the following:

$$A \ominus (B \cap C) \supseteq (A \ominus B) \cup (A \ominus C) \tag{3.32}$$

Note that the associative relations are of value in showing how large dilations and erosions might be factorized so that they can be implemented more efficiently as two smaller dilations and erosions applied in sequence. Similarly, the distributive relations show that a large mask may be split into two separate masks, which may then be applied separately and the resulting images *OR*ed together to create the same final image. These approaches can be useful for providing efficient implementations, especially in cases where very large masks are involved. For example, we could dilate an image horizontally and vertically by two separate operations, which would then be merged together, as in the following instance:



Next, let us consider the importance of the identity operation  $I$ , which corresponds to a mask with a single 1 at the central (A0) position:



By way of example, we take Eqs. (3.29) and (3.30) and replace  $C$  by  $I$  in each of them. If we write the union of  $B$  and  $I$  as  $D$ , so that mask  $D$  is bound to contain a central 1 (i.e.,  $D \supseteq I$ ), we have:

$$A \oplus D = A \oplus (B \cup I) = (A \oplus B) \cup (A \oplus I) = (A \oplus B) \cup A \tag{3.33}$$

which always contains  $A$ :

$$A \oplus D \supseteq A \tag{3.34}$$

Similarly:

$$A \ominus D = A \ominus (B \cup I) = (A \ominus B) \cap (A \ominus I) = (A \ominus B) \cap A \tag{3.35}$$

which is always contained within  $A$ :

$$A \ominus D \subseteq A \tag{3.36}$$

Operations (such as dilation by a mask containing a central 1), which give outputs that are guaranteed to contain the inputs are termed *extensive*, while those (such as erosion by a mask containing a central 1) for which the outputs are guaranteed to be contained by the inputs are termed *antiextensive*. Clearly, extensive operations extend objects and antiextensive operations contract them, or in either case, leave them unchanged.

Another important type of operation is the *increasing* type of operation. An increasing operation is one such as union that preserves order in the size of the objects on which it operates. If object  $F$  is small enough to be contained within object  $G$ , then applying erosions or dilations will not affect the situation, although the objects change their sizes and shapes considerably. We can write these conditions in the form:

if

$$F \subseteq G \tag{3.37}$$

then

$$F \oplus B \subseteq G \oplus B \tag{3.38}$$

and

$$F \ominus B \subseteq G \ominus B \tag{3.39}$$

Next, we note that erosion can be used for locating the boundaries of objects in binary images:

$$P = A - (A \ominus B) \tag{3.40}$$

Technically, we are here dealing with sets, and the appropriate set operation is the ANDNOT function  $\setminus$  rather than minus. However, the latter admirably conveys the required meaning without ambiguity.

There are many practical applications of dilation and erosion, which follow particularly from using them together, as we shall see below.

Finally, we explore why the morphological definition of erosion involves a reflection. The idea is that dilation and erosion are able, under the right circumstances, to cancel each other out. Take the left shift dilation operation and the right shift erosion operation. These are both achieved via the mask:



but in the erosion operation it is applied in its reflected form, thereby producing the right shift required to erode the left edge of any objects. This makes it clear why an operation of the type  $(A \oplus B) \ominus B$  has a chance of canceling to give  $A$ .

More specifically, there must be shifts in opposite directions as well as appropriate subtractions produced by ANDing instead of ORing in order for cancellation to be possible. Of course, in many cases the dilation mask will have 180° rotation symmetry, and then the distinction between  $B^r$  and  $B$  will be purely academic.

### 3.12.5 CLOSING AND OPENING

Dilation and erosion are basic operators from which many others can be derived. Earlier, we were interested in the possibility of an erosion canceling a dilation, and vice versa. Hence it is an obvious step to define two new operators that express the degree of cancellation: the first is called *closing* since it often has the effect of closing gaps between objects; the other is called *opening* because it often has the effect of opening gaps (Fig. 3.25). Closing ( $\bullet$ ) and opening ( $\circ$ ) are formally defined by the formulae:

$$A \bullet B = (A \oplus B) \ominus B \quad (3.41)$$

$$A \circ B = (A \ominus B) \oplus B \quad (3.42)$$

Closing is able to eliminate salt noise, narrow cracks, or channels and small holes or concavities: we continue to take the convention that dark objects have become 1's in binary images, and light background or other features have become 0's. Opening is able to eliminate pepper noise, fine hairs, and small protrusions. Thus these operators are extremely important for practical applications. Furthermore, by subtracting the derived image from the original image, it is possible to locate many sorts of defect, including those cited above as being eliminated by opening and closing: this possibility makes the two operations even more important. For example, we might use the following operation to locate all the fine hairs in an image:

$$Q = A - A \circ B \quad (3.43)$$

This operator and its dual using opening:

$$R = A \bullet B - A \quad (3.44)$$

are extremely important for defect detection tasks. They are often respectively called the white and black “top hat” operators. It is dubious whether “top hat” is a very appropriate name for this type of operator: a priori, the term “residue function” (or simply “residue”) would appear to be better, as it conjures up the right functional connotations. Practical applications of these two operators include location of solder bridges and cracks in printed circuit board tracks.

Closing and opening have the interesting property that they are idempotent: this means that repeated application of either operation has no further effect (this property contrasts strongly with what happens when dilation and erosion are applied a number of times). We can write these results formally as follows:

$$(A \bullet B) \bullet B = A \bullet B \quad (3.45)$$

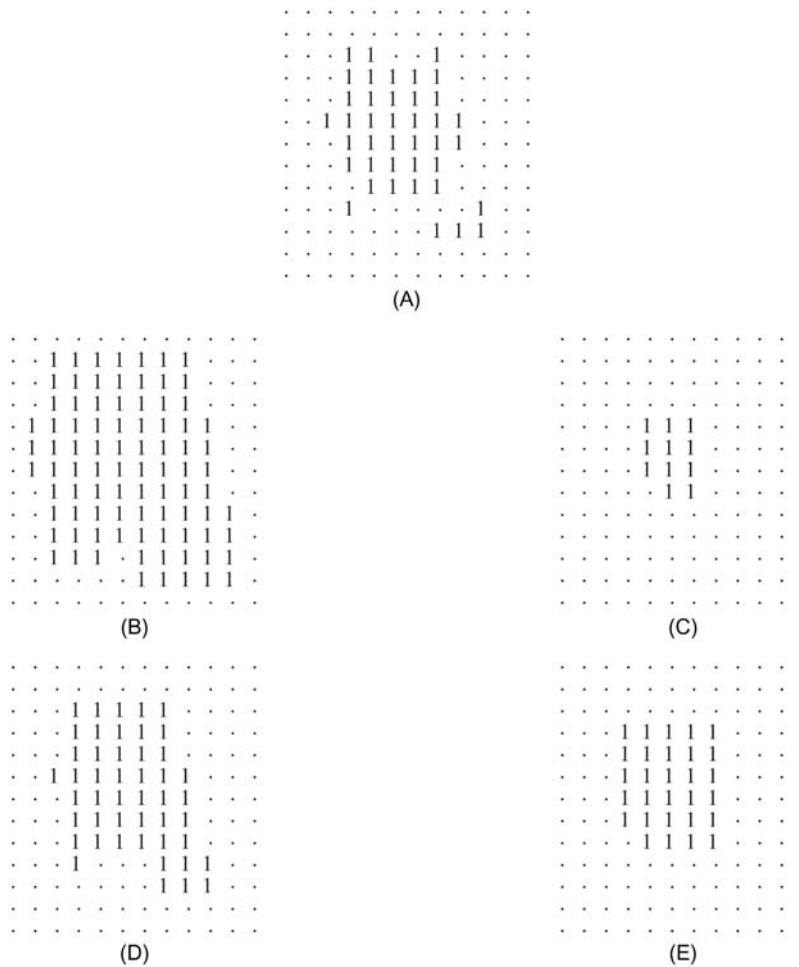


**FIGURE 3.25**

Results of morphological operations. (A) The original image; (B) the dilated image; (C) the eroded image; (D) the closed image; and (E) the opened image.

© World Scientific 2000.

$$(A \circ B) \circ B = A \circ B \tag{3.46}$$

From a practical point of view these properties are to be expected, since any hole or crack that has been filled in remains filled in, and there is no point in repeating the operation. Similarly, once a hair or protrusion has been removed, it cannot again be removed without first recreating it. Not quite so obvious is the fact that the combined closing and opening operation is idempotent:



$$\{[(A \bullet B) \circ C] \bullet B\} \circ C = (A \bullet B) \circ C \quad (3.47)$$

The same applies to the combined opening and closing operation. A simpler result is the following:

$$(A \oplus B) \circ B = (A \oplus B) \quad (3.48)$$

which shows that there is no point in opening with the same mask that has already been used for dilation: essentially, the first dilation produces some effects that are not reversed by the erosion (in the opening operation), and the second dilation then merely reverses the effects of the erosion. The dual of this result is also valid:

$$(A \ominus B) \bullet B = (A \ominus B) \quad (3.49)$$

There are a number of other properties of closing and opening; among the most important ones are the following set containment properties that apply when  $D \supseteq I$ :

$$A \oplus D \supseteq A \bullet D \supseteq A \quad (3.50)$$

$$A \ominus D \subseteq A \circ D \subseteq A \quad (3.51)$$

Thus, closing an image will if anything increase the sizes of objects, while opening an image will if anything make objects smaller, although there are clear limits on how much change closing and opening operations can induce.

Finally, note that closing and opening are subject to the same duality as for dilation and erosion:

$$(A \bullet B)^c = A^c \circ B^f \quad (3.52)$$

$$(A \circ B)^c = A^c \bullet B^f \quad (3.53)$$

### 3.12.6 SUMMARY OF BASIC MORPHOLOGICAL OPERATIONS

The past few sections have by no means exhausted the properties of the morphological operations dilate, erode, close, and open. However, they have outlined some of their properties and have demonstrated some of the practical results obtained using them. Perhaps the main aim of including the mathematical analysis has been to show that these operations are not ad hoc, and that their properties are mathematically provable. Furthermore, the analysis has also indicated (1) how sequences of operations can be devised for a number of eventualities and (2) how sequences of operations can be analyzed to save computation (for instance) by taking care not to use idempotent operations repeatedly and by breaking masks down into smaller more efficient ones.

Overall, the operations devised here can help to eliminate noise and irrelevant artefacts from images, so as to obtain more accurate recognition of shapes; they can also help to identify defects on objects by locating specific features of interest. In addition, they can perform grouping functions such as locating regions of

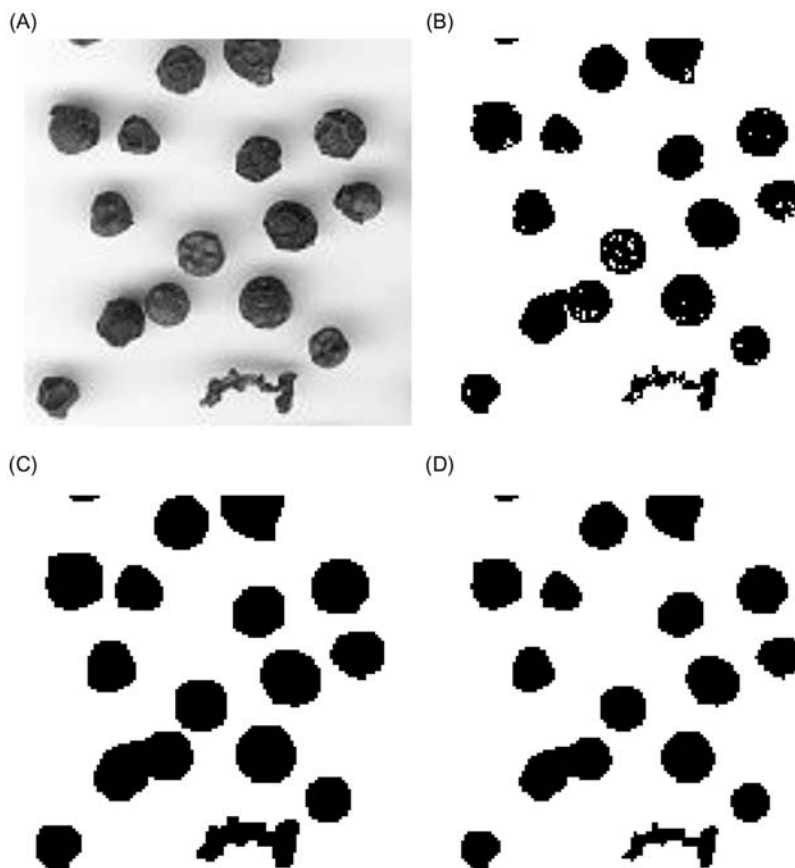
images where small objects such as seeds may reside (Section 3.13). In general, elimination of artefacts is carried out by operations such as closing and opening, while location of such features is carried out by finding how the results of these operations differ from the original image (cf. Eqs. (3.29) and (3.30)); and locating regions where clusters of small objects occur may be achieved by larger scale closing operations. Clearly, care in the choice of scales and mask sizes is of vital importance in the design of complete algorithms for all these tasks. Figs. 3.26 and 3.27 illustrate some of these possibilities in the case of a peppercorn image: some of the interest in this image relates to the presence of a twiglet and how it is eliminated from consideration and/or identified.

---

### 3.13 MORPHOLOGICAL GROUPING

Texture analysis is an important area of machine vision and is relevant not only for segmenting one region of an image from another (as in many remote sensing applications) but also for characterizing regions absolutely. Chapter 7, Texture Analysis, describes a number of approaches to texture analysis. While some of these require considerable computation, there are others that involve much less computation and which are applicable when the textures are particularly simple. For example, if it is required to locate regions containing small objects, simple morphological operations applied to thresholded versions of the image are often appropriate (Fig. 3.28) (Bangham and Marshall, 1998). Such approaches can be used for locating regions containing seeds, grains, nails, sand, or other materials, either for assessing the overall quantity or spread or for determining whether there are regions that have not yet been covered. The basic operation to be applied is the dilation operation, which combines the individual particles into fully connected regions. This method is suitable not only for connecting individual particles but also for separating regions containing high and low densities of such particles. The expansion characteristic of the dilation operation can be largely canceled by a subsequent erosion operation, using the same morphological kernel. Indeed, if the particles are always convex and well separated, the erosion should exactly cancel the dilation, although in general the combined closing operation is not a null operation, and this is relied upon in the above connecting operation.

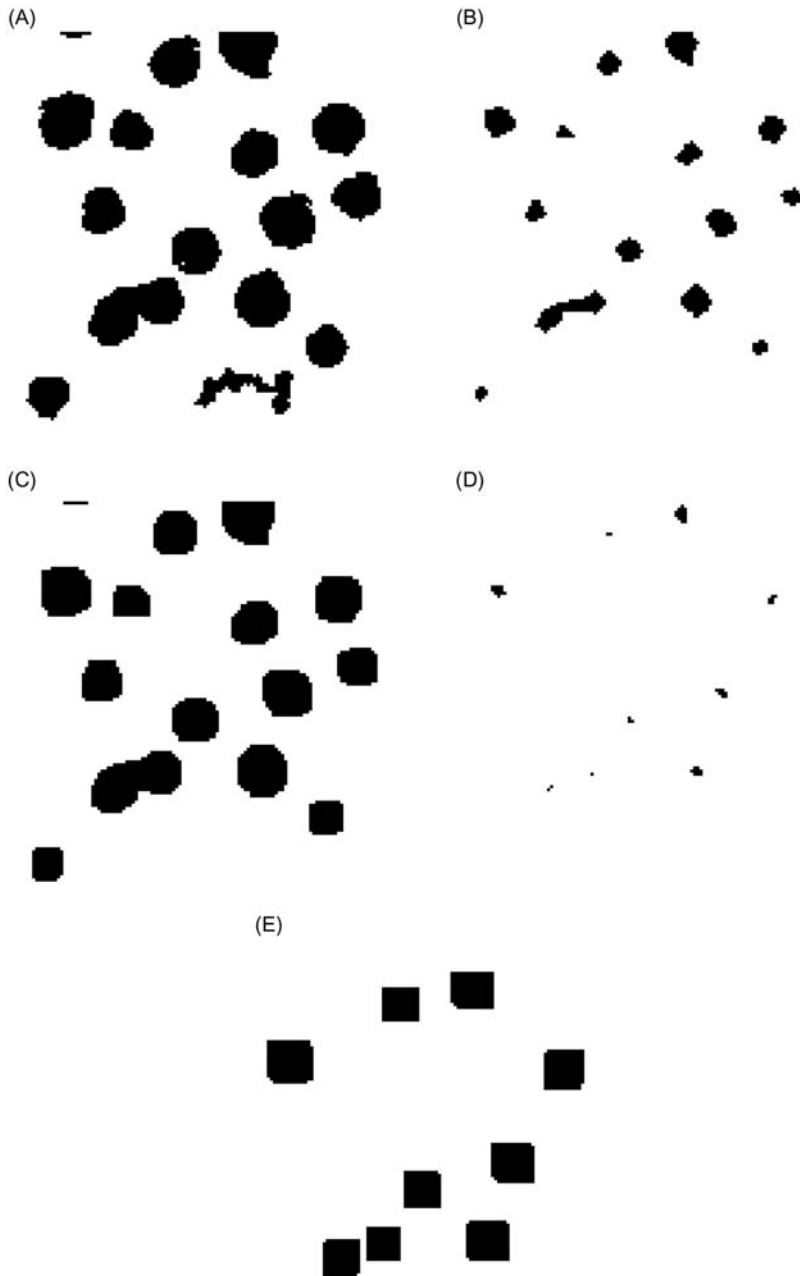
We next look at a simple inspection application and find that a slightly more sophisticated approach can lead to improved results. The application in question is the location of rodent droppings lying on a bed of cereal grains, as indicated in Fig. 3.29A. Fig. 3.29B shows a thresholded version of the original figure, which achieves a fair degree of detection of the contaminants. The obvious way of eliminating the undesirable speckled background is obtained by applying an erosion, followed by a dilation to restore the contaminants to their original sizes and shapes: the effect of this procedure is shown in Fig. 3.29C. Note that the method has been successful in eliminating the shadows between the grains but has been

**FIGURE 3.26**

Use of the closing operation. (A) A peppercorn image; (B) the result of thresholding; (C) the result of applying a  $3 \times 3$  dilation operation to the object shapes; and (D) the effect of subsequently applying a  $3 \times 3$  erosion operation. The overall effect of the two operations is a “closing” operation. In this case closing is useful for eliminating the small holes in the objects: this would, for example, be useful for helping to prevent misleading loops from appearing in skeletons. For this picture, extremely large window operations would be required to group peppercorns into regions.

© World Scientific 2000.

decidedly weak in coping with light regions on the contaminants. Remembering that while considerable uniformity might be expected between grains, the same cannot be said about rodent droppings, whose size, shape, and color vary quite markedly. Hence the erosion–dilation schema has limited effectiveness. To tackle this problem, it seemed worth attempting to consolidate the contaminants by applying dilation before erosion in order to eliminate any speckle or small light

**FIGURE 3.27**

Use of the opening operation. (A) A thresholded peppercorn image; (B) the result of applying a  $7 \times 7$  erosion operation to the object shapes; and (C) the effect of subsequently applying a  $7 \times 7$  dilation operation to the eroded image. (Continued)

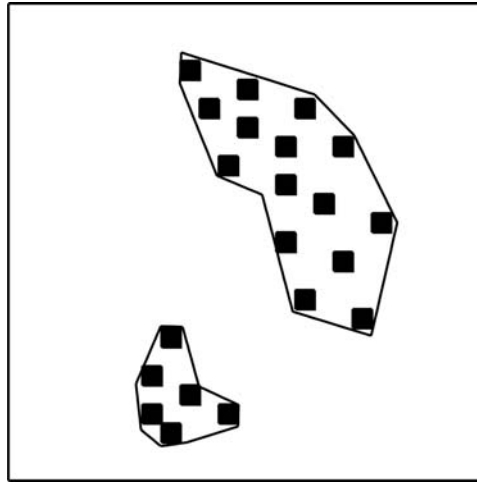


**FIGURE 3.28**

Idealized grouping of small objects into regions, such as might be attempted using closing operations.

© IEE 2000.

patches on them. The effect of this approach is shown in Fig. 3.29D. Notice that the result is to consolidate the shadows between grains even more than the shapes of the contaminants. Even when an additional few erosions are applied (Fig. 3.29E), the consolidated shadows do not disappear and are of comparable sizes to the contaminants. Hence the approach is not viable and creates more problems than it solves.

An alternative strategy was to try to consolidate the foreground and the background *simultaneously* by applying a large median filter to the thresholded image, as shown in Fig. 3.29F. This gives good segmentation of the contaminants, retaining their intrinsic shape to a reasonable degree: it also suppresses the shadows between grains quite well. In fact, the shadows immediately around the contaminants enhance the sizes of the latter in the median filtered image, while some shadows further away are consolidated and retained by the median filtering. As a final step in the analysis, it was found useful to perform a final erosion operation (Fig. 3.29G): this eliminates the extraneous shadows and brings the contaminants

- 
- ◀ applying a  $7 \times 7$  dilation operation. The overall effect of the two operations is an “opening” operation. In this case opening is useful for eliminating the twiglet. (D) and (E) The same respective operations when applied within an  $11 \times 11$  window. Here some size filtering of the peppercorns has been achieved and all the peppercorns have been separated, thereby helping with subsequent counting and labeling operations.

© World Scientific 2000.

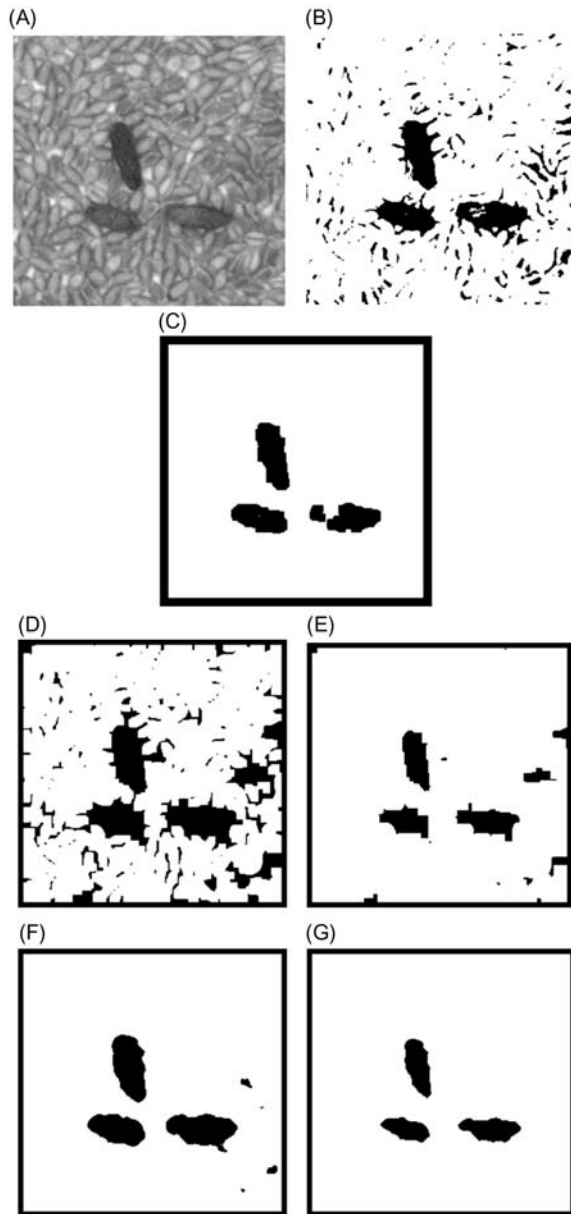


**FIGURE 3.29**

Effects of various operations and filters on a grain image. (A) Grain image containing several contaminants (rodent droppings). (B) Thresholded version of (A). (C) Result of erosion and dilation on (B). (D) Result of dilation and erosion on (B). (E) Result of erosion  
(Continued)

back to something like their proper size and shape. Overall, as is evident from Fig. 3.29G, the median filtering–erosion schema gave easily the greatest fidelity to the original contaminants, while being particularly successful at eliminating other artefacts (Davies et al. 1998). In this case it seems that the median filter is acting as an analytical device that carefully meditates and obtains the final result in a single rigorous stage, thereby avoiding the error-propagation inherent in a two-stage process.

---

### 3.14 MORPHOLOGY IN GRAYSCALE IMAGES

The generalization of morphology to grayscale images can be achieved in a number of ways. A particularly simple approach is to employ “flat” structuring elements. These perform morphological processing in the same way for each of the gray levels, acting as if the shapes at each level were separate, independent binary images. If dilation is carried out in this way, the result turns out to be identical to the effect of applying an intensity maximum operation of the same shape: i.e., we replace set inclusion by a magnitude comparison; needless to say, this is mathematically identical in action for a normal binary image, but when applied to a grayscale image it neatly generalizes the dilation concept. Similarly, erosion can be carried out by applying a minimum intensity structuring element of the same shape as the original binary structuring element. This discussion assumes that we focus on light objects against dark backgrounds. In fact, this is the opposite convention to that employed in Chapter 2, Images and Imaging Operations, but, as we shall see below, in grayscale processing it is probably more general to focus on intensities rather than on specific objects. Thus, light objects will be dilated when the maximum intensity operation is applied and eroded when the minimum intensity operation is applied; we could of course reverse the convention, depending on what type of objects we are concentrating on at any moment or in any application. We can summarize the situation as follows:

$$A \oplus B = \max_{b \in B} A_b \quad (3.54)$$

$$A \ominus B = \min_{b \in B} A_{-b} \quad (3.55)$$

There are other more complex grayscale analogs of dilation and erosion: these take the form of 3-D structuring elements whose output at any gray level depends not just on the shape of the image at that gray level but also on the shapes at a number of nearby gray levels. While such “nonflat” structuring elements are

---

◀ on (D). (F) Result of applying  $11 \times 11$  median filter to (B). (G) Result of erosion on (F). In all cases, “erosion” means three applications of the basic  $3 \times 3$  erosion operator, and similarly for “dilation.”

useful, for a good many applications they are not necessary, as flat structuring elements already embody a very considerable amount of generalization relative to the binary case.

We complete this section by showing that generalization to nonflat structuring is not unduly complex—far from it. In the case of the max operation the generalized form for a 1-D grayscale image of intensity  $I$  is simply:

$$(I \oplus K)(x) = \max[I(x - z) + K(z)] \quad (3.56)$$

where  $K(z)$  is the structuring element. In fact, it is much neater to present the operation geometrically as shown in Fig. 3.30, for the case of a triangular structuring element. Here the function  $K(z)$  appears as an inverted template, which is run over the image  $I(x)$  in such a way as to remain just in contact with it. Thus the origin of the inverted template traces out the top surface of the dilated image. The geometric presentation of Fig. 3.30 has the advantage of helping to visualize how the generalized operation works for 2-D images.

Similar relations apply for erosion, closing, opening, and a variety of set functions. This means that the standard binary morphological relations, Eqs. (3.24)–(3.32), apply for grayscale images as well as for binary images. Furthermore, the dilation–erosion and closing–opening dualities (Eqs. (3.21), (3.22), (3.52), and (3.53)) also apply for grayscale images. These are extremely powerful results and allow one to apply morphological concepts in an intuitive manner. In that

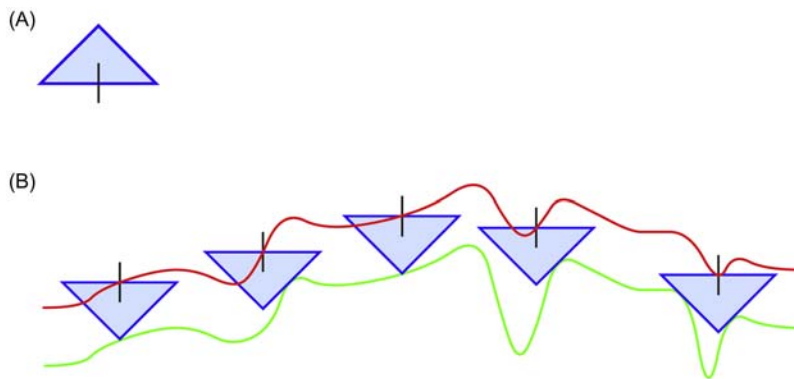


**FIGURE 3.30**

Dilation of 1-D grayscale image by triangular structuring element. (A) The structuring element, with the vertical line at the bottom indicating the origin of coordinates; (B) the original image (lower, continuous green line), several instances of the inverted structuring element being applied, and the output image (upper, continuous red line). This geometric construction automatically takes account of the maximum operation in Eq. (3.56). Note that as no part of the structuring element is below the origin in (A), the output intensity is increased at every point in the image.



case the practically important factor devolves into choosing the right gray scale structuring element for the application.

---

### 3.15 CONCLUDING REMARKS

Although this chapter has dwelt on the implementation of noise suppression and image enhancement operators based on the local intensity distribution, it has made certain other points. In particular, it has shown the need to make a specification of the required imaging process and only then to work out the algorithm design strategy. Not only does this ensure that the algorithm will perform its function effectively but also it makes it possible to optimize it for various practical criteria including speed, storage, and other parameters of interest. In addition, this chapter has demonstrated that any undesirable properties of the chosen design strategy—such as the inadvertent shifting of edges—should be sought and dealt with. Finally, the large edge shifts of certain types of rank order filter are particularly important, because they are turned to advantage in morphological operators.

Binary images contain all the data needed to analyze the shapes, sizes, positions, and orientations of objects in two dimensions, and thereby to recognize them and even to inspect them for defects. As we shall see in [Chapters 8](#), Binary Shape Analysis and [9](#), Boundary Pattern Analysis, many simple small neighborhood operations exist for processing binary images and moving towards the goals stated above. At first sight these may appear a somewhat random set, reflecting historical development rather than systematic analytic tools. However, in the past few decades, mathematical morphology has emerged as a unifying theory of shape analysis: we have aimed to give the flavor of the subject in this chapter. In fact, mathematical morphology, as its name suggests, is mathematical in nature, and this can be a source of difficulty, but there are a number of key theorems and results: a few of these have been considered here and placed in context. For example, generalized dilation and erosion have acquired a central importance, since further vital concepts and constructs are based on them—closing, opening, template matching, and even connectedness properties (although space has prevented a detailed discussion of its application to the last two topics). For further information on grayscale morphological processing, see Haralick and Shapiro (1992) and Soille (2003). Interestingly, the rigor of mathematics is a cause for celebration, but at the same time it can make the arguments and the results obtained from them less intuitive. On the other hand, the real benefit of mathematics is to leapfrog what is possible by intuition alone and to arrive at results that are new and unexpected.

*Median filters have long been used to eliminate impulse noise without blurring edges. However, this chapter has shown that significant shifting of edges can result from use of median filters, and this property extends to mode filters and a fortiori to rank order filters—so much so that the latter form the basis of morphological processing. Specifically, erosion, dilation and operations such as opening and closing are at the core of mathematical morphology. In addition, the mathematics helps to make the subject of shape analysis rigorous and less ad hoc. Its extensions to grey-scale image processing are also valuable.*

---

### 3.16 BIBLIOGRAPHICAL AND HISTORICAL NOTES

Much of the work of this chapter has built on a paper by the author (Davies, 1988c), which rests on considerable earlier work on Gaussian, median, and other rank order filters (Hodgson et al., 1985; Duin et al., 1986). Notice that the edge shifts that occur for median filters are not limited to this type of filter but apply almost equally to mean filters (Davies, 1991b). In addition, other inaccuracies have been found with median filters and methods have been devised for correcting them (Davies, 1992e).

The early literature hardly mentions mode filters, presumably because of the difficulty of finding simple mode estimators that are not unduly confused by noise and that still operate rapidly. Indeed, only one early reference appeared (Coleman and Andrews, 1979), although it was backed up by later work (e.g., Evans and Nixon, 1995; Griffin, 2000). Other work referred to here is that on decomposing Gaussian and median filters (Narendra, 1978; Wijek et al., 1985) and the many papers on fast implementation of median filters (e.g., Narendra, 1978; Huang et al., 1979; Danielsson, 1981; Davies, 1992a).

Considerable efforts have been devoted to studying the “root” behavior of the median filter, i.e., the result of applying median filtering operations until no further change occurs. In fact, much of this work was carried out on 1-D signals, including cardiac and speech waveforms, rather than on images (Gallagher and Wise, 1981; Fitch et al., 1985; Heinonen and Neuvo, 1987). Root behavior is of interest as it relates to the underlying structure of signals, although its realization involves considerable amounts of processing. Some of the work on filtering aims to improve on rather than to emulate the median filter. Work of this type includes the detail-preserving filters of Heinonen and others (Nieminen et al., 1987) and relates to the lower set of plots in Fig. 3.18. See also the neural network approach to this topic (e.g., Greenhill and Davies, 1994). More recent work on nonlinear filtering appears in Marshall et al. (1998); see Marshall (2004) for a new design method for weighted order statistics filters.

The author reported methods of optimizing linear smoothing filters in small neighborhoods by minimizing the total error in fitting them to a continuous Gaussian function (Davies, 1987b): a balance has to be struck between subpixel

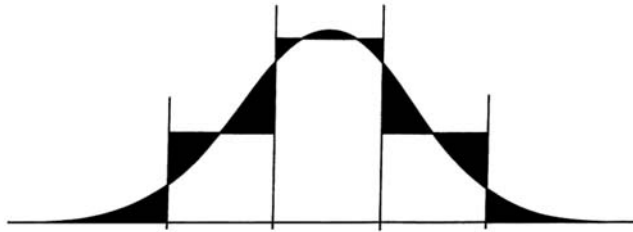


**FIGURE 3.31**

Approximating a discrete to a continuous Gaussian. This diagram shows how a balance needs to be struck between subpixel errors and those arising from the truncated part of the function.

errors within the neighborhood and errors that arise from the proportion of the distribution that lies outside the neighborhood (Fig. 3.31).

With the advent of extremely low-cost color frame grabbers on PCs and the widespread use of digital cameras, digital color images became ubiquitous; this resulted in much research on color filtering. A useful summary of work in this area up to 1998 appears in Sangwine and Horne (1998). More recent work on vector (color) filtering includes that of Lukac (2003). Charles and Davies (2003b) describe new distance-weighted median filters and their application to color images. They also extend the author's earlier mode filter work to color images (Charles and Davies, 2003a, 2004). Davies's (2000b) theorem shows that restricting a multichannel (color) filter output to the vector value of one of the input sample points (i.e., from the current window in the image) will increase the inaccuracy present in the final image, for a large proportion of pixels: since this represents the usual vector median strategy that is employed to minimize color bleeding, the effectiveness of color filtering algorithms needs to be looked at further.

Davies further analyzed the distortions and edge shifts produced by a range of rank order, mean, and mode filters, and produced a unified review of the subject (Davies, 2003c). In the case of median filters, it proved possible, and necessary for high accuracy, to produce a discrete model of the situation (Davies, 2003a), rather than extending the continuum model described much earlier (Davies, 1989b).

The book by Serra (1982) was an important early landmark in the development of morphology. Many subsequent papers helped to lay the mathematical foundations, perhaps the most important and influential being that by Haralick et al. (1987); see also Zhuang and Haralick (1986) for methods for decomposing morphological operators, and Crimmins and Brown (1985) for more practical aspects of shape recognition. The papers by Dougherty and Giardina (1988), Heijmans (1991), and Dougherty and Sinha (1995a,b) were important in the development of methods for grayscale morphological processing, while the work of Huang and Mitchell (1994) on grayscale morphology decomposition and that of Jackway and Deriche (1996) on multiscale morphological operators gave further impetus to the subject.

One problem is that it is by no means obvious how to decide on the sequence of morphological operations that is required in any application. This is an area where genetic algorithms have contributed to the systematic generation of complete systems (see, e.g., Harvey and Marshall, 1994).

### 3.16.1 MORE RECENT DEVELOPMENTS

The 2000s saw a new approach to filtering via “switched” types of filter that judge whether any pixel is corrupted by impulse noise: if the latter, they use a method such as the median or VMF to eliminate it; if the former, they adopt a policy of zero change by using the original pixel intensity or color. The zero change policy is useful because it helps to maintain image sharpness and fidelity. An early example of this approach was the work of Eng and Ma (2001); see Chen et al. (2009) and Smolka (2010) for recent more sophisticated versions of this concept (Smolka’s version falls in the category of a “peer group switching filter”).

Davies (2007b) studied the properties of the generalized (nonvector) median filter that has the capability for eliminating even more noise than the VMF, while not being targeted so specifically at eliminating color bleeding. He demonstrated ways of implementing the filter so that it runs sufficiently rapidly to make it a viable alternative to the VMF.

Celebi (2009) showed how to reduce the computational needs of directional vector filters based on order statistics without significant loss of accuracy. At another end of the scale, Rabbani and Gazor (2010) found how to reduce additive Gaussian noise by using local mixture models; they reported that, of the wavelet types of local representation, the discrete complex wavelet transform is preferable both in terms of peak noise performance and computational cost.

In the area of morphology, Bai and Zhou (2010) designed a “top-hat” selection transformation for locating and enhancing small dim infrared targets typified by aircraft in the sky. The selection transformation is based on the classical top-hat (residue) operator. A necessary parameter in the analysis is the value of  $n$ , the minimum difference in intensity between the target and the background, and methods are given for estimating it. Jiang et al. (2007) also use a residue operator to find thin low-contrast edges. The method uses five basic  $5 \times 5$  masks to detect edges of the right widths. Very high resistance to noise is demonstrated by the particular combination of techniques applied in this approach. Soille and Vogt (2009) show how binary images may be segmented to identify a range of different types of pattern. These include the following mutually exclusive foreground categories: core, islet, connector (loop and bridge), boundary (perforation and edge), branch, and segmented binary pattern. Lézoray and Charrier (2009) describe a new approach to color image segmentation, by analysis of color projections in 2D histograms to find the dominant colors: the important factor is that clustering in 2D histograms can proceed very effectively using standard image processing techniques, including morphological processing. Valero et al. (2010) use directional mathematical morphology to detect roads in remote sensing images. The paper

starts by taking roads to be linear connected paths; however, curved road segments and other network details can be dealt with by using “path openings” and “path closings” in order to obtain the required structural information.

---

### 3.17 PROBLEMS

1. Draw up a table showing the numbers of operations required to implement a median filter in various sizes of the neighborhood. Include in your table (1) results for a straight bubble sort of all  $n^2$  pixels, (2) results for bubble sorts in separated  $1 \times n$  and  $n \times 1$  neighborhoods, and (3) results for the histogram method of [Section 3.3](#). Discuss the results, taking account of possible computational overheads.
2. Show how to perform a median filtering operation on a binary image. Show also that if a set of binary images is formed by thresholding a grayscale image at various levels, and each of these binary images is median filtered, then a grayscale image can be reconstructed, which is a median filtered version of the original grayscale image. Consider to what extent the reduced amount of computation in filtering a binary image compensates for the number of separate thresholded images to be filtered.
3. An “extremum” filter is an image-parallel operation that assigns to every pixel the intensity value of the closer of the two extreme values in its local intensity distribution. Show that it should be possible to use such a filter to enhance images. What would be the *disadvantage* of such a filter?
4. Under what conditions is a 1-D signal that has been filtered once by a median filter a root signal? What truth is there in the statement that a straight edge in an image is neither shifted nor blurred by a median filter, whatever its cross-section?
5. a. Explain the action of the following median filtering algorithm:

```

for all pixels in image do {
    for (i = 0; i <= 255; i++) hist[i] = 0;
    for (m = 0; m <= 8; m++) hist[ P[m] ]++;
    i = 0; sum = 0;
    while (sum < 5) {
        sum = sum + hist[i];
        i = i + 1;
    }
    Q0 = i - 1;
}

```

- b. Show how this algorithm can be speeded up (1) by a more efficient histogram clearing technique and (2) by calculating the minimum intensity in each  $3 \times 3$  window. In each case estimate approximately how much the algorithm will be speeded up.

- c. Explain why a median filter is able to smooth images without introducing blurring.
- d. A 1-D cross-section of an image has the following intensity profile:

1 2 1 1 2 3 0 2 2 3 1 1 2 2 9 2 2 8 8 8 7 8 8 7 9 9 9

Apply (1) a three-element median filter and (2) a five-element median filter to this profile. With the aid of these examples, show that median filters tend to produce “runs” of constant values in 1-D profiles. Show also that under some circumstances, an edge in the profile can be shifted by a nearby spike: give a rule showing when this is likely to occur for an  $n$ -element median filter in one dimension.

- 6. a. A *mode* filter is defined as the one in which the new pixel intensity at any pixel takes the most probable value in the local intensity distribution of a window placed around that pixel in the original image space. Show for a grayscale image that a mode filter will if anything sharpen the image, while a *mean* filter will tend to blur the image.
- b. A *max* filter is the one that takes the maximum value of the local intensity distribution in a window around each pixel. Explain what will be seen when a max filter is applied to an image. Consider whether any similar effects are liable to happen when a mode filter is applied to an image.
- c. Explain the purpose of a *median* filter. Why are 2-D median filters sometimes implemented as two 1-D median filters applied in sequence?
- d. Contrast the behavior of five-element 1-D mean, max, and median filters as applied to the following waveform (for the mean filter, give the nearest integer value in each case):

0 1 1 2 3 2 2 0 2 3 9 3 2 4 4 6 5 6 7 0 8 8 9 1 1 8 9

- e. Work out what would happen if the 1-D median filters were applied many times, starting with this waveform.
- 7. a. Determine the effect of applying (1) a  $3 \times 3$  median filter and (2) a  $5 \times 5$  median filter to the portion of an image shown in [Fig. 3.P1](#).
- b. Show that it should be possible to develop a corner detector based on the properties of these median filters. What advantages or disadvantages might result from employing this design strategy?
- 8. a. Distinguish between *mean* and *median filtering*. Explain why a mean filter would be expected to blur an image, while a median filter would not have this effect. Illustrate your answer by showing what happens in the following 1-D case with a window of size  $1 \times 3$ :

1 1 1 1 2 1 1 2 3 4 4 0 4 4 4 5 6 7 6 5 4 3 3

- b. Give a complete median filter algorithm based on histograms and operating within a  $3 \times 3$  window. Explain why it operates relatively slowly.
- c. A computer language has the  $\max(a, b)$  operation as standard. Show how it may be used to find the maximum intensity within a  $3 \times 3$  window. Show also how it may be used to find the median by successively

```

0 0 0 0 0 0 0 0 0 0
0 0 0 0 0 0 0 2 0 0
0 1 0 0 0 0 0 0 0 0
0 0 1 0 0 0 0 0 0 0
0 0 0 0 9 9 9 9 9 9
0 0 0 0 9 9 8 9 9 9
0 0 1 0 9 8 9 9 7 9
0 0 0 0 7 9 9 8 9 9
0 1 0 8 9 9 9 9 9 9
0 0 0 0 9 9 9 9 9 9
0 0 0 0 8 9 9 9 9 9

```

FIGURE 3.P1 PORTION OF IMAGE FOR TESTS OF MEDIAN FILTER.

- replacing the maximum values by zeros. If the  $\max(a, b)$  operation is about the same speed as the  $a + b$  operation, determine whether the median can be found any faster by this method.
- d. Discuss whether splitting a  $3 \times 3$  median operation into  $1 \times 3$  and  $3 \times 1$  median operations is likely to be effective at eliminating impulse noise in images. How would the speed of this approach be affected by use of the  $\max(a, b)$  operation?
  9. a. Determine the result of applying a three-element median filter to the following 1-D signals:
    - i. 0 0 0 0 0 1 0 1 1 1 1 1 1 1
    - ii. 2 1 2 3 2 1 2 2 3 2 4 3 3 4
    - iii. 1 1 2 3 3 4 5 8 6 6 7 8 9 9
  - b. What general lessons can be learnt from the results? In the first case consider also the corresponding situation for a grayscale edge in a 2-D image.
  - c. 2-D median filters are sometimes implemented as two 1-D median filters applied in sequence in order to improve the speed of processing. Estimate the gain in speed that could be achieved in this way for (1) a  $3 \times 3$  median filter, (2) a  $7 \times 7$  median filter, and (3) in the general case.
  10. A morphological gradient binary edge enhancement operator is defined by the formula:

$$G = (A \oplus B) - (A \ominus B)$$

Using a 1-D model of an edge, or otherwise, show that this will give wide edges in binary images. If grayscale dilation ( $\oplus$ ) is equated to taking a local *maximum* of the intensity function within a  $3 \times 3$  window, and grayscale erosion ( $\ominus$ ) is equated to taking a local *minimum* within a  $3 \times 3$  window, sketch the result of applying the operator  $G$ . Show that it is similar in effect to a Sobel edge enhancement operator, if edge orientation effects are ignored by taking the Sobel magnitude:

$$g = (g_x^2 + g_y^2)^{1/2}$$

# The role of thresholding

# 4

One of the important practical aims of image processing is the demarcation of objects appearing in digital images. This process is called segmentation and a good approximation to it can often be achieved by thresholding. Broadly, this involves separating the dark and light regions of the image, and thus identifying dark objects on a light background (or vice versa). This chapter discusses the effectiveness of this idea and the means for achieving it.

*Look out for:*

- the segmentation, region-growing, and thresholding concepts
- the problem of threshold selection
- the limitations of global thresholding
- problems in the form of shadows or glints (highlights)
- what can be achieved with local adaptive thresholding algorithms
- more thoroughgoing variance, entropy-based and maximum likelihood methods
- the possibility of modeling images by multilevel thresholding
- the value of the global valley transformation
- how thresholds can be found in unimodal distributions.

Thresholding is limited in what it can achieve, and there are considerable difficulties in automatically estimating the optimum threshold—as evidenced by the many available techniques that have been devised for the purpose. In fact, segmentation is an ill-posed problem, and the fact that the human eye appears to perform thresholding reliably gives a misleading impression. Nevertheless, there are instances where the task can be simplified, e.g., by suitable lighting schemes, so that thresholding becomes effective. Hence it is a useful technique that needs to be included in the toolbox of available algorithms for use when appropriate. However, edge detection (see [Chapter 5: Edge Detection](#)) provides an alternative highly effective means to key into complex image data.

## 4.1 INTRODUCTION

One of the first tasks to be undertaken in vision applications is that of segmenting objects from their backgrounds. When objects are large and have little surface detail, segmentation can be imagined as splitting the image into a number of



regions each having a high level of uniformity in some parameter such as brightness, color, texture, or even motion. Hence it should be straightforward to separate objects from one another and from their background, and also to discern the different facets of solid objects such as cubes.

Unfortunately, the concept of segmentation presented above is an idealization that is sometimes reasonably accurate but more often in the real world it is an invention of the human mind, generalized inaccurately from certain simple cases. This problem arises because of the ability of the eye to understand real scenes at a glance and hence to segment and perceive objects within images in the form they are known to have. Introspection is not a good way of devising vision algorithms, and it must not be overlooked that segmentation is actually one of the central and most difficult practical problems of computer vision.

Thus the common view of segmentation as looking for regions possessing some degree of uniformity has limited validity. There are many examples of this in the world of 3-D objects: one is a sphere lit from one direction, the brightness in this case changing continuously over the surface, so that there is no distinct region of uniformity; another is a cube where the direction of the lighting may lead to several of the facets having equal brightness values, so that it is impossible from intensity data alone to segment the image completely as desired.

Nevertheless, there is sufficient correctness in the concept of segmentation by uniformity measures for it to be worth pursuing for practical applications. The reason is that in many (especially industrial) applications only a very restricted range and number of objects are involved, and in addition, it is possible to have almost complete control over the lighting and the general environment. The fact that a particular method may not be completely general need not be problematic, since by employing tools that are appropriate for the task in hand, a cost-effective solution will have been achieved in that case at least. However, in practical situations there is clearly a tension between simple cost-effective solutions and general purpose but more computationally expensive solutions; this tension must always be kept in mind in practical subjects such as computer vision.

---

## 4.2 REGION-GROWING METHODS

The segmentation idea outlined above leads naturally to the region-growing technique (Zucker, 1976b). Here pixels of like intensity (or other suitable property) are successively grouped together to form larger and larger regions until the whole image has been segmented. Clearly there have to be rules about not combining adjacent pixels that differ too much in intensity, while permitting combinations for which intensity changes gradually because of variations in background illumination over the field of view. However, this is not enough to make a viable strategy, and in practice the technique has to include the facility not only to merge regions together but also to split them if they become too large and

inhomogeneous (Horowitz and Pavlidis, 1974). Particular problems are noise and sharp edges and lines that form disconnected boundaries, and for which it is difficult to formulate simple criteria to decide whether they form true region boundaries. In remote sensing applications, for example, it is often difficult to separate fields rigorously when hedges are broken and do not provide continuous boundaries: in such applications segmentation may have to be performed interactively, with a human operator helping the computer. Hall (1979) found that in practice regions tend to grow too far, so that to make the technique work well it is necessary to limit their growth with the aid of edge detection schemes: the danger is clearly that even one small break could join two regions into a single larger one.

Thus the region-growing approach to segmentation turns out to be quite complex to apply in practice. In addition, region-growing schemes usually operate iteratively, gradually refining hypotheses about which pixels belong to which regions. The technique is complicated because, carried out properly, it involves global as well as local image operations. In view of all these factors, and the fact that more powerful methods are available and will be considered later in the book, it will not be worth pursuing region growing further here.

---

## 4.3 THRESHOLDING

If background lighting is arranged so as to be fairly uniform and we are looking for rather flat objects that can be silhouetted against a contrasting background, segmentation can be achieved simply by thresholding the image at a particular intensity level. The process of thresholding has already been covered in [Chapter 2](#), Images and Imaging Operations, the basic result being that the initial grayscale image is converted into a binary image in which objects appear as black figures on a white background ([Fig. 2.7](#)) or as white figures on a black background. Further analysis of the image then devolves into analysis of the shapes and dimensions of the figures: at this stage object identification should be straightforward. [Chapter 8](#), Binary Shape Analysis, concentrates on such tasks. Meanwhile there is one outstanding problem—how to devise an automatic procedure for determining the optimum thresholding level.

### 4.3.1 FINDING A SUITABLE THRESHOLD

One simple technique for finding a suitable threshold arises in situations such as optical character recognition (OCR) where the proportion of the background that is occupied by objects (i.e., print) is relatively constant in a variety of conditions. A preliminary analysis of relevant picture statistics then permits subsequent thresholds to be set by insisting on a fixed proportion of dark and light in a sequence of images (Doyle, 1962). In practice, a series of experiments is performed in which the thresholded image is examined as the threshold is adjusted: at that stage the

proportions of dark and light in the image are measured. Unfortunately, any unforeseen disturbance following the original measurement—such as a light bulb failing—will upset such a scheme, since it will affect the relative amounts of dark and light in the image. Nevertheless, this is frequently a useful technique in industrial applications, especially when particular details within an object are to be examined: typical examples of this are holes in mechanical components such as brackets.

The technique that is most frequently employed for determining thresholds involves analyzing the histogram of intensity levels in the digitized image (Fig. 4.1): if a significant minimum is found, it is interpreted as the required threshold value (Weska, 1978). Clearly, the assumption being made here is that the peak on the left of the histogram corresponds to dark objects and the peak on the right corresponds to light background (here it is assumed that, as in many industrial applications, objects appear dark on a light background).

This method is subject to the following major difficulties:

1. the valley may be so broad that it is difficult to locate a significant minimum;
2. there may be a number of minima because of the type of detail in the image, and selecting the most significant one will be difficult;
3. noise within the valley may inhibit location of the optimum position;
4. there may be no clearly visible valley in the distribution because noise may be excessive or because the background lighting may vary appreciably over the image;
5. either of the major peaks in the histogram (usually that due to the background) may be much larger than the other and this will then bias the position of the minimum;

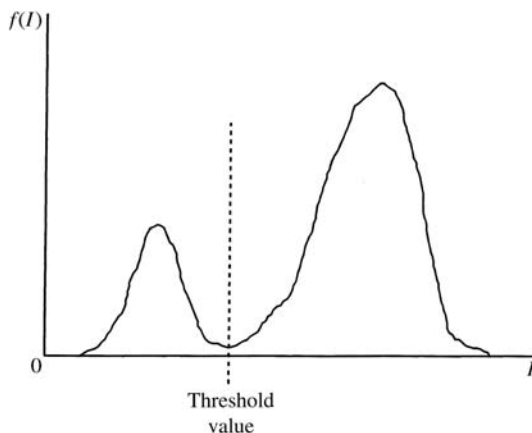


**FIGURE 4.1**

Idealized histogram of pixel intensity levels in an image. The large peak on the right results from the light background; the smaller peak on the left is due to dark foreground objects. The minimum of the distribution provides a convenient intensity value to use as a threshold.

6. the histogram may be inherently multimodal, making it difficult to determine which is the relevant thresholding level.

For simplicity, we will temporarily ignore the last problem and concentrate on how best to find a genuine single threshold when its position is partly obscured as indicated by problems 1–5 (these can be summarized as arising from image “clutter,” noise, and lighting variations).

### 4.3.2 TACKLING THE PROBLEM OF BIAS IN THRESHOLD SELECTION

This section considers problem 5 as mentioned above—that of eliminating the bias in the selection of thresholds that arises when one peak in the histogram is larger than the other. First, note that if the relative heights of the peaks are known, this effectively eliminates the problem, since the “fixed proportion” method of threshold selection outlined above can be used. However, this is not normally possible. A more useful approach is to prevent bias by weighting down the extreme, out of balance values of the intensity distribution. To achieve this, note that the intermediate values are special in that they correspond to object edges. Hence a good basic strategy is to find positions in the image where there is a significant intensity gradient—corresponding to pixels along edges—and to analyze the intensity values *immediately around* these locations, ignoring other points in the image. This will ensure that the numbers of foreground and background pixels examined will be approximately equal, so there should be no net bias.

At this point we have found techniques that are able to provide inherently reasonable threshold values. However, they do not solve all the problems caused by uneven lighting. In addition, they are unable to cope with glints, shadows, and image clutter. Unfortunately, such artefacts are common in most real situations (Figs. 4.2 and 4.3) and are only eliminated with difficulty in practice. Indeed, in industrial applications where shiny metal components are involved, glints are the rule rather than the exception, while shadows can seldom be avoided with any sort of object. Even flat objects are liable to have quite strong shadow contours around them because of the particular placement of lights. Note also that glints and shadows can only be allowed for properly in a two-stage image analysis system, where tentative assignments are made and then are firmed up by reexamining all pixel intensities in detail. We now return to the problem of making the most of the thresholding technique, by finding how variations in background lighting can be allowed for.

---

## 4.4 ADAPTIVE THRESHOLDING

The problem that arises when illumination is not sufficiently uniform may be tackled by permitting the threshold to vary adaptively over the whole image. In principle there are several ways of achieving this. One involves modeling the

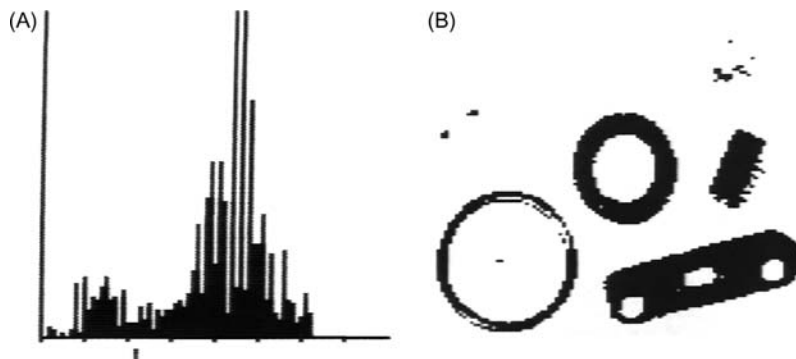


**FIGURE 4.2**

Histogram for the image shown in Fig. 2.7A. Note that the histogram is not particularly close to the ideal form of Fig. 4.1. Hence the threshold obtained from (A) (indicated by the short line beneath the scale) does not give ideal results with all the objects in the binarized image (B). Nevertheless, the results are better than for the arbitrarily thresholded image of Fig. 2.7B.

background within the image. Another is to work out a local threshold value for each pixel by examining the range of intensities in its neighborhood.

The problem of modeling the background can sometimes be solved rather neatly by obtaining an image of the background in the absence of any objects—a method that may well be applicable on a factory product line. In principle, it would appear to solve the problem of adaptive thresholding in a rigorous, exact manner. However, caution is needed because objects bring with them not only shadows (which can in a sense be regarded as parts of the objects) but also an additional effect due to the reflections they cast over the background and other objects. This additional effect is nonlinear, in the sense that it is necessary to add not only the difference between the object and the background intensity in each case but also an intensity that depends on the *products* of the reflectances of pairs of objects. These considerations mean that using the no-object background is ultimately invalid. Nevertheless, this approach is often useful as a first approximation, but if it proves impracticable, there is no option but to model the background from the actual image being segmented. It is worth noting that similar problems arise in surveillance, e.g., when cars or pedestrians are being located on roads or pavements (see [Chapter 22: Surveillance](#)).

#### 4.4.1 LOCAL THRESHOLDING METHODS

The other approach mentioned earlier is particularly useful for finding local thresholds. It involves analyzing intensities in the neighborhood of each pixel to determine the optimum local thresholding level. Thus it is necessary to obtain the vital information by an efficient sampling procedure. A simple means of

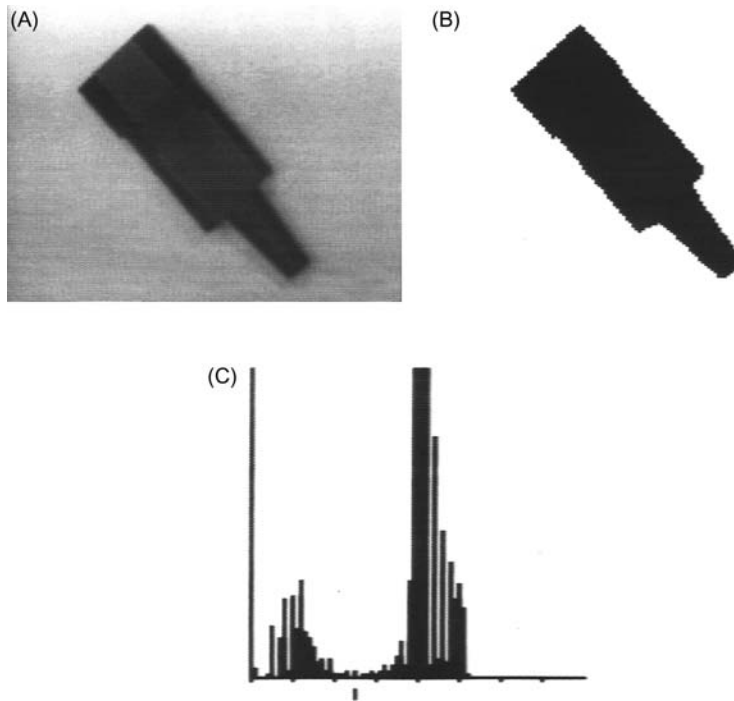


**FIGURE 4.3**

A picture with more ideal properties. (A) Image of a plug that has been lit fairly uniformly. The histogram (C) approximates to the ideal form, and the result of thresholding (B) is acceptable. However, much of the structure of the plug is lost during binarization.

achieving this is to take a suitably computed function of nearby intensity values as the threshold: often the mean of the local intensity distribution is taken, since this is a simple statistic and gives good results in some cases. For example, in astronomical images stars have been thresholded in this way. Niblack (1985) reported a case in which a proportion of the local standard deviation was added to the mean to give a more suitable threshold value, the reason (presumably) being to help suppress noise (clearly, addition is appropriate where bright objects such as stars are to be located, whereas subtraction will be more appropriate in the case of dark objects).

Another statistic that is frequently used is the mean of the maximum and minimum values in the local intensity distribution. The justification for this is that whatever the sizes of the two main peaks of the distribution, this statistic often gives a reasonable estimate of the position of the histogram minimum. Clearly, this method will only be accurate if (1) the intensity profiles of object edges are symmetrical, (2) noise acts uniformly everywhere in the image so that the widths of the two peaks of the distribution are similar, and (3) the heights of the two

distributions do not differ markedly. Sometimes these assumptions are definitely invalid—for example, when looking for (dark) cracks in eggs or other products. In such cases the mean and maximum of the local intensity distribution can be found and a threshold deduced using the statistic

$$T = \text{mean} - (\text{maximum} - \text{mean}) \quad (4.1)$$

where the strategy is to estimate the lowest intensity in the bright background assuming the distribution of noise to be symmetrical (Fig. 4.4): use of the mean here is realistic only if the crack is narrow and does not affect the value of the mean significantly. If it does, then the statistic can be adjusted by use of an ad hoc parameter:

$$T = \text{mean} - k(\text{maximum} - \text{mean}) \quad (4.2)$$

where  $k$  may be as low as 0.5 (Plummer and Dale, 1984).

This method is essentially the same as that of Niblack (1985), but the computational load in estimating the standard deviation is minimized. Each of the last two techniques relies on finding local extrema of intensity. Using these measures helps to save computation but they are clearly somewhat unreliable because of the effects of noise. If this is a serious problem, quartiles or other statistics of the distribution may be used. The alternative of prefiltering the image to remove noise is unlikely to work for crack thresholding, since cracks will almost certainly be removed at the same time as the noise. A better strategy is to form an image of  $T$ -values obtained using Eq. (4.1) or (4.2): smoothing this image should then permit the initial image to be thresholded effectively.

Unfortunately, all these methods work well only if the size of the neighborhood selected for estimating the required threshold is large enough to span a significant amount of foreground and background. In many practical cases this is not possible and the method then adjusts itself erroneously, for example, so that it

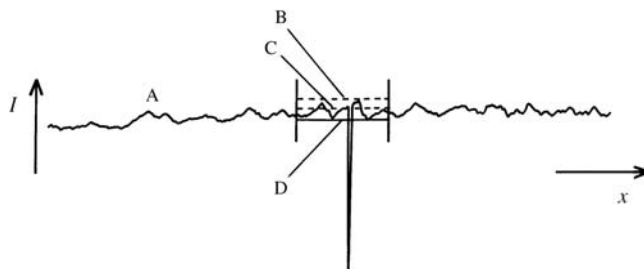


**FIGURE 4.4**

Method for thresholding the crack in an egg. (A) Intensity profile of an egg in the vicinity of a crack: the crack is assumed to appear dark (e.g., under oblique lighting); (B) local maximum of intensity on the surface of the egg; (C) local mean intensity. Eq. (4.2) gives a useful estimator  $T$  of the thresholding level (D).

**Table 4.1** A Simple Algorithm for Adaptively Thresholding Print

---

```

minrange = 255 / 5;
/* minimum likely difference in intensity between print and background:
this parameter can be preset manually or "learnt" by a previous routine */
for all pixels in image do {
    find minimum and maximum of local intensity distribution;
    range = maximum - minimum;
    if (range > minrange)
        T = (minimum + maximum) / 2; // print is visible in neighbourhood
    else T = maximum - minrange / 2; // neighbourhood is all white
    if (P0 > T) Q0 = 255; else Q0 = 0; // now binarize print
}

```

---

finds darker spots within dark objects as well as segmenting the dark objects themselves. However, there are certain applications where there is little risk of this occurring. One notable case is that of OCR. Here the widths of character limbs are likely to be known in advance and should not vary substantially. If this is so, then a neighborhood size can be chosen to span or at least sample both character and background, and it is thus possible to threshold the characters highly efficiently using a simple functional test of the type described above. The effectiveness of this procedure (Table 4.1) is demonstrated in Fig. 4.5.

Before leaving this topic, note that hysteresis thresholding is a type of adaptive thresholding—effectively permitting the threshold value to vary locally: this topic will be investigated in Section 5.10.

---

## 4.5 MORE THOROUGHGOING APPROACHES TO THRESHOLD SELECTION

At this point we return to global threshold selection and describe some especially important approaches that have a rigorous mathematical basis. The first of these is variance-based thresholding; the second is entropy-based thresholding; and the third is maximum likelihood thresholding. All three are widely used, the second having achieved an increasingly wide following over the past 20–30 years, and the third is a more broadly based technique that has its roots in statistical pattern recognition—a subject that is covered in Chapter 13, Basic Classification Concepts.

### 4.5.1 VARIANCE-BASED THRESHOLDING

The standard approach to thresholding outlined earlier involved finding the neck of the global image intensity histogram. However, this is impracticable when the



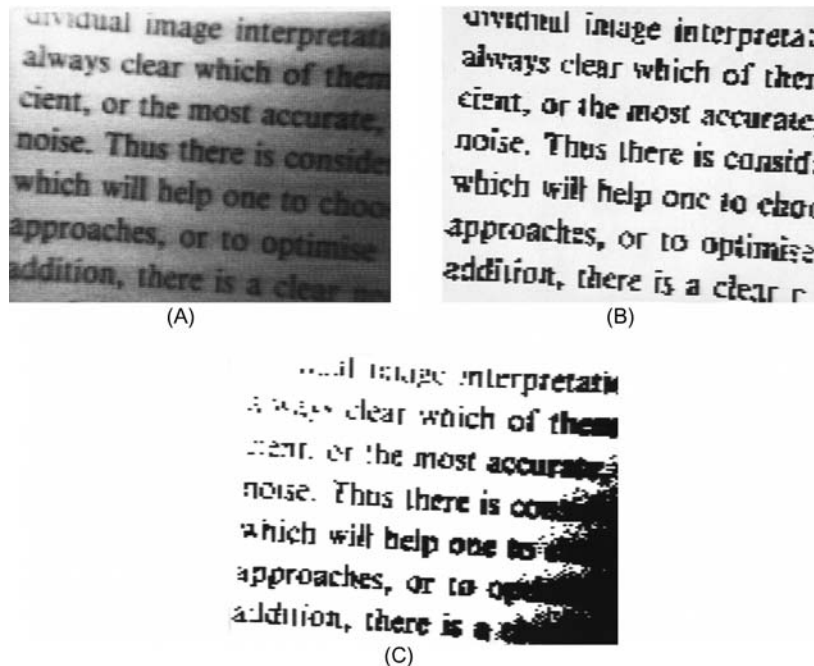


**FIGURE 4.5**

Effectiveness of local thresholding on printed text. Here a simple local thresholding procedure (Table 4.1), operating within a  $3 \times 3$  neighborhood, is used to binarize the image of a piece of printed text (A). Despite the poor illumination, binarization is performed quite effectively (B). Note the complete absence of isolated noise points in (B), while by contrast the dots on all the *i*'s are accurately reproduced. The best that could be achieved by uniform thresholding is shown in (C).

dark peak of the histogram is minuscule in size, as it will then be hidden among the noise in the histogram, and it will not be possible to extract it with the usual algorithms.

A good many investigators have studied this sort of problem (e.g., Otsu, 1979; Kittler et al., 1985; Sahoo et al., 1988; Abutaleb, 1989): among the most well-known approaches are the variance-based methods. In these methods, the image intensity histogram is analyzed to find where it can best be partitioned to optimize criteria based on ratios of the within-class, between-class, and total variance. The simplest approach (Otsu, 1979) is to calculate the between-class variance, as will now be described.

First we assume that the image has a grayscale resolution of  $L$  gray levels. The number of pixels with gray level  $i$  is written as  $n_i$ , so the total number of

pixels in the image is  $N = n_1 + n_2 + \dots + n_L$ . Thus the probability of a pixel having gray level  $i$  is:

$$p_i = n_i/N \quad (4.3)$$

where

$$p_i \geq 0 \quad \sum_{i=1}^L p_i = 1 \quad (4.4)$$

For ranges of intensities up to and above the threshold value  $k$ , we can now calculate the between-class variance  $\sigma_B^2$  and the total variance  $\sigma_T^2$ :

$$\sigma_B^2 = \pi_0(\mu_0 - \mu_T)^2 + \pi_1(\mu_1 - \mu_T)^2 \quad (4.5)$$

$$\sigma_T^2 = \sum_{i=1}^L (i - \mu_T)^2 p_i \quad (4.6)$$

where

$$\pi_0 = \sum_{i=1}^k p_i \quad \pi_1 = \sum_{i=k+1}^L p_i = 1 - \pi_0 \quad (4.7)$$

$$\mu_0 = \sum_{i=1}^k i p_i / \pi_0 \quad \mu_1 = \sum_{i=k+1}^L i p_i / \pi_1 \quad \mu_T = \sum_{i=1}^L i p_i \quad (4.8)$$

Making use of the latter definitions, the formula for the between-class variance can be simplified to:

$$\sigma_B^2 = \pi_0 \pi_1 (\mu_1 - \mu_0)^2 \quad (4.9)$$

For a single threshold the criterion to be maximized is the ratio of the between-class variance to the total variance:

$$\eta = \sigma_B^2 / \sigma_T^2 \quad (4.10)$$

However, the total variance is constant for a given image histogram, so maximizing  $\eta$  simplifies to maximizing the between-class variance.

The method can readily be extended to the dual threshold case  $1 \leq k_1 \leq k_2 \leq L$ , where the resultant classes,  $C_0$ ,  $C_1$ , and  $C_2$ , have respective gray level ranges of  $[1, \dots, k_1]$ ,  $[k_1 + 1, \dots, k_2]$  and  $[k_2 + 1, \dots, L]$ .

In some situations (e.g., Hannah et al., 1995) this approach is still not sensitive enough to cope with histogram noise, and more sophisticated methods must be used. One such technique is that of entropy-based thresholding, which has become firmly embedded in the subject (Pun, 1980; Kapur et al., 1985; Abutaleb, 1989; Brink, 1992). For further insight into the performance of the between-class variance method (BCVM), see [Section 4.7](#).

### 4.5.2 ENTROPY-BASED THRESHOLDING

Entropy measures of thresholding are based on the concept of entropy. The entropy statistic is high if a variable is well distributed over the available range and low if it is well ordered and narrowly distributed: specifically, entropy is a measure of disorder and is zero for a perfectly ordered system. The concept of entropy thresholding is to threshold at an intensity for which the sum of the entropies of the two intensity probability distributions thereby separated is maximized. The reason for this is to obtain the greatest reduction in entropy—i.e., the greatest increase in order—by applying the threshold: in other words, the most appropriate threshold level is the one that imposes the greatest order on the system and thus leads to the most meaningful result.

To proceed, the intensity probability distribution is again divided into two classes—those with gray levels up to the threshold value  $k$  and those with gray levels above  $k$  (Kapur et al., 1985). This leads to two probability distributions A and B:

$$A: \quad \frac{P_1}{P_k}, \frac{P_2}{P_k}, \dots, \frac{P_k}{P_k} \quad (4.11)$$

$$B: \quad \frac{P_{k+1}}{1-P_k}, \frac{P_{k+2}}{1-P_k}, \dots, \frac{P_L}{1-P_k} \quad (4.12)$$

where

$$P_k = \sum_{i=1}^k p_i \quad 1 - P_k = \sum_{i=k+1}^L p_i \quad (4.13)$$

The entropies for each class are given by:

$$H(A) = - \sum_{i=1}^k \frac{P_i}{P_k} \ln \frac{P_i}{P_k} \quad (4.14)$$

$$H(B) = - \sum_{i=k+1}^L \frac{P_i}{1-P_k} \ln \frac{P_i}{1-P_k} \quad (4.15)$$

and the total entropy is:

$$H(k) = H(A) + H(B) \quad (4.16)$$

Substitution leads to the final formula:

$$H(k) = \ln \left( \sum_{i=1}^k p_i \right) + \ln \left( \sum_{i=k+1}^L p_i \right) - \frac{\sum_{i=1}^k p_i \ln p_i}{\sum_{i=1}^k p_i} - \frac{\sum_{i=k+1}^L p_i \ln p_i}{\sum_{i=k+1}^L p_i} \quad (4.17)$$

and it is this parameter that has to be maximized.

This approach can give very good results—see for example Hannah et al. 1995. Again, it is straightforwardly extended to dual thresholds, but we shall not

go into the details here (Kapur et al., 1985). In fact, probabilistic analysis to find mathematically ideal dual thresholds may not be the best approach in practical situations: an alternative technique for determining dual thresholds sequentially has been devised by Hannah et al. (1995), and applied to an X-ray inspection task.

### 4.5.3 MAXIMUM LIKELIHOOD THRESHOLDING

When dealing with distributions such as intensity histograms, it is important to compare the actual data with the data that might be expected from a previously constructed model based on a training set: this is in keeping with the methods of statistical pattern recognition (see [Chapter 13: Basic Classification Concepts](#)), which takes full account of prior probabilities. For this purpose, one option is to model the training set data using a known distribution function such as a Gaussian. The latter has many advantages, including its accessibility to relatively straightforward mathematical analysis. In addition, it is specifiable in terms of two well-known parameters—the mean and the standard deviation, which are easily measured in practical situations. Indeed, for any Gaussian distribution we have:

$$p_i(x) = \frac{1}{(2\pi\sigma_i^2)^{1/2}} \exp\left[-\frac{(x-\mu_i)^2}{2\sigma_i^2}\right] \quad (4.18)$$

where the  $i$  refers to a specific distribution, and of course when thresholding is being carried out there is supposition that two such distributions are involved. Applying the respective a priori class probabilities  $P_1, P_2$  (see [Chapter 13: Basic Classification Concepts](#)), careful analysis (Gonzalez and Woods, 1992) shows that the condition  $p_1(x) = p_2(x)$  reduces to the form:

$$x^2\left(\frac{1}{\sigma_1^2} - \frac{1}{\sigma_2^2}\right) - 2x\left(\frac{\mu_1}{\sigma_1^2} - \frac{\mu_2}{\sigma_2^2}\right) + \left(\frac{\mu_1^2}{\sigma_1^2} - \frac{\mu_2^2}{\sigma_2^2}\right) + 2\log\left(\frac{P_2\sigma_1}{P_1\sigma_2}\right) = 0 \quad (4.19)$$

Note that, in general, this equation has two solutions, implying the need for two thresholds, although when  $\sigma_1 = \sigma_2$ , there is a single solution:

$$x = \frac{1}{2}(\mu_1 + \mu_2) + \frac{\sigma^2}{\mu_1 - \mu_2} \ln\left(\frac{P_2}{P_1}\right) \quad (4.20)$$

The reason for the existence of two solutions is that one solution represents a threshold in the area of overlap between the two Gaussians; the other solution is mathematically unavoidable and lies either at very high or very low intensities. It is this latter solution that disappears when the two Gaussians have equal variance, as the distributions clearly never cross again. In any case, it seems unlikely that the distributions being modeled would in practice approximate so well to Gaussians that the noncentral solution could ever be important—i.e., it is essentially a mathematical fiction that needs to be eliminated from consideration.

Next, when the prior probabilities for the two classes are equal, the equation reduces to the altogether simpler and more obvious form:

$$x = \frac{1}{2}(\mu_1 + \mu_2) \quad (4.21)$$

Of all the methods described in this chapter, only the maximum likelihood method makes use of a priori probabilities. While this makes it look as if it is the only rigorous method, and indeed that all other methods are automatically erroneous and biased in their estimations, this is not the actual position. The reason lies in the fact that the other methods incorporate actual frequencies of sample data, which embody the a priori probabilities (see [Section 13.3](#)). Hence the other methods should give correct results. Nevertheless, it is refreshing to see a priori probabilities brought in explicitly, as this gives a greater confidence of getting unbiased results in any doubtful situations.

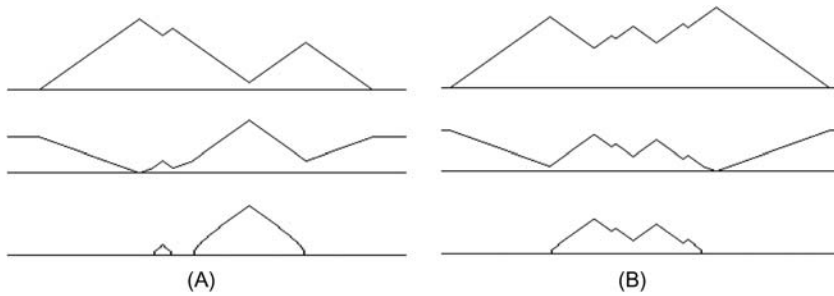
---

## 4.6 THE GLOBAL VALLEY APPROACH TO THRESHOLDING

An important disadvantage of the many approaches to threshold estimation, including particularly entropy thresholding and its variants, is that it is often unclear how they will react to unusual or demanding situations, such as where multiple thresholds have to be found in the same image (Kapur et al., 1985; Hannah et al., 1995; Tao et al., 2003; Wang and Bai, 2003; Sezgin and Sankur, 2004). In addition to this, there is the risk that the more complex approaches will miss important aspects of the original data. The global valley approach (Davies, 2007a) aimed to provide a rigorous means of going back to basics to find global valleys of intensity histograms in such a way as to embody the intrinsic meaning of the data.

The top trace of [Fig. 4.6A](#) shows the basic situation—where thresholding is effective and the optimum threshold should be simple to locate. However, the intensity histogram often contains such a welter of peaks and valleys that even the human eye, with its huge capability for analysis “at a glance,” can be confused—especially when it is necessary to identify global valley positions rather than local minima of lesser significance. The situation is made clearer by the example shown in the top trace of [Fig. 4.6B](#). Here, valley 1 (numbering from the left) is lower than valley 3, but valley 3 is deeper in the sense that it has two high peaks immediately around it; however, valley 1 also lies between the highest two peaks, and in that sense it is the *globally* deepest valley in the distribution.

Clearly, to judge global valley deepness, we need a mathematical criterion, so that comparisons between all the valleys can be carried out unambiguously. To proceed, for any potential global valley point (call it point  $j$ ), we need to look at all the points ( $i$ ) on the left of it to see which gives the highest peak to the left and to look at all the points ( $k$ ) on the right of it to see which of these gives the highest peak to the right, before we can construct a suitable criterion value for point  $j$ . Hence we need to take the maximum over all points  $i$  and the maximum


**FIGURE 4.6**

Result of applying global minimization algorithm to 1-D data sets. (A) A basic two-peak structure. (B) A basic multimode structure. Top trace: original 1-D datasets. Middle trace: results from Eq. (4.23). Bottom trace: results from Eq. (4.23).

© IET 2008.

over all points  $k$ . Furthermore, we need to do this for all points  $j$ , and for each of them we need to consider only points  $i$  ( $i < j$ ) and points  $k$  ( $k > j$ ), and take account of the corresponding heights  $h_i$ ,  $h_j$ ,  $h_k$  in the distribution. The maximum must then be taken for a criterion function  $C_j$  of general form  $\max_{i,k} \{Q(h_i - h_j, h_k - h_j)\}$ . An obvious criterion function of this form employs the arithmetic mean. However, to avoid complications from negative heights, we introduce a sign function  $s(\cdot)$  such that  $s(u) = u$  if  $u > 0$  and  $s(u) = 0$  if  $u \leq 0$ . The result is the following function:

$$F_j = \max_{i,k} \left\{ \frac{1}{2} [s(h_i - h_j) + s(h_k - h_j)] \right\} \quad (4.22)$$

When this is applied to the top trace of Fig. 4.6A, the result is a distribution (middle trace of Fig. 4.6A), which has a maximum at the required valley position. In addition, the values of  $i$  and  $k$  corresponding to this maximum are the first and third peak positions in the original intensity distribution. The sign function  $s(\cdot)$  has the effect of preventing negative responses that would complicate the situation unnecessarily.

While the function  $F$  used above is straightforward to apply and employs linear expressions that are often attractive in permitting in-depth analysis, it results in pedestals at either end of the output distribution: these could complicate the situation when there are many peaks and valleys. Fortunately, the geometric mean is not subject to this problem, and so it is the one that is adopted in the global valley method (GVM). Thus we use the following function instead of  $F_j$ :

$$K_j = \max_{i,k} \{[s(h_i - h_j)s(h_k - h_j)]\} \quad (4.23)$$

Note that the arithmetic and geometric means are very similar when the two arguments are nearly equal, but deviate a lot when the two arguments are

dissimilar: it is the dissimilar case that applies at the ends of the distribution, where it is required to suppress a potential valley that has only one peak near to it, and the geometric mean then offers a sound advantage over the arithmetic mean. These ideas are further confirmed by Fig. 4.6B.

Overall, the rationale for this approach is that we are looking for the most significant valley in an intensity distribution, corresponding to an optimum discriminating point between (for example) dark objects and light background in the original image. While in some cases the situation is obvious (Fig. 4.6A), in general it is difficult to sort out a confusing set of peaks and valleys and in particular to identify global valleys. So the concept embodied in Eq. (4.23) is that of aiming to guarantee an optimal global solution by automatic means. Clearly, by analysis of the output distribution, it is also possible to find a whole range of maxima corresponding to global valley positions in the input distribution: to this extent the method is able to cope with multimode distributions and to find multiple threshold positions.

With all histogramming methods, it is necessary to take due account of local noise in the distribution, as it could lead to inaccurate results. Hence the  $K$  distribution is smoothed before proceeding with further analysis to locate thresholds.

Another important factor is the amount of computation required for this approach. While it at first appears that a computationally intensive scan over all possible sets of sampling points  $i, j, k$  is required to obtain the optimal solution, it turns out that with care that computational load can be reduced from  $O(N^3)$  to  $O(N)$ , where  $N$  is the number of gray levels in the intensity distribution.

---

## 4.7 PRACTICAL RESULTS OBTAINED USING THE GLOBAL VALLEY METHOD

The ideas presented above are next tested using the image shown in Fig. 4.7A. Starting with this image, the following sequence of operations is applied: (1) an intensity histogram is generated (top trace in Fig. 4.7D); (2) the function  $K$  is applied (middle trace in Fig. 4.7D); (3) the output distribution is smoothed (bottom trace in Fig. 4.7D); (4) peaks are located (see the short vertical lines at the bottom of Fig. 4.7D); (5) the most significant peaks are chosen as threshold levels (here all eight are selected); (6) a new image is generated by applying the mean of the adjacent threshold intensity levels. The result (Fig. 4.7B) is a reasonably segmented likeness of the original image, albeit with clear limitations in the cloud regions—simply because accurate renditions of these would require a rather full range of gray levels, and thresholding is not appropriate in such regions. However, what is significant is the ease with which the approach automatically incorporates multilevel thresholding of multimode intensity distributions—a point that has been a difficulty with entropy thresholding, for example (Hannah et al., 1995). Finally, Fig. 4.7C gives a comparison with the maximum BCVM of Otsu (1979), which has recently undergone something of a resurgence of popularity

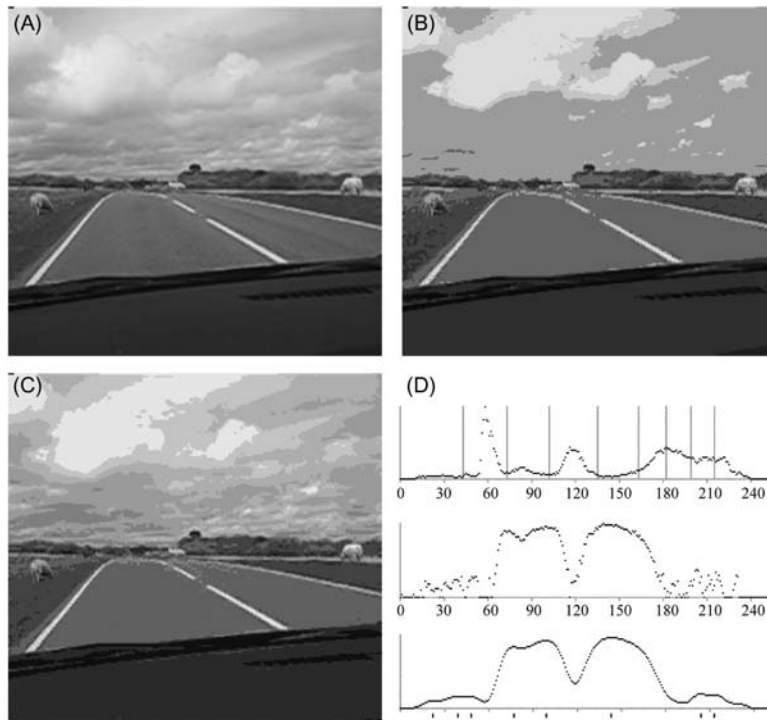


**FIGURE 4.7**

Result of applying the global valley algorithm to a multimode intensity distribution.

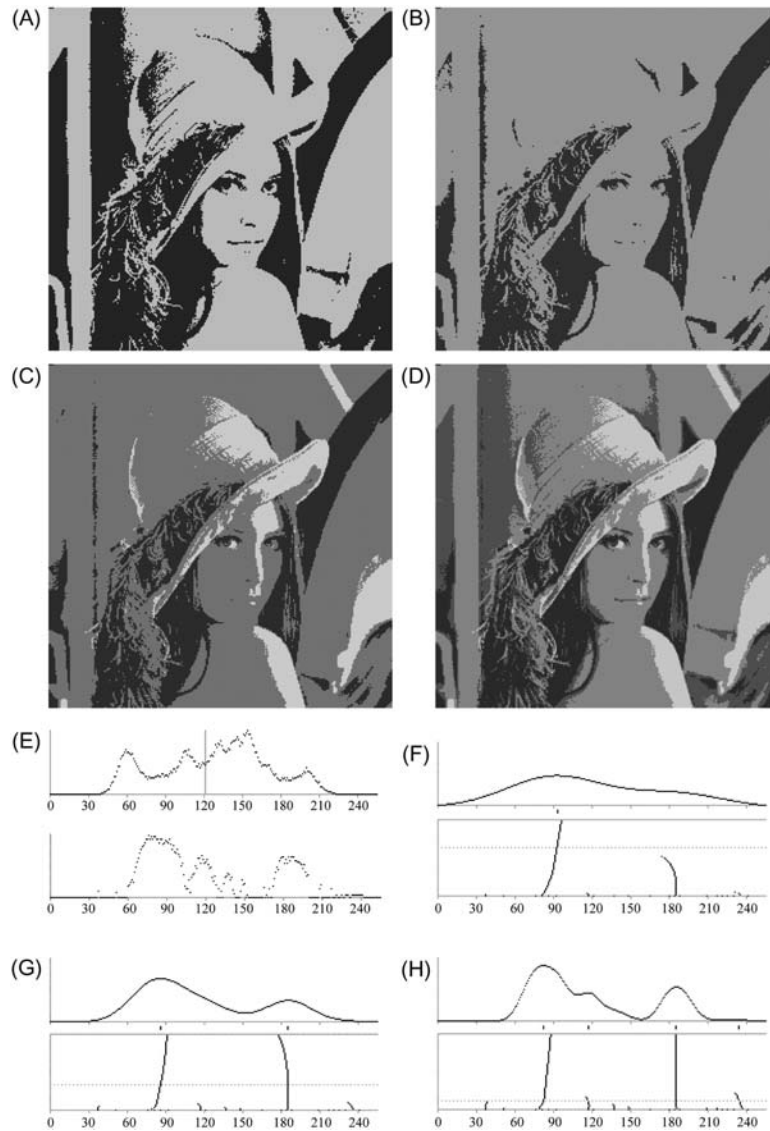
(A) Original grayscale image. (B) Reconstituted image after multiple thresholding using the eight peaks in the output distribution. (D) Top: original intensity histogram for (A). Middle: result of applying the global valley transformation. Bottom: result of smoothing. The eight short vertical lines at the very bottom indicate the peak positions. In (D), the intensity scale is 0–255; the vertical scale is normalized to a maximum height indicated by the height of the vertical axis. Note: The three traces are computed 25 times more accurately than the rounded values displayed, so the peak locations are determined as accurately as indicated. For comparison, (C) shows the result of applying the between class variance method to the same image: the eight thresholds are indicated by vertical lines in the top trace of (D).

© IET 2008.

and use, partly as a result of the ease with which it can be used for the systematic generation of multilevel thresholds (Liao et al., 2001; Otsu, 1979).

The reconstructability of the method (in the sense that much of the image is reconstructed so well that it is difficult to distinguish from the original) is an indication of success in that it is clear that the information removed was by no means arbitrary but was actually redundant and unhelpful. This property is also evident in Fig. 4.8, which shows the application of the method to the well-known Lena image.



**FIGURE 4.8**

Multilevel thresholding of the Lena image. For the original grayscale image, see “Miscellaneous” at the USC-SIPI Image Database (<http://sipi.usc.edu/database/database.php> (Accessed December 13, 2011)). (A) Result of applying the between-class variance method (BCVM) to original image. (B)–(D) Results of applying the global valley method to original image, producing respectively bi-level, tri-level, and five-level images. (E) Top: intensity histogram: the vertical line indicates the bi-level

(Continued)

The basic criterion used for smoothing is that of reducing noise as far as possible without eliminating relevant thresholding points. To achieve this, repeated convolutions of the  $K$  distributions are made with a three-element  $\frac{1}{4}[1\ 2\ 1]$  kernel until an appropriate amount of smoothing is obtained. Note that the GVM peaks are by no means static. In particular, as smoothing progresses, they gradually move and then merge, as can be seen in the bottom traces in Fig. 4.8F–H. Just before merger, there is often a rapid movement to align the merging peaks. To cope with this and to find suitable thresholding levels, a useful heuristic was to move one quarter of the way from the merged position to the next merger position (see horizontal dotted lines in Fig. 4.8F–H). To clarify the process, the basic GVM algorithm is given in Table 4.2.

Fig. 4.8F–H gives three examples of smoothing until 1, 2, or 4 thresholding points are produced (these give bi-level, tri-level, and five-level thresholding). They lead to the images shown in Fig. 4.8B–D: note particularly that the light shaded region on Lena’s nose is very stable and noise-free. Note that there is a potential confusion in the above process: as smoothing proceeds, the number of GVM thresholds progressively decreases. Hence the ordering of the respective images and traces in subfigures (F) to (H) appears inverted from this point of view. However, it is the logical order for the BCVM, for which computation increases approximately exponentially with the number of thresholds.

We concentrate next on a specific advantage of the GVM: that it produces robust judgments of minority intensities at the ends of the intensity range. Effectively, it amplifies such regions of the distribution and provides highly stable image segmentations: see in particular the under-vehicle shadows located in Fig. 23.1C and the ergot contaminant located in Fig. 4.9C. Note that these represent important vehicle guidance and inspection tasks: (1) use of under-vehicle shadows is a promising technique for locating vehicles on the road ahead (Liu et al., 2007); (2) ergot is poisonous and it is important to locate it among wheat or other grains that are to be used for human consumption (Davies, 2003b). The fact that GVM is able to make sense of the exceptionally noisy  $K$  distribution shown in Fig. 4.9D seems rather remarkable.

Comparing the GVM results with those of the BCVM (Fig. 4.8A, E), we see that the bi-level BCVM threshold appears to lie in an a priori quite

- 
- ◀ threshold selected by the BCVM. Bottom: the resulting  $K$  distribution. (F)–(H) The upper traces show smoothed versions of the  $K$  distribution, with short vertical lines indicating respectively one, two, or four threshold positions; the lower traces show threshold positions resulting from progressive smoothing of the  $K$  distribution: note that these are scaled and some are truncated as indicated by the horizontal gray line at the top; the horizontal dotted lines show how sets of threshold values are selected automatically (see text).

**Table 4.2** Basic Global Valley Algorithm

---

```

scan = 0;
do {
    numberofpeaks = 0;
    for (all intensity values in distribution) {
        if (peak found) {
            peakposition[scan, numberofpeaks] = intensity;
            numberofpeaks++;
        }
    }
    if (numberofpeaks == requirednumber) {
        if (previousnumberofpeaks > numberofpeaks) lowestscan = scan;
        else highestscan = scan;
    }
    previousnumberofpeaks = numberofpeaks;
    apply incremental smoothing kernel to distribution;
    scan++;
} while (numberofpeaks > 0);

optimumscan = (lowestscan*3 + highestscan)/4;
for (all peaks up to requirednumber)
    bestpeakposition[peak] = peakposition[optimumscan, peak];

```

---

*This version of the algorithm assumes that the required number of peaks (requirednumber) is known in advance, although the optimum amount of smoothing is unknown. Here the latter is estimated by taking a weighted mean of the lowest and highest numbers of smoothing scans that yield the required number of peaks. The final line of the algorithm gives the required number of peaks in the best positions. While this form of the algorithm obtains positions for a specific required number of peaks, the underlying process also maps out a complete set of stability graphs because it proceeds until the number of peaks is zero. For further details, see [Section 4.7](#).*

© IET 2008.

reasonable position in the intensity histogram: however, closer examination shows that the performance of the BCVM approximates to splitting the active area of the histogram into equal parts, corresponding to finding an approximate median. This means that for nearly unimodal histograms it has much less chance of leading to optimal segmentations. This view of its operation is supported by tests ([Fig. 4.10](#)) made on idealized histograms: these show that it is unable to locate the bottom of the valley. It is also noteworthy that, unlike the GVM, the multilevel BCVM sometimes misses thresholds at the ends of the range of intensities (see, for example, the vertical lines in the top trace of [Fig. 4.7D](#)).

Overall, it has been found that the GVM produces significantly more stable thresholds than the BCVM, it is less prone to producing noisy boundaries in the thresholded images, and its results tend to be more meaningful. In fact, the BCVM tends to split intensity distributions rather blindly into approximately

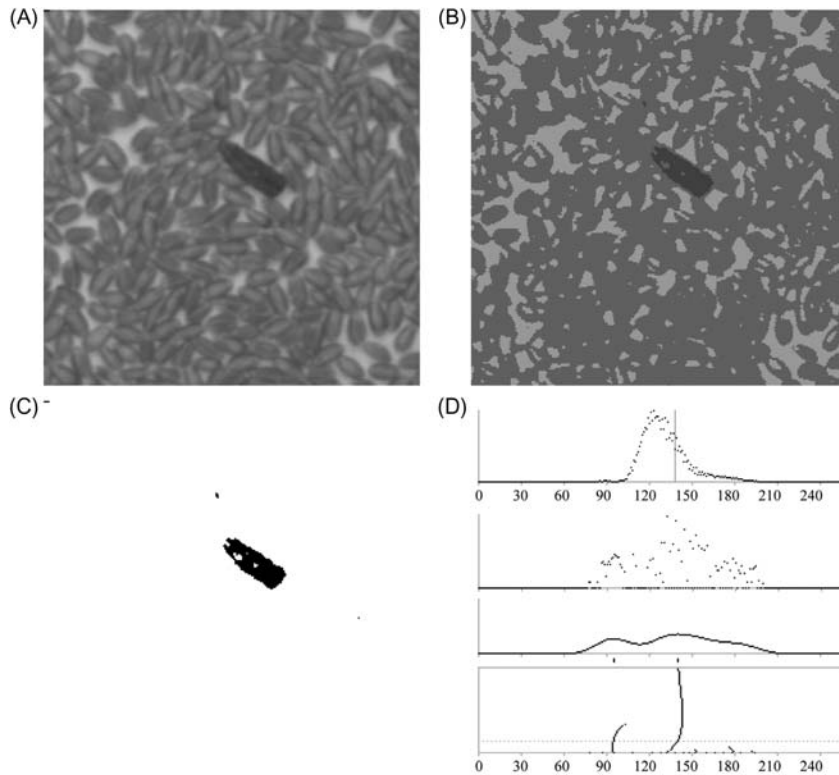


**FIGURE 4.9**

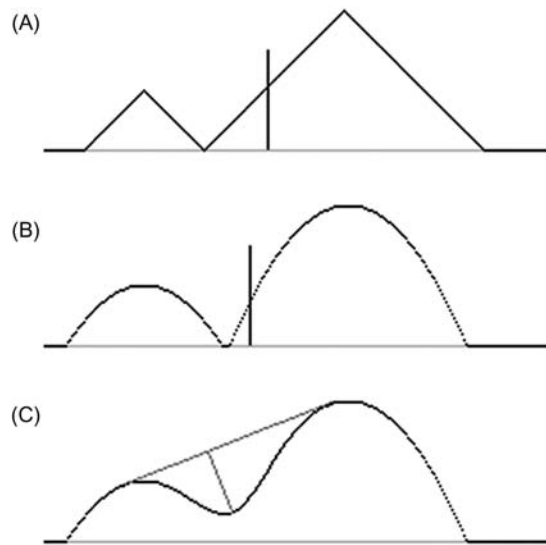
Location of ergot among wheat grains. (A) Original image. (B) Doubly thresholded image. (C) Result of only applying the lower threshold. (D) Top to bottom: intensity histogram of (A); result of applying the global valley transformation; result of smoothing the global valley transform; the two thresholds used in (B) are located automatically at the dotted line. The lower threshold is needed for locating any ergot, while the other can be used for separating wheat grains from the light conveyor background. For further details, see text.

© IET 2008.

equal areas: while its mathematical formulation does not explicitly aim at this, it often seems to have essentially this effect.

## 4.8 HISTOGRAM CONCAVITY ANALYSIS

In this section we briefly consider previous work on histogram concavity analysis. Rosin (2001) described how a simple geometrical construction (Fig. 4.10C) could be used to identify a suitable bi-level threshold. The technique depends on the

**FIGURE 4.10**

Results of applying the between class variance method (BCVM) and concavity analysis in idealized cases. Applying the BCVM to (A) a triangular histogram, and (B) a parabolic histogram. The vertical lines indicate the bi-level threshold selected by the BCVM: note that in each case it lies well away from the obvious global minimum of the histogram. (C) Finding thresholds by concavity analysis. The technique forms the convex hull of the distribution, takes each joining line, and uses the foot of the longest normal as an indicator of the threshold position. This approach is often highly effective but tends to give a result closer to the main peak than the optimum minimum location.

© IET 2008.

histogram having a “corner,” which is then easily identified, but when the corner is less well defined, bias can creep in and it becomes necessary to model the histogram distributions to obtain systematic corrections to the thresholding point. The approach will work for true unimodal distributions (including those produced by grayscale edge images) or for “nearly” unimodal distributions where there is a very weak mode in addition to the main mode. For true unimodal distributions the GVM will not work, because one of the component signals in function  $K$  is zero: in such cases it is imperative to use a method such as that described by Rosin—although others have been described over a long period, by Rosenfeld and de la Torre (1983), Tsai (1995) and others. For nearly unimodal distributions, the Rosin approach gives some intrinsic bias, as indicated in Fig. 4.10C: but it is presumably possible in many applications to perform modeling to overcome this problem. However, the need for modeling does not seem to arise with the GVM—as has already been demonstrated (see particularly Figs. 21.2 and 23.1).

---

## 4.9 CONCLUDING REMARKS

The preceding sections have revealed a number of factors that are crucial to the process of thresholding—in particular, to avoid bias in threshold selection by employing approximately equal populations in the dark and light regions of the intensity histogram and, when variations in illumination are present, to work within small neighborhoods so that the local intensity histograms have well-defined valleys.

In fact, these conditions are not necessarily compatible and compromises are needed in practical situations. In particular, it is generally not possible to find a neighborhood size that can be applied everywhere in an image, on all occasions yielding roughly equal populations of dark and light pixels. Indeed, if the chosen size is small enough to span edges ideally, hence yielding unbiased local thresholds, it will be valueless inside large objects. Attempting to avoid this situation by resorting to alternative methods of threshold calculation does not solve the problem since inherent to such methods is a built-in region size: this means that variable resolution solutions may be needed.

At this stage we call into question the complications involved in such thresholding procedures, which become even worse when intensity distributions start to become multimodal. Note that the overall procedure is to find local intensity gradients to obtain accurate, unbiased estimates of thresholds, so that it then becomes possible to take a horizontal slice through a grayscale image and hence, ultimately, find “vertical” (i.e., spatial) boundaries within the image. On the other hand, perhaps we should consider simplifying matters by using the gradients *directly* to estimate the boundary positions. Such an approach, for example, leads to no problems from large regions where intensity histograms are essentially unimodal, although it would be foolish to pretend that there are no other problems (see [Chapter 5](#): Edge Detection and [Chapter 10](#): Line, Circle, and Ellipse Detection).

On the whole, the author takes the view that many approaches (region-growing, thresholding, edge detection, etc.), *taken to the limits of approximation*, will give equally good results. After all, they are all limited by the same physical effects—image noise, variability of lighting, presence of shadows, etc. However, some methods are easier to coax into working well, need minimal computation, or have other useful properties such as robustness. Thus, thresholding can be a highly efficient means of aiding the interpretation of certain types of image: but as soon as image complexity rises above a certain critical level, it suddenly becomes more effective and considerably less complicated to rely on edge detection. This is studied in [Chapter 5](#), Edge Detection. Meanwhile, we must not overlook the possibility of easing the thresholding process by optimizing the lighting system and ensuring that any worktable or conveyor is kept clean and white: this turns out to be a viable approach in a surprisingly large number of industrial applications.

The end result of thresholding is a set of silhouettes representing the shapes of objects: these constitute a “binarized” version of the original image. Many techniques exist for performing binary shape analysis and some of these are described in [Chapter 8](#), Binary Shape Analysis. Meanwhile, note that many features of the original scene—for example, texture, grooves, or other surface structure—may not be present in the binarized image. Although the use of multiple thresholds to generate a number of binarized versions of the original image can preserve relevant information present in the original image, this approach is still limited, and eventually one may be forced to return to the original grayscale image for more detailed information.

*Thresholding is amongst the simplest of image processing operations and is an intrinsically appealing way of performing segmentation. While the approach is clearly limited, it would be a mistake to ignore it and its recent developments, which provide useful tools for the programmer's toolkit.*

---

## 4.10 BIBLIOGRAPHICAL AND HISTORICAL NOTES

Segmentation by thresholding started many years ago from simple beginnings and in recent years has been refined into a set of mature procedures. Among the notable early methods is the paradigm but computation intensive Chow and Kaneko method (1972), which was outlined in [Section 4.4.1](#). Nakagawa and Rosenfeld (1979) studied the method and developed it for cases of trimodal distributions but without improving computational load.

Fu and Mui (1981) provided a useful general survey on image segmentation: this was updated by Haralick and Shapiro (1985). These papers review many topics that could not be covered in the present chapter for reasons of space, which also applies for the valuable survey of thresholding techniques by Sahoo et al. (1988). Nevertheless, it is worth emphasizing the point made by Fu and Mui (1981) that “All the region extraction techniques process the pictures in an iterative manner and usually involve a great expenditure in computation time and memory.”

As hinted in [Section 4.4](#), thresholding (particularly local adaptive thresholding) has had many applications in OCR. Among the earliest were the algorithms described by Bartz (1968) and Ullmann (1974): two highly effective algorithms have been described by White and Rohrer (1983).

During the 1980s the entropy approach to automatic thresholding evolved (Pun, 1981; Kapur et al., 1985; Abutaleb, 1989; Pal and Pal, 1989): this approach ([Section 4.5.2](#)) proved highly effective, and its development continued during the 1990s (Hannah et al., 1995).

In the 2000s, the entropy approach to threshold selection has remained important, in respect to both conventional region location and ascertaining the transition region between objects and background to make the segmentation process more reliable (Yan et al., 2003). In one instance it was found useful to employ fuzzy entropy and genetic algorithms (Tao et al., 2003). Wang and Bai (2003) have shown how threshold selection may be made more reliable by clustering the intensities of boundary pixels, while ensuring that a continuous rather than a discrete boundary is considered (the problem being that in images that approximate to binary images over restricted regions, the edge points will lie preferentially in the object or the background, not neatly between both). However, in complex outdoor scenes and for many medical images such as brain scans, thresholding alone will not be sufficient, and resort may even have to be made to graph matching (see [Chapter 11](#): The Generalized Hough Transform) to produce the best results—reflecting the important fact that segmentation is necessarily a high-level rather than a low-level process (Wang and Siskind, 2003). In rather less demanding cases, deformable model-guided split-and-merge techniques may, however, still be sufficient (Liu and Sclaroff, 2004).

#### 4.10.1 MORE RECENT DEVELOPMENTS

Sezgin and Sankur (2004) give a thorough review and assessment of work on thresholding prior to 2004. More recently, there has been continued interest in thresholding in the case of unimodal (Coudray et al., 2010; Medina-Carnicer et al., 2011) and near-unimodal histograms (Davies, 2007a, 2008): the latter case is covered fairly fully in [Sections 4.6 and 4.7](#). In the case of Coudray et al. (2010), the aim is to threshold intensity gradient histograms to locate edges reliably: the approach taken is to model the contribution from noise as a Rayleigh distribution and then to devise heuristics for analyzing the overall distribution. With the same aim, Medina-Carnicer et al. (2011) show that applying a histogram transformation improves the performance of the Otsu (1979) and Rosin (2001) methods. Li et al. (2011) adopt the novel approach of constraining the gray-level ranges considered by the thresholding algorithm in such a way as to weaken gray-level changes in both foreground and background, thus simplifying the original image and making the intensity histogram more closely bimodal. After that several thresholding methods are found to operate more reliably. Ng (2006) describes a revised version of the Otsu (1979) method that operates well for unimodal distributions, and which is useful for defect detection. This “valley emphasis” method works by applying a weight to the Otsu threshold calculation. Overall, several of the recent developments can be construed as applying transformations or other improvements to older methods to make them more sophisticated and accurate: none is highly complex in any theoretical way. Finally, it may seem somewhat surprising that, after so many decades, thresholding is still something of a “hot” subject: that this is so must be because of its extreme simplicity and high level of utility.



---

## 4.11 PROBLEMS

1. Using the methods in Section 4.3.3, model the intensity distribution obtained by finding all the edge pixels in an image and including also all pixels adjacent to these pixels. Show that while this gives a sharper valley than for the original intensity distribution, it is not as sharp as for pixels located by the Laplacian operator.
2. Consider whether it is more accurate to estimate a suitable threshold for a bimodal, dual-Gaussian distribution by (a) finding the position of the minimum or (b) finding the mean of the two-peak positions. What corrections could be made by taking account of the magnitudes of the peaks?
3. Obtain a complete derivation of Eq. (4.19). Show that, in general (as stated in Section 4.5.3), it has two solutions. What is the physical reason for this? How can it have only one solution when  $\sigma_1 = \sigma_2$ ?
4. Prove the statement made in Section 4.6, that the computational load of the histogram analysis for the global value method can be reduced from  $O(N^3)$  to  $O(N)$ . Show also that the number of passes over the histogram required to achieve this is at most two.

Edge detection provides an intrinsically more rigorous means than thresholding for initiating image segmentation. However, there is a large history of ad hoc edge detection algorithms, and this chapter aims to distinguish what is principled from what is ad hoc and to provide theory and practical knowledge underpinning available techniques.

*Look out for:*

- the variety of template matching (TM) operators that have been used for edge detection—e.g., the Prewitt, Kirsch, and Robinson operators
- the differential gradient (DG) approach to edge detection—exemplified by the Roberts, Sobel, and Frei–Chen operators
- theory explaining the performance of the TM operators
- methods for the optimal design of DG operators, and the value of “circular” operators
- tradeoffs between resolution, noise suppression capability, location accuracy, and orientation accuracy
- the distinction between edge enhancement and edge detection
- outlines of more modern operators—the Canny and Laplacian-based operators.

In discussing the process of edge detection, this chapter shows that it is possible to estimate edge orientation with surprising accuracy within a small window—the secret being the considerable information residing in the grayscale values. High orientation accuracy turns out to be of particular value when using the Hough transform to locate extended objects in digital images—as will be seen in several chapters in Part 2, Intermediate-Level Vision, of this book.

## 5.1 INTRODUCTION

In [Chapter 4](#), The Role of Thresholding, segmentation was tackled by the general approach of finding regions of uniformity in images—on the basis that the areas found in this way would have a fair likelihood of coinciding with the surfaces and facets of objects. The most computationally efficient means of following this approach was that of thresholding, but for real images this turns out to be failure-prone or else quite difficult to implement satisfactorily. Indeed, to make it work well, it seems to require a multiresolution or hierarchical approach, coupled with

sensitive measures for obtaining suitable local thresholds. Such measures have to take account of local intensity gradients as well as pixel intensities, and the possibility of proceeding more simply—by taking account of intensity gradients alone—was suggested.

In fact, edge detection has long been an alternative path to image segmentation and is the method pursued in this chapter. Whichever way is inherently the better approach, edge detection has the additional advantage in that it immediately reduces by a large factor (typically around 100) the considerable redundancy of most image data: this is useful because it significantly reduces both the space needed to store the information and the amount of processing subsequently required to analyze it.

Edge detection has gone through an evolution spanning well over 30 years. Two main methods of edge detection have been apparent over this period, the first of these being TM and the second being the DG approach. In either case the aim is to find where the intensity gradient magnitude  $g$  is sufficiently large to be taken as a reliable indicator of the edge of an object. Then  $g$  can be thresholded in a similar way to that in which intensity was thresholded in Chapter 4, The Role of Thresholding (in fact, we shall see that it is possible to look for local maxima of  $g$  instead of, or as well as, thresholding it). The TM and DG methods differ mainly in how they proceed to estimate  $g$  locally: however, there are also important differences in how they determine local edge orientation, which is an important variable in certain object detection schemes. In Section 5.11 we look at the Canny operator, which was much more rigorously designed than previous edge detectors. Finally, we consider Laplacian-based operators.

Before proceeding to discuss the performance of the various edge detection operators, it will be useful to note that there is a variety of types of edge, including in particular the “sudden step” edge, the “slanted step” edge, the “planar” edge, and various intermediate edge profiles (Fig. 5.1). In most of this chapter we shall be concerned with edges that approximate to types (A)–(D) in Fig. 5.1: later on we shall consider those that approximate to types (E) and (F) in Fig. 5.1.

---

## 5.2 BASIC THEORY OF EDGE DETECTION

Both DG and TM operators estimate local intensity gradients with the aid of suitable convolution masks. In the case of the DG type of operator, only two such masks are required—for the  $x$  and  $y$  directions. In the TM case, it is usual to employ up to 12 convolution masks capable of estimating local components of gradient in the different directions (Prewitt, 1970; Kirsch, 1971; Robinson, 1977; Abdou and Pratt, 1979).

In the TM approach, the local edge gradient magnitude (for short, the edge “magnitude”) is approximated by taking the maximum of the responses for the component masks:

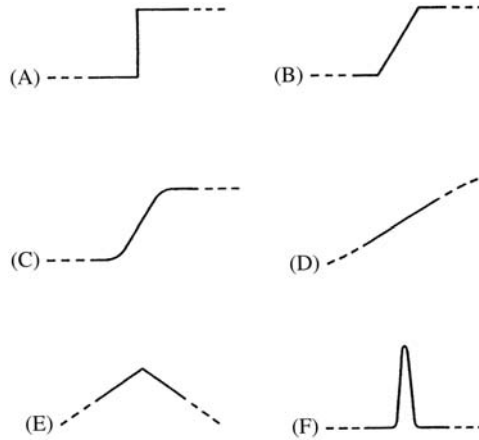


**FIGURE 5.1**

Edge models: (A) sudden step edge; (B) slanted step edge; (C) smooth step edge; (D) planar edge; (E) roof edge; and (F) line edge. The effective profiles of edge models are nonzero only within the stated neighborhood. The slanted step and the smooth step are approximations to realistic edge profiles: the sudden step and the planar edge are extreme forms that are useful for comparisons (see text). The roof and line edge models are shown for completeness only and are not considered further in this chapter.

$$g = \max(g_i; i = 1, \dots, n) \quad (5.1)$$

where  $n$  is usually 8 or 12.

In the DG approach, the local edge magnitude may be computed vectorially using the nonlinear transformation:

$$g = (g_x^2 + g_y^2)^{1/2} \quad (5.2)$$

In order to save computational effort, it is a common practice (Abdou and Pratt, 1979) to approximate this formula by one of the simpler forms:

$$g = |g_x| + |g_y| \quad (5.3)$$

or

$$g = \max(|g_x|, |g_y|) \quad (5.4)$$

which are, on average, equally accurate (Föglein, 1983).

In the TM approach, edge orientation is estimated simply as that of the mask giving rise to the largest value of gradient in Eq. (5.1). In the DG approach, it is estimated vectorially by the more complex equation:

$$\theta = \arctan(g_y/g_x) \quad (5.5)$$

Clearly, DG Eqs. (5.2) and (5.5) require considerably more computation than TM Eq. (5.1), although they are also more accurate. However, in some situations

orientation information is not required; in addition, image contrast may vary widely, so there may appear to be little gain from thresholding a more accurate estimate of  $g$ . This may explain why so many workers have employed the TM instead of the DG approach. Since both approaches essentially involve estimation of local intensity gradients, it is not surprising that TM masks often turn out to be identical to DG masks (Tables 5.1 and 5.2).

**Table 5.1** Masks of Well-known Differential Edge Operators

a. Masks for the Roberts  $2 \times 2$  operator:

$$R_{x'} = \begin{bmatrix} 0 & 1 \\ -1 & 0 \end{bmatrix} \quad R_{y'} = \begin{bmatrix} 1 & 0 \\ 0 & -1 \end{bmatrix}$$

b. Masks for the Sobel  $3 \times 3$  operator:

$$S_x = \begin{bmatrix} -1 & 0 & 1 \\ -2 & 0 & 2 \\ -1 & 0 & 1 \end{bmatrix} \quad S_y = \begin{bmatrix} 1 & 2 & 1 \\ 0 & 0 & 0 \\ -1 & -2 & -1 \end{bmatrix}$$

c. Masks for the Prewitt  $3 \times 3$  “smoothed gradient” operator:

$$P_x = \begin{bmatrix} -1 & 0 & 1 \\ -1 & 0 & 1 \\ -1 & 0 & 1 \end{bmatrix} \quad P_y = \begin{bmatrix} 1 & 1 & 1 \\ 0 & 0 & 0 \\ -1 & -1 & -1 \end{bmatrix}$$

*Masks are presented in an intuitive format (viz. coefficients increasing in the positive  $x$  and  $y$  directions) by rotating the normal convolution format through  $180^\circ$ . This convention is employed throughout this chapter. The Roberts  $2 \times 2$  operator masks (a) can be taken as being referred to axes  $x'$ ,  $y'$  at  $45^\circ$  to the usual  $x$ ,  $y$  axes.*

**Table 5.2** Masks of Well-known  $3 \times 3$  Template Matching Edge Operators

	$0^\circ$	$45^\circ$
a. Prewitt masks	$\begin{bmatrix} -1 & 1 & 1 \\ -1 & -2 & 1 \\ -1 & 1 & 1 \end{bmatrix}$	$\begin{bmatrix} 1 & 1 & 1 \\ -1 & -2 & 1 \\ -1 & -1 & 1 \end{bmatrix}$
b. Kirsch masks	$\begin{bmatrix} -3 & -3 & 5 \\ -3 & 0 & 5 \\ -3 & -3 & 5 \end{bmatrix}$	$\begin{bmatrix} -3 & 5 & 5 \\ -3 & 0 & 5 \\ -3 & -3 & -3 \end{bmatrix}$
c. Robinson “three-level” masks	$\begin{bmatrix} -1 & 0 & 1 \\ -1 & 0 & 1 \\ -1 & 0 & 1 \end{bmatrix}$	$\begin{bmatrix} 0 & 1 & 1 \\ -1 & 0 & 1 \\ -1 & -1 & 0 \end{bmatrix}$
d. Robinson “five-level” masks	$\begin{bmatrix} -1 & 0 & 1 \\ -2 & 0 & 2 \\ -1 & 0 & 1 \end{bmatrix}$	$\begin{bmatrix} 0 & 1 & 2 \\ -1 & 0 & 1 \\ -2 & -1 & 0 \end{bmatrix}$

*The table illustrates only two of the eight masks in each set: the remaining masks can in each case be generated by symmetry operations. For the three-level and five-level operators, four of the eight available masks are inverted versions of the other four (see text).*

### 5.3 THE TEMPLATE MATCHING APPROACH

Table 5.2 shows four sets of well-known TM masks for edge detection. These masks were originally (Prewitt, 1970; Kirsch, 1971; Robinson, 1977) introduced on an intuitive basis, starting in two cases from the DG masks shown in Table 5.1. In all cases the eight masks of each set are obtained from a given mask by permuting the mask coefficients cyclically. By symmetry, this is a good strategy for even permutations, but symmetry alone does not justify it for odd permutations—the situation is explored in more detail below.

Note first that four of the “three-level” and four of the “five-level” masks can be generated from the other four of their set by sign inversion. This means that in either case only four convolutions need to be performed at each pixel neighborhood, thereby saving computation. This is an obvious procedure if the basic idea of the TM approach is regarded as one of comparing intensity gradients in the eight directions. The two operators that do not employ this strategy were developed much earlier on some unknown intuitive basis.

Before proceeding, we note the rationale behind the Robinson “five-level” masks. These were intended (Robinson, 1977) to emphasize the weights of diagonal edges in order to compensate for the characteristics of the human eye, which tends to enhance vertical and horizontal lines in images. Normally, image analysis is concerned with computer interpretation of images and an isotropic set of responses is required. Thus the “five-level” operator is a special purpose one that need not be discussed further here.

These considerations show that the four template operators mentioned above have limited theoretical justification. It is therefore worth studying the situation in more depth: this is done in the next section.

### 5.4 THEORY OF $3 \times 3$ TEMPLATE OPERATORS

In the following it is assumed that eight masks are to be used, with angles differing by  $45^\circ$ . In addition, four of the masks differ from the others only in sign, since this seems unlikely to result in any loss of performance. Symmetry requirements then lead to the following masks for  $0^\circ$  and  $45^\circ$ , respectively.

$$\begin{bmatrix} -A & 0 & A \\ -B & 0 & B \\ -A & 0 & A \end{bmatrix} \quad \begin{bmatrix} 0 & C & D \\ -C & 0 & C \\ -D & -C & 0 \end{bmatrix}$$

It is clearly of great importance to design masks, so that they give consistent responses in different directions. To find how this affects the mask coefficients,

we employ the strategy of ensuring that intensity gradients follow the rules of vector addition. If the pixel intensity values within a  $3 \times 3$  neighborhood are

$$\begin{array}{|c|c|c|} \hline a & b & c \\ \hline d & e & f \\ \hline g & h & i \\ \hline \end{array}$$

then the above masks will give the following estimates of gradient in the  $0^\circ$ ,  $90^\circ$ , and  $45^\circ$  directions:

$$g_0 = A(c + i - a - g) + B(f - d) \quad (5.6)$$

$$g_{90} = A(a + c - g - i) + B(b - h) \quad (5.7)$$

$$g_{45} = C(b + f - d - h) + D(c - g) \quad (5.8)$$

If vector addition is to be valid, then:

$$g_{45} = (g_0 + g_{90})/\sqrt{2} \quad (5.9)$$

Equating coefficients of  $a$ ,  $b$ , ...,  $i$  leads to the self-consistent pair of conditions:

$$C = B/\sqrt{2} \quad (5.10)$$

$$D = A\sqrt{2} \quad (5.11)$$

A further requirement is for the  $0^\circ$  and  $45^\circ$  masks to give equal responses at  $22.5^\circ$ . This can be shown to lead to the formula

$$B/A = \sqrt{2} \frac{9t^2 - (14 - 4\sqrt{2})t + 1}{t^2 - (10 - 4\sqrt{2})t + 1} \quad (5.12)$$

where  $t = \tan 22.5^\circ$ , so that

$$B/A = (13\sqrt{2} - 4)/7 = 2.055 \quad (5.13)$$

We can now summarize our findings with regard to the design of TM masks. First, obtaining sets of masks by permuting coefficients “cyclically” in a square neighborhood is ad hoc and cannot be relied upon to produce useful results. Next, following the rules of vector addition and the need to obtain consistent responses in different directions, we have shown that ideal TM masks need to closely match the Sobel coefficients; we have also rigorously derived an accurate value for the ratio  $B/A$ .

Having obtained some insight into the process of designing TM masks for edge detection, we next move on to study the design of DG masks.

**Table 5.3** Masks for Estimating Components of Gradient in Square Neighborhoods

	$M_x$	$M_y$
a. $2 \times 2$ neighborhood	$\begin{bmatrix} -1 & 1 \\ -1 & 1 \end{bmatrix}$	$\begin{bmatrix} 1 & -1 \\ -1 & -1 \end{bmatrix}$
b. $3 \times 3$ neighborhood	$\begin{bmatrix} -1 & 0 & 1 \\ -1 & 0 & 1 \\ -1 & 0 & 1 \end{bmatrix}$	$\begin{bmatrix} 1 & 1 & 1 \\ 0 & 0 & 0 \\ -1 & -1 & -1 \end{bmatrix}$
c. $4 \times 4$ neighborhood	$\begin{bmatrix} -3 & -1 & 1 & 3 \\ -3 & -1 & 1 & 3 \\ -3 & -1 & 1 & 3 \\ -3 & -1 & 1 & 3 \end{bmatrix}$	$\begin{bmatrix} 3 & 3 & 3 & 3 \\ 1 & 1 & 1 & 1 \\ -1 & -1 & -1 & -1 \\ -3 & -3 & -3 & -3 \end{bmatrix}$
d. $5 \times 5$ neighborhood	$\begin{bmatrix} -2 & -1 & 0 & 1 & 2 \\ -2 & -1 & 0 & 1 & 2 \\ -2 & -1 & 0 & 1 & 2 \\ -2 & -1 & 0 & 1 & 2 \\ -2 & -1 & 0 & 1 & 2 \end{bmatrix}$	$\begin{bmatrix} 2 & 2 & 2 & 2 & 2 \\ 1 & 1 & 1 & 1 & 1 \\ 0 & 0 & 0 & 0 & 0 \\ -1 & -1 & -1 & -1 & -1 \\ -2 & -2 & -2 & -2 & -2 \end{bmatrix}$

The above masks can be regarded as extended Prewitt masks. The  $3 \times 3$  masks are Prewitt masks, included in this table for completeness. In all cases weighting factors have been omitted in the interests of simplicity, as they are throughout this chapter.

## 5.5 THE DESIGN OF DIFFERENTIAL GRADIENT OPERATORS

This section studies the design of DG operators. These include the Roberts  $2 \times 2$  operator and the Sobel and Prewitt  $3 \times 3$  operators (Roberts et al., 1965; Prewitt, 1970; for the Sobel operator, see Pringle, 1969; Duda and Hart, 1973, p. 271) (Table 5.1). The Prewitt or “gradient smoothing” type of operator has been extended to larger pixel neighborhoods by Prewitt (1970) and others (Brooks, 1978; Haralick, 1980) (Table 5.3). In these instances the basic rationale is to model local edges by the best fitting plane over a convenient size of neighborhood. Mathematically, this amounts to obtaining suitably weighted averages to estimate slope in the  $x$  and  $y$  directions. As pointed out by Haralick (1980), the use of equally weighted averages to measure slope in a given direction is incorrect: the proper weightings to use are given by the masks listed in Table 5.3. Thus the Roberts and Prewitt operators are apparently optimal, whereas the Sobel operator is not. This will be discussed in more detail below.

A full discussion of the edge detection problem involves consideration of the accuracy with which edge magnitude and orientation can be estimated when the local intensity pattern cannot be assumed to be planar. In fact, there have been a number of analyses of the angular dependencies of edge detection operators for a step edge approximation. In particular, O’Gorman (1978) considered the variation of estimated versus actual angle resulting from a step edge observed within a square neighborhood (see also Brooks, 1978): note that the case considered was that of a continuum rather



than a discrete lattice of pixels. This was found to lead to a smooth variation with angular error varying from zero at  $0^\circ$  and  $45^\circ$  to a maximum of  $6.63^\circ$  at  $28.37^\circ$  (where the estimated orientation was  $21.74^\circ$ ), the variation for angles outside this range being replicated by symmetry. Abdou and Pratt (1979) obtained similar variations for the Sobel and Prewitt operators in a discrete lattice, the respective maximum angular errors being  $1.36^\circ$  and  $7.38^\circ$  (Davies, 1984b). It seems that the Sobel operator has angular accuracy that is close to optimal because it is close to being a “truly circular” operator. This point is discussed in more detail below.

---

## 5.6 THE CONCEPT OF A CIRCULAR OPERATOR

It was stated above that when step edge orientation is estimated in a square neighborhood, an error of up to  $6.63^\circ$  can result. Such an error does not arise with a planar edge approximation, since fitting of a plane to a planar edge profile within a square window can be carried out exactly. Errors appear only when the edge profile differs from the ideal planar form, within the square neighborhood—with the step edge probably being something of a “worst case.”

One way to limit errors in the estimation of edge orientation might be to restrict observation of the edge to a circular neighborhood. In the continuous case this is sufficient to reduce the error to zero for all orientations, since symmetry dictates that there is only one way of fitting a plane to a step edge within a circular neighborhood, assuming that all planes pass through the same central point; the estimated orientation  $\theta$  is then equal to the actual angle  $\varphi$ . A rigorous calculation along the lines indicated by Brooks (1976), which results in the following formula for a square neighborhood (O’Gorman, 1978):

$$\tan \theta = 2 \tan \varphi / (3 - \tan^2 \varphi) \quad 0^\circ \leq \varphi \leq 45^\circ \quad (5.14)$$

leads to the following formula

$$\tan \theta = \tan \varphi, \quad \text{i.e., } \theta = \varphi \quad (5.15)$$

for a circular neighborhood (Davies, 1984b). Similarly, zero angular error results from fitting a plane to an edge of *any* profile within a circular neighborhood, in the continuous approximation. Indeed, for an edge surface of arbitrary shape, the only problem is whether the mathematical best-fit plane coincides with one that is subjectively desirable (and, if not, a fixed angular correction will be required). Ignoring such cases, the basic problem is how to approximate a circular neighborhood in a digitized image of small dimensions, containing typically  $3 \times 3$  or  $5 \times 5$  pixels.

To proceed systematically, we first recall a fundamental principle stated by Haralick (1980):

*the fact that the slopes in two orthogonal directions determine the slope in any direction is well known in vector calculus. However, it seems not to be so well known in the image processing community.*

Essentially, appropriate estimates of slopes in two orthogonal directions permit the slope in any direction to be computed. For this principle to apply, appropriate estimates of the slopes have first to be made: if the components of slope are inappropriate, they will not act as components of true vectors and the resulting estimates of edge orientation will be in error. This appears to be the main source of error with the Prewitt and other operators—it is not so much that the components of slope are in any instance incorrect, but rather that they are inappropriate for the purpose of vector computation since *they do not match one another adequately in the required way* (Davies, 1984b).

Following the arguments for the continuous case discussed earlier, slopes must be rigorously estimated within a circular neighborhood. Then the operator design problem devolves into determining how best to simulate a circular neighborhood on a discrete lattice so that errors are minimized. In order to carry this out, it is necessary to apply a close to circular weighting while computing the masks, so that correlations between the gradient weighting and circular weighting factors are taken properly into account.

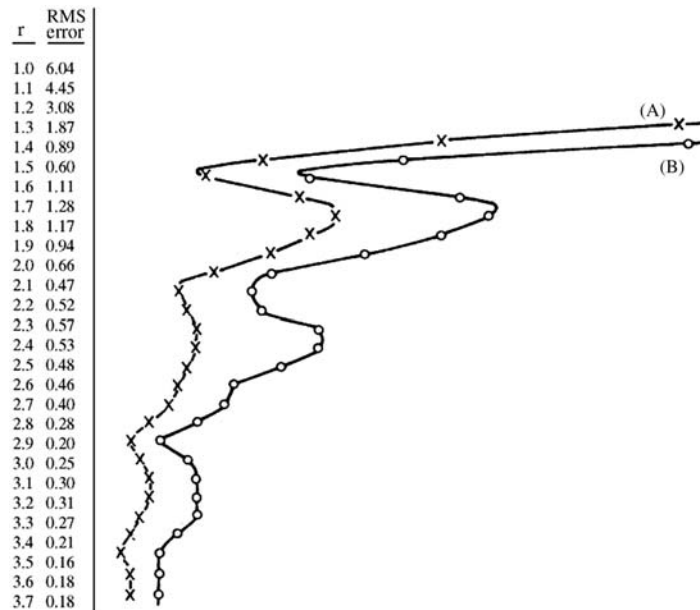
---

## 5.7 DETAILED IMPLEMENTATION OF CIRCULAR OPERATORS

In practice, the task of computing angular variations and error curves has to be tackled numerically, dividing each pixel in the neighborhood into arrays of suitably small subpixels. Each subpixel is then assigned a gradient weighting (equal to the  $x$  or  $y$  displacement) and a neighborhood weighting (equal to 1 for inside and 0 for outside a circle of radius  $r$ ). Clearly, the angular accuracy of “circular” DG edge detection operators must depend on the radius of the circular neighborhood. In particular, poor accuracy would be expected for small values of  $r$  and reasonable accuracy for large values of  $r$ , as the discrete neighborhood approaches a continuum.

The results of such a study are presented in [Fig. 5.2](#). The variations depicted represent (1) root mean square (RMS) angular errors and (2) maximum angular errors in the estimation of edge orientation. The structures on each variation are surprisingly smooth: they are so closely related and systematic that they can only represent statistics of the arrangement of pixels in neighborhoods of various sizes. Details of these statistics are discussed in [Section 5.8](#).

Overall, three features of [Fig. 5.2](#) are worthy of note. First, as expected, there is a general trend to zero angular error as  $r$  tends to infinity. Second, there is a very marked periodic variation, with particularly good accuracy resulting where the circular operators best match the tessellation of the digital lattice. The third feature of interest is the fact that errors do not vanish for any finite value of  $r$ —clearly, the constraints of the problem do not permit more than the minimization of errors. These curves show that it is possible to generate a family of optimal

**FIGURE 5.2**

Variations in angular error as a function of radius  $r$ : (A) RMS angular error; (B) maximum angular error.

operators (at the minima of the error curves), the first of which corresponds closely to an operator (the Sobel operator) that is known to be nearly optimal.

The variations shown in Fig. 5.2 can be explained (Davies, 1984b) as pixel centers lying in well packed or “closed” bands approximating to continua—indicated by the low error points in Fig. 5.2—between which centers would be more loosely packed. Thus we get the “closed band” operators listed in Table 5.4: their angular variations appear in Table 5.5. It is seen that the Sobel operator, which is already the most accurate of the  $3 \times 3$  edge gradient operators suggested previously, can be made some 30% more accurate by adjusting its coefficients to make it more circular. In addition, the closed bands idea indicates that the corner pixels of  $5 \times 5$  or larger operators are best removed altogether: not only does this require less computation but also it actually improves performance. It also seems likely that this situation would apply for many other operators and would not be specific to edge detection.

Before leaving this topic, note that the optimal  $3 \times 3$  masks obtained above numerically by consideration of circular operators are very close indeed to those obtained purely analytically in Section 5.4, for TM masks, following the rules of vector addition. In the latter case a value of 2.055 was obtained for the ratio of the two mask coefficients, whereas for circular operators the value

**Table 5.4** Masks of “Closed Band” Differential Gradient Edge Operators

a. Band containing shells a–c (effective radius = 1.500)

$$\begin{bmatrix} -0.464 & 0.000 & 0.464 \\ -0.959 & 0.000 & 0.959 \\ -0.464 & 0.000 & 0.464 \end{bmatrix}$$

b. Band containing shells a–e (effective radius = 2.121)

$$\begin{bmatrix} 0.000 & -0.294 & 0.000 & 0.294 & 0.000 \\ -0.582 & -1.000 & 0.000 & 1.000 & 0.582 \\ -1.085 & -1.000 & 0.000 & 1.000 & 1.085 \\ -0.582 & -1.000 & 0.000 & 1.000 & 0.582 \\ 0.000 & -0.294 & 0.000 & 0.294 & 0.000 \end{bmatrix}$$

c. Band containing shells a–h (effective radius = 2.915)

$$\begin{bmatrix} 0.000 & 0.000 & -0.191 & 0.000 & 0.191 & 0.000 & 0.000 \\ 0.000 & -1.085 & -1.000 & 0.000 & 1.000 & 1.085 & 0.000 \\ -0.585 & -2.000 & -1.000 & 0.000 & 1.000 & 2.000 & 0.585 \\ -1.083 & -2.000 & -1.000 & 0.000 & 1.000 & 2.000 & 1.083 \\ -0.585 & -2.000 & -1.000 & 0.000 & 1.000 & 2.000 & 0.585 \\ 0.000 & -1.085 & -1.000 & 0.000 & 1.000 & 1.085 & 0.000 \\ 0.000 & 0.000 & -0.191 & 0.000 & 0.191 & 0.000 & 0.000 \end{bmatrix}$$

*In all cases only the x-mask is shown: the y-mask may be obtained by a trivial symmetry operation. Mask coefficients are accurate to ~0.003 but would in normal practical applications be rounded to 1- or 2-figure accuracy.*

**Table 5.5** Angular Variations for the Best Operators Tested

Actual Angle (degrees)	Estimated Angle (degrees) <sup>a</sup>					
	Prew	Sob	a–c	circ	a–e	a–h
0	0.00	0.00	0.00	0.00	0.00	0.00
5	3.32	4.97	5.05	5.14	5.42	5.22
10	6.67	9.95	10.11	10.30	10.81	10.28
15	10.13	15.00	15.24	15.52	15.83	14.81
20	13.69	19.99	20.29	20.64	20.07	19.73
25	17.72	24.42	24.73	25.10	24.62	25.00
30	22.62	28.86	29.14	29.48	29.89	30.02
35	28.69	33.64	33.86	34.13	35.43	34.86
40	35.94	38.87	39.00	39.15	40.30	39.71
45	45.00	45.00	45.00	45.00	45.00	45.00
RMS error	5.18	0.73	0.60	0.53	0.47	0.19

Key: Prew, Prewitt. Sob, Sobel. a–c, theoretical optimum—closed band containing shells a–c. circ, actual optimum circular operator (as defined by the first minimum in Fig. 6.2). a–e, theoretical optimum—closed band containing shells a–e. a–h, theoretical optimum—closed band containing shells a–h.

<sup>a</sup>Values are accurate to within ~0.02° in each case.

$0.959/0.464 = 2.067 \pm 0.015$  is obtained. Clearly this is no accident and it is very satisfying that a coefficient that was formerly regarded as ad hoc (Kittler, 1983) is in fact optimizable and can be obtained in closed form (Section 5.4).

---

## 5.8 THE SYSTEMATIC DESIGN OF DIFFERENTIAL EDGE OPERATORS

The family of “circular” DG edge operators studied in Sections 5.6 and 5.7 incorporates only one design parameter—the radius  $r$ . Only a limited number of values of this parameter permit optimum accuracy for estimation of edge orientation to be attained.

It is worth considering what additional properties this one parameter can control and how it should be adjusted during operator design. In fact, it affects signal-to-noise ratio, resolution, measurement accuracy, and computational load. To understand this, note first that signal-to-noise ratio varies linearly with the radius of the circular neighborhood, since signal is proportional to area and Gaussian noise is proportional to the square root of area. Likewise, the measurement accuracy is determined by the number of pixels over which averaging occurs and hence is proportional to operator radius. Resolution and “scale” also vary with radius, since relevant linear properties of the image are averaged over the active area of the neighborhood. Finally, computational load, and the associated cost of hardware for speeding up the processing, is generally at least in proportion to the number of pixels in the neighborhood, and hence proportional to  $r^2$ .

Overall, the fact that four important parameters vary in a fixed way with the radius of the neighborhood means that there are exact tradeoffs between them, and that improvements in some are only obtained by losses to others: from an engineering point of view compromises between them will have to be made according to circumstances.

---

## 5.9 PROBLEMS WITH THE ABOVE APPROACH—SOME ALTERNATIVE SCHEMES

Although the above ideas may be interesting, they have their own inherent problems. In particular, they take no account of the displacement  $E$  of the edge from the center of the neighborhood or of the effects of noise in biasing the estimates of edge magnitude and orientation. In fact, it is possible to show that a Sobel operator gives *zero* error in the estimation of step edge orientation under the following condition:

$$|\theta| \leq \arctan(1/3) \quad \text{and} \quad |E| \leq (\cos \theta - 3 \sin|\theta|)/2 \quad (5.16)$$

Furthermore, for a  $3 \times 3$  operator of the form

$$\begin{bmatrix} -1 & 0 & 1 \\ -B & 0 & B \\ -1 & 0 & 1 \end{bmatrix} \begin{bmatrix} 1 & B & 1 \\ 0 & 0 & 0 \\ -1 & -B & -1 \end{bmatrix}$$

applied to the edge

$$\begin{array}{|ccc|} \hline a & a+h(0.5-E \sec \theta + \tan \theta) & a+h \\ a & a+h(0.5-E \sec \theta) & a+h \\ a & a+h(0.5-E \sec \theta - \tan \theta) & a+h \\ \hline \end{array}$$

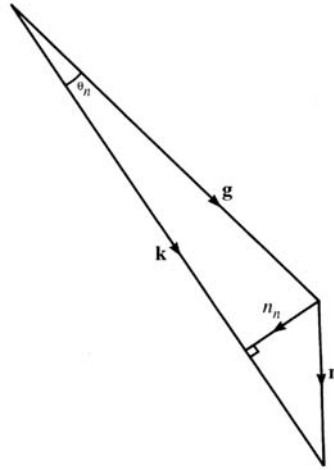
Lyvers and Mitchell (1988) found that the estimated orientation is:

$$\varphi = \arctan[2B \tan \theta / (B + 2)] \quad (5.17)$$

which immediately shows why the Sobel operator should give zero error for a specific range of  $\theta$  and  $E$ . However, this is somewhat misleading, since considerable errors arise outside this region. Not only do they arise when  $E = 0$ , as assumed in the foregoing sections but also they vary strongly with  $E$ . Indeed, the maximum errors for the Sobel and Prewitt operators rise to  $2.90^\circ$  and  $7.43^\circ$ , respectively, in this more general case (the corresponding RMS errors are  $1.20^\circ$  and  $4.50^\circ$ , respectively). Hence a full analysis should be performed to determine how to reduce the maximum and average errors. Lyvers and Mitchell (1988) carried out an empirical analysis and constructed a lookup table with which to correct the orientations estimated by the Sobel operator, the maximum error being reduced to  $2.06^\circ$ .

Another scheme that reduces the error is the moment-based operator of Reeves et al. (1983). This leads to Sobel-like  $3 \times 3$  masks that are essentially identical to the  $3 \times 3$  masks of Davies (1984b), both having  $B = 2.067$  (for  $A = 1$ ). However, the moment method can also be used to estimate the edge position  $E$  if additional masks are used to compute second-order moments of intensity. Hence it is possible to make a very significant improvement in performance by using a 2-D lookup table to estimate orientation: the result is that the maximum error is reduced from  $2.83^\circ$  to  $0.135^\circ$  for  $3 \times 3$  masks, and from  $0.996^\circ$  to  $0.0042^\circ$  for  $5 \times 5$  masks.

However, Lyvers and Mitchell (1988) found that much of this additional accuracy is lost in the presence of noise, and RMS standard deviations of edge orientation estimates are already around  $0.5^\circ$  for  $3 \times 3$  operators at 40 db signal-to-noise ratios. The reasons for this are quite simple. Each pixel intensity has a noise component that induces errors in its weighted mask components; the combined effects of these errors can be estimated assuming that they arise independently, so that their variances add (Davies, 1987b). Thus noise contributions to the  $x$  and  $y$  components of gradient can be computed. These provide estimates for the components of noise along and perpendicular to the edge gradient vector

**FIGURE 5.3**

Calculating angular errors arising from noise:  $\mathbf{g}$ , intensity gradient vector;  $\mathbf{n}$ , noise vector;  $\mathbf{k}$ , resultant of intensity gradient and noise vector;  $n_n$ , normal component of noise;  $\theta_n$ , noise-induced orientation error.

(Fig. 5.3): the edge orientation for a Sobel operator turns out to be affected by an amount  $\sqrt{12}\sigma/4h$  radians, where  $\sigma$  is the standard deviation on the pixel intensity values and  $h$  is the edge contrast. This explains the angular errors given by Lyvers and Mitchell, if Pratt's (2001) definition of signal-to-noise ratio (in decibels) is used:

$$S/N = 20 \log_{10}(h/\sigma) \quad (5.18)$$

A totally different approach to edge detection was developed by Canny (1986). He used functional analysis to derive an optimal function for edge detection, starting with three optimization criteria—good detection, good localization, and only one response per edge under white noise conditions. The analysis is too technical to be discussed in detail here. However, the 1-D function found by Canny is accurately approximated by the derivative of a Gaussian: this is then combined with a Gaussian of identical  $\sigma$  in the perpendicular direction, truncated at 0.001 of its peak value, and split into suitable masks. Underlying this method is the idea of locating edges at local maxima of gradient magnitude for a Gaussian-smoothed image. In addition, the Canny implementation employs a hysteresis operation (Section 5.10) on edge magnitude in order to make edges reasonably connected. Finally, a multiple scale method is employed to analyze the output of the edge detector. More details will be said about these points below. Lyvers and Mitchell (1988) tested the Canny operator and found it to be significantly less accurate for orientation estimation than the

moment and integrated directional derivative (IDD) operators described above. In addition, it needed to be implemented using 180 masks and hence took enormous computation time, although many practical implementations of this operator are much faster than this early paper indicates. Indeed, it is nowadays necessary to ask “Which Canny?”, as there are a great many implementations of it, and this leads to problems for any realistic comparison between operators. One such implementation is described in [Section 5.11](#).

An operator that has been of great historical importance is that of Marr and Hildreth (1980). The motivation for the design of this operator was the modeling of certain psychophysical processes in mammalian vision. The basic rationale is to find the Laplacian of the Gaussian-smoothed ( $\nabla^2 G$ ) image and then to obtain a “raw primal sketch” as a set of zero-crossing lines. The Marr–Hildreth operator does not use any form of threshold since it merely assesses where the  $\nabla^2 G$  image passes through zero. This feature is attractive, since working out threshold values is a difficult and unreliable task. However, the Gaussian smoothing procedure can be applied at a variety of scales, and in one sense the scale is a new parameter that substitutes for the threshold. In fact, a major feature of the Marr–Hildreth approach, which has been very influential in later work (Witkin, 1983; Bergholm, 1986), is the fact that zero-crossings can be obtained at several scales, giving the potential for more powerful semantic processing: clearly, this necessitates finding means for combining all the information in a systematic and meaningful way. This may be carried out by bottom-up or top-down approaches, and there has been much discussion in the literature about methods for carrying out these processes. However, it is worth remarking that in many (especially industrial inspection) applications, one is interested in working at a particular resolution and considerable savings in computation can then be made. It is also noteworthy that the Marr–Hildreth operator is reputed to require neighborhoods of at least  $35 \times 35$  for proper implementation (Brady, 1982). Nevertheless, other workers have implemented the operator in much smaller neighborhoods, down to  $5 \times 5$ . Wiejak et al. (1985) showed how to implement the operator using linear smoothing operations to save computation. Lyvers and Mitchell (1988) reported orientation accuracies using the Marr–Hildreth operator that are not especially high ( $2.47^\circ$  for a  $5 \times 5$  operator and  $0.912^\circ$  for a  $7 \times 7$  operator, in the absence of noise).

It was noted above that those edge detection operators that are applied at different scales lead to different edge maps at different scales. In such cases, certain edges that are present at lower scales disappear at larger scales; in addition, edges that are present at both low and high scales appear shifted or merged at higher scales. Bergholm (1986) demonstrated the occurrence of elimination, shifting, and merging, while Yuille and Poggio (1986) showed that edges that are present at high resolution should not disappear at some lower resolution. These aspects of edge location are by now well understood.



In what follows we first consider hysteresis thresholding, a process already mentioned with regard to the Canny operator. In [Section 5.11](#) we give a fuller appraisal of the Canny operator and show detailed results on real images. Then in [Section 5.12](#) we consider the Laplacian type of operator.

---

## 5.10 HYSTERESIS THRESHOLDING

The concept of hysteresis thresholding is a general one and can be applied in a range of applications, including both image and signal processing. In fact, the Schmitt trigger is a very widely used electronic circuit for converting a varying voltage into a pulsed (binary) waveform. In this latter case there are two thresholds, and the input has to rise above the upper threshold before the output is allowed to switch on and has to fall below the lower threshold before the output is allowed to switch off. This gives considerable immunity against noise in the input waveform—far more than where the difference between the upper and lower switching thresholds is zero (the case of zero hysteresis), since then a small amount of noise can cause an undue amount of switching between the upper and lower output levels.

When the concept is applied in image processing, it is usually with regard to edge detection, in which case there is an exactly analogous 1-D waveform to be negotiated around the boundary of an object, although as we shall see, some specifically 2-D complications arise. The basic rule is to threshold the edge at a high level and then to allow extension of the edge down to a lower level threshold but only adjacent to points that have already been assigned edge status.

[Fig. 5.4](#) shows the results of making tests on the edge gradient image in [Fig. 5.4E](#). [Figs. 5.4A and B](#) show the result of thresholding at the upper and lower hysteresis levels, respectively, and [Fig. 5.4C](#) shows the result of hysteresis thresholding using these two levels. For comparison, [Fig. 5.4D](#) shows the effect of thresholding at a suitably chosen intermediate level. Note that isolated edge points within the object boundaries are ignored by hysteresis thresholding, although noise spurs can occur and are retained. We can envision the process of hysteresis thresholding in an edge image as the location of points that

1. form a superset of the upper threshold edge image;
2. form a subset of the lower threshold edge image; and
3. form that subset of the lower threshold image that is connected to points in the upper threshold image via the usual rules of connectedness (see [Chapter 8: Binary Shape Analysis](#)).

Clearly, edge points only survive if they are seeded by points in the upper threshold image.

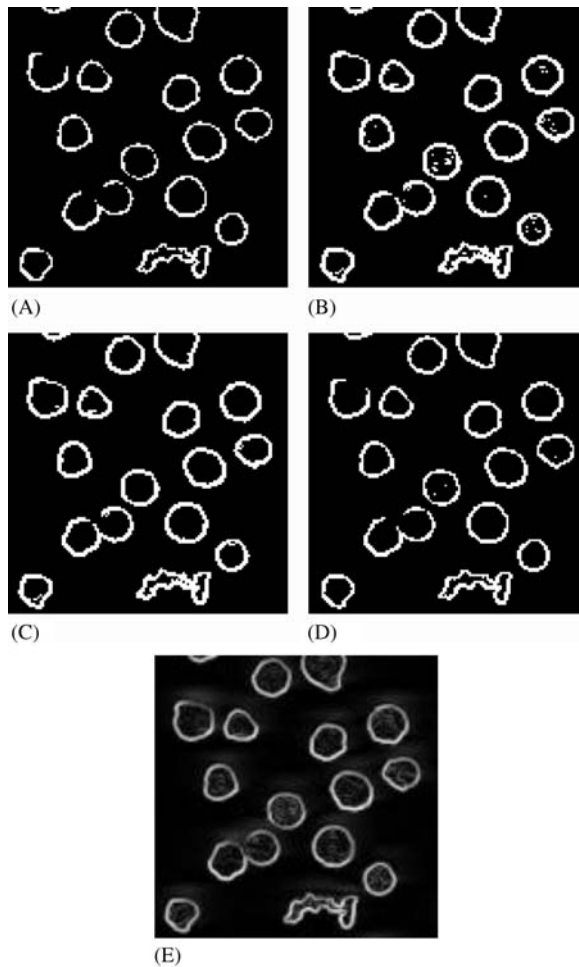


**FIGURE 5.4**

Effectiveness of hysteresis thresholding. (A) Effect of thresholding at the upper hysteresis level. (B) Effect of thresholding at the lower hysteresis level. (C) Effect of hysteresis thresholding. (D) Effect of thresholding at an intermediate level. This figure shows tests made on the edge gradient image in (E) (the latter was obtained by applying a Sobel operator to the image of Fig. 3.26A).

© World Scientific 2000.

While the result in Fig. 5.4C is better than in Fig. 5.4D, where gaps in the boundaries are eliminated or reduced in length, noise spurs are introduced in a few cases. Nevertheless, the aim of hysteresis thresholding is to obtain a better balance between false positives and false negatives by exploiting connectedness in the object boundaries. Indeed, if managed correctly, the additional parameter

will normally lead to a net (average) reduction in boundary pixel classification error. However, there are few simple guidelines for selection of hysteresis thresholds, apart from the following:

1. use a pair of hysteresis thresholds, which provides immunity against the known range of noise levels;
2. choose the lower threshold to limit the possible extent of noise spurs (in principle, the lowest threshold subset that contains *all* true boundary points); and
3. select the upper threshold to guarantee as far as possible the seeding of important boundary points (in principle, the highest threshold subset that is connected to *all* true boundary points).

Unfortunately, in the limit of high signal variability, rules 2 and 3 appear to suggest eliminating hysteresis altogether! Ultimately, this means that the only rigorous way of treating the problem is to perform a complete statistical analysis of false positives and false negatives for a large number of images in any new application.

---

## 5.11 THE CANNY OPERATOR

Since its publication in 1986 the Canny operator (Canny, 1986) has become one of the most widely used edge detection operators: there are good reasons for this, as it was aimed at getting away from a tradition of mask-based operators, many of which can hardly be regarded as “designed,” into one that is entirely principled and fully integrated. Intrinsic to the method is that of carefully specifying the spatial bandwidth within which it is expected to work, and also the exclusion of unnecessary thresholds, while at the same time permitting thin line structures to emerge, and ensuring that they are connected together as far as possible and indeed are meaningful at the particular scale and bandwidth. As a result of these considerations, the method involves a number of stages of processing:

1. low-pass spatial frequency filtering;
2. application of first-order differential masks;
3. nonmaximum suppression involving subpixel interpolation of pixel intensities; and
4. hysteresis thresholding.

In principle, low-pass filtering needs to be carried out by Gaussian convolution operators for which the standard deviation (or spatial bandwidth)  $\sigma$  is known and prespecified. Then first-order differential masks need to be applied: for this purpose the Sobel operator is acceptable. In this context note that the Sobel

operator masks can be regarded as convolutions ( $\otimes$ ) of a basic  $[-1 \ 1]$  type of mask with a  $[1 \ 1]$  smoothing mask. Thus taking the Sobel  $x$ -derivative we have:

$$\begin{bmatrix} -1 & 0 & 1 \\ -2 & 0 & 2 \\ -1 & 0 & 1 \end{bmatrix} = \begin{bmatrix} 1 \\ 2 \\ 1 \end{bmatrix} [-1 \ 0 \ 1] \quad (5.19)$$

where

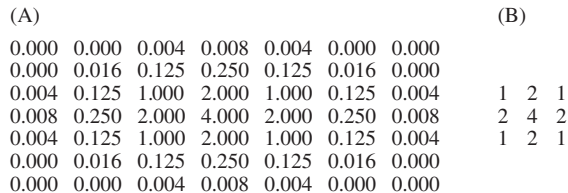
$$[1 \ 2 \ 1] = [1 \ 1] \otimes [1 \ 1] \quad (5.20)$$

and

$$[-1 \ 0 \ 1] = [-1 \ 1] \otimes [1 \ 1] \quad (5.21)$$

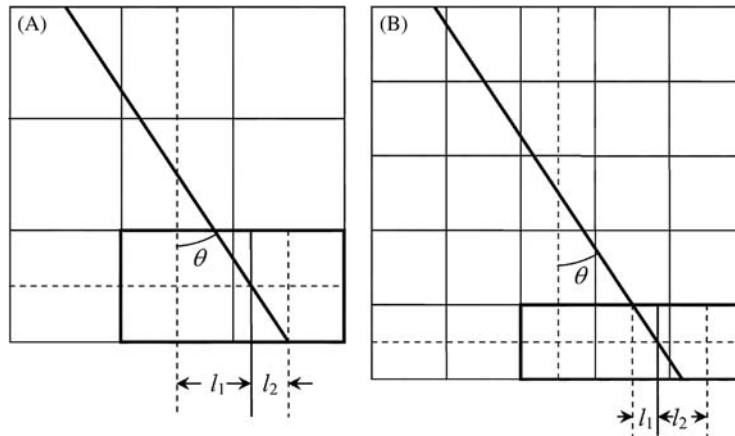
These equations make it clear that the Sobel operator itself includes a considerable amount of low-pass filtering, so the amount of additional filtering needed in stage 1 can reasonably be reduced. Another thing to bear in mind is that low-pass filtering can itself be carried out by a smoothing mask of the type shown in Fig. 5.5B, and it is interesting how close this mask is to the full 2-D Gaussian shown in Fig. 5.5A. Note also that the bandwidth of the mask in Fig. 5.5B is exactly known (it is 0.707), and when combined with that of the Sobel, the overall bandwidth becomes almost exactly 1.0.

Next, we turn our attention to stage 3, that of nonmaximum suppression. For this purpose, we need to determine the local edge normal direction using Eq. (5.5) and move either way along the normal to determine whether the current location is or is not a local maximum along it. If it is not, we suppress the edge output at the current location, only retaining edge points that are proven local maxima along the edge normal. Since only one point along this direction should be a local maximum, this procedure will necessarily thin the grayscale edges to



**FIGURE 5.5**

Exactness of the well-known  $3 \times 3$  smoothing kernel. This figure shows the Gaussian based smoothing kernel (A) that is closest to the well-known  $3 \times 3$  smoothing kernel (B) over the central ( $3 \times 3$ ) region. For clarity neither is normalized by the factor 1/16. The larger Gaussian envelope drops to 0.000 outside the region shown and integrates to 18.128 rather than 16. Hence the kernel in (B) can be said to approximate a Gaussian within  $\sim 13\%$ . Its actual standard deviation is 0.707 compared with 0.849 for the Gaussian.

**FIGURE 5.6**

Pixel interpolation in the Canny operator. (A) Interpolation between the two highlighted pixels at the bottom right in a  $3 \times 3$  neighborhood. (B) Interpolation in a  $5 \times 5$  neighborhood: note that two possibilities exist for interpolating between pairs of adjacent pixels, the relevant distances being marked for the one on the right.

unit width. Here a slight problem arises in that the edge normal direction will in general not pass through the centers of the adjacent pixels, and the Canny method requires the intensities along the normal to be estimated by interpolation. In a  $3 \times 3$  neighborhood this is simply achieved, as the edge normal in any octant will have to lie between a given pair of pixels, as shown in Fig. 5.6A. In a larger neighborhood, interpolation can take place between several pairs of pixels. For example, in a  $5 \times 5$  neighborhood, it will have to be determined which of two pairs is relevant (Fig. 5.6B), and an appropriate interpolation formula applied. However, it could be construed that there is no need to use larger neighborhoods, as a  $3 \times 3$  neighborhood will contain all the relevant information and given enough presmoothing in stage 1—negligible loss of accuracy will result. Of course, if impulse noise is present, this could lead to serious error, but low-pass filtering is in any case has not guaranteed to eliminate impulse noise so there are no special loss results from using the smaller neighborhood for nonmaximum suppression. Such considerations need to be examined carefully in the light of the particular image data and the noise it contains. Fig. 5.6 shows the two distances  $l_1$  and  $l_2$  that have to be determined. The pixel intensity along the edge normal is given by weighting the corresponding pixel intensities in *inverse* proportion to the distances:

$$I = (l_2 I_1 + l_1 I_2) / (l_1 + l_2) = (1 - l_1) I_1 + l_1 I_2 \quad (5.22)$$

where

$$l_1 = \tan \theta \quad (5.23)$$

This brings us to the final stage, that of hysteresis thresholding. By this point, as much as possible has been achieved without applying thresholds and it becomes necessary to take this final step. However, by applying the two hysteresis thresholds, it is intended to limit the damage that can be caused by a single threshold and repair it with another: that is to say, select the upper threshold to ensure capturing edges that are reliable and then select other points that have high likelihood of being viable edge points because they are adjacent to edge points of known reliability. In fact, this is still somewhat ad hoc but in practice it gives quite good results. A simple rule for choice of the lower threshold is that it should be about half the upper threshold. Again, this is only a rule of thumb, and it has to be examined carefully in the light of the particular image data.

Figs. 5.7 and 5.8 show results for the Canny operator at various stages and also comparisons for various thresholds—viz. (E) using hysteresis thresholding, (F) single thresholding at the lower level, and (G) single thresholding at the upper level. The evidence is that hysteresis thresholding is usually more reliable and more coherent than single level thresholding, in the sense of giving fewer false or misleading results.

---

## 5.12 THE LAPLACIAN OPERATOR

Whereas an edge detector such as the Sobel is a first derivative operator, the Laplacian is a second-derivative operator, and as such it is sensitive only to changes in intensity gradient. In 2-D its standard (mathematical) definition is given by:

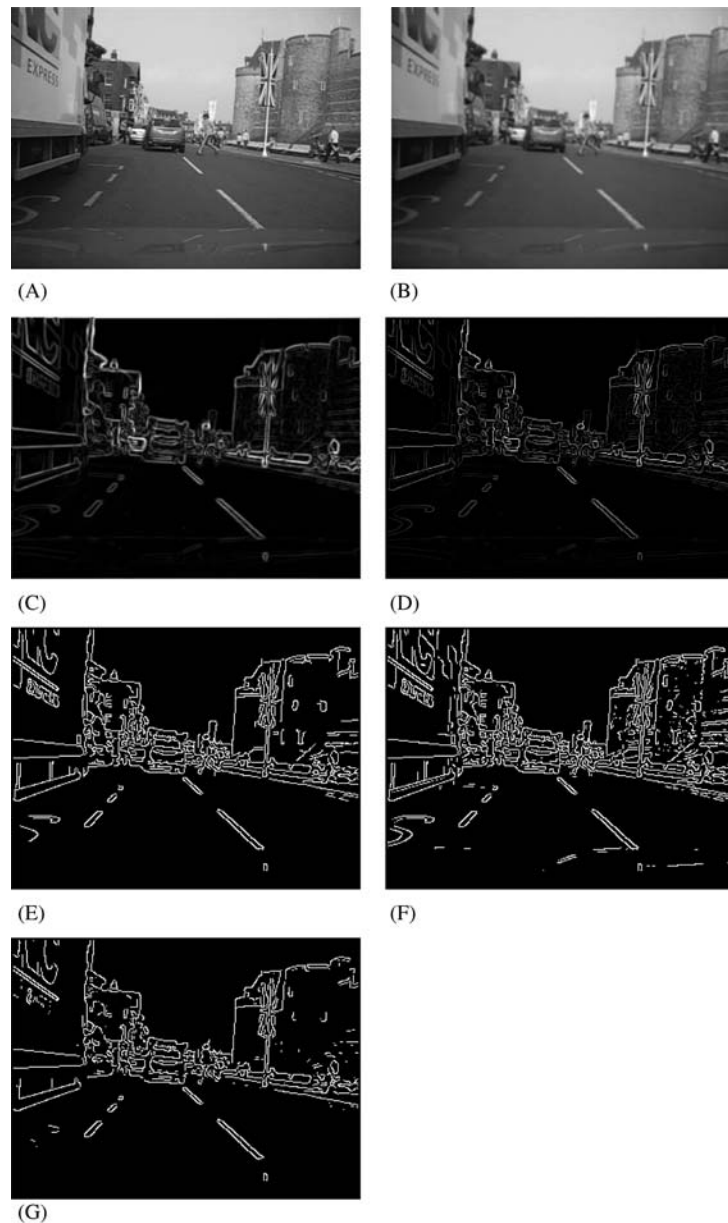
$$\nabla^2 = \frac{\partial^2}{\partial x^2} + \frac{\partial^2}{\partial y^2} \quad (5.24)$$

Localized masks for computing Laplacians can be derived by taking difference of Gaussian (DoG) kernels using two Gaussians of different bandwidth (for details of this procedure, see Section 6.7.4). This gives them an isotropic 2-D profile, with a positive center and a negative surround. This shape can be approximated in  $3 \times 3$  windows by masks such as the following:

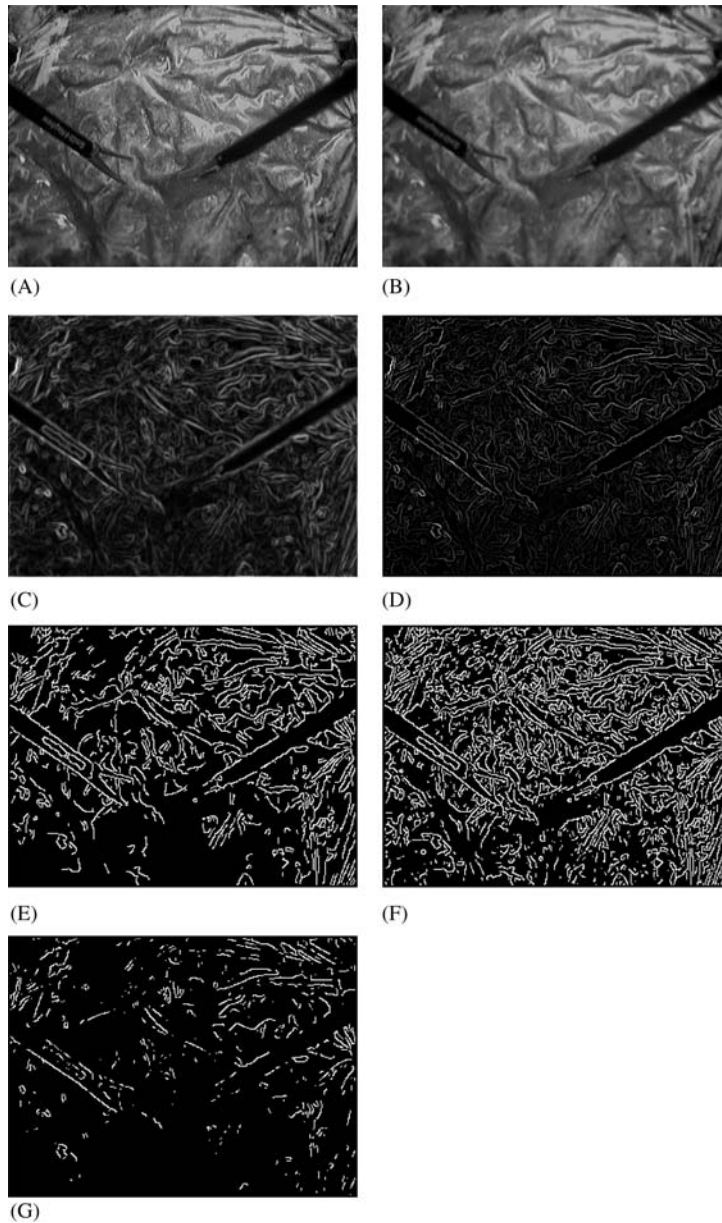
$$\begin{bmatrix} -1 & -1 & -1 \\ -1 & 8 & -1 \\ -1 & -1 & -1 \end{bmatrix} \quad (5.25)$$

Clearly, this mask is far from isotropic: nevertheless it exhibits many of the properties of larger masks, such as DoG kernels, which are much more accurately isotropic.

Here we present only an outline of the properties of this type of operator. These can be seen from Fig. 5.9. First, note that the Laplacian output ranges from positive to negative: hence in Fig. 5.9C it is presented on a medium gray

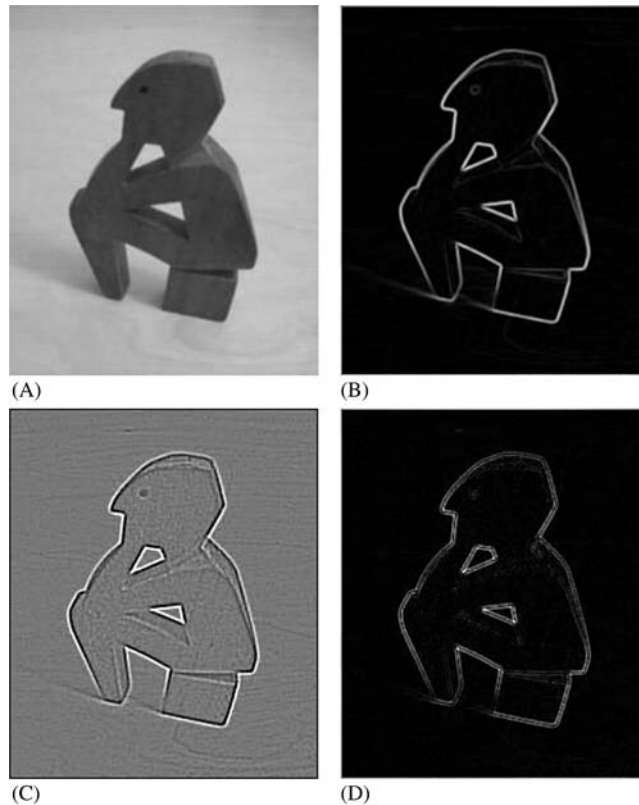
**FIGURE 5.7**

Application of the Canny edge detector. (A) Original image. (B) Smoothed image. (C) Result of applying Sobel operator. (D) Result of nonmaximum suppression. (E) Result of hysteresis thresholding. (F) Result of thresholding only at the lower threshold level. (G) Result of thresholding at the upper threshold level. Notice that there are fewer false or misleading outputs in (E) than would result from using a single threshold.

**FIGURE 5.8**

Another application of the Canny edge detector. (A) Original image. (B) Smoothed image. (C) Result of applying Sobel operator. (D) Result of nonmaximum suppression. (E) Result of hysteresis thresholding. (F) Result of thresholding only at the lower threshold level. (G) Result of thresholding at the upper threshold level. Again there are fewer false or misleading outputs in (E) than would result from using a single threshold.



**FIGURE 5.9**

Comparison of Sobel and Laplacian outputs. (A) Presmoothed version of original image. (B) Result of applying the Sobel operator. (C) Result of applying the Laplacian operator. Because the Laplacian output can be positive or negative, the output in (C) is displayed relative to a medium (128) gray level background. (D) Absolute magnitude Laplacian output. For clarity, (C) and (D) have been presented at increased contrast. Notice that the Laplacian output in (D) gives double edges—one just inside and one just outside the edge position indicated by a Sobel or Canny operator (to find edges using a Laplacian, zero crossings have to be located). Both the Sobel and the Laplacian used here operate within a  $3 \times 3$  window.

background, which indicates that on the exact edge of an object the Laplacian output is actually zero, as stated earlier. This is made clearer, in [Fig. 5.9D](#), where the magnitude of the Laplacian output is shown. It is seen that edges are highlighted by strong signals just inside and just outside the edge locations that are located by a Sobel or Canny operator ([Fig. 5.9B](#)). Ideally this effect is symmetrical, and if the Laplacian is to be used for edge detection, zero crossings of

the output will have to be located. However, in spite of preliminary smoothing of the image (Fig. 5.9A), the background in Fig. 5.9D has a great deal of noise in the background, and attempting to find zero crossings will therefore lead to a lot of noise being detected in addition to the edge points: in fact, it is well known that differentiation (especially double differentiation, as here) tends to accentuate noise. Nevertheless, this approach has been used highly successfully, usually with DoG operators working in much larger windows. Indeed, with much larger windows there will be a good number of pixels lying very near the zero crossings, and it will be possible to discriminate much more successfully between them and the pixels merely having low Laplacian output. A particular advantage of using Laplacian zero crossings is that theoretically they are bound to lead to closed contours around objects (albeit noise signals will also have their own separate closed contours).

---

## 5.13 CONCLUDING REMARKS

The above sections make it clear that the design of edge detection operators has by now been taken to quite an advanced stage, so that edges can be located to subpixel accuracy and orientated to fractions of a degree. In addition, edge maps may be made at several scales and the results correlated to aid image interpretation. Unfortunately, some of the schemes that have been devised to achieve these things are fairly complex and tend to consume considerable computation. In many applications this complexity may not be justified because the application requirements are, or can reasonably be made, quite restricted. Furthermore, there is often the need to save computation for real-time implementation. For these reasons, it will often be useful to explore what can be achieved using a single high-resolution detector such as the Sobel operator, which provides a good balance between computational load and orientation accuracy. Indeed, several of the examples in Part 2, Intermediate-Level Vision, of the book have been implemented using this type of operator, which is able to estimate edge orientation to within about  $1^\circ$ . This does not in any way invalidate the latest methods, particularly those involving studies of edges at various scales: such methods come into their own in applications such as general scene analysis, where vision systems are required to cope with largely unconstrained image data.

This chapter has completed another facet of the task of low-level image segmentation. Later chapters move on to consider the shapes of objects that have been found by the thresholding and edge detection schemes discussed in Chapter 3, Image Filtering and Morphology, and Chapter 4, The Role of Thresholding. In particular, Chapter 8, Binary Shape Analysis, studies shapes by analysis of the regions over which objects extend, while Chapter 9, Boundary Pattern Analysis, studies shapes by considering their boundary patterns.

*Edge detection is perhaps the most widely used means of locating and identifying objects in digital images. While different edge detection strategies vie with each other for acceptance, this chapter has shown that they obey fundamental laws—such as sensitivity, noise suppression capability and computation cost all increasing with footprint size.*

## 5.14 BIBLIOGRAPHICAL AND HISTORICAL NOTES

As seen in the first few sections of this chapter, early attempts at edge detection tended to employ numbers of template masks that could locate edges at various orientations. Often these masks were ad hoc in nature, and after 1980 this approach finally gave way to the DG approach that had already existed in various forms for a considerable period (see the influential paper by Haralick, 1980).

The Frei–Chen approach is of interest in that it takes a set of nine  $3 \times 3$  masks forming a complete set within this size of neighborhood—of which one tests for brightness, four test for edges, and four test for lines (Frei and Chen, 1977). Although interesting, the Frei–Chen edge masks do not correspond to those devised for optimal edge detection: Lacroix (1988) makes further useful remarks about the approach.

Meanwhile, psychophysical work by Marr (1976), Wilson and Giese (1977), and others provided another line of development for edge detection. This led to the well-known paper by Marr and Hildreth (1980), which was highly influential in the following few years. This spurred others to think of alternative schemes, and the Canny (1986) operator emerged from this vigorous milieu. In fact, the Marr–Hildreth operator was among the first to preprocess images in order to study them at different scales—a technique that has expanded considerably (see, for example, Yuille and Poggio, 1986), and which will be considered in more depth in [Chapter 6](#), Corner, Interest Point, and Invariant Feature Detection. The computational problems of the Marr–Hildreth operator kept others thinking along more traditional lines, and the work by Reeves et al. (1983), Haralick (1984), and Zuniga and Haralick (1987) fell into this category. Lyvers and Mitchell (1988) reviewed many of these papers and made their own suggestions. Another study (Petrou and Kittler, 1988) carried out further work on operator optimization. The work of Sjöberg and Bergholm (1988), which found rules for discerning shadow edges from object edges, is also of interest.

More recently, there was a move to achieving greater robustness and confidence in edge detection by careful elimination of local outliers: in Meer and Georgescu's (2001) method, this was achieved by estimating the gradient vector, suppressing nonmaxima, performing hysteresis thresholding, and integrating with a confidence measure to produce a more general robust result; in fact, each pixel was assigned a confidence value *before* the final two steps of the algorithm. Kim et al. (2004) took this technique a step further and eliminated the need for setting

a threshold by using a fuzzy reasoning approach. Similar sentiments were expressed by Yitzhaky and Peli (2003), and they aimed to find an optimal parameter set for edge detectors by receiver operating characteristic curve and chi-square measures, which actually gave very similar results. Prieto and Allen (2003) designed a similarity metric for edge images, which could be used to test the effectiveness of a variety of edge detectors. They pointed to the fact that metrics need to allow slight latitude in the positions of edges, in order to compare the similarity of edges reliably. They reported a new approach that took into account both displacement of edge positions and edge strengths in determining the similarity between edge images.

Not content with hand-crafted algorithms, Suzuki et al. (2003) devised a back-propagation neural edge enhancer that undergoes supervised learning on model data to permit it to cope well (in the sense of giving clear, continuous edges) with noisy images: it was found to give results superior to those of conventional algorithms (including Canny, Heuckel, Sobel, and Marr-Hildreth) in similarity tests relative to the desired edges. The disadvantage was a long learning time, although the final execution time was short.

### 5.14.1 MORE RECENT DEVELOPMENTS

Among the most recent developments, Shima et al. (2010) have described the design of more accurate gradient operators on hexagonal lattices. While the latter are not commonly used, there has long been a specialist interest in this area because of the greater number of nearest neighbors at equal distances from a given pixel in a hexagonal lattice: this makes certain types of window operation and algorithm more accurate and efficient, and is particularly useful for edge detection and thinning. Ren et al. (2010) have described an improved edge detection algorithm that operates via the fusion of intensity and chromatic difference, thereby making better use of intercomponent information in color images.

---

## 5.15 PROBLEMS

1. Prove Eqs. (5.12) and (5.13).
2. Check the results quoted in Section 5.9 giving the conditions under which the Sobel operator leads to zero error in the estimation of edge orientation. Proceed to prove Eq. (5.17).

This page intentionally left blank

# Corner, interest point, and invariant feature detection

# 6

Corner detection is valuable for locating complex objects and for tracking them in 2-D or 3-D. This chapter discusses this detection problem and considers which methods are best suited for the task.

*Look out for:*

- the ways in which corner features are useful
- the variety of methods available for corner detection—template matching, the second-order derivative method, the median-based method, the Harris interest point detector
- where the corner signal is a maximum: how detector bias arises
- how corner orientation may be estimated
- why invariant feature detectors are needed: the hierarchy of relevant types of invariance
- how feature detectors may be made invariant to similarity and affine transformations—SIFT, SURF, MSER, etc.
- the need for invariant detectors to embody multiparameter descriptors to help with subsequent matching tasks
- what criteria can be developed for measuring the performance of conventional and invariant types of feature and feature detector
- the histograms of oriented gradients (HOG) approach to feature detection.

Note the variety of methods available for performing interrelated detection tasks. However, different methods have different speeds, accuracies, sensitivities, and degrees of robustness: this chapter aims to bring out all these aspects of the problem.

## 6.1 INTRODUCTION

This chapter is concerned with the efficient detection of corners. It has been noted in previous chapters that objects are generally located most efficiently from their features. Prominent features include straight lines, circles, arcs, holes, and corners. Corners are particularly important since they may be used to locate and orientate objects and to provide measures of their dimensions; for example, knowledge about

orientation will be vital if a robot is to find the best way of picking up an object, while dimensional measurement will be necessary in most inspection applications. Hence efficient, accurate corner detectors are of great relevance in machine vision.

We start this chapter by considering what is perhaps the most obvious detection scheme—that of template matching. Then we move on to other types of detectors, based on the second-order derivatives of the local intensity function; subsequently, we find that median filters can lead to useful corner detectors, with properties similar to those of the second-order derivative–based detectors. Next, we consider detectors based on the second moments of the *first* derivatives of the local intensity function. While this will complete the traditional approach to corner detection, it opens the door for consideration of the highly important invariant local feature detectors that have in the past decade or so been developed for matching widely separated views of 3-D scenes, including those containing rapidly moving objects. By the end of the chapter the vital task of considering performance criteria for the various types of corner and feature detector will also be undertaken.

---

## 6.2 TEMPLATE MATCHING

Following our experience with template matching methods for edge detection ([Chapter 5: Edge Detection](#)), it would appear to be straightforward to devise suitable templates for corner detection. These would have the general appearance of corners, and in a  $3 \times 3$  neighborhood would take forms such as the following:

$$\begin{bmatrix} -4 & 5 & 5 \\ -4 & 5 & 5 \\ -4 & -4 & -4 \end{bmatrix} \quad \begin{bmatrix} 5 & 5 & 5 \\ -4 & 5 & -4 \\ -4 & -4 & -4 \end{bmatrix}.$$

The complete set of eight templates being generated by successive  $90^\circ$  rotations of the first two shown. An alternative set of templates was suggested by Bretsch (1981). As for edge detection templates, the mask coefficients are made to sum to zero so that corner detection is insensitive to absolute changes in light intensity. Ideally, this set of templates should be able to locate all corners and to estimate their orientation to within  $22.5^\circ$ .

Unfortunately, corners vary very much in a number of their characteristics, including in particular their degree of pointedness, internal angle, and the intensity gradient at the boundary. [The term “pointedness” is used as the opposite to “bluntness”, the term “sharpness” being reserved for the total angle  $\eta$  through which the boundary turns in the corner region, i.e.,  $\pi$  minus the internal angle.] Hence it is quite difficult to design optimal corner detectors. In addition, corners are generally insufficiently pointed for good results to be obtained with the  $3 \times 3$  template masks shown above. Another problem is that in larger neighborhoods, not only do the masks become larger but also more of them are needed to obtain

optimal corner responses, and it rapidly becomes clear that the template matching approach is likely to involve excessive computation for practical corner detection. The alternative is to approach the problem analytically, somehow deducing the ideal response for a corner at any arbitrary orientation, and thereby bypassing the problem of calculating very many individual responses to find which one gives the maximum signal. The methods described in the remainder of this chapter embody this alternative philosophy.

### 6.3 SECOND-ORDER DERIVATIVE SCHEMES

Second-order differential operator approaches have been used widely for corner detection and mimic the first-order operators used for edge detection. Indeed, the relationship lies deeper than this. By definition, corners in grayscale images occur in regions of rapidly changing intensity levels. By this token they are detected by the same operators that detect edges in images. However, corner pixels are much rarer than edge pixels—by one definition, they arise where two relatively straight-edged fragments intersect. (We might imagine a  $256 \times 256$  image of 64K pixels, of which 1000 ( $\sim 2\%$ ) lie on edges and a mere 30 ( $\sim 0.06\%$ ) are situated at corner points.) Thus it is useful to have operators that detect corners *directly*, i.e., *without unnecessarily locating edges*. To achieve this sort of discriminability it is clearly necessary to consider local variations in image intensity up to at least second order. Hence the local intensity variation is expanded as follows:

$$I(x, y) = I(0, 0) + I_x x + I_y y + I_{xx} x^2/2 + I_{xy} xy + I_{yy} y^2/2 + \dots \quad (6.1)$$

where the suffices indicate partial differentiation with respect to  $x$  and  $y$  and the expansion is performed about the origin  $X_0(0,0)$ . The symmetrical matrix of second derivatives is:

$$\mathcal{I}_{(2)} = \begin{bmatrix} I_{xx} & I_{xy} \\ I_{yx} & I_{yy} \end{bmatrix} \quad \text{where } I_{xy} = I_{yx} \quad (6.2)$$

This gives information on the local curvature at  $X_0$ . In fact, a suitable rotation of the coordinate system transforms  $\mathcal{I}_{(2)}$  into diagonal form:

$$\tilde{\mathcal{I}}_{(2)} = \begin{bmatrix} I_{\tilde{x}\tilde{x}} & 0 \\ 0 & I_{\tilde{y}\tilde{y}} \end{bmatrix} = \begin{bmatrix} \kappa_1 & 0 \\ 0 & \kappa_2 \end{bmatrix} \quad (6.3)$$

where appropriate derivatives have been reinterpreted as principal curvatures at  $X_0$ .

We are particularly interested in rotationally invariant operators and it is significant that the trace and determinant of a matrix such as  $\mathcal{I}_{(2)}$  are invariant under rotation. Thus we obtain the Beaudet (1978) operators:

$$\text{Laplacian} = I_{xx} + I_{yy} = \kappa_1 + \kappa_2 \quad (6.4)$$



and

$$\text{Hessian} = \det(\mathcal{I}_{(2)}) = I_{xx}I_{yy} - I_{xy}^2 = \kappa_1\kappa_2 \quad (6.5)$$

It is well known that the Laplacian operator gives significant responses along lines and edges and hence is not particularly suitable as a corner detector. On the other hand, Beaudet's "DET" operator does not respond to lines and edges but gives significant signals in the vicinity of corners: it should therefore form a useful corner detector. However, DET responds with one sign on one side of a corner and with the opposite sign on the other side of the corner: at the point of real interest—on the point of the corner—it gives a null response. Hence rather more complicated analysis is required to deduce the presence and exact position of each corner (Dreschler and Nagel, 1981; Nagel, 1983). The problem is clarified in Fig. 6.1. Here the dotted line shows the path of maximum horizontal curvature for various intensity values up the slope. The DET operator gives maximum response at positions P and Q on this line, and the parts of the line between P and Q must be explored to find the "ideal" corner point C where DET is zero.

Perhaps to avoid rather complicated procedures of this sort, Kitchen and Rosenfeld (1982) examined a variety of strategies for locating corners, starting from the consideration of local variation in the directions of edges. They found a highly effective operator which estimates the projection of the local rate of change of gradient direction vector along the horizontal edge tangent direction, and showed that it is mathematically identical to calculating the horizontal

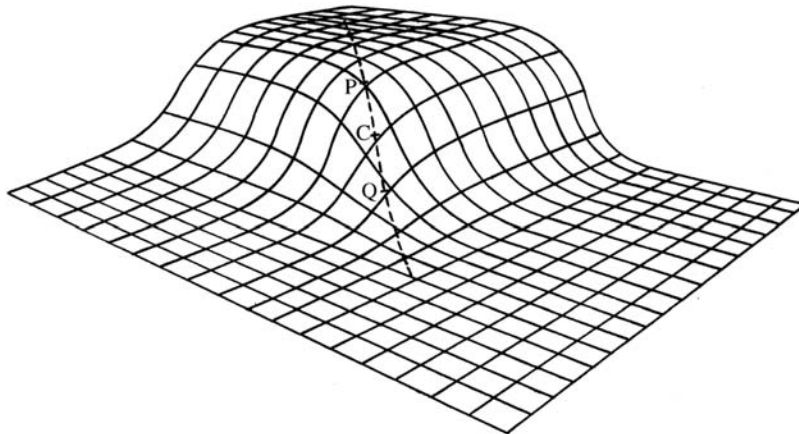


**FIGURE 6.1**

Sketch of an idealized corner, taken to give a smoothly varying intensity function. The dotted line shows the path of maximum horizontal curvature for various intensity values up the slope. The DET operator gives maximum responses at P and Q, and it is required to find the ideal corner position C where DET gives a null response.

curvature  $\kappa$  of the intensity function  $I$ . To obtain a realistic indication of the strength of a corner they multiplied  $\kappa$  by the magnitude of the local intensity gradient  $g$ :

$$\begin{aligned} C &= \kappa g = \kappa(I_x^2 + I_y^2)^{1/2} \\ &= \frac{I_{xx}I_y^2 - 2I_{xy}I_xI_y + I_{yy}I_x^2}{I_x^2 + I_y^2} \end{aligned} \quad (6.6)$$

Finally, they used the heuristic of nonmaximum suppression along the edge normal direction to localize the corner positions further.

In 1983 Nagel was able to show that the Kitchen and Rosenfeld (KR) corner detector using nonmaximum suppression is mathematically virtually identical to the Dreschler and Nagel (DN) corner detector. A year later, Shah and Jain (1984) studied the Zuniga and Haralick (ZH) corner detector (1983) based on a bicubic polynomial model of the intensity function: they showed that this is essentially equivalent to the KR corner detector. However, the ZH corner detector operates rather differently in that it thresholds the intensity gradient and then works with the subset of edge points in the image, only at that stage applying the curvature function as a corner strength criterion. By making edge detection explicit in the operator, the ZH detector eliminates a number of false corners that would otherwise be induced by noise.

The inherent near-equivalence of these three corner detectors need not be overly surprising, since in the end the different methods would be expected to reflect the same underlying physical phenomena (Davies, 1988d). However, it is gratifying that the ultimate result of these rather mathematical formulations is interpretable by something as easy to visualize as horizontal curvature multiplied by intensity gradient.

---

## 6.4 A MEDIAN FILTER–BASED CORNER DETECTOR

An entirely different strategy for detecting corners was developed by Paler et al. (1984). It adopts an initially surprising and rather nonmathematical approach based on the properties of the median filter. The technique involves applying a median filter to the input image, and then forming another image that is the difference between the input and the filtered images. This difference image contains a set of signals that are interpreted as local measures of corner strength.

Clearly, it seems risky to apply such a technique since its origins suggest that, far from giving a correct indication of corners, it may instead unearth all the noise in the original image and present this as a set of “corner” signals. Fortunately, analysis shows that these worries may not be too serious. First, in the absence of noise, strong signals are not expected in areas of background, nor are they expected near straight edges, since median filters do not shift or modify such edges significantly (see [Chapter 3: Image Filtering and Morphology](#)). However, if

a window is moved gradually from a background region until its central pixel is just over a convex object corner, there is no change in the output of the median filter: hence there is a strong difference signal indicating a corner.

Paler et al. (1984) analyzed the operator in some depth and concluded that the signal strength obtained from it is proportional to (1) the local contrast and (2) the “sharpness” of the corner. The definition of sharpness they used was that of Wang et al. (1983), meaning the angle  $\eta$  through which the boundary turns. Since it is assumed here that the boundary turns through a significant angle (perhaps the whole angle  $\eta$ ) within the filter neighborhood, the difference from the second-order intensity variation approach is a major one. Indeed, it is an implicit assumption in the latter approach that first- and second-order coefficients describe the local intensity characteristics reasonably rigorously, the intensity function being inherently continuous and differentiable. Thus the second-order methods may give unpredictable results with pointed corners where directions change within the range of a few pixels. Although there is some truth in this, it is worth looking at the similarities between the two approaches to corner detection before considering the differences. We proceed with this in the next subsection.

### 6.4.1 ANALYZING THE OPERATION OF THE MEDIAN DETECTOR

This subsection considers the performance of the median corner detector under conditions where the grayscale intensity varies by only a small amount within the median filter neighborhood region. This permits the performance of the corner detector to be related to low-order derivatives of the intensity variation, so that comparisons can be made with the second-order corner detectors mentioned earlier.

To proceed we assume a continuous analog image and a median filter operating in an idealized circular neighborhood. For simplicity, since we are attempting to relate signal strengths and differential coefficients, noise is ignored. Next, recall (Chapter 3: Image Filtering and Morphology) that for an intensity function that increases monotonically with distance in some arbitrary direction  $\tilde{x}$  but which does not vary in the perpendicular direction  $\tilde{y}$ , the median within the circular window is equal to the value at the center of the neighborhood. This means that the median corner detector gives zero signal if the horizontal curvature is locally zero.

If there is a small horizontal curvature  $\kappa$ , the situation can be modeled by envisaging a set of constant-intensity contours of roughly circular shape and approximately equal curvature, within the circular window, which will be taken to have radius  $a$  (Fig. 6.2). Consider the contour having the median intensity value. The center of this contour does not pass through the center of the window but is displaced to one side along the negative  $\tilde{x}$  axis. Furthermore, the signal obtained from the corner detector depends on this displacement. If the displacement is  $D$ , it is easy to see that the corner signal is  $Dg_{\tilde{x}}$  since  $g_{\tilde{x}}$  allows the intensity change over the distance  $D$  to be estimated (Fig. 6.2). The remaining problem

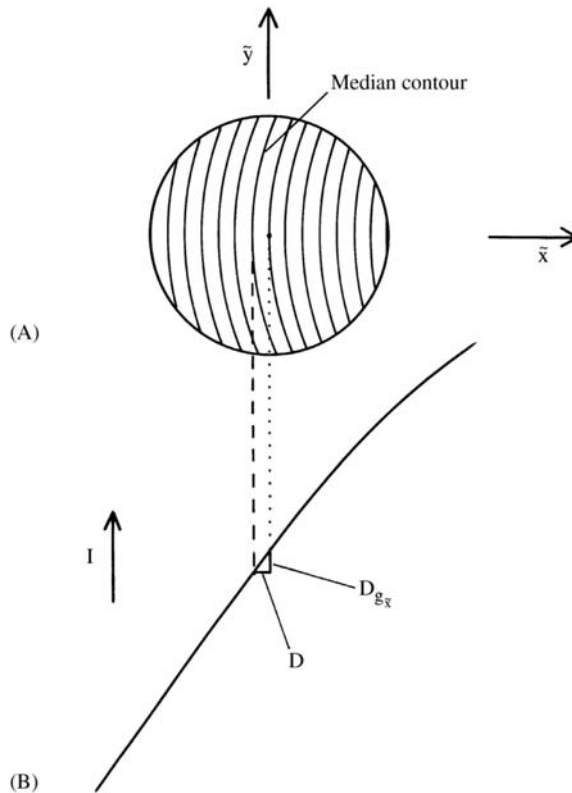


**FIGURE 6.2**

(A) Contours of constant intensity within a small neighborhood: ideally, these are parallel, circular, and of approximately equal curvature (the contour of median intensity does not pass through the center of the neighborhood); (B) Cross-section of intensity variation, indicating how the displacement  $D$  of the median contour leads to an estimate of corner strength.

© Springer 1988.

is to relate  $D$  to the horizontal curvature  $\kappa$ . A formula giving this relation has already been obtained in [Chapter 3](#), Image Filtering and Morphology. The required result is:

$$D = \frac{1}{6} \kappa a^2 \tag{6.7}$$

So the corner signal is

$$C = D g_{\bar{x}} = \frac{1}{6} \kappa g_{\bar{x}} a^2 \tag{6.8}$$

Note that  $C$  has the dimensions of intensity (contrast), and that the equation may be reexpressed in the form:

$$C = \frac{1}{12}(g_{\bar{x}}a) \cdot (2a\kappa) \quad (6.9)$$

so that, as in the formulation of Paler et al. (1984), corner strength is closely related to corner contrast and corner sharpness.

To summarize, the signal from the median-based corner detector is proportional to horizontal curvature and to intensity gradient. Thus this corner detector gives an identical response to the three second-order intensity variation detectors discussed in Section 6.3, the closest practically being the KR detector. However, this comparison is valid only when second-order variations in intensity give a complete description of the situation. Clearly, the situation might be significantly different where corners are so pointed that they turn through a large proportion of their total angle within the median neighborhood. In addition, the effects of noise might be expected to be rather different in the two cases, as the median filter is particularly good at suppressing impulse noise. Meanwhile, for small horizontal curvatures, there ought to be no difference in the positions at which median and second-order derivative methods locate corners, and accuracy of localization should be identical in the two cases.

### 6.4.2 PRACTICAL RESULTS

Experimental tests with the median approach to corner detection have shown that it is a highly effective procedure (Paler et al., 1984; Davies, 1988d). Corners are detected reliably and signal strength is indeed roughly proportional both to local image contrast and to corner sharpness (see Fig. 6.3). Noise is more apparent for  $3 \times 3$  implementations and this makes it better to use  $5 \times 5$  or larger neighborhoods to give good corner discrimination. However, the fact that median

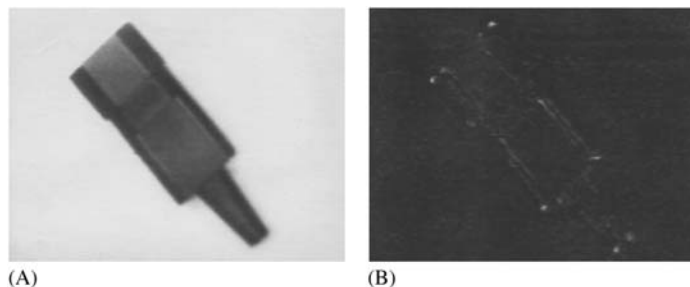


**FIGURE 6.3**

(A) Original off-camera  $128 \times 128$  6-bit grayscale image; (B) result of applying the median-based corner detector in a  $5 \times 5$  neighborhood. Note that corner signal strength is roughly proportional both to corner contrast and to corner sharpness.

operations are slow in large neighborhoods, and that background noise is still evident even in  $5 \times 5$  neighborhoods, means that the basic median-based approach gives poor performance by comparison with the second-order methods. However, both of these disadvantages are virtually eliminated by using a “skimming” procedure, in which edge points are first located by thresholding the edge gradient, and the edge points are then examined with the median detector to locate the corner points (Davies, 1988d). With this improved method, performance is found to be generally superior to that for the KR method in that corner signals are better localized and accuracy is enhanced. Indeed, the second-order methods appear to give rather fuzzy and blurred signals that contrast with the sharp signals obtained with the improved median approach (Fig. 6.4).

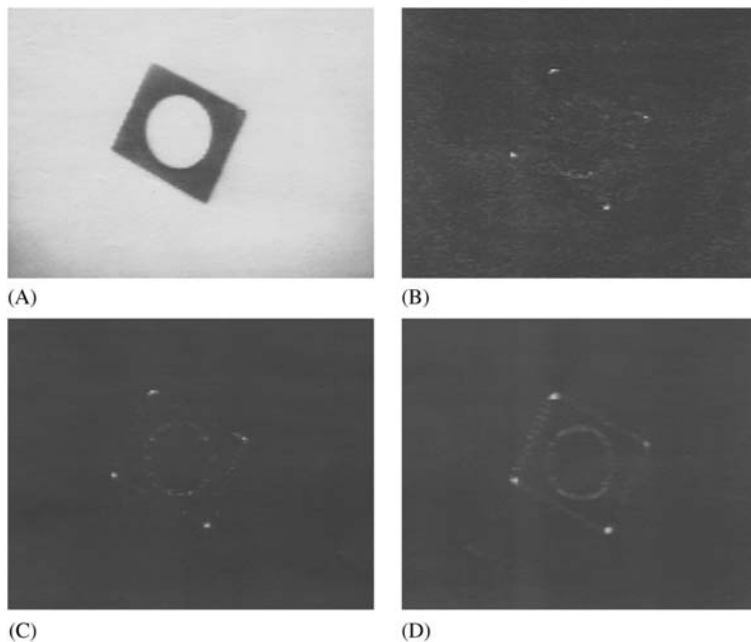


**FIGURE 6.4**

Comparison of the median and KR corner detectors: (A) original  $128 \times 128$  grayscale image; (B) result of applying a median detector; (C) result of including a suitable gradient threshold; (D) result of applying a KR detector. The considerable amount of background noise is saturated out in (A) but is evident from (B). To give a fair comparison between the median and KR detectors,  $5 \times 5$  neighborhoods are employed in each case, and nonmaximum suppression operations are not applied: the same gradient threshold is used in (C) and (D). *KR*, Kitchen and Rosenfeld.

At this stage the reason for the more blurred corner signals obtained using the second-order operators is not clear. Basically, there is no valid rationale for applying second-order operators to pointed corners, since higher derivatives of the intensity function will become important and will at least in principle interfere with their operation. However, it is evident that the second-order methods will probably give strong corner signals when the tip of a pointed corner appears anywhere in their neighborhood, so there is likely to be a minimum blur region of radius  $a$  for any corner signal. This appears to explain the observed results adequately. However, note that the sharpness of signals obtained by the KR method may be improved by nonmaximum suppression (Kitchen and Rosenfeld, 1982; Nagel, 1983). Furthermore, this technique can also be applied to the output of median-based corner detectors: hence, the fact remains that the median-based method gives inherently better localized signals than the second-order methods.

Overall, the inherent deficiencies of the median-based corner detector can be overcome by incorporating a skimming procedure, and then the method becomes superior to the second-order approaches in giving better localization of corner signals. The underlying reason for the difference in localization properties appears to be that the median-based signal is ultimately sensitive only to the particular few pixels whose intensities fall near the median contour within the window, whereas the second-order operators use typical convolution masks which are in general sensitive to the intensity values of all the pixels within the window. Thus the KR operator tends to give a strong signal when the tip of a pointed corner is present anywhere in the window.

---

## 6.5 THE HARRIS INTEREST POINT OPERATOR

Earlier in this chapter, we considered the second-order derivative type of corner detector, which was designed on the basis that corners are ideal, smoothly varying differentiable intensity profiles. We also examined median filter–based detectors: these had a totally different *modus operandi* and were found to be suitable for processing curved step edges whose profiles were quite likely *not* to be smoothly varying and differentiable. At this point we consider what other strategies are available for corner detection. An important one that has become extremely widely used is the Harris operator. Far from being a second-order derivative type of detector, the Harris operator only takes account of first-order derivatives of the intensity function. Thus there is a question of how it can acquire enough information to detect corners. In this section we construct a model of its operation in order to throw light on this crucial question.

The Harris operator is defined very simply, in terms of the local components of intensity gradient  $I_x, I_y$  in an image. The definition requires a window region to

be defined and averages  $\langle \cdot \rangle$  are taken over this whole window. We start by computing the following matrix:

$$\Delta = \begin{bmatrix} \langle I_x^2 \rangle & \langle I_x I_y \rangle \\ \langle I_x I_y \rangle & \langle I_y^2 \rangle \end{bmatrix} \quad (6.10)$$

where the suffixes indicate partial differentiation of the intensity  $I$ ; we then use the determinant and trace to estimate the corner signal:

$$C = \det \Delta / \text{trace } \Delta \quad (6.11)$$

While this definition involves averages, we shall find it more convenient to work with sums of quadratic products of intensity gradients:

$$\Delta = \begin{bmatrix} \Sigma I_x^2 & \Sigma I_x I_y \\ \Sigma I_x I_y & \Sigma I_y^2 \end{bmatrix} \quad (6.12)$$

To understand the operation of the detector, first consider its response for a single edge (Fig. 6.5A). In fact:

$$\det \Delta = 0 \quad (6.13)$$

because  $I_x$  is zero over the whole window region. Note that there is no loss in generality from selecting a horizontal edge, as  $\det \Delta$  and  $\text{trace } \Delta$  are invariant under rotation of axes.

Next consider the situation in a corner region (Fig. 6.5B). Here:

$$\Delta = \begin{bmatrix} l_2 g^2 \sin^2 \theta & l_2 g^2 \sin \theta \cos \theta \\ l_2 g^2 \sin \theta \cos \theta & l_2 g^2 \cos^2 \theta + l_1 g^2 \end{bmatrix} \quad (6.14)$$

where  $l_1$  and  $l_2$  are the lengths of the two edges bounding the corner, and  $g$  is the edge contrast, assumed constant over the whole window. We now find:

$$\det \Delta = l_1 l_2 g^4 \sin^2 \theta \quad (6.15)$$



**FIGURE 6.5**

Case of a straight edge and a general corner. (A) A single straight edge appearing in a circular window. (B) A general corner appearing in a circular window. Circular windows are taken as ideal in that they will not favor any direction over any other.



and

$$\text{trace } \Delta = (l_1 + l_2)g^2 \quad (6.16)$$

so

$$C = \frac{l_1 l_2}{l_1 + l_2} g^2 \sin^2 \theta \quad (6.17)$$

which may be interpreted as the product of (1) a strength factor  $\lambda$ , which depends on the edge lengths within the window, (2) a contrast factor  $g^2$ , and (3) a shape factor  $\sin^2 \theta$ , which depends on the edge “sharpness”  $\theta$ . Clearly,  $C$  is zero for  $\theta = 0$  and  $\theta = \pi$ , and is a maximum for  $\theta = \pi/2$ , all these results being intuitively correct and appropriate.

There is a useful theorem about the sets of lengths  $l_1$  and  $l_2$  for which the strength factor  $\lambda$ , and thus  $C$ , is a maximum. Suppose we set  $L = l_1 + l_2 = \text{constant}$ . Then  $l_1 = L - l_2$ , and substituting for  $l_1$  we find:

$$\lambda = \frac{l_1 l_2}{l_1 + l_2} = [L l_2 - l_2^2]/L \quad (6.18)$$

$$\therefore d\lambda/dl_2 = 1 - 2l_2/L \quad (6.19)$$

which is zero for  $l_2 = L/2$ , at which point  $l_1 = l_2$ . This means that the best way of obtaining maximum corner signal is to place the corner symmetrically within the window, following which the signal can be increased further by moving the corner so that  $L$  is maximized (Fig. 6.6).

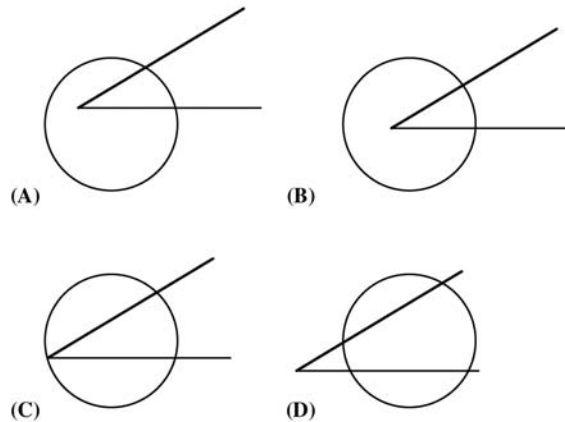


**FIGURE 6.6**

Possible geometries for a sharp corner being sampled by a circular window. (A) General case. (B) Symmetrical placement with  $l_1 = l_2$  (see notation in Fig. 6.5B). (C) Case of maximum signal. (D) Case where the signal is reduced in size as the tip of the corner goes outside the window.

We also notice another fact—that if  $l_i$  is small (for either value of  $i$ ), the corner signal at first increases linearly with  $l_i$ , and as noted earlier, the corner detector will ignore a single straight edge on its own.

Finally, the fact that we are exploring the properties of a symmetric matrix that can be represented using any convenient set of orthogonal axes means that we can find the eigenvalues and eigenvectors. However, it is illuminating to notice that these arise automatically when a symmetrically aligned set of axes is selected along the corner bisectors, as then the off-diagonal elements of the modified  $\Delta$  matrix acquire two components  $(L/2)g^2 \sin(\theta/2)\cos(\theta/2)$  of opposite sign and therefore cancel out. The on-diagonal elements are thus the eigenvalues themselves, and are  $(L/2)g^2 \times 2 \cos^2(\theta/2)$  and  $(L/2)g^2 \times 2 \sin^2(\theta/2)$ . Again, if  $\theta = 0$  or  $\pi$ , one or other of the eigenvalues is zero, so the determinant is zero and the corner signal vanishes; also, the maximum signal occurs for  $\theta = \pi/2$ .

### 6.5.1 CORNER SIGNALS AND SHIFTS FOR VARIOUS GEOMETRIC CONFIGURATIONS

In this section we seek the conditions for maximum corner signal for corners of different degrees of sharpness. We shall follow the observation of the previous section that maximum signal requires that  $l_1 = l_2 = L/2$ .

First, we take the case when  $\theta = 0$ : we have already seen that this leads to  $C = 0$ .

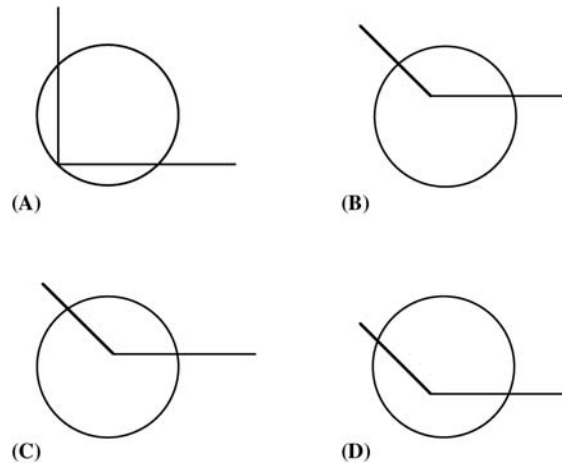
Next, when  $\theta$  is small, i.e., less than  $\pi/2$ , we can go on increasing  $L$  by moving the corner symmetrically. The optimum is reached exactly as the tip of the corner reaches the far side of the window (Fig. 6.6). We could envisage the corner moving even further, but then the portions of the sides that lie within the window will be moved laterally, so they will become shorter, and the signal will fall (Fig. 6.6D).

Now take the case  $\theta = \pi/2$ . Then we can again proceed as above, and the optimum will still occur when the tip of the corner lies on the far side of the window (Fig. 6.7A). However, further increase of  $\theta$  will result in a different optimum condition (Fig. 6.7B–D). In that case the optimum occurs for a reduced shift of the tip of the corner, the optimum occurring when the visible ends of the edges are exactly at opposite ends of a window diameter (Fig. 6.7D). Formally, we can see this in the symmetrical case ( $l_1 = l_2$ ) from the following equation:

$$\lambda_{\text{sym}} = (L^2/4)/L = L/4 \quad (6.20)$$

so reduction of  $L$  will reduce  $\lambda_{\text{sym}}$  and  $C$  will fall. This situation continues until  $\theta = \pi$ , at which point  $C$  again falls to zero.

We can now calculate the corner shift produced by the Harris detector. Specifically, the detector places the maximum output signal at the center of the window in the cases where the signal is stated to be “optimum” above. The shift produced has a size equal to the radius  $a$  of the window for small corner angles,

**FIGURE 6.7**

Possible geometries for right angle and obtuse corners. (A) Optimum case for a right-angle corner. This is the right-angle case corresponding to that shown in Fig. 6.6C. (B) General case for an obtuse corner. (C) Symmetrical placement with  $l_1 = l_2$ . (D) Case of maximum signal. In (D) the edges bounding the corner cross the boundary of the circular window at opposite ends of a diameter.

© IET 2005.

as then the tip of the corner is symmetrically placed on the boundary of the window. When  $\theta$  rises above  $\pi/2$ , simple geometry (Fig. 6.8A) shows that the shift is given by:

$$\delta = a \cot(\theta/2) \quad (6.21)$$

Hence  $\delta$  starts with value  $a$  at  $\theta = \pi/2$ , and falls to zero as  $\theta \rightarrow \pi$  (Fig. 6.8B).

### 6.5.2 PERFORMANCE WITH CROSSING POINTS AND T-JUNCTIONS

In this section we consider the performance of the Harris operator on other types of feature, which are not normally classed as simple corners. Examples are shown in Figs. 6.9 and 6.10. It turns out that the Harris operator picks these out with much the same efficiency as for corners. We start by considering crossing points.

One of the most important points to notice is that many of the same equations apply as for corners, and in particular Eq. (6.17) still applies. However,  $l_1$  and  $l_2$  must now be taken as the sum of the edge lengths in each of the two main directions. Here there is an important point to note—that along the two edge directions the signs of the contrast values both reverse at the crossing point. Nevertheless, this does not alter the response, because in Eq. (6.17) the contrast  $g$  is squared.

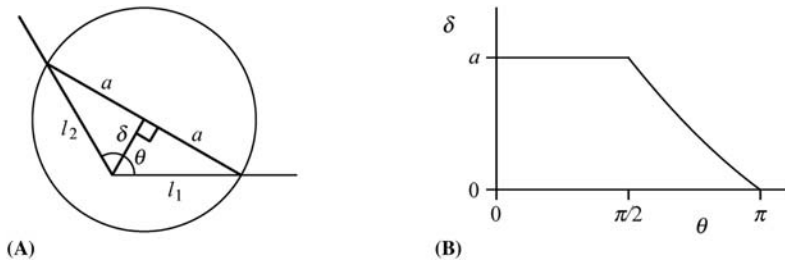


**FIGURE 6.8**

Geometry for calculating obtuse corner shifts and actual results. (A) Detailed geometry for calculating corner shift for the case shown in Fig. 6.7D. (B) Graph showing corner shift  $\delta$  as a function of corner sharpness  $\theta$ . The left of the graph corresponds to the constant shift of  $a$  obtained for sharp corners, while the right shows the varying results for obtuse angles.

© IET 2005.

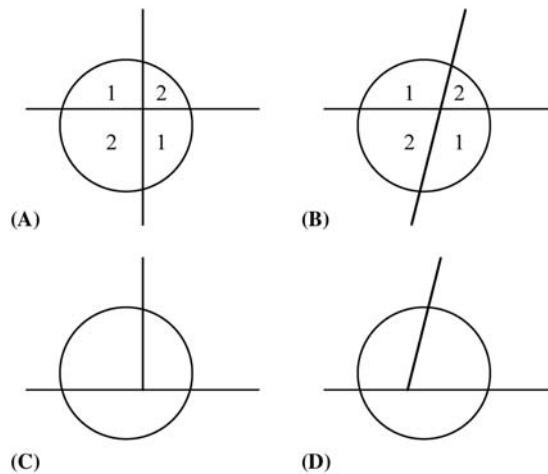


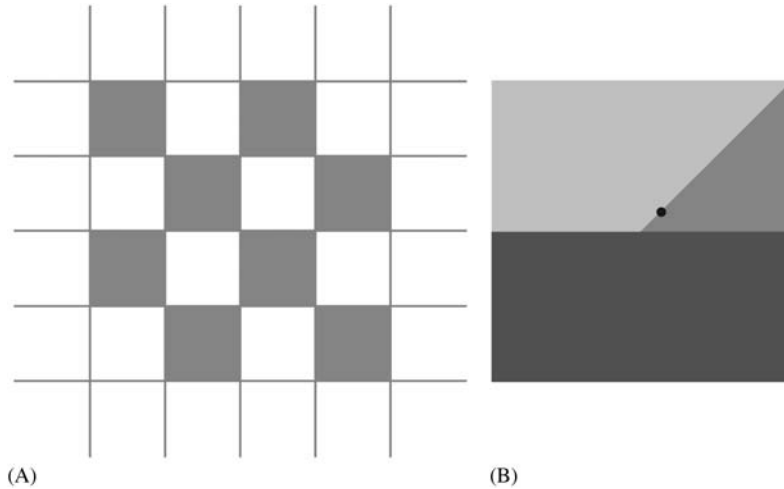
**FIGURE 6.9**

Other types of interest point. The types of interest point shown in this figure are those that cannot be classed as simple corner points. (A) Crossing point. (B) Oblique crossing point. (C) T-junction. (D) Oblique T-junction. In (A) and (B) the numbers indicate regions of equal, or different, intensity.

© IET 2005.

So when the window is centered at the crossing point, which is the tip of both constituent corners, the values of  $l_1$  and  $l_2$  are doubled.

Another relevant factor is that the corner configuration is now symmetric about the crossing point, so by symmetry this must also be the position of

**FIGURE 6.10**

Effect of the Harris corner detector. (A) shows a checkerboard pattern that gives high responses at each of the edge crossover points. Because of symmetry, the location of the peaks is exactly at the crossover locations. (B) Example of a T-junction. The black dot shows a typical peak location: in this case there is no symmetry to dictate that the peak must occur exactly at the T-junction.

maximum signal. In fact, the global maximum signal must occur when there is a maximum length of both edges within the window, and they must therefore be closely aligned along window diameters. These remarks apply both for  $\pi/2$  and for oblique crossovers (Figs. 6.9A,B and 6.10A).

We now consider another case that arises fairly often—the T-junction interest point. This can be either a  $\pi/2$  or an oblique junction. Such cases are more general than corners and the crossing point junctions discussed above, in that they are mediated by three regions with three different intensities (Figs. 6.9C,D and 6.10B). A complete analysis of the situation for all these cases cannot be undertaken here. Instead, we consider the interesting case of a high contrast edge that is reached but not crossed by a low contrast edge. In this case, the additional intensity breaks the symmetry of the junction, so that not only does the corner peak not lie on the junction point but also there will be a small lateral movement of the peak. However, if the low contrast edge has much lower contrast than the other two, the lateral shift will be minimal. To calculate the corner signal, we first generalize Eq. (6.17) to take account of the fact that one line will have higher contrast than the other:

$$C' = \frac{l_1 l_2 g_1^2 g_2^2}{l_1 g_1^2 + l_2 g_2^2} \sin^2 \theta \quad (6.22)$$

where  $l_1$  is taken as the straight edge with high contrast  $g_1$  and  $l_2$  is the straight edge with low contrast  $g_2$ . Proceeding as before we find that the optimal signal occurs where  $l_1|g_1| = l_2|g_2|$ . Interestingly, this can mean that the maximum signal occurs on the low contrast edge, in a highly asymmetric way (Fig. 6.10B). Part of the motivation of this study was the observation that the Harris operator peaks shown in the literature (e.g., Shen and Wang, 2002) often seem to be localized at such points, though this does not seem to have been remarked upon before 2005 when the author noted and explained the phenomenon (Davies, 2005). While apparently trivial it is actually important, as measurement bias can mislead and/or be the cause of error in subsequent algorithms. However, here the bias is known, systematic and calculable, and can be allowed for when the operator is used in practice.

Notice that the Harris operator is often called an “interest” operator, as it detects not only corners but also other interesting points such as crossovers and T-junctions, and we have seen that there is good reason why this happens. Indeed, it is difficult to imagine that a second-order derivative signal would give sizeable signals in these other cases, as the coherence of the second derivative would be largely absent, or even identically zero in the case of a crossover. Interestingly, the Harris operator often used to be called the Plessey operator, after the company at which it was originally developed.

### 6.5.3 DIFFERENT FORMS OF THE HARRIS OPERATOR

In this section, we consider the different forms the Harris operator can take. The form in Eq. (6.11) is due to Noble (1988) who actually gave the inverse of this expression and included a small positive constant in the denominator to prevent divide-by-zero situations. However, the original Harris operator had the rather different form:

$$C = \det \Delta - k(\text{trace } \Delta)^2 \quad (6.23)$$

where  $k \approx 0.04$ . Ignoring the constant, we find that the analysis presented above remains virtually unchanged, particularly concerning the optimal signal and the localization bias. The term involving  $k$  was added by Harris and Stevens (1988) in order to limit the number of false positives due to prominent edges. In principle, isolated edges should have no such effect, because as shown earlier, they lead to  $\det \Delta = 0$ . However, noise or clutter can affect this by introducing short extraneous edges, which interact with any existing strong edges to constitute pseudo-corners (in the absence of explanations in the literature, this seems to be the most reasonable interpretation of the situation): hence  $k$  has to be adjusted empirically to minimize the number of false positives. Searching the literature shows that in practice workers almost invariably give  $k$  a value close to 0.04 or 0.05: in fact, Rocket has investigated this, and has found that (1) making  $k$  equal to 0.04 rather than zero drastically cuts down the number of false positives due to

edges; and (2) there appears to be an optimum value for  $k$  which is actually much closer to 0.05 than to 0.04, but definitely below 0.06, the  $k$  response function being a smoothly varying curve (Rocket, 2003). Nevertheless, we must expect the optimum value of  $k$  to vary with the image data.

Interestingly, in tests carried out using the Harris operator, the form given in Eq. (6.11) was used without any attempt to introduce a term in  $k$  (though divide-by-zero was taken care of), with the results shown in Fig. 6.11. Excessive numbers of false positives due to edges were not evident, though possibly this was so because of the lack of sensitivity to that effect with this particular type of data.

Finally, it should be pointed out that, when making direct theoretical comparisons between the Harris and other operators (such as the second-order derivative and median-based operators), the square roots of the expressions in Eqs. (6.11) and (6.17) will need to be taken to ensure that the result is directly proportional to edge contrast  $g$ .

---

## 6.6 CORNER ORIENTATION

This chapter has so far considered the problem of corner detection as relating merely to corner location. However, of the possible point features by which objects might be detected, corners differ from holes in that they are not isotropic, and hence are able to provide orientation information. Such information can be used by procedures that collate the information from various features in order to deduce the presence and positions of objects containing them. In Chapter 11, The Generalized Hough Transform, it will be seen that orientation information is valuable in immediately eliminating a large number of possible interpretations of an image, and hence of quickly narrowing down the search problem and saving computation.

Clearly, when corners are not particularly pointed (Fig. 6.12), or are detected within rather small neighborhoods, the accuracy of orientation will be somewhat restricted. However, orientation errors will seldom be worse than  $45^\circ$ , and will generally be less than  $20^\circ$ . (In fact, accuracy of corner location will also suffer. However, a way of overcoming this problem will be described in Chapter 11, The Generalized Hough Transform, by making use of the generalized Hough transform.) Although these accuracies are far worse than those (around  $1^\circ$ ) for edge orientation (see Chapter 5: Edge Detection), they nevertheless provide valuable constraints on possible interpretations of an image.

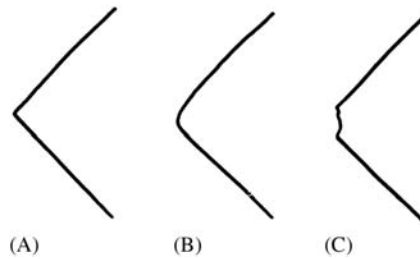
Here we consider only simple means of estimating corner orientation. Basically, once a corner has been located accurately, it is a rather trivial matter to estimate its orientation from that of the intensity gradient at that location. This estimate can be made more accurate by finding the mean intensity gradient over a small region surrounding the estimated corner position, i.e., using the components  $\langle I_x \rangle$  and  $\langle I_y \rangle$ .



**FIGURE 6.11**

Application of the Harris interest point detector. (A) Original image. (B) Interest point feature strength. (C) and (D) Placement of interest points giving greatest response over a distance of 5 pixels (C) and 7 pixels (D). (E) and (F) Placements for later frames in the sequence (using maximum responses over a distance of 7 pixels). (D)–(F) show a high consistency of feature identification, which is important for tracking purposes. Notice that interest points really do indicate locations of interest—corners, people’s feet, ends of white road markings, and castle window and battlement features. Also, the greater the significance as measured by the pixel suppression range, the greater relevance the feature tends to have.



**FIGURE 6.12**

Types of corner: (A) pointed; (B) rounded; (C) chipped. Corners of type (A) are normal with metal components, those of type (B) are usual with biscuits and other food products, whereas those of type (C) are common with food products but rarer with metal parts.

© IEE 1988.

## 6.7 LOCAL INVARIANT FEATURE DETECTORS AND DESCRIPTORS

The discussion in the former sections covered corner and interest point detectors that were useful for general-purpose object location, i.e., finding objects from their features. The specifications of the detectors were that they should be sensitive, reliable, and accurate, so that there would be little chance of missing any objects containing them and that object location would be accurate. In the context of the object inference schemes described in Part 2—and particularly in [Chapter 11](#), The Generalized Hough Transform—it does not matter if some features are missing or whether additional noise or clutter features arise, as the inferential schemes are sufficiently robust to be able to find the objects in spite of this. However, the whole context was the essentially 2-D situation where it was good enough to imagine that the objects were nearly flat, or had nearly flat faces, so that 3-D perspective types of distortion could be avoided. Even so, in 3-D, corners appear as corners from almost any viewpoint, so robust inference algorithms should still be able to perform object location. However, when viewing objects from quite different directions in 3-D, appearance can change dramatically, so it can become extremely difficult to recognize them, even if all the features are present in the images. Thus we arrive at the concept of viewing over wide baselines. In the case of binocular vision, which takes two views over quite a narrow baseline ( $\sim 7$  cm for human eyes), the difference between the views is necessary in order to convey depth information, but it is rarely so great that features recognized in one view cannot be re-identified in the second view (though when huge numbers of similar, e.g., textural, features occur, as when viewing a piece of material, this may not apply). On the other hand, when objects are viewed on a wide baseline, as happens after significant motion has occurred, the angular separation between the views may be as large as  $50^\circ$ . If even larger angular

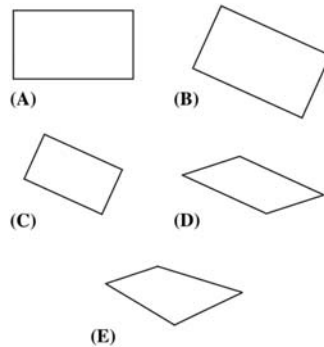
separations occur, there will be much less possibility of recognition. While this sort of situation can be tackled by memorizing sequences of views of objects, here we concentrate primarily on what can be discerned from local features that are seen in wide baseline views of up to  $\sim 50^\circ$ .

At this point we have established the need to be able to recognize local features from wide baseline views as far apart as  $50^\circ$  so that objects can be recognized and tracked or found in databases without especial difficulty. Clearly, the corner and interest point detectors described thus far have no special provision for this. To achieve this aim, additional criteria have to be fulfilled. The first is that feature detection must be consistent and repeatable in spite of substantial change of viewpoint. The second is that features must embody descriptions of their localities so that there is high probability that the same physical feature will be positively identified in each of the views. Imagine that each image contains  $\sim 1000$  corner features. Then there will be  $\sim 1$  million potential feature matches between two views. While a robust inference scheme could perform the match in the case of flat objects, the situation becomes so much more demanding for general views of 3-D objects that matching might not be possible, either at all, or more likely, within a reasonable time—or without large numbers of ambiguities occurring. So it is hugely important to minimize the feature matching task. Indeed, ideally, if a rich enough descriptor is provided for each feature, feature matching might be reducible to one-to-one between views. At this stage we are extremely far from this possibility, as the corners that we have detected can so far only be characterized on the basis of their enclosed angle and intensity or color (and note that the first of these parameters will generally be substantially changed by the altered viewing angle). In what follows we consider in turn the two requirements of consistent, repeatable feature detection and feature description. But first, we have to define the various types of feature normalization that are involved.

### 6.7.1 GEOMETRIC TRANSFORMATIONS AND FEATURE NORMALIZATION

Broadly speaking, obtaining consistent, repeatable feature detection involves allowing for and normalizing the variations between views. The obvious candidates for normalization are scale, affine distortion and perspective distortion. Of these, the first is straightforward, the second is difficult, and the third is impractical to implement. This is because of the number of parameters that need to be estimated for each feature. Bearing in mind that local features are necessarily small, the accuracy with which the parameters can be estimated decreases rapidly with increase in their number. Fig. 6.13 shows how various transformations affect a 2-D shape. The following equations respectively define Euclidean, similarity (scale variation) and affine transformations:

$$\begin{bmatrix} x' \\ y' \end{bmatrix} = \begin{bmatrix} r_{11} & r_{12} \\ r_{21} & r_{22} \end{bmatrix} \begin{bmatrix} x \\ y \end{bmatrix} + \begin{bmatrix} t_1 \\ t_2 \end{bmatrix} \quad (6.24)$$

**FIGURE 6.13**

Effects of various transformations on a convex 2-D shape. (A) Original shape. (B) Effect of Euclidean transform (translation + rotation). (C) Effect of similarity transform (change of scale). (D) Effect of affine transform (stretch + shear). (E) Effect of perspective transform. Note that in (D) parallel lines still remain parallel: this is not in general the case after a projective transform, as indicated in (E). Overall, each of the transforms illustrated is a generalization of the previous one. The respective numbers of degrees of freedom are 3, 4, 6, and 8: in the last case each of the four points is independent and has 2 degrees of freedom, though there are constraints, such as convexity having to be maintained.

$$\begin{bmatrix} x' \\ y' \end{bmatrix} = \begin{bmatrix} sr_{11} & sr_{12} \\ sr_{21} & sr_{22} \end{bmatrix} \begin{bmatrix} x \\ y \end{bmatrix} + \begin{bmatrix} t_1 \\ t_2 \end{bmatrix} \quad (6.25)$$

$$\begin{bmatrix} x' \\ y' \end{bmatrix} = \begin{bmatrix} a_{11} & a_{12} \\ a_{21} & a_{22} \end{bmatrix} \begin{bmatrix} x \\ y \end{bmatrix} + \begin{bmatrix} t_1 \\ t_2 \end{bmatrix} \quad (6.26)$$

where rotation takes place through an angle  $\theta$ , and the rotation matrix is:

$$\begin{bmatrix} r_{11} & r_{12} \\ r_{21} & r_{22} \end{bmatrix} = \begin{bmatrix} \cos \theta & -\sin \theta \\ \sin \theta & \cos \theta \end{bmatrix} \quad (6.27)$$

Euclidean transformations allow translation and rotation operations and have 3 degrees of freedom (DoF); similarity transformations include scaling operations and have 4 DoF; affine transformations include stretching and shearing operations, have 6 DoF, and are the most complex of the transformations that make parallel lines transform into parallel lines; projective transformations are much more complex, have 8 DoF, and include operations which (1) make parallel lines non-parallel, and (2) change *ratios* of lengths on straight lines. The steady increase in the number of parameters is what mitigates against estimation of perspective distortions in the feature points: in fact, it also tends to reduce accuracy for the scale parameter when estimating full affine distortion.

### 6.7.2 HARRIS SCALE AND AFFINE INVARIANT DETECTORS AND DESCRIPTORS

Before proceeding to consider the above ideas in more detail, note that feature detectors such as the Harris operator already estimate location and orientation, so normalization for translation and rotation is already allowed for. This leaves scale as the next candidate for normalization. Here, the basic concept is to apply a given feature detector at various scales, using larger and larger masks. In the case of the Harris operator, there are two relevant scales: one is the edge detection (differentiation) scale  $\sigma_D$  and the other is the overall feature (integration) scale  $\sigma_I$ . In practice these need to be linked together (this involves little loss of generality) so that  $\sigma_I = \gamma\sigma_D$ , where  $\gamma$  has a suitable value in the range 0–1 (typically  $\sim 0.5$ ).  $\sigma_I$  then represents the scale of the overall operator. The approach is now to vary  $\sigma_I$  and to find the value that provides the best match of the operator to the local image data: the best match (extremum value) is the one representing the local image structure: it is intended to be independent of image resolution, which is arbitrary. In fact, the resulting “scale-adapted” Harris operator rarely attains true maxima over scales in such a (“scale-space”) representation (Mikolajczyk and Schmid, 2004); this is because a corner appears as a corner over a wide range of scales (Tuytelaars and Mikolajczyk, 2008). To achieve an optimal scale for matching, a totally different approach is applied: that is to use the Harris operator to locate a suitable feature point, and then to examine its surroundings to find the ideal scale, using a Laplacian operator. The scale of the latter is then adjusted to determine, in a matched filter (i.e., optimum signal-to-noise ratio) way, when the profile of the Laplacian most accurately matches the local image structure (Fig. 6.14). The required operator is called a Laplacian of Gaussian (LoG). It corresponds to smoothing the image using a Gaussian and then applying the Laplacian  $\nabla^2 = \frac{\partial^2}{\partial x^2} + \frac{\partial^2}{\partial y^2}$  (see Chapter 5: Edge Detection). Also, as convolution

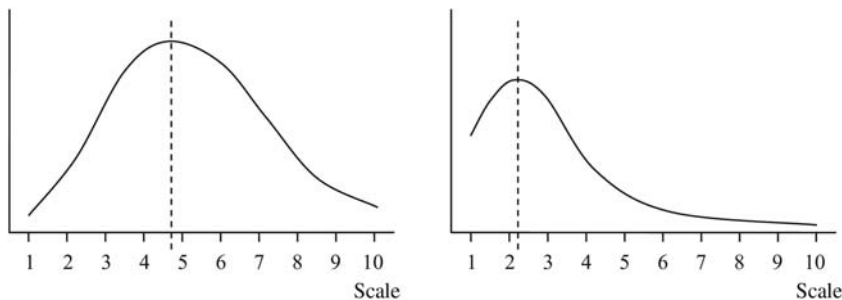


**FIGURE 6.14**

Scaling graphs for two objects which are being matched. The scaling graph on the left has an extremum at 4.7, and the one on the right has an extremum at 2.2. This shows that the best match occurs when the ratios of their scaling factors are approximately 2.14:1. The vertical scales of the graphs do not come into the optimization calculation.

( $\otimes$ ) is associative, we have  $\nabla^2 \otimes (G \otimes I) = (\nabla^2 \otimes G) \otimes I = LoG \otimes I$ . Hence we arrive at the following combined isotropic convolution operator:

$$LoG = \frac{(r^2 - 2\sigma^2)}{\sigma^4(2\pi\sigma^2)} \exp(-r^2/2\sigma^2) = \frac{(r^2 - 2\sigma^2)}{\sigma^4} G(\sigma) \quad (6.28)$$

where

$$G(\sigma) = \frac{1}{2\pi\sigma^2} \exp(-r^2/2\sigma^2) \quad (6.29)$$

Having optimized this operator, we know the scale of the corner, and also its location and 2-D orientation. This means that when comparing two such corner features we can maintain translation, rotation, and scale invariance. To obtain affine invariance we estimate the affine shape of the corner neighborhood. Examining the Harris matrix Eq. (6.10), we rewrite it in the scale-adapted form:

$$\Delta = \sigma_D^2 G(\sigma_1) \otimes \begin{bmatrix} I_x^2(\sigma_D) & I_x(\sigma_D)I_y(\sigma_D) \\ I_x(\sigma_D)I_y(\sigma_D) & I_y^2(\sigma_D) \end{bmatrix} \quad (6.30)$$

where

$$I_x(\sigma_D) = \frac{\partial}{\partial x} G(\sigma_D) \otimes I \quad (6.31)$$

and similarly for  $I_y(\sigma_D)$ . These equations take full account of the differentiation and integration scales  $\sigma_D$  and  $\sigma_I$ . Then for each scale of the scale-adapted Harris operator, we repeat the process that was applied while determining the scale using the Laplacian, this time iteratively determining the best-fit ellipse (rather than circle) profile that fits the local intensity pattern. In fact, in spite of starting at separate scales, the resulting elliptic fits are, for well-defined corner structures, highly consistent and a robust average can be selected. The corresponding ellipse will (compared with the original circle) be stretched by different amounts in two perpendicular directions: the degrees of stretch and skew are the output affine parameters.

The final step is to normalize the feature by transforming it so that the elliptic profile becomes isotropic, circular, and therefore affine invariant (i.e., the affine deformation is nullified). This corresponds to equalizing the eigenvalues of the optimum scale-adapted second-order matrix, Eq. (6.30).

When comparing two corners we require invariant parameters. To obtain these descriptors, it is necessary to determine Gaussian derivatives of the local neighborhood of the interest points, computed on the transformed isotropic feature profile. Clearly, the Gaussian derivatives have to be adjusted for a standardized isotropic profile size, and they have to be normalized to intensity variations by dividing the higher order derivatives by the first-order derivative (i.e., the average intensity gradient in the neighborhood). In the work of Mikolajczyk and Schmid (2004), descriptors of dimension 12 were obtained by using derivatives up to fourth order. (There are two first-order, three second-order, four third-order, and

five fourth-order derivatives: excluding the first-order derivatives, this leaves a total of 12 up to fourth order.) This set of descriptors proved highly effective for identifying corresponding pairs of features in widely different views of up to  $\sim 40^\circ$  angular separation with better than 40% repeatability, and in the affine case up to  $\sim 70^\circ$  with up to 40% repeatability. In addition, the localization accuracy for Harris–Laplace dropped off more or less linearly with angular separation, becoming excessive above  $40^\circ$ , whereas that for Harris–Affine remained at an acceptable level ( $\sim 1.5$  pixel error). The Harris–Laplace was described as having a breakdown point at a viewpoint change of  $40^\circ$ .

### 6.7.3 HESSIAN SCALE AND AFFINE INVARIANT DETECTORS AND DESCRIPTORS

Over the same period that scale and affine invariant detectors and descriptors based on the Harris operator were developed, investigations of similar operators based on the Hessian operator were being undertaken. Here it is useful to recall that the Harris operator is defined in terms of first derivatives of the intensity function  $I$ , while the Hessian operator (see Eq. (6.5)) is defined in terms of the second derivatives of  $I$ . Thus we can consider the Harris operator as being edge-based, and the Hessian operator as being blob-based. This matters for two reasons. One is that the two types of operator might, and do, bring in different information about objects and hence to some extent they are complementary. The other is that the Hessian is better matched than the Harris to the Laplacian scale estimator: indeed, the Hessian arises from the determinant and the Laplacian from the trace of the matrix of second-order derivatives (Eq. (6.2)). The better matching of the Hessian to the Laplacian results in improved scale selection accuracy for this operator (Mikolajczyk and Schmid, 2005). The other details of the Hessian–Laplacian and Hessian–Affine operators are similar to those for the corresponding Harris operators and will not be discussed in more detail here. However, it is worth remarking that in all four cases there are typically 200–3000 detected regions per image depending on the content (Mikolajczyk and Schmid, 2005).

### 6.7.4 THE SCALE INVARIANT FEATURE TRANSFORMS OPERATOR

Lowe’s scale invariant feature transform (widely known as “SIFT”) was first introduced in 1999, a much fuller account being given by Lowe (2004). While being restricted to a scale invariant version, it is important for two reasons: (1) for impressing on the vision community the existence, importance, and value of invariant types of detector; and (2) for demonstrating the richness that feature descriptors can bring to feature matching. For estimating scale, the SIFT operator uses the same basic principle as for the Harris and Hessian-based operators outlined above. However, it differs in using the Difference of Gaussians (DoG)

instead of the LoG, in order to save computation. This possibility is seen by differentiating  $G$  with respect to  $\sigma$  in Eq. (6.29):

$$\frac{\partial G}{\partial \sigma} = \left( \frac{r^2}{\sigma^3} - \frac{2}{\sigma} \right) G(\sigma) = \sigma \text{LoG} \quad (6.32)$$

which means that we can approximate LoG as the DoG of two scales:

$$\text{LoG} \approx \frac{G(\sigma') - G(\sigma)}{\sigma' - \sigma} = \frac{G(k\sigma) - G(\sigma)}{(k-1)\sigma^2} \quad (6.33)$$

where use of the constant scale factor  $k$  permits scale normalization to be carried out easily between scales.

In fact, it is in the design of the descriptors that SIFT is particularly different from the Harris and Hessian-based detectors. Here the operator divides the support region, at each scale, into a  $16 \times 16$  sample array and estimates the intensity gradient orientations for each of these. They are then grouped into sets of sixteen  $4 \times 4$  sub-arrays and orientation histograms are generated for each of these, the directions being restricted to one of eight directions. The final output is a  $4 \times 4$  array of histograms each containing entries for eight directions—amounting to a total output dimensionality of  $4 \times 4 \times 8 = 128$ .

The overall detector is found (Mikolajczyk, 2002) to be more repeatable than Harris–Affine and to retain a final matching accuracy above 50% out to a  $50^\circ$  angular separation. However, because of the limited stability of Harris–Affine, Lowe (2004) recommends the approach of Pritchard and Heidrich (2003) of including additional SIFT features with  $60^\circ$  viewpoint separation during training. We defer further discussion of the performance of this detector to Section 6.7.7 below.

### 6.7.5 THE SPEEDED-UP ROBUST FEATURES OPERATOR

The development of SIFT stimulated efforts to produce an effective invariant feature detector that was also highly efficient and required a smaller descriptor than the large one employed by SIFT. An important operator in this mold was the speeded-up robust features (SURF) method of Bay et al. (2006, 2008). This was based on the Hessian–Laplace operator. In order to increase speed, several measures were taken: (1) the integral image approach was used to perform rapid computation of the Hessian and was also used during scale space analysis; (2) the DoG was used in place of the LoG for assessing scale; (3) sums of Haar wavelets were used in place of gradient histograms, resulting in a descriptor dimensionality of 64—half that of SIFT; (4) the sign of the Laplacian was used at the matching stage; (5) various reduced forms of the operator were used to adapt it to different situations, notably an “upright” version capable of recognizing features within  $\pm 15^\circ$  of those pertaining to an upright stance, as occurs for outdoor buildings and other objects. By maintaining a rigorous, robust design, the operator was described as outperforming SIFT, and also proved capable of estimating

3-D object orientation within fractions of a degree and certainly more accurately than SIFT, Harris–Laplace, and Hessian–Laplace.

Of some importance for this implementation is the integral image approach (Simard et al., 1999), brought prominently to light by Viola and Jones (2001), but maybe not utilized as much as one might expect during the 2000s. This is extremely simple, yet radical in the levels of speedup it can bring. It involves computing an integral image  $I_{\Sigma}$ , which is an image that retains sums of all pixel intensities encountered in a single scan over the input image:

$$I_{\Sigma}(x,y) = \sum_{i=0}^x \sum_{j=0}^y I(i,j) \tag{6.34}$$

This not only permits any pixel intensity in the original image to be recovered:

$$I(i, j) = I_{\Sigma}(i, j) - I_{\Sigma}(i - 1, j) - I_{\Sigma}(i, j - 1) + I_{\Sigma}(i - 1, j - 1) \tag{6.35}$$

but also allows the sum of the pixel intensities in any upright rectangular block, such as those ranging from  $x = i$  to  $i + a$  and  $y = j$  to  $j + b$  within block D in Fig. 6.15, to be utilized:

$$\begin{aligned} \sum_D I &= \sum_A I - \sum_{A,B} I - \sum_{A,C} I + \sum_{A,B,C,D} I \\ &= I_{\Sigma}(i, j) - I_{\Sigma}(i + a, j) - I_{\Sigma}(i, j + b) + I_{\Sigma}(i + a, j + b) \end{aligned} \tag{6.36}$$

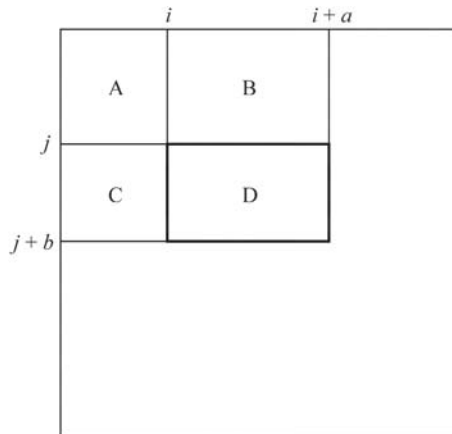


**FIGURE 6.15**

The integral image concept. Here block D can be considered as made up by taking block  $A + B + C + D$ , then subtracting block  $A + B$  and block  $C$ , in the latter case by subtracting  $A + C$  and adding  $A$ : see text for an exact mathematical treatment.



The method is exceptionally well adapted to computing Haar filters that typically consist of arrays containing blocks of identical values, for example:

$$\begin{bmatrix} -1 & -1 & 1 & 1 & 1 & 1 & -1 & -1 \\ -1 & -1 & 1 & 1 & 1 & 1 & -1 & -1 \\ -1 & -1 & 1 & 1 & 1 & 1 & -1 & -1 \\ -1 & -1 & 1 & 1 & 1 & 1 & -1 & -1 \end{bmatrix}$$

Note that once the integral image has been computed, it permits summations to be made over any block merely by performing four additions—taking a miniscule time that is independent of the size of the block. A simple generalization to the 3-D box filter (Simard et al., 1999) is also possible, and this is used in computing within scale-space in the SURF implementation.

### 6.7.6 MAXIMALLY STABLE EXTREMAL REGIONS

There is one class of invariant feature that does not fall into the pattern covered in the preceding sections—the invariant region type of feature. Among the most important examples of this type of feature is the maximally stable extremal region (MSER). The method analyses regions with increasing ranges of intensity and aims to determine those that are extremal in a particularly stable way. (Recall that finding extrema is a powerful general method for locating invariant features, as we have already seen in [Section 6.7.2](#).)

The method (Matas et al., 2002) starts by taking pixels of zero intensity and progressively adding pixels with higher intensity levels, at each stage monitoring the regions that form. At each stage largest connected regions or “connected components” will represent extremal regions. (See [Section 8.3](#) for a full explanation of connected components and their computation. Meanwhile, assume that a “connected component” means a region *containing everything that is connected to any part of that region*. Hence by definition, a connected component is an extremal region.) As more and more gray levels are added, the connected component regions will grow and some initially separate ones will merge. MSERs are those connected components that are close to stable (as conveniently measured by their area) over a range of intensities, i.e., each MSER is represented by the position of a local intensity minimum in the rate of change of the area function. Interestingly, relative area change is an affine-invariant property, so finding MSER regions guarantees both scale and affine invariance. In fact, because of the way that intensities are handled in this method, the results are also independent of monotonic transformation of image intensities.

While every MSER can be regarded as a connected component of a thresholded image, global thresholding is not carried out, and optimality is judged on the basis of the stability of the connected components that are located. Intrinsicly, MSERs have arbitrary shapes, though for matching purposes they can be converted into ellipses of appropriate areas, orientations, and moments. Perhaps surprisingly for affine features, they can be computed highly efficiently in times that are nearly linear in the number of pixels; they also have good

repeatability, though they are quite sensitive to image blur. This last problem is to be expected, given the dependence on individual gray levels and the precision with which connected components analysis is carried out; in fact, this difficulty has been addressed in a recent extension of the work (Perdoch et al., 2007).

### 6.7.7 COMPARISON OF THE VARIOUS INVARIANT FEATURE DETECTORS

While there are many more invariant feature detectors than we have been able to cover here (Salient regions, IBR, FAST, SFOP, . . .) and many variants of them (GLOH, PCA-SIFT, . . .), we next concentrate on comparisons between them. In fact, most of the papers describing new detectors make comparisons with older detectors, but often with limited data sets. Here we outline the conclusions of Ehsan et al. (2010), who compared SIFT, SURF, Harris–Laplace, Harris–Affine, Hessian–Laplace, and Hessian–Affine, using the following data sets: Bark, Bikes, Boat, Graffiti, Leuven, Trees, UBC, and Wall (viz. eight sequences of six images)—see Oxford Data Sets at <http://www.robots.ox.ac.uk/~vgg/research/affine/> (accessed April 19, 2011). Table 6.1 presents the results in a modified form with SURF placed after Hessian–Laplace, as it is based on the latter.

Apart from Table 6.1, Ehsan et al. (2010) showed the results of using three different criteria for judging repeatability of feature detector performance. The first was the standard repeatability criterion:

$$C_0 = N_{\text{rep}} / \min(N_1, N_2) \quad (6.37)$$

where  $N_1$  is the total number of points detected in the first image,  $N_2$  is the total number of points detected in the second image, and  $N_{\text{rep}}$  is the number of repeated points.

**Table 6.1** Comparison of Invariant Feature Detectors

Data sets	SIFT	Harris–Laplace	Hessian–Laplace	SURF	Harris–Affine	Hessian–Affine	Total
Bark	■■■	■	■	■■	■	■	9
Bikes	■	■■■	■■■	■■■	■■	■■■	14
Boat	■■	■■■	■■■	■■	■	■■	12
Graffiti	■	■	■	■	■■■	■■■	10
Leuven	■■■	■	■■	■■■	■	■■	12
Trees	■	■■■	■■■	■■■	■■	■■	13
UBC	■■	■■■	■■■	■■■	■■■	■■■	17
Wall	■■■	■■	■■	■■■	■■	■■	14
total	16	14	18	20	15	18	101

*The totals give some indication of the overall capabilities of the detectors, and of the complexity of the individual data sets. However, the detector totals must be interpreted in the light of the highest level of invariance achievable—viz. scale or affine.*

They emphasized that it has been remarked (Tuytelaars and Mikolajczyk, 2008) that repeatability “does not guarantee high performance in a given application.” They reasoned that this was due in part to comparing features within adjacent pairs of images rather than over whole image sequences: specifically, they recommended that each image should be compared taking the first frame of the sequence as a reference and using the following criterion:

$$C_1 = N_{\text{rep}}/N_{\text{ref}} \quad (6.38)$$

Nevertheless, they also proposed a more symmetric measure of repeatability:

$$C_2 = N_{\text{rep}}/(N_{\text{ref}} + N_c) \quad (6.39)$$

where  $N_c$  is the total number of points detected in the current frame. This proved to be a less harsh and more realistic criterion when compared with the trends of the observed ground truth for an image sequence. Further evidence for moving away from the standard repeatability criterion  $C_0$  is that it rewards failure to detect features (because decrease in  $N_1$  or  $N_2$  will, if anything, raise the value of  $C_0$ ). This suggests altering  $C_0$  to use the maximum instead of the minimum. However, using either the maximum or the minimum tends to emphasize extreme results, leading to nonrobust measures. From this point of view the most appropriate measure has to be  $C_2$ . In fact, this criterion gave optimal results and low error probability measures when run against ground truth using Pearson’s correlation coefficients (Ehsan et al., 2010). Using  $C_2$ , an important result was the dominance of the Hessian-based detectors, which is already very evident in [Table 6.1](#) (derived from their table 2), where the three Hessian-based totals are 18, 18, 20, vis-à-vis 14, 15, and 16 for the others (interestingly, the situation is even more polarized in favor of Hessian-based detectors when the data sets giving the best and worst results—Bark and UBC—are ignored). Note that Tuytelaars and Mikolajczyk (2008) did not come out so strongly in favor of the Hessian-based detectors, but this was probably because their analysis of data sets was not so extensive; also, Ehsan et al. (2010) were the first to look at image sequences so rigorously using  $C_2$ .

The review by Tuytelaars and Mikolajczyk (2008) is of great value in evaluating performance using several disparate criteria, viz. repeatability, localization accuracy, robustness, and efficiency. Some of their results are shown in [Table 6.2](#)—notably those for all the feature detectors covered in [Table 6.1](#) and those for the single-scale Harris and Hessian, and for the MSER detector (Matas et al., 2002) mentioned earlier. They also make the following valuable observations:

1. Scale invariant operators can normally be dealt with adequately by a robustness capability for viewpoint changes of less than  $30^\circ$ , as affine deformations only rise above those due to variations in object appearance beyond that level.
2. In different applications, different feature properties may be important, and thus success depends largely on appropriate selection of features.

**Table 6.2** Performance Evaluation of Various Feature Detectors

Detector	Invariance	Repeat-ability	Accuracy	Robust-ness	Efficiency	Total
Harris	Rotation	■■■	■■■	■■■	■	11
Hessian	Rotation	■■	■■	■■	■	7
SIFT	Scale	■■	■■	■■	■■	8
Harris–Laplace	Scale	■■■	■■■	■■	■	9
Hessian–Laplace	Scale	■■■	■■■	■■■	■	10
SURF	Scale	■■	■■	■■	■■■	9
Harris–Affine	Affine	■■■	■■■	■■	■■	10
Hessian–Affine	Affine	■■■	■■■	■■■	■■	11
MSER	Affine	■■■	■■■	■■	■■■	11

The totals give some indication of the overall capabilities of the detectors: however, they must be interpreted in the light of the highest level of invariance achievable (Column 2).

3. Repeatability may not always be the most important feature performance characteristic: not only is it hard to define and measure but robustness to small appearance variations matters more.
4. There is a need for work focusing on complementarity of features, leading either to complementary detectors or to detectors providing complementary features.

In the last respect, note that some ground work has recently been carried out by Ehsan et al. (2011) to measure the coverage of interest point detectors. They identify the recent SFOP scale invariant feature transform (Förstner et al., 2009) as the most outstanding detector in this respect, either used on its own or in conjunction with others. Ehsan et al.’s new criterion for coverage  $C$  is based on the harmonic mean so as not to overemphasize nearby features:

$$C = N(N-1) / \sum_{i=1}^{N-1} \sum_{j>1}^N (1/d_{ij}) \quad (6.40)$$

(In this formula  $d_{ij}$  is the Euclidean distance between feature points  $i$  and  $j$ .)

Note that a detector that has high coverage is not guaranteed to be sound: after all, a detector giving a random selection of feature points might fare well on this count. Hence a coverage criterion can only come into its own when it is used to select complementary types of feature and feature detector, or a detector that provides a good mix of types of feature, for which the output selection is known to be sound on other counts (repeatability, robustness, and so on).

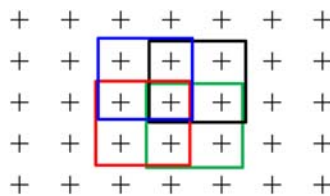
### 6.7.8 HISTOGRAMS OF ORIENTED GRADIENTS

This study of locally invariant feature detectors would be incomplete without including the histograms of oriented gradients (HOG) approach (Dalal and

Triggs, 2005), which appeared during much the same period as SIFT, SURF, and the other methods mentioned earlier. HOGs were designed for, and are well-matched to, the detection of human shapes. Basically, they focus on the straight limbs of the human body, which have many edge points aligned along the same direction—though the latter will naturally change with walking or other motions. The basis of the method is to divide the image into “cells” (sets of pixels) and to produce orientation histograms for all of them. Voting into the orientation histogram bins takes place with weighting proportional to gradient magnitude. The cells are combined into larger overlapping blocks, with the result that some of the blocks end up with larger signals indicating the presence of human limbs. Curiously, the HOG detectors cue mainly on silhouette contours and emphasize the head, shoulders, and feet.

Although the HOG approach and the SIFT operator have a certain resemblance in that they both use orientation histograms, they do so in different ways. In fact, the aim of SIFT is to provide orientation invariance by matching pairs of features by first canceling the difference in orientations between them (SIFT is intrinsically scale-invariant, though it is ultimately also translation and rotation invariant as its descriptor has full knowledge of the location and orientation of each feature). In contrast, the HOG approach does not provide orientation invariance but instead aims to present a cell map of orientation histograms over parts of an image, so that human or other shapes can be identified. Thus it should be described as a *regional image descriptor* rather than as a *local image descriptor*. However, it has the further advantage of providing a good measure of geometric and photometric invariance as it focuses only on local variations in orientation.

To provide illumination invariance, the histograms in the HOG operator are normalized with respect to image contrast. Dalal and Triggs achieved this by normalizing the contrast over neighboring (typically  $2 \times 2$ ) blocks of cells. Interestingly, they found it better to do this several times for each cell by using different overlapping blocks of cells and treating the results as independent signals. In the case of  $2 \times 2$  blocks of cells, this gave four results for each cell—as indicated by the four main squares in the following figure:



Overall, experiment showed that square cells of side 6–8 pixels together with block sizes of  $2 \times 2$  or  $3 \times 3$  cells worked best (in this context “best” meant giving the best match to the widths of human limbs in the particular image data set).

Another interesting detail was that nine histogram bins were used to cover the range  $0^\circ$ – $180^\circ$ , amounting to relatively fine quantization for orientation; in addition, no gain was found from using signed gradients when detecting humans (though the position was found to be reversed for car and motorbike recognition).

---

## 6.8 CONCLUDING REMARKS

Corner detection provides a useful start to the process of object location and to this end is often used in conjunction with the abstract pattern matching approaches discussed in [Chapter 11](#), The Generalized Hough Transform. Apart from the obvious template matching procedure, which is of limited applicability, three main approaches have been described. The first was the second-order derivative approach, which includes the KR, DN, and ZH methods—all of which embody the same basic schema; the second was the median-based method, which turned out to be equivalent to the second-order derivative methods in situations where corners have smoothly varying intensity functions; and the third was the Harris detector which is based on the matrix of second moments of the *first* derivatives of the intensity function. Perhaps surprisingly, the latter is able to extract the same information much as the other two approaches, though there are differences, in that the Harris detector is better described as an interest point detector than as a corner detector. In fact, the Harris detector has probably been the most widely used corner and interest point detector of all, and for general purpose (non-3-D) operation this still seems to be the case—in spite of the advent of the SUSAN detector (Smith and Brady, 1997), which is known to be faster and more efficient, but somewhat less resistant to noise.

Interestingly, the situation presented above started changing radically from about 1998, when workers started looking for approaches to object location, which were not merely robust to noise, distortion, partial occlusion, and extraneous features, but were able to overcome problems of gross distortion due to viewing the same scene from widely different directions. This “wide baseline” problem, which is prominent with 3-D and motion applications, including tracking moving objects, became the driving force for radical new thinking and development. As we have seen, attempts were made to adapt the Harris operator to this scenario, making it invariant to similarity (scale) and affine transformations, though in the end somewhat more success was achieved by returning to the Hessian operator discussed earlier in this chapter. Alternative approaches included the MSER approach, which is by no means based on the location of any sort of corner or interest points. Indeed, it harks back to the thresholding methods of [Chapter 4](#), The Role of Thresholding. But this is all to the good, as the underlying task is that of segmentation coupled with recognition and identification/matching: division of the subject into watertight topics such as thresholding, edge detection, and corner detection has limited validity or at least it is too restrictive to offer the

best solutions to the real problems of the subject. In this context it is relevant that the newly evolved feature detectors embody multiparameter descriptors, making them far better suited not only to detection per se but also to the more exacting task of wide baseline 3-D matching.

Overall, in this chapter we have seen the corner detector approach transmogrify itself to overcome the problems of viewing objects from directions as far apart as  $70^\circ$ —and with a great deal of success. Remarkably, all this was achieved in little more than a decade—evidence that progress in this subject has been accelerating. Importantly, the old computer adage “garbage in—garbage out” is relevant, because feature detection forms a crucial link between the original pictures and their high level interpretation.

*This chapter has studied how objects may be detected and located from their corners and interest points. It has developed both the classic approach to detector design and the more recent invariant approaches, which result in multiparameter feature descriptors to aid matching between widely separated views of objects.*

---

## 6.9 BIBLIOGRAPHICAL AND HISTORICAL NOTES

The subject of corner detection has been developing for over three decades. The scene was set for the development of parallel corner detection algorithms by Beaudet’s (1978) work on rotationally invariant image operators. This was soon followed by Dreschler and Nagel’s (1981) more sophisticated second-order corner detector: the motivation for this research was to map the motion of cars in traffic scenes, corners providing the key to unambiguous interpretation of image sequences. One year later, Kitchen and Rosenfeld (1982) had completed their study of corner detectors based mainly on edge orientation and had developed the second-order KR method described in [Section 6.3](#). The years 1983 and 1984 saw the development of the second-order ZH detector and the median-based detector (Zuniga and Haralick, 1983; Paler et al., 1984). Subsequently, the author’s work on the detection of blunt corners (see [Chapter 11](#): The Generalized Hough Transform) and on analyzing and improving the median-based detector appeared (Davies, 1988a,d, 1992a). Meanwhile, other methods had been developed, such as the Harris algorithm (Harris and Stephens, 1988; see also Noble, 1988). The Smith and Brady (1997) “SUSAN” algorithm marked a further turning point, needing no assumptions on the corner geometry, as it works by making simple comparisons of local gray levels: this is one of the most cited of all corner detection algorithms.

In the 2000s further corner detectors have been developed. Lüdtkke et al. (2002) designed a detector based on a mixture model of edge orientation: in addition to being effective in comparison with the Harris and SUSAN operators, particularly at large opening angles, the method provides accurate angles and

strengths for the corners. Olague and Hernández (2002) worked on a unit step edge function (USEF) concept, which is able to model complex corners well: this resulted in adaptable detectors that are able to detect corners with sub-pixel accuracy. Shen and Wang (2002) described a Hough transform–based detector: as this works in a 1-D parameter space it is fast enough for real-time operation; a useful feature of the paper is the comparison with, and between, the Wang and Brady detector, the Harris detector, and the SUSAN detector. The several example images show that it is difficult to be sure exactly what one is looking for in a corner detector (i.e., corner detection is an ill-posed problem) and that even the well-known detectors sometimes inexplicably fail to find corners in obvious places. Golightly and Jones (2003) present a practical problem in outdoor country scenery: they discuss not only the incidence of false positives and false negatives but also the probability of correct association in corner matching, e.g., during motion.

Rocket (2003) gives a performance assessment of three corner detection algorithms—the KR detector, the median-based detector, and the Harris detector: the results are complex, and the three detectors are found to have very different characteristics. The paper is valuable in showing how to optimize the three methods (not least showing that the Harris detector parameter  $k$  should be  $\sim 0.05$ ), and also because it concentrates on careful research rather than “selling” a new detector. Tissainayagam and Suter (2004) give an assessment of the performance of corner detectors, with vitally important coverage of point feature (motion) tracking applications. Interestingly, it finds that, in image sequence analysis, the Harris detector is more robust to noise than the SUSAN detector, a possible explanation being that it “has a built-in smoothing function as part of its formulation.” Finally, Davies (2005) analyzed the localization properties of the Harris operator: see [Section 6.5](#) for the main results of this work.

While the above discussion covers many of the developments on corner detection, it is not the whole story. This is because in many applications it is not specific corner detectors that are needed but “interest point” detectors, which are capable of detecting any characteristic patterns of intensity that can be used as reliable feature points. In fact, the Harris detector is often called an interest point detector—with good reason, as indicated in [Section 6.5.2](#). Moravec (1977) was among the first to refer to interest points and was followed by Schmid et al. (2000) and many others. However, Sebe and Lew (2003) and Sebe et al. (2003) call them salient points—a term more often reserved for points that attract the attention of the *human* visual system. Overall, it is probably safest to use the Haralick and Shapiro (1993) definition: a point being “interesting” if it is both distinctive and invariant—i.e., it stands out and is invariant to geometric distortions such as might result from moderate changes in scale or viewpoint (note that Haralick and Shapiro also list other desirable properties—stability, uniqueness, and interpretability). The invariance aspect is taken up by Kenney et al. (2003) who show how to remove ill-conditioned points from consideration, to make matching more reliable.



The subject of invariant feature detectors and descriptors has taken little over a decade to develop and over that period it has come a long way. It started with papers by Lindeberg (1998) and Lowe (1999) that indicated the way forward and provided basic techniques. It arose largely because of difficulties in wide baseline stereo work, and with tracking object features over many video frames—because features change their appearance over time and correspondences are easily lost. To proceed, it was necessary first to eliminate the relatively simple problem of features changing in size, thereby necessitating scale invariance (it being implicit that translation and rotation invariance have already been dealt with). Later, improvements became necessary to cope with affine invariance. Thus Lindeberg's pioneering theory (1998) was soon followed by Lowe's work (1999, 2004) on scale invariant feature transforms (SIFT). This was followed by affine invariant methods developed by Tuytelaars and Van Gool (2000), Mikolajczyk and Schmid (2002, 2004), Mikolajczyk et al. (2005), and others. In parallel with these developments, work was published on MSER (Matas et al., 2002) and other extremal methods (e.g., Kadir and Brady, 2001; Kadir et al., 2004).

Much of this work capitalized on the interest point work of Harris and Stephens (1988), and was underpinned by careful in-depth experimental investigations and comparisons (Schmid et al., 2000; Mikolajczyk and Schmid, 2005; Mikolajczyk et al., 2005). Next, the tide turned in other directions, in particular the design of feature detectors that aim at real-time operation—as in the case of the SURF approach (Bay et al., 2006, 2008).

A review article summarizing the main approaches was published by Tuytelaars and Mikolajczyk in 2008. However, that was by no means the end of the story. As outlined in [Section 6.7.7](#), Ehsan et al. (2010) briefly reviewed the status quo on repeatability of the main features and detectors, and reported on experiments to assess it: their work included two new repeatability criteria that more realistically reflected the underlying requirements for invariant detectors. In addition, they presented new work (Ehsan et al., 2011) on the coverage of invariant feature detectors, reflecting poignant remarks made in Tuytelaars and Mikolajczyk's (2008) review. It is clear that, with the passing of the first decade of the 2000s, an even more exacting phase of development is under way, with more rigorous performance evaluation: it will no longer be sufficient to produce new invariant feature detectors; instead it will be necessary to integrate them much more fully with the target applications, following rigorous design to ensure that all relevant criteria are being met and that the tradeoffs between the criteria are much more transparent.

### 6.9.1 MORE RECENT DEVELOPMENTS

Since the Tuytelaars and Mikolajczyk's (2008) review, further relevant work on feature detectors and descriptors has emerged. Rosten et al. (2010) have presented the FAST family of corner detectors that is designed on a new heuristic to be especially fast while at the same time to be highly repeatable; they also review

methods for comparing feature detectors and call for less concentration on how a feature detector should do its job than on what performance measure it is required to optimize. Cai et al. (2011) work on a “linear discriminant projections” procedure for reducing the dimensionality of local image descriptors and manage to bring the SIFT tally down from 128 to just 30. However, they warn that this seems to be achievable only by making the projections specific to the type of image data. With a similar motivation, Teixeira and Corte-Real (2009) quantize the SIFT descriptor to form visual words using a predefined vocabulary, though in this case the vocabulary is structured in the form of a tree; it is constructed using a generic data set related to the type of object tracking being performed. van de Sande et al. (2010) discuss the generation of color object descriptors. They find that the choice of a single-color descriptor for all categories of data is sub-optimal: but for unknown data, “OpponentSIFT” (using three sets of SIFT features for the three opponent colors) showed the highest degree of invariance with respect to photometric variations. Zhou et al. (2011) proposed a method to perform descriptor combination and classifier fusion. They cast the problem of object classification into a learning setting which again means that the method is adaptive and not applicable to new data without retraining. Overall, we see that trying to reduce the original 128 SIFT features (or the equivalent) tends to make such methods specific to particular training data.

---

## 6.10 PROBLEMS

1. By examining suitable binary images of corners, show that the median corner detector gives a maximal response within the corner boundary rather than half-way down the edge outside the corner. Show how the situation is modified for grayscale images. How will this affect the value of the gradient noise-skimming threshold to be used in the improved median detector?
2. Prove Eq. (6.6), starting with the following formula for curvature:

$$\kappa = (d^2y/dx^2) / [1 + (dy/dx)^2]^{3/2}$$

*Hint:* First express  $dy/dx$  in terms of the components of intensity gradient, remembering that the intensity gradient vector  $(I_x, I_y)$  is oriented along the edge normal; then replace the  $x, y$  variation by  $I_x, I_y$  variation in the formula for  $\kappa$ .

This page intentionally left blank

# Texture analysis

# 7

It is quite easy to understand what a texture is, although somewhat less easy to define it. For many reasons it is useful to be able to classify textures and to distinguish them from one another; it is also useful to be able to determine the boundaries between different textures, as they often signify the boundaries of real objects. This chapter studies the means for achieving these aims.

*Look out for:*

- basic measures by which textures can be classified—such as regularity, randomness, and directionality
- problems that arise with “obvious” texture analysis methods, such as autocorrelation
- the long-standing graylevel co-occurrence matrix method
- Laws’ method and Ade’s generalization of it
- the fact that textures have to be analyzed statistically, because of the random element in their construction.

Texture analysis is a core element in the vision repertoire, just as textures are core components of most images. It therefore seemed most appropriate to include this topic in Part 1, Low-Level Vision, of the book.

## 7.1 INTRODUCTION

In the foregoing chapters many aspects of image analysis and recognition have been studied. At the core of these matters has been the concept of segmentation, which involves the splitting of images into regions that have some degree of uniformity, whether in intensity, color, texture, depth, motion, or other relevant attributes. Care was taken in [Chapter 4](#), The Role of Thresholding, to emphasize that such a process will be largely ad hoc, since the boundaries produced will not necessarily correspond to those of real objects. Nevertheless, it is important to make the attempt, either as a preliminary to more accurate or iterative demarcation of objects and their facets or else as an end in itself, for example, to judge the quality of surfaces.

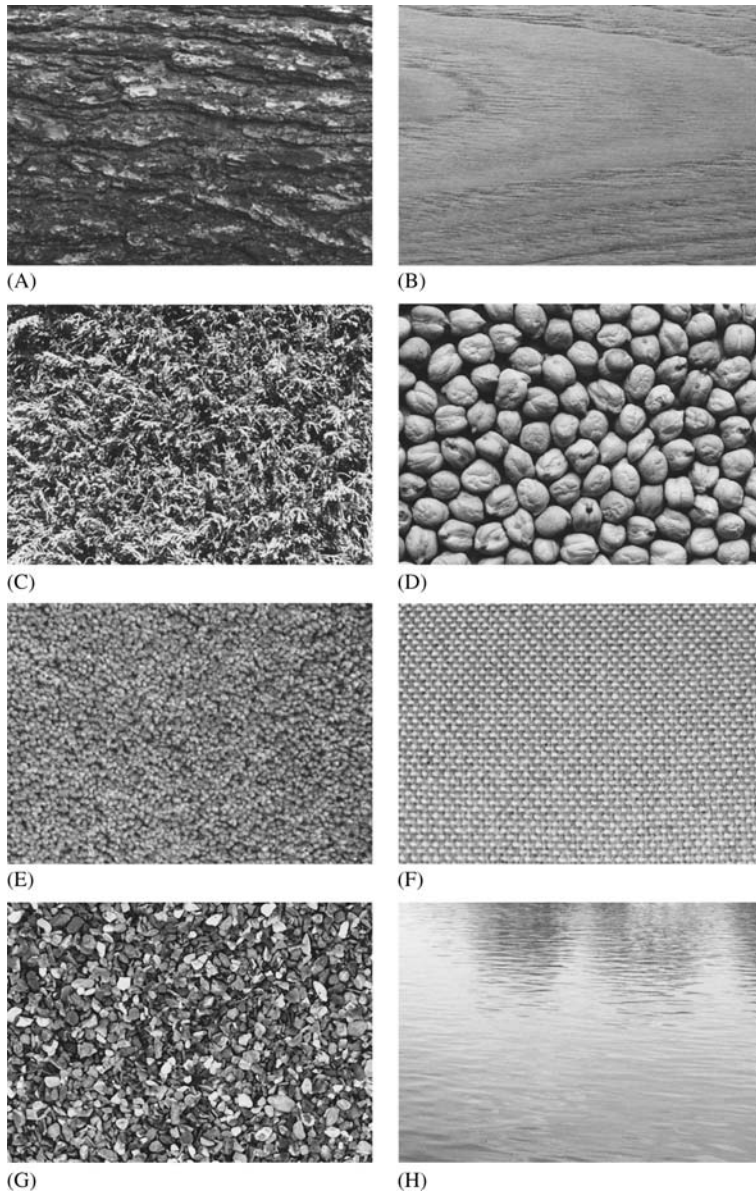
In this chapter we move on to the study of texture and its measurement. Texture is a difficult property to define: indeed, in 1979 Haralick reported that no satisfactory definition of it had up till then been produced. Perhaps, we should not be surprised by this, as the concept has rather separate meanings in the contexts of vision, touch, and taste, the particular nuances being understood by different people also being highly individual and subjective. Nevertheless, we require a working definition of texture, and in vision the particular aspect we focus on is the variation in intensity of a particular surface or region of an image. Even with this statement we are being indecisive about whether it is the physical object being observed which is being described or the image derived from it. This reflects the fact that it is the roughness of the surface or the structure or composition of the material that originally gives rise to its visual properties. However, in this chapter we are mainly interested in the interpretation of images, and so we define texture as the characteristic variation in intensity of a region of an image that should allow us to recognize and describe it and to outline its boundaries (Fig. 7.1).

This definition of texture implies that texture is nonexistent in a surface of uniform intensity and does not say anything about how the intensity might be expected to vary or how we might recognize and describe it. In fact, there are very many ways in which intensity might vary, but if the variation does not have sufficient uniformity, the texture may not be characterized sufficiently closely to permit recognition or segmentation.

We next consider ways in which intensity might vary. Clearly, it can vary rapidly or slowly, markedly or with low contrast, with a high or low degree of directionality, and with greater or lesser degrees of regularity. This last characteristic is often taken as key: either the textural pattern is regular as for a piece of cloth or it is random as for a sandy beach or a pile of grass cuttings. However, this ignores the fact that a regular textural pattern is often not wholly regular (again, as for a piece of cloth) or not wholly random (as for a mound of potatoes of similar size). Thus the degrees of randomness and of regularity will have to be measured and compared when characterizing a texture.

There are more profound things to say about the textures mentioned above. Often textures are derived from tiny objects or components which are themselves similar, but which are placed together in ways ranging from purely random to purely regular—be they bricks in a wall, grains of sand, blades of grass, strands of material, stripes on a shirt, wickerwork on a basket, or a host of other items. In texture analysis it is useful to have a name for the similar textural elements that are replicated over a region of the image: such textural elements are called *texels*. These considerations lead us to characterize textures in the following ways:

1. The texels will have various sizes and degrees of uniformity.
2. The texels will be orientated in various directions.
3. The texels will be spaced at varying distances in different directions.
4. The contrast will have various magnitudes and variations.
5. Various amounts of background may be visible between texels.
6. The variations composing the texture may each have varying degrees of regularity vis-à-vis randomness.

**FIGURE 7.1**

A variety of textures obtained from real objects. A Bark, B wood grain, C fir leaves, D chick peas, E carpet, F fabric, G stone chips, H water. These textures demonstrate the wide variety of familiar textures that are easily recognized from their characteristic intensity patterns.

It is quite clear from this discussion that a texture is a complicated entity to measure. The reason is primarily that many parameters are likely to be required to characterize it: in addition, when so many parameters are involved, it is difficult to disentangle the available data and measure the individual values or decide the ones that are most relevant for recognition. And of course, the statistical nature of many of the parameters is by no means helpful. However, we have so far only attempted to show how complex the situation can be. In the following, we attempt to show that quite simple measures can be used to recognize and segment textures in practical situations.

Before proceeding, it is useful to recall that in the analysis of shape there is a dichotomy between available analysis methods. We could, for example, use a set of measures, such as circularity and aspect ratio, which would permit a description of the shape but which would not allow it to be reconstructed; or else we could use descriptors such as skeletons with distance function values, or moments, which would permit full and accurate reconstruction, although the set of descriptors might have been curtailed so that only limited but predictable accuracy was available. In principle, such a reconstruction criterion should be possible with texture. However, in practice there are two levels of reconstruction. In the first, we could reproduce a pattern that, to human eyes, would be indistinguishable from the off-camera texture until one compared the two on a pixel-by-pixel basis. In the second, we could reproduce a textured pattern exactly. The point is that textures are normally partially statistical in nature, so it will be difficult to obtain a pixel-by-pixel match in intensities: neither, in general, will it be worth aiming to do so. Thus texture analysis generally only aims at obtaining accurate statistical descriptions of textures, from which *apparently* identical textures can be reproduced if desired.

Many workers have contributed to, and used, a wide range of approaches for texture analysis well over a period of 40 years. The sheer weight of the available material and the statistical nature of it can be daunting for many. Note that [Section 7.4](#) is particularly relevant to practitioners, as it describes the Laws' texture energy approach that is intuitive, straightforward to apply in both software and hardware, and highly effective in many application areas. However, [Section 7.3](#) on graylevel co-occurrence matrices (which were important historically) can be omitted on a first reading.

---

## 7.2 SOME BASIC APPROACHES TO TEXTURE ANALYSIS

In [Section 7.1](#) we defined texture as the characteristic variation in intensity of a region of an image that should allow us to recognize and describe it and to outline its boundaries. In view of the likely statistical nature of textures, this prompts us to characterize the texture by the variance in intensity values taken over the whole region of the texture. However, such an approach will not give a rich enough description of the texture for most purposes and will certainly not provide any

possibility of reconstruction: it will also be especially unsuitable in cases where the texels are well defined or where there is a high degree of periodicity in the texture. On the other hand, for highly periodic textures such as arise with many textiles, it is natural to consider the use of Fourier analysis. Indeed, in the early days of image analysis, this approach was tested thoroughly, although the results were not always encouraging. Finally, note that we have deferred for now the problem of finding the region of a texture, so that we can compute its characteristics in order to perform a segmentation function. However, some preliminary training of a classifier may clearly be used to overcome this problem for supervised texture segmentation tasks.

Bajcsy (1973) used a variety of ring and orientated strip filters in the Fourier domain to isolate texture features—an approach that was found to work successfully on natural textures such as grass, sand, and trees. However, there is a general difficulty in using the Fourier power spectrum in that the information is more scattered than might at first be expected. In addition, strong edges and image boundary effects can prevent accurate texture analysis by this method. Perhaps, more important is the fact that the Fourier approach is a global one, which is difficult to apply successfully to an image that is to be segmented by texture analysis (Weszka *et al.*, 1976).

Autocorrelation is another obvious approach to texture analysis, since it should show up both local intensity variations and also the repeatability of the texture (Fig. 7.2). An early study was carried out by Kaizer (1955). He examined how many pixels an image has to be shifted before the autocorrelation function drops to  $1/e$  of its initial value and produced a subjective measure of coarseness on this basis. However, Rosenfeld and Troy (1970a,b) later showed that autocorrelation is not a satisfactory measure of coarseness. In addition, autocorrelation is not a very good discriminator of isotropy in natural textures. Hence workers were quick to take up the co-occurrence matrix approach introduced by Haralick *et al.* in 1973: in fact, this approach not only replaced the use of autocorrelation but also became to a large degree during the 1970s, the “standard” approach to texture analysis.

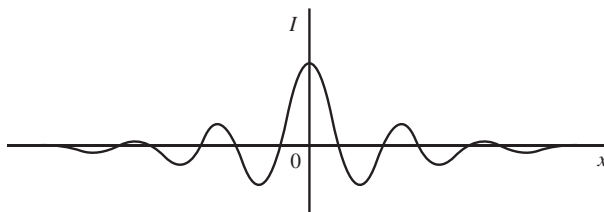


**FIGURE 7.2**

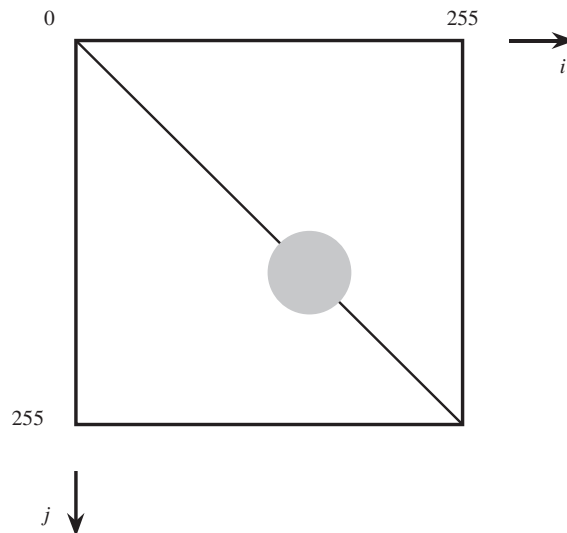
Use of autocorrelation function for texture analysis. This diagram shows the possible 1-D profile of the autocorrelation function for a piece of material in which the weave is subject to significant spatial variation: notice that the periodicity of the autocorrelation function is damped down over quite a short distance.



### 7.3 GRAYLEVEL CO-OCCURRENCE MATRICES

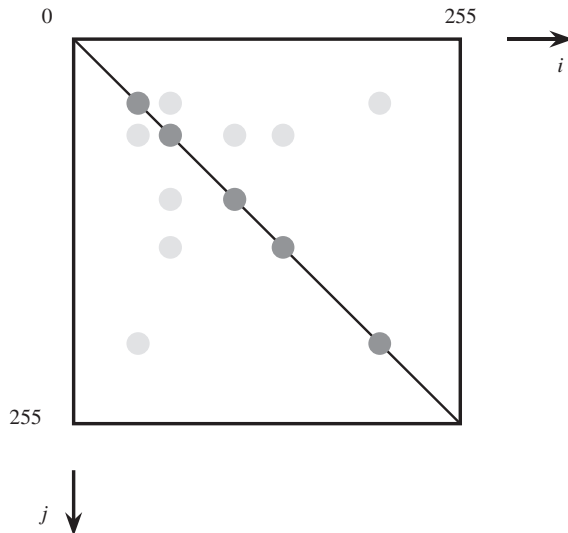
The graylevel co-occurrence matrix approach—also frequently called the spatial gray level dependence matrix (SGLDM) approach—is based on studies of the statistics of pixel intensity distributions. As hinted above with regard to the variance in pixel intensity values, single pixel statistics do not provide rich enough descriptions of textures for practical applications. Thus it is natural to consider the second-order statistics obtained by considering *pairs* of pixels in certain spatial relations to each other. Hence, co-occurrence matrices are used, which express the relative frequencies (or probabilities)  $P(i, j|d, \theta)$  with which two pixels having relative polar coordinates  $(d, \theta)$  appear with intensities  $i, j$ . The co-occurrence matrices provide raw numerical data on the texture, although these data must be condensed to relatively few numbers before they can be used to classify the texture. The early paper by Haralick *et al.* (1973) gave 14 such measures, and these were used successfully for classification of many types of material (including, for example, wood, corn, grass, and water). However, Connors and Harlow (1980a) found that only five of these measures were normally used, viz. “energy,” “entropy,” “correlation,” “local homogeneity,” and “inertia” (note that these names do not provide much indication of the modes of operation of the respective operators).

To obtain a more detailed idea of the operation of the technique, consider the co-occurrence matrix shown in Fig. 7.3. This corresponds to a nearly uniform grayscale image with superimposed Gaussian noise.



**FIGURE 7.3**

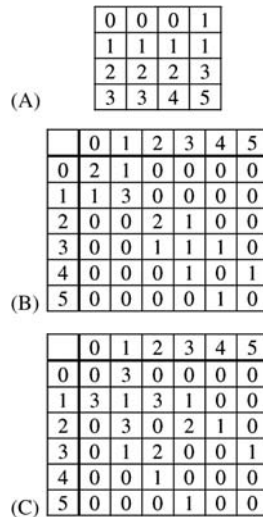
Co-occurrence matrix for a nearly uniform grayscale image with superimposed Gaussian noise. Here the intensity variation is taken to be almost continuous: normal convention is followed by making the  $j$  index increase downwards, as for a table of discrete values (cf. Fig. 7.4).

**FIGURE 7.4**

Co-occurrence matrix for an image with several distinct regions of nearly constant intensity. Again, the leading diagonal of the diagram is from the top left to the bottom right (cf. Figs. 7.2 and 7.5).

image containing a single region in which the pixel intensities are subject to an approximately Gaussian noise distribution, the attention being on pairs of pixels at a constant vector distance  $\mathbf{d} = (d, \theta)$  from each other. Next consider the co-occurrence matrix shown in Fig. 7.4, which corresponds to an almost noiseless image with several nearly uniform image regions. In this case, the two pixels in each pair may correspond either to the same image regions or to different ones, although if  $d$  is small, they will only correspond to adjacent image regions. Thus we have a set of  $N$  on-diagonal patches in the co-occurrence matrix but only a limited number  $L$  of the possible number  $M$  of off-diagonal patches linking them, where  $M = {}^N C_2$  and  $L \leq M$  (typically  $L$  will be of order  $N$  rather than  $N^2$ ). With textured images, if the texture is not too strong, it may be modeled as noise, and the  $N + L$  patches in the image will be larger but still not overlapping. However, in more complex cases the possibility of segmentation using the co-occurrence matrices will depend on the extent to which  $\mathbf{d}$  can be chosen to prevent the patches from overlapping. Since many textures are directional, careful choice of  $\theta$  will clearly help with this task, although the optimum value of  $d$  will depend on several other characteristics of the texture.

As a further illustration, we consider the small image shown in Fig. 7.5A. To produce the co-occurrence matrices for a given value of  $\mathbf{d}$ , we merely need to calculate the numbers of cases for which pixels a distance  $\mathbf{d}$  apart have intensity values  $i$  and  $j$ . Here, we content ourselves with the two cases  $\mathbf{d} = (1, 0)$  and  $\mathbf{d} = (1, \pi/2)$ . We thus obtain the matrices shown in Fig. 7.5B and C.

**FIGURE 7.5**

Co-occurrence matrices for a small image. (A) The original image; (B) the resulting co-occurrence matrix for  $\mathbf{d} = (1, 0)$ , and (C) the matrix for  $\mathbf{d} = (1, \pi/2)$ . Note that even in this simple case the matrices contain more data than the original image.

This simple example demonstrates that the amount of data in the matrices is liable to be many times more than in the original image—a situation that is exacerbated in more complex cases by the number of values of  $d$  and  $\theta$  that are required to accurately represent the texture. In addition, the number of gray levels will normally be closer to 256 than to 6, and the amount of matrix data varies as the square of this number. Finally, we should notice that the co-occurrence matrices merely provide a new representation—they do not themselves solve the recognition problem.

These factors mean that the gray scale has to be compressed into much a smaller set of values, and careful choice of specific sample  $d$ ,  $\theta$  values must be made: in most cases it is not at all obvious how such a choice should be made, and it is even more difficult to arrange for it to be made automatically. In addition, various functions of the matrix data must be tested before the texture can be properly characterized and classified.

These problems with the co-occurrence matrix approach have been tackled in many ways: just two are mentioned here. The first is to ignore the distinction between opposite directions in the image, thereby reducing storage by 50%. The second is to work with *differences* between gray levels; this amounts to performing a summation in the co-occurrence matrices along axes parallel to the main diagonal of the matrix. The result is a set of the *first-order difference* statistics. While these modifications have given some additional impetus to the approach, the 1980s saw a highly significant diversification of methods for

the analysis of textures. Of these, Laws' approach (1979, 1980a,b) is important in that it has led to other developments that provide a systematic, adaptive means of tackling texture analysis. This approach is covered in the following section.

## 7.4 LAWS' TEXTURE ENERGY APPROACH

In 1979 and 1980 Laws presented his novel texture energy approach to texture analysis (1979, 1980a,b). This involved the application of simple filters to digital images. The basic filters he used were common Gaussian, edge detector, and Laplacian-type filters, and were designed to highlight points of high "texture energy" in the image. By identifying these high-energy points, smoothing the various filtered images, and pooling the information from them, he was able to characterize textures highly efficiently. As remarked earlier, Laws' approach has strongly influenced much subsequent work, and it is therefore worth considering it here in some detail.

The Laws' masks are constructed by convolving together just three basic  $1 \times 3$  masks:

$$L3 = [1 \quad 2 \quad 1] \quad (7.1)$$

$$E3 = [-1 \quad 0 \quad 1] \quad (7.2)$$

$$S3 = [-1 \quad 2 \quad -1] \quad (7.3)$$

The initial letters of these masks indicate *Local* averaging, *Edge* detection, and *Spot* detection. In fact, these basic masks span the entire  $1 \times 3$  subspace and form a complete set. Similarly, the  $1 \times 5$  masks obtained by convolving pairs of these  $1 \times 3$  masks together form a complete set. Although in principle nine masks can be formed in this way, only five of them are distinct:

$$L5 = [1 \quad 4 \quad 6 \quad 4 \quad 1] \quad (7.4)$$

$$E5 = [-1 \quad -2 \quad 0 \quad 2 \quad 1] \quad (7.5)$$

$$S5 = [-1 \quad 0 \quad 2 \quad 0 \quad -1] \quad (7.6)$$

$$R5 = [1 \quad -4 \quad 6 \quad -4 \quad 1] \quad (7.7)$$

$$W5 = [-1 \quad 2 \quad 0 \quad -2 \quad 1] \quad (7.8)$$

(Here the initial letters are as before, with the addition of *Ripple* detection and *Wave* detection.) We can also use matrix multiplication to combine the  $1 \times 3$  and a similar set of  $3 \times 1$  masks to obtain nine  $3 \times 3$  masks—for example:

$$\begin{bmatrix} 1 \\ 2 \\ 1 \end{bmatrix} [-1 \quad 2 \quad -1] = \begin{bmatrix} -1 & 2 & -1 \\ -2 & 4 & -2 \\ -1 & 2 & -1 \end{bmatrix} \quad (7.9)$$

**Table 7.1** The Nine  $3 \times 3$  Laws Masks

<b>L3<sup>T</sup>L3</b>			<b>L3<sup>T</sup>E3</b>			<b>L3<sup>T</sup>S3</b>		
1	2	1	-1	0	1	-1	2	-1
2	4	2	-2	0	2	-2	4	-2
1	2	1	-1	0	1	-1	2	-1
<b>E3<sup>T</sup>L3</b>			<b>E3<sup>T</sup>E3</b>			<b>E3<sup>T</sup>S3</b>		
-1	-2	-1	1	0	-1	1	-2	1
0	0	0	0	0	0	0	0	0
1	2	1	-1	0	1	-1	2	-1
<b>S3<sup>T</sup>L3</b>			<b>S3<sup>T</sup>E3</b>			<b>S3<sup>T</sup>S3</b>		
-1	-2	-1	1	0	-1	1	-2	1
2	4	2	-2	0	2	-2	4	-2
-1	-2	-1	1	0	-1	1	-2	1

The resulting set of masks also forms a complete set (Table 7.1): note that two of these masks are identical to the Sobel operator masks. The corresponding  $5 \times 5$  masks are entirely similar but are not considered in detail here as all relevant principles are illustrated by the  $3 \times 3$  masks.

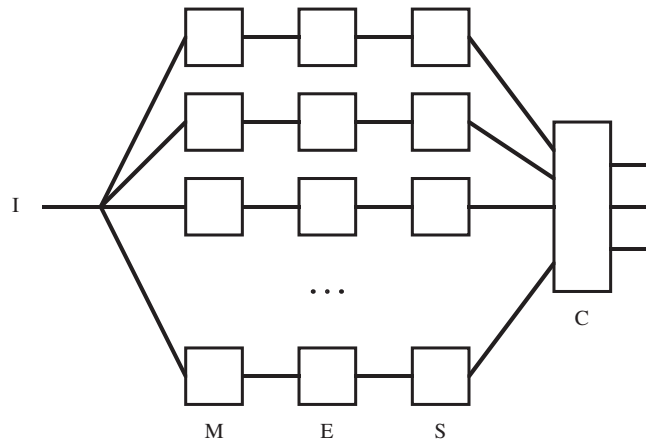
All such sets of masks include one whose components do not average to zero. Thus it is less useful for texture analysis since it will give results dependent more on image intensity than on texture. The remainder are sensitive to edge points, spots, lines, and combinations of these.

Having produced images that indicate local edginess, etc., the next stage is to deduce the local magnitudes of these quantities. These magnitudes are then smoothed over a fair-sized region rather greater than the basic filter mask size (e.g., Laws used a  $15 \times 15$  smoothing window after applying his  $3 \times 3$  masks): the effect of this is to smooth over the gaps between the texture edges and other microfeatures. At this point, the image has been transformed into a vector image, each component of which represents energy of a different type. While Laws (1980b) used both squared magnitudes and absolute magnitudes to estimate texture energy, the former corresponding to true energy and giving a better response, the latter are useful in requiring less computation:

$$E(l, m) = \sum_{i=l-p}^{l+p} \sum_{j=m-p}^{m+p} |F(i, j)| \quad (7.10)$$

$F(i, j)$  being the local magnitude of a typical microfeature, which is smoothed at a general scan position  $(l, m)$  in a  $(2p + 1) \times (2p + 1)$  window.

A further stage is required to combine the various energies in a number of different ways, providing several outputs that can be fed into a classifier to decide upon the particular type of texture at each pixel location (Fig. 7.6): if necessary, principal component analysis is used at this point to help select a suitable set of intermediate outputs.

**FIGURE 7.6**

Basic form for a Laws' texture classifier. Here *I* is the incoming image, *M* represents the microfeature calculation, *E* the energy calculation, *S* the smoothing, and *C* the final classification.

Laws' method resulted in excellent classification accuracy quoted at (for example) 87% compared with 72% for the co-occurrence matrix method, when applied to a composite texture image of grass, raffia, sand, wool, pigskin, leather, water, and wood (Laws, 1980b). He also found that the histogram equalization normally applied to images to eliminate first-order differences in texture field grayscale distributions gave little improvement in this case.

Research was undertaken by Pietikäinen *et al.* (1983) to determine whether the precise coefficients used in the Laws' masks are responsible for the performance of his method. They found that so long as the general forms of the masks were retained, performance did not deteriorate and could in some instances be improved. They were able to confirm that Laws' texture energy measures are more powerful than measures based on pairs of pixels (i.e., co-occurrence matrices).

## 7.5 ADE'S EIGENFILTER APPROACH

In 1983 Ade investigated the theory underlying the Laws' approach and developed a revised rationale in terms of eigenfilters. (At this point it is suggested that, before reading further, the reader may find it helpful to refer to [Section 14.5](#), where principal components analysis and eigenvalue problems are discussed.) He took all possible pairs of pixels within a  $3 \times 3$  window and characterized the image intensity data by a  $9 \times 9$  covariance matrix. He then determined the eigenvectors required to diagonalize this matrix. These correspond to filter masks similar to the Laws' masks, i.e., the use of these "eigenfilters" masks produces images that are principal

component images for the given texture. Furthermore, each eigenvalue gives that part of the variance of the original image that can be extracted by the corresponding filter. Essentially, the variances give an exhaustive description of a given texture in terms of the texture of the images from which the covariance matrix was originally derived. Clearly, the filters that give rise to low variances can be taken to be relatively unimportant for texture recognition.

It will be useful to illustrate the technique for a  $3 \times 3$  window. Here we follow Ade (1983) in numbering the pixels within a  $3 \times 3$  window in scan order:

1	2	3
4	5	6
7	8	9

This leads to a  $9 \times 9$  covariance matrix for describing relationships between pixel intensities within a  $3 \times 3$  window, as stated above. At this point we recall that we are describing a texture and assuming that its properties are not synchronous with the pixel tessellation, we would expect various coefficients of the covariance matrix  $\mathbf{C}$  to be equal: for example,  $C_{24}$  should equal  $C_{57}$ ; in addition,  $C_{57}$  must equal  $C_{75}$ . It is worth pursuing this matter, as a reduced number of parameters will lead to increased accuracy in determining the remaining ones. In fact, there are  ${}^9C_2 = 36$  ways of selecting pairs of pixels, but there are only 12 distinct spatial relationships between pixels if we disregard translations of whole pairs—or 13 if we include the null vector in the set (Table 7.2). Thus the covariance matrix (see Sections 14.1 and 14.5), whose components include the 13 parameters  $a$ – $m$ , takes the form:

$$\mathbf{C} = \begin{bmatrix} a & b & f & c & d & k & g & m & h \\ b & a & b & e & c & d & l & g & m \\ f & b & a & j & e & c & i & l & g \\ c & e & j & a & b & f & c & d & k \\ d & c & e & b & a & b & e & c & d \\ k & d & c & f & b & a & j & e & c \\ g & l & i & c & e & j & a & b & f \\ m & g & l & d & c & e & b & a & b \\ h & m & g & k & d & c & f & b & a \end{bmatrix} \quad (7.11)$$

$\mathbf{C}$  is symmetric; the eigenvalues of a real symmetric covariance matrix are real and positive, and the eigenvectors are mutually orthogonal (see Section 14.5).

**Table 7.2** Spatial Relationships Between Pixels in a  $3 \times 3$  Window

$a$	$b$	$c$	$d$	$e$	$f$	$g$	$h$	$i$	$j$	$k$	$l$	$m$
9	6	6	4	4	3	3	1	1	2	2	2	2

*This table shows the number of occurrences of the spatial relationships between pixels in a  $3 \times 3$  window. Note that  $a$  is the diagonal element of the covariance matrix  $\mathbf{C}$ , and that all others appear twice as many times in  $\mathbf{C}$  as indicated in the table.*

In addition, the eigenfilters thus produced reflect the proper structure of the texture being studied and are ideally suited to characterizing it. For example, for a texture with a prominent highly directional pattern, there will be one or more high-energy eigenvalues with eigenfilters having strong directionality in the corresponding direction.

---

## 7.6 APPRAISAL OF THE LAWS AND ADE APPROACHES

At this point, it will be worthwhile to compare the Laws and Ade approaches more carefully. In the Laws approach, standard filters are used, texture energy images are produced, and *then* principal component analysis may be applied to lead to recognition; whereas in the Ade approach, special filters (the eigenfilters) are applied, incorporating the results of principal component analysis, following which texture energy measures are calculated and a suitable number of these are applied for recognition.

The Ade approach is superior to the extent that it permits low-value energy components to be eliminated early on, thereby saving computation. For example, in Ade's application, the first five of the nine components contain 99.1% of the total texture energy, so the remainder can be ignored; in addition, it would appear that another two of the components containing 1.9% and 0.7% of the energy, respectively, could also be ignored, with little loss of recognition accuracy. However, in some applications textures could vary continually, and it may well be inadvisable to fine-tune a method to the particular data pertaining at any one time. For example, these remarks apply (1) to textiles, for which the degree of stretch will vary continuously during manufacture, (2) to raw food products such as beans, whose sizes will vary with the source of supply, and (3) to processed food products such as cakes, for which the crumbliness will vary with cooking temperature and water vapor content.

In 1986, Unser developed a more general version of the Ade technique that also covered the methods of Faugeras (1978), Granlund (1980), and Wermser and Liedtke (1982). This approach is not only performance optimized for texture classification but also optimized for discrimination between two textures by simultaneous diagonalization of two covariance matrices. The method was developed further by Unser and Eden (1989, 1990): this work makes a careful analysis of the use of nonlinear detectors. As a result, two levels of nonlinearity are employed, one immediately after the linear filters and designed (by employing a specific Gaussian texture model) to feed the smoothing stage with genuine variance or other suitable measures, and the other after the spatial smoothing stage to counteract the effect of the earlier filter, and aiming to provide a feature value that is in the same units as the input signal. In practical terms, this means having the capability for providing an root mean square (RMS) texture signal from each of the linear filter channels.



Overall, the originally intuitive Laws approach emerged during the 1980s as a serious alternative to the co-occurrence matrix approach. It is well to note that alternative methods that are potentially superior have also been devised; see, for example, the local rank correlation method of Harwood et al. (1985), and the forced-choice method of Vistnes (1989) for finding edges between different textures, which apparently has considerably better accuracy than the Laws approach. Vistnes's (1989) investigation concludes that the Laws approach is limited by (1) the small scale of the masks that can miss larger scale textural structures and (2) the fact that the texture energy smoothing operation blurs the texture feature values across the edge. The latter finding (or the even worse situation where a third class of texture appears to be located in the region of the border between two textures) has also been noted by Hsiao and Sawchuk (1989, 1990) who applied an improved technique for feature smoothing; they also used probabilistic relaxation for enforcing spatial organization on the resulting data.

---

## 7.7 CONCLUDING REMARKS

In this chapter we have seen the difficulties of analyzing textures: these arise from the potential and, in many cases, the frighteningly real complexities of textures—not least from the fact that their properties are often largely statistical in nature. The erstwhile widely used grayscale co-occurrence matrix approach has been seen to have distinct computational shortcomings. First, many co-occurrence matrices are in principle required (with different values of  $d$  and  $\theta$ ) in order to adequately describe a given texture; second, the co-occurrence matrices can be very large and, paradoxically, may hold more data than the images they are characterizing—especially if the range of grayscale values is large. In addition, many sets of co-occurrence matrices may be needed to allow for variation of the texture over the image and if necessary to initiate segmentation. Hence co-occurrence matrices need to be significantly compressed, although in most cases it is not at all obvious a priori how this should be achieved, and it is even more difficult to arrange for it to be carried out automatically. This probably explains why attention shifted during the 1980s to other approaches, including particularly Laws' technique and its variations (especially that of Ade). Other developments were fractal-based measures, Markov approaches, and the Gabor filter technique, although space has prevented a discussion of these methods here; see [Section 7.8](#) for further reading on these topics.

*Textures are recognized and segmented by humans with the same apparent ease as for plain objects. This chapter has shown that texture analysis needs to be sensitive to microstructures and then pulled into macrostructures—with PCA being a natural means of finding the optimum structure. The subject has great importance for new applications such as iris recognition.*

---

## 7.8 BIBLIOGRAPHICAL AND HISTORICAL NOTES

Early work on texture analysis was carried out by Haralick *et al.* (1973), and in 1976 Weska and Rosenfeld applied textural analysis to materials inspection. The area was reviewed by Zucker (1976a) and by Haralick (1979), and excellent accounts appear in the books by Ballard and Brown (1982) and Levine (1985).

At the end of the 1970s, the Laws technique (1979, 1980a,b) arrived upon the scene (which had up till then been dominated by the co-occurrence matrix approach) and led to the principal components approach of Ade (1983), which was further developed by Dewaele *et al.* (1988), Unser and Eden (1989, 1990), and others. The direction taken by Laws was particularly valuable as it showed how texture analysis could be implemented straightforwardly and in a manner consistent with real-time applications such as inspection.

The 1980s also saw other new developments, such as the fractal approach led by Pentland (1984) and a great amount of work on Markov random field models of texture. Here the work of Hansen and Elliott (1982) was very formative, although the names Cross, Derin, D. Geman, S. Geman, and Jain come up repeatedly in this context. Bajcsy and Liebermann (1976), Witkin (1981), and Kender (1983) pioneered the *shape from texture* concept, which has received considerable attention ever since. Later, much work appeared on the application of neural networks to texture analysis, for example, Greenhill and Davies (1993) and Patel *et al.* (1994). A number of reviews and useful comparative studies have been made, including Van Gool *et al.* (1985), Du Buf *et al.* (1990), Ohanian and Dubes (1992), and Reed and Du Buf (1993).

More recent developments include further work with automated visual inspection in mind (Davies, 2000a; Tsai and Huang, 2003; Ojala *et al.*, 2002; Manthalkar *et al.*, 2003; Pun and Lee, 2003), although several of these papers also cite medical, remote sensing, and other applications. Of these papers, the last three are specifically aimed at rotation invariant texture classification and the last one also aims at scale invariance. In previous years, there has not been quite this emphasis on rotation invariance, although it was by no means a new topic. Other work (Clerc and Mallat, 2002) was concerned with recovering shape from texture via a texture gradient equation, while Ma *et al.* (2003) were particularly concerned with person identification based on iris textures. Mirmehdi and Petrou (2000) described an in-depth investigation of color texture segmentation. In this context, the importance of “wavelets” as an increasingly used technique of texture analysis with interesting applications (such as human iris recognition) should be noted (e.g., Daugman, 1993, 2003). Wavelets are directional filters reminiscent of the Laws edges, bars, waves, and ripples, but have more rigorously defined shapes and envelopes, and are defined in multiresolution sets (Mallat, 1989).

Then, in a particularly exciting advance, Spence *et al.* (2004) managed to eliminate texture by using photometric stereo to find the underlying surface shape (or “bump map”), following which they were able to perform impressive

reconstructions, including texture, from a variety of viewpoints; McGunnigle and Chantler (2003) have shown that this sort of technique is also able to reveal hidden writing on textured surfaces, where only pen pressure marks have been made. Similarly, Pan et al. (2004) have shown how texture can be eliminated from ancient tablets (in particular, those made of lead and wood) to reveal clear images of the writing underneath.

### 7.8.1 MORE RECENT DEVELOPMENTS

Over the 2000s, the trend to scale and rotation invariant texture analysis mentioned above has continued, the paper by Janney and Geers (2010) describing an “invariant features of local textures” approach, using a strictly circular 1-D array of sampling positions around any given position. The method employs Haar wavelets and, as a result, is computationally efficient. It is applied at multiple scales in order to achieve scale invariance; in addition, intensity normalization is used to make the method illumination as well as scale and rotation invariant.

Two new books have recently been published on this rather specialist subject—Petrou and Sevilla (2006) and Mirmehdi *et al.* (2008). The former is a very sound textbook, starting from a low level and progressing through topics not covered in the present volume, such as fractals, Markov random fields, Gibbs distributions, Gabor functions, wavelets, and the Wigner distribution. The latter is an edited volume containing chapters by various researchers and providing much new information, as indicated by some of the more novel chapter titles: “TEXEMS: random texture representation and analysis,” “3D texture analysis,” “Texture for appearance models,” “From dynamic texture to dynamic shape and appearance models,” “Divide-and-texture: Hierarchical feature description,” “Practical implementation of the trace transform,” and “Face analysis using local binary patterns.”

# Intermediate-level vision

# 2

*In Part 2 we study intermediate-level image analysis, which is concerned with obtaining abstract information about images, starting with the images themselves: at this stage we are less interested in converting one image into another, as in the subject of image processing. In particular, transform methods will be used, which have been designed systematically for the purpose.*

*For the most part, the chapters in Part 2 result in abstract information on the positions and orientations of various image features: they do not aim to provide real-world data, a function that is left to Parts 3–5. Thus Part 2 may indicate that a circle exists in one part of an image: it is left to later parts to interpret this as a wheel and to find any defects it may have.*

This page intentionally left blank

# Binary shape analysis

# 8

Although binary images contain much less information than their gray-scale counterparts, they embody shape and size information that is highly relevant for object recognition. However, this information resides in a digital lattice of pixels, and this results in intricacies appearing in the geometry. This chapter resolves these problems and explores a number of important algorithms for processing shapes.

*Look out for:*

- the connectedness paradox and how it is resolved
- object labeling and how labeling conflicts are resolved
- problems related to measurement in binary images
- size filtering techniques
- the convex hull as a means of characterizing shape, and methods for determining it
- distance functions and how they are obtained using parallel and sequential algorithms
- the skeleton and how it is found by thinning: the crucial role played by the crossing number, both in determining the skeleton and in analyzing it
- simple measures for shape recognition, including circularity and aspect ratio
- more rigorous measures of shape, including moments and boundary descriptors.

In reality, this chapter almost exclusively covers area-based methods of shape analysis, leaving boundary-based procedures to [Chapter 9](#), Boundary Pattern Analysis—though circularity measures and boundary tracking are both covered. However, chapter boundaries cannot be completely exclusive, as any method requires “hooks” that have been laid down in a variety of places, and indeed, it is often valuable to meet a concept before finding out in detail how to put flesh on it.

Returning to the present chapter, it is interesting to note how intricate some of the algorithmic processes are: connectedness, in particular, pervades the whole subject of digital shape analysis and comes with a serious health warning.

## 8.1 INTRODUCTION

Over the past few decades 2-D shape analysis has provided the main means by which objects are recognized and located in digital images. Fundamentally, 2-D shape has been important because it uniquely characterizes many types of object, from keys to characters, from gaskets to spanners, and from fingerprints to

chromosomes, whereas in addition it can be represented by patterns in simple binary images. [Chapter 1](#), *Vision, The Challenge* showed how the template-matching approach leads to a combinatorial explosion even when fairly basic patterns are to be found, so preliminary analysis of images to find features constitutes a crucial stage in the process of efficient recognition and location. Thus, the capability for binary shape analysis is a very basic requirement for practical visual recognition systems.

In fact, 40 years of progress have provided an enormous range of shape analysis techniques and a correspondingly large range of applications. Clearly, it will be impossible to cover the whole field within the confines of a single chapter—so completeness will not even be attempted (the alternative of a catalogue of algorithms and methods, all of which are covered only in brief outline, is eschewed). At one level, the main topics covered are examples with their own intrinsic interest and practical application, and at another level they introduce matters of fundamental principle. Recurring themes are the central importance of connectedness for binary images; the contrasts between local and global operations on images and between different representations of image data; the need to optimize accuracy and computational efficiency; and the compatibility of algorithms and hardware. The chapter starts with a discussion of how connectedness is measured in binary images.

---

## 8.2 CONNECTEDNESS IN BINARY IMAGES

This section begins with the assumption that objects have been segmented, by thresholding or other procedures, into sets of 1s in a background of 0s (see [Chapters 2–4](#)). At this stage, it is important to realize that a second assumption is already being made implicitly—that it is easy to demarcate the boundaries between objects in binary images. However, in an image that is represented digitally in rectangular tessellation, a problem arises with the definition of connectedness. Consider the following dumbbell-shaped object, which is represented as an array of 1's (all unmarked image points are taken to have the binary value 0):

```

                1 1
               1 1 1 1
                1 1
                 1
                  1
                   1
                  1 1
                 1 1 1 1
                  1 1

```

At its center, this object has a segment of the form

$$\begin{array}{cc} 0 & 1 \\ 1 & 0 \end{array}$$

which separates two regions of background. At this point, diagonally adjacent 1s are regarded as being connected, whereas diagonally adjacent 0s are regarded as disconnected—a set of allocations which seems inconsistent. However, we can hardly accept a situation where a connected diagonal pair of 0s crosses a connected diagonal pair of 1s without causing a break in either case. Similarly, we cannot accept a situation in which a disconnected diagonal pair of 0s crosses a disconnected diagonal pair of 1s without there being a join in either case. Hence, a symmetrical definition of connectedness is not possible, and it is conventional to regard diagonal neighbors as connected only if they are foreground, i.e., the foreground is “8-connected,” and the background is “4-connected.” This convention is followed in the subsequent discussion.

---

## 8.3 OBJECT LABELING AND COUNTING

Now, we have a consistent definition of connectedness; we can unambiguously demarcate all objects in binary images and should be able to devise algorithms for labeling them uniquely and counting them. Labeling may be achieved by scanning the image sequentially until a 1 is encountered on the first object; a note is then made of the scanning position, and a “propagation” routine is initiated to label the whole of the object with a 1: as the original image space is already in use, a separate image space has to be allocated for labeling. Next, the scan is resumed, ignoring all points already labeled, until another object is found; this is labeled with a 2 in the separate image space. This procedure is continued until the whole image has been scanned, and all the objects have been labeled (Fig. 8.1). Implicit in this procedure is the possibility of propagating through a

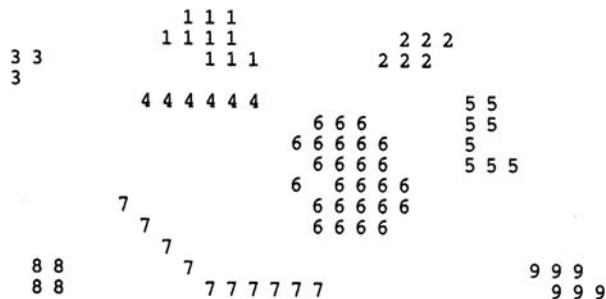


**FIGURE 8.1**

A process in which all binary objects are labeled.



connected object. Suppose at this stage that no method is available for limiting the field of the propagation routine, so that it has to scan the whole image space. Then, the propagation routine takes the form:

```
do {
  for all points in image
    if point is in an object
      and next to a propagating region labelled  $N$ 
      assign it the label  $N$ 
} until no further change;
```

(8.1)

the kernel of the do–until loop being expressed more explicitly as:

```
// original image in A-space; labels to be inserted in P-space
for all pixels in image do {
  if ((A0 == 1)
      && ((P1 == N)|(P2 == N)|(P3 == N)|(P4 == N)
          |(P5 == N)|(P6 == N)|(P7 == N)|(P8 == N)))
    P0 = N;
}
```

(8.2)

At this stage, a fairly simple type of algorithm for object labeling is obtained, as shown in [Table 8.1](#): the *for forward scan over image do {...}* notation denotes a *sequential* forward raster scan over the image.

Notice that the above object counting and labeling routine requires a *minimum* of  $2N + 1$  passes over the image space, and in practice, the number will be closer to  $NW/2$  where  $W$  is the average width of the objects: hence, the algorithm is inherently rather inefficient. This prompts us to consider how the number of passes over the image could be reduced to save computation. One possibility would be to scan forwards through the image, propagating new labels through objects as they are discovered. Although this would work mostly straightforwardly with convex objects, problems would be encountered with objects possessing concavities—e.g., “U” shapes—as different parts of the same object would end with different labels, and also means would have to be devised for coping with “collisions” of labels (e.g., the largest local label could be propagated through the remainder of the object: see [Fig. 8.2](#)). Then, inconsistencies could be resolved by a reverse scan through the image. However, this procedure will not resolve all problems that can arise, as in the case of more complex (e.g., spiral) objects. In such cases, a general parallel propagation, repeatedly applied until no further labeling occurs, might be preferable—though as we have seen, such a process is inherently rather computation intensive. However, it is implemented very conveniently on certain types of parallel processor, such as single instruction stream, multiple data stream (SIMD) machines.

Ultimately, the least computationally intensive procedures for propagation involve a different approach: objects and parts of objects are labeled on a *single* sequential pass through the image, at the same time noting which labels coexist on objects. Then, the labels are sorted separately, in a stage of abstract information processing, to determine how the initially rather ad hoc labels should

**Table 8.1** A Simple Algorithm for Object Labeling

---

```

// start with binary image containing objects in A-space
// clear label space
for all pixels in image do { P0 = 0; }
// start with no objects
N = 0;
/* look for objects using a sequential scan and propagate labels through them*/
do { // search for an unlabelled object
    found = false;
    for forward scan over image do {
        if ( (A0 == 1) && (P0 == 0) && not found) {
            N = N + 1;
            P0 = N;
            found = true;
        }
    }
    if (found) // label the object just found
        do {
            finished = true;
            for all pixels in image do {
                if ( (A0 == 1) && (P0 == 0)
                    && ( (P1 == N) || (P2 == N) || (P3 == N) || (P4 == N)
                        || (P5 == N) || (P6 == N) || (P7 == N) || (P8 == N) ) ) {
                    P0 = N;
                    finished = false;
                }
            }
        } until finished;
    } until not found; // i.e. no (more) objects
// N is the number of objects found and labelled

```

---

```

          1 1 1
          1 1 1   2 2
            3   1 1 1   2 2
          3 3 3   1 1 1   2 2 2 2
        3 3 3 3 1 1 1 2 2 2 2 2
      3 3 3 3 3 1 1 2 2 2 2 2 2
    3 3 3 3 3 3 3 3 3 3 3 3 3 3
  3 3 3 3 3 3 3 3 3 3 3 3 3 3 3
3 3 3 3 3 3 3 3 3 3 3 3 3 3 3
3 3 3 3 3 3 3 3 3 3 3 3 3 3
  3 3 3 3 3 3 3 3 3 3 3 3
    3 3 3   3 3 3 3 3
      4 4   3   3 3 3 3
        4 4   3   3 3 3
          4 4 4 4 4 4 4
            4 4 4 4 4

```

**FIGURE 8.2**

Labeling U-shaped objects: a problem that arises in labeling certain types of object if a simple propagation algorithm is used. Some provision has to be made to accept “collisions” of labels although the confusion can be removed by a subsequent stage of processing.

**Table 8.2** The Improved Algorithm for Object Labeling

---

```

// clear label space
for all pixels in image do { P0 = 0; }
// start with no objects
N = 0;
// clear the table that is to hold the label coexistence data
for (i = 1; i <= Nmax; i++)
    for (j = 1; j <= Nmax; j++)
        coexist[i][j] = false;
// label objects in a single sequential scan
for forward scan over image do {
    if (A0 == 1) {
    }
        if ( (P2 == 0) && (P3 == 0) && (P4 == 0) && (P5 == 0) ) {
            N = N + 1;
            P0 = N;
        }
        else {
            P0 = max(P2, P3, P4, P5);
            // now note which labels coexist in objects
            coexist[P0][P2] = true;
            coexist[P0][P3] = true;
            coexist[P0][P4] = true;
            coexist[P0][P5] = true;
        }
    }
}
analyse the coexist table and decide ideal labelling scheme;
relabel image if necessary;

```

---

be interpreted. Finally, the objects are relabeled appropriately in a second pass over the image (in fact, this latter pass is sometimes unnecessary, as the image data are merely labeled in an overcomplex manner and what is needed is simply a key to interpret them). The improved labeling algorithm now takes the form shown in Table 8.2. Clearly, this algorithm with its single sequential scan is intrinsically far more efficient than the previous one, although the presence of particular dedicated hardware or a suitable SIMD processor might alter the situation and justify the use of alternative procedures.

It will be clear that minor amendments to the above algorithms permit the areas and perimeters of objects to be determined: thus, objects may be labeled by their areas or perimeters instead of by numbers representing their order of appearance in the image. More important, the availability of propagation routines means that objects can be considered in turn in their entirety—if necessary by transferring them individually to separate image spaces or storage areas ready for unencumbered independent analysis. Evidently, if objects appear in individual binary spaces, maximum and minimum spatial coordinates are trivially measurable, centroids can readily be found and more detailed calculations of moments (see below) and other parameters can easily be undertaken.

### 8.3.1 SOLVING THE LABELING PROBLEM IN A MORE COMPLEX CASE

In this section, we add substance to the all too facile statement at the end of Table 8.2—“analyze coexist table and decide ideal labeling scheme.” First, we have to make the task nontrivial by providing a suitable example. Fig. 8.3 shows an example image, in which sequential labeling has been carried out in line with the algorithm of Table 8.2. However, one variation has been adopted—of using a minimum rather than a maximum labeling convention, so that the values are in general slightly closer to the eventual ideal labels. (This also serves to demonstrate that there is not just one way of designing a suitable labeling algorithm.) The algorithm itself indicates that the coexist table should now appear as in Table 8.3. However, the whole process of calculating ideal labels can be made more efficient by inserting numbers instead of ticks, and also adding the right numbers along the leading diagonal, as in Table 8.4; for the same reason, the numbers below the leading diagonal, which are technically redundant, are retained here.

The next step is to minimize the entries along the individual rows of the table, as in Table 8.5. Then, we minimize along the individual columns (Table 8.6). Then, we minimize along rows again (Table 8.7). This process is iterated to completion, which has already happened here after three stages of minimization. We can now read off the final result from the leading diagonal. Note that a further stage of computation is needed to make the resulting labels consecutive integers, starting with unity. However, the procedure needed to achieve this is much more basic and does not need to manipulate a 2-D table of data: this will be left as a simple programming task for the reader.

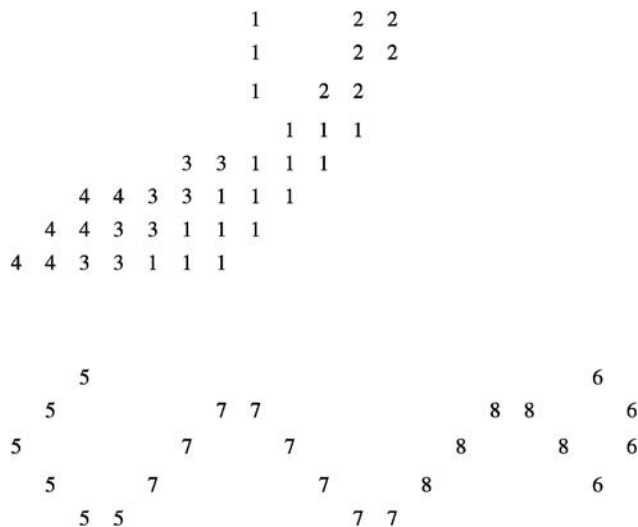


**FIGURE 8.3**

Solving the labeling problem in a more complex case.

**Table 8.3** Coexist Table for the Image of Fig. 8.3

	1	2	3	4	5	6	7	8
1		✓	✓					
2	✓							
3	✓			✓				
4			✓					
5							✓	
6								✓
7					✓			✓
8						✓	✓	

The ticks correspond to clashes of labels.

**Table 8.4** Coexist Table with Additional Numerical Information

	1	2	3	4	5	6	7	8
1	1	1	1					
2	1	2						
3	1		3	3				
4			3	4				
5					5		5	
6						6		6
7					5		7	7
8						6	7	8

This coexist table is an enhanced version of Table 8.3. Technically, the numbers along, and below, the leading diagonal are redundant, but nevertheless they speed up the subsequent computation.

**Table 8.5** Coexist Table Redrawn with Minimized Rows

	1	2	3	4	5	6	7	8
1	1	1	1					
2	1	1						
3	1		1	1				
4			3	3				
5					5		5	
6						6		6
7					5		5	5
8						6	6	6

At this stage, the table is no longer symmetric.

**Table 8.6** Coexist Table Redrawn Again With Minimized Columns

	1	2	3	4	5	6	7	8
1	1	1	1					
2	1	1						
3	1		1	1				
4			1	1				
5					5		5	
6						6		5
7					5		5	5
8						6	5	5

**Table 8.7** Coexist Table Redrawn Yet Again With Minimized Rows

	1	2	3	4	5	6	7	8
1	1	1	1					
2	1	1						
3	1		1	1				
4			1	1				
5					5		5	
6						5		5
7					5		5	5
8						5	5	5

*At this stage, the table is in its final form and is once again symmetric.*

At this point, some comment on the nature of the process described above will be appropriate. What has happened is that the original image data has effectively been condensed into the minimum space required to express the labels—namely just one entry per original clash. This explains why the table retains the 2-D format of the original image: lower dimensionality would not permit the image topology to be represented properly. It also explains why minimization has to be carried out, to completion, in two orthogonal directions. On the other hand, the particular implementation, including both above- and below-diagonal elements, is able to minimize computational overheads and finalize the operation in remarkably few iterations.

Finally, it might be felt that too much attention has been devoted to finding connected components of binary images. In fact, this is a highly important topic in practical applications such as industrial inspection, where it is crucial to locate all the objects unambiguously before they can individually be identified and scrutinized. In addition, Fig. 8.3 makes clear that it is not only U-shaped objects that give problems but also those that have shape subtleties—as happens at the left of the upper object in this figure.

## 8.4 SIZE FILTERING

Before proceeding to study size filtering, we draw attention to the fact that the 8-connected and 4-connected definitions of connectedness lead to the following measures of distance (or “metrics”) that apply to pairs of pixels, labeled  $i$  and  $j$ , in a digital lattice:

$$d_8 = \max(|x_i - x_j|, |y_i - y_j|) \quad (8.3)$$

and

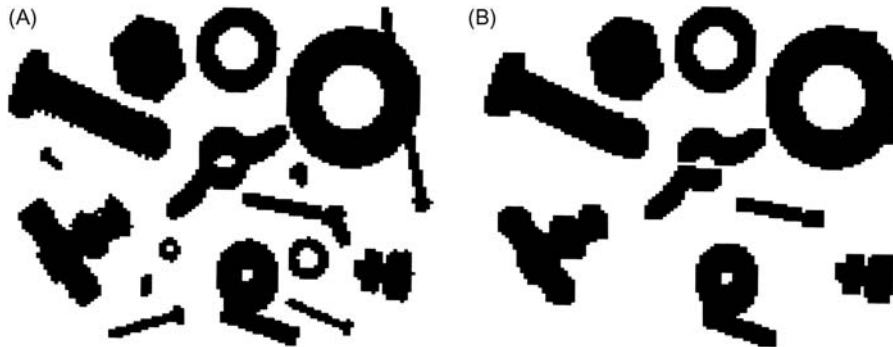
$$d_4 = |x_i - x_j| + |y_i - y_j| \quad (8.4)$$

Although the use of the  $d_4$  and  $d_8$  metrics is bound to lead to certain inaccuracies, it is useful to see what can be achieved with the use of local operations in binary images. This section studies how simple size filtering operations can be carried out, using merely local ( $3 \times 3$ ) operations. The basic idea is that small objects may be eliminated by applying a series of shrink operations. In fact,  $N$ -shrink operations will eliminate an object (or those parts of an object) that are  $2N$  or fewer pixels across their narrowest dimension. Of course, this process shrinks *all* the objects in the image, but in principle a subsequent  $N$  expand operations will restore the larger objects to their former size.

If complete elimination of small objects is required but perfect retention of larger objects, this will, however, not be achieved by the above procedure, as in many cases the larger objects will be distorted or fragmented by these operations (Fig. 8.4). To recover the larger objects in their *original* form, the proper approach is to use the shrunken versions as “seeds” from which to grow the originals via a propagation process. The algorithm of Table 8.8 is able to achieve this.

Having seen how to remove whole (connected) objects that are everywhere narrower than a specified width, it is possible to devise algorithms for removing any subset of objects that are characterized by a given range of widths: large objects may be filtered out by first removing lesser sized objects and then performing a logical masking operation with the original image, whereas intermediate-sized objects may be filtered out by removing a larger subset and then restoring small objects that have previously been stored in a separate image space. Ultimately, all these schemes depend on the availability of the propagation technique, which in turn depends on the internal connectedness of individual objects.

Finally, note that expand operations followed by shrink operations may be useful for joining nearby objects, filling in holes, and so on. Numerous refinements and additions to these simple techniques are possible. A particularly interesting one is to separate the silhouettes of touching objects such as chocolates by a shrinking operation: this then permits them to be counted reliably (Fig. 8.5).

**FIGURE 8.4**

The effect of a simple size filtering procedure. When size filtering is attempted by a set of  $N$  shrink and  $N$  expand operations, larger objects are restored approximately to their original size but their shapes frequently become distorted or even fragmented. In this example, (B) shows the effect of applying two shrink and then two expand operations to the image in (A).

**Table 8.8** Algorithm for Recovering Original Forms of Shrunken Objects

---

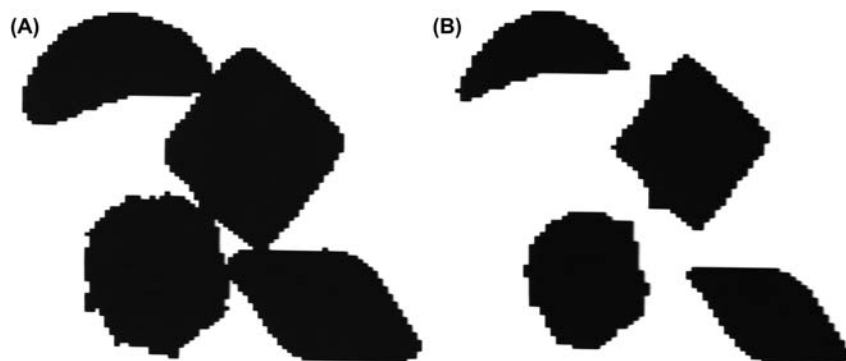
```

// save original image
for all pixels in image do { C0 = A0; }
// now shrink the original objects N times
for (i = 1; i <= N; i++) {
  for all pixels in image do {
    sigma = A1 + A2 + A3 + A4 + A5 + A6 + A7 + A8;
    if (sigma < 8) B0 = 0; else B0 = A0;
  }
  for all pixels in image do {A0 = B0; }
}
// next propagate the shrunken objects using the original image
do {
  finished = true;
  for all pixels in image do {
    sigma = A1 + A2 + A3 + A4 + A5 + A6 + A7 + A8;
    if ( (A0 == 0) && (sigma > 0) && (C0 == 1) ) {
      A0 = 1;
      finished = false;
    }
  }
} until finished;

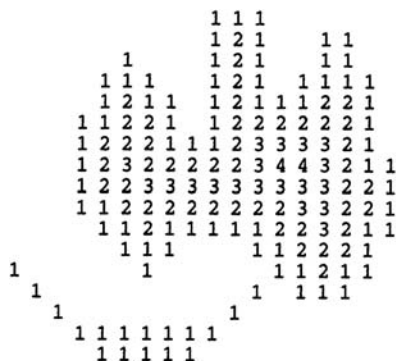
```

---



**FIGURE 8.5**

Separation of touching objects by shrink operations. Here, objects (chocolates) in (A) are shrunk (B) in order to separate them so that they may be counted reliably.

**FIGURE 8.6**

The distance function of a binary shape: the value at every pixel is the distance (in the  $d_8$  metric) from the background.

## 8.5 DISTANCE FUNCTIONS AND THEIR USES

The distance function of an object is a very simple and useful concept in shape analysis. Essentially, each pixel in the object is numbered according to its distance from the background. As usual, background pixels are taken as 0s; then edge pixels are counted as 1s; object pixels next to 1s become 2s; next to those are the 3s; and so on throughout all the object pixels (Fig. 8.6).

The parallel algorithm of Table 8.9 finds the distance function of binary objects by propagation. Note that this algorithm performs a final pass in which nothing happens; this is inevitable if we are to be certain that the process will run to completion.

**Table 8.9** A Parallel Algorithm for Propagating Distance Functions

---

```

// Start with binary image containing objects in A-space
for all pixels in image do { Q0 = A0*255; }
N = 0;
do {
  finished = true;
  for all pixels in image do {
    if ( (Q0 == 255) // in object and no answer yet
        && ( (Q1 == N) || (Q2 == N) || (Q3 == N) || (Q4 == N)
            || (Q5 == N) || (Q6 == N) || (Q7 == N) || (Q8 == N) ) ) {
      // next to an N
      Q0 = N + 1;
      finished = false; // some action has been taken
    }
  }
  N = N + 1;
} until finished;

```

---

It is possible to perform the propagation of a distance function with far fewer operations if sequential processing is used. In 1-D, the basic idea would be to build up ramps within objects using a routine like the following:

```

for all pixels in a row of pixels do {Q0 = A0*255;}
for forward scan over row of pixels do
  if (Q0 > Q5 + 1) Q0 = Q5 + 1;

```

Next, we need to insist on double-sided ramps within objects, both horizontally and vertically. This is elegantly achieved using two sequential operations, one being a normal forward raster scan and the other being a reverse raster scan:

```

for all pixels in image do {Q0 = A0*255;}
for forward scan over image do {
  minplusone = min(Q2, Q3, Q4, Q5) + 1;
  if (Q0 > minplusone) Q0 = minplusone;
}
for reverse scan over image do {
  minplusone = min(Q6, Q7, Q8, Q1) + 1;
  if (Q0 > minplusone) Q0 = minplusone;
}

```

(8.5)

Note the compact notation being used to distinguish between forward and reverse raster scans over the image: *for forward scan over image do {...}* denotes a forward raster scan, whereas *for reverse scan over image do {...}* denotes a reverse raster scan. A more succinct version of this algorithm is the following:

```

for all pixels in image do {Q0 = A0*255;}
for forward scan over image do {
  Q0 = min(Q0 - 1, Q2, Q3, Q4, Q5) + 1;
}
for reverse scan over image do {
  Q0 = min(Q0 - 1, Q6, Q7, Q8, Q1) + 1;
}

```

(8.6)

Before moving on, it will be useful to emphasize the value of sequential processing for propagating distance functions. In fact, when this sequential algorithm is run on a serial computer, it will be  $O(N)$  times *faster* than the corresponding parallel algorithm running on a serial computer, but  $O(N)$  times *slower* than the same parallel algorithm running on a parallel computer, for an  $N \times N$  image. Although this statement is specific to propagation of distance functions, similar statements can be made about a good many other operations. (Note that parallel processing is achieved very efficiently using parallel computers known SIMD machines.)

### 8.5.1 LOCAL MAXIMA AND DATA COMPRESSION

An interesting application of distance functions is that of data compression. To achieve this, operations are carried out to locate those pixels which are local maxima of the distance function (Fig. 8.7), as storing these pixel values and positions permits the original image to be regenerated by a process of downwards propagation (see below). Note that although finding the local maxima of the distance function provides the basic information for data compression, the actual compression occurs only when the data are stored as a list of points rather than in the original picture format. In order to locate the local maxima, the following parallel routine may be employed:

```
for all pixels in image do {
  maximum = max(Q1, Q2, Q3, Q4, Q5, Q6, Q7, Q8);
  if ((Q0 > 0) && (Q0 ≥ maximum)) B0 = 1; else B0 = 0;
}
```

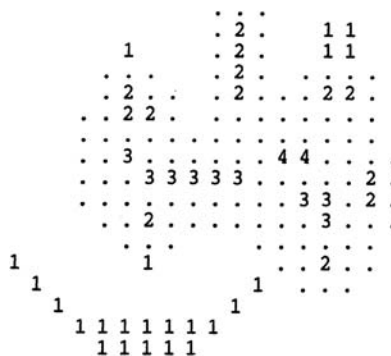
(8.7)


FIGURE 8.7

Local maxima of the distance function of the shape shown in Fig. 8.6, the remainder of the shape being indicated by dots and the background being blank. Notice that the local maxima group themselves into clusters each containing points of equal distance function value, whereas clusters of different values are clearly separated.

Alternatively, the compressed data can be transferred to a single image space:

```
for all pixels in image do {
  maximum = max(Q1, Q2, Q3, Q4, Q5, Q6, Q7, Q8);
  if ((Q0 > 0) && (Q0 ≥ maximum)) P0 = Q0; else P0 = 0;
}
```

(8.8)

Note that the local maxima that are retained for the purpose of data compression are not absolute maxima but are maximal in the sense of not being adjacent to larger values. If this were not so, insufficient numbers of points would be retained for completely regenerating the original object. As a result of this, it is found that the absolute maxima group themselves into clusters of connected points, each cluster having a common distance value and being separated from points of different distance values (Fig. 8.7). Thus, the set of local maxima of an object is not a connected subset. This fact has an important bearing on skeleton formation (see below).

Having seen how data compression may be performed by finding local maxima of the distance function, it is relevant to consider a parallel downwards propagation algorithm (Table 8.10) for recovering the shapes of objects from an image into which the values of the local maxima have been inserted. Note again that if it can be assumed that at most  $N$  passes are needed to propagate through objects of known maximum width, then the algorithm becomes simply:

```
for (i = 1; i ≤ N; i++)
  for all pixels in image do {
    Q0 = max(Q0 + 1, Q1, Q2, Q3, Q4, Q5, Q6, Q7, Q8) - 1;
  }
```

(8.9)

**Table 8.10** A Parallel Algorithm for Recovering Objects From Local Maxima of the Distance Functions

---

```
// assume that input image is in Q-space, and that non-maximum values have
// value 0
do {
  finished = true;
  for all pixels in image do {
    maxminusone = max(Q0 + 1, Q1, Q2, Q3, Q4, Q5, Q6, Q7, Q8) - 1;
    if (Q0 < maxminusone) {
      Q0 = maxminusone;
      finished = false; // some action has been taken
    }
  }
} until finished;
```

---

---

## 8.6 SKELETONS AND THINNING

The skeleton is a powerful analog concept which may be employed for the analysis and description of shapes in binary images. A skeleton may be defined as a connected set of medial lines along the limbs of a figure: for example, in the case of thick hand-drawn characters, the skeleton may be supposed to be the path actually traveled by the pen. In fact, the basic idea of the skeleton is that of eliminating redundant information while retaining only the topological information concerning the shape and structure of the object that can help with recognition. In the case of hand-drawn characters, the thickness of the limbs is taken to be irrelevant: it may be constant and therefore carry no useful information, or it may vary randomly and again be of no value for recognition (Fig. 1.2).

The definition presented above leads to the idea of finding the loci of the centers of maximal discs inserted within the object boundary. First, suppose the image space to be a continuum. Then, the discs are circles, and their centers form loci which may be modeled very conveniently when object boundaries are approximated by linear segments. In fact, sections of the loci fall into three categories:

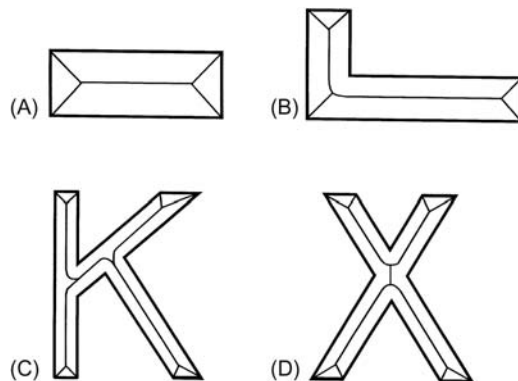
1. they may be angle bisectors, i.e., lines which bisect corner angles and reach right up to the apexes of corners;
2. they may be lines that lie half-way between boundary lines;
3. they may be parabolas which are equidistant from lines and from the nearest points of other lines—namely, corners where two lines join.

Clearly, Categories 1 and 2 are special forms of a more general case.

These ideas lead to unique skeletons for objects with linear boundaries, and the concepts are easily generalizable to curved shapes. In fact, this approach tends to give rather more detail than is commonly required, even the most obtuse corner having a skeleton line going into its apex (Fig. 8.8). Hence, a thresholding scheme is often employed such that skeleton lines only reach into corners having a specified minimum degree of sharpness.

We now have to see how the skeleton concept will work in a digital lattice. Here, we are presented with an immediate choice: which metric should we employ? If we select the Euclidean metric (i.e., lattice distance is measured as the Euclidean distance between pairs of pixels), there may be a considerable computational load. If we select the  $d_8$  metric, we will immediately lose accuracy but the computational requirements should be more modest (we do not here consider the  $d_4$  metric, as we are dealing with the shapes of foreground objects). In what follows we concentrate on the  $d_8$  metric.

At this stage, some thought shows that the application of maximal discs in order to locate skeleton lines amounts essentially to finding the positions of local maxima of the distance function. Unfortunately, as seen in the previous section, the set of local maxima does not form a connected graph within a given object, nor is it necessarily composed of thin lines, and indeed it may in places be 2 pixels

**FIGURE 8.8**

Four shapes whose boundaries consist entirely of straight line segments. The idealized skeletons go right to the apex of each corner, however obtuse. In certain parts of shapes (B), (C) and (D), the skeleton segments are parts of parabolas rather than straight lines. As a result, the detailed shape of the skeleton (or the approximations produced by most algorithms operating in discrete images) is not exactly what might initially be expected or what would be preferred in certain applications.

wide. Thus, problems arise in trying to use this approach to obtain a connected unit-width skeleton that can conveniently be used to represent the shape of the object. We shall return to this approach again below. Meanwhile, however, we pursue an alternative idea—that of thinning.

Thinning is perhaps the simplest approach to skeletonization. It may be defined as the process of systematically stripping away the outermost layers of a figure until only a connected unit-width skeleton remains (see e.g., Fig. 8.9). A number of algorithms are available to implement this process, with varying degrees of accuracy, and we discuss below how a specified level of precision can be achieved and tested for. First, however, it is necessary to discuss the mechanism by which points on the boundary of a figure may validly be removed in thinning algorithms.

### 8.6.1 CROSSING NUMBER

The exact mechanism for examining points to determine whether they can be removed in a thinning algorithm must now be considered. This may be decided by reference to the *crossing number*  $\chi$  (chi) for the 8 pixels around the outside of a particular  $3 \times 3$  neighborhood.  $\chi$  is defined as the total number of 0-to-1 and 1-to-0 transitions on going once round the outside of the neighborhood: this number is in fact twice the number of potential connections joining the remainder of the object to the center of the neighborhood (Fig. 8.10). Unfortunately, the formula for  $\chi$  is made more complex by the 8-connectedness

**FIGURE 8.9**

Typical result of a thinning algorithm operating in a discrete lattice.

0 0 0	0 0 0	1 0 0	1 0 0	1 0 1	1 0 0	1 0 1
0 1 0	0 1 1	0 1 1	0 1 0	0 1 0	0 1 0	0 1 0
0 0 0	1 1 1	1 1 1	0 1 0	1 1 1	1 0 1	1 0 1
0	2	4	4	6	6	8

**FIGURE 8.10**

Some examples of the crossing number values associated with given pixel neighborhood configurations (0, background; 1, foreground).

criterion. To express this efficiently, we use the C++ “(int)” construct to convert logical outcomes true and false to integer outcomes 1 and 0. Basically, we would expect

$$\begin{aligned}
 \text{badchi} = & (\text{int})(A1 \neq A2) + (\text{int})(A2 \neq A3) + (\text{int})(A3 \neq A4) \\
 & + (\text{int})(A4 \neq A5) + (\text{int})(A5 \neq A6) + (\text{int})(A6 \neq A7) \\
 & + (\text{int})(A7 \neq A8) + (\text{int})(A8 \neq A1)
 \end{aligned} \tag{8.10}$$

However, this is incorrect because of the 8-connectedness criterion. For example, in the case

$$\begin{array}{ccc}
 0 & 1 & 0 \\
 0 & 1 & 1 \\
 1 & 1 & 1
 \end{array}$$

the formula gives the value 4 for  $\chi$  instead of 2. The reason is that the isolated 0 in the top right-hand corner does not prevent the adjacent 1s from being joined. It is therefore tempting to use the modified formula:

$$\begin{aligned}
 \text{wrongchi} = & (\text{int})(A1 \neq A3) + (\text{int})(A3 \neq A5) + (\text{int})(A5 \neq A7) \\
 & + (\text{int})(A7 \neq A1);
 \end{aligned} \tag{8.11}$$

However, this too is wrong, as in the case

$$\begin{array}{ccc} 0 & 0 & 1 \\ 0 & 1 & 0 \\ 1 & 1 & 1 \end{array}$$

it gives the answer 2 instead of 4. It is therefore necessary to add four extra terms to deal with isolated 1s in the corners:

$$\begin{aligned} \text{chi} = & (\text{int})(A1 \neq A3) + (\text{int})(A3 \neq A5) + (\text{int})(A5 \neq A7) \\ & + (\text{int})(A7 \neq A1) \\ & + 2 * ((\text{int})((A2 > A1) \&\& (A2 > A3)) + (\text{int})((A4 > A3) \&\& (A4 > A5))) \\ & + (\text{int})((A6 > A5) \&\& (A6 > A7)) + (\text{int})((A8 > A7) \&\& (A8 > A1)); \end{aligned} \quad (8.12)$$

This (now correct) formula for crossing number gives values 0, 2, 4, 6, or 8 in different cases (Fig. 8.10). The rule for removing points during thinning is that points may only be removed if they are at those positions on the boundary of an object where  $\chi$  is 2: when  $\chi$  is greater than 2, the point *must* be retained, as it forms a vital connected point between two parts of the object; in addition, when it is 0, it must be retained as removing it would create a hole.

Finally, there is one more condition that must be fulfilled before a point can be removed during thinning—that the sum  $\sigma$  (sigma) of the eight pixel values around the outside of the  $3 \times 3$  neighborhood (see Chapter 2: Images and Imaging Operations) must not be equal to 1. The reason for this is to preserve line ends, as in the following cases:

$$\begin{array}{ccc} 0 & 0 & 0 \\ 0 & 1 & 0 \\ 0 & 1 & 0 \end{array} \quad \begin{array}{ccc} 0 & 0 & 0 \\ 0 & 1 & 0 \\ 0 & 0 & 1 \end{array}$$

Clearly, if line ends are eroded as thinning proceeds, the final skeleton will not represent the shape of an object (including the relative dimensions of its limbs) at all accurately (however, it is possible that we might sometimes wish to shrink an object while preserving connectedness, in which case this extra condition need not be implemented). Having covered these basics, we are now in a position to devise complete thinning algorithms.

## 8.6.2 PARALLEL AND SEQUENTIAL IMPLEMENTATIONS OF THINNING

Thinning is “essentially sequential” in that it is easiest to ensure that connectedness is maintained by arranging that only one point may be removed at a time. As indicated above, this is achieved by checking before removing a point that it has a crossing number of 2. Now imagine applying the “obvious” sequential algorithm of Table 8.11 to a binary image. Assuming a normal forward raster scan, the result of this process is to produce a highly distorted skeleton, consisting



**Table 8.11** An “Obvious” Sequential Thinning Algorithm

---

```

do {
    finished = true;
    for forward scan over image do {
        sigma = A1 + A2 + A3 + A4 + A5 + A6 + A7 + A8;
        chi = (int) (A1 != A3) + (int) (A3 != A5) + (int) (A5 != A7)
            + (int) (A7 != A1)
            + 2*((int) ((A2 > A1) && (A2 > A3)) + (int) ((A4 > A3) && (A4 > A5))
            + (int) ((A6 > A5) && (A6 > A7)) + (int) ((A8 > A7) && (A8 > A1)));
        if ((A0 == 1) && (chi == 2) && (sigma != 1)) {
            A0 = 0;
            finished = false; // some action has been taken
        }
    }
} until finished;

```

---

of lines along the right-hand and bottom edges of objects. It may now be seen that the  $\chi = 2$  condition is necessary but not sufficient, as it says nothing about the order in which points are removed. To produce a skeleton that is unbiased, giving a set of truly medial lines, it is necessary to remove points as evenly as possible around the object boundary. A scheme that helps with this involves a novel processing sequence: mark edge points on the first pass over an image; on the second pass, strip points sequentially as in the above algorithm, *but only where they have already been marked*; then mark a new set of edge points; then perform another stripping pass; then repeat this marking and stripping sequence until no further change occurs. An early algorithm working on this principle is that of Beun (1973).

Although the novel sequential thinning algorithm described above can be used to produce a reasonable skeleton, it would be far better if the stripping action could be performed symmetrically around the object, thereby removing any possible skeletal bias. In this respect, a parallel algorithm should have a distinct advantage. However, parallel algorithms result in several points being removed at once: this means that lines 2 pixels wide will disappear (as masks operating in a  $3 \times 3$  neighborhood cannot “see” enough of the object to judge whether a point may validly be removed or not), and as a result, shapes can become disconnected. The general principle for avoiding this problem is to strip points lying on different parts of the boundary in different passes, so that there is no risk of causing breaks. In fact, there is a very large number of ways of achieving this, by applying different masks and conditions to characterize different parts of the boundary. If boundaries were always convex, the problem would no doubt be reduced; however, boundaries can be very convoluted and are subject to quantization noise, so the problem is a complex one. With so many potential solutions to the problem, we concentrate here on one that can conveniently be analyzed and which gives acceptable results.

The method discussed is that of removing north, south, east, and west points cyclically until thinning is complete. North points are defined as the following:

$$\begin{array}{ccc} \times & 0 & \times \\ \times & 1 & \times \\ \times & 1 & \times \end{array}$$

where  $\times$  means either a 0 or a 1: south, east, and west points are defined similarly. It is easy to show that all north points for which  $\chi=2$  and  $\sigma \neq 1$  may be removed in parallel without any risk of causing a break in the skeleton—and similarly for south, east, and west points. Thus, a possible format for a parallel thinning algorithm in rectangular tessellation is the following:

```
do {
  strip appropriate north points;
  strip appropriate south points;
  strip appropriate east points;
  strip appropriate west points;
} until no further change;
```

(8.13)

where the basic parallel routine for stripping “appropriate” north points is:

```
for all pixels in image do {
  sigma = A1 + A2 + A3 + A4 + A5 + A6 + A7 + A8;
  chi = (int)(A1 != A3) + (int)(A3 != A5) + (int)(A5 != A7)
        + (int)(A7 != A1)
        + 2 * ((int)((A2 > A1) && (A2 > A3)) + (int)((A4 > A3) && (A4 > A5))
        + (int)((A6 > A5) && (A6 > A7)) + (int)((A8 > A7) && (A8 > A1)));
  if ((A3 == 0) && (A0 == 1) && (A7 == 1) //north point
      && (chi == 2) && (sigma != 1))
    B0 = 0;
  else B0 = A0;
}
```

(8.14)

(but extra code needs to be inserted to detect whether any changes have been made in a given pass over the image).

Algorithms of the above type can be highly effective, although their design tends to be rather intuitive and ad hoc. In a survey made by the author in 1981 (Davies and Plummer, 1981), a great many such algorithms exhibited problems. Ignoring cases where the algorithm design was insufficiently rigorous to maintain connectedness, four other problems were evident:

1. the problem of skeletal bias;
2. the problem of eliminating skeletal lines along certain limbs;
3. the problem of introducing “noise spurs”;
4. the problem of slow speed of operation.

In fact, problems 2 and 3 are opposites in many ways: if an algorithm is designed to suppress noise spurs, it is liable to eliminate skeletal lines in some circumstances; contrariwise, if an algorithm is designed never to eliminate

skeletal lines, it is unlikely to be able to suppress noise spurs. This situation arises as the masks and conditions for performing thinning are intuitive and ad hoc, and therefore have no basis for discriminating between valid and invalid skeletal lines: ultimately, this is because it is difficult to build overt global models of reality into purely local operators. In a similar way, algorithms that proceed with caution, i.e., which do not remove object points in the fear of making an error or causing bias, tend to be slower in operation than they might otherwise be. Again, it is difficult to design algorithms that can make correct global decisions rapidly via intuitively designed local operators. Hence, a totally different approach is needed if solving one of the above problems is not to cause difficulties with the others. Such an alternative approach is discussed in the next section.

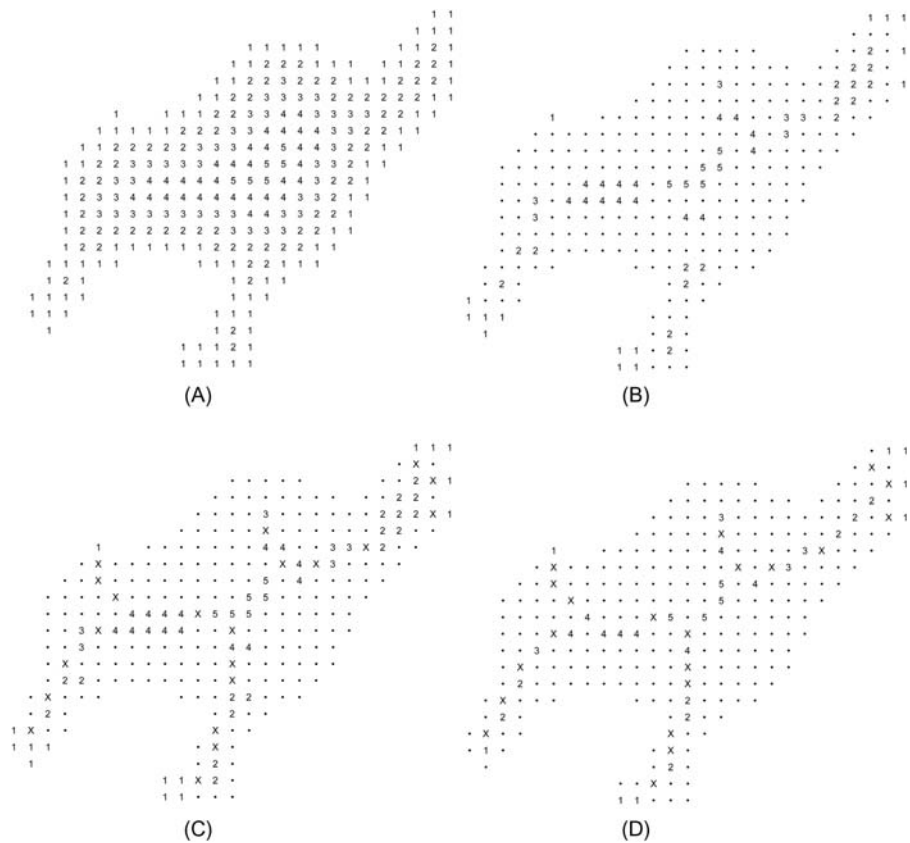
### 8.6.3 GUIDED THINNING

This section returns to the ideas of [Section 8.5.1](#), where it was found that the local maxima of the distance function do not form an ideal skeleton because they appear in clusters and are not connected. In addition, the clusters are often two pixels wide. On the plus side, the clusters are accurately in the correct positions and should therefore not be subject to skeletal bias. Hence, an ideal skeleton should result if (1) the clusters could be reconnected appropriately and (2) the resulting structure could be reduced to unit width—though, of course, a unit width skeleton can only be perfectly unbiased where the object is an odd number of pixels wide.

A simple means of reconnecting the clusters is to use them to guide a conventional thinning algorithm (see [Section 8.6.2](#)). As a first stage, thinning is allowed to proceed normally but with the proviso that no cluster points may be removed. This gives a connected graph which is in certain places 2 pixels wide. Then, a routine is applied to strip the graph down to unit width. At this stage an unbiased skeleton (within 1/2 pixel) should result. The main problem here is the presence of noise spurs. The opportunity now exists to eliminate these systematically by applying suitable global rules. A simple rule is that of eliminating lines on the skeletal graph that terminate in a local maximum of value (say) 1 (or, better, stripping them back to the next local maximum), as such a local maximum corresponds to fairly trivial detail on the boundary of the object. Thus, the level of detail that is ignored can be programmed into the system (Davies and Plummer, 1981). The whole guided thinning process is shown in [Fig. 8.11](#).

### 8.6.4 A COMMENT ON THE NATURE OF THE SKELETON

At the beginning of [Section 8.6](#), the case of character recognition was taken as an example, and it was stated that the skeleton may be supposed to be the path traveled by the pen in drawing out the character. However, in one important respect, this is not valid. The reason is seen both in the analog reasoning and from the results of thinning algorithms. Take the case of a letter K. The vertical limb on

**FIGURE 8.11**

Results of a guided thinning algorithm: (A) distance function on the original shape; (B) set of local maxima; (C) set of local maxima now connected by a simple thinning algorithm; (D) final thinned skeleton. The effect of removing noise spurs systematically, by cutting limbs terminating in a 1 back to the next local maximum, is easily discernible from the result in (D): the general shape of the object is not perturbed by this process.

the left of the skeleton will theoretically consist of two linear segments joined by two parabolic segments leading into the junction (Fig. 8.8). This limb will only become straight if a higher level model is used to constrain the result.

### 8.6.5 SKELETON NODE ANALYSIS

Skeleton node analysis may be carried out very simply with the aid of the crossing number concept. Points in the middle of a skeletal line have a crossing number of 4; points at the end of a line have crossing number 2; points at skeletal “T”

junctions have a crossing number of 6; and points at skeletal “X” junctions have a crossing number of 8. However, there is a situation to beware of—places which look like a “+” junction:

$$\begin{array}{ccc} 0 & 1 & 0 \\ 1 & 1 & 1 \\ 0 & 1 & 0 \end{array}$$

In such places, the crossing number is actually 0 (see formula), although the pattern is definitely that of a cross. At first, the situation seems to be that there is insufficient resolution in a  $3 \times 3$  neighborhood to identify a “+” cross, the best option being to look for this particular pattern of 0s and 1s and use a more sophisticated construct than the  $3 \times 3$  crossing number to check whether or not a cross is present. The problem is that of distinguishing between two situations such as:

$$\begin{array}{ccc} 0 & 0 & 0 & 0 & 0 & & 0 & 0 & 1 & 0 & 0 \\ 0 & 0 & 1 & 0 & 0 & & 1 & 0 & 1 & 0 & 0 \\ 0 & 1 & 1 & 1 & 0 & \text{and} & 1 & 1 & 1 & 1 & 1 \\ 0 & 0 & 1 & 0 & 0 & & 0 & 0 & 1 & 0 & 0 \\ 0 & 0 & 0 & 0 & 0 & & 0 & 0 & 0 & 1 & 0 \end{array}$$

However, further analysis shows that the first of these two cases would be thinned down to a dot (or a short bar), so that if a “+” node appears on the final skeleton (as in the second case), it actually signifies that a cross is present despite the contrary value of  $\chi$ . Davies and Celano (1993) have shown that the proper measure to use in such cases is the *modified* crossing number  $\chi_{\text{skel}} = 2\sigma$ , this crossing number being different from  $\chi$  because it is required not to test whether points can be eliminated from the skeleton, but to ascertain the meaning of points that are at that stage *known* to lie on the final skeleton. Note that  $\chi_{\text{skel}}$  can have values as high as 16—it is not restricted to the range 0 to 8!

Finally, note that sometimes insufficient resolution really is a problem, in that a cross with a shallow crossing angle appears as two “T” junctions:

$$\begin{array}{cccccccc} 0 & 0 & 0 & 0 & 0 & 0 & 0 & 1 \\ 1 & 1 & 1 & 0 & 0 & 1 & 1 & 0 \\ 0 & 0 & 0 & 1 & 1 & 0 & 0 & 0 \\ 0 & 1 & 1 & 0 & 0 & 1 & 1 & 1 \\ 1 & 0 & 0 & 0 & 0 & 0 & 0 & 0 \end{array}$$

Clearly, resolution makes it impossible to recognize an asterisk or more complex figure from its crossing number, within a  $3 \times 3$  neighborhood. Probably, the best solution is to label junctions tentatively, then to consider all the junction labels in the image, and to analyze whether a particular local combination of junctions should be reinterpreted—e.g., two “T” junctions may be deduced to form a cross. This is especially important in view of the distortions that appear on a skeleton in the region of a junction (see [Section 8.6.4](#)).

### 8.6.6 APPLICATION OF SKELETONS FOR SHAPE RECOGNITION

Shape analysis may be carried out simply and conveniently by analysis of skeleton shapes and dimensions. Clearly, study of the nodes of a skeleton (points for which there are other than two skeletal neighbors) can lead to the classification of simple shapes but not, for example, discrimination of all block capitals from each other. Many classification schemes exist which can complete the analysis, in terms of limb lengths and positions, and methods for achieving this are touched on in later chapters.

A similar situation exists for analysis of the shapes of chromosomes, which take the form of a cross or a “V.” For small industrial components, more detailed shape analysis is called for; this can still be approached with the skeleton technique, by examination of distance function values along the lines of the skeleton. In general, shape analysis using the skeleton proceeds by examination in turn of nodes, limb lengths and orientations, and distance function values, until the required level of characterization is obtained.

The particular importance of the skeleton as an aid in the analysis of connected shapes is not only that it is invariant under translations and rotations but also that it embodies what is for many purposes a highly convenient representation of the figure which (with the distance function values) essentially carries all the original information. If the original shape of an object can be deduced exactly from a representation, this is generally a good sign as it means that it is not merely an ad hoc descriptor of shape but that considerable reliance may be placed on it (compare other methods such as the circularity measure—see [Section 8.7](#)).

---

## 8.7 OTHER MEASURES FOR SHAPE RECOGNITION

There are many simple tests of shape that can be made to confirm the identity of objects or to check for items such as defects. These include measurements of product area and perimeter, length of maximum dimension, moments relative to the centroid, number and area of holes, area and dimensions of the convex hull (see below) and enclosing rectangle, number of sharp corners, number of intersections with a check circle and angles between intersections ([Fig. 8.12](#)), and numbers and types of skeleton nodes.

The list would not be complete without a mention of the widely used shape measure  $C = \text{areal/perimeter}^2$ . This quantity is often called “circularity” or “compactness”, as it has a maximum value of  $1/4\pi$  for a circle, decreases as shapes become more irregular, and approaches zero for long narrow objects: alternatively, its reciprocal is sometimes used, being called “complexity” as it increases in size as shapes become more complex. Note that both measures are dimensionless so that they are independent of size and are therefore sensitive only to the shape of an object. Other dimensionless measures of this type include rectangularity and aspect ratio.

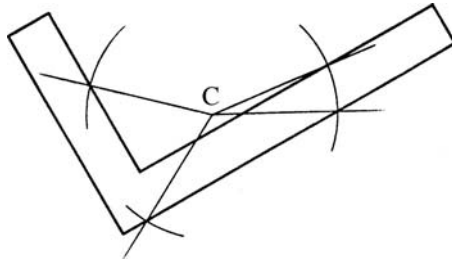


**FIGURE 8.12**

Rapid product inspection by polar checking.

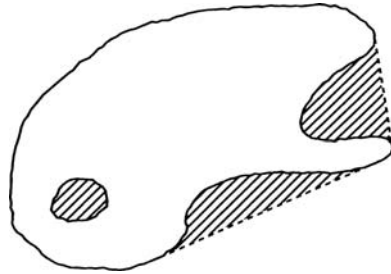
All these measures have the property of characterizing a shape but not of describing it uniquely. Thus, it is easy to see that there are in general many different shapes having the same values of parameters such as circularity. Hence, these rather ad hoc measures are on the whole less valuable than approaches such as skeletonization (Section 8.6) or moments (see below) that can be used to represent and reproduce a shape to any required degree of precision. Nevertheless, rigorous checking of even one measured number to high precision often permits a machined part to be identified positively.

The use of moments for shape analysis was mentioned above: these are widely used and should be covered in more detail. In fact, moment approximations provide a rigorous means of describing 2-D shapes and take the form of series expansions of the type:

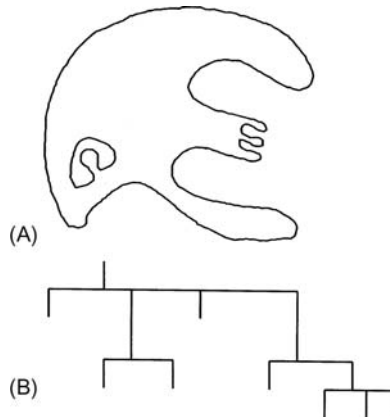
$$M_{pq} = \sum_x \sum_y x^p y^q f(x, y) \quad (8.15)$$

for a picture function  $f(x, y)$ ; such a series may be curtailed when the approximation is sufficiently accurate. By referring axes to the centroid of the shape, moments can be constructed that are position-invariant: they can also be normalized so that they are invariant under rotation and change of scale (Hu, 1962; see also Wong and Hall, 1978). The main value of using moment descriptors is that in certain applications the number of parameters may be made small without significant loss of precision—although the number required may not be clear without tests being made on a range of relevant shapes. Moments can prove particularly valuable in describing shapes such as cams and other fairly round objects, although they have also been used in a variety of other applications including aeroplane silhouette recognition (Dudani et al., 1977).

The convex hull was also mentioned above and has also been used as the basis for sophisticated, complete descriptions of shapes. The *convex hull* is defined as the smallest convex shape that contains the original shape (it may be envisaged as the shape contained by an elastic band placed around the original shape). The *convex deficiency* is defined as the shape that has to be added to a given shape to create the convex hull (Fig. 8.13). The convex hull may be used as

**FIGURE 8.13**

Convex hull and convex deficiency. The convex hull is the shape enclosed on placing an elastic band around an object. The shaded portion is the convex deficiency that is added to the shape to create the convex hull.

**FIGURE 8.14**

A simple shape and its concavity tree. The shape in (A) has been analyzed by repeated formation of convex hulls and convex deficiencies until all the constituent regions are convex (see text). The tree representing the entire process as shown in (B): at each node, the branch on the left is the convex hull and the branches on the right are convex deficiencies.

a simple approximation providing a rapid indication of the extent of an object. A fuller description of the shape of an object may be obtained by means of *concavity trees*: here, the convex hull of an object is first obtained with its convex deficiencies, then the convex hulls and deficiencies of the convex deficiencies are found, then the convex hulls and deficiencies of these convex deficiencies—and so on until all the derived shapes are convex, or until an adequate approximation to the original shape is obtained. Thus, a tree is formed which can be used for systematic shape analysis and recognition (Fig. 8.14). We shall not dwell on this



approach beyond noting its inherent utility and that at its core is the need for a reliable means of determining the convex hull of a shape.

A simple strategy for obtaining the convex hull is to repeatedly fill in the center pixel of all neighborhoods that exhibit a concavity, including each of the following:

$$\begin{array}{cccc} 1 & 1 & 1 & 0 & 1 & 1 \\ 1 & 0 & 0 & 1 & 0 & 0 \\ 0 & 0 & 0 & 0 & 0 & 0 \end{array}$$

until no further change occurs. In fact, the shapes obtained by the above approach are larger than ideal convex hulls and approximate to octagonal (or degenerate octagonal) shapes. Hence, more complex algorithms are required to generate convex hulls, a useful approach involving the use boundary tracking to search for positions on the boundary that have common tangent lines.

---

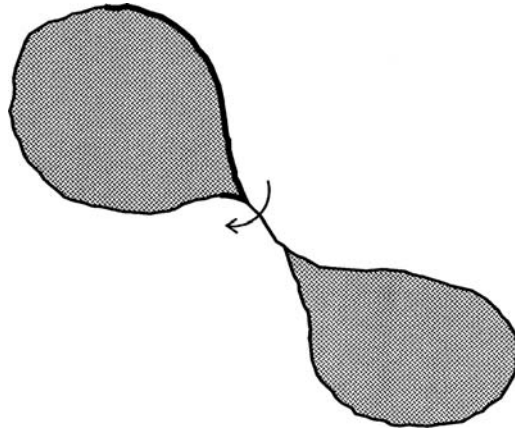
## 8.8 BOUNDARY TRACKING PROCEDURES

The preceding sections have described methods of analyzing shape on the basis of body representations of such as skeletons and moments. However, an important approach has so far been omitted—the use of boundary pattern analysis. This approach has the potential advantage of requiring considerably reduced computation, as the number of pixels to be examined is equal to the number of pixels on the boundary of any object rather than the much larger number of pixels within the boundary. Before proper use can be made of boundary pattern analysis techniques, means must be found for tracking systematically around the boundaries of all the objects in an image: in addition, care must be taken not to ignore any holes that are present or any objects within holes.

In one sense, the problem has been analyzed already, in that the object labeling algorithm of [Section 8.3](#) systematically visits and propagates through all objects in the image. All that is required now is some means of tracking round object boundaries, once they have been encountered. Quite clearly, it will be useful to mark in a separate image space all points that have been tracked: alternatively, an object boundary image may be constructed and the tracking performed in this space, all tracked points being eliminated as they are passed.

In the latter procedure, objects having unit width in certain places may become disconnected. Hence, we ignore this approach and adopt the previous one. There is still a problem when objects have unit-width sections, as these can cause badly designed tracking algorithms to choose a wrong path, going back around the previous section instead of on to the next ([Fig. 8.15](#)). To avoid this circumstance, it is best to adopt the following strategy:

1. track round each boundary, keeping to the left path consistently;
2. stop the tracking procedure only when passing through the starting point in the original direction (or passing through the first two points in the same order).

**FIGURE 8.15**

A problem with an oversimple boundary tracking algorithm: the boundary-tracking procedure takes a short-cut across a unit-width boundary segment instead of continuing and keeping to the left path at all times.

**Table 8.12** Basic Procedure for Tracking Around a Single Object

```
do {
    // find direction to move next
    start with current tracking direction;
    reverse it;
    do {
        rotate tracking direction clockwise
    } until the next 1 is met on outer pixels of 3 × 3 neighbourhood;
    record this as new current direction;
    move one pixel along this direction;
    increment boundary index;
    store current position in boundary list;
} until (position == original position) && (direction == original
direction)
```

Apart from necessary initialization at the start, a suitable tracking procedure is given in [Table 8.12](#).

Having seen how to track around the boundaries of objects in binary images, we are now in a position to embark on boundary pattern analysis. This is done in [Chapter 9](#), Boundary Pattern Analysis.

## 8.9 CONCLUDING REMARKS

This chapter has concentrated on rather traditional methods of performing image analysis—using image processing techniques. This has led naturally to area representations of objects, including for example moment and convex hull-based

schemes, although the skeleton approach appeared as a rather special case in that it converts objects into graphical structures. An alternative schema is to represent shapes by their boundary patterns, after applying suitable tracking algorithms: this latter approach is considered in the following chapter. Meanwhile, connectedness has been an underlying theme in the present chapter, objects being separated from each other by regions of background, thereby permitting objects to be considered and characterized individually. Connectedness has been seen to involve rather more intricate computations than might have been expected, and this necessitates great care in the design of algorithms: this must partly explain why after so many years, new thinning algorithms are still being developed (e.g., Kwok, 1989; Choy et al., 1995) (ultimately, these complexities arise because global properties of images are being computed by purely local means).

Although it will turn out that boundary pattern analysis is in certain ways more attractive than region pattern analysis, this comparison cannot be completely divorced from considerations of the hardware the algorithms have to run on. In this respect, note that many of the algorithms of this chapter can be performed efficiently on SIMD processors, which have one processing element per pixel, whereas boundary pattern analysis will be seen to match better the capabilities of more conventional serial computers.

*Shape analysis can be attempted by boundary or region representations. Both are deeply affected by connectedness and related metric issues for a digital lattice of pixels. This chapter has shown that these issues are only solved by carefully incorporating global knowledge alongside local information—e.g., by use of distance transforms.*

---

## 8.10 BIBLIOGRAPHICAL AND HISTORICAL NOTES

The development of shape analysis techniques has been particularly extensive: hence, only a brief perusal of the history is attempted here. The all-important theory of connectedness and the related concept of adjacency in digital images was developed largely by Rosenfeld (see e.g., Rosenfeld, 1970). The connectedness concept led to the idea of a distance function in a digital picture (Rosenfeld and Pfaltz, 1966, 1968), and the related skeleton concept (Pfaltz and Rosenfeld, 1967). However, the basic idea of a skeleton dates from the classic work by Blum (1967)—see also Blum and Nagel (1978). Important work on thinning has been carried out by Arcelli et al. (1975, 1981; Arcelli and di Baja, 1985) and parallels work by Davies and Plummer (1981). The latter paper demonstrates possibilities for limb pruning, and a rigorous method for testing the results of *any* thinning algorithm, however generated, and in particular for detecting skeletal bias. More recently, Arcelli and Ramella (1995) have reconsidered the problem of skeletons in gray-scale images. There have also been important developments to generalize

the distance function concept and to make distance functions uniform and isotropic: see for example Huttenlocher et al. (1993). The design of a modified crossing number  $\chi_{\text{skel}}$  for the analysis of skeletal shape dates from the same period: as pointed out in Section 8.6.5,  $\chi_{\text{skel}}$  is different from  $\chi$  as it evaluates the *remaining* (i.e., skeletal) points rather than points that *might* be eliminated from the skeleton (Davies and Celano, 1993).

Sklansky has carried out much work on convexity and convex hull determination (see e.g., Sklansky, 1970; Sklansky et al., 1976), whereas Batchelor (1979) developed concavity trees for shape description. Haralick et al. (1987) have generalized the underlying mathematical (morphological) concepts, including the case of gray-scale analysis. Use of invariant moments for pattern recognition dates from the two seminal papers by Hu (1961, 1962). Pavlidis has drawn attention to the importance of unambiguous (“asymptotic”) shape representation schemes (Pavlidis, 1980)—as distinct from ad hoc sets of shape measures.

In the 2000s, skeletons have maintained their interest and utility, becoming if anything more precise by reference to exact analog shapes (Kégl and Krzyżak, 2002), and giving rise to the concept of a shock graph, which characterizes the result of the much earlier grass-fire transformation (Blum, 1967) more rigorously (Giblin and Kimia, 2003). Wavelet transforms have also been used to implement skeletons more accurately in the discrete domain (Tang and You, 2003). In contrast, shape matching has been carried out using self-similarity analysis coupled with tree representation—an approach that has been especially valuable for tracking articulated object shapes, including human profiles and hand motions (Geiger et al., 2003). It is interesting to see graphical analysis of skeletonized hand-written character shapes performed taking account of catastrophe theory (Chakravarty and Kompella, 2003): this is relevant because (1) critical points—where points of inflection exist—can be deformed into pairs of points each corresponding to a curvature maximum plus a minimum; (2) crossing of  $t$ 's can be actual or noncrossing; and (3) loops can turn into cusps or corners (many other possibilities also exist). The point is that methods are needed for mapping between *variations* of shapes rather than making snap judgments as to classification (this corresponds to the difference between scientific understanding of process and ad hoc engineering).

### 8.10.1 MORE RECENT DEVELOPMENTS

More recently, increased attention has been devoted to processing skeletons and using them for object matching and classification. Bai and Latecki (2008) discuss how to prune skeletons meaningfully, by ensuring that endpoints of skeleton branches correspond to visual parts of objects (such as all the legs of a horse). Once this has been achieved, it should be possible to match objects (such as horses) in spite of any articulations or contour deformations that may have taken place. The method is found to permit much more efficient matching and to be

more resistant to partial occlusion: this is because meaningfulness is built into the final skeleton, whereas minor intricacies (which may originally have been due to noise forming tiny holes in the object) will have been eliminated. This approach is potentially useful for tracking, stereo matching, and database matching. Ward and Hamarneh (2010) attend to the order in which skeleton branches should be pruned. They report on several pruning algorithms and quantify their performance in terms of denoizing, classification, and within-class skeleton similarity measures. The work is important because of the well-known fact that the medial axis transform is unstable with respect to minor perturbations on the boundary of a shape: this means that before skeletons can be used reliably, noise spurs need to be pruned so that they correspond to the underlying shapes.

---

## 8.11 PROBLEMS

1. Write the full C++ routine required to sort the lists of labels, to be inserted at the end of the algorithm of [Table 8.2](#).
2. Show that, as stated in [Section 8.6.2](#) for a parallel thinning algorithm, all north points may be removed in parallel without any risk of causing a break in the skeleton.
3. Describe methods for locating, labeling, and counting objects in binary images. You should consider whether methods based on propagation from a “seed” pixel, or those based on progressively shrinking a skeleton to a point, would provide the more efficient means for achieving the stated aims. Give examples for objects of various shapes.
4.
  - a. Give a simple one-pass algorithm for labeling the objects appearing in a binary image, making clear the role played by connectedness. Give examples showing how this basic algorithm goes wrong with real objects: illustrate your answer with clear pixel diagrams, which show the numbers of labels that can appear on objects of different shapes.
  - b. Show how a table-orientated approach can be used to eliminate multiple labels in objects. Make clear how the table is set up and what numbers have to be inserted into it. Are the number of iterations needed to analyze the table similar to the number that would be needed in a multipass labeling algorithm taking place entirely within the original image? Consider how the *real* gain in using a table to analyze the labels arises.
5.
  - a. Using the following notation for a  $3 \times 3$  window:

A4	A3	A2
A5	A0	A1
A6	A7	A8

work out the effect of the following algorithm on a binary image containing small foreground objects of various shapes:

```
do {
  for all pixels in image do {
    sum = (int)(A1 + A3 == 2) + (int)(A3 + A5 == 2)
          + (int)(A5 + A7 == 2) + (int)(A7 + A1 == 2);
    if (sum > 0) B0 = 1; else B0 = A0;
  }
  for all pixels in image do {A0 = B0;}
} until no further change;
```

- b. Show in detail how to implement the *do ... until no further change* function in this algorithm.
6. a. Give a simple algorithm operating in a  $3 \times 3$  window for generating a *rectangular* convex hull around each object in a binary image. Include in your algorithm any necessary code for implementing the required *do ... until no further change* function.
    - b. A more sophisticated algorithm for finding accurate convex hulls is to be designed. Explain why this would employ a boundary tracking procedure. State the general strategy of an algorithm for tracking around the boundaries of objects in binary images and write a program for implementing it.
    - c. Suggest a strategy for designing the complete convex hull algorithm and indicate how rapidly you would expect it to operate, in terms of the size of the image.
  7. a. Explain the meaning of the term *distance function*. Give examples of the distance functions of simple shapes, including that shown in Fig. 8.P1.
    - b. Rapid image transmission is to be performed by sending only the coordinates and values of the local maxima of the distance functions. Give a complete algorithm for finding the local maxima of the distance

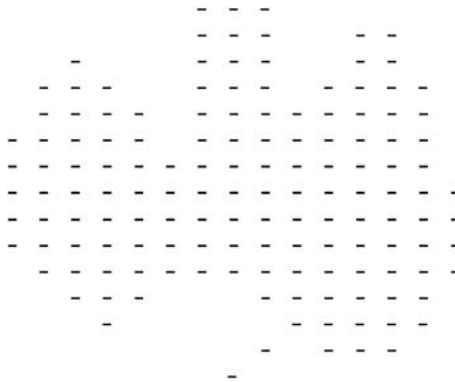


**FIGURE 8.P1**

Binary picture object for shape analysis tests.

- functions in an image and devise a further algorithm for reconstructing the original binary image.
- c. Discuss which of the following sets of data would give more compressed versions of the binary picture object shown in Fig. 8.P1:
    - i. the list of local maxima coordinates and values;
    - ii. a list of the coordinates of the boundary points of the object;
    - iii. a list consisting of one point on the boundary and the relative directions (each expressed as a 3-bit code) between each *pair* of boundary points on tracking round the boundary.
  8. a. What is the *distance function* of a binary image? Illustrate your answer for the case where a  $128 \times 128$  image P contains just the object shown in Fig. 8.P2. How many passes of (1) a parallel algorithm and (2) a sequential algorithm would be required to find the distance function of the image?

```

1 1 1 1 1 1 1 1 1 1 1 1 1 1 1 1
1 1 1 1 1 1 1 1 1 1 1 1 1 1 1 1
1 1 1 1 1 1 1 1 1 1 1 1 1 1 1 1
1 1 1 1 1 1 1 1 1 1 1 1 1 1 1 1
1 1 1 1 1 1 1 1 1 1 1 1 1 1 1 1
  1 1 1 1 1 1 1 1 1 1 1 1 1 1 1 1
                                     1 1 1 1 1 1 1
                                       1 1 1 1 1 1 1
                                         1 1 1 1 1 1 1
                                           1 1 1 1 1 1 1
                                             1 1 1 1 1 1 1
                                              1 1 1 1 1 1 1
                                               1 1 1 1 1 1 1
                                                1 1 1 1 1 1 1
                                                 1 1 1 1 1 1 1
                                                  1 1 1 1 1 1 1 1 1

```

**FIGURE 8.P2**

Binary picture object for distance function analysis.

- b. Give a complete parallel *or* sequential algorithm for finding the distance function and explain how it operates.
  - c. Image P is to be transmitted rapidly by determining the coordinates of locations where the distance function is locally maximum. Indicate the positions of the local maxima, and explain how the image could be reconstituted at the receiver.
  - d. Determine the compression factor  $\eta$  if image P is transmitted in this way. Show that  $\eta$  can be increased by eliminating some of the local maxima before transmission and estimate the resulting increase in  $\eta$ .
- a. The local maxima of the distance function can be defined in the following two ways:
    - i. those pixels whose values are greater than those of all the neighboring pixels;
    - ii. those pixels whose values are greater than *or equal to* the values of all the neighboring pixels. Which definition of the local maxima would be more useful for reproducing the original object shapes? Why is this?

- b. Give an algorithm that is capable of reproducing the original object shapes from the local maxima of the distance function and explain how it operates.
- c. Explain the *run-length-encoding* approach to image compression. Compare the run-length encoding and local maxima methods for compressing binary images. Explain why the one method would be expected to lead to a greater degree of compression with some types of image, whereas the other method would be expected to be better with other types of image.
10. a. Explain how propagation of a distance function may be carried out using a parallel algorithm. Give in full a simpler algorithm that operates using two sequential passes over the image.
- b. It has been suggested that a four-pass sequential algorithm will be even faster than the two-pass algorithm, as each pass can use just a 1-D window involving at most three pixels. Write down the code for *one* typical pass of the algorithm.
- c. Estimate the approximate speeds of these three algorithms for computing the distance function, in the case of an  $N \times N$  pixel image. Assume a conventional serial computer is used to perform the computation.
11. Small dark insects are to be located amongst cereal grains. The insects approximate to rectangular bars of dimensions 20 by 7 pixels, and the cereal grains are approximately elliptical with dimensions 40 by 24 pixels. The proposed algorithm design strategy is: (1) apply an edge detector which will mark all the edge points in the image as  $s$  in a  $1$ s background, (2) propagate a distance function in the *background* region, (3) locate the local maxima of the distance function, (4) analyze the values of the local maxima, and (5) carry out necessary further processing to identify the nearly parallel sides of the insects. Explain how to design stages (4) and (5) of the algorithm in order to identify the insects, ignoring the cereal grains. Assume that the image is not so large that the distance function will overflow the byte limit. Determine how robust the method will be if the edge is broken in a few places.
12. Give the general strategy of an algorithm for tracking around the boundaries of objects in binary images. If the tracker has reached a boundary point with crossing number  $\chi=2$  and neighborhood  $\begin{bmatrix} 0 & 0 & 1 \\ 0 & 1 & 1 \\ 1 & 1 & 1 \end{bmatrix}$ , decide in which direction it should now proceed. Hence, give a complete procedure for determining the direction code of the next position on the boundary for cases where  $\chi=2$ . Take the direction codes starting *from* the current pixel (\*) as being specified by the following diagram:

4	3	2
5	*	1
6	7	8



How should the procedure be modified for cases where  $\chi \neq 2$ ?

13. a. Explain the principles involved in tracking around the boundaries of objects in binary images to produce reliable outlines. Outline an algorithm which can be used for this purpose, assuming it is to get its information from a normal  $3 \times 3$  window.
  - b. A binary image is obtained and the data in it is to be compressed as much as possible. The following range of algorithms is to be tested for this purpose:
    - i. the boundary image;
    - ii. the skeleton image;
    - iii. the image of the local maxima of the distance function;
    - iv. the image of a suitably chosen subset of the local maxima of the distance function;
    - v. a set of run-length data, i.e., a series of numbers obtained by counting runs of 0s, then runs of 1s, then runs of 0s, etc., in a continuous line-by-line scan over the image.
  - c. In (i) and (ii), the lines may be encoded using chain code, i.e., giving the *coordinates* of the first point met, and the *direction* of each subsequent point using the direction codes 1 to 8 defined relative to the current position C by:
 

4	3	2
5	C	1
6	7	8
  - d. With the aid of suitably chosen examples, discuss which of the methods of data compression should be most suitable for different types of data. Wherever possible, give numerical estimates to support your arguments.
  - e. Indicate what you would expect to happen if noise were added to initially noise-free input images.
14. Test the two-mask strategy outlined in [Section 8.7](#) for obtaining the convex hulls of binary picture objects. Confirm that it operates consistently and give a geometrical construction that predicts the final shapes it produces. What happens if either the first or the second mask is used on its own? Show that the two-mask strategy will operate both as a sequential and as a parallel algorithm. Devise a version of the algorithm that does not permit nearby shapes to be merged.

# Boundary pattern analysis

# 9

Recognition of binary objects by boundary pattern analysis should be a straightforward process, but this chapter shows that there are a number of problems to be overcome. In particular, any boundary distortions such as those due to breakage or several objects being in contact may result in total failure of the matching process. This chapter discusses the problems and their solution.

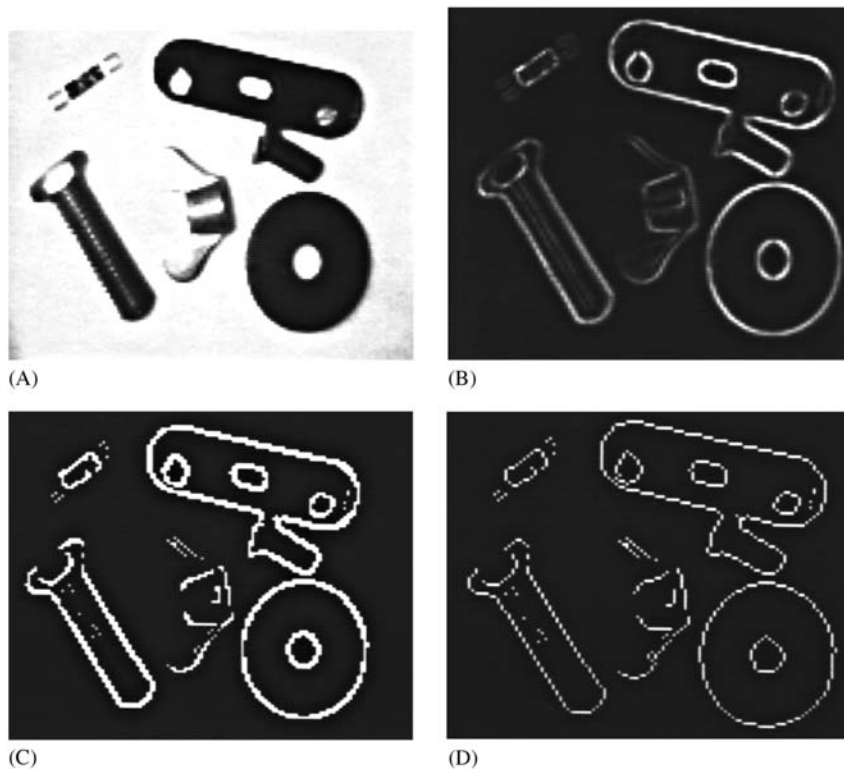
*Look out for:*

- the centroidal profile approach and its limitations
- how the method may be speeded up
- how recognition based on the  $(s, \psi)$  boundary plot is significantly more robust
- how the  $(s, \psi)$  plot leads on to the more convenient  $(s, \kappa)$  plot
- the relation between  $\kappa$  and  $\psi$
- more rigorous ways of dealing with the occlusion problem
- discussion of the accuracy of boundary length measures.

Disparate ways are available for representing object boundaries and for measuring and recognizing objects using them. All the methods are subject to the same ultimate difficulties—particularly that of managing occlusion (which necessarily removes relevant data), and that of inaccuracy in the pixel-based description. Sound ways of managing occlusion are indicated in [Section 9.6](#). This work presages later chapters in which the methods such as the Hough transform are widely employed for robust object recognition.

## 9.1 INTRODUCTION

An earlier chapter showed how thresholding may be used to binarize gray-scale images and hence to present objects as 2-D shapes. However, that method of segmenting objects is successful only when considerable care is taken with lighting and when the object can be presented conveniently, e.g., as dark patches on a light background. In other cases, adaptive thresholding may help to achieve the same end: as an alternative, edge detection schemes can be applied, these generally being rather more resistant to problems of lighting. Nevertheless, thresholding of edge-enhanced images still gives certain problems: in particular, edges may peter out in some places and may be thick in others ([Fig. 9.1](#)).

**FIGURE 9.1**

Some problems with edges. The edge-enhanced image (B) from an original image (A) is thresholded as in (C). The edges so detected are found to peter out in some places and to be thick in other places. A thinning algorithm is able to reduce the edges to unit thickness (D) but ad hoc (i.e., not model-based) linking algorithms are liable to produce erroneous results (not shown).

For many purposes, the output of an edge detector is ideally a connected unit-width line around the periphery of an object and steps need to be taken to convert edges to this form—if this has not already been achieved using a Canny or other operator employing nonmaximum suppression (see [Chapter 5: Edge Detection](#)).

Thinning algorithms can be used to reduce edges to unit thickness, whilst maintaining connectedness ([Fig. 9.1D](#)). Many algorithms have been developed for this purpose, and the main problems here are as follows: (1) slight bias and inaccuracy due to uneven stripping of pixels, especially in view of the fact that even the best algorithm can only produce a line that is locally within 1/2 pixel of the ideal position and (2) introduction of a certain number of noise spurs. The first of these problems can be minimized by using gray-scale edge thinning algorithms that act directly on the original gray-scale edge-enhanced image

(e.g., Paler and Kittler, 1983). Noise spurs around object boundaries can be eliminated quite efficiently by removing lines that are shorter than (say) 3 pixels. Overall, the major problem to be dealt with is that of reconnecting boundaries that have become fragmented during thresholding.

A number of rather ad hoc schemes are available for relinking broken boundaries: for example, line ends may be extended along their existing directions—a *very* limited procedure as there are (at least for binary edges) only eight possible directions, and it is quite possible for the extended line ends not to meet. Another approach is to join line ends that are sufficiently close together and point in similar directions, both to each other *and* to the direction of the vector between the two ends. In fact, this approach can be made quite credible in principle but in practice it can lead to all sorts of problems as it is still ad hoc and not model driven. Hence, adjacent lines that arise from genuine surface markings and shadows may be arbitrarily linked together by such algorithms. In many situations it is therefore best if the process is model driven—for example, by finding the best fit to some appropriate idealized boundary such as an ellipse. Yet another approach is that of relaxation labeling, which iteratively enhances the original image, progressively making decisions as to where the original gray levels reinforce each other. Thus edge linking is permitted only where evidence is available in the original image that this is appropriate. A similar but computationally more efficient line of attack is the hysteresis thresholding method described in [Chapter 5, Edge Detection](#): here intensity gradients above a certain upper threshold are taken to give definite indication of edge positions, whereas those above a second, lower threshold are taken to indicate edges only if they are adjacent to positions that have already been accepted as edges (for a more detailed analysis, see [Section 5.10](#)).

It may be thought that the Marr–Hildreth and related (Laplacian-based) edge detectors do not run into these problems, because they give edge contours that are necessarily connected. However, the result of using methods that force connectedness is that sometimes (e.g., when edges are diffuse, or of low contrast, so that image noise is an important factor) parts of a contour will lack meaning; indeed, a contour may meander over such regions following noise rather than useful object boundaries. Furthermore, it is as well to note that the problem is not merely one of pulling low-level signals out of noise, but rather that sometimes there is no signal at all present that could be enhanced to a meaningful level. Reasons for this include lighting being such as to give zero contrast (as, e.g., when a cube is lit in such a way that two faces have equal brightness) and occlusion. Lack of spatial resolution can also cause problems by merging together several lines on an object.

In what follows it will be assumed that all of these problems have been overcome by sufficient care with the lighting scheme, appropriate digitization and other means. It will also be assumed that suitable thinning and linking algorithms have been applied so that all objects are outlined by connected unit-width boundary lines. At this stage, it should be possible to locate the objects from the boundary image, and to identify and orientate them accurately.

---

## 9.2 BOUNDARY TRACKING PROCEDURES

Before objects can be matched from their boundary patterns, means must be found for tracking systematically around the boundaries of all the objects in an image: means have already been demonstrated for achieving this in the case of regions such as those that result from intensity thresholding routines (Chapter 8: Binary Shape Analysis). However, if a connected unit-width boundary is formed by an alternative process such as edge detection, the problem of tracking is much simpler, as it is necessary only to move repeatedly to the next edge pixel. Clearly, it will be necessary to ensure (1) that we never reverse direction, (2) that we know when we have been round the whole boundary once, and (3) that we record which object boundaries have been encountered. As when tracking around regions, we must ensure that in each case we end by passing through the starting point in the same direction.

---

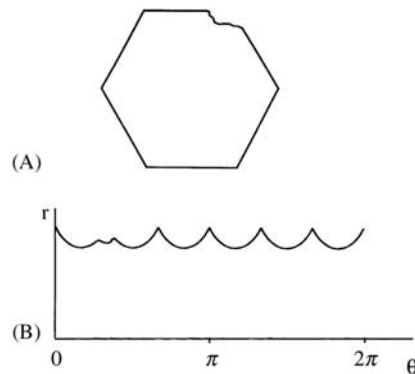
## 9.3 CENTROIDAL PROFILES

The substantial matching problems that occur with 2-D template matching make it attractive to attempt to locate objects in a less demanding search space. In fact, this is possible to achieve very simply by matching the boundary of each object in a single dimension. Perhaps the most obvious such scheme uses an  $(r, \theta)$  plot. Here, the centroid of the object is first located: its position is deducible directly from the list of boundary pixel coordinates—there is no need to start with a region-based description of the object. Then a polar coordinate system is set up relative to this point and the object boundary is plotted as an  $(r, \theta)$  graph—often called a “centroidal profile” (Fig. 9.2). Next, the 1-D graph so obtained is matched against the corresponding graph for an idealized object of the same type. As the object in general has an arbitrary orientation, it is necessary to “slide” the idealized graph along that obtained from the image data until the best match is obtained. The match for each possible orientation  $\alpha_j$  of the object is commonly tested by measuring the differences in radial distance between the boundary graph B and the template graph T for various values of  $\theta$  and summing their squares to give a difference measure  $D_j$  for the quality of the fit:

$$D_j = \sum_i [r_B(\theta_i) - r_T(\theta_i + \alpha_j)]^2 \quad (9.1)$$

Alternatively, the absolute magnitudes of the differences are used:

$$D_j = \sum_i |r_B(\theta_i) - r_T(\theta_i + \alpha_j)| \quad (9.2)$$

**FIGURE 9.2**

Centroidal profiles for object recognition and scrutiny: (A) hexagonal nut shape in which one corner has been damaged; (B) centroidal profile, which permits both straightforward identification of the object and detailed scrutiny of its shape.

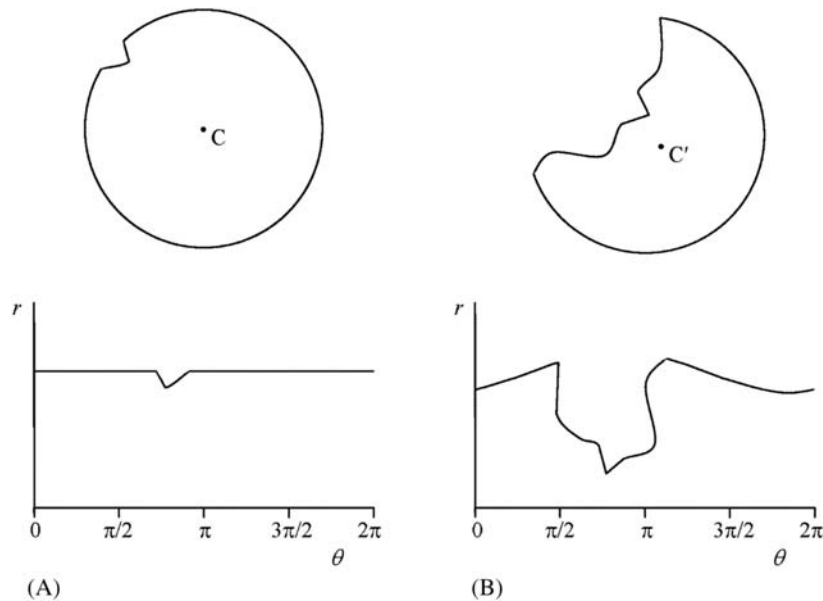
The latter measure has the advantage of being easier to compute and of being less biased by extreme or erroneous difference values. Note that the basic 2-D matching operation has now been reduced to 1-D, and if we need work in  $1^\circ$  steps, the orientation indices  $i$  and  $j$  will each have to range over 360 values. The result is that the number of operations that are required to test each object drops to around  $360^2$  (i.e.,  $\sim 100,000$ ), so boundary pattern analysis should give a very substantial saving in computation.

The 1-D boundary pattern matching approach described above is able to identify objects and also to find their orientations. In fact, initial location of the centroid of the object also solves one other part of the problem as specified at the end of [Section 9.1](#). At this stage it may be noted that the matching process also leads to the possibility of inspecting the object's shape as an inherent part of the process ([Fig. 9.2](#)). In principle, this combination of capabilities makes the centroidal profile technique quite powerful.

Finally, note that the method is able to cope with objects of identical shapes but different sizes. This is achieved by using the maximum value of  $r$  to normalize the profile, giving a variation  $(\rho, \theta)$  where  $\rho = r/r_{\max}$ .

## 9.4 PROBLEMS WITH THE CENTROIDAL PROFILE APPROACH

In practice, there are several problems with the procedure outlined above. First, any major defect or occlusion of the object boundary can cause the centroid to be moved away from its true position, and the matching process will be largely spoiled ([Fig. 9.3](#)). Thus, instead of concluding that this is an object of type X with a specific part of its boundary damaged, the algorithm will most probably

**FIGURE 9.3**

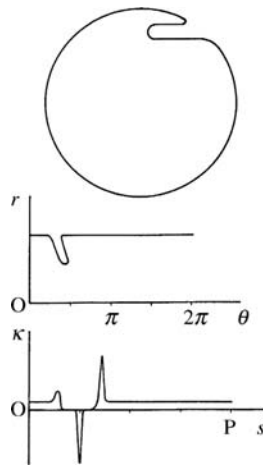
Problems with the centroidal profile descriptor. Part (A) shows a circular object with a minor defect on its boundary; its centroidal profile appears beneath it. Part (B) shows the same object, this time with a gross defect: because the centroid is shifted to  $C'$ , the *whole* of the centroidal profile is grossly distorted.

not recognize it at all. Such behavior would be inadequate in many automated inspection applications, in which positive identification and fault-finding are required, and the object would have to be rejected without a satisfactory diagnosis being made.

Second, the  $(r, \theta)$  plot will be multivalued for a certain class of object (Fig. 9.4). This has the effect of making the matching process partly 2-D and leads to complication and excessive computation.

Third, the very variable spacing of the pixels when plotted in  $(r, \theta)$  space is a source of complication. It leads to the requirement for considerable smoothing of the 1-D plots, especially in regions where the boundary comes close to the centroid—as for elongated objects such as spanners or screwdrivers (Fig. 9.5); however, in other places, accuracy will be greater than necessary and the overall process will be wasteful. The problem arises because quantization should ideally be uniform along the  $\theta$ -axis so that the two templates can be moved conveniently relative to one another to find the orientation of best match.

Finally, computation times can still be quite significant, so some timesaving procedure is required.

**FIGURE 9.4**

Boundary pattern analysis via  $(r, \theta)$  and  $(s, \kappa)$  plots.

**FIGURE 9.5**

A problem in obtaining a centroidal profile for elongated objects. This figure highlights the pixels around the boundary of an elongated object—a spanner—showing that it will be difficult to obtain an accurate centroidal profile for the region near the centroid.

### 9.4.1 SOME SOLUTIONS

All four of the above problems can be tackled in one way or another, with varying degrees of success. The first problem, that of coping with occlusions and gross defects, is probably the most fundamental and the most resistant to satisfactory solution. For the method to work successfully, a stable reference point must be found within the object. The centroid is naturally a good candidate for this as the averaging inherent in its location tends to eliminate most forms of noise or minor defect; however, major distortions such as those arising from breakages or occlusions are bound to affect it adversely. The centroid of the



boundary is no better, and may also be less successful at suppressing noise. Other possible candidates are the positions of prominent features such as corners, holes, centers of arcs, and so on. In general, the smaller such a feature, the more likely it is to be missed altogether in the event of a breakage or occlusion, whereas the larger such a feature, the more likely it is to be affected by the defect. In fact, circular arcs can be located accurately (at their centers) even if they are partly occluded (see [Chapter 10: Line, Circle, and Ellipse Detection](#)), so these features are very useful for leading to suitable reference points. A set of symmetrically placed holes may sometimes be suitable, as even if one of them is obscured, one of the others is likely to be visible and can act as a reference point.

Clearly, such features can help the method to work adequately but their presence also calls into question the value of the 1-D boundary pattern matching procedure, as they make it likely that superior methods can be used for object recognition (see later chapters in Part 2). For the present we therefore accept (1) that severe complications arise when part of an object is missing or occluded and (2) that it may be possible to provide some degree of resistance to such problems by using a prominent feature as a reference point instead of the centroid. Indeed, the only significant *further* change that is required to cope with occlusions is that difference ( $r_B - r_T$ ) values of greater than (say) 3 pixels should be ignored, and the best match then becomes one for which the greatest number of values of  $\theta$  give good agreement between B and T.

The second problem, of multivalued  $(r, \theta)$  plots, is solved very simply by employing the heuristic of taking the smallest value of  $r$  for any given  $\theta$  and then proceeding with matching as normal (here, it is assumed that the boundaries of any holes present within the boundary of the object are dealt with separately, information about any object and its holes being collated at the end of the recognition process). This ad hoc procedure should in fact be acceptable when making a preliminary match of the object to its 1-D template, and may be discarded at a later stage when the orientation of the object is known accurately.

The third problem described above arises because of uneven spacing of the pixel boundaries along the  $\theta$  dimension of the  $(r, \theta)$  graph. To some extent this problem can be avoided by deciding in advance on the permissible values of  $\theta$  and querying a list of boundary points to find which has the closest  $\theta$  to each permissible value. Some local smoothing of the ordered set of boundary points can be undertaken but this is in principle unnecessary, as for a connected boundary, there will always be one pixel that is closest to a line from the centroid at a given value of  $\theta$ .

The two-stage approach to matching hinted at above can also be used to help with the last of the problems mentioned above—the need to speed up the processing. First, a coarse match is obtained between the object and its 1-D template by taking  $\theta$  in relatively large steps of (say)  $5^\circ$  and ignoring intermediate angles in both the image data and the template; then a better match is obtained by making fine adjustments to the orientations, obtaining a match to within  $1^\circ$ .

In this way, the coarse match is obtained perhaps 20 times faster than the previous full match, whereas the final fine match takes a relatively short time, as very few distinct orientations have to be tested.

This two-stage process can be optimized by making a few simple calculations. The coarse match is given by steps  $\delta\theta$ , so the computational load is proportional to  $(360/\delta\theta)^2$ , whereas the load for the fine match is proportional to  $360 \delta\theta$ , giving a total load of:

$$\lambda = (360/\delta\theta)^2 + 360 \delta\theta \quad (9.3)$$

This should be compared with the original load of:

$$\lambda_0 = 360^2 \quad (9.4)$$

Hence, the load is reduced (and the algorithm speeded up) by the factor:

$$\eta = \lambda_0/\lambda = 1/[(1/\delta\theta)^2 + \delta\theta/360] \quad (9.5)$$

This is a maximum for  $d\eta/d\delta\theta = 0$ , giving:

$$\delta\theta = \sqrt[3]{2 \times 360} \approx 9^\circ \quad (9.6)$$

In practice this value of  $\delta\theta$  is rather large and there is a risk that the coarse match will give such a poor fit that the object will not be identified; hence, values of  $\delta\theta$  in the range  $2-5^\circ$  are more usual (see, e.g., Berman et al., 1985). Note that the optimum value of  $\eta$  is 26.8 and that this reduces only to 18.6 for  $\delta\theta = 5^\circ$ , whereas it goes down to 3.9 for  $\delta\theta = 2^\circ$ .

Another way of approaching the problem is to search the  $(r, \theta)$  graph for some characteristic feature such as a sharp corner (this step constituting the coarse match), and then to perform a fine match around the object orientation so deduced. Clearly there are possibilities of error here, in situations in which objects have several similar features—as in the case of a rectangle; however, the individual trials are relatively inexpensive and so it is worth invoking this procedure if the object possesses appropriate well-defined features. Note that it is possible to use the position of the maximum value,  $r_{\max}$ , as an orientating feature but this is frequently inappropriate because a smooth maximum gives a relatively large angular error.

---

## 9.5 THE $(s, \psi)$ Plot

It will be seen from the above considerations that boundary pattern analysis should usually be practicable except when problems from occlusions and gross defects can be expected. However, these latter problems do give motivation for employing alternative methods if these can be found. In fact, the  $(s, \psi)$  graph has proved particularly popular as it is inherently better suited than the  $(r, \theta)$  graph to

situations in which defects and occlusions may occur. In addition, it does not suffer from the multiple values encountered by the  $(r, \theta)$  method.

The  $(s, \psi)$  graph does not require prior estimation of the centroid or some other reference point as it is computed directly from the boundary, in the form of a plot of the tangential orientation  $\psi$  as a function of boundary distance  $s$ . The method is not without its problems and, in particular, distance along the boundary needs to be measured accurately. The commonly used approach is to count horizontal and vertical steps as unit distance, and to take diagonal steps as distance  $\sqrt{2}$ ; in fact, this idea must be regarded as a rather ad hoc solution and the situation is discussed further in [Section 9.7](#).

When considering application of the  $(s, \psi)$  graph for object recognition, it will immediately be noticed that the graph has a  $\psi$  value that increases by  $2\pi$  for each circuit of the boundary, i.e.,  $\psi(s)$  is not periodic in  $s$ . The result is that the graph becomes essentially 2-D, i.e., the shape has to be matched by moving the ideal object template both along the  $s$ -axis and along the  $\psi$ -axis directions. Ideally, the template could be moved diagonally along the direction of the graph. However, noise and other deviations of the actual shape relative to the ideal shape mean that in practice the match must be at least partly 2-D; hence, adding to the computational load.

One way of tackling this problem is to make a comparison with the shape of a circle of the same boundary length  $P$ . Thus, an  $(s, \Delta\psi)$  graph is plotted that reflects the difference  $\Delta\psi$  between the  $\psi$  expected for the shape and that expected for a circle of the same perimeter:

$$\Delta\psi = \psi - 2\pi s/P \quad (9.7)$$

This expression helps to keep the graph 1-D, as  $\Delta\psi$  automatically resets itself to its initial value after one circuit of the boundary (i.e.,  $\Delta\psi$  is periodic in  $s$ ).

Next, notice that the  $\Delta\psi(s)$  variation depends on the starting position where  $s = 0$  and that this is randomly sited on the boundary. It is useful to eliminate this dependence and this may be achieved by subtracting from  $\Delta\psi$  its mean value  $\mu$ . This gives the new variable:

$$\tilde{\psi} = \psi - 2\pi s/P - \mu \quad (9.8)$$

At this stage the graph is completely 1-D and is also periodic, being similar in these respects to an  $(r, \theta)$  graph. Matching should now reduce to the straightforward task of sliding the template along the  $\psi(s)$  graph until a good fit is achieved.

At this point, there should be no problems so long as (1) the scale of the object is known, and (2) occlusions or other disturbances cannot occur. Suppose next that the scale is unknown: then the perimeter  $P$  may be used to normalize the value of  $s$ . If, however, occlusions *can* occur, then no reliance can be placed on  $P$  for normalizing  $s$  and hence, the method cannot be guaranteed to work. This problem does not arise if the scale of the object is known, as a standard perimeter  $P_T$  can be assumed. However, the possibility of occlusion gives further problems that are discussed in the next section.

Another way in which the problem of nonperiodic  $\psi(s)$  can be solved is by replacing  $\psi$  by its derivative  $d\psi/ds$ . Then the problem of constantly expanding  $\psi$  (which results in its increasing by  $2\pi$  after each circuit of the boundary) is eliminated—the addition of  $2\pi$  to  $\psi$  does not affect  $d\psi/ds$  locally, as  $d(\psi + 2\pi)/ds = d\psi/ds$ . Notice that  $d\psi/ds$  is actually the local curvature function  $\kappa(s)$  (see Fig. 9.4), so the resulting graph has a simple physical interpretation. Unfortunately, this version of the method has its own problems in that  $\kappa$  approaches infinity at any sharp corner. For industrial components, which frequently have sharp corners, this is a genuine practical difficulty and may be tackled by approximating adjacent gradients and ensuring that  $\kappa$  integrates to the correct value in the region of a corner (Hall, 1979).

Many workers take the  $(s, \kappa)$  graph idea further and expand  $\kappa(s)$  as a Fourier series:

$$\kappa(s) = \sum_{n=-\infty}^{\infty} c_n \exp(2\pi i n s / P) \quad (9.9)$$

This results in the well-known Fourier descriptor method. In this method, shapes are analyzed in terms of a series of Fourier descriptor components that are truncated to zero after a sufficient number of terms. Unfortunately, the amount of computation involved in this approach is considerable and there is a tendency to approximate curves with relatively few terms. In industrial applications in which computations have to be performed in real time, this can give problems, so it is often more appropriate to match to the basic  $(s, \kappa)$  graph. In this way, critical measurements between object features can be made with adequate accuracy in real time.

---

## 9.6 TACKLING THE PROBLEMS OF OCCLUSION

Whatever means are used for tackling the problem of continuously increasing  $\psi$ , problems still arise when occlusions occur. However, the approach is not immediately invalidated by missing sections of boundary as it is for the basic  $(r, \theta)$  method. As noted above, the first effect of occlusions is that the perimeter of the object is altered, so  $P$  can no longer be used to indicate its scale. Hence, the latter has to be known in advance; this is assumed in what follows. Another practical result of occlusions is that certain sections correspond correctly to parts of the object, whereas other sections correspond to parts of occluding objects; alternatively, they may correspond to unpredictable boundary segments in which damage has occurred. Note that if the overall boundary is that of two overlapping objects, the observed perimeter  $P_B$  will be greater than the ideal perimeter  $P_T$ .

Segmenting the boundary between relevant and irrelevant sections is, a priori, a difficult task. However, a useful strategy is to start by making positive matches wherever possible and to ignore irrelevant sections—i.e., try to match as usual,

ignoring any section of the boundary that is a bad fit. We can imagine achieving a match by sliding the template  $T$  along the boundary  $B$ . However, a problem arises as  $T$  is periodic in  $s$  and should not be cut off at the ends of the range  $0 \leq s \leq P_T$ . As a result, it is necessary to attempt to match over a length  $2P_T$ . At first sight it might be thought that the situation ought to be symmetrical between  $B$  and  $T$ . However,  $T$  is known in advance whereas  $B$  is partly unknown, there being the possibility of one or more breaks in the ideal boundary into which foreign boundary segments have been included; indeed, the positions of the breaks are unknown, so it is necessary to try matching the whole of  $T$  at all positions on  $B$ . Taking a length  $2P_T$  in testing for a match effectively permits the required break to arise in  $T$  at any relevant position: see Fig. 9.6.

When carrying out the match we basically use the difference measure:

$$D_{jk} = \sum_i [\psi_B(s_i) - (\psi_T(s_i + s_k) + \alpha_j)]^2 \quad (9.10)$$

where  $j$  and  $k$  are the match parameters for orientation and boundary displacement, respectively. Notice that the resulting  $D_{jk}$  is roughly proportional to the length  $L$  of the boundary over which the fit is reasonable. Unfortunately, this

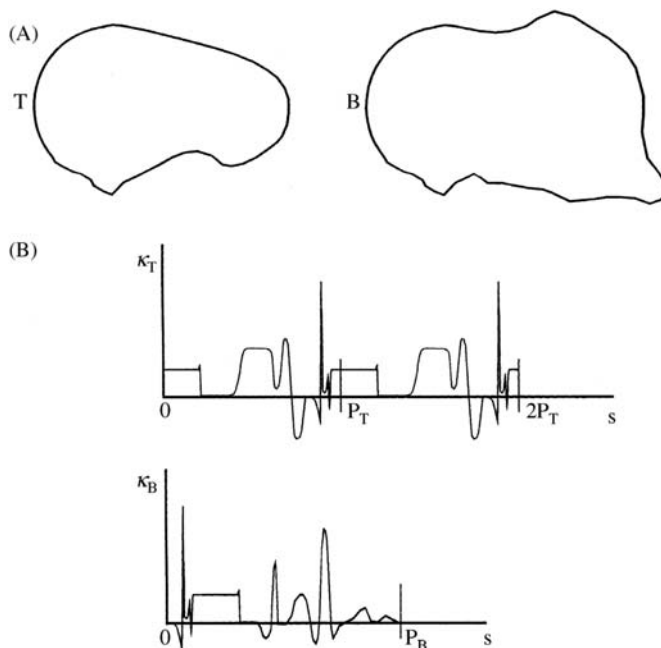


**FIGURE 9.6**

Matching a template against a distorted boundary. When a boundary  $B$  is broken (or partly occluded) but continuous, it is necessary to attempt to match between  $B$  and a template  $T$  that is doubled to length  $2P_T$ , to allow for  $T$  being severed at any point: (A) the basic problem; (B) matching in  $(s, \kappa)$ -space.

means that the measure  $D_{jk}$  appears to *improve* as  $L$  decreases; hence, when variable occlusions can occur, the best match must be taken as the one for which the greatest length  $L$  gives good agreement between B and T (this may be measured as the greatest number of values of  $s$  in the sum of Eq. (9.10) which give good agreement between B and T, i.e., the sum overall  $i$  such that the difference in square brackets is numerically less than, say,  $5^\circ$ ).

If the boundary is occluded in more than one place, then  $L$  is at most the largest single length of unoccluded boundary (not the total length of unoccluded boundary), as the separate segments will in general be “out of phase” with the template. This is a disadvantage when trying to obtain an accurate result, as extraneous matches add noise that degrades the fit that is obtainable—hence, adding to the risk that the object will not be identified and reducing accuracy of registration. This suggests that it might be better to use only short sections of the boundary template for matching. Indeed, this strategy can be advantageous as speed is enhanced and registration accuracy can be retained or even improved by careful selection of salient features (note that nonsalient features such as smooth curved segments could have originated from many places on object boundaries and are not very helpful for identifying and accurately locating objects; hence, it is reasonable to ignore them). In this version of the method we now have  $P_T < P_B$  and it is necessary to match over a length  $P_T$  rather than  $2P_T$ , as T is no longer periodic (Fig. 9.7). Once various segments have been located, the boundary can be reassembled as closely as possible into its full form, and at that stage defects, occlusions, and other distortions can be recognized overtly and recorded. Reassembly of the object boundaries can be performed by techniques such as the Hough transform and relational pattern matching techniques (see Chapter 11: The Generalized Hough Transform). Work of this type has been carried out by Turney et al. (1985), who found that the salient features should be short boundary segments where corners and other distinctive “kinks” occur.

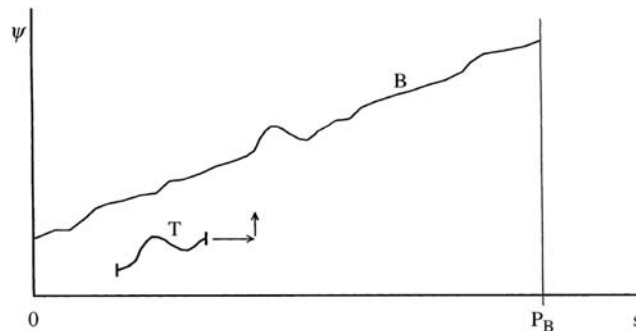


**FIGURE 9.7**

Matching a short template to part of a boundary. A short template T, corresponding to part of an idealized boundary, is matched against the observed boundary B. Strictly speaking, matching in  $(s, \psi)$ -space is 2-D although there is very little uncertainty in the vertical (orientation) dimension.

Before leaving this topic, note that  $\tilde{\psi}$  can no longer be used when occlusions are present, as although the perimeter can be assumed to be known, the mean value of  $\Delta\psi$  (Eq. (9.8)) cannot be deduced. Hence, the matching task reverts to a 2-D search (though, as stated earlier, very little unrestrained search in the  $\psi$  direction need be made). However, in the case when small salient features are being sought, it is a reasonable working assumption that no occlusion occurs in any of the individual cases—a feature is either entirely present or entirely absent. Hence, the average slope  $\bar{\psi}$  over  $T$  can validly be computed (Fig. 9.7), and this again reduces the search to 1-D (Turney et al., 1985).

Overall, missing sections of object boundaries necessitate a fundamental rethink as to how boundary pattern analysis should be carried out. For quite small defects the  $(r, \theta)$  method is sufficiently robust but in less trivial cases it is vital to use some form of the  $(s, \psi)$  approach, whereas for really gross occlusions, it is not particularly useful to try to match for the full boundary; rather, it is better to attempt to match small salient features. This sets the scene for the Hough transform and relational pattern matching techniques of later chapters.

---

## 9.7 ACCURACY OF BOUNDARY LENGTH MEASURES

Next we examine the accuracy of the idea expressed earlier, that adjacent pixels on an 8-connected curve should be regarded as separated by 1 pixel if the vector joining them is aligned along the major axes, and by  $\sqrt{2}$  pixels if the vector is in a diagonal orientation. In general, this estimator overestimates the distance along the boundary. The reason for this is quite simple to see by appealing to the following pair of situations:

```

1 1 1 1 1 1 1 1 1 1 1 1 1 1 1 1 1 1 1 1 1 1
1 1 1 1 1 1 1 1 1 1 1 1 1 1 1 1 1 1 1 1 1 1
1 1 1 1 1 1 1 1 1 1 1 1 1 1 1 1 1 1 1 1 1 1
...
                                1 1 1 1 1 1 1 1 1 1 1 1
1 1 1 1 1 1 1 1 1 1 1 1 1 1 1 1 1 1 1 1 1 1
1 1 1 1 1 1 1 1 1 1 1 1 1 1 1 1 1 1 1 1 1 1
...

```

In either case, we are considering only the top of the object. In the first example, the boundary length along the top of the object is exactly that given by the rule. However, in the second case the estimated length is increased by amount  $\sqrt{2} - 1$  because of the step. Now as the length of the top of the object tends to large values, say  $p$  pixels, the actual length approximates to  $p$  whereas the estimated length is  $p + \sqrt{2} - 1$ ; thus, a definite error exists. Indeed, this error initially increases in importance as  $p$  decreases, as the actual length of the top of the object (when there is one step) is still

$$L = (1+p^2)^{1/2} \approx p \quad (9.11)$$

so the fractional error is

$$\xi \approx (\sqrt{2} - 1)/p \quad (9.12)$$

which increases as  $p$  becomes smaller.

This result can be construed as meaning that the fractional error  $\xi$  in estimating boundary length increases initially as the boundary orientation  $\psi$  increases from zero. A similar effect occurs as the orientation decreases from  $45^\circ$ . Thus, the  $\xi$  variation possesses a maximum between  $0^\circ$  and  $45^\circ$ . This systematic overestimation of boundary length may be eliminated by employing an improved model in which the length per pixel is  $s_m$  along the major axes directions and  $s_d$  in diagonal directions. A complete calculation (Kulpa, 1977; see also Dorst and Smeulders, 1987) shows that

$$s_m = 0.948 \quad (9.13)$$

and

$$s_d = 1.343 \quad (9.14)$$

It is perhaps surprising that this solution corresponds to a ratio  $s_d/s_m$  that is still equal to  $\sqrt{2}$ , although the arguments given above make it obvious that  $s_m$  should be less than unity.

Unfortunately, an estimator that has just two free parameters can still permit quite large errors in estimating the perimeters of individual objects. To reduce this problem, it is necessary to perform more detailed modeling of the step pattern around the boundary (Koplowitz and Bruckstein, 1989), which seems certain to increase the computational load significantly.

It is important to underline that the basis of this work is to estimate the length of the original continuous boundary rather than that of the digitized boundary; furthermore, it must be noted that the digitization process loses information, so the best that can be done is to obtain a best estimate of the original boundary length. Thus, employing the values 0.948, 1.343 given above, rather than the values 1,  $\sqrt{2}$ , reduces the estimated errors in boundary length measurement from 6.6% to 2.3%—but then only under certain assumptions about correlations between orientations at neighboring boundary pixels (Dorst and Smeulders, 1987).

---

## 9.8 CONCLUDING REMARKS

This chapter has been concerned with boundary pattern analysis. The boundary patterns were imagined to arise from edge detection operations that have been processed to make them connected and of unit width. However, if intensity thresholding methods were employed for segmenting images, boundary tracking



procedures would also permit the boundary pattern analysis methods of this chapter to be used. Conversely, if edge detection operations led to the production of connected boundaries, these could be filled in by suitable algorithms (which are more tricky to devise than might at first be imagined) (Ali and Burge, 1988) and converted to regions to which the binary shape analysis methods of Chapter 8, Binary Shape Analysis, could be applied. Hence, shapes are representable in region or boundary form: if they initially arise in one representation, they may be converted to the alternative representation. This means that boundary or regional means may be employed for shape analysis, as appropriate.

An important factor here is that a positive advantage is often gained by employing boundary pattern analysis, as computation should be inherently lower (in proportion to the numbers of pixels that are required to describe the shapes in the two representations). Another important determining factor that has been seen in the present chapter is that of occlusion. If occlusions are present, then several of the methods will operate incorrectly—as also happens for the basic centroidal profile method described early in this chapter. The  $(s, \psi)$  method then provides a good starting point. As has been seen, this is best applied to detect small salient boundary features, which can then be reassembled into whole objects by relational pattern matching techniques (see especially Chapter 11: The Generalized Hough Transform).

*A variety of boundary representations is available for shape analysis. However, this chapter has shown that intuitive schemes raise fundamental robustness issues: these will only be resolved later on by forgoing deduction in favor of inference. Underlying analogue shape estimation in a digital lattice is also an issue.*

---

## 9.9 BIBLIOGRAPHICAL AND HISTORICAL NOTES

Many of the techniques described in this chapter have been known since the early days of image analysis. Boundary tracking has been known since 1961 when Freeman introduced his chain code. Indeed, Freeman is responsible for much subsequent work in this area (see, e.g., Freeman, 1974). Freeman (1978) introduced the notion of segmenting boundaries at “critical points” in order to facilitate matching: suitable critical points were corners (discontinuities in curvature), points of inflection, and curvature maxima. This work is clearly strongly related to that of Turney et al. (1985). Early work on Fourier boundary descriptors using the  $(r, \theta)$  and  $(s, \psi)$  approaches was carried out by Rutovitz (1970), Barrow and Popplestone (1971), and Zahn and Roskies (1972); another notable paper in this area is that by Persoon and Fu (1977). In an interesting development, Lin and Chellappa (1987) were able to classify partial (i.e., nonclosed) 2-D curves using Fourier descriptors.

At the beginning of the chapter it was noted that there are significant problems in obtaining a thin connected boundary for every object in an image. Since 1988, the concept of active contour models (or “snakes”) solved many of these problems. See [Chapter 12](#), Object Segmentation and Shape Models for an introduction to snakes and [Chapter 22](#), Surveillance for their application to vehicle location.

It is worth remarking on the increased attention to accuracy evident over the past 20–30 years; this is seen, for example, in the length estimators for digitized boundaries discussed in [Section 9.7](#) (see Kulpa, 1977; Dorst and Smeulders, 1987; Beckers and Smeulders, 1989; Koplowitz and Bruckstein, 1989; Davies, 1991c). For a later update on the topic, see Coeurjolly and Klette (2004).

In recent times there has been an emphasis on characterizing and classifying *families* of shapes rather than just individual isolated shapes: see in particular Cootes (1992), Amit (2002), Jacinto et al. (2003). Klassen et al. (2004) provide a further example of this in their analysis of planar (boundary) shapes using geodesic paths between the various shapes of the family: in their work they employ the Surrey fish database (Mokhtarian et al., 1996). The same general idea is also manifest in the self-similarity analysis and matching approach of Geiger et al. (2003), which they used for human profile and hand motion analysis. Horng (2003) describes an adaptive smoothing approach for fitting digital planar curves with line segments and circular arcs. The motivation for this approach is to obtain significantly greater accuracy than can be achieved with the widely used polygonal approximation, yet with lower computational load than the spline fitting type of approach. It can also be imagined that any fine accuracy restriction imposed by a line plus circular arc model will have little relevance in a discrete lattice of pixels. da Gama Leitão and Stolfi (2002) have developed a multiscale contour-based method for matching and reassembling 2-D fragmented objects. Although this method is targeted at reassembly of pottery fragments in archaeology, the authors imply that it is also likely to be of value in forensic science, in art conservation, and in assessing the causes of failure of mechanical parts following fatigue and the like.

Two useful books are available that cover the subject of shape and shape analysis in rather different ways: one is by Costa and Cesar (2000) and the other is by Mokhtarian and Bober (2003). The former is fairly general in coverage but emphasizes Fourier methods, wavelets and multiscale methods. The latter sets up a scale space (especially curvature scale space) representation (which is multiscale in nature), and develops the subject quite widely from there.

### 9.9.1 MORE RECENT DEVELOPMENTS

Ghosh and Petkov (2005) have described problems relating to the robust interpretation of incomplete object boundaries. They discuss the problems in relation to the ICR test—viz. assessing recognition rate performance as a function of the

percentage of the contour retained, in which deletions may occur either as segment deletions, or as occlusions, or as random pixel deletions. Experiments showed that occlusion was the most, and random pixel deletion the least, serious problem. Mori et al. (2005) considered problems relating to 3-D shape recognition from multiple 2-D views. They found that “shape contexts” were particularly important for efficient matching in such situations, shape contexts corresponding to representing shapes by a set of  $n$  samples on an object and examining the distribution of relative positions. This technique permitted shape matching to take place efficiently in two stages—fast pruning of possibilities followed by detailed matching.

---

## 9.10 PROBLEMS

1. Devise a program for finding a thinned (8-connected) boundary of an object in a binary image.
2.
  - a. Describe the centroidal profile approach to shape analysis. Illustrate your answer for a circle, a square, a triangle, and defective versions of these shapes.
  - b. Obtain a general formula expressing the shape a straight line presents in the centroidal profile.
  - c. Show that there are two means of recognizing objects from their centroidal profiles, one involving analysis of the profile and the other involving comparison with a template.
  - d. Show how the latter approach can be speeded up by implementing it in two stages, first at low resolution, and then at full resolution. If the low resolution has  $1/n$  of the detail of the full resolution, obtain a formula for the total computational load. Estimate from the formula for what value of  $n$  the load will be minimized. Assume that the full angular resolution involves 360 one-degree steps.
3.
  - a. Give a simple algorithm for eliminating salt and pepper noise in binary images, and show how it can be extended to eliminate short spurs on objects.
  - b. Show that a similar effect can be achieved by a “shrink” + “expand” type of procedure. Discuss how much such procedures affect the shapes of objects: give examples illustrating your arguments, and try to quantify exactly what sizes and shapes of object would be completely eliminated by such procedures.
  - c. Describe the  $(r, \theta)$  graph method for describing the shapes of objects. Show that applying 1-D median filtering operations to such graphs can be used to smooth the described object shapes. Would you expect this approach to be more or less effective at smoothing object boundaries than methods based on shrinking and expanding?

4.
  - a. Outline the  $(r, \theta)$  graph method for recognition of objects in two dimensions, and state its main advantages and limitations. Describe the shape of the  $(r, \theta)$  graph for an equilateral triangle.
  - b. Write down a complete algorithm, operating in a  $3 \times 3$  window, for producing an approximation to the convex hull of a 2-D object. Show that a more accurate approximation to the convex hull can be obtained by joining humps with straight lines in an  $(r, \theta)$  graph of the object. Give reasons why the result for the latter case will only be an approximation, and suggest how an exact convex hull might be obtained.
5. An alternative approach to shape analysis involves measuring distance around the boundary of any object, and estimating increments of distance as 1 unit when progressing to the next pixel in a horizontal or vertical direction and  $\sqrt{2}$  units when progressing in a diagonal direction. Taking a square of side 20 pixels that is aligned parallel to the image axes, and rotating it through small angles, show that distance around the boundary of the square is not estimated accurately by the  $1:\sqrt{2}$  model. Show that a similar effect occurs when the square is orientated at about  $45^\circ$  to the image axes. Suggest ways in which this problem might be tackled.

This page intentionally left blank

# Line, circle, and ellipse detection

# 10

Detection of macroscopic features is an important aspect of visual pattern recognition. Of particular interest is the identification of straight lines, which are ubiquitous both in manufacturing and in the built environment. Two methods—the Hough transform (HT) and RANSAC (random sample consensus)—provide the means for locating these features highly robustly. This chapter describes the principles and processes needed to achieve this. In addition, circle features occur very widely in images of manufactured objects and can also be located using HTs. This also applies for ellipses, which may appear in their own right or as oblique views of circular objects. However, locating ellipses is more complicated than locating circles because of the greater number of parameters needed to define them.

*Look out for:*

- how HTs may be used for locating straight lines in images
- why HTs are robust against noise and background clutter
- the RANSAC approach to line location, and its efficiency
- how laparoscopic tools may be located
- how HTs may be used for locating circular objects in images
- how they can be applied when circle radius is unknown
- how speed of processing can be increased
- the diameter bisection and chord–tangent methods for ellipse location
- how the human iris may be located.

This chapter describes two key methods for detecting important features in images. It is shown how the HT is able to locate a range of features including straight lines, circles, and ellipses, while the RANSAC approach is applied to the efficient location of straight lines, though its power greatly exceeds this single illustration. Both methods rely on voting schemes, and in each case their robustness stems from concentration on *positive* evidence for objects and features.

## 10.1 INTRODUCTION

Straight edges are amongst the most common features of the modern world, arising in perhaps the majority of manufactured objects and components—not

least in the very buildings in which we live. Yet, it is arguable whether true straight lines ever arise in the natural state: possibly the only example of their appearance in virgin outdoor scenes is the horizon—although even this is clearly seen from space as a circular boundary! The surface of water is essentially planar, although it is important to realize that this is a deduction: the fact remains that straight lines seldom appear in completely natural scenes. Be all this as it may, it is clearly vital both in city pictures and in the factory to have effective means of detecting straight edges. This chapter studies available methods for locating these important features.

Historically, the HT has been the main means of detecting straight edges, and since the method was originally invented (Hough, 1962), it has been developed and refined for this purpose. Hence this chapter concentrates on this particular technique; it also prepares the ground for applying the HT to the detection of circles, ellipses, corners, etc. in the next few chapters. We start by examining the original Hough scheme, even though it is now seen to be wasteful in computation, since important principles are involved. By the end of the chapter we shall see that the HT is not alone in its capabilities for line detection: RANSAC is also highly capable in this direction. In fact, both approaches have their advantages and limitations, as the discussion in [Section 10.6](#) will show.

This chapter also examines the location of round objects: these are important in many areas of image analysis but they are especially important in industrial applications such as automatic inspection and assembly. In the food industry alone, a very sizeable number of products are round—biscuits, cakes, pizzas, pies, oranges, and so on (Davies, 1984c). In the automotive industry many circular components are used—washers, wheels, pistons, heads of bolts, etc., while round holes of various sizes appear in such items as casings and cylinder blocks. In addition, buttons and many other everyday objects are round. Of course, when round objects are viewed obliquely they appear elliptical; furthermore, certain other objects are *actually* elliptical. This makes it clear that we need algorithms that are capable of finding both circles and ellipses. Finally, objects can frequently be located by their holes, so finding round holes or features is part of the larger problem: this chapter addresses various aspects of this problem.

An important facet of this work is how well object location algorithms cope in the presence of artifacts such as shadows and noise. In particular, the paradigm represented by [Table 10.1](#) was shown in [Chapter 9](#), Boundary Pattern Analysis to be insufficiently robust to cope in such situations. This chapter shows that the HT technique is particularly good at dealing with all sorts of difficulties, including quite severe occlusions. It achieves this not by adding robustness but by having robustness built in as an integral part of the technique.

The application of the HT to circle detection is one of the most straightforward uses of the technique. However, there are several enhancements and adaptations that can be applied in order to improve accuracy and speed of operation and in addition to make the method work efficiently when detecting circles with a range of sizes. These modifications are studied after covering the basic HT

**Table 10.1** Basic RANSAC Algorithm for Finding the Line With Greatest Support

---

```

Mmax = 0;
for all pairs of edge points do {
    find equation of line defined by the two points i, j;
    M = 0;
    for all N points in list do
        if (point k is within threshold distance d of line) M++;
    if (M > Mmax) {
        Mmax = M;
        imax = i;
        jmax = j;
        // this records the hypothesis giving the maximum support so far
    }
}
/* if Mmax > 0, (x[imax], y[imax]) and (x[jmax], y[jmax]) will be the
coordinates of the points defining the line having greatest support */

```

---

*This algorithm only returns one line: in fact it returns the specific line model that has greatest support, for the line that has greatest support. Lines with less support are in the end ignored.*

techniques. Versions of the HT that can perform ellipse detection are then considered. The chapter ends with a short section on an important application—that of human iris location.

---

## 10.2 APPLICATION OF THE HOUGH TRANSFORM TO LINE DETECTION

The basic concept involved in locating lines by the HT is point-line duality. A point  $P$  can be defined either as a pair of coordinates or in terms of the set of lines passing through it. The concept starts to make sense if we consider a set of collinear points  $P_i$ , then list the sets of lines passing through each of them, and finally note that there is just one line that is common to all these sets. Thus it is possible to find the line containing all the points  $P_i$  merely by eliminating those that are not multiple hits. Indeed, it is easy to see that if a number of noise points  $Q_j$  are intermingled with the signal points  $P_i$ , the method will be able to discriminate the collinear points from amongst the noise points at the same time as finding the line containing them, merely by searching for multiple hits. Thus the method is inherently robust against noise, as indeed it is in discriminating against currently unwanted signals such as circles.

In fact, the duality goes further. For just as a point can define (or be defined by) a set of lines, so a line can define (or be defined by) a set of points, as is obvious from the above argument. This makes the above approach to line detection a mathematically elegant one and it is perhaps surprising that the



Hough detection scheme was first published as a patent (Hough, 1962) of an electronic apparatus for detecting the tracks of high-energy particles, rather than as a paper in a learned journal.

The form in which the method was originally applied involves parametrizing lines using the slope-intercept equation

$$y = mx + c \quad (10.1)$$

Every point on a straight edge is then plotted as a line in  $(m, c)$  space corresponding to all the  $(m, c)$  values consistent with its coordinates, and lines are detected in this space. The embarrassment of unlimited ranges of the  $(m, c)$  values (near-vertical lines require near-infinite values of these parameters) is overcome by using two sets of plots, the first corresponding to slopes of less than 1.0 and the second to slopes of 1.0 or more; in the latter case, Eq. (10.1) is replaced by the form:

$$x = \tilde{m}x + \tilde{c} \quad (10.2)$$

where

$$\tilde{m} = 1/m \quad (10.3)$$

The need for this rather wasteful device was removed by the Duda and Hart (1972) approach, which replaces the slope-intercept formulation with the so-called “normal”  $(\theta, \rho)$  form for the straight line (see Fig. 10.1):

$$\rho = x \cos \theta + y \sin \theta \quad (10.4)$$

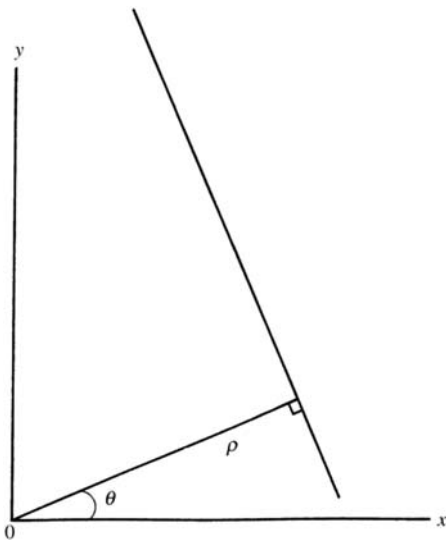


**FIGURE 10.1**

Normal  $(\theta, \rho)$  parametrization of a straight line.

To apply the method using this form, the set of lines passing through each point  $P_i$  is represented as a set of sine curves in  $(\theta, \rho)$  space: e.g., for point  $P_1(x_1, y_1)$  the sine curve has equation:

$$\rho = x_1 \cos \theta + y_1 \sin \theta \quad (10.5)$$

Then multiple hits in  $(\theta, \rho)$  space indicate, via their  $\theta, \rho$  values, the presence of lines in the original image.

Each of the methods described above has the feature that it employs an “abstract” parameter space in which multiple hits are sought. Above we talked about “plotting” points in parameter space but in fact the means of looking for hits is to seek peaks which have been built by *accumulation* of data from various sources. Although it might be possible to search for hits by logical operations such as use of the logical AND function, the Hough method gains considerably by *accumulating evidence* for events by a *voting scheme*. It will be seen below that this is the source of the method’s high degree of robustness.

Although the methods described above are mathematically elegant and are capable of detecting lines (or sets of collinear points—which may be completely isolated from each other) amid considerable interfering signals and noise, they are subject to considerable computational problems. The reason for this is that every prominent point in the original image gives rise to a great many votes in parameter space, so for a  $256 \times 256$  image the  $(m, c)$  parametrization requires 256 votes to be accumulated, while the  $(\theta, \rho)$  parametrization requires a similar number—360 if the  $\theta$  quantization is to be fine enough to resolve  $1^\circ$  changes in line orientation. (It should be remarked that it does not matter in what way the “prominent points” are prominent: they may in fact be edge points, dark specks, centers of holes, and so on. Later we shall consistently take them to be edge points.)

Several workers tried to overcome this problem, and Dudani and Luk (1978) tackled it by trying to separate out the  $\theta$  and  $\rho$  estimations. They accumulated votes first in a 1-D parameter space for  $\theta$ —i.e., a histogram of  $\theta$  values: note that such a histogram is itself a simple form of HT. (Indeed, it is now common for any process to be called an HT if it involves accumulating votes in a parameter space, with the intention of searching for significant peaks to find properties of the original data.) Having found suitable peaks in the  $\theta$  histogram, they then built a  $\rho$  histogram for all the points that contributed votes to a given  $\theta$  peak, and repeated this for all  $\theta$  peaks. Thus two 1-D spaces replace the original 2-D parameter space, with very significant savings in storage and load. However, two-stage methods of this type tend to be less accurate since the first stage is less selective: biased  $\theta$  values may result from pairs of lines that would be well separated in a 2-D space. In addition, any error in estimating  $\theta$  values is propagated to the  $\rho$  determination stage, making values of  $\rho$  even less accurate. For this reason Dudani and Luk added a final least-squares fitting stage to complete the accurate analysis of straight edges present in the image. (Note that many workers have found that using the least-squares technique tends to weight up the contribution of less accurate points, including those that have nothing to do with the line in

question. To understand the limitations of least squares, see the Appendix on Robust Statistics.)

From a practical point of view, to proceed with this method of line detection, it is first necessary to obtain the local components of intensity gradient, and then deduce the gradient magnitude  $g$  and threshold it to locate each edge pixel in the image.  $\theta$  may be estimated using the arctan function in conjunction with the local edge gradient components  $g_x$ ,  $g_y$ :

$$\theta = \arctan(g_y/g_x) \quad (10.6)$$

As the arctan function has period  $\pi$ ,  $\pm\pi$  may have to be added to obtain a principal value in the range  $-\pi$  to  $+\pi$ : this can be decided from the signs of  $g_x$  and  $g_y$ . (Note that in C++, the basic arctan function is *atan*, with a single argument, which should be  $g_y/g_x$  used as indicated above. However, the C++ *atan2* function has two arguments, and if  $g_y$  and  $g_x$  are used, respectively, for these, the function automatically returns an angle in the range  $-\pi$  to  $\pi$ .) Once  $\theta$  is known,  $\rho$  can be found from Eq. (10.4).

Finally, note that straight lines and straight edges are different and need to be detected differently. (Straight *edges* are probably more common and appear as object boundaries, whereas straight *lines* are typified by telephone wires in outdoor scenes.) In fact, we have concentrated above on using the HT to locate straight edges, starting with edge detectors. Straight line segments may be located using Laplacian-type operators and their orientations are defined over a range  $0^\circ$  to  $180^\circ$  rather than  $0^\circ$  to  $360^\circ$ : this makes HT design subtly different. For concreteness, in the remainder of this chapter we concentrate on straight *edge* detection.

### 10.2.1 LONGITUDINAL LINE LOCALIZATION

The preceding sections have provided a variety of means for locating lines in digital images and finding their orientations. However, these methods are insensitive to where along an infinite idealized line an observed segment appears. The reason for this is that the fit includes only two parameters. There is some advantage to be gained in this, in that partial occlusion of a line does not prevent its detection: indeed, if several segments of a line are visible, they can all contribute to the peak in parameter space, hence improving sensitivity. On the other hand, for full image interpretation, it is useful to have information about the longitudinal placement of line segments.

This is achieved by a further stage of processing. The additional stage involves finding which points contributed to each peak in the main parameter space, and carrying out connectivity analysis in each case. (When the slope of the line is less than  $45^\circ$ , this is most conveniently achieved by projecting it along the  $x$ -axis, and when greater than  $45^\circ$ , by projecting it along the  $y$ -axis: similarly for orientations in other quadrants.) Dudani and Luk (1978) called this process “*xy-grouping*.” It is not vital that the line segments should be 4- or 8-connected—just that

there should be sufficient points on them so that adjacent points are within a threshold distance apart, i.e., groups of points are merged if they are within the prespecified distance (typically, 5 pixels). Finally, segments shorter than a certain minimum length (also typically  $\sim 5$  pixels) can be ignored as too insignificant to help with image interpretation.

### 10.3 THE FOOT-OF-NORMAL METHOD

An alternative means of saving computation (Davies, 1986) eliminates the use of trigonometric functions such as arctan by employing a different parametrization scheme. As noted earlier, the methods so far described all employ abstract parameter spaces in which points bear no immediately obvious visual relation to image space. In the alternative scheme, the parameter space is a second image space, which is congruent to image space (i.e., parameter space is like image space, *and* each point in parameter space holds information that is immediately relevant to the corresponding point in image space).

This type of parameter space is obtained in the following way. First, each edge fragment in the image is produced much as required previously so that  $\rho$  can be measured, but this time the foot of the normal from the origin is itself taken as a voting position in parameter space (Fig. 10.1). Clearly, the foot-of-normal position embodies all the information previously carried by the  $\rho$  and  $\theta$  values, and mathematically the methods are essentially equivalent. However, the details differ, as will be seen.

The detection of straight edges starts with the analysis of (1) local pixel coordinates  $(x, y)$  and (2) the corresponding local components of intensity gradient  $(g_x, g_y)$  for each edge pixel. Taking  $(x_0, y_0)$  as the foot of the normal from the origin to the relevant line (produced if necessary—see Fig. 10.2), it is found that

$$g_y/g_x = y_0/x_0 \quad (10.7)$$

$$(x - x_0)x_0 + (y - y_0)y_0 = 0 \quad (10.8)$$

These two equations are sufficient to compute the two coordinates  $(x_0, y_0)$ . Solving for  $x_0$  and  $y_0$  gives

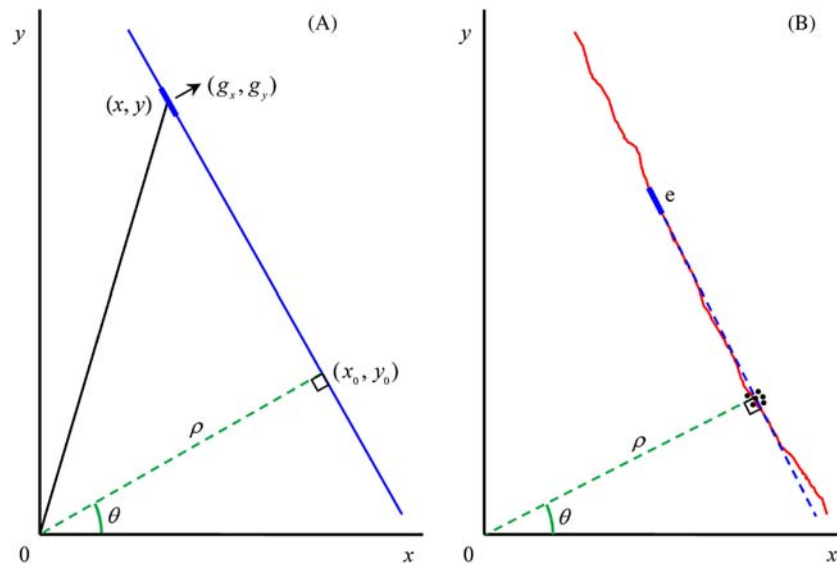
$$x_0 = v g_x \quad (10.9)$$

$$y_0 = v g_y \quad (10.10)$$

where

$$v = \frac{x g_x + y g_y}{g_x^2 + g_y^2} \quad (10.11)$$

Notice that these expressions involve only additions, multiplications, and just one division, so voting can be carried out efficiently using this formulation.



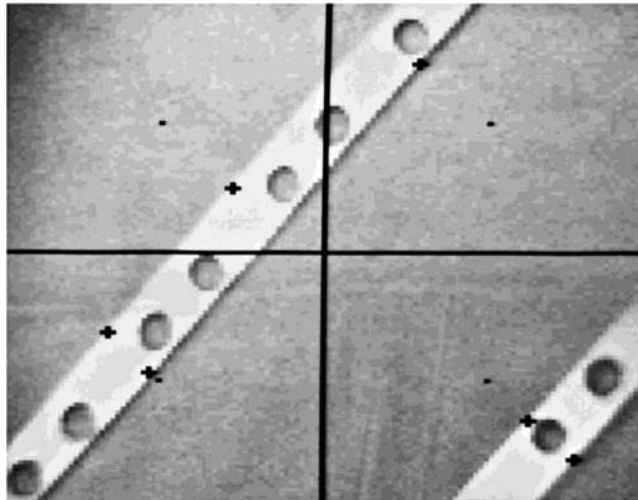
**FIGURE 10.2**

Image space parametrization of a straight line: (A) parameters involved in the calculation (see text); (B) buildup of foot-of-normal positions in parameter space for a more practical situation, where the line is not exactly straight:  $e$  is a typical edge fragment leading to a single vote in parameter space.

### 10.3.1 APPLICATION OF THE FOOT-OF-NORMAL METHOD

Although the foot-of-normal method is mathematically similar to the  $(\theta, \rho)$  method, it is unable to determine line orientation directly with quite the same degree of accuracy. This is because the orientation accuracy depends on the fractional accuracy in determining  $\rho$ —which in turn depends on the absolute magnitude of  $\rho$ . Hence for small  $\rho$  the orientation of a line that is predicted from the position of the peak in parameter space will be relatively inaccurate, even though the *position* of the foot-of-normal is known accurately. However, accurate values of line orientation can always be found by identifying the points that contributed to a given peak in the foot-of-normal parameter space and making them contribute to a  $\theta$  histogram, from which line orientation may be determined much more accurately.

Typical results with the above method are shown in Fig. 10.3: here it was applied in subimages of size  $64 \times 64$  within  $128 \times 128$  images. Clearly, some of the objects in these pictures are grossly overdetermined by their straight edges, so low  $\rho$  values are not a major problem. For those peaks where  $\rho > 10$ , line orientation is estimated within approximately  $2^\circ$ ; as a result, these objects are located within 1 pixel and orientated within  $1^\circ$  by this technique, without the necessity for  $\theta$  histograms. Two of the subimages in Fig. 10.3 contain line segments that



**FIGURE 10.3**

Results of image space parametrization of mechanical parts. The dot at the center of each quadrant is the origin used for computing the image space transform. The crosses are the positions of peaks in parameter space which mark the individual straight edges. For further explanation, see text.

are not detected. This is due partly to their relatively low contrast, higher noise levels, above average fuzziness, or short length. However, it is also due to the thresholds set on the initial edge detector and on the final peak detector: when these are set at lower values, additional lines are detected but other noise peaks also become prominent in parameter space, and each of these needs to be checked in detail to confirm the presence of the corresponding line in the image. This is one aspect of a general problem that arises right through the field of image analysis.

---

## 10.4 USING RANSAC FOR STRAIGHT LINE DETECTION

RANSAC is an alternative model-based search schema that can often be used instead of the HT. In fact, it is highly effective when used for line detection, which is why the method is introduced here. The strategy can be construed as a voting scheme, but it is used in a different way from that in the HT. The latter operates by building up the evidence for instances of target objects in the form of votes in parameter space, and then making decisions about their existence (or by making hypotheses about their existence that can subsequently be checked out). RANSAC operates by making a sequence of hypotheses about the target objects, and determines the support for each of them by counting how many data points agree with them. As might be expected, for any potential target object,

only the hypotheses with the maximum support are retained at each stage. This results in more compact information storage than for the HT: i.e., for RANSAC a list of hypotheses is held in current memory, whereas for the HT a whole parameter space, which is usually only sparsely populated, is held in memory. Thus the RANSAC data are abstract lists, whereas the HT data can often be viewed as pictures in parameter space—as in the case of the foot-of-normal line detector. None of this prevents the RANSAC output being displayed (e.g., as straight lines) in image space; nor does it prevent the HT being accumulated using a list representation.

To explain RANSAC in more detail, we take the case of line detection. As for the HT, we start by applying an edge detector and locating all the edge points in the image. As we shall see, RANSAC operates best with a limited number of points, so it is useful to find the edge points that are local maxima of the intensity gradient image. (This does not correspond to the type of nonmaximum suppression used in the Canny operator, which produces thin connected *strings* of edge points, but to individual *isolated* points: we shall return to this point below.) Next, to form a straight line hypothesis, all that is necessary is to take any pair of edge points from the list of  $N$  that remain after applying the local maximum operation. For each hypothesis we run through the list of  $N$  points finding how many points  $M$  support the hypothesis. Then we take more hypotheses (more pairs of edge points) and at each stage retain only the one giving maximum support  $M_{\max}$ . This process is shown in Table 10.1.

The algorithm in Table 10.1 corresponds to finding the center of the highest peak in parameter space in the case of the HT. To find all the lines in the image, the most obvious strategy is the following: find the first line, then eliminate all the points that gave it support; then find the next line and eliminate all the points that gave it support; and so on until all the points have been eliminated from the list. The process may be written more compactly in the form:

```
repeat {
  find line;
  eliminate support;
}
until no data points remain;
```

Such a strategy carries the problem that if lines cross each other, support for the second line (which will necessarily be the weaker one) could have less support than it deserves. However, this should only be a serious disadvantage if the image is severely cluttered with lines. Nevertheless, the process is sequential and as such the results (i.e., the exact line locations) will depend on the order in which lines are eliminated, as the support regions will be minutely altered at each stage. Overall, the interpretation of complex images almost certainly has to proceed sequentially, and there is significant evidence that the human eye-brain system interprets images in this way, following early cues in order to progressively make sense of the data. Interestingly, the HT seems to escape from this by the potential capability for *parallel* identification of peaks: while for simple images this may

well be true, for complicated images containing many overlapping edges, there will again be the need for sequential analysis of the type envisaged above (e.g., see the “back-projection” method of Gerig and Klein, 1986). The point is that with the particular list representation employed by RANSAC, we are *immediately* confronted with the problem of how to identify multiple targets, whereas for the reasons given above this doesn’t immediately happen with the HT. Finally, on the plus side, successive elimination of support points necessarily makes it progressively easier and less computation intensive to find subsequent target objects. But the process itself is not cost-free, as the whole RANSAC procedure in Table 10.1 has to be run twice per line in order to identify the support points that have to be eliminated.

Next we consider the computational load of the RANSAC process. If there are  $N$  edge points, the number of potential lines will be  ${}^N C_2$ , corresponding to a computational load of  $O(N^2)$ . However, finding the support for each line will involve  $O(N)$  operations, so the overall computational load will be  $O(N^3)$ . In addition, the need to eliminate the support points for each line found will require computation proportional to the number of lines  $n$ , amounting to only  $O(nN)$ , and this will have little effect on the overall computational load.

One point that has not yet been made is that all  $N$  edge points will not arise from straight lines: some will arise from lines, some from curves, some from general background clutter, and some from noise. To limit the number of false positives, it will be useful to set a support threshold  $M_{\text{thr}}$  such that potential lines for which  $M > M_{\text{thr}}$  are most likely to be true straight lines, while others are most likely to be artifacts, such as parts of curves or noise points. Thus the RANSAC procedure can be terminated when  $M_{\text{max}}$  drops below  $M_{\text{thr}}$ . Of course, it may be required to retain only “significant” lines, e.g., those having length greater than  $L$  pixels. In that case, analysis of each line could allow many more points to be eliminated as the RANSAC algorithm proceeds. Another factor is whether hypotheses corresponding to pairs whose points are too close together should be taken into account. In particular, it might be considered that points closer together than 5 pixels would be superfluous as they would be likely to have much reduced chance of pointing along the direction of a line. However, it turns out that RANSAC is fail-safe in this respect, and there is some gain from keeping pairs with quite small separations, as some of the resulting hypotheses can actually be more accurate than any others. Overall, restricting pairs by their separations can be a useful way of reducing computational load, bearing in mind that  $O(N^3)$  is rather high. Here, we should recall that the load for the HT is  $O(N^2)$  during voting, if pairs of points are used, or  $O(N)$  if single edge points and their gradients are used instead.

As we have just seen, RANSAC does not compare well with the HT regarding computational load, so it is better to employ RANSAC when  $N$  can be reduced in some way. This is why it is useful to use  $N$  local maxima rather than a full list of edge points in the form of strings of edge points generated by nonmaximum suppression or *a fortiori* those existing before nonmaximum suppression. Indeed,



there is much to be gained by repeated random sampling from the full list until sufficient hypotheses have been tested to be confident that all significant lines have been detected. [Note that these ideas reflect the original meaning of the term RANSAC, which stands for RANdom SAMpling Consensus—“consensus” indicating that any hypothesis has to form a consensus with the available support data.] Using this procedure, the computational load is reduced from  $O(N^3)$  toward  $O(N^2)$  or even  $O(N)$  (it is difficult to predict the resulting computational complexity: in any case, the achievable computational load will be highly data dependent). Confidence that all significant lines have been detected can be obtained by estimating the risk that a significant line will be missed because no representative pair of points lying on the line was considered. This aspect of the problem will be examined more fully in [Section A.6](#) of the Appendix on Robust Statistics.

Before proceeding further, we shall briefly consider another way of reducing computational load that is, by using the connected strings of edge points resulting from nonmaximum suppression, but in addition eliminating those that are very short and coding the longer ones as isolated points every  $p$  pixels, where  $p \approx 10$ . In this way, there would be far fewer points than for our earlier paradigm, and also those that are employed would have increased coherence and probability of lying on straight edges; hence there would be a concentration on high quality data, whereas the  $O(N^3)$  computation factor would be dramatically reduced. Clearly, in high noise situations this would not work well: it is left to the reader to judge how well it would work for the sets of edges located by the Canny operator in [Figs. 5.7 and 5.8](#).

We are now in a position to consider actual results obtained by applying RANSAC to straight line detection. In the tests described, pairs of points were employed as hypotheses, and all edge points were local maxima of the intensity gradient. The cases shown in [Fig. 10.4](#) correspond to detection of a block of wood in the shape of an icosahedron, and a pair of laparoscopic tools with parallel sides. Note that one line on the right of [Fig. 10.4A](#) was missed because a lower limit had to be placed on the level of support for each line: this was necessary because below this level of support the number of chance collinearities rose dramatically even for the relatively small number of edge points shown in [Fig. 10.4B](#), leading to a sharp rise in the number of false positive lines. [Figs. 23.2 and 23.3](#) show RANSAC being used to locate road lane markings. The same version of RANSAC was used in all the above cases, albeit in the case of [Fig. 23.3](#) a refinement was added to allow improved elimination of points on lines that had already been located (see below). Overall, this set of examples shows that RANSAC is a highly important contender for location of straight lines in digital images. Not discussed here is the fact that RANSAC is useful for obtaining robust fits to many other types of shape, in 2-D and in 3-D.

It should be mentioned that one characteristic of RANSAC is that it is less influenced by aliasing along straight lines than the HT. This is because HT peaks tend to be fragmented by aliasing, so the best hypotheses can be difficult to obtain without excessive smoothing of the image. The reason why RANSAC wins in

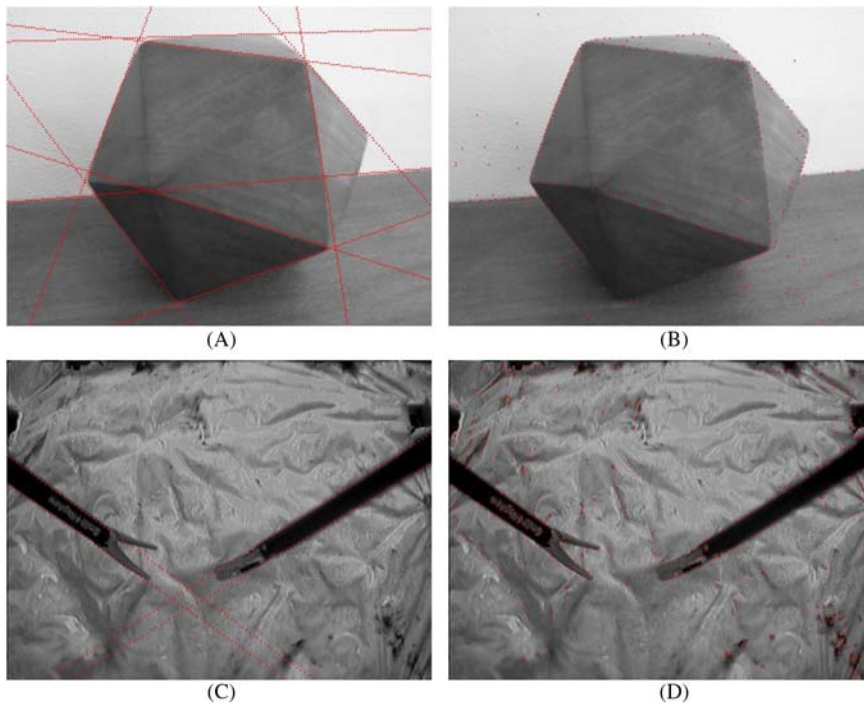


**FIGURE 10.4**

Straight line location using the RANSAC technique. (A) shows an original gray-scale image with various straight edges located using the RANSAC technique. (B) shows the edge points fed to RANSAC for (A). These were isolated points which were local maxima of the gradient image. (C) shows the straight edges of a pair of laparoscopic tools—a cutter and a gripper—which have been located by RANSAC. (D) shows the points fed to RANSAC for (C). In (A), three edges of the icosahedron are missed. This is because they are roof edges with low contrast and low intensity gradient. RANSAC missed a fourth edge because of a lower limit placed on the level of support (see text).

this context is that it does not rely on individual hypotheses being accurate: rather it relies on enough hypotheses easily being generatable, and by the same token, discardable.

Finally, we return to the above comment about obtaining improved deletion of points on lines that have already been located. Suppose the cross-section of a line is characterized by a (lateral) Gaussian distribution of edge points. As a true Gaussian extends to infinity in either direction, the support region is not well defined, but for high accuracy it is reasonable to take it as the region within  $\pm\sigma$  of the center-line of the line. However, if just these points are eliminated, the remaining points near the line could later on give rise to alternative lines or combine with other points to lead to false positives. It is therefore, better

(Mastorakis and Davies, 2011) to make the “delete distance”  $d_d$  larger than the “fit distance”  $d_f$  that is used for support during detection, e.g.,  $d_d = 2\sigma$  or  $3\sigma$ , where  $d_f = \sigma$ . ( $d_d \approx 3\sigma$  can be considered to be close to optimal because 99.9% of the samples in a Gaussian distribution lie within  $\pm 3\sigma$ .) Fig. 23.3 shows instances in which the fit distance is 3 pixels and the delete distance has values of 3, 6, 10, and 11 pixels, showing the advantages that can be gained by making  $d_d$  significantly greater than  $d_f$ . Fig. 23.4 shows a flowchart of the algorithm used in this case.

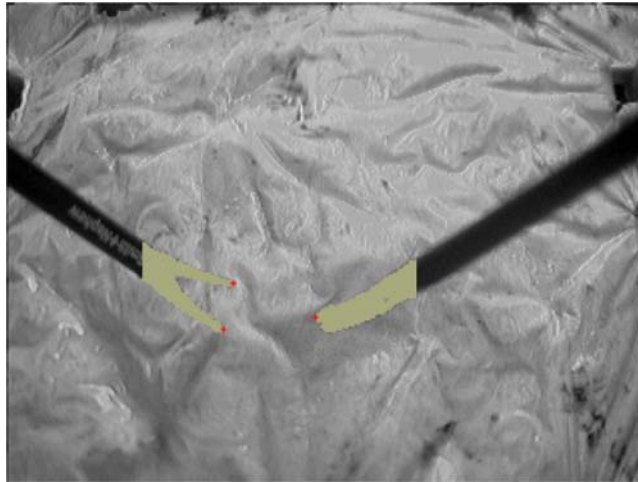
---

## 10.5 LOCATION OF LAPAROSCOPIC TOOLS

The previous section showed how RANSAC can provide a highly efficient means for locating straight edges in digital pictures, and gave an example of its use to locate the handles of laparoscopic tools. These are used for various forms of “key-hole” surgery: specifically, one tool (e.g., a cutter) might be inserted through one incision and another (e.g., a gripper) through a second incision. Additional incisions are needed for viewing via a laparoscope which employs optical fiber technology, and for inflating the cavity—for example, the abdominal or chest cavity. In this section, we consider what information can be obtained via the laparoscope.

Fig. 10.4C shows laparoscopic gripper and cutter tools being located in a simulated flesh background. The latter will normally be a wet surface that is largely red and will exhibit many regions that are close to being specularly reflective. The large variations in intensity that occur under these conditions make the scene quite difficult to interpret. Although the surgeon who is in control of the instruments can learn a lot about the scene through tactile feedback and thus bolster his understanding of it, other people viewing the scene, e.g., on a TV monitor or computer, are liable to find it highly confusing. The same will apply for any computer attempting to interpret, analyze, or record the progress of an operation. These latter tasks are potentially important for logging operations, for training other doctors, for communicating with specialists elsewhere, or for analyzing the progress of the operation during any subsequent debriefing. It would therefore be useful if the exact locations, orientations, and other parameters of the tools could be determined at least relative to the frame of reference of the laparoscope. To this end, RANSAC has provided important 2-D data on the location of the tool handles. Assessing the vanishing points of the pairs of lines from the handles also provides 3-D information. Clearly, further information can be obtained from the coordinates of the ends of the tools.

To identify the ends of the tools, the ends of the handles are first located: this is a straightforward task requiring knowledge of the exact ends of the RANSAC support regions for the tool handle edges. The remainder of the tool ends can now be located by initial approximate prediction, adaptive thresholding, and connected components analysis (Fig. 10.5), special attention being paid to accurate location of the tips of the tool ends. In Fig. 10.5 this is achieved within  $\sim 1$  pixel for the gripper on the left, and slightly less accurately for the closed cutter on the right.

**FIGURE 10.5**

Tips of laparoscopic tools located from the parts highlighted in gray.

If the gripper had been open, accuracy would have been similar to that for the gripper. Note that, because of the complex intensity patterns in the background, it would have been difficult to locate the tool ends without first identifying the tool handles.

Each of the laparoscopic tools referred to above has  $(X, Y, Z)$  position coordinates, together with rotations  $\psi$  within the image plane  $(x, y)$ ,  $\theta$  away from the image plane (toward the  $Z$ -axis), and  $\varphi$  about the axis of the handle; in addition, each tool end has an opening angle  $\alpha$  (Fig. 10.6). It is bound to be difficult to obtain all seven parameters with any great accuracy from a single monocular view. However, in principle, using an exact CAD model of the tool end, this should be possible with  $\sim 15\text{--}20^\circ$  accuracy for the angles. The 2-D information about the centerlines and widths of the handles, the convergence of the handle edges, the exact positions of the tips of the tools, should together permit such a 3-D analysis to be carried out. Here we have concentrated on the 2-D analysis: details of the relevant 3-D background theory needed to proceed further can be found in Part 3.

---

## 10.6 HOUGH-BASED SCHEMES FOR CIRCULAR OBJECT DETECTION

In this section we present a HT-based approach for circular object detection: the purpose will be to replace the non-robust centroidal profile method outlined in Chapter 9—which is usefully summarized in Table 10.2.

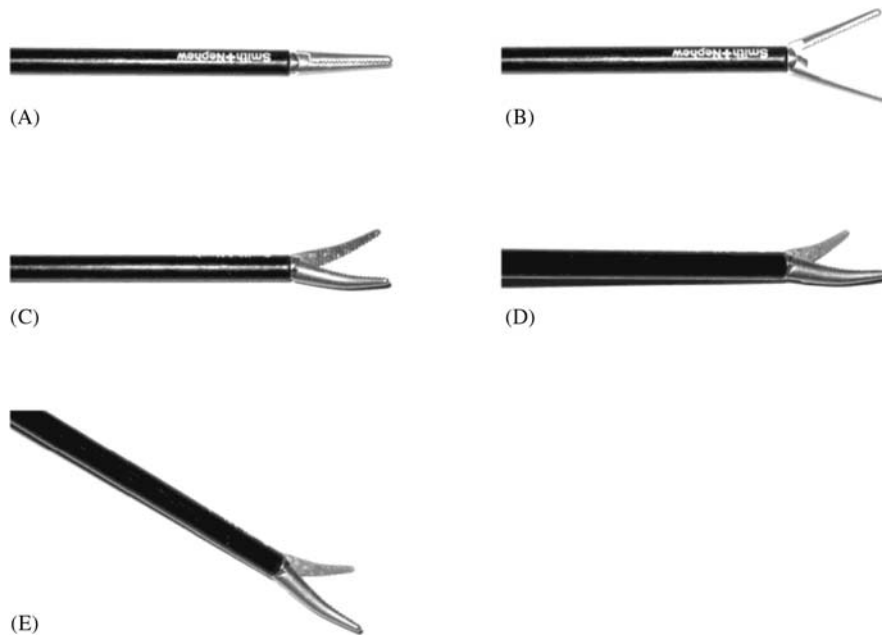


**FIGURE 10.6**

Orientation parameters for a laparoscopic tool. (A) A gripper tool with closed jaws. (B) Gripper with jaws separated by an angle  $\alpha$ . (C) Gripper rotated through an angle  $\varphi$  about a horizontal axis. (D) Gripper tipped through an angle  $\theta$  away from the image plane. (E) Gripper rotated through an angle  $\psi$  about the camera optical axis.

**Table 10.2** Procedure for Finding Objects Using  $(r, \theta)$  Boundary Graphs

1. Locate edges within the image
2. Link broken edges
3. Thin thick edges
4. Track around object outlines
5. Generate a set of  $(r, \theta)$  plots
6. Match  $(r, \theta)$  plots to standard templates

*This procedure is not sufficiently robust with many types of real data e.g., in the presence of noise, distortions in product shape, etc.: in fact, it is quite common to find the tracking procedure veering off and tracking around shadows or other artifacts.*

In the original HT method for finding circles (Duda and Hart, 1972), the intensity gradient is first estimated at all locations in the image and then thresholded to give the positions of significant edges. Then the positions of all possible center locations—namely all points a distance  $R$  away from every edge pixel—are accumulated in parameter space,  $R$  being the anticipated circle radius. Parameter space can be a general storage area but when looking for circles it is convenient to

make it congruent to image space: in that case possible circle centers are accumulated in a new plane of image space. Finally, parameter space is searched for peaks which correspond to the centers of circular objects. Since edges have nonzero width and noise will always interfere with the process of peak location, accurate center location requires the use of suitable averaging procedures (Davies, 1984c; Brown, 1984).

This approach clearly requires a very large number of points to be accumulated in parameter space and so a revised form of the method has now become standard: in this approach, locally available edge orientation information at each edge pixel is used to enable the exact positions of circle centers to be estimated (Kimme et al., 1975). This is achieved by moving a distance  $R$  along the edge normal at each edge location. Thus the number of points accumulated is equal to the number of edge pixels in the image: this represents a significant saving in computational load. (We assume here that objects are known to be *either* lighter *or* darker than the background, so that it is only necessary to move along the edge normal in one direction.) For this procedure to be practicable, the edge detection operator that is employed must be highly accurate. Fortunately, the Sobel operator is able to estimate edge orientation to  $1^\circ$  and is very simple to apply (Chapter 5: Edge Detection). Thus the revised form of the transform is viable in practice.

As was seen in Chapter 5, Edge Detection, once the Sobel convolution masks have been applied, the local components of intensity gradient  $g_x$  and  $g_y$  are available, and the magnitude and orientation of the local intensity gradient vector can be computed using the formulae:

$$g = (g_x^2 + g_y^2)^{1/2} \quad (10.12)$$

and

$$\theta = \arctan(g_y/g_x) \quad (10.13)$$

However, use of the arctan operation is not necessary when estimating center location coordinates  $(x_c, y_c)$  since the trigonometric functions can be made to cancel out:

$$x_c = x - R(g_x/g) \quad (10.14)$$

$$y_c = y - R(g_y/g) \quad (10.15)$$

the values of  $\cos \theta$  and  $\sin \theta$  being given by:

$$\cos \theta = g_x/g \quad (10.16)$$

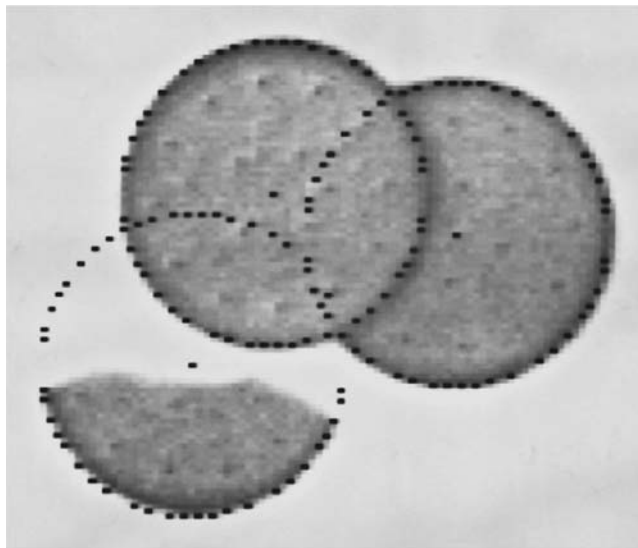
$$\sin \theta = g_y/g \quad (10.17)$$

In addition, the usual edge thinning and edge linking operations—which normally require considerable amounts of processing—can be avoided if a little extra smoothing of the cluster of candidate center points is performed (Davies, 1984c) (Table 10.3). Thus this Hough-based approach can be a very efficient one for locating the centers of circular objects, virtually all the superfluous operations having

**Table 10.3** A Hough-Based Procedure for Locating Circular Objects

1. Locate edges within the image
2. Link broken edges
3. Thin thick edges
4. For every edge pixel, find a candidate center point
5. Locate all clusters of candidate centers
6. Average each cluster to find accurate center locations

*This procedure is particularly robust. It is largely unaffected by shadows, image noise, shape distortions, and product defects. Note that stages 1–3 of the procedure are identical to stages 1–3 in Table 10.2. However, in the Hough-based method, computation can be saved, and accuracy actually increased, by omitting stages 2 and 3.*

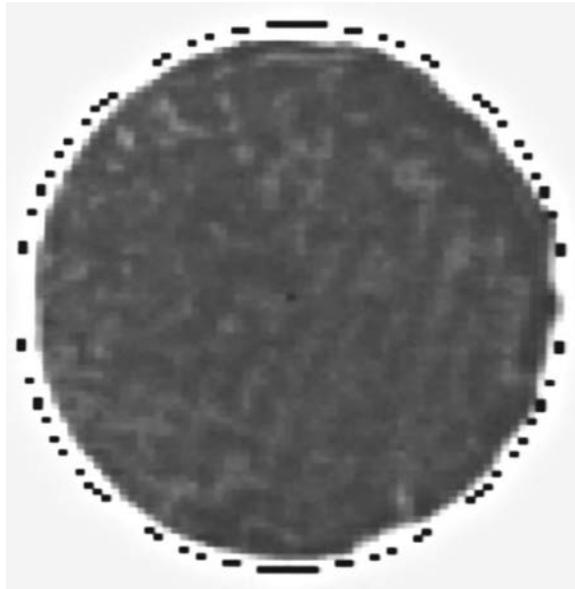
**FIGURE 10.7**

Location of broken and overlapping biscuits, showing the robustness of the center location technique. Accuracy is indicated by the black dots which are each within 1/2 pixel of the radial distance from the center.

© IFS 1984.

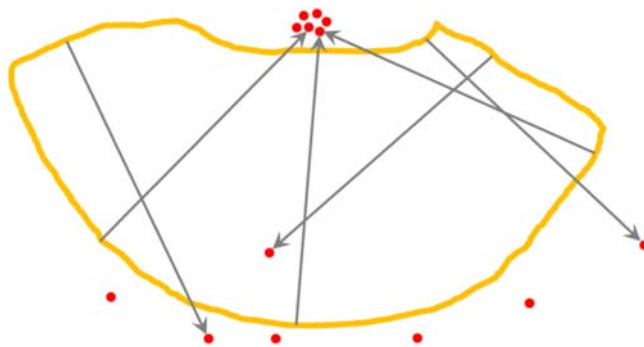
been eliminated, leaving only edge detection, location of candidate center points, and center point averaging to be carried out. In addition, the method is highly robust, so if part of the boundary of an object is obscured or distorted, the object center is still located accurately. In fact, the results are often quite impressive (see e.g., Figs. 10.7 and 10.8). The reason for this useful property is clear from Fig. 10.9.

The efficiency of the above technique means that it takes slightly less time to perform the actual HT part of the calculation than to evaluate and threshold the

**FIGURE 10.8**

Location of a biscuit with a distortion, showing a chocolate-coated biscuit with excess chocolate on one edge. Note that the computed center has not been “pulled” sideways by the protuberances. For clarity, the black dots are marked 2 pixels outside the normal radial distance.

© IFS 1984.

**FIGURE 10.9**

Robustness of the Hough transform when locating the center of a circular object. The circular part of the boundary gives candidate center points that focus on the true center, whereas the irregular broken boundary gives candidate center points at random positions. In this case, the boundary is approximately that of the broken biscuit shown in [Fig. 10.7](#).



intensity gradient over the whole image. Part of the reason for this is that the edge detector operates within a  $3 \times 3$  neighborhood and necessitates some 12 pixel accesses, four multiplications, eight additions, two subtractions, and an operation for the evaluation of the square root of sum of squares (Eq. (10.12)).

Overall, the dictates of accuracy imply that candidate center location requires significant computation. However, substantial increases in speed are still possible by software means alone, as will be seen later in the chapter. Meanwhile, we consider the problems that arise when images contain circles of many different radii, or for one reason, or another radii are not known in advance.

---

## 10.7 THE PROBLEM OF UNKNOWN CIRCLE RADIUS

There are a number of situations where circle radius is initially unknown. One such situation is where a number of circles of various sizes are being sought—as in the case of coins, or different types of washer. Another is where the circle size is variable—as for food products such as biscuits—so that some tolerance must be built into the system. In general, all circular objects have to be found and their radii measured. In such cases, the standard technique is to accumulate candidate center points simultaneously in a number of parameter planes in a suitably augmented parameter space, each plane corresponding to one possible radius value. The centers of the peaks detected in parameter space give not only the location of each circle in two dimensions but also its radius. Although this scheme is entirely viable in principle, there are several problems in practice:

1. many more points have to be accumulated in parameter space;
2. parameter space requires much more storage;
3. significantly greater computational effort is involved in searching parameter space for peaks.

To some extent this is to be expected, since the augmented scheme enables more objects to be detected directly in the original image.

It is shown below that the last two problems may largely be eliminated. This is achieved by using just one parameter plane to store all the information for locating circles of different radii, i.e., accumulating not just one point per edge pixel but a whole line of points along the direction of the edge normal in this one plane. In practice, the line need not be extended indefinitely in either direction but only over the restricted range of radii over which circular objects or holes might be expected.

Even with this restriction, a large number of points are being accumulated in a single parameter plane, and it might be thought initially that this would lead to such a proliferation of points that almost any “blob” shape would lead to a peak in parameter space which might be interpreted as a circle center. However, this is not so and significant peaks normally result only from genuine circles and closely related shapes.

To understand the situation, consider how a sizeable peak can arise at a particular position in parameter space. This can happen only when a large number of

radial vectors from this position meet the boundary of the object normally. In the absence of discontinuities in the boundary, a contiguous set of boundary points can only be normal to radius vectors if they lie on the arc of a circle. Nevertheless, errors in the measurement of local edge orientation make the scheme slightly less specific in its capability for detecting circular objects.

Finally, note that the information on radial distance has been lost by accumulating all votes in a single parameter plane. Hence, a further stage of analysis is needed to measure object radius. This extra stage of analysis normally involves negligible additional computation, because the search space has been narrowed down so severely by the initial circle location procedure: hence only a 1-D HT need be used, with radial distance as the relevant parameter.

### 10.7.1 PRACTICAL RESULTS

The method described above works much as expected, the main problems arising with small circular objects (of radii less than about 20 pixels) at low resolution (Davies, 1988b). Essentially, the problems are those of lack of discrimination in the precise shapes of small objects (see Fig. 10.10), as anticipated above. As suggested earlier, this can frequently be turned to advantage in that the method becomes a circular feature detector for small radii (see Fig. 10.10, where a wing nut is located).

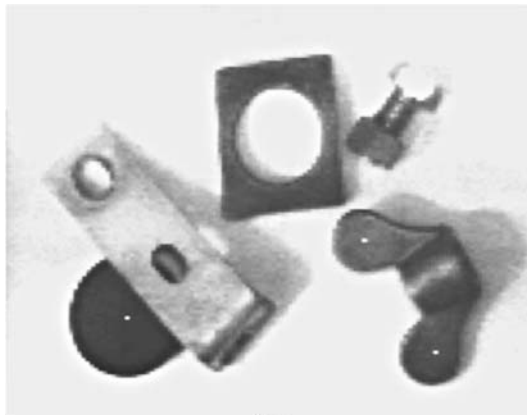
As required, objects are detected reliably even when they are partly occluded. However, it is clear from Fig. 10.10 that high accuracy of center location cannot be expected when a single parameter plane is used to detect objects over a large range of sizes: hence it is best to cut down the voting range as far as possible.

Overall, there is a tradeoff between speed and accuracy with this approach. However, the results confirm that it is possible to locate objects of various radii within a significantly conflated parameter space, thereby making substantial savings in storage and computation—even though the total number of votes that have to be accumulated in parameter space is not itself reduced.

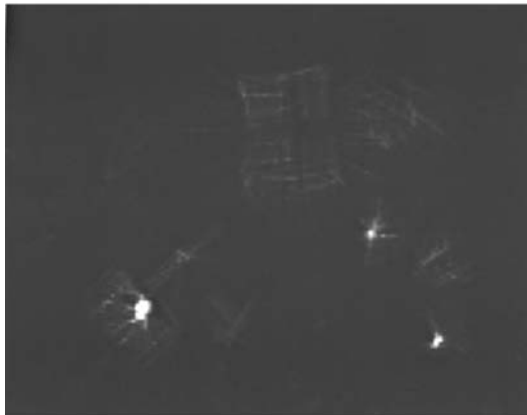
---

## 10.8 OVERCOMING THE SPEED PROBLEM

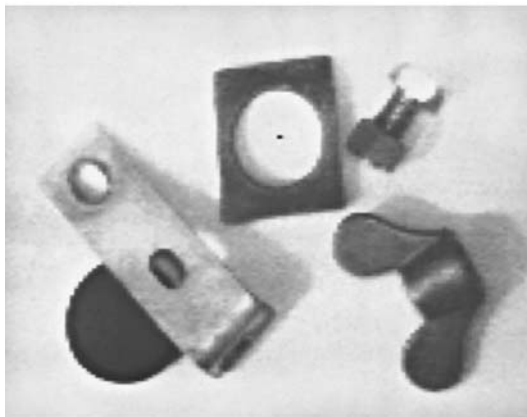
This section examines how circle detection may be carried out with significant improvement in speed. To achieve this, two methods are tried: (1) sampling the image data and (2) using a simpler edge detector. The most appropriate strategy for (1) appears to be to look only at every  $n$ th line in the image, while that for (2) involves using a small 2-element neighborhood while searching for edges (Davies, 1987d). Although this approach will lose the capability for estimating edge orientation, it will still permit horizontal and vertical chords of a circle to be bisected, thereby leading to values for the center coordinates  $x_c$ ,  $y_c$ . It also involves much less computation, the multiplications and square root calculations, and most of the divisions being eliminated or replaced by 2-element differencing



(A)



(B)



(C)

**FIGURE 10.10**

(A) Accurate simultaneous detection of a lens cap and a wing nut when radii are assumed to range from 4 to 17 pixels; (B) response in parameter space that arises with such a range of radii: note the overlap of the transforms from the lens cap and the bracket; (C) hole detection in the image of (A) when radii are assumed to fall in the range  $-26$  to  $-9$  pixels (negative radii are used since holes are taken to be objects of negative contrast): clearly, in *this* image a smaller range of negative radii could have been employed.

operations. Practical details showing the overall speed gain available using this approach are given below.

Both the original HT and the chord bisection approach lead to peak formation, though the former leads to a single 2-D peak and the latter to two 1-D peaks which have to be obtained separately. Robustness of circle detection depends on all peaks being found reliably, and this becomes less likely when objects are distorted. Clearly, if a reduced number of horizontal and vertical scan lines contribute to the 1-D peaks, this will also cause a potential reduction in the robustness of detection, i.e., the risk that a peak will be missed. In addition, there is a further factor to be considered: if only a proportion  $\alpha$  of all possible horizontal and vertical scan lines contribute to 1-D HT peaks, the signal-to-noise ratio will fall by a factor  $\sqrt{\alpha}$  and the accuracy with which the center can be located will be similarly reduced.

While the chord sampling strategy can be highly effective, it is susceptible to problems with highly textured objects: this is because too many false edges may be produced, and these can lead to chords that do not stretch across the whole object; as this leads to a further lowering of  $\alpha$  and further reduces the robustness and accuracy of the method.

### 10.8.1 PRACTICAL RESULTS

Tests (Davies, 1987d) with the images in Fig. 10.11 showed that gains in speed of more than 25 can be obtained, with values of  $\alpha$  down to less than 0.1

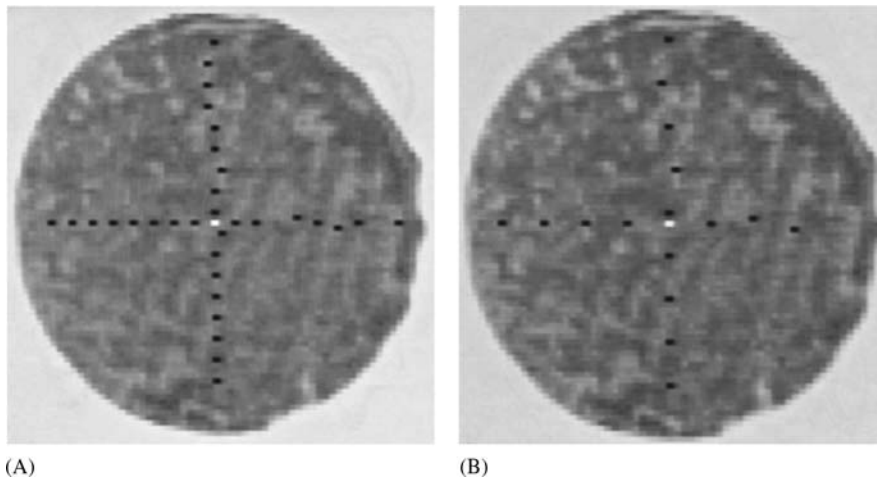


**FIGURE 10.11**

Successful object location using the chord bisection algorithm for the same initial image, using successive step sizes of 4 and 8 pixels. The black dots show the positions of the horizontal and vertical chord bisectors, and the white dot shows the position found for the center.

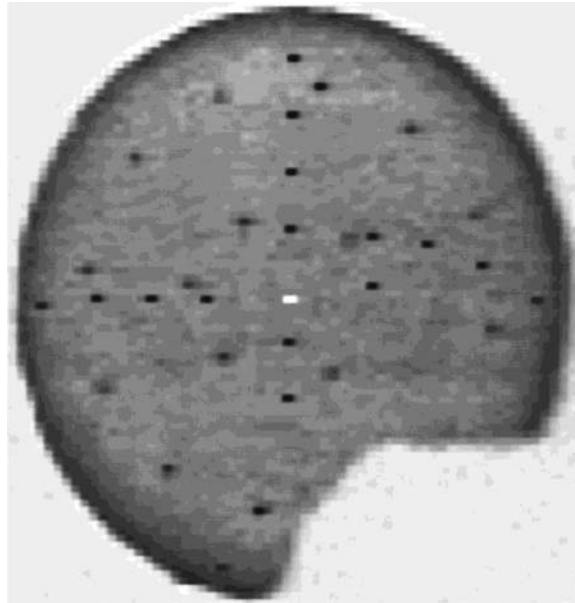


**FIGURE 10.12**

Successful location of a broken object using the chord bisection algorithm: only about one-quarter of the ideal boundary is missing.

(i.e., every 10th horizontal and vertical line scanned). The results for broken circular products (Fig. 10.12) are self-explanatory; they indicate the limits to which the method can be taken. An outline of the complete algorithm is given in Table 10.4 (note the relatively straightforward problem of disambiguating the results if there happen to be several peaks).

Fig. 11.13 shows the effect of adjusting the threshold in the 2-element edge detector. The result of setting it too low is seen in Fig. 10.13A. Here the surface texture of the object has triggered the edge detector, and the chord midpoints give rise to a series of false estimates of the center coordinates. Fig. 11.13B shows the result of setting the threshold at too high a level, so that the number of estimates of center coordinates is reduced and sensitivity suffers.

Overall, the center location procedure described above is more than an order of magnitude faster than the standard HT and often as much as 25 times faster. This could be quite important in exacting real-time applications. Robustness is so good that the method tolerates at least one-quarter of the circumference of an object being absent, making it adequate for many real applications. Importantly, it is entirely clear what types of image data would be likely to confuse the algorithm.

**Table 10.4** Outline of the Fast Center-Finding Algorithm

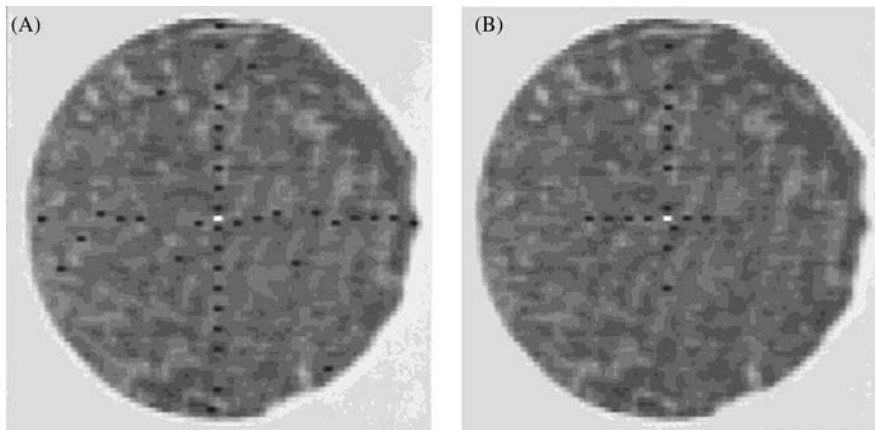
---

```

y = 0;
do {
    scan horizontal line y looking for start and end of each object;
    calculate midpoints of horizontal object segments;
    accumulate midpoints in 1-D parameter space (x space);
    // note that the same space, x space, is used for all lines y
    y = y + d;
} until y > ymax;
x = 0;
do {
    scan vertical line x looking for start and end of each object;
    calculate midpoints of vertical object segments;
    accumulate midpoints in 1-D parameter space (y space);
    // note that the same space, y space, is used for all lines x
    x = x + d;
} until x > xmax;
find peaks in x space;
find peaks in y space;
test all possible object centres arising from these peaks;
// the last step is necessary only if  $\exists > 1$  peak in each space
// d is the horizontal and vertical step-size (= 1/ $\alpha$ )

```

---

**FIGURE 10.13**

Effect of misadjustment of the gradient threshold: (A) effect of setting the threshold too low, so that surface texture muddles the algorithm; (B) loss of sensitivity on setting the threshold too high.

## 10.9 ELLIPSE DETECTION

The problem of detecting ellipses may seem only marginally more complex than that of detecting circles—as eccentricity is only a single parameter. However, eccentricity destroys the symmetry of the circle, so the direction of the major axis also has to be defined. As a result, five rather than four parameters are required to describe an ellipse, and ellipse detection has to take account of this, either explicitly or implicitly. In spite of this, one method for ellipse detection is especially simple and straightforward to implement: that is the diameter bisection method, which is described next.

### 10.9.1 THE DIAMETER BISECTION METHOD

The diameter bisection method of Tsuji and Matsumoto (1978) is very simple in concept. First, a list is compiled of all the edge points in the image. Then, the list is sorted to find those that are antiparallel, so that they could lie at opposite ends of ellipse diameters; next, the positions of the center points of the connecting lines for all such pairs are taken as voting positions in parameter space (Fig. 10.14). As for circle location, the parameter space that is used for this purpose is congruent to image space. Finally, the positions of significant peaks in parameter space are located to identify possible ellipse centers.

Naturally, in an image containing many ellipses and other shapes, there will be very many pairs of antiparallel edge points and for most of these the center points of the connecting lines will lead to nonuseful votes in parameter space. Clearly,

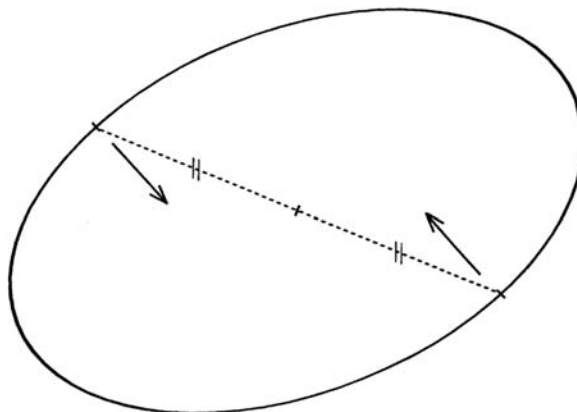


**FIGURE 10.14**

Principle of the diameter bisection method. A pair of points is located for which the edge orientations are antiparallel. If such a pair of points lies on an ellipse, the midpoint of the line joining the points will be situated at the center of the ellipse.

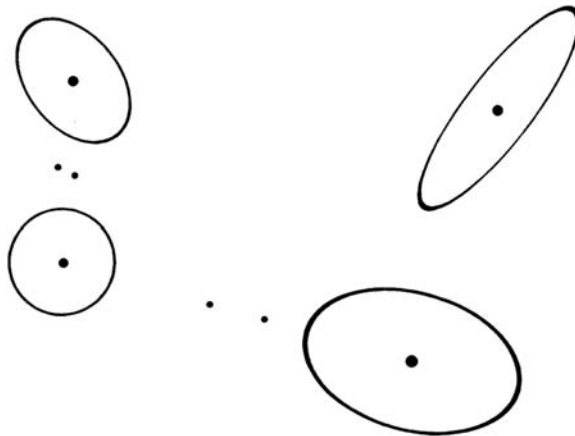
such clutter leads to wasted computation. However, it is a principle of the HT that votes must be accumulated in parameter space at all points which *could in principle* lead to correct object center location: it is left to the peak finder to find the voting positions that are most likely to correspond to object centers.

Not only does clutter lead to wasted computation but the method itself is computationally expensive. This is because it examines all *pairs* of edge points, and there are many more such pairs than there are edge points ( $m$  edge points lead to  ${}^m C_2 \approx m^2/2$  pairs of edge points). Indeed, since there are likely to be at least 1000 edge points in a typical image, the computational problems can be formidable.

Interestingly, the basic method is not particularly discriminating about ellipses. It picks out many symmetrical shapes—any indeed that possess  $180^\circ$  rotation symmetry, including rectangles, ellipses, circles, or superellipses (these have equations of the form  $x^s/a^s + y^s/b^s = 1$ , ellipses being a special case). In addition, the basic scheme sometimes gives rise to a number of false identifications even in an image in which only ellipses are present (Fig. 10.15). However, Tsuji and Matsumoto (1978) also proposed a technique by which true ellipses can be distinguished. The basis of the technique is the property of an ellipse that the lengths of perpendicular semidiameters OP, OQ (O being the centre of the ellipse and P and Q being boundary points) obey the relation:

$$1/OP^2 + 1/OQ^2 = 1/R^2 = \text{constant} \quad (10.18)$$

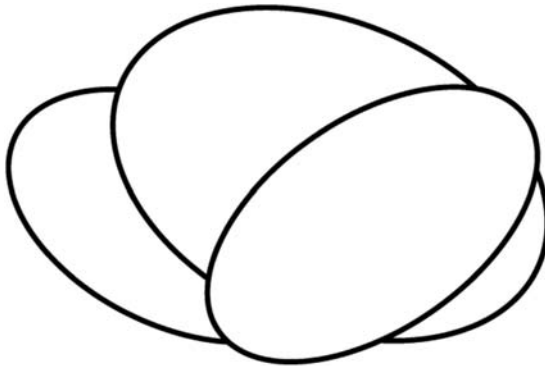
To proceed, the set of edge points that contribute to a given peak in parameter space is used to construct a histogram of  $R$  values (the latter being obtained from Eq. (10.18)). If a significant peak is found in this histogram, then there is clear



**FIGURE 10.15**

Result of using the basic diameter bisection method. The large dots show true ellipse centers found by the method, while the smaller dots show positions at which false alarms commonly occur. Such false alarms are eliminated by applying the test described in the text.



**FIGURE 10.16**

Limitations of the diameter bisection method: of the three ellipses shown, only the leftmost one cannot be located by the diameter bisection method.

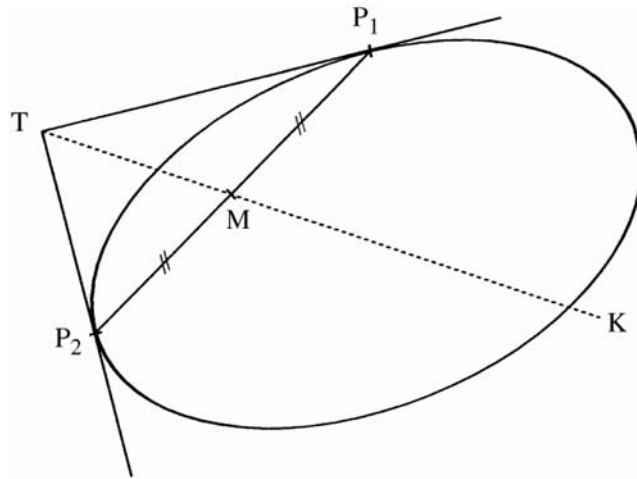
evidence of an ellipse at the specified location in the image. If two or more such peaks are found, then there is evidence of a corresponding number of concentric ellipses in the image. If, however, no such peaks are found, then a rectangle, superellipse, or other symmetrical shape may be present and each of these would need its own identifying test.

The method obviously relies on there being an appreciable number of pairs of edge points on an ellipse lying at opposite ends of diameters: hence there are strict limits on the amount of the boundary that must be visible (Fig. 10.16). Finally, it should not go unnoticed that the method wastes the signal available from unmatched edge points. These considerations have led to a search for further methods of ellipse detection.

### 10.9.2 THE CHORD–TANGENT METHOD

The chord–tangent method was devised by Yuen et al. (1988) and makes use of another simple geometric property of the ellipse. Again pairs of edge points are taken in turn, and for each point of the pair, tangents to the ellipse are constructed and found to cross at  $T$ ; the midpoint of the connecting line is found at  $M$ ; then the equation of line  $TM$  is calculated and all points that lie on the portion  $MK$  of this line are accumulated in parameter space (Fig. 10.17) (clearly,  $T$  and the center of the ellipse lie on the opposite sides of  $M$ ). Finally, peak location proceeds as before.

The proof that this method is correct is trivial. Symmetry ensures that the method works for circles, and projective properties then ensure that it also works for ellipses: under orthographic projection (see Chapter 16: The Three-Dimensional World), straight lines project into straight lines, midpoints into midpoints, tangents into tangents, and circles into ellipses; in addition, it is always

**FIGURE 10.17**

Principle of the chord–tangent method. The tangents at  $P_1$  and  $P_2$  meet at  $T$  and the midpoint of  $P_1P_2$  is  $M$ . The center  $C$  of the ellipse lies on the line  $TM$  produced. Notice that  $M$  lies between  $C$  and  $T$ . Hence the transform for points  $P_1$  and  $P_2$  need only include the portion  $MK$  of this line.

possible to find a viewpoint such that a circle can be projected into a given ellipse.

Unfortunately, this method suffers from significantly increased computation, since so many points have to be accumulated in parameter space. This is obviously the price to be paid for greater applicability. However, computation can be minimized in at least three ways: (1) cutting down the lengths of the lines of votes accumulated in parameter space by taking account of the expected sizes and spacings of ellipses; (2) not pairing edge points initially if they are too close together or too far apart; and (3) eliminating edge points once they have been identified as belonging to a particular ellipse.

### 10.9.3 FINDING THE REMAINING ELLIPSE PARAMETERS

Although the methods described above are designed to locate the center coordinates of ellipses, a more formal approach is required to determine other ellipse parameters. Accordingly, we write the equation of an ellipse in the form:

$$Ax^2 + 2Hxy + By^2 + 2Gx + 2Fy + C = 0 \quad (10.19)$$

an ellipse being distinguished from a hyperbola by the additional condition:

$$AB > H^2 \quad (10.20)$$

This condition guarantees that  $A$  can never be zero and that the ellipse equation may without loss of generality be rewritten with  $A = 1$ . This leaves five parameters, which can be related to the position of the ellipse, its orientation, and its size and shape (or eccentricity).

Having located the center of the ellipse, we may select a new origin of coordinates at its center  $(x_c, y_c)$ ; the equation then takes the form:

$$x'^2 + 2Hx'y' + By'^2 + C' = 0 \quad (10.21)$$

where

$$x' = x - x_c; \quad y' = y - y_c \quad (10.22)$$

It now remains to fit to Eq. (10.21) the edge points that gave evidence for the ellipse center under consideration. The problem will normally be vastly overdetermined. Hence an obvious approach is the method of least squares. Unfortunately, this technique tends to be very sensitive to outlier points and is therefore liable to be inaccurate. An alternative is to employ some form of HT. Here, we follow Tsukune and Goto (1983) by differentiating Eq. (10.21):

$$x' + By'/dx' + H(y' + x'dy'/dx') = 0 \quad (10.23)$$

Then  $dy'/dx'$  can be determined from the local edge orientation at  $(x', y')$  and a set of points accumulated in the new  $(H, B)$  parameter space. When a peak is eventually located in  $(H, B)$  space, the relevant data (a subset of a subset of the original set of edge points) can be used with Eq. (10.21) to obtain a histogram of  $C'$  values, from which the final parameter for the ellipse can be obtained.

The following formulae are needed to determine the orientation  $\theta$  and semi-axes  $a, b$  of an ellipse in terms of  $H, B$ , and  $C'$ :

$$\theta = \frac{1}{2} \arctan\left(\frac{2H}{1-B}\right) \quad (10.24)$$

$$a^2 = \frac{-2C'}{(B+1) - [(B-1)^2 + 4H^2]^{1/2}} \quad (10.25)$$

$$b^2 = \frac{-2C'}{(B+1) + [(B-1)^2 + 4H^2]^{1/2}} \quad (10.26)$$

Mathematically,  $\theta$  is the angle of rotation that diagonalizes the second-order terms in Eq. (10.21); having performed this diagonalization, the ellipse is then essentially in the standard form  $\tilde{x}^2/a^2 + \tilde{y}^2/b^2 = 1$ , so  $a$  and  $b$  are determined.

Note that the above method finds the five ellipse parameters in *three* stages: first the positional coordinates are obtained, then the orientation, and finally the size and eccentricity. (Strictly, the eccentricity is  $e = (1 - b^2/a^2)^{1/2}$ , but in most cases we are more interested in the ratio of semiminor to semimajor axes,  $b/a$ .) This three-stage calculation involves less computation but compounds any errors—in addition, edge orientation errors, though low, become a limiting factor. For this reason, Yuen et al. (1988) tackled the problem by speeding up the HT

procedure itself rather than by avoiding a direct assault on Eq. (10.21): i.e., they aimed at a fast implementation of a thoroughgoing second stage which finds all the parameters of Eq. (10.21) in one 3-D parameter space.

It is now clear that reasonably optimal means are available for finding the orientation and semiaxes of an ellipse once its position is known: the weak point in the process appears to be that of finding the ellipse initially. Indeed, the two approaches for achieving this that have been described above are particularly computation intensive, mainly because they examine all pairs of edge points; a possible alternative is to apply the generalized Hough transform (GHT), which locates objects by taking edge points singly: this possibility will be considered in [Chapter 11](#), The Generalized Hough Transform.

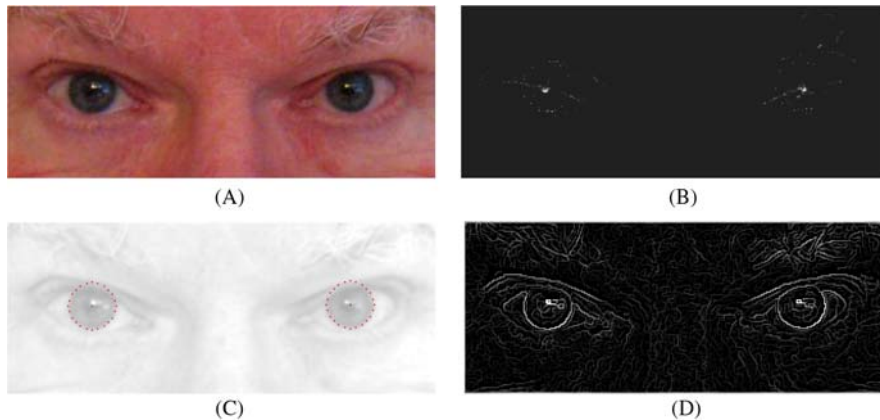
---

## 10.10 HUMAN IRIS LOCATION

Human iris location is an important application of computer vision for three reasons: (1) it provides a useful cue for human face analysis; (2) it can be used for the determination of gaze direction; (3) it is useful in its own right for biometric purposes, that is to say, for identifying individuals almost uniquely. The latter possibility has already been noted in [Chapter 7](#), Texture Analysis where textural methods for iris recognition were outlined and some key references were given. More details of human face location and analysis will be given in [Chapter 21](#), Face Detection and Recognition: the Impact of Deep Learning. Here we concentrate on iris location using the HT.

In fact, we can tackle the iris location and recognition task reasonably straightforwardly. First, if the head has been located with reasonable accuracy, then it can form a region of interest, inside which the iris can be sought. In a front view with the eyes looking ahead, the iris will be seen as a round often high-contrast object, and can be located straightforwardly with the aid of a HT (Ma et al., 2003). In some cases this will be less easy because the iris is relatively light and the color may not be distinctive—though a lot will depend on the quality of the illumination. Perhaps more important, in some human subjects, the eyelid and lower contour of the eye may partially overlap the iris ([Fig. 10.18A](#)), making it more difficult to identify, though, as confirmed below, HTs are capable of coping with a fair degree of occlusion.

Note that the iris will appear elliptical if the eyes are not be facing directly ahead; in addition, the shape of the eye is far from spherical and the horizontal diameter is larger than the vertical diameter—again making the iris appear elliptical (Wang and Sung, 2001). In either case the iris can still be detected using a HT. Furthermore, once this has been done, it should be possible to estimate the direction of gaze with a reasonable degree of accuracy (Gong et al., 2000), thereby taking us further than mere recognition. (The fact that measurement of ellipse eccentricity would lead to an ambiguity in the gaze direction can be offset by measuring the position of the ellipse on the eyeball.) Finally, Toennies et al. (2002) showed that the HT can be used to localize the irises for real-time

**FIGURE 10.18**

Iris location using the Hough transform. (A) Original image of the eye region of a face. (B) The gradient-weighted Hough transform (HT) in parameter space. (C) Accurate location of the irises from the peaks in (B). (D) Output from the Canny operator (incorporating smoothing, nonmaximum suppression and hysteresis) used to obtain the initial edge image. Gradient weighting has contributed significantly to the robustness and accuracy of object (iris) location. Notice the plethora of additional edges in (D): these give rise to substantial numbers of votes which interfere with those from the irises.

applications, in spite of quite substantial partial occlusion by the eyelid and lower contour of the eye.

A number of the points made above are illustrated by the example in Fig. 10.18. Far from being a trivial application of the HT, there are a surprisingly large number of edges in the eye region: these produce significant numbers of additional votes which interfere with those from the irises. These arise from the upper and lower eyelids and the folds of skin around them. Hence the accuracy of the method is not assured: this makes gradient weighting (see Section 11.4) especially valuable. The radii of the irises shown in Fig. 10.18 are about 17.5 pixels, and there is no particular evidence of ellipticity in their shape. However, more accurate location of the iris and measurement of ellipticity in order to estimate orientation (e.g., to determine the angle of gaze) require considerably greater resolution, with iris radii approaching 100 pixels, whereas pictures that analyze iris texture patterns for biometric purposes require even larger radii.

---

## 10.11 CONCLUDING REMARKS

This chapter has described a variety of techniques for finding straight lines and straight edges in digital images. Several of these were based on the HT, which is

important because it permits systematic extraction of global data from images and has the capability to ignore “local” problems, due for example, to occlusions and noise. This is what is required for “intermediate-level” processing, as will be seen repeatedly in later chapters.

The specific techniques covered have involved various parametrizations of a straight line, and means for improving efficiency and accuracy. In particular, speed is improved by using a two-stage line finding procedure—a method that is useful in other applications of the HT, as will be seen in later chapters. Accuracy tends to be reduced by such two-stage processing because of error propagation and because the first stage is liable to be subject to too many interfering signals. However, it is possible to improve the accuracy of approximate solutions by using least squares refinement procedures.

Subsequently, it became clear that the RANSAC approach also has line fitting capabilities, which are for some purposes superior to those of the HT, though RANSAC tends to be more computation intensive (with  $N$  edge points it has a computational load of  $O(N^3)$  rather than  $O(N^2)$ ). Suffice it to say that the final choice of approach will depend on the exact type of image data, including levels of noise and background clutter.

The chapter went on to describe techniques for circle and ellipse detection, starting with the HT approach. Although the HT is found to be effective and highly robust against occlusions, noise, and other artifacts, it requires considerable storage and computation—especially if circles of unknown radius are to be located. A method has been described for efficiently tackling the latter problem using a single 2-D parameter space. In addition, a technique has been described for markedly reducing the computational load involved in circle detection by sampling along every  $n$ th row and column. In essence, the technique replaces a 2-D search by two 1-D searches, which though more efficient limits the robustness and accuracy in a known way. This is in line with the principle that (as for the HT), robustness cannot be added as an afterthought but must be included as an integral part of the design of any vision algorithm.

Two HT-based schemes for ellipse detection have also been described—the diameter bisection method and the chord–tangent method. A further approach to ellipse detection, based on the generalized HT, will be covered in [Chapter 11](#), The Generalized Hough Transform. At that point further lessons will be drawn on the efficacies of the various methods.

As in the case of line detection, a trend running through the design of circle and ellipse detection schemes is the deliberate splitting of algorithms into two or more stages. This is useful for keying into the important and relevant parts of an image prior to finely discriminating one type of object or feature from another, or prior to measuring dimensions or other characteristics accurately. Indeed, the concept can be taken further, in that the efficiencies of all the algorithms discussed in this chapter have been improved by searching first for edge features in the image. The concept of two-stage template matching is therefore deep-seated in the methodology of the subject and is developed further in later chapters.

Although two-stage template matching is a standard means of increasing efficiency (VanderBrug and Rosenfeld, 1977; Davies, 1988f), it is not obvious that efficiency can always be increased in this way. It appears to be in the nature of the subject that ingenuity is needed to discover means of achieving this.

*The HT is one way of inferring the presence of objects from their feature points, and RANSAC is another. Both methods use voting schemes to select best fit lines, though only the HT employs a parameter space representation; and both methods are highly robust as they focus only on positive evidence for the existence of objects. The HT also achieves an impressive level of robustness for circle and ellipse detection. Practical issues such as speed and storage requirements can in some cases be improved by employing parameter spaces of reduced dimension.*

---

## 10.12 BIBLIOGRAPHICAL AND HISTORICAL NOTES

The HT was developed in 1962 (Hough, 1962) with the aim of finding (straight) particle tracks in high-energy nuclear physics, and was brought into the mainstream image analysis literature much later by Rosenfeld (1969). Duda and Hart (1972) developed the method further and applied it to the detection of lines and curves in digital pictures. O’Gorman and Clowes (1976) soon developed a Hough-based scheme for finding lines efficiently, by making use of edge orientation information, at much the same time that Kimme et al. (1975) applied the same method (apparently independently) to the efficient location of circles. Many of the ideas for fast effective line finding described in this chapter arose in a paper by Dudani and Luk (1978). The author’s foot-of-normal method (Davies, 1986) was developed much later. During the 1990s, work in this area progressed further—see for example, Atiquzzaman and Akhtar’s (1994) method for the efficient determination of lines together with their end coordinates and lengths; Lutton et al.’s (1994) application of the transform to the determination of vanishing points; and Kamat-Sadekar and Ganesan’s (1998) extensions of the technique to cover the reliable detection of multiple line segments, particularly in relation to road scene analysis.

Some mention should be made of the related Radon transform. This is formed by integrating the picture function  $I(x, y)$  along infinitely thin straight strips of the image, with normal coordinate parameters  $(\theta, \rho)$ , and recording the results in a  $(\theta, \rho)$  parameter space. The Radon transform is a generalization of the HT for line detection (Deans, 1981). In fact, for straight lines the Radon transform reduces to the Duda and Hart (1972) form of the HT. The transforms of real lines have a characteristic “butterfly” shape (a pencil of segments passing through the corresponding peak) in parameter space. This phenomenon was investigated by Leavers and Boyce (1987), who devised special  $3 \times 3$  convolution filters for sensitively detecting these peaks.

There has been strong continuing interest in the HT in spite of its computational difficulties: in fact, these reflect underlying matching problems that are inescapable in computer vision, so development of methods must continue. Thus Schaffalitsky and Zisserman (2000) carried out an interesting extension of earlier ideas on vanishing lines and points by considering the case of repeated lines such as those occurring on certain types of fences and brick buildings; Song et al. (2002) developed HT methods for coping with the problems of fuzzy edges and noise in large-sized images; and Guru et al. (2004) demonstrated viable alternatives to the HT, based for example, on heuristic search achieved by small eigenvalue analysis.

The author's work on circle detection for automated inspection required real-time implementation and also high accuracy. This spurred the development of the techniques described in [Sections 10.7–10.8](#) (Davies, 1987d, 1988b). In addition, the author considered the effect of noise on edge orientation computations, showing in particular their effect in reducing the accuracy of center location (Davies, 1987c): see [Section 5.9](#).

Yuen et al. (1989) reviewed various existing methods for circle detection using the HT. In general, their results confirmed the efficiency of the method of [Section 10.7](#) for unknown circle radius, although they found that the two-stage process that was involved can sometimes lead to slight loss of robustness. It appears that this problem can be reduced in some cases by using a modified version of the algorithm of Gerig and Klein (1986); but note that the Gerig and Klein approach is itself a two-stage procedure. More recently, Pan et al. (1995) have increased the speed of computation of the HT by prior grouping of edge pixels into arcs, for an underground pipe inspection application.

The two-stage template matching technique and related approaches for increasing search efficiency in digital images were known by 1977 (Nagel and Rosenfeld, 1972; Rosenfeld and VanderBrug, 1977; VanderBrug and Rosenfeld, 1977), and have undergone further development since then—especially in relation to particular applications such as those described in this chapter (Davies, 1988f).

The ellipse detection sections are based particularly on the work of Tsuji and Matsumoto (1978), Tsukune and Goto (1983), and Yuen et al. (1988); for a fourth method (Davies, 1989a) using the GHT idea of Ballard (1981) in order to save computation, see [Chapter 11](#), The Generalized Hough Transform. The contrasts between these methods are many and intricate, as this chapter has shown. In particular, the idea of saving dimensionality in the implementation of the GHT appears also in a general circle detector (Davies, 1988b). At that point in time, the necessity for a multistage approach to determination of ellipse parameters seemed proven, although somewhat surprisingly the optimum number of such stages was just two.

Later algorithms represented moves to greater degrees of robustness with real data by explicit inclusion of errors and error propagation (Ellis et al., 1992); increased attention was subsequently given to the verification stage of the Hough approach (Ser and Siu, 1995). In addition, work was carried out on the detection



of superellipses, which are shapes intermediate in shape between ellipses and rectangles, though the technique used (Rosin and West, 1995) was that of segmentation trees rather than HTs (nonspecific detection of superellipses can of course be achieved by the diameter bisection method—see [Section 10.9.1](#)); see also Rosin (2000).

For cereal grain inspection, with typical flow rates in excess of 300 grains per second, ultra-fast algorithms were needed and the resulting algorithms were limiting cases of chord-based versions of the HT (Davies, 1999a,b); a related approach was adopted by Xie and Ji (2002) for their efficient ellipse detection method; Lei and Wong (1999) employed a method which was based on symmetry, and this was found to be able to detect parabolas and hyperbolas as well as ellipses. Note that while this is advantageous in some applications, the lack of discrimination could prove to be a disadvantage in other applications. It was also reported as being more stable than other methods since it does not have to calculate tangents or curvatures; the latter advantage has also been reported by Sewisy and Leberl (2001). The fact that even in the 2000's, basic new ellipse detection schemes are being developed says something about the science of image analysis: even today the toolbox of algorithms is incomplete, and the science of how to choose between items in the toolbox, or how, *systematically*, to develop new items for the toolbox, is immature. Further, although all the parameters for specification of such a toolbox may be known, knowledge about the possible tradeoffs between them is still limited.

### 10.12.1 MORE RECENT DEVELOPMENTS

Advances are still being made in the application of the HT. In particular, Chung et al. (2010) have developed an orientation-based elimination strategy that they have shown to be more efficient than previous line-determination methods based on the HT. It operates by dividing edge pixels into sets with small (typically  $10^\circ$ ) ranges of orientation, and for each of these, it carries out the process of line detection. Since this process involves a parameter space of reduced size, both storage and search times are reduced.

The RANSAC procedure was published by Fischler and Bolles in 1981: this must be one of the most cited papers in computer vision, and the method must be one of the most used (more even than the HT, because it only relies on the existence of suitable hypotheses, *however* obtained). The original paper used it for tackling the full perspective  $n$ -point fitting problem in 3-D (see [Chapter 17: Tackling the Perspective  \$n\$ -Point Problem](#)). Clarke et al. (1996) used it for locating and tracking straight lines. Borkar et al. (2009) used it for locating lane markings on roads, and Mastorakis and Davies (2011) developed it further for the same purpose. Interestingly, Borkar et al. used a low resolution HT to feed RANSAC, and followed it by least squares fitting of the inliers. The paper does not report on how much was gained by this three-stage approach, either in accuracy or in reliability. (If enough hypotheses are employed—and there is certainly

no lack of these in such an application—both the HT and least squares fitting might be avoided, but here optimization for speed may make the inclusion of least squares essential.) For further discussion of RANSAC, see [Chapter 23](#), In-Vehicle Vision Systems and [Appendix A](#).

Much work has recently been carried out on iris detection using the HT. Jang et al. (2008) were particularly concerned with overlap of the iris region by the upper and lower eyelids, and used a parabolic version of the HT to accurately locate their boundaries, taking special care to limit the computational load. Li et al. (2010) used a circular HT to locate the iris and a RANSAC-like technique for locating the upper and lower eyelids, again using a parabolic model for the latter: their approach was designed to cope with very noisy iris images. Chen et al. (2010) used a circular HT to locate the iris and a straight line HT to locate up to two line segment approximations to the boundaries of each of the eyelids. Cauchie et al. (2008) produced a new version of the HT to accurately locate common circle centers from circular or partial circle segments, and demonstrated its value for iris location. Min and Park (2009) used a circular HT for iris detection, a parabolic HT for eyelid detection, and followed this with eyelash detection using thresholding.

Finally, we summarize work carried out by Guo et al. (2009) to overcome the problems of dense sets of edges in textured regions. To reduce the impact of such edges, a measure of isotropic surround suppression was introduced: the resulting algorithm gave small weights to edges in texture regions and large weights to edges on strong and clear boundaries when accumulating votes in Hough space. The approach gave good results when locating straight lines in scenes containing man-made structures such as buildings.

---

## 10.13 PROBLEMS

1.
  - a. In the foot-of-normal HT, straight edges are found by locating the foot of the normal  $F(x_f, y_f)$  from an origin  $O(0, 0)$  at the center of the image to an extended line containing each edge fragment  $E(x, y)$ , and placing a vote at  $F$  in a separate image space.
  - b. By examining the possible positions of lines within a square image and the resulting foot-of-normal positions, determine the exact extent of the parameter space that is theoretically required to form the HT.
  - c. Would this form of the HT be expected to be (1) more or less robust and (2) more or less computation intensive than the  $(\rho, \theta)$  HT for line location?
2.
  - a. Why is it sometimes stated that a HT generates *hypotheses* rather than actual solutions for object location? Is this statement justified?
  - b. A new type of HT is to be devised for detecting straight lines. It will take every edge fragment in the image and extend it in either direction until it meets the boundary of the image, and then accumulate a vote at each position. Thus *two* peaks should result for every line. Explain why

finding these peaks will require *less* computation than for the standard HT, but that deducing the presence of lines will then require *extra* computation. How will these amounts of computation be likely to vary with (1) the size of the image and (2) the number of lines in the image?

- c. Discuss whether this approach would be an improvement on the standard approach for straight line location, and whether it would have any disadvantages.
3.
    - a. Describe the HT approach to object location. Explain its advantages relative to the *centroidal*  $(r, \theta)$  *plot* approach: illustrate your answer with reference to location of circles of known radius  $R$ .
    - b. Describe how the HT may be used to locate straight edges. Explain what is seen in the parameter space if many curved edges also appear in the original image.
    - c. Explain what happens if the image contains a square object of arbitrary size and *nothing* else. How would you deduce from the information in parameter space that a square object is present in the image? Give the main features of an algorithm to decide that a square object is present and to locate it.
    - d. Examine in detail whether an algorithm using the strategy described in (c) would become confused if (1) parts of some sides of the square were occluded; (2) one or more sides of the square were missing; (3) several squares appeared in the image; (4) several of these complications occurred together.
    - e. How important is it to this type of algorithm to have edge detectors that are capable of accurately determining edge orientation? Describe a type of edge detector that is capable of achieving this.
  4.
    - a. Describe the use of the HT for circular object detection, assuming that object size is known in advance. Show also how a method for detecting ellipses could be adapted for detecting circles of unknown size.
    - b. A new method is suggested for circle location which involves scanning the image both horizontally and vertically. In each case, the midpoints of chords are determined and their  $x$  or  $y$  coordinates are accumulated in separate 1-D histograms. Show that these can be regarded as simple types of HT, from which the positions of circles can be deduced. Discuss whether any problems would arise with this approach; consider also whether it would lead to any advantages relative to the standard HT for circle detection.
    - c. A further method is suggested for circle location. This again involves scanning the image horizontally, but in this case, for every chord that is found, an estimate is immediately made of the *two* points at which the center could lie, and votes placed at those locations. Work out the geometry of this method, and determine whether this method is faster than the method outlined in (b). Determine whether the method has any disadvantages compared with method in (b)?

5. Determine which of the methods described in this chapter will detect (1) hyperbolas, (2) curves of the form  $Ax^3 + By^3 = 1$ , (3) curves of the form  $Ax^4 + Bx + Cy^4 = 1$ .
6. Prove Eq. (10.18) for an ellipse. *Hint:* Write the coordinates of P and Q in suitable parametric forms, and then use the fact that  $OP \perp OQ$  to eliminate one of the parameters from the left-hand side of the equation.
7. Describe the *diameter bisection* and *chord–tangent* methods for the location of ellipses in images, and compare their properties. Justify the use of the chord–tangent method by proving its validity for circle detection and then extending the proof to cover ellipse detection.
8. Round coins of a variety of sizes are to be located, identified, and sorted in a vending machine. Discuss whether the chord–tangent method should be used for this purpose instead of the usual form of HT circle location scheme operating within a 3D  $(x, y, r)$  parameter space.
9. Outline each of the following methods for locating ellipses using the HT: (1) the *diameter bisection* method; (2) the *chord–tangent* method. Explain the principles on which these methods rely. Determine which is the more robust and compare the amounts of computation each requires.
10. For the diameter bisection method, searching through lists of edge points with the right orientations can take excessive computation. It is suggested that a two-stage approach might speed up the process: (1) load the edge points into a table which may be addressed by orientation; (2) look up the right edge points by feeding appropriate orientations into the table. Estimate how much this would be likely to speed up the diameter bisection method.
11. It is found that the diameter bisection method sometimes becomes confused when several ellipses appear in the same image, and generates false “centers” that are not situated at the centers of any ellipses. It is also found that certain other shapes are detected by the diameter bisection method. Ascertain in each case quite what the method is sensitive to, and consider ways in which these problems might be overcome.

This page intentionally left blank

# The generalized Hough transform

# 11

In this chapter, we shall see how the Hough transform (HT) can be used to locate general shapes, and that it is broadly able to retain its robustness properties. On a slightly different tack, abstract pattern matching involves stepping back from the image itself and working at a higher level, grouping features in an abstract way to *infer* the presence of objects. Graph matching has long been a standard approach for achieving this, but in some circumstances, we shall see that the generalized Hough transform (GHT) is able to outperform it. This chapter discusses these inference procedures and goes on to consider the various types of search that can be used with image data.

*Look out for:*

- The GHT technique
- its relation to spatial matched filtering
- how sensitivity is optimized by gradient rather than uniform weighting
- how the GHT may be used for ellipse detection
- how the computational loads of the various HT techniques can be estimated
- the match graph approach for identifying objects from their point features
- why subgraph–subgraph isomorphism leads to maximum robustness
- how symmetry can be used to simplify the matching task
- situations where the GHT can outperform the maximal clique paradigm.

This chapter describes the GHT and extends our view of the HT as a generic computer vision technique. It also makes order calculations of computational load for three HT-based methods of ellipse detection. It goes on to show how the presence of objects can be inferred from sets of point features and that in some situations there is considerable advantage in using the GHT for this purpose.

## 11.1 INTRODUCTION

In the previous few chapters, it has been seen that the HT is of great importance for the detection of features such as lines, circles and ellipses, and for finding relevant image parameters. This makes it worthwhile to see the extent to which the

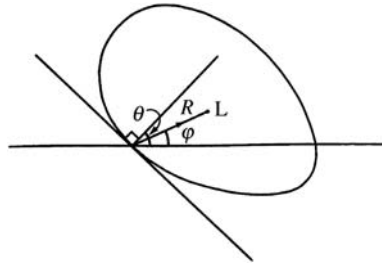
method can be generalized so that it can detect arbitrary shapes. The work of Merlin and Farber (1975) and Ballard (1981) was crucial historically and led to the development of the GHT. The GHT is studied in this chapter, showing first how it is implemented and then examining how it is optimized and adapted to particular types of image data. This requires us to go back to first principles, taking spatial matched filtering as a starting point. Having developed the relevant theory, the GHT is applied to the important case of ellipse detection, showing in particular how computational load may be minimized. The computational problems of the GHT and HT are then examined more generally.

For situations where objects have more complex shapes, it is common to locate them from salient features such as small holes, corners, straight, circular or elliptical segments, and indeed any readily localizable subpatterns: earlier chapters have shown how such features may be located. However, at some stage, it becomes necessary to find methods for collating the information from the various features, in order to recognize and locate the objects containing them. Graph-matching methods have often been employed to achieve this, and this approach will be examined later in the chapter. However, certain graph-matching methods such as the paradigm maximal clique approach have distinct computational problems as they are known to be NP-complete. Interestingly, in some cases, it is possible to use the GHT to carry out the point pattern matching task (of identifying objects from their point features) and thus find objects efficiently in polynomial time: this procedure is described in [Section 11.10](#). Attention is then drawn to the use of features that have additional attributes—such as the orientation and sharpness of corners—and how this can help to cut down computation and potential ambiguities in interpretation.

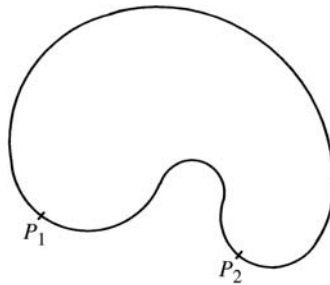
---

## 11.2 THE GENERALIZED HOUGH TRANSFORM

This section shows how the standard Hough technique is generalized so that it can detect arbitrary shapes. In principle, it is trivial to achieve this. First, we need to select a localization point  $L$  within a template of the idealized shape. Then, we need to arrange so that, instead of moving from an edge point a *fixed* distance  $R$  directly along the local edge normal to arrive at the center, as for circles, we move an appropriate *variable* distance  $R$  in a variable direction  $\varphi$  so as to arrive at  $L$ :  $R$  and  $\varphi$  are now functions of the local edge normal direction  $\theta$  ([Fig. 11.1](#)). Under these circumstances, votes will peak at the preselected object localization point  $L$ . The functions  $R(\theta)$  and  $\phi(\theta)$  can be stored analytically in the computer algorithm, or for completely arbitrary shapes, they may be stored as lookup tables. In either case, the scheme is beautifully simple in principle but two complications arise in practice. The first arises because some shapes have features such as concavities and holes, so that several values of  $R$  and  $\varphi$  are required for certain values of  $\theta$  ([Fig. 11.2](#)). The second arises because we are going from an

**FIGURE 11.1**

Computation of the generalized Hough transform.

**FIGURE 11.2**

A shape exhibiting a concavity: certain values of  $\theta$  correspond to several points on the boundary and hence require several values of  $R$  and  $\varphi$ —as for points  $P_1$  and  $P_2$ .

isotropic shape (a circle) to an anisotropic shape which may be in a completely arbitrary orientation.

To cope with the first of these complications, the lookup table (usually called the “ $R$ -table”) must contain a list of the positions  $\mathbf{r}$ , relative to  $L$ , of all points on the boundary of the object for each possible value of edge orientation  $\theta$  (or a similar effect must be achieved analytically): then, on encountering an edge fragment in the image whose orientation is  $\theta$ , estimates of the position of  $L$  may be obtained by moving a distance (or distances)  $\mathbf{R} = -\mathbf{r}$  from the given edge fragment. Clearly, if the  $R$ -table has multivalued entries (i.e., several values of  $\mathbf{r}$  for certain values of  $\theta$ ), only one of these entries (for given  $\theta$ ) can give a correct estimate of the position of  $L$ . However, at least the method is guaranteed to give optimum sensitivity, as all relevant edge fragments contribute to the peak at  $L$  in parameter space. This property of optimal sensitivity reflects the fact that the GHT is a form of spatial matched filter: this property is analyzed in more detail below.

The second complication arises because any shape other than a circle is anisotropic. As in most applications (including industrial applications such as automated assembly), object orientations are initially unknown, the algorithm has to obtain its own information on object orientation. This means adding an extra



dimension in parameter space (Ballard, 1981). Then, each edge point contributes a vote in each plane in parameter space at a position given by that expected for an object of given shape and given orientation. Finally, the whole of parameter space is searched for peaks, the highest points indicating both the locations of objects and their orientations. Clearly, if object size is also a parameter, the problem becomes far worse, and this complication is ignored here (although the method of [Section 10.7](#) is clearly relevant).

The changes made in proceeding to the GHT leave it just as robust as the HT circle detector described previously. This gives an incentive to improve the GHT so as to limit the computational problems in practical situations. In particular, the size of the parameter space must be cut down drastically both to save storage and to curtail the associated search task. Considerable ingenuity has been devoted to devising alternative schemes and adaptations to achieve this. Important special cases are those of ellipse detection and polygon detection, and in each of these, definite advances have been made: ellipse detection is covered in Chapter 10, Line, Circle, and Ellipse Detection for polygon detection, see Davies (1989a). Here, we proceed with some more basic studies of the GHT.

---

### 11.3 THE RELEVANCE OF SPATIAL MATCHED FILTERING

Many years ago, it was shown that the HT is equivalent to template matching (Stockman and Agrawala, 1977) and also to spatial matched filtering (Sklansky, 1978). Matched filtering dates from World War II when radar was being developed, and it was shown to be the ideal method for detecting signals: in particular, a filter that is “matched” to a given signal detects it with optimum signal-to-noise ratio (SNR) under white noise conditions (North, 1943; Turin, 1960). White noise is defined as noise that has equal power at all frequencies: in image science, white noise is understood to mean equal power at all *spatial* frequencies. The significance of this is that noise at different pixels is completely uncorrelated but is subject to the same gray-scale probability distribution—i.e., it has potentially the same range of amplitudes at all pixels.

Mathematically, using a matched filter is identical to correlation with a signal (or “template”) of the same temporal or spatial profile as the one to be detected (Rosie, 1966). Unfortunately, when applying correlation in image analysis, changes in background illumination cause large changes in signal from one image to another and from one part of an image to another. These problems have been tackled in two ways, which are as follows:

1. Adjusting templates so that they have a mean value of zero, to suppress the effects of varying levels of illumination;
2. Breaking up templates into a number of smaller templates each having zero mean: then as the sizes of the subtemplates approach zero, the effects of varying levels of illumination will tend to zero.

The first of these is widely used in image analysis and has been seen as the obvious one to apply when detecting edges, line segments, corners, or other small features. Indeed, when objects are detected by small features such as these, the second method is also tacitly being used. However, there is a problem in that if objects are detected from a set of small templates, they are not actually being detected in their entirety, so ways of inferring the presence of whole objects are required. And if this is not done sufficiently rigorously, the objects might be missed, or false alarms might be detected. Thus, deviation from the matched filter paradigm brings dangers with it.

Meanwhile, we are left with the idea that the GHT is a form of matched filter and incorporates both of the above ways of coping with uncontrolled variations in background illumination. It can also be said that these ways constitute a rather crude method for applying a noise-whitening filter, thereby bringing the matched filter closer to its ideal form.

Interestingly, employing zero-mean templates results in the absolute signal level being reduced to zero and only local relative signal levels being retained, so the GHT suppresses the signal from the bulk of the object, retaining only that near its boundary. As a result, the GHT is highly sensitive to object position but is not optimized for object detection. Overall, the GHT can therefore be viewed as a type of perimeter template around the outside of an object (Fig. 11.3)—though any internal high-contrast edges should also be included in the analysis.

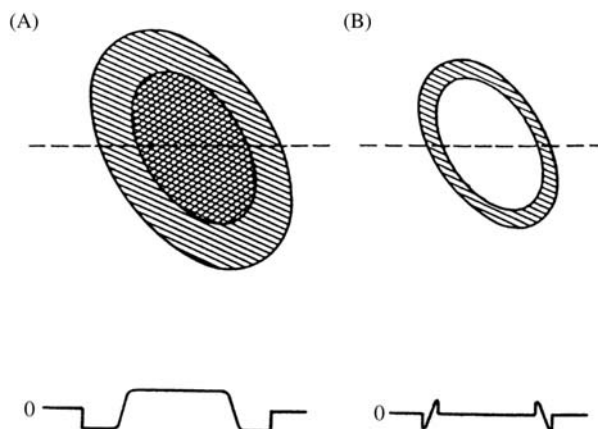


**FIGURE 11.3**

The idea of a perimeter template: both the original spatial matched filter template (A) and the corresponding “perimeter template” (B) have a zero mean (see text). The lower illustrations show the cross sections along the dotted lines.

## 11.4 GRADIENT WEIGHTING VERSUS UNIFORM WEIGHTING

Another long-standing problem regarding the GHT is how best to weight votes in parameter space in relation to the respective edge gradient magnitudes. To find an answer to this problem, we appeal to the spatial matched filter scenario for the ideal solution and then determine the corresponding solution for the GHT. First, note that the responses to the subtemplates (or to the perimeter template) are proportional to edge gradient magnitude. Next, note that with a spatial matched filter, signals are detected optimally by templates of the same shape. Each contribution to the spatial matched filter response therefore has to be proportional to the local magnitude of the signal and to that of the template. In view of the correspondence between (1) using a spatial matched filter to locate objects by looking for peaks in convolution space and (2) using a GHT to locate objects by looking for peaks in parameter space, we should use weights proportional to the gradients of the edge points *and* proportional to the a priori edge gradients.

There are two ways in which the choice of weighting is important. First, the use of uniform weighting implies that all edge pixels whose gradient magnitudes are above threshold will effectively have them reduced to the threshold value, so the signal will be curtailed: this can mean that the SNR of high-contrast objects will be reduced significantly. Second, the widths of edges of high-contrast objects will be broadened in a crude way by uniform weighting (see Fig. 11.4) but under gradient weighting this broadening will be controlled, giving a roughly Gaussian

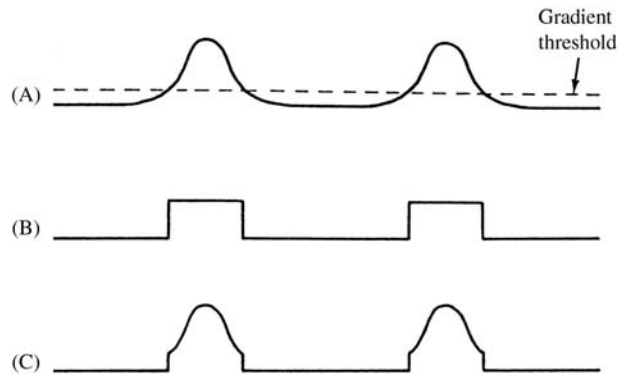


**FIGURE 11.4**

Effective gradient magnitude as a function of position within a section across an object of moderate contrast, thresholded at a fairly low level: (A) gradient magnitude for original image data and gradient thresholding level; (B) uniform weighting: the effective widths of edges are broadened rather crudely, adding significantly to the difficulty of locating the peak in parameter space; (C) gradient weighting: the position of the peak in parameter space can be estimated in a manner that is basically limited by the shape of the gradient profile for the original image data.

edge profile: thus, the peak in parameter space will be narrower and more rounded, and the object reference point  $L$  can be located more easily and with greater accuracy. This effect is visible in Fig. 11.5, which also shows the relatively increased noise level that results from uniform weighting.

Note also that low gradient magnitudes correspond to edges of poorly known location, whereas high values correspond to sharply defined edges: thus, the accuracy of the information relevant to object location is proportional to the magnitude of the gradient at each of the edge pixels, and appropriate weighting should therefore be used.

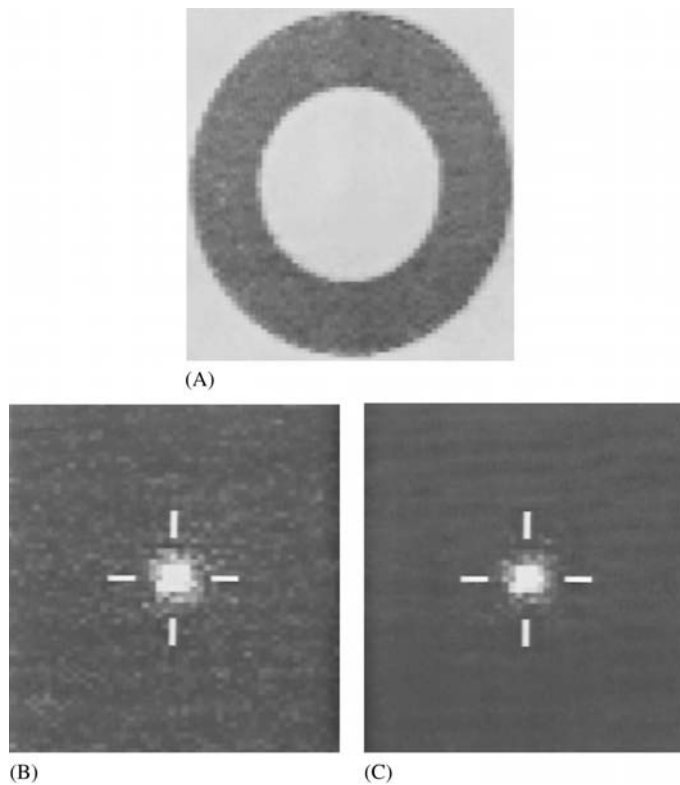


**FIGURE 11.5**

Results of applying the two types of weighting to a real image: (A) original image; (B) results in parameter space for uniform weighting; (C) results for gradient weighting. The peaks (which arise from the outer edges of the washer) are normalized to the same levels in the two cases: the increased level of noise in (B) is readily apparent. In this example, the gradient threshold is set at a low level (around 10% of the maximum level) so that low-contrast objects can also be detected.

### 11.4.1 CALCULATION OF SENSITIVITY AND COMPUTATIONAL LOAD

The aim of this subsection is to underline the above ideas by working out formulae for sensitivity and computational load. It is assumed that  $p$  objects of size around  $n \times n$  are being sought in an image of size  $N \times N$ .

Correlation requires  $N^2 n^2$  operations to compute the convolutions for all possible positions of the object in the image. Using the perimeter template, the number of basic operations is reduced to  $\sim N^2 n$ , corresponding to the reduced number of pixels in the template. The GHT requires  $\sim N^2$  operations to locate the edge pixels, plus a further  $\sim pn$  operations to accumulate the points in parameter space.

The situation for sensitivity is rather different. With correlation, the results for  $n^2$  pixels are summed, giving a signal proportional to  $n^2$ , although the noise (assumed to be independent at every pixel) is proportional to  $n$ : this is because of the well-known result that the noise powers of various independent noise components are additive (Rosie, 1966). Overall, this results in the SNR being proportional to  $n$ . The perimeter template possesses only  $\sim n$  pixels, and here, the overall result is that the SNR is proportional to  $\sqrt{n}$ . The situation for the GHT is inherently identical to that for the perimeter template method, so long as plots in parameter space are weighted in proportion to edge gradient  $g$  multiplied by a priori edge gradient  $G$ . It is now necessary to compute the constant of proportionality  $\alpha$ . Take  $s$  as the average signal, equal to the intensity (assumed to be roughly uniform) over the body of the object, and  $S$  as the magnitude of a full matched filter template. In the same units,  $g$  (and  $G$ ) is the magnitude of the signal within the perimeter template. Then,  $\alpha = 1/sS$ . This means that the perimeter template method and the GHT method lose sensitivity in two ways—first because they look at less of the available signal, and second because they look where the signal is low. For a high value of gradient magnitude, which occurs for a step edge (where most of the variation in intensity takes place within the range of 1 pixel), the values of  $g$  and  $G$  saturate out, so that they are nearly equal to  $s$  and  $S$  (see Fig. 11.6). Under these conditions, the perimeter template method and the GHT have sensitivities that depend only on the value of  $n$ .

Table 11.1 summarizes the situation discussed above. The oft-quoted statement that the computational load of the GHT is proportional to the number of

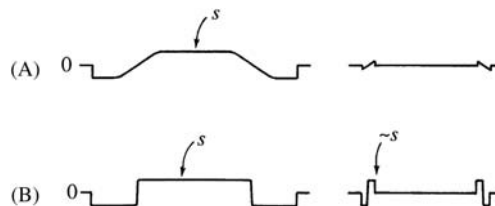


FIGURE 11.6

Effect of edge gradient on perimeter template signal: (A) low edge gradient: signal is proportional to gradient; (B) high edge gradient: signal saturates at value of  $s$ .

**Table 11.1** Formulae for Computational Load and Sensitivity<sup>a</sup>

	Template Matching	Perimeter Template Matching	Generalized Hough Transform
Number of operations	$O(N^2n^2)$	$O(N^2n)$	$O(N^2) + O(pn)$
Sensitivity	$O(n)$	$O(\sqrt{ng}G/sS)$	$O(\sqrt{ng}G/sS)$
Maximum sensitivity <sup>b</sup>	$O(n)$	$O(\sqrt{n})$	$O(\sqrt{n})$

<sup>a</sup>This table gives formulae for computational load and sensitivity when  $p$  objects of size  $n \times n$  are sought in an image of size  $N \times N$ . The intensity of the image within the whole object template is taken as  $s$  and the value for the ideal template is taken as  $S$ ; corresponding values for intensity gradient within the perimeter template are  $g$  and  $G$ .

<sup>b</sup>Maximum sensitivity refers to the case of a step edge, for which  $g \approx s$  and  $G \approx S$  (see Fig. 11.6).

perimeter pixels, rather than to the much greater number of pixels within the body of an object, is only an approximation. In addition, this saving is not obtained without cost: in particular, the sensitivity (SNR) is reduced (at best) as the square root of object area/perimeter (note that area and perimeter are measured in the same units, so it is valid to find their ratio).

Finally, the absolute sensitivity for the GHT varies as  $gG$ . As contrast changes so that  $g \rightarrow g'$ , we see that  $gG \rightarrow g'G$ : i.e., sensitivity changes by a factor  $g'/g$ . Hence, theory predicts that sensitivity is proportional to contrast. Although this result might have been anticipated, we now see that it is valid only under conditions of gradient weighting.

## 11.4.2 SUMMARY

The above sections examined the GHT and found that the following factors are involved in optimizing it:

1. Each point in parameter space should be weighted in proportion to the intensity gradient at the edge pixel giving rise to it, *and* in proportion to the a priori gradient, if sensitivity is to be optimized.
2. The computational load of the GHT can be minimized by ignoring pixels having low magnitudes of intensity gradient. If the threshold of gradient magnitude is set too high, fewer objects are likely to be detected; if it is set too low, computational savings will be diminished. Suitable means are required for setting the threshold, but little reduction in computation will be possible if the highest sensitivity in a low-contrast image is to be retained.
3. The GHT is inherently optimized for object location rather than object detection. This means that it may miss low-contrast objects which are detectable by other methods that take the whole area of an object into account. However, this consideration is often unimportant in applications where SNR is less of a problem than finding objects quickly in an uncluttered environment.

Overall, it is clear that the GHT is a spatial matched filter only in a particular sense, and as a result may not always achieve the highest possible sensitivity. The main advantage of the technique is that it is highly efficient, overall computational load in principle being proportional to the relatively few pixels on the perimeters of objects rather than to the much greater numbers of pixels within them. In addition, by concentrating on the boundaries of objects, the GHT retains its power to locate objects accurately. It is thus important to distinguish clearly between sensitivity in *detecting* objects and sensitivity in *locating* them.

---

## 11.5 USE OF THE GHT FOR ELLIPSE DETECTION

It has already been seen that when the GHT is used to detect anisotropic objects, there is an intrinsic need to employ a large number of planes in parameter space. However, it is shown below that by accumulating the votes for all possible orientations in a *single* plane in parameter space, significant savings in computation can sometimes be made. Basically, the idea is largely to reduce the considerable storage requirements of the GHT by using only one instead of (typically) 360 planes in parameter space, whereas at the same time significantly reducing the computation involved in the final search for peaks. Such a scheme could have concomitant disadvantages such as the production of spurious peaks, and this aspect will have to be examined carefully.

To achieve these aims, it is necessary to analyze the shape of the point spread function (PSF) to be accumulated for each edge pixel. To demonstrate this, we take the case of ellipses of unknown orientation. We start by taking a general edge fragment at a position defined by ellipse parameter  $\psi$  and deducing the bearing of the center of the ellipse relative to the local edge normal (Fig. 11.7). Working first in an ellipse-based axes system, for an ellipse with semimajor and semiminor axes  $a$  and  $b$ , respectively, it is clear that:

$$x = a \cos \psi \quad (11.1)$$

$$y = b \sin \psi \quad (11.2)$$

Hence,

$$dx/d\psi = -a \sin \psi \quad (11.3)$$

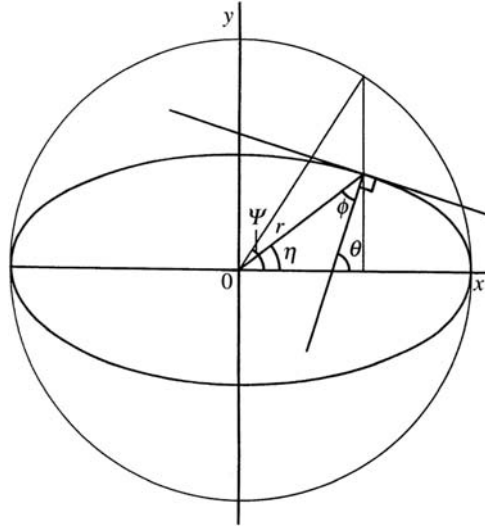
$$dy/d\psi = b \cos \psi \quad (11.4)$$

giving

$$dy/dx = -(b/a) \cot \psi \quad (11.5)$$

Hence, the orientation of the edge normal is given by:

$$\tan \theta = (a/b) \tan \psi \quad (11.6)$$


**FIGURE 11.7**

Geometry of an ellipse and its edge normal.

At this point, we wish to deduce the bearing of the center of the ellipse relative to the local edge normal. From Fig. 11.7:

$$\phi = \theta - \eta \quad (11.7)$$

where

$$\tan \eta = y/x = (b/a) \tan \psi \quad (11.8)$$

and

$$\begin{aligned} \tan \phi &= \tan (\theta - \eta) \\ &= \frac{\tan \theta - \tan \eta}{1 + \tan \theta \tan \eta} \end{aligned} \quad (11.9)$$

Substituting for  $\tan \theta$  and  $\tan \eta$ , and then rearranging, gives:

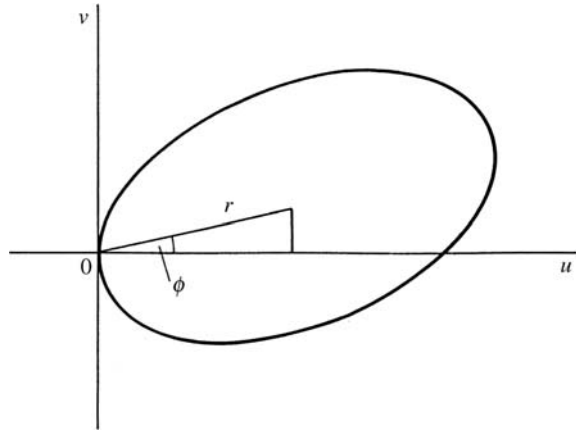
$$\tan \phi = \frac{(a^2 - b^2)}{2ab} \sin 2\psi \quad (11.10)$$

In addition:

$$r^2 = a^2 \cos^2 \psi + b^2 \sin^2 \psi \quad (11.11)$$

To obtain the PSF for an ellipse of unknown orientation, we now simplify matters by taking the current edge fragment to be at the origin and orientated with its normal along the  $u$ -axis (Fig. 11.8). The PSF is then the locus of all



**FIGURE 11.8**

Geometry for finding the PSF for ellipse detection by forming the locus of the centers of ellipses touching a given edge fragment.

possible positions of the center of the ellipse. To find its form, it is merely required to eliminate  $\psi$  between Eqs. (11.10) and (11.11). This is facilitated by reexpressing  $r^2$  in double angles (the significance of double angles lies in the  $180^\circ$  rotation symmetry of an ellipse):

$$r^2 = \frac{a^2 + b^2}{2} + \frac{a^2 - b^2}{2} \cos 2\psi \quad (11.12)$$

After some manipulations, the locus is obtained as:

$$r^4 - r^2(a^2 + b^2) + a^2b^2 \sec^2 \phi = 0 \quad (11.13)$$

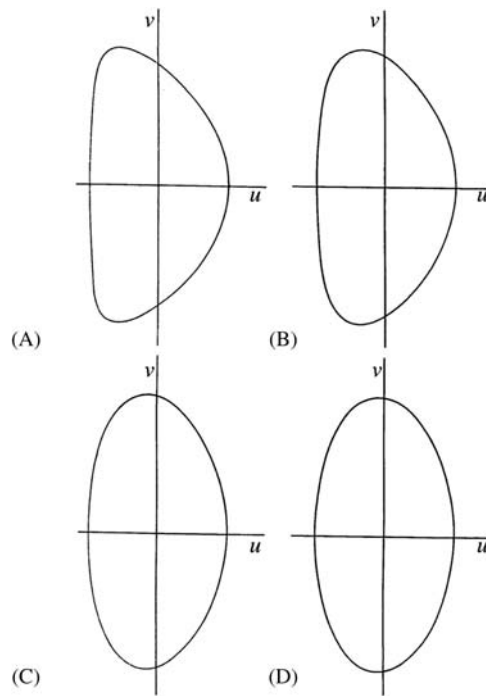
which can, in the edge-based coordinate system, also be expressed in the form:

$$v^2 = (a^2 + b^2) - u^2 - a^2b^2/u^2 \quad (11.14)$$

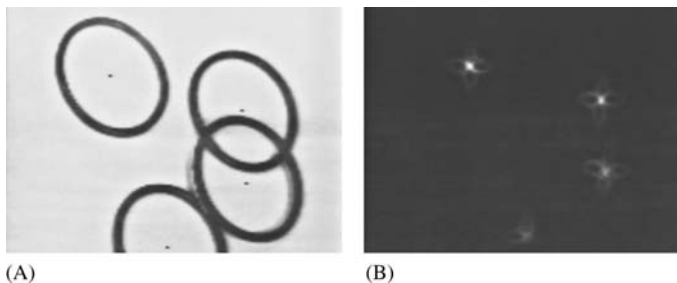
In fact, this is a complex and variable shape, as shown in Fig. 11.9, though for ellipses of low eccentricity, the PSF also approximates to an ellipse. However, it is normally better to implement it accurately using a specially constructed lookup table.

### 11.5.1 PRACTICAL DETAILS

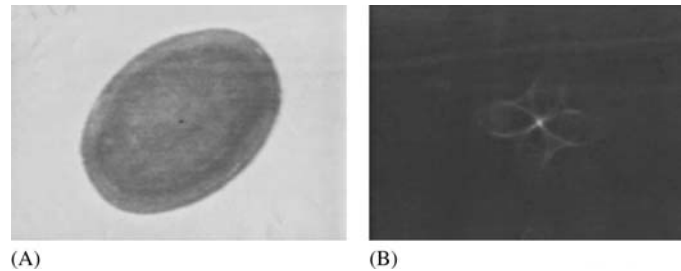
Having constructed a lookup table for ellipse detection, the detection algorithm has to scale it, position it, and rotate it so that points can be accumulated in parameter space. Fig. 11.10 shows the result of applying the above scheme to an image of some O-rings lying on a slope, whereas Fig. 11.11 shows the result obtained for an elliptical object; the respective PSFs contain 50 and 100 votes.

**FIGURE 11.9**

Typical PSF shapes for detection of ellipses with various eccentricities: (A) ellipse with  $a/b = 21.0$ ; (B) ellipse with  $a/b = 5.0$ ; (C) ellipse with  $a/b = 2.0$ ; (D) ellipse with  $a/b = 1.4$ . Notice how the PSF shape approaches a small ellipse of aspect ratio 2.00 as eccentricity tends to zero.

**FIGURE 11.10**

Applying the PSF to detection of tilted circles: (A) off-camera  $128 \times 128$  image of a set of circular O-rings on a  $45^\circ$  slope of arbitrary direction; (B) transform in parameter space: notice the peculiar shape of the ellipse transform, which is close to a "four-leaf clover" pattern. (A) also indicates the positions of the centers of the O-rings as located from (B): accuracy is limited by the presence of noise, shadows, clutter, and available resolution, to an overall standard deviation of about 0.6 pixels.




---

**FIGURE 11.11**

Applying the PSF to detection of elliptical objects: (A) off-camera  $128 \times 128$  image of an elliptical bar of soap of arbitrary orientation; (B) transform in parameter space: in this case, the clover-leaf pattern is better resolved. Accuracy of location is limited partly by distortions in the shape of the object but the peak location procedure results in an overall standard deviation of the order of 0.5 pixels.

In Fig. 11.10, the O-rings are found accurately and with a fair degree of robustness, despite overlap and occlusion.

Fig. 11.10 also shows the arrangement of points in parameter space that results from applying the PSF to every edge point on the boundary of an ellipse: The pattern is somewhat clearer in Fig. 11.11. In either case, it is seen to contain a high degree of structure (curiously, the votes seem to form approximate “four-leaved clover” patterns). For an ideal transform, there would be no structure apart from the main peak, and all points on the PSF *not* falling on the peak at the center of the ellipse would be randomly distributed nearby. Nevertheless, the peak at the center is very well defined and confirms that this form of GHT is completely viable.

---

## 11.6 COMPARING THE VARIOUS METHODS FOR ELLIPSE DETECTION

This section briefly compares the computational loads for the methods of ellipse detection discussed above. To make fair comparisons, we concentrate on ellipse detection per se and ignore any additional procedures concerned with (1) finding other ellipse parameters, (2) distinguishing ellipses from other shapes, or (3) separating concentric ellipses. We start by examining the GHT method and the diameter bisection method.

First, suppose that an  $N \times N$  pixel image contains  $p$  identical ellipses with semiaxes  $a$ ,  $b$ , and two PDF-orientated parameters defined by  $c = \frac{1}{2}(a + b)$ ,  $d = \frac{1}{2}(a - b)$ . By ignoring noise and general background clutter, we shall be favoring the diameter bisection method, as will be seen below. Next, the discussion is simplified by supposing that the computational load resides mainly

in the calculation of the positions at which votes should be accumulated in parameter space—the effort involved in locating edge pixels and in locating peaks in parameter space is much smaller.

Under these circumstances, the load for the GHT method may be approximated by the product of the number of edge pixels and the number of points per edge pixel that have to be accumulated in parameter space, the latter being equal to the number of points on the PSF. Hence, the load is proportional to:

$$\begin{aligned} L_G &\approx p \times 2\pi c \times 2\pi(2d + d)/2 = 6\pi^2 pcd \\ &\approx 60 pcd \end{aligned} \quad (11.15)$$

where the ellipse has been taken to have relatively low eccentricity so that, as indicated in Section 11.5, the PSF itself approximates to an ellipse, and its semi-axes have the values  $2d$  and  $d$ .

For the diameter bisection method, the actual voting is a minor part of the algorithm—as indeed it is in the GHT method (see the snippet of code listed in Table 11.1). In either case, most of the computational load concerns edge orientation calculations or comparisons. Assuming that these calculations and comparisons involve similar inherent effort, it is fair to assess the load for the diameter bisection method as:

$$\begin{aligned} L_D &\approx p \times 2\pi c C_2 \approx (2\pi p c)^2 / 2 \\ &\approx 20p^2 c^2 \end{aligned} \quad (11.16)$$

Hence,

$$L_D/L_G \approx pc/3d \quad (11.17)$$

When  $a$  is close to  $b$ , as for a circle,  $L_G \rightarrow 0$  and then the diameter bisection method becomes a poor option. However, in some cases, it is found that  $a$  is close to  $2b$ , so that  $c$  is close to  $3d$ . The ratio of the loads then becomes:

$$L_D/L_G \approx p \quad (11.18)$$

It is possible that  $p$  will be as low as 1 in some cases: however, such cases are likely to be rare and are offset by applications where there is significant background image clutter and noise, or where all  $p$  ellipses have other edge detail giving irrelevant signals that can be considered a type of self-induced clutter (see the O-ring example of Fig. 11.10).

It is also possible that some of the pairs of edge points in the diameter bisection method can be excluded before they are considered, e.g., by giving every edge point a range of interaction related to the size of the ellipses. This would tend to reduce the computational load by a factor of the order of (but not as small as)  $p$ . However, the computational overhead required for this would not be negligible.

Overall, the GHT method should be significantly faster than the diameter bisection method in most real applications, the diameter bisection method being at a definite disadvantage when image clutter and noise are strong. By

comparison, the chord–tangent method always requires more computation than the diameter bisection method, as not only does it examine every pair of edge points but also it generates a *line* of votes in parameter space for each pair.

Against these, computational limitations must be noted the different characteristics of the methods. First, the diameter bisection method is not particularly discriminating, in that it locates many symmetrical shapes, as remarked earlier. The chord–tangent method is selective for ellipses but is not selective about their size or eccentricity. The GHT method is selective about all of these factors. These types of discriminability, or lack of it, can turn out to be advantageous or disadvantageous, depending on the application: hence, we do no more here than draw attention to the situation. It is also relevant that the diameter bisection method is rather less robust than the other methods: this is so as if one edge point of an anti-parallel pair is not detected, then the other point of the pair cannot contribute to detection of the ellipse—a factor that does not apply for the other two methods as they take all edge information into account.

---

## 11.7 A GRAPH-THEORETIC APPROACH TO OBJECT LOCATION

This section considers a commonly occurring situation involving considerable constraints—objects appearing on a horizontal worktable or conveyor at a known distance from the camera. It is also assumed (1) that objects are flat or can appear in only a restricted number of stances in three dimensions, (2) that objects are viewed from directly overhead, and (3) that perspective distortions are small. In such situations, the objects may in principle be identified and located from very few point features. As such features are taken to have no structure of their own, it will be impossible to locate an object uniquely from a single feature, although positive identification and location would be possible using two features if these were distinguishable and if their distance apart were known. For truly indistinguishable point features, an ambiguity remains for all objects not possessing  $180^\circ$  rotation symmetry. Hence, at least three point features are in general required to locate and identify objects at known range. Clearly, noise and other artifacts such as occlusions modify this conclusion. In fact, when matching a template of the points in an idealized object with the points present in a real image, we may find that:

1. A great many feature points may be present because of multiple instances of the chosen type of object in the image
2. additional points may be present because of noise or clutter from irrelevant objects and structure in the background
3. certain points that should be present are missing because of noise or occlusion, or because of defects in the object being sought.

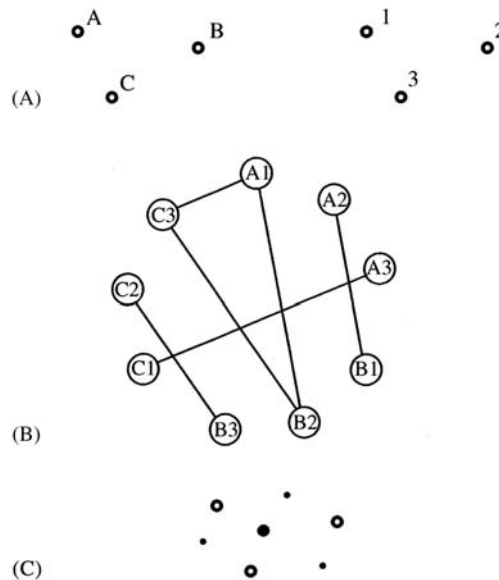
These problems mean that we should in general be attempting to match a subset of the points in the idealized template to various subsets of the points in the

image. If the point sets are considered to constitute *graphs* with the point features as *nodes*, the task devolves into the mathematical problem of subgraph–subgraph isomorphism, i.e., finding which subgraphs in the image graph are isomorphic to subgraphs of the idealized template graph. [Isomorphic means having the same basic shape and structure.] Of course, there may be a large number of matches involving rather few points: these would arise from sets of features that *happen* (see e.g., item 2 above) to lie at valid distances apart in the original image. The most significant matches will involve a fair number of features and will lead to correct object identification and location. Clearly, a point feature matching scheme will be most successful if it finds the most likely interpretation by searching for solutions with the greatest internal consistency—i.e., with the greatest number of point matches per object.

Unfortunately, the schema presented above is still too simplistic in many applications as it is insufficiently robust against distortions. In particular, optical (e.g., perspective) distortions may arise, or the objects themselves may be distorted, or by resting partly on other objects they may not be quite in the assumed stance: hence, distances between features may not be exactly as expected. These factors mean that some tolerance has to be accepted in the distances between pairs of features, and it is common to employ a threshold such that interfeature distances have to agree within this tolerance before matches are accepted as potentially valid. Clearly, distortions lay more strain on the point matching technique and make it all the more necessary to seek solutions with the greatest possible internal consistency. Thus, as many features as possible should be taken into account in locating and identifying objects. The maximal clique approach is intended to achieve this.

As a start, as many features as possible are identified in the original image, and these are numbered in some convenient order such as the order of appearance in a normal TV raster scan. The numbers then have to be matched against the letters corresponding to the features on the idealized object. A systematic way of achieving this is by constructing a *match graph* (or *association graph*) in which the nodes represent feature assignments and arcs joining nodes represent pairwise compatibilities between assignments. To find the best match, it is then necessary to find regions of the match graph where the cross-linkages are maximized. To achieve this, *cliques* are sought within the match graph. A clique is a *complete subgraph*—i.e., one for which all pairs of nodes are connected by arcs. However, the previous arguments indicate that if one clique is completely included within another clique, it is likely that the larger clique represents a better match—and indeed *maximal cliques* can be taken as leading to the most reliable matches between the observed image and the object model.

Fig. 11.12A illustrates the situation for a general triangle: For simplicity, the figure takes the observed image to contain only one triangle and assumes that lengths match exactly and that no occlusions occur. The match graph in this example is shown in Fig. 11.12B: there are nine possible feature assignments, six valid compatibilities, and four maximal cliques, only the largest corresponding to an exact match.



**FIGURE 11.12**

A simple matching problem—a general triangle: (A) basic labeling of model (*left*) and image (*right*); (B) match graph; (C) placement of votes in parameter space. In (B) the maximal cliques are: (1) A1, B2, C3; (2) A2, B1; (3) B3, C2; and (4) C1, A3. In (C), the following notation is used:  $\circ$ , positions of observed features;  $\bullet$ , positions of votes;  $\bullet$ , position of main voting peak.

© AVC 1988.

Fig. 11.13A shows the situation for the less trivial case of a quadrilateral, the match graph being shown in Fig. 11.13B. In this case, there are 16 possible feature assignments, 12 valid compatibilities, and seven maximal cliques. If occlusion of a feature occurs, this will (taken on its own) reduce the number of possible feature assignments and also the number of valid compatibilities: in addition, the number of maximal cliques and the size of the largest maximal clique will be reduced. On the other hand, noise or clutter can add erroneous features. If the latter are at arbitrary distances from existing features, then the number of possible feature assignments will be increased but there will not be any more compatibility in the match graph, so the latter will have only trivial additional complexity. However, if the extra features appear at *allowed* distances from existing features, this will introduce extra compatibilities into the match graph and make it more tedious to analyze. In the case shown in Fig. 11.14, both types of complication—an occlusion and an additional feature—arise: there are now eight pairwise assignments and six maximal cliques, rather fewer overall than in the original case of Fig. 11.13. However, the important factor is that the largest

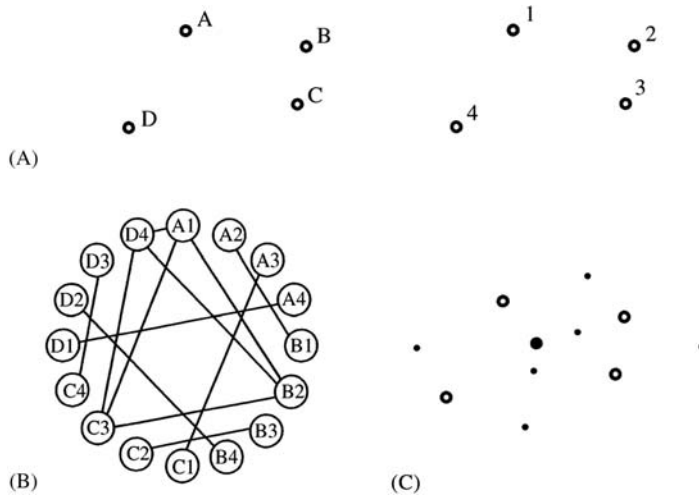


**FIGURE 11.13**

Another matching problem—a general quadrilateral: (A) basic labeling of model (*left*) and image (*right*); (B) match graph; (C) placement of votes in parameter space (notation as in Fig. 11.12).

© AVC 1988.

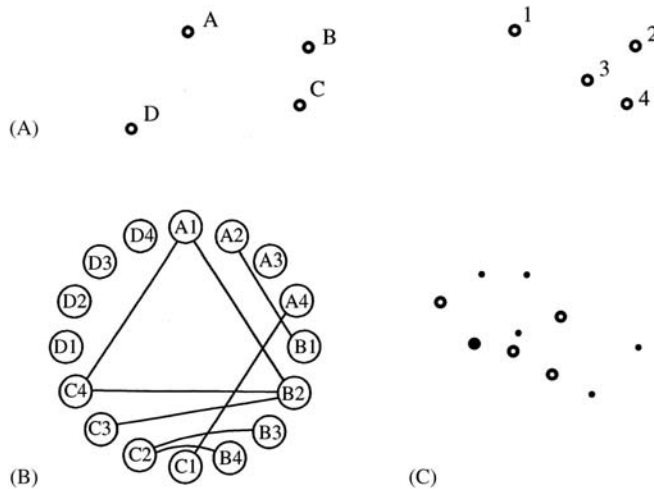


**FIGURE 11.14**

Matching when one feature is occluded and another is added: (A) basic labeling of model (*left*) and image (*right*); (B) match graph; (C) placement of votes in parameter space (notation as in Fig. 11.12).



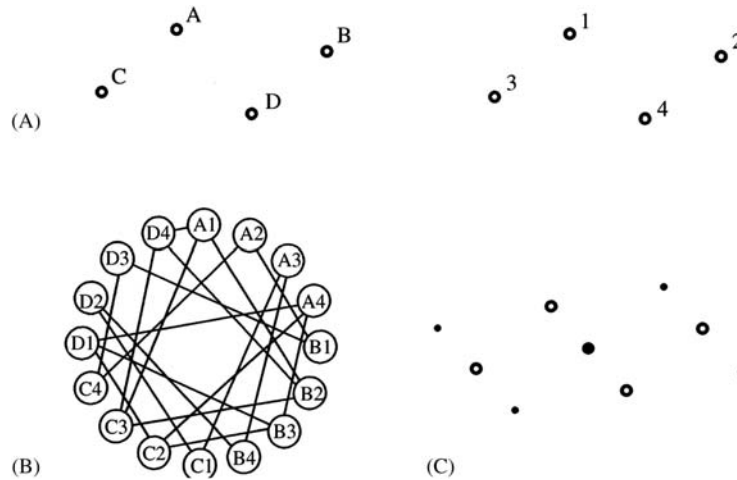


**FIGURE 11.15**

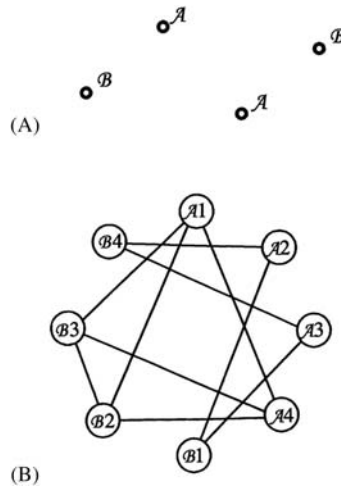
Matching a figure possessing some symmetry: (A) basic labeling of model (*left*) and image (*right*); (B) match graph; (C) placement of votes in parameter space (notation as in Fig. 11.12).

maximal clique still indicates the most likely interpretation of the image and that the technique is inherently highly robust.

When using methods such as the maximal clique approach which involve repetitive operations, it is useful to look for means of saving computation. In fact, when the objects being sought possess some symmetry, economies can be made. Consider the case of a parallelogram (Fig. 11.15). Here, the match graph has 20 valid compatibilities, and there are 10 maximal cliques. Of these, the largest two have equal numbers of nodes, and *both* identify the parallelogram within a symmetry operation. This means that the maximal clique approach is doing more computation than absolutely necessary: this can be avoided by producing a new “symmetry-reduced” match graph after relabeling the model template in accordance with the symmetry operations (see Fig. 11.16). This gives a much smaller match graph with half the number of pairwise compatibilities and half the number of maximal cliques. In particular, there is only one nontrivial maximal clique: note, however, that its size is not reduced by the application of symmetry.

### 11.7.1 A PRACTICAL EXAMPLE—LOCATING CREAM BISCUITS

Fig. 11.17A shows one of a pair of cream biscuits which are to be located from their “docket” holes—this strategy being advantageous as it has the potential for highly accurate product location prior to detailed inspection (in this case, the purpose is to locate the biscuits accurately from the holes, and then to check the alignment of the biscuit wafers and detect any excess cream around the sides of

**FIGURE 11.16**

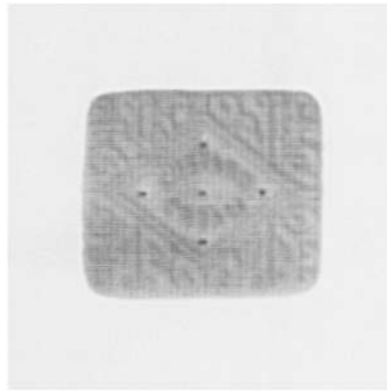
Using a symmetry-reduced match graph: (A) relabeled model template; (B) symmetry-reduced match graph.

the product). The holes found by a simple template-matching routine are indicated in Fig. 11.17B: the template used is rather small and, as a result, the routine is fairly fast but fails to locate all holes; in addition, it can give false alarms. Hence, an “intelligent” algorithm must be used to analyze the hole location data.

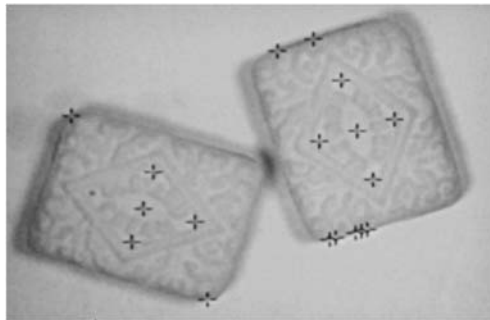
Clearly, this is a highly symmetrical type of object and so it should be beneficial to employ the symmetry-reduced match graph described above. To proceed, it is helpful to tabulate the distances between all pairs of holes in the object model (Fig. 11.18B). Then, this table can be regrouped to take account of symmetry operations (Fig. 11.18D). This will help when we come to build the match graph for a particular image. Analysis of the data in the above example shows that there are two nontrivial maximal cliques, each corresponding correctly to one of the two biscuits in the image. Note, however, that the reduced match graph does not give a *complete* interpretation of the image: it locates the two objects, but it does not confirm uniquely which hole is which. In particular, for a given starting hole of type A, it is not known which is which of the two holes of type B. This can be ascertained by applying simple geometry to the coordinates in order to determine (say) which hole of type B is reached by moving around the center hole E in a clockwise sense.

## 11.8 POSSIBILITIES FOR SAVING COMPUTATION

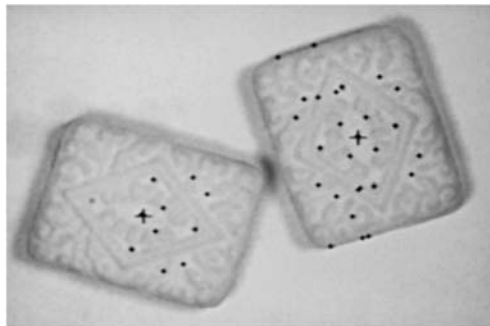
In these examples, the checking of which subgraphs are maximal cliques is a simple problem. However, in real matching tasks, it can quickly become



(A)



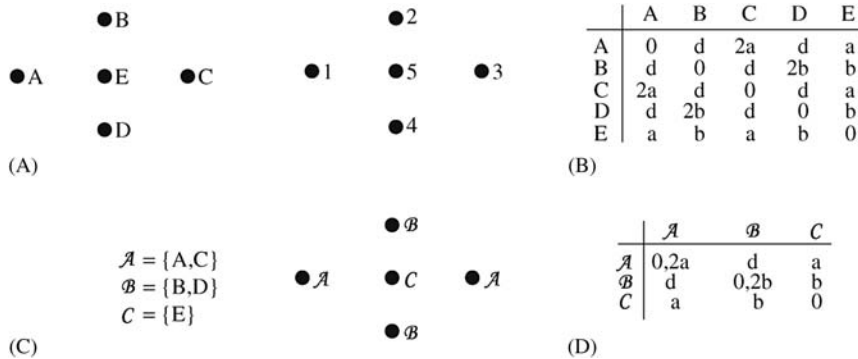
(B)



(C)

**FIGURE 11.17**

(A) A typical cream sandwich biscuit; (B) a pair of cream sandwich biscuits with crosses indicating the result of applying a simple hole detection routine; (C) the two biscuits reliably located by the GHT from the hole data in (B): the isolated small crosses indicate the positions of single votes.


**FIGURE 11.18**

Interfeature distances for holes on cream biscuits: (A) basic labeling of model (*left*) and image (*right*); (B) allowed distance values; (C) revised labeling of model using symmetric set notation; (D) allowed distance values. The cases of zero interfeature distance in the final table can be ignored as they do not lead to useful matches.

**Table 11.2** A Simple Maximal Clique Algorithm

```

set clique size to 2;
// this is the size already included by the match graph
while (newcliques = true) { // new cliques still being found
  increment clique size;
  set newcliques = false;
  for all cliques of previous size {
    set all cliques of previous size to status maxclique;
    for all possible extra nodes
      if extra node is joined to all existing nodes in clique {
        store as a clique of current size;
        set newcliques = true;
      }
  }
  // the larger cliques have now been found
  for all cliques of current size
    for all cliques of previous size
      if all nodes of smaller clique are included in current clique
        set smaller clique to status not maxclique;
  // the subcliques have now been relabelled
}
    
```

unmanageable (the reader is encouraged to draw the match graph for an image containing two objects of seven points!).

Table 11.2 shows what is perhaps the most obvious type of algorithm for finding maximal cliques. It operates by examining in turn all cliques of a given number of nodes and finding what cliques can be constructed from them by adding additional nodes (bearing in mind that any additional nodes must be compatible

with all existing nodes in the clique). This permits all cliques in the match graph to be identified. However, an additional step is needed to eliminate (or relabel) all cliques that are included as subgraphs of a new larger clique before it is known which cliques are maximal.

In view of the evident importance of finding maximal cliques, many algorithms have been devised for the purpose. It is probable that the best of these is now close to the fastest possible speed of operation. Unfortunately, the optimum execution time is known to be bounded not by a polynomial in  $M$  (for a match graph containing maximal cliques of up to  $M$  nodes) but by a much faster varying function. Specifically, the task of finding maximal cliques is akin to the well-known traveling salesman problem and is known to be “NP-complete,” implying that it runs in exponential time (see [Section 11.9.1](#)). Thus, whatever the run-time may be for values of  $M$  up to about 6, it will typically be 100 times slower for values of  $M$  up to about 10, and 100 times slower again for  $M$  greater than  $\sim 14$ . In practical situations, there are several ways of tackling this problem, which are as follows:

1. use the symmetry-reduced match graph wherever possible
2. choose the fastest available maximal clique algorithm
3. write critical loops of the maximal clique algorithm in machine code
4. build special hardware or multiprocessor systems to implement the algorithm
5. use the local–feature–focus (LFF) method (see below: this means searching for cliques of small  $M$  and then working with an alternative method)
6. use an alternative sequential strategy, which may however not be guaranteed to find all the objects in the image
7. use the GHT approach (see [Section 11.9](#)).

Of these methods, the first should be used wherever applicable. Methods 2–4 amount to improving the implementation and are subject to diminishing returns: note that the execution time varies so rapidly with  $M$  that even the best software implementations are unlikely to give a practical increase in  $M$  of more than 2 (i.e.,  $M \rightarrow M + 2$ ). Likewise, dedicated hardware implementations may only give increases in  $M$  of the order of 4 to 6. Method 5 is a “short-cut” approach which proves highly effective in practice. The idea is to search for specific subsets of the features of an object and then to hypothesize that the object exists and go back to the original image to check that it is actually present. Bolles and Cain (1982) devised this method when looking for hinges in quite complex images. In principle, the method has the disadvantage that the particular subset of an object that is chosen as a cue may be missing because of occlusion or some other artifact. Hence, it may be necessary to look for several such cues on each object. This is an example of further deviation from the matched filter paradigm, which reduces detection sensitivity yet again. The method is called the LFF method because objects are sought by cues or local foci.

The maximal clique approach is a type of exhaustive search procedure and is effectively a parallel algorithm. This has the effect of making it highly robust but

is also part of the reason for its slow speed. An alternative is to perform some sort of sequential search for objects, stopping when sufficient confidence is attained in the interpretation or partial interpretation of the image. For example, the search process may be terminated when a match has been obtained for a certain minimum number of features on a given number of objects. Such an approach may be useful in some applications and will generally be considerably faster than the full maximal clique procedure when  $M$  is greater than about 6. An analysis of several tree-search algorithms for subgraph isomorphism was carried out by Ullmann (1976): the paper tests algorithms using artificially generated data, and it is not clear how they relate to real images. The success or otherwise of all nonexhaustive search algorithms must, however, depend critically on the particular types of image data being analyzed: hence, it is difficult to give further general guidance on this matter (but see [Section 11.11](#) for additional comments on search procedures).

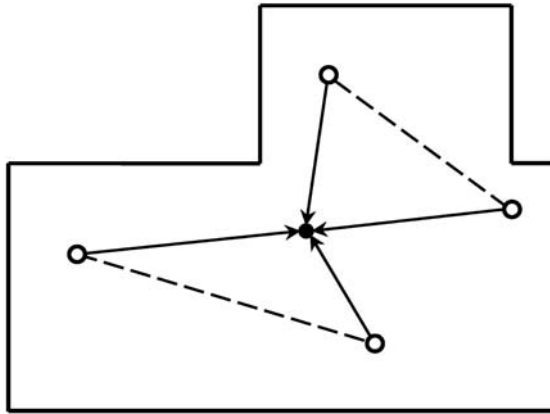
The final method listed above is based on the GHT. In many ways, this provides an ideal solution to the problem as it presents an exhaustive search technique that is essentially equivalent to the maximal clique approach, while not falling into the NP-complete category. This may seem contradictory, as any approach to a well-defined mathematical problem should be subject to the mathematical constraints known to be involved in its solution. However, although the abstract maximal clique problem is known to be NP-complete, the *subset* of maximal clique problems that arises from 2-D image-based data may well be solved with less computation by other means, and in particular, by a 2-D technique. This special circumstance does appear to be valid but it naturally offers no possibility of solving general NP-complete problems by reference to the specific solutions found using the GHT approach! The GHT approach is described in the following section.

---

## 11.9 USING THE GHT FOR FEATURE COLLATION

This section describes how the GHT can be used as an alternative to the maximal clique approach to collate information from point features in order to find objects. Initially, we consider situations where objects have no symmetries—as for the cases of [Figs. 11.12–11.14](#).

To apply the GHT, we first list all features and then accumulate votes in parameter space at every possible position of a localization point  $L$  consistent with each *pair* of features ([Fig. 11.19](#)). This strategy is particularly suitable in the present context, as it corresponds to the pairwise assignments used in the maximal clique method. To proceed, it is necessary merely to use the interfeature distance as a lookup parameter in the GHT  $R$ -table. For indistinguishable point features, this means that there must be two entries for the position of  $L$  for each value of the interfeature distance. Note that we have assumed that no symmetries exist and

**FIGURE 11.19**

Method for locating  $L$  from pairs of feature positions: each pair of feature points gives two possible voting positions in parameter space, when objects have no symmetries. When symmetries are present, certain pairs of features may give rise to up to four voting positions: this is confirmed on careful examination of Fig. 11.17C.

that all pairs of features have different interfeature distances. If this were not so, then more than two vectors would have to be stored in the  $R$ -table per interfeature distance value.

To illustrate the procedure, it is applied first to the triangle example of Fig. 11.12. Fig. 11.12C shows the positions at which votes are accumulated in parameter space. There are four peaks with heights of 3, 1, 1, 1, it being clear that, in the absence of complicating occlusions and defects, the object is locatable at the peak of maximum size. Next, the method is applied to the general quadrilateral example of Fig. 11.13: this leads to seven peaks in parameter space, whose sizes are 6, 1, 1, 1, 1, 1, 1 (Fig. 11.13C).

Close examination of Figs. 11.12–11.14 indicates that every peak in parameter space corresponds to a maximal clique in the match graph. Indeed, there is a one-to-one relation between the two. In the uncomplicated situation being examined here, this is bound to be so for any general arrangement of features within an object, as every pairwise compatibility between features corresponds to two potential object locations, one correct and one that can be correct only from the point of view of that pair of features. Hence, the correct locations all add to give a large maximal clique and a large peak in parameter space, whereas the incorrect ones give maximal cliques each containing two wrong assignments and each corresponding to a false peak of size 1 in parameter space. This situation still applies even when occlusions occur or additional features are present (see Fig. 11.14). The situation is slightly more complicated when symmetries are present, the two methods each deviating in a different way: space does not permit the matter to be explored in depth here but the solution for the case of Fig. 11.15A is presented in

Fig. 11.15C. Overall, it seems simplest to imagine that there is still a one-to-one relationship between the solutions from the two approaches.

Finally, consider again the example of Section 11.7.1 (Fig. 11.17A), this time obtaining a solution by the GHT. Fig. 11.17C shows the positions of candidate object centers as found by the GHT. The small isolated crosses indicate the positions of single votes, and those very close to the two large crosses lead to voting peaks of weights 10 and 6 at these respective positions. Hence, object location is both accurate and robust, as required.

### 11.9.1 COMPUTATIONAL LOAD

This subsection compares the computational requirements of the maximal clique and GHT approaches to object location. For simplicity, imagine an image that contains just one wholly visible example of the object being sought. Moreover, suppose that the object possesses  $n$  features and that we are trying to recognize it by seeking all possible pairwise compatibilities, whatever their distance apart (as for all examples in Section 11.7).

For an object possessing  $n$  features, the match graph contains  $n^2$  nodes (i.e., possible assignments), and there are  $n^2 C_2 = n^2(n^2 - 1)/2$  possible pairwise compatibilities to be checked in building the graph. The amount of computation at this stage of the analysis is  $O(n^4)$ . To this must be added the cost of finding the maximal cliques. As the problem is NP-complete, the load rises at a rate which is faster than polynomial, and probably exponential in  $n^2$  (Gibbons, 1985).

Now consider the cost of getting the GHT to find objects via pairwise compatibilities. As has been seen, the total height of all the peaks in parameter space is in general equal to the number of pairwise compatibilities in the match graph. Hence, the computational load is of the same order,  $O(n^4)$ . Next comes the problem of locating all the peaks in parameter space. In this case, parameter space is congruent to image space. Hence, for an  $N \times N$  image, only  $N^2$  points have to be visited in parameter space, and the computational load is  $O(N^2)$ . Note, however, that an alternative strategy is available in which a running record is kept of the relatively small numbers of voting positions in parameter space. The computational load for this strategy will be  $O(n^4)$ : although of a higher *order*, this often represents less computation in practice.

The reader may have noticed that the basic GHT scheme as outlined so far is able to locate objects from their features but does not determine their orientations. However, orientations can be computed by running the algorithm a second time and finding all the assignments that contribute to each peak. Alternatively, the second pass can aim to find a different localization point within each object. In either case, the overall task should be completed in little over twice the time, i.e., still in  $O(n^4 + N^2)$  time.

Although the GHT at first appears to solve the maximal clique problem in polynomial time, what it actually achieves is to solve a real-space template-matching problem in polynomial time: it does not solve an *abstract* graph-theoretic problem



in polynomial time. The overall lesson is that the graph theory representation is not well matched to real space, not that real space can be used to solve abstract NP-complete problems in polynomial time.

---

## 11.10 GENERALIZING THE MAXIMAL CLIQUE AND OTHER APPROACHES

This section considers how the graph-matching concept can be generalized to cover alternative types of feature and also various attributes of features. The earlier discussion was restricted to point features and in particular to small holes. Corners were also taken as point features by ignoring attributes other than position coordinates. Thus, holes and corners seem to be ideal, in that they give maximum localization and hence maximum accuracy for object location.

Other types of feature generally have more than two specifying parameters, one of which may be contrast and the other size. This applies for most holes and circular objects, although for the smallest holes, it is sometimes most practicable to take the central dip in intensity as the measured parameter. Corners may have a number of attributes, including contrast, color, sharpness, and orientation, though these may not be known to high accuracy. Finally, more complex shapes such as ellipses have orientation, size, and eccentricity, and again contrast or color may be a usable attribute.

In fact, so much information is available that we need to consider how best to use it for locating objects. For convenience, this is discussed in relation to the maximal clique method. In fact, the answer is very simple. When compatibilities are being considered and the arcs are being drawn in the match graph, *any* available information may be taken into account in deciding whether a pair of features in the image matches a pair of features in the object model. In [Section 11.7](#), the discussion was simplified by taking interfeature distances as the only relevant measurements. However, it is quite acceptable to describe the features in the object model more fully and to insist that they all match within prespecified tolerances. For example, holes and corners may be permitted to lead to a match only if the former are of the correct size, the latter are of the correct sharpness and orientation, and the interfeature distances are also appropriate. All relevant information has to be held in suitable lookup tables. In general, the gains easily outweigh the losses, as a considerable number of potential interpretations will be eliminated—hence, making the match graph significantly simpler and reducing, in many cases by a substantial factor, the amount of computation that is required to find the maximal cliques.

Overall, extrafeature attributes can be of great value in cutting down computation: they are also useful in reducing the possibility of erroneous interpretations.

---

## 11.11 SEARCH

The above sections have shown how the maximal clique approach may be used to locate objects in an image, or alternatively to label scenes according to predefined rules about what arrangements of regions are expected in scenes. In either case, the basic process being performed is that of search for solutions that are compatible with the observed data. This search takes place in assignment space, i.e., a space in which all combinations of assignments of observed features with possible interpretations exist. The problem is that of finding one or more valid sets of observed assignments.

It generally happens that the search space is very large, so that an exhaustive search for all solutions would involve enormous computational effort and would take considerable time. Unfortunately, one of the most obvious and appealing methods of obtaining solutions, the maximal clique approach, is NP-complete and can require impracticably large amounts of time to find solutions. It is therefore useful to clarify the nature of the maximal clique approach: to achieve this, we first describe the two main categories of search—breadth—first and depth—first search.

Breadth—first search is a form of search that systematically works down a tree of possibilities, never taking shortcuts to nearby solutions. Depth—first search, in contrast, involves taking as direct a path as possible to individual solutions, stopping the process when a solution is found and backtracking up the tree whenever a wrong decision is found to have been made. It is normal to curtail the depth—first search when sufficient solutions have been found, and this means that much of the tree of possibilities will not have been explored. Although breadth—first search can be curtailed similarly when enough solutions have been found, the maximal clique approach as described earlier is in fact a form of breadth—first search that is exhaustive and runs to completion.

In addition to being an exhaustive breadth—first search, the maximal clique approach may be described as being “blind” and “flat”—i.e., it involves neither heuristic nor hierarchical means of guiding the search. In fact, faster search methods involve guiding the search in various ways. First, heuristics are used to specify at various stages in which direction to proceed (which node of the tree to expand), or which paths to ignore (which nodes to prune). Second, the search can be made more “hierarchical,” so that it searches first for outline features of a solution, returning later (perhaps in several stages) to fill in the details. Details of these techniques are omitted here. However, an interesting approach was used by Rummel and Beutel (1984): they searched images for industrial components using features such as corners and holes, alternating at various stages between breadth—first and depth—first search by using a heuristic based on a dynamically adjusted parameter: this being computed on the basis of how far the search is still away from its goal, and the quality of the fit so far. Rummel and Beutel noted the existence of a trade-off between speed and accuracy as a “guide factor,” based on the number of features required for recognition, is adjusted—the problem being that trying to increase speed introduces some risk of not finding the optimum solution.

---

## 11.12 CONCLUDING REMARKS

The HT was introduced in Chapter 10, Line, Circle, and Ellipse Detection as a line detection scheme and then applied for detecting circles and ellipses. In that chapter, it appeared as a rather cunning method for aiding object detection; although it was seen to offer various advantages, particularly in its robustness in the face of noise and occlusion, there appeared to be no real significance in its rather novel voting scheme. The present chapter has shown that, far from being a trick method, the HT is much more general an approach than originally supposed: indeed, it embodies the properties of the spatial matched filter and is therefore capable of close-to-optimal sensitivity for object detection. However, this does not prevent its implementation from entailing considerable computational load, and significant effort and ingenuity has been devoted to overcoming this problem, both in general and in specific cases. The general case is tackled by the schemes discussed in the earlier sections of this chapter. It is important not to underestimate the value of specific solutions, both because such shapes as lines, circles, ellipses, and polygons cover a large proportion of (or approximations to) manufactured objects, and because methods for coping with specific cases have a habit (as for the original HT) of becoming more general as workers see possibilities for developing the underlying techniques.

To further underline the generality of the GHT, it has also been used for optimal location of lines of known length, by emulating a spatial matched filter detector; this result has been applied to the optimal detection of polygons and corners: for an example of the latter, see [Fig. 11.20](#) (Davies, 1988a, 1989a).

This chapter has also discussed the problem of recognizing objects from point features. The maximal clique approach was seen to be capable of finding solutions to this task, but is limited in being NP-complete. Interestingly, the GHT has been found capable of performing the same task in polynomial time. That this is possible is because the graph theory representation is not well matched to the relevant real-space template-matching task in the way that the GHT is. Here, recall that the GHT is particularly well suited to object detection in real space as it is one type of spatial matched filter, whereas this cannot be said of the maximal clique approach.

Finally, note that, on an absolute scale, the graph-matching approach takes very little note of detailed image structure, using at most only pairwise feature attributes. This is adequate for 2-D image interpretation but inadequate for situations such as 3-D image analysis where there are more degrees of freedom to contend with (normally three degrees of freedom for position and three for orientation, for each object in the scene). Hence, more specialized and complex approaches need to be taken in such cases: these are examined in Part 3.

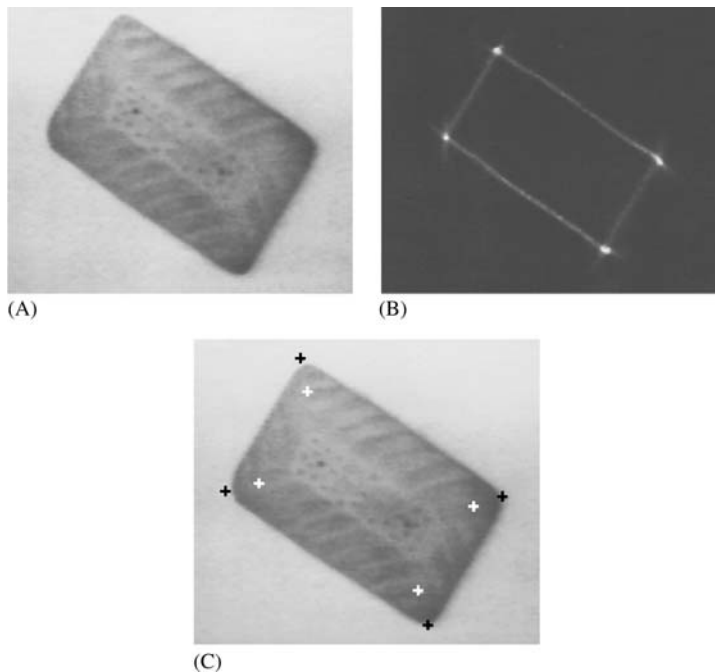


**FIGURE 11.20**

Example of the generalized Hough transform approach to corner detection. (A) original image of a biscuit ( $128 \times 128$  pixels, 64 gray levels); (B) transform with lateral displacement around 22% of the shorter side; (C) image with transform peaks located (white crosses) and idealized corner positions deduced (black crosses). The lateral displacement employed here is close to the optimum for this type of object.

(A,B) © IEE 1988

*Although the HT may appear to have a somewhat arbitrary design, this chapter has shown that it has solid roots in matched filtering, which in turn implies that votes should be gradient weighted for optimal sensitivity. The chapter also contrasts three methods for ellipse detection, showing how computational load may be estimated and minimized. In addition, searching for objects via their features is far more efficient than template matching. This chapter has shown that this raises the need to **infer** the presence of objects—a process that can still be computation intensive. In this respect, tests show that the GHT can be much more efficient than graph matching.*

## 11.13 BIBLIOGRAPHICAL AND HISTORICAL NOTES

Although the HT was introduced as early as 1962, a number of earlier ideas—including especially those of Merlin and Farber (1975) and Kimme

et al. (1975)—were required before the GHT could be developed (Ballard, 1981). By that time, the HT was already known to be formally equivalent to template matching (Stockman and Agrawala, 1977) and to spatial matched filtering (Sklansky, 1978).

By 1985, the computational load of the HT became the critical factor preventing its more general use—particularly as it could be used for most types of arbitrary shape detection, with well-attested sensitivity and considerable robustness. Li et al. (1985, 1986) showed the possibility of much faster peak location by using nonuniformly quantized parameter spaces. This work was developed further by Princen et al. (1989a,b) and Davies (1992g). An important development has been the randomized Hough transform, pioneered by Xu and Oja (1993) amongst others: it involves casting votes until specific peaks in parameter space become evident, thereby saving unnecessary computation.

Accurate peak location remains an important aspect of the HT approach. Properly, this is the domain of robust statistics which handles the elimination of outliers (see Appendix A). Davies (1992f) has shown a computationally efficient means of accurately locating HT peaks and has found why peaks sometimes appear narrower than a priori considerations would indicate (Davies, 1992b). Kiryati and Bruckstein (1991) have tackled aliasing effects which can arise with the HT, and which have the effect of cutting down accuracy.

Over time, the GHT approach has been broadened by geometric hashing, structural indexing, and other approaches (e.g., Lamdan and Wolfson, 1988; Gavrilu and Groen, 1992; Califano and Mohan, 1994). At the same time, a probabilistic approach to the subject has been developed (Stephens, 1991) which puts it on a firmer footing. Grimson and Huttenlocher (1990) warn (possibly overpessimistically) against the blithe use of the GHT for complex object recognition tasks, because of the false peaks that can appear in such cases. For further review of the state of the subject up to 1993, see Leavers (1993).

In various chapters of Part 2, the statement has been made that the HT carries out a search leading to hypotheses that should be checked before a final decision about the presence of an object can be made. (A similar statement can be made in the case of graph-matching methods such as the maximal clique approach to object location.) However, Princen et al. (1994) show that the performance of the HT can be improved if it is itself regarded as a hypothesis testing framework: this is in line with the concept that the HT is a model-based approach to object location. Kadyrov and Petrou (2001) have developed the trace transform, which can be regarded as a generalized form of the Radon transform—itsself closely related to the HT.

Other workers have used the HT for affine-invariant search: Montiel et al. (2001) made an improvement to reduce the incidence of erroneous evidence in the gathered data, whereas Kimura and Watanabe (2002) made an extension for 2-D shape detection that is less sensitive to the problems of occlusion and broken boundaries. Kadyrov and Petrou (2002) have adapted the trace transform to cope with affine parameter estimation.

In a generalization of the work of Atherton and Kerbyson (1999), and of Davies (1987a) on gradient weighting (see [Section 11.4](#)), Anil Bharath and his colleagues have examined how to optimize the sensitivity of the HT (private communication, 2004). Their method is particularly valuable in solving the problems of early threshold setting that limit many HT techniques. Similar sentiments come out in a different way in the work of Kesidis and Papamarkos (2000), which maintains the gray-scale information throughout the transform process, thereby leading to more exact representations of the original images.

Olson (1999) has shown that localization accuracy can be improved efficiently by transferring local error information into the HT and handling it rigorously. An important finding is that the HT can be divided into several subproblems without decrease in performance. This finding is elaborated in a 3-D model-based vision application where it is shown to lead to reduced false positive rates (Olson, 1998). Wu et al. (2002) extend the 3-D possibilities further by using a 3-D HT to find glasses: first a set of features are located that lie on the same plane, and this is then interpreted as the glasses rim plane. This approach allows the glasses to be separated from the face, and then they can be located in their entirety.

van Dijck and van der Heijden (2003) develop the geometric hashing method of Lamdan and Wolfson (1988) to perform 3-D correspondence matching using full 3-D hashing. This is found to have advantages in that knowledge of 3-D structure can be used to reduce the number of votes and spurious matches. Tuytelaars et al. (2003) describe how invariant-based matching and HTs can be used to identify regular repetitions in planes appearing within visual (3-D) scenes in spite of perspective skew: the overall system has the ability to reason about consistency and is able to cope with periodicities, mirror symmetries, and reflections about a point.

Graph-matching and clique-finding algorithms started to appear in the literature around 1970: for an early solution to the graph isomorphism problem, see Corneil and Gottlieb (1970). The subgraph isomorphism problem was tackled soon after by Barrow et al. (1972): see also Ullmann (1976). The double subgraph isomorphism (or subgraph–subgraph isomorphism) problem was commonly tackled by seeking maximal cliques in the match graph, and algorithms for achieving this have been described by Bron and Kerbosch (1973), Osteen and Tou (1973), and Ambler et al. (1975) (note that in 1989, Kehtarnavaz and Mohan reported preferring the algorithm of Osteen and Tou on the grounds of speed). Improved speed has also been achieved using the minimal match graph concept (Davies, 1991a).

Bolles (1979) applied the maximal clique technique to real-world problems (notably the location of engine covers) and showed how operation could be made more robust by taking additional features into account. By 1982, Bolles and Cain had formulated the LFF method, which (1) searches for restricted sets of features on an object, (2) takes symmetry into account to save computation, and (3) reconsiders the original image data in order to confirm a valid match: the paper gives various criteria for ensuring satisfactory solutions with this type of method.

Not satisfied with the speed of operation of maximal clique methods, other workers have tended to use depth-first search techniques. Rummel and Beutel (1984) developed the idea of alternating between depth-first and breadth-first search as dictated by the data—a powerful approach, although the heuristics that they used for this may well lack generality. Meanwhile, Kasif et al. (1983) showed how a modified GHT (the “relational HT”) could be used for graph matching, although their paper gives few practical details. A somewhat different application of the GHT to perform 2-D matching was described in [Section 11.9](#) and has been extended to optimize accuracy (Davies, 1992c). Geometric hashing has been developed to perform similar tasks on objects with complex polygonal shapes (Tsai, 1996).

Over the past decades inexact matching algorithms have acquired increasing predominance over exact matching methods, because of the ubiquitous presence of noise, distortions, and missing or added feature points, together with inaccuracies and thus mismatches of feature attributes. One class of work on inexact (or “error-tolerant”) matching considers how structural representations should be compared (Shapiro and Haralick, 1985); this early work on similarity measures shows how the concept of “string edit distance” can be applied to graphical structures (Sanfeliu and Fu, 1983); the formal concept of edit distance was later extended by Bunke and Shearer (1998) and Bunke (1999), who considered and rationalized the cost functions for methods such as graph isomorphisms, subgraph isomorphisms, and maximum common subgraph isomorphisms: choice of cost functions was shown to be of crucial importance to success in each particular data set, though detailed analysis demonstrated important subtleties in the situation (Bunke, 1999).

Yet another class of work is that on optimization. This has included work on simulated annealing (Herauld et al., 1990), genetic search (Cross et al., 1997), and neural processing (Pelillo, 1999). The work of Umeyama (1988) develops the least squares approach using a matrix eigendecomposition method to recover the permutation matrix relating the two graphs being matched. One of the most recent developments has been the use of spectral graph theory to recover the permutation structure. Spectral graph theory involves analysis of the structural properties of graphs using the eigenvalues and eigenvectors of the adjacency matrix. In fact, the Umeyama (1988) approach only matches graphs of the same size. Other related methods have emerged (e.g., Horaud and Sossa, 1995), but they have all suffered from an inability to cope with graphs of different sizes. However, Luo and Hancock (2001) have demonstrated how this particular problem can be overcome—by showing how the graph-matching task can be posed as maximum likelihood estimation using the EM algorithm formalism. Hence, singular value decomposition is used efficiently to solve correspondence problems. Ultimately, the method is important because it helps to move graph matching away from a discrete process in which a combinatorial search problem exists toward a continuous optimization problem which moves systematically toward the optimum solution. It ought to be added that the method works under considerable levels of

structural corruption—such as when 50% of the initial entries in the data-graph adjacency matrix are in error (Luo and Hancock, 2001). In a later development, Robles-Kelly and Hancock (2002) managed to achieve the same end, and to achieve even better performance within the spectral graph formalism itself.

Meanwhile, other developments included a fast, phased approach to inexact graph matching (Hlaoui and Wang, 2002); a reproducible kernel Hilbert space (RKHS) interpolator-based graph-matching algorithm capable of efficiently matching huge graphs of more than 500 vertices (e.g., those extracted from aerial scenes) on a PC (van Wyk et al., 2002). For a more detailed appraisal of inexact matching algorithms, see Lladós et al. (2001): note that the latter appears in a special section of IEEE Trans. PAMI on *Graph Algorithms and Computer Vision* (Dickinson et al., 2001).

### 11.13.1 MORE RECENT DEVELOPMENTS

Amongst the most recent developments are the following. Aragon-Camarasa and Siebert (2010) considered using the GHT for clustering SIFT feature matches. However, it turned out that a *continuous* rather than discretized HT space was needed for this application. This meant that each matched point had to be stored at the full machine precision in a Hough space consisting of a list data structure. Therefore, peak location had to take the form of standard unsupervised clustering algorithms. This was an interesting case where the intended GHT could not follow the standard voting and accumulating procedure. Assheton and Hunter (2011) also deviated sharply from the standard GHT approach when performing pedestrian detection and tracking: they used a shape-based voting algorithm based on Gaussian mixture models. The algorithm was stated to be highly effective for detecting pedestrians based on the silhouette shape. Chung et al. (2010) studied the problem of information retrieval from databases. They produced a region-based solution for object retrieval using the GHT and adaptive image segmentation. A key aspect of the overall scheme was the location of affine invariant MSERs (see Chapter 6: Corner, Interest Point, and Invariant Feature Detection) in the database and query images. Roy et al. (2011) applied the GHT to the detection and verification of seals (stamps) containing lettering and geometric patterns. This is a difficult problem because of the likely presence of noise, interfering text and signatures as well as incompleteness due to the application of uneven pressure to the stamp. In practice, a seal has to be located using scale and rotation invariant features (particularly text characters); it is then detected as a GHT peak resulting from application of a spatial feature descriptor of neighboring connected component pairs: i.e., in this application, the text characters in the seal are used as basic features for seal detection instead of individual edge or feature points. Memory demands are limited by splitting the  $R$ -table into two different look-up-tables—the character pair table and the distance table.

Silletti et al. (2011) have devised a variant approach to spectral graph matching in which new similarity measures are applied. The approach permits



application to a variety of types of image and yields results that are said to show significant improvements over certain preexisting methods. Gope and Kehtarnavaz (2007) have demonstrated a new method for affine matching between planar point sets. The method makes use of the convex hulls of the point sets and performs matching between them: this is a useful approach because (1) convexity is affine invariant, and (2) use of the convex hull is intrinsically robust. Property (2) follows from the fact that convex hulls are only locally altered by point perturbations including insertions and deletions. The method makes use of an enhanced modified Hausdorff distance and achieves better results in the presence of noise and occlusion than a number of standard methods. Aguilar et al. (2009) have developed a new “graph transformation matching” algorithm, to match points between pairs of images. It validates each match through the spatial configuration of the points by constructing a  $k$ -nearest-neighbor graph for each image; vertices that introduce structural dissimilarity between the graphs are iteratively eliminated, thereby yielding a consensus graph representing a correct set of point matches between the images.

---

## 11.14 PROBLEMS

1. a. Describe the main stages in the application of the HT to locate objects in digital images. What are the particular advantages offered by the HT technique? Give reasons why they arise.  
 b. It is said that the HT only leads to *hypotheses* about the presence of objects in images, and that they should all be checked independently before making a final decision about the contents of any image. Comment on the accuracy of this statement.
2. Devise a GHT version of the spatial matched filter for detecting lines of known length  $L$ . Show that when used to detect an ideal line of length  $L$ , it gives a distributed response of length  $2L$  that peaks at the center of the line, but when used to detect a partially occluded version of the line, it gives a response that is flat-topped over a range that includes the center of the line.
3. Show how a GHT version of the spatial matched filter can be devised to detect an equilateral triangle, leading to a star-shaped transform that peaks at the center the triangle. How may this approach be adapted for (1) a general triangle, (2) a regular polygon having  $N$  sides?
4. Find the match graph for a set of features arranged in the form of an isosceles triangle. Find how much simplification occurs by taking account of symmetry and using the symmetry-reduced match graph. Extend your results to the case of a kite (two isosceles triangles arranged symmetrically base-to-base).
5. Two lino-cutter blades (trapeziums) are to be located from their corners. Consider images in which two corners of one blade are occluded by the other blade. Sketch the possible configurations, counting the number of

corners in each case. If corners are treated like point features with no other attributes, show that the match graph will lead to an ambiguous solution. Show further that the ambiguity can in general be eliminated if proper account is taken of corner orientation. Specify how accurately corner orientation would need to be determined for this to be possible.

6. In problem 11.5, would the situation be any better if the GHT were used?
7. a. Metal flanges are to be located from their holes using a graph-matching (maximal clique) technique. Each bar has four identical holes at distances from the narrow end of the bar of 1, 2, 3, 5 cm, as shown in Fig. 11.P1. Draw match graphs for the four different cases in which one of the four holes of a given flange is obscured: determine in each case whether the method is able to locate the metal flange without any error, and whether any ambiguity arises.

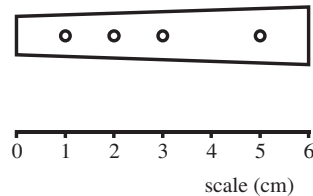


**FIGURE 11.P1**

Metal flanges for location using the GHT.

- b. Do your results tally with the results for human perception? How would any error or ambiguity be resolved in practical situations?
8. a. Describe the maximal clique approach to object location. Explain why the largest maximal clique will normally represent the most likely solution to any object location task.
- b. If symmetrical objects with four feature points are to be located, show that suitable labeling of the object template will permit the task to be simplified. Does the type of symmetry matter? What happens in the case of a rectangle? What happens in the case of a parallelogram? (In the latter case, see points A, B, C, D in Fig. 11.P2.)

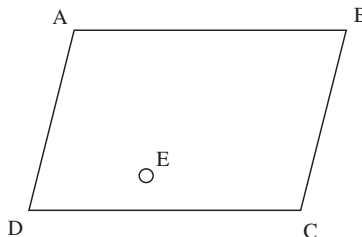


**FIGURE 11.P2**

Object with five feature points.

- c. A nearly symmetrical object with *five* feature points (see Fig. 11.P2) is to be located. This is to be achieved by looking initially for the feature points A, B, C, D and ignoring the fifth point E. Discuss how the fifth point may be brought into play to finally determine the orientation of the object, using the maximal clique approach. What disadvantage might there be in adopting this two-stage approach?
9. a. What is template matching? Explain why objects are normally located from their features rather than using whole object templates. What are the features that are commonly used for this purpose?
- b. Describe templates that can be used for corner and hole detection.
- c. An improved type of lino-cutter blade (Fig. 11.P3) is to be placed into packs of six by a robot. Show how the robot vision system could locate the blades *either* from their corners *or* from their holes by applying the maximal clique method (i.e., show that *both* schemes would work).

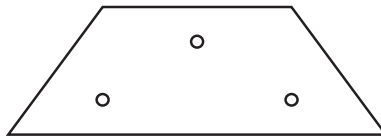


FIGURE 11.P3

---

Symmetrical lino-cutter blade.

- d. After a time, it appears that the robot is occasionally confused when the blades overlap. It is then decided to locate the blades from their holes *and* their corners. Show why this helps to eliminate any confusion. Show also how finally distinguishing the corners from the holes can help in extreme cases of overlap.
10. a. A certain type of lino-cutter blade has four corners and two fixing holes (Fig. 11.P4). Blades of this type are to be located using the maximal clique technique. Assume the objects lie on a worktable and that they are viewed orthogonally at a known distance.

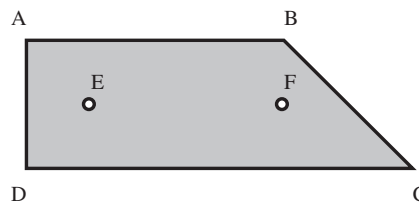


FIGURE 11.P4

---

Non-symmetrical lino-cutter blade.

- b. Draw match graphs for the following situations:
- i. the objects are to be located by their holes and their corners, regarding these as *indistinguishable* point features;

- ii. the objects are to be located solely by their corners (i.e., matching corners in the image with corners on an idealized object);
  - iii. the objects are to be located solely by their holes;
  - iv. the objects are to be located by their holes *and* their corners, but these are to be regarded as *distinguishable* features.
- c. Discuss your results with particular reference to:
- i. the robustness that can be achieved;
  - ii. the speed of computation.
- d. In the latter case, distinguish the time taken to build the basic match graph from the time taken to find all the maximal cliques in it. State any assumptions you make about the time taken to find a maximal clique of  $m$  nodes in a match graph of  $n$  nodes.
11. a. Decorative biscuits are to be inspected after first locating them from their holes. Show how the maximal clique graph-matching technique can be applied to identify and locate the biscuits shown in Fig. 11.P5A, which are of the same size and shape.

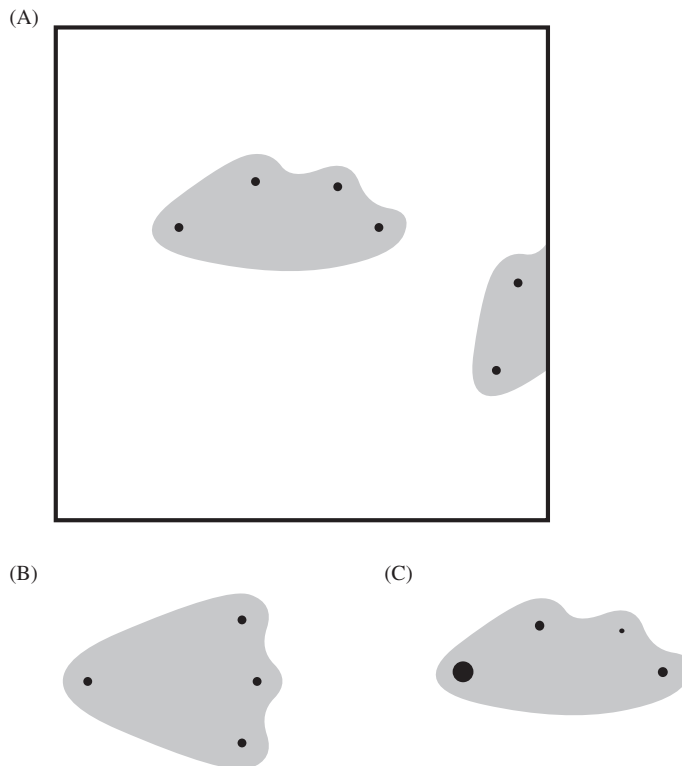


**FIGURE 11.P5**

Decorative biscuits for inspection.

- b. Show how the analysis will be affected for biscuits which have an axis of symmetry, as shown in Fig. 11.P5B. Show also how the technique may be modified to simplify the computation for such a case.
  - c. A more detailed model of the first type of biscuit shows it has holes of *three* sizes, as shown in Fig. 11.P5C. Analyze the situation and show that a much simplified match graph can be produced from the image data, leading to successful object location.
  - d. A further matching strategy is devised to make use of the hole size information: matches are *only* shown in the match graph if they arise between pairs of holes of *different* sizes. Determine how successful this strategy is, and discuss whether it is likely to be generally useful, e.g., for objects with increased numbers of features.
  - e. Work out an optimal object identification strategy, which will be capable of dealing with cases where holes and/or corners are to be used as point features, where the holes might have different sizes, the corners might have different angles and orientations, the object surfaces might have different colors or textures, and objects might have larger numbers of features. Make clear what the term “optimal” should be taken to mean in such cases.
12. a. Fig. 11.P6 shows a 2-D view of a widget with four corners. Explain how the maximal clique technique can be used to locate widgets even if they are partly obscured by various types of object including other widgets.

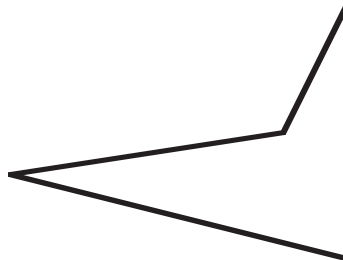


**FIGURE 11.P6**

Diagram of a widget.

- b. Explain why the basic algorithm will not distinguish between widgets that are normally presented from those that are upside down. Consider how the basic method could be extended to ensure that a robot only picks up those that are the right way up.
- c. The camera used to view the widgets is accidentally jarred and then reset at a different, unknown height above the worktable. State clearly why the usual maximal clique technique will now be unable to identify the widgets. Discuss how the overall program could be modified to make

sense of the data and make correct interpretations in which all the widgets are identified. Assume *first* that widgets are the only objects appearing in the scene, and *second* that a variety of other objects may appear.

- d. The camera is jarred again, and this time is set at a small, unknown angle to the vertical. To be sure of detecting such situations and of correcting for them, a flat calibration object of known shape is to be stuck on the worktable. Decide on a suitable shape and explain how it should be used to make the necessary corrections.
13. Show that flat convex shapes remain convex under affine transformations.

This page intentionally left blank

# Object segmentation and shape models

# 12

Object segmentation can be carried out using raw thresholding or edge detection, but such processes are liable to stray far-off course because of random image artifacts such as noise and shadows. The idea of using shape models is to control the situation so that the segmentations obtained are more meaningful. Active contour models or “snakes” provide a means for tackling this problem: principal components analysis (PCA)-based methods provide another.

*Look out for:*

- the need for shape models during segmentation
- the use of active contour models (snakes) for segmenting object boundaries
- the principle of energy minimization
- problems in handling snake evolution: model constraints
- the “level set” approach to object segmentation
- the “fast-marching” and “front-propagation” methods
- the use of PCA for learning shape models
- how the list of eigenvalues is limited
- how the system is trained using landmark points
- speeding up search by implementing it at various scales to improve matching
- improving on the Mahalanobis distance model using gray-scale boundary profiles.

The snake approach is subject to difficulties because all the necessary rules have to be incorporated into the snake analytically without acknowledging exactly what type of shape it will have: PCA-based methods are more powerful as they train the system to know exactly what type of shape is being sought. However, they involve substantial amounts of complication and computation, though as a result, they can extract objects from regions of considerable noise.

## 12.1 INTRODUCTION

This chapter follows on naturally from [Chapter 5](#) on edge detection. It takes as its basis the idea that edges have already been found in the image and that they need to be connected up to form objects in a systematic way. In fact, it is not



absolutely necessary to find the edge points first, so long as they can be found on the fly as a shape model develops. Indeed, the snake “active contour” approach can adopt the latter strategy—in which case, the snake model is forced to grow in a systematic way until it is found to match the edges that are present in the picture. As we shall see in the following section, snakes are made to be subject to rules that force them to develop under the influence of energy minimization and other constraints. That approach and the ensuing level-set technique are guided by general segmentation principles but do not include exact models of the shapes that are to be found. On the other hand, alternative approaches such as PCA are available for generating shape models: these act more like recognition algorithms than segmentation algorithms. In addition, they have become extremely widely used and deserve to be covered in fair depth. We start with a basic description of the active contour approach.

---

## 12.2 ACTIVE CONTOURS

Active contour models (also known as “deformable contours” or “snakes”) are widely used for systematically refining object contours. The basic concept is to obtain a complete and accurate outline of an object that may be ill-defined in places, whether through lack of contrast, or noise or fuzzy edges. A starting approximation is made, either by instituting a large contour that may be shrunk to size, or a small contour that may be expanded suitably, until its shape matches that of the object. In principle, the initial boundary can be rather arbitrary, whether mostly outside or within the object in question. Then, its shape is made to evolve subject to an energy minimization process: on the one hand, it is desired to minimize the *external* energy corresponding to imperfections in the degree of fit; on the other hand, it is desired to minimize the *internal* energy, so that the shape of the snake does not become unnecessarily intricate, e.g., by taking on any of the characteristics of image noise. There are also model constraints that are represented in the formulation as contributions to the external energy: typical of such constraints is that of preventing the snake from moving into prohibited regions, such as beyond the image boundary, or, for a moving vehicle, off the region of the road.

The snake’s internal energy includes elastic energy which might be needed to extend or compress it, and bending energy. If no bending energy terms were included, sharp corners and spikes in the snake would be free to occur with no restriction. Similarly, if no elastic energy terms were included, the snake would be permitted to grow or shrink without penalty.

The image data is normally taken to interact with the snake via three main types of image feature—lines, edges, and terminations (the latter can be line terminations or corners). Various weights can be given to these features according to the behavior required of the snake. For example, it might be required to hug edges and go around corners, and only to follow lines in the absence of edges: so the line weights would be made much lower than the edge and corner weights.

These considerations lead to the following breakdown of the snake energy:

$$\begin{aligned}
 E_{\text{snake}} &= E_{\text{internal}} + E_{\text{external}} \\
 &= E_{\text{internal}} + E_{\text{image}} + E_{\text{constraints}} \\
 &= E_{\text{stretch}} + E_{\text{bend}} + E_{\text{line}} + E_{\text{edge}} + E_{\text{term}} + E_{\text{repel}}
 \end{aligned}
 \tag{12.1}$$

The energies are written down in terms of small changes in position  $\mathbf{x}(s) = (x(s), y(s))$  of each point on the snake, the parameter  $s$  being the arc length distance along the snake boundary. Thus, we have:

$$E_{\text{stretch}} = \int \kappa(s) \|\mathbf{x}_s(s)\|^2 ds \tag{12.2}$$

and

$$E_{\text{bend}} = \int \lambda(s) \|\mathbf{x}_{ss}(s)\|^2 ds \tag{12.3}$$

where the suffices  $s, ss$  imply first and second order differentiation, respectively. Similarly,  $E_{\text{edge}}$  is calculated in terms of the intensity gradient  $|\text{grad } I|$ , leading to:

$$E_{\text{edge}} = - \int \mu(s) \|\text{grad } I\|^2 ds \tag{12.4}$$

where  $\mu(s)$  is the edge weighting factor.

The overall snake energy is obtained by summing the energies for all positions on the snake: a set of simultaneous differential equations is then set up to minimize the total energy. Space prevents a full discussion of this process here. Suffice it to say that the equations cannot be solved analytically, and recourse has to be made to iterative numerical solution, during which the shape of the snake evolves from some high energy initialization state to the final low energy equilibrium state, defining the contour of interest in the image.

In the general case, there are several possible complications to be tackled, which are as follows:

1. several snakes may be required to locate an initially unknown number of relevant image contours;
2. different types of snake will need different initialization conditions;
3. snakes will sometimes have to split up as they approach contours that turn out to be fragmented.

There are also procedural problems. The intrinsic snake concept is that of well-behaved differentiability. However, lines, edges, and terminations are usually highly localized, so there is no means by which a snake even a few pixels away could be expected to learn about them and hence to move toward them. In these circumstances, the snake would “thrash around,” and fail to systematically zone in on a contour representing a global minimum of energy. To overcome this problem, smoothing of the image is required, so that edges can communicate with the snake some distance away, and the smoothing must gradually be reduced as the

snake nears its target position. Ultimately, the problem is that the algorithm has no high-level appreciation of the overall situation but merely reacts to a conglomerate of local pieces of information in the image: this makes segmentation using snakes somewhat risky despite the intuitive attractiveness of the concept.

In spite of these potential problems, a valuable feature of the snake concept is that, if set up correctly, the snake can be rendered insensitive to minor discontinuities in a boundary: this is important, as this makes it capable of negotiating practical situations such as fuzzy or low contrast edges, or places where small artifacts get in the way (this may happen with resistor leads for example); this capability is possible because the snake energy is set up *globally*—quite unlike the situation for boundary tracking where error propagation can cause wild deviations from the desired path. The reader is referred to the abundant literature on the subject, not only to clarify the basic theory (Kass and Witkin, 1987; Kass et al., 1988) but also to find how it may be made to work well in real situations.

---

## 12.3 PRACTICAL RESULTS OBTAINED USING ACTIVE CONTOURS

In this section, we briefly explore a simple implementation of the active contour concept. Arguably, the implementation chosen is amongst the simplest that will work in practical situations while still adhering to the active contour concept. To make it work without undue complication or high levels of computation, a “greedy” algorithm is used—that is, one that makes local optimizations (energy minimizations) in the expectation that this will result in global optimization. Naturally, it could lead to solutions that do not correspond to absolute minima of the energy function, though this is by no means a problem that is caused solely by using a greedy algorithm, as almost all forms of iterative energy minimization method can fall into this trap.

The first thing to do when devising such an algorithm is to interpret the theory in practical terms. Thus, we rewrite the snake stretch function (Eq. (12.2)) in the discrete form:

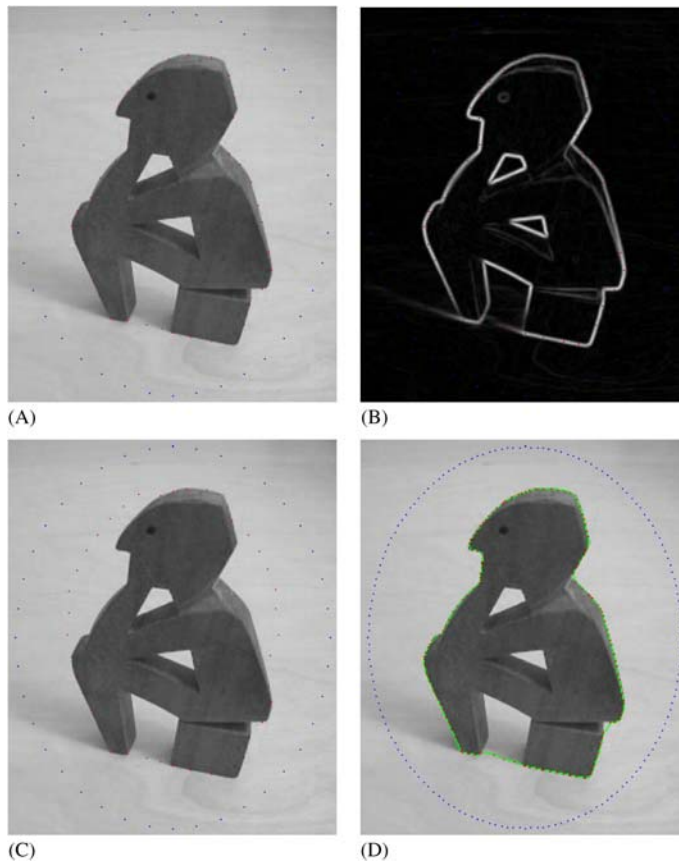
$$E_{\text{stretch}} = \sum_{i=1}^N \kappa \|\mathbf{x}_i - \mathbf{x}_{i+1}\|^2 \quad (12.5)$$

where there are  $N$  snake points  $\mathbf{x}_i$ ,  $i = 1, \dots, N$ : note that this set must be accessed cyclically. In addition, when using a greedy algorithm and updating the position of the  $i$ th snake point, the following local form of Eq. (12.5) has to be used:

$$\varepsilon_{\text{stretch}, i} = \kappa (\|\mathbf{x}_i - \mathbf{x}_{i-1}\|^2 + \|\mathbf{x}_i - \mathbf{x}_{i+1}\|^2) \quad (12.6)$$

Unfortunately, although this function causes the snake to be tightened, it can also result in clustering of snake points. To avoid this, the following alternative form can be useful:

$$\varepsilon_{\text{stretch}, i} = \kappa [(d - \|\mathbf{x}_i - \mathbf{x}_{i-1}\|)^2 + (d - \|\mathbf{x}_i - \mathbf{x}_{i+1}\|)^2] \quad (12.7)$$

**FIGURE 12.1**

Generation of active contour models (snakes). (A) Original picture with snake initialization points (blue) near the image boundary; the final snake locations (red) hug the outside of the object but hardly penetrate the large concavity at the bottom: they actually lie approximately along a weak shadow edge. (B) Result of smoothing and application of Sobel operator to (A); the snake algorithm used this image as its input. The snake output is superimposed in (red) on (B), so that the high degree of colocation with the edge maxima can readily be seen. (C) Intermediate result, after half (30) the total number of iterations (60): this illustrates that, after one edge point has been captured, it becomes much easier for other such points to be captured. (D) Result of using an increased number of initialization points (blue) and joining (green) the final locations (red) to give a connected boundary: some remanent deficiencies are evident.

where  $d$  is a fixed number representing the smallest likely value of the mean distance between adjacent pairs of snake points, for the given type of target object. In the implementation used in Fig. 12.1,  $d$  had the noncritical value of 8 pixels; interestingly, this also resulted in faster convergence toward the final form of the

snake, as it was encouraged to move further to minimize the magnitudes of the terms in round brackets.

The contour shown in Fig. 12.1 fills the concavity at the top right, but hardly moves into the concavity at the bottom because of a low contrast shadow edge: note that more or less influence by weak edges can readily be obtained by adjusting the  $\text{grad}^2$  coefficient  $\mu$  in Eq. (12.4). Elsewhere the snake ends up with almost exact adherence to the object boundary. The snake shown in the figure employs  $p = 40$  points, and  $r = 60$  iterations are needed to bring it to its final position. In each iteration, the greedy optimization for each snake point is over an  $n \times n$  pixel region with  $n = 11$ . Overall, the computation time is controlled by and essentially proportional to the quantity  $prn^2$ .

The final contour in Fig. 12.1D shows the result of using an increased number of initialization points and joining the final locations to give a connected boundary: some of the remaining deficiencies could be reduced by fitting with splines or other means instead of simply joining the dots.

As indicated earlier, this was a simple implementation—so much so that no attempt was made to take corners and bends into account, though in the case shown in Fig. 12.1, no disadvantages or deviations can be seen, except in (D). Clearly, a suitable redesign involving additional energy terms would have to be included to cope with more complex image data. It is interesting that so much can be achieved by just two terms, viz. the stretch and edge terms in Eq. (12.1). However, an important factor in getting the greedy algorithm to work optimally, one snake point at a time is the need to include the energies for *both* adjacent links (as in Eqs. (12.6) and (12.7)), so as to limit bias and other complications.

---

## 12.4 THE LEVEL-SET APPROACH TO OBJECT SEGMENTATION

Although the active contour approach described in the previous two sections can be effective in many situations, it nevertheless has several drawbacks (Cremers et al., 2007), which are as follows:

1. There is the possibility of snake self-intersection.
2. Topological changes like splitting or merging of the evolving contour are not allowed.
3. The algorithm is highly dependent on the initialization, and this can result in the snake being biased or getting stuck in local minima.
4. Snakes lack meaningful probabilistic interpretation, so generalizing their action to cover color, texture, or motion is not straightforward.

The level-set approach is intended to remedy these deficiencies. The basic approach is to work with whole regions rather than edges and to evolve an

“embedding function” in which contours are represented implicitly rather than directly. In fact, the embedding function is a function  $\phi(\mathbf{x}, t)$ , and the contour is defined as the zero level of this function:

$$C(t) = \{\mathbf{x} | \phi(\mathbf{x}, t) = 0\} \quad (12.8)$$

For a contour which evolves (by gradient descent) along each local normal  $\mathbf{n}$  with a speed  $F$ , we have:

$$\phi(C(t), t) = 0 \quad (12.9)$$

which leads to

$$\frac{d}{dt} \phi(C(t), t) = \nabla \phi \frac{\partial C}{\partial t} + \frac{\partial \phi}{\partial t} = F \nabla \phi \cdot \mathbf{n} + \frac{\partial \phi}{\partial t} = 0 \quad (12.10)$$

Substituting for  $\mathbf{n}$  using:

$$\mathbf{n} = \frac{\nabla \phi}{|\nabla \phi|} \quad (12.11)$$

we obtain:

$$\frac{\partial \phi}{\partial t} = -|\nabla \phi| F \quad (12.12)$$

Next, we need to substitute for  $F$ . Following Caselles et al. (1997), we have:

$$\frac{\partial \phi}{\partial t} = |\nabla \phi| \operatorname{div} \left( g(I) \frac{\nabla \phi}{|\nabla \phi|} \right) \quad (12.13)$$

where  $g(I)$  is a generalized version of  $|\nabla \phi|$  in the snake potential.

Note that because the contour  $C$  is not mentioned explicitly, the updating takes place over all pixels, thereby involving a great many useless calculations: thus, the “narrow band” method was devised to overcome this problem and involves updating only in a narrow strip around the current contour. However, the need to continually update this strip means that the computational load remains considerable. An alternative approach is the “fast-marching” method, which essentially propagates a solution rapidly along an active wavefront, while leaving pixel values frozen behind it. As a result, this method involves maintaining the sign of the speed values  $F$ . The Hermes algorithm of Paragios and Deriche (2000) seeks to combine the two approaches. It aims at a *final* solution where all the necessary constraints are fulfilled, while maintaining these constraints only loosely at intermediate stages. The overall front propagation algorithm overcomes the four problems mentioned above: in particular, it is able to track nonrigid objects, copes with splitting and merging, and has low computational cost. The paper confirms these claims by showing traffic scenes in which vehicles and pedestrians are successfully tracked.

Rather than developing this method further here, we move on to describe a rather different and exceedingly widely used approach in which shape models are explicitly trained using PCA.

## 12.5 SHAPE MODELS

In order to model shapes, it is necessary to work in a specific representation. The representations used for boundary pattern analysis in Chapter 9, Boundary Pattern Analysis included  $(r, \theta)$ ,  $(s, \psi)$ , and  $(s, \kappa)$  boundary plots. Although such plots can be further modeled by Fourier methods, this can be cumbersome, and the complications conferred by translation, rotation, and shape distortions make it preferable to retreat from representation by continuous boundaries to representation by sets of discrete boundary points. This leads to advantages when moving from low to high resolution, in that, the boundary can still be represented by the same number of points in the same relative positions. Furthermore, if the representation is discrete, methods like PCA can be used to process the data: as we shall see below, this is of particular value when a training approach is to be used to learn shapes and obtain minimal descriptors of them. It is also relevant that PCA involves considerable computation, but nowadays that is a far less important consideration than it was 15–20 years ago; hence, if a method is accurate, robust, trainable, and provides valuable information as part of its normal running, then it should be considered for serious use. In fact, what we need to keep in mind here as part of the “valuable information” that is provided is the capability for eliminating the later (smaller) terms in a series—namely, the low energy eigenvalues that correspond largely to noise—and thereby reducing the redundancy and computational burden later on.

To implement shape models based on discrete boundary points, we need to start with definitive information on the models themselves. To achieve this, “landmark” points are marked around the shapes of interest, often with the aid of a mouse. Although this approach has obvious limitations in terms of human labor, it can nevertheless be highly accurate and reliable when small numbers of points are needed to define shapes. In addition, it has particular value when medical images are to be analyzed, as these are often rather fuzzy and require expert interpretation, consistency being of fundamental importance when using a computer algorithm to analyze them. In any case, once a few highly specific landmark points have been accurately identified, further points can often be derived with virtually no additional human interaction. In what follows we illustrate this using a series of hand images derived from a short motion video.

Fig. 12.2A shows a picture of a human hand, and Fig. 12.2B shows nine landmark points that have been marked on it using a mouse: these include five fingertip points ( $t_1 - t_5$ ) and four finger-base points ( $b_1 - b_4$ ). Fig. 12.2C shows how a further set of five mid-finger points ( $m_1 - m_5$ ) can be derived, using the white construction lines. Numbering the three sets of points from the top, we can write down the following vector relations giving the positions of  $m_1 - m_5$  as

$$\mathbf{m}_1 = \mathbf{b}_1 + c(\mathbf{b}_1 - \mathbf{b}_4) \quad (12.14)$$

$$\mathbf{m}_2 = \mathbf{b}_2 + \frac{1}{2}(\mathbf{b}_2 - \mathbf{b}_3) \quad (12.15)$$

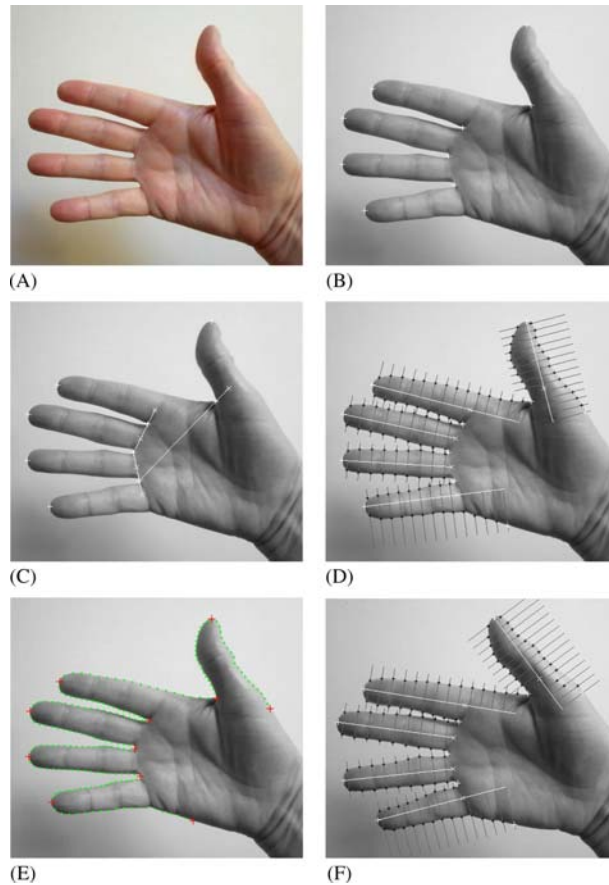


**FIGURE 12.2**

Producing boundary features for PCA analysis. (A) Original image of a hand. (B) Result of using a mouse to generate landmark points at the tips and bases of the fingers. (C) The geometric constructions used to generate mid-base finger locations. (D) White lines generated by joining finger tips to base points and producing dark lines perpendicular to the white lines used to locate boundary points. (E) Boundary points interpolated and equally spaced boundary points found. (F) A shiny light patch leading to misplaced boundary points, which PCA has to be able to cope with. See text for further details of the various stages.

$$\mathbf{m}_3 = \frac{1}{2}(\mathbf{b}_2 + \mathbf{b}_3) \quad (12.16)$$

$$\mathbf{m}_4 = \frac{1}{2}(\mathbf{b}_3 + \mathbf{b}_4) \quad (12.17)$$

$$\mathbf{m}_5 = \mathbf{b}_4 + \frac{1}{2}(\mathbf{b}_4 - \mathbf{b}_3) \quad (12.18)$$



Of these, the formulae for  $m_3$  and  $m_4$  are obviously appropriate, and those for  $m_2$  and  $m_5$  are also reasonable: although in principle, the last of these could be adjusted for the smaller width of the little finger, this doesn't seem to be necessary in practice. The formula for  $m_1$  is more problematic, but it works well if parameter  $c$  is taken to be  $1/6$ . It should be remarked that this vector method is based on the assumption that the shape of the hand will remain approximately planar, thereby making affine stretching acceptable: on the other hand, if intricate 3-D stretching or clenching were to take place, it would not yield good results, and many more landmark points would be needed.

The next stage is to construct five mid-finger lines from  $t_i$  to  $m_i$  ( $i = 1$  to  $5$ ), produced as necessary to cover the extended sides of fingers 1, 2, and 5. These lines are divided into equal sections, and perpendiculars are dropped from them far enough to enter the background regions. This permits a number of approximately equally spaced finger boundary points to be located, as shown in Fig. 12.2D. Finally, these boundary points are interpolated and smoothed by suitable algorithms, and sets of equally spaced points are found on the finger boundaries (Fig. 12.2E). The purpose of this is to ensure that the boundary points are as accurately reproducible as possible, and thus that they match corresponding points on similar hand shapes. In general, none of the points are more accurately located than the original nine landmark points, but at least the boundary points obtained (114 for each hand in the set) are located accurately without further human intervention. Notice that, in some cases, lack of boundary contrast, coupled with shiny light patches particularly within the thumb, resulted in a few undesirable deviations in the boundary points (Fig. 12.2F). However, as we shall see, PCA was able to average out effects such as these: no efforts were made in these tests to eliminate such effects before passing the boundary points to the PCA algorithm, though it would have been reasonably straightforward to do so (e.g., a median-based outlier detector together with a suitable interpolation scheme could have been used).

Before applying PCA, it is necessary to eliminate translation and rotation parameters. First, translation is eliminated by subtracting the mean location of all the boundary points. Then, the mean orientation of all the boundary points is found, and this is subtracted from all the orientations, and new coordinates for the boundary points are determined. These actions are achieved by using the arctan function (specifically the C++ or Matlab "atan2" function), followed by cosine and sine functions to reconstruct the new object coordinates. It is important to remember that averaging angles directly can lead to meaningless results, because of their periodicity (this comment also applies for median filtering in the rotationally symmetric hue domain, and in many other such cases): the most rigorous approach is to convert all points to the unit circle, then average their sines and cosines, and then deduce the mean direction. Finally, it is also useful to normalize object sizes by minimizing the sum of square distances between the model and the new image points. These normalizations and alignments are aimed at removing variations from the incoming data and making the work of the PCA algorithm

easier, and the final model independent of object position, orientation, and size. Put another way, it makes the resulting point distributions closer to Gaussian—which would be the case in an ideal PCA implementation.

Returning to our hand problem, and applying PCA to the 17 sets of 114 boundary points, the results shown in Table 12.1 were obtained. It is common to curtail the list of eigenvalues when the cumulative sum *csum* is more than  $\eta$  times the maximum,  $\eta$  typically being in the range 90%–99.5%, depending on the specific type of image data. Cootes and Taylor (1996), who originally developed the active shape model (ASM) approach, normally used a value of 98%. Applying this to the *csum* values listed in Table 12.1, we find that the first five eigenvalues should be retained. In fact, looking at the hand model modes shown in Fig. 12.3, five is a reasonable number to take, as the image variations resulting from smaller modes are almost undetectable. We can get further insight into the situation by examining Fig. 12.4. Here, the modes are not multiplied by the eigenvalue weights (which are  $\pm\sqrt{\lambda}$  rather than  $\pm\lambda$ ) but are multiplied instead by a fixed value of 100, so that their underlying nature can be seen. Certainly, the largest eigenvalues represent interesting coherent motions of the fingers, but after the

**Table 12.1** Eigenvalues for 17 Hand Images

Order	$\lambda$	<i>csum</i>	$\sqrt{\lambda}$	$\sqrt{\lambda/n}$
1	36,590.6	36,590.6	191.3	17.9
2	8400.7	44,991.3	91.7	8.6
3	4572.9	49,564.2	67.6	6.3
4	868.1	50,432.3	29.5	2.8
5	687.0	51,119.3	26.2	2.5
6	388.3	51,507.6	19.7	1.8
7	156.9	51,664.5	12.5	1.2
8	103.8	51,768.3	10.2	1.0
9	81.0	51,849.3	9.0	0.8
10	44.9	51,894.2	6.7	0.6
11	32.2	51,926.4	5.7	0.5
12	23.2	51,949.6	4.8	0.5
13	16.7	51,966.2	4.1	0.4
14	10.4	51,976.6	3.2	0.3
15	7.0	51,983.6	2.6	0.2
16	5.5	51,989.1	2.4	0.2

*The eigenvalues  $\lambda$  for the set of 17 hand images of the type shown in Fig. 12.2A are listed in decreasing order of size below, together with the cumulative sums, *csum*. Also listed are the square roots of the eigenvalues, which represent standard deviations. See text for the significance of the cumulative sums. The final column gives an approximation to the mean variation for the boundary points, showing where it takes subpixel levels. In general, boundary noise would be expected to lead to s.d.s. of 1 pixel or less, and strong modes (eigenvalues) to give s.d.s. representing coherences over several pixels.*

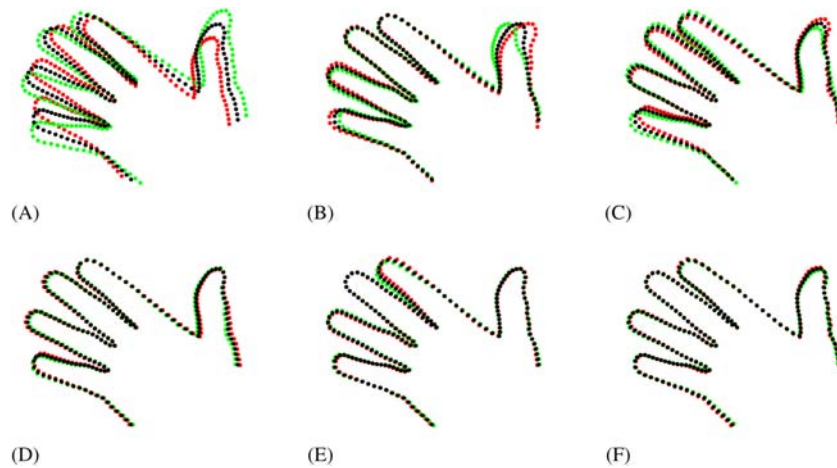


**FIGURE 12.3**

Effects produced by the various eigenvectors. Here, the effects for the six largest eigenvalues are shown in sequence, after training on 17 hands of the type presented in Fig. 12.2. The black dots show the mean hand position, and the red and green dots show the effects of moving either way from the mean position by the square root of the relevant eigenvalue (which represents the true strength of the eigenvector). Clearly, very little variation is produced by the sixth or higher eigenvalues.

fifth eigenvalue, few such coherences are discernible, and the remaining motions can be attributed largely to boundary noise. In some instances, these almost certainly result from uncertainties due to the shiny light patches mentioned earlier. (Interestingly, the reason for calling the eigenvectors “modes” stems from the physics of molecular vibrations, where the eigenvectors correspond to modes of vibration. This is not totally irrelevant, as we can imagine each hand mode sets the whole hand into a mode of vibration, which is all the more relevant for the video from which the 17 hand images were derived.)

The fact that the PCA eigenvalues are commonly interpreted as “energies” is not especially useful. Indeed, the boundary variations from the smaller eigenvalues appear in Fig. 12.4 as noise and their effects are better described, and measured in images, in terms of standard deviations (s.ds.). This gives us a better idea about which eigenvalues to curtail. To understand this, it is necessary to consider how the variations affect individual boundary points. Specifically, the eigenvalues given in Table 12.1 arise from the motions of  $n = 114$  boundary points. We can approximate the mean boundary variations by taking the mean square variations as  $\lambda/n$  and the corresponding s.d. as  $\sqrt{\lambda/n}$ : the latter are listed in Table 12.1. In our hand problem, the boundary variations for the modes vary from around 20 pixels to subpixel values  $\sim 0.2$  pixels, the latter figure being low because the boundary interpolation algorithm has significantly smoothed the boundary noise.

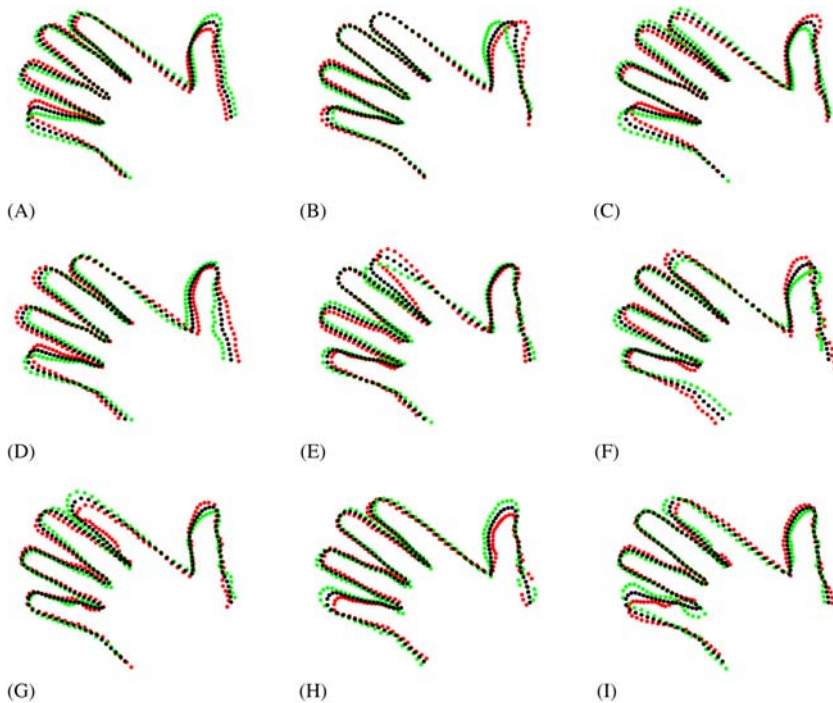


**FIGURE 12.4**

Clarification of the effects produced by the smaller eigenvalues. Here, the effects of the nine largest eigenvalues are shown in sequence. This figure differs from that of Fig. 12.3, in that, there is a fixed multiplier of 100 on the eigenvectors, which are now no longer weighted by the square root of the relevant eigenvalue. The resulting magnification reveals that rather than governing coherent motions of the fingers, the smaller eigenvalues tend to reflect random boundary noise. The result of the particular boundary uncertainties arising from shiny light patches (e.g., see Fig. 12.2F) are clearly visible to the right of (F)–(I).

In general, the most relevant level at which to curtail the eigenvalues ought to be where the boundary point variation s.d. ( $\sqrt{\lambda/n}$ ) drops to a value close to the expected pixel noise level s.d.

### 12.5.1 LOCATING OBJECTS USING SHAPE MODELS

Before examining how the trained PCA system can be used to locate test objects in images, it will be useful to summarize the progress we have made so far. First, we have seen that it is necessary to apply similarity transformations to bring the training set examples into alignment—specifically, by normalizing the translation, rotation, and size parameters, so that the sum of squared distances between corresponding landmark points is minimized: consistency at this preliminary stage is

key to making the PCA eigenvectors more accurate. Of course, the test patterns will have to be treated in the same way as the training set patterns and subjected to similar transformations so that their translations, rotations, and sizes are also prenormalized (see below).

Having brought the training set samples into alignment, their shapes can be stacked into  $s$  long shape vectors covering the  $N$  landmark points  $(x_{ij}, y_{ij})$ ,  $j = 1$  to  $N$ :

$$\mathbf{x}_i = (x_{i1}, y_{i1}, x_{i2}, y_{i2}, \dots, x_{iN}, y_{iN})^T, i = 1 \text{ to } s \quad (12.19)$$

We can now define a mean shape for the training set objects

$$\bar{\mathbf{x}} = \frac{1}{s} \sum_{i=1}^s \mathbf{x}_i \quad (12.20)$$

(It is also sensible to find the means of the  $N$  individual landmark positions, using the similar equation  $\bar{\xi} = \frac{1}{N} \sum_{j=1}^N \xi_j$ , where  $\xi_j = (x_{1j}, y_{1j}, x_{2j}, y_{2j}, \dots, x_{sj}, y_{sj})^T$ ,  $j = 1$  to  $N$ . Indeed, at first sight Eq. (12.20) may confusingly appear more like a point averaging equation than one for averaging shapes.)

We can also compute the shape covariance

$$\mathbf{S} = \frac{1}{s-1} \sum_{i=1}^s (\mathbf{x}_i - \bar{\mathbf{x}})(\mathbf{x}_i - \bar{\mathbf{x}})^T \quad (12.21)$$

To perform PCA fitting, we first approximate the normalized test pattern by the weighted sum of its component eigenvectors

$$\mathbf{x} = \bar{\mathbf{x}} + \Phi \mathbf{b} \quad (12.22)$$

Here,  $\mathbf{b}$  is the weighting vector containing the  $t$  model parameter values corresponding to the  $t$  eigenvalues that have been chosen as the largest and most significant ones (see previous section), and  $\Phi$  is the stacked matrix of the corresponding eigenvectors  $\Phi = (\phi_1, \phi_2, \dots, \phi_t)$ . Inverting Eq. (12.22) gives the weighting vector  $\mathbf{b}$

$$\mathbf{b} = \Phi^T (\mathbf{x} - \bar{\mathbf{x}}) \quad (12.23)$$

(Note that  $\Phi$  is symmetric, so its inverse is equal to its transpose.)

The next part of the task is more difficult, because it involves matching test data represented by raw pixel values to training data expressed in terms of landmark points. Furthermore, it would be nonsense to try to generate landmark points manually for more than one or two test images. Instead, we need to find a way of matching gray-scale points directly between the test and training images. In fact, it is possible to start the process by generating a local gray-level appearance profile along the edge normal at each landmark point. (For simplicity, the local normal at each landmark point can be found by taking the perpendicular bisector of the adjacent two landmark points.) This profile can then be matched against the normalized test pattern profile along the same line, and the position of the best fit for a suitable boundary point determined. If this procedure is carried out for each landmark point, we will end up with a new shape model for the test

object. The fitting process can be carried out iteratively at several—typically two or three—scales until convergence takes place.

The local gray-level appearance model was originally taken as the normalized first derivative ( $\mathbf{g}_i$ ) profile (Cootes and Taylor, 1996). In fact, Cootes et al. performed the match by minimizing the Mahalanobis distance  $M$  from the mean  $\bar{\mathbf{g}}$  of the training set profiles ( $\mathbf{g}_i$ ,  $i = 1$  to  $s$ ) to each unknown test sample  $\mathbf{g}_u$ ,  $M$  being given by

$$M^2 = (\mathbf{g}_u - \bar{\mathbf{g}})^T \mathbf{S}_g^{-1} (\mathbf{g}_u - \bar{\mathbf{g}}) \quad (12.24)$$

In this equation,  $\mathbf{S}_g^{-1}$  is the inverse of the gradient covariance matrix  $\mathbf{S}_g$ . Note that  $M$  reduces to the Euclidean distance when  $\mathbf{S}_g$  is the identity matrix. The reason for minimizing Mahalanobis distance is to maximize the probability that  $\mathbf{g}_u$  is drawn from the same multivariate Gaussian distribution as the training set data. It is clear that the inverse is appropriate because for a 1-D Gaussian distribution  $\mathbf{S}_g^{-1}$  reduces correctly to the inverse of the variance (the factor  $1/2\sigma^2$  has to appear in the Gaussian exponent).

The result of applying this procedure to the PCA model obtained from our set of 17 hand images (see Figs. 12.2–12.4) is shown in Fig. 12.5. The

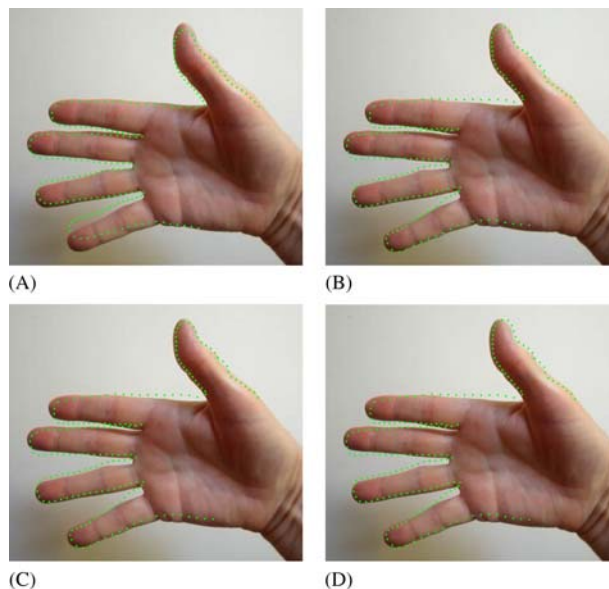


**FIGURE 12.5**

Result of fitting hand picture to PCA model. (A) Initial approximation. (B)–(D) Convergence of the fit with the Mahalanobis distance approach, after 40, 80, and 120 iterations. Note the restrictions produced using this approach—ultimately because of large intensity variations over the hand region.

successive images (A)–(D) show convergence after about 120 iterations, but the accuracy is seen to be limited. Ultimately, this problem is due to some relatively large intensity variations over the hand region—specifically, shiny regions such as those on the thumb noted earlier, and darker shadow regions around the lower edges of the fingers. Indeed, the individual points on the boundary where Mahalanobis matches are located (see Fig. 12.6) are frequently several pixels away from their ideal positions; and although the matches do improve slightly over the sequence, in this case, they remain biased and noisy.

Many workers have produced improved methods for carrying out gray-scale profile matching in cases where the images are nonideal and cannot be well matched by a linear Mahalanobis distance model. For example, van Ginneken et al. (2002) point to cases where the background of the object may be one of several possible types, and the best match can be identified using a  $k$ -NN classifier. Similarly, Kroon (2011) quotes situations where large gray-level variations including instances of shadows and/or specular highlights appear near the object boundaries. Kroon develops a rigorous approach to this problem, based on

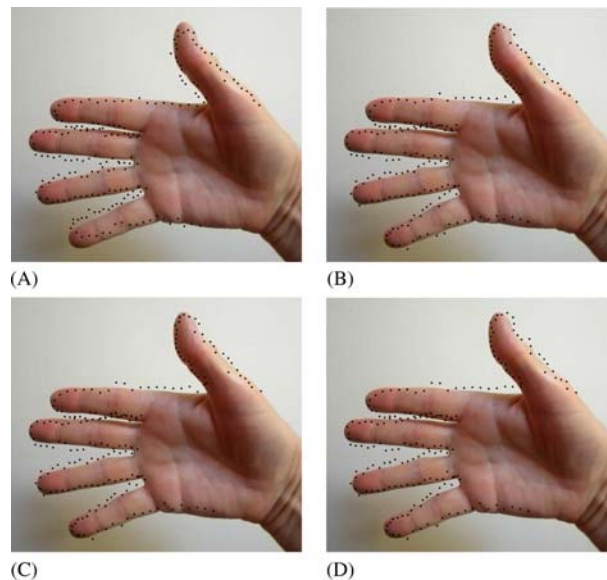


**FIGURE 12.6**

Local predictions produced by the Mahalanobis distance approach. (A)–(D) show the respective predictions after 1, 41, 81, and 121 iterations. Note that although these improve over the sequence, they remain biased and noisy.

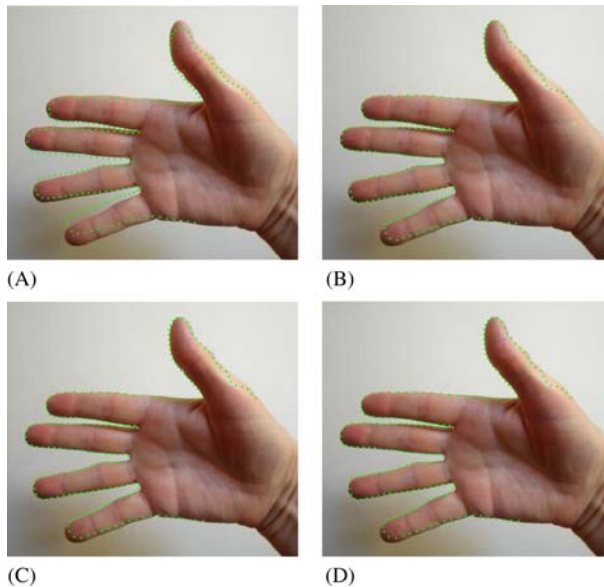


**FIGURE 12.7**

Result of fitting hand picture to PCA model using improved intensity profiles. (A) Initial approximation. (B)–(D) Convergence of the fit with the PCA intensity profile approach, after 8, 16, and 24 iterations. Here, the restrictions caused by intensity variations over the hand are largely eliminated, resulting in an almost perfect fit after significantly fewer iterations.

applying PCA to the local gray-level appearance profiles to identify the most common modes of variation: this application of PCA (*viz.*, to gray-scale *intensity* profiles) is distinct from that which has already been applied to the boundary *shape* profiles. Following training and finding the eigenvectors, model parameters are determined for the unknown test profile: each parameter is divided by the corresponding s.d. obtained during training, and the matching distance is then calculated as the quadratic sum of the normalized model values: this matching distance is minimized to optimize the fit. [Figs. 12.7 and 12.8](#) show that this approach is highly successful for this particular hand location problem. In particular, the resulting fit is accurate and appears after far fewer iterations than for the Mahalanobis distance approach; clearly, the ultimate reason for this is that the match locations feeding the overall fit are themselves much more reliable and accurate.

Finally, we give a summary of the overall algorithm that has to be used for training the system and fitting test objects ([Table 12.2](#)). This has several



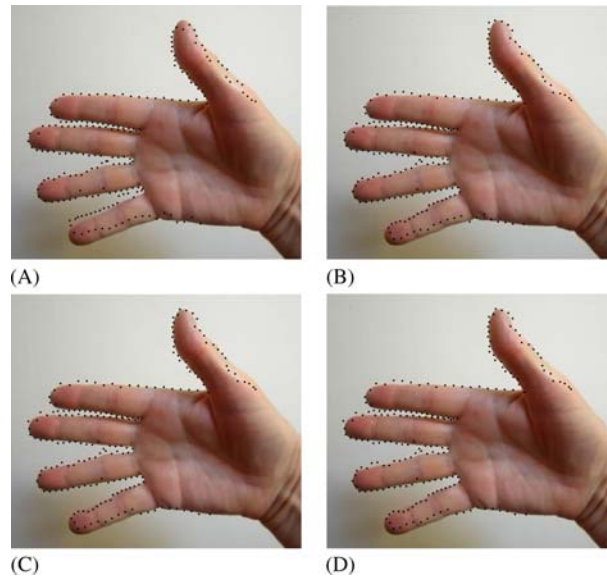


**FIGURE 12.8**

Local predictions produced by the PCA intensity profile approach. (A)–(D) show the respective predictions after 1, 9, 17, and 25 iterations. Note that these improve over the sequence and are significantly more controlled than for the Mahalanobis distance approach.

intricacies due, for example, to the repeated changes in the frames of reference at different stages of the calculation. There are also several further aspects of the algorithm that it would have been confusing to include in the table, but which should nevertheless be highlighted are as follows:

1. Transformation  $\mathbf{T}$  involves normalizing the pose parameters (translation, rotation, and size).
2. During matching, a total of  $2k + 1$  sample points centered around each landmark point are used for matching, and a range of movement of  $\pm l$  is allowed, where  $l \approx k$ .
3. Typical values of parameters are as follows:  $k = 6$ ,  $l = 6$ ,  $m = 3$ .
4. Search may be speeded up by implementing it at several scales, from coarse to fine, e.g., in steps of 4, 2, and finally 1 pixel.
5. The algorithm is written in a general form that allows either Mahalanobis or PCA profile matching distance to be used.

**Table 12.2** Summary of the PCA Object Modeling and Fitting Algorithm

	Reference Frame
<b>Training</b>	
Generate landmark points on training shapes	I
Normalize the landmark coordinates using a suitable transformation, and thus align training shapes to a common reference frame N. Take $\mathbf{T}_0$ as the mean of all the training set transformations	I $\rightarrow$ N
Perform PCA	N
Limit the number of eigenvalues to the $t$ largest, most significant ones	N
Obtain (trained) intensity profile for each landmark point	I
<b>Testing</b>	
Initialize the model shape parameters to those of the mean (trained) shape (i.e., set $\mathbf{b} = 0$ )	N
Place the mean object shape (including landmark points) close to the test object, either manually or using the inverted transformation $\mathbf{T}_0^{-1}$	N $\rightarrow$ I
do {	
Create appearance map of test object by sampling gray profiles along the contour normals, including $k$ sample points on each side of each landmark point	I
Search along each contour normal for the section of length $2k + 1$ having the closest appearance profile to that on the model normal	I
Take each section center as the new landmark position	I
Normalize the landmark coordinates using an updated transformation $\mathbf{T}$ , employing the same normalization technique as for training	I $\rightarrow$ N
Calculate the new model parameters using equation $\mathbf{b} = \Phi^T(\mathbf{x} - \bar{\mathbf{x}})$	N
Limit the model parameters to the range $\pm m\sqrt{\lambda}$	N
Convert the model parameters back to normalized contour positions using equation $\mathbf{x} = \bar{\mathbf{x}} + \Phi\mathbf{b}$	N
Convert the contour positions back to real image locations using the inverted normalization transformation $\mathbf{T}^{-1}$	N $\rightarrow$ I
} until sufficiently converged or the maximum number of iterations is reached	

*The column on the right indicates where the action is—either in the image frame I, or in the normalized frame N, or moving between them.*

## 12.6 CONCLUDING REMARKS

This chapter has introduced the idea of shape models for object segmentation. Over many years, it has been found that raw thresholding and edge detection do not provide straightforward means of segmenting images, as they are liable to stray far-off course: in particular, this is because of the effects of

random image artifacts such as noise and shadows, not to mention the clutter of nontarget objects in the background. The idea of using shape models is to control the situation so that the segmentations obtained become more meaningful. Active contour models (snakes) and level-set models provide means for tackling this problem: PCA-based methods provide another. The snake and level-set approaches are subject to difficulties because all the necessary rules have to be incorporated into the segmentation algorithm analytically without acknowledging exactly what type of shape it will have: PCA-based methods are more powerful as they train the system to know exactly what type of shape is being sought. Clearly, they involve far more sophistication because of the often huge efforts needed to train the system on real data. Thus, they involve vastly more complication and computation, though on the positive side, they can extract the required (learnt) objects from regions of considerable noise.

*Over many years, thresholding-based methods and region growing formed the basis of object segmentation. Subsequently, active contour models (snakes) and level-set methods were aimed at solving the same problem but using more subtle iterative, analytically based methods. However, it was only when PCA-based methods started to be applied to search for objects as instances of models that had been trained on specific target objects that reliability was able to increase dramatically—with the result that objects could be recovered from regions of considerable noise.*

---

## 12.7 BIBLIOGRAPHICAL AND HISTORICAL NOTES

The basic theory of active contour models and snakes was derived many years ago by Kass, Witkin, and Terzopoulos (Kass and Witkin, 1987; Kass et al., 1988). Subsequently, many workers aimed to produce methods that had the same purpose but which could also overcome the manifest disadvantages of normal snakes. Amongst these were those who promoted the level-set approach—Cremers et al. (2007), Caselles et al. (1997), and Paragios and Deriche (2000). Cootes and Taylor (1996) were almost solely responsible for the PCA-based ASM methods and later developed the more general active appearance model method (Cootes et al., 2001).

Cosío et al. (2010) used simplex search in ASMs for improved boundary segmentation: this involves fast numerical optimization to find the most suitable values of nonlinear functions without the need to calculate function derivatives. Their approach typically employs four pose parameters and ten shape parameters for defining a shape such as the prostate. The method significantly increases the range of object poses and thus results in more accurate boundary segmentation. Chiverton et al. (2008) describe a method that is closely related to the active contour concept: it zones in on objects using parameters relating to

foreground similarity and background dissimilarity and employs a new variational logistic maximum a posteriori contextual modeling schema. In this case, the (achieved) aim is to permit tracking of moving objects by iterative adaptive matching. Mishra et al. (2011) identify five basic limitations of preexisting active contour methods. Their solution is to decouple the internal and external active contour energies and to perform updating for each of them separately. The method is shown to be faster and to have at least comparable segmentation accuracy to five earlier methods.

This page intentionally left blank

# Machine learning and deep learning networks

# 3

*Part 3 covers the understanding and use of Machine Learning, including the very recent subject of Deep Learning networks. It starts in [Chapter 13](#), Basic classification concepts, by introducing the subject of abstract pattern classification—or “pattern recognition” as it was originally known—the word “abstract” being intended to convey the idea that whatever the nature of the*

*input data, the output will be a much more compact description of the input data: in the simplest case, optical character recognition yields the ASCII codes of the characters, and face recognition provides the names of the people being viewed.*

*Over the years, the subject of pattern classification has matured and its more modern form—Machine Learning—aims to provide a probabilistic framework for interpreting patterns, giving the exact probabilities for all possible interpretations (and thus indicating reliability as well as the most probable interpretation). Machine Learning is introduced in [Chapter 14](#), *Machine learning: probabilistic methods*, and concentrates on two prime areas: one is the rigorous “expectation maximization” approach; and the other is “boosting,” which aims at high speed and efficiency by combining the outputs of many weak classifiers in order to generate powerful high accuracy combined classifiers.*

*[Chapter 15](#), *Deep-learning networks*, goes on to examine how the concept of “Deep Learning” arose from the earlier artificial neural networks outlined in [Chapter 13](#), *Basic classification concepts*. In particular, it follows the huge advances in accuracy and speed obtained by deep learning architectures, and shows how much has been achieved in this area since the explosive advances that took place around 2012.*

*Finally, note that [Chapter 21](#), *Face detection and recognition: the impact of deep learning*, (the first chapter in Part 5) continues the study of deep learning, describing how it has been applied in the important area of face detection and recognition.*

# Basic classification concepts

# 13

Pattern recognition (PR) is a task that humans are able to achieve “at a glance” with little apparent effort. Much of PR is structural, being achieved essentially by analyzing shape. In contrast, statistical PR (SPR) treats sets of extracted features as abstract entities that can be used to classify objects on a statistical basis, often by mathematical similarity to sets of features for objects with known classes. This chapter explores the subject, presenting relevant theory where appropriate, and shows how artificial neural networks (ANNs) are able to help with recognition tasks.

*Look out for:*

- The nearest neighbor (NN) algorithm—probably the most intuitive of all SPR techniques
- Bayes’ theory, which forms the ideal minimum error classification system
- The relation linking the NN algorithm to Bayes’ theory
- The reason why the optimum number of features will always be finite
- The distinction between supervised and unsupervised learning
- The cluster analysis approach to unsupervised learning
- The support vector machine (SVM) approach to supervised learning
- How ANNs can be trained, avoiding problems of inadequate training and overfitting to training data.

SPR is a core methodology in the design of practical vision systems. As such, it has to be used in conjunction with structural PR methods and many other relevant techniques. In [Chapter 14](#), Machine Learning: Probabilistic Methods, we shall see how these foundations are extended to cover probabilistic PR (PPR) and the modern subject of machine learning (ML).

## 13.1 INTRODUCTION

Parts 1 and 2 of this book tackle the task of interpreting images on the basis that when suitable cues have been found, the identities and positions of various objects will emerge in a natural and straightforward way. When the objects that appear in



an image have simple shapes, just one stage of processing may be required—as in the case of circular washers on a conveyor. For more complex objects such as flat brackets and hinges, location requires at least two stages—as when graph matching methods are used. For situations where the full complexity of three dimensions occurs, more subtle procedures are usually required, as will be seen in Part 4. Indeed, the very ambiguity involved in interpreting 2-D images from a set of 3-D objects generally requires cues to be sought and hypotheses to be proposed before any serious attempt can be made with the task. Thus, cues are vital to keying into the complex data structures of many images. However, for simpler situations, concentration on small features is valuable in permitting image interpretation to be carried out efficiently and rapidly; neither must it be forgotten that in many applications of computer vision, the task is made simpler by the fact that the main interest lies in specific types of object, e.g., the widgets to be inspected on a widget line or the vehicles to be seen on a highway. Indeed, there are many more constrained types of situation in which the various possible solutions can be evaluated carefully before a final interpretation is reached. These situations arise practically where small relevant parts of images can be segmented and interpreted in isolation. One such case is that of optical character recognition (OCR): a commonly used approach for tackling it is that of SPR.

### FROM “STATISTICAL PATTERN RECOGNITION” TO “MACHINE LEARNING”

In practical situations, measurements of prominent features allow most objects to be classified straightforwardly. In fact, this is commonly achieved with varying degrees of certainty, but by comparing object features with those of a great many other known objects, we arrive at classifications that are statistically the most likely ones. Hence, this sort of classification procedure is called *SPR*.

A good number of early PR techniques and algorithms have followed this statistical approach without proceeding to the next stage—that of determining the solution that is mathematically the most *probable* one. Thus, an important goal has been to move the subject from *statistical PR* to *PPR*, i.e., from solutions that are not merely statistically good to those that are known to be probabilistically optimal. Indeed, it is a key aim of ML to progress toward probabilistic optimization of measurement and recognition. In [Chapter 14](#), Machine Learning: Probabilistic Methods, we shall see how ML achieves this aim in a number of important cases. The purpose of the present chapter is to lay firm foundations that lead to the core of ML.

The following sections study the principles of SPR. A description of all the work that has been carried out in this area would take several volumes to cover and cannot be attempted here. Fortunately, SPR has been researched for well over four decades and an overview chapter at this early stage in this book will be useful. We start by describing the NN approach to SPR and then go on to consider Bayes’ decision theory that provides a more general model of the underlying process.

## 13.2 THE NEAREST NEIGHBOR ALGORITHM

The principle of the NN algorithm is that of comparing input image patterns against a number of paradigms and then classifying them according to the class of the paradigm that gives the closest match (Fig. 13.1). An instructive but rather trivial example is shown in Fig. 1.1. Here, a number of binary patterns are presented to the computer in the training phase of the algorithm: then the test patterns are presented one at a time and compared bit by bit against each of the training patterns. It is clear that this gives a generally reasonable result, the main problems arise when (1) training patterns of different classes are close together in Hamming distance (i.e., they differ in too few bits to be readily distinguishable), and (2) minor translations, rotations, or noise cause variations that inhibit accurate recognition. More generally, problem (2) means that the training patterns are insufficiently representative of what will appear during the test phase. The latter statement encapsulates an exceptionally important principle, and it implies that there must be sufficient patterns in the training set for the algorithm to be able to generalize over all possible patterns of each class. However, problem (1) implies that patterns of two different classes may in some cases be so similar as to be indistinguishable by any algorithm, and then it is inevitable that erroneous classifications will be made. It is seen below that this is because the underlying distributions in feature space overlap. (Note that a number of the methods discussed in this chapter—such as the NN algorithm outlined above—are very general and can be applied to the recognition of widely different datasets, including for example speech and electrocardiograph waveforms.)

The example of Fig. 1.1 is rather trivial but nevertheless carries important lessons. Note that general images have many more pixels than those in Fig. 1.1 and

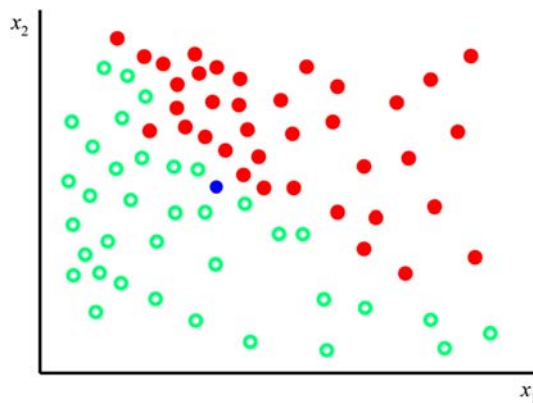


**FIGURE 13.1**

Principle of the nearest neighbor algorithm for a two-class problem: the class 1 training set patterns are shown in red, the class 2 training set patterns are shown in green, and the single test pattern is shown in blue.

also are not merely binary. However, as it is pertinent to simplify the data as far as possible to save computation, it is usual to concentrate on various features of a typical image and classify on the basis of these. One example is provided by a more realistic version of the OCR problem where characters have linear dimensions of at least 32 pixels (although we continue to assume that the characters have been located *reasonably* accurately so that it remains only to classify the subimages containing them). We can start by thinning the characters to their skeletons and making measurements on the skeleton nodes and limbs (see also [Chapter 1: Vision, the Challenge](#) and [Chapter 8: Binary Shape Analysis](#)): this gives (1) the numbers of nodes and limbs of various types, (2) the lengths and relative orientations of limbs, and perhaps (3) information on curvatures of limbs. Thus, we arrive at a set of numerical features that describe the character in the subimage.

The general technique is now to plot the characters in the training set in a multidimensional feature space and to tag the plots with the classification index. Then, test patterns are placed in turn in the feature space and classified according to the class of the nearest training set pattern. Clearly, this generalizes the method adopted in [Fig. 13.1](#). In the general case, the distance in feature space is no longer Hamming distance but some more general measures such as Mahalanobis distance (Duda and Hart, 1973). In fact, a problem arises as there is no reason why the different dimensions in feature space should contribute equally to distance; rather, they should each have different weights in order to match the physical problem more closely. The problem of weighting cannot be discussed in detail here, and the reader is referred to other texts such as that by Duda and Hart (1973). Suffice to say that with an appropriate definition of distance, the generalization of the method outlined above is adequate to cope with a variety of problems.

In order to achieve a suitably low error rate, large numbers of training set patterns are normally required. This then leads to significant storage and computation problems. Means have been found for reducing these problems by several important strategies. Notable amongst these is that of pruning the training set by eliminating patterns that are not near the boundaries of class regions in feature space, as such patterns do not materially help in reducing the misclassification rate.

An alternative strategy for obtaining equivalent performance at lower computational cost is to employ a piecewise linear or other functional classifier instead of the original training set. Clearly, the NN method itself can be replaced, with no change in performance, by a set of planar decision surfaces that are the perpendicular bisectors (or their analogues in multidimensional space) of the lines joining pairs of training patterns of different classes that are on the boundaries of class regions. If this system of planar surfaces is simplified by any convenient means, then the computational load may be reduced further ([Fig. 13.2](#)). This may be achieved either indirectly by some smoothing process, as implied above, or directly by finding training procedures that act to update the positions of decision surfaces immediately on receipt of each new training set pattern. The latter

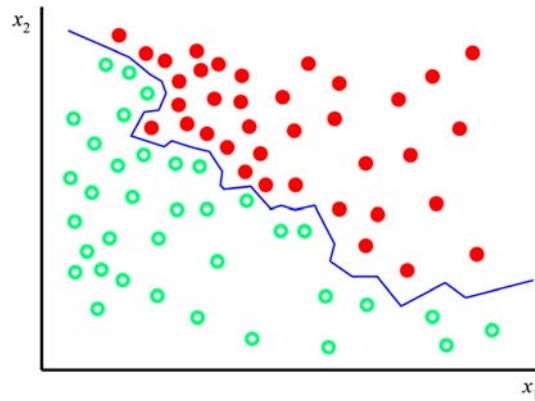


**FIGURE 13.2**

Use of planar decision surfaces for pattern classification; in this example, the “planar decision surface” reduces to a piecewise linear decision boundary in two dimensions. Once the decision boundary is known, the training set patterns themselves need no longer be stored.

approach is in many ways more attractive, as it drastically cuts down storage requirements—although it must be confirmed that a training procedure is selected that converges sufficiently rapidly. Again, discussion of this well-researched topic is left to other texts (Nilsson, 1965; Duda and Hart, 1973; Devijver and Kittler, 1982).

We now turn to a more generalized approach—that of Bayes' decision theory—as it underpins all the possibilities thrown up by the NN method and its derivatives.

### 13.3 BAYES' DECISION THEORY

The basis of Bayes' decision theory will now be examined. If we are trying to get a computer to classify objects, a sound approach is to get it to measure some prominent feature of each object such as its length and to use this feature as an aid to classification. Sometimes, such a feature may give very little indication of the pattern class—perhaps because of the effects of manufacturing variation. For example, a hand-written character may be so ill formed that its features are of little help in interpreting it; it then becomes much more reliable to make use of the known relative frequencies of letters, or to invoke context. In fact, either of these strategies can give a greatly increased probability of correct interpretation. In other words, when feature measurements are found to be giving an error rate above a certain threshold, it is more reliable to employ the a priori probability of a given pattern appearing.

The next step in improving recognition performance is to combine the information from feature measurements and from a priori probabilities; this is achieved by applying Bayes' rule. For a single feature  $x$ , this takes the form:

$$P(C_i|x) = p(x|C_i)P(C_i)/p(x) \quad (13.1)$$

where

$$p(x) = \sum_j p(x|C_j)P(C_j) \quad (13.2)$$

Mathematically, the variables here are (1) the a priori probability of class  $C_i$ ,  $P(C_i)$ ; (2) the probability density for feature  $x$ ,  $p(x)$ ; (3) the class-conditional probability density for feature  $x$  in class  $C_i$ ,  $p(x|C_i)$ —i.e., the probability that feature  $x$  arises for objects known to be in class  $C_i$ ; and (4) the a posteriori probability of class  $C_i$  when  $x$  is observed,  $P(C_i|x)$ .

The notation  $P(C_i|x)$  is a standard one, being defined as the probability that the class is  $C_i$  when the feature is known to have the value  $x$ . Bayes' rule says that to find the class of an object, we need to know two sets of information about the objects that might be viewed: the first is the basic probability  $P(C_i)$  that a particular class might arise; the second is the distribution of values of the feature  $x$  for each class. Fortunately, each of these sets of information can be found straightforwardly by observing a sequence of objects, e.g., as they move along a conveyor. As before, such a sequence of objects is called a training set.

Many common image analysis techniques give features that may be used to help identify or classify objects. These include the area of an object, its perimeter, the number of holes it possesses, and so on. It is important to note that classification performance may be improved not only by making use of the a priori probability but also by employing a number of features simultaneously. Generally, increasing the number of features helps to resolve object classes and reduce classification errors (Fig. 13.3); however, the error rate is rarely reduced to zero merely by adding more and more features, and indeed the situation eventually deteriorates for reasons explained in Section 13.5.

Bayes' rule can be generalized to cover the case of a generalized feature  $\mathbf{x}$ , in multidimensional feature-space, by using the modified formula:

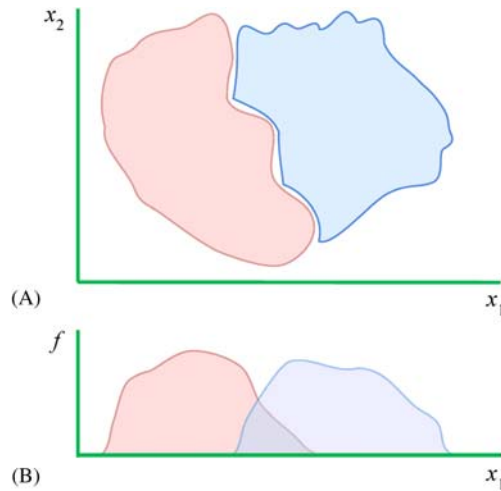
$$P(C_i|\mathbf{x}) = p(\mathbf{x}|C_i)P(C_i)/p(\mathbf{x}) \quad (13.3)$$

where  $P(C_i)$  is the a priori probability of class  $C_i$ , and  $p(\mathbf{x})$  is the overall probability density for feature vector  $\mathbf{x}$ :

$$p(\mathbf{x}) = \sum_j p(\mathbf{x}|C_j)P(C_j) \quad (13.4)$$

The classification procedure is then to compare the values of all the  $P(C_j|\mathbf{x})$  and to classify an object as class  $C_i$  if:

$$P(C_i|\mathbf{x}) > P(C_j|\mathbf{x}) \quad \text{for all } j \neq i \quad (13.5)$$

**FIGURE 13.3**

Use of several features to reduce classification errors: (A) the two regions to be separated in 2-D ( $x_1$ ,  $x_2$ ) feature space; (B) frequencies of occurrence of the two classes when the pattern vectors are projected onto the  $x_1$ -axis. Clearly, error rates will be high when either feature is used on its own but will be reduced to a low level when both features are employed together.

### 13.3.1 THE NAÏVE BAYES' CLASSIFIER

Many classification methods, including the NN algorithm and the Bayes' classifier, can involve substantial amounts of storage and computation if the amount of training is to be sufficient to achieve low error rates. Hence, there is considerable value in employing methods that minimize computation while retaining adequate classification accuracy. In fact, the naïve Bayes' classifier is able to achieve this in many applications—in particular, those where individual features can be selected that are approximately independent. Features in this category include roundness, size, and redness in the case of oranges.

To understand this, take the expression  $p(\mathbf{x}|C_i)P(C_i) = p(x_1, x_2, \dots, x_N|C_i) P(C_i)$  in Eq. (13.4), and reexpress it as appropriate for independent (uncorrelated) features  $x_1, x_2, \dots, x_N$ :

$$p(\mathbf{x}|C_i)P(C_i) = p(x_1|C_i)p(x_2|C_i) \dots p(x_N|C_i) \cdot P(C_i) = \prod_j p(x_j|C_i) \cdot P(C_i) \quad (13.6)$$

This is valid because the overall probability of a set of independent variables is the product of the individual probabilities. First, note that this is a significant simplification of the original general expression. Second, its computation involves only the means and variances of the  $N$  individual variables and not the whole  $N \times N$  covariance matrix. Clearly, reducing the number of parameters makes the

naïve Bayes' classifier less powerful. However, this is counterbalanced by the fact that, if the same training set is used, the remaining parameters will be much more accurately determined. The result is that, given the right combination of features, the naïve Bayes' classifier can indeed be highly effective in practice.

---

## 13.4 RELATION OF THE NEAREST NEIGHBOR AND BAYES' APPROACHES

When Bayes' theory is applied to simple PR tasks, it is immediately clear that a priori probabilities are important in determining the final classification of any pattern, as these probabilities arise explicitly in the calculation. However, this is not so for the NN type of classifier. Indeed, the whole idea of the NN classifier appears to be to get away from such considerations; instead, classifying patterns on the basis of training set patterns that lie nearby in feature space: In this respect, the NN type of classifier seems to fall neatly in the SPR camp. However, there must be a definite answer to the question of whether a priori probabilities are or are not taken into account *implicitly* in the NN formulation, and therefore, whether an adjustment needs to be made to the NN classifier to minimize the error rate. As it is clearly important to have a categorical statement of the situation, the next subsection is devoted to provide such a statement, together with necessary analysis.

### 13.4.1 MATHEMATICAL STATEMENT OF THE PROBLEM

This subsection considers in detail the relation between the NN algorithm and Bayes' theory. For simplicity (and with no ultimate loss of generality), we here take all dimensions in feature space to have equal weight, so that the measure of distance in feature space is not a complicating factor.

For greatest accuracy of classification, many training set patterns will be used and it will be possible to define a density of training set patterns in feature space,  $D_i(\mathbf{x})$ , for position  $\mathbf{x}$  in feature space and class  $C_i$ . Clearly, if  $D_k(\mathbf{x})$  is large at position  $\mathbf{x}$  in class  $C_k$ , then training set patterns lie close together, and a test pattern at  $\mathbf{x}$  will be likely to fall in class  $C_k$ . More particularly, if

$$D_k(\mathbf{x}) = \max_i D_i(\mathbf{x}) \quad (13.7)$$

then our basic statement of the NN rule implies that the class of a test pattern  $\mathbf{x}$  will be  $C_k$ .

However, according to the outline given above, this analysis is flawed in not showing explicitly how the classification depends on the a priori probability of class  $C_k$ . To proceed, note that  $D_i(\mathbf{x})$  is closely related to the conditional probability density  $p(\mathbf{x}|C_i)$  that a training set pattern will appear at position  $\mathbf{x}$  in

feature space if it is in class  $C_i$ . Indeed, the  $D_i(\mathbf{x})$  are merely nonnormalized value of the  $p(\mathbf{x}|C_i)$ :

$$p(\mathbf{x}|C_i) = \frac{D_i(\mathbf{x})}{\int D_i(\mathbf{x}) \, d\mathbf{x}} \quad (13.8)$$

The standard Bayes' formulae (Eqs. (13.3) and (13.4)) can now be used to calculate the a posteriori probability of class  $C_i$ .

So far, it has been seen that the a priori probability should be combined with the training set density data before valid classifications can be made using the NN rule; as a result, it seems invalid merely to take the nearest training set pattern in feature space as an indicator of pattern class. However, note that when clusters of training set patterns and the underlying within-class distributions scarcely overlap, there is anyway a rather low probability of error in the overlap region, and the result of using  $p(\mathbf{x}|C_i)$  rather than  $P(\mathbf{x}|C_i)$  to indicate class often introduces only a very small bias in the decision surface. Hence, although invalid *mathematically*, the error introduced need not be disastrous.

We now consider the situation in more detail, finding how the need to multiply by the a priori probability affects the NN approach. In fact, multiplying by the a priori probability can be achieved either *directly*, by multiplying the densities of each class by the appropriate  $P(\mathbf{x}|C_i)$ , or *indirectly*, by providing a suitable amount of additional training for classes with high a priori probability. It may now be seen that the amount of additional training required is *precisely* the amount that would be obtained if the training set patterns were allowed to appear with their natural frequencies (see equations below). For example, if objects of different classes are moving along a conveyor, we should not first separate them and then train with equal numbers of patterns from each class; we should instead allow them to proceed normally and train on them all at their normal frequencies of occurrence in the training stream. Clearly, if training set patterns do not appear for a time with their proper natural frequencies, this will introduce a bias into the properties of the classifier. Thus, we must make every effort to permit the training set to be representative not only of the *types* of pattern of each class but also of the *frequencies* with which they are presented to the classifier during training.

*The following proof of the density-based decision rule (Eqs. (13.3)–(13.4)) may be bypassed on a first reading.*

The above ideas for *indirect* inclusion of a priori probabilities may be expressed as follows:

$$P(C_i) = \frac{\int D_i(\mathbf{x}) \, d\mathbf{x}}{\sum_j \int D_j(\mathbf{x}) \, d\mathbf{x}} \quad (13.9)$$



Hence

$$P(C_i|\mathbf{x}) = \frac{D_i(\mathbf{x})}{\left(\sum_j \int D_j(\mathbf{x}) d\mathbf{x}\right) p(\mathbf{x})} \quad (13.10)$$

where

$$p(\mathbf{x}) = \frac{\sum_k D_k(\mathbf{x})}{\sum_j \int D_j(\mathbf{x}) d\mathbf{x}} \quad (13.11)$$

Substituting for  $p(\mathbf{x})$  now gives

$$P(C_i|\mathbf{x}) = \frac{D_i(\mathbf{x})}{\sum_k D_k(\mathbf{x})} \quad (13.12)$$

so the decision rule to be applied is to classify an object as class  $C_i$  if

$$D_i(\mathbf{x}) > D_j(\mathbf{x}) \quad \text{for all } j \neq i \quad (13.13)$$

The following conclusions have now been arrived at:

1. The NN classifier may well not include a priori probabilities and hence could give a classification bias;
2. It is in general wrong to train a NN classifier in such a way that an equal number of training set patterns of each class are applied;
3. The correct way to train a NN classifier is to apply training set patterns at the natural rates at which they arise in raw training set data.

The third conclusion is perhaps the most surprising and the most gratifying. Essentially, it adds further fire to the principle that training set patterns should be representative of the class distributions from which they are taken, although we now see that it should be generalized to the following: *training sets should be fully representative of the populations from which they are drawn*, where “fully representative” includes ensuring that the frequencies of occurrence of the various classes are representative of those in the whole population of patterns. Phrased in this way, the principle becomes a general one which is relevant to many types of trainable classifier.

### 13.4.2 THE IMPORTANCE OF THE NEAREST NEIGHBOR ALGORITHM

The NN algorithm is important in being perhaps the simplest of all classifiers to implement on a computer; in addition, it has the advantage of being guaranteed to give an error rate within a factor of two of the ideal error rate (obtainable with a Bayes' classifier). By modifying the method to base classification of any test pattern on the most commonly occurring class amongst the  $k$  nearest training set patterns (giving the “ $k$ -NN” method), the error rate can be reduced further until it is

arbitrarily close to that of a Bayes' classifier (note that Eq. (13.12) can be interpreted as covering this case too). However, both the NN and (a fortiori) the  $k$ -NN methods have the disadvantage that they often require enormous storage to record enough training set pattern vectors, and correspondingly large amounts of computation to search through them to find an optimal match for each test pattern—hence, necessitating the pruning and other methods mentioned earlier for cutting down the load.

Finally, we can conclude that the implicit incorporation of a priori probabilities into the NN and  $k$ -NN types of classifier essentially moves them out of the SPR category and into the realm of PPR (see box in Section 13.1).

---

## 13.5 THE OPTIMUM NUMBER OF FEATURES

It was stated in Section 13.3 that error rates can be reduced by increasing the number of features used by a classifier, but that there is a limit to this, after which performance actually deteriorates. We here consider why this should happen. Basically, the reason is similar to the situation where many parameters are used to fit a curve to a set of  $D$  data points. As the number of parameters  $P$  is increased, the fit of the curve becomes better and better, and in general becomes perfect when  $P = D$ . However, by that stage, the significance of the fit is poor, as the parameters are no longer overdetermined and no averaging of their values is taking place. Essentially, all the noise in the raw input data is being transferred to the parameters. The same thing happens with training set patterns in feature space. Eventually, training set patterns are so sparsely packed in feature space that the test patterns have reduced probability of being nearest to a pattern of the same class, so error rates become very high. This situation can also be regarded as due to a proportion of the features having negligible statistical significance, i.e., they add little additional information and serve merely to add uncertainty to the system.

However, an important factor is that the optimum number of features depends on the amount of training a classifier receives. If the number of training set patterns is increased, more evidence is available to support the determination of a greater number of features and hence to provide more accurate classification of test patterns. Indeed, in the limit of very large numbers of training set patterns, performance continues to increase as the number of features is increased.

This situation was first clarified by Hughes (1968) and verified in the case of  $n$ -tuple PR (a variant of the NN classifier due to Bledsoe and Browning, 1959) by Ullmann (1969). Both workers produced clear curves showing the initial improvement in classifier performance as the number of features increased, this improvement being followed by a fall in performance for large numbers of features.

Before leaving this topic, note that the above arguments relate to the number of features that should be used but not to their selection. Clearly, some features are more significant than others, the situation being very data-dependent. It is left

as a topic for experimental tests to determine in any instance which subset of features will minimize classification errors (see also Chittineni, 1980).

### 13.6 COST FUNCTIONS AND ERROR—REJECT TRADEOFF

In the foregoing sections it has been implied that the main criterion for correct classification is that of maximum a posteriori probability. However, although probability is always relevant, in a practical engineering environment, it can be more important to minimize costs. Hence, it is necessary to compare the costs involved in making correct or wrong decisions. Such considerations can be expressed mathematically by invoking a loss function  $L(C_i|C_j)$  that represents the cost involved in making a decision  $C_i$  when the true class for feature  $\mathbf{x}$  is  $C_j$ .

To find a modified decision rule based on minimizing costs, we first define a function known as the conditional risk:

$$R(C_i|\mathbf{x}) = \sum_j L(C_i|C_j)P(C_j|\mathbf{x}) \quad (13.14)$$

This function expresses the expected cost of deciding on class  $C_i$  when  $\mathbf{x}$  is observed. As it is wished to minimize this function, we decide on class  $C_i$  only if:

$$R(C_i|\mathbf{x}) < R(C_j|\mathbf{x}) \text{ for all } j \neq i \quad (13.15)$$

If we were to choose a particularly simple cost function, of the form:

$$L(C_i|C_j) = \begin{cases} 0 & \text{for } i=j \\ 1 & \text{for } i \neq j \end{cases} \quad (13.16)$$

then the result would turn out to be identical to the previous probability-based decision rule, relation (13.5). Clearly, it is only when certain errors lead to relatively large (or small) costs that it pays to deviate from the normal decision rule. Such cases arise when we are in a hostile environment and must, for example, give precedence to the sound of an enemy tank over that of other vehicles—it is better to be oversensitive and risk a false alarm than to retain a small chance of not noticing the hostile agent. Similarly, on a production line, it may in some circumstances be better to reject a small number of good products than to risk selling a defective product. Cost functions therefore permit classifications to be biased in favor of a safe decision in a rigorous, predetermined, and controlled manner, and the desired balance of properties obtained from the classifier.

Another way of minimizing costs is to arrange for the classifier to recognize when it is “doubtful” about a particular classification, because two or more classes are almost equally likely. Then, one solution is to make a safe decision, the decision plane in feature space being biased away from its position for maximum probability classification. An alternative is to reject the pattern, i.e., place it into an “unknown” category; in that case, some other means can be employed for making an appropriate classification. Such a classification could be made by

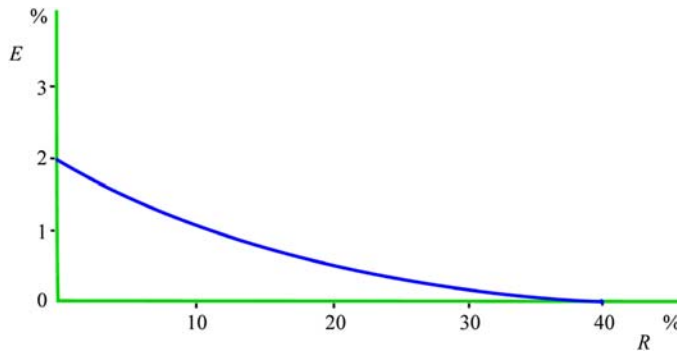


**FIGURE 13.4**

An error-reject tradeoff curve ( $E$ , error rate;  $R$ , reject rate). In this example, the error rate  $E$  drops substantially to zero for a reject rate  $R$  of 40%. More usually,  $E$  cannot be reduced to zero until  $R$  is 100%.

going back to the original data and measuring further features, but in many cases, it is more appropriate for a human operator to be available to make the final decision. Clearly, the latter approach is more expensive, and so introducing a “reject” classification can incur a relatively large cost factor. A further problem is that the error rate is reduced only by a fraction of the amount that the rejection rate is increased. (Here, all errors and reject rates are assumed to be calculated as proportions of the total number of test patterns to be classified.) Indeed, in a simple two-class system, the initial decrease in error rate is only one half the initial increase in reject rate (i.e., a 1% decrease in error rate is obtained only at the expense of a 2% increase in reject rate), and the situation gets rapidly worse as progressively lower error rates are attempted (Fig. 13.4). Thus, very careful cost analysis of the error–reject tradeoff curve must be made before an optimal scheme can be developed. Finally, note that the overall error rate of the classification system depends on the error rate of the classifier that examines the rejects (e.g., the human operator), and this needs to be taken into account in determining the exact tradeoff to be used.

## 13.7 SUPERVISED AND UNSUPERVISED LEARNING

In the earlier parts of this chapter, we made the implicit assumption that the classes of all the training set patterns are known, and in addition, that they should be used in training the classifier. Indeed, this assumption might be thought of as inescapable. However, classifiers may actually use two approaches for learning—*supervised learning* (in which the classes are known and used in training) and *unsupervised learning* (in which they are either unknown or else known and not used in training). Unsupervised learning can

frequently be advantageous in practical situations. For example, a human operator is not required to label all the products coming along a conveyor, as the computer can find out for itself both how many classes of product there are and which categories they fall into; in this way considerable operator effort is eliminated. In addition, it is possible that a number of errors would thereby be circumvented. On the contrary, unsupervised learning involves a number of difficulties, as will be seen in the following sections.

Before proceeding, we give two other reasons why unsupervised learning is useful. First, when the characteristics of objects vary with time—for example, beans change in size and color as the season develops—it will be necessary to track these characteristics within the classifier, and unsupervised learning provides a valuable means of approaching this task. Second, when setting up a recognition system, the characteristics of objects, and in particular their most important parameters (e.g., from the point of view of quality control) may well be unknown, and it will be useful to gain some insight into the nature of the data. Thus, types of fault will need to be logged, and permissible variants on objects will need to be noted. As an example, many OCR fonts (such as Times Roman) have a letter “a” with a stroke bent over the top from right to left, though other fonts (such as Monaco) do not have this feature. An unsupervised classifier will be able to flag this up by locating a cluster of training set patterns in a totally separate part of feature space (see Fig. 13.5). In general, unsupervised learning is about the location of clusters in feature space.

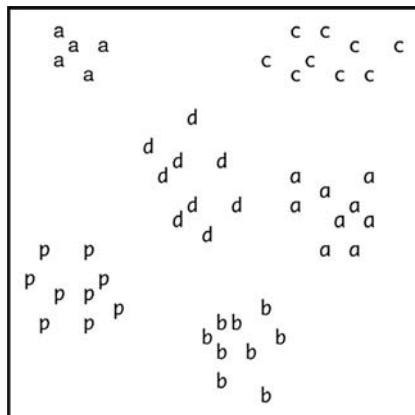


**FIGURE 13.5**

Location of clusters in feature space. Here, the letters correspond to samples of characters taken from various fonts. The small cluster of a’s with strokes bents over the top from right to left appear at a separate location in feature space; this type of deviation should be detectable by cluster analysis.

---

## 13.8 CLUSTER ANALYSIS

As indicated above, an important reason for performing cluster analysis is characterization of the input data. However, the underlying motivation is normally to classify test data patterns reliably. To achieve these aims, it will be necessary both to partition feature space into regions corresponding to significant clusters, and to label each region (and cluster) according to the type of data involved. In practice, this can happen in the following two ways:

1. By performing cluster analysis, and then labeling the clusters by specific queries to human operators on the classes of a small number individual training set patterns.
2. By performing supervised learning on a small number of training set patterns, and then performing unsupervised learning to expand the training set to realistic numbers of examples.

In either case, there is ultimately no escape from the need for supervised classification. However, by placing the main emphasis on unsupervised learning, we limit tedium and the possibility of preconceived ideas about possible classes from affecting the final recognition performance.

Before proceeding further, notice that there are cases where we may have absolutely no idea in advance about the number of clusters in feature space; this occurs in classifying the various regions in satellite images. Such cases are in direct contrast with applications such as OCR or recognizing chocolates being placed in a chocolate box.

Cluster analysis involves a number of very significant problems. Not least is the visualization problem. First, in one, two, or even three dimensions, we can easily visualize and decide on the number and location of any clusters, but this capability is misleading; we cannot extend this capability to feature spaces of many dimensions. Second, computers do not visualize as we do, and special algorithms will be needed to enable them to do so. Although computers could be made to emulate our capability in low-dimensional feature spaces, a combinatorial explosion would occur if we attempted this for high-dimensional spaces. This means that we will have to develop algorithms that operate on *lists* of feature vectors, if we are to produce automatic procedures for cluster location.

Available algorithms for cluster analysis fall into two main groups—*agglomerative* and *divisive*. Agglomerative algorithms start by taking the individual feature points (training set patterns, excluding class) and progressively grouping them together according to some similarity function until a suitable target criterion is reached. Divisive algorithms start by taking the whole set of feature points as a single large cluster, and progressively dividing it until some suitable target criterion is reached. Let us assume that there are  $P$  feature points. Then, in the worst case, the number of comparisons between pairs of individual feature point

positions which will be required to decide whether to combine a pair of clusters in an agglomerative algorithm will be

$${}^P C_2 = \frac{1}{2}P(P - 1) \quad (13.17)$$

while the number of iterations required to complete the process will be of order  $P - K$  (here we are assuming that the final number of clusters to be found is  $K$ , where  $K \leq P$ ). On the other hand, for a divisive algorithm, the number of comparisons between pairs of individual feature point positions will be reduced to:

$${}^K C_2 = \frac{1}{2}K(K - 1) \quad (13.18)$$

while the number of iterations required to complete the process will be of order  $K$ .

Although it would appear that divisive algorithms require far less computation than agglomerative algorithms, this is not so. This is because any cluster containing  $p$  feature points will have to be examined for a huge number of potential splits into subclusters, the actual number being of order:

$$\sum_{q=1}^p {}^p C_q = \sum_{q=1}^p \frac{p!(p - q)!}{q!} \quad (13.19)$$

This means that in general, the agglomerative approach will have to be adopted. In fact, the type of agglomerative approach outlined above is exhaustive and rigorous, and a less exacting, iterative approach can be used. First, a suitable number  $K$  of cluster centers are set (these can be decided from a priori considerations, or by making arbitrary choices). Second, each feature vector is assigned to the closest cluster center. Third, the cluster centers are recalculated. This process is repeated if any feature points have moved from one cluster to another during the iteration, though termination can also be instituted if the quality of clustering ceases to improve. A basic form of the algorithm originated by Forgy (1965) is given in Table 13.1.

Clearly, the effectiveness of this algorithm will be highly data-dependent—in particular, with regard to the order in which the data points are presented. In addition, the result could be oscillatory or nonoptimal (in the sense of not arriving at the best solution). This could happen if at any stage a single cluster center arose near the center of a pair of small clusters. In addition, the method gives no indication of the most appropriate number of clusters. Accordingly, a number of variant and alternative algorithms have been devised. One such algorithm is the

**Table 13.1** Basis of Forgy's Algorithm for Cluster Analysis

---

```

choose target number K of clusters;
set initial cluster centres;
calculate quality of clustering;
do {
    assign each data point to the closest cluster centre;
    recalculate cluster centres;
    recalculate quality of clustering;
} until no further change in the clusters or the quality of the clusters;
```

---

**Table 13.2** Basis of MacQueen's *K-means* Algorithm

---

```

choose target number K of clusters;
set the K initial cluster centres at K data points;
for all other data points { // first pass
    assign data point to closest cluster centre;
    recalculate relevant cluster centre;
}
for all data points // second pass
    re-assign data point to closest cluster centre;

```

---

ISODATA algorithm (Ball and Hall, 1966); this is similar to Forgy's method, but is able to merge clusters which are close together, and to split elongated clusters.

Another disadvantage of iterative algorithms is that it may not be obvious when they should terminate; as a result, they are liable to be too computation intensive. Thus, there has been some support for noniterative algorithms. MacQueen's *K-means* algorithm (MacQueen, 1967) is one of the best known noniterative clustering algorithms: it involves two runs over the data points, one being required to find the cluster centers and the other being required to finally classify the patterns (see Table 13.2). Again, the choice of which data points are to act as the initial cluster centers can be either arbitrary or on some more informed basis.

Noniterative algorithms are, as indicated earlier, very dependent on the order of presentation of the data points. With image data, this is especially problematic, as the first few data points are quite likely to be similar (e.g., all derived from sky or other background pixels). A useful way of overcoming this problem is to randomize the choice of data points, so that they can arise from anywhere in the image. In general, noniterative clustering algorithms are less effective than iterative algorithms, because they are overinfluenced by the order of presentation of the data.

Overall, one of the main problems with the algorithms described above is the lack of indication they give of the most appropriate value of  $K$ . However, if a range of possible values for  $K$  is known, all of them can be tried, and the one giving the best performance in respect of some suitable target criterion can be taken as providing an optimal result. In that case, we will have found the set of clusters which, in some specified sense, gives the best overall description of the data. Alternatively, some method of analyzing the data to determine  $K$  can be used before final cluster analysis: the Zhang and Modestino (1990) approach falls into this category.

Finally, note that none of the above discussion on cluster analysis involves any probabilistic formulation, so the approaches covered in this section are purely those of SPR. However, Chapter 14, Machine Learning: Probabilistic Methods presents new theory and methodology showing how this problem is overcome.

---

## 13.9 THE SUPPORT VECTOR MACHINE

The SVM is a new paradigm for SPR, and emerged during the 1990s as an important contender for practical applications. The basic concept relates to linearly separable feature spaces and is illustrated in Fig. 13.6A. The idea is to find the pair



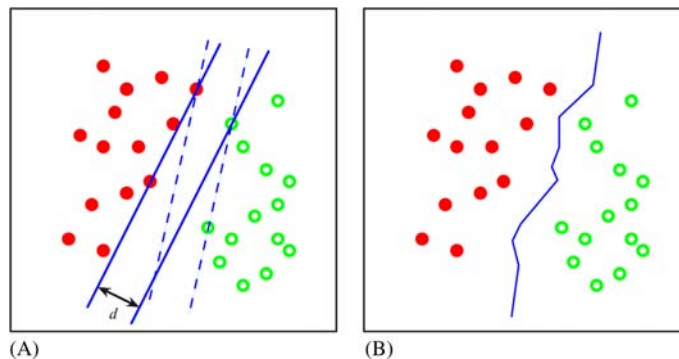


**FIGURE 13.6**

Principle of the support vector machine. Part (A) shows two sets of linearly separable feature points: the two parallel hyperplanes have the maximum possible separation  $d$  and should be compared with alternatives such as the pair shown dashed. Part (B) shows the optimal piecewise linear solution that would be found by the nearest neighbor method.

of parallel hyperplanes that lead to the maximum separation between two classes of feature so as to provide the greatest protection against errors. In Fig. 13.6A, the dashed set of hyperplanes has lower separation and thus represents a less ideal choice, with reduced protection against errors. Each pair of parallel hyperplanes is characterized by specific sets of feature points—the so-called support vectors. In the feature space shown in Fig. 13.6A, the planes are fully defined by three support vectors, though clearly this particular value only applies for 2-D feature spaces: in  $N$  dimensions, the number of support vectors required is  $N + 1$ . This provides an important safeguard against overfitting, as, however, many data points exist in a feature space, the maximum number of vectors needed to describe it is  $N + 1$ .

For comparison, Fig. 13.6B shows the situation that would exist if the NN algorithm were employed. In this case, the protection against errors would be higher, as each position on the separating surface is optimized to the highest local separation distance. However, this increase in accuracy comes at quite high cost in the much larger number of defining example patterns. Indeed, as indicated above, much of the gain of the SVM comes from its use of the smallest possible number of defining example patterns (the support vectors). The disadvantage is that the basic method only works when the dataset is linearly separable.

To overcome this problem, it is usual to transform the training and test data to a feature space of higher dimension where the data do become linearly separable. In fact, this approach will tend to reduce or even eliminate the main advantage of the SVM and lead to overfitting of the data and to poor generalizing ability. However, if the transformation that is employed is nonlinear, the final (linearly separable) feature space could have a manageable number of dimensions, and the advantage of the SVM may not be eroded. Nevertheless, there comes a point where the restriction of linear separability has to be questioned. At that point, it

has been found useful to build “slack” variables  $s_i$  into the optimization equations to represent the amount by which the separability constraint can be violated. This is engineered by adding a cost term  $C \sum_i s_i$  to the normal error function:  $C$  is adjustable and acts as a regularizing parameter, which is optimized by monitoring the performance of the classifier on a range of training data.

For further information on this topic, the reader should consult either the original papers by Vapnik, including Vapnik (1998), or the specialized text by Cristianini and Shawe-Taylor (2000), or else other texts on SPR, such as Webb (2002).

---

## 13.10 ARTIFICIAL NEURAL NETWORKS

The concept of an ANN that could be useful for PR started in the 1950s and continued right through the 1960s. For example, Bledsoe and Browning (1959) developed the “ $n$ -tuple” type of classifier that involved bit-wise recording and lookup of binary feature data, leading to the “weightless” or “logical” type of ANN. Although the latter type of classifier maintained a following for some years, there can be little exaggeration in saying that Rosenblatt’s “perceptron” (1958, 1962) has had a far greater influence on the subject.

The simple perceptron is a linear classifier that classifies patterns into two classes. It takes a feature vector  $\mathbf{x} = (x_1, x_2, \dots, x_N)$  as its input, and produces a single scalar output  $\sum_{i=1}^N w_i x_i$ , the classification process being completed by applying a threshold (Heaviside step) function at  $\theta$  (see Fig. 13.7). The mathematics is simplified by writing  $-\theta$  as  $w_0$ , and taking it to correspond to an input  $x_0$  which is maintained at a constant value of unity. The output of the linear part of the classifier is then written in the form:

$$d = \sum_{i=1}^N w_i x_i - \theta = \sum_{i=1}^N w_i x_i + w_0 = \sum_{i=0}^N w_i x_i \quad (13.20)$$

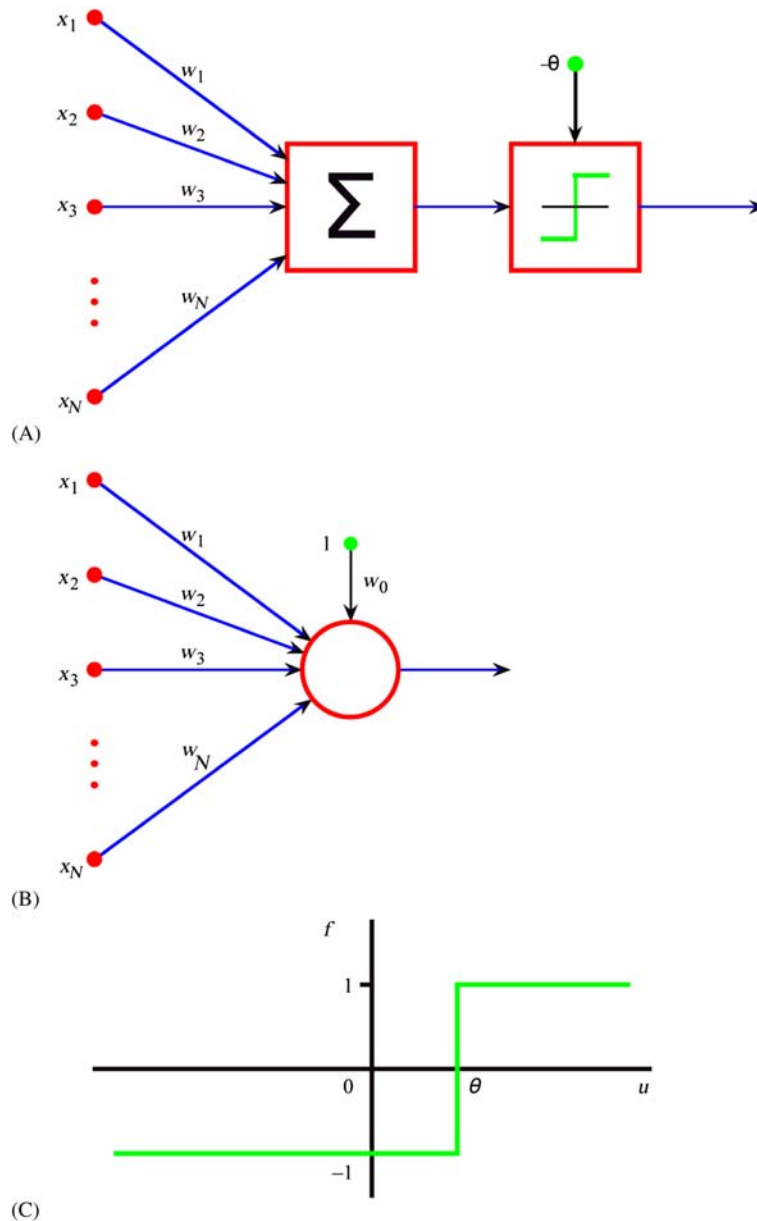
and the final output of the classifier is given by:

$$y = f(d) = f\left(\sum_{i=0}^N w_i x_i\right) \quad (13.21)$$

This type of neuron can be trained using a variety of procedures, such as the *fixed increment rule* given in Table 13.3. (The original fixed increment rule used a learning rate coefficient  $\eta$  equal to unity.) The basic concept of this algorithm was to try to improve the overall error rate by moving the linear discriminant plane a fixed distance toward a position where no misclassification would occur—but only doing this when a classification error had occurred:

$$w_i(k+1) = w_i(k) \quad y(k) = \omega(k) \quad (13.22)$$

$$w_i(k+1) = w_i(k) + \eta[\omega(k) - y(k)]x_i(k) \quad y(k) \neq \omega(k) \quad (13.23)$$

**FIGURE 13.7**

Simple perceptron. Part (A) shows the basic form of a simple perceptron: input feature values are weighted and summed, and the result fed via a threshold unit to the output connection. Part (B) gives a convenient shorthand notation for the perceptron, and Part (C) shows the activation function of the threshold unit.

**Table 13.3** Perceptron *Fixed Increment* Algorithm

---

```

initialise weights with small random numbers;
select suitable value of learning rate coefficient  $\eta$  in the range 0 to 1;
do {
  for all patterns in the training set {
    obtain feature vector  $\mathbf{x}$  and class  $\omega$ ;
    compute perceptron output  $y$ ;
    if ( $y \neq \omega$ ) adjust weights according to  $w_i = w_i + \eta(\omega - y)x_i$ ;
  }
} until no further change;

```

---

In these equations, the parameter  $k$  represents the  $k$ th iteration of the classifier, and  $\omega(k)$  is the class of the  $k$ th training pattern. It is clearly important to know whether this training scheme is effective in practice. In fact, it is possible to show that if the algorithm is modified so that its main loop is applied sufficiently many times, *and* if the feature vectors are linearly separable, then the algorithm will converge to a correct error-free solution.

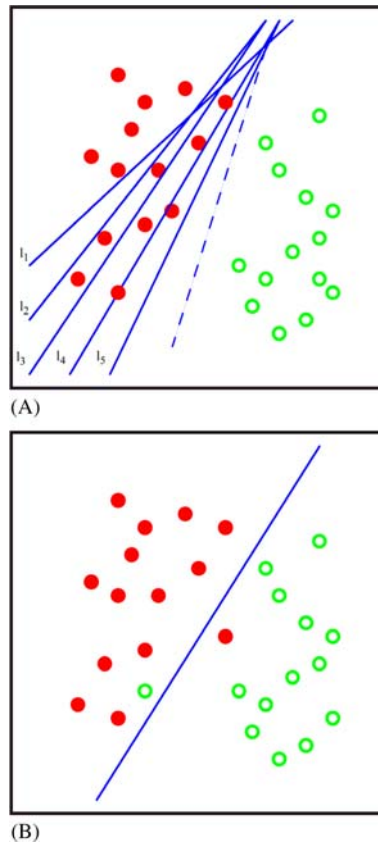
On the contrary, most sets of feature vectors are not linearly separable; thus, it is necessary to find an alternative procedure for adjusting the weights. This is achieved by the Widrow–Hoff delta rule that involves making changes in the weights in proportion to the error  $\delta = \omega - d$  made by the classifier. (Note that the error is calculated *before* thresholding to determine the actual class: i.e.,  $\delta$  is calculated using  $d$  rather than  $f(d)$ ). Thus, we obtain the Widrow–Hoff delta rule in the form:

$$w_i(k+1) = w_i(k) + \eta \delta x_i(k) = w_i(k) + \eta[\omega(k) - d(k)]x_i(k) \quad (13.24)$$

There are two important ways in which the Widrow–Hoff rule differs from the fixed increment rule:

1. An adjustment is made to the weights whether or not the classifier makes an actual classification error.
2. The output function  $d$  used for training is different from the function  $y = f(d)$  used for testing.

These differences underline the revised aim of being able to cope with nonlinearly separable feature data. Fig. 13.8 clarifies the situation by appealing to a 2-D case. Fig. 13.8A shows separable data which are straightforwardly fitted by the fixed increment rule. However, the fixed increment rule is not designed to cope with nonseparable data of the type shown in Fig. 13.8B and results in instability during training, and inability to arrive at an optimal solution. On the other hand, the Widrow–Hoff rule copes satisfactorily with this type of data. An interesting addendum to the case of Fig. 13.8A is that although the fixed increment rule apparently reaches an optimal solution, the rule becomes “complacent” once a zero error situation has occurred, whereas an ideal classifier would arrive at a solution which minimizes the probability of error. Clearly, the Widrow–Hoff rule goes some way to solving this problem.

**FIGURE 13.8**

Separable and nonseparable data. Part (A) shows two sets of pattern data: lines  $l_1$ – $l_5$  indicate possible successive positions of a linear decision surface produced by the fixed increment rule. Note that the latter is satisfied by the final position  $l_5$ . The dotted line shows the final position that would have been produced by the Widrow–Hoff delta rule. Part (B) shows the stable position that would be produced by the Widrow–Hoff rule in the case of nonseparable data; in this case, the fixed increment rule would oscillate over a range of positions during training.

So far, we have considered what can be achieved by a simple perceptron. Clearly, though it is only capable of dichotomizing feature data, a suitably trained array of simple perceptrons—the “single-layer perceptron” of Fig. 13.9—should be able to divide feature space into a large number of subregions bounded (in multidimensional space) by hyperplanes. However, in a multiclass application, this approach would require a very large number of simple perceptrons—up to  ${}^c C_2 = \frac{1}{2}c(c - 1)$  for a  $c$ -class system. Hence, there is a need to generalize the

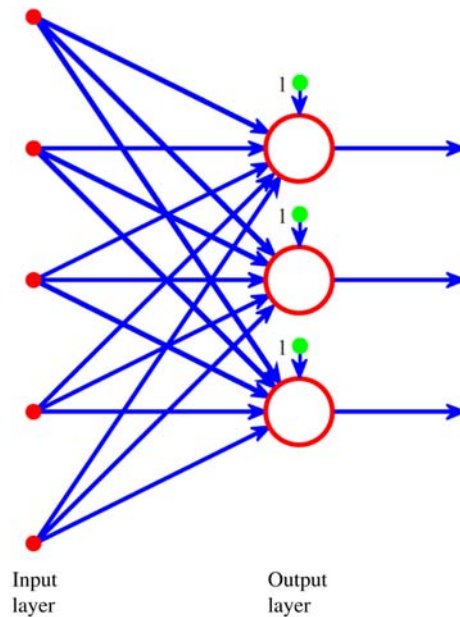


**FIGURE 13.9**

Single-layer perceptron. The single-layer perceptron employs a number of simple perceptrons in a single layer. Each output indicates a different class (or region of feature space). In more complex diagrams, the bias units (labeled “1”) are generally omitted for clarity.

approach by other means. In particular, multilayer perceptron (MLP) networks (see Fig. 13.10)—which would emulate the neural networks in the brain—seem poised to provide a solution as they should be able to recode the outputs of the first layer of simple perceptrons.

Rosenblatt himself proposed such networks, but was unable to find a general means for training them systematically. In 1969, Minsky and Papert published their famous monograph, and in discussing the MLP raised the specter of “the monster of vacuous generality;” they drew attention to certain problems that apparently would never be solved using MLPs. For example, diameter-limited perceptrons (those that view only small regions of an image within a restricted diameter) would be unable to measure large-scale connectedness within images. These considerations discouraged effort in this area, and for many years, attention was diverted to other areas such as expert systems. It was not until 1986 that Rumelhart *et al.* were successful in proposing a systematic approach to the training of MLPs. Their solution is known as the back-propagation algorithm.

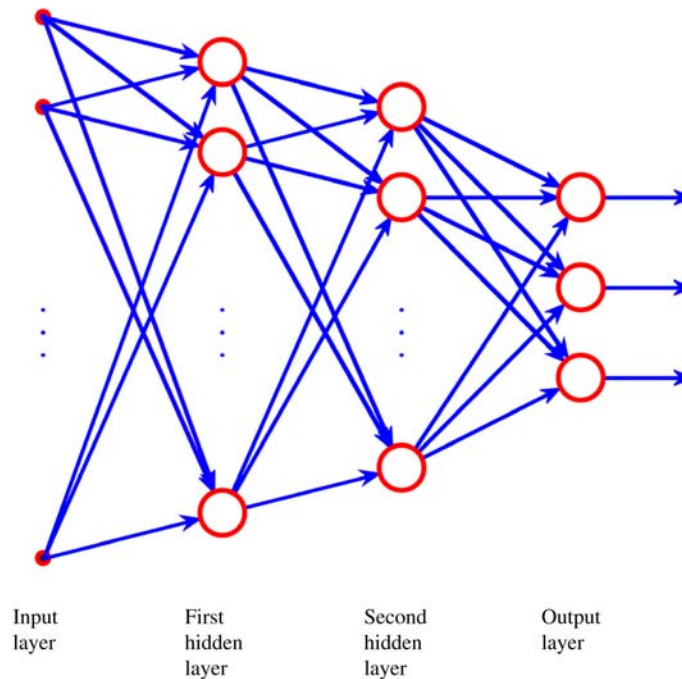


**FIGURE 13.10**

Multilayer perceptron. The multilayer perceptron employs several layers of perceptrons. In principle, this topology permits the network to define more complex regions of feature space and thus performs much more precise pattern recognition tasks. Finding systematic means of training the separate layers becomes the vital issue. For clarity, the bias units have been omitted from this and later diagrams.

### 13.11 THE BACK-PROPAGATION ALGORITHM

The problem of training a MLP can be simply stated: a general layer of a MLP obtains its feature data from the lower layers and receives its class data from higher layers. Hence, if all the weights in the MLP are potentially changeable, the information reaching a particular layer cannot be relied upon. There is no reason why training a layer in isolation should lead to overall convergence of the MLP toward an ideal classifier (however defined). Although it might be thought that this is a rather minor difficulty, in fact, this is not so; indeed, this is but one example of the so-called credit assignment problem. This is probably not a good first example by which to define the credit assignment problem (in this case, it would appear to be more of a *deficit* assignment problem). The credit assignment problem is the problem of correctly determining the local origins of global

properties and making the right assignments of rewards, punishments, corrections, and so on, thereby permitting the whole system to be optimized systematically.

One of the main difficulties in predicting the properties of MLPs and hence of training them reliably is the fact that neuron outputs swing suddenly from one state to another as their inputs change by infinitesimal amounts. Hence, we might consider removing the thresholding functions from the lower layers of MLP networks to make them easier to train. On the contrary, this would result in these layers acting together as larger linear classifiers, with far less discriminatory power than the original classifier (in the limit we would have a single linear classifier with a single thresholded output connection, so the overall MLP would act as a single-layer perceptron).

The key to solving to these problems was to modify the perceptrons composing the MLP by giving them a less “hard” activation function than the Heaviside function. As we have seen, a linear activation function would be of little use, but one of “sigmoid” shape, such as the tanh function (Fig. 13.11) is effective, and indeed is almost certainly the most widely used of the available functions. (We do not here make a marked distinction between symmetrical activation functions and alternatives that are related to them by shifts of axes, though the symmetrical formulation seems preferable as it emphasizes bidirectional functionality. In fact, the tanh function, which ranges from  $-1$  to  $1$ , can be expressed in the form:  $\tanh u = (e^u - e^{-u}) / (e^u + e^{-u}) = 1 - 2 / (1 + e^{2u})$  and is thereby closely related to the commonly used function  $(1 + e^{-v})^{-1}$ . It can now be deduced that the latter function is symmetrical, though it ranges from  $0$  to  $1$  as  $v$  goes from  $-\infty$  to  $\infty$ .)

Once these softer activation functions were used, it became possible for each layer of the MLP to “feel” the data more precisely and thus training procedures could be set up on a systematic basis. In particular, the rate of change of the data at each individual neuron could be communicated to other layers that could then be trained appropriately—though only on an incremental basis. We shall not go through the detailed mathematical procedure, or proof of convergence, beyond stating that it is equivalent to energy minimization and gradient descent on a (generalized) energy surface. Instead, we give an outline of the backpropagation algorithm (see Table 13.4). Nevertheless, some notes on the algorithm are in order:

1. The outputs of one node are the inputs of the next, and an arbitrary choice is made to label all variables as output ( $y$ ) parameters rather than as input ( $x$ ) variables; all output parameters are in the range  $0$  to  $1$ .
2. The class parameter  $\omega$  has been generalized as the target value  $t$  of the output variable  $y$ .
3. For all except the final outputs, the quantity  $\delta_j$  has to be calculated using the formula  $\delta_j = y_j(1 - y_j)(\sum_m \delta_m w_{jm})$ , the summation having to be taken over all the nodes in the layer *above* node  $j$ .
4. The sequence for computing the node weights involves starting with the output nodes and then proceeding downwards one layer at a time.



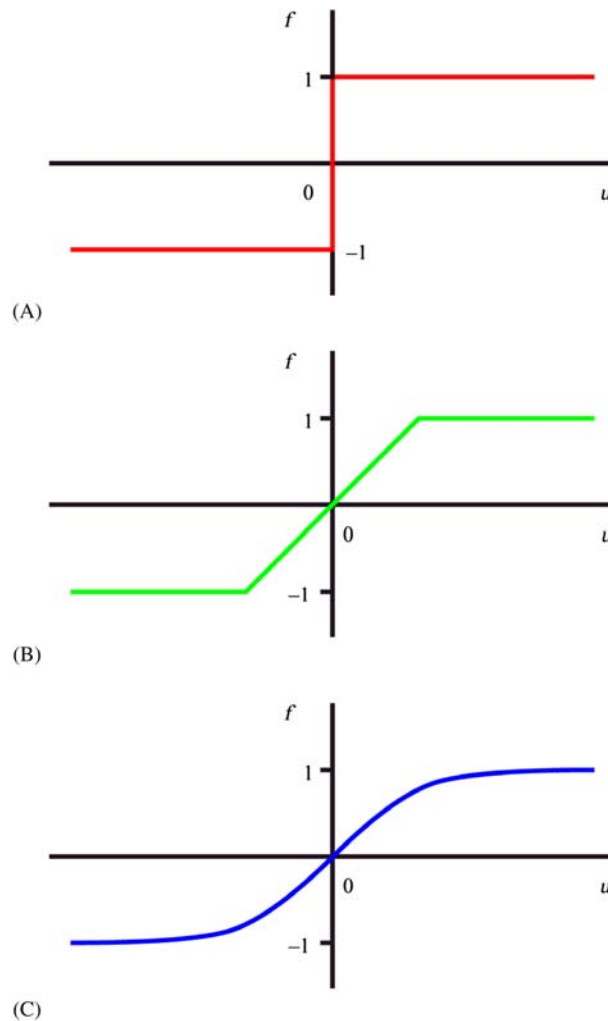


**FIGURE 13.11**

Symmetric activation functions. This figure shows a series of symmetric activation functions. Part (A) shows the Heaviside activation function used in the simple perceptron. Part (B) shows a linear activation function, which is, however, limited by saturation mechanisms. Part (C) shows a sigmoidal activation function which approximates to the hyperbolic tangent function.

5. If there are no hidden nodes, the formula reverts to the Widrow–Hoff delta rule, except that the input parameters are now labeled  $y_i$ , as indicated above.
6. It is important to initialize the weights with random numbers to minimize the chance of the system becoming stuck in some symmetrical state from which it might be difficult to recover.

**Table 13.4** The Back-Propagation Algorithm

---

```

initialise weights with small random numbers;
select suitable value of learning rate coefficient  $\eta$  in the range 0 to 1;
do {
  for all patterns in the training set
    for all nodes  $j$  in the MLP {
      obtain feature vector  $x$  and target output value  $t$ ;
      compute MLP output  $y$ ;
      if (node is in output layer)
         $\delta_j = y_j(1 - y_j)(t_j - y_j)$ ;
      else  $\delta_j = y_j(1 - y_j)(\sum_m \delta_m w_{jm})$ ;
      adjust weights  $i$  of node  $j$  according to  $w_{ij} = w_{ij} + \eta \delta_j y_i$ ;
    }
} until changes are reduced to some predetermined level;

```

---

7. Choice of value for the learning rate coefficient  $\eta$  will be a balance between achieving a high rate of learning and avoidance of overshoot: normally a value of around 0.8 is selected.

When there are many hidden nodes, convergence of the weights can be very slow, and indeed, this is one disadvantage of MLP networks. Many attempts have been made to speed convergence, and a method that has been very widely used is to add a “momentum” term to the weight update formula, it being assumed that weights will change in a similar manner during iteration  $k$  to the change during iteration  $k - 1$ :

$$w_{ij}(k+1) = w_{ij}(k) + \eta \delta_j y_i + \alpha [w_{ij}(k) - w_{ij}(k-1)] \quad (13.25)$$

where  $\alpha$  is the momentum factor. This technique is primarily intended to prevent networks from becoming stuck at local minima of the energy surface.

---

## 13.12 MULTILAYER PERCEPTRON ARCHITECTURES

The preceding sections gave the motivation for designing a MLP and for finding a suitable training procedure, and then outlined a general MLP architecture and the widely used back-propagation training algorithm. However, having a general solution is only one part of the answer. The next question is how best to adapt the general architecture to specific types of problem. We shall not give a full answer to this question here. However, Lippmann attempted to answer this problem in 1987. He showed that a two-layer (single hidden layer) MLP can implement arbitrary convex decision boundaries and indicated that a three-layer (two-hidden layer) network is required to implement more complex decision boundaries. It was subsequently found that it should never be necessary to exceed two hidden layers, as a three-layer network can tackle quite general situations if sufficient neurons are used (Cybenko, 1988). Subsequently, Cybenko (1989) and Hornik *et al.* (1989)

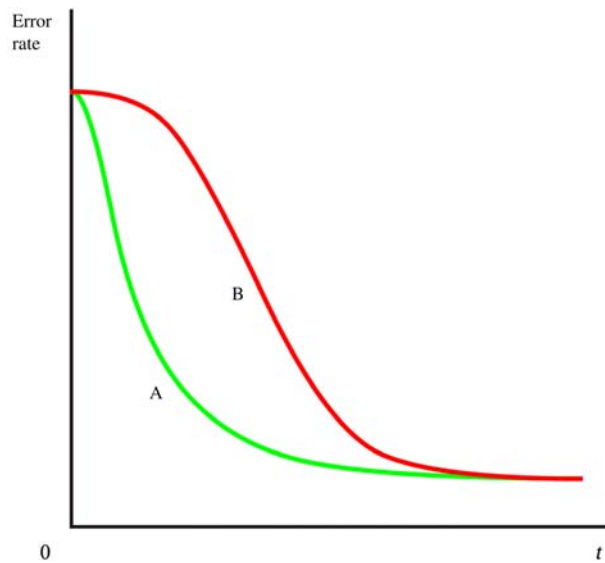


**FIGURE 13.12**

Learning curve for the multilayer perceptron. Here, (A) shows the learning curve for a single-layer perceptron, and (B) shows that for a multilayer perceptron. Note that the multilayer perceptron takes considerable time to get going, as initially each layer receives relatively little useful training information from the other layers. Note also that the lower part of the diagram has been idealized to the case of identical asymptotic error rates—though this situation would seldom occur in practice.

showed that a two-layer MLP can approximate any continuous function, though nevertheless there may sometimes be advantages in using more than two layers.

Although the back-propagation algorithm can train MLPs containing any number of layers, in practice, training one layer “through” several others introduces an element of uncertainty that is commonly reflected in increased training times (see Fig. 13.12). Thus, there is some advantage to be gained from using a minimal number of layers of neurons. In this context, the above findings on the necessary numbers of hidden layers have proved to be valuable.

### 13.13 OVERFITTING TO THE TRAINING DATA

When training MLPs and many other types of ANN, there is a problem of overfitting the network to the training data. One of the fundamental aims of SPR is for the learning machine to be able to generalize from the particular set of data it is trained on to other types of data it might meet during testing. In particular, the machine should be able to cope with noise, distortions, and fuzziness in the data,

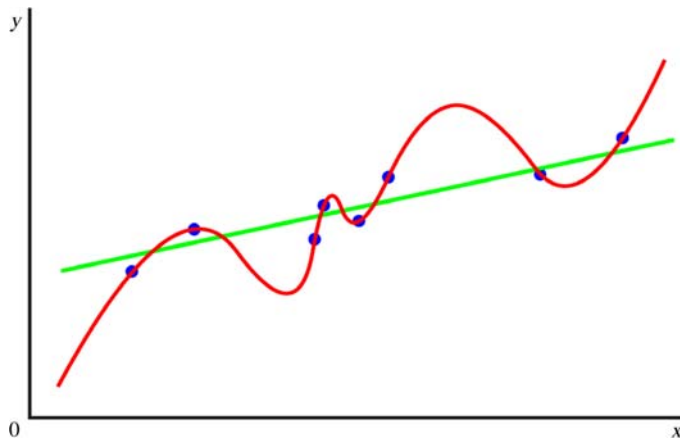


**FIGURE 13.13**

Overfitting of data. In this graph, the data points are rather too well fitted by the red curve, which matches every nuance exactly. Unless there are strong theoretic reasons why the red curve should be used, the green line will give a higher confidence level.

though clearly not to the extent of being able to respond correctly to types of data different from those on which it has been trained. The main points to be made here are (1) that the machine should learn to respond to the underlying population from which the training data have been drawn, and (2) that it must not be so well adapted to the specific training data that it responds less well to other data from the same population. Fig. 13.13 shows in a 2-D case both a fairly ideal degree of fit, and a situation where every nuance of the set of data has been fitted, thereby achieving a degree of overfit.

Typically, overfitting can arise if the learning machine has more adjustable parameters than are strictly necessary for modeling the training data: with too few parameters such a situation should not arise. However, if the learning machine has enough parameters to ensure that relevant details of the underlying population are fitted, there may be overmodeling of part of the training set; thus, the overall recognition performance will deteriorate. Ultimately, the reason for this is that recognition is a delicate balance between capability to discriminate and capability to generalize, and it is unlikely that any complex learning machine will get the balance right for all the features it has to take account of.

Be this as it may, we clearly need to have some means of preventing overadaptation to the training data. One way of achieving this is to curtail the training process before overadaptation can occur. (It is often stated that this procedure aims to prevent overtraining. However, the term “overtraining” is ambiguous. On the one hand, it can mean recycling through the *same* set of training data until eventually the learning machine is overadapted to it. On the other hand, it can mean using more and more *totally new* data—a procedure that cannot produce

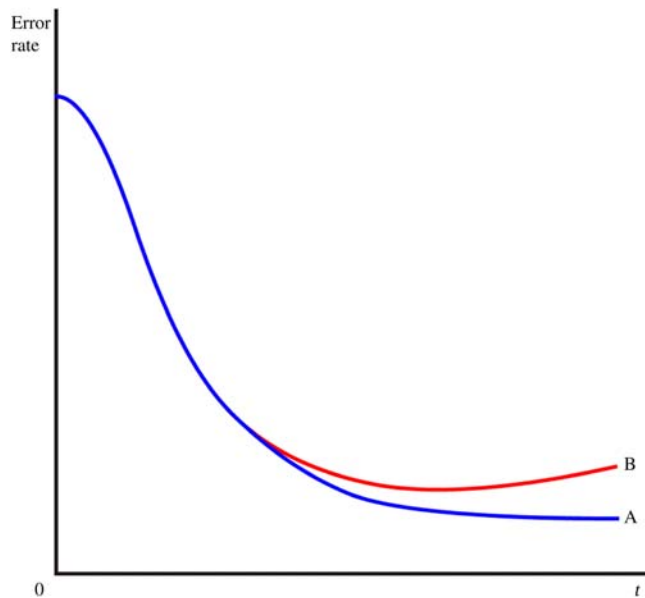


**FIGURE 13.14**

Cross-validation tests. This diagram shows the learning curve for a multilayer perceptron (A) when tested on the training data and (B) when tested on a special validation set. Part (A) tends to go on improving even when overfitting is occurring. However, this situation is detected when (B) starts deteriorating. To offset the effects of noise (not shown on curves (A) and (B)), it is usual to allow 5%–10% deterioration relative to the minimum in (B).

overadaptation to the data, and on the contrary is almost certain to improve performance. In view of this ambiguity, it seems better not to use the term.) In fact, curtailing the training process is not difficult to manage: we merely need to test the system periodically during training to ensure that the point of overadaptation has not been reached. Fig. 13.14 shows what happens when testing is carried out simultaneously on a separate dataset: at first, performance on the test data closely matches that on the training data, being slightly superior for the latter because a small degree of overadaptation is already occurring. But after a time, performance starts deteriorating on the test data, whereas that on the training data appears to go on improving. This is the point where serious overfitting is occurring, and the training process needs to be curtailed. The aim, then, is to make the overall training process far more rigorous by splitting the original training set into two parts—the first being retained as a normal training set, and the second being called the *validation set*. Note that the latter is actually part of the training set in the sense that it is not part of the eventual test set.

The process of checking the degree of training by use of a validation set is called *cross-validation* and is vitally important to proper use of an ANN.

The training algorithm should include cross-validation as a fully integrated part of the whole training schedule: it should not be regarded as an optional extra.

It is useful to speculate how overadaptation could occur when the training procedure is completely determined by the back propagation (or other) provably correct algorithm. In fact, there are specific mechanisms by which overadaptation can occur. For example, when the training data do not control particular weights sufficiently closely, some could drift to large positive or negative values, while retaining a sufficient degree of cancellation so that no problems appear to arise with the training data; yet, when test or validation data are employed, the problems become all too clear. The fact that the form of the sigmoid function will permit some nodes to become “saturated out” does not help the situation, as it inactivates parameters and hides certain aspects of the incoming data. Yet, it is intrinsic to the MLP architecture and the way it is trained that some nodes are *intended* to be saturated out in order to ignore irrelevant features of the training set. The problem is whether inactivation is inadvertent or designed. The answer probably lies in the quality of the training set and how well it covers the available or potential feature space.

Finally, let us suppose a MLP is being set up, and it is initially unknown how many hidden layers will be required or how many nodes there will have to be in each layer; it will also be unknown how many training set patterns will be required or how many training iterations will be needed—or what values of the momentum or learning parameters will be appropriate. A quite substantial number of tests will be required to decide all the relevant parameters. There is therefore a definite risk that the final system will be overadapted not only to the training set but also to the validation set. In such circumstances, what we need is a second validation set that can be used after the whole network has been finalized and final training is being undertaken.

---

## 13.14 CONCLUDING REMARKS

The methods of this chapter make it rather surprising that so much of image processing and analysis is possible without any reference to a priori probabilities. It seems likely that this situation is due to the fact that algorithms are designed and implemented by humans who have knowledge of the types of input data and thereby incorporate a priori probabilities implicitly, e.g., via the application of suitable threshold values. Nonetheless, SPR is extremely valuable within its own range of utility. This includes identifying objects on conveyors and making value judgments of their quality, reading labels and codes, verifying signatures, checking fingerprints, and so on. Indeed, the number of distinct applications of SPR is huge, and it forms an essential counterpart to the other methods described in this book.

This chapter has concentrated mainly on the supervised learning approach to SPR. However, unsupervised learning is also vitally important, particularly when training on huge numbers of samples (e.g., in a factory environment) is involved. The section on this topic should therefore not be ignored as a minor, insignificant perturbation.

In summary, the only methods of this chapter that transcend SPR and include probabilistic analysis are NN-based methods (though only when suitably trained) and of course Bayes theory. In [Chapter 14](#), *Machine Learning: Probabilistic Methods*, it will be seen how new methods can be developed that incorporate probability as an intrinsic part of their design.

*Vision is largely a recognition process with both structural and statistical aspects. This chapter has reviewed SPR, emphasizing fundamental classification error limits, and has shown the part played by Bayes' theory, the NN algorithm and ANNs. Note that the last of these is subject to the same limitations as other SPR methods, particularly with regard to adequacy of training and the possibility of overfitting. Further methods incorporating probability as part of their formulation are left to later chapters, notably Chapter 14, *Machine Learning: Probabilistic Methods*.*

---

### 13.15 BIBLIOGRAPHICAL AND HISTORICAL NOTES

Although the subject of SPR tends not to be at the center of attention in image analysis work, it provides an important background—especially in the area of automated visual inspection where decisions continually have to be made on the adequacy of products. (Note, however, that SPR is vital to the analysis of multi-spectral data from satellite imagery: see for example, Landgrebe (1981).) Most of the relevant works on this topic were already in place by the early 1970s, including the work of Hughes (1968) and Ullmann (1969) relating to the optimum number of features to be used in a classifier. At that stage, a number of important volumes appeared—see for example, Duda and Hart (1973) and Ullmann (1973), and these were followed a little later by Devijver and Kittler (1982).

In fact, the use of SPR for image interpretation dates from the 1950s. For example, in 1959, Bledsoe and Browning developed the  $n$ -tuple method of PR, which turned out (Ullmann, 1973) to be a form of NN classifier; however, it has been useful in leading to a range of simple hardware machines based on RAM ( $n$ -tuple) lookups (see e.g., Aleksander *et al.*, 1984), thereby demonstrating the importance of marrying algorithms and readily implementable architectures.

Many of the most important developments in this area have probably been those comparing the detailed performance of one classifier with another, particularly with respect to cutting down the amount of storage and computational effort. Papers in these categories include those by Hart (1968) and Devijver and Kittler (1980). Oddly, there appeared to be no overt mention in the literature of how

a priori probabilities should be used with the NN algorithm, until the author's paper on this topic (Davies, 1988e): see [Section 13.4](#).

On the unsupervised approach to SPR, Forgy's (1965) method for clustering data was soon followed by the famous ISODATA approach of Ball and Hall (1966), and then by MacQueen's (1967) *K-means* algorithm. Much related work ensued, and this was summarized by Jain and Dubes (1988), which became a classic text. However, cluster analysis is an exacting process and various workers have felt the need to push the subject further forward: e.g., Postaire and Touzani (1989) required more accurate cluster boundaries; Jolion and Rosenfeld (1989) wanted better detection of clusters in noise; Chauduri (1994) needed to cope with time-varying data; and Juan and Vidal (1994) required faster *K-means* clustering. Note that all this work can be described as conventional and did not involve the use of robust statistics per se. However, elimination of outliers is central to the problem of reliable cluster analysis: for a discussion of this aspect of the problem, see [Appendix A](#) and the references listed therein.

Although the field of PR has moved forward substantially since 1990, there are fortunately several quite recent texts that cover the subject relatively painlessly (Duda *et al.*, 2001; Webb, 2002; Theodoridis and Koutroumbas, 2009).

SVMs also came into prominence over the 1990s and have found an increasing number of applications: the concept was invented by Vapnik and the historical perspective is covered in Vapnik (1998). Cristianini and Shawe-Taylor (2000) provide a student-orientated text on the subject.

Next, we turn our attention to the history of ANNs. After a promising start in the 1950s and 1960s, they fell into disrepute (or at least, disregard) following the pronouncements of Minsky and Papert in 1969; they picked up again in the early 1980s, were subjected to an explosion in interest after the announcement of the backpropagation algorithm by Rumelhart *et al.* in 1986, and in the mid-1990s settled into the role of normal tools for vision and other applications. Note that the backpropagation algorithm was invented several times (Werbos, 1974; Parker, 1985) before its relevance was finally recognized. In parallel with these MLP developments, Oja (1982) developed his Hebbian principal components network. Useful early references on ANNs include the volumes by Haykin (1999) and Bishop (1995), and papers on their application to segmentation and object location, such as Toulson and Boyce (1992) and Vaillant *et al.* (1994); for work on contextual image labeling, see Mackeown *et al.* (1994).

After the euphoria of the early 1990s, during which papers on ANNs applied to vision were ubiquitous, it was seen that the main value of ANNs lay in their unified approach to feature extraction and selection (even if this necessarily carries the disadvantage that the statistics are hidden from the user), and their intrinsic capability for finding moderately nonlinear solutions with relative ease. Later papers include the ANN face detection work of Rowley *et al.* (1998), amongst others (Fasel, 2002; Garcia and Delakis, 2002). For further general information on ANNs, see the book by Bishop (2006).



### 13.15.1 MORE RECENT DEVELOPMENTS

Returning to mainstream SPR, Jain (2010) presented a review of the subject of clustering, entitled “Data clustering: 50 years beyond *K-means*”. He noted that “In spite of the fact that *K-means* was proposed over 50 years ago and thousands of clustering algorithms have been published since then, *K-means* is still widely used”—thereby reflecting the difficulty of designing a general purpose clustering algorithm and the ill-posed nature of the problem; emerging and useful research directions include semisupervised clustering and ensemble clustering. The review presents the main challenges and issues facing the subject as of 2010: above all is the plea for a suite of benchmark data with ground truth to test and evaluate clustering methods.

Youn and Jeong (2009) describe a class-dependent feature-scaling method employing a naïve Bayes’ classifier for text data mining, including functions such as text categorization and search. Although the reasons why the naïve Bayes independence assumption works well in many cases have not been well explained or understood until recently, this paper confirms that it is often a good choice for text analysis because the amount of data used is large (e.g., the number of features is about 100,000 for protein sequence data). In particular, the simplicity and the effectiveness of the naïve Bayes’ classifier maps well to text categorization. Rish (2001) provides an empirical study of naïve Bayes, containing much useful information.

---

### 13.16 PROBLEMS

1. Show that if the cost function of Eq. (13.16) is chosen, then the decision rule (13.15) can be expressed in the form of relation (13.5).
2. Show that in a simple two-class system, introducing a reject classification to reduce the number of errors by  $R$  in fact requires  $2R$  test patterns to be rejected, assuming that  $R$  is small. What is likely to happen as  $R$  increases?
3. In a 1-D feature space, show that the feature value at which the a posteriori probability curves cross over corresponds to a decision boundary giving the minimum possible classification error.

# Machine learning: probabilistic methods

# 14

This chapter introduces two main fiercely probabilistic methods, the expectation maximization (EM) algorithm—together with mixture models, its major outlet—and multiple classifiers, including in particular boosted classifiers. The methods by which the underlying probabilistic theory is developed are explored, and it is shown how rigorously adhering to this approach can yield more accurate practical results. Other topics appearing in the chapter include principal components analysis (PCA) and performance analysis.

*Look out for:*

- the EM algorithm and Gaussian mixture models
- use of  $K$ -means for initializing the EM algorithm
- histogram-based image segmentation using mixture models
- PCA and its value
- multiple classifiers and boosting
- comparisons between loss functions for boosting
- the means by which boosting is achieved with multiple classes
- the various ways in which probabilistic optimization is formulated
- the receiver-operating-characteristic (ROC) curve, which allows an optimum balance between false positives and false negatives to be achieved.

Probabilistic methods are key to machine learning and the need to take us away from the tedium of (re)programming conventional code for every application. To this end, the EM algorithm and the boosting approach are paradigms for the subject and help us to understand quite how the probabilistic approach is applied in practice. It is left to later chapters to cover further theory, advanced applications, and also deep learning, which is an exceptionally rapidly developing topic.

## 14.1 INTRODUCTION

In this chapter, we progress from the pattern recognition beginnings, outlined in [Chapter 13](#), Basic Classification Concepts to the more modern subject of machine learning. That doesn't mean we have to unlearn the knowledge we acquired in [Chapter 13](#), Basic Classification Concepts, but it will mean that we move with a

heightened mind-set into a more principled scenario. We start by taking the example of the  $K$ -means clustering algorithm of [Section 13.8](#). Although powerful, this approach had important limitations—in particular, that of there being no absolute arbiter of correctness or direction in the calculations or indeed completeness in the knowledge of how closely we were approaching ideal solutions. Here we move on to a powerful approach based on probabilistic optimization—the EM algorithm. In many ways, we will be using the EM algorithm as a vehicle for learning about probabilistic optimization. This could prove challenging, not least because of the amount of mathematics that we will be handling. On the other hand, the experimental outcomes—for example, via mixture models—will make the results highly tangible and visible and will provide confirmation that we are on the path to progress.

Perhaps the main point about probabilistic optimization is that we are always in a situation where we have an absolute mathematical goal—to ensure that the solutions we are seeking are subject to ever-increasing probability. This is important because, when analyzing data involving a large component of randomness, we can never be sure whether any real improvement is being made. But if we can prove mathematically that the process of change can only increase the probability of correct interpretation, we have a crucially important tool at our fingertips. Indeed, probability will often be our only arbiter of value: Using any other criteria instead or at the same time might only serve to fool us that we are making progress.

Such ideas and motivations are undoubtedly good, but exactly how will we formulate probabilistic arguments in such a way as to achieve our aims? In principle, it is even possible that enough is not known about probability and probabilistic approaches to achieve anything at all. Above all, by what route will we be able to achieve such goals? The answer to these questions lies in the fact that by the 2010s many tools have been developed to permit this to happen, and at this very moment in time progress in this area is accelerating, so work and perseverance will lead to increasing returns in the future—a fact that applies rather strongly in computer vision.

To give a foretaste of all this and to indicate that there are concrete underpinnings to our probabilistic methodology, let me cite a few basic methods and techniques: among the most powerful is Bayes theory, the sine qua non in the area of applied statistics. Next, there are important mathematical constraints, such as Jensen's inequality, and the Kulback–Leibler divergence formula, which gives a distance measure showing how different two probabilistic distributions are. Then there is Newton's method of approximation, which is fundamental, but which can be bettered in relevant cases by the EM algorithm. Amongst all this theory, we must not forget such basic probability ideas as the vertical bar (“knowing that”) notation, which allows probabilities to be reexpressed using the product rule  $p(A, B) = p(A|B)p(B)$ .

Finally, much of what we shall do in the probabilistic formulism is to make models of the input data—this being particularly true of the EM algorithm, which

is designed for generating accurate statistical models of data. But what types of model are to be used? Here, the Gaussian distribution is key. This is because it accurately models inaccuracies of measurement due to random noise. I ought somewhat tautologically to be saying *Gaussian* random noise because there are other sorts of random noise—e.g., Rayleigh noise which appears on electrical signals output from a rectifier and which are necessarily always positive, thereby biasing the type of noise superimposed on the signals. However, Gaussian noise is rendered exceptionally important because of the central limit theorem: this states that when noise is due to many different independent disturbances, the overall disturbance will take the form of a Gaussian distribution. By way of example, notice from Fig. 14.1, how quickly a square pulse distribution changes into a shape similar to a Gaussian when combining (convolving) it with an identical distribution just twice and is at least superficially identical to a Gaussian after three or four such combinations. More formally, the sum of a set of  $N$  independent random variables is itself a random variable whose distribution tends toward a Gaussian distribution as  $N$  increases. This fact gives the Gaussian distribution high practical importance, which is augmented by its simplicity of form, and further augmented by the fact that its basic extension to the multidimensional case is trivial. Here, the word “basic” indicates that the mean and standard deviation for the 1-D case must obviously generalize immediately to two means and two standard deviations for 2-D (and so on for higher dimensionalities); however, the fully generalized 2-D Gaussian will actually have a  $2 \times 2$  covariance matrix containing a total of four parameters (the  $n$ -D Gaussian has an  $n \times n$  covariance matrix with a total of  $n^2$  parameters, though only  $\frac{1}{2}(n^2 + n)$  of them are distinct). Of course, inclusion of increased numbers of parameters in a single formalism is a mark of power and value; on the other hand, it can also be regarded as something of a problem, as calculation of greater numbers of parameters requires increased computation. Nevertheless, there is a paucity of functions that can be applied to make viable probabilistic models, and the Gaussian distribution is almost always the first contender, in either its 1-D or multivariate forms. Further contenders are those such as Student’s  $t$ -distribution and other exponentially-based distributions such as the beta and gamma distributions. Interestingly, as we shall see, it is often useful to apply the log function in probability calculations, and the fact that it is

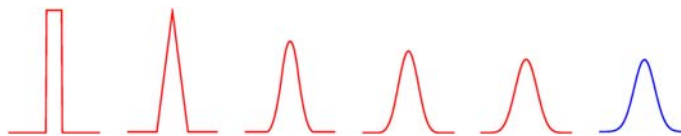


**FIGURE 14.1**

The central limit theorem in action. The sequence of shapes obtained after successive convolutions with the square pulse on the left: the final blue shape is a true Gaussian. Notice how quickly the shapes become indistinguishable from the Gaussian.

the inverse of the exponential function means that mathematical optimization often becomes more tractable for exponentially-based distributions.

Overall, taken together, the various factors given above yield a subject area of great power, though sometimes it might appear that proofs center on mathematical tricks rather than on straightforward calculations. However, proofs normally rely on previous results and theorems: only familiarization with the techniques allows one to understand the situation fully—though the short-cut for understanding is appreciation of practical demonstrations that the theory applies to real applications including those of computer vision, as we shall see for the EM algorithm and the other methods that are to follow.

---

## 14.2 MIXTURES OF GAUSSIANS AND THE EM ALGORITHM

Before proceeding to describe the EM algorithm and its justification, it will be useful to look at the sort of problems that we will want to apply it to. In particular, suppose, we have a 1-D distribution of data points which we wish to fit: Perhaps, the most obvious way to model it is by using a set of individual Gaussian distributions, each of which will correspond to one of the peaks of the input distribution. Mathematically, we can model this as a mixture of Gaussians in which each Gaussian has its own mixture coefficient  $m$ . Furthermore, if we are to follow our probabilistic strategy, we will need to express both the input distribution and the result as probability distributions.

The first thing to do is to represent the Gaussian distribution as a probability distribution integrating to unity:

$$\mathcal{N}(x|\mu, \sigma) = \frac{1}{(2\pi\sigma^2)^{1/2}} \exp\left[-\frac{(x-\mu)^2}{2\sigma^2}\right] \quad (14.1)$$

$\mu$  and  $\sigma$  being, respectively, the mean and standard deviation of the distribution: In addition, we follow standard usage in denoting the Gaussian by its alternate name, the *normal* distribution, and represent it using the symbol  $\mathcal{N}$ . We can now write the joint (probability) distribution of our problem as follows:

$$p(x) = \sum_{k=1}^K m_k \mathcal{N}(x|\mu_k, \sigma_k) \quad (14.2)$$

where  $k$  is the index of the set of mixture coefficients. To ensure that the joint distribution  $p(x)$  is a true probability, we integrate both sides of Eq. (14.2) and obtain the condition

$$\sum_{k=1}^K m_k = 1 \quad (14.3)$$

Note that the mixture coefficients  $m_k$  can be regarded as a priori probabilities for the mixture values. There are many potential ways of determining the set of parameters  $m_k, \mu_k, \sigma_k$  that lead to a best fit for all the data points,  $x_i, i = 1, \dots, N$ , including some form of nonlinear optimization such as the Gauss–Newton method. However, it is possible to split the problem into two sub-problems, each involving reduced complexity and reduced computation. This approach is called the EM (“Expectation Maximization”) algorithm. In the E-step we take the Gaussian parameters to be fixed, and merely solve for the mixture parameters  $m_k$  (or rather their “responsibilities,”  $\rho_k$ —see below); and in the M-step we take the mixture parameters to be fixed and solve for the Gaussian parameters  $\mu_k, \sigma_k$ . The two steps are recycled as many times as necessary to proceed from an initial approximation to a final, much more accurate one.

To proceed, it will be useful to reexpress the mixture coefficients  $m_k$  in terms of “hidden” variables  $z_k$ , as this will permit us to apply Bayes theorem and obtain an important result. [The nomenclature of “hidden” or “latent” variables has long been standard in this area, but some workers regard it as an artifice. After all, why make an arbitrary distinction between Gaussian amplitudes and their means and standard deviations? However, it is worth noting that the EM algorithm at least makes it *useful* to consider the two sets of variables separately and to optimize them in turn.] In fact, the vector  $\mathbf{z} = (z_1, \dots, z_K)$  will be a 1-of- $K$  variable in which the various  $z_k$  will satisfy  $z_k \in \{0, 1\}$  and  $\sum_k z_k = 1$ . The relation between  $z_k$  and  $m_k$  is

$$\left. \begin{aligned} p(z_k = 1) &= m_k \\ p(z_{j \neq k} = 0) &= 1 \end{aligned} \right\} \quad (14.4)$$

Hence,

$$p(\mathbf{z}) = \prod_{j=1}^K m_j^{z_j} \quad (14.5)$$

Similarly,

$$p(x|z_k = 1) = \mathcal{N}(x|\mu_k, \sigma_k) \quad (14.6)$$

$$\therefore p(x|\mathbf{z}) = \prod_{j=1}^K \mathcal{N}(x|\mu_j, \sigma_j)^{z_j} \quad (14.7)$$

Summing the joint distribution  $p(x, \mathbf{z}) = p(x|\mathbf{z})p(\mathbf{z})$  to include all states of  $\mathbf{z}$ , we find

$$p(x) = \sum_{\mathbf{z}} p(x|\mathbf{z})p(\mathbf{z}) = \sum_{k=1}^K m_k \mathcal{N}(x|\mu_k, \sigma_k) \quad (14.8)$$

This result is in line with Eq. (14.2) and shows we now have two different ways of formulating the 1-D distribution of data points. Importantly, we can now

use Bayes theorem to determine the posterior probability of  $z_k$  knowing  $x$ , viz.,  $p(z_k = 1|x)$ :

$$\rho(z_k) \equiv p(z_k = 1|x) = \frac{p(x|z_k = 1)p(z_k = 1)}{\sum_{j=1}^K p(x|z_j = 1)p(z_j = 1)} = \frac{p(x|\mathbf{z})p(\mathbf{z})}{\sum_{\mathbf{z}} p(x|\mathbf{z})p(\mathbf{z})} \quad (14.9)$$

We shall call this quantity the *responsibility*  $\rho(z_k)$  of the  $k$ th mixture component for explaining observation  $x$ , and evaluate it using Eqs. (14.4) and (14.6):

$$\rho(z_k) = \frac{m_k \mathcal{N}(x|\mu_k, \sigma_k)}{\sum_{j=1}^K m_j \mathcal{N}(x|\mu_j, \sigma_j)} \quad (14.10)$$

Finally, we estimate the responsibilities of the different Gaussian distributions for explaining the individual data points  $x_i$ ,  $i = 1, \dots, N$ :

$$\rho(z_{ik}) = \frac{m_k \mathcal{N}(x_i|\mu_k, \sigma_k)}{\sum_{j=1}^K m_j \mathcal{N}(x_i|\mu_j, \sigma_j)} \quad (14.11)$$

Here,  $m_k$  can be regarded as the prior probability and  $\rho(z_{ik})$  as the posterior probability.

This completes the theory for the E-step of the EM algorithm. Thus, we have now moved a good proportion of the way to applying the EM or “Expectation Maximization” algorithm, which is the means by which we shall be optimizing the fit of the joint distribution  $p(x)$  to the data points. In our case, we only need to optimize the likelihood function (probability) obtained above following from the application of Bayes theorem. However, it is a common practice instead to optimize the *log* likelihood function, as this can lead to considerable simplification when Gaussians or other exponentially-based functions are used to model the data. In particular, when fitting data to a single Gaussian distribution, we proceed by taking the products of the pdfs for all the individual data points, assumed to be measured independently and to have the same Gaussian form:

$$p(x_1, \dots, x_I|\mu, \sigma) = \prod_{i=1}^N p(x_i|\mu, \sigma) = \prod_{i=1}^N \mathcal{N}(x_i|\mu, \sigma) \quad (14.12)$$

Although we could obtain a maximum likelihood solution by finding the peak of this distribution, we can choose to use the log likelihood function  $\mathcal{L}$  as log is a monotonically increasing function which will have a maximum at exactly the same position. Proceeding with this gives

$$\begin{aligned} \mathcal{L} &= \ln \prod_{i=1}^N \mathcal{N}(x_i|\mu, \sigma) = \sum_{i=1}^N \ln[\mathcal{N}(x_i|\mu, \sigma)] \\ &= \sum_{i=1}^N \left[ -\frac{1}{2} \ln(2\pi\sigma^2) - \frac{(x_i - \mu)^2}{2\sigma^2} \right] \end{aligned} \quad (14.13)$$

This immediately shows the required simplification, and indeed confirms that the mean of  $x$  is at  $\mu$ : a formula for the standard deviation can be obtained with just a few more lines of calculation.

Clearly, when our mixture of Gaussians distribution is needed to fit the data, finding a maximum is somewhat more complicated to achieve: that is why the EM algorithm is needed.

### 14.2.1 DETAILS OF THE EXPECTATION MAXIMIZATION ALGORITHM

*On a first reading, details of the calculations in Eqs. (14.15)–(14.20) may be by-passed: the focus of attention should then be on the E- and M-steps in the computation, which are given by Eqs. (14.22) and (14.23).*

We now proceed to look at the log likelihood function for the mixture of Gaussians case. This takes the following form:

$$\mathcal{L} = \sum_{i=1}^N \ln \sum_{k=1}^K m_k \mathcal{N}(x_i | \mu_k, \sigma_k) \quad (14.14)$$

Differentiating Eq. (14.14) with respect to  $\mu_k$  gives

$$\begin{aligned} \frac{d\mathcal{L}}{d\mu_k} &= \sum_{i=1}^N \frac{m_k}{\sum_{j=1}^K m_j \mathcal{N}(x_i | \mu_j, \sigma_j)} \times \frac{d\mathcal{N}(x_i | \mu_k, \sigma_k)}{d\mu_k} \\ &= \sum_{i=1}^N \frac{m_k \mathcal{N}(x_i | \mu_k, \sigma_k)}{\sum_{j=1}^K m_j \mathcal{N}(x_i | \mu_j, \sigma_j)} \times \frac{(x_i - \mu_k)}{\sigma_k^2} \\ &= \sum_{i=1}^N \rho(z_{ik}) \times \frac{(x_i - \mu_k)}{\sigma_k^2} \end{aligned} \quad (14.15)$$

where we have identified the first factor under the summation as the responsibility  $\rho(z_{ik})$ , defined in Eq. (14.11). The condition for a maximum,  $d\mathcal{L}/d\mu_k = 0$ , occurs when

$$\mu_k = \frac{\sum_{i=1}^N \rho(z_{ik}) x_i}{\sum_{i=1}^N \rho(z_{ik})} \quad (14.16)$$

A similar calculation shows that  $d\mathcal{L}/d\sigma_k = 0$  when

$$\sigma_k^2 = \frac{\sum_{i=1}^N \rho(z_{ik}) (x_i - \mu_k)^2}{\sum_{i=1}^N \rho(z_{ik})} \quad (14.17)$$



However, a subtlety occurs when optimizing to determine the updated value of  $m_k$ . This arises because it is necessary to ensure that  $\sum_{k=1}^K m_k = 1$  (see Eq. (14.3)). We can achieve this methodically by using a Lagrange multiplier  $\lambda$ —in this case by maximizing  $\mathcal{L} + \lambda[(\sum_{k=1}^K m_k) - 1]$  rather than  $\mathcal{L}$  itself. Differentiating with respect to  $m_k$  and setting the result to zero, we find

$$\sum_{i=1}^N \frac{\mathcal{N}(x_i | \mu_k, \sigma_k)}{\sum_{j=1}^K m_j \mathcal{N}(x_i | \mu_j, \sigma_j)} + \lambda = 0 \quad (14.18)$$

To determine  $\lambda$ , if we multiply both sides of Eq. (14.18) by  $m_k$ , sum over  $k$ , and apply the constraint condition (Eq. (14.3)) we immediately obtain the result  $\lambda = \sum_{i=1}^N \frac{1}{m_k} - 1 = -N$ . Next, multiplying both sides by  $m_k$  and identifying the formula for the responsibility  $\rho(z_{ik})$ —as defined in Eq. (14.11)—we find

$$\sum_{i=1}^N \rho(z_{ik}) = -\lambda m_k = N m_k \quad (14.19)$$

$$\therefore m_k = \frac{1}{N} \sum_{i=1}^N \rho(z_{ik}) \quad (14.20)$$

(Notice that summing this result over  $k$  shows that  $\sum_{i=1}^N \sum_{k=1}^K \rho(z_{ik}) = N$ , which means that the responsibilities for the  $N$  data points necessarily sum to  $N$  and are shared one way or another between the  $K$  Gaussian distributions.)

The overall result of the maximum likelihood calculation is to give updated values of the Gaussian means and variances that are weighted by the responsibilities of the relevant data points, and to adjust the mixture coefficients to the average values, they need to have for fitting the data points.

Finally, note that the above treatment has been simplified by taking the 1-D form of the Gaussian. However, it is straightforward to generalize this to the  $n$ -dimensional case:

$$\mathcal{N}(\mathbf{x} | \boldsymbol{\mu}, \boldsymbol{\Sigma}) = \frac{1}{(2\pi)^{n/2} |\boldsymbol{\Sigma}|^{1/2}} \exp \left[ -\frac{1}{2} (\mathbf{x} - \boldsymbol{\mu})^T \boldsymbol{\Sigma}^{-1} (\mathbf{x} - \boldsymbol{\mu}) \right] \quad (14.21)$$

where  $\boldsymbol{\mu}$  and  $\boldsymbol{\Sigma}$  are, respectively, the mean and ( $n \times n$ ) covariance matrix of the distribution. As a result, the maximum likelihood solutions (obtained with only fairly minor changes to the proofs) become:

*E-step: Initial evaluation of the responsibilities*

$$\rho(z_{ik}) = \frac{m_k \mathcal{N}(\mathbf{x}_i | \boldsymbol{\mu}_k, \boldsymbol{\Sigma}_k)}{\sum_{j=1}^K m_j \mathcal{N}(\mathbf{x}_i | \boldsymbol{\mu}_j, \boldsymbol{\Sigma}_j)} \quad (14.22)$$

*M-step: update of the Gaussian parameters and mixture coefficients*

$$\begin{aligned} \boldsymbol{\mu}'_k &= \frac{\sum_{i=1}^N \rho(z_{ik}) \mathbf{x}_i}{\sum_{i=1}^N \rho(z_{ik})} \\ \boldsymbol{\Sigma}'_k &= \frac{\sum_{i=1}^N \rho(z_{ik}) (\mathbf{x}_i - \boldsymbol{\mu}_k) (\mathbf{x}_i - \boldsymbol{\mu}_k)^T}{\sum_{i=1}^N \rho(z_{ik})} \\ m'_k &= \frac{1}{N} \sum_{i=1}^N \rho(z_{ik}) \end{aligned} \tag{14.23}$$

where each prime indicates that the relevant parameter is being updated. (Note that the calculation of the  $\boldsymbol{\Sigma}_k$  update uses the *nonupdated*  $\boldsymbol{\mu}_k$ , as the  $\boldsymbol{\mu}_k$  and  $\boldsymbol{\Sigma}_k$  updates are presumed to occur simultaneously.)

There is one stage left in the complete EM algorithm, and that is the evaluation of the log likelihood, which is mainly needed to check for convergence:

$$\mathcal{L}' = \sum_{i=1}^N \ln \sum_{k=1}^K m'_k \mathcal{N}(\mathbf{x}_i | \boldsymbol{\mu}'_k, \boldsymbol{\Sigma}'_k) \tag{14.24}$$

The overall EM algorithm as applied for the generation of Gaussian mixture models may then be very simply summarized as in [Table 14.1](#). Note that although convergence can in principle be judged from the magnitude of the log likelihood, it is quite common to judge it from the *smallness* of the changes to it, i.e., whether  $\Delta \mathcal{L} = \mathcal{L}' - \mathcal{L}$  is smaller than a preset threshold. We shall say more about this later.

At this point, it is worth reiterating what has been achieved so far. Specifically, instead of optimizing the likelihood function by adjusting all parameters together, which would require a tedious search operation, we have managed to split the task into two—first optimizing the responsibilities on their own, and then updating the Gaussian parameters: Each of the latter processes can be achieved by following analytically defined procedures that are each much less complex than a general search. Admittedly, neither procedure moves directly toward the optimum solution and nor procedure is complete in itself, as the whole

**Table 14.1** Summary of the EM Algorithm

---

```

obtain initial approximation to the solution
do {
    apply M-step to estimate responsibilities
    apply E-step to update Gaussian parameters and mixture coefficients
} until log likelihood shows sufficient convergence
    
```

---

process has to be iterated until a satisfactory degree of convergence is achieved. An interesting analogy for the whole process is that of “tacking” in a yacht while sailing into the wind (though the analogy is imperfect as exactly the same process is carried out in the alternate direction when changing tack).

Another point that should be emphasized is that we have not yet proved that the log likelihood is bound to be improved by the EM algorithm. Although this does seem likely for the M-step, all we have actually shown is that  $\mathcal{L}$  moves toward a stationary value, though not necessarily a maximum. We next look at this and other problems by examining the EM algorithm more generally.

### 14.3 A MORE GENERAL VIEW OF THE EM ALGORITHM

*Much of the theory in this section—especially Eqs. (14.25)–(14.29) and (14.31)–(14.33)—can be by-passed on a first reading, though some attention should be paid to Fig. 14.2 which clarifies the overall process of the EM algorithm.*

To proceed with this, we move away from the Gaussian formulation and replace the Gaussian parameters  $\mu_k$  and  $\Sigma_k$  with a general set of parameters  $\theta$ . Thus, we replace  $\mathcal{N}(\mathbf{x}|\mu, \Sigma)$  by  $P(\mathbf{x}|z, \theta)$ , where  $z$  is a hidden variable representing a mixture or other coefficient. Generalizing further, we take  $\mathbf{z}$  to be a set of hidden variables, and obtain the log likelihood function:

$$\mathcal{L} = \ln p(\mathbf{x}|\theta) = \sum_z p(\mathbf{x}, \mathbf{z}|\theta) \quad (14.25)$$

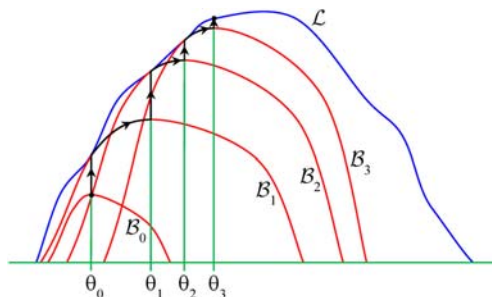


**FIGURE 14.2**

E and M steps in the EM algorithm.  $B_0$  is the initial lower bound on the likelihood function, and adjustment of the hidden ( $z$ ) parameters results in a vertical “E” step to meet the optimum log likelihood curve  $\mathcal{L}$  (marked blue). Thereafter, adjustment of the  $\theta$  parameters results in an “M” step along the red  $B_1$  curve until a local maximum is reached. Subsequent E and M steps (both indicated by black arrows) follow until the highest position on the  $\mathcal{L}$  curve is reached. For clarity, only the first few steps are shown.

The problem is how to maximize this function systematically and examine its optimality. To achieve this we make use of the Kullback–Leibler (KL) divergence function,  $\text{KL}(q||p)$ , which is a measure of the difference between two probability distributions (here  $q$  and  $p$ ) for which it is known that  $\text{KL}(q||p) \geq 0$ , equality only occurring only when  $q(\mathbf{z}) = p(\mathbf{z}|\mathbf{x}, \boldsymbol{\theta})$ . In fact, the formula for the KL divergence is

$$\text{KL}(q||p) = - \sum_{\mathbf{z}} q(\mathbf{z}) \ln \frac{p(\mathbf{z}|\mathbf{x}, \boldsymbol{\theta})}{q(\mathbf{z})} \quad (14.26)$$

To make use of this formula and its inequality, we need to make a clever choice of starting function—i.e., one that suitably matches the form of  $\mathcal{L}$ . Accordingly, we define

$$\mathcal{B}(q, \boldsymbol{\theta}) = \sum_{\mathbf{z}} q(\mathbf{z}) \ln \frac{p(\mathbf{x}, \mathbf{z}|\boldsymbol{\theta})}{q(\mathbf{z})} \quad (14.27)$$

Using the product rule, we find

$$\begin{aligned} \mathcal{B}(q, \boldsymbol{\theta}) &= \sum_{\mathbf{z}} q(\mathbf{z}) \ln \frac{p(\mathbf{z}|\mathbf{x}, \boldsymbol{\theta})p(\mathbf{x}|\boldsymbol{\theta})}{q(\mathbf{z})} \\ &= \sum_{\mathbf{z}} q(\mathbf{z}) \ln \frac{p(\mathbf{z}|\mathbf{x}, \boldsymbol{\theta})}{q(\mathbf{z})} + \sum_{\mathbf{z}} q(\mathbf{z}) \ln p(\mathbf{x}|\boldsymbol{\theta}) \end{aligned} \quad (14.28)$$

We now see why this choice of  $\mathcal{B}(q, \boldsymbol{\theta})$  was judicial—because, when added to the KL divergence, substantial cancellation occurs and we obtain

$$\begin{aligned} \mathcal{B}(q, \boldsymbol{\theta}) + \text{KL}(q||p) &= \sum_{\mathbf{z}} q(\mathbf{z}) \ln p(\mathbf{x}|\boldsymbol{\theta}) \\ &= \ln p(\mathbf{x}|\boldsymbol{\theta}) \end{aligned} \quad (14.29)$$

The last line follows because  $\sum_{\mathbf{z}} q(\mathbf{z}) = 1$ , leaving just the log likelihood,  $\mathcal{L}$ .

Applying the KL divergence inequality,  $\text{KL}(q||p) \geq 0$ , we finally obtain the important result:

$$\mathcal{B} \leq \mathcal{L} \quad (14.30)$$

which means that  $\mathcal{L}(\mathbf{x}|\boldsymbol{\theta})$  is an upper bound on  $\mathcal{B}(q, \boldsymbol{\theta})$ . In addition, the fact that equality can be achieved when  $q(\mathbf{z}) = p(\mathbf{z}|\mathbf{x}, \boldsymbol{\theta})$  means that  $\mathcal{B}$  has a maximum value equal to  $\mathcal{L}$ , which can be located by adjusting  $\mathbf{z}$ . In general, there will be a single maximum value, so any variation of  $\boldsymbol{\theta}$  for fixed  $\mathbf{z}$  around the optimum will pull the  $\mathcal{B}$  curve away from the  $\mathcal{L}$  curve: this shows that the two curves touch at the optimal value of  $\mathbf{z}$  (Fig. 14.2). It also implies that keeping  $\mathbf{z}$  fixed, adjustment of  $\boldsymbol{\theta}$  will lead to an even higher maximum of  $\mathcal{L}$ . Note that the fact that the  $\mathcal{B}$  curve pulls away from the  $\mathcal{L}$  curve during the M-step (when  $\boldsymbol{\theta}$  is being adjusted), so that the KL divergence is no longer zero, does not prevent even higher values of  $\mathcal{L}$  from being attained during the M-step. In fact, each step of the EM

algorithm can only increase the value of  $\mathcal{L}$ , or at worst leave it unchanged (in the case where the maximum has already been reached).

Unfortunately, there are circumstances when an optimum cannot be reached in this way: indeed, everything depends on the reliability of the KL divergence formula. Interestingly, the latter is derived by application of Jensen's inequality to convex or concave functions. A convex function is one such as  $y = x^2$  for which points on any chord lie above the function. For such a case, Jensen's inequality is

$$\int F(x)p(x)dx \geq F\left[\int xp(x)\right]dx \quad (14.31)$$

Applying this formula to the KL divergence gives

$$\text{KL}(q||p) = -\int q(x)\ln\frac{p(x)}{q(x)}dx \geq -\ln\left[\int\frac{p(x)}{q(x)}q(x)dx\right] \quad (14.32)$$

(Note that log is a concave function, so the inequality should in principle be reversed. However, the minus signs in Eq. (14.32) take care of that problem.)

After canceling  $q(x)$  and normalizing  $p(x)$  to unity we obtain the desired inequality:

$$\text{KL}(q||p) \geq 0 \quad (14.33)$$

(Be warned that this relation is not symmetrical between  $q$  and  $p$ .)

We can now see that one major reason why the EM algorithm might not find the maximum arises when  $\mathcal{L}$  is not convex, which clearly means that EM may get stuck at a local maximum. Hence it is usual to initialize the EM algorithm with a variety of starting positions and states. In any case, many types of problem require a number of solutions, each corresponding to a local maximum. Therefore, to ensure getting all the relevant solutions, at least the same number of starting locations need to be employed. In fact, it is often necessary to use more starting points than should be necessary; furthermore, to be sure of finding all the solutions, there is a need (1) to randomize the starting locations, (2) to present them in random order, and (3) to repeat the process several times. Finally, it will be necessary to *identify* all the solutions: even if all solutions have been found, their identities will be unknown. In particular, if  $\kappa$  solutions are found, there could be  $\sim \kappa!$  possible assignments for them. (In an ideal case, e.g., for a model employing  $K$  Gaussians, there would be exactly  $K!$  identity assignments.) This matters particularly in time-varying situations where the ordering of the solutions will change as time goes on, so ongoing tests will be needed to match the identities of the various solutions: In surveillance applications, for example, this will make it difficult to track objects between frames without estimating and matching velocities of travel.

Finally, the  $K$ -means algorithm is often used to initialize the EM algorithm. This is because  $K$ -means is significantly less computation-intensive than EM. On the other hand, this does not help with the problem of determining the optimum value of  $K$  for either method. In both cases, trial and error are necessary, though more advanced methods such as variational mixture modeling and relevance vector machine EM (Vetrov et al., 2010) can be used to solve the problem systematically.

## 14.4 SOME PRACTICAL EXAMPLES

We will now demonstrate the use of the EM algorithm in some practical cases. First, we take a 2-D distribution of points arising from three Gaussians. In the instance taken, the Gaussians have respective mean positions  $(1, 1.5)$ ,  $(2, 5)$ ,  $(-2, 5)$  and covariance matrices:

$$\begin{bmatrix} 2 & 0 \\ 0 & 0.4 \end{bmatrix}, \begin{bmatrix} 0.5 & 0 \\ 0 & 1.5 \end{bmatrix}, \begin{bmatrix} 1 & -0.5 \\ -0.5 & 1 \end{bmatrix}.$$

As can be seen in Fig. 14.3A, the 200 points randomly extracted from each of these Gaussians overlap in nontrivial ways, thereby providing a reasonably complex task for the EM algorithm. (Systematic means for extracting sample points from pre-specified distributions are described in Appendix D.) Fig. 14.3B–F shows the performance over 25 iterations, at which stage the successive changes in the log likelihood have fallen below a suitable threshold of  $\Delta\mathcal{L} = 0.01$ . Fig. 14.4 shows the convergence of  $\mathcal{L}$ : note that  $\mathcal{L}$  is always negative, because it is the logarithm of a probability necessarily lying in the range 0–1.

Another test was carried out using the same starting data, but with the six sets of data points tackled in different random orders (Fig. 14.5). In each case (A–F), the results after 10 iterations were quite dissimilar, but after 25 iterations the results were essentially identical to those in Fig. 14.3F.

We now move on to a more immediately useful situation, as indicated in Fig. 14.6A. Here the task is to segment the image into a number of subareas, exactly as for the multilevel thresholding algorithm of Section 4.7. In this case, the EM algorithm is used to directly model the intensity histogram of Fig. 14.6C (green trace) using a series of Gaussians (red traces). Looking at the data it is clear that six Gaussians will be optimal, and indeed the blue summation trace is very close to the unprocessed green data. The optimum fit is obtained after 10–20 iterations, depending on the initialization—a typical case being shown in Fig. 14.6D. The final segmentation is shown in Fig. 14.6B, and—except in the cloud region—is very similar to that in Fig. 4.7. In this case, pixels between adjacent Gaussian crossings have been assigned the mean intensity of the intervening Gaussian and reinserted into the image. This is optimal because equal a posteriori probabilities necessarily indicate decision boundaries leading to minimum overall error.

In this example, some care was taken to analyze exactly when iteration should be terminated. It turned out *not* to be ideal to take a preset value of  $\Delta\mathcal{L}$  to achieve this. However, careful thought shows that  $\mathcal{L}$  is a maximum when  $\Delta\mathcal{L} = 0$ —and the graph in Fig. 14.6D makes it very clear when this happens. On the other hand, why should  $\mathcal{L}$  go through a maximum and start decreasing? The only reasonable explanation is that overtraining is occurring, in the sense that the model is becoming over-adapted to the data. In an ideal case with ideal data (as is perhaps the case for Fig. 14.3), this might not happen. But in a case like this where there is considerable

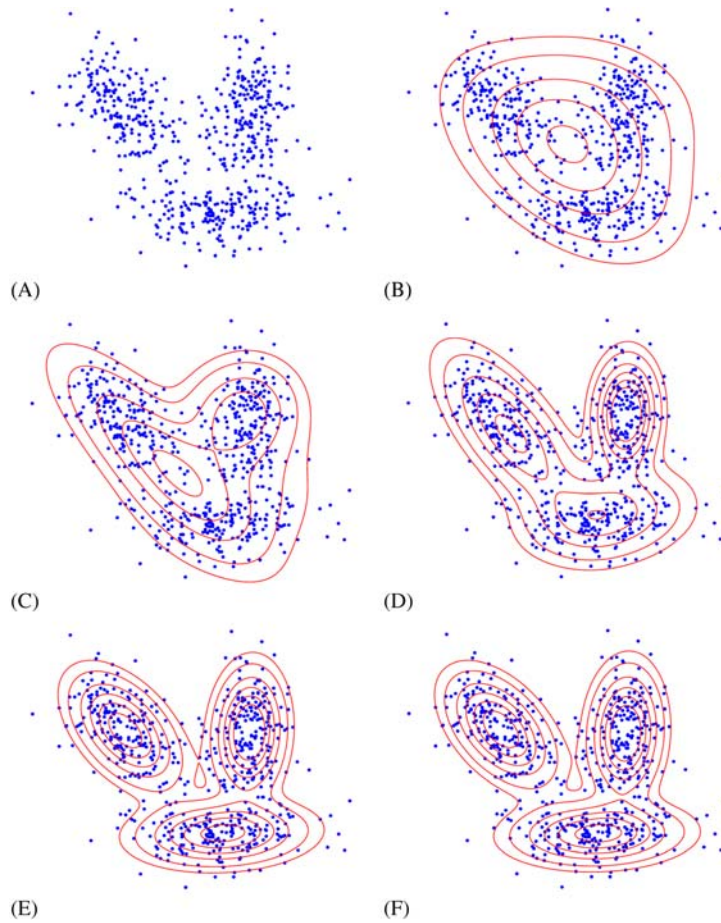


**FIGURE 14.3**

Three Gaussian mixture distributions being fitted by the EM algorithm. (A)–(F) show, respectively, the raw data and the results of 5, 10, 15, 20, and 25 iterations: the algorithm needed exactly 25 iterations to reduce the changes in log likelihood to less than 0.01. Apart from lowest contour, those shown are equally spaced, with heights 0.005, 0.01, 0.02, 0.03, 0.04, and 0.05. Exactly the same data points were used in all cases (see text for details). Similarly, the algorithm was initialized identically in all five cases.

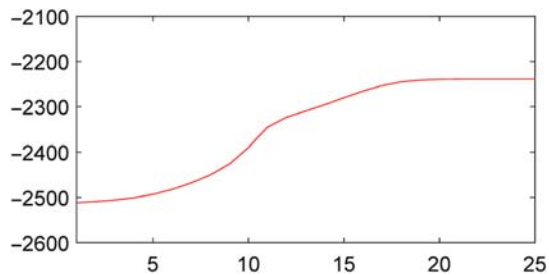


**FIGURE 14.4**

Convergence plot of  $\mathcal{L}$  over 25 iterations of the EM algorithm for the data shown in Fig. 14.3A.

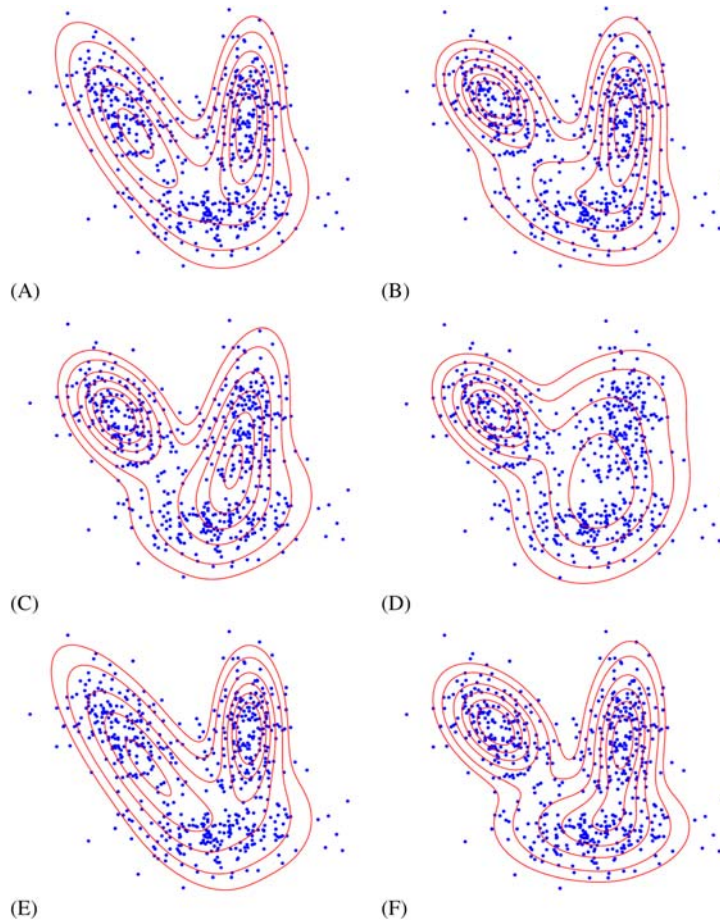


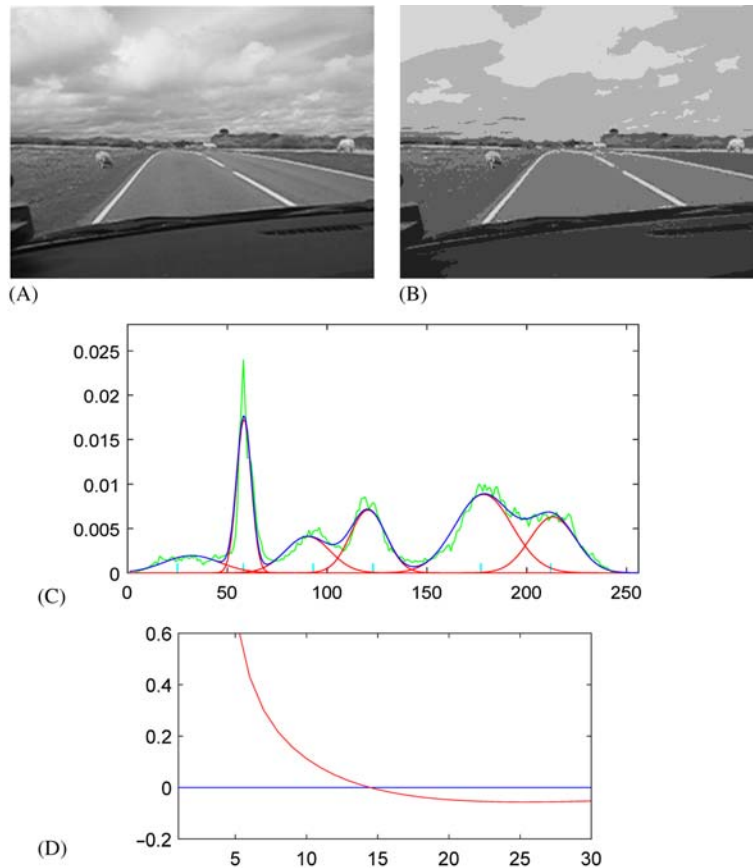
**FIGURE 14.5**

Effect of different data orderings on the progress of the EM algorithm. These results arise from exactly the same data points as for Fig. 14.3. However, the data were shuffled differently in each of the six cases. All the cases show the progress after 10 iterations, as in Fig. 14.3C. Nevertheless, after 25 iterations, the results were essentially identical to those in Fig. 14.3F.

noise and clutter on the intensity histogram, it is all too easy for the algorithm to fall into a niche which is locally optimal but which is certainly not a global maximum. Hence it seems far better to terminate the algorithm when  $\Delta\mathcal{L} = 0$ .

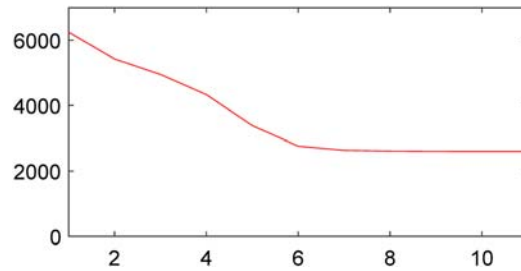
Returning to the problem of initialization, it is often said that the *K*-means algorithm provides a useful way to obtain a starting approximation. In the case of Fig. 14.6A, tests showed *K*-means to be far more robust than EM, having a



**FIGURE 14.6**

Application of the EM algorithm to multilevel thresholding. The intensity histogram of the image (A) is shown as a green trace in (C). The EM algorithm is used to obtain a GMM as shown in red by the six Gaussians in (C). The blue summation trace in (C) shows an excellent fit to the green trace, with no systematic variations—indicating that in this case a six-Gaussian fit is optimal. All pixels contributing to the green trace between adjacent Gaussian crossings are assigned the mean intensity of the intervening Gaussian and reinserted into the image, as in (B). The fit to the cloud intensities is naturally relatively poor, but the other intensities are reasonably matched. (D) Shows the changes in  $\Delta\mathcal{L}$  over 30 iterations of the algorithm. In (C), the six cyan markers just above the horizontal axis indicate the means located by the *K*-means algorithm.

significantly wider capture region together with faster convergence. The latter is indicated by the graph of Fig. 14.7, which gives the sum of squares of the closest distances to the final mean values taken over all the data points. The result of preliminary (and highly consistent) *K*-means analysis is shown by the six cyan

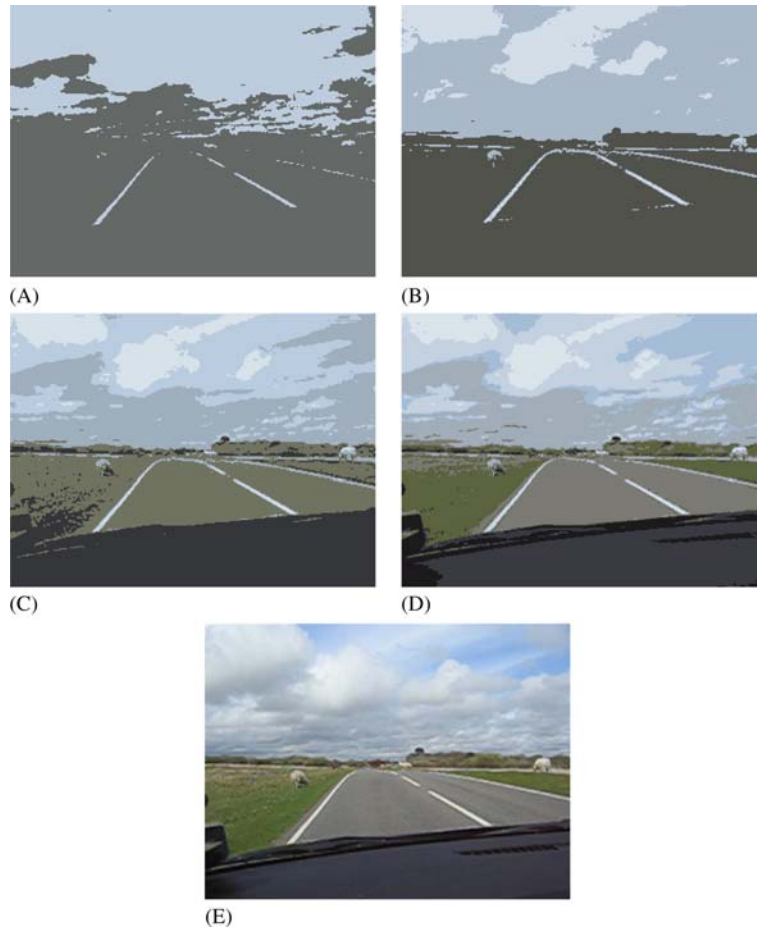
**FIGURE 14.7**

Convergence plot of  $\mathcal{D}$  over 11 iterations of the  $K$ -means algorithm for the grayscale image in Fig. 14.6A.  $\mathcal{D}$  is the sum of the squares of the closest distances to the final mean values taken over all the data points.

markers just above the horizontal axis of the graph in Fig. 14.6C. Notice that these are very close to the final EM Gaussian peak locations, and thus they provide good initialization for the EM algorithm, as was confirmed by a series of tests. However, the differences between the  $K$ -means estimates and those of the EM algorithm are very real. This is because the two methods measure different things. In the histogram example,  $K$ -means finds mean values for its particular domains, whereas EM computes properly modeled peak values. Furthermore, through its hidden parameters, EM rigorously estimates what happens in the cross-over regions of its Gaussians. Finally, EM is firmly based on rigorous probabilistic optimization rather than on simple ad-hoc rules. What is surprising is how well  $K$ -means performs when compared with the EM paradigm. Yet in addition, we must not overlook the fact that this version of the EM algorithm is targeted at situations where Gaussians are well suited to building the models—which certainly seems to be the case for the histogram example presented here.

With these factors in mind, it is pertinent to inquire further about the value of the  $K$ -means algorithm. In particular, it will be useful to see how well it copes with color images. Interestingly, it is close to trivial to arrange this. Fig. 14.8 shows the result of such a test, for a small range of values of  $K$ . In this case, eight colors were needed to segment the image to reasonable accuracy and identify the grass, road, two portions of the car, blue sky and clouds. The reason why  $K$  needs to be greater than six (the value in the grayscale case) is that more information is required for segmentation into color regions, i.e., more complex data requires more parameters to describe it. A similar finding occurred for the images shown in Fig. 14.9: In this case, the greenish patches on the face show that  $K = 8$  is still not sufficient to be sure of providing an accurate description of important regions of the image.

But how can it be “close to trivial” to use  $K$ -means for segmenting color images? The reason lies in the method that  $K$ -means uses to perform its basic function, viz.,

**FIGURE 14.8**

Segmentation using  $K$ -means. Use of the  $K$ -means algorithm to segment an original image (E) into  $K$  regions of uniform color. The values of  $K$  are, respectively, 2, 3, 5, and 8 in images (A)–(D). Apart from the clouds, the image in (D) is a reasonable rendition of image (E).

assigning data points to the closest cluster center (Table 13.2). This simply requires that, for each pixel, we minimize  $(I - \mu_k)^2$  over all  $k$  color channels and make the result average into the new values of  $\mu_k$ . All we need to do to make a generalization to color is to minimize  $(I_{\text{red}} - \mu_{\text{red},k})^2 + (I_{\text{green}} - \mu_{\text{green},k})^2 + (I_{\text{blue}} - \mu_{\text{blue},k})^2$  over all  $k$ . (In fact, this is somewhat simplistic as it weights all color components equally: we return to this point below.) However, matters are not quite so simple in practice. Note that in the grayscale case, most of the work is done on the intensity histogram,

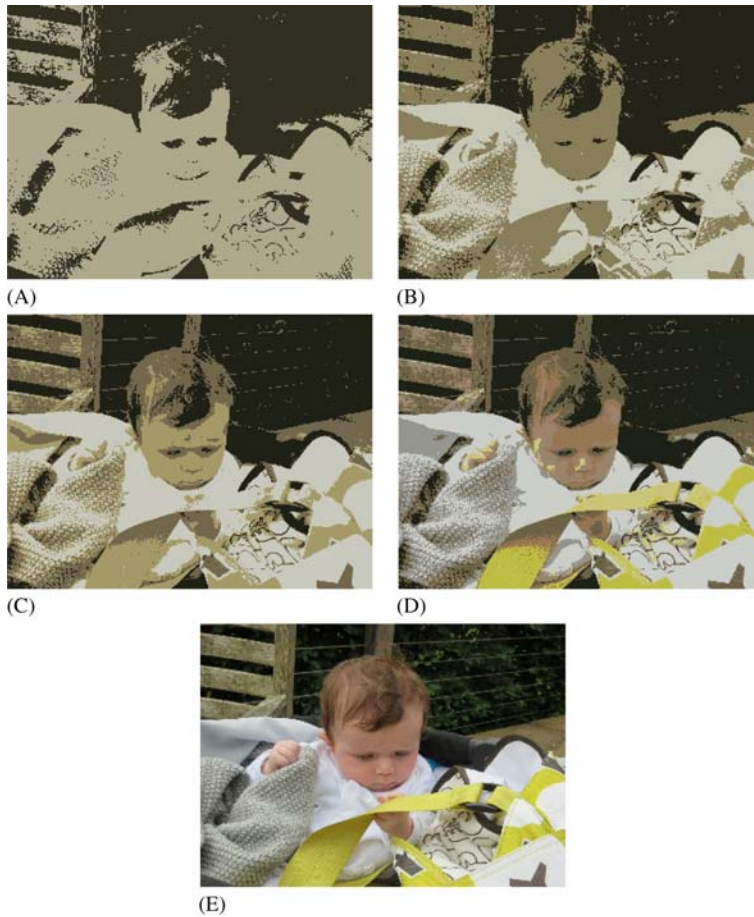


**FIGURE 14.9**

Segmentation using  $K$ -means. Use of the  $K$ -means algorithm to segment an original image (E) into  $K$  regions of uniform color. The values of  $K$  are, respectively, 2, 3, 4, and 8 in images (A)–(D). Apart from some details in the face, the image in (D) is a reasonable rendition of image (E).

whose index typically ranges from 0 to 255. In the color domain, the 3-D histogram space would have  $256^3$  cells. This means that working with the full color domain would be a computational nightmare. The normal way around this problem is to reduce the size of the space by a large factor by quantizing into larger buckets (e.g.,  $8^3$  cells per bucket), resulting in a color space of size  $32^3$  ( $\approx 32K$ ), which is practical. However, in the case we have been considering, it is better to scan over

the image space ( $\approx 64\text{K}$  pixels) than over the color space, as that will not lead to any loss of resolution.

Looking at the problem in another way, there are two possible representations that can be used: one is (generalized) histogram space and the other is image space. For grayscale images, it pays to use the former, whereas for color images, it pays to use the latter. One other possibility remains and that is when the color space is sparsely populated—in which case a list of active elements could be used. Ignoring this arguably rare possibility, applying  $K$ -means to color images is bound to lead to relatively high computation, as all the  $K$  values have to be compared for all pixels at every iteration. Nevertheless,  $K$ -means can win out as it tends to converge quite rapidly and, in addition, has no complex functions such as Gaussians to compute.

Finally, it will be far less trivial applying the EM algorithm to color images, as the computational load will tend to be excessive, especially if we are to preserve the full probabilistic formalism of this type of algorithm. In addition, color tends to be a more complex entity to handle, not least because hue, saturation, intensity (HSI) and similar representations are often used, and hue is problematic as it has cyclic boundary conditions; ultimately, the problem of color constancy (the need for invariance to varying illumination) also has to be dealt with, and this further complicates the situation (see [Appendix C](#) for elaboration of these points).

Rather than dwell on such complexities, it is important to draw attention to perhaps the most crucial problem for EM—that of the number of parameters that have to be fitted. This is important because it increases in the number of parameters impact on the speed and reliability of convergence. For each 1-D Gaussian that has to be fitted, there will be one mixture parameter plus one mean parameter and one variance parameter. However, for  $n$ -D multivariate Gaussians, there will be one mixture parameter plus  $n$  mean parameters (i.e., one per dimension) and an  $n \times n$  covariance matrix. In fact, the situation is slightly simplified because covariance matrices have to be symmetric. This means that a single  $n$ -D Gaussian will have one mixture parameter,  $n$  mean parameters and  $\frac{1}{2}(n^2 + n)$  covariance parameters. Further simplifications can sometimes be made by taking the covariance matrix to be diagonal (with a total of  $n$  parameters) or even isotropic (with just one independent parameter), as in the following respective cases:

$$\begin{bmatrix} a & f & e \\ f & b & d \\ e & d & c \end{bmatrix}, \begin{bmatrix} a & 0 & 0 \\ 0 & b & 0 \\ 0 & 0 & c \end{bmatrix}, \begin{bmatrix} a & 0 & 0 \\ 0 & a & 0 \\ 0 & 0 & a \end{bmatrix}.$$

[Table 14.2](#) summarizes the numbers of parameters for cases that are relevant to the previous discussion. Interestingly, the problems of [Figs. 14.3 and 14.6](#) have identical numbers of adjustable parameters (both are 18) and converge reliably, whereas the color segmentation problem (80 adjustable parameters) is bound to be far more computation intensive and could be subject to convergence problems. Clearly, it is a matter of test and experiment whether the covariance matrices obtained using real data can be approximated as either diagonal or isotropic

**Table 14.2** Numbers of Gaussian Parameters for Cases Discussed in the Text

Configuration of Gaussians	Number of Parameters				Relevance to Figures
	Mixture	Mean	Covariance	Total	
3: general 2-D	3	$3 \times 2$	$3 \times 3$	18	<a href="#">Fig. 14.3</a>
6: 1-D (grayscale)	6	$6 \times 1$	$6 \times 1$	18	<a href="#">Fig. 14.6</a>
8: 3-D (color)	8	$8 \times 3$	$8 \times 6$	80	<a href="#">Fig. 14.8: ideal</a>
8: 3-D (color)	8	$8 \times 3$	$8 \times 1$	40	<a href="#">Fig. 14.8: K-means</a>

*In the last row, the reference to K-means is only an indicator of the number of effective parameters, as Gaussians are not employed explicitly in the algorithm, though an equivalent complexity does apply to the task itself.*

matrices. However, the EM algorithm is more sophisticated and far more likely to benefit from use of a general covariance matrix, whereas the *K*-means algorithm is probably most appropriately served by an isotropic matrix—as used to generate the images in [Figs. 14.8 and 14.9](#). Interestingly, it is common practice to provide the EM algorithm with a first approximation that is either diagonal or isotropic: in the case of [Fig. 14.3](#), the latter was employed.

## 14.5 PRINCIPAL COMPONENTS ANALYSIS

Closely related to cluster analysis is the concept of data representation. One powerful way of approaching this task is that of PCA. This involves finding the mean of a cluster of points in feature space, and then finding the principal axes of the cluster in the following way. First, an axis is found which passes through the mean position and which gives the maximum variance when the data are projected onto it. Then, a second such axis is found which maximizes variance in a direction normal to the first. This process is carried out until a total of  $N$  principal axes have been found for an  $N$ -dimensional feature space. The process is illustrated in [Fig. 14.10](#). In fact, the process is entirely mathematical and need not be undertaken in the strict sequence indicated above: it merely involves finding a set of orthogonal axes which diagonalizes the covariance matrix.

The covariance matrix for the input population is defined as

$$\Sigma = \mathbb{E}((\mathbf{x}_{(p)} - \boldsymbol{\mu})(\mathbf{x}_{(p)} - \boldsymbol{\mu})^T) \quad (14.34)$$

where  $\mathbf{x}_{(p)}$  is the location of the  $p$ th data point and  $\boldsymbol{\mu}$  is the mean of the  $P$  data points;  $\mathbb{E}(\cdot)$  indicates expectation value for the underlying population. We can estimate  $\Sigma$  from the equations

$$\Sigma = \frac{1}{P} \sum_{p=1}^P \mathbf{x}_{(p)} \mathbf{x}_{(p)}^T - \boldsymbol{\mu} \boldsymbol{\mu}^T \quad (14.35)$$

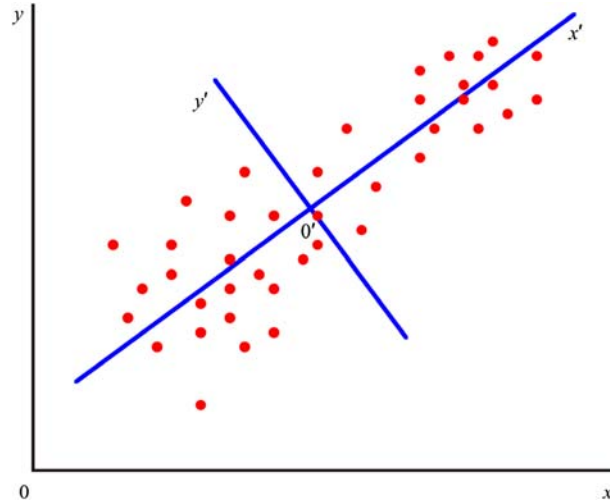
**FIGURE 14.10**

Illustration of principal components analysis. Here, the dots represent patterns in feature space and are initially measured relative to the  $x$ - and  $y$ -axes. Then the sample mean is located at  $O'$ , and the direction  $O'x'$  of the first principal component is found as the direction along which the variance is maximized. The direction  $O'y'$  of the second principal component is normal to  $O'x'$ ; in a higher dimensional space, it would be found as the direction normal to  $O'x'$  along which the variance is maximized.

$$\boldsymbol{\mu} = \frac{1}{P} \sum_{p=1}^P \mathbf{x}_{(p)} \quad (14.36)$$

As  $\boldsymbol{\Sigma}$  is real and symmetric, it is possible to diagonalize it using a suitable orthogonal transformation matrix  $\mathbf{A}$ , obtaining a set of  $N$  orthonormal eigenvectors  $\mathbf{u}_i$  with eigenvalues  $\lambda_i$  given by

$$\boldsymbol{\Sigma} \mathbf{u}_i = \lambda_i \mathbf{u}_i \quad (i = 1, 2, \dots, N) \quad (14.37)$$

The vectors  $\mathbf{u}_i$  are derived from the original vectors  $\mathbf{x}_i$  by

$$\mathbf{u}_i = \mathbf{A}(\mathbf{x}_i - \boldsymbol{\mu}) \quad (14.38)$$

and the inverse transformation needed to recover the original data vectors is

$$\mathbf{x}_i = \boldsymbol{\mu} + \mathbf{A}^T \mathbf{u}_i \quad (14.39)$$

Here, we have recalled that for an orthogonal matrix

$$\mathbf{A}^{-1} = \mathbf{A}^T \quad (14.40)$$

In fact, it may be shown that  $\mathbf{A}$  is the matrix whose rows are formed from the eigenvectors of  $\boldsymbol{\Sigma}$ , and that the diagonalized covariance matrix  $\boldsymbol{\Sigma}'$  is given by

$$\boldsymbol{\Sigma}' = \mathbf{A} \boldsymbol{\Sigma} \mathbf{A}^T \quad (14.41)$$

so that

$$\Sigma' = \begin{bmatrix} \lambda_1 & 0 & \cdots & 0 \\ 0 & \lambda_2 & & 0 \\ \vdots & & \ddots & \vdots \\ 0 & 0 & \cdots & \lambda_N \end{bmatrix} \quad (14.42)$$

Note that in an orthogonal transformation, the trace of a matrix remains unchanged. Thus, the trace of the input data is given by

$$\text{trace } \Sigma = \text{trace } \Sigma' = \sum_{i=1}^N \lambda_i = \sum_{i=1}^N s_i^2 \quad (14.43)$$

where we have interpreted the  $\lambda_i$  as the variances of the data in the directions of the principal component axes (note that for a real symmetric matrix, the eigenvalues are all real and positive).

In what follows, we shall assume that the eigenvalues have been placed in an ordered sequence, starting with the largest. In that case,  $\lambda_1$  represents the most significant characteristic of the set of data points, with the later eigenvalues representing successively less significant characteristics. We could even go so far as to say that, in some sense,  $\lambda_1$  represents the most interesting characteristic of the data, whereas  $\lambda_N$  would be largely devoid of “interest.” More practically, if we ignored  $\lambda_N$ , we might not lose much useful information, and indeed the last few eigenvalues would frequently represent characteristics which are not statistically significant and are essentially noise. For these reasons, PCA is commonly used for reduction in the dimensionality of the feature space from  $N$  to some lower value  $N'$ . In some applications, this would be taken as leading to a useful amount of data compression. In other applications, it would be taken as providing a reduction in the enormous redundancy present in the input data.

We can quantify these results by writing the variance of the data in the reduced dimensionality space as

$$\text{trace } (\Sigma')_{\text{reduced}} = \sum_{i=1}^{N'} \lambda_i = \sum_{i=1}^{N'} s_i^2 \quad (14.44)$$

Not only is it now clear why this leads to reduced variance in the data, but also we can see that the mean square error obtained by making the inverse transformation (Eq. (14.39)) will be

$$\bar{\epsilon}^2 = \sum_{i=1}^N s_i^2 - \sum_{i=1}^{N'} s_i^2 = \sum_{i=N'+1}^N s_i^2 \quad (14.45)$$

One application in which PCA has become especially important is the analysis of multispectral images, e.g., from earth-orbiting satellites. Typically, there will be six separate input channels (e.g., three colors and three infra-red), each providing an image of the same ground region. If these images are  $512 \times 512$  pixels in size, there will be about a quarter of a million data points and these will have to



be inserted into a six-dimensional feature space. After finding the mean and covariance matrix for these data points, the latter is diagonalized and a total of six principal component images can be formed. Commonly, only two or three of these will contain immediately useful information, and the rest can be ignored. (For example, the first three of the six principal component images may well possess 95% of the variance of the input images.) Ideally, the first few principal component images in such a case will highlight such areas as fields, roads, and rivers, and this will be precisely the data that are required for mapmaking or other purposes. In general, the vital pattern recognition tasks can be aided *and* considerable savings in storage can be achieved on the incoming image data by attending to just the first few principal components.

Finally, it is as well to note that PCA really provides a particular form of data representation. In itself, it does not deal with pattern classification, and methods which are required to be useful for the latter type of task must possess useful discrimination. Thus, selection of features simply because they possess the highest variability does not mean that they will necessarily perform well in pattern classifiers. Another important factor which is relevant to the whole study of data analysis in feature space is the scales of the various features. Often, these will be an extremely variegated set, including length, weight, color, numbers of holes, and so on. Clearly, such a set of features will have no special comparability and are unlikely even to be measurable in the same units. This means that placing them in the same feature space and assuming that the scales on the various axes should have the same weighting factors must be invalid. One way of tackling this problem is to normalize the individual features to some standard scale given by measuring their variances. Such a procedure will naturally radically change the results of principal components calculations and further mitigates against principal components methodology being used thoughtlessly. On the other hand, there are some occasions on which different features can be compatible, and where PCA can be performed without such worries: One such situation is where all the features are pixel intensities in the same window (this case is discussed in [Section 7.5](#)).

---

## 14.6 MULTIPLE CLASSIFIERS

In recent years, there have been moves to make the classification process more reliable by application of multiple classifiers working in cooperation. The basic concept is much like that of three magistrates coming together to make a more reliable judgment than any one can make alone. Each is expert in a variety of things, but not in everything, so putting their knowledge together in an appropriate way should permit more reliable judgments to be made. A similar concept applies to expert AI systems: Multiple expert systems should be able to make up for each other's shortcomings. In all these cases, some way should exist for getting the most out of the individual classifiers without confusion reigning.

Note that the idea is not just to take all the feature detectors that the classifiers use and to replace their output decision-making devices with a single more complex decision-making unit. Indeed, such a strategy could well run into the problem discussed in [Section 14.5](#)—of exceeding the optimum number of features: at best, only a minor improvement would result from such a strategy, and at worst, the system would be grossly failure prone. On the contrary, the idea is to take the final classification of a number of complete but totally separate classifiers and to combine their outputs to obtain a substantially improved output. Furthermore, it could happen that the separate classifiers use totally different strategies to arrive at their decisions: one may be a nearest neighbor classifier, another may be a Bayes' classifier, and another may be a neural network classifier (see [Sections 13.10–13.13](#)). Likewise, one may employ structural pattern recognition, one might use statistical pattern recognition, and another might use syntactic pattern recognition. Each will be respectable in its own right and each will have its own strengths and weaknesses. Part of the idea is one of convenience: to make use of any soundly based classifier that is available, and to boost its effectiveness by using it in conjunction with other soundly based classifiers.

The next task is to see how to achieve this in practice. Perhaps, the most obvious way forward is to get the individual classifiers to vote for the class of each input pattern. Although this is a nice idea, it will often fail because the weaknesses of the individual classifiers may be worse than their strengths. Thus, the concept must be made more sophisticated.

Another strategy is again to allow the individual classifiers to vote, but this time to make them do so in an exclusive manner, so that as many classes as possible are eliminated for each input pattern. This is achievable with a simple intersection rule: A class is accepted as a possibility only if *all* the classifiers indicate that it is a possibility. The strategy is implemented by applying a threshold to each classifier in a special way, which will now be described.

A prerequisite for this strategy to work is that each classifier must not only give a class decision for each input pattern, it must also give the ranks of all possible classes for each pattern. In other words, it must give its first choice of class for any pattern, its second choice for that pattern, and so on. Then the classifier is labeled with the rank it assigned to the true class of that pattern. In fact, we apply each classifier to the whole training set and get a table of ranks ([Table 14.3](#)). Finally, we find the worst case (largest rank) for each classifier and take that as a threshold value which will be used in the final multiple classifiers. (In everyday parlance, the worst case corresponds to the lowest rank, which is here the largest numerical rank; similarly, the highest rank is the smallest numerical rank. It is obviously necessary to be totally unambiguous about this nomenclature.) When using this method for testing input patterns, only those classifiers that are not excluded by the threshold have their outputs intersected to give the final list of classes for the input pattern.

The above “intersection strategy” focuses on the worst-case behavior of the individual classifiers, and the result could be that a number of classifiers will

**Table 14.3** Determining a Set of Classifiers for the Intersection Strategy

	Classifier Ranks				
	C <sub>1</sub>	C <sub>2</sub>	C <sub>3</sub>	C <sub>4</sub>	C <sub>5</sub>
D <sub>1</sub>	5	3	7	1	8
D <sub>2</sub>	4	9	6	4	2
D <sub>3</sub>	5	6	7	1	4
D <sub>4</sub>	4	7	5	3	5
D <sub>5</sub>	3	5	6	5	4
D <sub>6</sub>	6	5	4	3	2
D <sub>7</sub>	2	6	1	3	8
thr	6	9	7	5	8

*In the upper section of this table, the original classifier ranks are shown for each input pattern; in the bottom line of the table, only the worst case rank is retained. When later applying test patterns, this can be used as the threshold (marked “thr”) to determine which classifiers should be employed.*

**Table 14.4** Determining a Set of Classifiers for the Union Strategy

	Classifier Ranks					Best Classifiers				
	C <sub>1</sub>	C <sub>2</sub>	C <sub>3</sub>	C <sub>4</sub>	C <sub>5</sub>	C <sub>1</sub>	C <sub>2</sub>	C <sub>3</sub>	C <sub>4</sub>	C <sub>5</sub>
D <sub>1</sub>	5	3	7	1	8	0	0	0	1	0
D <sub>2</sub>	4	9	6	4	2	0	0	0	0	2
D <sub>3</sub>	5	6	7	1	4	0	0	0	1	0
D <sub>4</sub>	4	7	5	3	5	0	0	0	3	0
D <sub>5</sub>	3	5	6	5	4	3	0	0	0	0
D <sub>6</sub>	6	5	4	3	2	0	0	0	0	2
D <sub>7</sub>	2	6	1	3	8	0	0	1	0	0
Min–max threshold						3	0	1	3	2

*In the left-hand section of this table, the original classifier ranks are shown for each input pattern; in the right-hand section of the table, only one rank is retained; namely, that obtaining for the classifier that is best able to recognize that pattern. Note that to facilitate the next piece of analysis—finding the thresholds on the classifier ranks—all remaining places in the table are packed with zeros. A zero final threshold then indicates a classifier that is of no help in analyzing the input data.*

hardly reduce the list of possible classes for the input patterns. This tendency can be tackled by an alternative “union strategy” which focuses on the specialisms of the individual classifiers: The aim is then to find a classifier that recognizes each particular pattern well. To achieve this, we look for the classifier with the smallest rank (classifier rank being defined exactly as already defined above for the intersection strategy) for each individual pattern (Table 14.4). Having found the smallest rank for the individual input patterns, we determine the largest of these ranks that arises for each classifier as we go through all the input patterns.

Applying this value as a threshold now determines whether the output of the classifier should be used to help determine the class of a pattern. Note that the threshold is determined in this way using the training set and is later used to decide which classifiers to apply to individual test patterns. Thus for any pattern, a restricted set of classifiers is identified that can best judge its class.

To clarify the operation of the union strategy, let us examine how well it will work on the training set. In fact, it is guaranteed to retain enough classifiers to ensure that the true class of any pattern is not excluded (though naturally, this is not guaranteed for any member of the test set). Hence, the aim of employing a classifier that recognizes each particular pattern well is definitely achieved.

Unfortunately, this guarantee is not obtained without cost. Specifically, if a member of the training set is actually an outlier, the guarantee will still apply, and the overall performance may be compromised. This problem can be tackled in many ways, but a simple possibility is to eliminate excessively bad exemplars from the training set. Another way is to abandon the union strategy altogether and go for a more sophisticated voting strategy. Other approaches involve reordering the data to improve the rank of the correct class (Ho et al., 1994).

---

## 14.7 THE BOOSTING APPROACH

The concept of boosting originated in the late 1980s. It was based on the idea that it should be possible to improve the performance of a weak learner—one that performs slightly better than chance—by combining it with other weak learners. Indeed, Schapire (1990) showed that a set of three weak learners  $C_1$ – $C_3$  would be guaranteed to have improved performance if they were trained in a rigorously defined way:  $C_1$  would first be trained on  $N$  points; then,  $C_2$  would be trained on a different set of  $N$  points, half of which were misclassified by  $C_1$ ; then,  $C_3$  would be trained on a further set of  $N$  points for all of which  $C_1$  and  $C_2$  disagreed. Finally, the improved (“boosted”) classifier would be obtained by taking the majority vote of  $C_1$ ,  $C_2$ , and  $C_3$ .

Following this existence theorem, progress was rapid and the widely used Discrete AdaBoost algorithm was published by Freund and Schapire in 1996. It first defined a set of weak binary classifiers  $f_m(x)$ :  $m = 1, \dots, M$ . It then trained them on weighted versions of the training points, increasing the weights of misclassified points and decreasing those of correctly classified points. After training, the final classifier was obtained as the sum of the  $M$  individual classifier outputs. The complete algorithm is shown in [Table 14.5](#). Note that it makes significant use of the set indicator function  $\mathcal{I}(A)$ —best regarded here as a logic function that takes the value 1 when  $A$  is true and 0 otherwise. Thus, in the algorithm,  $\mathcal{I}(f_m(x) \neq y_i) = 1$  indicates an instance of misclassification. Built into the algorithm is the fact that, in each of the  $M$  stages of the algorithm, the best (remaining) weak classifier is identified and used to update the weights; this reveals that

**Table 14.5** The Discrete AdaBoost Algorithm

---

Input  $N$  training points  $x_i$  together with their binary classes  $y_i \in \{-1, 1\}$ .  
 Initialise the weights  $w_i$  to  $1/N$ : this also normalises them so that  $\sum_{i=1}^N w_i = 1$ .  
 for  $m = 1, \dots, M$  do {  
   Find the best-fit classifier by minimising the weighted classification error

$$e_m = \sum_{i=1}^N w_{i,m} \mathcal{I}(f_m(x_i) \neq y_i).$$

Evaluate  $c_m = \ln[(1 - e_m)/e_m]$ .  
 Update the weights:  $w_i = w_i \exp[c_m \mathcal{I}(f_m(x_i) \neq y_i)]$ , for all  $i = 1, \dots, N$ .  
 Renormalise the weights  $w_i$  so that  $\sum_{i=1}^N w_i = 1$ .  
 }  
 Output the final classifier as  $S(x) = \text{sign} \left[ \sum_{m=1}^M c_m f_m(x) \right]$ .

---

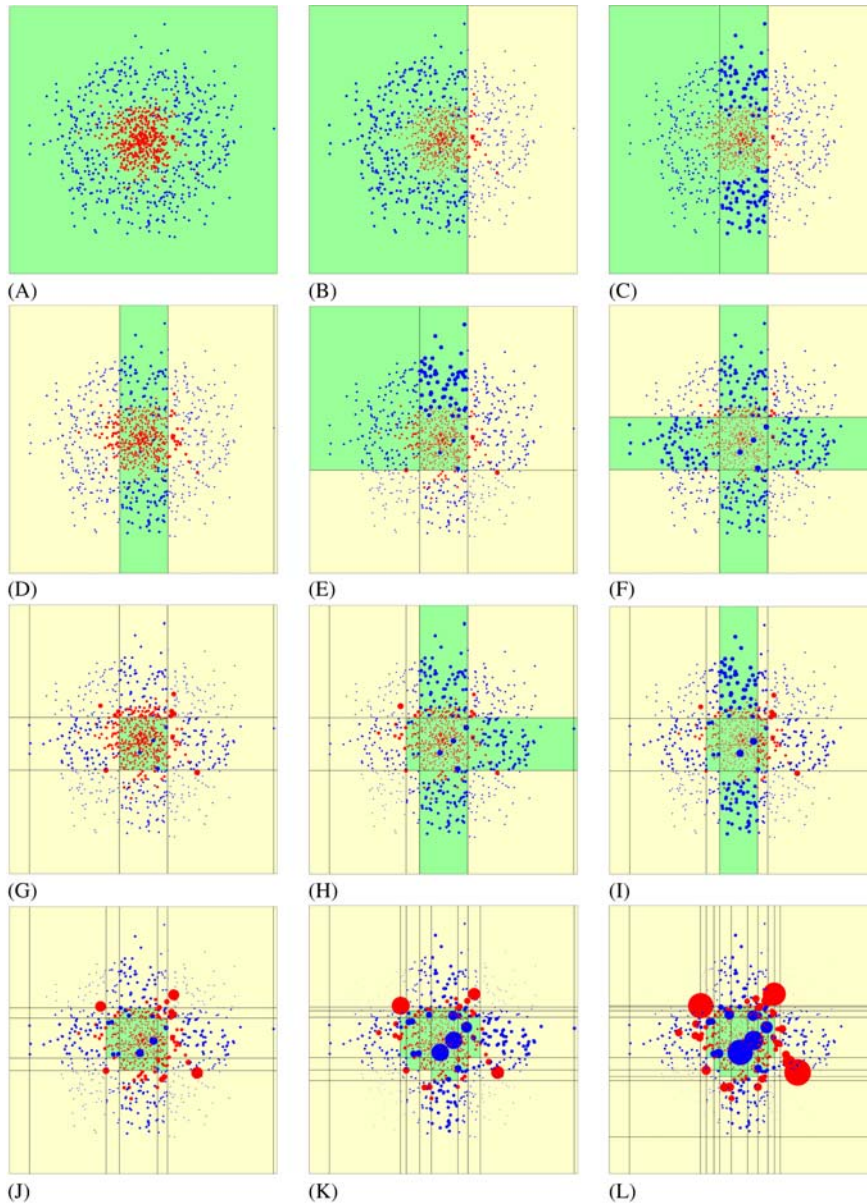
during operation, the algorithm sorts the weak classifiers into best first order—a strategy that postpones use of the worst weak classifiers and at the same time allows performance to be improved via weight updates.

Although the sum of a set of hyperplanes would result in a single hyperplane decision surface, this is certainly not the case for the AdaBoost algorithm, because the component functions  $f_m(x)$  are highly nonlinear.

It is important to understand why the weights of the data points are adjusted before each stage of training: First, points that have already been correctly classified by the first  $m$  stages can reasonably be deemphasized as the information they have provided has already been embedded in the coefficients of the first  $m$  weak classifiers; thus, the latter have already achieved their purpose. However, this is not true for the incorrectly classified points: hence, the latter need to be given more emphasis when training subsequent weak classifiers. How this approach works in practice is demonstrated in Fig. 14.11.

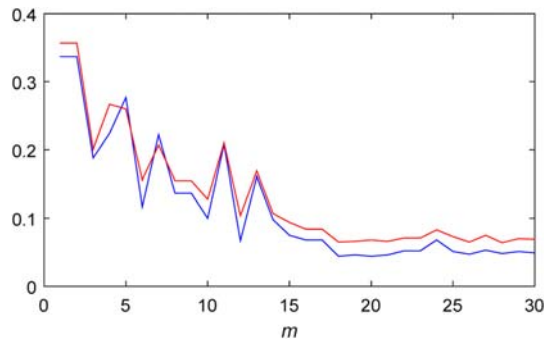
Fig. 14.11A shows the training data, and subsequent pictures show the result of applying various numbers of weak classifiers; the latter have simple straight line decision surfaces. Overall, we see that the combined classifiers are able to achieve what there is no hope of any of the individual weak classifiers doing on its own. Notice also states that the weights of the data points seem to get adjusted in quite a reasonable way during the first few stages; however, later on, we start seeing a small number of points acquiring quite large weights, and after 20 stages, there is excessive concentration on a tiny proportion of the weak classifiers. The latter situation represents the possibility or even the likelihood of overtraining. To investigate this further, we need to look at the error rates during training and testing.

Fig. 14.12 shows the error classification graphs for training and testing. It is clear that the training classification error initially improves rapidly, but then levels off after about 18 weak classifiers have been trained. Similarly, when the overall classifier is tested on previously unseen samples from the same source,



**FIGURE 14.11**

Result of training AdaBoost on a sequence of weak classifiers. Part (A) shows the disposition of the initial training set, consisting of 500 red and 500 blue data points. Parts (B)–(L) show, respectively, the result of training on 1, 2, 3, 4, 5, 6, 7, 8, 12, 20, and 30 weak classifiers, each consisting of a single straight-line decision surface. After each best-fit weak classifier is applied, the weights of the data points are adjusted—being made smaller for correctly classified points and larger for incorrectly classified points. In (J)–(L), it is possible to identify a few points—those with large red or blue spots—that should be considered as overtrained.



**FIGURE 14.12**

Error classification graphs for training and testing. The lower (blue) graph shows the error classification plots for training, and the upper (red) graph shows those for testing. Initially, there is a rapid fall in the error rates in both cases, but these levels out at somewhat higher error rates for test set: testing is always expected to lead to better performance when carried out on the training set. After 18–20 weak classifiers have been applied, no further improvement occurs and some overtraining becomes apparent.

the initial improvement is almost identical, but it again levels off after about 18 weak classifiers have been trained, the final error rate being about 30% higher. In addition, both curves seem to rise slightly as further weak classifiers are trained, the global minima falling around 18–20 weak classifiers. Nevertheless, there is little indication of the poor performance normally expected when classifiers are overtrained. Indeed, it was originally thought that boosted classifiers were not subject to overtraining: Later work indicated that this is not so, though boosted classifiers do seem to be fairly resistant to overtraining. This is because, as more and more weak classifiers are brought in, fewer and fewer data samples are being used for further training (see Fig. 14.11), so the overall level of overtraining is minimal. The other factor to be borne in mind is that each stage of training with totally independent weak classifiers correctly identifies and then *largely* eliminates a substantial fraction  $\eta$  of the data samples from further consideration, so only a fraction  $(1-\eta)^m$  will remain after  $m$  stages. If  $\eta \approx 0.3$ , the fraction remaining will fall according to the series 1.00, 0.70, 0.49, 0.34, 0.24—which amounts to a near-exponential fall in the error rates for  $m$  up to  $\sim 20$  (see Fig. 14.12).

## 14.8 MODELING ADABOOST

So far, we have effectively defined the AdaBoost algorithm as a recipe for achieving improved classification. The next step is to carry out a theoretical

analysis of its operation. The theoretical model presented by Friedman et al. (2000) was that of an exponential loss function

$$E = \sum_{i=1}^N \exp(-y_i F(x)) \quad (14.46)$$

with

$$F(x) = \sum_{m=1}^M c_m f_m(x) \quad (14.47)$$

$y_i$  being the training set classes:  $y_i \in \{-1, 1\}$ .

To use the model for function minimization, it is necessary to know what is and what is not being minimized. First, we observe that it is only necessary to attend to the training of the stage  $m$  weak classifier, as all other weak classifiers will follow the same pattern at other stages of the algorithm. This means that we only have to minimize  $E_m$  with respect to  $c_m$  and  $f_m(x)$ . Though straightforward in principle, significant care is needed with the indicator function  $\mathcal{I}(\cdot)$  and other aspects of the calculation, so details of the proof may be omitted on a first reading. However, it should be noted that Eq. (14.52) is the main result that is used in the AdaBoost algorithm (Table 14.5). Writing  $E_m$  as

$$E_m = \sum_{i=1}^N w_{i,m} \exp(-y_i c_m f_m(x_i)) \quad (14.48)$$

where the weights  $w_{i,k}$ :  $k = 1, \dots, m$  take care of the exponential factors for weak classes  $1, \dots, m-1$  from previous stages, it only remains to perform the minimizations with respect to  $c_m$  and  $f_m(x)$ . Thus, the  $w_{i,k}$ :  $k = 1, \dots, m$  can be taken as constant and ignored over these minimizations. To proceed, it is necessary to separate the  $c_m$  variations for correctly classified points (for which  $y$  and  $f$  have identical signs) from those for incorrectly classified points (for which  $y$  and  $f$  have opposite signs):

$$\begin{aligned} E_m &= e^{-c_m} \sum_{i:\text{correct}} w_{i,m} + e^{c_m} \sum_{i:\text{incorrect}} w_{i,m} \\ &= e^{-c_m} \sum_{i=1}^N w_{i,m} - e^{-c_m} \sum_{i:\text{incorrect}} w_{i,m} + e^{c_m} \sum_{i:\text{incorrect}} w_{i,m} \\ &= e^{-c_m} \sum_{i=1}^N w_{i,m} + (e^{c_m} - e^{-c_m}) \sum_{i:\text{incorrect}} w_{i,m} \\ &= e^{-c_m} \sum_{i=1}^N w_{i,m} + (e^{c_m} - e^{-c_m}) \sum_{i=1}^N w_{i,m} \mathcal{I}(f_m(x) \neq y_i) \end{aligned} \quad (14.49)$$

As the first term in this equation is independent of  $f_m(x)$ , minimizing  $E_m$  with respect to  $f_m(x)$  is equivalent to minimizing the term  $e_m = \sum_{i=1}^N w_{i,m} \mathcal{I}(f_m(x_i) \neq y_i)$



in the AdaBoost algorithm. To minimize  $E_m$  with respect to  $c_m$ , we differentiate and find

$$\frac{\partial E}{\partial c_m} = (e^{c_m} + e^{-c_m}) \sum_{i=1}^N w_{i,m} \mathcal{I}(f_m(x_i) \neq y_i) - e^{-c_m} \sum_{i=1}^N w_{i,m} \quad (14.50)$$

Setting  $\frac{\partial E}{\partial c_m} = 0$  gives

$$e_m = \frac{\sum_{i=1}^N w_{i,m} \mathcal{I}(f_m(x_i) \neq y_i)}{\sum_{i=1}^N w_{i,m}} = \frac{e^{-c_m}}{e^{c_m} + e^{-c_m}} = \frac{1}{e^{2c_m} + 1} \quad (14.51)$$

(The discrepancy between  $e_m$  as defined here and as defined following Eq. (14.49) arises because AdaBoost normalizes the weights  $w_i$  after each iteration: see Table 14.5.)

After a few straightforward steps, we find that

$$c_m = \frac{1}{2} \ln \left[ \frac{1 - e_m}{e_m} \right] \quad (14.52)$$

This proves the validity of the last few optimization steps in the AdaBoost algorithm, within a constant factor of one half for *all* the weak classifier coefficients. The important point is that the characteristics and minimization properties of the whole algorithm have been determined with the *single* assumption that there is an exponential loss function  $E$ .

### 14.8.1 REAL ADABOOST

*This version of the AdaBoost algorithm and its proof (Eqs. (14.53)–(14.56)) may be omitted on a first reading. Its main relevance here is to help pave the way for more rigorous probabilistic theory, in line with the principles of machine learning.*

Real AdaBoost is a version of the AdaBoost algorithm that is formulated in terms of probabilities rather than in terms of errors, and which can still be derived using the exponential loss function. To see this, we express the expected loss for the  $m$ th weak classifier in the following form:

$$\mathbb{E}(E_m) = \mathbb{E}(\exp[-yf_m(x)]|x) = P_m(y = 1|x)e^{-f_m(x)} + P_m(y = -1|x)e^{f_m(x)} \quad (14.53)$$

$$\therefore \frac{\partial \mathbb{E}(E_m)}{\partial f_m(x)} = -P_m(y = 1|x)e^{-f_m(x)} + P_m(y = -1|x)e^{f_m(x)} \quad (14.54)$$

Setting  $\frac{\partial \mathbb{E}(E_m)}{\partial f_m(x)} = 0$  to minimize the expected loss—or equivalently, to maximize the class probability estimate—gives

$$e^{2f_m(x)} = \frac{P_m(y = 1|x)}{P_m(y = -1|x)} = \frac{P_m(y = 1|x)}{1 - P_m(y = 1|x)} \quad (14.55)$$

**Table 14.6** The Real AdaBoost Algorithm

---

Input  $N$  training points  $x_i$  with their binary classes  $y_i \in \{-1, 1\}$ .  
 Initialise the weights  $w_i$  to  $1/N$ : this also normalises them so that  $\sum_{i=1}^N w_i = 1$ .  
 for  $m = 1, \dots, M$  do {  
   Find the best-fit classifier by optimising the class probability estimate  $\rho_m(x)$ ,  
   using weights  $w_i$  on the training data.  
   Evaluate  $f_m(x_i) = \frac{1}{2} \ln[\rho_m(x_i)/(1 - \rho_m(x_i))]$ .  
   Update the weights:  $w_i = w_i \exp[-y_i f_m(x_i)]$ , for all  $i = 1, \dots, N$ .  
   Renormalise the weights  $w_i$  so that  $\sum_{i=1}^N w_i = 1$ .  
 }  
 Output the final classifier as  $S(x) = \text{sign}[\sum_{m=1}^M f_m(x)]$ .

---

$$\therefore f_m(x) = \frac{1}{2} \ln \left[ \frac{P_m(y = 1|x)}{1 - P_m(y = 1|x)} \right] \quad (14.56)$$

In an algorithm, we would estimate  $P_m(y = 1|x)$  using  $\frac{1}{N} \sum_{i=1}^N \mathcal{I}(y_i = 1)$  and proceed to find a best fit to the data, expressing the final result in the form  $\rho_m(x) = \hat{P}_m(y = 1|x)$ : for a best fit, the argmin function would be used. Thus, we arrive at the Real AdaBoost algorithm (Table 14.6).

---

## 14.9 LOSS FUNCTIONS FOR BOOSTING

It turns out that there is a whole family of possible loss functions. Of these,  $E$  is simple to handle but has the problem that it gives far too much weight to misclassified points: Potentially at least, this leads to distinct loss of robustness. However, a simple way to overcome this problem is to use the “log-loss” function

$$L = \ln[1 + \exp(-yF(x))] \quad (14.57)$$

(For clarity, we here drop the  $i$  suffix and the summation over the  $N$  training set points.) To compare  $E$  and  $L$ , it is best to normalize  $L$  so that, like  $E$ , it is equal to 1 at  $yF = 0$ . In addition, it is useful to adjust it so that it has the same gradient at  $yF = 0$ . This leads to the modified function

$$\tilde{L} = \ln[1 + \exp(-2yF(x))] + 1 - \ln 2 \quad (14.58)$$

whose gradient is

$$\frac{d\tilde{L}}{d(yF)} = \frac{-2}{1 + \exp(2yF(x))} \quad (14.59)$$

In addition,

$$\frac{d^2 \tilde{L}}{d(yF)^2} = \frac{4\exp(2yF(x))}{[1 + \exp(2yF(x))]^2} \quad (14.60)$$

which has value 1 at  $yF = 0$ . This is the same as for the exponential loss function  $E$ . Fig. 14.13 confirms that  $E$  and  $\tilde{L}$  have the same values, gradients, and curvatures at  $yF = 0$ . In addition, for negative values of  $yF$ ,  $\tilde{L}$  tends to a linear asymptote  $A$  with gradient  $-2$ , whereas for positive values of  $yF$ , it tends to a horizontal asymptote: both asymptotes pass through the point  $(0, 1 - \ln 2)$ , i.e.,  $(0, 0.31)$ , as shown in Fig. 14.13.

Overall,  $\tilde{L}$  seems to have the advantages of  $E$  without the exponential blow-up for negative  $yF$ , instead having a controlled near-linear response in that region. In the same region (see Fig. 14.13), it is similar to the “hinge” function  $H$ , which forms the basis of the support vector machine (SVM) classification method: this also has gradient 1 at the point  $(0, 1)$ , where the  $E$  and  $\tilde{L}$  curves touch.

The binary misclassification (step) function  $S$  is also shown in Fig. 14.13, this being 1 for misclassification and 0 for correct interpretation. In fact, the idea of a loss function is to mimic and thereby represent  $S$  mathematically. Note that it

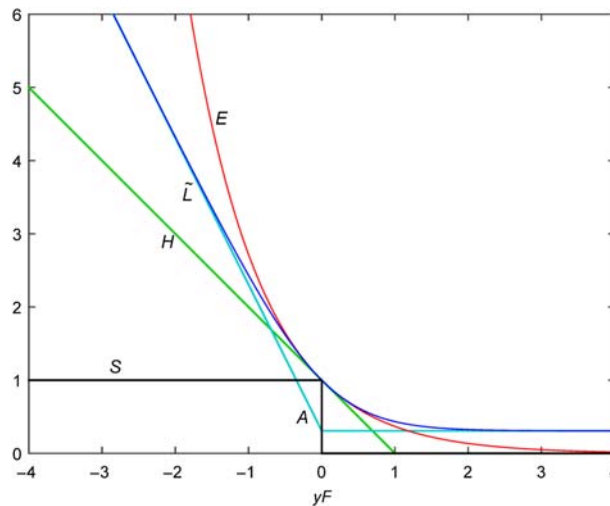


**FIGURE 14.13**

Comparison of loss functions used for boosting.  $E$  and  $\tilde{L}$  are the exponential (red) and log-loss (blue) functions and  $H$  is the hinge function (green) used in SVM classifiers.  $S$  is the binary misclassification step function (black) which loss functions have to mimic in a smooth, monotonically varying way. The two linear asymptotes (cyan) of  $\tilde{L}$  are labeled as  $A$  near their junction at  $yF = 0$ . Note that  $E$  and  $\tilde{L}$  have equal values, gradients, and curvatures at the point where they meet  $S$ : it is important that  $\tilde{L}$  maintains this characteristic but moves toward linear variation for large negative values of  $yF$ .

should be differentiable and should vary monotonically (i.e., its gradient should never change sign). In addition, it should ideally be upward convex, as this helps to guarantee straightforward optimization. All these conditions apply for  $E$  and  $L$ , but they rule out not only  $S$  but also  $H$  and  $A$  as suitable loss functions (even if the latter were combined with the positive  $yF$ -axis or with a horizontal asymptote, as piecewise linear functions are not differentiable).

So far, we have taken the log-loss function  $L$  (or  $\tilde{L}$ ) on trust, as having the right sort of variation, but without providing any proof of viability. However, if we use the function  $f_m(x)$  derived in Eq. (14.56) and solve it to determine  $p_m(x)$ , we find

$$p_m(x) = \frac{e^{f_m(x)}}{e^{-f_m(x)} + e^{f_m(x)}} = \frac{1}{1 + e^{-2f_m(x)}} \tag{14.61}$$

or, writing the combined probability in full

$$P(y = 1|x) = \frac{1}{1 + e^{-2F(x)}} \tag{14.62}$$

Hence, by definition, the log likelihood is

$$\mathcal{L} = -\ln[1 + \exp(-2yF(x))] \tag{14.63}$$

The value of this result is that it gives us a probabilistic basis for the log-loss function: specifically, we will be able to extract probabilities from the trained log-loss function. One of the main problems of the exponential loss function  $E$  was that it didn't provide this opportunity: in fact,  $E$  is not a proper log-likelihood as it does not equal the log of any probability mass function acting on binary variables, neither does taking log  $E$  help with this. *As a result, AdaBoost cannot be used to obtain probability estimates from  $f(x)$ .*

*Details of the log-loss function and its minimization (Eqs. (14.64)–(14.68)) may be omitted on a first reading. Suffice it to say that it provides a substantive step toward the development of a proper probability-based algorithm—and specifically the LogitBoost algorithm of Section 14.10.*

Next, we need to find the function that minimizes the mean of the log-loss function. Writing

$$\begin{aligned} \mathbb{E}(L) &= \mathbb{E}(\ln[1 + \exp(-2yF(x))]) \\ &= P(y = 1|x) \ln(1 + e^{-2F(x)}) + P(y = -1|x) \ln(1 + e^{2F(x)}) \end{aligned} \tag{14.64}$$

and differentiating with respect to  $F(x)$  gives

$$\frac{\partial \mathbb{E}(L)}{\partial F(x)} = \frac{-2P(y = 1|x) e^{-2F(x)}}{1 + e^{-2F(x)}} + \frac{2P(y = -1|x) e^{2F(x)}}{1 + e^{2F(x)}} \tag{14.65}$$

For a minimum, we set  $\frac{\partial \mathbb{E}(L)}{\partial F(x)} = 0$ . After some cancellation, this leads to

$$\frac{P(y = 1|x)}{P(y = -1|x)} = e^{2F(x)} \tag{14.66}$$

Noting that  $P(y = 1|x) + P(y = -1|x) = 1$ , we can solve for the two probabilities

$$P(y = 1|x) = \frac{1}{1 + e^{-2F(x)}} \quad (14.67)$$

and

$$P(y = -1|x) = \frac{1}{1 + e^{2F(x)}} \quad (14.68)$$

As  $y$  is completely contained in the set  $\{-1, +1\}$ , we can summarize these results as

$$P(y|x) = \frac{1}{1 + e^{-2yF(x)}} \quad (14.69)$$

(In binomial calculations, recombining the results in this way—via a single parameter—is a useful trick to bear in mind.)

We also obtain the well-known “population minimizer” in the somewhat simplified form as follows:

$$F(x) = \frac{1}{2} \ln \left[ \frac{p(x)}{1 - p(x)} \right] \quad (14.70)$$

We can clarify the notion of a population minimizer (sometimes described as a risk minimizer) by noting that a median filter carries out this function in each window of an image—median regression otherwise being known as  $L_1$  regression.

Curiously, this is essentially the same as the population minimizer that we obtained for the exponential loss function in Eq. (14.56). It is worthwhile to question how such different loss functions can validly have the same minimizers. In fact, a simple calculation (simpler than the one given above for  $L$ ) shows that any loss function of the form  $g(e^{-yF(x)})$  has a population minimizer of the form given in Eq. (14.70). (It is an instructive exercise for the student to prove this and to determine any restrictions on the function  $g(\cdot)$ .)

Interestingly, Eq. (14.69) is a special case of the sigmoid activation function we met in Section 13.11, where it was used to regularize the training of artificial neural networks. Formally, the *logistic sigmoid function* (Fig. 14.14) is defined as

$$\sigma(v) = \frac{1}{1 + e^{-v}} \quad (14.71)$$

(This function is called the logistic sigmoid function to distinguish it from other sigmoid (S-shaped) functions, such as the arctan function and probit function—the latter being a cumulative Gaussian distribution ranging upwards from  $-\infty$ .)

Its inverse, which is used in Eq. (14.70), is known as the *logit function*:

$$v = \ln \left[ \frac{\sigma}{1 - \sigma} \right] \quad (14.72)$$

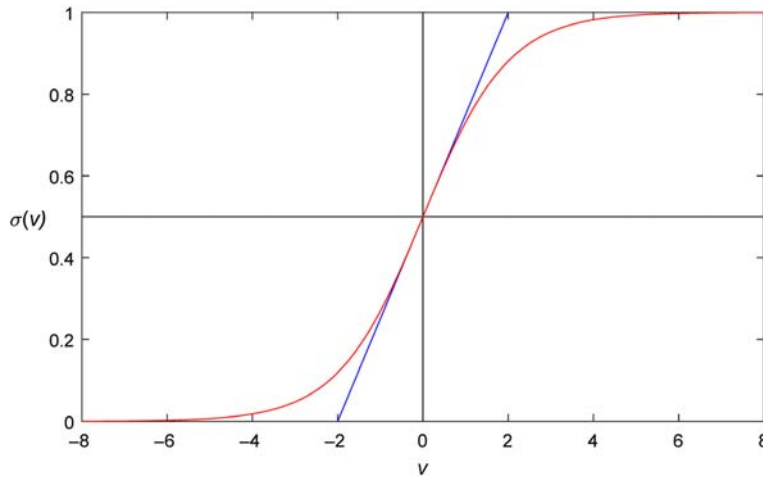


**FIGURE 14.14**

Logistic sigmoid function. This symmetric curve is a shifted version of that shown in Fig. 13.11C, which is centered around the origin. The blue line shows the tangent at the center: its gradient of 0.25 is here disguised by axis scaling.

## 14.10 THE LOGITBOOST ALGORITHM

Much has been said above about the value of the log-loss function  $L$ . Unfortunately, it is somewhat more complicated than the exponential loss function  $E$  and this gives rise to the need for a substantial change in strategy when designing a suitable optimization algorithm. The LogitBoost algorithm (Table 14.7) devised by Friedman et al. (2000) reflects this. First, it is forced to use a least squares approach for optimization. Second, at first sight, its strategy does not appear to employ the loss function, but in fact it employs its derivatives. Third, it does not aim directly at minimizing classification error but instead starts by using an equation in which the loss function is matched with a piecewise linear data-driven model given by the function  $2uF(x)$ . Here, for compatibility with probabilities, the class is represented by  $u \in \{0, 1\}$  rather than by  $y \in \{-1, 1\}$ , the two parameters being related by the formulae

$$u = (y + 1)/2 \quad (14.73)$$

$$y = 2u - 1 \quad (14.74)$$

Thus, the function  $2uF(x)$  has two linear sections—along the  $F(x)$  axis when  $u = 0$ , and along the line  $2F(x)$  when  $u = 1$ . With this representation, we should expect to find that the result of optimization is intended to be that the expectation value of  $u$  will equal the probability  $p$  of class  $u = 1$  occurring.

**Table 14.7** The LogitBoost Algorithm

---

Input  $N$  training points  $x_i$  with their binary classes  $u_i = (y_i + 1)/2$ , where  $u_i \in \{0, 1\}$ .  
 Initialise the weights  $w_i$  to  $1/N$ .  
 Initialise the probability estimates  $p(x_i)$  to  $1/2$ .  
 for  $m = 1, \dots, M$  do {  
   Evaluate the working responses  $r_i = \frac{u_i - p(x_i)}{p(x_i)[1 - p(x_i)]}$ .  
   Evaluate the weights  $w_i = p(x_i)[1 - p(x_i)]$ .  
   Find the best-fit classifier by least squares regression of  $r_i$  using weights  $w_i$ .  
   Update  $F(x) = F(x) + \frac{1}{2} f_m(x)$ .  
   Update  $p(x_i) = 1/[1 + \exp(-2F(x_i))]$ .  
 }  
 Output the final classifier as  $S(x) = \text{sign} \left[ \sum_{m=1}^M f_m(x) \right]$ .

---

We will now follow the above reasoning in more detail. The equations for the working responses  $r_i$  and weights  $w_i$  appearing in Table 14.7 are derived by Friedman et al. (2000). Specifically, Friedman et al. combine the update  $F(x) + f(x)$  and the expected log-likelihood and start with the equation

$$\mathbb{E}(L) = \mathbb{E}(2u[F(x) + f(x)] - \ln(1 + e^{2[F(x) + f(x)]})) \quad (14.75)$$

where  $F(x)$  is the extracted result for stages previous to  $m$  and  $f(x)$  is the expected addition for stage  $m$ . Note that the minus sign in the exponent (see Eq. (14.57)) has been dropped by including it in  $F(x)$ , whereas the  $y$  has been replaced by the  $u$  in the function  $2uF(x)$  earlier in the equation: but overall, the equation *consistently* embodies all the necessary components for optimization. The point of the calculation is to minimize the expected log-loss by weighted least squares regression. The calculation finds the first and second derivatives of  $\mathbb{E}(L)$  with respect to  $f(x)$  and calculates the results at  $f(x) = 0$ . Here, we simplify the proof by ignoring the  $f(x)$  terms and differentiating straight away with respect to  $F(x)$ :

$$\begin{aligned} L' &= \frac{\partial \mathbb{E}(L)}{\partial F(x)} = \mathbb{E} \left( 2u - \frac{2e^{2F(x)}}{1 + e^{2F(x)}} \middle| x \right) \\ &= 2 \mathbb{E} \left( u - \frac{1}{1 + e^{-2F(x)}} \middle| x \right) = 2 \mathbb{E}(u - p(x) | x) \end{aligned} \quad (14.76)$$

$$\begin{aligned} L'' &= \frac{\partial^2 \mathbb{E}(L)}{\partial F(x)^2} = -2 \mathbb{E} \left( \frac{2e^{-2F(x)}}{[1 + e^{-2F(x)}]^2} \middle| x \right) \\ &= -4 \mathbb{E} \left( \frac{1}{1 + e^{-2F(x)}} \times \frac{1}{1 + e^{2F(x)}} \middle| x \right) = -4 \mathbb{E}(p(x)[1 - p(x)] | x) \end{aligned} \quad (14.77)$$

Next, using the Newton update appropriate for an optimization function, we have

$$F(x) = F(x) - \frac{L'}{L''} = F(x) + \frac{1}{2} \mathbb{E} \left( \frac{u - p(x)}{p(x)[1 - p(x)]} \middle| x \right) \quad (14.78)$$

(Newton's method is conventionally used to find roots of an equation by successive approximation, according to  $x_{i+1} = x_i - g(x)/g'(x)$ . However, when applied for optimization, it needs to locate maxima or minima, so it needs to find roots of the *derivative* function. Thus, first and second derivatives become relevant.)

The factor of one half is reflected by the same factor appearing in the expression for  $F(x)$  in Table 14.7. The argmin function is used to perform weighted least squares regression—in this case minimizing  $\sum_{i=1}^N w_i [r_i - f_m(x_i)]^2$ .

Fig. 14.15 indicates something of the performance of the LogitBoost algorithm. Although the results are not directly comparable to those for AdaBoost (Fig. 14.11), because of the finer angular increments used in creating the weak classifiers, they are actually quite impressive, as they show what can be achieved with relatively few weak classifiers.

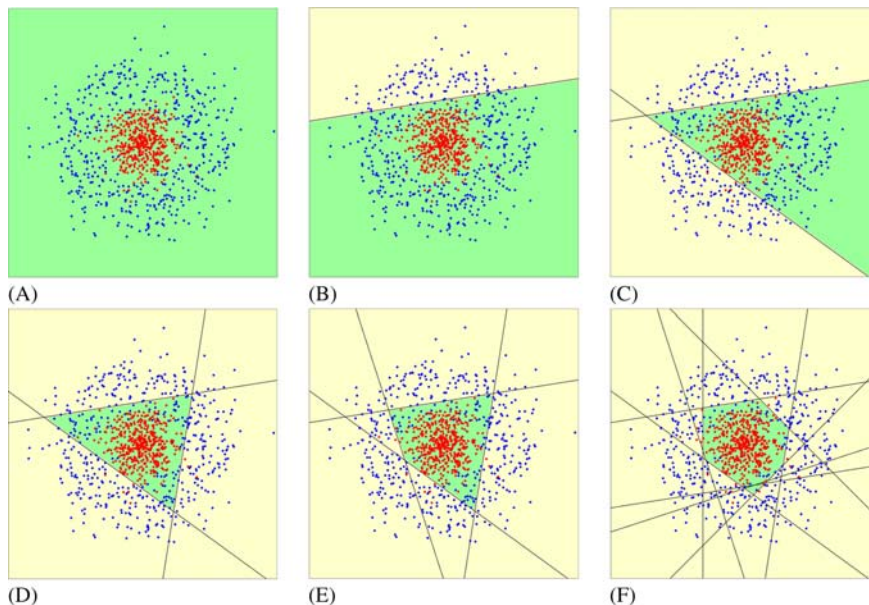


**FIGURE 14.15**

Result of training LogitBoost on a sequence of weak classifiers. Part (A) shows the disposition of the initial training set, consisting of 500 red and 500 blue data points. Parts (B)–(F) show, respectively, the results of training on 1, 2, 3, 4, and 10 weak classifiers, each consisting of a single straight-line decision surface.



Overall, LogitBoost relies on a loss function that is far more robust against outliers than the exponential function embodied in AdaBoost. However, the main problem with LogitBoost is that optimization becomes more difficult, with the result that gradient descent- or Newton-based schemes have to be used for optimization. Such methods fall into the category of iteratively reweighted least squares, and they impose a significantly increased computational load on the technique. It should also be mentioned that as  $p(x_i)$  approaches 0 or 1, the  $r_i$  term in LogitBoost becomes very large and can become numerically unstable. For this reason is it necessary to enforce upper limits on the absolute value of  $r_i$  and on the lowest value of  $w_i$ .

---

### 14.11 THE EFFECTIVENESS OF BOOSTING

We now need to look back and see why boosting is so effective. A simple answer can be found by considering the Hughes (1968) effect: This applies when very large numbers of features are employed in an attempt to obtain highly accurate classification. In fact, in such circumstances, the “curse of dimensionality” creeps in, and, with limited training data, the additional features can’t be estimated sufficiently accurately to improve performance, which therefore falls off. On the other hand, in boosting, trying a great many weak classifiers does not result in a commensurate number of features, as only the best remaining weak classifier survives each stage, and those that survive include only those that improve the predictive power of the model. Nevertheless, overtraining will eventually occur because the specific training set is mapped ever more closely into the boosted classifier. This analysis is confirmed by the success of the Viola–Jones (2001) work on object detection by boosting, which will be described in [Chapter 21](#), Face Detection and Recognition: the Impact of Deep Learning.

---

### 14.12 BOOSTING WITH MULTIPLE CLASSES

*This whole section may be omitted on a first reading as the number of additional complications is significant: It has been included here to show the type of theory that is involved and also to demonstrate that it is tractable. Note particularly the necessity for the symmetric multiple logistic transformation (Eq. (14.79)) and the salutary warnings before Eq. (14.98) and after Eq. (14.99).*

So far, we have concentrated on boosting when there are only two classes to be distinguished. In a world where very many objects have to be distinguished and recognized, this may seem to be a rather slight achievement. However, this case is important in its own right as it represents situations where specific objects such as faces need to be *detected* against a variegated background. In any case, there are also situations where objects such as rats and mice need to be distinguished from

**Table 14.8** Complexities of Different Types of Multiclassifier

No. of Classes	All Pairs	Binary Cut	OVR
2	1	1	1
3	3	2	2
4	6	2	3
5	10	3	4
6	15	3	5
7	21	3	6
8	28	3	7
9	36	4	8
10	45	4	9
100	~ 5000	7	99
1000	~ 500,000	10	999

*This table shows the number of dichotomizers needed to distinguish between  $K$  classes, using various strategies, OVR being the “one-versus-the-rest” classifier.*

each other. In fact, once we have achieved 2-class recognition, we have conquered the main problem. This is because  $K$ -class recognition can immediately be achieved by taking each pair of object types and generating a 2-class machine to distinguish between them. The problem then becomes one of managing the considerable number of 2-class machines—or dichotomizers as they are called—that are required under this strategy. This number is  ${}^K C_2 = \frac{1}{2}K(K-1)$ . Note that for values of  $K$  up to 5, this number is 10 or less, which is manageable. An alternative strategy is to aim at a sequence of binary cuts, in which case we should be able to separate up to 1000 or so classes with just 10 cuts: in such a case, the number of dichotomizers needed is just  $\log_2 K$ . It needs to be emphasized that this represents an ideal solution which would need some extra redundancy to be sure of attaining reasonable performance. An alternative is the “one-versus-the-rest” (OVR) classifier, for which exactly  $K-1$  dichotomizers are needed. This scales linearly with  $K$ , though clearly it is not as minimal as the binary cut strategy (Table 14.8).

Returning to the boosting environment, the OVR classifier is the one that has commonly been adopted. To make it work successfully, we need a suitable logistic transform, such as the following symmetric multiple logistic transformation:

$$F_j(x) = \ln p_j(x) - \frac{1}{K} \sum_{k=1}^K \ln p_k(x) \quad (14.79)$$

When  $K = 2$  this becomes

$$\begin{aligned} F_j(x) &= \ln p_j(x) - \frac{1}{2} \sum_{k=1}^2 \ln p_k(x) \\ &= \frac{1}{2} [\ln p_1(x) - \ln p_2(x)] = \frac{1}{2} \ln \left[ \frac{p(x)}{1-p(x)} \right] \end{aligned} \quad (14.80)$$

where we have successively taken  $j = 1$  and  $k = 1, 2$  and finally dropped the suffices on  $p(x)$ . Eq. (14.80) gives exactly the same result as Eq. (14.70), which confirms that Eq. (14.79) is an acceptable symmetric generalization of Eq. (14.70). Notice that there are  $K$  functions of this form, so  $F_j(x)$  fully embodies the OVR classification strategy.

Next, we need to find the probabilities resulting from this definition of  $F_j(x)$ . Writing Eq. (14.79) in the form

$$\ln \left[ \frac{p_j(x)}{e^{F_j(x)}} \right] = \frac{1}{K} \sum_{k=1}^K \ln p_k(x) \quad (14.81)$$

we see that the expression on the right-hand side has to be a constant function  $\beta(x)$  of  $x$ . We can now readily solve for  $p_j(x)$ :

$$p_j(x) = e^{\beta(x)} e^{F_j(x)} \quad (14.82)$$

As the probabilities have to sum to unity, we immediately find that

$$e^{\beta(x)} \sum_{k=1}^K e^{F_k(x)} = 1 \quad (14.83)$$

so

$$p_j(x) = \frac{e^{F_j(x)}}{\sum_{k=1}^K e^{F_k(x)}} \quad (14.84)$$

It is also clear on summing Eq. (14.79) from  $k = 1$  to  $K$  that

$$\sum_{k=1}^K F_k(x) = 0 \quad (14.85)$$

It should be pointed out that Eq. (14.85) can be useful for ensuring numerical stability during computation. It has no effects on the probabilities (it can be seen from Eqs. (14.82) and (14.84) that adding a constant to each  $F_j(x)$  would change  $\beta(x)$  but would leave the  $p_j(x)$  unchanged).

Eqs. (14.79), (14.84), and (14.85) were introduced by Friedman et al. (2000) and form the basis for multiclass boosting algorithms. The AdaBoost.MH algorithm—one of the more successful of the multiclass AdaBoost variants—is based on this general idea. However, it is equivalent to running separate boosting algorithms on  $K$  dichotomizers each having datasets of  $N$  samples (starting with a total of  $KN$  samples), and “there is no guarantee that the implied probabilities sum to 1” (Friedman et al., 2000). Friedman et al. sought to overcome this problem by rigorously adhering to their symmetric multiple logistic transformation (Eq. (14.79)) in a new multiclass version of LogitBoost (Table 14.9). Note also that if probabilities are used to formulate the problem and its solution, mismatches between classifiers should not occur, as the probabilities provide an absolute measure of coherence between classes. Interestingly, the multiclass version of LogitBoost and proof of its validity match those of the 2-class case extremely

**Table 14.9** Multiclass LogitBoost Algorithm

---

Input  $NK$  training points  $x_{ij}$  with their classes  $u_{ij} \quad i = 1, \dots, N, j = 1, \dots, K$ .  
 Initialise the weights  $w_{ij}$  to  $1/N$ .  
 Initialise probability estimates  $p_j(x_{ij})$  to  $1/K$ , and functions  $F_j(x_{ij})$  to 0.  
 for  $m = 1, \dots, M$  do {  
   for  $j = 1, \dots, K$  do {  
     Evaluate the working responses  $r_{ij} = \frac{u_{ij} - p_j(x_{ij})}{p_j(x_{ij})[1 - p_j(x_{ij})]}$ .  
     Evaluate the weights  $w_{ij} = p_j(x_{ij})[1 - p_j(x_{ij})]$ .  
     Fit the function  $f_{mj}(x)$  by least squares regression of  $r_{ij}$  using weights  $w_{ij}$ .  
   }  
   Apply symmetrisation  $f_{mj}(x) = \frac{K-1}{K} \left[ f_{mj}(x) - \frac{1}{K} \sum_{k=1}^K f_{mk}(x) \right]$ .  
   Update  $F_j(x) = F_j(x) + f_{mj}(x)$ .  
   Update  $p_j(x) = e^{F_j(x)} / \sum_{k=1}^K e^{F_k(x)}$ .  
 }  
 Output the final classifier as  $Q(x) = \arg \max_j [F_j(x)]$ .

---

closely, with only minor additional complexity. This is a testament to the value of starting with a particularly powerful formulation in the 2-class case.

To start the derivation, we take an arbitrary base class  $J$  from the  $K$  classes and compare all other classes with this one. However, the proof will be mathematically neater if we reorder the classes so that the  $J$ th class is the  $K$ th class: this can be done with no loss of generality. We again combine the expected update plus log-likelihood, generalized to cover all  $K - 1$  nonbase classes:

$$\mathbb{E}(L) = \mathbb{E} \left( u_j [F_j(x) + f_j(x)] - \ln \left( 1 + \sum_{k=1}^{K-1} e^{[F_k(x) + f_k(x)]} \right) \right) \quad (14.86)$$

We first find the first and second derivatives of  $\mathbb{E}(L)$  with respect to  $f_j(x)$  and calculate the results at  $f_j(x) = 0$ . We again simplify the proof by ignoring the  $f_j(x)$  terms and differentiating straight away with respect to  $F_j(x)$ :

$$G_j = \frac{\partial \mathbb{E}(L)}{\partial F_j(x)} = \mathbb{E} \left( u_j - \frac{e^{F_j(x)}}{1 + \sum_{l=1}^{K-1} e^{F_l(x)}} \middle| x \right) \quad (14.87)$$

$$H_{jj} = \frac{\partial^2 \mathbb{E}(L)}{\partial F_j(x)^2} = - \mathbb{E} \left( \frac{e^{F_j(x)}}{1 + \sum_{l=1}^{K-1} e^{F_l(x)}} \times \frac{\left[ 1 + \sum_{l=1}^{K-1} e^{F_l(x)} \right] - e^{F_j(x)}}{1 + \sum_{l=1}^{K-1} e^{F_l(x)}} \middle| x \right) \quad (14.88)$$

$$H_{jk: k \neq j} = \frac{\partial^2 \mathbb{E}(L)}{\partial F_j(x) \partial F_k(x)} = \mathbb{E} \left( \frac{e^{F_j(x)}}{1 + \sum_{l=1}^{K-1} e^{F_l(x)}} \times \frac{e^{F_k(x)}}{1 + \sum_{l=1}^{K-1} e^{F_l(x)}} \middle| x \right) \quad (14.89)$$

To progress further, we need to use a multilogit version of Eq. (14.72):

$$F_j(x) = \ln \left[ \frac{P(u_j = 1|x)}{P(u_K = 1|x)} \right] \quad j = 1, \dots, K-1 \quad (14.90)$$

This is now the appropriate form of the function—i.e., without the factor one half in front of the logarithm—as for clarity (and following Friedman et al., 2000) we have omitted the factor 2 in the update and the exponent in Eq. (14.75). The corresponding formulae for the probabilities are:

$$p_j(x) = \frac{e^{F_j(x)}}{1 + \sum_{k=1}^{K-1} e^{F_k(x)}} \quad j = 1, \dots, K-1 \quad (14.91)$$

$$p_K(x) = \frac{1}{1 + \sum_{k=1}^{K-1} e^{F_k(x)}} \quad (14.92)$$

Substituting in Eqs. (14.87)–(14.89), we find

$$G_j = \mathbb{E}(u_j - p_j(x)|x) \quad j = 1, \dots, K-1 \quad (14.93)$$

$$H_{jj} = -\mathbb{E}(p_j(x)[1 - p_j(x)]|x) \quad j = 1, \dots, K-1 \quad (14.94)$$

$$H_{jk:k \neq j} = \mathbb{E}(p_j(x)p_k(x)) \quad j, k = 1, \dots, K-1 \quad (14.95)$$

In fact, the latter two equations can be written more compactly in the form

$$H_{jk} = -\mathbb{E}(p_j(x)[\delta_{jk} - p_k(x)]|x) \quad j, k = 1, \dots, K-1 \quad (14.96)$$

In the multiclass LogitBoost algorithm (Table 14.9), least squares fitting is again needed, and a quasi-Newton update involves taking a diagonal approximation to the Hessian  $H_{jk}$ , the update equation now being

$$F_j(x) = F_j(x) - \frac{G_j}{H_{jj}} = F_j(x) + \mathbb{E} \left( \frac{u_j - p_j(x)}{p_j(x)[1 - p_j(x)]} \middle| x \right) \quad (14.97)$$

Finally, we need to convert to a symmetric parametrization by applying Eq. (14.79). As indicated above, this is necessary so that probability is strictly and consistently maintained over all the dichotomizers. In addition, we need to average over all possible choices for the base class (this amounts to dividing the original  $K - 1$  contributions between  $K$  classes):

$$F_j(x) = F_j(x) + f_j(x) \quad (14.98)$$

where

$$f_j(x) = \frac{K-1}{K} \left[ \mathbb{E} \left( \frac{u_j - p_j(x)}{p_j(x)[1 - p_j(x)]} \middle| x \right) - \frac{1}{K} \sum_{k=1}^K \mathbb{E} \left( \frac{u_k - p_k(x)}{p_k(x)[1 - p_k(x)]} \middle| x \right) \right] \quad (14.99)$$

Note that, because of symmetrization, the final update equation for  $p_j(x)$  in the multiclass LogitBoost algorithm (Table 14.9) is Eq. (14.84) rather than Eq. (14.91).

## 14.13 THE RECEIVER OPERATING CHARACTERISTIC

In the early sections of this chapter, there was an implicit understanding that classification error rates have to be reduced as far as possible, though in Section 13.6, it was acknowledged that it is cost rather than error that is the practically important parameter. It was also found that a trade-off between error rate and reject rate allows a further refinement to be made to the analysis.

Here, we consider another refinement that is required in many practical cases where binary decisions have to be made. Radar provides a good illustration of this, showing that there are two basic types of misclassification: First, radar displays may indicate an aircraft or missile when none is present—in which case the error is called a false positive (or in popular parlance, a false alarm); second, they may indicate that no aircraft or missile is present when there actually is one—in which case the error is called a false negative. Similarly, in automated industrial inspection, when searching for deficient products, a false positive corresponds to finding one when none is present, whereas a false negative corresponds to missing a deficient product when one is present.

In fact, there are four relevant categories: (1) true positives (positives that are correctly classified), (2) true negatives (negatives that are correctly classified), (3) false positives (positives that are incorrectly classified), and (4) false negatives (negatives that are incorrectly classified). If many experiments are carried out to determine the proportions of these four categories in a given application, we can obtain the four probabilities of occurrence. Using an obvious notation, these will be related by the following formulae:

$$P_{TP} + P_{FN} = 1 \quad (14.100)$$

$$P_{TN} + P_{FP} = 1 \quad (14.101)$$

(In case the reader finds the combinations of probabilities in these formulae confusing, note that an object that is actually a faulty product will either be *correctly* detected as such or else it will be *incorrectly* categorized as acceptable—in which case it is a false negative.)

It will be apparent that the probability of error  $P_E$  is the sum:

$$P_E = P_{FP} + P_{FN} \quad (14.102)$$

In general, false positives and false negatives will have different costs. Thus, the loss function  $L(C_1|C_2)$  will not be the same as the loss function  $L(C_2|C_1)$ . For example, missing an enemy missile or failing to find a glass splinter in baby food may be far more costly than the cost of a few false alarms (which in the case of food inspection merely means the rejection of a few good products). In fact, there

are a good many applications where there is a prime need to reduce as far as possible the number of false negatives (the number of failures to detect the requisite targets).

But how far should we go in aiming to reduce the number of false negatives? This is an important question that should be answered by systematic analysis rather than by ad hoc means. The key to achieving this is to note that the proportions of false positives and false negatives will vary independently with the system setup parameters, though frequently only a single threshold parameter needs to be considered in any detail. In that case, we can eliminate this parameter and determine how the numbers of false positives and false negatives depend on each other. The result is the receiver operating characteristic or “ROC” curve (Fig. 14.16). (Although this text defines the ROC curve in terms of  $P_{FP}$  and  $P_{FN}$ , many other texts use alternative definitions, based for example on  $P_{TP}$  and  $P_{FP}$ —in which case the graph will appear inverted.)

The ROC curve will often be approximately symmetrical, and, if expressed in terms of probabilities rather than numbers of items, will pass through the points (1, 0) and (0, 1)—as shown in Fig. 14.16. It will generally be highly concave so it will pass well below the line  $P_{FP} + P_{FN} = 1$ , except at its two ends. The point closest to the origin will often be close to the line  $P_{FP} = P_{FN}$ . This means that if false positives and false negatives are assigned equal costs, the classifier can be

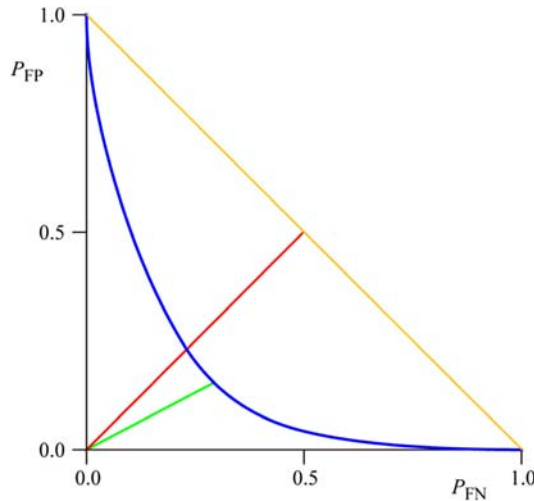


**FIGURE 14.16**

Idealized ROC curve (shown in blue). The red line of gradient +1 indicates the position which a priori might be expected to lead to minimum error. In fact, the optimum working point is that indicated by the green line, where the gradient on the curve is  $-1$ . The orange line of gradient  $-1$  indicates the limiting worst case scenario: all practical ROC curves will lie below this line.

optimized simply by minimizing  $P_E$  with the constraint  $P_{FP} = P_{FN}$ . Note, however, that in general the point closest to the origin is *not* the point that minimizes  $P_E$ : The point that minimizes total error is actually the point on the ROC curve where the gradient is  $-1$  (Fig. 14.16).

Unfortunately, there is no general theory predicting the shape of the ROC curve. Furthermore, the number of samples in the training set may be limited (especially in inspection if rare contaminants are being sought), and then it may not prove possible to make an accurate assessment of the shape—especially in the extreme wings of the curve. In some cases, this problem can be tackled by modeling, e.g., using exponential or other functions—as shown in Fig. 14.17 where the exponential functions lead to reasonably accurate descriptions. However, the underlying shape can hardly be exactly exponential, as this would suggest that the ROC curve tends to zero at infinity rather than at the points  $(1, 0)$  and  $(0, 1)$ . Also, there will in principle be a continuity problem at the join of two exponentials. Nevertheless, if the model is reasonably accurate over a good range of thresholds, the relative cost factors for false positives and false negatives can be adjusted appropriately, and an ideal working point determined systematically. Of course, there may be other considerations: e.g., it may not be permissible for the

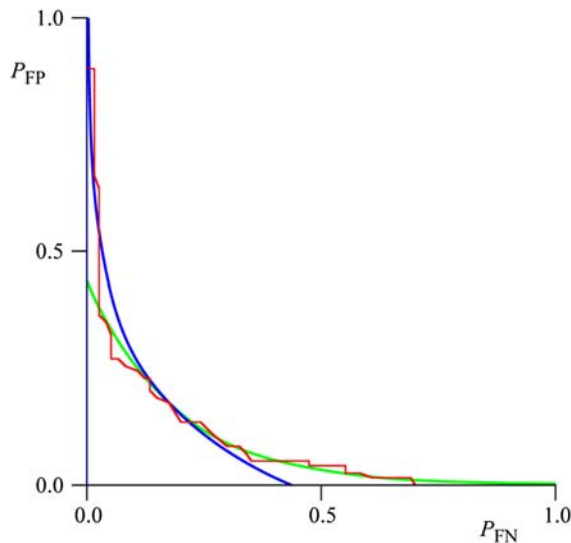


**FIGURE 14.17**

Fitting a ROC curve using exponential functions. Here, the given (red) ROC curve (see Davies et al., 2003c) has distinctive steps resulting from a limited set of data points. A pair of exponential curves (shown in green and blue) fits the ROC curve quite well along the two axes, each having an obvious region that it models best. In this case, the crossover region is reasonably smooth, but there is no real theoretical reason for this. Furthermore, exponential functions will not pass through the limiting points  $(0, 1)$  and  $(1, 0)$ .



false-negative rate to rise above a certain critical level. For examples of the use of the ROC analysis, see Keagy et al. (1995, 1996) and Davies et al. (2003).

### 14.13.1 PERFORMANCE MEASURES RELATING TO ERROR RATES

In signal-detection theory (typified by the radar type of application), it is usual to work with error rates rather than the probabilities used in the above section. Hence, we define the following:

$$\text{True positive rate : } tpr = \frac{TP}{P} = \frac{TP}{TP + FN} \quad (14.103)$$

$$\text{True negative rate : } tnr = \frac{TN}{N} = \frac{TN}{TN + FP} \quad (14.104)$$

$$\text{False positive rate : } fpr = \frac{FP}{N} = \frac{FP}{TN + FP} \quad (14.105)$$

$$\text{False negative rate : } fnr = \frac{FN}{P} = \frac{FN}{TP + FN} \quad (14.106)$$

where  $P$  and  $N$  are the actual numbers of objects in classes P and N, respectively. Following Eqs. (14.100) and (14.101) we have

$$tpr + fnr = 1 \quad (14.107)$$

and

$$tnr + fpr = 1 \quad (14.108)$$

These two equations show the consistency of the four definitions presented above.

It is unfortunate and sometimes confusing that a plethora of names for these and related parameters have arisen in various fields of pattern recognition. Below, we aim to make sense of these names as well as defining them:

<i>Sensitivity</i>	A parameter describing the success in finding a particular type of target. It is also a synonym for <i>hit rate</i> . It is therefore equal to $tpr$
<i>Recall</i>	A term used when describing the success in finding an item in a database. It is therefore also equal to $tpr$
<i>Specificity</i>	A term that is important in medicine and relates to the proportion of <i>well</i> patients who are accurately told after a test that they are not ill. It is therefore equal to $tnr = 1 - fpr$
<i>Discriminability</i>	A term used when describing the success in differentiating a particular type of target from a similar type of target. It is therefore equal to $TP/(TP + FP)$
<i>Precision</i>	A term describing the accuracy in picking out a particular type of target from any distractors, including noise and clutter. It is also equal to $TP/(TP + FP)$

(Continued)

*Continued*

<i>Accuracy</i>	A term used to describe the overall success rate when distinguishing between foreground and background. We can deduce that it must be equal to $(TP + TN)/(P + N)$
<i>False alarm rate</i>	Another synonym for <i>fpr</i>
<i>Positive predictive value</i>	Another synonym for <i>precision</i>
<i>F-measure</i>	A measure that is used as an overall performance indicator, combining the <i>recall</i> and <i>precision</i> measures (or alternatively, the sensitivity and discriminability measures). Because it is the numbers of errors ( $FP + FN$ ) that have to be combined (rather than the error rates themselves), the formula for <i>F-measure</i> may initially appear overcomplex: $\frac{2}{1/recall + 1/precision}$

A more general formula for F-measure is the following:

$$F_{\gamma}\text{-measure} = \frac{1}{\gamma/recall + (1 - \gamma)/precision} \quad (14.109)$$

where  $\gamma$  can be adjusted to give the most appropriate weighting between *recall* and *precision*: it is normally given a value close to 0.5.

Quite often, *recall* and *precision* are used together to form ROC-like graphs, though they are distinct from ROC curves which typically show *tpr* versus *fpr*. (Note that, although  $recall = tpr$ ,  $precision \neq fpr$ .)

Finally, a valuable performance indicator for binary classifiers is obtained by finding the area under the curve (AUC) for a *tpr* versus *fpr* ROC curve. It is largest when the ROC curve lies close to the  $tpr = 1$ ,  $fpr = 0$  axes. Using this measure, the best classifier is the one that has the largest AUC.

---

## 14.14 CONCLUDING REMARKS

This chapter has covered two main topics that are solidly in the domain of probabilistic machine learning—the EM algorithm and classification by boosting. These embody distinct ways of embodying probabilistic methods, and even in the boosting case, there are several strategies for achieving this. Thus, while in principle probability provides an absolute and unique way of doing things, in practice theoretical innovation will only permit some ideas to be taken forward and turned into working probabilistic approaches: in the end, some possible approaches will approximate better to reality than others. Indeed, given that other criteria such as robustness are also important, and that different criteria will have to be taken into account to different extents with different datasets, different approximations to probability may be needed in different applications. A case in point is when the Student *t*-distribution is used in place of the Gaussian in mixture models because

it can be adjusted to put more weight into the tails of the distribution: this allows for more robust treatment of data containing outliers (Sfikas et al., 2007). Another case is when the theory underlying the LogitBoost algorithm takes on a different starting point than that for AdaBoost. In general, it is found that the mathematics of the problem only permits one to include probability in specific ways. All this is natural, as in many or even most applications, the relevant natural probability distributions are not known with any certainty, but they still have to be modeled in order to approximate suitable probabilistic methods.

In this chapter, it has also been necessary to include other important methods. One of these is PCA, which has applications in a variety of vision topics. These are as diverse as optimizing the representation of multispectral images, constructing shape models, and matching varying facial expressions, e.g., using the “eigenface” approach (see Chapters 12 and 21).

Finally, ROC and performance analysis have been discussed in some detail because of their importance in most vision applications: it is all very well having relevant theory underpinning algorithms, and using learning approaches for implementing them, but it is also necessary to analyze their performance. Interestingly, though this is normally carried out in terms of success and failure rates (e.g., *tp<sub>r</sub>*, *fn<sub>r</sub>*, etc.), such quantities are not a million miles away from the probabilities we have been discussing in most of this chapter.

*This chapter has covered the EM algorithm and how it is applied to mixture modeling. Its success when applied to histogram-based segmentation has been made clear. K-means provides a useful initial approximation for mixture modeling: however, though related, it is not a probabilistic method and it is therefore liable to be less accurate. Boosted classifiers make systematic use of weak classifiers and are surprisingly good at this, even to the extent of being fairly resistant to overtraining.*

---

## 14.15 BIBLIOGRAPHICAL AND HISTORICAL NOTES

Relative to many other topics covered in this chapter, the EM algorithm is fairly old, originating in a paper by Dempster et al. (1977): Nevertheless, it has stood the test of time and its use in vision is largely undiminished. Mixture models came to vision much later, and important applications include those of background subtraction (Stauffer and Grimson, 1999) and skin detection (Jones and Rehg, 2002). Later work using mixture models for segmentation includes that of Ma et al. (2007) and Sfikas et al. (2007). In the latter case, the Student *t*-distribution was used instead of the Gaussian, as its wings can be made to extend far further: this was turned to advantage to allow for robust treatment of data containing outliers. Specifically, the Student *t*-distribution contains more parameters than the Gaussian so it can be adjusted to put more weight into the tails of the distribution.

PCA is an age-old mathematical technique which was invented by Karl Pearson in 1901. It has been much used for data fitting in all the sciences, having undergone a big spurt in the 1960s with the advent of the digital computer. Its use is characterized by different names depending on the application area, e.g., Hotelling transform, Karhunen–Loève transform, and singular value decomposition. More recently, it has been developed in a number of ways, e.g., to Kernel PCA (Schölkopf et al., 1997) and Probabilistic PCA (Tipping and Bishop, 1999).

The multiple classifier approach is a relatively recent development and is well reviewed by Duin (2002). Ho et al. (1994) dates from when the topic was rather younger and lists an interesting set of options as seen at that point.

“Bagging” and “boosting” are further variants on the multiple classifier theme: they were developed by Breiman (1996) and Freund and Schapire (1996). Bagging (short for “bootstrap aggregating”) means sampling the training set  $n$  times, with replacement, generating  $b$  bootstrap sets to train  $b$  subclassifiers, and assigning any test pattern to the class most often predicted by the subclassifiers. The method is particularly useful for unstable situations (such as when classification trees are used) but is almost valueless when stable classification algorithms are used (such as the nearest neighbor algorithm). Boosting is useful for aiding the performance of weak classifiers. In contrast with bagging, which is a parallel procedure, boosting is a sequential deterministic procedure. It operates by assigning different weights to different training set patterns according to their intrinsic (estimated) accuracy. For further progress with these techniques, see Rätsch et al. (2002), Fischer and Buhmann (2003), and Lockton and Fitzgibbon (2002). Finally, Beiden et al. (2003) discuss a variety of factors involved in the training and testing of competing classifiers; in addition, much of the discussion relates to multivariate ROC analysis.

Li and Zhang (2004) describe how a new boosting algorithm “FloatBoost” has been applied to produce the first real-time multiview face-detection system reported. The method uses a backtrack mechanism after each iteration of AdaBoost learning to minimize the error rate directly; it also uses a novel statistical model for learning the best weak classifiers and a stagewise approximation to the posterior probability, thereby requiring fewer weak classifiers than AdaBoost. Gao et al. (2010) report on a modified version of AdaBoost to resolve the key problems of how to *select* the most discriminative weak learners and how to optimally *combine* the selected weak learners. Experiments confirm the utility of the algorithm including the capability to solve these two key problems; both synthetic and real scene data (car and noncar patterns) are used for the tests. Fumera et al. (2008) present a theoretical analysis of bagging as a linear combination of classifiers, thereby giving an analytical model of bagging misclassification probability as a function of ensemble size.

Decision trees provide a convenient fast-operating method of pattern recognition, and the methodology has developed quite rapidly in recent years. Chandra et al. (2010) describe a new node-splitting procedure called the distinct class-based splitting measure (DCSM) for decision tree construction.

Node-splitting measures are important as they help to produce compact decision trees with improved generalization abilities. Chandra et al. have shown that DCSM is well behaved and produces decision trees that are more compact and provide better classification accuracy than trees constructed using other common node-splitting measures. The DCSM measure also helps with pruning (which produces compact trees with better classification accuracy). Köktas et al. (2010) describe a multiclassifier for grading knee osteoarthritis using gait analysis. It employs a decision tree with multilayer perceptrons (MLP) at the leaves. In fact, three different MLPs (different “experts”) with binary classifications are employed at different leaves of the tree. They showed that, for this type of data, this produced better results than a single multiclass classifier. Rodríguez et al. (2010) describe tests made on a large number of datasets using ensemble methods to generate more accurate classifiers. They show that, for multiclass problems, ensembles of decision trees (“forests”) can successfully be combined with ensembles of nested dichotomies. The direct approach, using ensembles of nested dichotomies with a forest method as the base classifier, can be improved using ensemble methods with a nested dichotomy of decision trees as the base classifier.

Fawcett (2006) produced an excellent, largely tutorial summary of ROC analysis in which many descriptors employing true and false positives and negatives are used; a valuable feature of the paper is the unification of a subject in which many apparently different descriptors appear with different names according to the varying backgrounds of the workers. In particular, the recently much more widely used terms “precision” and “recall” are related to “sensitivity,” “specificity,” “accuracy,” and others (for definitions and further discussion of these performance measures, see [Section 14.13.1](#)). In addition, measures such as “F-measure” are defined, and problems and pitfalls of using ROC graphs are pointed out. Ooms et al. (2010) underline the value of Fawcett’s summary but show that the ROC concept is limited and is not an optimal measure for *sorting* as distinct from cases where *misclassification costs* are the main concern. They propose a sorting optimization curve (SOC) to cope with sorting problems and help identify the best choice of operating point in that case. In contrast with the ROC curve which plots *FP* rate versus *FN* rate or *TP* rate versus *FP* rate, the SOC curve plots yield rate ( $Y$ ) versus relative quality improvement rate ( $Q$ ), where  $Y = (TP + FP)/(P + N)$ : this formula arises because no distinction is made between true and false positives when selling a product. Quality  $Q$  is defined in terms of the precision  $Pr = TP/(TP + FP)$ , viz.  $Q = f(Pr)$ , and uses whatever function  $f$  is needed to achieve this when sorting a particular commodity (such as apples). Typically, optimization involves moving up the  $Y$  versus  $Q$  curve until reaching the lowest level of quality that is acceptable or legal.

Assessing the quality of the ROC curve has acquired some importance in the past decade or so, and the AUC measure has been the main performance indicator for this (Fawcett, 2006). For example, Hu et al. (2008) have used it to advantage for optimal evaluation and selection of features.

---

## 14.16 PROBLEMS

1. Give a complete proof of Eq. (14.17).
2. Give complete proofs of the three equations listed as Eq. (14.23).
3. Prove the statement made following Eq. (14.70), that this population minimizer applies for any loss function of the form  $g(e^{-yF(x)})$  and determines any restrictions on the function  $g(\cdot)$ , including its range of values and gradients.
4. Repeat the calculation following Eq. (14.75) and determine whether the two  $2$ s included in this equation are really necessary, i.e., whether they affect the final outcome.
5. Why is the point on a ROC curve closest to the origin *not* the point that minimizes total error? Prove that the point that minimizes the total error on a ROC curve is actually the point where the gradient is  $-1$  (see Section 14.13).
6. Consider the four quantities  $TP$ ,  $TN$ ,  $FP$ ,  $FN$  defined in Section 14.13. Arrange them in order of size for situations where positives are rare and recognition errors are likely to be low. If the rates  $tpr$ ,  $tnr$ ,  $fpr$ ,  $fnr$  are also arranged in order of size, will the order be the same as for  $TP$ ,  $TN$ ,  $FP$ ,  $FN$ ?
7. Compare the shapes of ROC curves and *precision–recall* curves for identical classifiers. What mathematical relations link their shapes? Determine whether the ROC curves for two classifiers will cross each other the same number of times as the *precision–recall* curves.
8. Prove that Eq. (14.109) provides a mathematically sound way of combining *precision* and *recall* into a single measure. What are the mathematical criteria that need to be considered?

This page intentionally left blank

This chapter introduces deep-learning networks. It starts with the observation that convolutional neural networks (CNNs) have gradually taken over from the more general artificial neural networks (ANNs) described in [Chapter 13](#), Basic Classification Concepts and develops ideas on CNN architectures. With the aid of a number of key case studies, it gives reasons for the sudden explosion in the application of CNNs to classification and segmentation and also points to valuable progress being made in other areas such as automatic image caption generation.

*Look out for:*

- reasons why CNNs give improved performance over earlier types of ANN
- design of typical CNN architectures
- technical features such as depth, stride, zero padding, receptive field and pooling
- ways in which AlexNet was an improvement over LeNet
- how Zeiler and Fergus improved AlexNet still further
- how VGGNet achieved even better performance
- the value of deconvolution networks (DNNs) for visualizing the operation of CNNs
- the role of pooling and unpooling in CNN–DNN (encoder–decoder) nets
- how CNN–DNN nets are able to perform semantic segmentation
- how recurrent neural networks (RNNs) are used for tasks like image annotation.

One of the reasons why interest in the early ANNs waned was lack of knowledge about their internal operation and fear that they would be failure-prone because of improper or inadequate training. Eventually, such fears were dispelled by use of DNNs to help visualize the internal workings of CNNs. Coupled with this were the vastly greater datasets that have gradually become available. Today, it looks as if the future of deep networks is assured: the current problem is finding out in quite what ways they should be used vis-à-vis more conventional approaches.

## 15.1 INTRODUCTION

The original aim of designing ANNs was to emulate what is known to happen in the human brain, when information passes from the eyes, first to the lateral geniculate nuclei and then to the visual cortex, being processed in sequence by areas V1, V2, V4, IT (the inferior temporal cortex), and onward, until recognition is achieved and acted upon. All this appeared to happen so straightforwardly in the



human brain—whole scenes being analyzed “at a glance” with no apparent effort—that it seemed worthwhile attempting it in computerized systems. Clearly, an ANN should emulate the human visual system and should consist of a number of layers, each modifying the data, first locally and then by larger and larger sets of neurons until tasks such as recognition and scene analysis are achieved. However, in the early days, full control of ANNs tended to be restricted to very few layers: indeed, a working maximum depth consisted of one input layer, three hidden layers, and one output layer—though it was later found that it should never be necessary to use more than two hidden layers, and that many basic tasks could be tackled using a three-layer network with a single hidden layer (see [Section 13.12](#)).

One of the reasons for the restriction to few layers was the credit assignment problem, which meant that it became trickier to train many layers “through” others, and at the same time, more layers meant more neurons to be trained and more computation being required to complete the task. All this being so, ANNs tended to be called on to carry out only the classical recognition process and to be fed by standard feature detectors applied in earlier nonlearning layers. Thus, the standard paradigm was that of an image preprocessor, followed by trained classifier ([Fig. 15.1](#)). As very good feature detectors could be designed by hand, this did not cause any obvious problems. However, as time went on, there was pressure to do full-scale scene analysis of real scenes, which could contain images of many types of object in many positions and poses. Thus, there was a growing need to move to much more complex multilayer recognition systems for which the early types of ANN were simply inadequate. At the same time, it became desirable to train the preprocessing system itself, so that it closely matched the requirements of the following object analysis system; clearly, it was becoming necessary to produce integrated multilayer neural networks.

Meanwhile, some workers tried other types of classifier, and ANNs were gradually ousted, support vector machines (SVMs) providing a valuable alternative: the old type of ANN was no longer up to the task and was eschewed. This happened in the late 1990s. In fact, ANNs had also had another problem, in that a “suck-it-and-see” approach was necessary when applying them to any new task: i.e., there was no scientifically based rationale for determining how many neurons or layers would be needed, how much training would be needed, or indeed quite how complex the training set would have to be. (Looking at this in another way, the ideal profile of the network was unknown: in practice profiles varied—some



**FIGURE 15.1**

Classic paradigm for a classification system. The main function of the classic image preprocessor was to perform feature detection, using hand-coded, nonlearning procedures. The trained classifier would typically use ANNs trained by backpropagation.

networks being narrow and some wide in the middle.) Neither was it understood how ANNs were working internally, and few, if any methods for achieving a true scientific analysis of their operation were available. This meant that industrialists and others who might be in a position to apply them in anger did not know how reliable they would be or have the confidence to use them in real applications. In summary, traditional ANNs fell out of favor, the main reasons being the following:

1. Effective training was limited to a small number of layers and nodes per layer.
2. They had to be trained on carefully selected sets of samples, which tended to impose limits on the amount of training that could be done.
3. Their operation was not sufficiently underpinned by scientific analysis.
4. It was never certain how reliable they would be in practice, and there was significant fear that training would end up focusing on local minima.
5. SVM and other techniques had been found to outperform them.
6. In spite of the attempt to emulate biological systems, they did not scale well to direct application to large images.
7. Their architecture gave poor spatial invariance across images.

In the last case, the poor invariance arose was because in each hidden layer, the neurons were individually trained: each neuron saw different training data from the other neurons in its layer, and in any case the weights needed to be initialized randomly. This was a significant disadvantage, as it is highly preferable that the same decision should be made about any object wherever it appears in an image. The scaling problem (item 6) was also particularly serious because finding correlations between objects in a large image (e.g., finding a vehicle by locating its four wheels) required networks that scaled in size and complexity with (at least) the square of the image dimensions: it is one thing to apply an ANN to a  $20 \times 20$ -pixel image of a numeral in a box, and quite another to apply an ANN to a  $400 \times 400$ -pixel image which might well require many more hidden layers.

Overall, it was becoming clear that a different type of architecture was required to handle these direct imaging problems: in particular, it had to have spatial invariance and also it had to be able to correlate data over several scales. In principle, such a scheme would probably best be handled by starting with wide networks the same size as the input image, and looking at their outputs using smaller networks, and so on until the final layer—perhaps even a single connection—would indicate for example, that there is a fire somewhere in the viewed scene; alternatively, a small output interface could indicate where all the relevant objects are and identify them—as in the case of faces or car wheels.

In fact, there were several variants on the basic ANN idea in the late 1990s, but few of them were taken very seriously at the time and most of them died along with the other ANNs. (One should not take their “death” too literally: it merely means that they fell out of use and were effectively dead.) Nevertheless, some aficionados continued working on alternative architectures, one of which

was the CNN. This was to come to the forefront in the late 2000s, and particularly in 2011 and 2012, when the tide turned around completely, as we shall see below. The day of “deep” learning networks had finally arrived—a *deep network* being defined as one with more than three nonlinear hidden layers, which placed them beyond the scope of regular ANNs. (In an extension of this metaphor, a *very deep network* is defined as one having more than 10 hidden layers.)

---

## 15.2 CONVOLUTIONAL NEURAL NETWORKS

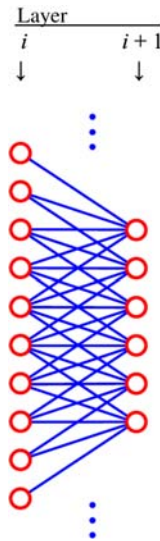
CNNs depart from regular ANNs in a number of key ways, which are as follows:

1. CNN neurons have local connectivity, so they do not have to be connected to *all* the outputs from the previous layer of neurons.
2. Their input fields can overlap.
3. In any layer, neurons have the same weight parameters across the whole layer.
4. CNNs abandon the old sigmoidal output function and instead use the rectified linear unit (ReLU) nonlinear function (though each convolutional layer does not have to be fed directly to a ReLU layer).
5. They intersperse convolution layers with subsampling or “pooling” layers.
6. They may have normalization layers to keep signals from each layer at suitable levels.

However, they still use supervised learning, and they still train the network by backpropagation.

Now let us consider the above differences in more detail. First, we note that a network of the general ANN type multiplies each input by an already determined weight and adds them all together. Next, if the neurons and weights are identical across a whole layer (see item 3), the resulting mathematical operation is by definition a convolution—hence, the term CNN. Regarding the overlap condition (item 2), if a given layer is to have the same dimensions as the previous layer, the input fields at each pixel will overlap almost completely (see Fig. 15.2). Interestingly, in this book, we have already seen many examples of convolutions, notably for feature detection—prominent examples being edge, corner, and interest point detection—though in each of these cases the convolutions are followed by nonlinear detectors. Item 4 deals with the necessary nonlinearity. ReLU means Rectified Linear Unit and is a nonlinear function defined by  $\max(0, x)$  (see Fig. 15.3), where  $x$  is the output value of the immediately preceding convolution layer (in fact, the ReLU shadows each output connection and is a 1-to-1 filter).

Pooling (item 5) involves taking all the outputs from a locality and deriving a single output from them: usually, this takes the form of a sum or maximum operation on all the inputs. It is generally carried out in  $2 \times 2$  or  $3 \times 3$  windows, the former being more common, and the maximum pooling operation is more common than the sum (or averaging) operation. In each of the latter pairs of options,

**FIGURE 15.2**

Part of a convolutional neural network. Note that the input fields of the neurons in layer  $i+1$  overlap almost completely as they progress from layer  $i$ : here, the inputs to adjacent neurons in layer  $i+1$  differ in at most 1 connection (the difference would be somewhat greater in 2-D). In this case, the input fields of the output neurons all have value 5.

**FIGURE 15.3**

The ReLU nonlinear function  $\max(0, x)$ . The function operates independently on all output connections of the immediately preceding CNN layer.

the aim is to modify the data minimally, so as to remove a significant proportion of the redundancy in a particular layer of the network, while at the same time keeping the most useful data. (Use of a maximum operation may seem somewhat surprising, as finding the maximum of a set of numbers is more likely than averaging to accentuate impulse noise: on the other hand, many convolutions contain a modicum of smoothing/low pass filtering, so the max operation need not degrade the final output significantly.)

Note that all the listed changes to the original ANN format fall within the same linear mathematical  $(\sum_i w_i x_i)$  specification, except where ReLU or pooling

operations are carried out. However, the latter still permit signal gradients to be passed through the system, so backpropagation can be applied in exactly the same way as for ANNs.

It ought to be added that several convolutional layers can be placed immediately after one another. In fact, this is equivalent to a single larger convolution. Although this arrangement may appear pointless, it can strongly affect the overall computational load. For example, three  $3 \times 3$  convolutions are equivalent to a single  $7 \times 7$  convolution: this means applying 27 operations instead of 49 operations, so the former implementation would appear to be more suitable. On the other hand, when the CNN calculation is implemented on a graphics processing unit (GPU—see below), this is not necessarily the case.

Overall, we can see that CNNs provide reasonable alternatives to ANNs. In addition, they seem better adapted to the model presented in [Section 15.1](#), of moving steadily from local to global operations on images, and looking for larger and larger features or objects in the process. It is also worth emphasizing that the spatial invariance achieved by CNNs is particularly valuable and is not realizable with ANNs.

Although proceeding through the network takes us from local to more global operations, it is also common for the first few layers of a CNN to look for specific low-level features: Hence, these will typically have sizes matching that of the image. Further on in the network, it is common for pooling operations to be applied, thereby reducing the sizes of subsequent layers. After several stages of convolution and pooling, the network will have narrowed down considerably, so it is possible to make the final few layers fully connected—i.e., in any layer, each neuron is connected to *all* the outputs of the previous layer. At that stage, there are likely to be very few outputs, and those that remain will be dictated by whatever parameters must in the end be supplied by the network: these may include classifications and associated parameters such as the absolute or relative positions.

Another master-move on progressing from ANNs to CNNs is that bringing in spatial invariance greatly reduces the number of weights in the network. This makes training far more straightforward and drastically decreases the computational load for a given size of network. For a receptive field width of  $R$ , there will be only  $R$  parameters per layer, compared with a total of  $W$  in the case of an ANN. When processing 2-D images, the corresponding numbers are squared, and we have to compare  $R^2$  with  $W^2$  (or strictly, with  $WH$ —see the following section). Thus, we see the computational load increasing rapidly with image size for ANNs, but staying at the same low value for CNNs. In addition, the ReLU function is simpler than the ANN sigmoid function and this also speeds up processing. Indeed, it is difficult to imagine a simpler calculation than the ReLU—as we can see from the 1-line routine needed to implement it: if  $(x < 0)$  output = 0 else output =  $x$ . In contrast, the sigmoid function can be written in one line as output =  $\tanh x$ , though this is misleading as the  $\tanh$  function requires far more computation. Finally, the ReLU avoids the saturation problems that ANNs are

subject to [a neuron giving an output close to the limits ( $\pm 1$ ) of the tanh function tends to get stuck at the same value because there is no gradient to guide the backpropagation algorithm away from it]. Indeed, the ReLU gradient is constant over the input range  $x \geq 0$ , and the fact that it is not attenuated over part of this range tends to speed up learning.

### 15.3 PARAMETERS FOR DEFINING CNN ARCHITECTURES

When analyzing CNN architectures, there are a number of points that deserve attention. In particular, several quantities and terms need to be defined—*width*  $W$ , *height*  $H$ , *depth*  $D$ , *stride*  $S$ , *zero padding*  $P$ , and *receptive field*  $R$ . In fact, the width and height are merely the dimensions of the input image, or else the dimensions of a specific layer of the neural network. The depth  $D$  of the network or of a specific block in it is the number of layers it contains.

The width  $W$  and height  $H$  of a layer are the numbers of neurons it has in each dimension. The stride  $S$  is the distance between adjacent neurons in the output field measured in units corresponding to the distance between adjacent neurons in the input field (see Fig. 15.4): stride  $S$  can be defined along the width and

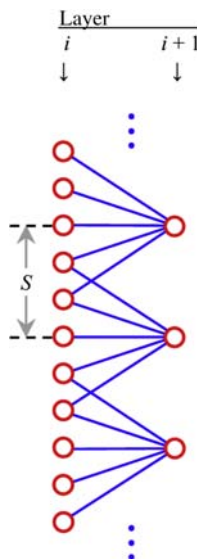


**FIGURE 15.4**

Illustration of the stride distance  $S$ .  $S$  is defined as the distance between adjacent neurons in the output field measured in units corresponding to the distance between adjacent neurons in the input field. Here, it is indicated by the length of the double-ended arrow. In this case, the input fields of the output neurons all have value 5, and the stride has value 3.

height dimensions but is usually the same for each. If  $S = 1$ , adjoining layers have the same dimensions (but see below how the size of the receptive field  $R$  can modify this). Note that increasing the stride  $S$  can be useful, as this saves memory and computation. In principle, it achieves a similar effect to pooling. However, pooling involves some averaging, while increasing the stride merely decreases the number of samples taken.

$R_i$  is the width of the receptive field for each neuron in level  $i$ , i.e., the number of inputs for all neurons in that level. Zero padding is the addition of  $P$  “virtual” neurons providing static inputs at each end of the width dimension (here we simplify the analysis by considering only the width  $W$  of each layer, and the placement of neurons across it: ignoring the height dimension involves no loss of generality). The zero padding neurons are given fixed weights of zero, the idea being to ensure that all neurons in the same layer have equal numbers of inputs, thereby facilitating programing. However, it also ensures that successive convolutions don’t lead to smaller and smaller active widths; in particular, when  $S = 1$ , it permits us to make the widths of adjacent layers exactly equal (i.e.,  $W_{i+1} = W_i$ ). Zero padding is actually the same concept that was used in [Section 2.4](#) on image processing.

A simple formula connects several of these quantities: see Eq. (15.1). (It is left as an exercise for the reader to prove this formula, which is a straightforward task once the significance of each of the parameters is fully understood.)

$$W_{i+1} = (W_i + 2P_i - R_i)/S_i + 1 \quad (15.1)$$

where the suffices pertain to the inputs to layer  $i$  and the outputs feeding layer  $i+1$ . It is worth underlining the null situation  $W_{i+1} = W_i$  that applies when  $S_i = 1$ ,  $R_i = 1$ , and  $P_i = 0$ . (These values can be taken as base values for the design of architectures, though the next step will normally be to increase  $R_i$  to a higher value.)

By way of example, if  $W_i = 7$ ,  $P_i = 1$ ,  $R_i = 3$ , and  $S_i = 1$ , we get  $W_{i+1} = 7$ , which justifies the statement made earlier—namely that  $W_{i+1} = W_i$  if  $S_i = 1$ . Next consider what happens when  $S_i$  is changed to 2 without altering the other parameters: in that case, we find  $W_{i+1} = (7 + 2 - 3)/2 + 1 = 4$  ([Fig. 15.5](#)). Now consider what happens when  $W_i$  is changed to 9: we then find that a stride of 3 will not work (the result is not an integer) because it will not fit the width of the following layer:  $W_{i+1} = (9 + 2 - 3)/3 + 1 = 3.67$ . As a result, data will be lost around the edges of the image. This situation could be tackled by having different padding values (e.g., larger at the right of the image), though when  $R_i$  has a low value, the larger of the two padding values would probably not work well (the increased numbers of zeros in the corresponding receptive fields would eliminate too much information). This situation is illustrated by the last example, but now replacing  $P_i = 1$  with  $P_{iL} = 1$  and  $P_{iR} = 2$  leads to a

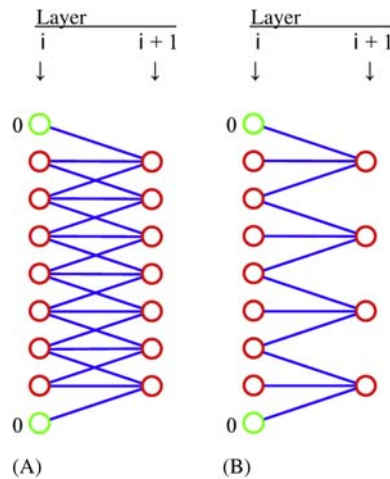


**FIGURE 15.5**

Details of the use of stride and zero padding for a small CNN. Part (A) shows how a seven-neuron layer is connected to the following seven-neuron layer in a case where a single “virtual” neuron (marked green) is applied at either end of the input layer to ensure that all the output neurons have the same number of input connections  $R$ . Part (B) shows what happens when the stride is increased to 2. In each case, the padding parameter  $P=1$  and  $R=3$ . (See also [Table 15.1](#), rows 2 and 3.).

width  $W_{i+1} = (9 + 1 + 2 - 3)/3 + 1 = 4$ . Here, we have used a slightly more general version of [Eq. \(15.1\)](#):

$$W_{i+1} = (W_i + P_{iL} + P_{iR} - R_i)/S_i + 1 \quad (15.2)$$

Overall, the purpose of padding is to (systematically) allow for end effects at the extremes of each layer, by ensuring that the number of zeros is adjusted to accommodate the desired stride and receptive field values. A summary of all the cases discussed above appears in [Table 15.1](#).

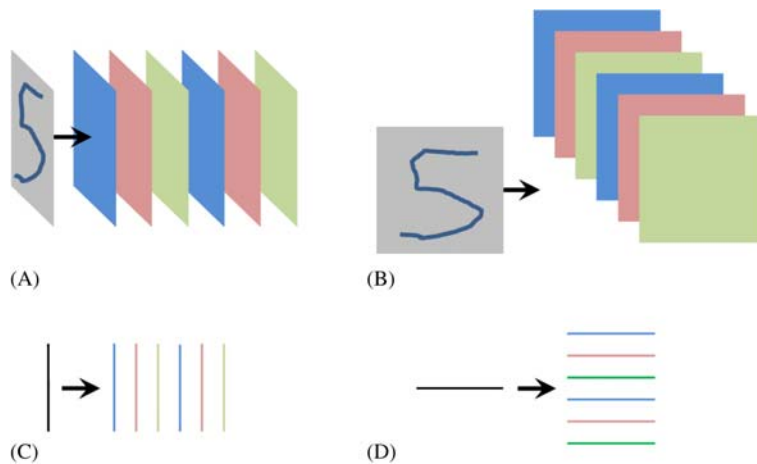
Finally, an important point must be made about the definition of the depth of a number of layers of a CNN. The earlier discussion has implied that a number of adjacent layers of a CNN are normally accessed one after another in sequence—as would indeed be the case if larger and larger convolutions were implemented one after another in an effort to detect larger and larger features or even objects. However, there is another possibility—that the various layers are fed in parallel from a given starting point in the network, for example, the input image. [Fig. 15.6](#) contrasts these two possibilities. The second possibility arises typically when an image is to be searched for a variety of different features, such as lines, edges, or corners, and the results fed in parallel to a more holistic detector. We shall see below that this strategy was adopted in the LeNet architecture, which LeCun and others developed to identify handwritten numerals and zip codes.



**Table 15.1** Consistency of CNN Parameters

$W_i$	$S_i$	$R_i$	$P_{iL}$	$P_{iR}$	$W_{i+1}$	Comment
7	1	1	0	0	7	Null case
7	1	3	1	1	7	
7	2	3	1	1	4	
9	3	3	1	1	3.67	Incorrectly mapped
9	3	3	1	2	4	$P_{iL} \neq P_{iR}$
9	3	3	0	0	3	

This table shows the values of various parameters and how they affect the number of outputs fed to the following layer of neurons. Definitions of the parameters and discussions of most of the examples below are given in the text (see also Fig. 15.5). The results are calculated using Eq. (15.2), which permits different padding values at opposite ends of the width dimension. The purpose of the formula is to permit rigorous checks to be made of the consistency of the architectural parameters: specifically, nonintegral values of  $W_{i+1}$  indicate that the architecture is incorrectly mapped.

**FIGURE 15.6**

Visualizing depth in a CNN. Part (A) shows how an input image is applied to the first layer of a CNN: it is implied by the layout that the image is processed in turn by the six layers of the network. Part (B) shows how the image information could instead be fed in parallel to all six layers, in which case, they would act independently to locate six different sets of features in the input image. Both layouts are valid and can be represented, respectively, by the line diagrams in (C) and (D): for simplicity, the height dimension is not shown in these diagrams so that the width and depth can easily be visualized. In this example, both types of depth have the value 6.

## 15.4 LECUN *ET AL.*'S LENET ARCHITECTURE

In 1998, LeCun *et al.* published the now landmark case of a CNN that employed many of the stages noted above (Fig. 15.7). The input image was fed in parallel to a stack of 6 layers performing convolution operations, each immediately being followed by its own subsampling (pooling) layer; the 6 pooling layers were followed by another stack of 16 convolution layers, each followed by its own pooling layer; there then followed a sequence of two fully connected convolution layers which in turn were fully connected to a final output network containing a radial basis function (RBF) classifier.

The details of this architecture are presented in Fig. 15.7 and Table 15.2: These two forms of presentation are provided as an aid to understanding the complexities of the overall LeNet architecture, and to be sure that there is no in clarity as to what is being done. *Why* it is being done in this way is another important question which we shall also aim to understand. But first, we attend to the *what* aspect and consider some of the design features in detail:

1. The six hidden layers in LeNet are labeled C1, S2, C3, S4, C5, F6, where “C,” “S,” and “F” indicate respectively convolution, subsampling (pooling),

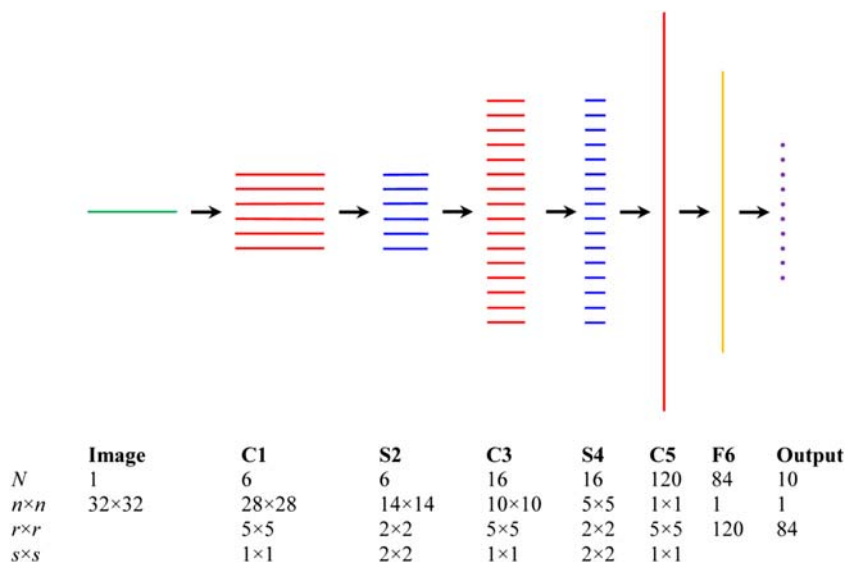


**FIGURE 15.7**

Schematic of the LeNet architecture. This schematic carries much the same information as Table 15.2: both are provided as an aid to understanding the details of the overall LeNet architecture.  $N$  indicates the number of layers of each type;  $n \times n$  indicates the dimensions in the case of a 2-D image format;  $n \times n$  indicates the dimensions in the case of a 2-D image format; and  $r \times r$  is the size of a 2-D neuron input field (a single number indicates that the input is abstract 1-D data). Layers C5, F6, and Output are fully connected to each other.

**Table 15.2** Summary of the LeNet Connections and Trainable Parameters

Layers	Layer Size	Connections			Parameters		
	$N: n \times n$ $r \times r$	Inputs	Outputs	Total	Inputs	Outputs	Total
Image	1: $32 \times 32$		1024 ( $32^2$ )	1024			
<b>C1</b>	6: $28 \times 28$ $5 \times 5$	117,600 ( $6 \times 28^2 \times 5^2$ )	4704 ( $6 \times 28^2 \times 1$ )	122,304	150 ( $6 \times 5^2$ )	6 ( $6 \times 1$ )	156
S2	6: $14 \times 14$ $2 \times 2$	4704 ( $6 \times 14^2 \times 2^2$ )	1176 ( $6 \times 14^2 \times 1$ )	5880		12 ( $6 \times 2$ )	12
<b>C3</b>	16: $10 \times 10$ $5 \times 5$	150,000 ( $60 \times 10^2 \times 5^2$ )	1600 ( $16 \times 10^2 \times 1$ )	151,600	1500 ( $60 \times 5^2$ )	16 ( $16 \times 1$ )	1516
S4	16: $5 \times 5$ $2 \times 2$	1600 ( $16 \times 5^2 \times 2^2$ )	400 ( $16 \times 5^2 \times 1$ )	2000		32 ( $60 \times 2$ )	32
<b>C5</b>	120: $1 \times 1$	48,000	120	48,120	48,000	120	48,120
(f.c.)	$5 \times 5$	( $120 \times 16 \times 5^2$ )	( $120 \times 1$ )		( $120 \times 16 \times 5^2$ )	( $120 \times 1$ )	
<b>F6</b>	84: 1	10,080	84	10,164	10,080	84	10,164
(f.c.)	120	( $84 \times 120$ )	( $84 \times 1$ )		( $84 \times 120$ )	( $84 \times 1$ )	
Outputs	10: 1	840	10	850	(Excludes RBF parameters)		—
(f.c.)	84	( $10 \times 84$ )	(10)				
<b>Total</b> (C,F,S only)		331,984	8084	340,068			60,000

LeNet has six hidden layers between the image layer and the output layer. This table gives details of the connections and the numbers of trainable parameters in each layer. Column 1 gives the name of each layer—"C," "S," and "F," indicating respectively convolution, subsampling (pooling), and fully connected convolution. The following sets of layers are fully connected (f.c.) to each other: S4–C5, C5–F6, and F6–Outputs. In each case, Column 2 indicates the number of layers N and their dimensions:  $n \times n$  indicates the sizes of the layers for 2-D image format, a bare "1" indicating that a layer has abstract (1-D) format;  $r \times r$  indicates the convolution or subsampling window size. Columns 3–5 and 6–8 give the numerical values and also show, in brackets, how they are calculated. For justification of the numbers 60, 120, and 84 appearing in some of the calculations, see text. For convolutions C1, C3, and C5, the padding parameter  $P = 2$ .

and fully connected convolution. Thus, convolution and subsampling layers alternate until C5 is reached: at that point (i.e., from layer S4 onward), the network becomes fully connected, and further subsampling layers are not needed, as *every* input connection is trained. (This explains why the numbers in the “Parameters” columns become identical to those in the “Connections” columns in Table 15.2.) S4 cannot be described as fully connected as that applies only to its outputs.

2. In Table 15.2, column 2 indicates the number of layers  $N$  of each type and their dimensions:  $n \times n$  indicates that the layer has 2-D image format; a bare “1” indicates that it has abstract (1-D) format;  $r \times r$  indicates the input field of each neuron. The purpose of Table 15.2 is to give details of the connections and the numbers of trainable parameters in each layer. Columns 3–5 and 6–8 give the numerical values and also show, in brackets, how they are calculated.
3. In principle, the convolution inputs and outputs should match, i.e., the numbers of inputs should be  $r \times r$  times the numbers of outputs. In fact, this only happens for C1. In the other three cases, we also have to take account of the following:
  - a. For C3, an attempt is made to look not just at one previous layer but at all previous layers. However, this would require inordinate amounts of computation, so a feature map is used in which the actual number of features selected is limited to 60—as indicated in detail in Table 15.3.
  - b. For C5, there is a question as to why 120 layers have been used, as the LeCun *et al.* (1998) paper doesn’t clarify this (but note that the layers are situated along the depth dimension and can nevertheless be considered as neurons). However, C5 is fully connected, and it seems likely that 120 layers constituted the largest reasonable number that could be fully connected (in the list of connections and trained parameters in Table 15.2,

**Table 15.3** How the 6 Feature Maps From S2 are Fed to the 16 C4 Inputs

	1	2	3	4	5	6		7	8	9	10	11	12		13	14	15		16
1	+				+	+	1	+			+	+	+	1	+		+	1	+
2	+	+				+	2	+	+			+	+	2	+	+		2	+
3	+	+	+				3	+	+	+			+	3		+	+	3	+
4		+	+	+			4	+	+	+	+			4	+		+	4	+
5			+	+	+		5		+	+	+	+		5	+	+		5	+
6				+	+	+	6			+	+	+	+	6		+	+	6	+

*This table indicates (by + signs) how outputs from S2 layers are selected as inputs to the C4 layers. This is achieved by combining the following selections, containing respectively 18, 24, 12, and 6 values to be carried across from S2 to C3, the total being 60. This is many more than could come from one layer of S2 but many less than the 96 that would come from full connection. The reasons for employing this sampling technique are not only to reduce memory and computation but also to include an element of randomness by breaking symmetry (too regular an arrangement might give more chance of missing important combinations of features).*

120 is multiplied by 485, which leads to a total of 58,200 connections and parameters).

- c. For F6, the main consideration is making the convolution fully connected, and the number of inputs is no longer described as  $r \times r$  but has the 1-D value 120. The number 84 arose because the output of layer F6 returns to image format with a  $7 \times 12$  image array giving a stylized rendition of the digit in the input image. It turns out that this is useful as the usual 1-of- $N$  code for classifying characters has insufficient redundancy to distinguish between dozens of possibilities: this made it better practice to convert to a stylized character format, even though the LeNet was tested primarily on digits.
4. The final output interprets the stylized  $7 \times 12$  image array as one of 10 digits, using a RBF operator to make the classification.
5. The subsampling layers S2 and S4 have  $2 \times 2$  inputs and perform an averaging operation. They also include a learning function with just two parameters, which respectively apply a trainable multiplying factor and a trainable bias value.
6. The  $5 \times 5$  output from S4 results in C5 having a single ( $1 \times 1$ ) neuron per layer. However, it was felt preferable to take C5 as providing a 2-D output, in case the network was later increased in size. Nevertheless, given the architecture as presented in Fig. 15.7 and Table 15.2, C5 is fully connected and has been marked as such in the table.
7. “Fully-connected” means that any layer is fully connected at its inputs. (By convention, fully connected layers do not use padded inputs but merely connect all relevant inputs and outputs that contain actual signals.) We can now write down the following simple relation between the numbers of inputs and outputs:

$$\text{inputs}_{i+1} = \text{outputs}_i \times \text{outputs}_{i+1} \quad (15.3)$$

This can be used to confirm the self-consistency of the fully connected parts of a CNN architecture and gives correct values for the numbers of input connections of C5, F6, and Output. However, when applied to C3, and ignoring the padding inputs, it gives the following input value:  $\text{inputs}_{C3} = 96 \times 10^4$ , which is much greater than the value given in Table 15.2 ( $15 \times 10^4$ ). This shows that C3 is far from being fully connected.

8. As a further check on the self-consistency of the architecture, we can check that the following rule applies for layer  $S_i$ , where  $i = 2$  or 4

$$\text{inputs}_i = \text{outputs}_{i-1} \quad (15.4)$$

Having dealt with the details of the architecture, it will now be useful to see why this particular architecture was chosen for the given task of numerical digit recognition.

In the handwritten Zip code and digit recognition scenario, digits appear as imprecisely located signs that are also imprecisely scaled; furthermore, they are

subject to a myriad of style variations and distortions: the latter include local malformations, incorrectly placed dots, crosses, joins, and a modicum of noise that might already be on the paper or inadvertently added after drawing, in the form of smudges, blotches, or specks of food. All these factors make it difficult for a human to read the codes correctly—and arguably no less difficult for machines. To solve these problems, it is useful to start by ensuring that reading algorithms have spatial, scale, and distortion invariance.

Fortunately, CNNs have spatial invariance built into them by the use of convolution—the same small kernel being replicated and applied right across any specific CNN layer. Similarly, many of the variations caused by scale, style, and distortion changes can be alleviated by eliminating the need for exact correspondence between the positions of small features. In particular, stacks of convolution layers each of which detects a different subfeature—such as line segments of various orientations, endpoints, crossings, and corners—can be combined in ways that are insensitive to slight changes in position. This is achieved by introducing subsampling (pooling) layers between convolutions. Thus, we can see that the LeNet architecture embodies the most important invariances by its use of stacks of convolution and pooling layers. In fact, many of the problems cited above are random in nature, and the simplest way of tackling them is by training the network on large quantities of data. However, there is one more technique that can help with this, and that is normalization of the input data by ensuring that the pooling layers also employ a trainable multiplicative coefficient and a trainable bias before passing the data through a sigmoid function. Note that if a sigmoid function is made too wide, it will become linear, tending to make the whole network linear and unable to make strong decisions; whereas if it is made too narrow, it will lose its linearity, and backpropagation training will become slow and inefficient: Clearly, a balance has to be struck between these two extremes, and it is desirable for the network to be able to make its own decisions about the best working point by learning the relevant parameters.

Next, although each pooling layer averages the inputs from the previous convolution layers and follows this by multiplying by a trainable parameter as well as adding a trainable bias, the relative weights of the inputs also have to be trained: this mechanism is required to ensure that the inputs are finely balanced for the best performance. This is achieved by including a further trainable multiplicative weight at the output of each convolution layer—as indicated in the column marked “output parameters” in [Table 15.2](#).

In LeNet, we can now interpret layers C1–S4 as multiple stages of feature detection in image space (or in reduced scale versions of image space); in addition, we can interpret the subsequent layers as performing more abstract feature detection processes—no longer being tied to image space—and resulting in classification of the digits presented in the input images. Apart from the final RBF layer, this rather complex network was trained using the standard backpropagation algorithm: in spite of its overall depth, training did not prove intractable—as it would have been if an ANN of this size had been used. In fact, as we can now

see, the design was put together in a hand-crafted way, the various numbers of layers and their sizes being adjusted to cope optimally with Zip code and digit identification. Although the detailed weights were obtained by large amounts of training, the architecture itself was built using logic and expertise in understanding the underlying problem.

Perhaps the most interesting thing about the design is that the network is deliberately made to look for large features with *reduced* location accuracy, and if any larger network were to be devised along the same lines, this principle would probably have to be extended further.

---

## 15.5 KRIZHEVSKY *ET AL.*'S ALEXNET ARCHITECTURE

AlexNet was designed specifically to target the ImageNet Challenge, which took place in 2012. (This statement is not meant to belittle the on-going projects being conducted in the designers' laboratories. However, such a challenge necessitates that, for a while, huge efforts are devoted to targeting the specific problem in hand—in this case, the ImageNet Large-Scale Visual Recognition Object Challenge (ILSVRC) in 2012.) In general, such challenges are extremely valuable as they force competitors to reach into the inner recesses of available knowledge and technology and come up with new approaches and new ideas that give the chance of making dramatic progress. Indeed, the extreme nature of these challenges leads to the possibility of making radical developments to the underlying science, and also of making breakthroughs in the technology. Nevertheless, it is best to be circumspect as one or two of the characteristics of a winning solution could still be ad hoc in nature, and therefore not worthy of slavish replication in future systems.

In this case, the AlexNet designers (Krizhevsky et al., 2012) seem to have made sound achievements at every level. First, they found it necessary to eliminate any inhibitions about using a by then quite old schema based on CNNs which hadn't obviously been at the forefront of classification research, and forcing it into shape as a winning approach. To achieve this, they had to radically improve the CNN architecture, and this necessarily gave rise to a very large software machine; they then had to speed it up dramatically with the aid of GPUs—by no means a small task as it meant reoptimizing the software to match the hardware; finally, they had to find how to feed the software system with a very large training set—again no mean task, as an unprecedentedly large number of parameters had to be trained rigorously, and several innovations were required in order to achieve this.

First, we shall attend to the architecture of the software system. We shall return later to the development of suitable training sets, and of necessary innovations for managing them and ensuring that the CNN software system is adequately trained.

The CNN architecture is shown in [Fig. 15.8](#): Further details of the various layers are presented in [Table 15.4](#). The number of hidden layers is 10, which is

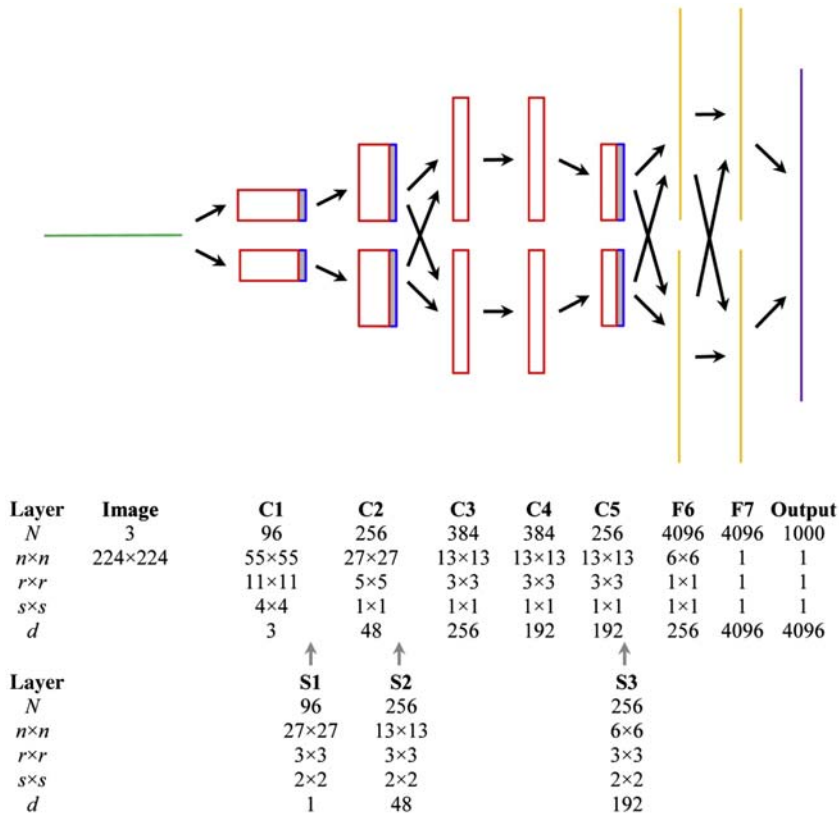


**FIGURE 15.8**

Schematic of the AlexNet architecture. This schematic carries much the same information as Table 15.4: both are provided as an aid to understanding the details of the overall AlexNet architecture.  $N$  indicates the number of layers of each type;  $n \times n$  indicates the dimensions in the case of a 2-D image format;  $r \times r$  is the size of a 2-D neuron input field (a single number indicates that the input is abstract 1-D data);  $s \times s$  is the 2-D stride;  $d$  indicates the number of connections arising from the depth of the immediately preceding layer: in three cases, it is half of the actual depth ( $N$ ) because the architecture is split between two GPUs. To aid clarity, subsampling layers are shaded and are shown attached to the preceding convolution layer. Layers F6, F7, and Output are fully connected.

only 4 more than for LeNet. However, these numbers are misleading as the *depths* of the various layers in AlexNet sum to 11,176 compared with 258 for LeNet. Similarly, AlexNet contains  $\sim 650,000$  neurons compared with 6508 for LeNet, whereas the number of trainable parameters is some 60 million compared with 60,000 for LeNet. And when we look at the size of the input image, we find that



Table 15.4 Summary of the AlexNet Connections and Trainable Parameters

Layers	Layer Size	Connections		Parameters
	$N: n \times n$	Inputs	Outputs	
Image	3: $224 \times 224$		150,528 ( $3 \times 224^2$ )	—
<b>C1</b>	96: $55 \times 55$ 11 $\times$ 11: 3	$105.42 \times 10^6$ ( $3 \times 96 \times 55^2 \times 11^2$ )	290,400 ( $96 \times 55^2 \times 1$ )	$0.03 \times 10^6$ ( $3 \times 96 \times 11^2$ )
S1	96: $27 \times 27$ 3 $\times$ 3: 48	$0.63 \times 10^6$ ( $96 \times 27^2 \times 3^2$ )	69,984 ( $96 \times 27^2 \times 1$ )	192 ( $96 \times 2$ )
<b>C2</b>	256: $27 \times 27$ 5 $\times$ 5: 48	$223.95 \times 10^6$ ( $48 \times 256 \times 27^2 \times 5^2$ )	186,624 ( $256 \times 27^2 \times 1$ )	$0.61 \times 10^6$ ( $96 \times 256 \times 5^2$ )
S2	256: $13 \times 13$ 3 $\times$ 3: 192	$0.39 \times 10^6$ ( $256 \times 13^2 \times 3^2$ )	43,264 ( $256 \times 13^2 \times 1$ )	512 ( $256 \times 2$ )
<b>C3</b>	384: $13 \times 13$ 3 $\times$ 3: 256	$149.52 \times 10^6$ ( $256 \times 384 \times 13^2 \times 3^2$ )	64,896 ( $384 \times 13^2 \times 1$ )	$0.89 \times 10^6$ ( $256 \times 384 \times 3^2$ )
<b>C4</b>	384: $13 \times 13$ 3 $\times$ 3: 192	$112.14 \times 10^6$ ( $192 \times 384 \times 13^2 \times 3^2$ )	64,896 ( $384 \times 13^2 \times 1$ )	$1.33 \times 10^6$ ( $384 \times 384 \times 3^2$ )
<b>C5</b>	256: $13 \times 13$ 3 $\times$ 3: 192	$74.76 \times 10^6$ ( $192 \times 256 \times 13^2 \times 3^2$ )	43,264 ( $256 \times 13^2 \times 1$ )	$0.89 \times 10^6$ ( $384 \times 256 \times 3^2$ )
S3	256: $6 \times 6$ 3 $\times$ 3: 192	$0.08 \times 10^6$ ( $256 \times 6^2 \times 3^2$ )	9216 ( $256 \times 6^2 \times 1$ )	512 ( $256 \times 2$ )
<b>F6</b> (f.c.)	4096: $6 \times 6$ 256	$37.75 \times 10^6$ ( $256 \times 4096 \times 6^2$ )	4096	$37.75 \times 10^6$ ( $256 \times 4096 \times 6^2$ )
<b>F7</b> (f.c.)	4096:1 4096	$16.78 \times 10^6$ ( $4096 \times 4096$ )	4096	$16.78 \times 10^6$ ( $4096 \times 4096$ )
Outputs (f.c.)	1000:1 4096	$4.10 \times 10^6$ ( $1000 \times 4096$ )	1000	— (softmax)
<b>Total</b> (C,F only)		$720.32 \times 10^6$	658,272	$58.28 \times 10^6$

AlexNet has 10 hidden layers between the image layer and the output layer. This table gives details of the connections and the numbers of trainable parameters in each layer. Column 1 gives the name of each layer—"C," "S," and "F," indicating respectively convolution, subsampling (pooling), and fully connected convolution. In each case, Column 2 indicates the number of layers  $N$  and their dimensions:  $n \times n$  indicates the sizes of the layers for 2-D image format, a bare "1" indicating that a layer has abstract (1-D) format;  $r \times r$  indicates the convolution or subsampling window size. C1 has a  $4 \times 4$  stride; the three subsampling windows have a  $2 \times 2$  stride. Columns 3–5 give the numerical values and also show, in brackets, how they are calculated. Bias parameters are presumed to number 1 per neuron output for convolution layers (C, F) and 2 per output for subsampling layers (S), as for LeNet.

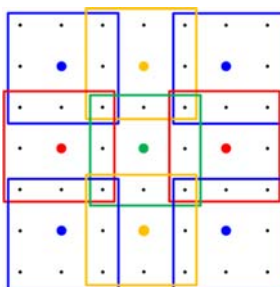
AlexNet takes a color image of size  $224 \times 224$ , whereas LeNet could only manage a bilevel  $32 \times 32$  input image. So overall, AlexNet is larger than LeNet by a factor between 100 and 1000, depending on which factors should be regarded as the most relevant. However, the real change wrought by AlexNet was the

possibility of working with huge numbers of layers and managing the credit assignment problem in spite of this—while still using the backpropagation algorithm for training. At the time, this was unprecedented, but it was made possible partly by the already reduced number of parameters required by CNNs, because, as we have seen, all the neurons in any given layer of neurons are forced to use identical parameters; it was also made possible by employing exceptionally large training sets, and by other methods to be described below.

Before proceeding further, we shall examine various details of the AlexNet architecture. One prominent feature of the architecture is the horizontal split right across the network, above and below which a single GPU is used for implementation (Fig. 15.8). In principle, this should impose serious limitations upon the architecture, but in practice, it turned out not to be an insoluble problem. (In fact, this could perhaps be regarded as one of the most cunning innovations in the system.) This is because it is reasonable to let the each GPU chunter away at half the image and its features, and because at one juncture (between layers C2 and C3) data from the other half of the data is brought back again; as an added measure, all the data is brought together once again for the final two fully connected layers (F6 and F7)—and for the fully connected Output layer embodying the softmax computations. Next, note that all the convolution layers take in the neuron  $r \times r$  fields of view for *all* the available depth outputs from the previous layer. However, in layers C2, C4, and C5, the *available* depth outputs  $d$  number only half of those from the previous layers—because transference of data across the inter-GPU divide is not possible: i.e., in those three cases,  $d$  is only half the value of  $N$  for the previous layer.

There is also a definite need to reduce redundancy in the system at an early stage. This is achieved rather brutally by applying a  $4 \times 4$  stride in layer C1, though excessive damage is prevented by applying an  $11 \times 11$  pixel window to help gather sufficient information at the same time. In fact, this is the only place in the whole system where a stride of greater than 1 is used—except in the case of the three subsampling layers S1, S2, S3. Interestingly, excessive damage is prevented in the latter cases by using a  $3 \times 3$  rather than the more usual  $2 \times 2$  pooling window. These three subsampling layers are termed “overlapping pooling,” and are particularly easy to visualize (Fig. 15.9): in fact, they employ max-pooling rather than averaging.

Notice that the dimensions ( $n \times n$ ) of the layers fall rapidly first from  $224 \times 224$  to  $55 \times 55$ , then successively to  $27 \times 27$ ,  $13 \times 13$  (three times),  $6 \times 6$  and finally down to  $1 \times 1$ . The published paper (Krizhevsky *et al.*, 2012) makes no mention of padding niceties and perhaps this was due to the need to the rush to complete the machine in 2012 (of course, the published paper had to report what was actually done, rather than to overidealize it). But in any case rapid convergence to size  $1 \times 1$  and thereby to purely abstract pattern classification processes is of value, both for minimizing storage and for maximizing speed. Interestingly, almost all the trainable parameters are in layers F6 and F7, only 1000 inputs being left for the final softmax (nonneural) classifier.

**FIGURE 15.9**

A simple case of overlapping pooling. This figure shows a small  $7 \times 7$  pixel image (small dots) in which the sampled output points (large dots) represent a  $2 \times 2$  stride mapping. The squares show how each output point is fed from a  $3 \times 3$  pooling window. To prevent confusion, the square windows are offset slightly from each other, but they all still contain nine pixel centers.

One of the features of AlexNet that set it apart from LeNet was the use of the then recently developed ReLU nonlinear transfer function. Krizhevsky et al. found that this was able to speed up training by a factor of about 6 relative to the usual *tanh* function. As huge amounts of training were needed in AlexNet, this was a valuable innovation. In fact, ReLUs do not need input normalization to prevent them from saturating (it is obvious that a linear response can never saturate). Nevertheless, Krizhevsky et al. found that it was still useful to include an element of what they called “brightness normalization,” which they considered to perform a function similar to that of lateral inhibition in the human visual system. They found that including it improved error rates by between 1% and 2%.

Very shortly before AlexNet was completed, a new technique called “dropout” was introduced by Hinton et al. (2012); see also Hinton (2002). The purpose of this was to limit the incidence of overtraining. This was achieved by randomly setting a proportion (typically as high as 50%) of the weights to zero for each training pattern; this rather surprising technique appeared to work well: it did so by preventing hidden layers from relying too much on the specific data fed to them. (Another way of looking at this is that random sampling from  $2^{WH}$  different architectures is taking place, so the possibility of any of them being overtrained should be negligible: in effect, the network is being trained via many independent pathways, so any individual overtrained pathway should not affect the overall performance.)

Krizhevsky et al. (2012) included this feature in AlexNet. To apply it, the output of each neuron is randomly set to zero with probability 0.5. This is done before the forward pass of the input data, and the affected neurons do not contribute to the ensuing backpropagation. On the next forward pass, a different set of neuron outputs is set to zero with probability 0.5, and again the affected neurons do not

contribute to backpropagation; and similarly for later passes. During testing, an alternate procedure occurs, with all neuron outputs being multiplied by 0.5. In fact, multiplying *all* neuron outputs by 0.5 is an approximation to taking the statistical geometric mean of all the local neuron output probability distributions and relies on the geometric mean being not too far from the arithmetic mean. Dropout was incorporated into the first two layers of AlexNet, and significantly reduced the amount of overfitting (undertraining because of too little training data): the main disadvantage of including it was to double the number of iterations needed for convergence. Effectively, the training time was doubled but the effectiveness of training was significantly improved—all of which was far better than the usual outcome of excessive training resulting in poorer performance!

AlexNet was trained using the 1.2 million images available from the ImageNet ILSVRC challenge, this number being a subset of the full 15 million in the ImageNet database. In fact, ILSVRC-2010 was the only subset for which test labels were available, there being about 1000 images in each of 1000 categories. However, it was found that these images were far too few to specify a CNN of the complexity required to perform accurate classification of this immense task. Therefore, means were required for expanding the dataset sufficiently to train AlexNet and achieve classification error rates in the 10% to 20% bracket.

Two main means of augmenting the dataset were considered and implemented. One was to apply realistic translations and reflections to the images in order to generate more images of the same type. The transformations even extended to extracting five  $224 \times 224$  patches and their horizontal reflections from the initial  $256 \times 256$  ImageNet images, giving a total of 10 patches per image. Another was to alter the intensities and colors of the input images. To make this exercise more rigorous, it was carried out by first using principal components analysis (PCA) to identify color principal components for the ImageNet dataset, and then to generate random magnitudes by which to multiply the eigenvalues, thereby producing viable variants of the original images. Together, these two approaches were able to validly generalize and multiply the size of the original dataset by a factor of  $\sim 2000$ —the principle being to generate natural changes in position, intensity, and color (the latter would naturally change with the color of the ambient illumination).

At this stage, it ought to be emphasized that the aim of the challenge was to find the best vision machine (giving the lowest classification error rates) that is able to recognize an example of a flea, a dog, a car, or other common object in any position in an image and in any reasonable (i.e., naturally occurring) pose. Furthermore, the machine should prioritize its classifications to give at least the first five most probable interpretations. Then, each machine can be rated not only on the accuracy of its top classification but also on whether the object classified appears within the machine's top five classifications. AlexNet was able to achieve a winning top-5 error-rating of 15.3%, compared with 26.2% for the runner up. Another first was the dramatic drop to below 20% error rate for such an exercise, which spelt a new lease of life for deep neural networks, and brought them sharply back into the limelight.

Note that all this was achieved not merely by designing a winning architecture and generating the right dataset to train it adequately, but also it was necessary to bring the training time down to realizable levels. In this respect, GPU implementation proved to be crucial. Even with a pair of GPUs, the training time took approximately a week, working 24 hours a day, to manage the task. Without GPUs, it would have taken some 50 times longer—most probably, about a year—so the machine would have had to be submitted to the following year’s challenge! [A commonly accepted figure is that a GPU has a speed advantage  $\sim 50$  relative to a typical host CPU.]

Finally, it should be noted that GPUs provide a very good implementation because of their intrinsic parallelism, and thus their capability for handling large datasets in fewer cycles. Note that each layer of a CNN is completely homogeneous and is therefore well adapted for parallel processing. Note also that GPUs are well adapted to working in parallel as they are able to read from and write to each other’s memories directly, avoiding the need to move data through the host CPU memory.

---

## 15.6 ZEILER AND FERGUS’S WORK ON CNN ARCHITECTURES

Following the almost unprecedented success of AlexNet relative to previous CNN architectures such as LeNet, many workers concentrated on consolidating this progress and augmenting it further. In particular, Zeiler and Fergus (2014) made a detailed analysis of its optimality and means for improving it. They started with statements including the following, “There is no clear understanding of why [CNNs] perform so well, or how they might be improved;” “there is still little insight into the internal operation and behavior of these complex models, or how they achieve such good performance;” “from a scientific standpoint, this is deeply unsatisfactory.”

Their most immediate task was to reimplement AlexNet and to test it thoroughly, with the aim of finding its limitations and developing it further. They employed the same ImageNet 2012 training data and augmented it in the same way—by resizing the images, cropping to  $256 \times 256$ , and using 10 different sub-crops to  $224 \times 224$  pixels, again incorporating horizontal flipping. The main difference between the new implementation and AlexNet was the use of a single GPU in place of the original two. This allowed Zeiler and Fergus to replace the sparse connections between layers C3 and C5 with a complete set of dense connections. In addition, they used a powerful visualization technique (described in more detail in the next section) to improve performance further. One such improvement was to renormalize the various filters in the convolutional layers to prevent any of them dominating (effectively, a dominant layer prevents other layers from contributing fully to object recognition).

Visualization also helped with the selection of optimal architectures. In particular, it showed that the first and second layers of AlexNet were weak in the middle spatial-frequency range—with hindsight, this was a fairly obvious result of jumping straight from an  $11 \times 11$  filter of large ( $4 \times 4$ ) stride to a  $5 \times 5$  filter with a  $1 \times 1$  stride: they also showed that the large stride was the cause of aliasing problems, which had not been anticipated. They dealt with these problems by placing a  $7 \times 7$  filter in C1 and reducing the stride to  $2 \times 2$ . However, these changes necessitated modifications in later layers, because the image size had not been reduced sufficiently in the first few layers: this will be seen from the ZFNet architecture schematic shown in Fig. 15.10; we name this the “ZFNet architecture” to avoid confusion with AlexNet and other architectures. As a result of all

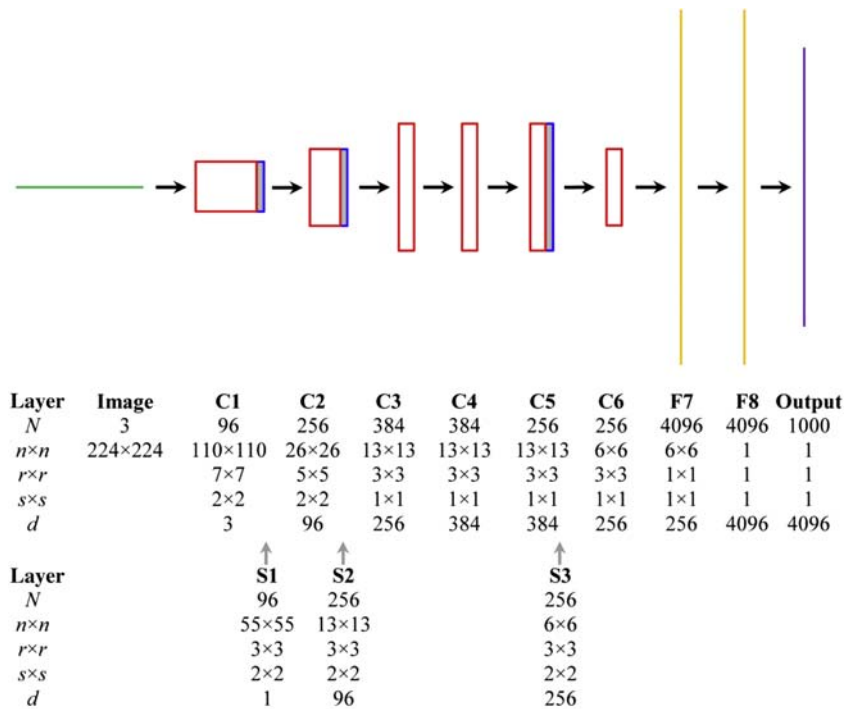


FIGURE 15.10

Schematic of the ZFNet architecture. This schematic is very similar to that for AlexNet, as shown in Fig. 15.8. Indeed, it is so close that the meanings of all terms should be clear from Fig. 15.8. Notice that AlexNet contains seven hidden layers, whereas ZFNet contains eight hidden layers (these figures are exclusive of the three subsampling layers in each network). Note that ZFNet is implemented using only a single GPU, and its architecture is not split. Hence,  $d$  is now equal to the number of connections arising from the depth of the immediately preceding layer. The main feature to focus on here is how the values of  $n \times n$ ,  $r \times r$  and  $s \times s$  vary between AlexNet and ZFNet.

these changes, ZFNet was able to achieve a top-5 error-rating of 14.8%, which should be compared with the AlexNet figure of 15.3%. (It turned out that Clarifai did even better in the 2013 ImageNet competition, attaining a figure of 11.7%, but space precludes including a detailed discussion of that story here.)

Zeiler and Fergus (2014) carried out further experiments to explore the reasons for the success of the AlexNet architecture. They tried adjusting the sizes of the different layers and also removing them entirely—each time completely retraining the architecture on the same data. Many of these changes made little difference to the overall performance, leading only to slight increases in the error rate. Nevertheless, removing several layers at once led to much worse performance, whereas increasing the size of the middle convolution layers improved performance significantly. They concluded that maintaining the overall depth of the architectural model, whereas making detailed changes is important for achieving good performance. One can argue that the “intelligence” of a net intrinsically increases with depth, but to capitalize on this intelligence requires increased training and thus substantially increased computation.

This sort of approach is sometimes called an “ablation study,” the word “ablation” being a commonly used medical term meaning, shaving off diseased flesh, layer by layer. Applied to classification systems such as CNNs, progressive removal of layers aims to reveal which layers are critical to the architecture. Interestingly, in this case, it revealed something different—that the minimum depth is more critical rather than any individual layer.

To proceed further, Zeiler and Fergus showed that it was possible to use the previously trained CNN layers to perform totally different tasks using the Caltech-101, Caltech-256, and Pascal VOC 2012 datasets, whose main characteristics we now briefly describe:

- **Caltech-101:** This dataset contains pictures of objects in 101 categories, with  $\sim 50$  images per category, though some categories have up to  $\sim 800$  images. The image size is  $\sim 300 \times 200$  pixels. This dataset was collected in 2003 by Fei-Fei Li et al. The images have little clutter and are approximately centered.
- **Caltech-256:** This dataset contains pictures of objects in 256 categories and contains a total of 30607 images, i.e., around 120 per category, with a minimum per category of between 30 and 80. The dataset has two valuable features: artefacts due to image rotation are avoided and a substantial clutter category is introduced for testing background rejection. The dataset was published in 2006 by Griffin et al.
- **PASCAL VOC 2012:** This dataset contains 20 classes. Note that the images can contain several objects: the training/validation data has 11,530 images containing 27,450 ROI annotated objects and 5,034 segmentations. However, the annotations are incomplete: only people are annotated and some people are not annotated. See van de Sande et al. (2012) for further details.

To achieve this, they merely retrained the softmax output classifier appropriately: as this classifier contains relatively few parameters, it can be trained quite

quickly. The retrained ZFNet system performed better on the two Caltech datasets than the best previously reported performance, whereas on the PASCAL dataset, it performed much less well. This was because the PASCAL dataset images can contain multiple objects, whereas the ZFNet system only provided a single exclusive prediction for each image. Concentrating on the two Caltech datasets, the considerable success achieved was presumably due to the extensive training of the CNN core: this couldn't be matched by the previous leading systems because of the paucity of the data they had available for training. On the other hand, when ZFNet was retrained on this data, it performed poorly in each case: this reflects the enormous thirst for training data of such a powerful neural classifier.

## 15.7 ZEILER AND FERGUS'S VISUALIZATION EXPERIMENTS

We now move on to Zeiler and Fergus's visualization experiments. These were designed to reveal the inner workings of CNNs. Basically, they sought to analyze quite how a properly trained CNN processes incoming data. It proved difficult to do this holistically; in fact, it could only be done one layer at a time. What they needed to do was to feed a new image into the system, look at the output from layer  $i$ , and try to work out what happened to the signals in passing through that layer (Fig. 15.11). Suppose that at that point the data has just passed through a

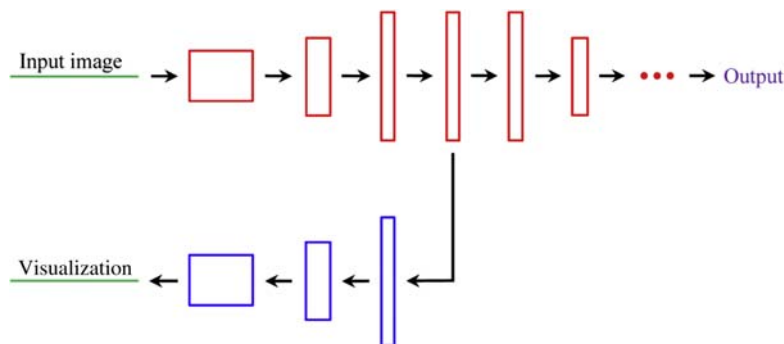


**FIGURE 15.11**

The idea of a deconvolution network. This schematic shows (top) the normal pathway from the input image to the output. This pathway is trained as usual by backpropagation, and the learnt parameters are then fixed. Next, a new input image is applied, and data is extracted laterally and passed to the visualization pathway. The aim is to deconstruct the learnt parameters to see how the new input image activates the network. However, the latter process is more complicated than might initially be imagined, as pooled maxima have to be unpooled (i.e., passed back to the correct channels), reversed ReLUs have to be included, and convolution coefficients have to be “deconvolved.”



subsampling layer, and specifically its max-pooling layer. At that point, it is unknown which of the  $r \times r$  inputs (typically, a total of 4 or 9 inputs) gave rise to the maximum signal. However, for that particular input image, we need to go down to the next layer to determine which it is. Then, we need to go one stage further, to the next lower layer, and track the maximum signal even further. At each layer, the unit that does the backward recursion (in the original Latin sense of running back, not of using a recursive procedure that calls itself) is called an “unpooling” layer, and as it operates it invokes so-called “switches” that locate the path back to the previous maximum.

Looking more closely at the process of downwards recursion, the whole downwards orientated system is actually put into reverse—not merely the pooling operation. Even the ReLUs are pointed downwards—as they have to ensure that the signals moving downwards remain mutually compatible and positive. (Although some aspects of the inversion process may seem strange and somewhat arbitrary, much will become clear from the revised approach adopted in the following section.) Lastly, the convolution filters themselves have to be inverted by using “transposed” versions of the filters (in practice, this is approximately achieved by rotating them through  $180^\circ$ : Zeiler and Fergus, 2014). Interpreting the resulting pictures can be quite difficult. However, the observation that signals in AlexNet’s middle spatial-frequency range were weak is typical of what is possible with this approach. Similarly, occlusion sensitivity can be analyzed to find quite where in the trained network crucial losses in activity occur as a result of (partial) occlusion.

Although the work carried out on visualization is highly useful to answer questions such as these about the operation of the CNN, it is also rather limited. In particular, it applies only to the particular image input at any one time: i.e., it only visualizes a single activation and does not automatically carry lessons about the overall operation of the network. As a result, only an approximate version of the convnet features from the layer underneath the current location in the network can be recovered from the system.

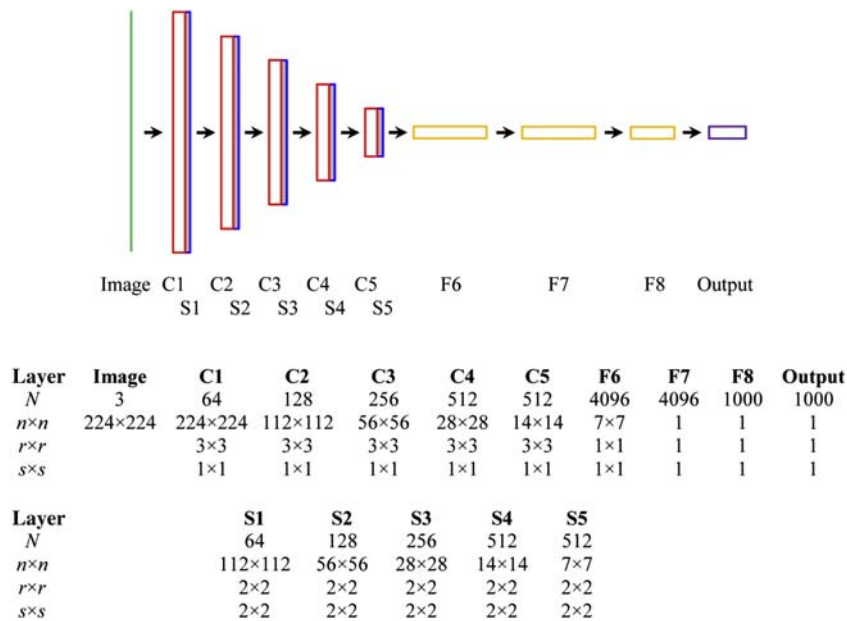
Finally, note that the complete system architecture that carries out the visualization is called a “DNN:” this is because it includes not only the components of the original convolutional network but also, at the same time, the same components used in reverse. Thus, it contains unpooling elements as well as pooling elements and also has to reverse both the ReLUs and the convolutions. In the case of convolutions, it is impossible to achieve exact reversal, for the same reason that removing blur from images cannot be done exactly: however, see Zeiler et al. (2010) for a way forward using a regularization approach. Overall, what Zeiler and Fergus have achieved is (1) to significantly improve our confidence about the operation and validity of CNNs and (2) to identify a number of viable methods for improving their performance. Nevertheless, advance design of all the details of a CNN in terms of the number of layers, and profiles of the image sizes ( $n \times n$ ), and the neuron input field sizes ( $r \times r$ )—not to mention optimum stride sizes ( $s \times s$ )—still seems rather out of reach.

---

## 15.8 SIMONYAN AND ZISSERMAN'S VGGNET ARCHITECTURE

In the continued absence of knowledge about the form of an ideal architecture, Simonyan and Zisserman (2015) set out to determine the effect of further increases in depth. To achieve this, they significantly reduced the number of parameters in the basic network by limiting the maximum neuron input field to  $3 \times 3$ . In fact, they restricted the convolution input field and stride to  $3 \times 3$  and  $1 \times 1$ , respectively, and set both the input field and the stride of each subsampling layer to  $2 \times 2$ . In addition, they arranged for the systematic and rapid convergence of the successive layers from  $224 \times 224$  down to  $7 \times 7$  in 5 stages, followed by a transition to  $1 \times 1$  in a single fully connected stage; this was followed two further fully connected layers and then a final softmax output layer (Fig. 15.12). All the hidden layers included a ReLU nonlinearity stage (not shown in the figure): local response normalization—which had been used by Krizhevsky et al. in AlexNet—was excluded as it was found not to improve performance. Apart from the  $N$  “channels,” the 5 convolutional layers C1–C5, respectively, contained 2, 2, 3, 3, 3 identical sublayers, though these are not marked in Fig. 15.12. Finally, it should be remarked that, for reasons of experimentation, Simonyan and Zisserman devised six variations on the VGGNet architecture, with 11 to 19 weighted hidden layers: Here, we only cover configuration D (with 16 weighted hidden layers), for which the numbers of identical sublayers in layers C1–C5 are as listed above. Configuration D is of particular interest as it was used in the work of Noh et al. (2015), to be described in detail in the next section.

As mentioned above, Simonyan and Zisserman saved on the basic number of parameters by restricting the convolution input field to  $3 \times 3$ . This meant that larger convolutions had to be produced by applying several  $3 \times 3$  convolutions in sequence. Clearly, a  $5 \times 5$  input field would necessitate applying two  $3 \times 3$  convolutions, and a  $7 \times 7$  field would require three  $3 \times 3$  convolutions. In the latter case, this would reduce the total number of parameters from  $7^2 = 49$  to three times  $3^2 = 27$ . In fact, not only did this way of implementing a  $7 \times 7$  convolution reduce the number of parameters, but also it forced an additional regularization on the convolution, as a ReLU nonlinearity was interposed between each of the  $3 \times 3$  component convolutions. It is also relevant that both the input and output of each three-layer  $3 \times 3$  convolution stack can have  $N$  channels, in which case it will contain a total of  $27N^2$  parameters, and it is that figure which should be compared with  $49N^2$  parameters. The numbers of parameters in the various layers of VGGNet (configuration D) are given in Table 15.5, the underlying formula for C1–C5 being  $M \times 3^2N^2$  for a stack of  $M$   $3 \times 3$  convolutions. However, note that this formula only applies if the previous convolution layer has the same value of  $N$ , which is valid for C5 but is not the case for C1–C4: see Table 15.5 for the detailed picture.

**FIGURE 15.12**

Architecture of VGGNet. This architecture shows a more recent optimization of the standard type of CNN network. Unlike the schematics in Figs. 15.7, 15.8, and 15.10, this one is arranged to show the relative sizes of the convolution layers, which range from image size down to  $1 \times 1$ . Note that the convolution layers all have unit stride, and that their input fields are limited to a maximum size of  $3 \times 3$ : the subsampling layers all have  $2 \times 2$  input fields and  $2 \times 2$  strides.

VGGNet has a number of possible configurations, with numbers of weighted hidden layers ranging from 11 to 19. Configuration D (shown above) has 16 layers, layers C1–F8, respectively, containing 2, 2, 3, 3, 3; 1, 1, 1 weighted sublayers. The number of weighted layers determines the number of parameters: see Table 15.5.

In spite of its increased depth, VGGNet contains only about 2.4 times as many parameters as AlexNet, it is much simpler and doesn't split the architecture to fit it to a 2-GPU system (see Fig. 15.8). On the contrary, it immediately obtains a speedup of 3.75 times over a single GPU when using an off-the-shelf 4-GPU system.

Details of the training methodology are similar to those for AlexNet: see the original paper by Simonyan and Zisserman (2015). However, these authors include one interesting innovation: that is to use “scale jittering,” while training—i.e., to augment the training set using objects over a wide range of scales. In fact, random scaling was applied over an image scale factor of 2.

The outcome was that VGGNet achieved top-5 test error results of 7.0% using a single net, compared with 7.9% for GoogLeNet (Szegedy et al., 2014). In fact, GoogLeNet achieved a figure of 6.7%, but only by employing seven nets. Thus,

**Table 15.5** VGGNet Parameters

Configuration D	<i>N</i>	Sublayer	Formula	Parameters
C1	64	1	$(3 \times 3) \times 3 \times 64$	$0.04 \times 10^6$
		2	$(3 \times 3) \times 64^2$	
C2	128	1	$(3 \times 3) \times 64 \times 128$	$0.22 \times 10^6$
		2	$(3 \times 3) \times 128^2$	
C3	256	1	$(3 \times 3) \times 128 \times 256$	$1.47 \times 10^6$
		2	$(3 \times 3) \times 256^2$	
		3	$(3 \times 3) \times 256^2$	
C4	512	1	$(3 \times 3) \times 256 \times 512$	$5.90 \times 10^6$
		2	$(3 \times 3) \times 512^2$	
		3	$(3 \times 3) \times 512^2$	
C5	512	1	$(3 \times 3) \times 512^2$	$7.08 \times 10^6$
		2	$(3 \times 3) \times 512^2$	
		3	$(3 \times 3) \times 512^2$	
F6	4096		$(7 \times 7) \times 512 \times 4096$	$102.76 \times 10^6$
F7	4096		$4096 \times 4096$	$16.78 \times 10^6$
F8	1000		$4096 \times 1000$	$4.10 \times 10^6$
<b>Total</b>				<b><math>138.35 \times 10^6</math></b>

*This table summarizes the numbers of parameters in the various convolution layers of VGGNet, configuration D. Note that most of the parameters appear in the early fully connected layers, particularly F6.*

VGGNet achieved second place in the ILSVRC-2014 challenge. However, after submission, the authors managed to decrease the error rate to 6.8% using an ensemble of two models—substantially the same performance as for GoogLeNet, but with significantly fewer nets. Interestingly, all this was achieved even though the VGGNet architecture did not depart from the classical LeNet architecture of LeCun *et al.* (1989), the main improvement being the significantly increased depth of the network.

In spite of being placed second in the ILSVRC-2014 challenge, VGGNet has proved more versatile and adaptable to different datasets and is a preferred choice in the vision community for extracting features from images. This seems to be because VGGNet actually provides more robust features even though it turned out to have slightly weaker classification performance on a specific dataset. As we shall see in the next section, VGGNet was the network chosen by Noh *et al.* (2015) for their work on DNNs.

## 15.9 NOH *ET AL.*'S DECONVNET ARCHITECTURE

Inspired by the work of Zeiler and Fergus, as outlined in [Sections 15.6 and 15.7](#), Noh *et al.* (2015) produced a “learning DNN” (DeconvNet) that learnt *from*

*training* how to deconvolve the sets of convolution coefficients in each layer of a CNN. In fact, the overall architecture of their system seems inspired and far simpler than indicated by the explanations in Section 15.7: Once again, hindsight radically clarifies the progress made. Their architecture is shown in Fig. 15.13: note that its initial CNN section is borrowed from layers C1–F7 of VGGNet but excludes layer F8 and the Output softmax layer. In this architecture, we see no downflowing paths, but that is because the partial downflowing path of Zeiler and Fergus’s deconvolution (deconv) network has been rotated, extended, and added after the upflowing section. Indeed, it can also be said that this architecture is a

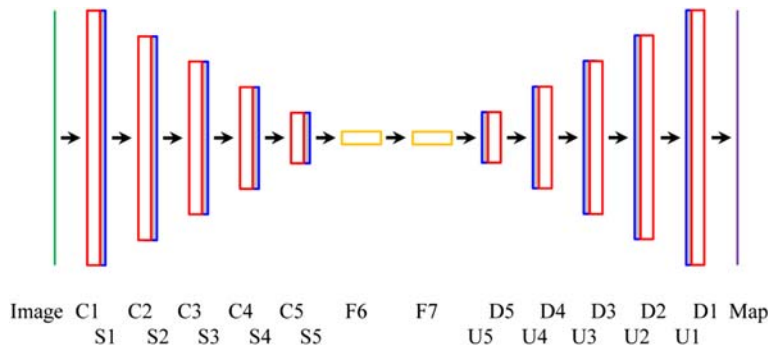


**FIGURE 15.13**

Schematic of Noh et al.’s learning deconvolution network. This network contains two networks back to back. On the left is a standard CNN network, and on the right is the corresponding DNN “deconvolution” network that seems to operate in reverse. The CNN network (on the left) has no output (e.g., softmax) classifier, as the ultimate purpose is not to classify objects but to present a map of where they are on a pixel-by-pixel basis throughout the area of the image. Deconv layers D5 down to D1 are intended to progressively unpick layers C5–C1. Similarly, unpooling layers U5 down to U1 are intended to progressively unpick pooling layers S5–S1. To achieve this, the position parameters from the max-pooling layers have to be fed to corresponding locations in corresponding unpooling layers (i.e., locations from  $S_i$  should be fed to  $U_i$ ).

This schematic is arranged to show the relative sizes of the convolution layers, which range from image size down to  $1 \times 1$ , and then up again to give a full-size segmentation map of the input image. Overall, this architecture can be regarded as a single CNN and could in principle be trained accordingly. However, its large depth dictates that a different strategy needs to be adopted (see text for further details).

Note that the CNN network was borrowed from VGGNet (Fig. 15.12), but excluded both its layer F8 and its Output softmax layer. For details of layers C1–F7 and S1–S5, see Fig. 15.12. The details of  $D_i$  are as for  $C_i$ , and those for  $U_i$  are as for  $S_i$ —except that  $D_i$  and  $U_i$  expand rather than contract the dataflow. In many ways, it is useful to regard the expansion process as *mirroring* the original contraction process. Although suitable combination rules are needed to define what happens with overlapping output windows, the system is *trained* to perform the relevant deconvolutions.

generalization of Zeiler and Fergus's deconv network. It will be useful to provide a rationale for this. First, an upflowing CNN is needed for identifying objects in the input image. Second, if objects are to be located in particular parts of an image, another CNN is needed to point to the positions, and this necessarily has to follow the identification process (a network aimed at achieving all this is called a semantic segmentation network). Undertaking both tasks in one enormous unconstrained CNN would be prohibitive of memory and training, so the two networks have to be linked closely together. The means of connecting them together is to provide feedforward paths from the pooling units to later unpooling units. So the very means by which the CNN output was generalized to *eliminate* the effects of sample variations has led to the second CNN being augmented to *yield* the required location maps. Crucially, we also see that the overall single upflowing data-path makes it obvious why the ReLU units must now all point in the same direction. (Remember that they have now all been turned to face forwards again.) It is also clear that with such a huge network, training will have to be carried out carefully, and it would appear obvious that the originally upflowing (object detection) section should initially be trained on its own.

Overall, the system works by mirroring the input CNN by including a DNN after it. The operation may be summarized as follows: unpooling layer  $U_i$  is non-linear and redirects (unpools) the  $C_i$  maximum signals; then deconvolution layer  $D_i$  operates linearly on the data, and therefore has to sum the overlapping inputs, weighted as necessary. However, rather than constructing suitable combination rules to define what happens with the overlapping output windows of each  $D_i$  layer—and doing this in some very approximate way (such as “transposed” versions of the convolution filters)—the deconvolution layers are trained as normal parts of the overall network. Although this is a rigorous approach, it does increase the burden involved in training the network.

It is also useful to have a mental model of the whole process occurring in the DNN. First, each unpooling layer recovers the information from the corresponding pooling layer and reconstitutes the dimensions the dataspace had before pooling. However, it only populates it sparsely, with the local maximum values in appropriate positions. The purpose of the following deconvolutional layer is to reconstruct a dense map in its dataspace. So, although the CNN reduces the size of the activations, the following DNN enlarges the activations and makes them dense again. However, the situation is not completely unraveled, as only the maximum values have been reinserted. As Noh *et al.* (2015) say in their paper, “unpooling captures *example-specific* structures by tracing the original locations with strong activations back to image space,” whereas “learned filters in the deconvolutional layers tend to capture *class-specific* shapes.” What this means is that the deconvolutional layers rebuild the example shapes to correspond more accurately to what would be expected for objects of the specific classes.

In spite of this assurance, the network has to be trained appropriately. However, the surmise given above about training in two stages has been improved by Noh *et al.* as follows: to beat the problem of the space of semantic

segmentation being extremely large, the network is first trained on easy examples, and then trained on more challenging examples: this amounts to a sort of bootstrapping approach. In more detail, the first of the training processes involves limiting the variations in object size and location by centering and cropping them in their bounding boxes; the second stage involves ensuring that the more challenging objects are adequately overlapped with ground-truth segmentations: to achieve this the widely used intersection over union measure is used and is taken to be acceptable only if it is at least 0.5.

In fact, the first stage uses a “tight” bounding box, and this is extended by a factor 1.2 and further expanded into a square in order to include sufficient local context around each object. In this first stage, the box is rated according to the object located at its center, other pixels being labeled as background. However, in the second stage, this simplification is not applied, and all relevant class labels are used for annotation.

The method is shown to be more accurate than the earlier “fully convolutional” network (FCN) of Long et al. (2015): these have respective mean accuracies of 70.5% and 62.2%. (Space precludes a full explanation of the FCN here. However, it may be envisaged as a simplified network constructed of convolution layers, including stride and pooling, but with no unpooling, no final pooling layer, and no final classifier layer—all fully connected layers having been converted to convolutions.) However, Noh et al. also show that the two types of network are, to a significant degree, complementary, and combining them into an ensemble gives better results (72.5%) than either taken alone. Specifically, FCN is better at extracting the overall shape of an object, whereas DeconvNet is better at capturing the fine details of the shape. To achieve the best results, the ensemble method takes the mean of the output maps from the two methods and then applies a conditional random field (CRF) to obtain the final segmentation. (Taking the mean of the output maps is justified, as the output maps of FCN and DeconvNet are class-conditional probability maps, each computed independently from the input image. Note also that in computer vision, CRFs are often used for object recognition and image segmentation: a CRF can take context into account by the use of prior probabilities.) In view of the slightly confused situation, we shall not pursue either of these methods further here: instead, we look at another closely related method—that of Badrinarayanan et al. (2015), which uses much less memory and has several other advantages.

---

## 15.10 BADRINARAYANAN *ET AL.*'S SEGNET ARCHITECTURE

The SegNet architecture strongly resembles that of DeconvNet and is also aimed at semantic segmentation. However, its authors demonstrated the need for returning to a significantly simpler architecture in order to make it more easily trainable (Badrinarayanan et al., 2015). Basically, their architecture was identical to

DeconvNet (Fig. 15.13) but with F6 and F7 excluded. In addition, it was clear to the authors that use of max-pooling and subsampling reduce feature map resolution and thereby reduce location accuracy in the final segmented images. Nevertheless, they start by eliminating the fully connected layers of VGGNet, retain the encoding–decoding (CNN–DNN) structure of DeconvNet, and also retain max-pooling and unpooling. In fact, it is the move away from using of fully connected layers that helps SegNet the most, as this drastically reduces the number of parameters to be learnt (see Table 15.5), and thereby also drastically reduces the training requirements of the method. Accordingly, the whole network can be considered a single rather than a dual network and trained efficiently “end-to-end.” Furthermore, the authors identified a far more efficient way to store object location information: they do so by storing *only* the max-pooling indices, viz. the locations of the maximum feature values in each pooling window in each encoder feature map. As a result only 2 bits of information are needed for each  $2 \times 2$  pooling window (cf. Fig. 15.12). This means that even for the initial CNN (encoder) layers, it is not necessary to store the feature maps themselves: what has to be stored is the object location information. By this means the encoder storage requirement is reduced from 134M (corresponding to layers C1–F7 of VGGNet in Table 15.5) down to 14.7M—or only a small fraction of this if it were recoded as 2 bits (instead of two floating point numbers) per pooling window. The total storage for SegNet is rated at twice this, as the same amount of information has to be saved in the decoder layers. However, the same applies to other deconvnets, so in all cases the total amount of data has to be doubled relative to the contents of the initial CNN encoder.

The smaller size of SegNet makes end-to-end training possible, and thereby far more suitable for real-time applications. The authors acknowledge that larger networks can work better—though at the cost of far more complex training procedures, increased memory, and considerably increased inference time. Furthermore, it is difficult to assess their true performance. Basically, the decoders have to be trained via very large and cumbersome encoders, and the latter are general purpose rather than being targeted at specific applications (note that the amount of effort required to train such encoders is so great as to discourage workers from retraining them to adapt them to their own applications). In the majority of instances, such networks have been based on a VGGNet front end, typically containing all 13 sublayers of C1–C5, together with a variable (very small) number of fully connected layers.

These considerations make it no surprise that Badrinarayanan *et al.* successfully applied SegNet to the CamVid dataset (Brostow *et al.*, 2009) by training it end-to-end for optimum adaptation. They found it outperformed seven conventional (nonneural) methods, including local label descriptors and superparsing (Yang *et al.*, 2012; Tighe and Lazebnik, 2013), obtaining scores averaging to 80.1%, in comparison with 51.2% and 62.0%, respectively; the 11 categories to be recognized were building, tree, sky, vehicle, sign, road, pedestrian, fence, pole, pavement, and cyclist, and the accuracies attained for these ranged from 52.9%



(cyclist) to 94.7% (pavement). Their success with this task may be judged from the results of their online demo (<http://mi.eng.cam.ac.uk/projects/segnet/>—website accessed 7 October 2016), which was used to generate the pictures in Fig. 15.14: In fact, this demo placed pixels in 12 categories, including road markings in addition to the 11 listed above: see Fig. 15.14.



**FIGURE 15.14**

Three road scenes taken from the front passenger seat. In each case, the image on the left is the original, and the image on the right is the segmentation produced by SegNet. The key indicates the 12 possible meanings assigned by SegNet. Although location accuracy is not perfect, the assigned meanings are generally reasonable, given the limited number of allowed interpretations and the variety of objects within the fields of view. These pictures were processed using the online demo at <http://mi.eng.cam.ac.uk/projects/segnet/> (Badrinarayanan et al., 2015).

They also did a careful comparison of SegNet with other recent semantic segmentation networks, including FCN and DeconvNet. FCN and DeconvNet have the same encoder size (134M); note that FCN reduces the decoder size down to 0.5M, though DeconvNet continues with a 134M decoder. Class averages for the three methods are 59.1%, 62.2%, and 69.6%, making SegNet the numerically worst of the three, though its accuracy is still competitive, and it has the distinct advantage of being more adaptable by virtue of being trained end-to-end. In fact, it is also easily the fastest running, being  $\sim 2.2$  times faster than FCN and  $\sim 3.3$  times faster than DeconvNet, albeit (because of availability of results) on different sized images.

Overall, the authors state that architectures “which store the encoder network feature maps in full perform best but consume more memory during inference time,” which also means that they run more slowly. On the other hand, SegNet is more efficient as it only stores the max-pooling indices; in addition, it has competitive accuracy, and its capability for end-to-end training on currently relevant data make it significantly more adaptable.

---

## 15.11 RECURRENT NEURAL NETWORKS

No sooner had we embarked upon this chapter on deep-learning networks than we realized that the most obvious upgrade path from traditional ANNs was that of using convolutional neural elements. No other possibility seemed to arise for modifying or upgrading the architecture. In retrospect, that was largely because we were primarily intent on recognition—whether of single objects or in the end for performing semantic segmentation of whole images. But while we had a firm mind-set for analyzing static images, in practice, we also need to have our eyes set on video interpretation. In fact, image sequences are best and most compactly described by telling the story underlying any video. The next step is to find how best to manage the time element. To achieve this, it is natural to use a state machine approach, and a simple way forward is to feed the outputs of the network back into its own inputs—thereby giving rise to a RNN.

It will be recalled that both ANNs and CNNs were structured carefully into layers, so that each output could only be fed to the inputs of the *following* layer. We now generalize this, so that each neuron output can be fed to at least one input on each neuron. As a result, not only will each neuron be looking at normal, current input signals, but also it will emit signals that reflect the history of the network. Note also that the feedback that is now present has the capability of making the neurons act like flip-flops containing memory, so the entire network will react with strongly time-dependent behavior. Furthermore, although a network of this type is used for testing, it will automatically be subject to continuous training, and the result will also be strongly order-dependent.

In fact, the above description of the new RNN is rather too unconstrained and general: it is better to think of its structure unfolding along the time dimension (Fig. 15.15) and to interpret its operation as performing the same task for every element of an image sequence. Notice that, just as the CNN neurons in each layer performed exactly the same operation at every neuron in a layer, so now the RNN

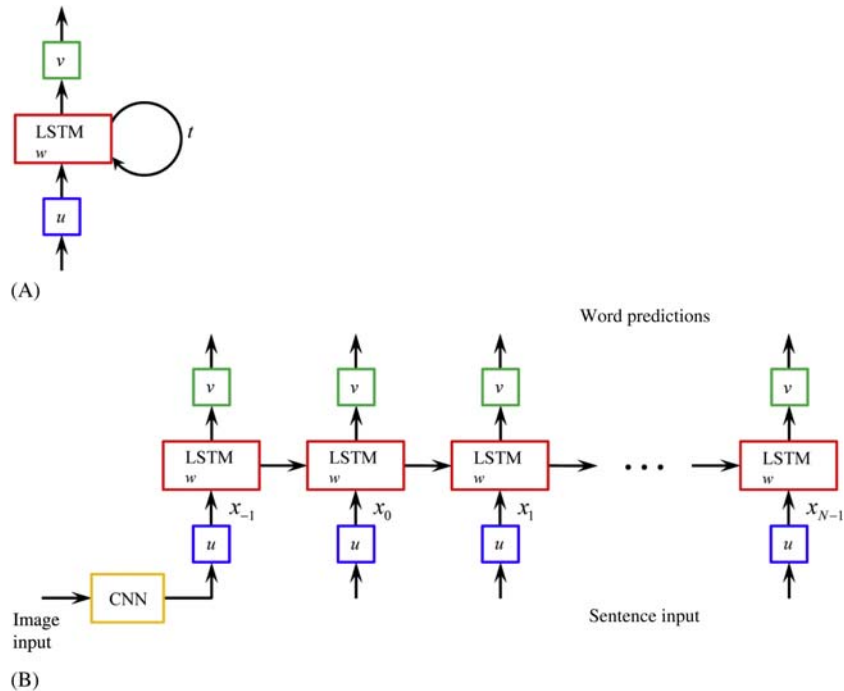


**FIGURE 15.15**

Recurrent neural networks and their application. Part (A) shows how a neuron (here marked “LSTM”: see text) is employed in a recurrent neural network: a single feedback loop has been connected between an output and an input in order to allow the neuron to undergo temporal development (as indicated by  $t$ ). Part (B) shows how the feedback loop can be “unfolded,” to clarify how the network operates after initialization at  $t = -1$ . Note that the same parameters  $u$ ,  $v$ , and  $w$  apply at each instant of time:  $u$  and  $v$  are multiplicative parameters that are applied at each input and output, whereas  $w$  is the weight of the neuron, which is applied internally. In fact, (B) shows more than just the temporal development of the neuron in (A): it actually shows the caption-generating system of Vinyals et al. (2015). In particular, it shows how an image is fed to the RNN via a CNN which extracts and identifies various image features, and these are then analyzed by the RNN to give word predictions. To achieve this,  $N$  sentence inputs [Basically, the system is trained using images accompanied by word inputs—though these can be “sentence” inputs consisting of word vectors (see Mikolov et al., 2013).] are also provided after  $t = -1$ , i.e., for  $t = 0, \dots, N - 1$ . In fact, the word applied at  $t = 0$  is the “start” signal and that applied at  $t = N$  is the “stop” signal.

will perform exactly the same operation at every time element. In practice, this means that the inputs are all equally weighted as  $u$ , the outputs are all equally weighted as  $v$ , and the multiplicative weights in each neuron are all equally weighted as  $w$ .

So far, we have not shown how training will proceed, but this is simply achieved by replacing the backpropagation algorithm by an exactly analogous backpropagation through time (BPTT) algorithm. The overall architecture can now be imagined as a set of identical copies of the same network, with each stage passing data to its temporal successor. There is also the possibility of making the network bidirectional, so that data can be passed from the future back to the past. Stated in this way, the concept makes little sense, but it is actually a useful recipe when dealing with natural language, as sentences have to make global sense, and each word has to be a good contextual fit for its location in a sentence. Moreover, if image sequences are to be interpreted correctly, the output sentence descriptions will also have to make global sense. For clarity, and in spite of its recent popularity, we shall ignore the bidirectional possibility in what follows.

There is one particular difficulty that RNNs have been subject to that did not arise with ANNs or CNNs: whereas the latter could be imagined as completely analogue in operation, with each set of neuron inputs immediately giving rise to a corresponding output, and each set of output signals quickly rippling through the entire machine, with an RNN this process would lead to “race” conditions and it would not be clear how the old memory states would propagate through the system and whether they would result in robust, reliable stored memories, and output signals. These considerations led to neurons having to be very carefully designed with three logistic gates being included inside each neuron. The resulting neurons were called LSTM units. These incorporate safeguards to make the whole network operate reliably, and they have been almost universally employed ever since they were invented by Hochreiter and Schmidhuber in 1997. It should be added that part of their function is to arrange forgetting of old, now irrelevant data; to terminate complete sentences; and to start new ones when appropriate. Finally, note that in many texts, the failure modes of RNNs were originally described as vanishing and exploding gradients (which are particularly serious for the BPTT algorithm) and arose as the analog signals they represented were not properly controlled. The reason for using long short-term memories (LSTMs) was to allow the network parameters to learn reliably and consistently over many time steps.

Considerable work has now been carried out using RNNs. Amongst the most important topics in this area has been that of automatic annotation of images and videos. Notable amongst the most recent papers is that of Vinyals et al. (2015) describing their automatic image caption generating system. This carefully maps both the image and the words into the same space, with the image entering the vision CNN and the words entering as a word embedding into the RNN (Fig. 15.15B). Interestingly, the image is only fed to the first LSTM input: indeed, Vinyals et al. found that feeding the image in repeatedly (i.e., at each time step) led to inferior results as image noise then made the network more prone to overfitting. Overall, the network is trained to minimize the sum of the negative log

likelihood of the correct word being used at each time step, i.e., to ensure that the sentence (sequence of words) that is output for each image is the one with maximum likelihood of being correct. Typical captions include “A group of young people playing a game of frisbee” and “A herd of elephants walking across a dry grass field”—which, in the examples given (Vinyals et al., 2015), were not only correct descriptions of actual video actions but also quite perceptive comments. It is salutary to note that in this work, the RNN is essentially performing a translation function—in this case between the internal codes issuing from the CNN classifier output and the real (English) words the RNN is trained on.

In other work (Vondrick et al., 2016), a relatively simple RNN using an AlexNet CNN front end was trained to make predictions 1 second before an event (e.g., whether two people would hug, kiss, or “high-five”) that were at least 19% more accurate than for previous methods—albeit the absolute performance was some way below that of human operators.

---

## 15.12 CONCLUDING REMARKS

This has been an unusual chapter, in that about 80% of the material has only been published in the last 4–5 years—though of course that material rested strongly on foundations that had been developing over the previous quarter century. The hugely accelerating progress over these past few years is evidenced—unusually for a subject like computer vision—by a considerable proportion of the key papers being made available first on arXiv—a feature that has hitherto been more familiar in particle physics and cosmology than in computer vision. All this created difficulties in gathering together the vital information and in presenting it in any ordered way. In fact, it presented the need for writing it as a series of key case studies, and those that were selected for this purpose were made to tell a developmental story about the subject. However, there is a pitfall in this approach, as it risked putting together a hotchpotch of facts and of claims and counterclaims, but without providing sufficient guidance for the reader on the underlying science or indeed the logic underlying all the work. Therefore, care had to be taken to allow these aspects to emerge. As a result, some of the case study descriptions turned out to be longer than expected, though in the end, this is all to the good as underlying explanations are the nonnegotiable part of any book: thus, the case studies have to be taken as vehicles upon which the principles and explanations of scientific detail are carried along. Then, there are the many terms that are passed around in the research literature, but which one often finds are undefined—“everyone” knows what they mean but in many cases they are never clearly written down, at least in citable places. Indeed, one suspects that they are often handed down solely by word of mouth at conferences and private meetings. As far as possible, to provide a logical development, all such terms have been sought out and defined as and where necessary.

The account starts by describing CNNs and how they are put together—this being followed immediately by an explanation of CNN architectures and the relevant technical terms for describing them: these include terms such as depth, stride, zero padding, receptive field, pooling, and ReLU. But of course, the main important question at this early stage is why convolutional networks won out: in short, this was because of the insistence on position invariance in each layer, which in turn limited the number of network parameters to be learnt by training. Understanding of all these considerations allowed us to go on to study LeCun et al.’s LeNet architecture: this originated in the 1990s and culminated in their key paper in 1998. Although this architecture remained a paradigm approach, it was not especially successful vis-à-vis other nonneural approaches. It was only in 2012, when it was radically updated in various key ways by Krizhevsky et al. in the form of AlexNet, that this approach really took off, and was shown to be superior to previous nonneural approaches. Hence, AlexNet formed the basis for the next case study, which was pursued at length in [Section 15.5](#). In fact, it wasn’t merely the architecture that was original but also the methods for generating and augmenting training sets: it had become clear when training huge networks containing  $\sim 650,000$  neurons with  $\sim 60$  million trainable parameters, that a mere million images (1000 from each of 1000 classes) is wildly insufficient. And so additional images were obtained (1) by extracting numerous patches and expanding numbers of examples by applying horizontal reflections and (2) by applying transformations to the intensities and colors in order to further increase the quantity of valid training samples—both of these strategies proving successful.

Almost before the ink had dried on the AlexNet paper, Zeiler and Fergus (2014) found how to optimize the architecture further and produced means for visualizing its operation—on the basis that understanding its *modus operandi* would lead to further improvement. This did turn out to be possible, and so-called ablation studies helped further. (At this point, ablation was another technical term that had to be explored and explained.)

Zeiler and Fergus’s ideas on deconvolution for analyzing the internal operation of a CNN proved vital to others for producing the new deconv networks which would not only allow objects to be classified, but also by inverting the process, to allow the classes to be transformed into pixel maps, thereby leading to semantic segmentation of the original images. In this area, the works of Noh et al. (2015) and Badrinarayanan et al. (2015) were seminal—though others also made valuable contributions. However, not to be forgotten was Simonyan and Zisserman’s VGGNet architecture (2015), which the latter two papers very much relied upon: this was because Simonyan and Zisserman found how to make CNNs of the AlexNet ilk significantly deeper (theirs was the first to be reasonably termed “very deep”)—by various means, including in particular that of narrowing the receptive fields of the convolution kernels down to a maximum of  $3 \times 3$ .

All this was a long story—and future work will show that it is still far from being complete. Indeed, even if the VGGNet architecture is near the optimum that is possible for a multioutput classifier that is fed with raw images, it remains to be seen how well it can be applied for similar applications in acoustics and seismology

or in 3-D applications; and how widely it can be used in more general situations than those of classification and semantic segmentation. For example—as outlined in [Section 15.11](#)—Google have published a paper (Vinyals et al., 2015) in which they show nontrivial pictures that have been described by their automatic image-captioning system: when sufficiently developed, this will be of distinct value for searching the web for specific types of picture. Even at this stage, the work involves sentence generation combined with deep neural analysis of images and will have to be watched closely for further progress. This sort of work will clearly be of value in talking to and controlling robots. However, here, we avoid the temptation to include excessive speculation: our aim is merely to show what has so far been achieved and to hint at what might be possible. In any case, even if the basic theory of deep neural networks progresses little further for some time, maximizing the impact of what has been done so far and advancing the methodology will best be achieved by wide exploration of potential applications.

Finally, perhaps the most lasting impact of CNNs such as VGGNet is that of providing highly effective pretrained feature spaces for other classifiers, to which SVM and other networks can readily be added to tackle and solve new tasks. As has already been remarked, VGGNet has been the preferred choice in the vision community for performing this function, but it should be emphasized that it has not been alone: e.g., GoogLeNet has also been applied in this way. In a case in point, Bejiga et al. (2017) have described how they combined a pretrained GoogLeNet front end with a linear SVM classifier to assist avalanche search and rescue operations by analyzing unmanned aerial vehicle (UAV) image sequences. Interestingly, their combined CNN–SVM classifier easily outperformed a traditional HOG–SVM classifier on two datasets and resulted in accuracies well in excess of 90% for several videos. In another case, Ravanbakhsh et al (2015) used an AlexNet front end with an SVM classifier for performing human action recognition, again attaining performance levels well above those of traditional methods when applied to sports and other videos.

*This chapter has covered deep-learning networks and their application to classification and segmentation. Their explosive development in the 2010s has been highlighted, and the ground rules for deep-learning architectures have been explained at some length with the aid of a number of key case studies. What happened in 2012 was the sudden realization that deep neural networks are now superior in performance to even the best conventional (nonneural) approaches in a handful of important application areas. They also seem to be making valuable progress in other areas such as automatic image caption generation.*

---

### 15.13 BIBLIOGRAPHICAL AND HISTORICAL NOTES

This rather unusual chapter reflects a slow systematic advance in the development and use of ANNs—during which CNNs gradually came to dominate the scene—

this being followed by an explosive series of advances which took place from 2011 onward. The key event that initiated the latter change was the attempt by Krizhevsky et al. to respond to the ILSVRC in 2012. After augmenting the by then standard LeCun et al. (1998) LeNet architecture, and making various what might in 2011–12 have been classed as ‘daring’ moves—including use of ReLUs, together with overlapping (max-) pooling, huge numbers of layers, and use of dropout—they implemented the whole machine as a dual GPU architecture joined only at a limited number of layers; finally, they trained the system not only on the 1.2 million images supplied for the challenge but in the end  $\sim 2000$  times that number. To achieve all that within a year was a formidable task, bearing in mind that it was not known in advance that these measures would actually work in practice. Needless to say, in the following year or two, many other workers followed this advance with improvements of their own—notable amongst these being Simonyan and Zisserman (2015), who found how to make networks “very deep”—in particular, by narrowing the receptive fields of the convolution kernels to a *maximum* of  $3 \times 3$ . A notable application of this type of work was that of Badrinarayanan et al. (2015), which was aimed at semantic segmentation.

At this point, the theoretical development of the CNN approach seemed to slow down, and attention turned to finding what applications could be dealt with using existing theory and the experimental methods so far developed. This meant that large numbers of papers suddenly started to be produced in various application areas. Notably, these included face detection and recognition. Developments in the latter areas will be covered more fully in [Chapter 21](#), Face Detection and Recognition: the Impact of Deep Learning. However, the work done by Taigman et al. (2014) is worth recalling: their “DeepFace” approach to face recognition brought the performance level up to 97.35%, which was extremely close to that for human recognition. Interestingly, they achieved this using an initial “frontalization” technique aimed at standardizing faces to a symmetric frontal view. Sagonas et al. (2015) developed their own frontalization technique obtaining that can best be described as a trained eigenset of frontal images. At about the same time, Yang et al. (2015, 2017) developed a high-performance Faceness-Net face detector using a CNN architecture for finding attributes of face images. This was run forwards to find the intrinsic face features and “in reverse” to regenerate localized face-part response maps: here, they followed the coding–decoding procedures set out by Zeiler and Fergus (2014). Finally, Bai et al. (2016) produced a very much simpler and faster design: this is a FCN working at multiple scales, with five shared convolutional layers followed by a branching out into two further convolutional layers—the latter respectively coping with (1) the multiple scales and (2) the sliding window effect needed to perform the final matching. An interesting and actually quite powerful conclusion is that a simpler system that is trained end-to-end has a better chance of achieving superior performance than one that is put together using separately pretrained sections.



This page intentionally left blank

# 3D vision and motion

# 4

*Part 4 covers the developments needed for an understanding of real scenes, which necessarily contain 3D objects—a number of which may be in motion. 3D vision is considerably more complex than 2D vision, not least because the number of degrees of freedom of an object will typically have increased from three to six, with an accompanying combinatorial increase in the number of scene configurations to be considered.*

*This part of the book starts ([Chapter 16](#): The three-dimensional world) by airing the problems, before considering the complexities of full perspective projection ([Chapter 17](#): Tackling the perspective n-point problem). Next, it is*

*useful to see what shortcuts can be achieved by taking invariants into account (Chapter 18: Invariants and perspective). Chapter 19, Image transformations and camera calibration, deals with camera calibration but also shows how recent research has attempted to avoid the need for explicit calibration by making careful computations that interrelate multiple scenes: here the emphasis is on taking opportunities that permit some of the complexities to be bypassed. Finally, Chapter 20, Motion, examines the problems of motion in the context of 3D vision.*

# The three-dimensional world

# 16

Humans are able to employ 3-D vision with consummate ease, and according to conventional wisdom, binocular vision is the key to this success. The truth is more complex than this, and this chapter demonstrates why.

*Look out for:*

- What can be achieved using binocular vision
- How the shading of surfaces can be used in place of binocular vision to achieve similar ends
- How these basic methods provide dimensional information for 3-D scenes but do not immediately lead to object recognition
- How the process of 3-D object recognition can be tackled by studies of 3-D geometry.

Note that this is an introductory chapter on 3-D vision, designed to give the flavor of the subject and to show its origins in human vision. It will be followed by the other four chapters (Chapters 17–20) that comprise Part 4 of this volume.

At a more detailed level, notice the importance of the epipolar line approach in solving the correspondence problem: the concept is deservedly taken considerably further in Chapter 19, Image Transformations and Camera Calibration, in conjunction with the required mathematical formulation.

## 16.1 INTRODUCTION

In the foregoing chapters, it has generally been assumed that objects are essentially flat and are viewed from above in such a way that there are only three degrees of freedom—namely, the two associated with position, and a further one concerned with orientation. Although this approach was adequate for carrying out many useful visual tasks, it is inadequate for interpreting outdoor or factory scenes or even for helping with quite simple robot assembly and inspection tasks. Indeed, over the past few decades, a considerable amount of quite sophisticated theory has been developed and backed up by experiment to find how scenes composed of real 3-D objects can be understood in detail.

In general, this means attempting to interpret scenes in which objects may appear in totally arbitrary positions and orientations—corresponding to six degrees of freedom. Interpreting such scenes, and deducing the translation and orientation parameters of arbitrary sets of objects, takes a substantial amount of computation—partly because of the inherent ambiguity in inferring 3-D information from 2-D images.

A variety of approaches are now available for proceeding with 3-D vision. A single chapter will be unable to describe all of them but the intention here is to provide an overview, outlining the basic principles and classifying the methods according to generality, applicability, etc. Although computer vision need not necessarily mimic the capabilities of the human eye–brain system, much research on 3-D vision has been aimed at biological modeling. This type of research shows that the human visual system makes use of a number of different methods simultaneously, taking appropriate cues from the input data and forming hypotheses about the content of a scene, progressively enhancing these hypotheses until a useful working model of what is present is produced. Thus, individual methods are not expected to work in isolation: rather, they need to provide the model generator with whatever data become available. Clearly, biological machinery of various types will lie idle for much of the time until triggered by specific input stimuli. Computer vision systems are currently less sophisticated than this and tend to be built on specific processing models, so that they can be applied efficiently to more restricted types of image data. In this chapter, we adopt the pragmatic view that particular methods need to be (or have been) developed for specific types of situation, and that they should be used only when appropriate—although some care is taken to elucidate what the appropriate types of application are.

---

## 16.2 THREE-DIMENSIONAL VISION—THE VARIETY OF METHODS

One of the most obvious characteristics of the human visual system is that it employs two eyes, and it is well known to the layman that binocular (or “stereo”) vision permits depth to be discerned within a scene. However, the loss of vision that results when one eye is shut is relatively insignificant and is by no means a disqualification from driving a car or even an airplane. On the contrary, depth can readily be deduced in monocular vision from a plethora of cues that are buried in an image. Naturally, to achieve this the eye–brain system is able to call on a huge amount of prestored data about the physical world and about the types of object in it, be they manmade or natural entities. For example, the size of any car being viewed is strongly constrained; likewise, most objects have highly restricted sizes, both absolutely and in their depths relative to their frontal dimensions. Nevertheless, in a single view of a scene, it is normally impossible to deduce

absolute sizes—all the objects and their depths can be scaled up or down by arbitrary factors and this cannot be discerned from a monocular view.

Although it is clear that the eye–brain system makes use of a huge database relating to the physical world, there is much that can be learnt with negligible prior knowledge, even from a single monocular view. The main key to this is the “shape from shading” concept. For 3-D shape to be deducible from shading information (i.e., from the gray-scale intensities in an image), something has to be known about how the scene is lit—the simplest situation being when the scene is illuminated by a single point light source at a known position: note that indoors a single overhead tungsten light is still the most usual illuminator, whereas outdoors the sun performs a similar function. In either case, an obvious result is that a single source will illuminate one part of an object and not another—which then remains in shadow—and parts that are orientated in various ways relative to the source and the observer appear with different brightness values, so that orientation can in principle be deduced. In fact, as will be seen below, deduction of orientation and position is not at all trivial and may even be ambiguous. Nevertheless, successful methods have been developed for carrying out this task. One problem that often arises is that the position of the light source is unknown but this information can generally be extracted (at least by the eye) from the scene being examined, so a bootstrapping procedure is then able to unlock the image data gradually and proceed to an interpretation.

Although these methods enable the eye to interpret real scenes, it is difficult to say quite to what degree of precision they are carried out. With computer vision, the required precision levels are liable to be higher, although the machine will be aided by knowing exactly where the source of illumination is. However, with computer vision we can go further and arrange artificial lighting schemes that would not appear in nature, so the computer can acquire an advantage over the human visual system. In particular, a set of light sources can be applied in sequence to the scene—an approach known as photometric stereo—which can in certain cases help the computer to interpret the scene more rigorously and efficiently. In other cases, structured light may be applied: this means projecting onto the scene a pattern of spots or stripes, or even a grid of lines, and measuring their positions in the resulting image. By this means, depth information can be obtained much as for pairs of stereo images.

Finally, a number of methods have been developed for analyzing images on the basis of readily identifiable sets of features. These methods are the 3-D analogs of the graph matching and Generalized Hough Transform (GHT) approaches of [Chapter 11](#), The Generalized Hough Transform. However, they are significantly more complex because they generally involve six degrees of freedom in place of the three assumed throughout [Chapter 11](#), The Generalized Hough Transform. It should also be noted that such methods make strong assumptions about the particular objects to be located within the scene. In general situations, it is unlikely that such assumptions could be made, and so initial analysis of any images must be made on the basis that the entire scene must be mapped out in 3-D, then 3-D

models built up and finally deductions must be made by noticing what relation one part of the scene bears to another part. Note that if a scene is composed from an entirely new set of objects, all that can be done is to *describe* what is present and say perhaps what the set most closely *resembles*: recognition per se cannot be performed. Notice that scene analysis is—at least from a single monocular image—an inherently ambiguous process: every scene can have a number of possible interpretations and there is evidence that the eye looks for the simplest and most probable explanation rather than an absolute interpretation. Indeed, it is underlined by the many illusions to which the eye–brain system is subject that decisions must repeatedly be made concerning the most likely interpretation of a scene and that there is some risk that its internal model builder will lock on to an interpretation or part-interpretation that is suboptimal (see the paintings of Escher!).

This section has indicated that methods of 3-D vision can be categorized according to whether they start by mapping out the shapes of objects in 3-D space and then attempt to interpret the resulting shapes, or whether they try to identify objects directly from their features. In either case, a knowledge base is ultimately called for. It has also been seen that methods of mapping objects in real space include monocular and binocular methods, although structured lighting can help to offset the deficiencies of employing a single “eye.” Laser scanning and ranging techniques must also be included in methods of 3-D mapping, although space precludes detailed discussion of these techniques in this book.

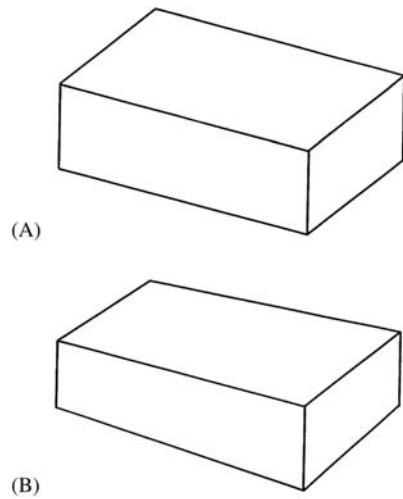
---

### 16.3 PROJECTION SCHEMES FOR THREE-DIMENSIONAL VISION

It is common in engineering drawings to provide three views of an object to be manufactured—the plan, the side view, and the elevation. Traditionally, these views are simple orthographic (nondistorting) projections of the object—that is, they are made by taking sets of parallel lines from points on the object to the flat plane on which it is being projected.

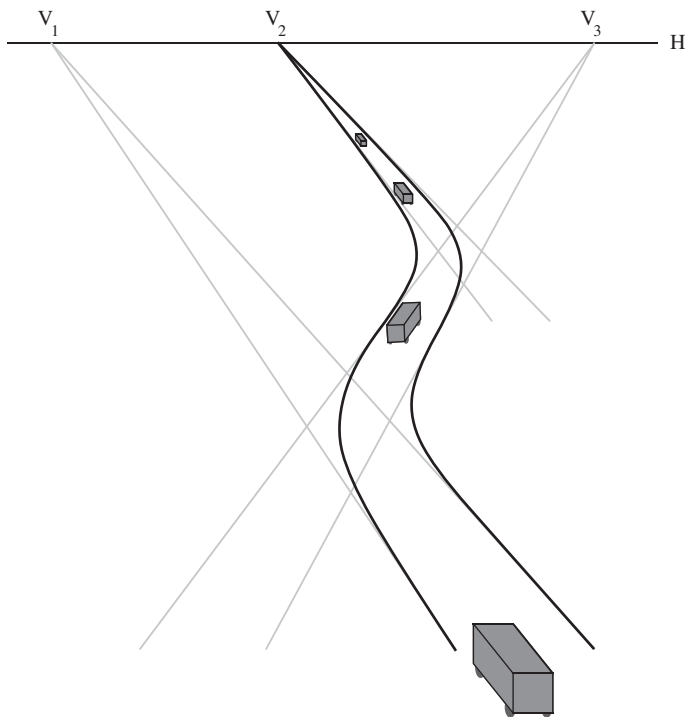
However, when objects are viewed by eye or from a camera, rays converge to the lens and so images formed in this way are subject not only to change of scale but also to perspective distortions (Fig. 16.1). This type of projection is called perspective projection, although it includes orthographic projection as the special case of viewing from a distant point. Unfortunately, perspective projections have the disadvantage that they tend to make objects appear more complex than they really are by destroying simple relationships between their features: thus, parallel edges no longer appear parallel and midpoints no longer appear as such (although many useful geometric properties still hold—e.g., a tangent line remains a tangent line and the order of points on a straight line remains unchanged).

In outdoor scenes, it is very common to see lines which are known to be parallel apparently converging toward a vanishing point on the horizon line (Fig. 16.2).



**FIGURE 16.1**

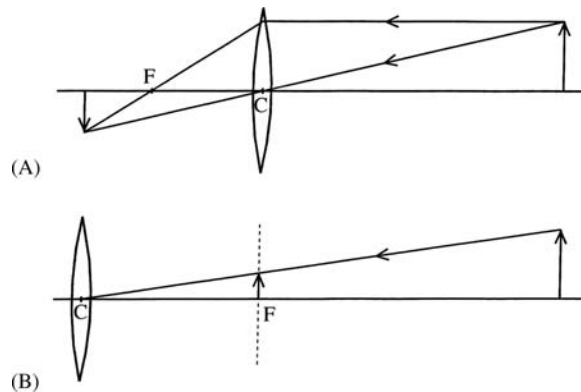
(A) Image of a rectangular box taken using orthographic projection; (B) the same box taken using perspective projection. In (B) note that parallel lines no longer appear parallel, although paradoxically the box appears more realistic.



**FIGURE 16.2**

Vanishing points and the horizon line. This figure shows how parallel lines on the ground plane appear, under perspective projection, to meet at vanishing points  $V_i$  on the horizon line  $H$ . (Note that  $V_i$  and  $H$  lie in the *image plane*.) If two parallel lines do not lie on the ground plane, their vanishing point will lie on a different vanishing line. Hence, it should be possible to determine whether any roads are on an incline by computing all the vanishing points for the scene.



**FIGURE 16.3**

(A) Projection of an image into the image plane by a convex lens; note that a single image plane only brings objects at a single distance into focus but that for far-off objects the image plane may be taken to be the focal plane, a distance  $f$  from the lens; (B) a commonly used convention which imagines the projected image to appear noninverted at a focal plane  $F$  in front of the lens. The center of the lens is said to be the center of projection for image formation.

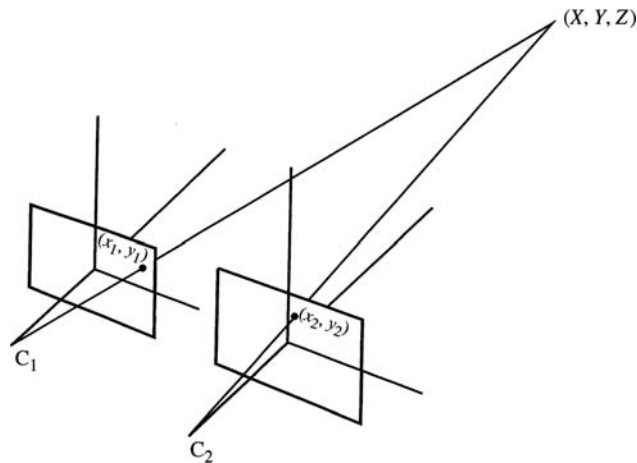
In fact, the horizon line is the projection onto the image plane of the line at infinity on the ground plane  $G$ : it is the set of all possible vanishing points for parallel lines on  $G$ . In general, the vanishing points of a plane  $P$  are defined as the projections onto the image plane corresponding to points at infinity in a given direction on  $P$ . Thus, any plane  $Q$  within the field of view may have vanishing points in the image plane, and these will lie on a vanishing line which is the analog of the horizon line for  $Q$ .

Fig. 16.3A shows how an image is projected into the image plane by a convex (eye or camera) lens at the origin. It is inconvenient to have to consider inverted images, and it is a commonly used convention in image analysis to set the center of the lens at the origin  $(0, 0, 0)$  and to imagine the image plane to be the plane  $Z=f$ ,  $f$  being the focal length of the lens; with this simplified geometry (Fig. 16.3B), images in the image plane appear noninverted. Taking a general point in the scene as  $(X, Y, Z)$ , which appears in the image as  $(x_1, y_1)$ , perspective projection now gives:

$$(x_1, y_1) = (fX/Z, fY/Z) \quad (16.1)$$

### 16.3.1 BINOCULAR IMAGES

Fig. 16.4 shows the situation when two lenses are used to obtain a stereo pair of images. In general, the two optical systems do not have parallel optical axes but exhibit a “vergence” (which may be variable, as it is for human eyes), so that they intersect at some point within the scene. Then a general point  $(X, Y, Z)$  in the



**FIGURE 16.4**

Stereo imaging using two lenses. The axes of the optical systems are parallel, i.e., there is no “vergence” between the optical axes.

scene has two different pairs of coordinates,  $(x_1, y_1)$  and  $(x_2, y_2)$ , in its two images, which differ both because of the vergence between the optical axes and because the baseline  $b$  between the lenses causes relative displacement or “disparity” of the points in the two images.

For simplicity, we now take the vergence to be zero, i.e., the optic axes are parallel. Then, with suitable choice of  $Z$  axis on the perpendicular bisector of the baseline  $b$ , we obtain two equations:

$$x_1 = (X + b/2)f/Z \quad (16.2)$$

$$x_2 = (X - b/2)f/Z \quad (16.3)$$

so that the disparity is

$$D = x_1 - x_2 = bf/Z \quad (16.4)$$

Rewriting this equation in the form:

$$Z = bf/(x_1 - x_2) \quad (16.5)$$

now permits the depth  $Z$  to be calculated. In fact, computation of  $Z$  only requires the disparity for a stereo pair of image points to be found and parameters of the optical systems to be known. However, confirming that both points in a stereo pair actually correspond to the same point in the original scene is in general not at all trivial, and much of the computation in stereo vision is devoted to this task. In addition, to obtain good accuracy in the determination of depth, a large baseline  $b$  is required: unfortunately, as  $b$  is increased the correspondence between the images decreases, so it becomes more difficult to find matching points.

### 16.3.2 THE CORRESPONDENCE PROBLEM

There are two important approaches to finding pairs of points that match in the two images of a stereo pair. One is that of “light striping” (one form of structured lighting), which encodes the two images so that it is easy to see pairs of corresponding points. If a single vertical stripe is used, for every value of  $y$  there is in principle only one light stripe point in each image and so the matching problem is solved. We return to this problem in a later section.

The second important approach is to employ epipolar lines. To understand this approach, imagine that we have located a distinctive point in the first image and that we are marking all possible points in the object field which could have given rise to it. This will mark out a line of points at various depths in the scene and, when viewed in the second image plane, a locus of points can be constructed in that plane. This locus is the *epipolar line* corresponding to the original image point in the alternate image (Fig. 16.5). If we now search along the epipolar line for a similarly distinctive point in the second image, the chance of finding the correct match is significantly enhanced. This method has the advantage not only of cutting down the amount of computation required to find corresponding points, but also of reducing significantly the chance of false alarms. Note that the concept of an epipolar line applies to both images—a point in one image gives an epipolar line in the other image. Note also that in the simple geometry of Fig. 16.4, all epipolar lines are parallel to the  $x$ -axis, although this is

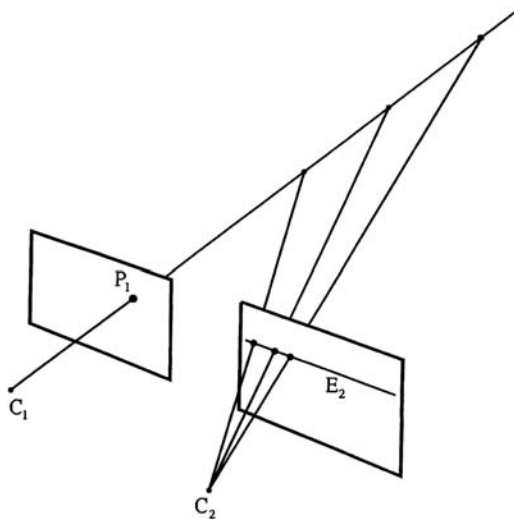


**FIGURE 16.5**

Geometry of epipolar lines. A point  $P_1$  in one image plane may have arisen from any one of a line of points in the scene and may appear in the alternate image plane at any point on the so-called epipolar line  $E_2$ .

not so in general (in fact, the general situation is that all epipolar lines in one image plane pass through the point that is the image of the projection point of the alternate image plane).

The correspondence problem is rendered considerably more difficult by the fact that there will be points in the scene which give rise to points in one image but not in the other. Such points are either occluded in the one image, or else are so distorted as not to give a recognizable match in the two images (e.g., the different background might mask a corner point in one image while permitting it to stand out in the other). Any attempt to match such points can then only lead to false alarms. Thus, it is necessary to search for consistent sets of solutions in the form of continuous object surfaces in the scene. For this reason, iterative “relaxation” schemes are widely used to implement stereo matching.

Broadly speaking, correspondences are sought by two methods: one is the matching of near-vertical edge points in the two images (near-horizontal edge points do not give the required precision); the other is the matching of local intensity patterns using correlation techniques. Correlation is an expensive operation and, in this case, is relatively unreliable—principally because intensity patterns frequently appear significantly foreshortened (i.e., distorted by the effects of perspective) in one or other image and hence are difficult to match reliably. In such cases, the most practical solution is to reduce the baseline; as noted earlier, this has the effect of reducing the accuracy of depth measurement. Further details of these techniques are to be found in Shirai (1987).

Before leaving this topic, we consider in slightly more detail how the above-mentioned problems of visibility arise. Fig. 16.6 shows a situation in which an object is being observed by two cameras giving stereo images. Clearly, much of the object will not be visible in either image because of self-occlusion, whereas some feature points will only be visible in one or the other image. Now consider the order in which the points appear in the two images (Fig. 16.7). The points which are visible appear in the same order as in the scene, and the points which are just going out of sight are those for which the order between the scene and the image is just about to change. Points which provide information about the front surface of the object can thus only bear a simple geometrical relation to each other: in particular, for points not to obscure, or be obscured by, a given point  $P$ , they must not lie within a double-ended cone region defined by  $P$  and the centers of projection  $C_1, C_2$  of the two cameras: this region is shown shaded in Fig. 16.7. A surface passing through  $P$  for which full-depth information can be retrieved must lie entirely within the nonshaded region. (Of course, a new double-ended cone must be considered for each point on the surface being viewed.) Note that the possibility of objects containing holes, or having transparent sections, must not be forgotten (such cases can be detected from differences in the ordering of feature points in the two views—see Fig. 16.7); neither must it be ignored that the foregoing figures represent a single horizontal cross section of an object which can have totally different shapes and depths in different cross-sections.

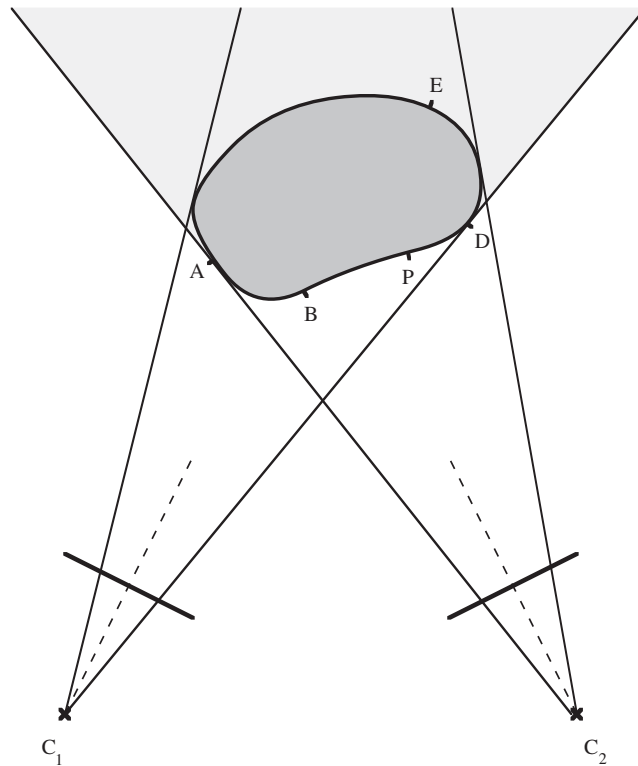


**FIGURE 16.6**

Visibility of feature points in two stereo views. Here, an object is viewed from two directions. Only feature points which appear in both views are of value for depth estimation. This eliminates all points in the shaded region, such as E, from consideration.

## 16.4 SHAPE FROM SHADING

It was mentioned in [Section 16.2](#) that it is possible to analyze the pattern of intensities in a single (monocular) image and to deduce the shapes of objects from the shading information. The principle underlying this technique is that of modeling the reflectance of objects in the scene as a function of the angles of incidence  $i$  and emergence  $e$  of light from their surfaces. In fact, a third angle is also involved, and it is called the “phase”  $g$  ([Fig. 16.8](#)).

A general model of the situation gives the radiance  $I$  (light intensity in the image) in terms of the irradiance  $E$  (energy per unit area falling on the surface of the object) and the reflectance  $R$ :

$$I(x_1, y_1) = E(x, y, z)R(\mathbf{n}, \mathbf{s}, \mathbf{v}) \quad (16.6)$$

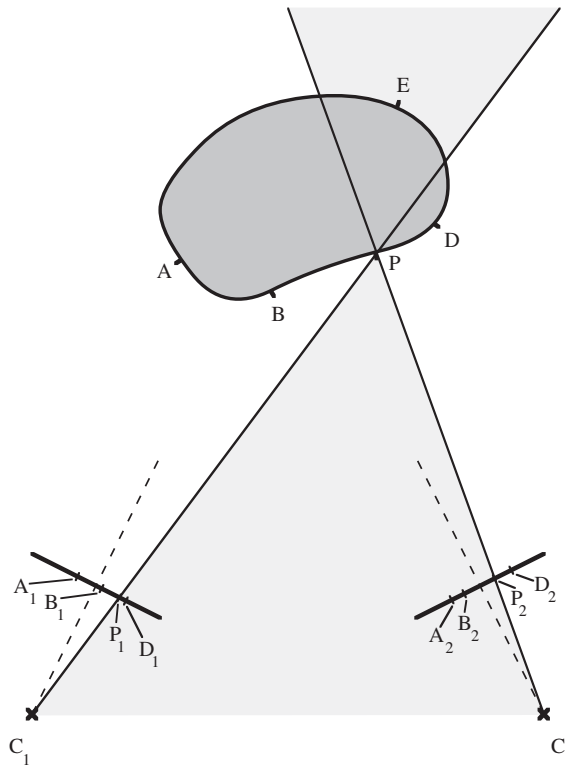


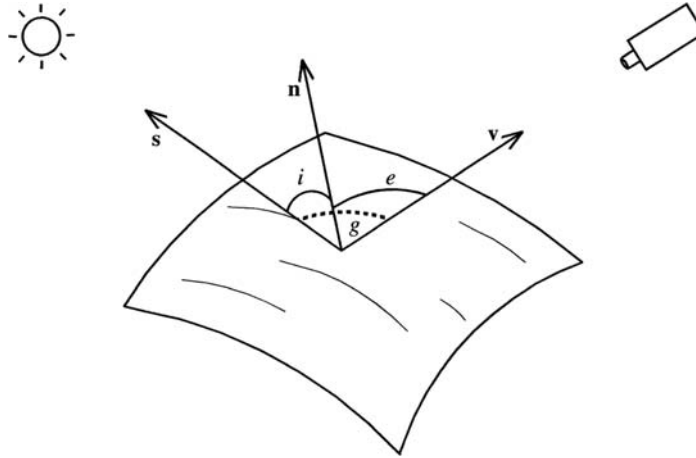
**FIGURE 16.7**

Ordering of feature points on an object. In the two views of the object shown here, the feature points all appear in the same order  $A, B, P, D$  as on the surface of the object. Points for which this would not be valid, such as  $E$ , are behind the object and are obscured from view. Relative to a given visible feature  $P$ , there is a double-ended cone (shaded) in which feature points must not appear if they are not to obscure the feature under consideration. An exception to these rules might be if the object had a semitransparent window through which an additional feature  $T$  were visible: in that case, interpretation would be facilitated by noting that the orderings of the features seen in the two views were different—e.g.,  $A_1, T_1, B_1, P_1, D_1$  and  $A_2, B_2, T_2, P_2, D_2$ .

It is well known that a number of matt surfaces approximate reasonably well to an ideal Lambertian surface whose reflectance function depends only on the angle of incidence  $i$ —that is, the angles of emergence and phase are immaterial:

$$I = (1/\pi)E \cos i \quad (16.7)$$

For the present purpose  $E$  is regarded as a constant and is combined with other constants for the camera and the optical system (including, e.g., the


**FIGURE 16.8**

Geometry of reflection. An incident ray from source direction  $\mathbf{s}$  is reflected along the viewer direction  $\mathbf{v}$  by an element of the surface whose local normal direction is  $\mathbf{n}$ ;  $i$ ,  $e$ , and  $g$  are defined respectively as the incident, emergent, and phase angles.

$f$ -number). In this way, a normalized reflectance is obtained, which in this case is

$$\begin{aligned} R &= R_0 \cos i = R_0 \mathbf{s} \cdot \mathbf{n} \\ &= \frac{R_0(1 + pp_s + qq_s)}{(1 + p^2 + q^2)^{1/2}(1 + p_s^2 + q_s^2)^{1/2}} \end{aligned} \quad (16.8)$$

where we have used the standard convention of writing orientations in 3-D in terms of  $p$  and  $q$  values. These are not direction cosines but correspond to the coordinates of the point  $(p, q, l)$  at which a particular direction vector from the origin meets the plane  $z=1$ : hence, they need suitable normalization, as in the above equation.

The above equation gives a reflectance map in gradient  $(p, q)$  space. We now temporarily set the absolute reflectance value  $R_0$  equal to unity. The reflectance map can be drawn as a set of contours of equal brightness, starting with a point having  $R = 1$  at  $\mathbf{s} = \mathbf{n}$ , and going down to zero for  $\mathbf{n}$  perpendicular to  $\mathbf{s}$ . When  $\mathbf{s} = \mathbf{v}$ , so that the light source is along the viewing direction (here taken to be the direction  $p = q = 0$ ), zero brightness occurs only for infinite distances on the reflectance map [ $(p^2 + q^2)^{1/2}$  approaching infinity] (Fig. 16.9A). In a more general case, when  $\mathbf{s} \neq \mathbf{v}$ , zero brightness occurs along a straight line in gradient space (Fig. 16.9B). To find the exact shapes of the contours, we can set  $R$  at a constant value  $a$ , which results in

$$a(1 + p^2 + q^2)^{1/2}(1 + p_s^2 + q_s^2)^{1/2} = 1 + pp_s + qq_s \quad (16.9)$$

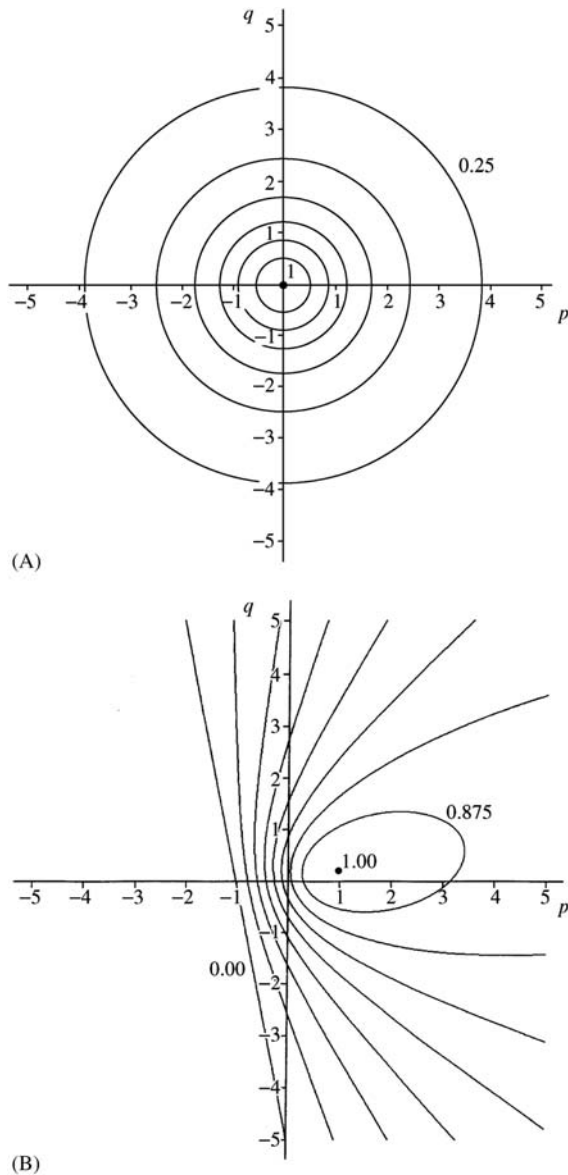


**FIGURE 16.9**

Reflectance maps for Lambertian surfaces: (A) contours of constant intensity plotted in gradient  $(p, q)$  space for the case where the source direction  $\mathbf{s}$  (marked by a black dot) is along the viewing direction  $\mathbf{v}$   $(0, 0)$  (the contours are taken in steps of 0.125 between the values shown); (B) the contours that arise where the source direction  $(p_s, q_s)$  is at a point (marked by a black dot) in the positive quadrant of  $(p, q)$  space: note that there is a well-defined region, bounded by the straight line  $1 + \rho p_s + q q_s = 0$ , for which the intensity is zero (the contours are again taken in steps of 0.125).



Squaring this equation clearly gives a quadratic in  $p$  and  $q$ , which could be simplified by a suitable change of axes. Thus, the contours must be curves of conic section, namely circles, ellipses, parabolas, hyperbolas, lines, or points (the case of a point arises only when  $a = 1$ , when we get  $p = p_s$ ,  $q = q_s$ ; and that of a line only if  $a = 0$ , when we get the equation  $1 + pp_s + qq_s = 0$ : both of these solutions were implied above).

Unfortunately, object reflectances are not all Lambertian and an obvious exception is for surfaces that approximate to pure specular reflection. In that case  $e = i$  and  $g = i + e$  ( $\mathbf{s}$ ,  $\mathbf{n}$ ,  $\mathbf{v}$  are coplanar); the only nonzero reflectance position in gradient space is the point representing the bisector of the angle between the source direction  $\mathbf{s}$  ( $p$ ,  $q$ ) and the viewing direction  $\mathbf{v}$  ( $0$ ,  $0$ )—that is,  $\mathbf{n}$  is along  $\mathbf{s} + \mathbf{v}$ —and very approximately:

$$p \approx p_s/2 \quad (16.10)$$

$$q \approx q_s/2 \quad (16.11)$$

For less perfect specularity, a peak is obtained around this position. A good approximation to the reflectance of many real surfaces is obtained by modeling them as basically Lambertian but with a strong additional reflectance near the specular reflectance position. Using the Phong (1975) model for the latter component gives

$$R = R_0 \cos i + R_1 \cos^m \theta \quad (16.12)$$

$\theta$  being the angle between the actual emergence direction and the ideal specular reflectance direction.

The resulting contours now have two centers around which to peak: the first is the ideal specular reflection direction ( $p \approx p_s/2$ ,  $q \approx q_s/2$ ), and the second is that of the source direction ( $p = p_s$ ,  $q = q_s$ ). When objects are at all shiny—such as metal, plastic, liquid, or even wood surfaces—the specular peak is quite sharp and rather intense: casual observation may not even indicate the presence of another peak as Lambertian reflection is so diffuse (Fig. 16.10). In other cases, the specular peak can broaden and become more diffuse: hence it may merge with the Lambertian peak and effectively disappear.

Some remarks should be made about the Phong model employed above. First, it is adapted to different materials by adjusting the values of  $R_0$ ,  $R_1$ , and  $m$ . Phong remarks that  $R_1$  typically lies between 10% and 80%, whereas  $m$  is in the range 1–10. However, Rogers (1985) indicates that  $m$  may be as high as 50. Note that there is no physical significance in these numbers—the model is simply a phenomenological one. This being so, care should be taken to prevent the  $\cos^m \theta$  term from contributing to reflectance estimates when  $|\theta| > 90^\circ$ . The Phong model is reasonably accurate but has been improved by Cook and Torrance (1982). This is important in computer graphics applications but the improvement is difficult to apply in computer vision, because of lack of data concerning the reflectances of real objects and because of variability in the current state (cleanliness, degree of

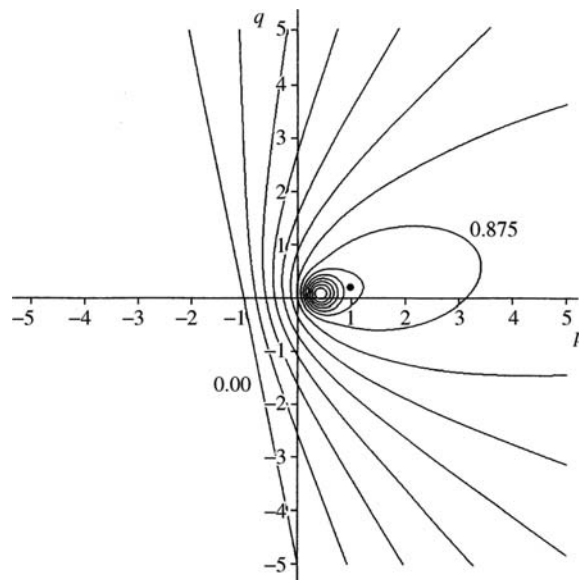


**FIGURE 16.10**

Reflectance map for a non-Lambertian surface: a modified form of Fig. 16.9B for the case where the surface has a marked specular component ( $R_0 = 1.0$ ,  $R_1 = 0.8$ ): note that the specular peak can have very high intensity (much greater than the maximum value of unity for the Lambertian component). In this case, the specular component is modeled with a  $\cos^8\theta$  variation (the contours are again taken in steps of 0.125).

polish, etc.) of a given surface. However, the method of photometric stereo gives some possibility of overcoming these problems.

## 16.5 PHOTOMETRIC STEREO

Photometric stereo is a form of structured lighting that increases the information available from surface reflectance variations. Basically, instead of taking a single monocular image of a scene illuminated from a single source, several images are taken, from the same vantage point, with the scene illuminated in turn by separate light sources. These light sources are ideally point sources some distance away in various directions, so that there is in each case a well-defined light source direction from which to measure surface orientation.

The basic idea of photometric stereo is that of cutting down the number of possible positions in gradient space for a given point on the surface of an object. It has already been seen that, for known absolute reflectance  $R_0$ , a constant brightness in one image permits the surface orientation to be limited to a curve of conic

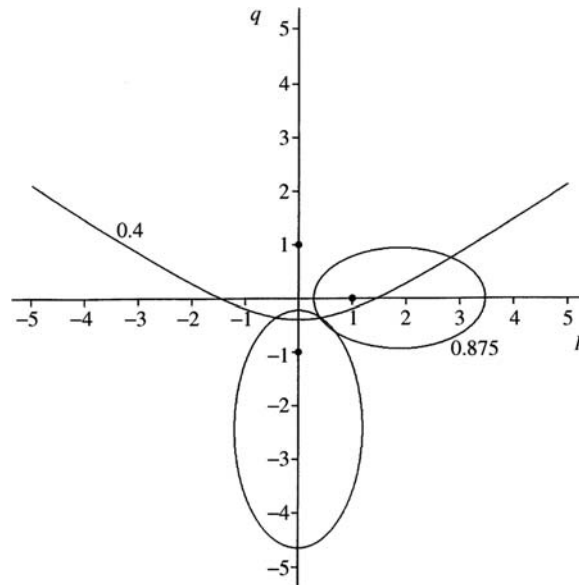


**FIGURE 16.11**

Obtaining a unique surface orientation by photometric stereo. Three contours of constant intensity arise for different light sources of equal strength: all three contours pass through a single point in  $(p, q)$  space and result in a unique solution for the local gradient.

cross section in gradient space. This would also be true for a second such image, the curve being a new one if the illuminating source is different. In general, two such conic curves meet at two points, so there is now only a single ambiguity in the gradient of the surface at any given point in the image. To resolve this ambiguity, a third source of illumination can be employed (this must not be in the plane containing the first two and the surface point being examined), and the third image gives another curve in gradient space which should pass through the appropriate crossing point of the first two curves (Fig. 16.11). If a third source of illumination cannot be used, it is sometimes possible to arrange that the inclination of each of the sources is so high that  $(p^2 + q^2)^{1/2}$  on the surface is always lower than  $(p_s^2 + q_s^2)^{1/2}$  for each of the sources, so that only one interpretation of the data is possible. This method is prone to difficulty, however, as it means that parts of the surface could be in shadow, thereby preventing the gradient for these parts of the surface from being measured. Another possibility is to assume that the surface is reasonably smooth, so that  $p$  and  $q$  vary continuously over it. This itself ensures that ambiguities are resolved over most of the surface.

However, there are other advantages to be gained from using more than two sources of illumination. One is that information on the absolute surface reflectance can be obtained. Another is that the assumption of a Lambertian surface can

be tested. Thus, three sources of illumination ensure that the remaining ambiguity is resolved *and* permit absolute reflectivity to be measured: this is obvious as if the three contours in gradient space do not pass through the same point, then the absolute reflectivity cannot be unity, so corresponding contours should be sought which do pass through the same point. In practice the calculation is normally carried out by defining a set of nine matrix components of irradiance,  $s_{ij}$  being the  $j$ th component of light source vector  $\mathbf{s}_i$ . Then, in matrix notation:

$$\mathbf{E} = R_0 \mathbf{S} \mathbf{n} \quad (16.13)$$

where

$$\mathbf{E} = (E_1, E_2, E_3)^T \quad (16.14)$$

and

$$S = \begin{bmatrix} s_{11} & s_{12} & s_{13} \\ s_{21} & s_{22} & s_{23} \\ s_{31} & s_{32} & s_{33} \end{bmatrix} \quad (16.15)$$

Provided that the three vectors  $\mathbf{s}_1, \mathbf{s}_2, \mathbf{s}_3$  are not coplanar, so that  $S$  is not a singular matrix,  $R_0$  and  $\mathbf{n}$  can now be determined from the formulae:

$$R_0 = |S^{-1} \mathbf{E}| \quad (16.16)$$

$$\mathbf{n} = \frac{S^{-1} \mathbf{E}}{R_0} \quad (16.17)$$

An interesting special case arises if the three source directions are mutually perpendicular; taking them to be aligned along the respective major axes directions,  $S$  is now the unit matrix, so that:

$$R_0 = (E_1^2 + E_2^2 + E_3^2)^{1/2} \quad (16.18)$$

and

$$\mathbf{n} = (E_1, E_2, E_3)^T / R_0 \quad (16.19)$$

If four or more images are obtained using further illumination sources, more information can be obtained: for example, the coefficient of specular reflectance,  $R_1$ . In practice, this coefficient varies somewhat randomly with the cleanness of the surface and it may not be relevant to determine it accurately. More probably, it will be sufficient to check whether significant specularity is present, so that the corresponding region of the surface can be ignored for absolute reflectance calculations. Nonetheless, finding the specularity peak can itself give important surface orientation information, as will be clear from the previous section. Note that, although the information from several illumination sources should ideally be collated using least-squares analysis, this method requires significant computation. Hence, it seems better to use the images resulting from further illumination sources as confirmatory—or, instead, to select the three that exhibit the

least evidence of specularly as giving the most reliable information on local surface orientation.

---

## 16.6 THE ASSUMPTION OF SURFACE SMOOTHNESS

It was hinted above that the assumption of a reasonably smooth surface permits ambiguities to be removed in situations where there are two illuminating sources. In fact, this method can be used to help analyze the brightness map even for situations where a single source is employed: indeed, the fact that the eye can perform this feat of interpretation indicates that it should be possible to find computer methods for achieving it. Much research has been carried out on this topic and a set of methods is available, although the calculations are complex, iterative, computation intensive procedures. For this reason, they are not studied in depth here: the reader is referred to the volume by Horn (1986) for detailed information on this topic. However, one or two remarks are in order.

First, consider the representation to be employed for this type of analysis. In fact, normal gradient  $(p, q)$  space is not very appropriate for the purpose. In particular, it is necessary to average gradient (i.e., the  $\mathbf{n}$  values) locally within the image; however,  $(p, q)$ -space is not “linear,” in that a simple average of  $(p, q)$  values within a window would give biased results. It turns out that a conformal representation of gradient (i.e., one which preserves small shapes) is closer to the ideal, in that the distances between points in such a representation provide better approximations to the relative orientations of surface normals: averaging in such a representation gives reasonably accurate results. The required representation is obtained by a stereographic projection, which maps the unit (Gaussian) sphere onto a plane ( $z = 1$ ) through its north pole but this time using as a projection point not its center but its south pole. This projection has the additional advantage that it projects all possible orientations of a surface onto the plane, not merely those from the northern hemisphere. Hence, backlit objects can be represented conveniently in the same map as used for frontlit objects.

Second, the relaxation methods used to estimate surface orientation have to be provided with accurate boundary conditions: in principle, the more correct the orientations that are presented initially to such procedures, the more quickly and accurately the iterations proceed. There are normally two sets of boundary condition that can be applied in such programs. One is the set of positions in the image where the surface normal is perpendicular to the viewing direction. The other is the set of positions in the image where the surface normal is perpendicular to the direction of illumination: this set of positions corresponds to the set of shadow edges (Fig. 16.12). Careful analysis of the image must be undertaken to find each set of positions, but once they have been located they provide valuable cues for unlocking the information content of the monocular image, and mapping out surfaces in detail.

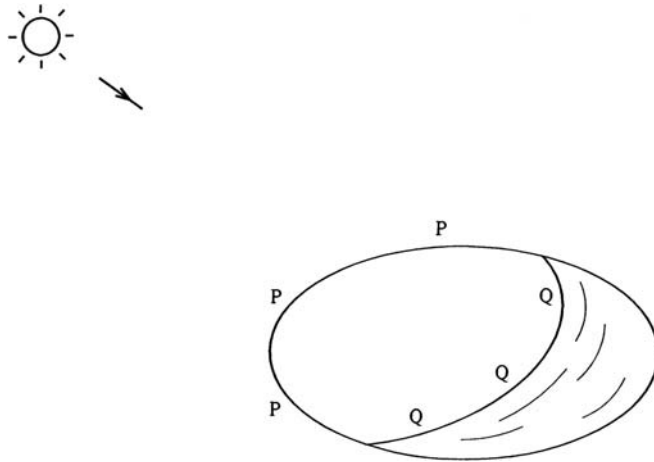


**FIGURE 16.12**

The two types of boundary condition that can be used in shape-from-shading computations of surface orientation: (1) positions P where the surface normal is perpendicular to the viewing direction; (2) positions Q where the surface normal is perpendicular to the direction of illumination (i.e., shadow boundaries).

Finally, all shapes from shading techniques provide information which initially takes the form of surface orientation maps. Dimensions are not obtainable directly but these can be computed by integration across the image from known starting points. In practice, this tends to mean that absolute dimensions are unknown and that dimensional maps are obtainable only if the size of an object is given or if its depth within the scene is known.

## 16.7 SHAPE FROM TEXTURE

Texture can be very helpful to the human eye in permitting depth to be perceived. Although textured patterns can be very complex, even the simplest textural elements can carry depth information. Ohta et al. (1981) showed how circular patches on a flat surface viewed more and more obliquely in the distance become first elliptical and then progressively flatter and flatter. At infinite distance, on the horizon line (here defined as the line at infinity in the given plane), they would clearly become very short line segments. To disentangle such textured images sufficiently to deduce depths within the scene, it is first necessary to find the horizon line reliably. This is achieved by taking all pairs of texture elements and deducing from their areas where the horizon line would have to be. To proceed, we make use of the rule:

$$d_1^3/d_2^3 = A_1/A_2 \quad (16.20)$$

which applies as circles at various depths would give a square law, although the progressive eccentricity also reduces the area linearly in proportion to the depth. This information is accumulated in a separate image space and a line is then fitted to these data: false alarms are eliminated automatically by this Hough-based procedure. At this stage the original data—the ellipse areas—provide direct information on depth, although some averaging is required to obtain accurate results. Although this type of method has been demonstrated in certain instances, it is in practice highly restricted unless very considerable amounts of computation are performed. Hence, it is doubtful whether it can be of general practical use in machine vision applications.

---

## 16.8 USE OF STRUCTURED LIGHTING

Structured lighting has already been considered briefly in [Section 16.2](#) as an alternative to stereo for mapping out depth in scenes. Basically, a pattern of light stripes, or other arrangement of light spots or grids, is projected onto the object field. Then these patterns are enhanced in a (generally) single monocular image and analyzed to extract the depth information. To obtain the maximum information, the light pattern must be close-knit and the received images must be of very high resolution. When shapes are at all complex, the lines can in places appear so close together that they are unresolvable. It then becomes necessary to separate the elements in the projected pattern, trading resolution and accuracy for reliability of interpretation. Even so, if parts of the objects are along the line of sight, the lines can merge together and even cross back and fore, so unambiguous interpretation is never assured. In fact, this is part of a larger problem, in that parts of the object will be obscured from the projected pattern by occluding bodies or by self-occlusion: the method has this feature in common with the shape from shading technique and with stereo vision, which relies on *both* cameras being able to view various parts of the objects simultaneously. Hence, the structured light approach is subject to similar restrictions to those found for other methods of 3-D vision and is not a panacea. Nevertheless, it is a useful technique that is generally simple to set up so as to acquire specific 3-D information which can enable a computer to start the process of cueing into complex images.

Light spots provide perhaps the most obvious form of structured light. However, they are restricted because for each spot an analysis has to be performed to determine which spot is being viewed: connected lines, in contrast, carry a large amount of coding information with them so that ambiguities are less likely to arise. Grids of lines carry even more coding information but do not necessarily give any more depth information. Indeed, if a pattern of light stripes can be projected (for example) from the left of the camera so that they are parallel to the  $y$ -axis in the observed image, then there is no point in projecting another set of lines parallel to the  $x$ -axis, as these merely replicate information that is already

available from the rows of pixels in the image—all the depth information is carried by the vertical lines and their horizontal displacements in the image. This analysis assumes that the camera and projected beams are carefully aligned, and that no perspective or other distortions are present. In fact, most practical structured lighting systems in current use employ light stripe patterns rather than spot patterns or full-grid patterns.

This section ends with an analysis of the situations that can arise when a single stripe is incident on objects as simple as rectangular blocks. Fig. 16.13 shows three types of structure in observed stripes: (1) the effect of a sharp angle being encountered; (2) the effect of “jump edges” at which light stripes jump horizontally and vertically at the same time; and (3) the effect of discontinuous edges at which light stripes jump horizontally but not vertically. The reasons for these circumstances will be obvious from Fig. 16.13. Basically, the problem to be tackled with jump and discontinuous edges is to find whether a given stripe end marks an occluding edge or an occluded edge. The importance of this distinction is that occluding edges mark actual edges of the object being observed, whereas occluded edges may be merely edges of shadow regions and are then not *directly* significant (more precisely, they involve interactions of light with two objects rather than with one and are therefore more complex to interpret). A simple rule is that, if stripes are projected from the left, the left-hand component of a discontinuous edge will be the occluding edge and the right-hand component will be the

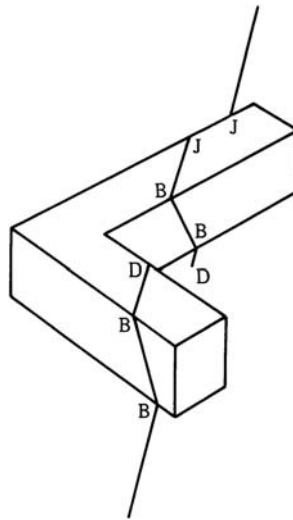


**FIGURE 16.13**

Three of the structures that are observed when a light stripe is incident on even quite simple shapes: bends (B), jumps (J), and discontinuities (D).



occluded edge. Angle edges are located by applying a Laplacian type of operator which detects the change in orientation of the light stripe.

The ideas outlined above correspond to possible 1-D operators that interpret light stripe information to locate nonvertical edges of objects. The method provides no direct information concerning vertical edges. To obtain such information, it is necessary to analyze the information from sets of light stripes. For this purpose 2-D edge operators are required, which collect sufficient data from at least two or three adjacent light stripes. Further details are beyond the scope of this chapter.

Overall, light stripes provide a very useful means of recognizing planes forming the faces of polyhedra and other types of manufactured object. The characteristic sets of parallel lines can be found and demarcated relatively easily, and the fact that the lines usually give rather strong signals means that line-tracking techniques can be applied and that algorithms can operate quite rapidly. However, whole-scene interpretation, including inferring the presence and relative positions of different objects, remains a more complex task, as will be seen below.

---

## 16.9 THREE-DIMENSIONAL OBJECT RECOGNITION SCHEMES

The methods described so far in this chapter employ various means for finding depth at all places in a scene and are hence able to map out 3-D surfaces in a fair amount of detail. However, they do not give any clue as to what these surfaces represent. In some situations, it may be clear that certain planar surfaces are parts of the background, e.g., the floor and the walls of a room, but in general individual objects will not be inherently identifiable. Indeed, objects tend to merge with each other and with the background, so specific methods are needed to segment the 3-D space map and finally recognize the objects, giving detailed information on their positions and orientations. [A 3-D space map may be defined as an imagined 3-D map showing, without interpretation, the surfaces of all objects in the scene and incorporating all the information from depth or range images. Note that it will generally include only the front surfaces of objects seen from the vantage point of the camera.]

Before proceeding to study this problem, notice that further general processing can be carried out to analyze the 3-D shapes. Agin and Binford (1976) and others have developed techniques for likening 3-D shapes to “generalized cylinders”, these being like normal (right circular) cylinders but with additional degrees of freedom so that the axes can bend and the cross-sections can vary, both in size and in detailed shape: even an animal like a sheep can be likened to a distorted cylinder. On the whole, this approach is elegant but may not be well adapted to describe many industrial objects, and it is therefore not pursued further here. A simpler approach may be to model the 3-D surfaces as planar, quadratic, cubic, and quartic surfaces, and then to try to understand these model surfaces in terms of what is known about existing objects. This approach was adopted by Hall et al.

(1982) and was found to be viable, at least for certain quite simple objects such as cups. Shirai (1987) has taken the approach even further so that a whole range of objects can be found and identified in quite complex indoor scenes.

We next consider what we are trying to achieve regarding recognition. First, can recognition be carried out *directly* on the mapped out 3-D surfaces, just as it could for the 2-D images of earlier chapters? Second, if we can bypass the 3-D modeling process, and still recognize objects, might it not be possible to save even more computation and omit the stage of mapping out 3-D surfaces, instead identifying 3-D objects directly in 2-D images? It might even be possible to locate 3-D objects from a single 2-D image.

Consider the first of these problems. When we studied 2-D recognition, many instances were found where the Hough Transform (HT) approach was of great help. It turned out to give trouble in more complex cases, particularly when attempts were made to find objects where there were more than two or at most three degrees of freedom. Here, however, we have situations where objects normally have six degrees of freedom—three degrees of freedom for translation and another three for rotation. This doubling of the number of free parameters on going from 2-D to 3-D makes the situation far worse, as the search space is proportional in size not to the number of degrees of freedom, but to its exponent: for example, if each degree of freedom in translation or rotation can have 256 values, the number of possible locations in parameter space changes from  $256^3$  in 2-D to  $256^6$  in 3-D. This will be seen to have a very profound effect on object location schemes and tends to make the HT technique difficult to implement. In the next section, we study an interesting approach to the 3-D recognition problem, which uses a subtle combination of 2-D and 3-D techniques.

---

## 16.10 HORAUD'S JUNCTION ORIENTATION TECHNIQUE

This and related techniques are sometimes referred to as “shape from angle.”

Horaud's (1987) technique is special in that it uses as its starting point 2-D images of 3-D scenes and “backprojects” them into the scene, with the aim of making interpretations in 3-D rather than 2-D frames of reference. This has the initial effect of increasing mathematical complexity, although in the end useful, more accurate results emerge.

Initially, the boundaries of planar surfaces on objects are backprojected. Each boundary line is thus transformed into an “interpretation plane” defined by the center of the camera projection system and the boundary line in the image plane: clearly, the interpretation plane must contain the line that originally projected into the boundary line in the image. Similarly, angles between boundary lines in the image are backprojected into two interpretation planes, which must contain the original two object lines. Finally, junctions between three boundary lines are backprojected into three interpretation planes which must contain a corner in the

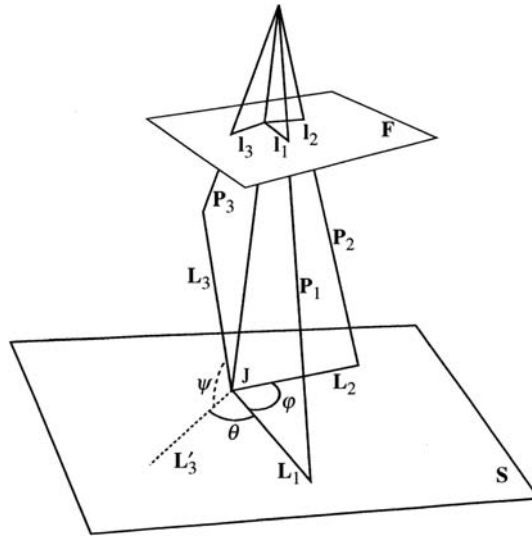


**FIGURE 16.14**

Geometry for backprojection from junctions: a junction of three lines in an image may be backprojected into three planes, from which the orientation in space of the original corner  $J$  may be deduced.

space map (Fig. 16.14). The paper focuses on the backprojection of junctions and shows how measurements of the junction angles in the image relate to those of the original corner; it also shows how the space orientation of the corner can be computed. In fact, it is interesting that the orientation of an object in 3-D can in general be deduced from the appearance of just one of its corners in a single image. This is a powerful result and in principle permits objects to be recognized and located from extremely sparse data.

To understand the method, the mathematics first needs to be set up with some care. Assumes that lines  $L_1$ ,  $L_2$ ,  $L_3$  meet at a junction in an object and appear as lines  $l_1$ ,  $l_2$ ,  $l_3$  in the image (Fig. 16.14). Take respective interpretation planes containing the three lines and label them by unit vectors  $P_1$ ,  $P_2$ ,  $P_3$  along their normals, so that:

$$P_1 \cdot L_1 = 0 \quad (16.21)$$

$$P_2 \cdot L_2 = 0 \quad (16.22)$$

$$P_3 \cdot L_3 = 0 \quad (16.23)$$

In addition, take the space plane containing  $L_1$  and  $L_2$ , and label it by a unit vector  $S$  along its normal, so that

$$S_1 \cdot L_1 = 0 \quad (16.24)$$

$$S_2 \cdot L_2 = 0 \quad (16.25)$$

As  $\mathbf{L}_1$  is perpendicular to  $\mathbf{S}$  and to  $\mathbf{P}_1$ , and  $\mathbf{L}_2$  is perpendicular to  $\mathbf{S}$  and to  $\mathbf{P}_2$ , it is found that

$$\mathbf{L}_1 = \mathbf{S} \times \mathbf{P}_1 \quad (16.26)$$

$$\mathbf{L}_2 = \mathbf{S} \times \mathbf{P}_2 \quad (16.27)$$

Note that  $\mathbf{S}$  is not in general perpendicular to  $\mathbf{P}_1$  and  $\mathbf{P}_2$ , so  $\mathbf{L}_1$  and  $\mathbf{L}_2$  are not in general unit vectors. Defining  $\varphi$  as the angle between  $\mathbf{L}_1$  and  $\mathbf{L}_2$ , we now have

$$\mathbf{L}_1 \cdot \mathbf{L}_2 = L_1 L_2 \cos \varphi \quad (16.28)$$

which can be reexpressed in the form:

$$(\mathbf{S} \times \mathbf{P}_1) \cdot (\mathbf{S} \times \mathbf{P}_2) = |\mathbf{S} \times \mathbf{P}_1| |\mathbf{S} \times \mathbf{P}_2| \cos \varphi \quad (16.29)$$

Next, we need to consider the junction between  $\mathbf{L}_1$ ,  $\mathbf{L}_2$ ,  $\mathbf{L}_3$ . To proceed, it is necessary to specify the relative orientations in space of the three lines.  $\theta$  is the angle between  $\mathbf{L}_1$  and the projection  $\mathbf{L}'_3$  of  $\mathbf{L}_3$  on plane  $\mathbf{S}$ , whereas  $\psi$  is the angle between  $\mathbf{L}'_3$  and  $\mathbf{L}_3$  (Fig. 16.14). Thus, the structure of the junction  $J$  is described completely by the three angles  $\varphi, \theta, \psi$ .  $\mathbf{L}_3$  can now be found in terms of other quantities:

$$\mathbf{L}_3 = \mathbf{S} \sin \psi + \mathbf{L}_1 \cos \theta \cos \psi + (\mathbf{S} \times \mathbf{L}_1) \sin \theta \cos \psi \quad (16.30)$$

Applying Eq. (16.23), we find

$$\mathbf{S} \cdot \mathbf{P}_3 \sin \psi + \mathbf{L}_1 \cdot \mathbf{P}_3 \cos \theta \cos \psi + (\mathbf{S} \times \mathbf{L}_1) \cdot \mathbf{P}_3 \sin \theta \cos \psi = 0 \quad (16.31)$$

Substituting for  $\mathbf{L}_1$  from Eq. (16.26), and simplifying, we finally obtain

$$\begin{aligned} (\mathbf{S} \cdot \mathbf{P}_3) |\mathbf{S} \times \mathbf{P}_1| \sin \psi + \mathbf{S} \cdot (\mathbf{P}_1 \times \mathbf{P}_3) \cos \theta \cos \psi \\ + (\mathbf{S} \cdot \mathbf{P}_1) (\mathbf{S} \cdot \mathbf{P}_3) \sin \theta \cos \psi = (\mathbf{P}_1 \cdot \mathbf{P}_3) \sin \theta \cos \psi \end{aligned} \quad (16.32)$$

Eqs. (16.31) and (16.34) now exclude the unknown vectors  $\mathbf{L}_1$ ,  $\mathbf{L}_2$ ,  $\mathbf{L}_3$  but they retain  $\mathbf{S}$ ,  $\mathbf{P}_1$ ,  $\mathbf{P}_2$ ,  $\mathbf{P}_3$  and the three angles  $\varphi, \theta, \psi$ .  $\mathbf{P}_1$ ,  $\mathbf{P}_2$ ,  $\mathbf{P}_3$  are known from the image geometry, and the angles  $\varphi, \theta, \psi$  are presumed to be known from the object geometry; in addition, only two components  $(\alpha, \beta)$  of the unit vector  $\mathbf{S}$  are independent, so the two equations should be sufficient to determine the orientation of the space plane  $\mathbf{S}$ . Unfortunately, the two equations are highly nonlinear, and it is necessary to solve them numerically. Horaud (1987) achieved this by reexpressing the formulae in the forms:

$$\cos \varphi = f(\alpha, \beta) \quad (16.33)$$

$$\begin{aligned} \sin \theta \cos \psi = g_1(\alpha, \beta) \sin \psi + g_2(\alpha, \beta) \cos \theta \cos \psi \\ + g_3(\alpha, \beta) \sin \theta \cos \psi \end{aligned} \quad (16.34)$$

For each image junction,  $\mathbf{P}_1$ ,  $\mathbf{P}_2$ ,  $\mathbf{P}_3$  are known and it is possible to evaluate  $f$ ,  $g_1$ ,  $g_2$ ,  $g_3$ . Then, assuming a particular interpretation of the junction, values are assigned to  $\varphi, \theta, \psi$  and curves giving the relation between  $\alpha$  and  $\beta$  are plotted for each equation. Possible orientations for the space plane  $\mathbf{S}$  are then given by

positions in  $(\alpha, \beta)$  space where the curves cross. Horaud showed that, in general, 0, 1, or 2 solutions are possible: the case of no solutions corresponds to trying to make an impossible match between a corner and an image junction when totally the wrong angles  $\varphi, \theta, \psi$  are assumed; one solution is the normal situation; and two solutions arise in the interesting special case when orthographic or near-orthographic projection permits perceptual reversals—that is, a convex corner is interpreted as a concave corner or vice versa. In fact, under orthographic projection the image data from a single corner are insufficient, taken on their own, to give a unique interpretation: in this situation, even the human visual system makes mistakes—as in the case of the well-known Necker cube illusion (see [Chapter 17: Tackling the Perspective n-Point Problem](#)). However, when such cases arise in practical situations, it may be better to take the convex rather than the concave corner interpretation as a working assumption, as it has slightly greater likelihood of being correct.

Horaud has shown that such ambiguities are frequently resolved if the space plane orientation is estimated simultaneously for all the junctions bordering the object face in question, by plotting the  $\alpha$  and  $\beta$  values for all such junctions on the same  $\alpha, \beta$  graph. For example, with a cube face on which there are three such junctions, nine curves are coincident at the correct solution, and there are nine points where only two curves cross, indicating false solutions. On the other hand, if the same cube is viewed under conditions approximating very closely to orthographic projection, two solutions with nine coincident curves appear and the situation remains unresolved, as before.

Overall, this technique is important in showing that although lines and angles individually lead to virtually unlimited numbers of possible interpretations of 3-D scenes, junctions lead individually to at most two solutions and any remaining ambiguity can normally be eliminated if junctions on the same face are considered together. As has been seen, the exception to this rule occurs when projection is accurately orthographic, although this is a situation that can often be avoided in practice.

So far, we have considered only how a given hypothesis about the scene may be tested: nothing has been said about how assignments of the angles  $\varphi, \theta, \psi$  are made to the observed junctions. Horaud's paper discussed this aspect of the work in some depth. In general, the approach is to use a depth-first search technique in which a match is "grown" from the initial most promising junction assignment. In fact, considerable preprocessing of sample data is carried out to find how to rank image features for their utility during depth-first search interpretation. The idea is to order possible alternatives such as linear or circular arcs, convex or concave junctions, short or long lines, etc. In this way, the tree search becomes more planned and efficient at run time. Generally, the more frequently occurring types of feature should be weighted down in favor of the rarer types of feature, for greater search efficiency. In addition, remember that hypothesis generation is relatively expensive in that it demands a stage of backprojection, as described above. Ideally, this stage need be employed only once for each object (in the case that

only a single corner is, initially, considered). Subsequent stages of processing then involve hypothesis verification in which other features of the object are predicted and their presence sought in the image: if found, they are used to refine the existing match; if the match at any stage becomes worse, then the algorithm backtracks and eliminates one or more features and proceeds with other ones. This process is unavoidable, as more than one image feature may be present near a predicted feature.

One of the factors that has been found to make the method converge quickly is the use of grouped rather than individual features, as this tends to decrease the combinatorial explosion in the size of the search: in the present context, this means that attempts should be made to match first all junctions or angles bordering a given object face, and further that a face should be selected that has the greatest number of matchable features around it.

In summary, this approach is successful, as it backprojects from the image and then uses geometrical constraints and heuristic assumptions for matching in 3-D space. It is suitable for matching objects that possess planar faces and straight-line boundaries, hence giving angle and junction features. However, extending the backprojection technique to situations where object faces are curved and have curved boundaries could be significantly more difficult.

---

## 16.11 AN IMPORTANT PARADIGM—LOCATION OF INDUSTRIAL PARTS

In this section, we consider the location of a common class of industrial part: this constitutes an important example that has to be solved in one way or another. Here, we go along with the Bolles and Horaud (1986) approach as it leads to sensible solutions and embodies a number of useful didactic lessons. The method starts with a depth map of the scene (obtained in this case using structured lighting).

Fig. 16.15 shows in simplified form the type of industrial part being sought in the images. In typical scenes, several of these parts may appear jumbled on a worktable, with perhaps three or four being piled on top of each other in some places. In such cases, it is vital that the matching scheme be highly robust if most of the parts are to be found, since even when a part is unoccluded, it appears against a highly cluttered and confusing background. However, the parts themselves have reasonably simple shapes and possess certain salient features. In the particular problem cited, each has a cylindrical base with a concentric cylindrical head and also a planar shelf attached symmetrically to the base. To locate such objects, it is natural to attempt to search for circular and straight dihedral edges. In addition, because of the type of data being used, it is useful to search for straight tangential edges, which appear where the sides of curved cylinders are viewed obliquely.

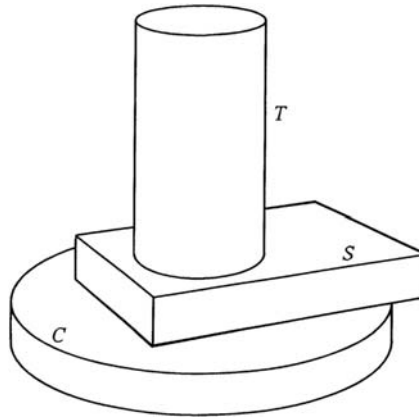


**FIGURE 16.15**

The essential features of the industrial components located by the 3-D PO system of Bolles and Horaud (1986). S, C, and T indicate, respectively, straight and circular dihedral edges and straight tangential edges, all of which are searched for by the system.

In general, circular dihedral edges appear elliptical, and parameters for five of the six degrees of freedom of the part can be determined by analyzing these edges. The parameter that cannot be determined in this way corresponds to rotation about the axis of symmetry of the cylinder.

Straight dihedral edges also permit five free parameters to be determined, as location of one plane eliminates three degrees of freedom and location of an adjacent plane eliminates a further two degrees of freedom. The parameter that remains undetermined is that of linear motion along the direction of the edge. However, there is also a further ambiguity in that the part may appear either way around on the dihedral edge.

Straight tangential edges determine only four free parameters, as the part is free to rotate about the axis of the cylinder and can also move along the tangential edge. Note that these edges are the most difficult to locate accurately, as range data are subject to greater levels of noise as surfaces curve away from the sensor.

All three of these types of edge are planar. They also provide useful additional information that can help to identify where they are on a part. For example, straight and curved dihedral edges both provide information on the size of the included angle, and the curved edges also give radius values. In fact, curved dihedral edges provide significantly more parametric information about a part than either of the other two types of edge, and therefore they are of most use to form initial hypotheses about the pose (position and orientation) of a part. Having found such an edge, it is necessary to try out various hypotheses about which edge it is, for example, by searching for other circular dihedral edges at specific relative positions: this is a vital hypothesis verification step. Next, the problem of

how to determine the remaining free parameter is solved by searching for the linear straight dihedral edge features from the planar shelf on the part.

At this stage, hypothesis generation is complete and the part is essentially found, but hypothesis verification is required (1) to confirm that the part is genuine and not an accidental grouping of independent features in the image, (2) to refine the pose estimate, and (3) to determine the “configuration” of the part, i.e., to what extent, it is buried under other parts (making it difficult for a robot to pick it up). When the most accurate pose has been obtained, the overall degree of fit can be considered and the hypothesis rejected if some relevant criterion is not met.

In common with other researchers (Faugeras and Hebert, 1983; Grimson and Lozano-Perez, 1984), Bolles and Horaud took a depth-first tree search as the basic matching strategy. Their scheme uses a minimum number of features to key into the data, first generating hypotheses and then taking care to ensure verification. [Note that Bolles and Cain (1982) had earlier used this technique in a 2-D part location problem.] This contrasts with much work (especially that based on the HT) which makes hypotheses but does not check them. (Note that forming the initial hypotheses is the difficult and computation intensive part of the work: researchers will therefore write about this aspect of their work and perhaps not state the minor amount of computation that went into confirming that objects had indeed been located: note also that in much 2-D work, images can be significantly simpler and the size of the peak in parameter space can be so large as to make it virtually certain that an object has been located—thus rendering verification unnecessary.)

---

## 16.12 CONCLUDING REMARKS

To the layman, 3-D vision is an obvious and automatic result of the fact that the human visual system is binocular and presumes both that binocular vision is the only way to arrive at depth maps and that once they have been obtained the subsequent recognition process is trivial. However, what this chapter has actually demonstrated is that neither of these commonly held views is valid. First, there are a good many ways of arriving at depth maps, and some of them are available using monocular vision. Second, the complexity of the mathematical calculations involved in locating objects and the amount of abstract reasoning involved in obtaining robust solutions—plus the need to ensure that the latter are not ambiguous—are taxing even in simple cases, including those where the objects have well-defined salient features.

Despite the diversity of methods covered in this chapter, there are certain important themes: the use of “trigger” features, the value of combining features into groups that are analyzed together, the need for working hypotheses to be generated at an early stage, the use of depth-first heuristic search (combined where appropriate with more rigorous breadth-first evaluation of the possible



interpretations), and the detailed verification of hypotheses. All these can be taken as parts of current methodology; *details*, however, vary with the data set. More specifically, if a new type of industrial part is to be considered, some study must be made of its most salient features: then this causes not only the feature detection scheme to vary but also the heuristics of the search employed—and also the mathematics of the hypothesis mechanism. The reader is referred to the following chapter for further discussion of object recognition under perspective projection.

Although the previous two sections have concentrated on object recognition and have perhaps tended to eschew the value of range measurements and depth maps, it is possible that this might give a misleading impression of the situation. In fact, there are many situations where recognition is largely irrelevant but where it is mandatory to map out 3-D surfaces in great detail. Turbine blades, automobile body parts or even food products such as fruit may need to be measured accurately in 3-D: in such cases it is known in advance what object is in what position, but some inspection or measurement function has to be carried out and a diagnosis made. In such instances, the methods of structured lighting, stereopsis or photometric stereo come into their own and are highly effective methods. Ultimately, also, one might expect that a robot vision system will have to use all the tricks of the human visual system if it is to be as adaptable and useful when operating in an unconstrained environment rather than at a particular worktable.

This has been a preliminary chapter on 3-D vision, setting the scene for Parts 4 and 5. In particular, [Chapter 17](#), Tackling the Perspective n-Point Problem will be devoted to a careful analysis of the distinction between weak and full perspective projection and how this affects the object recognition process; [Chapter 18](#), Invariants and Perspective will aim to show something of the elegance and value of invariants in providing short cuts around some of the complexities of full perspective projection; [Chapter 19](#), Image Transformations and Camera Calibration will consider camera calibration and will also consider how recent research on inter-relating multiple views of a scene has allowed some of the tedium of camera calibration to be by-passed; and [Chapter 20](#), Motion will introduce the topic of motion analysis in 3-D scenes.

*Conventional wisdom indicates that binocular vision is the key to understanding the 3-D world. This chapter has shown that the correspondence problem makes the practice of binocular vision tedious, although the solutions it provides are only depth maps and require further intricate analysis before the 3-D world can fully be understood.*

---

### 16.13 BIBLIOGRAPHICAL AND HISTORICAL NOTES

As noted earlier in the chapter, the most obvious approach to 3-D perception is to employ a binocular camera system. Burr and Chien (1977) and Arnold (1978) showed how a correspondence could be set up between the two input images by

use of edges and edge segments. Forming a correspondence can involve considerable computation: Barnea and Silverman (1972) showed how this problem could be alleviated by passing quickly over unfavorable matches. Likewise, Moravec (1980) devised a coarse-to-fine matching procedure which arrives systematically at an accurate correspondence between images. Marr and Poggio (1979) formulated two constraints—those of uniqueness and continuity—that have to be satisfied in choosing global correspondences: these constraints are important in leading to the simplest available surface interpretation. Ito and Ishii (1986) found that there is something to be gained from three-view stereo in offsetting ambiguity and the effects of occlusions.

The structured lighting approach to 3-D vision was introduced independently by Shirai (1972) and Agin and Binford (1973, 1976), in the form of a single plane of light, whereas Will and Pennington (1971) developed the grid coding technique. Nitzan et al. (1977) employed an alternative light detecting and ranging scheme for mapping objects in 3-D; here short light pulses were timed as they traveled to the object surface and back.

Meanwhile, other workers were attempting monocular approaches to 3-D vision. Some basic ideas underlying shape-from-shading date from as long ago as 1929, with Fesenkov's investigations of the lunar surface: see also van Digellen (1951). However, the first shape-from-shading problem to be solved both theoretically and in an operating algorithm appears to have been that of Rindfleisch (1966), also relating to lunar landscapes. Thereafter, Horn systematically tackled the problem both theoretically and with computer investigations, starting with a notable review (1975) and resulting in prominent papers (e.g., Horn, 1977; Ikeuchi and Horn, 1981; Horn and Brooks, 1986), an important book (Horn, 1986) and an edited work (Horn and Brooks, 1989). Interesting papers by other workers in this area include Blake et al. (1985), Bruckstein (1988) and Ferrie and Levine (1989). Woodham (1978, 1980, 1981) must be credited with the photometric stereo idea. Finally, the vital contributions made by workers on computer graphics in this area must not be forgotten—see, for example, Phong (1975), Cook and Torrance (1982).

The concept of shape-from-texture arose from the work of Gibson (1950) and was developed by Bajcsy and Liebermann (1976), Stevens (1980), and notably by Kender (1980), who carefully explored the underlying theoretical constraints.

The paper by Barrow and Tenenbaum (1981) provides a very readable review of much of this earlier work. 1980 marked a turning point, when the emphasis in 3-D vision shifted from mapping out surfaces to interpreting images as sets of 3-D objects. Possibly, this segmentation task could not be tackled earlier because basic tools such as the HT were not sufficiently well developed. The work of Koenderink and van Doorn (1979) and Chakravarty and Freeman (1982) was probably also crucial in providing a framework for interpretation schemes to be developed by using potential 3-D views of objects. The work of Ballard and Sabbah (1983) provided an early breakthrough in segmentation of real objects in 3-D and this was followed by vital further work by Faugeras and Hebert (1983),

Silberberg et al. (1984), Bolles and Horaud (1986), Horaud (1987), Pollard et al. (1987), and many others.

Other interesting work includes that of Horaud et al. (1989) on solving the perspective 4-point problem (finding the position and orientation of the camera relative to known points): for further references on this topic, see [Section 17.6](#).

Though already a well worked-through topic, research on finding vanishing points proceeded further in the 1990s (e.g., Lutton et al., 1994; Straforini et al., 1993; Shufelt, 1999). Similarly, stereo correlation matching techniques were still under development, to maintain robustness in real-time applications (Lane et al., 1994).

Since 2000, work on stereo vision has continued unabated as a main-line topic (e.g., Lee et al., 2002; Brown et al., 2003), but Horn's approach to shape from shading has been largely superseded. One new technique is the Green's function approach to shape from shading (Torreão, 2001, 2003), whereas local shape from shading has been used to improve the photometric stereo technique (Sakarya and Erkmén, 2003). Photometric stereo has itself been developed considerably further in a new 4-source technique capable of coping with highlights and shadows (Barsky and Petrou, 2003). Another development is the application of shape from shading to radar data—a translation that required significant new theory (Frankot and Chellappa, 1990; Bors et al., 2003). Finally, a thoroughgoing new approach to the whole study of 3-D vision and its dependence on the light field has been initiated (Baker et al., 2003). This paper starts by comparing what can be learned from (1) stereo vision and (2) a shape from silhouette approach (observing object silhouettes from all directions in the given light field). An important conclusion is that the shapes of Lambertian objects can be uniquely determined with  $n$ -camera stereo, unless there are regions of constant intensity present: indeed, constant intensity is found *always* to lead to ambiguity. Essentially, this is because there may be a concavity whose light properties outside the concavity hull will be indistinguishable from those of the hull itself (Laurentini, 1994). Finally, we note that the paper by Baker et al. (2003) is important not only in giving a fresh view of the problems of 3-D vision in general, and shape from shading in particular, but also in demonstrating certain open questions.

### 16.13.1 MORE RECENT DEVELOPMENTS

Although the complexity of the image acquisition needed for photometric stereo should perhaps have made it relevant only during the early stages of the subject, the opposite now seems to be the case. First, Hernandez et al. (2011) indicate why this could be so: if a set of lights of different colors is arranged, there is no need to switch them, as the different color channels can be handled independently. However, this means that normally only three lights can be used, so the Barsky and Petrou (2003) 4-light technique cannot be employed, and this makes it difficult to confirm the interpretations obtained using the (usual) minimum number of three lights—an especially important factor when shadows occur.

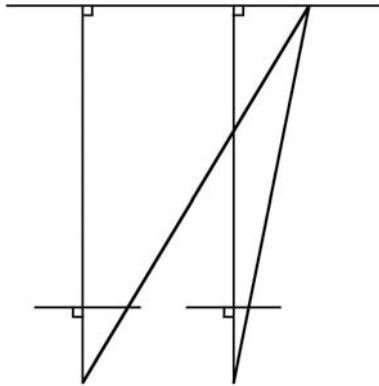
Nevertheless, Hernandez et al. (2011) are able to use regularization methods that cope with as few as two light sources. Wu and Tang (2010) employ the opposite approach of using a dense image set and exploit the resulting data redundancy to determine how well the observations fit a Lambertian model. An expectation maximization approach is used to interpret the data in two stages, concentrating first on surface normals and then on surface properties including orientation discontinuities. The approach is robust and produces good reconstruction results. Goldman et al. (2010) note that most objects are composed of only a small number of fundamental materials: they therefore constrain pixel representations to at most two such materials, and thereby recover not only the shape but also material bidirectional reflectance distribution functions and weight maps. McGunnigle and Dong (2011) propose a photometric stereo method in which a conventional four-light scheme is augmented with coaxial illumination. Their investigations show that coaxial illumination makes photometric stereo more robust to shadow and specularly.

Chen et al. (2011) devise a fast stereo matching algorithm that uses a global graph-cuts framework, but which is as efficient as some local approaches. By concentrating on region boundaries and cleverly limiting the number of disparity candidates, the number of vertices in the constructed graph is significantly reduced. As a result, promising disparities can readily be selected and partial occlusions can be handled efficiently, thereby improving stereo matching speed.

---

## 16.14 PROBLEMS

1. Prove that all epipolar lines in one image plane pass through the point that is the image of the projection point of the alternate image plane.
2. What is the physical significance of the straight line contour in gradient space (see Fig. 16.9B)?
3. Sketch a curve of the function  $\cos^m\theta$ . Estimate what value  $m$  would have to have for 90% of the  $R_1$  component to be reflected within  $10^\circ$  of the direction for pure specular reflection.
4. An alien has three eyes. Does this permit it to perceive or estimate depth more accurately than a human? What would be the best placement for a third eye?
5. A cube is viewed in orthographic projection. Show that although the cube is opaque, it is easy to compute the theoretical position of its centroid in the image. Show also that the orientation of the cube can be deduced by considering the apparent areas of its faces. If the contrast between the faces becomes so low that only a hexagonal outline is seen, show that ambiguities will arise in our knowledge of the orientation of the cube. Are ambiguities specific to cubes, or do they arise with other shapes? Why?

**FIGURE 16.P.1**

Geometry of a binocular imaging system

6. a. A feature at  $(X, Y, Z)$  appears at locations  $(x_1, y_1)$ , and  $(x_2, y_2)$  in the two images of a binocular imaging system. The image planes of both cameras lie in the same plane,  $f$  is the focal length of both camera lenses, and  $b$  is the separation of the optical axes of the lenses. Label Fig. 16.P.1 appropriately: by considering pairs of similar triangles, show that:

$$\frac{Z}{f} = \frac{X + b/2}{x_1} = \frac{X - b/2}{x_2}$$

- b. Hence, derive a formula which can be used to determine depth  $Z$  from the observed disparity.
7. Give a full proof that the error with which the fractional depth  $Z$  in a scene can be computed is (1) proportional to pixel size, (2) proportional to  $Z$ , and (3) inversely proportional to the baseline  $b$  between the stereo cameras. What other parameter appears in the final formula? Determine under what pair of conditions two very tiny cameras fabricated by nanotechnological methods could still perform viable depth measurement.
8. a. Draw a diagram which shows that the ordering of visible points is normally the same in both images seen by a binocular vision system.  
b. An object has a semitransparent front surface through which an interior feature  $F$  is just visible. Show that the ordering of the features in the two views of the object may be sufficient to prove that  $F$  is inside, or perhaps behind, the object.
9. a. State the conditions under which matt surfaces may properly be described as “Lambertian.” Show that the normal at a point on a Lambertian surface must lie on a cone of directions whose axis points to the point course of illumination. Show that a minimum of three independent light sources will be needed to identify the exact orientation of a matt surface. Why might four light sources help to determine surface orientation for a surface of unknown or nonideal properties?

- b. Compare the effectiveness of binocular vision and photometric stereo if it is desired to obtain a depth map for each object in a scene. In each case, consider the properties of the object surface and the distance from the observer.
- 10.
- a. Compare the properties of matt surfaces with those which exhibit “normal” specular reflection. Matt surfaces are sometimes described as “Lambertian.” Describe how the brightness of the surface varies according to the Lambertian model.
  - b. Show that for a given surface brightness, the orientation of any point on a Lambertian surface must lie on a certain cone of orientations.
  - c. Three images of a surface are obtained on illuminating it in sequence by three independent point light sources. Show with the aid of a diagram how this can lead to unambiguous estimates of surface orientation. Would surface orientation of any points on the surface *not* be estimated by this method? Are there any constraints on the allowable positions of the three light sources? Would it help if *four* independent point light sources were used instead of three?
  - d. Discuss whether the surface map that is obtained by shape from shading is identical to that obtained by stereo (binocular) vision. Are the two approaches best applied in the same or different applications? To what extent is the application of structured light able to give better or more accurate information than these basic approaches?
  - e. Consider what further processing is required before 3-D objects can be recognized by any of these approaches.

This page intentionally left blank

# Tackling the perspective $n$ -point problem

# 17

It is possible to recognize 3-D objects from very few point features, even when they are seen in a single view. In fact, the pose of the 3-D object can also be ascertained from a single view. However, ambiguities of interpretation do arise, and this chapter discusses the disambiguation problem.

*Look out for:*

- The distinction between weak and full perspective projection
- How the “perspective inversion” type of ambiguity arises under weak perspective projection
- How more serious ambiguities arise under full perspective projection
- How full perspective projection has the capability to provide more interpretative information than weak perspective projection
- How coplanarity can impose quite strong constraints on 3-D data, which can be sometimes helpful and at other times an impediment
- How symmetry can help with 3-D image interpretation.

Note that although this chapter considers only one aspect of 3-D vision, it raises very important issues that are relevant right through the subject of 3-D object recognition.

## 17.1 INTRODUCTION

This chapter follows on from the previous introductory chapter, and tackles a problem of central importance in the analysis of images from 3-D scenes. It has been kept separate and fairly short so as to focus carefully on relevant factors in the analysis. First, we look at the phenomenon of perspective inversion, which has already been alluded to several times in [Chapter 16](#), The Three-Dimensional World. Then we refine our ideas on perspective and proceed to consider the determination of object pose from salient features that are located in the images. It will be useful to consider how many salient features are required for unambiguous determination of pose.

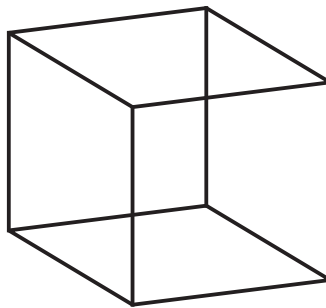


## 17.2 THE PHENOMENON OF PERSPECTIVE INVERSION

In this section, we study first the phenomenon of *perspective inversion*. This is actually a rather well-known effect that appears in the following “Necker cube” illusion. Consider a wire cube made from 12 pieces of wire welded together at the corners. Looking at it from approximately the direction of one corner, it is difficult to tell which way round the cube is, i.e., which of the opposite corners of the cube is the nearer (Fig. 17.1). Indeed, on looking at the cube for a time, one gradually comes to feel one knows which way round it is, but then it suddenly appears to reverse itself; then that perception remains for some time, until it too reverses itself. [In psychology, this shifting of attention is known as *perceptual reversal*, which is unfortunately rather similar to the term *perspective inversion* but is actually a much more general effect which leads to a host of other types of optical illusion—see Gregory (1971) and the many illustrations produced by M.C. Escher.] The perspective inversion illusion reflects the fact that the brain is making various hypotheses about the scene and even making decisions based on incomplete evidence about the situation (Gregory, 1971, 1972).

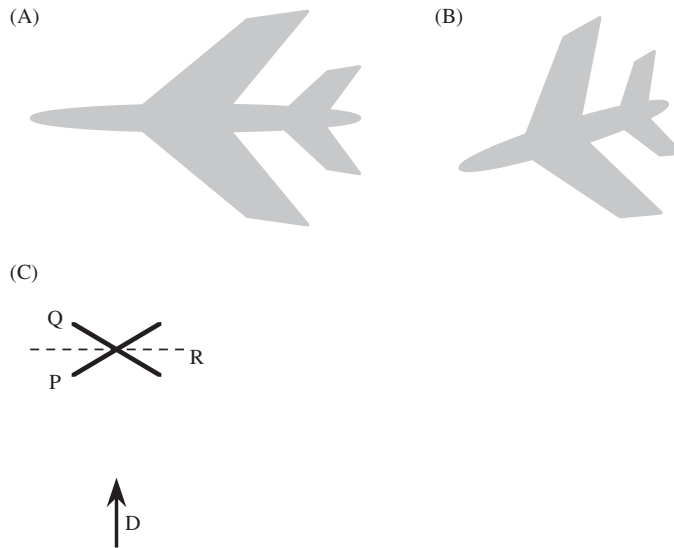
The wire cube illusion could perhaps be regarded as somewhat artificial. But consider instead an aeroplane (Fig. 17.2A) that is seen in the distance (Fig. 17.2B) against a bright sky. The silhouetting of the object means that its surface details are not visible. In that case, interpretation requires that a hypothesis be made about the scene, and it is possible to make the wrong one. Clearly (Fig. 17.2C), the aeroplane could be at an angle  $\alpha$  (as for P), though it could equally well be at an angle  $-\alpha$  (as for Q). The two hypotheses about the orientation of the object are related by the fact that the one can be obtained from the other by reflection in a plane R normal to the viewing direction D.

Strictly, there is only an ambiguity in this case if the object is viewed under orthographic or scaled orthographic projection. [*Scaled orthographic projection* is orthographic projection with the final image scaled in size by a constant factor.]



**FIGURE 17.1**

The phenomenon of perspective inversion. This figure shows a wire cube viewed approximately from the direction of one corner. The phenomenon of perspective inversion makes it difficult to see which of the opposite corners of the cube is the nearer: in fact, there are two stable interpretations of the cube, either of which may be perceived at any moment.

**FIGURE 17.2**

Perspective inversion for an aeroplane. Here, an aeroplane (A) is silhouetted against the sky and appears as in (B). Part (C) shows the two planes P and Q in which the aeroplane could lie, relative to the direction D of viewing: R is the reflection plane relating the planes P and Q.

However, in the distance, perspective projection approximates to scaled orthographic projection, and it is often difficult to detect the difference. (In this case, the object is said to be viewed under *weak perspective projection*. For weak perspective, the depth  $\Delta Z$  within the object has to be much less than its depth  $Z$  in the scene. On the other hand, the perspective scaling factor can be different for each object and will depend on its depth in the scene: so the perspective can validly be locally weak and globally normal.) If the aeroplane in Fig. 17.2 was quite near, it would be obvious that one part of the silhouette was nearer, as the perspective would distort it in a particular way. In general, perspective projection will break down symmetries, so searching for symmetries that are known to be present in the object should reveal which way around it is; however, if the object is in the distance, as in Fig. 17.2B, it will be virtually impossible to see the breakdown. On the contrary, short term study of the motion of the aeroplane will not help with interpretation in the case shown in Fig. 17.2B. Eventually, however, the aeroplane will appear to become smaller or larger, and this will give the additional information needed to resolve the issue.

---

### 17.3 AMBIGUITY OF POSE UNDER WEAK PERSPECTIVE PROJECTION

It is instructive to examine to what extent the pose of an object can be deduced under weak perspective projection. We can reduce the above problem to a

simplest case in which three points have to be located and identified. Any set of three points is coplanar, and the common plane corresponds to that of the silhouette shown in Fig. 17.2A (we assume here that the three points are not collinear, so that they do in fact define a plane). The problem then is to match the corresponding points on the idealized object (Fig. 17.2A) with those on the observed object (Fig. 17.2B). It is not yet completely obvious that this is possible, or that the solution is unique, even apart from the reflection operation noted earlier. It could be that more than three points will be required—especially if the scale is unknown—or it could be that there are several solutions, even if we ignore the reflection ambiguity. Of particular interest will be the extent to which it is possible to deduce which is which of the three points in the observed image.

To understand the degree of difficulty, let us briefly consider full perspective projection. In this case, any set of three noncollinear points can be mapped into any other three. This means that it may not be possible to deduce much about the original object just from this information: we will certainly not be able to deduce which point maps to which other point. However, we shall see that the situation is rather less ambiguous when viewing the object under weak perspective projection.

Perhaps, the simplest approach (due to Huang et al. as recently as 1995) is to imagine a circle drawn through the original set of points  $P_1$ ,  $P_2$ , and  $P_3$  (Fig. 17.3A). We then find the centroid  $C$  of the set of points and draw additional lines through the points, all passing through  $C$  and meeting the circle in another three points  $Q_1$ ,  $Q_2$ , and  $Q_3$  (Fig. 17.3A). Now, in common with orthographic projection, scaled orthographic projection maintains ratios of distances on the same straight line, and weak perspective projection approximates to this. Thus, the distance ratio  $P_iC:CQ_i$  remains unchanged after projection. Thus, when we project the whole figure, as in Fig. 17.3B, we find that the circle has become an ellipse, though all lines remain lines, and all linear distance ratios remain unchanged. The significance of this is as follows. When the points  $P'_1$ ,  $P'_2$ , and  $P'_3$  are observed in the image, the centroid  $C'$  can be computed, as can the positions of  $Q'_1$ ,  $Q'_2$ , and  $Q'_3$ . Thus, we have six points by which to deduce the position and parameters of the ellipse (in fact, five are sufficient). Once the ellipse is known, the orientation of its major axis gives the axis of rotation of the object; whereas the ratio of the lengths of the minor to major axes immediately gives the value of  $\cos \alpha$ . (Notice how the ambiguity in the sign of  $\alpha$  comes up naturally in this calculation.) Finally, the length of the major axis of the ellipse permits the depth of the object in the scene to be deduced.

We have now shown that observing three projected points permits a unique ellipse to be computed passing through them, and when this is back projected into a circle, the axis of rotation of the object, and the angle of rotation can be deduced, but not the sign of the angle of rotation. There are two important comments to be made about the above calculation. The first is that the three distance ratios must be stored in memory, before interpretation of the observed scene can begin. The second is that the order of the three points apparently has to be known before interpretation can be undertaken; otherwise, we will have to perform six computations in which all possible assignments of the distance ratios are tried; furthermore, it might appear from the earlier introductory remarks that several solutions are possible.

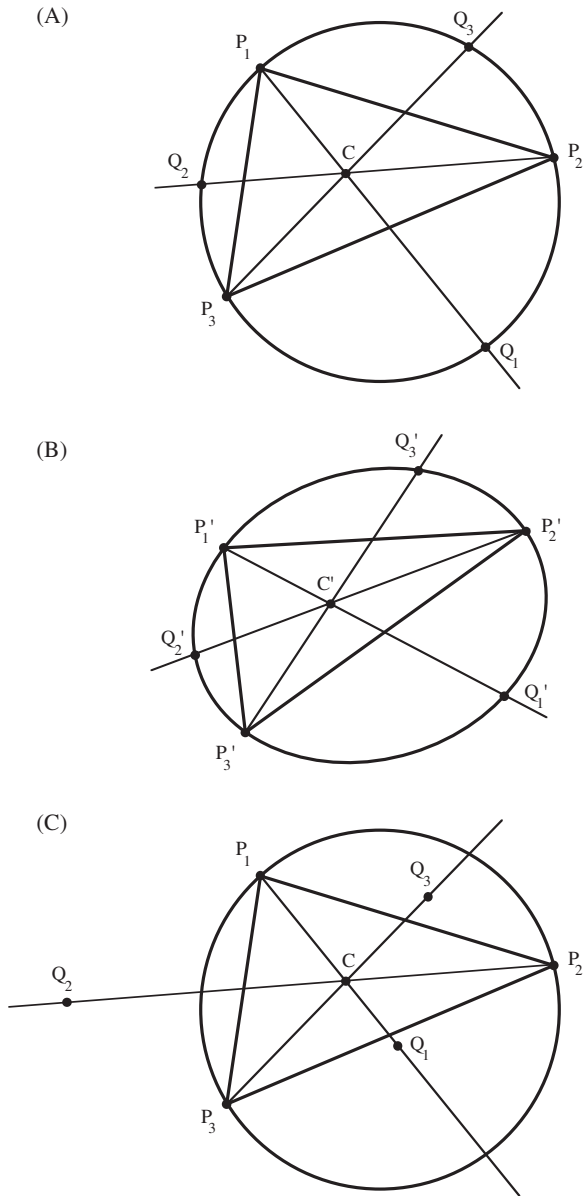


**FIGURE 17.3**

Determination of pose for three points viewed under weak perspective projection. Part (A) shows three feature points  $P_1, P_2, P_3$  which lie on a known type of object. The circle passing through  $P_1, P_2, P_3$  is drawn, and lines through the points and their centroid  $C$  meet the circle in  $Q_1, Q_2, Q_3$ . The ratios  $P_iC:CQ_i$  are then deduced. Part (B) shows the three points observed under weak perspective as  $P'_1, P'_2, P'_3$ , together with their centroid  $C'$  and the three points  $Q'_1, Q'_2, Q'_3$  located using the original distance ratios. An ellipse drawn through the six points  $P'_1, P'_2, P'_3, Q'_1, Q'_2, Q'_3$  can now be used to determine the orientation of the plane in which  $P_1, P_2, P_3$  must lie, and also (from the major axis of the ellipse) the distance of viewing. Part (C) shows how an erroneous interpretation of the three points does not permit a circle to be drawn passing through  $P_1, P_2, P_3, Q_1, Q_2, Q_3$  and hence no ellipse can be found which passes through the observed and the derived points  $P'_1, P'_2, P'_3, Q'_1, Q'_2, Q'_3$ .

Although there are some instances in which feature points might be distinguishable, there are many cases when they are not (especially in 3-D situations where corner features might vary considerably when viewed from different positions). Thus, the potential ambiguity is important. However, if we can try out each of the six cases, little difficulty will generally arise. For immediately, we deduce the positions  $Q_1'$ ,  $Q_2'$ ,  $Q_3'$ , we will find that it is not possible in general to fit the six resulting points to an ellipse. The reason is easily seen on returning to the original circle. In that case, if the wrong distance ratios are assigned, the  $Q_i$  will clearly not lie on the circle, as the only values of the distance ratios for which the  $Q_i$  do lie on the circle are the correctly assigned ones (Fig. 17.3C). This means that though computation is wasted testing the incorrect assignments, there appears to be no risk of their leading to ambiguous solutions. Nevertheless, there is one contingency under which things could go wrong. Suppose the original set of points  $P_1$ ,  $P_2$ ,  $P_3$  forms an almost perfect equilateral triangle. Then, the distance ratios will be very similar, and, taking numerical inaccuracies into account, it may not be clear which ellipse provides the best and most likely fit. This mitigates against taking sets of feature points which form approximately isosceles or equilateral triangles. However, in practice, more than three coplanar points will generally be used to optimize the fit, making fortuitous solutions rather unlikely.

Overall, it is fortunate that weak perspective projection requires such weak conditions for the identification of unique (to within a reflection) solutions, especially as full perspective projection demands four points before a unique solution can be found (see below). However, under weak perspective projection, additional points lead to greater accuracy but no reduction in the reflection ambiguity: this is because the information content from weak perspective projection is impoverished in the lack of depth cues which could (at least in principle) resolve the ambiguity. To understand this, lack of additional information from more than three points under weak perspective projection, note that each additional feature point in the same plane is predetermined once three points have been identified (here, we are assuming that the model object with the correct distance ratios can be referred to).

These considerations indicate that we have two potential routes to unique location of objects from limited numbers of feature points. The first is to resort to use of noncoplanar points viewed still under weak perspective projection. The second is to use full perspective projection to view coplanar or noncoplanar sets of feature points. We shall see below that whichever of these options we take, a unique solution demands that a minimum of four feature points be located on any object.

---

## 17.4 OBTAINING UNIQUE SOLUTIONS TO THE POSE PROBLEM

The overall situation is summarized in Table 17.1. Looking first at the case of weak perspective projection, the number of solutions only becomes finite for three

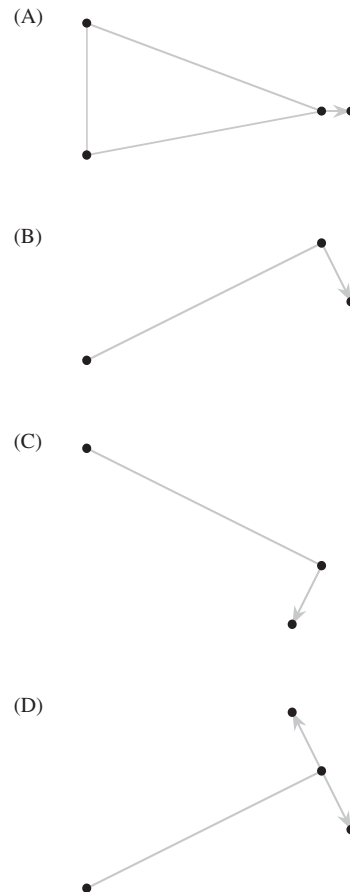
**Table 17.1** Ambiguities When Estimating Pose From Point Features

Arrangement of the Points	$n$	WPP	FPP
Coplanar	$\leq 2$	$\infty$	$\infty$
	3	2	4
	4	2	1
	5	2	1
	$\geq 6$	2	1
Noncoplanar	$\leq 2$	$\infty$	$\infty$
	3	2	4
	4	1	2
	5	1	2
	$\geq 6$	1	1

*This table summarizes the numbers of solutions that will be obtained when estimating the pose of a rigid object from point features located in a single image. It is assumed that  $n$  point features are detected and identified correctly and in the correct order. The columns WPP and FPP signify weak perspective projection and full perspective projection, respectively. The upper half of the table applies when all  $n$  points are coplanar; the lower half of the table applies when the  $n$  points are noncoplanar. Note that when  $n \leq 3$ , the results strictly apply only in the coplanar case. However, the top two lines in the lower half of the table are retained for easy comparison.*

or more point features. Once three points have been employed, in the coplanar case, there is no further reduction in the number of solutions, as (as noted earlier) the positions of any additional points can be deduced from the existing ones. However, this does not apply when the additional points are noncoplanar as they are able to provide just the right information to eliminate any ambiguity (see Fig. 17.4). (Although this might appear to contradict what was said earlier about perspective inversion, note that we are assuming here that the body is rigid and that all its features are at *known* fixed points on it in three dimensions; hence, this particular ambiguity no longer applies, except for objects with special symmetries which we shall ignore here—see Fig. 17.4D).

Considering next the case of full perspective projection, the number of solutions again becomes finite only for three or more point features. The lack of information provided by three point features means that four solutions are in principle possible (see the example in Fig. 17.5 and the detailed explanation in Section 17.4.1), but the number of solutions drops to one as soon as four coplanar points are employed (the correct solution can be found by making cross-checks between subsets of three points, and eliminating inconsistent solutions); when the points are noncoplanar, it is only when six or more points are employed that there is sufficient information to unambiguously determine the pose: there is necessarily no ambiguity with six or more points, as all 11 camera calibration parameters can be deduced from the 12 linear equations that then arise (see Chapter 19: Image Transformations and Camera Calibration). Correspondingly, it is deduced

**FIGURE 17.4**

Determination of pose for four points viewed under weak perspective projection. Part (A) shows an object containing four noncoplanar points, as seen under weak perspective projection. Part (B) shows a side view of the object. If the first three points (connected by nonarrowed gray lines) were viewed alone, perspective inversion would give rise to a second interpretation (C). However, the fourth point gives additional information about the pose which permits only one overall interpretation. This would not be the case for an object containing an additional symmetry as in (D), as its reflection would be identical to the original view (not shown).

that five noncoplanar points will in general be *insufficient* for all 11 parameters to be deduced, so there will still be some ambiguity in this case.

Next, it should be questioned why the coplanar case is at first ( $n = 3$ ) better under weak perspective projection and then ( $n > 3$ ) better under full perspective projection, whereas the noncoplanar case is always better, or as good, under weak

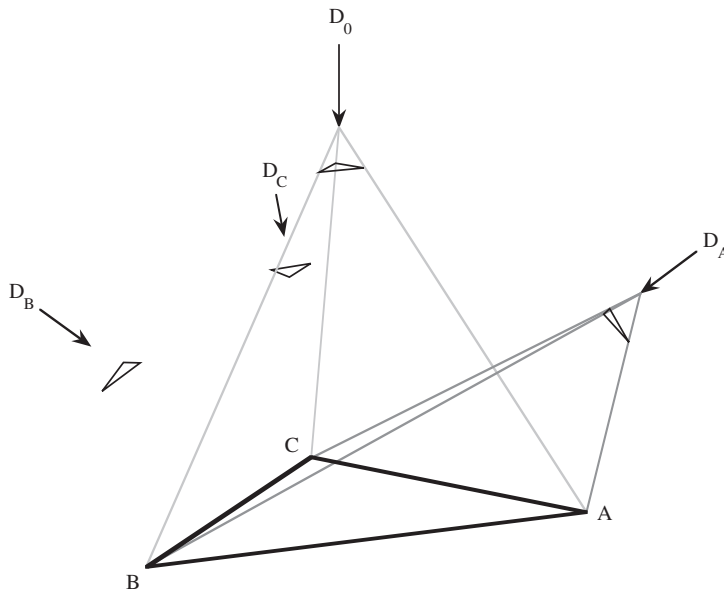


**FIGURE 17.5**

Ambiguity for three points viewed under full perspective projection. Under full perspective projection, the camera sees three points A, B, C as three directions in space, and this can lead to fourfold ambiguity in interpreting a known object. The figure shows the four possible viewing directions and centers of projection of the camera (indicated by the directions and tips of the bold arrows): in each case, the image at each camera is indicated by a small triangle.  $D_A$ ,  $D_B$ ,  $D_C$  correspond approximately to views from the general directions of A, B, C, respectively.

perspective projection. [In this context, “better” means less ambiguous and leading to fewer solutions.] The reason must be that intrinsically full perspective projection provides more detailed information but is frustrated by lack of data when there are relatively few points: however, the exact stage at which the additional information becomes available is different in the coplanar and noncoplanar cases. In this respect, it is important to note that when coplanar points are being observed under weak perspective projection, there is never enough information to eliminate the ambiguity.

It should be emphasized that the above discussion assumes that the correspondences between object and image features are all known, i.e., that  $n$  point features are detected and identified correctly and in the correct order. If this is not so, the number of possible solutions could increase substantially, considering the number of possible permutations of quite small numbers of points. This makes it attractive to use the minimum number of features for ascertaining the most probable match (Horaud et al., 1989). Other workers have used heuristics to help reduce the number



of possibilities. For example, Tan (1995) used a simple compactness measure (see Section 8.7) to determine which geometric solution is the most likely: extreme obliqueness is perhaps unlikely, and the most likely solution is taken to be the one with highest compactness value. This idea follows on from the extremum principle of Brady and Yuille (1984), which states that the most probable solutions are those nearest to extrema of relevant (e.g., rotation) parameters. (Perhaps the simplest way of understanding this principle is obtained by considering a pendulum, whose extreme positions are also its most probable! However, in this case, the extremum occurs when the angle  $\alpha$  (see Fig. 17.1) is close to zero.) In this context, note that coplanar points viewed under weak or full perspective projection always appear in the same cyclic order: this is not trivial to check given the possible distortions of an object, though if a convex polygon can be drawn through the points, the cyclic order around its boundary will not change on projection. (The reason for this is that planar convexity is an invariant of projection.) However, for noncoplanar points, the pattern of the perceived points can reorder itself almost randomly: this means that a considerably greater number of permutations of the points have to be considered for noncoplanar points than for coplanar points.

Finally, note that the above discussion has concentrated on the existence and uniqueness of solutions to the pose problem. The stability of the solutions has not so far been discussed. However, the concept of stability gives a totally different dimension to the data presented in Table 17.1. In particular, noncoplanar points tend to give more stable solutions to the pose problem. For example, if the plane containing a set of coplanar points is viewed almost head-on ( $\alpha \approx 0$ ), there will be very little information on the exact orientation of the plane, because the changes in lateral displacement of the points will vary as  $\cos \alpha$  (see Section 17.2), and there will be no linear term in the Taylor expansion of the orientation dependence.

### 17.4.1 SOLUTION OF THE THREE-POINT PROBLEM

Fig. 17.5 showed how four solutions can arise when three point features are viewed under full perspective projection. Here, we briefly explore this situation by considering the relevant equations. Fig. 17.5 shows that the camera sees the points as three image points representing three directions in space. This means that we can compute the angles  $\alpha$ ,  $\beta$ ,  $\gamma$  between these three directions. If the distances between the three points A, B, C on the object are the known values  $D_{AB}$ ,  $D_{BC}$ ,  $D_{CA}$ , we can now apply the cosine rule in an attempt to determine the distances  $R_A$ ,  $R_B$ ,  $R_C$  of the feature points from the center of projection:

$$D_{BC}^2 = R_B^2 + R_C^2 - 2R_B R_C \cos \alpha \quad (17.1)$$

$$D_{CA}^2 = R_C^2 + R_A^2 - 2R_C R_A \cos \beta \quad (17.2)$$

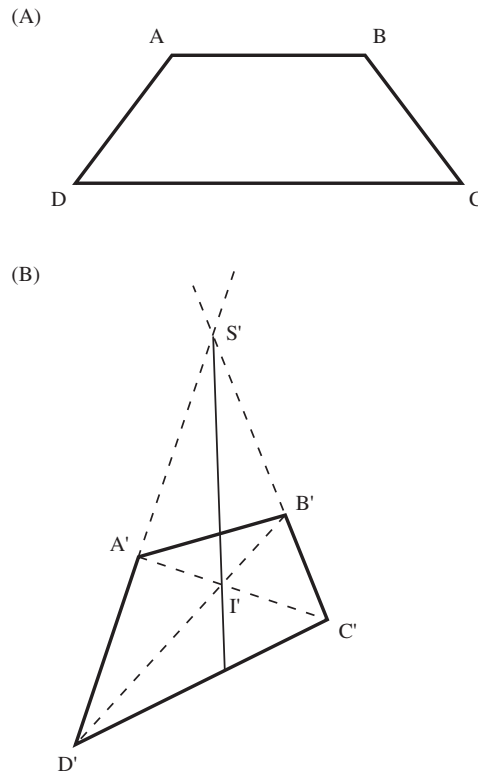
$$D_{AB}^2 = R_A^2 + R_B^2 - 2R_A R_B \cos \gamma \quad (17.3)$$

Eliminating any two of the variables  $R_A$ ,  $R_B$ ,  $R_C$  yields an eighth degree equation in the other variable, indicating that eight solutions to the system of equations could be available (Fischler and Bolles, 1981). However, the above cosine rule equations contain only constants and second degree terms: hence, for every positive solution, there is another solution which differs only by a sign change in all the variables. These solutions correspond to inversion through the center of projection and are hence unrealizable. Thus, there are at most four realizable solutions to the system of equations. In fact, we can quickly demonstrate that there may sometimes be fewer than four solutions: as in some cases, for one or more of the “flipped” positions shown in Fig. 17.5, one of the features could be on the negative side of the center of projection, and hence would be unrealizable.

Before leaving this topic, note that the homogeneity of Eqs. (17.1)–(17.3) implies that observation of the angles  $\alpha$ ,  $\beta$ ,  $\gamma$  permits the orientation of the object to be estimated independently of any knowledge of its scale: in fact, estimation of scale depends directly on estimation of range, and vice versa. Thus, knowledge of just one range parameter (e.g.,  $R_A$ ) will permit the scale of the object to be deduced. Alternatively, knowledge of its area will permit the remaining parameters to be deduced. This concept provides a slight generalization of the main results of Sections 17.2 and 17.3, which generally start with the assumption that all the dimensions of the object are known.

### 17.4.2 USING SYMMETRIC TRAPEZIA FOR ESTIMATING POSE

One more example will be of interest here. That is the case of a four points arranged at the corners of a symmetric trapezium (Tan, 1995). When viewed under weak perspective projection, the midpoints of the parallel sides are easily measured, but under full perspective projection, midpoints do not remain midpoints, so the axis of symmetry cannot be obtained in this way. However, producing the skewed sides to meet at  $S'$  and forming the intersection  $I'$  of the diagonals permits the axis of symmetry to be located as the line  $I'S'$  (Fig. 17.6). Thus, we now have not four points but six to describe the perspective view of the trapezium. What is more important is that the axis of symmetry has been located, and this is known to be perpendicular to the parallel sides of the trapezium. This is a great help in making the mathematics more tractable, and in obtaining solutions quickly so that, for example, object motion can be tracked in real time. Again, this is a case where object orientation can be deduced straightforwardly, even when the situation is one of strong perspective, and even when the size of the object is unknown. This result is a generalization from that of Haralick (1989) who noted that a single view of a rectangle of unknown size is sufficient to determine its pose. In either case, the range of the object can be found if its area is known, or its size can be deduced if a single range value can be found from other data (see also Section 17.4.1).

**FIGURE 17.6**

Trapezium viewed under full perspective projection. Part (A) shows a symmetrical trapezium, and (B) shows how it appears when viewed under full perspective projection. In spite of the fact that midpoints do not project into midpoints under perspective projection, the two points  $S'$  and  $I'$  on the symmetry axis can be located unambiguously as the intersection of two nonparallel sides and two diagonals, respectively. This gives six points (from which the two midpoints on the symmetry axis can be deduced if necessary), which is sufficient to compute the pose of the object, albeit with a single ambiguity of interpretation (see text).

## 17.5 CONCLUDING REMARKS

This chapter has aimed to cover certain aspects of 3-D vision that were not studied in depth in the previous chapter. In particular, it was worth investigating the topic of perspective inversion in some detail, and exploring how it was affected by the method of projection. Orthographic projection, scaled orthographic projection, weak perspective projection, and full perspective projection were considered, and the numbers of object points that would lead to correct or ambiguous interpretations were analyzed. It was found that scaled orthographic projection and its approximation, weak perspective projection, led to straightforward interpretation when four or

more noncoplanar points were considered, though the perspective inversion ambiguity remained when all the points were coplanar. This latter ambiguity was resolved with four or more points viewed under full perspective projection. However, in the noncoplanar case, some ambiguity remained until six points were being viewed. The key to understanding the situation is the fact that full perspective projection makes the situation more complex, though at the same time, it provides more information by which, ultimately, to resolve the ambiguity.

Additional problems were found to arise when the points being viewed are indistinguishable, and then a good many solutions may have to be tried before a minimally ambiguous result is obtained. With coplanar points fewer possibilities arise, and this leads to less computational complexity: the key to success here is the natural ordering that can arise for points in a plane—as for example, when they form a convex set which can be ordered uniquely around a bounding polygon. In this context, the role that can be played by the extremum principle of Brady and Yuille (1984) in reducing the number of solutions is significant (for further insight on the topic, see Horaud and Brady, 1988).

It is of great relevance to devise methods for rapid interpretation in real-time applications. To achieve this, it is important to work with a minimal set of points, and to obtain analytic solutions which move directly to solutions without computationally expensive iterative procedures: for example, Horaud et al. (1989) found an analytic solution for the perspective four-point problem which works both in the general noncoplanar case and in the planar case. Other low-computation methods are still being developed, as with pose determination for symmetrical trapezia (Tan, 1995). It should also be noted that understanding is still advancing, as demonstrated by Huang et al.'s (1995) neat geometrical solution to the pose determination problem for three points viewed under weak perspective projection.

This chapter has covered a specific 3-D recognition problem. [Chapter 18](#), Invariants and Perspective covers another—that of invariants, which provides speedy and convenient means of bypassing the difficulties associated with full perspective projection. [Chapter 19](#), Image Transformations and Camera Calibration aims to finalize the study of 3-D vision by showing how camera calibration can be achieved or, to some extent, circumvented.

*Perspective makes interpretation of images of 3-D scenes intrinsically difficult. However, this chapter has demonstrated that “weak perspective” views of distant objects are much simplified, so objects are commonly located using fewer features: for planar objects, a pose ambiguity remains, though it is eliminated under full perspective.*

---

## 17.6 BIBLIOGRAPHICAL AND HISTORICAL NOTES

The development of solutions to the so-called *perspective n-point (PnP) problem* (finding the pose of objects from  $n$  features under various forms of perspective)

has been proceeding for more than two decades and is by no means complete. Fischler and Bolles summarized the situation as they saw it in 1981, and several new algorithms were described by them. However, they did not discuss pose determination under weak perspective, and perhaps surprisingly, considering its reduced complexity, this has subsequently been the subject of much research (e.g., Alter, 1994; Huang et al., 1995). Horaud et al. (1989) discussed the problem of finding rapid solutions to the  $PnP$  problem by reducing  $n$  as far as possible: they also obtained an analytic solution for the case  $n = 4$  which should help considerably with real-time implementations. Their solution is related to Horaud's earlier (1987) corner interpretation scheme—described in [Section 16.10](#), whereas Haralick et al. (1984) provided useful basic theory for matching wire frame objects.

In a later paper, Liu and Wong (1999) described an algorithm for pose estimation from four corresponding points under full perspective projection (FPP) when the points are not coplanar. Strictly, according to [Table 17.1](#), this will lead to an ambiguity. However, Liu and Wong made the point “that the possibility for the occurrence of multiple solutions in the perspective four-point problem is much smaller than that in the perspective three-point problem,” so that “using a four-point model is much more reliable than using a three-point model;” and they actually only claim “good results.” Also, much of the emphasis of the paper is on errors and reliability. Hence, it seems that it is the *scope* for making errors in the sense of misinterpreting the situation that is significantly reduced. Added to this, Liu and Wong's (1999) work involves tracking a known object within a somewhat restricted region of space: this must again cut down the scope for error considerably. Hence, it is not clear that their work violates the relevant entry in [Table 17.1](#)—namely, FPP; noncoplanar;  $n = 4$  (see Fischler and Bolles, 1981)—rather than merely making it *unlikely* that a real ambiguity will arise.

Between them, Faugeras (1993), Hartley and Zisserman (2000), Faugeras and Luong (2001), and Forsyth and Ponce (2003) provide good coverage of the whole area of 3-D vision; for an interesting viewpoint on the subject, with particular emphasis on pose refinement, see Sullivan (1992). For further references on specific aspects of 3-D vision, see [Sections 16.13](#), [18.12](#), [19.16](#). ([Section 20.10](#) gives references on motion but also covers aspects of 3-D vision.)

### 17.6.1 MORE RECENT DEVELOPMENTS

Xu et al. (2008) present a new method for tackling the  $PnP$  problem. The linear method for the case of four coplanar points is extended to find coarse solutions for the general P3P problem. Once all the accurate solutions for the P3P problem have been found, the algorithm is applied to the general  $PnP$  problem. Solution stability issues and possible ambiguities are investigated, and experiments are performed to verify the effectiveness of the proposed method. Significantly, the case of four coplanar points has to be divided into two mutually exclusive cases, in which one point lies, or does not lie, within the triangle presented by the other

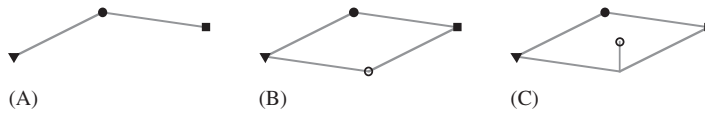


**FIGURE 17.P1**

In this diagram, the gray edges are construction lines, *not* parts of the objects. Parts (A) and (B) are completely planar objects, whereas Part (C) is not planar.

three points. Lepetit et al. (2008) propose an  $O(n)$  noniterative solution to the  $PnP$  problem that is far faster and more accurate than earlier methods and also more stable. The central idea is to express the 3-D points as a weighted sum of four virtual control points and to solve this case in terms of the coordinates. (The computational load of previous methods can be as high as  $O(n^5)$  or even  $O(n^8)$ .)

## 17.7 PROBLEMS

1. Draw up a complete table of pose ambiguities that arise for *weak* perspective projection, for various numbers of object points identified in the image. Your answer should cover both coplanar points and noncoplanar points and should make clear in each case how much ambiguity would remain in the limit of an infinite number of object points being seen. Give justification for your results.
2. Distinguish between *full perspective projection* and *weak perspective projection*. Explain how each of these projections presents oblique views of the following real objects: (1) Straight lines, (2) several concurrent lines (i.e., lines meeting in a single point), (3) parallel lines, (4) midpoints of lines, (5) tangents to curves, (6) circles whose centers are marked with a dot. Give justification for your results.
3. Explain each of the following: (1) Why weak perspective projection leads to an ambiguity in viewing an object such as that in Fig. 17.P1A? (2) Why the ambiguity doesn't disappear for the case of Fig. 17.P1B? (3) Why the ambiguity *does* disappear in the case of Fig. 17.P1C, if the true nature of the object is known? (4) Why the ambiguity doesn't occur in the case of Fig. 17.P1B viewed under full perspective projection? In the last case, illustrate your answer by means of a sketch.

This page intentionally left blank

# Invariants and perspective 18

Invariants are important for achieving recognition in both 2-D and 3-D. The basic idea is to identify some parameter or parameters that do not vary between different instances of the same object. Unfortunately, perspective projection makes the issue far harder in the general 3-D case. This chapter explores the problem and demonstrates a number of useful techniques. At the same time, it explores the problems of perspective projection, with some interesting outcomes.

*Look out for:*

- How a ratio of distances between features along the same straight line can act as a convenient invariant under weak perspective projection
- How a ratio of ratios (or “cross ratio”) can act as a convenient invariant under full perspective projection
- How the cross-ratio type of invariant can rather cunningly be generalized to cover many wider possibilities
- how the cross-ratio type of invariant seems largely unable to provide invariance outside any given plane
- Vanishing point (VP) detection and its relevance to image interpretation
- How to optimize views of 2-D pictures to limit perspective distortions
- Problems involved in “stitching” photographs.

While this chapter considers only one aspect of 3-D vision, it is extremely useful both in helping to cue into complex images (see particularly the egomotion example of Fig. 18.4) and in taking short cuts around the tedious analysis of 3-D geometry (see, e.g., Sections 18.8 and 18.9).

## 18.1 INTRODUCTION

Pattern recognition is a complex task and, as stated in [Chapter 1, Vision, the Challenge](#), involves the twin processes of discrimination and generalization. Indeed, the latter process is in many ways more important than the first—especially in the initial stages of recognition—since there is so much redundant information in a typical image. Thus, we need to find ways of helping to eliminate invalid matches. This is where the study of invariants comes into its own.

An invariant is a property of an object or class of objects that does not change with changes of viewpoint or object pose and which can therefore be used to help



distinguish it from other objects. The procedure is to search for objects with a specific invariant so that those which do not possess the invariant can immediately be discarded from consideration. An invariant property can be regarded as a necessary condition for an object to be in the chosen class, though in principle, only detailed subsequent analysis will confirm that it is. In addition, if an object is found to possess the correct invariant, it will then be profitable to pursue the analysis further and find its pose, size, or other relevant data. Ideally, an invariant would uniquely identify an object as being of a particular type or class. Thus, an invariant should not merely be a property which leads to further hypotheses being made about the object, but one which fully characterizes it. However, the difference is a subtle one, more a matter of degree and purpose than an absolute criterion. We shall see below the extent of the difference by appealing to a number of specific cases.

Let us first consider an object being viewed from directly overhead at a known distance by a camera whose optical axis is normal to the plane on which the object is lying. We shall assume that the object is flat. Take two point features on the object such as corners or small holes. If we measure the image distance between these features, then this acts as an invariant, in that:

1. It has a value independent of the translation and orientation parameters of the object;
2. It will be unchanged for different objects of the same type; and
3. It will in general be different from the distance parameters of other objects that might be on the object plane.

Thus, measurement of distance provides a certain lookup or indexing quality which will ideally identify the object uniquely, though further analysis will be required to fully locate it and ascertain its orientation. Hence, distance has all the requirements of an invariant, though it could also be argued that it is only a feature which *helps* to classify objects. Clearly, we are here ignoring an important factor—the effect of imprecision in measurement, due to spatial quantization (or inadequate spatial resolution), noise, lens distortions, and so on; in addition, the effects of partial occlusion or breakage are also being ignored. Most definitely, there is a limit to what can be achieved with a single invariant measure, though in what follows we attempt to reveal what is possible and demonstrate the advantages of employing an invariant-orientated approach.

The above ideas relating to distance as an invariant measure showed it to be useful in suppressing the effects of translations and rotations of objects in 2-D. Hence, it is of little direct value when considering translations and rotations in 3-D. Furthermore, it is not even able to cope with scale variations of objects in 2-D. Moving the camera closer to the object plane and refocusing totally change the situation and all values of the distance invariant residing in the object indexing table must be changed and the old values ignored. However, a little thought will show that this last problem could be overcome. All we need to do is to take *ratios* of distances. This requires a minimum of three-point features to be identified in the image and the interfeature distances measured. If we call two of these

distances  $d_1$  and  $d_2$ , then the ratio  $d_1/d_2$  will act as a scale-independent invariant, i.e., we will be able to identify objects using a single indexing operation whatever their 2-D translation, orientation, or apparent size or scale. An alternative to this idea is to measure the angle between pairs of distance vectors,  $\cos^{-1}(\mathbf{d}_1 \cdot \mathbf{d}_2 / d_1 d_2)$ , which will again be scale invariant.

Of course, this consideration has already been invoked in our earlier work on shape analysis. If objects are subject only to 2-D translations and rotations but not to changes of scale, they can be characterized by their perimeters or areas as well as their normal linear dimensions; furthermore, parameters such as compactness and aspect ratio, which employ dimensionless ratios of image measurements, were acknowledged in [Chapter 9](#), Boundary Pattern Analysis to overcome the size/scale problem.

Nevertheless, the main motivation for using invariants is to obtain mathematical measures of configurations of object features which are carefully designed to be independent of the viewpoint or coordinate system used and indeed not to require specific setup or calibration of the image acquisition system. However, it must be emphasized that camera distortions are assumed to be absent or to have been compensated for by suitable postcamera transformations (see [Chapter 19](#): Image Transformations and Camera Calibration).

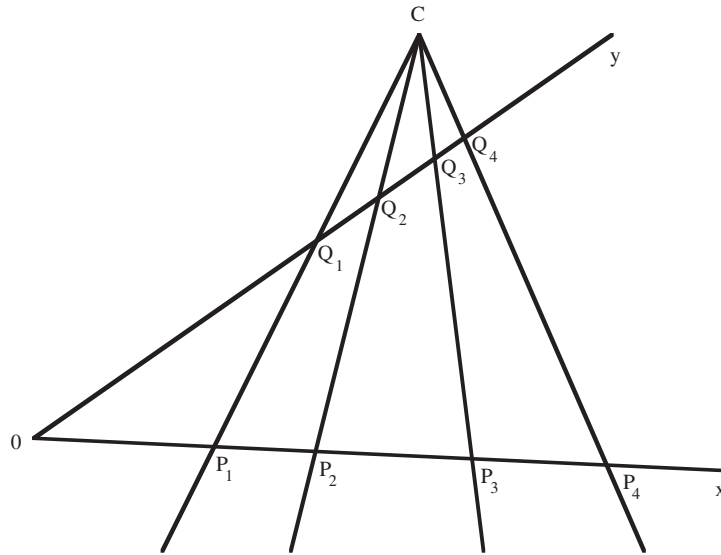
This chapter proceeds to develop the above ideas and later applies them to VP detection ([Sections 18.8 and 18.9](#)), obtaining optimal views of 2-D pictures and the “stitching” of digital photographs ([Section 18.10](#)). Interestingly, with the small intellectual outlay of the initial sections, these applications emerge with very little additional effort—demonstrating the value of the basic theory presented here.

---

## 18.2 CROSS RATIOS: THE “RATIO OF RATIOS” CONCEPT

It would be most useful if we could extend the above ideas to permit indexing for general transformations in 3-D. Indeed, an obvious question is whether finding ratios of ratios of distances will provide suitable invariants and lead to such a generalization. The answer is that ratios of ratios do provide useful further invariants, though going further than this leads to considerable complication, and there are restrictions on what can be achieved with limited computation. In addition, noise ultimately becomes a limiting factor, since so many parameters become involved in the computation of complex invariants that the method ultimately loses steam (it becomes just one of many ways of raising hypotheses and therefore has to compete with other approaches in a manner appropriate to the particular problem application being studied).

We now consider the ratio of ratios approach. Initially, we only examine a set of four collinear points on an object. [Fig. 18.1](#) shows such a set of four points ( $P_1, P_2, P_3, P_4$ ) and a transformation of them ( $Q_1, Q_2, Q_3, Q_4$ ) such as that produced by an imaging system with optical center  $C(c, d)$ . Choice of a suitable pair

**FIGURE 18.1**

Perspective transformation of four collinear points. This figure shows four collinear points ( $P_1, P_2, P_3, P_4$ ) and a transformation of them ( $Q_1, Q_2, Q_3, Q_4$ ) similar to that produced by an imaging system with optical center  $C$ . Such a transformation is called a *perspective transformation*.

of oblique axes permits the coordinates of the points in the separate sets to be expressed, respectively, as

$$\begin{aligned} (x_1, 0), (x_2, 0), (x_3, 0), (x_4, 0) \\ (0, y_1), (0, y_2), (0, y_3), (0, y_4) \end{aligned}$$

Taking points  $P_i, Q_i$ , we can write the ratio  $CQ_i:PQ_i$  both as  $\frac{c}{-x_i}$  and as  $\frac{d-y_i}{y_i}$ . Hence,

$$\frac{c}{x_i} + \frac{d}{y_i} = 1 \quad (18.1)$$

which must be valid for all  $i$ . Subtraction of the  $i$ th and  $j$ th relations now gives

$$\frac{c(x_j - x_i)}{x_i x_j} = \frac{-d(y_j - y_i)}{y_i y_j} \quad (18.2)$$

Forming a ratio between two such relations will now eliminate the unknowns  $c$  and  $d$ . For example, we will have:

$$\frac{x_3(x_2 - x_1)}{x_2(x_3 - x_1)} = \frac{y_3(y_2 - y_1)}{y_2(y_3 - y_1)} \quad (18.3)$$

However, the result still contains factors such as  $x_3/x_2$  which depend on absolute position. Hence, it is necessary to form a suitable ratio of such results which cancels out the effects of absolute positions:

$$\left(\frac{x_2 - x_4}{x_3 - x_4}\right) \bigg/ \left(\frac{x_2 - x_1}{x_3 - x_1}\right) = \left(\frac{y_2 - y_4}{y_3 - y_4}\right) \bigg/ \left(\frac{y_2 - y_1}{y_3 - y_1}\right) \quad (18.4)$$

Thus, our original intuition that a ratio of ratios type of invariant might exist which would cancel out the effects of a perspective transformation is correct. In particular, four collinear points viewed from any perspective viewpoint yield the same value of the cross ratio, defined as above. The value of the cross ratio of the four points is written as

$$C(P_1, P_2, P_3, P_4) = \frac{(x_3 - x_1)(x_2 - x_4)}{(x_2 - x_1)(x_3 - x_4)} \quad (18.5)$$

For clarity, we shall write this particular cross ratio as  $\kappa$  in what follows. Note that there are  $4! = 24$  possible ways in which 4 collinear points can be ordered on a straight line, and hence, there could be 24 cross ratios. However, they are not all distinct, and in fact, there are only 6 different values. To verify this, we start by interchanging pairs of points:

$$C(P_2, P_1, P_3, P_4) = \frac{(x_3 - x_2)(x_1 - x_4)}{(x_1 - x_2)(x_3 - x_4)} = 1 - \kappa \quad (18.6)$$

$$C(P_1, P_3, P_2, P_4) = \frac{(x_2 - x_1)(x_3 - x_4)}{(x_3 - x_1)(x_2 - x_4)} = \frac{1}{\kappa} \quad (18.7)$$

$$C(P_1, P_2, P_4, P_3) = \frac{(x_4 - x_1)(x_2 - x_3)}{(x_2 - x_1)(x_4 - x_3)} = 1 - \kappa \quad (18.8)$$

$$C(P_4, P_2, P_3, P_1) = \frac{(x_3 - x_4)(x_2 - x_1)}{(x_2 - x_4)(x_3 - x_1)} = \frac{1}{\kappa} \quad (18.9)$$

$$C(P_3, P_2, P_1, P_4) = \frac{(x_1 - x_3)(x_2 - x_4)}{(x_2 - x_3)(x_1 - x_4)} = \frac{\kappa}{\kappa - 1} \quad (18.10)$$

$$C(P_1, P_4, P_3, P_2) = \frac{(x_3 - x_1)(x_4 - x_2)}{(x_4 - x_1)(x_3 - x_2)} = \frac{\kappa}{\kappa - 1} \quad (18.11)$$

These cases provide the main possibilities, but of course interchanging more points will yield a limited number of further values—in particular:

$$C(P_3, P_1, P_2, P_4) = 1 - C(P_1, P_3, P_2, P_4) = 1 - \frac{1}{\kappa} = \frac{\kappa - 1}{\kappa} \quad (18.12)$$

$$C(P_2, P_3, P_1, P_4) = \frac{1}{C(P_2, P_1, P_3, P_4)} = \frac{1}{1 - \kappa} \quad (18.13)$$

This covers all six cases, and a little thought (based on trying further interchanges of points) will show that there can be no others (we can only repeat  $\kappa$ ,  $1 - \kappa$ ,  $\kappa/(\kappa - 1)$ , and their inverses). Of particular interest is the fact that

numbering the points in reverse (which would correspond to viewing the line from the other side) leaves the cross ratio unchanged. Nevertheless, it is inconvenient that the same invariant has six different manifestations, as this implies that six different index values have to be looked up before the class of an object can be ascertained. On the other hand, if points are labeled in order along the line rather than randomly, it should generally be possible to circumvent this situation.

So far, we have been able to produce only one projective invariant, and this corresponds to the rather simple case of four collinear points. The usefulness of this measure is augmented considerably when it is noted that four collinear points, taken in conjunction with another point, define a pencil of concurrent coplanar lines passing through the latter point. (It is a common nomenclature of projective geometry to call a set of concurrent lines a *pencil* (e.g., Tuckey and Armistead, 1953).) Clearly, we can assign a unique cross ratio to this pencil of lines, equal to the cross ratio of the collinear points on any line passing through them. We can clarify the situation by considering the angles between the various lines (Fig. 18.2). Applying the sine rule four times to determine the four distances in the cross ratio  $C(P_1, P_2, P_3, P_4)$  gives

$$\frac{x_3 - x_1}{\sin \alpha_{13}} = \frac{OP_1}{\sin \beta_3} \quad (18.14)$$

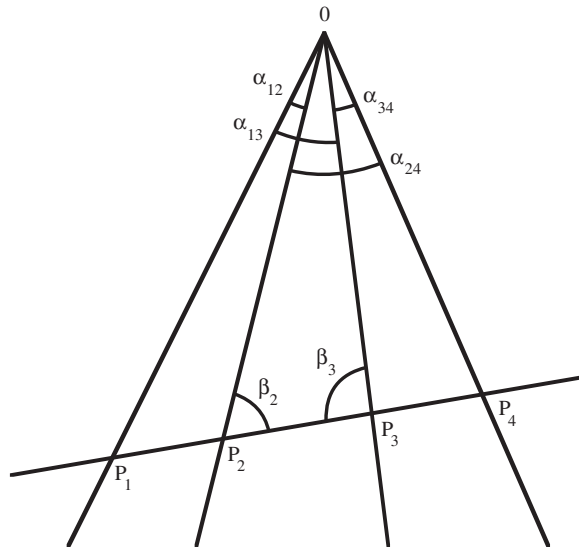


**FIGURE 18.2**

Geometry for calculation of the cross ratio of a pencil of lines. The figure shows the geometry required to calculate the cross ratio of a pencil of lines, in terms of the angles between them.

$$\frac{x_2 - x_4}{\sin \alpha_{24}} = \frac{OP_4}{\sin \beta_2} \quad (18.15)$$

$$\frac{x_2 - x_1}{\sin \alpha_{12}} = \frac{OP_1}{\sin \beta_2} \quad (18.16)$$

$$\frac{x_3 - x_4}{\sin \alpha_{34}} = \frac{OP_4}{\sin \beta_3} \quad (18.17)$$

Substituting in the cross-ratio formula (Eq. (18.5)) and canceling the factors  $OP_1$ ,  $OP_4$ ,  $\sin \beta_2$ , and  $\sin \beta_3$  now gives:

$$C(P_1, P_2, P_3, P_4) = \frac{\sin \alpha_{13} \sin \alpha_{24}}{\sin \alpha_{12} \sin \alpha_{34}} \quad (18.18)$$

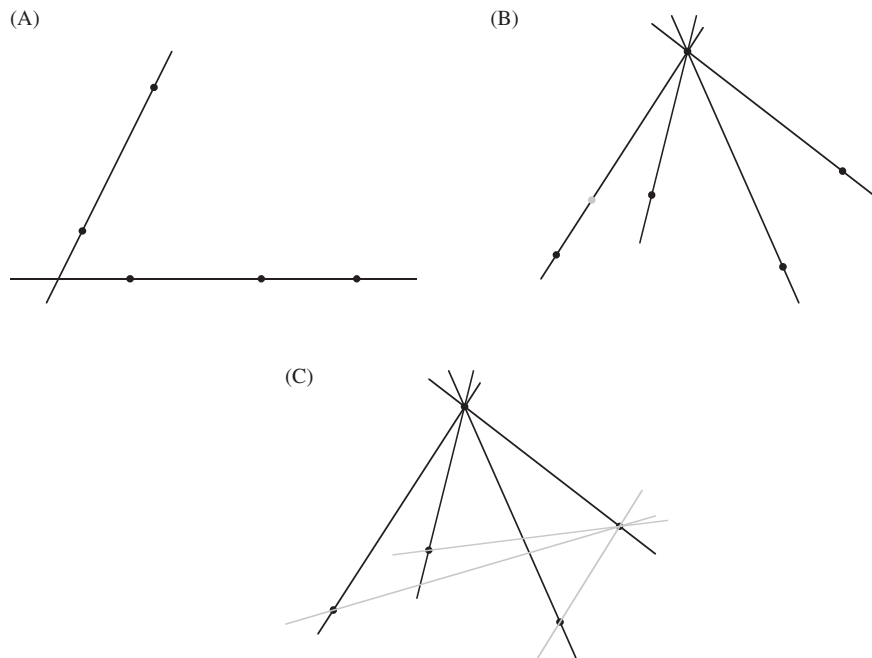
Thus, the cross ratio depends only on the angles of the pencil of lines. It is interesting that appropriate juxtaposition of the sines of the angles gives the final formula invariance under perspective projection: Using the angles themselves would not give the desired degree of mathematical invariance. Indeed, we can immediately see one reason for this: Inversion of the direction of any line must leave the situation unchanged; so, the formula must be tolerant to adding  $\pi$  to each of the two angles linking the line; this could not be achieved if the angles appeared without suitable trigonometric functions.

We can extend this concept to four concurrent planes since the concurrent lines can be projected into four concurrent planes once a separate axis for the concurrency has been defined. As there are infinitely many such axes, there are infinitely many ways in which sets of planes can be chosen. Thus, the original simple result on collinear points can be extended to a much more general case.

Finally, note that we started by trying to generalize the case of four collinear points, but what we achieved was first to find a dual situation in which points become lines also described by a cross ratio and then to find an extension in which planes are described by a cross ratio. We now return to the case of four collinear points and see how we can extend it in other ways.

## 18.3 INVARIANTS FOR NONCOLLINEAR POINTS

First, imagine that not all the points are collinear: Specifically let us assume that one point is not in the line of the other three. If this is the case, then there is not enough information to calculate a cross ratio. However, if a further coplanar point is available, we can draw an imaginary line between the noncollinear points to intersect their common line in a unique point, which will then permit a cross ratio to be computed (Fig. 18.3A). Nevertheless, this is some way from a general solution to the characterization of a set of noncollinear points. We might inquire how many point features in general position on a plane will be required to calculate an invariant. (Points on a plane which are chosen at random, and which are not

**FIGURE 18.3**

Calculation of invariants for a set of noncollinear points. (A) Shows how the addition of a fifth point to a set of four points, one of which is not collinear with the rest, permits the cross ratio to be calculated. (B) Shows how the calculation can be extended to any set of noncollinear points; also shown is an additional (gray) point which a single cross ratio fails to distinguish from other points on the same line. (C) Shows how any failure to identify a point uniquely can be overcome by calculating the cross ratio of a second pencil generated from the five original points.

collinear or in any special pattern such as a regular polygon, are described as being *in general position*.) In fact, the answer is five, since the fact that we can form a cross ratio from the angles between four lines immediately means that forming a pencil of four lines from five points defines a cross-ratio invariant (Fig. 18.3B).

While the value of this cross ratio provides a necessary condition for a match between two sets of five general coplanar points, it could be a fortuitous match, as the condition depends only on the relative directions between the various points and the reference point, i.e., any of the nonreference points is only defined to the extent that it lies on a given line. Clearly, two cross ratios formed by taking two reference points will define the directions of all the remaining points uniquely (Fig. 18.3C).

We can now summarize the general result, which stipulates that for five general coplanar points, no three of which are collinear, and two different cross ratios

are required to characterize the shape. These cross ratios correspond to taking in turn two separate points and producing pencils of lines passing through them and (in each case) the remaining four points (Fig. 18.3C). While it might appear that at least five cross ratios result from this sort of procedure, there are only two functionally independent cross ratios—essentially because the position of any point is defined once its direction relative to two other points is known.

Next, we consider the problem of finding the ground plane in practical situations—especially that of egomotion including vehicle guidance (Fig. 18.4). Here, a set of four collinear points can be observed from one frame to the next. If they are on a single plane, then the cross ratio will remain constant, but if one is elevated above the ground plane (as, e.g., a bridge or another vehicle), then the cross ratio will vary over time. Taking a larger number of points, it should clearly be

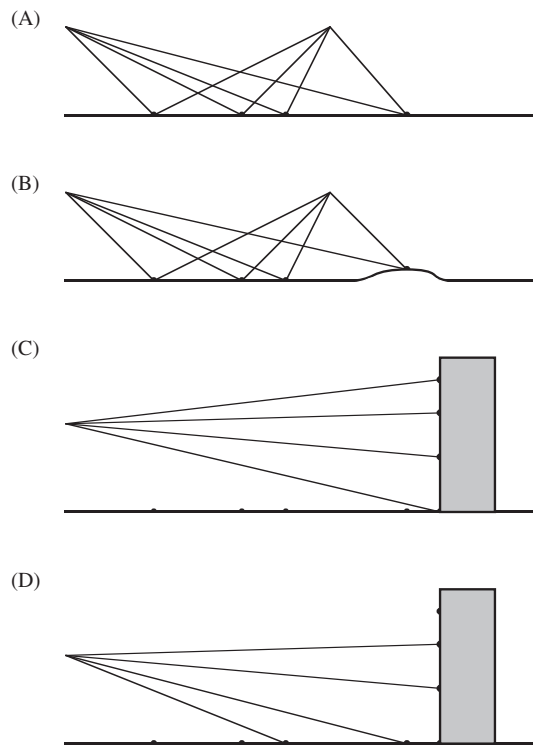


**FIGURE 18.4**

Use of cross ratio for egomotion guidance. (A) Shows how the cross ratio for a set of four collinear points can be tracked to confirm that the points are collinear: This suggests that they lie on the ground plane. (B) Shows a case where the cross ratio will not be constant. (C) Shows a case where the cross ratio is constant, though they actually lie on a plane which is not the ground plane. (D) Shows a case where all four points lie on planes; yet, the cross ratio will not be constant.



possible to deduce by a process of elimination which are on the ground plane and which are not (though the amount of noise and clutter will determine the computational complexity of the task): Note that all this is possible without any calibration of the camera, this being perhaps the main value of concentrating attention on projective invariants. Note that there is a potential problem regarding irrelevant planes, such as the vertical faces of buildings. The cross-ratio test is so resistant to viewpoint and pose that it merely ascertains whether the points being tested are coplanar. It is only by using a sufficiently large number of independent sets of points that one plane can be discriminated from another (for simplicity, we ignore here any subsequent stages of pose analysis that might be carried out).

### 18.3.1 FURTHER REMARKS ABOUT THE 5-POINT CONFIGURATION

The above description outlines the principles for solving the 5-point invariance problem but does not show clearly the conditions under which it is guaranteed to operate properly. In fact, these are straightforward to demonstrate. First, the cross ratio can be expressed in terms of the sines of the angles  $\alpha_{13}$ ,  $\alpha_{24}$ ,  $\alpha_{12}$ ,  $\alpha_{34}$ . Next, these can be reexpressed in terms of areas of relevant triangles, using equations typified by the following to express area:

$$\Delta_{513} = \frac{1}{2} a_{51} a_{53} \sin \alpha_{13} \quad (18.19)$$

Finally, the area can be reexpressed in terms of the point coordinates in the following way:

$$\Delta_{513} = \frac{1}{2} \begin{vmatrix} p_{5x} & p_{1x} & p_{3x} \\ p_{5y} & p_{1y} & p_{3y} \\ p_{5z} & p_{1z} & p_{3z} \end{vmatrix} = \frac{1}{2} |\mathbf{p}_5 \mathbf{p}_1 \mathbf{p}_3| \quad (18.20)$$

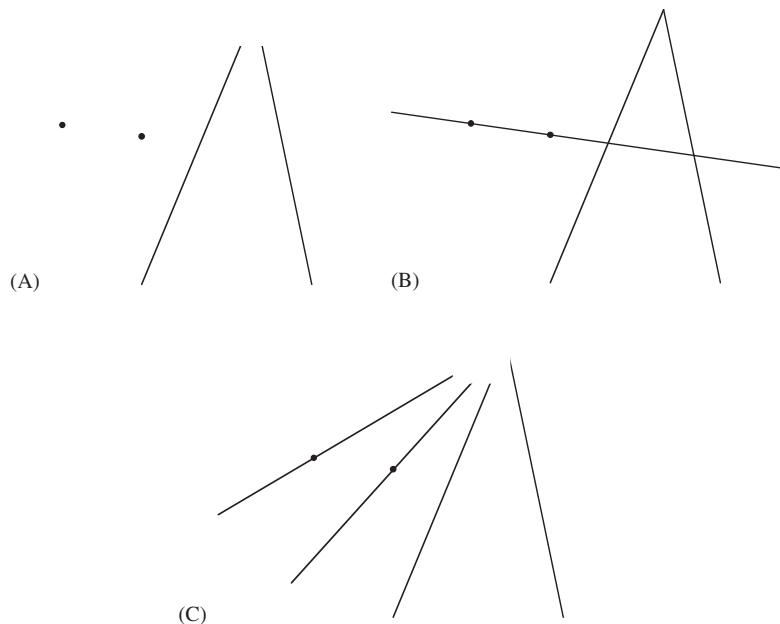
Using this notation, a suitable final pair of cross-ratio invariants for the configuration of five points may be written as follows:

$$C_a = \frac{\Delta_{513} \Delta_{524}}{\Delta_{512} \Delta_{534}} \quad (18.21)$$

$$C_b = \frac{\Delta_{124} \Delta_{135}}{\Delta_{123} \Delta_{145}} \quad (18.22)$$

While three more such equations may be written down, these will not be independent of the other two and will not carry any further useful information.

Note that a determinant will go to zero or infinity if the three points it relates to are collinear, corresponding to the situation when the area of the triangle is zero. Clearly, when this happens, any cross ratio containing this determinant will no longer be able to pass on any useful information. On the other hand, there is actually no further information to pass on, as this now constitutes a special case that is describable by a single cross ratio: thus we have reverted to the situation shown in Fig. 18.3A.

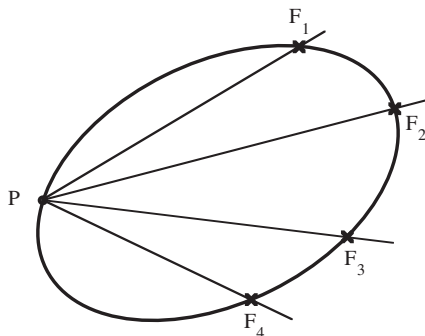
**FIGURE 18.5**

Cross ratio for two lines and two points. (A) Basic configuration. (B) How the line joining the two points introduces four collinear points to which a cross ratio may be applied. (C) How joining the two points to the junction of the two lines creates a pencil of four lines to which a cross ratio may be applied.

Finally, Fig. 18.3 misses out one further interesting case: This is the situation of two points and two lines (Fig. 18.5). Constructing a line joining the two points and producing it until it meets the two lines, we then have four points on a single line; thus, the configuration is characterized by a single cross ratio. Notice also that the two lines can be extended until they join, and further lines can be constructed from the join to meet the two points: This gives a pencil of lines characterized by a single cross ratio (Fig. 18.5C); the latter must have the same value as that computed for the four collinear points.

## 18.4 INVARIANTS FOR POINTS ON CONICS

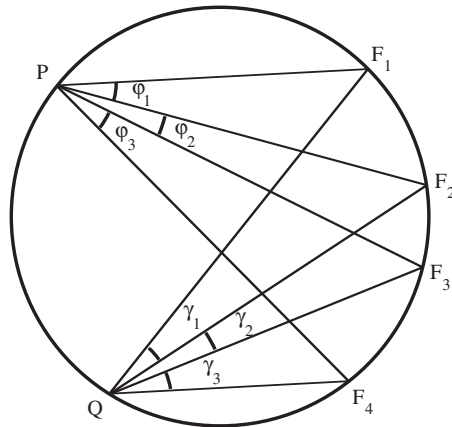
These discussions clearly help to build up an understanding of how geometric invariants can be designed to cope with sets of points, lines, and planes in 3-D. Significantly, more difficult is the case of curved lines and surfaces, though much headway has now been made with regard to the understanding of conics and certain other surfaces (see Mundy and Zisserman, 1992a). It will not be possible to examine all such cases in depth here. However, it will be useful to consider conic sections and particularly ellipses in more detail.

**FIGURE 18.6**

Definition of a conic using a cross ratio. Here,  $P$  is constrained to move so that the cross ratio of the pencil from  $P$  to  $F_1, F_2, F_3, F_4$  remains constant. By Chasles' theorem,  $P$  traces out a conic curve.

First, we consider Chasles' theorem, which dates from the 19th century. (The history of projective geometry is quite rich and was initially carried out totally independently of the requirements of machine vision.) Suppose we have four fixed coplanar points  $F_1, F_2, F_3, F_4$  on a conic section curve and one variable point  $P$  in the same plane (Fig. 18.6). Then, the four lines joining  $P$  to the fixed points form a pencil whose cross ratio will in general vary with the position of  $P$ . Chasles' theorem states that if  $P$  now moves so as to keep the cross-ratio constant, then  $P$  will trace out a conic section. This clearly provides a means of checking whether a set of points lies on a planar curve such as an ellipse. Note the close analogy with the problem of ground plane detection already mentioned. Again, the amount of computation could become excessive if there were a lot of noise or clutter in the image. When the image contains  $N$  boundary features which need to be checked out, the problem complexity is intrinsically  $O(N^5)$ , since there are  $O(N^4)$  ways of selecting the first four points, and for each such selection,  $N - 4$  points must be examined to determine whether they lie on the same conic. However, choice of suitable heuristics would be expected to limit the computation. Note the problem of ensuring that the first four points are tested in the same order around the ellipse, which is liable to be tedious (1) for point features, and (2) for disconnected boundary features.

While Chasles' theorem gives an excellent opportunity to use invariants to locate conics in images, it is not at all discriminatory in this. The theorem applies to a general conic: Hence, it does not immediately permit circles, ellipses, parabolas, or hyperbolas to be distinguished, a fact that would sometimes be a distinct disadvantage. This is an example of a more general problem in pattern recognition system design—of deciding exactly how and in what sequence one object should be differentiated from another: Space will not permit this point to be considered further here.

**FIGURE 18.7**

Proof of Chasles' theorem. This diagram shows that the four points  $F_1, F_2, F_3, F_4$  subtend the same angles at  $P$  as they do at the fixed point  $Q$ . Thus, the cross ratio is the same for all points on the circle. This means that Chasles' theorem is valid for a circle.

Finally, we state without proof that conic section curves can all be transformed under perspective projection to other types of conic section, and thus into ellipses; subsequently, they can be transformed into circles. Thus, any conic section curve can be transformed projectively into a circle, while the inverse transformation can transform it back again (Mundy and Zisserman, 1992b). This means that simple properties of the circle can frequently be generalized to ellipses or other conic sections. In this context, points to bear in mind are that, after perspective projection, lines intersecting curves do so in the same number of points, and thus, tangents transform into tangents, chords into chords, 3-point contact (in the case of nonconic curves) remains 3-point contact, and so on. Returning to Chasles' theorem, a simple proof in the case of circles will automatically generalize to more complex conic section curves.

In response to this assertion, we can in fact derive Chasles' theorem almost trivially for a circle. Appealing to Fig. 18.7, we see that the angles  $\varphi_1, \varphi_2, \varphi_3$  are equal to the respective angles  $\gamma_1, \gamma_2, \gamma_3$  (angles in the same segment of a circle). Thus, the pencils  $PF_1, PF_2, PF_3, PF_4$  and  $QF_1, QF_2, QF_3, QF_4$  have equal angles, their *relative* directions being superposable. This means that they will have the same cross ratio, defined by Eq. (18.18). Hence, the cross ratio of the pencil will remain constant as  $P$  traces out the circle. As stated above, the property will automatically generalize to any other conic.

## 18.5 DIFFERENTIAL AND SEMIDIFFERENTIAL INVARIANTS

There have been many attempts to characterize continuous curves by invariants. The obvious way forward is to represent points on a curve in terms of local curve

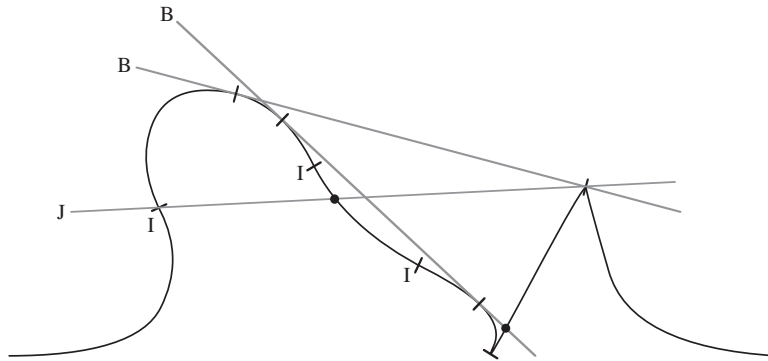


**FIGURE 18.8**

Means for finding distinguished points on a curve. The two bitangents contact the curve in a total of four bitangent points. Three points of inflection *I* provide another three distinguished points. A cusp and a corner provide a further two distinguished points (the latter also being a bitangent point). The line marked *J* contributes a further distinguished point on the curve, as does one of the bitangents: These are marked as large dots rather than as short lines.

derivatives: If a sufficient number of these can be obtained, invariants can be formed and computed. However, the noise (including digitization noise) that always exists on curves limits the accuracy of higher derivatives, and as a result it is difficult to form useful invariants in this way. In general, the second derivative of the curve function is the highest that can normally be used, and this corresponds to curvature, which is only an invariant for Euclidean transformations (translation and rotation without change of scale).

As a result of this problem, semidifferential invariants are often used instead of differential invariants. They involve considering only a few “distinguished” points on curves, and using these to generate invariants. The most common distinguished points to be used in this way are (Fig. 18.8):

1. Points of inflection,
2. Sharp corners on curves,
3. Cusps on curves (corners where the bounding tangents are coincident),
4. Bitangent points (points of contact of a line that touches the curve twice), and
5. Other points whose locations can be derived from existing distinguished points by geometric constructions.

Tangent points are unlikely to be suitable and hence are not included in this list, as a smooth curve will have tangents along its entire length. This is because they are characterized merely by 2-point contact between a limiting chord and the curve. However, a point of inflection represents a 3-point contact, and this means that it will be reasonably well localized, and its tangent will have a well-defined direction. On the other hand, bitangent points will be even more accurately

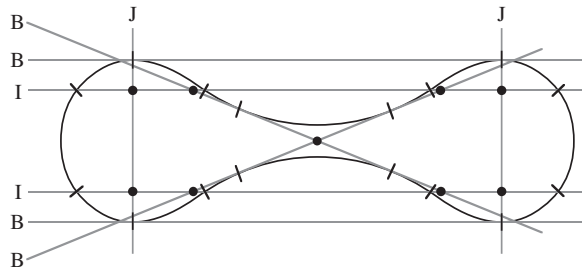


**FIGURE 18.9**

Means for finding direct and indirect distinguished points for an object. The four lines marked B are bitangents which contribute six bitangent points: Two of the bitangents contact the object on opposite sides of its boundary. The two lines marked I arise from points of inflection. The two lines marked J are joins of bitangent points. The nine large dots are indirect distinguished points, which do not lie on the object boundary. Clearly, a good many more indirect distinguished points could be generated, though not all would have accurately defined locations.

represented, as the tangent direction will be accurately defined by two well-separated points on the curve (Fig. 18.8): Nevertheless, bitangent points will still incur some longitudinal errors.

Bitangents can be of several sorts: In particular, they can contact the same shape on the same side; they can also cross the body and contact it on both sides. This latter case is more complex and is therefore sometimes discounted in machine vision applications. Nevertheless, it provides a means of finding further invariant reference points on an object. Note that this clearly happens directly, in that the bitangent points are already distinguished points: It also happens indirectly, as the bitangent may cross other reference lines—thereby defining further distinguished points. Fig. 18.9 shows several cases of direct and indirect distinguished points, the most accurate of which arise from bitangents, while slightly less accurate ones arise from points of inflection.

Once enough distinguished points and reference lines between them have been found, cross-ratio invariants may be obtained (1) from the incidence of distinguished points lying along suitable reference lines and (2) from pencils of lines drawn from distinguished points to line crossings or to other distinguished points.

A remark is needed to confirm that points of inflection can act as suitable distinguished points which are invariant under perspective transformations. Starting from the premise that perspective transformations preserve straight lines and points arising from crossings between curves and lines, we note that a chord which crosses a curve three times will also cross it three times under perspective projection: This will still apply even when the three crossing points merge into 3-point contact. (Three-point contact is distinguishable from 2-point contact in that the tangent crosses the curve at the point of contact.) Hence, points of inflection *are* suitable distinguished points and *are* perspective invariant.

This treatment has only dealt with planar curves and has not covered spatial nonplanar curves. The latter is a significantly more difficult area, as concepts such as bitangents and points of inflection have to be assigned new meaning in this more general domain: It is a subject we shall not be able to broach here.

## 18.6 SYMMETRIC CROSS-RATIO FUNCTIONS

When applying a cross ratio to a set of points on a line, it frequently happens that the order of the points on the line is known. For example, this will almost certainly be the case if feature detection of an image is carried out in a forward raster scan. Hence, the only confusion in the ordering will be the direction in which the line has been traversed. However, the cross ratio is independent of the end from which the line is scanned, since  $C(P_1, P_2, P_3, P_4) = C(P_4, P_3, P_2, P_1)$ . Nevertheless, there are situations in which the ordering of the cross-ratio features will not be known with certainty. This may occur for the situations shown in Figs. 18.3 and 18.5, where the features themselves do not all lie on a single line, or where the features are angles, or where the points lie on a conic whose equation is as yet unknown. In such circumstances, it will be useful to have an invariant which takes in all possible orders of the features.

To derive such an invariant, note first that if there is a confusion in the ordering of the points such that the value could be either  $\kappa$  or  $(1 - \kappa)$ , then we could apply the function  $f(\kappa) = \kappa(1 - \kappa)$ , which has the property  $f(\kappa) = f(1 - \kappa)$ , and this will solve the problem. Alternatively, if there is confusion between  $\kappa$  and  $1/\kappa$ , then we could apply the function  $g(\kappa) = \kappa + 1/\kappa$ , which has the property  $g(\kappa) = g(1/\kappa)$ , and again, this will solve the problem.

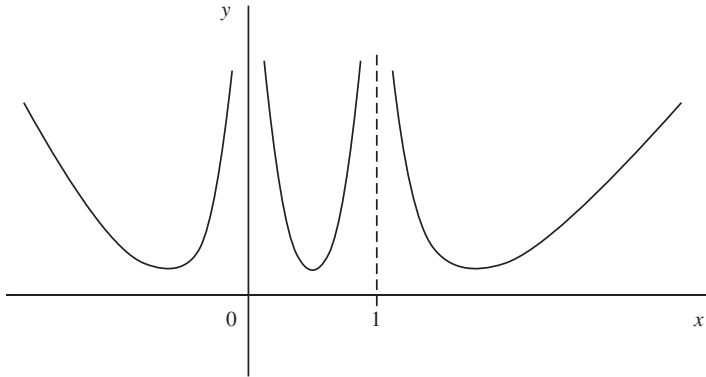
However, if there is potential confusion between the values  $\kappa$ ,  $(1 - \kappa)$ , and  $1/\kappa$ , the situation becomes more complicated. It is difficult to write down any obvious function that satisfies the double condition  $h(\kappa) = h(1 - \kappa) = h(1/\kappa)$ , though we may have soundly based intuition that it will involve symmetric functions such as  $f(\kappa)$  and  $g(\kappa)$ . In fact, the simplest answer seems to be:

$$j(\kappa) = \frac{(1 - \kappa + \kappa^2)^3}{\kappa^2(1 - \kappa)^2} \quad (18.23)$$

which obeys the symmetry idea as it can be reexpressed in the two forms:

$$j(\kappa) = \frac{[(1 - \kappa(1 - \kappa))]^3}{[\kappa(1 - \kappa)]^2} = \frac{(\kappa + 1/\kappa - 1)^3}{\kappa + 1/\kappa - 2} \quad (18.24)$$

Fortunately, we need go no further in our quest to obey the six conditions required to recognize all six of the cross-ratio values  $\kappa$ ,  $(1 - \kappa)$ ,  $1/\kappa$ ,  $1/(1 - \kappa)$ ,  $(\kappa - 1)/\kappa$ , and  $\kappa/(\kappa - 1)$ . The reason is that they are all deducible from each other by further applications of the initial negation and inversion rules. (The ultimate reason for this is that the operations to transform the function from one to another

**FIGURE 18.10**

Symmetric cross-ratio function. This is the function defined by Eq. (18.23).

of the six forms form a group of order six, which is generated from the negation and inversion transforms.)

While this is a powerful result, it does not come without loss. The reason is that there is now a sixfold ambiguity inherent in the solution so that once we have shown that the set of points satisfies the symmetric cross-ratio function, we still have to make tests to determine which of the six possibilities is the correct one. This is reflected by the complexity of the  $j$ -function, which contains a sixth degree polynomial and for every value of  $j$ , there are six possible values of  $\kappa$  (Fig. 18.10).

The situation can be described by saying that the function  $j(\kappa)$  is not “complete,” in the sense that this function alone is insufficient to recognize the set of features unambiguously. To underline this, observe that the original cross ratio *is* complete: once the value of  $\kappa$  is known, we can uniquely determine the position of one of the points from the other three points. This is obvious from the graph of  $\kappa$  as a function of  $x$  (where  $x = x_{34}$  gives the position of the fourth point), which, according to Eq. (18.25), is a hyperbola. (In projective geometry, it is well known that there are three degrees of freedom on a line: the positions of three points on a line are not predictable from other views of the three points, without further information on the viewpoint.)

$$\kappa = \frac{x_{31}x_{24}}{x_{21}x_{34}} = \frac{x_{31}(x_{23} + x)}{x_{21}x} = \frac{x_{31}x_{23}}{x_{21}} \left( \frac{1}{x} + \frac{1}{x_{23}} \right) \quad (18.25)$$

## 18.7 VANISHING POINT DETECTION

In this section, we consider how VPs can be detected. It is usual to carry this out in two stages: First, we locate all the straight lines in the image; next, we find



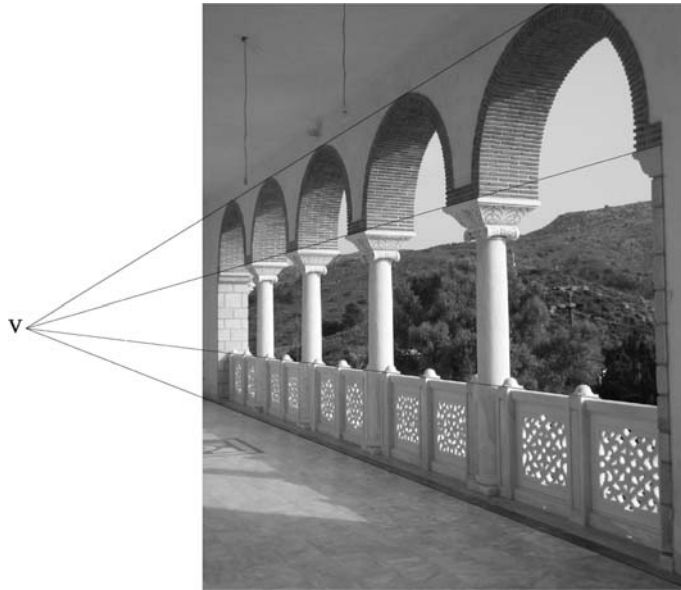


**FIGURE 18.11**

Position of the vanishing point. In this figure, parallel lines on the arches appear to converge to a vanishing point  $V$  outside the image. In general, vanishing points can lie at any distance and may even be situated at infinity.

which of the lines pass through common points—the latter being interpreted as VPs. Finding the lines using the Hough transform should be straightforward, though texture edges will sometimes prevent lines from being located accurately and consistently. Basically, locating the VPs requires a second Hough transform in which whole lines are accumulated in parameter space, leading to well-defined peaks (the VPs) where multiple lines overlap. In practice, the lines of votes will have to be extended to cover all possible VP locations. This procedure is adequate when the VPs appear within the original image space, but it often happens that they will be outside the original image (Fig. 18.11) and may even be situated at infinity. This means that a normal image-like parameter space cannot be used successfully, even if it is extended beyond the original image space. Another problem is that for distant VPs, the peaks in parameter space will be spread out over a considerable distance; so, detection sensitivity will be poor and accuracy of location will be low.

Fortunately, Magee and Aggarwal (1984) found an improved representation for locating VPs. They constructed a unit sphere  $G$ , called a Gaussian sphere, around the center of projection of the camera, and used  $G$  instead of an extended image plane as a parameter space. In this representation (Fig. 18.12), VPs appear at finite distances even in cases where they would otherwise appear to be at infinity. For this method to work, there has to be a one-to-one correspondence between

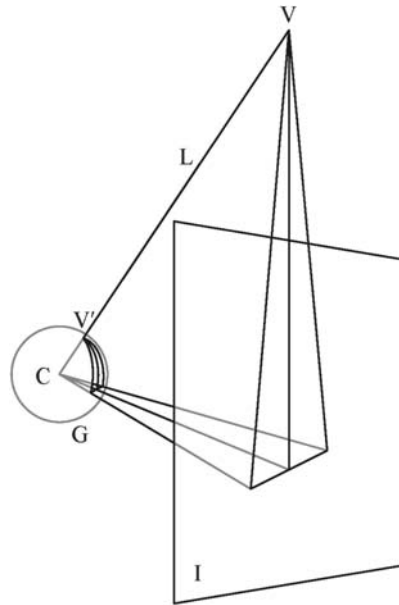


**FIGURE 18.12**

Detection of vanishing points using the Gaussian sphere. Parallel lines in space lead to converging lines in the image  $I$ . While the vanishing point  $V$  is here well above the image, it is easily located by projecting the lines onto the Gaussian sphere  $G$ . As discussed in the text,  $G$  is commonly used as a parameter space for accumulating vanishing point votes.  $C$  is the center of projection of the camera lens.

points in the two representations, and this is clearly valid (note that the back half of the Gaussian sphere is not used). However, the Gaussian sphere representation is not without problems: In particular, many irrelevant votes will be cast from lines that are not parallel in real 3-D space (generally only a small subset of the lines in the image will pass through VPs). To solve this problem, *pairs* of lines are considered in turn, and their crossing points are only accumulated as votes if the lines of each pair are judged likely to originate from parallel lines in 3-D space (e.g., they should have compatible gradients in the image). This procedure drastically limits both the number of votes recorded in parameter space and the number of irrelevant peaks. Nevertheless, the overall cost is still substantial, being proportional to the number of pairs of lines. Thus, if there are  $N$  lines, the number of pairs is  ${}^N C_2 = N(N-1)$ , so the result is  $O(N^2)$ .

The above procedure is important as it provides a highly reliable means for performing the search for VPs, and for largely discriminating against isolated lines and image clutter. Note that for a moving robot or other system, the correspondences between the VPs seen in successive images will lead to considerably greater certainty in the interpretation of each image.

## 18.8 MORE ON VANISHING POINTS

One advantage of the cross ratio is that it can turn up in many situations and on each occasion provide yet another neat result. A further example is when a road or pavement has flagstones whose boundaries are well demarcated and easily measurable. They can then be used to estimate the position of the VP on the ground plane. Imagine viewing the flagstones obliquely from above, with the camera or the eyes aligned horizontally (e.g., as for Fig. 23.12A). Then, we have the geometry of Fig. 18.13 where the points  $O$ ,  $H_1$ ,  $H_2$  lie on the ground plane while  $O$ ,  $V_1$ ,  $V_2$ ,  $V_3$  are in the image plane. (Notice that slightly oblique measurement of the flagstones, along a line that is not parallel to the sides of the flagstones, still permits the same cross ratio value to be obtained, as the same angular factor applies to all distances along the line.)

If we regard  $C$  as a center of projection, the cross ratio formed from the points  $O$ ,  $V_1$ ,  $V_2$ ,  $V_3$  must have the same value as that formed from the points

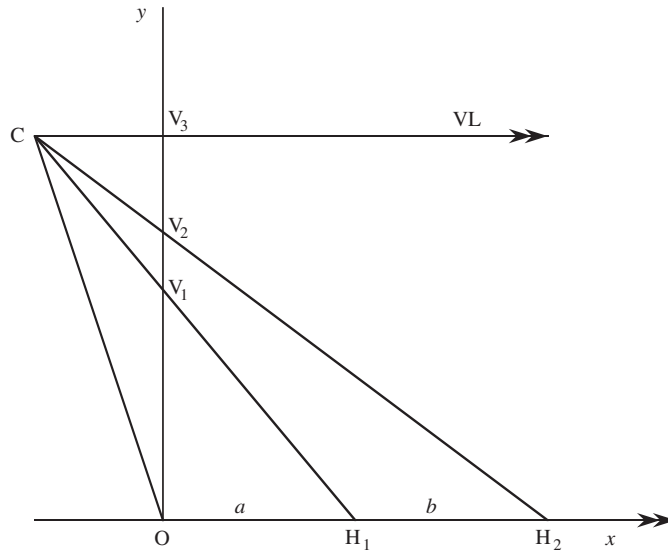


**FIGURE 18.13**

Geometry for finding the vanishing line from a known pair of spacings.  $C$  is the center of projection.  $VL$  is the vanishing line direction, which is parallel to the ground plane  $OH_1H_2$ . Although the camera plane  $OV_1V_2V_3$  is drawn perpendicular to the ground plane, this is not necessary for successful operation of the algorithm (see text).

O,  $H_1$ ,  $H_2$ , and infinity in the horizontal direction. Supposing that  $OH_1$  and  $H_1H_2$  have known lengths  $a$  and  $b$ , equating the cross-ratio values gives:

$$\frac{y_1(y_3 - y_2)}{y_2(y_3 - y_1)} = \frac{x_1}{x_2} = \frac{a}{a + b} \quad (18.26)$$

(Note that, in the case of Fig. 18.13, the  $y$  values are measured from O rather than from  $V_3$ .) This allows us to estimate  $y_3$ :

$$(a + b)(y_1y_3 - y_1y_2) = ay_2y_3 - ay_2y_1 \quad (18.27)$$

$$\therefore y_3(ay_1 + by_1 - ay_2) = ay_1y_2 + by_1y_2 - ay_1y_2 \quad (18.28)$$

$$\therefore y_3 = by_1y_2 / (ay_1 + by_1 - ay_2) \quad (18.29)$$

If  $a = b$  (as is likely to be the case for flagstones):

$$y_3 = \frac{y_1y_2}{2y_1 - y_2} \quad (18.30)$$

Notice that this proof does not actually assume that points  $V_1$ ,  $V_2$ ,  $V_3$  are vertically above the origin, or that line  $OH_1H_2$  is horizontal, just that these points lie along two coplanar straight lines, and that C is in the same plane. Also, note that it is only the ratio of  $a$  to  $b$ , not their absolute values, that is relevant in this calculation.

Having found  $y_3$ , we have calculated the direction of the VP, whether or not the ground plane on which it lies is actually horizontal, and whether or not the camera axis is horizontal.

Finally, notice that Eq. (18.30) can be rewritten in the simpler form:

$$\frac{1}{y_3} = \frac{2}{y_2} - \frac{1}{y_1} \quad (18.31)$$

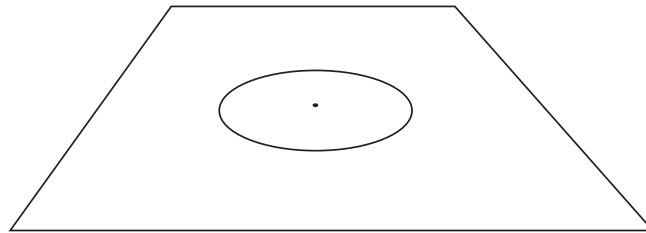
The inverse factors give some intuition into the processes involved—not least considering the inverse relation  $Z = Hf/y$  between distance along the ground plane and image distance from the vanishing line; and similarly, the inverse relation between depth and disparity shown in Eq. (16.4).

---

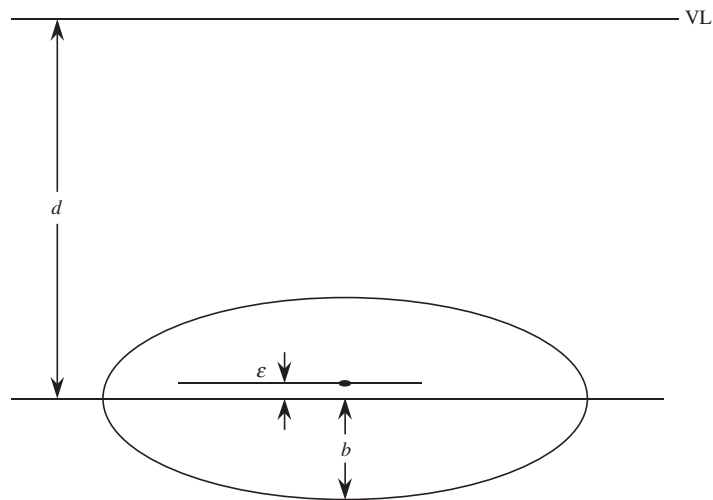
## 18.9 APPARENT CENTERS OF CIRCLES AND ELLIPSES

It is well known that circles and ellipses project into ellipses (or occasionally into circles). This statement is widely applicable and is valid for orthographic projection, scaled orthographic projection, weak perspective projection, and full perspective projection.

Another factor that can easily be overlooked is what happens to the center of the circle or ellipse under these transformations. It turns out that the ellipse (or circle) center does not project into the ellipse (or circle) center under full perspective projection: There will in general be a small offset (Fig. 18.14). The fact that

**FIGURE 18.14**

Projected position of a circle center under full perspective projection. Note that the projected center is not at the center of the ellipse in the image plane.

**FIGURE 18.15**

Geometry for calculating the offset of the circle center. The projected center of the circle is shown as the elongated dot, and the center of the ellipse in the image plane is a distance  $d$  below the vanishing line VL.

this happens may perhaps suggest that ellipses will be slightly distorted under projection. In fact, there is *no* such distortion, and the source of the shift in the center is merely that full perspective projection does not preserve length ratios—and in particular, mid-points do not remain mid-points.

If the position of the vanishing line of the plane can be identified in the image, the calculation of the offset for a circle is quite simple using the theory of [Section 18.8](#), which applies as the center of a circle bisects its diameter ([Fig. 18.15](#)). First, let  $\varepsilon$  be the shift in the center, let  $d$  be the distance of the

center of the ellipse from the vanishing line, and  $b$  be the length of the semiminor axis. Next, identify  $b + \varepsilon$  with  $y_1$ ,  $2b$  with  $y_2$ , and  $b + d$  with  $y_3$ . Finally, substituting  $y_1$ ,  $y_2$ , and  $y_3$  in Eq. (18.30), we then obtain the result:

$$\varepsilon = b^2/d \quad (18.32)$$

Notice that, unlike the situation in Section 18.8, we are here assuming that  $y_3$  is known and we are using its value to calculate  $y_1$  and hence  $\varepsilon$ .

If the vanishing line is not known, but the orientation of the plane on which the circle lies is known, and also the orientation of the image plane, then the vanishing line can be deduced, and the calculation can again proceed as above. However, this approach assumes that the camera has been calibrated (see Chapter 19: Image Transformations and Camera Calibration).

The problem of center determination when an ellipse is projected into an ellipse is a little harder to solve: Not only is the longitudinal position of the center unknown, but so is the lateral position. Nevertheless, the same basic projective ideas apply. Specifically, let us consider a pair of parallel tangents to the ellipse, which in the image become a pair of lines  $\lambda_1$ ,  $\lambda_2$  meeting on the vanishing line (Fig. 18.16). As the chord joining the contact points of the tangents passes through the center of the original ellipse, and as this property is projectively invariant; so, the projected center must lie on the chord joining the contact points of the line-pair  $\lambda_1$ ,  $\lambda_2$ . As the same applies for all pairs of parallel tangents to the original ellipse, we can straightforwardly locate the projected center of the ellipse in the image plane. (Students who are familiar with

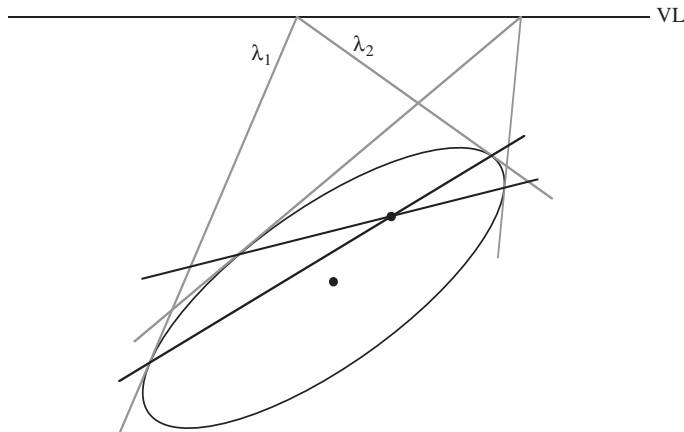


**FIGURE 18.16**

Construction for calculating the offsets for a projected ellipse. The two lines  $\lambda_1$ ,  $\lambda_2$  from a point on the vanishing line VL touch the ellipse, and the joins of the points of contact for all such line pairs pass through the projected center. (The figure shows just two chords of contact.)

projective geometry will be able to relate this to the “pole–polar” construction for a conic: In this case, the polar line is the vanishing line and its pole is the projected center. In general, the pole is not at the center of an ellipse and will not be so unless the polar is at infinite distance. Indeed, from this point of view, Eq. (18.31) can be understood in terms of “harmonic ranges,”  $y_2$  being the “harmonic mean” of  $y_1$  and  $y_3$ .) For an alternative, numerical analysis of the situation, see Zhang and Wei (2003).

Both the circle result and the ellipse result are important in cases of inspection of mechanical parts, where accurate results of center positions have to be made irrespective of any perspective distortions that may arise. Indeed, circles can also be used for camera calibration purposes, and again high accuracy is required (Heikkilä, 2000).

---

## 18.10 PERSPECTIVE EFFECTS IN ART AND PHOTOGRAPHY

An artist is painting a picture somewhere on the countryside. Every now and again, he looks up from his easel and surveys the scene; then, he turns back to his picture and adds a few more touches. He has chosen his location carefully and has set his easel at the right angle for best effect. We will suppose that he is not aiming to be impressionist but wishes to present the scene as he sees it. Although his painting is in 2-D, he is able to present all the information needed for others to perceive the scene in 3-D. However, there is a problem: The picture needs to be viewed from precisely the right angle and distance which must correspond to the artist’s original viewpoint. Of course, the artist had to rotate his head and mentally rotate the scene between the moments that he viewed it and painted it (he had to do this because the canvas he was painting on was opaque: Other artists such as Canaletto have used camera obscura methods to overcome this difficulty). However, we can overcome the problem by temporarily assuming that the canvas is transparent, which significantly simplifies the geometry (Fig. 18.17).

Interestingly, from his viewpoint, the artist could have painted a whole range of pictures of the scene, with his easel set at different angles (Fig. 18.17). All these pictures would be very closely related to each other and in fact would be related by homographies. But each of them would have exactly one proper viewing position and orientation, and when each was viewed from its proper viewing position, exactly the same 3-D regenerative effect would be perceived by the viewer. Thus, the fact that a homography exists between the various views does not change the constraint that each version of a picture is best viewed from a single location.

However, there is a circumstance when this is no longer true, that is, when the scene contains a flat (2-D) surface  $F$  which is then to be presented in 2-D. Immediately, we have a homography between the original scene and the canvas, and we also have homographies with all the possible rotated versions of the

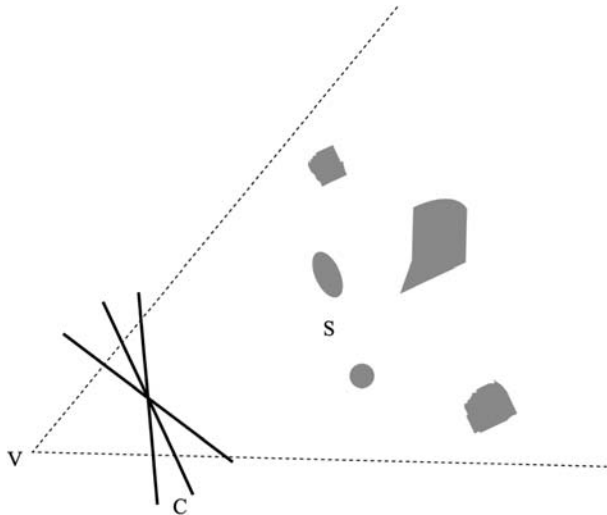


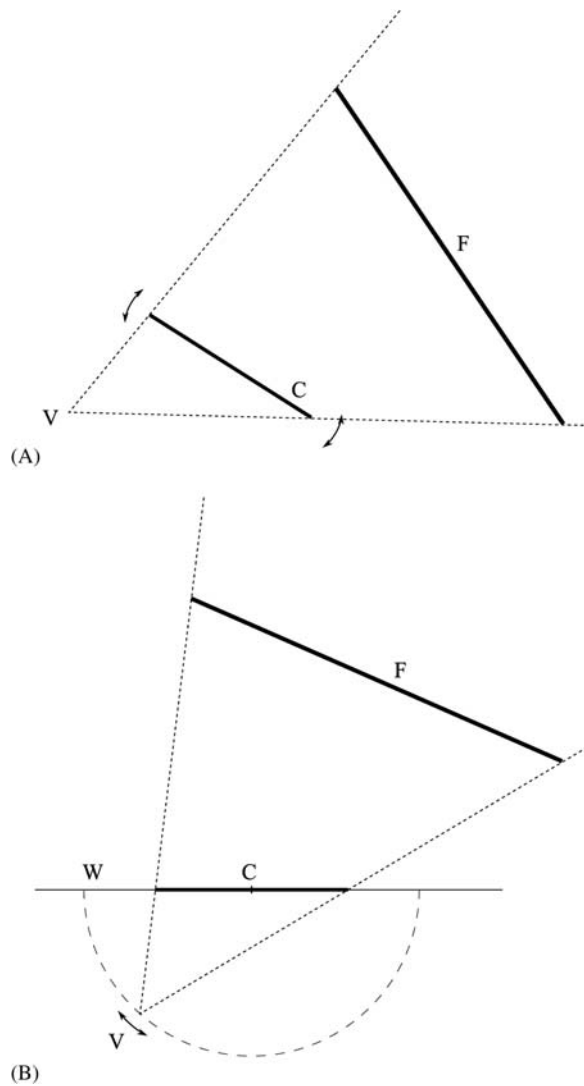
**FIGURE 18.17**

Effective viewpoint of artist painting a picture. The artist views the scene *S* from viewpoint *V* and paints what he sees on the canvas at *C*. The picture painted at *C* could be one of many depending on the orientation of the canvas.

canvas. But what of the viewing positions? To understand the situation properly, we need to think of the possible viewing points relative to the frame of reference of the canvas *C*, which we must now regard as fixed, e.g., on a gallery wall *W*. We can see that as the original canvas is rotated, so the ideal viewing point relative to its location on the gallery wall will rotate, albeit remaining at the distance corresponding to the distance of the artist's eye from the canvas. In fact, as one walks (along a circle) around the painting in the gallery, all the possible pictures that the artist might have painted from his original position unfold before us (Fig. 18.18). They all embody valid perspective distortions and thus, all would appear entirely natural. Note that a circular path is appropriate because it corresponds to the (constant) overall angle of the artist's view (angles in the same segment of a circle are equal).

But what of the case not of the flat wall of a house but of a face? In fact, substantial parts of the face approximate to a flat 2-D surface, e.g., the forehead, eyes, cheeks, mouth, and chin. Considering them alone, a considerable range of viewing points would be acceptable. Then, there is the human propensity for focusing on the eyes and largely ignoring the rest of the face. If this is done, acceptable views will be obtained by viewing the painting from many directions. Indeed when focusing on the eyes and ignoring the rest, it seems entirely understandable why people would report after visiting a stately home and seeing a painting of the 17th Earl that his eyes "followed them around the room."



**FIGURE 18.18**

Viewing a painted picture. Process of (A) painting and (B) viewing a picture. As the orientation of the canvas changes in (A), so the proper viewing point  $V$  in (B) moves along the path of a circle. For a flat object  $F$ , the circular path sweeps out all possible pictures the artist might have painted, and all will be related by homographies (see text).

A further factor is involved in this analysis—the orientation of the face when the picture was painted. If the face was originally at an angle  $\alpha$ , then the eyes would appear a factor  $\cos \alpha$  closer together than in the head-on painting. However, if the canvas were rotated through an angle  $\beta$ , the eyes would be

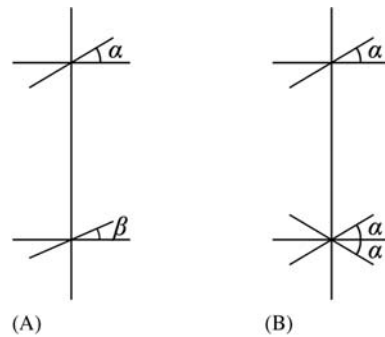


**FIGURE 18.19**

Effect of rotations relative to the viewing direction. In (A),  $\alpha$  represents the original orientation of the face, and  $\beta$  represents the orientation of the canvas. (B) Shows the situation both when  $\beta = \alpha$  and when  $\beta = -\alpha$ . In both instances, the two orientation effects cancel and the eyes appear to have their original separation.

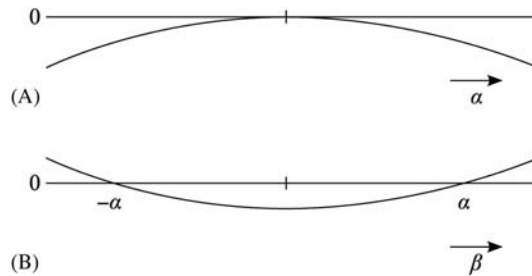


**FIGURE 18.20**

Effect of varying the viewing orientations. (A) Shows how the separation of the eyes becomes reduced as  $|\alpha|$  increases from zero. (B) Shows how the change in separation of the eyes for a fixed value of  $\alpha$  is first canceled out by increasing  $|\beta|$  from zero and then increased so that the change in separation becomes positive. The average magnitude of the change in separation can clearly be lower in (B) than in (A).

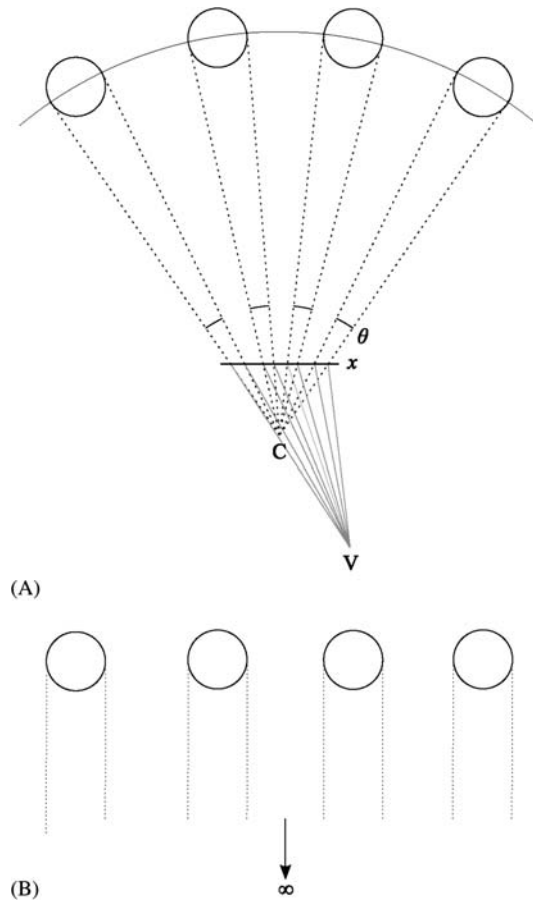
enlarged by a factor  $\sec \beta$ . Hence, there would be an overall magnification  $\cos \alpha / \cos \beta$ . Cancellation would occur when  $\beta = \alpha$ , which corresponds to the canvas being parallel to the face. However, cancellation would also occur when  $\beta = -\alpha$ , and this corresponds to the canvas and the face being rotated through equal and opposite angles  $\alpha$  relative to the final viewing direction (Fig. 18.19). Next, suppose that a certain amount of enlargement or diminution of the apparent distance between the eyes is acceptable (note especially that if one doesn't know the 17th Earl in the painting, some enlargement would be acceptable). The result is that the range of acceptable orientations of the final viewing direction will be increased, with the  $\beta$  distortion tending to cancel the  $\alpha$  distortion, the largest distortions for given  $\alpha$  occurring at high or low  $|\beta|$  (Fig. 18.20). Equalizing these

extreme distortions by making  $|\alpha| > 0$  would give the maximum permissible range of acceptable orientations (e.g.,  $\alpha = 20^\circ$ ,  $|\beta| = 0^\circ - 40^\circ$  with  $|\beta| = \alpha$  in the middle of the range).

In photography, there is also a correct viewing position, but when examining family photographs, there are no exceptional situations where people would look only at the eyes: People would want to look at facial expressions, hair styles, and so on (they would also be quite sensitive to whether everyone's eyes were open). Unfortunately, photographs of groups often appear distorted around the outside, a factor that could sometimes be partly due to pincushion or barrel distortion (these are lens aberrations—see [Chapter 19: Image Transformations and Camera Calibration](#)). However, this effect could also be due to an incorrect viewing position: The camera doesn't lie but only shows the true geometry according to the perspective it had when the button was pressed. It is a fact that photographs are often viewed at arms length—a distance far greater than the correct viewing distance ([Fig. 18.21](#)). If photographs were meant to be viewed at that distance, the photograph should be taken from much further away, to be sure that the camera doesn't lie inadvertently. Of course, there is a complication that people will normally look at the camera; so, taking the photograph from a different distance will affect the material content of the scene itself.

Until quite recently, photographs were best taken close up, because of the limited resolution of the film. Nowadays, digital cameras have such phenomenal resolution that there is some advantage from taking pictures further away, or even from a considerable distance, with the aid of a zoom lens. (The latter confers the added advantage that real-life shots can be taken without the subject being embarrassed or even aware they are being taken.) But there is a quite different advantage to be gained from taking photographs much further away: Although the correct viewing distance could then be rather larger than ideal from the perspective point of view, all people at all locations in the photograph can be viewed individually without perspective distortions creeping in. Note again that it is common practice for photographs to be handed around, and for each person in them to be scrutinized *individually*—so, the overall global composition might well be less important than the individual people who are portrayed (this is all the more true when one knows the people in the photograph, which is much more likely than with a painting of the 17th Earl). Optimization not only of each locality in a photograph but also of the global view is plainly impossible, but taking the photograph from a distance gives a very good compromise ([Fig. 18.21B](#)). However, taking it from infinity would lead to zero foreshortening of the faces and thereby make them appear flatter. Here, a lot depends on whether the lighting provides other cues that can give a good impression of depth.

Another possibility that digital photography offers is that of automatically stitching together several frames to create a wide scene or panorama. Here, best results are obtained if the camera is put into stitching mode so that it can make exposures constant over a sequence of frames or at least record what they were. Then, it could be expected that the edges of various frames would match up

**FIGURE 18.21**

Process of taking and viewing a photograph. (A) Shows the geometry for taking a photograph of a group of people all facing the camera at C. Also shown is the effective viewing location V of the photograph. (Clearly, the photograph would be enlarged before viewing, in which case the part of the illustration just above V would be scaled, but not otherwise changed.) (B) Shows a potentially more ideal way of taking the photograph, from a large distance. By following (B), people examining the photograph would be viewing from an ideal viewing point; in addition, all people shown in the picture could be examined individually without distortion.

without any sudden changes between them. To achieve a proper match, the frames obviously have to overlap, and then, special software can be used to find the best set of lines for trimming and stitching. This involves moving the trim lines in such a way—generally in plain background regions—that the breaks will be imperceptible. Of course, some smoothing along the trimmed edges will often

help, as long as this process doesn't encroach on regions of totally different intensity. Unfortunately, stitching can't easily cope with situations containing moving objects, and in this context, the author had an interesting early experience of the final country scene containing too many sheep!

The exact algorithms to be used for image stitching are quite intricate. This is because a time-consuming search is required to identify the best trimming lines. The criteria to be used are important, but these obviously involve minimization of intensity and color change along the borders—and there is also advantage in minimizing the intensity and color *gradients* along the borders. Then, there are rules for smoothing along the borders, after stitching has been carried out. Here, the simplest rule is not to do any smoothing at all, but this rule can be relaxed if the changes in intensity and intensity gradient have successfully been minimized.

There is one major problem with stitching: That scenes containing straight edges that go at angles across the whole scene are almost impossible to deal with (Fig. 18.22). This is because each (flat) frame will have been taken from a different direction in order to obtain a wider overall view. Thus, a straight line, such as a path, will appear straight in each frame, but the orientation will normally have to change at the join (Fig. 18.22): That this is not mere theory is demonstrated clearly by the examples in Fig. 18.23. The only way to overcome the problem is to present the scene on a sphere or cylinder in order to prevent kinks from appearing at the joins. But then, the original straight line will become a curved line, especially when the final picture is presented as a flat scene. Here again, the specter of the single viewpoint of each original picture is upon us. The best way of handling it seems to be to present it as a picture that is apparently taken from infinity (as for the earlier example of photographing a group of people) so that any straight line will appear straight, at least at every local position, even if a ruler placed along it will show that it is not straight globally. In fact, this is what the special rotating line-scan cameras were able to achieve in the 1960s and earlier, when they were used to take school photographs—and the time taken to gather enough light was often sufficient for at least one small boy to run from one end to the other and be photographed twice!

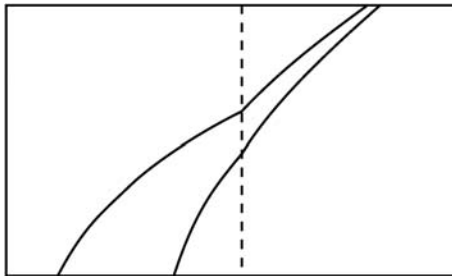


**FIGURE 18.22**

Effect of stitching two pictures depicting parts of a path. Apparently correct stitching will actually lead to a kink at the join.



(A)



(B)

**FIGURE 18.23**

Practical instances of stitching. (A) Shows that the surmise of Fig. 18.22 is correct. (B) shows the result of using an (effectively) overenthusiastic stitching package that manages to avoid a kink but ends up with perspective nonsense. If the lower end of the road boundary had been visible, the software might have avoided the latter problem but would then have introduced a kink.

---

## 18.11 CONCLUDING REMARKS

This chapter has aimed to give some insight into the important subject of invariants and its application in image recognition. The subject takes off when ratios of ratios of distances are considered, and this idea leads in a natural way to the cross-ratio invariant. While its immediate manifestation lies in its application to recognition of the spacings of points on a line, it generalizes immediately to angular spacings for pencils of lines, and also to angular separations of concurrent planes. A further extension of the idea is the development of invariants which can describe sets of noncollinear points, and two cross ratios suffice to characterize a set of five noncollinear points on a plane. The cross ratio can also be applied to conics: Indeed, Chasles' theorem describes a conic as the locus of points which maintains a pencil of constant cross ratio with a given set of four points. However, this theorem does not permit one type of conic curve to be distinguished from another.

Many other theorems and types of invariant exist, but space prevents more than a mention being made of them. As an extension to the line and conic examples given in this chapter, invariants have been produced which cover a conic and

two coplanar nontangent lines, a conic and two coplanar points, and two coplanar conics. Of particular value is the group approach to the design of invariants (Mundy and Zisserman, 1992a). However, certain mathematically viable invariants, such as those which describe local shape parameters on curves, prove to be too unstable to use in their full generality because of image noise. Nevertheless, semidifferential invariants have been shown (Section 18.5) to be capable of fulfilling essentially the same function.

Next, there is the warning of Åström (1995) that perspective transformations can produce such incredible changes in shape that a duck silhouette can be projected arbitrarily closely into something that looks like a rabbit or a circle, hence upsetting invariant-based recognition. (It could of course be argued that all recognition methods will be subject to the effects of perspective transformations. However, invariant-based recognition will not flinch from invoking highly extreme transformations which appear to grossly distort the objects in question, whereas more conventional methods are likely to be designed to cope with a reasonable range of expected shape distortions.) While such reports seem absent from the previous literature, Åström's work indicates that care must be taken to regard recognition via invariants as hypothesis formation which is capable of leading to false alarms.

Overall, the value of invariants lies in making computationally efficient checks of whether points or other features might belong to specific objects. In addition, they achieve this without the necessity for camera calibration or knowing the viewpoint of the camera—though there is an implicit assumption that the camera is Euclidean. (Here, we assume that the aim is location of specific objects in the image. If the objects are then to be located in the world coordinates, camera calibration or some use of reference points will of course be needed. However, there are many applications, such as inspection, surveillance and identification (e.g., of faces or signatures) where location of objects in the image can be entirely adequate.)

While invariants have been known within the vision community for well over 20 years, it is only during the last ~15 years that they have been systematically developed and applied for machine vision. Such is their power that they will undoubtedly assume a stronger and more central role in the future. Nowhere is this power better indicated than by the application to VP detection described in Sections 18.7–18.9. Note also the perspective projection problems that led not only to the need for invariants but also to the need for further insight into the problems of viewing and stitching 2-D pictures (Section 18.10).

*The problems of perspective projection are ubiquitous in 3-D vision, appearing even in simple situations such as viewing 2-D pictures and stitching digital photographs. However, vital interpretive information is provided by projective invariants which slice right through such complexities and are able to help, e.g., with VP detection.*

---

## 18.12 BIBLIOGRAPHICAL AND HISTORICAL NOTES

The mathematical subject of invariance is very old (cf. the work of Chasles, 1855), but it has only relatively recently been developed systematically for machine vision. Notable in this context is the work of Rothwell, Zisserman, and their coworkers, as reported by Forsyth et al. (1991), Mundy and Zisserman (1992a,b), Rothwell et al. (1992a,b), and Zisserman et al., (1990). In particular, the paper by Forsyth et al. (1991) shows the range of available invariant techniques and discusses the problems of stability which arise in certain cases. The appendix (Mundy and Zisserman, 1992b) on projective geometry for machine vision, which appears in Mundy and Zisserman (1992a), is especially valuable and provides the background needed for understanding the other papers in the volume. On the whole, the latter volume has a theoretical flavor which demonstrates what ought to be possible using invariants, though comparisons between invariants and other approaches to recognition are perhaps lacking. Thus, it is only by examining whether workers choose to use invariants in real applications that the full story will emerge. In this respect, the paper by Kamel et al. (1994) on face recognition is of great interest, as it shows how invariants helped to achieve more than had been achieved earlier after many attempts using other approaches—specifically in correcting for perspective distortions during face recognition.

Other more recent work appears in a special issue of *Image and Vision Computing* (Mohr and Wu, 1998): In particular, the paper by Van Gool et al. (1998) shows how shadows can be allowed for in aerial images, and the paper by Boufama et al. (1998) shows how invariants can help with object positioning. Startchik et al. (1998) provides a useful demonstration of the semidifferential invariant methods covered in [Section 18.5](#). Maybank (1996) deals with the problem of accuracy with invariants, making the point that this can be serious even for cross ratios (which contain only four parameters). Another early work, by a totally different set of workers, is Barrett et al. (1991) and contains a number of useful derivations, together with a practical example of aircraft recognition, complete with accuracy assessments.

Rothwell's (1995) book covers the early work on invariance in a thoughtful manner, and the later 3-D books by Hartley and Zisserman (2000) and Faugeras and Luong (2001) integrate the ideas into their structure but are not always easy to understand by students starting out in the subject. Semple and Kneebone (1952) is a standard work on projective geometry which is still widely used in its later reprints.

VP determination has often been considered both in relation to egomotion for mobile robots (Lebègue and Aggarwal, 1993; Shuster et al., 1993), and in general, with regard to the vision methodology (Magee and Aggarwal, 1984; Shufelt, 1999; Almansa et al., 2003), which is prone to suffer from inaccuracy when real off-camera data are used in any context. The seminal paper that gave rise to the



crucial Gaussian sphere technique was that by Barnard (1983). In an interesting twist, Clark and Mirmehdi (2002, 2003) use VPs to recover text that has been distorted by perspective. The approach permits them to recover paragraph formats; in addition to line spacings, various forms of text justification can be recognized and managed.

### 18.12.1 MORE RECENT DEVELOPMENTS

More recently, Shioyama and Uddin (2004) have used cross-ratio invariants for the reliable location of pedestrian crossings by analyzing multiple crossing points of transverse straight lines with the alternating patterns on the road. Kelly et al. (2005) have used homographies between stereo views to locate shadows and low-lying objects: To achieve this, they used the direct linear transformation (see Hartley and Zisserman, 2003) to identify homographies for sets of four or more points. Once homographies are found, they are used to eliminate the corresponding objects from consideration, thereby avoiding costly computation of 3-D depth values from the stereo views for those objects. Rajashekhar et al. (2007) use cross-ratio values to identify man-made structures in images to aid image retrieval. Hough transforms are used to find line structures in images; then, feature points on the lines are found and sets of cross-ratio values are computed and presented in the form of histograms (in each case, all six possible cross-ratio values are included in the histograms). It is found that values in the range 0 to 5 are most suitable for identifying man-made structures, in that the histograms are suitably densely concentrated. Structures such as buildings are well recognized from the histograms, as long as they are quantized with upwards of 200 bins. Li and Tan (2010) use a similar approach, but their cross-ratio values occur in continuous streams as outlines of characters or symbols are tracked. The resulting “cross-ratio spectra” allow characters to be recognized even with severe perspective distortions.

In the area of face recognition, An et al. (2010) describe a new illumination normalization model that is able to cope with varied lighting conditions. It works by decomposing the face into a high-frequency part and a low-frequency part: The main innovation is to divide the original intensity pattern by a smoothed version of the low-frequency part (though several other equalization and normalization processes are carried out as well). Hansen and Ji (2010) survey models for eye detection and gaze estimation and summarize the developments that are still needed in this area. Fang et al. (2010) describe a new method of multiscale image stitching. The paper discusses the problems of obtaining global and local alignment. A number of strategies are needed to overcome the various problems, and an iterative processing pipeline is required to integrate the different strategies.

## 18.13 PROBLEMS

1. Show that the six operations required to transform the cross ratio  $\kappa$  into the six different values for four points on a line form a group  $G$  of order six (see Sections 18.2 and 18.6). Show that  $G$  is a noncyclic group and has two subgroups of order 2 and 3, respectively. *Hint:* Show that all possible combined operations fall within the same set of six and also that this set contains the identity operation and the inverses of all the elements of the set.
2. Show that a conic and two points can be used to define an invariant cross ratio.
3. Show that two conics can be used to define an invariant cross ratio (1) if they intersect in four points, (2) if they intersect in two points, (3) if they do not intersect at all, so long as they have common tangents. (Note that the case of nonintersecting conics with no common tangents requires complex algebra: see for example, Rothwell (1995). The possibility of ambiguity and incompleteness in cases (1)–(3) is also discussed in Rothwell (1995).)
4. a. Perform a geometric calculation based on the sine rule which shows that the angles  $\alpha$ ,  $\beta$ , and  $\gamma$  are related to the distances  $a$ ,  $b$ , and  $c$  in Fig. 18.P.1 by the equation:

$$\frac{a}{\sin \alpha} \times \frac{c}{\sin \gamma} = \frac{a+b}{\sin(\alpha+\beta)} \times \frac{b+c}{\sin(\beta+\gamma)}$$

- b. Show that this leads to a relation between the cross ratios for various distances on the line and for the sines of various angles. Hence show that this also leads to the constancy of the cross ratios on any two lines crossing the pencil of four lines passing through O.

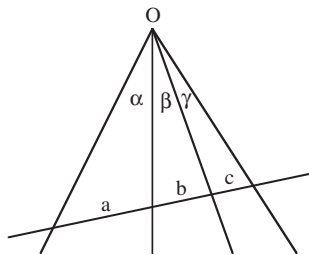


FIGURE 18.P.1

Geometry for cross-ratio calculation.

5. a. Explain the value of using *invariants* in relation to pattern recognition systems. Illustrate your answer by considering the value of thinning algorithms in optical character recognition.

- b. The *cross ratio* of four points ( $P_1, P_2, P_3, P_4$ ) on a line is defined as the ratio:

$$C(P_1, P_2, P_3, P_4) = \frac{(x_3 - x_1)(x_2 - x_4)}{(x_2 - x_1)(x_3 - x_4)}$$

Explain why this is a useful type of invariant for objects viewed under full perspective projection. Show that labeling the points in reverse order will not change the value of the cross ratio.

- c. Give arguments why the cross-ratio concept should also be valid for weak perspective projection. Work out a simpler invariant that is valid for straight lines viewed under weak perspective projection.
- d. A flat lino-cutter blade has two parallel sides of different lengths: It is viewed under weak perspective projection. Discuss whether it can be identified from any orientation in three dimensions by measuring the lengths of its sides.
6. a. Flagstones are viewed on a pavement, providing a large number of coplanar feature points. Show that a correspondence can be made between five coplanar feature points in two images—however, the camera has been moved between the shots—by checking the values of two cross ratios.
- b. It is required to compose a panorama of a scene by taking a number of photographs and “stitching” them together after making appropriate image transformations. To achieve this, it is necessary to make correspondences between the images. Show that the two cross-ratios type of planar invariant can be used for this purpose, even if the chosen scene features do not lie on a common plane. Determine under what conditions this is possible.
7. Redraw Fig. 18.16 using VPs aligned along the observed ellipse axes. Show that the problem of finding the transformed center location now reduces to two 1-D cases and that Eq. (18.32) can be used to obtain the transformed center coordinates.
8. A robot is walking along a path paved with rectangular flagstones. It is able to rotate its camera head so that one set of flagstone lines appears parallel while the other set converges toward a VP. Show that the robot can calculate the position of the VP in two ways: (1) By measuring the varying widths of individual flagstones, or (2) By measuring the lengths of adjacent flagstones and proceeding according to Eq. (18.30). In case (1), obtain a formula which could be used to determine the position of the VP. Which is the more general approach? Which would be applicable if the flagstones appeared in a flower garden in random locations and orientations?

# Image transformations and camera calibration

# 19

When setting up a measurement system it is natural to calibrate it carefully before use. This task has been left to last because (1) it is mathematically more demanding, (2) there are instances where it can be bypassed, (3) it is not always possible to perform the calibration entirely in advance, but rather it has to be updated to a sufficient extent as measurements proceed. This chapter outlines some of the problems of calibration and some of the results of recent research which allow the process to be at least partially bypassed.

*Look out for:*

- the homogeneous coordinates technique for representing general 3-D positions and transformations
- “extrinsic” (external world) and “intrinsic” (camera) parameters
- methods for achieving absolute camera calibration
- the need for correction of camera lens distortions
- the idea of a generalized epipolar geometry
- the “essential” and “fundamental” matrix formulations, relating the observed positions of any point in two camera frames of reference
- the central position of the eight-point algorithm
- the possibility of image “rectification”
- the possibility of 3-D reconstruction.

This is one of the key chapters constituting Part 3 of this book. These chapters should be taken together as they involve not merely different topics but also different *aspects* of the subject, and in addition, the aim has been to cover them in as gentle an order as possible considering the mathematical complexities involved in extracting 3-D and motion information from 2-D images.

## 19.1 INTRODUCTION

When images are obtained from 3-D scenes, the exact position and orientation of the camera-sensing device is often unknown, and there is a need for it to be related to some global frame of reference. This is especially important if accurate measurements of objects are to be made from their images, e.g., in inspection

applications. On the other hand, it may in certain cases be possible to dispense with such detailed information—as in the case of a security system for detecting intruders, or a system for counting cars on a motorway. There are also more complicated cases, such as those in which cameras can be rotated or moved on a robot arm, or the objects being examined can move freely in space. In such cases, camera calibration becomes a central issue. Before we can consider camera calibration, we need to understand in some detail the transformations that can occur between the original world points and the formation of the final image. We attend to these image transformations in the following section, and then move on to details of camera parameters and camera calibration in the subsequent two sections. Then, in [Section 19.5](#), we consider how any radial distortions of the image introduced by the camera lens can be corrected.

[Section 19.6](#) signals a break with previous work and introduces “multiple view” vision. This topic has become important in recent years, as it uses new theory to bypass the need for formal camera calibration, and makes it possible to update the vision system parameters during actual use. The basis for this work is generalized epipolar geometry: this takes the epipolar line ideas of [Section 16.3.2](#) considerably further. At the core of this, new work are the “essential” and “fundamental” matrix formulations, which relate the observed positions of any point in two camera frames of reference. Short sections on image “rectification” (obtaining a new image as it would be seen from an idealized camera position) and 3-D reconstruction follow.

---

## 19.2 IMAGE TRANSFORMATIONS

First, we consider the rotations and translations of object points relative to a global frame. After a rotation through an angle  $\theta$  about the  $Z$ -axis ([Fig. 19.1](#)), the coordinates of a general point  $(X, Y)$  change to:

$$X' = X \cos \theta - Y \sin \theta \quad (19.1)$$

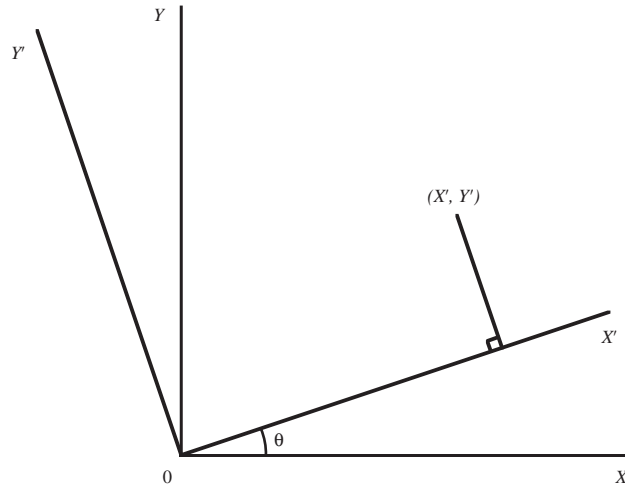
$$Y' = X \sin \theta + Y \cos \theta \quad (19.2)$$

This result is neatly expressed by the matrix equation:

$$\begin{bmatrix} X' \\ Y' \end{bmatrix} = \begin{bmatrix} \cos \theta & -\sin \theta \\ \sin \theta & \cos \theta \end{bmatrix} \begin{bmatrix} X \\ Y \end{bmatrix} \quad (19.3)$$

Clearly, similar rotations are possible about the  $X$  and  $Y$  axes. To satisfactorily express rotations in 3-D, we require a more general notation using  $3 \times 3$  matrices, the matrix for a rotation  $\theta$  about the  $Z$ -axis being:

$$\mathbf{Z}(\theta) = \begin{bmatrix} \cos \theta & -\sin \theta & 0 \\ \sin \theta & \cos \theta & 0 \\ 0 & 0 & 1 \end{bmatrix} \quad (19.4)$$

**FIGURE 19.1**

Effect of a rotation  $\theta$  about the origin.

Those for rotations  $\psi$  about the  $X$ -axis and  $\varphi$  about the  $Y$ -axis are:

$$\mathbf{X}(\psi) = \begin{bmatrix} 1 & 0 & 0 \\ 0 & \cos \psi & -\sin \psi \\ 0 & \sin \psi & \cos \psi \end{bmatrix} \quad (19.5)$$

$$\mathbf{Y}(\varphi) = \begin{bmatrix} \cos \varphi & 0 & \sin \varphi \\ 0 & 1 & 0 \\ -\sin \varphi & 0 & \cos \varphi \end{bmatrix} \quad (19.6)$$

We can make up arbitrary rotations in 3-D by applying sequences of such rotations. Similarly, we can express arbitrary rotations as sequences of rotations about the coordinate axes. Thus,  $\mathbf{R} = \mathbf{X}(\psi)\mathbf{Y}(\varphi)\mathbf{Z}(\theta)$  is a composite rotation in which  $\mathbf{Z}(\theta)$  is applied first, then  $\mathbf{Y}(\varphi)$ , and finally  $\mathbf{X}(\psi)$ . Rather than multiplying out these matrices, we write down here the general result expressing an arbitrary rotation  $\mathbf{R}$ :

$$\begin{bmatrix} X' \\ Y' \\ Z' \end{bmatrix} = \begin{bmatrix} R_{11} & R_{12} & R_{13} \\ R_{21} & R_{22} & R_{23} \\ R_{31} & R_{32} & R_{33} \end{bmatrix} \begin{bmatrix} X \\ Y \\ Z \end{bmatrix} \quad (19.7)$$

Note that the rotation matrix  $\mathbf{R}$  is not completely general: it is orthogonal and thus has the property that  $\mathbf{R}^{-1} = \mathbf{R}^T$ .

In contrast with rotation, translation through a distance  $(T_1, T_2, T_3)$  is given by:

$$X' = X + T_1 \quad (19.8)$$

$$Y' = Y + T_2 \quad (19.9)$$

$$Z' = Z + T_3 \quad (19.10)$$

which is not expressible in terms of a multiplicative  $3 \times 3$  matrix. However, just as general rotations can be expressed as rotations about various coordinate axes, so general translations and rotations can be expressed as sequences of basic rotations and translations relative to individual coordinate axes. Thus, it would be most useful to have a notation which unified the mathematical treatment so that a generalized displacement could be expressed as a product of matrices. This is indeed possible if so-called *homogeneous coordinates* are used. To achieve this, the matrices must be augmented to  $4 \times 4$ . A general rotation can then be expressed in the form:

$$\begin{bmatrix} X' \\ Y' \\ Z' \\ 1 \end{bmatrix} = \begin{bmatrix} R_{11} & R_{12} & R_{13} & 0 \\ R_{21} & R_{22} & R_{23} & 0 \\ R_{31} & R_{32} & R_{33} & 0 \\ 0 & 0 & 0 & 1 \end{bmatrix} \begin{bmatrix} X \\ Y \\ Z \\ 1 \end{bmatrix} \quad (19.11)$$

whereas the general translation matrix becomes:

$$\begin{bmatrix} X' \\ Y' \\ Z' \\ 1 \end{bmatrix} = \begin{bmatrix} 1 & 0 & 0 & T_1 \\ 0 & 1 & 0 & T_2 \\ 0 & 0 & 1 & T_3 \\ 0 & 0 & 0 & 1 \end{bmatrix} \begin{bmatrix} X \\ Y \\ Z \\ 1 \end{bmatrix} \quad (19.12)$$

The generalized displacement (i.e., translation plus rotation) transformation clearly takes the form:

$$\begin{bmatrix} X' \\ Y' \\ Z' \\ 1 \end{bmatrix} = \begin{bmatrix} R_{11} & R_{12} & R_{13} & T_1 \\ R_{21} & R_{22} & R_{23} & T_2 \\ R_{31} & R_{32} & R_{33} & T_3 \\ 0 & 0 & 0 & 1 \end{bmatrix} \begin{bmatrix} X \\ Y \\ Z \\ 1 \end{bmatrix} \quad (19.13)$$

We now have a convenient notation for expressing generalized transformations including operations other than the translations and rotations which account for the normal motions of rigid bodies. First, we take a scaling in size of an object, the simplest case being given by the matrix:

$$\begin{bmatrix} S & 0 & 0 & 0 \\ 0 & S & 0 & 0 \\ 0 & 0 & S & 0 \\ 0 & 0 & 0 & 1 \end{bmatrix}$$

The more general case:

$$\begin{bmatrix} S_1 & 0 & 0 & 0 \\ 0 & S_2 & 0 & 0 \\ 0 & 0 & S_3 & 0 \\ 0 & 0 & 0 & 1 \end{bmatrix}$$

introduces a shear in which an object line  $\lambda$  will be transformed into a line that is not in general parallel to  $\lambda$ . Skewing is another interesting transformation, being given by linear translations varying from the simple case:

$$\begin{bmatrix} 1 & B & 0 & 0 \\ 0 & 1 & 0 & 0 \\ 0 & 0 & 1 & 0 \\ 0 & 0 & 0 & 1 \end{bmatrix}$$

to the general case:

$$\begin{bmatrix} 1 & B & C & 0 \\ D & 1 & F & 0 \\ G & H & 1 & 0 \\ 0 & 0 & 0 & 1 \end{bmatrix}$$

Rotations can be regarded as combinations of scaling and skewing and are sometimes implemented as such (Weiman, 1976).

The other simple but interesting case is that of reflection, which is typified by:

$$\begin{bmatrix} 0 & 1 & 0 & 0 \\ 1 & 0 & 0 & 0 \\ 0 & 0 & 1 & 0 \\ 0 & 0 & 0 & 1 \end{bmatrix}$$

This generalizes to other cases of improper rotation where the determinant of the top left  $3 \times 3$  matrix is  $-1$ .

In all the cases discussed above, it will be observed that the bottom row of the generalized displacement matrix is redundant. In fact, we can put this row to good use in certain other types of transformation. Of particular interest in this context is the case of perspective projection. Following [Section 16.3, Eq. \(16.1\)](#), the equations for projection of object points into image points are as follows:

$$x = fX/Z \quad (19.14)$$

$$y = fY/Z \quad (19.15)$$

$$z = f \quad (19.16)$$

We next make full use of the bottom row of the transformation matrix by defining the homogeneous coordinates as  $(X_h, Y_h, Z_h, h) = (hX, hY, hZ, h)$ , where  $h$  is a nonzero constant which we can take to be unity. To proceed, we examine the homogeneous transformation:

$$\begin{bmatrix} 1 & 0 & 0 & 0 \\ 0 & 1 & 0 & 0 \\ 0 & 0 & 1 & 0 \\ 0 & 0 & 1/f & 0 \end{bmatrix} \begin{bmatrix} X \\ Y \\ Z \\ 1 \end{bmatrix} = \begin{bmatrix} X \\ Y \\ Z \\ Z/f \end{bmatrix} \quad (19.17)$$

We see that dividing by the fourth coordinate gives the required values of the transformed Cartesian coordinates  $(fX/Z, fY/Z, f)$ .



Let us now review this result. First, we have found a  $4 \times 4$  matrix transformation which operates on 4-D homogeneous coordinates. These do not correspond directly to real coordinates, but real 3-D coordinates can be calculated from them by dividing the first three by the fourth homogeneous coordinate. Thus, there is an arbitrariness in the homogeneous coordinates in that they can all be multiplied by the same constant factor without producing any change in the final interpretation. Likewise, when deriving homogeneous coordinates from real 3-D coordinates, we can employ any convenient constant multiplicative factor  $h$ , though we will normally take  $h$  to be unity.

The advantage to be gained from use of homogeneous coordinates is the convenience of having a single multiplicative matrix for any transformation, in spite of the fact that perspective transformations are intrinsically nonlinear: thus, a quite complex nonlinear transformation can be reduced to a more straightforward linear transformation. This eases computer calculation of object coordinate transformations, and other computations such as those for camera calibration (see below). We may also note that almost every transformation can be inverted by inverting the corresponding homogeneous transformation matrix. The exception is the perspective transformation, for which the fixed value of  $z$  leads merely to  $Z$  being unknown, and  $X, Y$  only being known relative to the value of  $Z$  (hence the need for binocular vision or other means of discerning depth in a scene).

---

### 19.3 CAMERA CALIBRATION

The above discussion has shown how homogeneous coordinate systems are used to help provide a convenient linear  $4 \times 4$  matrix representation for 3-D transformations including rigid body translations and rotations, and nonrigid operations including scaling, skewing, and perspective projection. In this last case, it was implicitly assumed that the camera and world coordinate systems are identical, as the image coordinates were expressed in the same frame of reference. However, in general, the objects viewed by the camera will have positions which may be known in world coordinates, but which will not a priori be known in camera coordinates, as the camera will in general be mounted in a somewhat arbitrary position and will point in a somewhat arbitrary direction. Indeed, it may well be on adjustable gimbals, and may also be motor driven, with no precise calibration system. If the camera is on a robot arm, there are likely to be position sensors which could inform the control system of the camera position and orientation in world coordinates, though the amount of slack may well make the information too imprecise for practical purposes (e.g., to guide the robot toward objects).

These factors mean that the camera system will have to be calibrated very carefully before the images can be used for practical applications such as robot pick-and-place. A useful approach is to assume a general transformation between the world coordinates and the image seen by the camera under perspective

projection, and to locate in the image various calibration points which have been placed in known positions in the scene. If enough such points are available, it should be possible to compute the transformation parameters, and then all image points can be interpreted accurately until recalibration becomes necessary.

The general transformation  $\mathbf{G}$  takes the form:

$$\begin{bmatrix} X_H \\ Y_H \\ Z_H \\ H \end{bmatrix} = \begin{bmatrix} G_{11} & G_{12} & G_{13} & G_{14} \\ G_{21} & G_{22} & G_{23} & G_{24} \\ G_{31} & G_{32} & G_{33} & G_{34} \\ G_{41} & G_{42} & G_{43} & G_{44} \end{bmatrix} \begin{bmatrix} X \\ Y \\ Z \\ 1 \end{bmatrix} \quad (19.18)$$

where the final Cartesian coordinates appearing in the image are  $(x, y, z) = (x, y, f)$ , and these are calculated from the first three homogeneous coordinates by dividing by the fourth:

$$x = X_H/H = (G_{11}X + G_{12}Y + G_{13}Z + G_{14})/(G_{41}X + G_{42}Y + G_{43}Z + G_{44}) \quad (19.19)$$

$$y = Y_H/H = (G_{21}X + G_{22}Y + G_{23}Z + G_{24})/(G_{41}X + G_{42}Y + G_{43}Z + G_{44}) \quad (19.20)$$

$$z = Z_H/H = (G_{31}X + G_{32}Y + G_{33}Z + G_{34})/(G_{41}X + G_{42}Y + G_{43}Z + G_{44}) \quad (19.21)$$

However, as we know  $z$ , there is no point in determining parameters  $G_{31}$ ,  $G_{32}$ ,  $G_{33}$ ,  $G_{34}$ . Accordingly, we proceed to develop the means for finding the other parameters. In fact, because only the ratios of the homogeneous coordinates are meaningful, only the ratios of the  $G_{ij}$  values need be computed, and it is usual to take  $G_{44}$  as unity: this leaves only 11 parameters to be determined. Multiplying out the first two equations and rearranging gives:

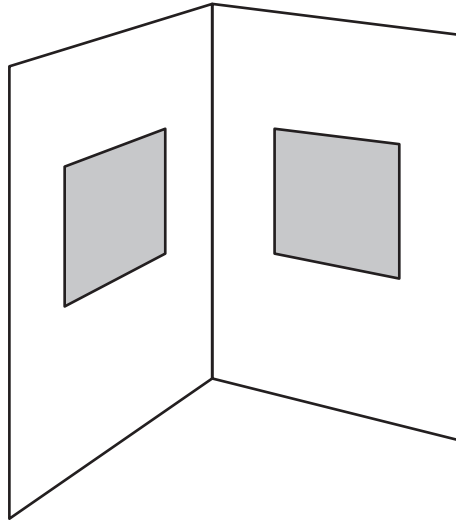
$$G_{11}X + G_{12}Y + G_{13}Z + G_{14} - x(G_{41}X + G_{42}Y + G_{43}Z) = x \quad (19.22)$$

$$G_{21}X + G_{22}Y + G_{23}Z + G_{24} - y(G_{41}X + G_{42}Y + G_{43}Z) = y \quad (19.23)$$

Noting that a single world point  $(X, Y, Z)$  which is known to correspond to image point  $(x, y)$  gives us *two* equations of the above form; it requires a minimum of six such points to provide values for all 11  $G_{ij}$  parameters: Fig. 19.2 shows a convenient near-minimum case. An important factor is that the world points used for the calculation should lead to independent equations: thus, it is important that they should not be coplanar. More precisely, there must be at least six points, no four of which are coplanar. However, further points are useful in that they lead to overdetermination of the parameters and increase the accuracy with which the latter can be computed. There is no reason why the additional points should not be coplanar with existing points: indeed, a common arrangement is to set up a cube so that three of its faces are visible, each face having a pattern of squares with 30–40 easily discerned corner features (as for a Rubic cube).

Least squares analysis can be used to perform the computation of the 11 parameters, e.g., via the pseudoinverse method. First, the  $2n$  equations have to be expressed in matrix form:

$$\mathbf{A}\mathbf{g} = \boldsymbol{\xi} \quad (19.24)$$

**FIGURE 19.2**

A convenient near-minimum case for camera calibration. Here, two sets of four coplanar points, each set of four being at the corners of a square, provide more than the absolute minimum number of points required for camera calibration.

where  $\mathbf{A}$  is a  $2n \times 11$  matrix of coefficients, which multiplies the  $G$ -matrix, now in the form:

$$\mathbf{g} = (G_{11}G_{12}G_{13}G_{14}G_{21}G_{22}G_{23}G_{24}G_{41}G_{42}G_{43})^T \quad (19.25)$$

and  $\xi$  is a  $2n$ -element column vector of image coordinates. The pseudoinverse solution is:

$$\mathbf{g} = \mathbf{A}^\dagger \xi \quad (19.26)$$

where

$$\mathbf{A}^\dagger = (\mathbf{A}^T \mathbf{A})^{-1} \mathbf{A}^T \quad (19.27)$$

The solution is more complex than might have been expected, as a normal matrix inverse is only defined, and can only be computed, for a square matrix. Note that solutions are only obtainable by this method if the matrix  $\mathbf{A}^T \mathbf{A}$  is invertible. For further details of this method, see Golub and van Loan (1983).

## 19.4 INTRINSIC AND EXTRINSIC PARAMETERS

At this point, it is useful to look in more detail at the general transformation leading to camera calibration. When we are calibrating the camera, we are actually trying to bring the camera and world coordinate systems into coincidence. The

first step is to move the origin of the world coordinates to the origin of the camera coordinate system. The second step is to rotate the world coordinate system until its axes are coincident with those of the camera coordinate system. The third step is to move the image plane laterally until there is complete agreement between the two coordinate systems: this step is required as it is not known initially which point in the world coordinate system corresponds to the principal point in the image. [The *principal point* is the image point lying on the principal axis of the camera: it is the point in the image which is closest to the center of projection. Correspondingly, the *principal axis* (or *optical axis*) of the camera is the line through the center of projection normal to the image plane.]

There is an important point to be borne in mind during this process. If the camera coordinates are given by  $\mathbf{C}$ , then the translation  $\mathbf{T}$  required in the first step will be  $-\mathbf{C}$ . Similarly, the rotations that are required will be the inverses of those which correspond to the actual camera orientations. The reason for these reversals is that (for example) rotating an object (here the camera) forwards gives the same effect as rotating the axes backwards. Thus, all operations have to be carried out with the reverse arguments to those indicated above in Section 19.1. The complete transformation for camera calibration is hence:

$$\mathbf{G} = \mathbf{PLRT}$$

$$= \begin{bmatrix} 1 & 0 & 0 & 0 \\ 0 & 1 & 0 & 0 \\ 0 & 0 & 1 & 0 \\ 0 & 0 & 1/f & 0 \end{bmatrix} \begin{bmatrix} 1 & 0 & 0 & t_1 \\ 0 & 1 & 0 & t_2 \\ 0 & 0 & 1 & t_3 \\ 0 & 0 & 0 & 1 \end{bmatrix} \begin{bmatrix} R_{11} & R_{12} & R_{13} & 0 \\ R_{21} & R_{22} & R_{23} & 0 \\ R_{31} & R_{32} & R_{33} & 0 \\ 0 & 0 & 0 & 1 \end{bmatrix} \begin{bmatrix} 1 & 0 & 0 & T_1 \\ 0 & 1 & 0 & T_2 \\ 0 & 0 & 1 & T_3 \\ 0 & 0 & 0 & 1 \end{bmatrix} \quad (19.28)$$

where matrix  $\mathbf{P}$  takes account of the perspective transformation required to form the image. In fact, it is usual to group together the transformations  $\mathbf{P}$  and  $\mathbf{L}$  and call them internal camera transformations which include the *intrinsic camera parameters*, whereas  $\mathbf{R}$  and  $\mathbf{T}$  are taken together as external camera transformations corresponding to *extrinsic camera parameters*:

$$\mathbf{G} = \mathbf{G}_{\text{internal}} \mathbf{G}_{\text{external}} \quad (19.29)$$

where

$$\mathbf{G}_{\text{internal}} = \mathbf{PL} = \begin{bmatrix} 1 & 0 & 0 & t_1 \\ 0 & 1 & 0 & t_2 \\ 0 & 0 & 1 & t_3 \\ 0 & 0 & 1/f & t_3/f \end{bmatrix} \rightarrow \begin{bmatrix} 1 & 0 & t_1 \\ 0 & 1 & t_2 \\ 0 & 0 & 1/f \end{bmatrix} \quad (19.30)$$

$$\mathbf{G}_{\text{external}} = \mathbf{RT} = \begin{bmatrix} \mathbf{R}_1 & \mathbf{R}_1 \cdot \mathbf{T} \\ \mathbf{R}_2 & \mathbf{R}_2 \cdot \mathbf{T} \\ \mathbf{R}_3 & \mathbf{R}_3 \cdot \mathbf{T} \\ \mathbf{0} & \mathbf{1} \end{bmatrix} \quad (19.31)$$

In the matrix for  $\mathbf{G}_{\text{internal}}$ , we have assumed that the initial translation matrix  $\mathbf{T}$  moves the camera's center of projection to the correct position, so that the value of  $t_3$  can be made equal to zero: in that case, the effect of  $\mathbf{L}$  will indeed be lateral as indicated above. At that point, we can express the (2-D) result in terms of a  $3 \times 3$  homogeneous coordinate matrix. In the matrix for  $\mathbf{G}_{\text{external}}$ , we have expressed the result succinctly in terms of the rows  $\mathbf{R}_1$ ,  $\mathbf{R}_2$ ,  $\mathbf{R}_3$  of  $\mathbf{R}$ , and have taken dot products with  $\mathbf{T}$ : the (3-D) result is a  $4 \times 4$  homogenous coordinate matrix.

Although the above treatment gives a good indication of the underlying meaning of  $\mathbf{G}$ , it is not general because we have not so far included scaling and skew parameters in the internal matrix. In fact, the generalized form of  $\mathbf{G}_{\text{internal}}$  is:

$$\mathbf{G}_{\text{internal}} = \begin{bmatrix} s_1 & b_1 & t_1 \\ b_2 & s_2 & t_2 \\ 0 & 0 & 1/f \end{bmatrix} \quad (19.32)$$

Potentially,  $\mathbf{G}_{\text{internal}}$  should include the following:

1. A transform for correcting scaling errors.
2. A transform for correcting translation errors. (For this purpose, the origin of the image should be on the principal axis of the camera. Misalignment of the sensor may prevent this point from being at the center of the image.)
3. A transform for correcting sensor skewing errors (due to nonorthogonality of the sensor axes).
4. A transform for correcting sensor shearing errors (due to unequal scaling along the sensor axes).
5. A transform for correcting for unknown sensor orientation within the image plane.

Clearly, translation errors (Item 2) are corrected by adjusting  $t_1$  and  $t_2$ . All the other adjustments are concerned with the values of the  $2 \times 2$  submatrix:

$$\begin{bmatrix} s_1 & b_1 \\ b_2 & s_2 \end{bmatrix}$$

However, note that application of this matrix performs rotation within the image plane immediately after rotation has been performed in the world coordinates by  $\mathbf{G}_{\text{external}}$ , and it is virtually impossible to separate the two rotations. This explains why we now have a total of 6 external and 6 internal parameters totaling 12 rather than the expected 11 parameters (we return to the factor  $1/f$  below). As a result, it is better to exclude Item 5 in the above list of internal transforms and to subsume it into the external parameters. (While doing so may not be ideal, there is no way of separating the two rotational components by purely optical means: only measurements on the internal dimensions of the camera system could determine the internal component, but separation is not likely to be a cogent or even meaningful matter. On the other hand, the internal component is likely to be stable, whereas the external component may be prone to variation if the camera is

not mounted securely.) As the rotational component in  $\mathbf{G}_{\text{internal}}$  has been excluded,  $b_1$  and  $b_2$  must now be equal, and the internal parameters will be:  $s_1, s_2, b, t_1, t_2$ . Note that the factor  $1/f$  provides a scaling which cannot be separated from the other scaling factors during camera calibration, without specific (i.e., separate) measurement of  $f$ . Thus, we have a total of 6 parameters from  $\mathbf{G}_{\text{external}}$  and 5 parameters from  $\mathbf{G}_{\text{internal}}$ : this totals 11 and equals the number cited in the previous section.

We next consider the special case where the sensor is known to be Euclidean to a high degree of accuracy. This will mean that  $b = b_1 = b_2 = 0$ , and  $s_1 = s_2$ , bringing the number of internal parameters down to three. In addition, if care has been taken over sensor alignment, and there are no other offsets to be allowed for, it may be known that  $t_1 = t_2 = 0$ . This will bring the total number of internal parameters down to just one, namely  $s = s_1 = s_2$ , or  $sf$ , if we take proper account of the focal length. In this case, there will be a total of seven calibration parameters for the whole camera system, and this may permit it to be set up unambiguously by viewing a known object having four clearly marked features instead of the six that would normally be required (see Section 19.3).

---

## 19.5 CORRECTING FOR RADIAL DISTORTIONS

Photographs generally appear so distortion free that there is a tendency to imagine that camera lenses are virtually perfect. However, it sometimes happens that a photograph will show odd curvatures of straight lines, particularly those appearing around the periphery of the picture. The results commonly take the form of “pincushion” or “barrel” distortion: these terms arise because pincushions have a tendency to be overextended at the corners, whereas barrels usually bulge in the middle. In images of paving stones or brick walls, the amount of distortion is usually not more than a few pixels in a total of the order of 512, i.e., typically less than 2%, and this explains why in the absence of particular straight line markers such distortions can be missed (Fig. 19.3). However, it is important both for recognition and for interimage matching purposes that any distortions should be eliminated. Indeed, image interpretation is nowadays targeted at, and frequently achieves, subpixel accuracy. In addition, disparities between stereo images are in the first order of small quantities, and single pixel errors would lead to significant errors in depth measurement. Hence, it is more the rule than the exception that 3-D image analysis will need to make corrections for barrel or pincushion distortion.

For reasons of symmetry, the distortions that arise in images tend to involve radial expansions or contractions relative to the optical axis—corresponding respectively to pincushion or barrel distortion. As with many types of error, series solutions can be useful. Thus, it is worthwhile to model the distortions as

$$\mathbf{r}' = \mathbf{r}f(r) = \mathbf{r}(a_0 + a_2r^2 + a_4r^4 + a_6r^6 + \dots) \quad (19.33)$$

**FIGURE 19.3**

Photograph of a brick wall showing radial (barrel) distortion.

the odd orders in the brackets canceling to zero, again for reasons of symmetry. It is usual to set  $a_0$  to unity, as this coefficient can be taken up by the scale parameters in the camera calibration matrix.

To fully define the effect, we write the  $x$  and  $y$  distortions as

$$x' - x_c = (x - x_c)(1 + a_2r^2 + a_4r^4 + a_6r^6 + \dots) \quad (19.34)$$

$$y' - y_c = (y - y_c)(1 + a_2r^2 + a_4r^4 + a_6r^6 + \dots) \quad (19.35)$$

Here,  $x$  and  $y$  are measured relative to the position of the optical axis of the lens  $(x_c, y_c)$ , so  $\mathbf{r} = (x - x_c, y - y_c)$ ,  $\mathbf{r}' = (x' - x_c, y' - y_c)$ .

As remarked above, the errors to be expected are in the range 2% or less. This means that it is normally sufficiently accurate to take just the first correction term in the expansion and disregard the rest. At the very least, this will introduce such a large improvement in the accuracy that it will be difficult to detect any discrepancies, especially if the image dimensions are  $512 \times 512$  pixels or less. (This remark will not apply to many web cameras, which are sold at extremely low prices on the mainly amateur market. Although the camera chip and electronics are often very good value, the accompanying low-cost lens may well require extensive correction to ensure that distortion-free measurements are possible.) In addition, computation errors in matrix inversion and convergence of 3-D algorithms will add to the digitization errors, tending further to hide higher powers of radial distortion. Thus, in most cases, the latter can be modeled using a single parameter equation:

$$\mathbf{r}' = \mathbf{r}f(r) = \mathbf{r}(1 + a_2r^2) \quad (19.36)$$

Note that the above theory only models the distortion: clearly, it has to be corrected by the corresponding inverse transformation.

It is instructive to consider the apparent shape of a straight line which appears, for example, along the top of an image (Fig. 19.3). Take the image dimensions to range over  $-x_1 \leq x \leq x_1$ ,  $-y_1 \leq y \leq y_1$ , and the optical axis of the camera to be at the center of the image. Then, the straight line will have the approximate equation:

$$y' = y_1 [1 + a_2(x^2 + y_1^2)] = y_1 + a_2y_1^3 + a_2y_1x^2 \quad (19.37)$$

which represents a parabola. The vertical error at the center of the parabola is  $a_2y_1^3$ , and the additional vertical error at the ends is  $a_2y_1x_1^2$ . If the image is square ( $x_1 = y_1$ ), these two errors are equal (the erroneous impression is given by the parabola shape that the error at  $x = 0$  is zero).

Finally, note that digital scanners are very different from single lens cameras, in that their lenses travel along the object space during acquisition. Thus, longitudinal errors are unlikely to arise to anything like the same extent, though lateral errors could in principle be problematic.

---

## 19.6 MULTIPLE VIEW VISION

Over the 1990s, a considerable advance in 3-D vision was made by examining what could be learnt from uncalibrated cameras using multiple views. At first sight, considering the efforts made in earlier sections of this chapter to understand exactly how cameras should be calibrated, this may seem nonsensical. Nevertheless, there are considerable potential advantages in examining multiple views—not least, many thousands of videotapes are available from uncalibrated cameras, including those used for surveillance and those produced in the film industry. In such cases, as much must be made of the available material as possible, whether or not any regrets over “what might have been” are entertained. However, the need is deeper than this. Many situations exist in which the camera parameters might vary because of thermal variations, or because the zoom or focus setting has been adjusted: and it is impracticable to keep recalibrating a camera using accurately made test objects. Finally, if multiple (e.g., stereo) cameras are used, each will have to be calibrated separately, and the results compared to minimize the combined error: far better to examine the system as a whole and to calibrate it on the real scenes that are being viewed.

In fact, we have already met some aspects of these aspirations, in the form of invariants that are obtained in sequence by a single camera. For example, if a series of four collinear points are viewed and their cross ratio is checked, it will be found to be constant as the camera moves forward, changes orientation, or views the points increasingly obliquely—so long as they all remain within the field of view. For this purpose, all that is required to perform the recognition and maintain awareness of the object (the four points) is an uncalibrated but



distortion-free camera. By distortion-free, we here mean not the ability to correct perspective distortion—which is, after all, the function of the cross ratio invariant—but the lack of radial distortion, or at least the capability in the following software for eliminating it (see [Section 19.5](#)).

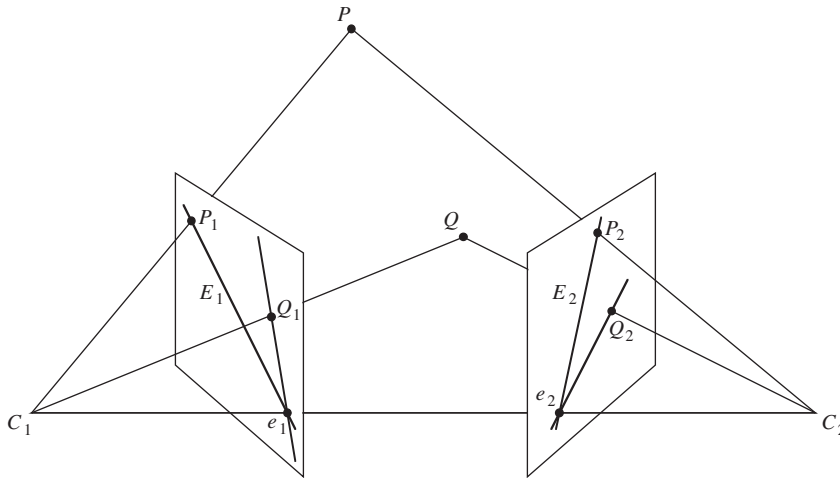
To understand how image interpretation can be carried out more generally, using multiple views—whether from the same camera moved to a variety of places, or multiple cameras with overlapping views of the world—we shall need to go back to basics and start afresh with a more general attack on concepts such as binocular vision and epipolar constraints. In particular, two important matrices will be called into play—the “essential” matrix and the “fundamental” matrix. We start with the essential matrix and then generalize the idea to the fundamental matrix. But first, we need to look at the geometry of two cameras with general views of the world.

---

## 19.7 GENERALIZED EPIPOLAR GEOMETRY

In [Section 16.3](#), we considered the stereo correspondence problem and had already simplified the task by choosing two cameras whose image planes were not only parallel but in the same plane. This made the geometry of depth perception especially simple, but suppressed possibilities allowed for in the human visual system (HVS), of having a nonzero vergence angle between the two images. Indeed, the HVS is special in adjusting vergence so that the current focus of attention in the field of view has almost zero disparity between the two images, and it seems likely that the HVS estimates depth not merely by measuring disparity but rather by measuring the vergence together with remanent small variations in disparity.

Here, we generalize the situation to cover the possibility of disparity coupled with substantial vergence. [Fig. 19.4](#) shows the revised geometry. Note first that observation of a real point  $P$  in the scene leads to points  $P_1$  and  $P_2$  in the two images; that  $P_1$  could correspond to any point on the epipolar line  $E_2$  in Image 2; and similarly, that point  $P_2$  could correspond to any point on the epipolar line  $E_1$  in Image 1. Indeed, the so-called epipolar plane of  $P$  is the plane containing  $P$  and the projection points  $C_1$  and  $C_2$  of the two cameras: the epipolar lines (see [Section 16.3](#)) are thus the straight lines in which this plane cuts the two image planes. Furthermore, the line joining  $C_1$  and  $C_2$  cuts the image planes in the so-called epipoles  $e_1$  and  $e_2$ : these can be regarded as the images of the alternate camera projection points. Note that all epipolar planes pass through points  $C_1$ ,  $C_2$  and  $e_1$ ,  $e_2$ : this means that all epipolar lines in the two images pass through the respective epipoles. However, if the vergence angle were zero (as in [Fig. 16.5](#)), the epipoles would be at infinity in either direction, and all epipolar lines in either image would be parallel, and indeed parallel to the vector  $C$  from  $C_1$  to  $C_2$ .

**FIGURE 19.4**

Generalized imaging of a scene from two viewpoints. In this case, there is substantial vergence. All epipolar lines in the left image pass through epipole  $e_1$ : of these, only  $E_1$  is shown. Similar comments apply for the right image.

## 19.8 THE ESSENTIAL MATRIX

In this section, we start with the vectors  $\mathbf{P}_1$ ,  $\mathbf{P}_2$ , from  $C_1$ ,  $C_2$  to  $P$ , and also the vector  $\mathbf{C}$  from  $C_1$  to  $C_2$ . Vector subtraction gives:

$$\mathbf{P}_2 = \mathbf{P}_1 - \mathbf{C} \quad (19.38)$$

We also know that  $\mathbf{P}_1$ ,  $\mathbf{P}_2$ , and  $\mathbf{C}$  are coplanar, the condition of coplanarity being:

$$\mathbf{P}_2 \cdot \mathbf{C} \times \mathbf{P}_1 = 0 \quad (19.39)$$

(This can be thought of as bringing to zero the volume of the parallelepiped with sides  $\mathbf{P}_1$ ,  $\mathbf{P}_2$ , and  $\mathbf{C}$ .)

To progress, we need to relate the vectors  $\mathbf{P}_1$  and  $\mathbf{P}_2$  when these are expressed relative to their own frames of reference. If we take these vectors as having been defined in the  $C_1$  frame of reference, we now reexpress  $\mathbf{P}_2$  in its own ( $C_2$ ) frame of reference, by applying a translation  $\mathbf{C}$  and a rotation of coordinates expressed as the orthogonal matrix  $R$ . This leads to:

$$\mathbf{P}'_2 = R\mathbf{P}_2 = R(\mathbf{P}_1 - \mathbf{C}) \quad (19.40)$$

so that:

$$\mathbf{P}_2 = R^{-1}\mathbf{P}'_2 = R^T\mathbf{P}'_2 \quad (19.41)$$

Substituting in the coplanarity condition gives:

$$(R^T \mathbf{P}'_2) \cdot \mathbf{C} \times \mathbf{P}_1 = 0 \quad (19.42)$$

At this point, it is useful to replace the vector product notation by using a skew-symmetric matrix  $C_\times$  to denote  $\mathbf{C} \times$ , where:

$$C_\times = \begin{bmatrix} 0 & -C_z & C_y \\ C_z & 0 & -C_x \\ -C_y & C_x & 0 \end{bmatrix} \quad (19.43)$$

At the same time, we observe the correct matrix formulation of all the vectors by transposing appropriately. We now find that:

$$(R^T \mathbf{P}'_2)^T C_\times \mathbf{P}_1 = 0 \quad (19.44)$$

$$\therefore \mathbf{P}'_2{}^T R C_\times \mathbf{P}_1 = 0 \quad (19.45)$$

Finally, we obtain the “essential matrix” formulation:

$$\mathbf{P}'_2{}^T E \mathbf{P}_1 = 0 \quad (19.46)$$

where the essential matrix has been found to be:

$$E = R C_\times \quad (19.47)$$

Eq. (19.46) is actually the desired result: it expresses the relation between the observed positions of the same point in the two camera frames of reference. Furthermore, it immediately leads to formulae for the epipolar lines. To see this, first note that in the  $C_1$  camera frame:

$$\mathbf{p}_1 = (f_1/Z_1) \mathbf{P}_1 \quad (19.48)$$

whereas in the  $C_2$  camera frame (and expressed in terms of that frame of reference):

$$\mathbf{p}'_2 = (f_2/Z_2) \mathbf{P}'_2 \quad (19.49)$$

Eliminating  $\mathbf{P}_1$  and  $\mathbf{P}'_2$ , and dropping the prime (as within the respective image planes the numbers 1 and 2 are sufficient to specify the coordinates unambiguously), we find:

$$\mathbf{p}_2{}^T E \mathbf{p}_1 = 0 \quad (19.50)$$

as  $Z_1, Z_2$  and  $f_1, f_2$  can be canceled from this matrix equation.

Now note that writing  $\mathbf{p}_2{}^T E = \mathbf{l}_1{}^T$  and  $\mathbf{l}_2 = E \mathbf{p}_1$  leads to the following relations:

$$\mathbf{p}_1{}^T \mathbf{l}_1 = 0 \quad (19.51)$$

$$\mathbf{p}_2{}^T \mathbf{l}_2 = 0 \quad (19.52)$$

This means that  $\mathbf{l}_2 = E\mathbf{p}_1$  and  $\mathbf{l}_1 = E^T\mathbf{p}_2$  are the epipolar lines corresponding to  $\mathbf{p}_1$  and  $\mathbf{p}_2$ , respectively. (To fully understand this, consider a line  $\mathbf{l}$  and a point  $\mathbf{p}$ :  $\mathbf{p}^T\mathbf{l} = 0$  means that  $\mathbf{p}$  lies on the line  $\mathbf{l}$ , or dually,  $\mathbf{l}$  passes through the point  $\mathbf{p}$ .)

Finally, we can find the epipoles from the above formulation. In fact, the epipole lies on every epipolar line within the same image. Thus,  $\mathbf{e}_2$  satisfies (can be substituted for  $\mathbf{p}_2$  in) Eq. (19.52), and hence:

$$\begin{aligned} \mathbf{e}_2^T\mathbf{l}_2 &= 0 \\ \therefore \mathbf{e}_2^TE\mathbf{p}_1 &= 0 \text{ for all } \mathbf{p}_1. \end{aligned}$$

This means that  $\mathbf{e}_2^TE = 0$ , i.e.,  $E^T\mathbf{e}_2 = 0$ . Similarly,  $E\mathbf{e}_1 = 0$ .

---

## 19.9 THE FUNDAMENTAL MATRIX

Notice that in the last part of the essential matrix calculation, we implicitly assumed that the cameras are correctly calibrated. Specifically,  $\mathbf{p}_1$  and  $\mathbf{p}_2$  are corrected (calibrated) image coordinates. However, there is a need to work with uncalibrated images, using the raw pixel measurements—for all the reasons given in Section 19.6. (Note also that any radial distortions need to be eliminated, so as to idealize the camera, but not to calibrate it in the sense of Sections 19.3 and 19.4.) Applying the camera intrinsic matrices  $G_1$ ,  $G_2$  to the calibrated image coordinates (Section 19.4), we get the raw image coordinates:

$$\mathbf{q}_1 = G_1\mathbf{p}_1 \quad (19.53)$$

$$\mathbf{q}_2 = G_2\mathbf{p}_2 \quad (19.54)$$

In fact, we here need to go in the reverse direction, so we use the inverse equations:

$$\mathbf{p}_1 = G_1^{-1}\mathbf{q}_1 \quad (19.55)$$

$$\mathbf{p}_2 = G_2^{-1}\mathbf{q}_2 \quad (19.56)$$

Substituting for  $\mathbf{p}_1$  and  $\mathbf{p}_2$  in Eq. (19.50), we find the desired equation linking the raw pixel coordinates:

$$\mathbf{q}_2^T(G_2^{-1})^TEG_1^{-1}\mathbf{q}_1 = 0 \quad (19.57)$$

which can be expressed as

$$\mathbf{q}_2^TF\mathbf{q}_1 = 0 \quad (19.58)$$

where

$$F = (G_2^{-1})^TEG_1^{-1} \quad (19.59)$$

$F$  is defined as the “fundamental matrix.” Because it contains all the information that would be needed to calibrate the cameras, it contains more free

parameters than the essential matrix. However, in other respects, the two matrices are intended to convey the same basic information, as is confirmed by the resemblance between the two formulations—Eqs. (19.46) and (19.58).

Finally, just as in the case of the essential matrix, the epipoles are given by  $F\mathbf{f}_1 = 0$  and  $F^T\mathbf{f}_2 = 0$ , though this time in raw image coordinates  $\mathbf{f}_1$  and  $\mathbf{f}_2$ .

---

## 19.10 PROPERTIES OF THE ESSENTIAL AND FUNDAMENTAL MATRICES

Next, we consider the composition of the essential and fundamental matrices. In particular, note that  $C_\times$  is a factor of  $E$  and also, indirectly, of  $F$ . In fact, they are homogeneous in  $C_\times$ , so the scale of  $\mathbf{C}$  will make no difference to the two matrix formulations (Eqs. (19.46) and (19.58)), only the *direction* of  $\mathbf{C}$  being important: indeed, the scales of both  $E$  and  $F$  are immaterial, and as a result, only the relative values of their coefficients are of importance. This means that there are at most only eight independent coefficients in  $E$  and  $F$ . In fact, in the case of  $F$ , there are only *seven*, as  $C_\times$  is skew-symmetric, and this ensures that it has Rank 2 rather than Rank 3—a property that is passed on to  $F$ . The same argument applies for  $E$ , but the lower complexity of  $E$  (by virtue of its not containing the image calibration information) means that it has only *five* free parameters. In the latter case, it is easy to see what they are: they arise from the original three translation ( $\mathbf{C}$ ) and three rotation ( $\mathbf{R}$ ) parameters, but the scale parameter is excluded.

In this context, note that if  $\mathbf{C}$  arises from a translation of a single camera, the same essential matrix will result whatever the scale of  $\mathbf{C}$ : only the direction of  $\mathbf{C}$  actually matters, and the same epipolar lines will result from continued motion in the same direction. In fact, in this case, we can interpret the epipoles as foci of expansion or contraction. This underlines the power of this formulation: specifically, it treats motion and displacement a single entity.

Finally, we should try to understand why there are seven free parameters in the fundamental matrix. The solution is relatively simple. Each epipole requires two parameters to specify it. In addition, three parameters are needed to map any three epipolar lines from one image to the other. But why do just three epipolar lines have to be mapped? This is because the family of epipolar lines is a pencil whose orientations are related by cross ratios, so once three epipolar lines have been specified, the mapping of any other can be deduced. (Knowing the properties of the cross ratio, it is seen that fewer than three epipolar lines would be insufficient, and that more than three would yield no additional information.) This fact is sometimes stated in the following form: a homography (a projective transformation) between two 1-D projective spaces has three degrees of freedom.

---

## 19.11 ESTIMATING THE FUNDAMENTAL MATRIX

In the previous section, we showed that the fundamental matrix has seven free parameters. This means that it ought to be possible to estimate it by identifying the same seven features in the two images. However, using the minimum number of points in this way carries the health warning that they must be in general position: special configurations of points can lead to numerical instabilities in the computations, total failure to converge, or unnecessary ambiguities in the results. In general, coplanar points are to be avoided. In any case, although this is mathematically possible in principle, and a suitable nonlinear algorithm has been devised by Faugeras et al. (1992) to implement it, it has been shown that the computation can be numerically unstable. Essentially, noise acts as an additional variable boosting the effective number of degrees of freedom in the problem to eight. However, a linear algorithm called the *eight-point algorithm* has been devised to overcome the problem. Curiously, this algorithm had been proposed many years earlier by Longuet-Higgins (1981) to estimate the *essential* matrix, but it came into its own when Hartley (1995) showed how to control the errors by first normalizing the values. In addition, by using more than eight points, increased accuracy can be attained, but then a suitable algorithm must be found that can cope with the now overdetermined parameters. Principal component analysis can be used for this, an appropriate procedure being singular value decomposition.

Apart from noise, gross mismatches in forming trial point correspondences between images can be a source of practical problems. If so, the normal least squares types of solution can profitably be replaced by the least median of squares robust estimation method ([Appendix A](#)).

---

## 19.12 AN UPDATE ON THE EIGHT-POINT ALGORITHM

[Section 19.11](#) outlined the value of the eight-point algorithm for estimating the fundamental matrix. Over a period of about 8 years (1995–2003), this essentially became the standard solution to the problem. However, a key contribution by Torr and Fitzgibbon (2003, 2004) has shown that the eight-point algorithm might after all not be the best possible method, as the solutions it obtains depend on the particular coordinate system used for the computation. This is because the normalization normally used, namely  $\sum_i f_i^2 = 1$ , is not invariant to shifts in the coordinate system. In fact, it is by no means obvious how to find an invariant normalization: note, for example, that the simple normalization  $f_9 = 1$  suggested by Tsai and Huang (1984) leads to biased solutions and excludes those with  $f_9 = 0$ . Nevertheless, Torr and Fitzgibbon's logical analysis of the situation, in

which they were forced to disregard the affine transform case appropriate for weak perspective, led to the following normalization of  $F$ :

$$f_1^2 + f_2^2 + f_4^2 + f_5^2 = K \quad (19.60)$$

where  $K$  is a constant and:

$$F = \begin{bmatrix} f_1 & f_2 & f_3 \\ f_4 & f_5 & f_6 \\ f_7 & f_8 & f_9 \end{bmatrix} \quad (19.61)$$

Finally, to determine  $F$ , Eq. (19.60) can be applied as a Lagrangian multiplier constraint, and this leads to an eigenvector solution for  $F$ . Overall, the  $8 \times 8$  eigenvalue problem solved by the eight-point algorithm is replaced by a  $5 \times 5$  eigenvalue problem. Furthermore, this approach not only yields the required invariance properties, thus ensuring a more accurate solution, but also it gives a much faster computation that loses significantly fewer tracks in image sequence analysis.

---

### 19.13 IMAGE RECTIFICATION

In Section 19.7, we took some pains to generalize the epipolar approach and subsequently arrived at general solutions, corresponding to arbitrary overlapping views of scenes. However, there are distinct advantages in special views obtained from cameras with parallel axes—as in the case of Fig. 16.5 where the vergence is zero. Specifically, it is easier to find correspondences between scenes that are closely related in this way. Unfortunately, such well-prepared pairs of images are not in keeping with the aims promoted in Section 19.6, of insisting on closely aligned and calibrated cameras, and this certainly doesn't apply to frames taken by a single moving camera unless its motion is severely constrained by special means. In fact, the solution is straightforward: take images with uncalibrated cameras, estimate the fundamental matrix, and then apply suitable linear transformations to compute the images for any desired idealized camera positions. The latter technique is called image rectification and ensures for example, that the epipolar lines are all parallel to the baseline  $\mathbf{C}$  between the centers of projection. This then results in correspondences being found by searching along points with the same ordinate in the alternate image: for a point with coordinates  $(x_1, y_1)$  in the first image, search for a matching point  $(x_2, y_1)$  in the second image.

When rectifying an image, it will in general be rotated in 3-D, and the obvious way of achieving this is to transfer each individual pixel to its new location in the rectified image. (Of course, it may also be translated and scaled, in which case the effect described here may be even more significant.). However, rotations are nonlinear processes and will in some cases have the effect of mapping several pixels into a single pixel; furthermore, a number of pixels may well not have intensity values assigned to them. While the first of these problems could be

tackled by some sort of intensity averaging process, and the latter problem could be tackled by applying a median or other type of filter to the transformed image, such techniques are insufficiently thoroughgoing to provide accurate, reliable solutions. The *proper* way of overcoming these intrinsic difficulties is to backproject the pixel locations from the transformed image space to the source image, use interpolation to compute the ideal pixel intensities, and then transfer these intensities to the transformed image space.

Bilinear interpolation is used most often in the transformation process. This works by performing interpolation in the  $x$ -direction and then in the  $y$ -direction. Thus, if the location to be interpolated to is  $(x + a, y + b)$  where  $x$  and  $y$  are integer pixel locations, and  $0 \leq a, b \leq 1$ , then the interpolated intensities in the  $x$ -direction are as follows:

$$I(x + a, y) = (1 - a)I(x, y) + aI(x + 1, y) \quad (19.62)$$

$$I(x + a, y + 1) = (1 - a)I(x, y + 1) + aI(x + 1, y + 1) \quad (19.63)$$

and the final result after interpolating in the  $y$ -direction is as follows:

$$I(x + a, y + b) = (1 - a)(1 - b)I(x, y) + a(1 - b)I(x + 1, y) \\ + (1 - a)bI(x, y + 1) + abI(x + 1, y + 1) \quad (19.64)$$

The symmetry of the result shows that it makes no difference which axis is chosen for the first pair of interpolations, and this limits the arbitrariness of the method. Note that the method does not assume a locally planar intensity variation in 2-D: this is clear as the value of the  $I(x + 1, y + 1)$  intensity is taken into account as well as the other three intensity values. Nevertheless, bilinear interpolation is not a totally ideal solution, as it takes no account of the sampling theorem, and for this reason, the bi-cubic interpolation method (which involves more computation) is sometimes used instead. In addition, all such methods introduce slight local blurring of the image as they involve averaging of local intensity values. Overall, transformation processes such as this are bound to result in slight degradation of the image data.

---

## 19.14 3-D RECONSTRUCTION

In [Section 19.10](#), the fact that  $F$  is determined only up to an unknown scale factor (or equivalently that the actual scales of its coefficients as obtained are arbitrary) was strongly emphasized. This reflected the deliberate avoidance of camera calibration in this work. In practice, this means that if the results of computations of  $F$  are to be related back to the real world, the scaling factor must be reinstated. In principle, this can be achieved by viewing a single yardstick: it is unnecessary to view an object such as a Rubik cube, as knowledge of  $F$  carries with it a lot of information on relative dimensions in the real world. This factor is important when reconstructing a real scene with a real depth map.

There are a number of methods for image reconstruction, of which perhaps the most obvious is triangulation. This starts by taking two camera positions



containing normalized images and projecting rays for a given point  $P$  back into the real world until they meet. In fact, attempting to do this meets with an immediate problem: the inaccuracies in the available parameters, coupled with the pixelation of the images, ensure that in most cases rays will not actually meet, as they are skew lines. The best that can be done with skew lines is to determine the position of closest approach. Once this has been found, the bisector of the line of closest approach (which is perpendicular to each of the rays) is, in *this* model, the most accurate estimate of the position of  $P$  in space.

Unfortunately, the above model is not guaranteed to give the most accurate prediction of the position of  $P$ . This is because perspective projection is a highly nonlinear process: in particular, slight misjudgment of the orientation of the point from either of the images can cause a substantial depth error, coupled with a significant lateral error: so much is indeed obvious from Fig. 19.5. This being so, it has to be asked where the error might still be linear, so that, at that position at least, error calculation can be based on Gaussian distributions. (Here, we ignore the possibility of gross errors arising from mismatches between images, which is



**FIGURE 19.5**

Error in locating a feature in space using binocular imaging. The dark-shaded regions represent the regions of space that could arise for small errors in the image planes. The crossover region, shaded black, confirms that longitudinal errors will be much larger than lateral errors. A full analysis would involve applying Gaussian or other error functions (see text).

the subject of further discussion in [Section 19.11](#) and elsewhere.) In fact, the errors can be taken to be approximately Gaussian in the images themselves. This means that the point in space that has to be chosen as representing the most accurate interpretation of the data is that which results in the minimum error (in a least mean square sense) when reprojected onto the image planes. Typically, the error obtained using this approach is a factor of two smaller than that for the triangulation method described above (Hartley and Zisserman, 2000).

Finally, it is useful to mention a further type of error that can arise with two cameras. This applies when they both view an object with a smoothly varying boundary. For example, if both cameras are viewing the right hand edge of a vase of circular cross section, each will see a different point on the boundary and a discrepancy will arise in the estimated boundary position ([Fig. 19.6](#)). It is left as an

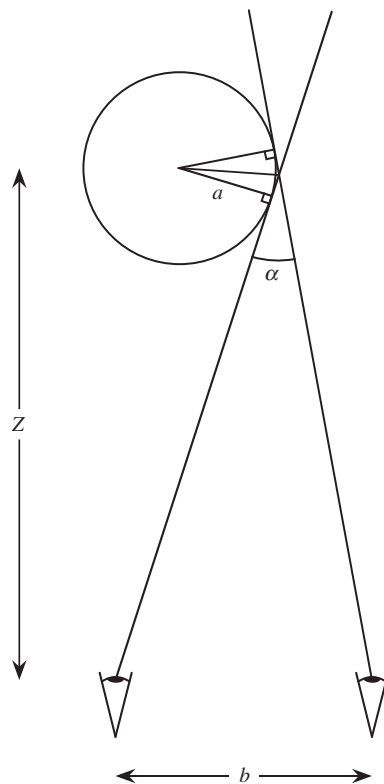


**FIGURE 19.6**

Lateral estimation error arising with a smoothly varying boundary. The error arises in estimating the boundary position when information from two views is fused in the standard way.  $a$  is the radius of a vase being observed,  $\alpha$  is the disparity in direction of its right hand boundary,  $Z$  is its depth in the scene, and  $b$  is the stereo baseline.

exercise (Section 19.17) to determine the exact magnitude of such errors. In fact, the error is proportional both to  $a$ , where  $a$  is the local radius of curvature of the observed boundary, and to  $Z^{-2}$ , where  $Z$  is the depth in the scene. This means that the error (and the percentage error) tends to zero at large distances, and also that the error falls properly to zero for sharp corners.

---

### 19.15 CONCLUDING REMARKS

This chapter has discussed the transformations required for camera calibration and has outlined how calibration can be achieved. The camera parameters have been classified as “internal” and “external,” thereby simplifying the conceptual problem and throwing light on the origins of errors in the system. It has been shown that a minimum of six points is required to perform calibration in the general case where 11 transformation parameters are involved; however, the number of points required might be reduced somewhat in special cases, e.g., where the sensor is known to be Euclidean. Nevertheless, it is normally more important to increase the number of points used for calibration than to attempt to reduce it, as substantial gains in accuracy can be obtained via the resulting averaging process.

In an apparent break with the previous work, Section 19.5 introduced multiple view vision. This important topic was seen to rest on generalized epipolar geometry and led to the essential and fundamental matrix formulations, which relate the observed positions of any point in two camera frames of reference. The importance of the eight-point algorithm for estimating either of these matrices—and particularly the fundamental matrix, which is relevant when the cameras are uncalibrated—was stressed. In addition, the need for accuracy in estimating the fundamental matrix is still a research issue.

*The obvious way of tackling vision problems is to set up a camera and calibrate it, and only then to use it in anger. This chapter has shown how, to a large extent, calibration can be avoided or carried out adaptively “on the fly”—by performing multiple view vision and analyzing the various key matrices that arise from the generalized epipolar problems.*

---

### 19.16 BIBLIOGRAPHICAL AND HISTORICAL NOTES

One of the first to use the various transformations described in this chapter was Roberts (1965). Important early references for camera calibration are the *Manual of Photogrammetry* (Slama, 1980), Tsai and Huang (1984), and Tsai (1986). Tsai’s paper is especially useful in that he provides an extended, highly effective treatment which copes with nonlinear lens distortions. More recent papers on this topic include Haralick (1989), Crowley et al. (1993), Cumani and Guiducci

(1995), and Robert (1996): see also Zhang (1995). Note that parametrized plane curves can be used instead of points for the purpose of camera calibration (Haralick and Chu, 1984).

Clearly, camera calibration is an old topic that is revisited every time 3-D vision has to be used for measurement, and otherwise when rigorous analysis of 3-D scenes is called for. The calibration scenario started to undergo a metamorphosis in the early 1990s, when it was realized that much could be learnt without overt calibration, but rather by *comparing* images taken from moving sequences or from multiple views (Faugeras, 1992; Faugeras et al., 1992; Hartley, 1992; Maybank and Faugeras, 1992). In fact, although it was appreciated that much could be learnt without overt calibration, it was not at that stage known how much *might* be learnt, and there ensued a rapid sequence of developments as the frontiers were progressively pushed back (e.g., Hartley, 1995; Hartley, 1997; Luong and Faugeras, 1997). By the late 1990s, the fast evolution phase was over, and definitive, albeit quite complex, texts appeared covering these developments (Hartley and Zisserman, 2000; Faugeras and Luong, 2001; Gruen and Huang, 2001). Nevertheless, many refinements of the standard methods were still emerging (Faugeras et al., 2000; Heikkilä, 2000; Sturm, 2000; Roth and Whitehead, 2002). It is in this light that the innovative insights of Torr and Fitzgibbon (2003, 2004) and Chojnacki et al. (2003) expressing similar but not identical sentiments relating to the eight-point algorithm should be considered.

In retrospect, it is amusing that the early, incisive paper by Longuet-Higgins (1981) presaged many of these developments: although his eight-point algorithm applied specifically to the essential matrix, it was only very much later (Faugeras, 1992; Hartley, 1992) that it was applied to the fundamental matrix, and even later, in a crucial step, that its accuracy was greatly improved by prenormalizing the image data (Hartley, 1997). As already noted, the eight-point algorithm continued to be a focus for new research.

### 19.16.1 MORE RECENT DEVELOPMENTS

Most recently, Gallo et al. (2011) have studied how planes may be fitted to surfaces that are obtained from range data (i.e., sets of data points whose real-world  $(X, Y, Z)$  coordinates are approximately known). Although RANSAC should provide useful solutions, it sometimes fails when finding pairs of planar patches, and a single plane is fitted to both, with the result that it contains more inliers than the correct models. To cope with this, they devised an alternate form of random sample consensus (RANSAC), connected components-RANSAC (CC-RANSAC), which only considers the largest connected components of inliers for a given plane hypothesis. The method requires an inlier threshold to be set, and this has to be adjusted for the particular application in question. One relevant application is automatic car parking where a single level near a curb has to be identified.

Although the 8-point algorithm has become standard for solving the fundamental matrix, the latter only contains seven independent parameters so only

identifying the same seven features in two images should be enough to solve it. Bartoli and Sturm (2004) have found that this is realizable if nonlinear estimation is used. The method converges faster than other approaches, though it is somewhat more likely to fall into local minima than methods based on redundant parameters. Fathy et al. (2011) study error criteria for fundamental matrix estimation. They show that the symmetric epipolar distance criterion is biased and find that of a number of available criteria, the recently developed Kanatani distance criterion (Kanatani et al., 2008) appears to be the most accurate. Ansar and Daniilidis (2003) have devised a novel set of algorithms for linear pose estimation from  $n$  points or  $n$  lines. The methods will find solutions for cases of  $n \geq 4$ , for points in general position. Although two similar existing noniterative methods exist in the case of estimation from  $n$  points (to which the new method is shown to be superior), there is no directly competing case for  $n$  lines.

---

## 19.17 PROBLEMS

1. For a 2-camera stereo system, obtain a formula for the depth error that arises for a given error in disparity. Hence, show that the percentage error in depth is numerically equal to the percentage error in disparity. What does this result mean in practical terms? How does the pixellation of the image affect the result?
2. A cylindrical vase with a circular cross section of local radius  $a$  is viewed by two cameras (Fig. 19.6). Obtain a formula giving the error  $\delta$  in the estimated position of the boundary of the vase. Simplify the calculation by assuming that the boundary is on the perpendicular bisector of the line joining the centers of projection of the two cameras, and hence find  $\alpha$  (Fig. 19.6) in terms of  $b$  and  $Z$ . Determine  $\delta$  in terms of  $\alpha$  and then substitute for  $\alpha$  from the previous formula. Hence, justify the statements made at the end of Section 19.14.
3. Discuss the potential advantages of trinocular vision in the light of the theory of Section 19.8. What would be the best placement for a third camera? Where should the third camera *not* be placed? Would any gain be achieved by incorporating even more views of a scene?

Motion is another aspect of 3D vision that humans are able to interpret with ease. This chapter studies the basic theoretical concepts: it is left to [Chapters 22 and 23](#) to apply them to real problems where motion is crucial, including the monitoring of traffic flow and the tracking of people.

*Look out for:*

- The basic concepts of optical flow, and its limitations
- The idea of a focus of expansion, and how it leads to the possibility of “structure from motion”
- How motion stereo is achieved
- The important status of the Kalman filter in motion applications
- The ways in which invariant features may be used for wide baseline matching.

Note that this introductory chapter on 3D motion leads to important methods for performing vital surveillance tasks—as will be seen in [Chapters 22 and 23](#).

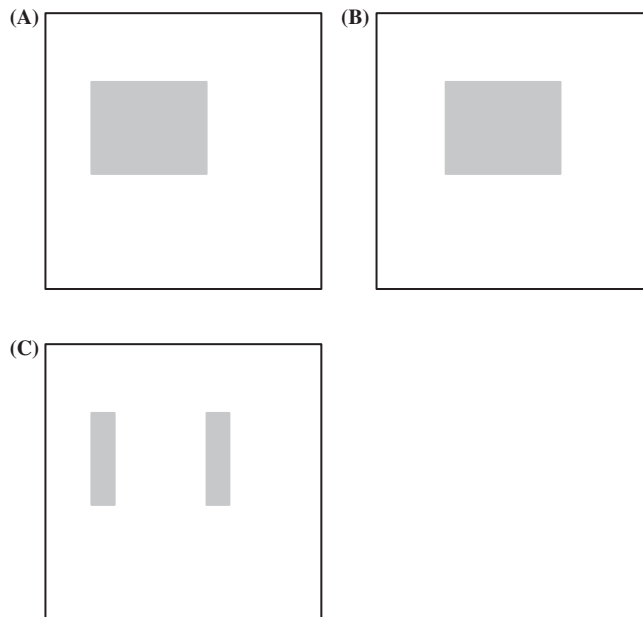
## 20.1 INTRODUCTION

This chapter is concerned with the analysis of motion in digital images. In the space available, it will not be possible to cover the whole subject comprehensively: Instead the aim will be to give the flavor of the subject, airing some of the principles that have proved important over the past two or three decades. Over much of this time, optical flow has been topical: It is appropriate to study it in fair detail, because of its importance for surveillance and other applications. Later in the chapter, the use of the Kalman filter for tracking moving objects will be discussed, and the use of invariant features such as SIFT for wide baseline matching, also relevant to motion tracking, will be covered.

## 20.2 OPTICAL FLOW

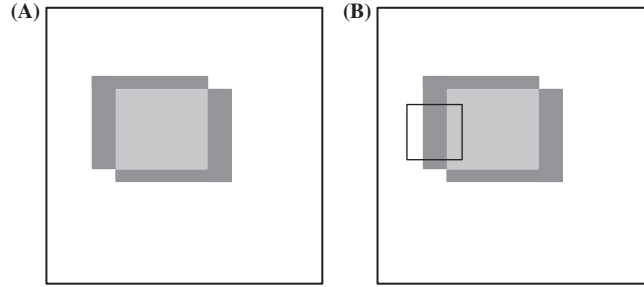
When scenes contain moving objects, analysis is necessarily more complex than for scenes where everything is stationary, since temporal variations in intensity have to be taken into account. However, intuition suggests that it should be possible—even straightforward—to segment moving objects by virtue of their motion: Image differencing over successive pairs of frames should permit this to be achieved. More careful consideration shows that things are not quite so simple, as illustrated in Fig. 20.1. The reason is that regions of constant intensity give no sign of motion, while edges parallel to the direction of motion also give the appearance of not moving: only edges with a component normal to the direction of motion carry information about the motion. In addition, there is some ambiguity in the direction of the velocity vector. This arises partly because there is too little information available within a small aperture to permit the full velocity vector to be computed (Fig. 20.2): This is hence called the *aperture problem*.

These elementary ideas can be taken further, and they lead to the notion of optical flow, wherein a local operator which is applied at all pixels in the image



**FIGURE 20.1**

Effect of image differencing. This figure shows an object which has moved between frames (A) and (B). (C) shows the result of performing an image differencing operation. Note that the edges parallel to the direction of motion do not show up in the difference image. Also, regions of constant intensity give no sign of motion.

**FIGURE 20.2**

The aperture problem. This figure illustrates the aperture problem. (A) shows (dark gray) regions of motion of an object whose central uniform region (light gray) gives no sign of motion. (B) shows how little is visible in a small aperture (black border), thereby leading to ambiguity in the deduced direction of motion of the object.

will lead to a motion vector field which varies smoothly over the whole image. The attraction lies in the use of a local operator, with its limited computational burden. Ideally, it would have an overhead comparable to an edge detector in a normal intensity image—though clearly, it will have to be applied locally to pairs of images in an image sequence.

We start by considering the intensity function  $I(x, y, t)$  and expanding it in a Taylor series:

$$I(x + dx, y + dy, t + dt) = I(x, y, t) + I_x dx + I_y dy + I_t dt + \dots \quad (20.1)$$

where second and higher order terms have been ignored. In this formula,  $I_x$ ,  $I_y$ ,  $I_t$  denote respective partial derivatives with respect to  $x$ ,  $y$ , and  $t$ .

We next set the local condition that the image has shifted by amount  $(dx, dy)$  in time  $dt$  so that it is functionally identical at  $(x + dx, y + dy, t + dt)$  and  $(x, y, t)$ :

$$I(x + dx, y + dy, t + dt) = I(x, y, t) \quad (20.2)$$

Hence, we can deduce:

$$I_t = - (I_x \dot{x} + I_y \dot{y}) \quad (20.3)$$

Writing the local velocity  $\mathbf{v}$  in the form:

$$\mathbf{v} = (v_x, v_y) = (\dot{x}, \dot{y}) \quad (20.4)$$

we find:

$$I_t = - (I_x v_x + I_y v_y) = - \nabla I \cdot \mathbf{v} \quad (20.5)$$

$I_t$  can be measured by subtracting pairs of images in the input sequence, while  $\nabla I$  can be estimated by Sobel or other gradient operators. Hence, it should be possible to deduce the velocity field  $\mathbf{v}(x, y)$  using the above equation. Unfortunately, this equation is a scalar equation and will not suffice for determining the two



local components of the velocity field as we require. There is a further problem with this equation—that the velocity value will depend on the values of both  $I_t$  and  $\nabla I$ , and these quantities are only estimated approximately by the respective differencing operators: In both cases, significant noise will arise, and this will be exacerbated by taking the ratio in order to calculate  $\mathbf{v}$ .

Let us now return to the problem of computing the full velocity field  $\mathbf{v}(x, y)$ . All we know about  $\mathbf{v}$  is that its components lie on the following line in  $(v_x, v_y)$  space (Fig. 20.3):

$$I_x v_x + I_y v_y + I_t = 0 \quad (20.6)$$

This line is normal to the direction  $(I_x, I_y)$  and has a distance from the (velocity) origin which is equal to

$$|\mathbf{v}| = -I_t / (I_x^2 + I_y^2)^{1/2} \quad (20.7)$$

Clearly, we need to deduce the component of  $\mathbf{v}$  along the line given by Eq. (20.6). However, there is no purely local means of achieving this with first derivatives of the intensity function. The accepted solution (Horn and Schunck, 1981) is to use relaxation labeling to arrive iteratively at a self-consistent solution

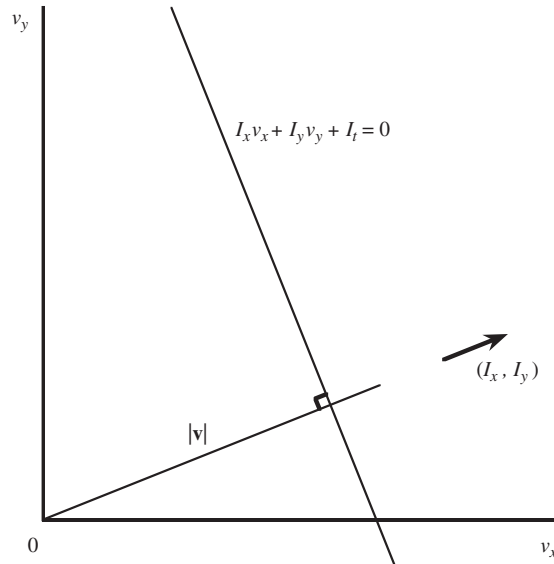


**FIGURE 20.3**

Computation of the velocity field. This graph shows the line in velocity space on which the velocity vector  $\mathbf{v}$  must lie. The line is normal to the direction  $(I_x, I_y)$  and its distance from the origin is known to be  $|\mathbf{v}|$  (see text).

which minimizes the global error. In principle, this approach will also minimize the noise problem indicated earlier.

In fact, there are still problems with the method. Essentially, these arise as there are liable to be vast expanses of the image where the intensity gradient is low. In that case, only very inaccurate information is available about the velocity component parallel to  $\nabla I$ , and the whole problem becomes ill-conditioned. On the other hand, in a highly textured image, this situation should not arise (assuming that the texture has a large enough grain size to give good differential signals).

Finally, we return to the idea mentioned at the beginning of this section—that edges parallel to the direction of motion would not give useful motion information. Such edges will have edge normals normal to the direction of motion, so  $\nabla I$  will be normal to  $\mathbf{v}$ . Thus, from Eq. (20.5),  $I_t$  will be zero. In addition, regions of constant intensity will have  $\nabla I = 0$ , so again  $I_t$  will be zero. It is interesting and highly useful that such a simple Eq. (20.5) embodies all the cases that were suggested earlier on the basis of intuition.

In what follows we assume that the optical flow (velocity field) image has been computed satisfactorily, i.e., without the disadvantages of inaccuracy or ill-conditioning. It must now be interpreted in terms of moving objects and in some cases a moving camera. In fact, we shall ignore motion of the camera by remaining within its frame of reference.

---

## 20.3 INTERPRETATION OF OPTICAL FLOW FIELDS

We start by considering a case where no motion is visible. In that case, the velocity field image contains only vectors of zero length (Fig. 20.4A). Next, we take a case where one object is moving towards the right, with a simple effect on the velocity field image (Fig. 20.4B). Next, we consider the case where the camera is moving forwards; in this case, all the stationary objects in the field of view appear to be diverging from a point which is called the *focus of expansion* (FoE)—see Fig. 20.4C; this image also shows an object which is moving rapidly past the camera, and which has its own separate FoE. Fig. 20.4D shows the case of an object moving directly towards the camera: In this case, its FoE lies within its outline. Similarly, objects which are receding appear to move away from the *focus of contraction*. Next, there are objects which are stationary but which are rotating about the line of sight: For these, the vector field appears as in Fig. 20.4E. There is a final case which is also quite simple—that of an object which is stationary but rotating about an axis normal to the line of sight; if the axis is horizontal, then the features on the object will appear to be moving up or down, while paradoxically the object itself remains stationary (Fig. 20.4F)—though its outline could oscillate as it rotates.

So far, we have only dealt with cases in which pure translational or pure rotational motion is occurring. If a rotating meteor is rushing past, or a spinning cricket

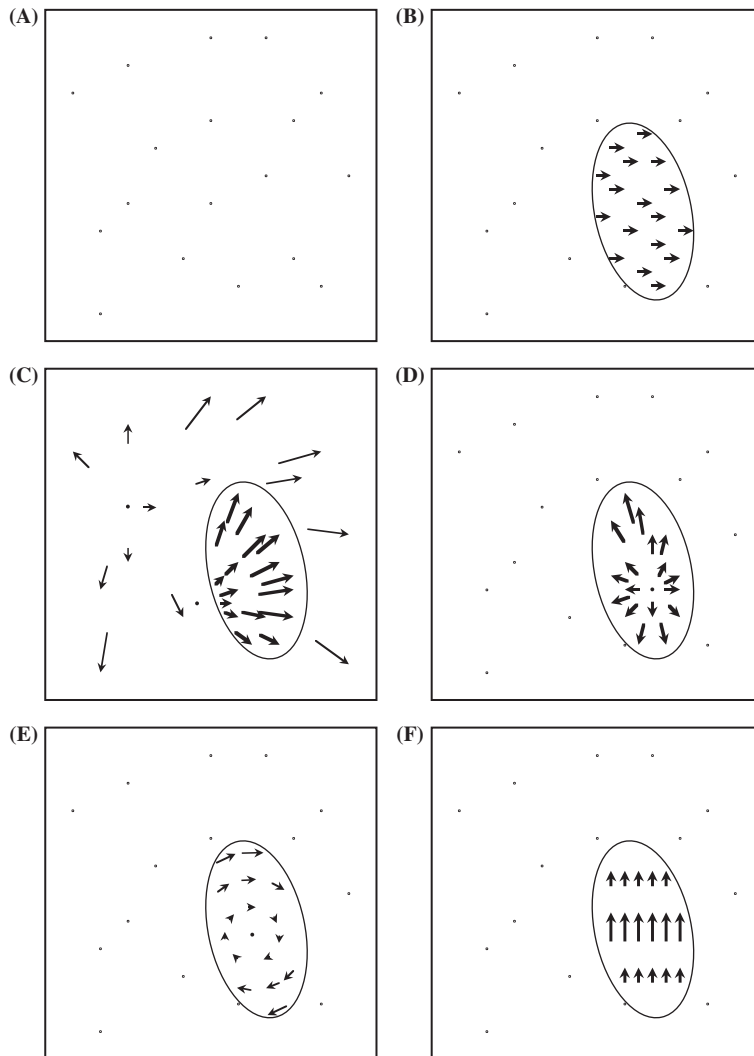


**FIGURE 20.4**

Interpretation of velocity flow fields. (A) shows a case where the object features all have zero velocity. (B) depicts a case where an object is moving to the right. (C) shows a case where the camera is moving into the scene, and the stationary object features appear to be diverging from a focus of expansion (FOE), while a single large object is moving past the camera and away from a separate FOE. In (D), an object is moving directly towards the camera which is stationary: The object's FOE lies within its outline. In (E), an object is rotating about the line of sight to the camera, and in (F), the object is rotating about an axis perpendicular to the line of sight. In all cases, the length of the arrow indicates the magnitude of the velocity vector.

ball is approaching, then both types of motion will occur together. In that case, unraveling the motion will be far more complex. We shall not solve this problem here but refer the reader to more specialized texts (e.g., Maybank, 1992). However, the complexity is due to the way depth ( $Z$ ) creeps into the calculations. First, note that pure rotational motion with rotation about the line of sight does not depend on  $Z$ : All we have to measure is the angular velocity, and this can be done quite simply.

## 20.4 USING FOCUS OF EXPANSION TO AVOID COLLISION

We now take a simple case in which a FoE is located in an image and show how it is possible to deduce the distance of closest approach of the camera to a fixed object of known coordinates. This type of information is valuable for guiding robot arms or robot vehicles and helping to avoid collisions.

In the notation of [Chapter 16](#), *The Three-Dimensional World*, we have the following formulae for the location of an image point ( $x, y, z$ ) resulting from a world point ( $X, Y, Z$ ):

$$x = fX/Z \quad (20.8)$$

$$y = fY/Z \quad (20.9)$$

$$z = f \quad (20.10)$$

Assuming that the camera has a motion vector  $(-\dot{X}, -\dot{Y}, -\dot{Z}) = (-u, -v, -w)$ , fixed world points will have velocity  $(u, v, w)$  relative to the camera. Now, a point  $(X_0, Y_0, Z_0)$  will after a time  $t$  appear to move to  $(X, Y, Z) = (X_0 + ut, Y_0 + vt, Z_0 + wt)$  with image coordinates:

$$(x, y) = \left( \frac{f(X_0 + ut)}{Z_0 + wt}, \frac{f(Y_0 + vt)}{Z_0 + wt} \right) \quad (20.11)$$

and as  $t \rightarrow \infty$ , this approaches the FoE  $F(fu/w, fv/w)$ . This point is in the image, but the true interpretation is that the actual motion of the center of projection of the imaging system is towards the point:

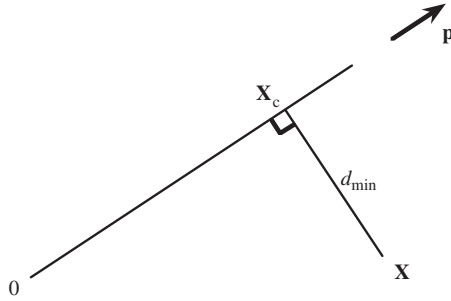
$$\mathbf{p} = (fu/w, fv/w, f) \quad (20.12)$$

(This is of course consistent with the motion vector  $(u, v, w)$  assumed initially.) The distance moved during time  $t$  can now be modeled as

$$\mathbf{X}_c = (X_c, Y_c, Z_c) = \alpha t \mathbf{p} = f\alpha t(u/w, v/w, 1) \quad (20.13)$$

where  $\alpha$  is a normalization constant. To calculate the distance of closest approach of the camera to the world point  $\mathbf{X} = (X, Y, Z)$ , we merely specify that the vector  $\mathbf{X}_c - \mathbf{X}$  be perpendicular to  $\mathbf{p}$  ([Fig. 20.5](#)) so that

$$(\mathbf{X}_c - \mathbf{X}) \cdot \mathbf{p} = 0 \quad (20.14)$$

**FIGURE 20.5**

Calculation of distance of closest approach. Here, the camera is moving from 0 to  $\mathbf{X}_c$  in the direction  $\mathbf{p}$ , not in a direct line to the object at  $\mathbf{X}$ .  $d_{\min}$  is the distance of closest approach.

That is,

$$(\alpha t \mathbf{p} - \mathbf{X}) \cdot \mathbf{p} = 0 \quad (20.15)$$

$$\therefore \alpha t \mathbf{p} \cdot \mathbf{p} = \mathbf{X} \cdot \mathbf{p} \quad (20.16)$$

$$\therefore t = (\mathbf{X} \cdot \mathbf{p}) / \alpha(\mathbf{p} \cdot \mathbf{p}) \quad (20.17)$$

Substituting in the equation for  $\mathbf{X}_c$  now gives:

$$\mathbf{X}_c = \mathbf{p}(\mathbf{X} \cdot \mathbf{p}) / (\mathbf{p} \cdot \mathbf{p}) \quad (20.18)$$

Hence, the minimum distance of approach is given by

$$\begin{aligned} d_{\min}^2 &= \left[ \frac{\mathbf{p}(\mathbf{X} \cdot \mathbf{p})}{(\mathbf{p} \cdot \mathbf{p})} - \mathbf{X} \right]^2 = \frac{(\mathbf{X} \cdot \mathbf{p})^2}{(\mathbf{p} \cdot \mathbf{p})} - \frac{2(\mathbf{X} \cdot \mathbf{p})^2}{(\mathbf{p} \cdot \mathbf{p})} + (\mathbf{X} \cdot \mathbf{X}) \\ &= (\mathbf{X} \cdot \mathbf{X}) - \frac{(\mathbf{X} \cdot \mathbf{p})^2}{(\mathbf{p} \cdot \mathbf{p})} \end{aligned} \quad (20.19)$$

which is naturally zero when  $\mathbf{p}$  is aligned along  $\mathbf{X}$ . Clearly, avoidance of collisions requires an estimate of the size of the machine (e.g., robot or vehicle) attached to the camera and the size to be associated with the world point feature  $\mathbf{X}$ . Finally, note that while  $\mathbf{p}$  is obtained from the image data,  $\mathbf{X}$  can only be deduced from the image data if the depth  $Z$  can be estimated from other information. In fact, this information should be available from time-to-adjacency analysis (see below) if the speed of the camera through space (and specifically  $w$ ) is known.

## 20.5 TIME-TO-ADJACENCY ANALYSIS

Next, we consider the extent to which the depths of objects can be deduced from optical flow. First, note that features on the same object share the same FoE, and this can help us to identify them. But how can we get information on the depths

of the various features on the object from optical flow? The basic approach is to start with the coordinates of a general image point  $(x, y)$ , deduce its flow velocity, and then find an equation linking this with the depth  $Z$ .

Taking the general image point  $(x, y)$  given in Eq. (20.11), we find:

$$\begin{aligned}\dot{x} &= f[(Z_0 + wt)u - (X_0 + ut)w]/(Z_0 + wt)^2 \\ &= f(Zu - Xw)/Z^2\end{aligned}\quad (20.20)$$

and

$$\dot{y} = f(Zv - Yw)/Z^2 \quad (20.21)$$

Hence:

$$\begin{aligned}\dot{x}/\dot{y} &= (Zu - Xw)/(Zv - Yw) = (u/w - X/Z)/(v/w - Y/Z) \\ &= (x - x_F)/(y - y_F)\end{aligned}\quad (20.22)$$

This result was to be expected, as the motion of the image point has to be directly away from the FoE  $(x_F, y_F)$ . With no loss of generality, we now take a set of axes such that the image point considered is moving along the  $x$ -axis. Then, we have:

$$\dot{y} = 0 \quad (20.23)$$

$$y_F = y = fY/Z \quad (20.24)$$

Defining the distance from the FoE as  $\Delta r$  (see Fig. 20.6), we find:

$$\Delta r = \Delta x = x - x_F = fX/Z - fu/w = f(Xw - Zu)/Zw \quad (20.25)$$

$$\therefore \Delta r/\dot{r} = \Delta x/\dot{x} = -Z/w \quad (20.26)$$

What this equation means is that the *time to adjacency*, when the origin of the camera coordinate system will arrive at the object point, is the same ( $Z/w$ ) when seen in real-world coordinates as when seen in image coordinates ( $-\Delta r/\dot{r}$ ). Hence, it is possible to relate the optical flow vectors for object points at different depths in the scene. This is important, as the assumption of identical values of  $w$  now allows us to determine the relative depths of object points merely from their apparent motion parameters:

$$\frac{Z_1}{Z_2} = \frac{\Delta r_1/\Delta r_2}{\dot{r}_1/\dot{r}_2} \quad (20.27)$$

This is thus the first step in the determination of structure from motion. In this context, note how the implicit assumption that the objects under observation are rigid is included—namely that all points on the same object are characterized by identical values of  $w$ . The assumption of rigidity underlies much of the work on interpretation of motion in images.

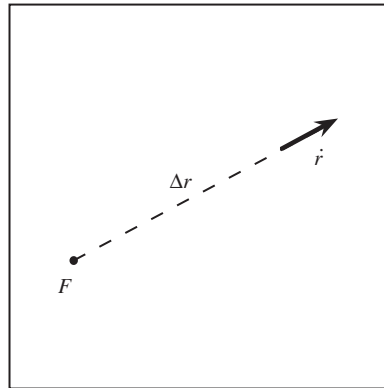


**FIGURE 20.6**

Calculation of time to adjacency. Here, an object feature is moving directly away from the focus of expansion  $F$  with speed  $\dot{r}$ . At the time of observation, the distance of the feature from  $F$  is  $\Delta r$ . These measurements permit the time to adjacency and hence also the relative depth of the feature to be calculated.

## 20.6 BASIC DIFFICULTIES WITH THE OPTICAL FLOW MODEL

When the optical flow ideas presented above are tried on real images, certain problems arise which are not apparent from the above model. First, not all edge points which should appear in the motion image are actually present. This is due to the contrast between the moving object and the background vanishing locally and limiting visibility. The situation is exactly as for edges which are located by edge-detection operators in nonmoving images: The contrast simply drops to a low value in certain localities and the edge peters out. This signals that the edge model, and now the velocity flow model, is limited and such local procedures are ad hoc and too impoverished to permit proper segmentation unaided.

Here, we take the view that simple models can be useful, but they become inadequate on certain occasions and robust methods are required to overcome the problems that then arise. Some of the problems were noticed by Horn as early as 1986. First, a smooth sphere may be rotating but the motion will not show up in an optical flow (difference) image. We can if we wish regard this as a simple optical illusion, as the rotation of the sphere may well be invisible to the eye too. Second, a motionless sphere may *appear* to rotate as the light rotates around it: The object is simply subject to the laws of Lambertian optics, and again we may if we wish regard this effect as an optical illusion. (The illusion is relative to the baseline provided by the *normally correct* optical flow model.)

We next return to the optical flow model and see where it could be wrong or misleading. The answer is at once apparent: We stated in writing Eq. (20.2) that

we were assuming that the *image* is being shifted. Yet, it is not images that shift but the objects imaged within them. Thus, we ought to be considering the images of objects moving against a fixed background (or a variable background if the camera is moving). This will then permit us to see how sections of the motion edge can go from high to low contrast and back again in a rather fickle way, which we must nevertheless allow for in our algorithms. With this in mind, it should be permissible to go on using optical flow and difference imaging, even though these concepts have distinctly limited theoretical validity. (For a more thoroughgoing analysis of the underlying theory, see Faugeras, 1993.)

---

## 20.7 STEREO FROM MOTION

An interesting aspect of camera motion is that over time, the camera sees a succession of images that span a baseline in a similar way to binocular (stereo) images. Thus, it should be possible to obtain depth information by taking two such images and tracking object features between them. The technique is in principle more straightforward than normal stereo imaging in that feature tracking is possible, so the correspondence problem should be nonexistent. However, there is a difficulty in that the object field is viewed from almost the same direction in the succession of images so that the full benefit of the available baseline is not obtained (Fig. 20.7). We can analyze the effect as follows:

First, in the case of camera motion, the equations for lateral displacement in the image depend not only on  $X$  but also on  $Y$ , though we can make a simplification in the theory by working with  $R$ , the radial distance of an object point from the optical axis of the camera, where

$$R = (X^2 + Y^2)^{1/2} \quad (20.28)$$

We now obtain the radial distances in the two images as

$$r_1 = Rf/Z_1 \quad (20.29)$$

$$r_2 = Rf/Z_2 \quad (20.30)$$

So, the disparity is

$$D = r_2 - r_1 = Rf(1/Z_2 - 1/Z_1) \quad (20.31)$$

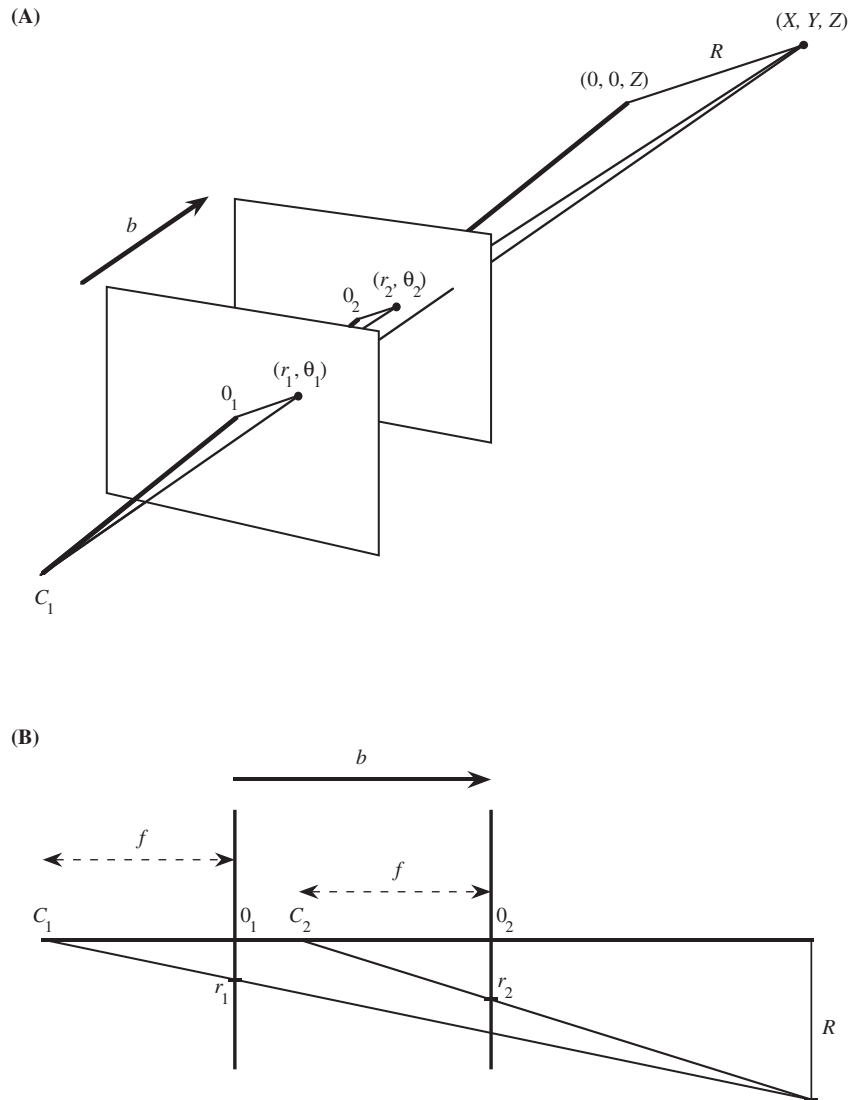
Writing the baseline as

$$b = Z_1 - Z_2 \quad (20.32)$$

and assuming that  $b \ll Z_1, Z_2$ , and then dropping the suffices, gives

$$D = Rbf/Z^2 \quad (20.33)$$



**FIGURE 20.7**

Calculation of stereo from camera motion. (A) shows how stereo imaging can result from camera motion, the vector  $\mathbf{b}$  representing the baseline. (B) shows the simplified planar geometry required to calculate the disparity. It is assumed that the motion is directly along the optical axis of the camera.

While this would appear to mitigate against finding  $Z$  without knowing  $R$ , we can overcome this problem by observing that

$$R/Z = r/f \quad (20.34)$$

where  $r$  is approximately the mean value  $\frac{1}{2}(r_1 + r_2)$ . Substituting  $R$  now gives

$$D = br/Z \quad (20.35)$$

Hence, we can deduce the depth of the object point as

$$Z = br/D = br/(r_2 - r_1) \quad (20.36)$$

This equation should be compared with Eq. (15.5) representing the normal stereo situation. The important point to note is that for motion stereo, the disparity depends on the radial distance  $r$  of the image point from the optical axis of the camera, whereas for normal stereo, the disparity is independent of  $r$ ; as a result, motion stereo gives no depth information for points on the optical axis, and the accuracy of depth information depends on the magnitude of  $r$ .

---

## 20.8 THE KALMAN FILTER

When tracking moving objects, it is desirable to be able to predict where they will be in future frames, as this will make maximum use of preexisting information and permit the least amount of search in the subsequent frames. It will also serve to offset the problems of temporary occlusion, such as when one vehicle passes behind another, or one person passes behind another, or even when one limb of a person passes behind another. (There are also many military needs for tracking prediction, and others on the sports field.) The obvious equations to employ for this purpose involve sequentially updating the position and the velocity of points on the object being tracked:

$$x_i = x_{i-1} + v_{i-1} \quad (20.37)$$

$$v_i = x_i - x_{i-1} \quad (20.38)$$

assuming for convenience a unit time interval between each pair of samples.

In fact, this approach is too crude to yield the best results. First, it is necessary to make three quantities explicit: (1) the raw measurements (e.g.,  $x$ ), (2) the best estimates of the values of the corresponding variables *before* observation (denoted by “−”), and (3) the best estimates of these same model parameters *following* observation (denoted by “+”). In addition, it is necessary to include explicit noise terms so that rigorous optimization procedures can be derived for making the best estimates.

In the particular case outlined above, the velocity—and possible variations on it which we shall ignore here for simplicity—constitutes a best estimate model parameter. We include position measurement noise by the parameter  $u$  and

velocity (model) estimation noise by the parameter  $w$ . The above equations now become

$$x_i^- = x_{i-1}^+ + v_{i-1} + u_{i-1} \quad (20.39)$$

$$v_i^- = v_{i-1}^+ + w_{i-1} \quad (20.40)$$

In the case that the velocity is constant and the noise is Gaussian, we can spot the optimum solutions to this problem:

$$x_i^- = x_{i-1}^+ \quad (20.41)$$

$$\sigma_i^- = \sigma_{i-1}^+ \quad (20.42)$$

these being called the *prediction* equations, and

$$x_i^+ = \frac{x_i/\sigma_i^2 + (x_i^-)/(\sigma_i^-)^2}{1/\sigma_i^2 + 1/(\sigma_i^-)^2} \quad (20.43)$$

$$\sigma_i^+ = \left[ \frac{1}{1/\sigma_i^2 + 1/(\sigma_i^-)^2} \right]^{1/2} \quad (20.44)$$

these being called the *correction* equations: these are nothing more than the well-known equations for weighted averages (Cowan, 1998). In these equations,  $\sigma^\pm$  are the standard deviations for the respective model estimates  $x^\pm$ , and  $\sigma$  is the standard deviation for the raw measurement  $x$ .

What these equations show is how repeated measurements improve the estimate of the position parameter and the error upon it at each iteration. Notice the particularly important feature—that the noise is being modeled as well as the position itself. This permits all positions earlier than  $i - 1$  to be forgotten. The fact that there were many such positions, whose values can all be averaged to improve the accuracy of the latest estimate, is of course rolled up into the values of  $x_i^-$  and  $\sigma_i^-$ , and eventually into the values for  $x_i^+$  and  $\sigma_i^+$ .

The next problem is how to generalize this result, both to multiple variables and to possibly varying velocity and acceleration. This is the function of the widely used Kalman filter. It achieves this by continuing with a linear approximation and by employing a state vector comprising position, velocity, and acceleration (or other relevant parameters), all in one state vector  $\mathbf{s}$ . This constitutes the dynamic model. The raw measurements  $x$  have to be considered separately.

In the general case, the state vector is not updated simply by writing:

$$\mathbf{s}_i^- = \mathbf{s}_{i-1}^+ \quad (20.45)$$

but requires a fuller exposition because of the interdependence of position, velocity, and acceleration; hence, we have:

$$\mathbf{s}_i^- = K_i \mathbf{s}_{i-1}^+ \quad (20.46)$$

Some authors write  $K_{i-1}$  in this equation, but it is only a matter of definition whether the label matches the previous or the new state. Similarly, the standard

deviations  $\sigma_i$ ,  $\sigma_i^\pm$  in Eqs. (20.42)–(20.44) (or rather, the corresponding variances) have to be replaced by the covariance matrices  $\Sigma_i$ ,  $\Sigma_i^\pm$ , and the equations become significantly more complicated. We will not go into the calculations fully here as they are nontrivial and need several pages to iterate. Suffice it to say that the aim is to produce an optimum linear filter by a least-squares calculation (see, e.g., Maybeck, 1979).

Overall, the Kalman filter is the optimal estimator for a linear system for which the noise is zero mean, white and Gaussian, though it will often provide good estimates even if the noise is not Gaussian.

Finally, it will be noticed that the Kalman filter itself works by averaging processes which will give erroneous results if any outliers are present. This will certainly occur in most motion applications. Thus, there is a need to test each prediction to determine if it is too far away from reality. If this is the case, it is not unlikely that the object in question has become partially or fully occluded: A simple option is to assume that the object continues in the same motion (albeit with a larger uncertainty as time goes on), and to wait for it to emerge from behind another object. At the very least, it is prudent to keep a number of such possibilities alive for some time, but the extent of this will naturally vary from situation to situation and from application to application.

---

## 20.9 WIDE BASELINE MATCHING

The need for wide baseline matching was noted in [Chapter 6](#), Corner, Interest Point and Invariant Feature Detection, where considerable discussion was included on detection of suitable invariant features (see [Section 6.7](#) and its various subsections). The topic has been left until the present chapter, because it is relevant for both 3D vision and motion analysis, and the latter topic has only been covered in this chapter. The wide baseline scenario arises from situations where the same object is viewed from widely different directions, with the result that its appearance may change dramatically so that it may become extremely difficult to recognize. While narrow baseline stereo is the norm for depth estimation using two cameras, wide baselines are common in surveillance applications—e.g., where a pedestrian precinct is viewed by several independent cameras that are widely separated, as described in [Chapter 22](#), Surveillance. They are also the norm when objects are being sought in image databases. However, one of the most likely situations when they occur is with objects that are in motion. While this may appear to be immaterial in surveillance or with driver assistance systems, because every pair of frames will give instances of narrow baseline stereo, it can easily happen that objects will be *temporarily occluded* and come back into view with different orientations or backgrounds; in addition, the *attention* of the software (like that of a human operator) may only be on part of the scene for part of the time. Hence, wide baseline viewing is bound to be a common consequence of motion. Overall, then, wide baseline matching techniques will be needed in a variety of instances of 3D viewing and motion tracking.

Chapter 6, Corner, Interest Point, and Invariant Feature Detection showed how features could be designed to cover a variety of wide baseline views as far apart as  $50^\circ$ . In these circumstances, an important factor in designing suitable feature detectors is to make them invariant to scale and affine distortions. However, that alone is not enough: The feature detectors must also provide descriptors of each feature that are sufficiently rich in information that matching between views is made as unambiguous as possible. In that way, wide baseline matching has a chance of being highly reliable. Lowe (2004) has found that reliable recognition of objects is possible with as few as three features. Indeed, it is highly important to aim to achieve this when images typically contain several thousand features which come from many different objects as well as background clutter. In this way, the number of false positives is reduced to minimal levels, and there is a high chance of detecting all objects of the chosen type in the input image. That this can be possible is underlined by the richness of Lowe's SIFT features whose descriptors contain 128 parameters. (As discussed in Chapter 6: Corner, Interest Point, and Invariant Feature Detection, features devised by other workers may contain fewer parameters, but in the end risk not working in all possible scenarios.)

Granted that wide baseline matching is desirable, and that SIFT and other features have rich descriptor sets, how should the matching actually be achieved? Ideally, all that is necessary is to compare the feature descriptors from each pair of images and find which ones match well, and which therefore lead to corecognition of objects in the two views. Clearly, the first requirement is a similarity test for pairs of features. Lowe (2004) achieved this using a nearest neighbor (Euclidean) distance measure in his 128-dimensional descriptor space. He then used a Hough transform to identify clusters of features giving the same interpretations of poses for objects appearing in the two images. Because of the relatively small number of inliers that may occur in this type of situation, he found that the Hough transform approach performed significantly better than RANSAC. Mikolajczyk and Schmid (2004) used a Mahalanobis distance measure for selecting the most similar descriptors to obtain a set of initial matches; they then used cross correlation to reject low-score matches; finally, they performed a robust estimation of the transformation between the two images using RANSAC. Tuytelaars and Van Gool (2004) developed this further, using semi-local constraints involving geometric consistency and photometric constraints to refine the selection of matches before (again) relying on RANSAC to perform the final robust estimation of poses. In contrast to the approaches outlined above, Bay et al. (2008) fed the descriptor information to a naïve Bayes classifier working on a "bag-of-words" representation (Dance et al., 2004) in order to perform object recognition. Bay et al. (2008) make no mention of determination of object pose in this application, which was targeted more at recognizing objects in an image database—though it could equally well have been targeted at repeated recognition of cars on the road, for which pose would not be especially relevant.

Overall, it is clear that the new regime of utilizing invariant feature detectors with rich descriptors of local image content forms a powerful approach to wide baseline object matching and takes much of the heat out of the subsequent algorithms.

---

## 20.10 CONCLUDING REMARKS

Early in this chapter, we described the formation of optical flow fields and showed how a moving object or a moving camera leads to a FoE. In the case of moving objects, the FoE can be used to decide whether a collision will occur. In addition, analysis of the motion taking account of the position of the FoE led to the possibility of determining structure from motion. Specifically, this can be achieved via time-to-adjacency analysis, which yields the relative depth in terms of the motion parameters measurable directly from the image. We then went on to demonstrate some basic difficulties with the optical flow model, which arise since the motion edge can have a wide range of contrast values, making it difficult to measure motion accurately. In practice, this means that larger time intervals may have to be employed to increase the motion signal. Otherwise, feature-based processing related to that of [Chapter 11](#), The Generalized Hough Transform can be used. Corners are the features which are the most widely used for this purpose, because of their ubiquity and because they are highly localized in 3D. Space prevents details of this approach from being described here: Details may be found in Barnard and Thompson (1980), Scott (1988), Shah and Jain (1984), and Ullman (1979). However, the value of the Kalman filter for alleviating the difficulties of temporary occlusion has been considered, and the use of invariant features for wide baseline matching (which includes motion tracking applications) has been covered.

Further work on motion as it arises in real applications will be dealt with in [Chapters 22 and 23](#), which address the problems of surveillance and in-vehicle vision systems.

*The obvious way to understand motion is by image differencing and determination of optical flow. This chapter has shown that the “aperture problem” is a difficulty that is avoidable by using corner tracking. Further difficulties are caused by temporary occlusions, thus necessitating techniques such as occlusion reasoning and Kalman filtering.*

---

## 20.11 BIBLIOGRAPHICAL AND HISTORICAL NOTES

Optical flow has been investigated by many workers over a good many years: See, e.g., Horn and Schunck (1981) and Heikkonen (1995). A definitive account of the mathematics relating to FoE appeared in 1980 (Longuet-Higgins and Prazdny, 1980). In fact, foci of expansion can be obtained either from the optical flow field or directly (Jain, 1983). The results of [Section 20.5](#) on time-to-adjacency analysis stem originally from the work of Longuet-Higgins and Prazdny (1980) which provides some deep insights into the whole problem of optical flow and the possibilities of using its shear components. Note that numerical solution of the velocity

field problem is not trivial; typically, least-squares analysis is required to overcome the effects of measurement inaccuracies and noise, and to finally obtain the required position measurements and motion parameters (Maybank, 1986). Overall, resolving ambiguities of interpretation is one of the main problems and challenges of image sequence analysis [see Longuet-Higgins (1984) for an interesting analysis of ambiguity in the case of a moving plane].

Unfortunately, the substantial and important literature on motion, image sequence analysis, and optical flow, which impinges heavily on 3D vision, could not be discussed in detail here for reasons of space. For seminal work on these topics, see, e.g., Huang (1983), Jain (1983), Nagel (1983, 1986), and Hildreth (1984).

For early work on the use of Kalman filters for tracking, see Marslin et al. (1991). For the huge amount of more recent work on tracking and surveillance of moving objects, including the tracking of people and vehicles, see [Chapters 22 and 23](#) (in fact, [Chapter 23: In-Vehicle Vision Systems](#) is especially concerned with monitoring moving objects from within vehicles). For recent references on tracking, particle filters, and detection of moving objects, see the bibliographies in [Chapters 22 and 23](#).

For further references on invariant features for wide baseline matching, see [Chapter 6](#), Corner, Interest Point, and Invariant Feature Detection.

---

## 20.12 PROBLEM

1. Explain why, in [Eq. \(20.44\)](#), the variances are combined in this particular way (in most applications of statistics, variances are combined by addition).

# Putting computer vision to work

# 5

*Part 5 takes all the techniques that have been covered in Parts 1–4 of the book and looks at their use when Computer Vision is put to work in key practical applications. Evidently, Part 5 cannot cover all possible application areas, so three key areas were selected for special treatment, reflecting the global pressures and needs of Society and the intrinsic capabilities of Computer Vision in the state in which it exists today (i.e., taking into account all the techniques and methods covered in Parts 1–4).*

*Chapter 21, Face detection and recognition: the impact of deep learning, describes much of the progress made in the past two decades in the*



*important area of face detection and recognition. It includes a significant discussion of the impact of deep learning on facial analysis, and shows that the latter provides a prime vector for the explosive advances that have been made in deep learning since 2011–12.*

*The other two subjects covered in Part 5 are those of Surveillance and In-Vehicle Vision Systems, both of which have been developing ever more strongly over the past 15–20 years, with In-Vehicle Vision Systems currently being particularly in vogue with the advent of driverless vehicles. (Here the word “driverless” has to be taken lightly, (1) because most vehicles still retain drivers and (2) because making vehicles truly driverless tends to result in their being, or being felt to be, less reliable, whatever the future may hold.)*

# Face detection and recognition: the impact of deep learning

# 21

Face recognition is highly important in modern society and crucial in security applications. Similarly, detection of faces in scenes is a starting point in many practical situations. This chapter covers both areas, using contrasting methods such as principal components analysis (PCA) to obtain “eigenfaces” and “boosting” to locate faces extremely rapidly. However, these early methods are becoming marginalized, e.g., by the frontalization approach and by deep learning so that computers can attain human levels of successful recognition.

*Look out for:*

- What can be achieved using simple techniques for efficient face detection
- Detection of facial features such as eyes, nose, and mouth
- The Viola–Jones boosting face detector
- The eigenface approach to face recognition
- The use of frontalization for transforming faces to a standard frontal form
- How deep learning may be applied to face detection and recognition (FDR)
- How faces may be considered as parts of 3-D objects
- Use of invariance for initiating face recognition.

Although this chapter is especially involved with FDR, it is forced to consider the use of modern deep learning architectures. Although the latter was dealt with mainly in [Chapter 15](#), Deep Learning Networks, this chapter develops the ideas further and can be regarded as highlighting the practical issues: Indeed, by the end of the chapter, the impact of deep learning emerges much more clearly.

## 21.1 INTRODUCTION

Face detection has become important in many modern situations, ranging from crowd control to monitoring people entering a building. In many cases, face detection alone will be insufficient, and faces will need to be recognized or in

some cases verified, as when entering a bank vault or logging into a computer. It can be argued that the most basic need is that of face detection, as that can not only permit people to be counted but also initiate recognition. It can also be argued that the act of recognition necessarily includes detection; and that verification is an instance of recognition where there is only one person to be recognized. In the overall scheme of things, face detection is the simplest of these tasks. In principle, it can be automated by applying a matched filter based on an “average” face, which could, as implied, be obtained by averaging a large number of faces available in a database. However, huge complications would be involved in achieving this, because face images are liable to be taken in widely different lighting conditions, and because faces are unlikely to be taken frontally. Indeed, heads will have different positions and poses; so, even a fully frontal view may display heads differing in roll or pitch. As for ships, roll, pitch, and yaw are the three important angles to be controlled or allowed for when attempting face detection or recognition. Of course, there are situations in which face pose is controlled, such as when a passport or driving license photograph is being taken, though such cases must be regarded as exceptional. Finally, it must not be forgotten that faces are flexible objects: Not only can the jaws be moved, and the mouth and eyes opened or closed, but also very large numbers of facial expressions (and thus emotions) can be instigated. All these inter- and intraface variations make facial analysis and recognition a highly complex business, which is further complicated by varieties of facial and cranial hair, and by glasses, hats, and other apparel. Needless to say that all these factors have to be dealt with in efforts to recognize terrorists.

In this context, it is instructive to look at the many “faces in the wild” that have been extracted from Internet pictures. We shall examine some of these below—in particular, using examples from the well-known set of George W. Bush (Fig. 21.1). We now move on to see how face detection can be attempted using skin tones as the basic means of proceeding.

---

## 21.2 A SIMPLE APPROACH TO FACE DETECTION

The widely used “labeled faces in the wild” (LFW) datasets contain pictures that have been collected from the Internet and approximately centered and sized. For the most part, they show frontal faces with a relatively small range of 3-D roll, pitch, and yaw orientations—all typically within the range  $\pm 30^\circ$  (see e.g., Fig. 21.1). In this section, we consider how face detection can be performed with reasonable speed and efficiency. One obvious approach is to aim to detect skin tones using both color and intensity controls. In Fig. 21.1, we have attempted this using a simple hue and intensity range test: *hue* +180° has to be in the range  $180^\circ \pm 20^\circ$ , and intensity has to be in the range  $140 \pm 50$  (in an overall intensity range 0–255). This range was obtained empirically: In a complete practical

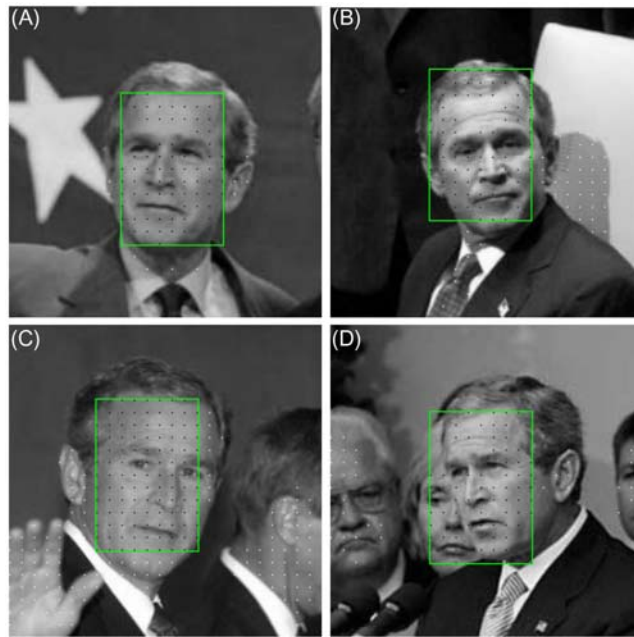


**FIGURE 21.1**

Face detection using a simple sampling approach. Here, four Bush faces (A–D) from the LFW database are detected using the simple sampling approach. First, skin tones are detected and recorded as white dots. Then, the best fit 2:3 aspect ratio bounding box is used to find the most likely face location. Within each best-fit box, white dots are changed to (inlier) black dots, and the remaining white dots indicate outliers. In cases (B) and (C), significant numbers of white dots remain, and in (C), they exceed the number of black dots. Note that the method actually indicates the best fit to skin tone regions rather than to faces as such: This is because the method does not include any specific within-face feature detection.

system, it would be determined by rigorous training. Here, it seemed appropriate to show what is possible with a simple schema.

In Fig. 21.1, processing was speeded up by sampling every 10th pixel in each direction. All pixels that have a skin tone signaled by the above test are marked with white dots. Next, a box with approximately 2:3 aspect ratio, corresponding roughly to LFW facial dimensions, is applied and the locations containing the greatest numbers of skin-tone signals are found: At this stage, the inlier dots are relabeled black, and the remaining white dots are regarded as outliers. In all four cases, the true faces are correctly found and labeled, and the decisions are not confused by the remaining outliers—even where they correspond to partial faces or other bright patches in the background. Clearly, the approach is robust and reasonably accurate: It is also very fast in operation as only every 100th pixel is

visited. The fact that the skin-tone detector is relatively crude and is not adapted to the individual faces seems not to matter. In fact, the most important parameter should be the box size. Oddly, this parameter is actually noncritical: It has been applied to a fair number of the LFW faces without any omissions occurring. Overall, the main problem is that this face detector will always find the object most akin to a face, even if there isn't one present. In this situation, the most obvious way forward would appear to be to find suitable facial feature detectors—such as eyes, ears, nose, or mouth—to verify that any face that is found is actually a face. Interestingly, though eyes are probably the features that are most widely used for this purpose, they are relatively indistinct in the pictures presented in Fig. 21.2, except perhaps for the last three. This makes it problematic to decide quite what features should be sought, and how accurately they could be detected.

---

### 21.3 FACIAL FEATURE DETECTION

Detection of faces via their skin tones can be unreliable, because (1) hands and other regions of the body can mimic faces, (2) clothes can have similar tones and colors, and (3) even background regions composed of sand or other materials can have similar tones and colors. Hence, alternative methods of face detection based on facial features or facial shapes can be used in place of those based simply on skin tones. In addition, they can be used *as well as* skin-tone region detection, to ensure that the overall approach is sufficiently robust.

Prominent amongst relevant facial features are eyes, nose, mouth, and ears—and their subfeatures such as corners. These can be detected by correlation using trained templates, as shown in Fig. 21.3 for eye detection. For reliability, such templates need to be quite small, to offset the problems of variability that plague face detection. As shown in Fig. 21.3, eyes can be detected separately, and the results combined adaptively, if they appear to correspond within sufficiently accurate limits. Clearly, combining detections of several features can be carried out not just for eyes but also for multiple features, though a priori information on how to achieve this sufficiently robustly may be lacking, especially in cases where degrees of roll, pitch, and yaw are large and unknown. Overall, perhaps the worst aspect of the multifeature approach is that a number of detectors need to be designed and trained and also that the fusion of the feature data can be even more difficult to manage and train. Note also that handling all these factors and complications can involve considerable computation. Thus, it is not too surprising that in recent years, this rather complex approach has become less evident in the literature. It was in this context that Viola and Jones (VJ) looked at the situation again and arrived at their innovative Haar filter-based approach, which is outlined in the following section.

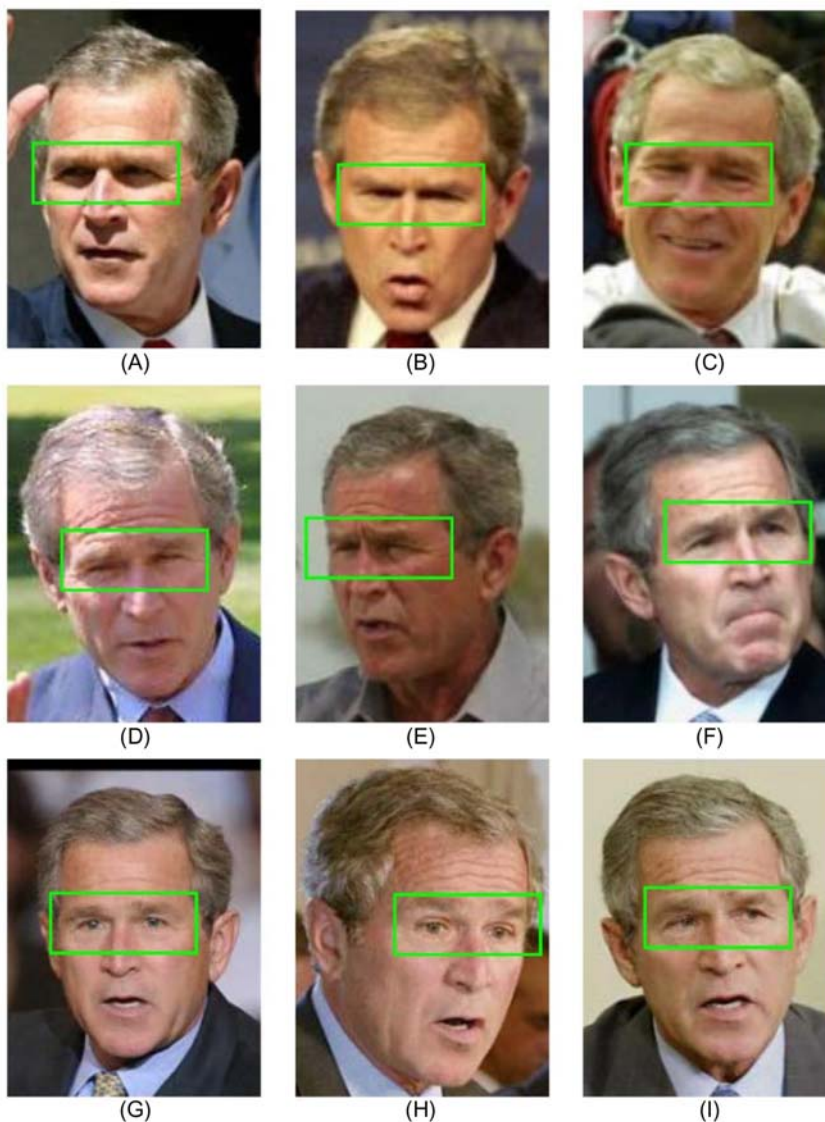


**FIGURE 21.2**

Variations in the eye regions for Bush LFW faces. In cases (A)–(E), there is strong shadow; so, it is impossible to apply obvious eye detectors—such as Hough transforms—based on iris detection. However, this starts becoming possible in cases (F)–(I), though it should be noted that the visible boundary of the iris in each of these cases is quite low (significantly less than 50%): At such low resolution, this becomes a problem. In addition, the well-known dark region around the eyes is almost completely absent in cases (G)–(I), making it difficult to locate the eyes reliably: In such cases, feature detectors for nose, mouth, or other features would also have to be employed.

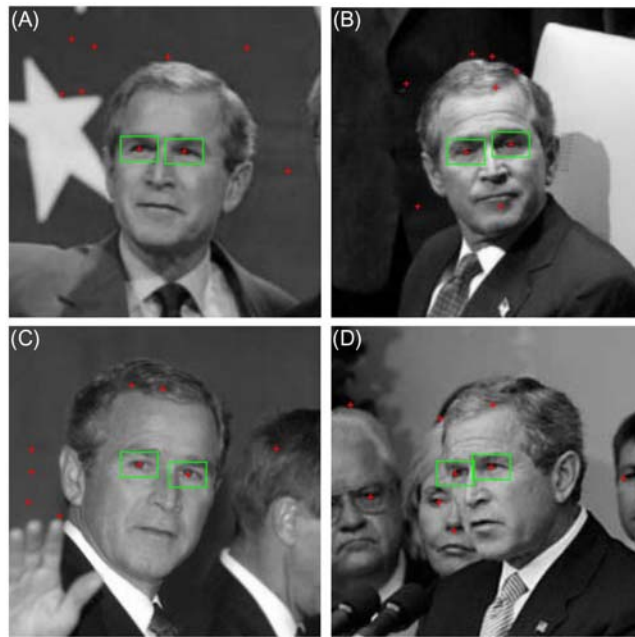


**FIGURE 21.3**

Detection of eye features. In these images (A–D), potential eye features are located using correlation with a trained eye template, the number recorded being limited to the nine most likely feature locations, these being marked with red crosses in each image. Then, a search is made for *pairs* of eye features that are within expected horizontal and vertical distance bounds (29 to 42 and  $\pm 8$  pixels, respectively), and the results are marked with green boxes. The box sizes indicate the size of the feature template used for eye detection. Note that many of the outliers arise from hidden likenesses in the hair and background, though in case (D), they also indicate isolated eyes from other people. Interestingly, the method copes well with faces exhibiting up to 20° roll and 30° yaw.

## 21.4 THE VIOLA–JONES APPROACH TO RAPID FACE DETECTION

The face detection problem outlined in the last section was analyzed in depth by Viola and Jones (2001). They decided on a totally new approach. First, they eschewed concentration on “obvious” features such as those mentioned above—viz. eyes, ears, nose, and mouth; in addition, they eschewed color and skin-tone detection, preferring to analyze faces in terms of intensity profile characteristics: Finally, they made no direct analysis of shape. What they sought above all was a set of features that worked in practice as a result of careful, sufficiently general

training on known datasets. For this reason, they decided to train the software system using Haar-like basis functions as general-purpose features. These had the possibility of locating relatively dark regions of the face: Indeed, it is often the case that the part of the face just below the eyebrows, which contains the eyes, is relatively shadowed and is significantly darker than the forehead or the region containing the nose and cheeks. Similarly, the part between the eyes is often significantly lighter than the nose region. If and when such intensity variations are actually present, Haar-like filters would be expected to show them up.

It should first be explained that a typical Haar filter consists of two adjacent, touching rectangles of equal size, but with opposite weights (normally  $\pm 1$ ): Hence, the sum of the weights will be zero, making the filter insensitive to the background illumination level. Such a filter will approximate to a differential edge detector. Other Haar filters will consist of three adjacent, touching rectangles, and if these are equal in area, their weights will have to be in the ratio  $-1:2:-1$ . Yet other Haar filters will consist of four adjacent, touching rectangles, whose weights alternate between rows:  $-1, 1$  and  $1, -1$ . These basic filters are illustrated in Fig. 21.4. The reasons for using such simple filters are (1) that very many of them may be constructed and applied easily, and (2) that their use involves minimal computation.

In Viola and Jones' (2001) work, the face images used for training were  $24 \times 24$  pixels in size, and it was assumed that relevant features could arise anywhere within each image. Furthermore, relevant features could have any size within this area. They developed the idea that each feature could appear anywhere within an image and at any scale, and its discriminatory power should be determined during training.

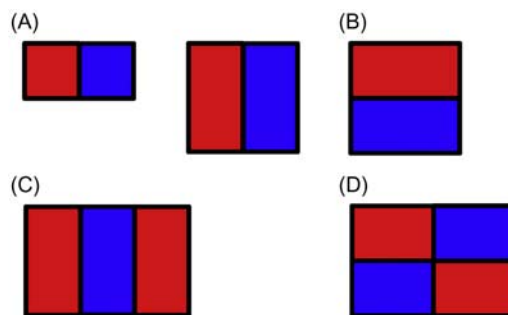


**FIGURE 21.4**

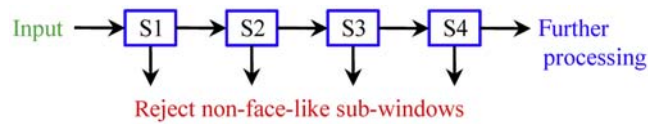
Typical Haar filters. (A) Basic two-element differential edge detector type filters. (B) Two-element differential edge detector operating in the vertical direction. (C) Three-element 1-D Laplacian type filter. (D) Four-element Roberts cross-type filter. If the red and blue elements have respective weights  $+1$  and  $-1$ , the filters will be zero sum, though in case (C), the blue element must be assigned double the weight.



Considering a general Haar filter as being defined by an enclosing rectangle, it is straightforward to calculate the total number of such filters: First, the vertical boundaries of the filter can be chosen in  ${}^{25}C_2 = 300$  ways, and similarly, for the horizontal boundaries: This makes the total number of features under consideration as being  $300^2 = 90,000$ . However, if the features are internally asymmetrical, e.g., containing two horizontally adjacent rectangles of opposite weights, there will in principle be twice this number, viz., 180,000. In fact, internal structures also act to limit the numbers of possibilities, as the overall width of the rectangle will then (as in the last case) have to contain an even number of pixels, leading to the total number of features of this type being  $6 \times 24 \times 300 = 43,200$ , or, including horizontally and vertically adjacent rectangles, a total of 86,400 features. Clearly, if we add the numbers of triple and quadruple rectangle features, and all other possible combinations, the total number will approach the total of 180,000 cited by Viola and Jones (2001). This is a very large number and far exceeds the number ( $24^2 = 576$ ) required for a complete set of basis functions for images of size  $24 \times 24$ —i.e., it is many times “overcomplete.” However, what is needed is a set of features that is, easily sufficient to accurately and compactly describe all the faces that can arise in practice. Of course, it would be impossible to include such large numbers of features in a practical face detector. Nevertheless, it is necessary to test a significant proportion of them during training, so as to make an accurate, rapidly operating face detector.

The approach adopted by VJ was to use a boosted classifier, based on Adaboost (see [Chapter 14: Machine Learning: Probabilistic Methods](#)), in which each feature would act as a weak classifier. A large proportion of these weak classifiers (features) would prove ineffective and would be rejected, and those that were retained would be assigned an optimum threshold and a parity value giving the sign of the filter (i.e., which way around the filter should be applied). At each stage, the weak learner selected would be the one that gives the best discrimination between faces and nonfaces: Note that, contrary to the statement given above that the training set consists of face images, it also has to contain many images that contain no faces. In VJ case, there were 4916 face images, plus their vertical mirror images, totaling 9832 images, and 10,000 nonface images of the same size. Making proper use of the latter is essential for training the classifier to eliminate false positives.

One of the factors that make the VJ detector operate rapidly is the fact that at each stage a good many negative subwindows are eliminated while retaining almost all the positive instances. This means that the false negative rate is kept close to zero. Indeed, this happens progressively, in that simpler more rapidly operating classifiers eliminate the majority of the subwindows, leaving it to later more complex classifiers to gradually reduce the false positive rate. The overall process is best described as a cascade of classifiers ([Fig. 21.5](#)): Each classifier in the sequence eliminates negative subwindows but virtually guarantees retaining and passing on all positive subwindows. Such sequential processing carries risks, because once a positive subwindow is rejected, it can't be recovered, and the error

**FIGURE 21.5**

Viola–Jones cascade detector. This figure shows only the first four stages, S1–S4. All the subwindows stream into the input, and nonface-like subwindows are filtered out, leaving the remainder to undergo further processing. The complete detector contained 38 stages. By the very end, all the windows look very face-like, though exactly how many are actually false positives or false negatives must depend on the quality of the training.

rate necessarily rises. The overall classifier obtained by the VJ detector contained 38 layers and included a total of 6061 features. In fact, the first five layers contained, respectively, 1, 10, 25, 25, and 50 features, reflecting the increasing complexity of the stages of the cascade.

Another factor that made the VJ detector considerably more rapid and efficient was the use of the integral image method (see [Section 6.7.5](#) and [Fig. 6.15](#)) for implementing every feature. The Haar filters are all composed of rectangles, and this made the integral image method a particularly natural way forward. Indeed, rectangular Haar filters are not especially ideal as feature detectors. However, when implemented using the integral image method, the process is so fast that a great many similar features can be added efficiently and their outputs combined together optimally, easily overcoming any losses in optimality of individual filters. In any case, it should be remembered that the Haar features form a (complete) basis set that is, guaranteed to be able to generate all possible shapes.

Overall, the VJ detector was about 15 times faster than the best previous detector (Rowley et al., 1998) and amounted to a breakthrough whose possibility had not previously been envisaged. In fact, it set the scene for more learning-based systems that rely less on conventional vision algorithm design, albeit relying far more on the use of specially constructed datasets for training. Interestingly, the fact that shape, color, and skin-tone analysis were eschewed early in the design, in favor of pure gray-scale processing and intensity profile analysis, is salutary, though in the end, it must be limiting—particularly if recognition rather than mere detection is involved.

Finally, we compare the VJ detector with the simple sampling detector described in the previous section. Both methods found all the faces in the image of [Fig. 21.6](#), but the sampling detector had two specific faults which the VJ detector did not succumb to: One was that it was more susceptible to false positives, because it did not have the additional information about the eye regions being relatively dark; and the other was that, for the same reason, it sometimes biased the faces toward locations where there were larger patches of skin tone, rather than ensuring that the eyes were both present in the final boxes: In fact, this problem only occurred when the faces were subject to in-plane rotation (i.e., roll).

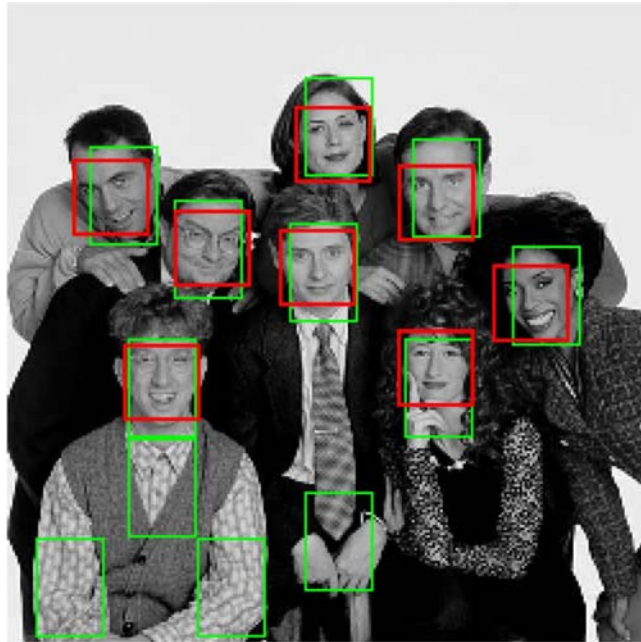


**FIGURE 21.6**

Detection of faces using two methods. Here, the green bounding boxes show the results obtained using the simple sampling method of Fig. 21.1; the red bounding boxes indicate the approximate locations found by the Viola–Jones detector. As might be expected, the latter finds the faces more accurately, without the bias toward skin-tone regions exhibited by the sampling method—though when properly combined with an eye detector, the latter method should be able to overcome this limitation. Note also that the sampling method is sometimes fooled by light regions—in this case containing hands and/or light clothing. In fact, the false positives could in this case be eliminated by ignoring the lower regions of the image, where faces are unlikely. Note that, to make this test, the simple sampling algorithm had to be modified to search sequentially for multiple nonoverlapping faces.

## 21.5 THE EIGENFACE APPROACH TO FACE RECOGNITION

The eigenface method of face recognition was invented by Sirovich and Kirby (1987) and developed into a successful practical technique by Turk and Pentland (1991). The basic idea was to take a set of face images as vectors in a face space and to perform PCA to form a basis set of standard face vectors. Faces could then be represented as linear combinations of this basis set, and each face could therefore be represented by the numerical weights in its own linear combination. The advantage of representing faces in this way is that each face would be represented

by a limited set of coefficients rather than by the large number of pixels in the original image. This means that any test face image can be compared with the training set images and classified by applying the nearest neighbor algorithm to determine the closest match.

As so far stated, there is a serious flaw in this approach—that the training set may be so large that the number of coefficients to be compared when testing could exceed the number of pixels in each image—in which case, the recognition problem will have been made worse rather than better. However, one of the main advantages of PCA is that each eigenvector is also assigned an eigenvalue, which effectively expresses its relative importance—at least in regard to the particular training set that has been employed. By arranging the eigenvalues in descending numerical order, it is possible to curtail the list of eigenvalues (and the corresponding eigenvectors) at a point where they become so small that the eigenvectors represent noise rather than useful features and scarcely contribute to the recognition process: for example, to include 95% of the total variation of the face images in the Extended Yale Face Database B of 16,128 images, the first 43 eigenfaces must be retained. This is a general point that has already been treated in [Section 14.5](#). Thus, we start with  $M$  training vectors and reduce this to a basis set of  $N$ . It is now the number  $N$  that has to be compared with the number of pixels  $P$  in each face image. Note that all the face images used in the training set must have the same dimensions, which we shall take as  $r \times c$ , or typically as  $100 \times 100$ . Fortunately, to span a space of  $M$  faces, a lot can be achieved with a relatively small basis set of size  $N$ , and it is generally reasonable to assume that  $N \ll P = rc$ : Indeed,  $N$  is typically 50, and  $P$  is typically  $\sim 10,000$ , so the assumption is more or less guaranteed.

To use the Eigenface system, the training set must first be set up. Note that it is important to ensure that all the faces in the training set are as similar as possible in form: The pictures must be taken under the same lighting conditions; they must be normalized and cropped as necessary so that the eyes and mouth are aligned in all the images; they must be resampled to the same pixel resolution; they must be converted from their initial 2-D (pixel) format into a 1-D vector of standard length  $P$ ; finally, they must be concatenated into a single training matrix  $\mathbf{T}$  of width  $M$ . Another important factor is that, to proceed with PCA, each input image (i.e., each column of  $\mathbf{T}$ ) must be converted to zero-mean by subtracting its mean value.

At this point, PCA is carried out to determine the eigenvalues and eigenvectors of the covariance matrix  $\mathbf{S}$  (in the face recognition, scenario eigenvectors are commonly called “eigenfaces”). After this, the  $M$  eigenvalues are placed in descending order and the smallest ones discarded, leaving a basis set of  $N$ , as discussed above.

Unfortunately, PCA is highly computation intensive, and it must be remembered that it involves diagonalizing the covariance matrix  $\mathbf{S}$  which is defined for pairs of images, each containing  $P$  elements: This means that  $\mathbf{S}$  is typically a  $10,000 \times 10,000$  element matrix. This is what makes PCA so computation intensive. However, when the number of training images  $M$  is smaller than the number

of pixels  $P$  in each image, it is simpler to compute the principal components as indicated below. First, we consider the usual way of computing the principal components, i.e., in terms of the following equation:

$$\mathbf{S}v_i = \lambda_i v_i \quad (21.1)$$

Next, we represent the covariance matrix in terms of  $\mathbf{T}$ :

$$\mathbf{S} = \mathbf{T}\mathbf{T}^T \quad (21.2)$$

Substituting for  $\mathbf{S}$ , we obtain

$$\mathbf{T}\mathbf{T}^T v_i = \lambda_i v_i \quad (21.3)$$

As  $\mathbf{T}\mathbf{T}^T$  is a large matrix, we consider what happens when applying the smaller matrix  $\mathbf{T}^T\mathbf{T}$ :

$$\mathbf{T}^T\mathbf{T}u_j = \lambda_j u_j \quad (21.4)$$

Premultiplying by  $\mathbf{T}$ , we obtain:

$$\mathbf{T}\mathbf{T}^T\mathbf{T}u_j = \lambda_j \mathbf{T}u_j \quad (21.5)$$

This shows that if  $u_j$  is an eigenvector of  $\mathbf{T}^T\mathbf{T}$ ,  $v_j = \mathbf{T}u_j$  is an eigenvector of  $\mathbf{S}$ .

As  $\mathbf{T}\mathbf{T}^T$  is a large matrix (typically  $\sim 10,000 \times 10,000$ ), and  $\mathbf{T}^T\mathbf{T}$  is a much smaller matrix (e.g.,  $200 \times 200$ ), it makes very good sense to compute the eigenvalues and eigenvectors from the smaller matrix, to obtain results for the larger matrix. The main problem with this approach is that the resulting vectors  $v_i$  are not normalized, and normalization has to be carried out later, if necessary.

Note that the coefficients used to record the projections of any face image against the eigenfaces are specific to the particular image rather than to the subject appearing in the image. This is a severe limiting factor of the method, as the weights for a subject seen under two sorts of lighting (e.g., left and right lighting) may differ radically even for the same subject.

Interestingly, in spite of the warnings given about how to prepare training set images, it is usually the case that the first three eigenfaces in the dataset have to be discarded. This is because they normally arise from variations in illumination rather than from differences in the faces themselves. Hence, eliminating them will tend to boost recognition accuracy (Belhumeur et al., 1997). However, it should be asked why the first *three* eigenfaces should be eliminated. First, note that mean image intensity has already been eliminated from the PCA analysis, so we have to look for further possibilities. The first is that of contrast: Two other candidates are linear intensity variations in two perpendicular directions. Note that once these have been eliminated, all possible linear intensity variations will have been covered. Higher order variations probably always have to be retained as it would be difficult for the computer to distinguish between variations due to lighting illumination and those due to facial characteristics.

It is also worth pointing out that the eigenfaces themselves bear little pictorial relation to real faces: Indeed, they can be regarded as potential incremental

adjustments to existing weighted sums of eigenfaces applied so as to model real faces better: At most, they will only add minor details to the models. Another point is that PCA is more an efficient mathematically based *representation* procedure than one designed for optimum classification: i.e., it provides a descriptor rather than an ideal decision surface. However, it is useful in the realm of face recognition for the purpose of dimensionality reduction.

Another area in which the eigenface approach ought perhaps to be useful is in determining modes of variation, such as degrees of opening of the eyes or mouth, and even in representing differing facial expressions. However, it seems that this is too hopeful in an approach that is, more orientated toward face recognition. For analysis of facial expression, active shape and appearance models (which employ PCA internally) are tools that are more overtly adapted to this purpose.

Finally, “Fisherfaces” constitutes another approach that has been successful in this area. Invented in 1997 by Belhumeur et al., it was based on linear discriminant analysis and included labeled data to retain more class information during dimension reduction; as a result, it was rather more successful than the eigenface approach: In particular, it was less sensitive to lighting variations, and thereby attained higher recognition accuracy. In fact, its classification error rates were around 7.3% compared with 24.4% for eigenfaces and 15.3% for eigenfaces with the first three principal components excluded (Belhumeur et al., 1997).

---

## 21.6 MORE ON THE DIFFICULTIES OF FACE RECOGNITION

By now, it will have become clear that faces are exceptionally variable objects. Here, we clarify the reasons for this. First, faces come in many sizes, shapes, colors, albedos, and expressions—not to mention the possibility of partial self-occlusion, and occlusion by glasses, hair, hats, and even disguises; age is also a serious factor when considering face variations of given individuals. Furthermore, the original 3-D shapes largely determine the appearance in 2-D images. This means that the full pose of the original shape may have to be taken into account in analyzing the 2-D image. Indeed, the three generally unknown orientations—roll, pitch, and yaw—form a substantial part of what makes face recognition difficult. However, another factor is also of vital importance, and that is, ambient illumination—and in particular, which direction or directions the face is lit from. Indeed, this factor is responsible for something like half the difficulty of managing face recognition. Not surprisingly, as a result of all the variations mentioned above, early work of face recognition concentrated on controlling the viewpoint and the lighting, insisting that faces were viewed from directly in front. However, the systems that were produced in this way were necessarily severely limited in their application and accuracy. Nevertheless, by arranging to view faces from several directions during training, comparisons with test faces could be improved, each training image only having to cope with angles over a range  $\sim 20^\circ$  instead

of the whole range. In fact, numerous schemes were devised for managing face recognition across pose: In particular, 2-D statistically based algorithms and 3-D algorithms have often been used to generate a 3-D model of each individual's head (e.g., Blanz and Vetter, 2003; Gross et al., 2004; Yan et al., 2007). In such cases, each test image had to be compared with a rendered image derived from the 3-D model. In fact, the 3-D-based algorithms were significantly more computation intensive, and it was difficult to arrange that up to 10 images were available per individual in order to synthesize sound 3-D models. Overall, by 2007–2008, such approaches yielded performance accuracies of up to 87%, though still being limited to overall pose variations of up to  $\sim 30^\circ$ : In some cases, the results were shown to exceed human performance—though it gradually became clear that such conclusions were misleading because of the artificial conditions under which the photographs had been taken.

At that stage, a shift took place from controlled to uncontrolled environments, and the LFW database was introduced (Huang et al., 2007), so that researchers could utilize realistic sets of images for training. At that point, the performance achievable by available algorithms plummeted—though in very few years, performance had again risen markedly (e.g., Wolf et al., 2009 claimed 89.5% classification accuracy).

In 2014, Taigman et al. published a paper on their “DeepFace” approach to face recognition. This used a deep learning architecture (Fig. 21.7) which brought the performance level up to 97.35%: They compared it with the performance obtained by humans, for which the corresponding figure was 97.53%, giving little doubt—at least with the LFW dataset—that human performance was extremely close to being matched. To some extent, it came as no surprise that a deep learning network could achieve this. However, a closer look at the architecture reveals (1) that it employed an initial nonneural “frontalization” procedure (see Section 21.7) and (2) that the deep learning network employed a two-layer convolutional network (these were separated by a max-pool layer), followed by a three-layer locally connected section followed in turn by two fully connected layers (Fig. 21.7). The two convolutional layers, respectively, contained 32 filters of size  $11 \times 11 \times 3$  and 16 filters of size  $9 \times 9 \times 16$ ; the max-pool layer had an input field of  $3 \times 3$  and a stride of 2; and the three locally connected layers each had 16 filters with respective sizes of  $9 \times 9 \times 16$ ,  $7 \times 7 \times 16$ , and  $5 \times 5 \times 16$ . (Note that in Fig. 21.7, the first two figures in the sizes are listed in the row labeled  $r \times r$ , whereas the last appears in the row labeled  $N$ .)

The reason for having locally connected layers was to retain localization of the data from the input image. In face analysis, we are far from the situation where any object has to be detected anywhere in the image: In fact, eyes will be predominantly in one place and mouth and nose predominantly in others; in addition, they will usually be in similar relative positions. Nevertheless, the additional numbers of parameters required for localization can only be afforded when a large labeled dataset is available for training. Finally, the second fully connected layer is fed to a  $K$ -way softmax layer which produces a probability distribution over all

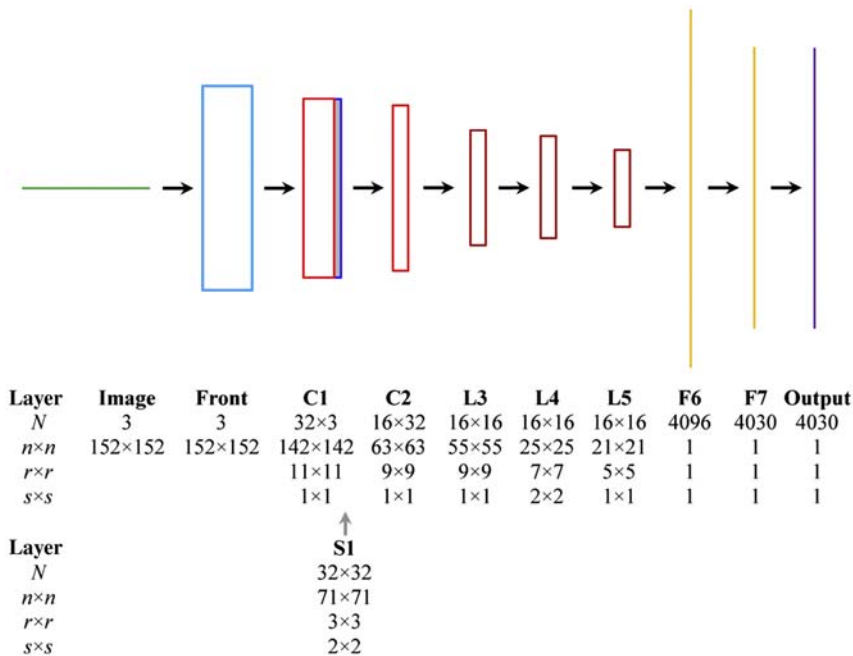


**FIGURE 21.7**

Schematic of Taigman et al.'s DeepFace face recognition architecture. The previous architecture that this most strongly resembles is that of ZFNet in Fig. 15.10. However, it differs in including the “Front” nonneural frontalization module (see Section 21.7), reducing the six convolution layers to just two, reducing the three sampling (max-pool) layers to one, adding three locally connected layers L3–L5, and maintaining higher layer dimensions ( $n \times n$ ) before moving on to the fully connected layers. The reason for having locally connected layers is to retain localization of the data from the input image, bearing in mind that face features such as eyes, nose, and mouth are likely to be similarly placed within each image and also need to be assessed as quite large individual features.

the class outputs. For the Facebook Social Face Classification dataset,  $K = 4030$ ; for the LFW dataset,  $K = 5749$ ; and for the YouTube Faces video dataset,  $K = 1595$ : all three of these datasets were used to test the DeepFace system. (In fact, the last two values of  $K$  need to be interpreted carefully, because the images and videos were used to compare *pairs* of faces.)

## 21.7 FRONTALIZATION

The idea of frontalization needs to be considered in some detail. The basic concept is that if all face images can be converted to a standardized frontal view,



comparison between test and training images will become far easier and much more accurate. The problem is quite how to achieve this: In the past few years, several approaches have been devised for the purpose—as we will see below. First, in spite of the fact that 3-D models had “fallen out of favor,” Taigman et al. (2014) decided to proceed by incorporating fiducial points to guide the modeling process. They identified six fiducial points—at the centers of the eyes, tip of the nose, ends of the mouth, and center of the lower lip (Fig. 21.8A); starting with these locations, they carried out 2-D similarity transformations to move them to a set of anchor points. In fact, this operation did not allow for out-of-plane rotation, so 3-D modeling had to be carried out as well. Here, a further 67 fiducial points were *manually* placed on the 3-D model and fitted by a least squares procedure—a process involving Delaunay triangulation derived from the 67 fiducial points. Once this had been achieved, obtaining a frontalized image of the face became trivial. Note that an affine camera model was used in the calculation, so full perspective projection was *not* taken into account, and the result was stated to be “only an approximation”—though the results achieved using the model were nonetheless impressive, as indicated above.

Sagonas et al. (2015) developed a totally different approach to frontalization. They started with the idea that, by collecting sets of frontal images, all that was necessary was to reexpress any new image in terms of these, i.e., we use the set

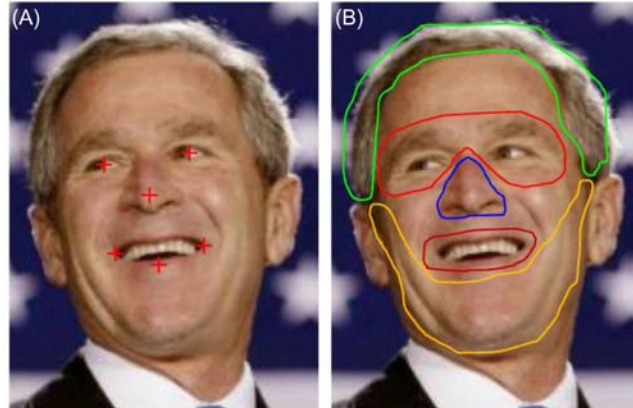


**FIGURE 21.8**

Facial features sought by several prominent methods. (A) Shows the six landmark points used by Taigman et al.’s Deepface recognition method—namely, the centers of the eyes, tip of the nose, ends of the mouth, and center of the lower lip. (B) Shows the five facial regions used by Yang et al.’s Faceness-Net detection system. Note that Sun et al.’s DeepID face recognition scheme started by detecting all the landmark points in (A) *except* for the center of the lower lip. Finally, note that the eye centers marked with red crosses in (A) do not coincide with iris centers, and this has implications about how the resulting landmarks are used in practice.

of frontal images as a basis set spanning a generic frontal face subspace, and then warp any new nonfrontal image to express it optimally as a linear combination of images in this basis set. In fact, it is clear that as a face is rotated in front of a camera, there will be one point at which an optimal match with an appropriate frontal image will occur, and at this point, the “nuclear norm” has been reached. The full calculation expresses this idea. However, it also has to express another fact: that when a face is viewed nonfrontally, part of it may well not be visible from the camera. This arises because even at quite small angles, the nose tends to partially obscure a small part of the cheek behind it (Fig. 21.9), whereas for larger rotations, an entire cheek, and also an ear, is likely to be occluded; in addition, a substantial region immediately under the chin will often be occluded. These factors play havoc with the optimization problem as so far described, because there is no possible single-valued warping that can cover the situation. In fact, part of the nonfrontal image has to be cut away. This immediately means that least squares fitting on its own will not work: Instead, it has to be replaced by, or



**FIGURE 21.9**

Face frontalization occlusion problem. Here, the author's face is viewed frontally, but the illumination is mainly from a light source about  $40^\circ$  to the right. The shadow to the left of the nose indicates the region that will *not* be visible from a camera placed at the light source position. Hence, if face frontalization is carried out for such a camera, the occluded region will have to be replaced by using either a transformed and reflected version of the face or by a trained map from a set of frontally viewed faces. The latter possibility is employed by the FAR technique devised by Sagonas et al. (2015).

combined with,  $l_1$  norm analysis. Sagonas et al. developed a systematic iterative procedure for achieving this: It automatically eliminated occlusions in the form of large-magnitude sparse errors. The fact that the algorithm typically took  $\sim 100$  iterations to achieve this meant that it could successfully manage progressively larger occlusions—of the sort that can occur for head rotations of up to  $\sim 30^\circ$ . The authors compared the effectiveness of their “Face frontalization for Alignment and Recognition” (FAR) technique with the 3-D modeling approach of Taigman et al., and found that the average r.m.s. error for FAR and DeepFace were 0.082 and 0.103, respectively. They explained their improved performance as due to not using any kind of 3-D modeling in their analysis. Overall, the FAR approach is superior to many previous approaches for producing statistical models of images: This is because it uses only a few hundred frontal images, which are simply obtained, rather than many thousands of labeled faces of many orientations.

Remembering that this is a fast-moving subject, it is worth drawing attention to a further approach to face frontalization, in this case, by Hassner et al. (2015). This method reverts to the 3-D modeling approach. However, it uses a standard 3-D surface and makes all images fit it accurately: It also extracts frontal face images from it by projection. In each case, a  $3 \times 4$ -projection matrix is used for the purpose, no attempt being made to use full perspective projection. It can be said that the method uses the standard 3-D surface as a proxy for moving face images around. To achieve all this, the authors use a total of 49 facial features, avoiding points along the jawline as these are not as distinct or as accurately defined as many others. In fact, the features used are all points lying close to the 3-D plane at the front of the face. Because of this, there is less reliance on the exact shape of the 3-D surface.

As is bound to happen, the nose and head as a whole can occlude parts of the face, and this is analyzed using the 3-D model surface. It soon becomes clear when this is happening, and in this situation, the visibility of each pixel in the frontalized picture is determined, using a clearly defined formula. Intensities of poorly visible pixels are replaced not merely by those of the corresponding pixels on the other side of the face but by a suitably weighted mean of the two intensities. The paper goes on to describe cases where this strategy does not work well—e.g., when the occlusion is due to other objects than the face itself (e.g., a hand or a microphone), when the face has an asymmetric expression, or when an eye is occluded: In this last case, a cross-eyed effect can result. There will also be problems when a person has a bandage or eye patch on one side of the face, or is wearing a monocle.

The advantage of this approach (in contrast with other 3-D methods) is that it results in retaining crisp details and sharp edges, and above all, it results in “aggressive alignment” and high accuracy. Even if the adherence to the 3-D model surface is slightly artificial and can result in absolute errors (e.g., potentially, a narrowed or widened face), it results in exceptional consistency. Essentially, the frontalizations lose negligible identifiable detail and remain

highly aligned. Remarkably, the lines on President Bush’s face remain so well aligned from one derived frontal image to another that they are retained accurately and are recognizable in each case.

The authors tested the method using the “Image-Restricted, Label-Free Outside Data” (IRLFOD) protocol, developed in 2014 by Huang and Learned-Miller—two of the authors of the original LFW dataset (Huang et al., 2007). The reason that IRLFOD was produced was to act as even more rigorous and stringent test of algorithm performance. In fact, the authors’ method gave the highest score (91.7%) achieved “to date” (i.e., 2015) reported in the IRLFOD category, attesting its quality as a high-performance approach: Numerically, its performance exceeded that of Cao et al. (2013) by  $\sim 2\%$ .

Of the three methods listed described above, the last probably requires the least computation and gives the highest alignment accuracy, though the various checks that have to be made to overcome problems that may have been introduced by the symmetry operation would appear to add a significant overhead. Interestingly, the method of Sagonas et al. should not have any such problems, as it takes standard frontal views as a basis set and automatically reverts to these (via the  $l_1$  norm) when a fault due to self-occlusion arises. However, its optimization algorithm probably has a higher computational load. The Taigman et al. approach to frontalization seems to require excessive labor to set up (it involves the manual placement of 67 anchor points), and its reliance on a model using Delaunay triangulation would appear to cut down the achievable accuracy—as noted by both Sagonas et al. and Hassner et al. This has to be weighed against the close-to-human performance which their overall system achieved. It remains to be seen which schemes win in the end, as datasets such as LFW come with ever more stringent protocols setting out how to make fair comparisons using them. In this respect, Huang and Learned-Miller (2014) point out the need for care with “outside data” that is, not part of the dataset in question: Adding additional outside data to a given dataset can give clues to a classifier about the ground truth, thereby preventing a fair comparison with other classifiers.

---

## 21.8 THE SUN ET AL. DEEPID FACE REPRESENTATION SYSTEM

In [Section 21.6](#), we looked closely at Taigman et al.’s approach to face recognition: At this point, it is worth comparing it with another recent method, which is claimed to be superior, but which follows a rather different route forward. That is, the method of Sun et al. (2014a,b). In fact, their DeepID face recognition scheme relies strongly on their face-point detector, which was published the previous year (2013). We shall consider the latter first.

[Fig. 21.10](#) shows the F1 whole-face network for the detection of eyes, nose, and mouth: For this purpose, the specific features sought are the eye centers, the

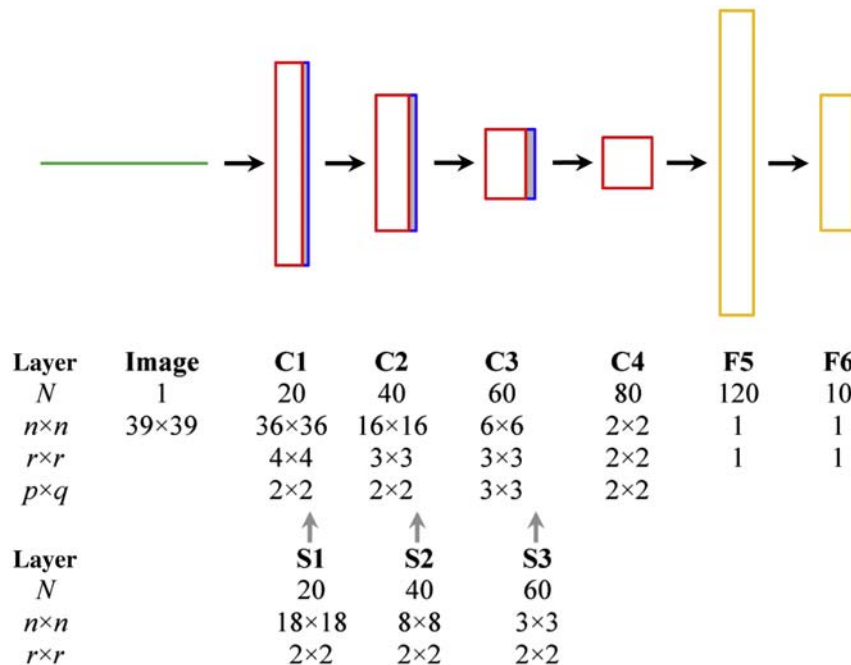


FIGURE 21.10

Schematic of Sun et al.'s CNN facial point detection architecture. This diagram shows the F1 whole-face network for detection of eyes, nose, and mouth. Similar networks are used to detect eyes and nose (EN1) and nose and mouth (NM1). The three networks form the first level of a cascade, the next two quite similar levels being targeted at refining the location of the five features. In all layers, the stride  $s$  is kept at 1. Parameters  $p$  and  $q$  indicate that the convolutional layers are divided into  $p \times q$  equal-sized patches within each of which the convolutional weights are shared. Note that for EN1 and NM1, the values of  $p$  and  $q$  are different from those listed above for F1. For cascade Levels 2 and 3,  $p = q = 1$ ; so, the convolutional layers remain undivided, which is best for accurately locating low-level features. Note also that cascade Levels 2 and 3 have only two convolutional layers and one max-pooling layer. Overall, there are three networks in cascade Level 1, 10 in cascade Level 2, and 10 in cascade Level 3: For further details, see Sun et al. (2013).

tip of the nose, and the corners of the mouth (Fig. 21.8A). Similar networks are used to detect eyes and nose (EN1) and nose and mouth (NM1): The predictions of the three networks are averaged to increase location accuracy. The three networks form the first level of a cascade, the next two quite similar levels being targeted at refining the location of the five features: Carefully constructed rules are employed to ensure that the last two layers of the cascade don't pull the point locations too far. In all layers, the stride  $s$  is kept at 1. Parameters  $p$  and  $q$  indicate

that the convolutional layers are divided into  $p \times q$  equal-sized patches within each of which the convolutional weights are shared. Note that for EN1 and NM1, the values of  $p$  and  $q$  are different from those listed above for F1. For cascade Levels 2 and 3,  $p = q = 1$ , so the convolutional layers remain undivided, which is best for accurately locating low-level features. Note also that cascade Levels 2 and 3 have only two convolutional layers and two max-pooling layers, though both retain two fully connected layers. Overall, there are three networks in cascade Level 1, 10 in cascade Level 2 and 10 in cascade Level 3—all 23 of which are similar to, and in many cases, simpler than, that shown in Fig. 21.10: For further details, see Sun et al. (2013).

The original idea of using convolution networks was to save computation and to ensure positional invariance when locating objects. Here, the reason for using patches which internally share parameters is to specialize location of objects such as eyes, NM1 to various subregions. This was also seen in Taigman et al.'s DeepFace architecture, where layers L3–L5 were labeled as local. In the Sun face-point detector, there are tensions between reliable detection of the five types of feature and accuracy of location. Their architecture achieves this by several means: Using small patches for sharing weights, keeping detection of the five types of feature separate as far as possible, and progressively refining their locations (via the cascade levels). The type of nonlinearity used is the tanh function followed by an abs function (an empirical study showed that the latter led to improved performance).

Oddly, the paper says little about how sets of five keypoints were marked on the 10,000 images used in training and testing, which were obtained from the web or from the LFW dataset. However, the approach gave higher detection reliability and location accuracy than previous face-point detectors, including those of Belhumeur et al. (2011) and Cao et al. (2012), when tested on LFPW (labeled face parts in the wild). On the BioID test set, the new method gave detection failure rates approaching zero—better than five earlier methods. Interestingly, the method gave reliable detections under large variations in pose, illumination, and facial expression and also gave accurate predictions under near occlusion, e.g., when an eye was closed or the head rotated so far that an eye was barely visible.

We can now move to the DeepID face recognition scheme (Sun et al., 2014a,b), which uses the above face-point detector. In fact, it starts by detecting the five facial landmark points (eye centers, nose tip, and mouth corners) and aligns the face globally using a similarity transform. As the latter involves only in-plane translation, rotation, and scaling, by following the two eye centers and the midpoint of the mouth corners, the face is only weakly aligned. Such a similarity transform will convert a square into a square: By comparison, an affine transform will convert a square into a parallelogram (see Section 6.7.1), but a perspective transformation is needed to contort a square into a (convex) quadrilateral: This carries immediate lessons for realistic 2-D face representation. Nevertheless, as we shall see, the authors manage to get the recognition system to work impressively on this basis.

After aligning a face image, 10 rectangular patches are extracted from it: Five of these are global regions, and five are local, the latter being centered around the five landmark features. All 10 patches are scaled by three factors  $\sim 0.75$ ,  $1.0$ ,  $\sim 1.2$  and expressed (1) in gray scale and (2) in color, giving a total of 60 patches. Finally, 60 DeepID convnets (Fig. 21.11) are trained to extract two 160-dimensional DeepID vectors using 10,000 original faces and leading to 10,000 identity classes. (The process can be called identification, verification, or recognition, depending on one's mind-set.) Notice that the total length of the DeepID vector is  $160 \times 2 \times 60$ , factor 2 signifying that the face has been flipped horizontally (though the patches around the eye centers and mouth corners are dealt with by flipping the opposite ones!).

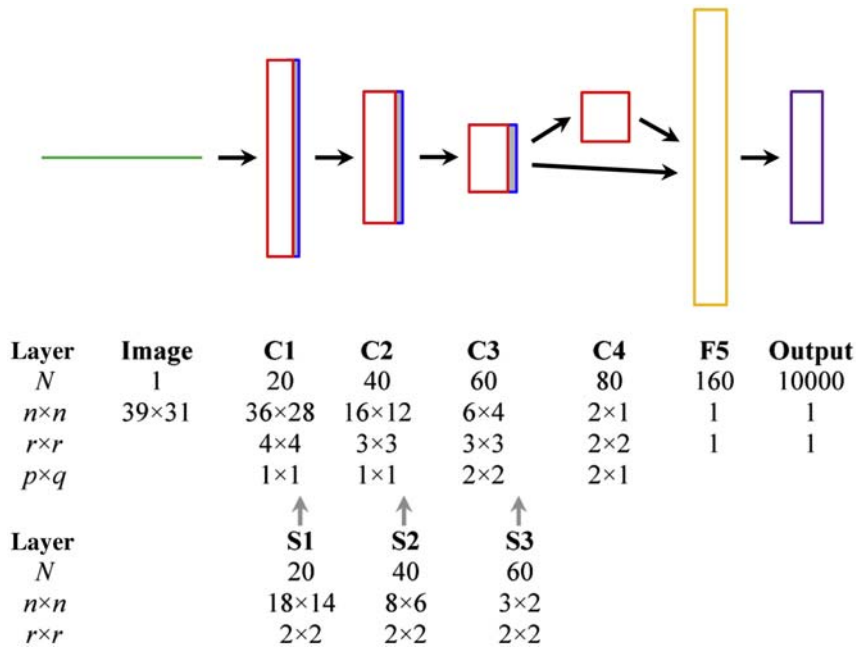


FIGURE 21.11

Schematic of Sun et al.'s DeepID face recognition architecture. This architecture starts with much the same form as that of Fig. 21.10, but in one crucial detail, it is different—in that layer, F5 is fed from C3 both directly and indirectly via C4. This prevents the small C4 from becoming a bottleneck in the information flow to F5—C4 nevertheless being important for capturing multiscale features. In all layers, the stride  $s$  is kept at 1. Parameters  $p$  and  $q$  indicate that the convolutional layers are divided into  $p \times q$  equal-sized patches within each of which the convolutional weights are shared, though these operate mainly in the higher levels of the network: Weights in higher convolutional levels are locally shared to ensure that they can learn *different* higher level features in different regions.

Next, it ought to be emphasized that the locations of the five landmark points are only brought into the learning system via the patches that are centered on them. The system has to learn for itself what the meanings of the individual patches are, and the fact that half of them are global patches and half are landmark-centered.

An even more important point is that, when the network has learned to recognize the 10,000 face identities under quite variable conditions, it has a highly accurate knowledge of the compact identity-related features residing in its topmost layers—principally the 60 F5 layers. Indeed, after so much training, the system can be described as having “overlearned” the features characteristic of a human face. We can say that the 60 F5 layers contain complementary sets of vectors and form an over-complete representation. Also, because the DeepID output vector is so large, the learned features are far from being overfitted to the data, but on the contrary should be well generalized to faces not seen during training. Above all, the number of neurons in the last hidden layer is much smaller than the number in the output layer: This forces the last hidden layer to learn “shared hidden representations” (Sun et al., 2014a,b) for faces of different people, and to be both discriminative and compact.

Although it is easy to claim that the method is well generalized to faces not seen in training, and the paper does not expand on this, there is one way in which it is obvious that it has actually achieved this. Notice first that each face image is trained on CelebFaces + as well as LFW, so that the number of face images available is  $\sim 200,000$  and the number of identities (people) is  $\sim 10,000$ , i.e., there are  $\sim 20$  faces per identity. Even with this number, the method is able to cope with the huge number of possible 3-D poses, which means it is successfully interpolating between them, and above all, it is doing so without making any overt 3-D models. The pure training and the method’s intrinsic generalization capability is managing to achieve this. This is in direct contrast with Taigman et al.’s DeepFace approach. In fact, DeepID proved to be even more accurate than DeepFace, and to have classification performance of 97.45% compared with 97.25% for DeepFace, and 97.53% for human-level performance. Among the most valuable contribution to this performance came from the number of patches used per face image—namely 60—and amounted to an improvement of some 5.27%.

All this leads to a strong conclusion—that in spite of the obvious fact that faces are attached to a 3-D head that has considerable variation in expression (including joint articulation and variable degrees of opening of the eyes and mouth), high performance face recognition approaching that of the human can be achieved by systems with no built-in knowledge of 3-D and 3-D pose. One can ask whether the architecture itself has been constructed using human knowledge of 3-D. Looking at the architectures in [Figs. 21.10 and 21.11](#), this does not seem to be the case. Admittedly, they have evolved to be sufficiently complex to achieve this, but in the main, the complexities are more to do with appreciation of possible low-to-high-level facial features than with anything to do with 3-D. One can even argue that the whole evolution of face recognition systems has only got where it has by ignoring 3-D aspects and freeing CNN-based learning systems to learn what they can in their own way.



---

## 21.9 FAST FACE DETECTION REVISITED

Having seen the considerable success that has been achieved in face classification, which in turn depends on facial feature detection and on face detection itself (face features only being found in face regions), it seems worth revisiting the problem of fast face detection. Following the ground-breaking work of Viola and Jones (2001), and the advances they made quite soon after (2004), Felzenszwalb et al. (2010) made a further big step forward by developing the concept of deformable parts models (DPM). These are based on the idea that faces can be considered collections of parts. Thus, to detect faces, it should only be necessary to locate the parts and examine their interrelationships. This can be carried out by identifying parts and their bounding boxes and then making proposals for combining them into larger bounding boxes representing (in Felzenszwalb et al.'s case) objects or in our case faces. Basically, once object or face bounding boxes have been found, these regions are protected from further analysis by nonmaximum suppression. In practice, this means giving each potential bounding box a score, keeping the highest scored and skipping any that overlap an already existing bounding box by a critical percentage, e.g., 50%. This highly successful approach achieved state-of-the-art results on the PASCAL VOC 2006, 2007, and 2008 benchmarks (Everingham et al., 2006, 2007, 2008) and “established itself as the de-facto standard for generic object detection” (Mathias et al., 2014).

Mathias et al. (2014) tested the DPM approach very thoroughly and showed that it could achieve top performance for face detection. They then went on to develop their own “HeadHunter” detector and showed that even if such a detector is based on *rigid* templates, it can also realize near-top performance: e.g., the two methods gave respective responses of 97.21% and 97.14% on the AFW test set: see Zhu and Ramanan (2012) for details of this test set. The conclusion they drew was that “parts are useful but not critical to reach top performance.” The main problem with the rigid template approach was found to be its need for large quantities of training data.

Yang et al. (2015a,b) called HeadHunter “the state-of-the-art method”: They then went on to show that their own new method outperformed it by 2.91% on the Fddb (face detection data set and benchmark) benchmark (defined by Jain and Learned-Miller, 2013). In fact, Yang et al.'s Faceness-Net was amongst the first face detectors to be developed along CNN lines. First, Yang et al. devised a CNN architecture for finding attributes of face images (Fig. 21.12). This was to be run forward to find the intrinsic face features and “in reverse”—by up-sampling—to regenerate localized face-part response maps: Here, they followed the methods set out by Zeiler and Fergus (2014), Simonyan et al. (2014), and Noh et al. (2015) on deconv nets, as outlined in Chapter 15, Deep Learning Networks. Then, face proposals were produced with the aid of a pipeline, using a faceness score to rank the resulting bounding boxes. Finally, nonmaximum suppression was used to identify the most reliable set of bounding box proposals.

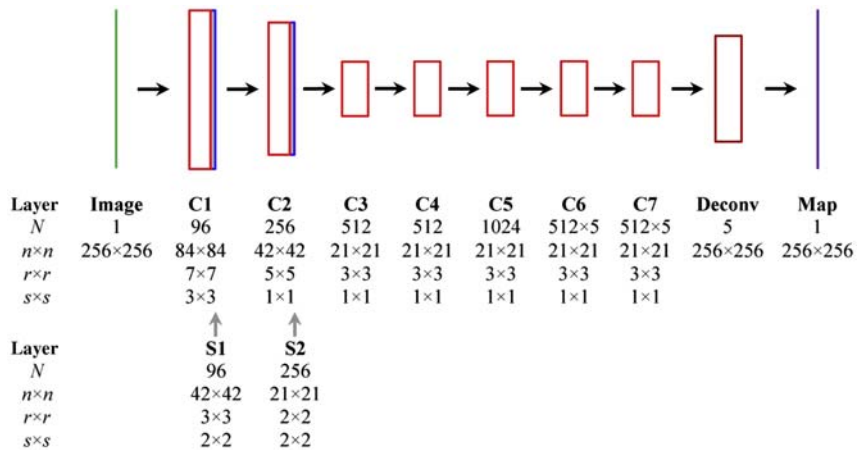


FIGURE 21.12

Schematic of Yang et al.'s Faceness-Net face detection architecture. [This schematic is as close to the Faceness-Net architecture as can be achieved from the details given in the paper by Yang et al. (2015a,b), which is slightly incomplete, e.g., in regard to stride, padding, convolution dimensions, and image sizes. In addition, compressing the whole architecture into one diagram itself risks introducing inaccuracies in order to make the underlying structure clearer to the reader.] The basic structure is that of a standard convolution net, with seven convolutional layers C1–C7 and two max-pooling layers S1, S2. There follows a Deconv network that effectively reverses the previous Conv network by applying unpooling and up-sampling units: This can be construed as taking the strongest activations in C7 and tracking them forward to a full-size face-parts map (see column heading “Deconv”). Note that layers C1–C5 are shared and C6 and C7 are distributed over five times as many channels in order to lead to five different face attributes: See “ $\times 5$ ” (twice) under row heading “ $N$ .” These also lead to the five face-part results produced by the end of the Deconv operation. Finally, by optimally combining face-part bounding boxes, these are grouped together to produce a single faces map: See text for details.

Much of the success of this method was due to adequately defining the five categories of part faces and indicating their likely relative placement. The five collective categories were labeled as follows (moving downwards from the top of the face, as in Fig. 21.8B):

1. “Hair”: Including possible colors, waviness, straightness, baldness, hairline, and fringe;
2. “Eye”: Including eyebrow and eye attributes, bags under eyes, and glasses;
3. “Nose”: Including size and shape;
4. “Mouth”: Including size of lips, openness of mouth, and use of lipstick; and
5. “Beard”: Including presence of beard, sideboards, goatee, mustache, and stubble.

Note that hair is categorized differently in the top, middle, and bottom half of the face. As for their likely spatial arrangements, the various attributes should appear in the top-to-bottom order given above—though allowing for any items that are missing, hidden, or occluded. The faceness score would be penalized for any inconsistencies. The scores would then be used to rank potential object proposals for whole faces. At each stage, a bounding box would be generated and (trained) bounding box regression used to predict the optimum position for each final face proposal.

The above approach owes much to the original VJ method in its use of a pipeline, to Zeiler and Fergus and others for the deconv net approach, and to Felzenszwalb et al. (2010) for their DPM methodology, including the use of non-maximum suppression.

In this context, it should be noted that Bai et al. (2016) have produced a very much simpler and faster design: This is a fully convolutional network working at multiple scales, with five shared convolutional layers followed by a branching out into two further convolutional layers—the latter, respectively, coping with (1) the multiple scales and (2) the sliding window effect needed to perform the final matching. The network makes no use of pooling, though a convolution layer with a stride of 2 is used following each of the first three layers. Bai et al. compared their method with what they regarded as the prior leading approaches—Faceness-Net (Yang et al., 2015a,b), HeadHunter (Mathias et al., 2014), DenseBox (Huang et al., 2015), and others. Their conclusion was that their method outperformed all but two of the state-of-the-art methods (see below), while (because of its greater simplicity and efficiency) keeping real-time performance. In particular, it achieved an average precision of 97.7% on the AFW dataset, compared with 97.2% for Yang et al.’s Faceness-Net detector, with an even wider margin for all the others: Arguably, this is because it is simply trained end-to-end rather than having to go through deconvolution with the possibility of introducing further uncertainties or inaccuracies. Furthermore, on the PASCAL face dataset (Yan et al., 2014), it performed slightly less well (91.8%) than Faceness-Net (92.1%) but outperformed all the other methods. And, on the FDDB dataset, it managed to beat all the tested *CNN-based* detectors other than DenseBox. In this context, note that DenseBox used three times as much training data as Bai et al.’s method. Overall, it seems that a simpler system that is trained end-to-end has a better chance of achieving superior performance.

### 21.9.1 EVEN MORE POWERFUL OBJECT DETECTION SCHEMES

In [Section 21.9](#), we saw something of the power of the Felzenszwalb et al.’s (2010) DPM approach to object detection. Interestingly, this approach is already in the process of being ousted by alternative approaches, one of which is the “Regions with CNN features” (R-CNN) method (Girshick et al., 2014). The latter involves using region proposal methods to generate potential bounding boxes: These are then classified and refined before duplicate detections are eliminated and the remaining ones are rescored. Overall, this is a slow and complex process,

though it has been speeded up in later versions (Girshick, 2015; Ren et al., 2015; Lenc and Vedaldi, 2015). However, all these versions have been radically improved upon by the YOLO approach (Redmon et al., 2015). YOLO stands for “You only look once,” which means that all the multiple pipeline processes of the previously mentioned methods are dealt with in just one pass through the convolution net: During this one pass, it notes all bounding box possibilities and gradually refines the judgments made about each possibility, until by the end of the single pass a set of mutually consistent decisions has been arrived at. Although this may initially seem like an impossibility, this merely shows that the approach is ahead of its time, and there is nothing impossible about it. That is, not to say that the method has no problems and no faults. Indeed, it has some difficulty in coping with multiplicities of small objects, and its main fault is that of inaccurate object localization. On the other hand, it makes far fewer background mistakes than other methods: Specifically, it makes far fewer false predictions of objects in background regions.

Another important factor is that the single-pass approach is far faster and results in immediate real-time performance, at rates  $\sim 45$  frames per second. The main feature of the architecture is that it contains 24 convolutional layers followed by two fully connected layers and ends very neatly with a  $7 \times 7 \times 30$  tensor consisting of a  $7 \times 7$  image grid containing the five parameters  $x$ ,  $y$ ,  $w$ ,  $h$ , and *confidence* (all times two to allow for touching objects) + 20 conditional class probabilities,  $Pr(Class_i|Object)$ . It ought to be added that an even more impressive version of this approach has already been published (Redmon and Farhadi, 2016). This detects objects in 200 classes in more than 9000 different object categories and is still fast enough to run in real time. The many refinements described in the paper cannot be covered fully here, but it is interesting that the final architecture (called “Darknet-19”) has 19 convolutional layers and 5 maxpooling layers and is able to perform joint classification and detection.

---

## 21.10 THE FACE AS PART OF A 3-D OBJECT

It has been noted several times in [Sections 21.6–21.8](#) that workers have used a 2-D similarity transform—or at most an affine transform—for modeling facial features, in spite of the fact that the head is a 3-D object. They have done this (1) in the interests of simplicity and (2) to keep computation within reasonable limits. However, there is the possibility that it would sometimes be useful to apply more accurate methods so as to improve classification performance. Hence, we indicate below how the analysis might be carried out.

To proceed, note that we can define a plane  $\Pi$  containing the outer corners of the eyes and the mouth. To a very good approximation, it can also be assumed that the inner corners of the eyes will be in the same plane ([Fig. 21.13A–C](#)). The next step is to estimate the position of the vanishing point  $V$  for the three horizontal lines  $\lambda_1$ ,  $\lambda_2$ ,  $\lambda_3$  joining these three pairs of features ([Fig. 21.13D](#)). Once this

has been done, it is possible to use the relevant cross-ratio invariants (see Chapter 18: Invariants and perspective) to determine the points that in 3-D lie mid-way between the two features of each pair: This will give the symmetry line  $\lambda_s$  of the face. It will also be possible to determine the horizontal orientation  $\theta$  of

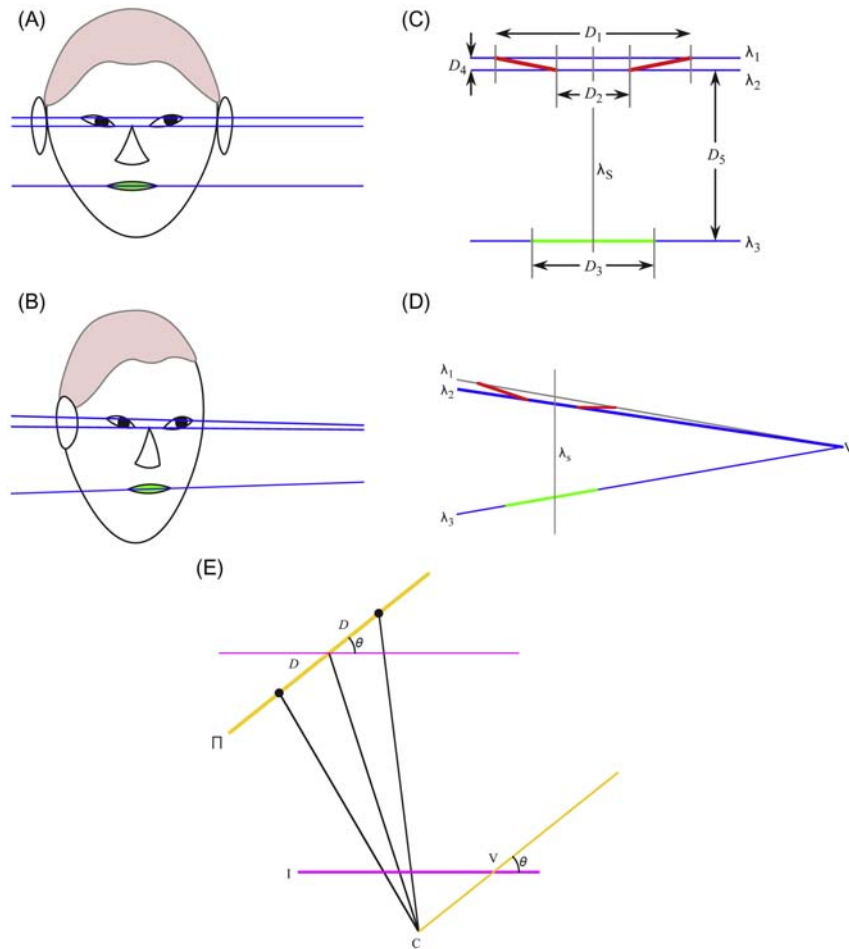


**FIGURE 21.13**

3-D analysis of facial parameters. (A) Front view of face. (B) Oblique view of face, showing perspective lines for corners of the eye and mouth. (C) Labeling of eye and mouth features and definition of five interfeature distance parameters. (D) Position of vanishing point  $V$  under an oblique view. (E) Positions of one pair of features and their midpoint on the facial plane  $\Pi$ . Note how the midpoint is no longer the midpoint in the image plane  $I$  when viewed under perspective projection. Note also how the vanishing point  $V$  gives the horizontal orientation of  $\Pi$ .

the facial plane  $\Pi$ , i.e., the (yaw) angle through which it has been rotated about a vertical axis, from a full frontal view. The geometry for these calculations is shown in Fig. 21.13E. Finally, it will be possible to convert the interfeature distances along  $\lambda_1$ ,  $\lambda_2$ ,  $\lambda_3$  to the corresponding full frontal values, taking proper account of perspective, but not yet taking account of the vertical orientation  $\varphi$  of  $\Pi$ , which is still unknown. Note that the theory underlying these procedures is closely related to that of Section 18.8: see also Fig. 18.13.

In fact, there is insufficient information to estimate the vertical orientation  $\varphi$  (the pitch) without making further assumptions: Ultimately, this is because the face has no horizontal axis of symmetry. If we can assume that  $\varphi$  is zero (i.e., the head is held neither up nor down, and the camera is on the same level), then we can gain some information on the relative vertical distances of the face, the raw measurements for these being obtained from the intercepts of  $\lambda_1$ ,  $\lambda_2$ ,  $\lambda_3$  with the symmetry line  $\lambda_s$ . Alternatively, we can assume average values for the interfeature distances and deduce the vertical orientation of the face. A further alternative is to make other estimates based on the chin, nose, ears, or hairline, but as these are not guaranteed to be in the facial plane  $\Pi$ , the whole assessment of facial pose may not then be accurate and invariant to perspective effects.

Overall, we are moving toward measurements either of facial pose or of facial interfeature measurements, with the possibility of obtaining some information on both, even when perspective distortions have to be allowed for (Kamel et al., 1994, Wang et al., 2003). Of course, the analysis will be significantly simpler in the absence of perspective distortions, when the face is viewed from a distance, or when a full frontal view is guaranteed. Indeed, the bulk of the work on facial recognition and pose estimation to date has been done in the context of weak perspective, making the analysis altogether simpler. Even then, the possibility of wide varieties of facial expression brings in a great deal of complexity. Clearly, the face is not merely a rubber mask (or deformable template) which can be distorted “tidily”: The capability for opening and closing the mouth and eyes creates additional nonlinear effects that are not modeled merely by stretching rubber masks.

---

## 21.11 CONCLUDING REMARKS

Over many years, face recognition has been an ongoing target for practitioners of computer vision. On a number of occasions, it has been claimed that the problem has been solved, only for criminologists to deny this and confirm that there is still some distance to go before reliable identification of people can be attained in *practical* situations. Not least, there are problems of hats, glasses, hairstyles, beards, degree of facial stubble, wildly variable facial expressions, and of course variations in lighting and shadow—and this does not even touch on the problem of deliberate disguise. Added to this, there is the all-too-obvious problem that the face is not flat, but part of a solid, albeit malleable object—the head—which can

appear in a variety of orientations and positions in space. Interestingly, it is part of the human psyche and mind-set that the face is representable as a flat photograph: humans are so good at understanding imagery that they don't perceive what they are really seeing, i.e., the process of seeing is a nonpassive one, and the 2-D input is confused with its 3-D interpretation.

Of course, criminologists are not the only workers who need face recognition algorithms and methodology. Indeed, there is also the need to measure facial expression, for reasons as diverse as determining whether a person is telling the truth, and finding how to mimic real people as accurately as possible in films (over the next few years, it is possible to anticipate that a good proportion of films will contain no human actors as this has the potential for making them quicker and cheaper to produce). In addition, medical diagnosis or facial reconstruction can also benefit from facial measurement procedures. Nevertheless, person verification for computers, banks, and other security applications is vital in many walks of life, though it needs to be carried out quickly and with negligible error. In the latter respect, efforts moved in the direction of identifying people highly accurately from their iris patterns (e.g., Daugman, 1993, 2003), and even more accurately from their retinal blood vessels, using the methods of retinal angiography. Here, some of the main signals are commercial rather than academic, though an important message is that it only becomes cost-effective to deal with the technical difficulties where there is need for the highest security: in that case, "the false acceptance rate for a correctly installed retina scan system falls below 0.0001 percent" (ru.computers.toshiba-europe.com: website accessed 19 May 2004). Although retinal methods are bound to be rather expensive to implement, the iris method is not, and much progress has been made in this direction.

In this chapter, we have only covered the beginnings of this subject but have successfully broached the topics of FDR, and of facial feature location: Note that the latter is a key to FDR but is also useful in its own right, e.g., for lip reading and for analyzing eye movement and attention patterns. The history of the subject has proceeded in distinct jumps, none being more ground breaking than the ultra-fast yet highly effective Viola–Jones (2001) face detector. Subsequently, considerable advances were made by Mathias et al. (2014)—on the back of vital work by Felzenszwalb et al. (2010) and others, on object detection using trained part-based models. However, these advances were immediately followed by breakthroughs using deep neural networks: See, for example, Yang et al. (2015a,b).

Likewise, face recognition followed a similar path, with very substantial improvements in classification performance from  $\sim 87\%$  around 2007 to  $\sim 97\%$  subsequently—notably by Taigman et al. (2014), Sun et al. (2014a,b), Sagonas et al. (2015, 2016), and Bai et al. (2016)—all of these achieving close-to-human performance levels, but again obtaining their successes by means of convolutional networks. As already outlined in [Chapter 15](#), Deep Learning Networks, CNNs only took off in 2012 (in the sense of suddenly being seen to be capable of outperforming standard approaches such as SVMs)—a factor that has already hit FDR hard. It has permitted training and testing on realistic databases such as

LFW and has necessitated improved protocols for use of these datasets. It seems clear that deep networks are here to stay, though just as the internal combustion engine survived the arrival of the jet engine, so will the standard vision algorithms from the pre-2012 era and probably new ones from the next swing of the pendulum. Meanwhile, face recognition is in a far more comfortable state than it was less than a decade ago.

*The eigenface method was the earliest systematic approach to face analysis and held promise of coping with huge numbers of facial variations, though it was soon overtaken by the Fisherface method. Face detection was also of vital importance and, when the boosting-based method of VJ emerged, it was 15 times faster than previous methods. Meanwhile, face recognition was found to be vastly inferior to human recognition on faces “from the wild.” Eventually, the real breakthrough came when applying deep learning to the task, using hundreds of thousands of faces and even more face patches, allowing “overlearning” to take place. By 2016, deep learning had also rerevolutionized face detection.*

---

## 21.12 BIBLIOGRAPHICAL AND HISTORICAL NOTES

Amongst the earliest systematic approaches to face analysis and recognition was the eigenface method which was invented by Sirovich and Kirby (1987) and developed into a successful practical technique by Turk and Pentland (1991). The basic idea was to take a set of face images as vectors in a face space, and to perform PCA to form a basis set of standard face vectors. Much effort was placed on this approach as it held the promise of analyzing faces into types, together with their modes of variation—interfacial and intrafacial (the latter including facial expressions), and even including different facial poses and lighting conditions. However, all this was too much for a single method to handle, and the Fisherfaces approach of Belhumeur et al. (1997) evolved out of it, in particular being less sensitive to lighting conditions and not needing the arbitrary elimination of the first three principal components. Indeed, Fisherfaces were found to reduce classification error rates from  $\sim 24\%$  to  $\sim 7\%$ —a notable success.

Another aspect of the face analysis problem was that of rapid detection. In 2001, VJ cut right across the existing methods and developed a highly novel approach using boosting to achieve the required speed and power. They also reduced the feature set to rudimentary rectangular-shaped Haar filters and achieved a 15-fold speed improvement over the best previous detector (that of Rowley et al., 1998): This amounted to a staggering breakthrough whose possibility had not hitherto been dreamed of.

By 2007, there was a contention between 2-D and 3-D-based face recognition algorithms, and performance was stuck at successful recognition rates  $\sim 87\%$ . At this point, it became apparent that face recognition was far from being a mature field as performance lagged well behind human performance on real images



“from the wild.” Thus, attention shifted from controlled to uncontrolled environments, and the LFW database was introduced (Huang et al., 2007). Although this led to an immediate drop in performance from available algorithms, by 2009, performance had again risen markedly: For example, Wolf et al. (2009) claimed 89.5% classification accuracy. However, the tide turned markedly in 2014 when Taigman et al. published their “DeepFace” (deep learning) approach to face recognition. This brought the performance level up to 97.35%, compared with a human performance level of 97.53%. Key to their success was the initial “frontalization” technique aimed at standardizing faces to a symmetric frontal view. Sagonas et al. (2015, 2016) developed their own frontalization technique obtaining what can best be described as a trained eigenset of frontal images. At about the same time, Yang et al. (2015a,b) developed a high-performance Faceness-Net face detector using a CNN architecture for finding attributes of face images (see also Yang et al., 2017). This was run forward to find the intrinsic face features and “in reverse” to regenerate localized face-part response maps: Here, they followed the coding–decoding procedures set out by Zeiler and Fergus (2014) and others. Finally, Bai et al. (2016) produced a very much simpler and faster design: This is a fully convolutional network working at multiple scales, with five shared convolutional layers followed by a branching out into two further convolutional layers—the latter, respectively, coping with (1) the multiple scales and (2) the sliding window effect needed to perform the final matching. An interesting and actually quite powerful conclusion is that a simpler system that is trained end-to-end has a better chance of achieving superior performance than one that is put together using separately pretrained sections.

Overall, although face recognition is in a far more comfortable state than it was less than a decade ago, it is difficult to say that the subject has stabilized. To a large extent, we are now in an area where the controlling algorithms are completely trained, and—apart from principled approaches such as the new one based on frontalization—we are arguably in a situation wherein we have relatively little knowledge of what the computer recognition system is actually doing and how close to optimality it actually is. But at least the introduction of CNN-based systems has given the subject a distinct shakeup and moved it from the doldrums to broad, sunlit uplands (cf. Part of the speech made by Winston Spencer Churchill in June 1940, following the Battle of Britain; “. . . the life of the world may move forward into broad, sunlit uplands”).

Surveillance is nowadays used very widely in transport and civil centers for monitoring traffic and people and is increasingly being carried out by computer. The motivation is largely to locate instances of undesirable behavior—theft, loitering with intent, speeding, and so on. What is special about surveillance is the rate at which pictorial information is delivered, and the fact that many of the objects being monitored are in motion. To cope with this, there is considerable emphasis on identification and elimination of the background and effective tracking of moving objects. At the same time, algorithms need to be fast in operation, though some help can be obtained with fast-dedicated hardware systems.

*Look out for:*

- The geometry of surveillance
- The need to separate foreground from background
- The basics of particle filters and their use for tracking
- The use of color histograms for tracking
- Chamfer matching and its use for identification and tracking
- How multiple cameras are used to obtain coverage over wide areas
- Systems for monitoring traffic flow
- Identification of the ground plane as an early stage in the analysis of many types of scene incorporating motion
- The need for “occlusion reasoning” when objects repeatedly pass behind one another and then reemerge
- The importance of the Kalman filter in motion applications
- License plate location
- How studies of the motions of complex objects may have to take into account 3D articulated models of linked parts
- Basic concepts of human gait analysis
- Animal tracking.

While this chapter covers the situation of static cameras being used to monitor moving objects, the following chapter covers the more complex case of in-vehicle vision systems, where moving cameras are used to monitor both stationary and moving objects.

“T is Cinna; I do know him by his gait” (William Shakespeare, 1599)

---

## 22.1 INTRODUCTION

Visual surveillance is a long-standing area of computer vision, and one of its main early uses was to obtain information on military activities—whether from high flying aircraft or from satellites. However, with the advent of ever cheaper video cameras, it subsequently became widely used for monitoring road traffic, and most recently it has become ubiquitous for monitoring pedestrians. In fact, its application has actually become much wider than this, the aim being to locate criminals or people acting suspiciously—for example, wandering around car-parks with the potential purpose of theft. However, by far, the majority of visual surveillance cameras are connected to video recorders and gather miles of videotape, most of which will never be looked at—though, following criminal or other activity, some hours of videotape may be scanned for relevant events. Further cameras will be attached to closed circuit television monitors where human operators may be able to extract some fraction of the events displayed, though human attentiveness and reliability when overseeing a dozen or so screens will not be high. Clearly, it would be far better if video cameras could be connected to automatic computer vision monitoring systems, which would call human operators' attention to potential hazards or misdemeanors of various types. Even if this were not carried out in real time in specific applications, it would be useful if it could be achieved at high speed with selected videotapes: This could save huge amounts of police time in locating and identifying perpetrators of crime.

Surveillance can cover other useful activities, including riot control, monitoring of crowds on football pitches, checking for overcrowding on underground stations, and generally helping with safety as well as crime. To some extent, human privacy must suffer when surveillance is called into play, and there is clearly a tradeoff between privacy and security: Suffice it to say here that many would be happier to have increased levels of security, a small loss of privacy being a welcome price to pay to achieve it.

In fact, there are many difficulties to be solved before the “people tracking” aspects of surveillance are fully solved. First, in comparison to cars, people are articulated objects that change shape markedly as they move: That their motion is often largely periodic can help visual analysis, though the irregularities in human motion may be considerable—especially if obstacles have to be avoided. Second, human motions are partly self-occluding, one leg regularly disappearing behind another, while arms can similarly disappear from view. Third, people vary in size and apparent shape, having a variety of clothes that can disguise their outlines. Fourth, when pedestrians are observed on a pavement, or on the underground, there is some possibility of losing track when one person passes behind another, as the two outlines tend to coalesce before reemerging from the combined object shape.

It could be said that all these problems have been solved. However, many of the algorithms that have been applied to these tasks have limited intelligence: Indeed, some employ rather simplified algorithms, as the need to operate continuously in

real time generally overrides the need for absolute accuracy. In any case, given the visual data that the computer actually receives, it is doubtful whether a human operator could always guarantee making correct interpretations: For example, there are occasions when humans turn around in their tracks because they have forgotten something, and this could cause confusion when trying to track every person in a complex scene. Further complexities can be caused by varying illumination, fixed shadows from buildings, moving shadows from clouds or vehicles, and so on.

In the following sections, we cover two main areas of surveillance—those in which people or pedestrians are the prime targets, and those in which vehicles are the prime targets. Of course, there are many transport scenarios where both would be observed by the same systems. In addition, similar techniques and considerations would apply in both cases. The next section, on the geometry underlying camera positioning, talks mainly about pedestrians: This is done for definiteness, though most of the considerations apply equally when vehicles are the prime targets, as happens on motorways, for example.

---

## 22.2 SURVEILLANCE—THE BASIC GEOMETRY

Perhaps the most obvious way of monitoring pedestrians is indicated in [Fig. 22.1A](#). As we have seen in [Chapter 16](#), *The Three-Dimensional World*, this leads to the following relations between real-world ( $X, Y, Z$ ) and image coordinates ( $x, y$ ):

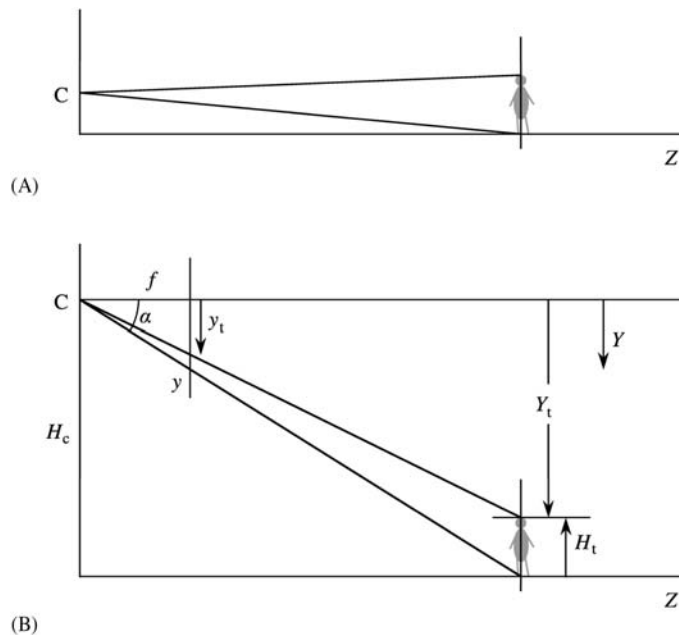
$$x = fX/Z \quad (22.1)$$

$$y = fY/Z \quad (22.2)$$

Here,  $Z$  is the (horizontal) depth in the scene,  $X$  represents lateral position,  $Y$  represents vertical position (downward from the camera axis), and  $f$  is the focal length of the camera lens. This method of observation is useful in providing undistorted profiles of pedestrians from which they may be recognized. However, it provides virtually no information about depth in the scene beyond what can be deduced from knowledge of the pedestrian's size; and as size may be one of the key parameters to be determined by the vision system, this is an unsatisfactory situation. Note also that this view of the scene is subject to gross occlusion of one pedestrian by another.

To overcome these problems, an overhead view would be better. However, it is difficult to obtain views from directly overhead; in any case, any one view would give a highly restricted range, and again pedestrian height could not be measured. An alternative approach is to place the camera in [Fig. 22.1A](#) higher up, as shown in [Fig. 22.1B](#), so that the positions of the feet of any pedestrian on the ground plane can be seen: This makes it possible to obtain a reasonable estimate of depth in the scene. In fact, if the camera is at a height  $H_c$  above the ground plane, [Eq. \(22.2\)](#) gives the depth  $Z$  as

$$Z = fH_c/y \quad (22.3)$$

**FIGURE 22.1**

3D monitoring: camera axis horizontal. (A) Camera axis mounted at eye level. (B) Camera mounted higher up to obtain a less restricted view.

while the modified value of  $y$  at the top of the pedestrian is given by

$$y_t = fY_t/Z = yY_t/H_c \quad (22.4)$$

The height of the pedestrian  $H_t$  can now be estimated from the following equation:

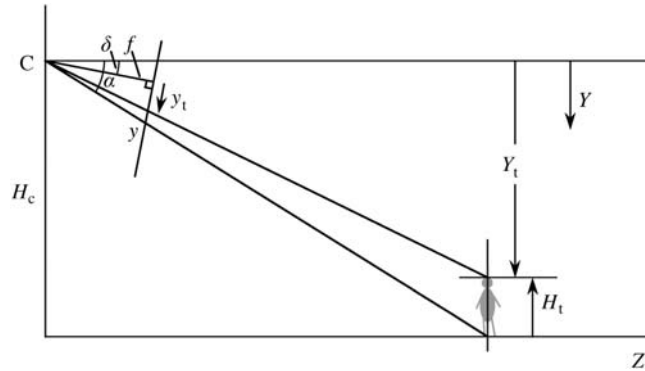
$$H_t = H_c - Y_t = H_c(1 - y_t/y) \quad (22.5)$$

Notice that to achieve this,  $H_c$  must be known from prior on-site measurements, or alternatively by camera calibration using test objects.

In practice, it is better to modify the above scheme by tilting the optical axis of the camera slightly downward (see Fig. 22.2), as this allows the range of observation to be increased, and particularly for nearby pedestrians to be kept in view. However, the geometry of the situation becomes somewhat more complicated, leading to the following basic formulae:

$$\tan \alpha = H_c/Z \quad (22.6)$$

$$\tan(\alpha - \delta) = y/f \quad (22.7)$$

**FIGURE 22.2**

3D monitoring: camera tilted downward.  $\delta$  is the angle of declination of the camera optical axis.

where  $\delta$  is the angle of declination of the camera. Substituting for  $\tan(\alpha - \delta)$  using the formula:

$$\tan(\alpha - \delta) = (\tan \alpha - \tan \delta) / (1 + \tan \alpha \tan \delta) \quad (22.8)$$

and using the above equations to eliminate  $\alpha$ , we obtain the following formula for  $Z$  in terms of  $y$ :

$$Z = H_c(f - y \tan \delta) / (y + f \tan \delta) \quad (22.9)$$

So far, we have not allowed for the heights of any objects but have only considered points on the ground plane. To estimate the heights of pedestrians, we need to bring in the additional equation:

$$Z = Y_t(f - y_t \tan \delta) / (y_t + f \tan \delta) \quad (22.10)$$

which is simply derived by substituting  $Y_t$  for  $H_c$  and  $y_t$  for  $y$  in Eq. (22.9). Eliminating  $Z$  between these two equations now allows us to find  $Y_t$ :

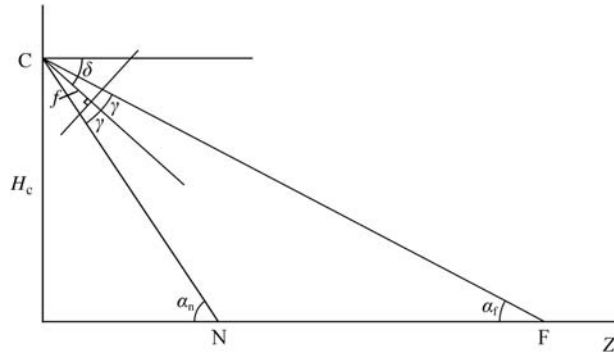
$$Y_t = H_c(f - y \tan \delta)(y_t + f \tan \delta) / (y + f \tan \delta)(f - y_t \tan \delta) \quad (22.11)$$

thereby permitting  $H_t = H_c - Y_t$  to be calculated in this case too.

Next, we consider the optimum value for the angle of declination  $\delta$  of the camera optical axis. We assume that the viewing range of the camera has to vary from a near point given by  $Z_n$  to a far point given by  $Z_f$ , corresponding to respective values of  $\alpha$ ,  $\alpha_n$ , and  $\alpha_f$  (Fig. 22.3). We also assume that the overall vertical field of view (FOV) of the camera is  $2\gamma$ . This immediately results in the following formulae:

$$H_c/Z_n = \tan \alpha_n = \tan(\delta + \gamma) \quad (22.12)$$

$$H_c/Z_f = \tan \alpha_f = \tan(\delta - \gamma) \quad (22.13)$$


**FIGURE 22.3**

Geometry for considering optimum camera tilt.  $\delta$  is the angle of declination of the camera optical axis.  $2\gamma$  is the overall vertical field of view of the camera.

Taking the ratio between these equations now shows that

$$\eta = Z_n/Z_f = \tan(\delta - \gamma)/\tan(\delta + \gamma) \quad (22.14)$$

so specifying either  $Z_n$  or  $Z_f$  immediately gives the alternate value. In the case that  $Z_f$  is taken to be infinity, Eq. (22.13) shows that  $\delta$  has to be equal to  $\gamma$ , in which case Eq. (22.12) leads to the relation  $Z_n = H_c \cot 2\gamma$ . Note that  $\delta = \gamma = 45^\circ$  is a limiting case that covers all points on the ground plane, that is,  $Z_n = 0$  and  $Z_f = \infty$ . For smaller values of  $\gamma$ , values of  $Z_n$  and  $Z_f$  are determined by  $\delta$ : e.g., for  $\gamma = 30^\circ$ , the optimum value of  $\eta$  (namely, 0) occurs both at  $\delta = 30^\circ$  and at  $\delta = 60^\circ$ , and the worst case ( $\eta \approx 0.072$ ) occurs at  $\delta = 45^\circ$ .

Finally, it is instructive to consider the minimum separation  $Z_s$  that is needed between pedestrians if they are not to occlude each other at all. By equating  $\tan\alpha$  to both  $H_t/Z_s$  and  $H_c/Z$  [see Eq. (22.6)], we find:

$$Z_s = H_t Z / H_c \quad (22.15)$$

As might have been expected, this varies inversely with camera height, but note that it is also proportional to  $Z$ .

Overall, we have seen that placing the camera high up permits both depth and height to be estimated and the incidence of occlusion to be considerably reduced. In addition, tilting the camera downward permits the maximum range to be achieved. Importantly, two cameras placed at the far ends of a courtyard should be able to cover it quite well. Pedestrians can be identified as having a particular position on the ground plane, though they could then be recognized pictorially from knowledge of their size, shape, and coloring. The formulae that are involved reflect all the complications of perspective projection, and some are quite complex. Notice that even in the simple case of Fig. 22.1B, the inverse relation between  $y$  and  $Z$  is highly nonlinear [see Eq. (22.3)], and equal intervals in the  $Z$

direction by no means correspond to equal vertical intervals in the image plane: See [Section 18.8](#) for further theory underpinning this point.

---

## 22.3 FOREGROUND–BACKGROUND SEPARATION

One of the first problems of surveillance is to locate the targets that are to be placed under observation. In principle, we could follow all the recognition methods of earlier chapters and just proceed to recognize the targets individually. However, there are two reasons why we should approach this differently. First, cars moving along a road, or pedestrians in a precinct, are highly variegated, unlike the situation for products appearing on a product line. Second, there is usually a significant real-time problem, especially when vehicles are moving at up to 100 mph on a highway, and cameras typically deliver 30 frames per second under highly variable conditions. Thus, it pays to capitalize on the motion of the targets and performs motion-based segmentation.

In these circumstances, it is natural to think of frame differencing and optical flow. Indeed, frame differencing has been applied to this task, but it is prone to noise problems and consequent unreliability. In any case, when applied between adjacent frames, it locates only limited sections of target outlines—in accordance with the  $-\nabla I \cdot \mathbf{v}$  formula of [Chapter 20](#), Motion. The simplest way out of this difficulty is that of background modeling.

### 22.3.1 BACKGROUND MODELING

The idea of background modeling is to create an idealized background image that can be subtracted from any frame to yield the target or foreground image. To achieve this, the simplest strategy is to take a frame when there are known to be no targets present and use that as the background model. In addition, to eliminate noise, it is useful to average a number of frames prior to making observations of targets. The problems with this strategy are (1) how to know when there are no targets present so that frames represent true background and (2) how to cope with the usual outdoor situation of illumination that varies with the weather and the time of day.

To solve the latter problem, only the most recent frames can reasonably be used, and if this path is followed, it is difficult to tackle the former problem (in any case, on highways with a lot of traffic, or precincts with a continuous *mêlée* of people, there may seldom be a chance of obtaining a clear background frame). One compromise solution is to take an average of many background frames over the most recent period  $\Delta t$ , whether or not targets are present. If targets are reasonably rare, most of the frames will be clear and a good approximation to an ideal background model will be built: Of course, any targets will not be eliminated so much as averaged in, and the result will sometimes be visible “tails” in the model.



To optimize the model,  $\Delta t$  can be increased, thereby minimizing problem (1), or decreased, thereby minimizing problem (2). Clearly, there is a tradeoff between the two difficulties: while it can be adjusted to suit the time of day and prevailing weather and illumination levels, this approach is limited.

Part of the problem is due to the “averaging in” mentioned above, and this can be partially eliminated by using a temporal median filter. Note that this means applying a median filter to the **I** (intensity and color) values of each pixel, over the sequence of frames arising during the most recent period  $\Delta t$ . This is a computation intensive process but is considerably better than taking a raw average, as mentioned above. It is effective to take the median because it eliminates outliers, but ultimately it will still lead to biased estimates. In particular, if we suppose that vehicles are on the whole darker than the road, then the temporal median will also tend to end up darker than the road. To overcome this problem, a temporal mode filter can be used, and hopefully, the intensity distribution will have separate modes—one from the road and one from the vehicles, so the former can be used and could probably be identified even if it became a minor mode when there were a lot of vehicles. However, there is no guarantee that there would only be one mode for vehicles, or even that any such modes would be clearly separated from the one corresponding to the road, and bias would again be the most likely result. Figs. 22.4–22.6 in Section 22.3.2 illustrate some of the problems.

In fact, there are significant further problems with background modeling. In many situations, the background objects are themselves subject to motion. In particular, shadows will move with time and their crispness will change with the weather; while leaves, branches of trees, and flags will flutter and sway in the wind, with highly variable frequencies, even the camera may sway, especially if it is mounted on a pole, but we defer that type of problem until Chapter 23, In-Vehicle Vision Systems. Motions of small animals and birds may also have to be considered. At this point, we shall concentrate on fluttering vegetation, which is often prevalent in outdoor scenarios, even within cities.

The fluttering of vegetation can be more serious than might at first be imagined. It can result in the **I** values of some pixels oscillating between those of leaves, branches, and sky (or ground, buildings, etc.). Thus, the distributions of intensities and colors for any pixel may best be regarded as the superposition of several distributions corresponding to two or three component sources. Here, what is important is that each of the component distributions could be quite narrow and well defined. This means that if each is known from ongoing training, any current intensity **I** can be checked to determine whether it is likely to correspond to background. If not, it has to correspond to a new foreground object.

Models formed from multiple component distributions are commonly called mixture models: In practice, the component distributions are approximated by Gaussians, because the odd shape of the overall distributions is largely attributable to the existence of the separate components. Thus, we arrive at the terms Gaussian mixture models (GMMs) and mixtures of Gaussians. Notice that the number of components at any pixel is initially unknown: Indeed, a large

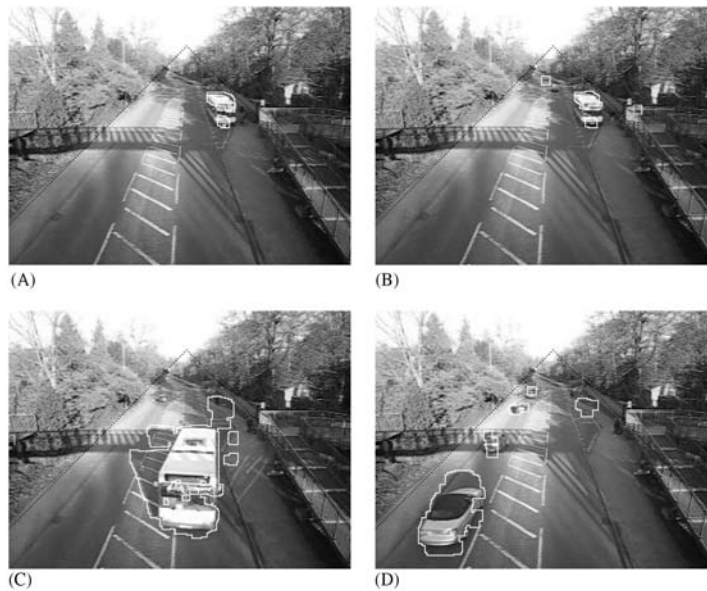


**FIGURE 22.4**

Background subtraction using a temporal median filter. The lines of black graphics dots demarcate the relevant road region: Almost all of the fluttering vegetation lies outside this region [it is indicated by fainter boundaries than for the foreground objects: see (B)]. Note the plethora of stationary shadows that are completely eliminated during the process of background subtraction. The stationary bus is progressively eaten away in (A) and (B), while in (C) and (D), the ghost of the bus appears and then starts to merge back into the background. These problems are largely eliminated in Fig. 22.5, which includes the same four frames.

proportion of pixels will have only a single component, and it may seem unlikely that the number would be much larger than three in practice. However, the fact that every pixel will have to be analyzed to determine its GMM is computationally burdensome, while the analysis can be unstable if the component distributions are not as tidy as suggested above. These factors mean that a computation intensive algorithm, the expectation maximization (EM) algorithm, has to be used to analyze the situation. In fact, while it is usual to use this rigorous approach to *initialize* the background generation process, many workers use simpler more efficient techniques for updating it so that the ongoing process can proceed in real time. The GMM method determines for itself the number of component distributions to use, the judgment being based on a threshold value for the fraction of the total weight given to the background model.

Unfortunately, the GMM approach fails when the background has very high frequency variations. Essentially, this is because the algorithm has to cope with

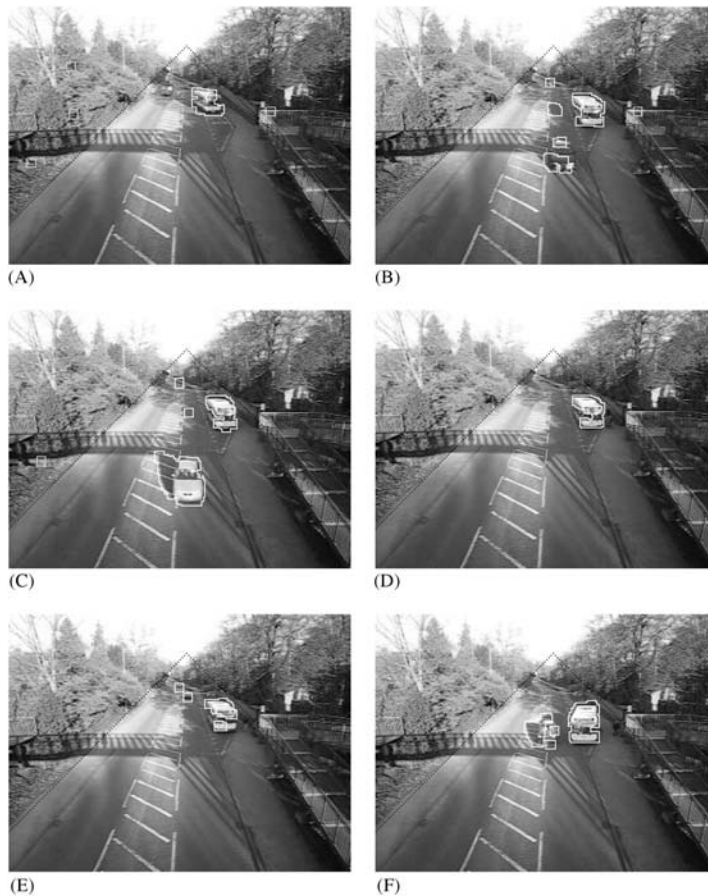


**FIGURE 22.5**

Background subtraction using a restrained temporal median filter. This figure shows a much more comprehensive set of frames than Fig. 22.4 because the method is more accurate. In particular, its responses (D, E, G, H) to the bus problems of Fig. 22.4 are vastly improved. Fluttering vegetation problems are indicated by fainter boundaries than for vehicles but are entirely absent from the road region. In all frames, the stationary shadows are completely eliminated by background subtraction: even the prominent bridge shadow is ignored; neither does it have much effect on the integrity of foreground objects. Note the low false-negative rate for vehicles, and the fact that they only tend to be joined together in the distance. Overall, foreground object fragmentation and false shapes (including the effects of moving shadows) are the worst problems.

**FIGURE 22.5**

(continued)

rapidly varying distributions, which change dramatically over very short periods of time, so the statistics become too poorly defined. To tackle this problem, Elgammal et al. (2000) moved away from the parametric approach of the GMM (the latter essentially finds the weights and variances of the component distributions, and thus is parametric). Their nonparametric method involves taking a kernel smoothing function (typically a Gaussian) and for each pixel, applying it to the  $N$  samples of  $\mathbf{I}$  for frames appearing during the period  $\Delta t$  prior to the current time  $t$ . This approach is able to rapidly adapt to jumps from one intensity value to another, while at the same time obtaining the local variances at each pixel. Thus, its value lies in its capability to quickly forget old intensities and to reflect local variances rather than random intensity jumps. In addition, it is a probabilistic approach but has no need of the EM algorithm, and this enables it to run highly

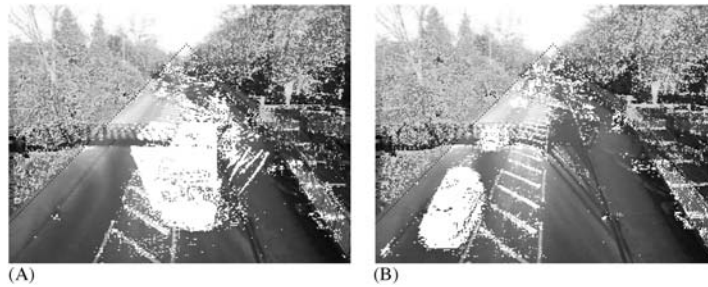


**FIGURE 22.6**

Problems arising immediately after background subtraction. These two frames show clearly the noise problems that arise during background subtraction: the white pixels indicate where the current image fails to closely match the background model. Most of the noise effects occur for fluttering vegetation outside the road region. Morphological operations (see text) are used to largely eliminate the noise and to integrate the vehicle shapes as far as possible, as shown in [Figs. 22.4 and 22.5](#).

efficiently in real time. In addition, it is capable of sensitive detection of foreground objects coupled with low false alarm rates. To achieve all this, it incorporates two further features:

1. It assumes independence between three different color channels, each having its own kernel bandwidth (variance). Together with the adoption of a Gaussian kernel function, this leads to a probability estimate given by

$$P(\mathbf{I}) = \frac{1}{N} \sum_{i=1}^N \prod_{j=1}^C \frac{1}{(2\pi\sigma_j^2)^{1/2}} e^{-(I_j - I_{ji})^2 / 2\sigma_j^2} \quad (22.16)$$

where  $i$  runs over the  $N$  samples taken in the time period  $\Delta t$  and  $j$  runs over the  $C$  color channels; this function is simple to calculate, though computation is further speeded up by use of precalculated kernel function lookup tables.

2. It uses chromaticity coordinates for suppressing shadows. As these coordinates are independent of the level of illumination, and shadows can be regarded as poorly lit background, this means that they should largely merge back into the background. Hence, the foreground is much less likely to have shadows accompanying it after background subtraction. The chromaticity coordinates  $r$ ,  $g$ ,  $b$  are derived from the usual  $R$ ,  $G$ ,  $B$  coordinates by the equations  $r = R/(R + G + B)$ , etc., with  $r + g + b = 1$ .

In fact, shadows can be particularly problematic: Not only do they distort the apparent shapes of foreground objects after background subtraction, but also they can connect separate foreground objects, and thus cause undersegmentation. The problem is reviewed by Prati et al. (2003), while Xu et al. (2005) have proposed a

hybrid shadow removal method that makes use of morphology: See also Guan (2010).

Whatever method is used for background modeling leading to background subtraction and hence to foreground detection, the various blobs will need to be clustered and labeled using connected components analysis. Frame-to-frame tracking is then carried out by making correspondences between the blobs in the different frames. As in the case of Xu et al. (2005), morphology can be used to help with this process. Nevertheless, false positives tend to arise because of shadows and illumination effects, while false negatives can arise from color similarities between foreground and background.

Overall, failures arise in two categories: (1) *the stationary background problem*, in which the shape of the foreground object is not defined accurately enough; and (2) *the transient background problem*, in which the start and stop of the foreground object aren't found quickly enough. If the accuracy or reactivity of the background model is inadequate, background subtraction will lead to the detection of false objects: These are called “ghosts” by Cucchiara et al. (2003). In addition, as indicated above, shadows tend to compound these problems.

### 22.3.2 PRACTICAL EXAMPLES OF BACKGROUND MODELING

To add concreteness to the above discussion, a traffic surveillance video was taken and submitted to some of the algorithms mentioned above. For illustrative purposes, the algorithms were kept as simple as possible. The raw data consisted of an AVI video from a digital camera (Canon Ixus 850 IS), which was decompiled into individual JPG frames, and though the JPG artifacts were fairly severe, no specific attempt was made to eliminate them. The frame size was  $320 \times 240$  pixels in RGB color, but only the 8-bit lightness component was used for the main tests. While the video was taken at 15 frames per second, only every 10th frame was used for the test, which comprised 113 frames. Of these, the first 10 can be regarded as initialization training material and these are not considered further. During the test, a bus arrived and was stationary at a bus stop for some time. The overall sequence is illustrated in Fig. 22.5: However, for reasons of space, the only frames included in the figures are those that illustrate the problems well. Note that the video was taken on a sunny day, and that there are a great many shadows, which over the minute or so of the video did not change markedly. On the other hand, some camera motion is detectable, possibly due to movement of the bridge. Thus, there are many ways in which the raw data were not ideal: These therefore impose exacting conditions on the success of any algorithm.

Fig. 22.4 shows some of the results obtained by applying a temporal median. Parts (A) and (B) show the bus stationary at the bus stop and being progressively eaten up as it starts to merge with the background. Part (C) shows the bus moving away from the bus stop, leaving a large “ghost” behind it. Part (D) shows that the ghost remains for some time and is a substantial factor to be taken into account by any foreground interpretation procedure.

To overcome these problems, the median was restrained so that it could only take into account pixel intensities within a limited number of gray levels of the current median value: In this way, it took on something of the characteristics of a mode filter (a temporal mode filter per se would lock on to the current value too inflexibly and not adapt well to the changing intensity distribution). The results are shown in Fig. 22.5. It is clear that the restrained median largely eliminates the two problems mentioned above (viz., the observed vehicle being eaten away while stationary and leaving a ghost behind it when moving on). For this reason, the remainder of the tests used only the restrained median. Problems that are seen in Fig. 22.5 include the following:

1. Eating away of foreground objects, leaving unusual shapes [e.g., (D), (I)].
2. Fragmentation of foreground objects [e.g., (B), (F)].
3. Shadows accompanying the moving foreground objects [e.g., (C), (G), (J)].
4. Joining of foreground objects that should appear separated [e.g., (I), (J)].
5. Signals from fluttering vegetation [e.g., (A), (K)].

Item 2 can be considered as an extreme case of item 1. Item 3 is bound to arise as the shadows are moving at the same speed as the vehicles that give rise to them, and straightforward background suppression or alternatively moving object detection alone will not eliminate them: in general, unless color interpretation will help (we return to this possibility below), high-level interpretation is needed to achieve satisfactory elimination. Item 4 is due partly to the effects of vehicle shadows, which tend to connect vehicles, especially when seen in the distance. The morphological operations that were applied (see below) also tended to make vehicles become joined. Item 5 is never manifest in the road region, i.e., between the lines of black graphics dots shown in the frames. This is because, in this case, the vegetation is high up, away from the road region. In addition, it is largely eliminated by morphological operations. In fact, Fig. 22.6 shows the results obtained immediately after background subtraction. It is clear that there is a serious noise problem, caused largely by (1) camera noise, (2) the effects of JPG artifacts, (3) fluttering vegetation, and (4) the effects of slight camera motion. Interestingly, two applications of a single pixel erosion operation were sufficient to eliminate the noise almost completely, these being followed by four applications of a single dilation operation to help restore vehicle shapes. (Overall, this corresponds to a 2-pixel opening operation followed by a 2-pixel dilation operation.) These morphological operations were selected to give roughly optimal results—in particular, low probability of failing to capture foreground objects in any individual frame, coupled with pressure to maintain object shapes as far as reasonable, and not to join vehicles together unavoidably. The point is that background subtraction must aim to pass on sufficient useful information to subsequent foreground object identification, tracking, and interpretation stages.

One of the remarkable aspects of the results is the total elimination of stationary shadows and lack of problems arising from this. On the other hand, two other sorts of shadows are manifest—those arising from moving objects, and those

falling on moving objects (the latter arise in the video both from the bridge and from the other causes of ground shadows): neither of these sorts of shadows are eliminated. Other problems are those of reflections, particularly from the windows of the bus (see the frame in Fig. 22.5G), and secondary illumination from moving vehicles.

Lastly, it was felt worthwhile to attempt utilizing the original color images and augmenting the background model by using the chromaticity coordinates as outlined in the previous section. In fact, while in some respects improvements occurred, these were more than canceled out by increased numbers of false negatives and fragmented shapes of the foreground objects. No results are shown here, but whereas Elgammal et al. (2000) were able to show excellent results obtained in this way, with the video used here no improvement seemed to be achievable by this approach. This requires some explanation. High up amongst the reasons is the effect of the highly variegated colors and intensities of the many different vehicles. In particular, some vehicles turned out to have body intensities close to those of shadows, whereas others had windows or transparent roofs of similar intensity. These had the effect of eliminating large portions of vehicles together with the shadows, thereby increasing the incidence of false-negative and false-shape information. However, even Elgammal et al. (2000) point out that intensities have to be used carefully in a way that will bolster up the shadow-removing capabilities of the chromaticity information, and here there appeared to be no way this could be achieved. Overall, all the color and grayscale information has to be taken into account in a more considered and strategic way, and this demands a thoroughgoing statistical pattern recognition approach in which objects are identified one by one in a high-level schema rather than by relatively chancy ad hoc methods: the latter definitely have their place, but their use must not be pushed beyond what is reasonable. One example of the use of object-by-object recognition is the identification of road markings, which need to be, and could easily be, identified whether or not vehicle shadows cover them. This could then lead to a much more viable strategy for identifying, tracking, and eliminating vehicle shadows. Meanwhile, in situations where the road has almost no color content, as in the traffic surveillance trials described above, it is difficult to remove shadows effectively merely by using chromaticity information.

### 22.3.3 DIRECT DETECTION OF THE FOREGROUND

In the previous subsection, it has been seen that background modeling followed by background subtraction constitutes a powerful strategy for the location of moving targets in image sequences. Nevertheless, for all sorts of reasons, it is limited in what it can achieve. While these reasons devolve into problems such as changes in ambient illumination, effects of shadows, irrelevant motions such as fluttering leaves, and color similarities between foreground and background, there is one whole tranche of information that is absent: Specifically, there is a total lack of information on the nature of the target objects, including size, shape,



location, orientation, color, speed, and probability of occurrence. If this sort of information were obtainable, there would be some chance of incorporating it into a complete target-detection system and achieving close to perfect detection capability. Indeed, it seems possible that in some cases, ignoring the background and attempting direct detection of the foreground might be a better first approximation. Such a procedure might well be both effective and efficient for the case of face detection, for example. In what follows, we consider how direct foreground detection might be achieved.

Direct foreground detection is only possible if a suitable foreground model is available or can be constructed. It would seem that this requires a specialization to each particular application, such as pedestrian detection or vehicle detection. However, some workers (e.g., Khan and Shah, 2000) have managed to achieve it more generically by a bootstrapping process. They start with background modeling and background subtraction, locate foreground objects by an “exception to background” procedure, and thus create initial foreground models. In subsequent frames, these are enhanced, mostly using Gaussian-based models: GMMs and nonparametric models have been employed for this. However, a difference relative to background modeling is that the latter applies continuously (with updates) for the same camera, whereas each foreground object must have its own individual model which is learnt anew for that object. So background modeling is only applied to initially locate the foreground object: thereafter, the foreground model is built and tracked, albeit in a similar way to what happens with background modeling.

More recently, in a new class of algorithm, Yu et al. (2007) use a GMM for simultaneously modeling both foreground and background. In this way, a tension is built between foreground and background that potentially leads to higher segmentation accuracy, and this does seem to have been achieved in practice. Against this, the algorithm has to be initialized by marking areas of definite foreground and background, and then it continues to track autonomously. However, there seems to be no reason why initialization should not also be carried out autonomously with the help of an initial stage of background modeling.

---

## 22.4 PARTICLE FILTERS

When trying to track foreground objects, independent detection in each frame, followed by appropriate linking, does not make best use of available information; neither does it achieve optimum sensitivity: this will be obvious when noting that averaging slowly moving objects over a number of frames can boost signal-to-noise ratio. In addition, over time—and sometimes over very few frames—objects can change radically in appearance, so tracking is needed in order to ensure continued capture. Nowhere is this more obvious than in the case of a guided missile approaching a target over several miles, as during the time of flight, the size,

scale, and resolution will increase dramatically. But even in cases where a person is being tracked, rotation of the head will present if anything even more dramatic changes in appearance. With the radically changing backgrounds arising with moving and rotating objects, sensitive robust tracking is clearly of fundamental importance. To achieve this, optimal methods are needed. In particular, in the face of radical change, we need to know what is the most *likely* position of an object that is being tracked. Optimal estimation of likelihood implies the need for Bayesian filtering.

To achieve this, we start by considering the observations  $\mathbf{z}_1$  to  $\mathbf{z}_k$  of an object in successive frames, and the corresponding deduced states of the object  $\mathbf{x}_0$  to  $\mathbf{x}_k$  (there is no zeroth value of  $\mathbf{z}$  because it takes at least two frames to estimate the velocity  $\mathbf{v}_k$ , which forms part of  $\mathbf{z}$  of the state information). At each stage, we need to estimate the most probable state of the object, and Bayes rule gives us the a posteriori probability density shown in Eq. (22.17) below. (Note that it is much easier to see the relation to Bayes rule if conditional dependence on  $\mathbf{z}_{1:k}$  is eliminated; once this is done, all remaining subscripts are equal to  $k + 1$ , and suppressing them, Eqs. (22.17) and (22.18) become standard Bayes rule. Reinstating dependence on  $\mathbf{z}_{1:k}$  is of course necessary when dealing with tracking over  $k + 1$  frames involving previous observations  $\mathbf{z}_{1:k}$ .)

$$p(\mathbf{x}_{k+1}|\mathbf{z}_{1:k+1}) = \frac{p(\mathbf{z}_{k+1}|\mathbf{x}_{k+1})p(\mathbf{x}_{k+1}|\mathbf{z}_{1:k})}{p(\mathbf{z}_{k+1}|\mathbf{z}_{1:k})} \quad (22.17)$$

where the normalizing constant is

$$p(\mathbf{z}_{k+1}|\mathbf{z}_{1:k}) = \int p(\mathbf{z}_{k+1}|\mathbf{x}_{k+1})p(\mathbf{x}_{k+1}|\mathbf{z}_{1:k}) d\mathbf{x}_{k+1} \quad (22.18)$$

The prior density is obtained from the previous time-step:

$$p(\mathbf{x}_{k+1}|\mathbf{z}_{1:k}) = \int p(\mathbf{x}_{k+1}|\mathbf{x}_k)p(\mathbf{x}_k|\mathbf{z}_{1:k}) d\mathbf{x}_k \quad (22.19)$$

but note that this is only valid because of the Markov process (of order one) assumption commonly taken to simplify Bayesian analysis, which leads to

$$p(\mathbf{x}_{k+1}|\mathbf{x}_k, \mathbf{z}_{1:k}) = p(\mathbf{x}_{k+1}|\mathbf{x}_k) \quad (22.20)$$

In other words, the transition probability for the update  $\mathbf{x}_k \rightarrow \mathbf{x}_{k+1}$  depends only indirectly on  $\mathbf{z}_{1:k}$ , via previous updates.

General solutions of this set of equations—in particular, Eqs. (22.17) and (22.19)—do not exist. However, restricted solutions are possible, as in the case of the Kalman filter (see Chapter 20: Motion), which assumes that all posterior densities are Gaussian. In addition, particle filters can be used to approximate the optimal Bayesian solution when Gaussian constraints are inapplicable.

The particle filter, also known as sequential importance sampling (SIS), the sequential Monte Carlo approach, bootstrap filtering, and condensation, is a recursive (iteratively applied) Bayesian approach that at each stage employs a set of

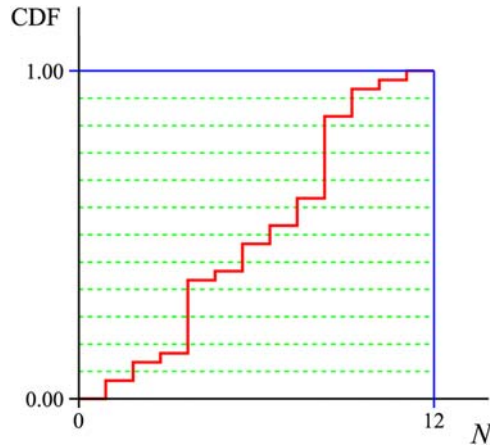


**FIGURE 22.7**

Use of the cumulative distribution function (CDF) to perform systematic resampling. Applying the regularly spaced horizontal sampling lines shows the cuts needed to find appropriate indexes ( $N$ ) for the new samples. The cuts tend to ignore the small steps in the CDF and to accentuate the large steps by duplicating samples.

samples of the posterior density function (see [Appendix D](#) for basic concepts on sampling from distributions). It is an attractive concept because in the limit of large numbers of samples (or “particles”), the filter is known to approach the optimal Bayesian estimate (Arulampalam et al., 2002).

To apply this method, the posterior density is reformulated as a sum of delta function samples:

$$p(\mathbf{x}_k | \mathbf{z}_{1:k}) \approx \sum_{i=1}^N w_k^i \delta(\mathbf{x}_k - \mathbf{x}_k^i) \quad (22.21)$$

where the weights are normalized by

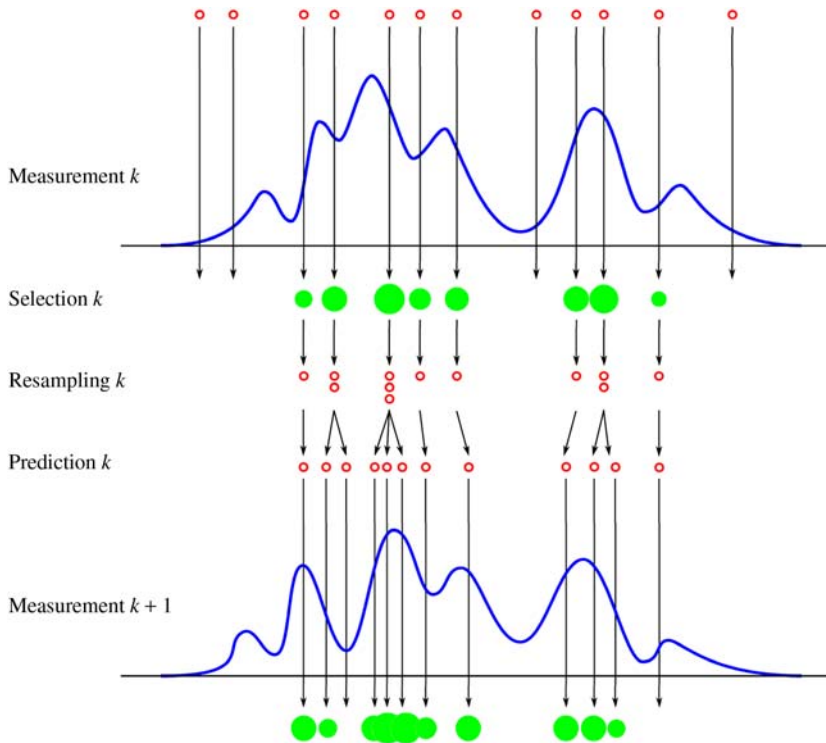
$$\sum_{i=1}^N w_k^i = 1 \quad (22.22)$$

Substituting into [Eqs. \(22.17\)–\(22.19\)](#), we obtain the posterior as follows:

$$p(\mathbf{x}_{k+1} | \mathbf{z}_{1:k+1}) \propto p(\mathbf{z}_{k+1} | \mathbf{x}_{k+1}) \sum_{i=1}^N w_k^i p(\mathbf{x}_{k+1} | \mathbf{x}_k^i) \quad (22.23)$$

where the prior now takes the form of a mixture of  $N$  components.

In principle, this gives us a discrete weighted approximation to the true posterior density. In fact, it is often difficult to sample directly from the posterior density: this problem is normally solved by SIS from a suitable “proposal” density


**FIGURE 22.8**

Perspective on the processes involved in particle filtering. Notice, how the filter cycles repeatedly through the same basic sequence.

function  $q(\mathbf{x}_{0:k} | \mathbf{z}_{1:k})$ . It is useful to take an importance density function that can be factorized:

$$q(\mathbf{x}_{0:k+1} | \mathbf{z}_{1:k+1}) = q(\mathbf{x}_{k+1} | \mathbf{x}_{0:k}, \mathbf{z}_{1:k+1})q(\mathbf{x}_{0:k} | \mathbf{z}_{1:k}) \quad (22.24)$$

following which, the weight update equation can be obtained (Arulampalam et al., 2002) in the form:

$$\begin{aligned} w_{k+1}^i &= w_k^i \frac{p(\mathbf{z}_{k+1} | \mathbf{x}_{k+1}^i) p(\mathbf{x}_{k+1}^i | \mathbf{x}_k^i)}{q(\mathbf{x}_{k+1}^i | \mathbf{x}_{0:k}^i, \mathbf{z}_{1:k+1})} \\ &= w_k^i \frac{p(\mathbf{z}_{k+1} | \mathbf{x}_{k+1}^i) p(\mathbf{x}_{k+1}^i | \mathbf{x}_k^i)}{q(\mathbf{x}_{k+1}^i | \mathbf{x}_k^i, \mathbf{z}_{k+1})} \end{aligned} \quad (22.25)$$

where the path  $\mathbf{x}_{0:k}^i$  and history of observations  $\mathbf{z}_{1:k}$  have been eliminated—as is necessary if the particle filter is to be able to track recursively in a manageable way.

In fact, pure SIS has the largely unavoidable problem that all but one particle will have negligible weight after a few iterations. More precisely, the variance of the importance weights is only able to increase over time, leading ineluctably to this degeneracy problem. However, one simple means of limiting the problem is to resample particles so that those with small weights are eliminated, while those with large weights are enhanced by duplication. Duplication can be implemented relatively easily, but it also leads to so-called sample impoverishment, i.e., it still results in some loss of diversity among the particles, which is itself a form of degeneracy. Nevertheless, if there is sufficient process noise, the result may prove to be adequate.

One basic algorithm for performing the resampling is “systematic resampling” and involves taking the cumulative discrete probability distribution (in which the original delta function samples are integrated into a series of steps) and subjecting it to uniform cuts over the range 0 to 1 to find appropriate indexes for the new samples. As will be seen from Fig. 22.7, this leads to small samples being eliminated and strong samples being duplicated, possibly several times. The result is called sampling importance resampling (Sir) and is a useful first step on the way to producing stable sets of samples. With this particular approach, the importance density is chosen to be the prior density:

$$q(\mathbf{x}_{k+1}|\mathbf{x}_k^i, \mathbf{z}_{k+1}) = p(\mathbf{x}_{k+1}|\mathbf{x}_k^i) \quad (22.26)$$

Appealing to Eqs. (22.25) shows that the weight update equation becomes enormously simplified to

$$w_{k+1}^i = w_k^i p(\mathbf{z}_{k+1}|\mathbf{x}_{k+1}^i) \quad (22.27)$$

Moreover, as resampling is applied at every time index, previous weights  $w_k^i$  are all given the value  $1/N$ , so we can simplify this equation to

$$w_{k+1}^i \propto p(\mathbf{z}_{k+1}|\mathbf{x}_{k+1}^i) \quad (22.28)$$

As can be seen in Eq. (22.26), the importance density is taken to be independent of measurement  $\mathbf{z}_{k+1}$ , so the algorithm is restricted with regard to observational evidence, and this is one cause of the loss of particle diversity mentioned earlier.

The Condensation method of Isard and Blake (1996) goes some way to eliminating these problems by following the resampling with a prediction phase during which a diffusion process separates any duplicated samples, thereby helping to maintain sample diversity. This is achieved by applying a stochastic dynamical model that has been trained on sample object motions. Fig. 22.8 gives an overall perspective on the approach and includes all the sampling and other processes that have been discussed above.

The concept is taken further in the ICondensation approach (Isard and Blake, 1998) by using a mixture of samples, some using standard Sir and some using an importance function depending on the most recent measurement  $\mathbf{z}_{k+1}$  but ignoring the dynamics. Thus, this complex method reflects the need to ensure continued

sample diversity: It also aims to combine low- and high-level approaches to tracking by noting that model switching may be necessary when handling real-world tasks such as tracking human hands.

Similar ideas and motivation were employed by Pitt and Shephard (1999) in their auxiliary particle filter (APF). This generates particles from an importance distribution depending on the most recent observations, and then samples the posterior using this importance density. The algorithm involves an additional likelihood computation for each particle, but overall, the computational efficiency is improved because fewer particles are needed. Nevertheless, Nait-Charif and McKenna (2004) found that the method gave only limited improvement relative to Sir. They went on to make a comparison with the iterated likelihood weighting (ILW) scheme. In this approach, after an initial iteration of Sir, the sample set is split randomly into two sets of equal size; one of these is migrated to regions of high likelihood and the other is handled normally. The purpose is to cope on the one hand with situations where the prior is sound and on the other hand, with situations where it is not and regions of high likelihood need to be explored. When tracking human heads, the method proved to be a significantly more robust tracker than either Sir or the APF. Perhaps oddly, the ILW is designed to reduce approximation error rather than to give unbiased estimates of a posterior. This means that it is not based completely on probabilistic methods. On the other hand, as for the Isard and Blake ICondensation approach mentioned above, it is intended to match a variety of scenarios that can be found when tracking under real-world conditions, where it is difficult to model all probabilities accurately.

Many more particle filter methods have been developed over the past decade or so. Several incorporate the Kalman filter and its extended and “unscented” versions, in attempts to optimize likelihoods when sample diversity turns out to be insufficient. More recently “regularized” and “kernel” particle filters (Schmidt et al., 2006) have been developed to tackle the problem of sample impoverishment. These perform resampling using a continuous approximation to the posterior density, typically using the Epanechnikov kernel (Comaniciu and Meer, 2002). The mean shift approach is in this category. Essentially, the mean shift algorithm is a means of climbing density gradients to identify underlying modes in sparse distributions and involves moving a sampling sphere around the space being searched. This makes it a good iterative search technique, though it is only suitable for locating one mode at a time. It complements the particle filter formalism well, as it can be used to refine the accuracy with which objects may be found, and works well even if a limited number of particles are employed. It has recently been applied by Chang and Lin (2010) for tracking various parts of the moving human body.

At this stage, it is starting to become apparent that different tracking applications will demand different types of particle filter. This will depend on a variety of factors including how jerky the motion is, whether rotations will be involved, whether occlusions will occur, and if so for how long—and of course on the appearance and variability of the objects being tracked. It should be noted that all

the theory and most of the ideas presented above reflect abstract situations and the concentration is on relatively small, well-localized objects that are considered locally, i.e., the filters themselves will not have a global understanding of the situation. Thus, they must be categorized as low or intermediate level vision. In contrast, the human eye is an excellent tracker by virtue of its capability for thinking about what objects are present and which ones have moved where, including passing behind other objects or even temporarily out of the scene. Clearly, we must not expect too much from particle filters just because they are based on probabilistic models.

An important advantage of particle filters is that they can be used to track multiple objects in an image sequence. This is because there is no record of which object is being tracked by which particles. However, this possibility arises only because no restrictions are placed on the posterior densities: In particular, they are not assumed to be Gaussian as in the case of Kalman filters. Indeed, if Kalman filters are used for tracking, each object must be tracked by its own Kalman filter.

Once a suitable approach to particle filtering has been arrived at, it is necessary to determine how to implement it. The basic means of achieving this is via appearance models. In particular, color and shape models are frequently used for this purpose. However, before delving into this topic, it will be useful to find what can be achieved by color analysis using what is by now quite an old approach—that of color indexing via color histogram matching.

---

## 22.5 USE OF COLOR HISTOGRAMS FOR TRACKING

One of the most useful tools that is available for object tracking was developed as early as 1991 by Swain and Ballard (1991) in a paper called “Color indexing.” The aim of that work was to index from a color image into a large database of models. In a sense that idea is the inverse of the tracking problem, as its purpose was to search for the model with the best match to a given image rather than to search for instances of a given model in frames from an image sequence. Actually, database searches fall in the realm of classification, whereas the process of tracking assumes implicitly that the object in question has already been identified. However, apart from one important difference which will be discussed below, this is a rather minor point.

The main idea behind the color indexing approach is that of matching color histograms rather than the images themselves. There is an obvious validity in this approach, in that if the images match, so will their color histograms. What is more, as the histograms have no memory of where in the image a particular color originated, histograms are invariant to translation and rotation about the viewing axis (so-called “in-plane rotation”). Also relevant is the fact that a planar object that is subject to out-of-plane rotation will still have the same color histogram,

although it will involve different numbers of pixels, so normalization will be required. The same applies for objects that are at different depths in the scene: The histogram profile will be unchanged, but it will have to be normalized to allow for the different numbers of pixels that are involved. Finally, a spherical or cylindrical object with the same set of colors distributed similarly over its surface will again have the same histogram. While exact adherence to this scenario might be relatively rare, it would apply almost perfectly for a ball of wool or a football, and with varying degrees of exactness for a shaven human head or torso. In fact, the main problem with use of histograms for recognition is the possible ambiguity it could bring, but when tracking a known object that has moved only a small distance between frames, this problem should be a minor one.

The above explanation demonstrates the potential power of the histogram approach but raises an important question about what happens when the object moves in such a way as to be larger or smaller than the model, whether through depth scaling or through out-of-plane rotation. In particular, if it becomes smaller, this will mean that the model will be matched partly against the object background. Swain and Ballard sought to minimize this effect by taking the following intersection measure rather than any sort of correlation between the image  $I$  and model  $M$  histograms:

$$\sum_{i=1}^n \min(I_i, M_i) \quad (22.29)$$

This would have the effect of discounting any pixels of a given color in excess of those expected in the model histogram (including both those whose colors are simply not represented in the model and those that have limited representation). The above expression was then normalized by the number of pixels in the model histogram. However, here, we follow Birchfield (1998) in normalizing by the number of pixels in the image histogram, to reflect the point made earlier that we are searching for the best image match rather than the best model match:

$$H_N(I, M) = \frac{\sum_{i=1}^n \min(I_i, M_i)}{\sum_{i=1}^n I_i} \quad (22.30)$$

At first sight, this formula might appear wrong, in that a match over fewer pixels would be normalized out, still representing perfect agreement and giving a normalized intersection of unity. Note, for example, that in shape matching, it is common to use the formula  $(A \cap B)/(A \cup B)$ , where  $A$  and  $B$  are sets representing object areas, which would give a value less than unity in the case  $A \supset B$ . However, Eq. (22.30) is designed to cope well with partial occlusions in the image, which will lead to the intersection with  $M$  being reduced, yielding the  $I$  values, which would then cancel with the denominator, giving the answer 1.

The overall effect of using the normalized intersection of Eq. (22.30) is that the method has the twin advantages of minimizing the effects of background and



canceling the effects of occlusion, while also coping well (and in some cases exactly) with varying viewpoints. The problem of varying scale remains, but this can be countered by preliminary segmentation of the object and scaling its histogram to the size of the model histogram.

There remains one further important consideration when matching an image against a model—that the model might have become out of date under varying levels of illumination. To a large extent, the latter can be considered as varying levels of *luminance*, with the *chrominance* parameters remaining more or less unchanged. This problem can be addressed by changing to different color representations. For example, we can move from the RGB representation to the HSI (hue, saturation, intensity) representation (see [Appendix C](#)), and then use the hue ( $H$ ) and saturation ( $S$ ) parameters. However, more protection will be available by color normalization (dividing by  $I$ )—though it is far easier and less computation intensive to normalize the RGB parameters directly:

$$r = R/(R + G + B) \quad (22.31)$$

$$g = G/(R + G + B) \quad (22.32)$$

$$b = B/(R + G + B) \quad (22.33)$$

but because  $r + g + b = 1$ , we should ignore one of the parameters, e.g.,  $b$ .

While the above arguments suggest that luminance should be totally ignored, this is inadvisable, as colors that are close to the black–white line in color space (where saturation  $S \approx 0$ ) would be indistinguishable. Indeed, Birchfield (1998) cites the “dangerous” case of dark-brown hair looking similar to a white wall if luminance is ignored. For these reasons, most workers use different sizes and numbers of histogram bins for luminance and chrominance information. Here, we have to remember that a full-sized color histogram with 256 bins in each of the color dimensions would be both large and clumsy and would not easily be searchable in real time—an especially important factor in tracking applications. In addition, such a histogram would not be well populated and would lead to very noisy statistics. For this reason, 16–40 bins per color dimension are much more typical. In particular,  $16 \times 16 \times 8$  bins are widely used, 8 being the number in the luminance channel. Note that these numbers correspond, respectively, to 16, 16, and 32 levels per channel, and that a  $512 \times 512$  image would lead to an average occupation number of 128 per bin: However, a  $256 \times 256$  image would give an average occupation of just 32 per bin, which is distinctly low and liable to be inaccurate (though this would depend very much on the type of data).

Birchfield (1998) reported that when used for head tracking, the color histogram method was able to follow a head reliably, though it became “unstable” when the head was in front of a white board whose color was quite close to that of skin. This behavior is understandable, as it has already been noted that the histogram approach is invariant to translation (hence, as long as the head is somewhere within the image, the histogram tracker will be unlikely to lose it). These points show that ultimately the histogram tracker approach is limited, and needs

to be enhanced by other means, in particular some means of detecting object outlines. To achieve this, Fieguth and Terzopoulos (1997) used (1) simple  $M$ -ary hypothesis testing of position around the previous position, the displacements merely being those at the  $M = 9$  points in a  $3 \times 3$  window; (2) a highly nonlinear velocity prediction scheme involving step incremental corrections for acceleration, deceleration, and damping to avoid oscillations; and (3) color histograms bins based exclusively on chrominance. The reason for these simplifications was to achieve real-time operation for full frames ( $640 \times 480$  pixels) at 30 frames per second—at which rate, object displacements become much smaller and easier to track.

Birchfield (1998) developed a more sophisticated approach, based on approximating the shape of the human head by a vertical ellipse with a fixed aspect ratio of 1:2. Then, in common with previous contour trackers, he measured the goodness of match by computing the normalized sum of gradient magnitudes around the boundary of the ellipse, though (1) he summed the gradient values at all points on the boundary rather than just at selected points (in fact, this is unusual: most workers sample at a set of 100 or so points on the boundary), and (2) he took the component of the gradient along the perpendicular to the boundary. This led to a shape model  $\mathbf{s}(x, y, \sigma)$  with three parameters— $x, y$  denoting the ellipse location and  $\sigma$  denoting its semiminor axis—and the following goodness of fit parameter:

$$\psi(\mathbf{s}) = \frac{1}{N_\sigma} \sum_{i=1}^{N_\sigma} |\mathbf{n}_\sigma(i) \cdot \mathbf{g}_s(i)| \quad (22.34)$$

Here,  $N_\sigma$  is the number of pixels on the boundary of an ellipse with semiminor axis  $\sigma$ ,  $\mathbf{n}_\sigma(i)$  is the unit vector normal to the ellipse at pixel  $i$ , and  $\mathbf{g}_s(i)$  is the local intensity gradient vector. Normalized goodness of fit parameters for boundary shape ( $\psi_b$ ) and color ( $\psi_c$ ) is added and used to obtain an optimum fit:

$$\mathbf{s}_{\text{opt}} = \arg \max_{\mathbf{s}_i} \{\psi_b(\mathbf{s}_i) + \psi_c(\mathbf{s}_i)\} \quad (22.35)$$

As discussed earlier, when the color module was tested on its own, it performed well, but somewhat unstably when the background color was close to that of skin. All this was corrected by adding the gradient module. However, the gradient module on its own performed less well than the color module on its own. As time progressed, the gradient model tended to become distracted by the background, not having any inbuilt design features to counteract this. Moreover, in a cluttered background, it behaved even less well; and it was not able to handle large accelerations adequately because of its limited ability to probe for high gradient regions, and its consequent propensity for attaching itself to the wrong ones. Fortunately, the two modules were able to complement each other's capabilities: in particular, the color module helped the gradient module by its ability to ignore background clutter, and by providing a larger region of attraction. Finally, when the human subject turned around, so that only his hair was visible,

the gradient module was able to take over and handle rescaling correctly as the subject moved; and it was able to prevent the color tracker from slipping down the subject's neck, which had a similar color histogram. All this signals that two or more strategies for tracking can be useful in real-world situations where enough information needs to be brought to bear to provide correct tracking interpretations on an ongoing basis. It also signals that the color histogram type of tracking module is exceptionally powerful and tends to need only minor tweaks to keep it properly on lock. Overall, however, the outstanding factor that needs further detailed attention and development is the handling of occlusion: this needs to be arranged by design rather than by tweaks, as we shall see in a later section.

---

## 22.6 IMPLEMENTATION OF PARTICLE FILTERS

The particle filter formalism is a very powerful one, mediated by generic probability-based optimization, yet needing to be taken further to achieve its promise. To arrange this, it needs to be applied to real objects and thus appearance models have to be taken into account—though in the present context, it will be more accurate and general to refer to them as observation models. Our particle filter formalism already embodies these in the form of conditional densities  $p(\mathbf{z}_k|\mathbf{x}_k)$ : See Eq. (22.28).

At this stage, we need to specialize the observations: here, we illustrate the process by considering the color and assumed elliptical shape of a human head: these can be thought of as region-based ( $r$ ) and boundary-based ( $b$ ) properties, each with their own likelihoods. Taking the latter to be conditionally independent, we can factorize  $p(\mathbf{z}_k|\mathbf{x}_k)$  as follows:

$$p(\mathbf{z}_k|\mathbf{x}_k) = p(\mathbf{z}_k^r|\mathbf{x}_k)p(\mathbf{z}_k^b|\mathbf{x}_k) \quad (22.36)$$

Clearly, the region-based likelihood will depend not only on the color but also on the shape of the region it is in. Nevertheless, the conditional independence assumption will be valid, as we are really interested in the colors within the boundary and the gradient values along it.

To proceed further, we assume that color histograms  $I$  and  $M$  have been obtained for the image and the target model, within the current region  $r$ . Following Nummiaro et al. (2003) and many other workers—and at this point, abandoning the Swain and Ballard (1991) normalized intersection formalism—we normalize them to unity as  $p^I, p^M$ , respectively. To compare these distributions, it is convenient to use the Bhattacharyya coefficient (here, expressed as a sum rather than an integral) which expresses the similarity between the distributions:

$$\rho(p^I, p^M) = \sum_{i=1}^m \sqrt{p_i^I p_i^M} \quad (22.37)$$

To display the *distance* between the distributions, we simply apply the measure

$$d = \sqrt{1 - \rho(p^I, p^M)} \quad (22.38)$$

Ideally, the color distribution will be close to the target distribution, so these should differ only as a Gaussian error function. Remembering that  $p^I$  is actually a function of  $\mathbf{x}_k$ , we now find the region (and color) conditional likelihood:

$$p(\mathbf{z}_k^I | \mathbf{x}_k) = \frac{1}{(2\pi\sigma_r^2)^{1/2}} e^{-\frac{d^2}{2\sigma_r^2}} = \frac{1}{(2\pi\sigma_r^2)^{1/2}} e^{-\frac{1-\rho(p^I(\mathbf{x}_k), p^M)}{2\sigma_r^2}} \quad (22.39)$$

Making a similar assumption that the estimated gradient positions in the image  $I$  will differ from those in the target model  $M$  by a Gaussian error function, we find the boundary conditional likelihood as follows:

$$p(\mathbf{z}_k^b | \mathbf{x}_k) = \frac{1}{(2\pi\sigma_b^2)^{1/2}} e^{-\frac{G^2}{2\sigma_b^2}} \quad (22.40)$$

where  $G$  represents the sum of the gradient magnitude values perpendicular to the local boundary positions.

Combining the last two equations, as specified by Eq. (22.36), now provides the required estimate of  $p(\mathbf{z}_k | \mathbf{x}_k)$ , which in turn leads via the particle filter formulation to an estimate of  $p(\mathbf{x}_k | \mathbf{z}_{1:k})$ . This essentially completes the long series of arguments and calculations comprising the particle filter scenario.

In fact, there are several further aspects to consider. The first is that it is natural to weight the contributions made by the various pixels to the color histograms. In particular, the pixels nearest to the centers of the ellipses should be weighted higher than those near their boundaries, so that any inaccuracies in the center locations will be minimized. For example, Nummiaro et al. (2003) used the weighting function as follows:

$$k(r) = \begin{cases} 1 - \frac{r^2}{r_0^2} & r < r_0 \\ 0 & r \geq r_0 \end{cases} \quad (22.41)$$

with  $r_0 = \sqrt{a^2 + b^2}$ ,  $a$  and  $b$  being the semimajor and semiminor axes of the ellipses. In fact, Nummiaro et al. (2003) placed such reliance on this weighting that their particle filter did not use a separate boundary likelihood  $p(\mathbf{z}_k^b | \mathbf{x}_k)$ . In contrast, Zhang et al. (2006) used both, almost exactly as described above, albeit with an APF incorporating mean shift filtering.

Another important aspect not so far mentioned is the need to adapt the target model  $M$  to keep it up to date, e.g., with regard to the size and orientation of the real-world target. Nummiaro et al. (2003) achieved this using the commonly applied “learning/forgetting” operation:

$$p_{k+1,i}^M = \alpha p_{k,i}^M + (1 - \alpha) p_{k,i}^I \quad i = 1, 2, \dots, m \quad (22.42)$$

which mixes in a little of the recent image data while forgetting a correspondingly small amount of the old model data. During this process, care is taken to avoid mixing in outlier data, such as when an object is partly occluded. Even with this precaution, it should be borne in mind that use of an adaptive model is potentially dangerous: while it helps by valid adaptation to appearance changes, it gives an increased sensitivity to extended occlusions and loss of target.

While heads are typically tracked using 2-D position  $(x, y)$  and ellipse shape parameters  $(a, b)$ , it can normally be assumed that the ellipse is vertically aligned. However, when viewed from overhead, in-plane orientation  $(\theta)$  is also an important parameter. Sometimes, similar models are used for individual human limbs, though rectangles have also been employed. However, ellipses provide a simple, easily parameterized shape and can be specified with as few as three parameters  $(x, y, b)$ ; they can even be used to track whole human figures using three or four parameters (Nummiaro et al., 2003). On the other hand, when torsos or hands are being tracked, closed curves may not be appropriate, and it is common to use parametric spline curves.

With the type of particle filter design outlined above, performance in the event of occlusions is a vexed question. Indeed, in this area, many claims and counter-claims about relative effectiveness of tracking and occlusion handling capabilities are made in various papers. As the claims are often made on different datasets, it is difficult to know the true position. However, the particle filter has quite a high level of intrinsic robustness. This is because “less likely object states have a chance to temporarily remain in the tracking process, (so) particle filters can deal with short-lived occlusions” (Nummiaro et al., 2003). Hence, minor propping up in a judicious way using other modules can often boost performance significantly. In principle, if a significant change such as a strong partial occlusion occurs, the simple artifice of putting the tracker on hold is often sufficient to allow it to recover and continue tracking. However, to be surer of recovery, the tracker might have to wait for a background subtraction routine to signal that the object is again present (Nait-Charif and McKenna, 2006). In any case, a background subtraction module is useful for signaling when a totally new object has entered the scene. Finally, when objects leave the scene, some memory of their appearance and position is useful in case they reenter the scene after a short time in the same or other location (when humans appear indoors, there are usually a limited number of entry and exit points, and reentry via the same one will generally be the most likely possibility). However, there is a danger of instituting a rather ad hoc set of algorithms to solve such problems, when what is needed is a more absolute object recognition module to positively identify individuals, or at least to search for the most likely identifications, together with sets of probabilities. A particular example of this type of situation is when two pedestrians walking in opposite directions (1) pass each other without interacting, but with the one momentarily occluding the other; or (2) stop, shake hands, and then proceed; or (3) stop, shake hands, and then retrace their steps. Scenario (3) involves merging of profiles and can be as difficult to handle as occlusion: In any case, temporary partial occlusion involves merging of the figures;

only seldom does complete occlusion and total disappearance of one figure occur. It ought to be stressed that scenario (1) is handled well by use of a Kalman filter module, which uses continuity of velocity to aid interpretation; scenario (2) is handled badly or not at all by such a module, depending on the time delay; while scenario (3) is not handled at all by such a module. (These points about use of Kalman filters are well illustrated by Nummiaro et al. (2003) in relation to a quite different scenario—that of a bouncing ball.) In general, human interactions have to use a Kalman filter at most tentatively, to throw up possible hypotheses about the motion: this being so, it is possible to incorporate Kalman filters usefully into a particle filter (van der Merwe et al., 2000); equally, they can be incorporated into supervisory programs that oversee the whole tracking process, as indicated above (see also Comaniciu et al., 2003).

---

## 22.7 CHAMFER MATCHING, TRACKING, AND OCCLUSION

As we have seen, one of the perennial problems of matching and tracking is that of occlusion of objects within the FOV. A variety of measures can be applied to make single camera systems as robust as possible against overlap. Leibe et al. (2005) have devised methods based on chamfer matching and segmentation, together with a minimum description length procedure for hypothesis verification. The latter evaluates hypotheses in terms of the savings that can be made by explaining part of the image by the hypotheses. Here, we concentrate on the concept of chamfer matching, as it has achieved considerable use for matching pedestrians, notably by Gavrilă (e.g., Gavrilă, 1998, 2000).

The basic idea behind chamfer matching relates to the process of matching objects to templates via their boundaries—a strategy that should be much less computation intensive than matching via whole object regions. However, since this would not give much indication of a potential match until very close to the match position, some means is required of making the approach to a match far smoother. This should also permit substantial speedup of the process by employing a hierarchical coarse-to-fine search. To achieve a smoother transition, edge points in the image are first located, and then a distance function image is generated, starting with the edge points, which are initialized to zero distance values. Application of the template, also in the form of edge points, will ideally yield a zero sum (of image distance function values) along the template points: This will rise to a higher value when the template is misplaced or the shape of the object is distorted, corresponding to the sum of distances of each image point from the ideal position. Taking the distance function as  $DF_1(i)$ , we can express the degree of match by the average “chamfer” distance, i.e., the average distance from each edge point to the nearest edge point in the template  $T$ :

$$D_{\text{chamfer}}(T, I) = \frac{1}{N_T} \sum_{i=1}^{N_T} DF_1(i) \quad (22.43)$$

where  $N_T$  is the number of edge points within the template.  $D_{\text{chamfer}}(T, I)$  is actually a dissimilarity measure, having a value of zero for a perfect match.

In fact, there is no necessity to take edge points for the image and the template: corner points or other feature points can be utilized, and the method is quite general. However, the method works best when the point set is sparse, so that (1) accurate location is achieved and (2) computation is reduced. On the other hand, reducing the number of points too far will result in lack of sensitivity and robustness as parts of the image and template will not be adequately represented.

As it stands, this approach is limited because any outliers (caused by occlusion or segmentation errors, for example) will lead to substantial matching problems. To limit this problem, Leibe et al. (2005) used a truncated distance for matching

$$D_{\text{chamfer}}(T, I) = \frac{1}{N_T} \sum_{i=1}^{N_T} \min(DF_1(i), d) \quad (22.44)$$

with a suitable empirical value of  $d$ . On the other hand, Gavrilu (Gavrilu, 1998) applied an order-based method for limiting the number of interfering distance function values, taking the  $k$ th of the ordered values (1 to  $N_T$ ) as the solution value:

$$D_{\text{chamfer}}(T, I) = \arg \text{order}_k^{i=1:N_T} DF_1(i) \quad (22.45)$$

When applying this formula, it may seem attractive to use the median value, for which  $k = \frac{1}{2}(N_T + 1)$ . However, it can easily happen that a large proportion of the template area is obscured, so we need to take a smaller value of  $k$  (e.g.,  $0.25N_T$ ) that reflects this. In fact, this will reduce accuracy when none of the template is obscured, so, in the end, Eq. (22.44) might give a more useful result. We take this discussion no further here, as a lot depends on the type of data that is involved. In passing, it is worth observing that when  $k = N_T$ , Eq. (22.45) gives the well-known Hausdorff distance (Huttenlocher et al., 1993):

$$D_{\text{chamfer}}(T, I) = \max_{i=1:N_T} DF_1(i) \quad (22.46)$$

This formula for the Hausdorff distance may appear different from the usual one, which involves a max–min operation: However, as computation of a distance function involves taking local minima of possible distances (see Chapter 8: Binary Shape Analysis), there is concurrence in the two formulations.

Note that, in the foregoing discussion, the distance function of the image is used rather than that of the template. This is because in practical situations, many templates will have to be applied in order to cover expected variations in the objects being detected. For example, if the method is being applied for pedestrian detection, various sizes, poses, positions of limbs, and types of clothing will have to be allowed for, as well as variations in the background and possible overlaps. In these circumstances, it is far more efficient to use  $DF_I$  than  $DF_T$ . Gavrilu (1998) showed with considerable success, how all the variations listed above can be dealt with and how the method can be made to work well to detect pedestrians.

Finally, returning to the work of Leibe et al. (2005), limitations of the chamfer matching technique were compensated by using segmentation information. This meant obtaining a similarity function from the chamfer distance (which is a dissimilarity measure), and then combining with a Bhattacharyya coefficient representing overlap with the hypothesized segmentation  $Seg_I(i)$  to produce an overall similarity measure:

$$S = a \left[ 1 - \frac{1}{b} D_{\text{chamfer}}(T, I) \right] + (1 - a) \sum_i \sqrt{Seg_I(i) R_T(i)} \quad (22.47)$$

Here,  $R_T(i)$  is the region within  $T$ , and the sum covers the pixels in this region. In addition, a somewhat arbitrary but nonetheless reasonable pair of weights is applied to balance the two similarity measures:  $a$  is the proportion of the overall similarity allotted to chamfer matching, and  $b$  is a weight expressing the fact that chamfer matching is applied over a significant boundary distance; in the work of Leibe et al. (2005),  $a$  and  $b$  were taken to be 0.45 and 50, respectively. The overall effect was to produce much improved solutions in respect of placement accuracy and elimination of false positives, relative to the chamfer distance method taken on its own (Eq. (22.44)).

---

## 22.8 COMBINING VIEWS FROM MULTIPLE CAMERAS

Over the past decade or so, there has been a surge of interest in multicamera surveillance systems. Multiple cameras are clearly necessary if, for example, long stretches of motorway are to be monitored, or if pedestrians are to be tracked around cities or shopping precincts. The FOV of a single camera is quite restricted and the resolution available for viewing in the distance will almost certainly be inadequate for detailed observation. Another reason for the use of several cameras is that of viewing in stereo and obtaining sufficient depth information. A further reason is that pedestrians in a precinct will frequently be partially or wholly occluded by architectural features such as statues or other pedestrians, but the chance of missing a pedestrian will be less, much less if the scene is viewed by multiple cameras; this sort of situation will also apply on roads, where many other possibilities for occlusion exist.

On roads, cameras are often mounted on overhead gantries, and maintaining observation over long distances will require many cameras. This raises the question of whether the observation should be unbroken, i.e., whether the cameras will have overlapping, contiguous, or nonoverlapping views. On motorways, cameras may be separated by several miles, and can usefully be sited at junctions, so it will be possible to keep track of all vehicles without too much expense, though breakdowns at intermediate locations may not be observed. On the other hand, in a shopping precinct, if pedestrians are to be monitored closely enough for attacks or terrorist activities to be detected, contiguous or overlapping views will be



mandatory. In fact, there will be a problem in ensuring that all pedestrians are positively identified as they progress from one FOV to the next: To facilitate this, and for ease of setting up the system, overlapping views are normally required.

Next, we consider the layout of a multicamera system. To do this, we must examine the area of the ground plane that lies within the FOV of the camera. First, note that the optical axis of the camera passes through the center of the image plane and that the latter has a rectangular shape given by the minimum and maximum values of  $x$  and  $y$ ,  $\pm x_m$  and  $\pm y_m$ . The FOV is therefore limited by four planes, at horizontal and vertical angles  $\pm \alpha$  and  $\pm \beta$ , where  $\tan \alpha = x_m/f$  and  $\tan \beta = y_m/f$ ,  $f$  being the focal length of the camera lens. Each plane will intersect with the ground plane in a line, and for a camera with a horizontal  $x$ -axis, the viewed area on the ground plane will be a symmetrical trapezium (Fig. 22.9). However, following on from the discussion in Section 22.2, if the camera is not inclined slightly downward, the distant side of the trapezium will not be visible. Since this would not make the most of the camera FOV, we will assume that it has been arranged for the distant side to fall on the ground plane.

When an adjacent camera views an adjacent section of the ground plane, there are two possibilities: (1) it will view the next stretch in the same direction, as on a motorway and (2) it will not be restricted to lie, or point, in the same direction, but just to overlap in some convenient way. For example, in a precinct or park, a typical placement would be that shown in Fig. 22.10A, where two opposite sides of the common viewing area would arise from the FOV of the first camera and the other two from that of the second camera—thereby forming a quadrilateral rather than a trapezium. However, other situations are possible, as shown in Fig. 22.10B, where the trapezia of the two cameras overlap in a more complex way, and the common viewing area is not a quadrilateral.

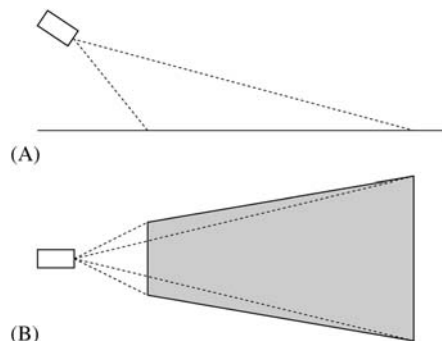


**FIGURE 22.9**

Area on the ground plane viewed by a camera. (A) Side view with the camera canted slightly downward. (B) Plan view of the symmetrical trapezium seen by the camera on the ground plane.

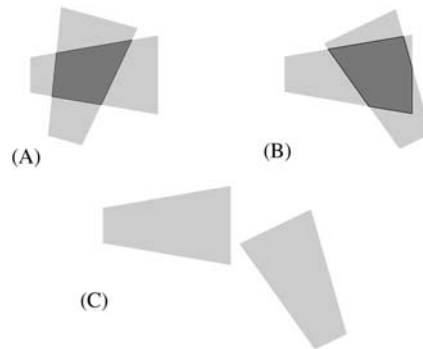


**FIGURE 22.10**

Areas on the ground plane viewed by multiple cameras. (A) Overlapping trapezia forming a quadrilateral. (B) Overlapping trapezia forming another shape—here, a pentagon. (C) Trapezia that do not overlap, though tracking across the gap can in some cases be achieved by making spatial and temporal correspondences (see text).

No matter which of the reasons for using a multicamera system apply, there is a need to relate the views from the separate cameras in order to obtain a consistent labeling of the objects passing between them. The obvious means of achieving this is by appearance, i.e., to apply recognition algorithms to establish that the same person or vehicle is being tracked across the various camera fields of view. Unfortunately, while this correspondence problem can normally be solved straightforwardly in binocular vision, when the two cameras are close together and pointing in a similar direction, this is by no means true for wide baseline cases such as those shown in Fig. 22.10. This is so for two reasons: (1) A person seen in two disparate views may have an altogether different appearance: e.g., the face may be visible in one and the back of the head in the other, or the back of a shirt may have a different design or color from the front and (2) the illumination may be quite different for each of the views, and this will make it even more difficult to confirm the person's identity from the other camera.

The obvious solution to this problem is to confirm identity not by appearance but by position and time. If we know that person  $P$  is at position  $X$  in the scene at time  $t$ , this must be the case in all views. So, all that has to be done is to relate the common areas of the ground plane uniquely between cameras. Following the widely used and usually sufficiently accurate assumption that everything is happening on the same flat ground plane, we only need to set up a homography between the two cameras to arrange for the same correct interpretation from any view. Under perspective projection, it requires a minimum of four common feature points to set up a homography (the number is as small as this because of the planar constraint, as is made clear in Table 16.1), though more points can be used to improve accuracy; note also that at least one more point is needed to validate the homography.

In the work of Calderara et al. (2008), greater accuracy was achieved by finding the straight lines bounding the common quadrilateral and using its corners as highly accurate points by which to define the homography. While this might seem trivial, in fact, the common quadrilateral has to be located by experiment. This can be achieved most easily when the scene is empty (e.g., overnight), and one individual can be sent to walk repeatedly around the site until a sufficient number of boundary points—as determined by the individual entering or leaving one of the fields of view—have been measured in both views. Note that to ensure that this gives sound results, temporal synchronization of the two camera systems is crucial. Once all this has been carried out, methods such as Hough transforms or RANSAC are applied to collate the boundary points into the straight lines bounding the quadrilateral: and because of the averaging inherent in this process, the straight lines will be known accurately; therefore, the corner positions will be known accurately, so there will be no need to use more points to establish an accurate homography.

Interestingly, Khan and Shah (2003) consider this approach an overkill to solve the consistent labeling problem. They assert that there is no need to determine the homography in this numerical sort of way: rather, it should be done by finding the FOV boundary lines and then merely noting when a pedestrian passes over one of these lines and making the identity at that point in time. That is, if an individual crosses a line at time  $t$ , this will be detected at the same time  $t$  in each camera and the person's identity can be passed across at that moment. This process is commonly called camera "handoff" (whereas it might appear to be more natural to call it "handover," there is a subtlety in that the latter term would tend to imply that the fields of view are contiguous rather than overlapping). However, if a group of people all cross the line together, this could obviously give rise to difficulties. Indeed, the whole problem of tracking groups of individuals is a difficult one and becomes almost insuperable in dense crowd situations.

While finding FOV boundary lines can be carried out when no crowds are present, and ideally when a single individual walks around, there are limits to the performance of the trained system. This is because a homography relates to a plane, and the simplest way of defining and using a plane is to use the foot locations to provide the plane contact points. (In principle, this is easily done by taking the lowest point on the individual.) However, when the calibrated system is used, the feet of one individual will often be obscured by another individual—a situation that will be virtually unavoidable in crowds. Consequently, there has been a fair amount of attention to recognizing and locating individuals from the tops of their heads (e.g., Eshel and Moses, 2008, 2010). Clearly, tops of heads are much less likely than feet to be occluded. Hence, even in crowd conditions, as long as cameras are quite high up and canted down at quite high angles (say  $40^\circ$ ), all but the shortest individuals should be identifiable. Interestingly, apart from orientation, tops of heads may actually look similar in different views. As the camera cant angle will be known, altered head orientation can be allowed for and recognition and cross identification between cameras can proceed. With fully

calibrated cameras (see [Chapter 19: Image Transformations and Camera Calibration](#)), tops of heads can be located in 3D space, and the positions of feet and heights of individuals can be deduced. Unfortunately, full camera calibration is a tedious process and may need frequent updating, so it is better not to rely on that approach in “informal” (and therefore changeable) surveillance situations such as shopping centers. Instead, camera views can be related using the fundamental matrix formulation ([Chapter 19: Image Transformations and Camera Calibration](#)), which requires only that epipoles should be known so that epipolar lines can be determined; however, finding them requires considerable computation, though this can be done offline prior to actual use (Calderara et al., 2008).

An intriguing approach to top-of-head location is to try various homographies differing only in the parameter  $H$  signifying distance from the floor. When a homography is found that indicates the same value of  $H$ , the foot locations can be calculated for each camera view, even though the feet themselves are obscured. However, to achieve this, a somewhat complex and subtle process is required (Eshel and Moses, 2008, 2010). Four vertical poles are set up at the corners of each viewing quadrilateral (or other convenient location), each pole having three bright lights along it (e.g., at the top, bottom, and middle of the pole). Then standard homographies are set up for each of these, so that at any location in an image, three heights can be deduced. Finally, a height that is to be measured can be related to the three known ones for that location, a cross ratio calculated along a vertical line, and the actual height deduced; at the same time, the foot position in each camera view can be identified unambiguously.

Overall, the simplest and most powerful approach is that of prior training by getting someone to walk around the site and thus demarcate the boundaries of each common viewing zone. Then, applying the fundamental matrix for pairs of cameras will permit homographies to be set up relating all the mutually viewable regions of ground planes. The paper by Calderara et al. (2008) contains a number of other subtleties, but space prevents them from being described in detail here. Finally, if heights and exact locations of people are to be found from top-of-head positions, elegant though fairly complex methods using several homographies have to be used, but in some applications, such as observation of crowds, the additional complexity may well be justified. However, segmentation of crowd views and identification of all individuals remains a research topic, especially when the people are tightly packed—as can easily happen in metro stations and football matches.

### 22.8.1 THE CASE OF NONOVERLAPPING FIELDS OF VIEW

Next, we move on to the case of nonoverlapping fields of view. Here, there seems to be no basis for homographies or for reliable camera handoff. However, some degree of similarity in appearance will still be detectable between views; in addition, there will be strong correlations between the time of leaving one FOV and arriving in another. The situation will often be helped if there is some

restriction of access, such as would occur if there is a single adjoining door. (On a motorway, there is anyway such a restriction, and temporal correlations can be strong.) Pflugfelder and Bischof (2008) have obtained significant success in this sort of situation and make no assumptions about appearance. In particular, they have found how to relate the camera calibration matrices when overlapping views are not available. While this seems intrinsically impossible because no common image points can be found and hence no equations can be obtained linking the parameters (recall that the 8-point algorithm requires eight points in order to obtain a sufficient number of equations), they have found that if velocities are assumed to be more or less constant across the intervening space, this provides the continuity needed to permit enough equations to be found. Thus, a minimum of two positions per view for each trajectory is sufficient, these being immediately before and after camera handoff. Strict temporal correspondences are required, as are data on relative camera orientations, but a common ground plane is not assumed. Under these conditions, tracking across gaps of up to 4 m was achieved (Fig. 22.10C). The method works because Rother and Carlsson's (2001) 2-point technique shows how to determine the relative positions of two cameras with overlapping views, and the new method simulates this situation by utilizing a separate two points in the second nonoverlapping view in order to emulate and replace the two points that would ideally have been present in an overlapping view.

For a differently motivated probabilistic strategy tackling this problem, based on transition probabilities between nonoverlapping views, see Makris et al. (2004): What is special about this approach is that it is quite general as it is entirely unsupervised and has no direct knowledge of camera placement or camera characteristics.

---

## 22.9 APPLICATIONS TO THE MONITORING OF TRAFFIC FLOW

### 22.9.1 THE SYSTEM OF BASCLE *ET AL.*

One important area of surveillance is the visual analysis of traffic flow. In an early study (Bascle *et al.*, 1994), it was found that the complexity of the analysis was reduced because vehicles run on the roadway and because their motions are generally smooth. Nevertheless, the methods that had to be used to make scene interpretation reliable and robust were nontrivial.

First, motion-based segmentation is used to initialize the interpretation of the sequence of scenes. The motion image is used to obtain a rough mask of the object, and then the object outline is refined by classical edge detection and linking. B-splines are used to obtain a smoother version of the outline, which is fed to a snake-based tracking algorithm. The latter updates the fit of the object outline and proceeds to repeat this for each incoming image.

However, snake-based segmentation concentrates on isolation of the object boundary and therefore ignores motion information from the main region of the object. It is therefore more reliable to perform motion-based segmentation of the entire region bounded by the snake, and to use this information to refine the description of the motion and to predict the position of the object in the next image. The overall process is thus to feed the output of the snake boundary estimator into a motion-based segmenter and position predictor which reinitializes the snake for the next image—so both constituent algorithms perform the operations they are best adapted to. It is especially relevant that the snake has a good starting approximation in each frame, both to help eliminate ambiguities and to save on computation. The motion-based region segmenter operates principally by analysis of optical flow, though in practice, the increments between frames are not especially small: this means that while true derivatives are not obtained, the result is not as bedevilled by noise as it might otherwise be.

Various refinements were incorporated into the basic procedure:

- B-splines are used to smooth the outlines.
- The motion predictions are carried out using an affine motion model that works on a point-by-point basis. (The affine model is sufficiently accurate for this purpose if perspective is weak so that motion can be approximated locally by a set of linear equations.)
- A multiresolution procedure is invoked to perform a more reliable analysis of the motion parameters.
- Temporal filtering of the motion is performed over several image frames.
- The overall trajectories of the boundary points are smoothed by a Kalman filter (a basic treatment of Kalman filters is given in [Section 20.8](#)).

Before proceeding to set up an affine motion model, recall that an affine transformation is one which is linear in the coordinates employed. This type of transformation includes the following geometric transformations: translation, rotation, scaling, and skewing (see [Chapters 6 and 19](#)). Hence, the relevant affine motion model involves six parameters:

$$\begin{bmatrix} x(t+1) \\ y(t+1) \end{bmatrix} = \begin{bmatrix} a_{11}(t) & a_{12}(t) \\ a_{21}(t) & a_{22}(t) \end{bmatrix} \begin{bmatrix} x(t) \\ y(t) \end{bmatrix} + \begin{bmatrix} b_1(t) \\ b_2(t) \end{bmatrix} \quad (22.48)$$

This leads to an affine model of image velocities, also with six parameters:

$$\begin{bmatrix} u(t+1) \\ v(t+1) \end{bmatrix} = \begin{bmatrix} m_{11}(t) & m_{12}(t) \\ m_{21}(t) & m_{22}(t) \end{bmatrix} \begin{bmatrix} u(t) \\ v(t) \end{bmatrix} + \begin{bmatrix} c_1(t) \\ c_2(t) \end{bmatrix} \quad (22.49)$$

Once the motion parameters have been found from the optical flow field, it is straightforward to estimate the following snake position.

An important factor in the application of this type of algorithm is the degree of robustness it permits. In this case, both the snake algorithm and the motion-based region segmentation scheme are claimed to be relatively robust to partial occlusions: the abundance of available motion information for each object, the

insistence on consistent motion, and the recursive application of smoothing procedures including a Kalman filter, all help to achieve this end. However, no specific nonlinear outlier rejection process is mentioned, which could help if two vehicles merged together and became separated later on or if total occlusion occurred.

Finally, the initial motion segmentation scheme locates the vehicles with their shadows since these are also moving (see Fig. 22.11); subsequent analysis seems able to eliminate the shadows and arrive at smooth vehicle boundaries.

### 22.9.2 THE SYSTEM OF KOLLER *ET AL.*

Another scheme for automatic traffic scene analysis was described by Koller *et al.* (1994). This contrasts with the system described above by placing heavy reliance on high-level scene interpretation through use of belief networks. The basic system incorporates a low-level vision system employing optical flow, intensity gradient, and temporal derivatives. These provide feature extraction and lead to snake approximations to contours; since convex polygons would be difficult to track from image to image (because the control points would tend to move randomly), the boundaries are smoothed by closed cubic splines having 12 control points: tracking is then achieved using Kalman filters. The motion is again approximated by an affine model, though in this case, only three parameters are used, one being a scale parameter and the other two being velocity parameters:

$$\Delta \mathbf{x} = s(\mathbf{x} - \mathbf{x}_m) + \Delta \mathbf{x}_m \quad (22.50)$$

Here, the second term gives the basic velocity component of the center of a vehicle region, and the first term gives the relative velocity for other points in the

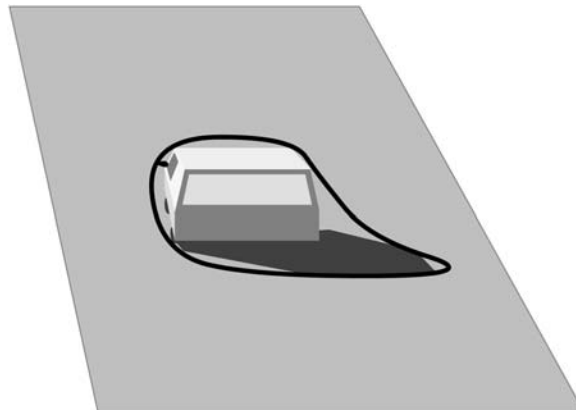


**FIGURE 22.11**

Vehicles located with their shadows. In many practical situations, shadows move with the objects that cause them, and simple motion segmentation procedures produce composite objects that include the shadows. Here, a snake tracker envelops the car and its shadow.

region,  $s$  being the change in scale of the vehicle ( $s = 0$  if there is no change in scale). The rationale for this is that vehicles are constrained to move on the roadway and rotations will be small. In addition, motion with a component toward the camera will result in an increase in size of the object and a corresponding increase in its apparent speed of motion.

Occlusion reasoning is achieved by assuming that the vehicles are moving along the roadway, and are proceeding in a definite order, so that later vehicles (when viewed from behind) may partly or wholly obscure earlier ones. This depth ordering defines the order in which vehicles are able to occlude each other and appears to be the minimum necessary to rigorously overcome problems of occlusion.

As stated above, belief networks are employed in this system to distinguish between various possible interpretations of the image sequence. Belief networks are directed acyclic graphs in which the nodes represent random variables and arcs between them represent causal connections. In fact, each node has an associated list of the conditional probabilities of its various states corresponding to assumed states of its parents (i.e., the previous nodes on the directed network). Thus, observed states for subsets of nodes permit deductions to be made about the probabilities of the states of other nodes. The reason for using such networks is to permit rigorous analysis of probabilities of different outcomes when a limited amount of knowledge is available about the system. Likewise, once various outcomes are known with certainty (e.g., a particular vehicle has passed beneath a bridge), parts of the network will become redundant and can be removed: however, before removal, their influence must be “rolled up” by updating the probabilities for the remainder of the network. Clearly, when applied to traffic, the belief network has to be updated in a manner appropriate to the vehicles that are currently being observed; indeed, each vehicle will have its own belief network that will contribute a complete description of the entire traffic scene. However, one vehicle will have some influence on other vehicles, and special note will have to be taken of stalled vehicles or those making lane changes. In addition, one vehicle slowing down will have some influence on the decisions made by drivers in following vehicles. All these factors can be encoded into the belief network and can aid in arriving at globally correct interpretations. General road and weather conditions can also be taken into account.

Further work was planned to enable the vision part of the system to deal with shadows, brake lights and other signals, and a wide enough variety of weather conditions. Overall, the system was designed in a very similar manner to that of Basche *et al.* (1994), though its use of belief networks made it rather more sophisticated.

In a later version of the system (Coifman *et al.*, 1998), it was decided that a greater degree of robustness with regard to partial occlusion was required. Hence, the idea of tracking objects as a whole was abandoned and corner features were used for detection. This led to a different problem—that of grouping corner features to infer the presence of the vehicles, a process that was simplified by using a common motion constraint, so that features that were seen to be rigidly moving together were grouped together. The new version of the system also applied a



homography between the image plane and the ground plane. The reason for this was to generate world parameters so that ground-based positions, trajectories, velocities, and densities could be established. Note for example that a vehicle traveling at constant speed on the road would have variable speed when viewed in an image. In addition, the right information could more easily be brought to bear when problems of partial or total occlusion are being investigated.

When designing a much later system, Magee (2004) made several interesting observations: (1) corner features are unreliable because of the small size of the objects of interest, (2) connected components analysis is a poor tool for combining parts of vehicles because of fragmentation and similarity of some object foreground points to background, and (3) particle filter trackers have high computational cost that does not scale linearly with the number of objects present—a serious matter when 30 or more vehicles in close proximity are being tracked simultaneously. He found that a sound way to track vehicles was to dynamically model vehicle invariants such as size, color, and speed: in other words, object appearance and recognition were important to systematic and accurate tracking; and the only way they could be achieved was by establishing a homography between the image and the ground plane. In that way, vehicle parameters properly became invariants as required. The homography is expressible as a nonlinear perspective transformation (or “inverse perspective mapping”), and some care is required in setting it up. (Note that such a mapping is mathematically valid only for points known to lie on the ground plane. When points not lying on the ground plane are back-projected to it, they give rise to weird, nonsensical effects, such as buildings that appear to lean backwards.) In fact, if the camera  $x$ -axis is horizontal, the homography only requires a rotation through an angle  $\theta$  about the image  $x$ -axis, together with a scaling, in order to relate the image coordinates to the ground plane coordinates. Ignoring the scaling, there is only one parameter ( $\theta$ ) to be determined. Magee adopted the simple strategy of estimating  $\theta$  as the angle required to make the roadway appear to have constant width, a procedure that proved to be adequate in his particular application (Fig. 22.12). The calculation was made sufficiently accurate by approximating the road centerlines and outlines by three polynomials and performing a fit by iteratively adjusting  $\theta$ . The reason for adopting this procedure is that the roadway has no absolute predefined shape, so a heuristic approach seemed appropriate. Ideally, however, the ground truth for the road centerlines and outlines would be known and the value of  $\theta$  could be adjusted to fit the ground truth without having to assume that the roadway has constant width.

---

## 22.10 LICENSE PLATE LOCATION

Over the past decade, there has been intensive effort to identify vehicles automatically by their license plates. Although license plates were introduced many years ago for the purpose of checking ownership and detecting stolen vehicles, nowadays two other important reasons for automatically identifying vehicles are (1) for

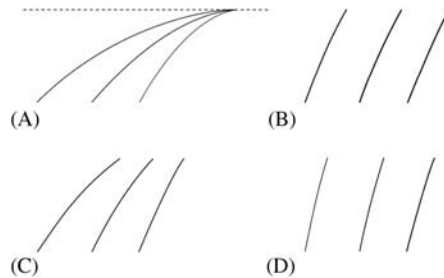


**FIGURE 22.12**

Adjusting the inverse perspective mapping of the roadway (A) shows the roadway as observed by the camera, (B) shows an inverse perspective mapping with the roadway adjusted for constant width, and (C) and (D) show cases of incorrect adjustment of the mapping.

taxation within tolling zones and (2) for exacting fines in the case of parking offenses—because considerable sums of money can be obtained in these ways with very little human intervention. Also, considering all the possible applications of computer vision in surveillance, identification of license plates represents a potentially straightforward application of current methodology. Nevertheless, there are many problems, not least because of the different styles of license plate from different countries.

Identification of license plates progresses through three main stages: (1) location and segmentation of the license plate, (2) segmentation of the individual characters, and (3) recognition of the individual characters. Here, we concentrate on the first of these stages, as the other two are more specialized and less generic, considering the different styles, fonts, and character sets in use in different countries. In any case, the first stage is probably the most difficult to engineer.

A priori, it might be thought that the best way of locating license plates would be via their colors, which are generally well specified for each country. However, many problems arise from variations in ambient lighting, particularly with the seasons, the weather and time of day, while shadows are also a source of difficulty. In this milieu, one of the best starting points has been found to be use of a simple Sobel or other vertical edge-detection operator, in conjunction with horizontal nonmaximum suppression and thresholding. This has been found to locate not only the vertical lines at the ends of the number plates but also the vertical lines at the sides of the characters (Zheng et al., 2005). This generally gives a relatively dense set of vertical edges within the region of the license plate. To proceed further, long background edges and short noise edges are eliminated. Finally, moving a rectangle of license plate size over the image and counting the edge pixels within it turns out to be a highly reliable way of locating license plates (in fact, this process is a form of correlation). The whole process is shown in Fig. 22.13, with the difference that in the case shown, the final stages are

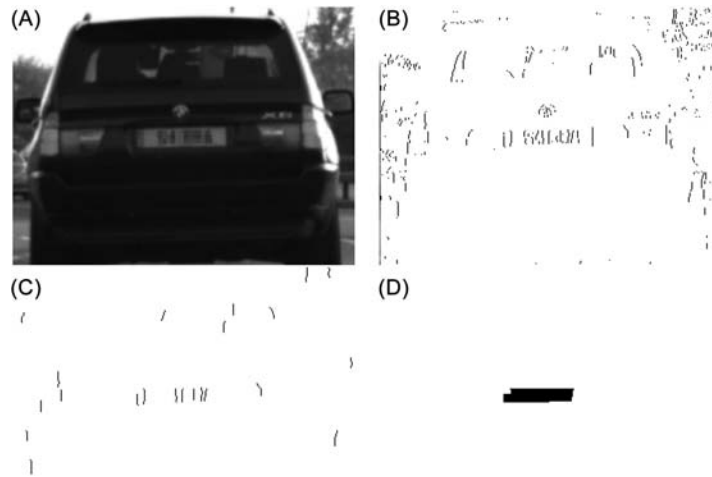


**FIGURE 22.13**

Simple procedure for locating license plates. (A) Original image with license plate pixelated to prevent identification. (B) Vertical edges of original image. (C) Vertical edges selected for length. (D) Region of license plate located by horizontal closing followed by horizontal opening, each over a substantial distance (in this case 16 pixels).

carried out solely using morphological operations (horizontal closing followed by horizontal opening, in each case by 16 pixels).

This method has been developed considerably further by Abolghasemi and Ahmadyfard (2009) using color and texture cues. They found that a particular advantage of color object analysis is robustness to viewpoint changes. They also used morphological closing to link all the vertical edge points and followed this by opening to eliminate the effects of isolated noise points.

Before characters can be segmented and recognized, another stage is needed—that of license plate distortion correction. This arises because license plates may not be observed from the most ideal viewpoint. This is something that requires careful attention. If vehicles are too far away from the camera, the resolution will be too low to permit vertical edges to be found; likewise, accurate identification of the characters will not be possible. If the license plate is viewed obliquely, it will appear misorientated and will not even appear rectangular. However, if license plates were always viewed at a particular distance and location, a standard perspective transformation could be applied to correct such distortions. While it is acknowledged in the literature (e.g., Chang et al., 2004) that adding such a step would improve the performance of license number recognition, few systems seem to incorporate such a step. The reason is probably that OCR (optical character recognition) systems are already very accurate even when characters are slightly sheared and rotated.

---

## 22.11 OCCLUSION CLASSIFICATION FOR TRACKING

It will be clear from the many remarks made about occlusion on the preceding pages that this is a serious problem that needs in-depth analysis and careful algorithm design, particularly with regard to people tracking. To this end, Vezzani and Cucchiara (2008) and Vezzani et al. (2011) have made a careful analysis of the means by which occlusion can arise, starting with the definition of *nonvisible regions* as the parts of objects that are not visible in the current frame. They proceeded to classify these as “dynamic,” “scene,” or “apparent” occlusions:

1. *Dynamic occlusions* are due to moving objects that are readily identified.
2. *Scene occlusions* are due to static objects that are part of the background, but which can nevertheless be in front of moving objects.
3. *Apparent occlusions* are sets of pixels that arise from shape variations of objects being tracked.

Here, it is important to note the distinction between background and foreground. To the layman, “background” merely means a backdrop in front of which the actors perform: it is regarded as static, while the foreground is considered to consist of more interesting moving objects. However, in computer vision, we have to consider the background as static wherever it is, with the moving “foreground” objects ranged at different distances from the camera and sometimes moving *behind* background objects (Fig. 22.14). Note that the background that is identified by background modeling algorithms is the static part of the scene. Of course, a complication that can disrupt this tidy situation is that the background may be composed partly of objects that have come to rest, either permanently or temporarily, and it will be up to the vision algorithm to consider the available evidence from watching the scene and to assess the various possibilities and probabilities.

Another factor to consider is whether occlusions are partial or total. For many static scenes and static situations, total occlusion is an eventuality that is normally disregarded; hence, all occlusions are taken to be partial, and they are simply referred to as “occlusions.” However, when tracking objects, total occlusion is a possibility that has to be borne in mind indefinitely (though in practical situations a time limit may have to be set).

So, when viewing image sequences containing motion, objects may temporarily be totally occluded, *or* they may be partially occluded—in which case, they may be broken into several sections. And when the objects reemerge later on, these sections need to be reassembled into whole objects: this scenario arises when a person passes behind a table, for example. In addition, when a person passes behind a low fence, and the lower body is temporarily invisible, it is necessary for the model of the complete person to be remembered; for if the model becomes adapted to the changed situation, it may not be able to cope properly when the whole person reemerges and it will continue to track only the top of the

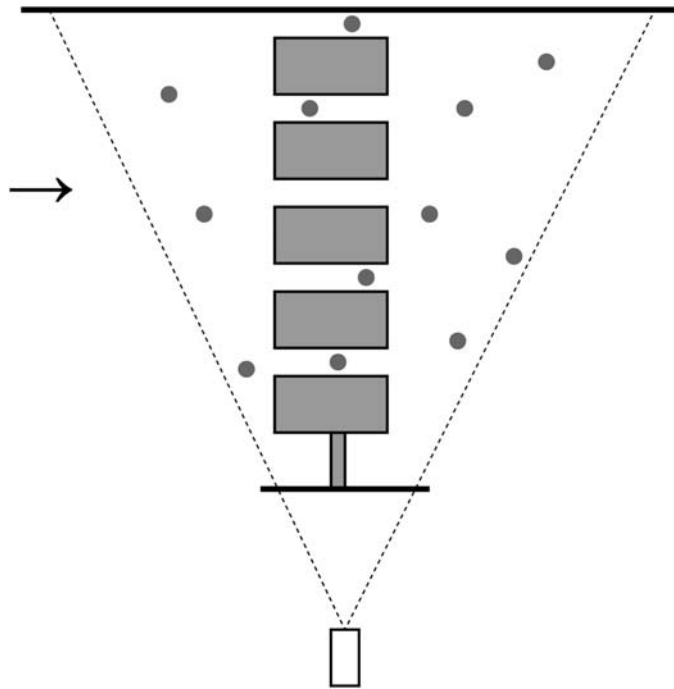


**FIGURE 22.14**

Typical situation of occlusion. This illustrates the case of turnstiles leading to underground trains, viewed from the side. The dots represent people (moving in the direction of the arrow) ranged at different distances from the camera.

body. Clearly, to cope successfully with such situations (Fig. 22.15), the computer needs to have the means to deal with them holistically. Similarly, when two people merge into a larger blob when walking together, the computer will need to have the means to recall that two people were involved so that their identities will be preserved and reinstated when they separate again. Thus, we require substantial intelligence to be incorporated into tracking algorithms.

The various components that have to be incorporated into the algorithm would appear to be the following: (1) the usual background extraction capability, (2) the usual blob tracking capability, (3) full appearance and identity recall, (4) merge capability, (5) split capability, and (6) probabilistic analysis of interpretations. Indeed, (6) will probably have to be the unifying force that drives the whole algorithm.

All these aspects are included in the work of Vezzani and Cucchiara (2008) and Vezzani et al. (2011). In particular, they employ an appearance-based formalism that integrates the possible shape variations of each object and represents them by probabilistic maps. This means that when part of an object is obscured,

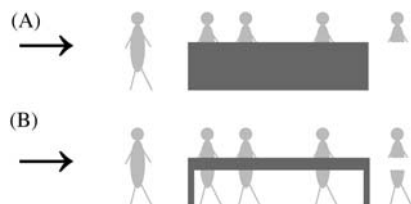


**FIGURE 22.15**

Further examples of occlusion. (A) Case of people walking behind a fence or barrier, potentially resulting in only the head and shoulders being tracked afterward. (B) Case of people walking behind a table, potentially resulting in two parts of the body being tracked independently afterward.

its shape model hallucinates the whole of the object in the probabilistic shape it ought to have, so that when it reemerges, it is automatically reintegrated virtually instantaneously into its natural form.

So far, we have not examined item 3 (see the beginning of this section), which mentioned apparent partial occlusions due to changes in shape. These arise because as a body rotates or bends slightly, or otherwise deforms, new parts will become visible though other parts will become invisible. While these could be regarded as arising through self-occlusion, this may not be the only possibility, e.g., if stretching is involved. We shall not delve further into this point, but merely underline that apparent partial occlusions are not caused by any other objects. This is quite an innovative observation relating to occlusion and may be part of the reason why progress with occlusion has been drawn out over many years. Suffice it to say that the work of Vezzani et al. represents a sound and impressive advance through its cognizance of the many aspects of occlusion in tracking scenarios.

The overall system is very robust and fast and is well able to cope with upward of 40 people in videos from the PETS2006 dataset. Nevertheless, it gives rise to some failures, which devolve into the following categories: (1) identity change of one person, (2) split head/feet, (3) incorrect splitting of groups containing two or three people, and (4) identity change of luggage. In fact, it appears that these are failures not of the *overall* system, including the handling of objects and occlusions, but of the part of the system handling appearance, which is arguably the part to which relatively little design effort has been devoted. Furthermore, it is not clear from the two papers whether a human observer could have performed better using the same video input. Nevertheless, the way forward, including the ability to handle problems (2) and (3) above, is probably to enhance the system using stick-figure-based models of humans, which can take proper account of limb articulation constraints (see the following section): the performance of a system that looks at the body as a whole and models it as a holistic probabilistic shape profile must in the end be limited without suitable enhancement.

## 22.12 DISTINGUISHING PEDESTRIANS BY THEIR GAIT

This section outlines a method for distinguishing pedestrians by their gait. Clearly, unlike many other moving objects such as vehicles, pedestrians have cyclical motions, and it is actually possible to recognize individual people by their gait. However, here, we consider only the methodology needed to locate pedestrians in image sequences.

The basis of the approach is to perform spatiotemporal differencing operations, in which spatiotemporal averaging is followed by temporal differencing. This “motion distillation” method (Sugrue and Davies, 2008) is implemented as a Haar wavelet and leads to a nonbinary motion map of the video at each time-step, according to the equation:

$$W = \sum_{t=t_0}^t \sum_i \sum_j x_{tij} - \sum_{t=t_1}^t \sum_i \sum_j x_{tij} \quad (22.51)$$

where  $x_{tij}$  represents the video pixel data at the point  $(t, i, j)$  in spatiotemporal space.

In this method, undesirable contrast dependence is removed by normalizing  $W$  values across the detected object: the process involves taking the ratio  $R$  of positive ( $W_+$ ) to negative ( $W_-$ ) filter outputs:

$$R = \frac{\sum |W_+|}{\sum |W_-|} \quad (22.52)$$

For a rigid object that retains its orientation relative to the camera,  $R$  will remain approximately constant over time. On the other hand, pedestrians deform as they move and can quickly be detected by testing for changes, and particularly oscillations in the “rigidity parameter”  $R$ .

Fig. 22.17A compares the motion signals  $R$  of a typical vehicle and a pedestrian (see Fig. 22.16 for typical frames from the original videos). While the vehicle signal changes only gradually as a result of slight rotation, changing perspective, and noise, the pedestrian signal is highly variable and oscillatory because of gait motion. Note that over the period shown in Fig. 22.17A, the area of the vehicle changes by a factor  $\sim 10$ , while the area of the pedestrian changes by only a few percent. This makes it all the more significant that  $R$  is so constant for the vehicle, demonstrating that it is a useful invariant of the motion.

After detection, a pedestrian’s motion field can be further analyzed for a variety of behavior patterns. Normal behavior can be modeled by fitting a rectangular box to the subject’s motion field. The rectangle is the full height of the figure with a width typically set at half the height (see below). The total motion area  $A$  is calculated as

$$A = \sum |W_+| + \sum |W_-| \quad (22.53)$$

**FIGURE 22.16**

Portions of frames extracted from video sequences by motion detector. Left: Three frames of moving vehicle. Right: Respective frames of pedestrian, runner and group of walkers.

© IET 2007.

where the sums are taken over the whole object; in addition, the corresponding area  $A_{\text{ex}}$  is calculated for the region outside the box. The box parameter  $\eta$  is then defined as the ratio of the two areas:

$$\eta = \frac{A_{\text{ex}}}{A} \quad (22.54)$$

This parameter should also be an invariant both for rigid motion and for “compact” motion where  $A_{\text{ex}}$  is small, giving a measure of the type of behavior: this is because  $\eta$  is dimensionless and compares like with like but still contrasts two motions (viz., exterior to the box and overall). If the pedestrian is walking normally, the  $\eta$  value will be low at all times (see, e.g., the bottom trace in Fig. 22.17A): the higher values typical of runners are demonstrated clearly in Fig. 22.17B. In addition, individual sudden actions such as waving and jumping will result in spikes in  $\eta$ .

A third type of invariant  $R_{\text{ex}}$  has also been developed to help discriminate other more complex cases. This has the same definition as for  $R$ , except that it applies only for the part of the object external to the box. It provides additional useful information helping to discriminate runners from groups of walkers (see Fig. 22.16). Both of these categories have been found to have values of  $\eta$  around 0.5, so  $R_{\text{ex}}$  is useful in enabling them to be discriminated. (Specifically,  $R_{\text{ex}} \approx 1.5R$  for runners and  $R_{\text{ex}} \approx R$  for groups of walkers, though additionally  $R$  and  $R_{\text{ex}}$  are only well synchronized for runners.) While the  $R_{\text{ex}}$  information cannot be described as being specific to groups, it is nevertheless valuable, though ultimately, only detailed analysis leading for example to stick-figure models of people may provide the information that is required in a particular application (see the following section).

Because of the importance of box size in determining the values of  $\eta$  and  $R_{\text{ex}}$ , a careful study was made to optimize discrimination between single walkers and runners. This gave the optimum box width/height ratio as close to 0.5, for which the walker–runner threshold was best set at about 0.1 (see Fig. 22.18).



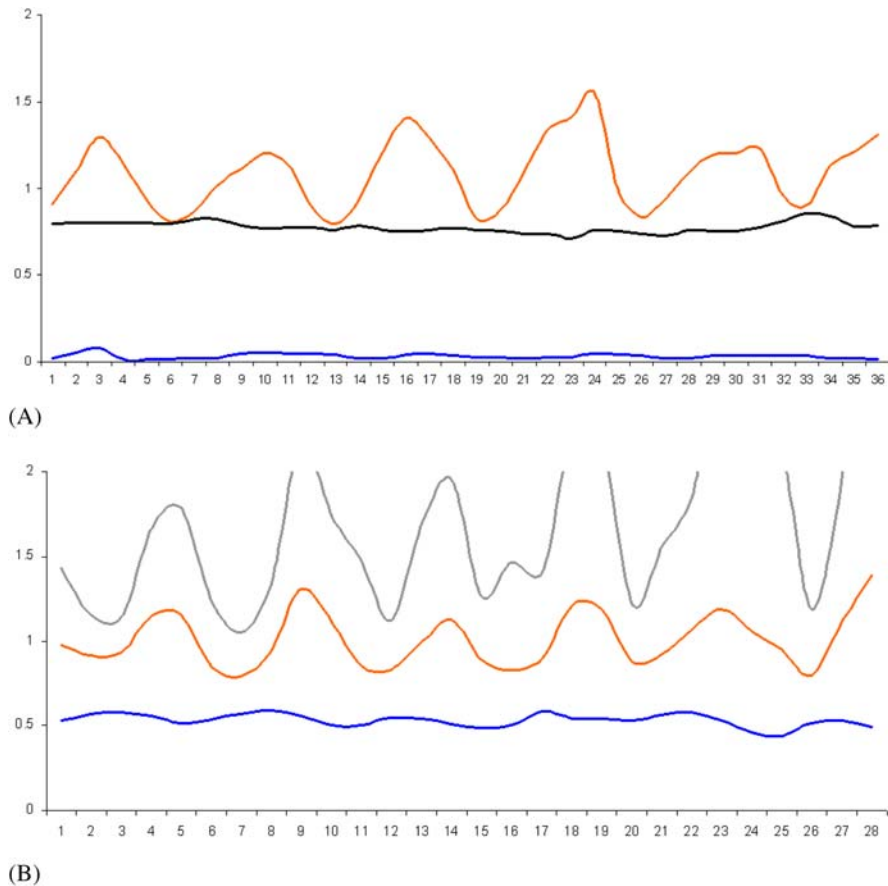


**FIGURE 22.17**

Motion analysis using rigidity and box parameters. (A) Top to bottom: result of applying the rigidity parameter  $R$  for the pedestrian; and result of applying  $R$  for the vehicle; result of applying box parameter  $\eta$  for the pedestrian. The horizontal scales indicate video frames. (B) Top to bottom: result of applying the respective parameters  $R_{ex}$ ,  $R$ ,  $\eta$  for the runner. In all cases the originals are shown in Fig. 22.16.

© IET 2007.

Overall, the methods described here have been found to distinguish motions of rigid and nonrigid objects with  $\sim 97\%$  accuracy. They are also able to classify single walkers with  $\sim 95\%$  accuracy, and runners and groups of walkers with  $\sim 87\%$  accuracy; in addition, they give useful indications of “extravagant” activities such as waving and jumping. Interestingly, all this was achieved via use of specially designed invariants, which save complexity and computation while being straightforward to set up and adjust.

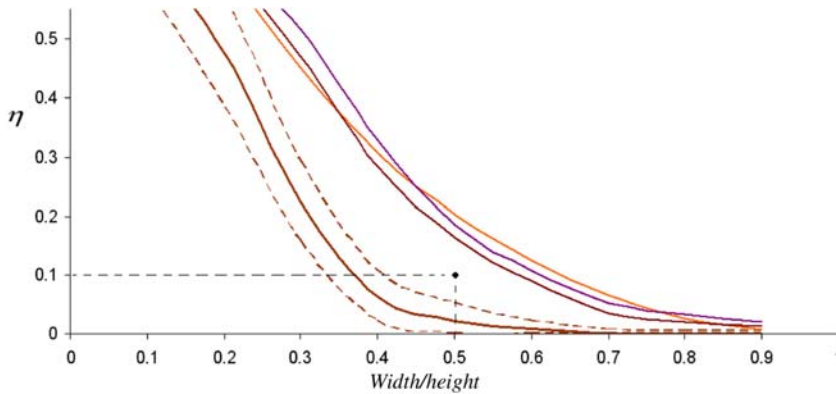


**FIGURE 22.18**

Discrimination permitted by box parameter  $\eta$ . The lower solid line represents the mean value of a sample of walkers (the broken lines indicate  $\pm \sigma$  error bars), and the upper solid lines record runners. To discriminate between walkers and runners, the best operating point is close to (0.5, 0.1), as shown.

© IET 2007.

## 22.13 HUMAN GAIT ANALYSIS

For several decades, human motion has been studied using conventional cinematography. Often, the aim of this work has been to analyze human movements in the context of various sports—in particular, tracking the swing of a golf club and thus helping the player to improve his game. To make the actions clearer, stroboscopic analysis coupled with bright markers attached to the body have been employed and have resulted in highly effective action displays. In the 1990s, machine vision was applied to the same task. At this point, the studies became much more serious and there was increased focus on accuracy. The reason for this was a widening of the area of application not only to other sports but also to medical diagnosis and to animation for modern types of film containing artificial sequences.

Because high accuracy is needed for many of these purposes—not least measuring limbs or other imperfections of human gait—analysis of the motion of the whole human body in normally lit scenes proved insufficient, and body markers remained important. Typically, two are needed per limb, so that the 3D orientation of each limb is deducible. Some work has been done to analyze human motions using single cameras, but the majority of the work employs two or more cameras: multiple cameras are valuable because of the occlusion that occurs when one limb passes behind another, or behind the body.

To proceed with the analysis, a kinematic model of the human body is required. In general, such models assume that limbs are rigid links between a limited number of ball and socket joints, which can be approximated as point

junctions between stick limbs. For example, one such model (Ringer and Lazenby, 2000) employs two rotation parameters at the point where the hips join the backbone, three for the joint where the thigh bone joins the hips, plus one for the knee, and another for the ankle. Thus, each leg has seven degrees of freedom, two of these being common (at the backbone): this leads to a total of 12 parameters covering leg movements (Fig. 22.19). Clearly, it is part of the nature of the skeleton that the joints are basically rotational, though there is some slack in the system, especially in the shoulders, while the knees have some lateral freedom. Finally, the whole situation is made more complex by constraints such as the inability of the knee to extend the lower leg too far forward.

Once a kinematic model has been established, tracking can be undertaken. It is relatively straightforward to identify the markers on the body with reasonable accuracy. The next problem is to distinguish one marker from another and to label them. Considering the huge number of combinations of labels that are possible, and the frequency with which occlusions of parts of a leg or arm are bound to take place, special association algorithms are required for the purpose. These include the Kalman filter that helps to predict how unseen markers will move until they come back into view. Such models can be improved by including acceleration parameters as well as position and velocity parameters (Dockstader and Tekalp, 2002). Their model is not merely theoretically deduced: it has to be trained, typically on sequences of 2500 images each separated by 1/30 seconds. In

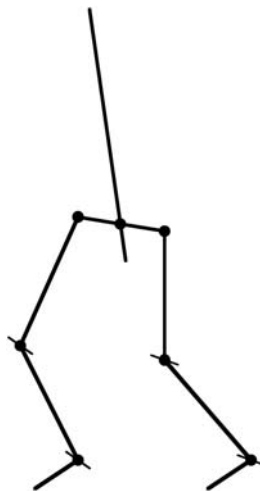


**FIGURE 22.19**

Stick-skeleton model of the lower human body. This model takes the main joints on the skeleton as being universal ball-and-socket joints, which can be approximated by point junctions—albeit with additional constraints on the possible motions (see text). Here, a thin line through a joint indicates the single rotational axis of that joint.

addition, the stick model of each human subject has to be initialized manually. Considerable training is necessary to overcome the slight inaccuracies of measurement and to build up the statistics sufficiently for practical application when testing. Errors are greatest when measuring hand and arm movements, because of the frequent occlusions they are subject to.

Overall, articulated motion analysis involves complex processing and a lot of training data. It is a key area of computer vision and the subject is evolving rapidly. It has already reached the stage of producing useful output, but accuracy will improve over the next few years and this will set the scene for practical medical monitoring and diagnosis, completely natural animation, detailed help with sports activities at affordable costs, not to mention recognition of criminals by their characteristic gaits. Certain requirements—such as multiple cameras—will probably remain, though the trend to markerless monitoring can be expected to continue. For further information, the reader could start by referring to the monograph by Nixon et al. (2006).

---

## 22.14 MODEL-BASED TRACKING OF ANIMALS

This section is concerned with the care of farm animals. Good stockmen notice many aspects of the behavior of the animals and learn to respond to them. Fighting, bullying, tail biting, activity, resting behavior, and posture are useful indicators of states of health, potential lameness, or heat stress, while group behavior may indicate the presence of predators or human intruders. In addition, feeding behavior is all important, as is the incidence of animals giving birth or breaking away from the confinement of the pen. In all these aspects, automatic observation of animals by computer vision systems is potentially useful.

Some animals such as pigs and sheep are lighter than their usual backgrounds of soil and grass, and thus they can in principle be located by thresholding. However, the backgrounds may be cluttered with other objects such as fences, pen walls, drinking troughs, and so on—all of which can complicate interpretation. Thus, straightforward thresholding will rarely work well in normal farm scenes. McFarlane and Schofield (1995) tackled this problem by background subtraction. They used a background image obtained by temporal median filtering for a whole range of images taken over a fair period: during this process, care was taken to mask out regions where piglets were known to be resting. Their algorithm modeled piglets as simple ellipses and achieved fair success in its task of monitoring the animals.

We next examine the more rigorous modeling approach adopted by Marchant and Onyango (1995) and developed further by Onyango and Marchant (1996) and Tillet *et al.* (1997). These workers aimed to track movements of pigs within a pen by viewing them from overhead under not very uniform lighting conditions. The main aim of the work at this early stage was tracking the animals, though, as

indicated above, it was intended to lead on to behavioral analysis in later work. To find the animals, some form of template matching is required. Shape matching is an attractive concept, but with live animals such as pigs, the shapes are highly variable: specifically, animals which are standing up or walking around will bend from side to side and may also bend their necks sideways or up and down as they feed. It is insufficient to use a small number of template masks to match the shapes, as there is an infinity of shapes related by various values of the shape parameters mentioned. These parameters are additional to the obvious ones of position, orientation, and size.

Careful trials showed that matching with all these parameters is insufficient, as the model is quite likely to be shifted laterally by variations in illumination: If one side of a pig is closer to the source of illumination, it will be brighter, and hence the final template used for matching will also shift in that direction. The resulting fit could be so poor that many possible “goodness of fit” criteria will deny the presence of a pig. These factors mean that possible variations in lighting have to be taken into account in fitting the animal’s intensity profile.

A rigorous approach involves principal components analysis (PCA). The deviation in position and intensity between the training objects and the model at a series of carefully chosen points is fed to a PCA system: the highest energy eigenvalues indicate the main modes of variation to be expected; then any specific test example is fitted to the model and amplitudes for each of these modes of variation are extracted, together with an overall parameter representing the goodness of fit. Unfortunately, this sort of approach is highly computation intensive because of the large number of free parameters; in addition, the position and intensity parameters are disparate measures that require quite different scale factors to be used to coax the schema into working. This means that some means is required for decoupling the position and intensity information. This is achieved by performing two independent PCAs in sequence—first on the position coordinates and then on the intensity values.

When this procedure is carried out, three significant shape parameters are found, the first being lateral bending of the pig’s back, accounting for 78% of the variance from the mean; and the second being nodding of the pig’s head: as the latter corresponded to only ~20% of the total variance, it was ignored in later analysis. In addition, the gray-level distribution model had three modes of variation amounting to a total of 77% of the intensity variance: the first two modes corresponded to (1) a general amplitude variation in which the distribution is symmetrical about the backbone, and (2) a more complex variation in which the intensity distribution is laterally shifted relative to the backbone (this arises largely from lateral illumination of the animal)—see [Fig. 22.20](#).

While PCAs yield the important modes of variation in shape and intensity, in any given case the animal’s profile has still to be fitted using the requisite number of parameters—one for shape and two for intensity. The Simplex algorithm (Press *et al.*, 1992) proved effective for this purpose. The objective function to be minimized to optimize the fit takes account of (1) the average difference in intensity

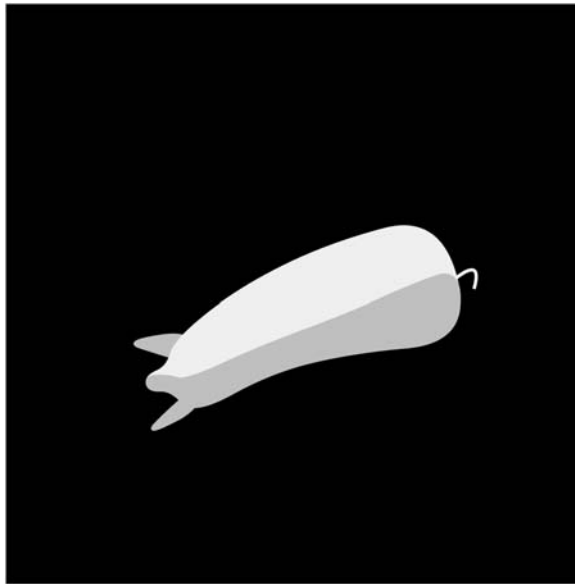


**FIGURE 22.20**

Effect of one mode of intensity variation found by PCA. This mode clearly arises from lateral illumination of the pig.

© World Scientific 2000.

between the rendered (gray-level) model and the image over the region of the model, and (2) the negative of the local intensity gradient in the image normal to the model boundary averaged along the model boundary (the local intensity gradient will be a maximum right around the animal if this is correctly outlined by the model).

One crucial factor has been skirted around in the preceding discussion: that the positioning and alignment of the model to the animal must be highly accurate (Cootes *et al.*, 1992). This applies both for the initial PCA and later when fitting individual animals to the model is in progress. Here, we concentrate on the PCA task. When using PCA, it should be borne in mind that it is a method of characterizing deviations: this means that the deviations must already be minimized by referring all variations to the mean of the distribution. Thus, it is very important when setting up the data to bring all objects to a common position, orientation, and scale before attempting PCA. In the present context, the PCA relates to shape analysis, and it is assumed that prior normalizations of position, orientation, and scale have already been carried out. (Note that in more general cases, scaling may be included within PCA if required. However, PCA is a computation intensive task, and it is best to encumber it as little as possible with unnecessary parameters.)

Overall, the achievements outlined above are notable, particularly in the effective method for decoupling shape and intensity analysis. In addition, the work holds significant promise for application in animal husbandry, demonstrating that animal monitoring and ultimately behavioral analysis should be attainable with the aid of computer vision.

---

## 22.15 CONCLUDING REMARKS

This chapter has shown something of the purpose of surveillance—which is largely to do with monitoring the behavior patterns of people and vehicles on roads and precincts. It has also shown a number of the principles and methods by which surveillance may be implemented: these include identification and elimination of background, detection and tracking of moving objects, identification of the ground plane, occlusion reasoning, Kalman and particle filtering, capability for modeling complex motions including those of articulated objects, and use of multiple cameras for widening coverage in time and space.

Over time, some specialized application areas have appeared, such as location and identification of license plates, identification of vehicles exceeding the speed limit, human gait analysis, and even animal tracking: the chapter has aimed to indicate how all these can be achieved. Early methods included Kalman filters and chamfer matching, and later ones included particle filters, which rely on a probabilistic approach to tracking. Particle filters have come a long way, but it is doubtful whether they can go much further if based on probability assessment alone, as it is clear that humans bring to bear huge databases of relevant information when tracking moving objects.

An important lesson is that detection and tracking are distinct, complementary functions, and there is no reason why the same algorithms will be optimal for both. As indicated in [Section 22.3.3](#), foreground detection requires the application of a suitable foreground model, or else a bootstrapping process involving an “exception to background” procedure. But once detection has been achieved, tracking can in principle proceed as a much simpler, more blinkered process. It remains to be seen whether future work will find ways of streamlining the detection + tracking model. Most likely, it will be found lacking, because objects such as people radically alter in appearance as they walk by; hence, it is more natural to have both processes working in parallel (not necessarily at constant rates) all the time, rather than being applied serially. The same applies when a guided missile approaches a tank but can be misled into tracking a different object in the background as the scale of the target radically changes by several orders of magnitude: again the tracking algorithm needs to be monitored by a continuously acting detection algorithm. These points are labored because detection and tracking are at the core of surveillance, whatever the application area, and are thus very much the generic backcloth to this chapter.

While the chapter has covered the situation of static cameras being used to monitor moving objects, the following chapter covers the intrinsically more complex case of in-vehicle vision systems, where moving cameras are used to monitor both stationary and moving objects. This will call for a radical rethink of vision system strategy, because all parts of the scene will be eternally shifting and changing, and it will generally not be possible to rely on relatively trivial preliminary identification of a stationary background.

*This chapter has shown that surveillance is largely about the detection and tracking of moving objects, and that different types of algorithm will often be needed to achieve each of these functions. In most cases, locating the ground plane is a necessary first step in the analysis, while occlusion reasoning, Kalman filtering, capability for modeling complex motions, and multiple cameras will often be needed to achieve the ultimate aim of analyzing developing behavior patterns.*

---

## 22.16 BIBLIOGRAPHICAL AND HISTORICAL NOTES

As we have seen, surveillance involves many factors, from 3D to motion, but paramount amongst these is the tracking of moving objects—in particular, vehicles and people. For some years, tracking meant the use of Kalman filters, but the deficiencies of this approach led in the 1990s to the development of particle filters, including particularly the work of Isard and Blake (1996, 1998), Pitt and Shepherd (1999), van der Merwe et al. (2000), Nummiaro et al. (2003), Nait-Charif and McKenna (2004, 2006), Schmidt et al. (2006), and many others. Much of the early work is summarized in a tutorial paper by Arulampalam et al. (2002), though Doucet and Johansen (2011) have justifiably felt it necessary to produce another. The first of these and a 2008 preprint of the second might better be called reviews than tutorials, as the going is difficult—partly because of the lack of explanatory figures—and often it is easier to appeal to the original works than to them.

In parallel with these developments, much work took place on background modeling using both parametric and nonparametric methods: See for example Elgammal et al. (2000). Cucchiara et al. (2003) helped by defining the stationary and transient background problems and by clarifying the problem of “ghosts.” Shadows have been a source of problems over the whole period, not least because they can be static or moving, and also because they can fall on static or moving objects: Elgammal et al. (2000) and Prati et al. (2003) carried out seminal work on this topic.

Khan and Shah (2000, 2003, 2009) were responsible for a thoroughgoing approach to the tracking of people both with single and with multiple cameras, this work being followed up by Eshel and Moses (2008, 2010) who found how to



make good use of top-of-head tracking in crowd scenes. Pflugfelder and Bischof (2008, 2010) developed the approach to cover nonoverlapping views—a task that had previously (Makris *et al.*, 2004) been solved with some degree of generality, but without knowledge of scene geometry, by learning transition probabilities for objects passing between views.

Vezzani and Cucchiara (2008) and Vezzani *et al.* (2011) made a careful analysis of the means by which occlusions can arise, and this enabled them to devise algorithms that cope better with temporary partial or full occlusions or temporary merging of moving objects—in the sense of not getting confused, and recovering faster from such events.

Work on traffic monitoring has stretched over many years (e.g., Fathy and Siyal, 1995; Kastinaki *et al.*, 2003). Early work on the application of snakes to tracking was carried out by Delagnes *et al.* (1995); on the use of Kalman filters for tracking by Marslin *et al.* (1991); and on the recognition of vehicles on the ground plane by Tan *et al.* (1994). For details of belief networks see Pearl (1988). Note that corner detectors (Chapter 6: Corner, Interest Point, and Invariant Feature Detection) have also been widely used for tracking: See Tissainayagam and Suter (2004) for an assessment of performance.

A huge amount of work has been carried out on the analysis of human motions (Aggarwal and Cai, 1999; Gavrilu, 1999; Collins *et al.*, 2000; Haritaoglu *et al.*, 2000; Siebel and Maybank, 2002; Maybank and Tan, 2004). See Sugrue and Davies (2007) for a simple method of distinguishing pedestrians. However, note that rigorous analysis of human motion involves studies of articulated motion (Ringer and Lazenby, 2000; Dockstader and Tekalp, 2001), one of the earliest enabling techniques being that of Wolfson (1991). As a result, a number of workers have been able to characterize or even recognize human gait patterns (Foster *et al.*, 2001; Dockstader and Tekalp, 2002; Vega and Sarkar, 2003): See Nixon *et al.* (2006) for a recent monograph on the subject. A particular purpose for this type of work has been the identification and avoidance of pedestrians from moving vehicles (Broggi *et al.*, 2000; Gavrilu, 2000). Much of this work has its roots in the early farsighted paper by Hogg (1983), which was later followed up by crucial work on eigenshape and deformable models (Cootes *et al.*, 1992; Baumberg and Hogg, 1995; Shen and Hogg, 1995). Gavrilu's work on pedestrian detection (Gavrilu, 1998, 2000) used chamfer matching, while Leibe *et al.* (2005) developed the method further, albeit with the help of a minimum distance length top-down segmentation scheme capable of handling multiple hypotheses.

In our concentration on complex topics such as articulated motion and complications caused by occlusion, it is important not to lose sight of simple but elegant developments such as histograms of orientated gradients (HOGs), which have only appeared relatively recently (Dalal and Triggs, 2005). These were designed for, and are well-matched to, the detection of human shapes. Basically, they focus on the straight limbs of the human body, which have many edge points aligned along the same direction—though the latter will naturally change with walking or other motions. The basis of the method is to divide the image into “cells” (sets of

pixels) and to produce orientation histograms for each of them. Voting into the orientation histogram bins takes place with weighting proportional to gradient magnitude. To provide strong illumination invariance, a robust normalization method is used. The cells are combined into larger overlapping blocks in several ways, with the result that some of the blocks end up with larger signals indicating the presence of human limbs. However, the result is curiously that the HOG detectors cue mainly on silhouette contours and emphasize the head, shoulders, and feet. In a later paper, Dalal, Triggs, and Schmid (2006) combined the HOG detector with motion detectors and were able to achieve even better results (motion detection improved the false alarm rate by a factor of 10 relative to the best appearance-based detector). An interesting feature of the HOG approach is that it outperforms wavelet analysis because the latter eliminates vital abrupt edge information by prematurely blurring the image data.

Overall, work on surveillance has stretched over many years but has vastly accelerated since the mid-1990s as workers have had access to more powerful computers that made it realistic to think of real-time implementation, both for experimentation and for on-road systems. Note that the past few years have seen developments in real-time systems involving FPGAs (field programmable gate arrays)—a trend that was already present circa 2000—and GPUs (graphics processing units)—a trend that is especially recent and has arisen as a result of natural interaction between the video games industry and computer vision.

### 22.16.1 MORE RECENT DEVELOPMENTS

Amongst the most recent works, Kim et al. (2010) have proposed a robust method for recognizing humans by their gait by using a hierarchical active shape model. The approach is novel in that it is prediction based and overcomes the drawbacks of existing methods by extracting a set of model parameters instead of directly analyzing the gait. Feature extraction proceeds by motion detection, object region detection, and Kalman prediction of the active shape model parameters. The method is able to alleviate tasks such as background generation, shadow removal, and obtaining high recognition rates. Ramanan (2006) has obtained good results by a new iterative parsing method for analyzing motions of articulated bodies ranging from humans playing games to horses frolicking and cantering. The approach has the advantage of being generic and does not depend on the location of skin or human faces. Lian et al. (2011) have obtained impressive performance when tracking pedestrians between camera view separations of more than 20 m—much greater than the separations  $\sim 4$  m obtained by Pflugfelder and Bischof (2008, 2010).

Ulusoy and Yuruk (2011) have analyzed the problems of fusing data from visual and thermal images in order to make good use of their complementary properties to improve overall performance. They show that fusion should lead to a better recall rate (fewer false negatives) but, at the same time, result in a decrease in precision rate (more false positives); they also note that the infrared

(thermal) domain always has higher precision (the underlying reasons for these observations are that thermal images effectively provide the *foreground* information containing the object pixels). In fact, it is only worth attempting fusion when an improved recall rate is required. This paper presents a more efficient method for fusing the data from the two domains and at the same time obtaining recall rates better than those previously obtained. The method was tested on outdoor images of human groups including those from a well-known database. The work in this paper leans heavily on the earlier work of Davis and Sharma (2007). Both papers refer to thermal imagery in spite of the title of the first which refers to “infrared” images.

---

### 22.17 PROBLEM

1. When an inverse perspective mapping onto the ground plane is carried out, points on the ground plane are well represented in the new representation. Explain why this does not apply for buildings or people, and why they always appear to lean backward when presented in this representation.

This chapter considers the value of in-vehicle vision as part of the means for providing driver assistance systems. To achieve this, many objects have to be identified, including not only the roadway itself but also the lane and other markings on it, road signs, other vehicles, and pedestrians. The latter are particularly important as their actions are relatively unpredictable, and people who wander into the roadway are liable to cause accidents—unless the driver assistance system can help to avoid them.

Designing in-vehicle vision systems is anything but trivial, as they necessarily deploy moving cameras, which means that all objects in a scene are moving; hence, it becomes quite difficult to eliminate the background from consideration. For these reasons, it becomes necessary to rely more on recognition of individual objects than on motion-based segmentation.

*Look out for:*

- how the roadway, road signs, and road markings may be located
- the availability of several distinct methods for locating vehicles
- what information can be obtained by viewing license plates and wheels
- how pedestrians may be located
- how vanishing points (VPs) can be used to provide a basic understanding of the scene
- how the ground plane may be identified
- how a plan view of the ground plane can be obtained and used to help with navigation
- how vehicles can be guided using vision to compensate for roll, pitch and yaw.

While it is easy to set out strategies for building in-vehicle vision systems that will work well in normal conditions on the roadway, it is far from simple to design them to operate on the less structured environments of farms or fields. Indeed, much additional reliance on GPS (global positioning system) and other methodologies will often be needed for the purpose.

## 23.1 INTRODUCTION

This chapter provides an introduction to in-vehicle vision systems. The topic clearly overlaps with many of the ideas of the previous chapter, particularly regarding traffic surveillance, as here we are regarding the flow from inside a vehicle rather than from a stationary camera mounted (typically) on an overhead gantry. However, although the environment may be similar, the situation is

essentially different, because the camera platform is in motion and almost nothing that is viewed appears stationary (Table 23.1). This means that it is extremely difficult to use methods such as background subtraction. Note that while it is theoretically possible to find a general perspective transformation that makes a sequence of frames exactly coincide so that background subtraction can be achieved, to do this would be to replace a technique that is intended to be a simple way of cueing into images into one that is, highly complex, and the process of finding a sufficiently exact perspective transformation would itself require considerable computation, so this is unlikely to provide a useful strategy for analyzing image sequences.

Given the more difficult problem of analyzing scenes containing moving objects from a moving platform, we have to find ways of tackling the task equitably. Fortunately, with vehicles on a road, the range of types of scene is highly restricted. In particular, the roadway is always present in the image foreground and thus is easily identifiable. Likewise, it normally has a characteristic dark intensity, and thus its recognition right into the distance need not be too problematic: the fact that it is moving relative to the camera is relatively immaterial. In fact, it may even be quite difficult to detect motion by looking downward toward the road surface. Next, there are a whole host of standard types of object that are likely to be visible from within a vehicle—buildings, other vehicles, pedestrians, road markings, road signs, telegraph poles, lamp standards, bollards, and so on. The high frequency with which each of these can appear indicates that it will be necessary to have the capability of recognizing each of them independently, at any range and at any speed. This means that it is better, *as a first stage in the analysis*, to revert to ignoring speed of motion and to concentrate on pattern recognition. In fact, recognition can be helped by considering the range, which is readily deduced, approximately at first, from the lowest location on the object, which is where it meets the road (it is here assumed that the road has already been segmented from the remainder of the scene as an important preliminary stage of the analysis). Note that depending on the aim of the analysis (a point to which we shall return below), it is likely to be more important to identify objects that lie within the road region, so segmentation of the latter is all the more important as a first stage. Then, these objects—now restricted mainly to the subset, other vehicles, pedestrians, road markings, road signs, traffic lights—each needs to be identified in its own right. Later, the exact motion of the moving platform, and subsequently its location relative to all the other objects, will need to be ascertained.

**Table 23.1** Levels of Difficulty When Motions Can Occur

- 
1. Locating stationary objects from a stationary platform
  2. Locating moving objects from a stationary platform
  3. Locating stationary objects from a moving platform
  4. Locating moving objects from a moving platform
-

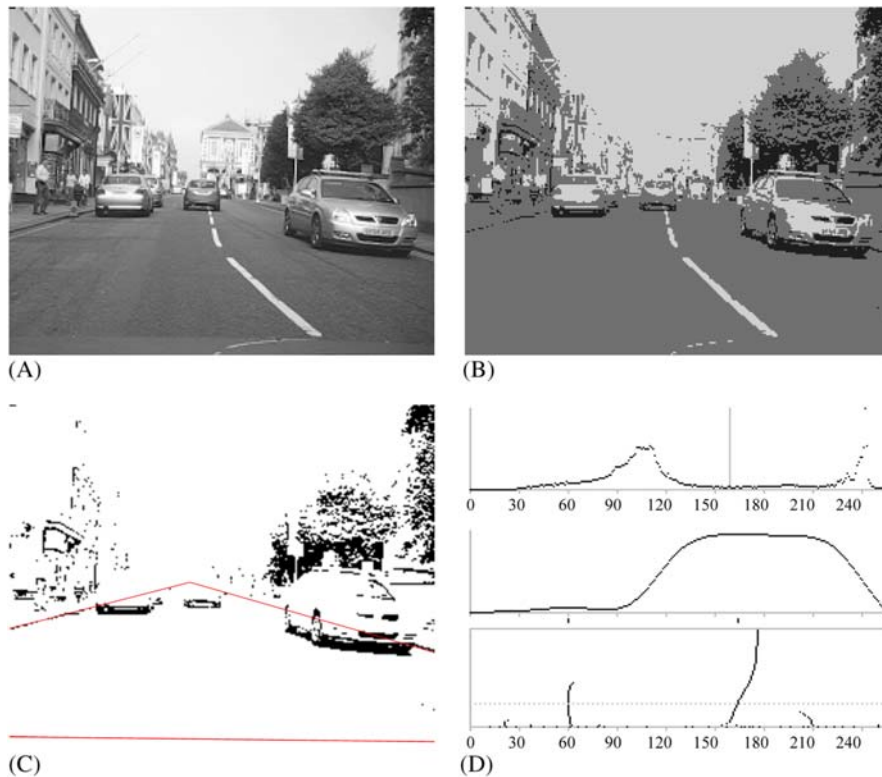
We next consider the aims of implementing in-vehicle vision systems. Broadly, there are two: (1) navigation along the road, including staying in lane and finding out from road signs and traffic signals where to go, when to stop and other such information (here, to simplify matters, we ignore use of GPS and other types of help, and how information from the various sources can be fused together reliably); (2) driver assistance, which can include a variety of matters, particularly informing the driver of all aspects included in (1), and alerting him or her to important factors, such as vehicles that are braking, or pedestrians who are moving onto the roadway. In fact, much of the information that is acquired by the vision system will need to be conveyed to the driver in one way or another. However, of particular interest is the fact that drivers will sometimes not be able to act rapidly enough to avoid pedestrians, vehicles that brake unpredictably, overtaking vehicles that suddenly cut in, and so on. There is also the problem that drivers may be drowsy or may for various reasons—e.g., because of distractions from other occupants or those caused by the simultaneous need to navigate—react too slowly, so that an accident could become imminent. In such cases, driver assistance that could automatically initiate breaking or swerving might be crucial. We can also envisage various situations where the vision system would be part of a fully automatic driving system: here, there is bound to be a problem of legality, and who or what would be to blame for an accident (*viz.* the driver, car manufacturer, vision system designer, or whoever). We shall not delve into such problems here, but just consider the vision system as an enabling technology. However, once vision and driver assistance systems become sufficiently powerful, they will doubtlessly become part of other schemes such as those for driving in tight convoys—deemed by many to be the best way of achieving rapid safe transit along our motorways. In addition, there are other ways in which driver assistance can be valuable: these range from cruise control to automatic parking.

In this chapter, we focus generally on providing a vision system that can perceive all that might be needed for vehicle guidance and driver assistance, with emphasis on locating the roadway and road lanes, identifying other vehicles and locating pedestrians close to or on the roadway. As indicated above, the whole process starts by locating the roadway, as discussed in the following section.

---

## 23.2 LOCATING THE ROADWAY

**Chapter 4**, The Role of Thresholding described a technique that was capable of locating the roadway using a multilevel thresholding approach (see [Fig. 4.9B](#)). In fact, the roadway was identified by the third and fourth thresholds as that section of the image with gray levels in the approximate range 100–140. Similar results are obtained in other cases, e.g., [Fig. 23.1B](#), where the two threshold values demarcate an even greater gray-scale range, c. 60–160. While these can be construed as being reasonably ideal cases, thresholding is such a basic technique that it should be

**FIGURE 23.1**

Frame of video taken from a moving vehicle. (A) Original image. (B) Doubly thresholded image. (C) Result of only applying the lower threshold. (D) Top: intensity histogram of the original scene. Middle: result of applying the global valley transformation and smoothing. Bottom: the dotted line shows the two thresholds used in (B) being located automatically. For further details, see text in [Chapter 4](#), The Role of Thresholding. The red lines in (C) demonstrate that, within the road area, the lower threshold predominantly identifies under-vehicle shadows.

© IET 2008.

possible to extend it to cover less ideal situations. For example, if shadows appear on the roadway, the latter would in many cases appear as two contiguous sets of regions with two prominent intensity levels and could indeed be identified by the same method. Note also that varying illumination levels would be likely to make one intensity elide smoothly into another, and if a suitable range of intensities between thresholds (as in [Figs. 4.9](#) and [23.1](#)) were taken into account, the segmentation problem might still be solved in exactly the same way. However, ultimately the problem is one of pattern recognition and can be solved by (1) eliminating other

objects, such as road lane markings, (2) identifying the limits to the roadway, and (3) taking other features such as color or texture into account. Note that as the color of the roadway is often a bland gray, it may only be made to stand out by noting the colors of the other surroundings, such as grass, trees, or brickwork on buildings. Clearly, this would make the whole system more complex, but in a well-known and well-worn way—pattern recognition by now being a reasonably mature subject. To some extent, the situation may be helped by bringing the motion of the vehicle into the picture (we have so far resisted this, to bring the discussion to the simplest possible base level). In that case, without calculating the exact motion of the vehicle, we can take account of the fact that the roadway stretches for a long distance ahead, so any part of it that is established to be roadway will remain so until the vehicle passes over it. Furthermore, on the road ahead, any vehicle that is located evidently runs on the roadway, so parts of it are continuously being identified. Thus, the camera vehicle merely needs to keep a record of all candidate regions that have been positively identified, so that any ambiguities from identification via intensities can be eliminated. Finally, this time taking motion parameters into account, keeping a tally on the road boundaries with the aid of Kalman filters will solve many of the remaining issues.

---

### 23.3 LOCATION OF ROAD MARKINGS

It will have been noticed from Figs. 4.9 and 23.1 that the multilevel thresholding technique used to locate the gray surface of the road simultaneously segments white road markings. However, white road markings are seldom pure white and may be worn or even partly duplicated by older markings. In any case, segmenting them by thresholding is not the same as absolute identification. One way around this dilemma is that of fitting the road markings to suitable models. Often straight lines are adequate, though sometimes parabolas have been used for the purpose. Fig. 23.2 shows a case where continuous and broken road markings have been identified using the RANSAC (random sample consensus) technique, which helps to locate the VP on the horizon to a reasonable approximation. The widths of the road lane markings can also be measured in this way. Fig. 23.3 takes this even further. In this case, a greater degree of reliability and accuracy is obtained by locally bisecting each lane marking horizontally before feeding the data to RANSAC. In this way, extraneous signals can be eliminated—if necessary by filtering the horizontal widths. Note how RANSAC is able to find the best fit straight line section even when the road lane markings are curved. Likewise, it is able to eliminate lane markings that have been distorted by the presence of older lane markings (Fig. 23.3A). As described in Chapter 10, Line, Circle, and Ellipse Detection, the version of RANSAC used for the tests successively eliminates the data points used to fit line segments, and the width delete threshold  $d_d$  is made larger than the fit threshold  $d_f$  so that no data points are retained that could



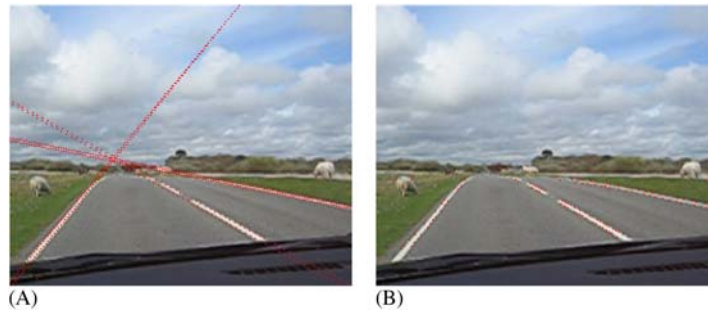


**FIGURE 23.2**

Application of RANSAC for locating road lane markings. (A) Original image of road scene with lane markings identified by RANSAC. (B) The edge point local maxima used by RANSAC for locating the road lane markings. While the lane markings converge to approximately the right point on the horizon line, the parallel sides of the individual lane markings do not converge quite so accurately, indicating the limits achievable with so few edge points. This is more a failure of the edge detector than of RANSAC itself.

mislead the algorithm while searching for subsequent line segments (see the algorithm flowchart in [Fig. 23.4](#)).

## 23.4 LOCATION OF ROAD SIGNS

We now continue with the process of analyzing the vehicle's environment and consider the most relevant remaining stationary parts that lie on or adjacent to the roadway. These include the traffic signs. It will not be possible to examine more than one or two cases, but amongst these are various relevant warnings, including those for road bumps and "GIVE WAY": note that many others appear in the same style—with the message in black on a white background and enclosed in a red triangle. To locate these signs, some tests were made without using the color aspect as this might represent too easy an approach (note also that in the wrong lighting conditions, color can be misleading): instead, an idealized small binary template of size  $22 \times 19$  pixels was employed. While apparently crude, this small template had the advantage of requiring very little computation to locate the relevant objects. In fact, the chamfer-matching technique ([Section 22.7](#)) was used for detecting the traffic signs shown in [Fig. 23.5](#). While the template was primarily designed to detect the road bump sign, it also gave a sizeable signal for the GIVE WAY sign. Indeed, the two signals found using the template were both well above the signal-to-noise ratio elsewhere in the image, the closest possible false alarms being high up in the trees, which contain a plethora of random shapes. Note that the picture was taken under highly nonideal conditions on a wet day when there were a number of reflective areas on the road. Overall, the chamfer-

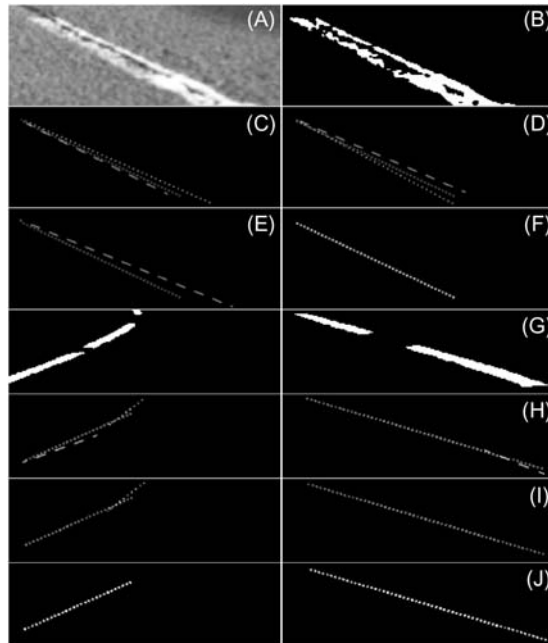


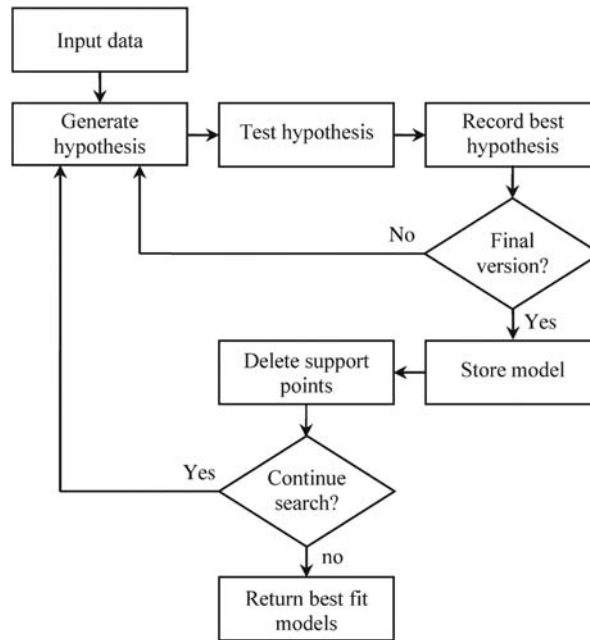
**FIGURE 23.3**

Further tests of RANSAC for locating road lane markings. (A) Original Image 1: a distorted set of double line road markings. (B) Thresholded version of (A). (C) 3–3. (D) 3–6. (E) 3–10. (F) 3–11. (The notation “ $d_f-d_d$ ” means that  $d_f$  is the “fit distance,” and  $d_d$  is the “delete distance;” see text.) (G) Original Image 2, already thresholded: the central section of the road containing no markings has been eliminated to save space. (H) 3–3, (I) 3–6, (J) 3–11. Parts (F) and (J) show the final results as dense dotted lines: in other cases, dots and dashes are used to distinguish the different lines. Note that immediately after thresholding, the horizontal bisector algorithm finds the midpoints of white regions along horizontal lines and feeds them to RANSAC for fitting.

© IET 2011.

matching technique seems well suited to rapidly locating fixed road signs of various sorts.

There is some possibility of designing a single idealized template for locating all triangular signs. Note first that a blank white interior would be more suitable than the road bump structure in Fig. 23.5E: this corresponds to disregarding the center of the template, taking it as being composed of “don’t care” locations. In fact, the template should really be designed by a suitable training approach such as the one outlined by Davies (1992d). In this method, a matched filter approach is used in designing templates, with local variability of training samples (represented by standard deviation  $\sigma(\mathbf{x})$ ) being taken to correspond to noise, thereby necessitating reduced local weighting: the local matched filter

**FIGURE 23.4**

Flowchart of the lane detector algorithm used for the tests in Fig. 23.3.

© IET 2011.

weighting is thus (Davies, 1992d) taken as  $\bar{S}(\mathbf{x})/\sigma(\mathbf{x})^2$  rather than  $\bar{S}(\mathbf{x})$ , where  $\bar{S}(\mathbf{x})$  is the mean local signal at  $\mathbf{x}$  during training. For the types of road sign considered above, variable distributions of black within the central white area would be treated optimally by this method.

## 23.5 LOCATION OF VEHICLES

In recent years, a number of algorithms have been designed for locating vehicles on the road, whether in surveillance applications or by in-vehicle vision systems. One notable means for achieving this has been by looking for the shadows induced by vehicles (Tzomakas and von Seelen, 1998; Lee and Park, 2006). Importantly, the strongest shadows are those appearing beneath the vehicle, not least because these are present even when the sky is overcast and no other shadows are visible. Such shadows are again identified by the multilevel thresholding approach of Chapter 4, The Role of Thresholding. Fig. 23.1 shows a particular instance of this, where almost the only dark pixels appearing within the roadway region are the under-vehicle shadows. In fact, as under-vehicle shadows lie under

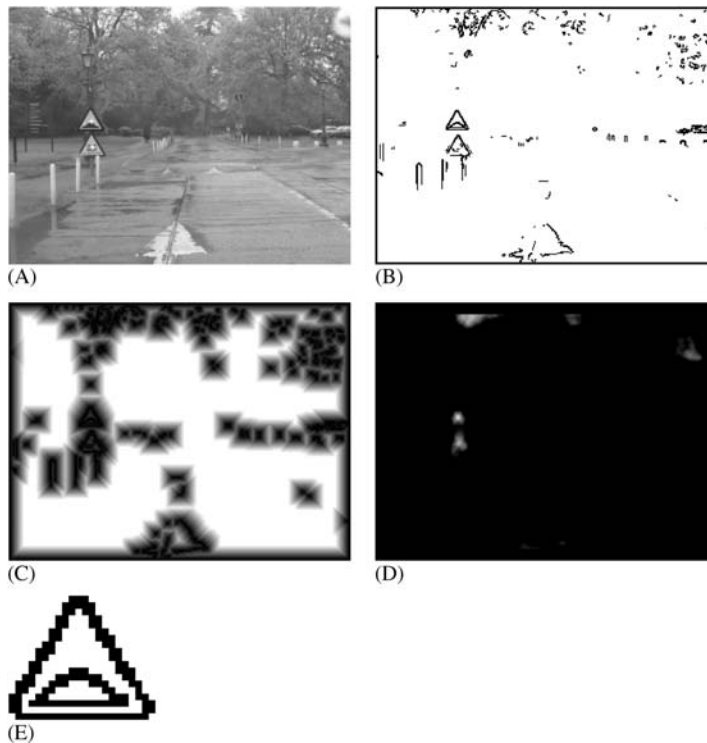


**FIGURE 23.5**

Locating road signs using chamfer matching. (A) Original image showing two triangular road signs (indicating a road bump and “GIVE WAY”): each of the signs is marked with a white cross where it has been located by the chamfer-matching algorithm. (B) Thresholded edge image after nonmaximum suppression. (C) Distance function image: note that with the display enhancement factor of 20 used here, the distance appears to saturate at 13 pixels. (D) The response obtained when moving the template (E) over the image.

vehicles, an excellent way of locating nearby vehicles is to move upward from the lowest part of the roadway until a dark entity appears: there is then a high probability that it will only locate vehicles. Note that in [Fig. 23.1C](#), the other main candidates are trees, but these are discounted as being well above the road region—as indicated by the dotted triangle.

As pointed out earlier when considering methods for locating the road region, it is useful to have a number of methods available for locating objects such as vehicles, in case of peculiar illumination conditions or other factors. Following this line of analysis, we consider symmetry, which was first used for this purpose some years ago (e.g., Kuehnle, 1991; Zielke et al., 1993). [Fig. 23.6](#) shows a

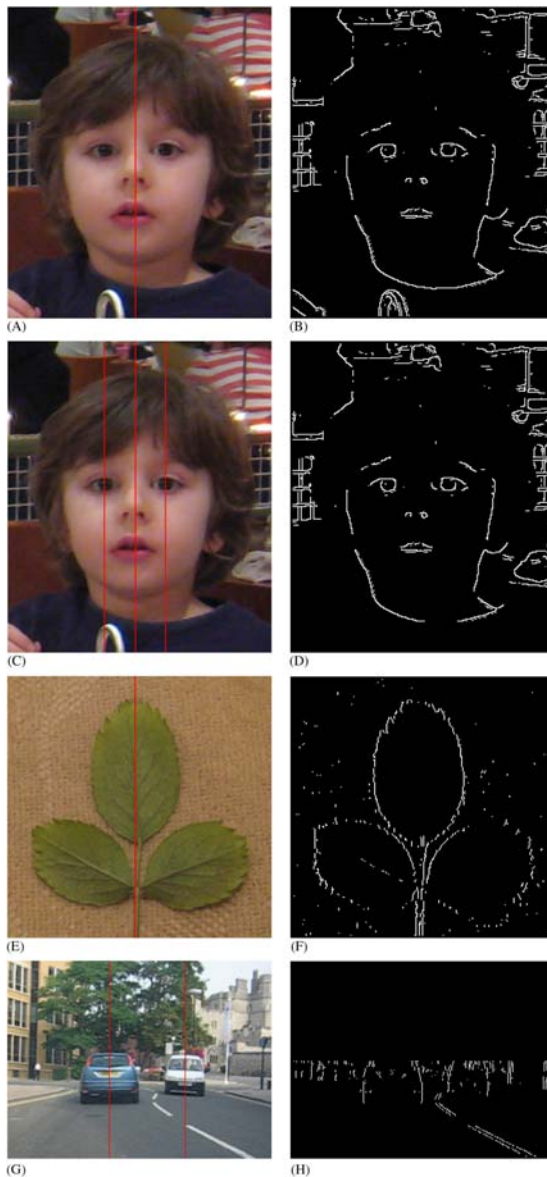


**FIGURE 23.6**

Searching for symmetry in images. (A) Original image of a face with a vertical axis of symmetry. (B) Edge image used for determining the axis of symmetry in (A). (C) Original image with symmetry axes of the eyes. (D) Slightly restricted edge image used for determining the symmetry axes of the eyes. (E) Original image of a leaf triplet, with symmetry axis. (F) Vertical edge image used to determine the symmetry axis in (E). (G) Original image of a traffic scene, with symmetry axes marked. (H) Vertical edge image used for determining the symmetry axes in (F). The slight bias of the left-most symmetry axis in (C) is not surprising in view of the few pixels involved and the interfering effects of other edge pixels in the image.

number of trials in which symmetry is applied to locate objects exhibiting a vertical axis of symmetry. The approach used is the 1-D Hough transform (HT), taking the form of a histogram in which the bisector positions from pairs of edge points along horizontal lines through the image are accumulated. When applied to face detection, the technique is so sensitive that it will locate not only the center-lines of faces but also those of the eyes. In the case of Fig. 23.6C, the algorithm was confused by the metal object at the bottom when locating the eye on the left, but when tested without that present, it was found without difficulty. Note that some bias occurs there because the algorithm is averaging the contribution of the whole eye, and the displacement between the iris and the rest of the eye becomes important. Similarly, the set of leaves in Fig. 23.6E is located without trouble, but the exact vertical axis that is located represents the combined peak signal from the lower two leaves and the uppermost leaf: in such a case, it would be better to identify each one separately. These sorts of problem are less important in Fig. 23.6G where both vehicles are located quite accurately—in spite of the fact that the car on the right is not exactly horizontal. Interestingly, both vehicles would also be found using the under-vehicle shadow method. The fact that they both lie within their respective lanes also aids positive identification.

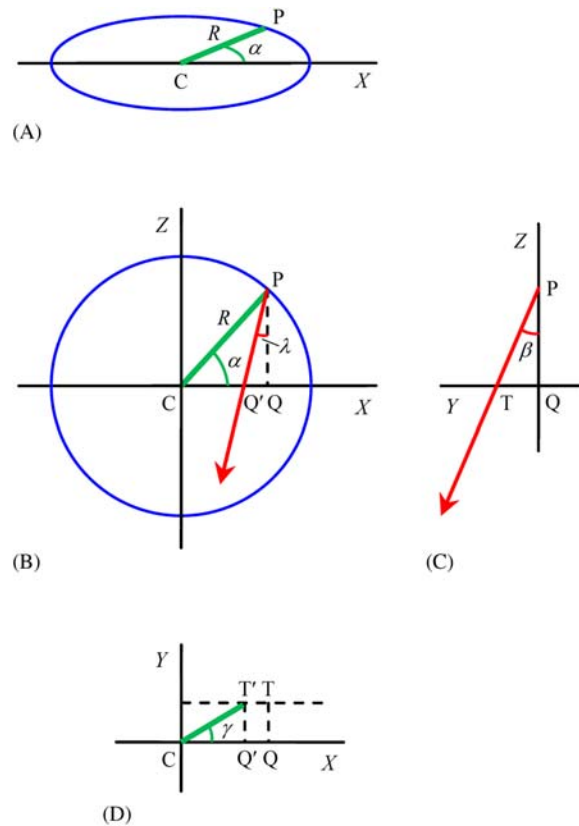
In spite of these successful applications of symmetry, note that the approach needs to be used with caution. In particular, the building on the left in Fig. 23.6G gives a plethora of signals because of the multiple symmetries between its windows. An interesting lesson is that three equally spaced vertical lines at locations  $x = 1, 3, 5$  will have a symmetry not only at  $x = 3$  but also at  $x = 2$  and  $4$ .

Finally, rotation symmetries and reflection symmetries about nonvertical axes are not especially useful in the present context. However, just as a 1-D HT can be used to locate symmetries about vertical axes, so 2-D HTs can be used to locate symmetries about lines of arbitrary direction. Thus, one can build a single 2-D parameter space, each horizontal line of which represents the symmetry in a different direction in the image. Such a parameter space might be expected to have a minor amount of coherence in the vertical direction, but we do not consider this further here.

---

## 23.6 INFORMATION OBTAINED BY VIEWING LICENSE PLATES AND OTHER STRUCTURAL FEATURES

License plate location has already been covered in Section 22.10. In this section, we consider what can be deduced from an oblique view of a license plate of length  $R$ . We simplify the situation by assuming that both the image plane and the license plate are vertical and that they have their main axes aligned horizontally and vertically. Fig. 23.7A and B shows respectively the oblique and plan views of the license plate horizontal axis. The apparent horizontal projection (CQ) of the center-line of the license plate is  $R \cos \alpha$  when viewed in the direction PT. Following Fig. 23.7C, its vertical projection (QT) is  $R \sin \alpha \tan \beta$ .

**FIGURE 23.7**

Horizontal line pose viewing geometry. (A) Oblique view of a horizontal straight line of length  $R$  rotated through an angle  $\alpha$  from the  $X$ -axis. (B) Plan view of the line. (C) Side view showing the viewing direction, along  $PT'$ , with a lateral angle  $\lambda$ ; the angle of elevation  $\beta$  is that of  $T$ , not of  $T'$ . (D) Front view in the  $X$ - $Y$  plane, which is parallel to the image plane  $x$ - $y$ . Note that the horizontal line  $CP$  in (B) appears to lie at an angle  $\gamma$  in (D); it has an apparent length ( $CT'$ ) of  $R'$ .

However, when viewed in the more general direction  $PT'$ , with lateral angle  $\lambda$ , its horizontal projection is  $CQ'$ , which is equal to  $R \cos \alpha - R \sin \alpha \tan \lambda$ . From Fig. 23.7D, we deduce that its apparent angle  $\gamma$  and length  $R'$  are given by the equations:

$$\tan \gamma = \frac{\tan \alpha \tan \beta}{1 - \tan \alpha \tan \lambda} \quad (23.1)$$

$$\begin{aligned} R' &= R \cos \alpha (1 - \tan \alpha \tan \lambda) \sec \gamma \\ &= R \sin \alpha \tan \beta \operatorname{cosec} \gamma \end{aligned} \quad (23.2)$$

These formulae seem intuitively correct, as for example,  $\gamma = 0$  if  $\alpha = 0$  or  $\beta = 0$ . In addition, under nonoblique viewing,  $\beta = 0$ ,  $\lambda = 0$ , and  $\gamma = 0$ , so Eq. (23.2) reverts to the standard result for nonoblique viewing,  $R' = R \cos \alpha$ .

Perhaps a more important case is that of  $\alpha = \pi/2$ , leading to  $\tan \gamma = -\tan \beta / \tan \lambda$ . We can interpret this result by taking image plane coordinates  $(x, y)$  and 3-D coordinates  $(X, Y, Z)$ . Noting that  $\tan \beta = y/f$  and  $\tan \lambda = x/f$ , we deduce that  $\tan \gamma = -y/x = -Y/X$ . This corresponds to viewing perspective lines on the roadway that are parallel to the optical axis of the camera. (Note that the minus sign in these equations corresponds to the fact that  $\gamma$  will be viewed in the range  $\pi/2$  to  $\pi$  when  $\alpha = \pi/2$ .)

Finally, note that instead of obtaining the projection of the line as it would appear in the direction of viewing, we have determined its projection in the vertical plane  $X-Y$ , which is parallel to the image plane  $x-y$ . As a result, the equations correspond *exactly* to projective projection into the image plane, rather than merely to orthographic projection.

We now need to obtain an equation for  $\alpha$  in terms of the other parameters. Solving Eq. (23.1) for  $\alpha$ , we find:

$$\tan \alpha = \frac{\tan \gamma}{\tan \beta + \tan \gamma \tan \lambda} \quad (23.3)$$

Next, taking the projections of the center-line of the license plate along the image  $x$  and  $y$  axes to be  $\delta x, \delta y$ , we find that the parameters  $\beta, \gamma, \lambda$  are all measurable, so  $\alpha$  can be estimated:

$$\tan \alpha = \frac{\delta y / \delta x}{(y/f) + (\delta y / \delta x)(x/f)} = \frac{f \delta y}{y \delta x + x \delta y} \quad (23.4)$$

Thus, we now know the orientation in space of the license plate. In principle, we can use Eq. (23.2) to estimate the range of the license plate. To achieve this, we need to know the value of  $R$ . In fact, for standard UK license plates,  $R$  is reasonably well defined (this assumes that the number of characters in the license plate is known), and so Eq. (23.2) can be used to estimate  $R'$ . Next, the ratio of  $R'$  to the apparent length  $r$  of the license plate gives the range  $Z$ :

$$Z = fR' / r = \frac{fR'}{[(\delta x)^2 + (\delta y)^2]^{1/2}} \quad (23.5)$$

If we had also made use of the apparent lengths and orientations of the shorter sides of the license plate, we could have eliminated dependence on the assumptions that the latter are vertical. However, it is unlikely that these short lines could be measured accurately enough to improve the situation significantly: instead we presume that the best that can be done is to use measurements on the longer sides to obtain preliminary estimates of the positions of vehicles, which can then be improved by other measurements.

Unfortunately, all the above theory is somewhat confounded by the variable camber of the road. But note that, while the camber will be considerably different on the opposite side of the road, its effects will tend to cancel when observing the



**FIGURE 23.8**

Vehicles viewed obliquely. More accurate information about orientation is often obtained from the side of the vehicle than from its rear.

license plates of vehicles on the same side of the road. Next, the size of  $\gamma$  depends on  $y$ , and hence on the height of the camera above the target feature: this means that the observed value of  $\gamma$  will be smaller for the license plate than for the rear wheels; hence, if the rear wheels are not occluded, it is likely that they will give a more accurate estimate of  $\alpha$  than that from the license plate. Nevertheless, license plates are more satisfactory indicators than rear wheels both because they are less likely to be occluded and because they are uniquely recognizable: in fact, the rear wheels of one vehicle can sometimes be confused with those of other vehicles, and even the front wheels can cause confusion. Finally, another factor needs to be borne in mind—that we are attempting to estimate an often small quantity  $\alpha$  from another small quantity  $\gamma$  when both are comparable to the interfering effect of the camber angle. Interestingly, this problem can be overcome more effectively by estimating  $\tilde{\alpha} = \pi/2 - \alpha$  from  $\tilde{\gamma} = \pi/2 - \gamma$  and applying these measures to views of the sides (particularly the sides of the wheels) of other vehicles. All this can be achieved by recalling that  $\tan \alpha$  and  $\tan \gamma$  should, respectively, be replaced by  $\cot \tilde{\alpha}$  and  $\cot \tilde{\gamma}$  in Eqs. (23.1) and (23.2). Overall, it might be expected that side views of vehicles will be more valuable for estimating orientation than rear views, whether the latter use rear wheels or license plates as indicators (though, obviously, only the rear view of a vehicle will be relevant when driving directly behind it). Consideration of Figs. 23.1, 23.6, 23.8, and 23.9 will provide adequate confirmation of these observations.

Finally, it might be asked why so much emphasis has been placed on measurement of angles vis-à-vis distances. This is basically because angles represent ratios of distances, and thus they tend to provide scale-invariant information. In addition, they do not demand knowledge of absolute distances for interpretation.

---

## 23.7 LOCATING PEDESTRIANS

In principle, locating whole pedestrians would require many chamfer templates of varying shapes and sizes, to cover the many body profiles of moving people. The



**FIGURE 23.9**

Chamfer matching to locate pedestrians from their lower legs. Parts (A) and (B) show original images of road scenes containing pedestrians. The red dots are the peak signals after chamfer matching using an idealized binary U template. Note the plethora of false positives because of the number of vertical edges able to stimulate signals—as seen in (C) and (D).

alternative chosen here is to look for specific subshapes that would be more general and invariant. Possibilities include leg, arm, head, and body sections. Fig. 23.9 shows lower legs being located using an idealized “U” template with parallel sides. However, a plethora of false positives arises because of the large number of vertical edges that are able to stimulate signals. Their presence means that the distance functions do not have the ideal maximum values that might be expected because the spurious edges reset the distance functions to zero in many places. This does not affect the sensitivity of the method in the sense that the templates are bound to locate instances of the profiles they represent. However, it does affect the numbers of false positives that are detected. In fact, in the examples shown, the result is not disastrous, because the lowest objects found, once road markings are eliminated, are the feet of the pedestrians. However, the fact that the method does not give ideal results makes it essential to back it up using alternative methods.

The Harris operator provides a useful alternative approach. As Fig. 23.10 shows, it is able to locate a range of features, including feet and heads, as well as road lane markings. Note that in the case shown in Fig. 23.10A, the right foot has not been found as it is larger than the other foot, and the particular Harris operator

**FIGURE 23.10**

Alternative approach to pedestrian location using the Harris operator. Here, the operator has the effect of locating corners and interest points, some of which include pedestrian feet and heads: above all, road lane markings are also located with high probability. The operator has not been tuned in any way to recognize such features. In addition, it has no sense of polarity (preference for dark or light).

employed stretched over a range of only seven pixels. Note that the Harris operator has no sense of polarity (preference for black or white): in the case of pedestrians, this is useful as the clothing and shoes (or feet) are unpredictable and can appear dark on a light background or vice versa. (Lack of polarity also applies to chamfer matching, but for different reasons.)

Further approaches are useful to back up the two mentioned above and also to confirm detections that have already been made. In this respect, unique identification of human skin color can be useful. That this is possible is shown in Fig. 23.11, one of the main problems clearly being the rather small numbers of pixels in the face regions. To carry out skin detection rigorously, it is necessary to train the color classifier on a set of training images. This was carried out for Fig. 23.11E. While the method was highly successful (see Fig. 23.11F), it corresponded to supervised learning of skin color; in practice, with less tight control of the training images, this process could be compromised by the presence of sand, stone, cement, and a host of brown variants, which have colors close to those of darker or lighter people. Another important factor is that in-vehicle vision systems will not have sufficient time to gather enough training data, considering particularly that the whole point of a vehicle is to travel and thus adaptation from dark to light and other environmental factors are bound to be a source of serious problems. In this respect, in-vehicle systems are subject to far worse conditions than will be usual for surveillance systems.

Overall, we find that in-vehicle pedestrian detection systems involve a demanding set of pattern recognition problems. Earlier we emphasized the potential value of pattern recognition when moving objects are being detected from moving platforms: this approach to the subject was also useful for didactic reasons. However, we are now finding that there are limits to this. In fact, it would

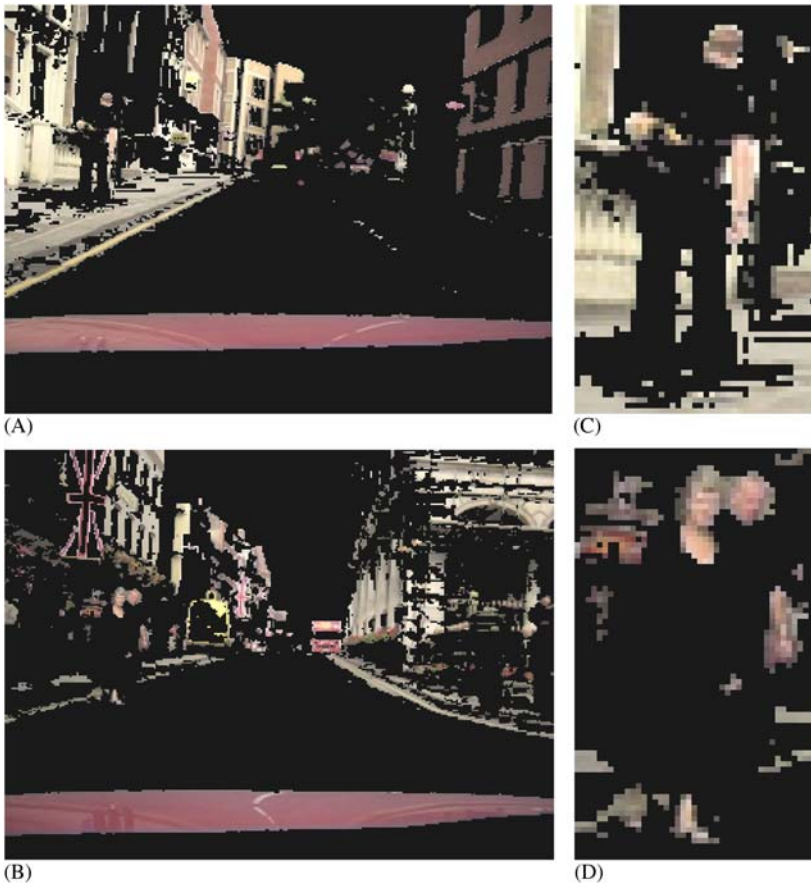


**FIGURE 23.11**

Another approach to pedestrian location via skin color detection. Parts (A) and (B) show that a lot can be achieved via skin color detection, detecting not only faces but also neck, chest, arms, and feet: see also the detail in (C) and (D). With proper color classifier training, even more can be achieved, as shown in (E) and (F).

be an artificial restriction not to make use of motion by at least tracking features and grouping them according to velocity (a process that was already mentioned in [Chapter 22: Surveillance](#)). The problem with this approach is the large number of, for example, interest point features that exist in an entire image, where almost all the features are moving. If each of them (say  $N$ ) is to be compared with all others in a pair of adjacent frames, then  $O(N^2)$  operations will have to be undertaken. However, by acknowledging the individuality and different characteristics of the various features, and their spatial arrangements, this vast number can be cut down



(E)



(F)

**FIGURE 23.11**

*(Continued).*

to manageable proportions. In particular, feature points should only move a limited distance between frames, so there will only be a small number  $n$  of candidates that match a given feature as it moves from one frame to the next. This leaves us with  $O(Nn)$  pairs of feature points to consider, a number that can be further minimized by examining the relative strengths and colors of the various pairs (ideally, the final result will be  $O(N)$ ). Here, some of the ideas of [Section 6.7](#), where features were characterized by a great many descriptors, may prove useful, even though wide baseline matching is not relevant for frame to frame tracking.

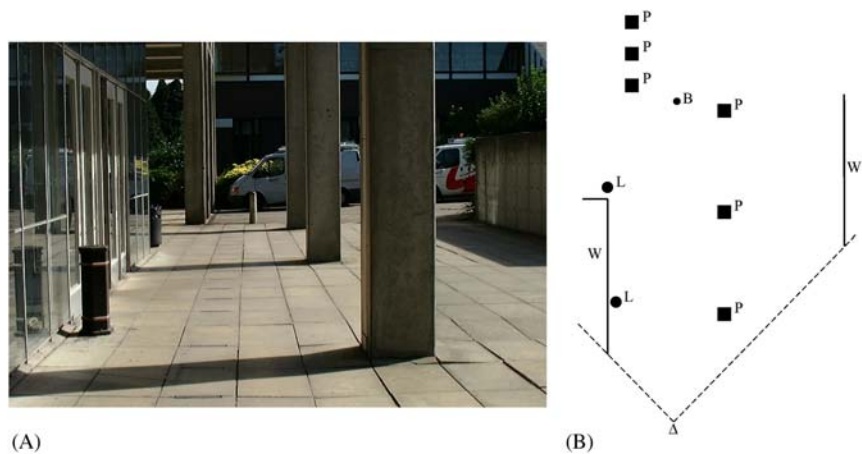
---

## 23.8 GUIDANCE AND EGOMOTION

An important aspect of driver assistance systems is that of vehicle guidance. In fact, this aspect is important both for vehicles with human drivers and for autonomous robot vehicles. In either case, vehicle egomotion is handled by a controlling computer which has to be fully aware of the situation. Incoming images contain complex information and reliable cues have to be found to key into them. Amongst the most widely used such cues are VPs, which are often very evident in city scenes (e.g., [Fig. 17.11](#)).

One of the ways in which VPs are most useful is in helping to identify the ground plane, and a lot of other information follows from this. In particular, local scale can be deduced: for example, objects on the ground plane have width that is referable to, and a known fraction of, the local width of the ground plane; in addition, VPs permit an estimate to be made of distance along the ground plane, by measuring the distance from the relevant image point to the VP, as we shall see below. Thus, they are useful for initiating the process of recognizing and measuring objects, determining their positions and orientations, and helping with the task of navigation.

Here, a lot will depend on the type of environment and the type of vehicle. There are many possibilities such as vacuum-cleaning robots, window-cleaning robots, lawn-mowing robots, invalid chair robots, weeding and spraying robots, maze-running robots, not to mention vehicles running autonomously on roads, or cars that park themselves automatically. In some cases, robots will have to undertake mapping, path planning, and navigational modeling and engage in detailed high-level analysis: this sort of situation has been explored by Kortenkamp et al. (1998). This approach will be important if a path has obstacles such as bollards or pillars ([Fig. 23.12](#)), and it will be vital for a maze-running robot. In many such cases, vision or other sensors will provide only limited information about the working area, and knowledge will have to be augmented in a suitable representation: this makes a plan view model of the working area a natural solution. To proceed with this idea, we need to transfer the information from individual images into the plan view representation (see the algorithm of [Table 23.2](#)).

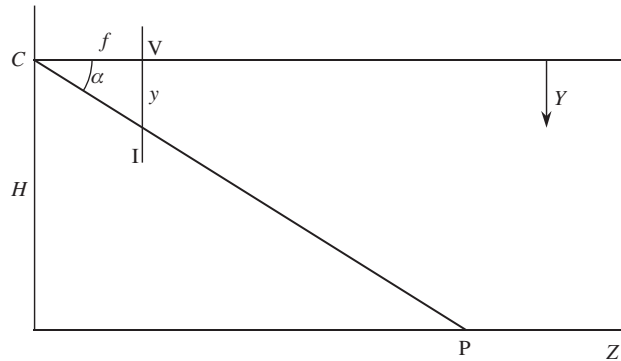
**FIGURE 23.12**

Plan view obtained for navigation. (A) View of a scene showing the obstacles to be avoided. (B) Plan view of the ground plane showing what is visible from viewpoint  $\Delta$  (for clarity, the full areas of the pillars P, bollards B, and litter-bins L are shown). The walls are marked W.

**Table 23.2** Computing Ongoing Plan Views of the Ground Plane

1. Detect all edges in the current frame
2. Locate all straight lines in the current frame: e.g., use an Hough transform
3. Locate all VPs: use a further HT, as described in [Section 18.7](#)
4. Find the VP closest to the direction of motion: eliminate all other VPs
5. Determine the closest section of G: this should be the part of the frame immediately in front of the robot
6. Use this and other information to determine which lines through the primary VP lie on G: eliminate all other lines
7. Segment objects on G
8. Eliminate object boundaries on G that are unrelated to lines passing through the primary VP
9. Tentatively identify as shadows any dark regions lying on G
10. Take the remaining object and shadow boundaries and check for consistency between frames: e.g., use the 5-point cross ratio values, as described in [Section 18.3](#)
11. Label all remaining feature points on G with their  $(X, Z)$  coordinates: use Eqs. (23.7) and (23.8)
12. Check for consistency with previous frames
13. Update list of objects with inconsistent boundaries as not lying on G, or as being otherwise unreliable: these could be due to moving shadows or noise
14. Update history of feature point coordinates on G

*This table presents an algorithm showing how a plan view of the ground plane G may be computed. It is assumed that the robot sees a sequence of video frames, and that it has to update its knowledge base as each frame comes along. The algorithm is set up assuming that it is best to analyze each frame ab initio, and then to look for consistency with previous frames.*

**FIGURE 23.13**

Geometry relating the image and the ground plane.  $C$  is the center of projection of the camera,  $I$  is the image plane,  $V$  is the vanishing point, and  $P$  is a general point on the ground plane.  $f$  is the focal length of the camera lens, and  $H$  is the height of  $C$  above the ground plane. The optical axis of the camera is assumed to be parallel to the ground plane.

Basically, to construct a plan view of the ground plane, we start with a single view of a scene in which the VP  $V$  has been determined and significant feature points on the ground plane (particularly regarding its boundaries) have been identified. Next, distance along the ground plane can be deduced as shown in Fig. 23.13. The angle of declination  $\alpha$  of a general feature point  $P$  ( $X$ ,  $H$ ,  $Z$ ) on the ground plane, seen in the image as point  $(x, y)$ , is given by:

$$\tan \alpha = H/Z = y/f \quad (23.6)$$

The value of  $Z$  is therefore given by:

$$Z = Hf/y \quad (23.7)$$

After obtaining a similar formula giving the lateral distance  $X$ , we deduce that:

$$X = Hx/y \quad (23.8)$$

The world (plan view) coordinates  $(X, Z)$  have now been found in terms of the image coordinates  $(x, y)$ . Note that  $y$  has to be measured from the VP  $V$  rather than the top of the image. Note also that as  $X$  and  $Z$  vary inversely with  $y$ , they vary rapidly when  $y$  is small, so digitization and other errors will markedly affect the accuracy with which far-away objects can be located from the plan view.

When the optical axis of the camera is not parallel to the ground plane, the calculations are best dealt with using homogeneous coordinates as shown in Chapter 19, Image Transformations and Camera Calibration.



### 23.8.1 A SIMPLE PATH-PLANNING ALGORITHM

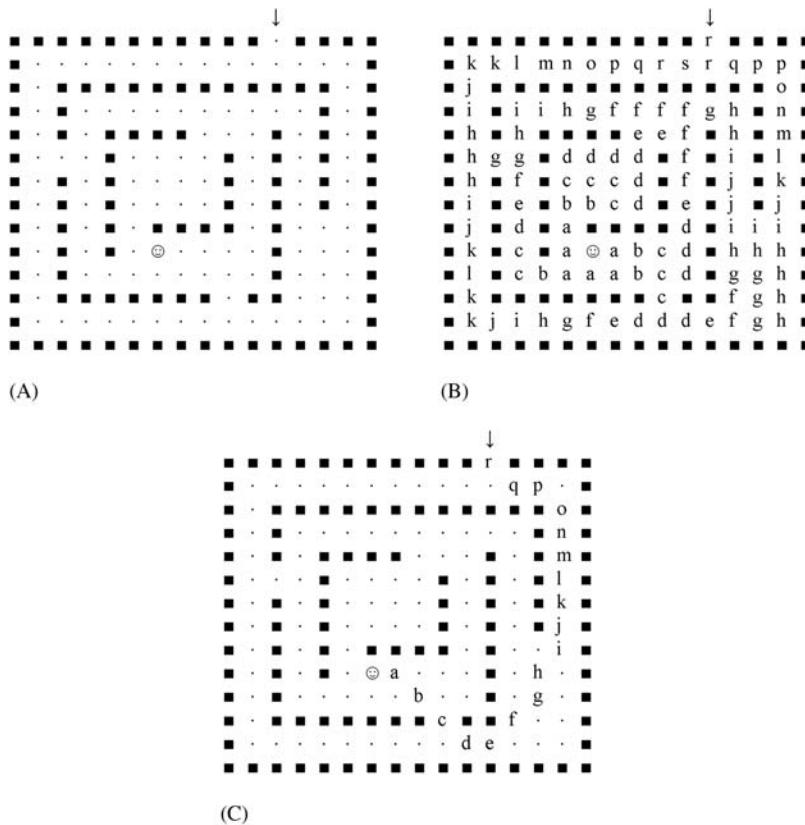
In this subsection, we assume that a plan view of the environment has been built up using the methods of the previous section. While it is by no means clear that humans use an instantaneous plan view model to help them to walk or drive around an environment (an image-based representation seems more likely), it is clear that they use plan views for deductive, logical analysis of the situation and when reading maps. In any case, plan views probably constitute the most natural means for storing navigational knowledge and arriving at globally optimal routes. Here, we leave aside conjecture of exactly how humans juggle the information between the two representations and concentrate on how a robot might reasonably undertake path planning using a plan view it has built up. In fact, a maze-running robot would need to be provided with a suitable algorithm for this purpose.

Fig. 23.14A shows a simple maze in which the robot has to proceed from the entrance E to the final goal G (respectively, marked “↓” and “☺” in the figure). We assume that a plan view of the maze has been built up and that a systematic means is needed to find the optimum path to the goal G. The envisaged algorithm starts from G and propagates a distance function over the whole region, constrained only by the walls of the maze (Fig. 23.14). If a parallel algorithm is used, it is terminated when the distance function arrives at E; if a sequential algorithm is used, it must carry on until the whole maze has been covered—assuming that an optimal path is required. When the distance function has been completed, finding an optimum path necessitates proceeding downhill along the distance function until G is reached: at each point, the locally greatest gradient must be used (Kanesalingam et al., 1998). Connected components analysis could be used to confirm that a path exists, but a distance function has to be used to guarantee finding the shortest path. Note that the method will find only one of several paths of equal length: these arise because of the limitations of this type of method that assigns integer values to distances between adjacent pixels.

---

## 23.9 VEHICLE GUIDANCE IN AGRICULTURE

In recent years, there has been increasing pressure on farmers to reduce the quantities of chemicals used for crop protection. This cry has come both from environmentalists and from the consumers themselves. The solution to this problem lies in more selective spraying of crops. For example, it would be useful to have a machine which would recognize and spray weeds with herbicides, leaving the vegetable crops themselves unharmed: alternatively, the individual plants could be sprayed with pesticides. This case study relates to the design of a vehicle which is capable of tracking plant rows and selecting individual plants for spraying (Marchant and Brivot, 1995; Marchant, 1996; Brivot and Marchant, 1996; Sanchiz et al., 1996; Marchant et al., 1998). Interestingly, many of the details of

**FIGURE 23.14**

Method for finding an optimal path through a maze. (A) Plan view of maze. (B) Distance function of the maze, starting at the goal (marked ⊕), and presenting distance values by successive letters, starting with  $a = 1$ . (C) Optimum path obtained by tracking from the maze entrance (marked ↓) along maximum gradient directions.

this work are remarkably similar to those for the totally independent project undertaken in Australia by Billingsley and Schoenfisch (1995).

The problem would be enormously simplified if plants grew in highly regular placement patterns, so that the machine could tell from their positions whether they were weeds or plants, and deal with them accordingly. However, the growth of biological systems is somewhat unpredictable and renders such a simplistic approach impracticable. Nevertheless, if plants are grown from seed in a greenhouse and transplanted to the field when they are approaching 100 mm high, they can be placed in straight parallel rows, which will be approximately retained as they grow to full size. There is then the hope (as in the case shown in Fig. 23.15)



**FIGURE 23.15**

Value of color in agricultural applications. In agricultural scenes, such as this, color helps with segmentation and with recognition. It may be crucial in discriminating between weeds and crops if selective robot weed killing is to be carried out.

© World Scientific 2000.

that the straight rows can be extracted by relatively simple vision algorithms, and the plants themselves located and identified straightforwardly.

At this stage, the main problems are (1) the plants will have grown to one side or another and will thus be out of line; (2) some will have died; (3) weeds will have appeared near some of the plants; (4) some plants will have grown too slowly and will not be recognized as plants. Thus, a robust algorithm will be required to perform the initial search for the plant rows. The HT approach is well adapted to this type of situation: specifically, it is well suited to looking for line structure in images.

The first step in the process is to locate the plants. This can be achieved with reasonable accuracy by thresholding the input images (this process is eased if infrared wavelengths are used to enhance contrast). However, at this stage, the plant images become shapeless blobs or clumps (Fig. 23.16). These contain holes and lobes (the leaves, in the case of cabbages or cauliflowers), but a certain amount of tidying up can be achieved either by placing a bounding box around the object shape, or by performing a dilation of the shape which will regularize it and fill in the major concavities (the real-time solution employed the first of these methods). Then, the position of the center of mass of the shape is determined, and

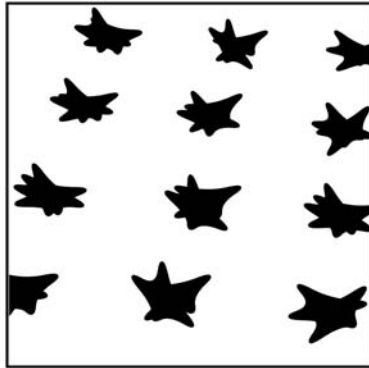


**FIGURE 23.16**

Perspective view of plant rows after thresholding. In this idealized sketch, no background clutter is shown.

© World Scientific 2000.

it is this that is fed to the HT straight line (plant row) detector. In common with the usual HT approach, votes are accumulated in parameter space for all possible parameter combinations consistent with the input data. Here, this means taking all possible line gradients and intercepts for lines passing through a given plant center and accumulating them in parameter space. To help find the most meaningful solution, it is useful to accumulate values in proportion to the plant area. In addition, note that if three rows of plants appear in any image, it will not initially be known which plant is in which row, and therefore each plant should be allowed to vote for all the row positions: this will naturally only be possible if the inter-row spacing is known and can be assumed in the analysis. However, if this procedure is followed, the method will be far more resistant to missing plants and to weeds which are initially mistakenly assumed to be plants.

The algorithm is improved by preferentially eliminating weeds from the images before applying the HT. Weed elimination is achieved by three techniques—hysteresis thresholding, dilation, and blob size filtering. Dilation refers to the standard shape expansion technique described in [Chapter 3, Image Filtering and Morphology](#) and is used here to fill in the holes in the plant blobs. Filtering by blob area is reasonable as the weeds are seldom as strong as the plants, which were transplanted only when they had become well established.

Hysteresis thresholding is a widely used technique which involves use of two threshold levels. In this case, if the intensity is greater than the upper level  $t_u$ , the object is taken to be plant; if lower than the lower level  $t_l$ , it is taken to be weed; if at an intermediate level and next to a region classified as plant, it is taken to be plant; the plant region is allowed to extend sequentially as far as necessary, given only that there is a contiguous region of intensity between  $t_l$  and  $t_u$  connecting a given point to a true plant ( $\geq t_u$ ) region. Note that this application is unusual in

that whole-object segmentation is achieved using hysteresis thresholding: more usually the technique is used to help create connected object boundaries (see Section 5.10).

Once the HT has been obtained, the parameter space has to be analyzed to find the most significant peak position. Normally, there will be no doubt as to the correct peak—even though the method of accumulation permits plants from adjacent rows to contribute to each peak. The reason for this is that with three rows each permitted to contribute to adjacent peaks, the resultant voting patterns in parameter space are as follows: 1,1,1,0,0; 0,1,1,1,0; 0,0,1,1,1—totaling 1,2,3,2,1—thereby making the true center position the most prominent (actually, the position is more complicated than this as several plants will be visible in each row, thus augmenting the central position further). However, the situation could be erroneous if any plants are missing. It is therefore useful to help the HT arrive at the true central position. This can be achieved by applying a Kalman filter (Section 20.8) to keep track of the previous central positions and anticipate where the next one will be—thereby eliminating false solutions. This concept is taken furthest in the paper by Sanchiz et al. (1996), where the individual plants are all identified on a reliable map of the crop field and errors from any random motions of the vehicle are systematically allowed for.

### 23.9.1 3-D ASPECTS OF THE TASK

So far we have assumed that we are looking at simple 2-D images which represent the true 3-D situation in detail. In practice, this is not so. The reason for this is that the rows of plants are being viewed obliquely and therefore appear as straight lines but with perspective distortions which shift and rotate their positions. The full position can only be worked out if the vehicle motions are kept in mind. In practice, vehicles moving along the rows of plants exhibit variations in speed and are subject to roll, pitch, and yaw. The first two of these motions correspond respectively to rotations about horizontal axes along and perpendicular to the direction of motion: these are less relevant and are ignored here. The last is important as it corresponds to rotation about a vertical axis and affects the immediate direction of motion of the vehicle.

To proceed, we have to relate the position  $(X, Y, Z)$  of a plant in 3-D with its location  $(x, y)$  in an image. We can achieve this with a general translation:

$$T = (t_x, t_y, t_z)^T \quad (23.9)$$

together with a general rotation:

$$R = \begin{bmatrix} r_1 & r_2 & r_3 \\ r_4 & r_5 & r_6 \\ r_7 & r_8 & r_9 \end{bmatrix} \quad (23.10)$$

giving:

$$\begin{bmatrix} X \\ Y \\ Z \end{bmatrix} = \begin{bmatrix} r_1 & r_2 & r_3 \\ r_4 & r_5 & r_6 \\ r_7 & r_8 & r_9 \end{bmatrix} \begin{bmatrix} x \\ y \\ z \end{bmatrix} + \begin{bmatrix} t_x \\ t_y \\ t_z \end{bmatrix} \quad (23.11)$$

The lens projection formulae are also relevant:

$$x = fX/Z \quad (23.12)$$

$$y = fY/Z \quad (23.13)$$

We shall not give a full analysis here, but assuming that roll and pitch are zero, and that the heading angle (direction of motion relative to the rows of plants) is  $\psi$ , and that this is small, we obtain a quadratic equation for  $\psi$  in terms of  $t_x$ . This means that two sets of solutions are in general possible. However, it is soon found that only one solution matches the situation, as the wrong solution is not supported by the other feature point positions. This shows the complications introduced by perspective projection—even when highly restrictive assumptions can be made about the geometrical configuration (in particular,  $\psi$  being small).

### 23.9.2 REAL-TIME IMPLEMENTATION

Finally, it was found to be possible to implement the vehicle guidance system on a single processor augmented by two special hardware units—a color classifier and a chaincoder. The latter is useful for fast shape analysis following boundary tracking. The overall system was able to process the input images at a rate of 10 Hz, which is sufficient for reliable vehicle guidance. Perhaps more important, the claimed accuracy was in the region of 10 mm and 1° of angle, making the whole guidance system adequate to cope with the particular slightly constrained application considered. A later implementation (Marchant et al., 1998) did a more thorough job of segmenting the individual plants (though still not using the blob size filter), obtaining a final 5 Hz sampling rate—again fast enough for real-time application in the field. All in all, this case study demonstrates the possibility of highly accurate selective spraying of weeds, thereby very significantly cutting down the amount of herbicide needed for crops such as cabbages, cauliflowers, and wheat.

---

## 23.10 CONCLUDING REMARKS

This chapter has considered the value of in-vehicle vision as part of the means for providing driver assistance systems. It has also considered the design of such systems. This process is rendered far from trivial because the camera is necessarily moving, so all objects in a scene will appear to be in motion. Hence, it becomes quite difficult to eliminate the background from consideration, and less easy to

rely on motion-based segmentation. This makes it natural to adopt the alternative approach of placing reliance on recognition of individual objects. Sections 23.2 and 23.3 showed how this concept can be applied to the location not only of the roadway but also of road markings and road signs. The principle also applied to location of vehicles, but as these vary in appearance, it proved necessary to have several distinct methods for locating them, including under-vehicle shadows, symmetry, wheels, and license plates (the latter acting not merely as unique vehicle identifiers but also as characteristics of vehicles in general). Curiously, license plates offered a possible means of finding the orientations of vehicles on roads as well as their locations, though the result was dependent on the relative heights of the camera and license plate under observation. This meant that, when they are not occluded, tire and wheel location will probably be more accurate indicators of vehicle orientation.

Pedestrian location was also seen to be a challenge—particularly as people are articulated objects, and walk with bobbing motions, and also because they tend to have unique appearances and clothing. This makes it natural to use specific templates for leg, arm, head, and body detection rather than whole-body templates. Here, symmetry is also a possible cue as well as skin color. All these approaches were studied in Section 23.7 and tallied with findings in the literature.

The chapter also included aspects of path planning consequent on projecting vehicles and other obstructions onto a plan view of the ground plane: this has some consequence for robot egomotion and navigation. It is also relevant for guidance of agricultural vehicles that are being used for cultivation, selective spraying, and so on. Here, it is also important to consider the much greater degrees of roll, pitch, and yaw that will be experienced by a tractor or other vehicle moving over plowed fields, and the visual compensation needed to cope with this. Some indication was given about how these factors have been coped with: because the principles are known, it seemed better for readers to refer to the original papers for further details.

Finally, we should remark on the almost explosive growth of interest in in-vehicle driver assistance systems, particularly since 2000. This is so important that the following section looks very closely at developments in this area and provides separate bibliographies relating to the various aspects. It was felt that it would be clearer presenting these separately once the principles of the subject had been dealt with, as has been done relatively didactically in the preceding sections.

*In-vehicle vision systems necessarily deploy moving cameras, so the usual surveillance strategy of eliminating the stationary background becomes difficult to apply. However, considerable success can be achieved using the alternative strategy of directly locating the most relevant objects, such as the roadway, road signs, road markings, vehicles (e.g., via their symmetry, shadows, wheel, and license plates), and pedestrians (e.g., via their legs, arms, body, and head). Plan views of the ground plane form useful adjuncts to the information obtained in these ways.*

---

## 23.11 MORE DETAILED DEVELOPMENTS AND BIBLIOGRAPHIES RELATING TO ADVANCED DRIVER ASSISTANCE SYSTEMS

As indicated earlier in the chapter, in recent years (and particularly since 2000), there has been an almost explosive growth of interest in in-vehicle vision systems. The prime though often unwritten underlying aim has been that of driver assistance—a general term that ultimately includes vehicle guidance. However, in 1998, it at first appeared that Bertozzi and Broggi (1998) had largely solved the problem. In fact, they had laid down many of the ground rules, including finding lane markings with the aid of morphological filters, locating obstacles without constraints on symmetry or shape, analyzing stereo images to find free space on the road ahead, removing the perspective effect, implementing the system on a rapidly operating software plus massively parallel hardware architecture, presenting feedback information to the driver via a TV monitor and control panel, testing the system on the road, and above all demonstrating robustness with respect to shadows, changing illumination conditions, varying road texture, and typical motions on the road. Nevertheless, the system was subject to basic assumptions such as the road being flat and road markings being visible; in addition, it placed a great deal of reliance on the stereo system, which had limited range; furthermore, it treated each pair of stereo images individually and was unable to exploit temporal correlations. Finally, while it never failed to detect vehicles on the road ahead, it sometimes detected false obstacles because of noise arising from the various image-remapping processes.

In the light of this work, other workers continued development with increased pace, pressing to eliminate deficiencies with the basic strategy; interestingly, many abandoned the stereo vision approach which brings with it many complications: in fact, appeal to the human vision system demonstrates all too clearly that stereo brings few real advantages for the restricted tasks involved in driving a vehicle (whatever is the case when assembling a gyroscope or other instrument on a workbench). We shall return to this point below.

First, it is worth outlining the findings of Connolly (2009) who has described in a general way the gains to be achieved by advanced driver assistance systems (ADASs). The main keys to success appear to be the provision of lane departure warnings, help for lane changing, collision avoidance, adaptive cruise control, and driver vigilance monitoring. However, it is important that the ADAS should not give too many warnings, or the driver may become annoyed and deactivate it: neither should it fail to act soon enough or give the driver too much confidence or too much freedom. In fact, it is vital for drowsiness to be detected because c. 30% of motorway accidents are caused by drivers undergoing micro or macro-sleeps. While much work has been carried out on blink-rate analysis for detecting these conditions, the method has limited effectiveness in probing the state of the brain itself. Nevertheless, it is clear that vision systems can do much to monitor



the driver's behavior, and specifically to monitor his direction of gaze and state of *apparent* awareness. Overall, it is probably in the realm of lane departure warnings and of collision avoidance that an ADAS can do the most good, without annoying the driver. Indeed, in the event of the driver's unawareness of an impending collision, or incapability of acting soon enough, the ADAS should be permitted to act autonomously. While this could in principle be legally contentious, it is not without precedent, as antilock braking systems are in common use.

There are many causes of collision, and a large proportion of them are due to driver error, even when drowsiness is not a specific factor. Failure to see a vehicle or pedestrian because of preoccupation with other events on or off the road, failure to estimate speeds or trajectories of vehicles sufficiently accurately, failure to judge how rapidly braking can be performed in the prevailing conditions, and lack of awareness of what other drivers intend to do are all involved in causing accidents: this list does not include gross vehicle malfunctions such as unpredictable tire bursts. In fact, all these factors arise from or are exacerbated by lack of the right information being available soon enough. Thus, it is obvious that vision has a large part to play in overcoming the problems. While radar, lidar, ultrasonics, or other technologies may help, vision provides far more of the right sort of information with the right sort of response rates, and computer vision should be able to cope reliably and rapidly enough to make this possible. The main questions are as follows: What will be the cost? Where will the cameras be placed? Can enough of them be used to ensure that relevant information is made available? Fortunately, cameras are by now so cheap that cost—relative to that of a vehicle or of the damage caused in a crash—is no longer a serious problem. On the other hand, the real problems are the sophistication and speed of the associated software (or in the latter case, how the system is to be implemented in hardware—a topic for which the reader should refer to other works such as Bailey, 2011). For the remainder of the chapter, we therefore concentrate mainly on the sophisticated software aspects, and what has been achieved since the turn of the millennium.

### 23.11.1 DEVELOPMENTS IN VEHICLE DETECTION

One area of vital concern has been the detection of other vehicles, especially those overtaking (Zhu et al., 2004; Wang et al., 2005; Hilario et al., 2006; Cherng et al., 2009). The last of these papers considers patterns of driving, such as “cutting” in after overtaking, but more subtly how interactions between events involving more than two vehicles can cause distractions that prevent optimal actions being taken: this is because not all dynamic obstacles are predicable; in fact, multiple critical situations can occur simultaneously. The paper takes the line that the computer must follow attention patterns that emulate those of the human brain and concentrate cyclically on eliminating the various critical phases that are being experienced. The necessary dynamic visual model is in this case tackled using a

spatiotemporal attention neural network. The system of Kuo et al. (2011) concentrates on detecting vehicles on the road ahead but is also able to assess longitudinal distance information and thus to provide adaptive cruise control (albeit no indications of accuracy are given in the paper). Note that this system uses a monocular camera and thus avoids the difficulties of stereo systems mentioned earlier.

Sun et al. (2004, 2006) reviewed the methods used by various workers to detect vehicles. They reported knowledge-based methods using symmetry, color, shadow, corners, horizontal and vertical edges, texture, and lights. In addition, stereo and motion approaches have been used. They also reported template matching and appearance-based methods and noted that sensor fusion is needed to ensure that sufficient information is brought to bear to make vehicle detection reliable. They emphasized that hypothesis generation and verification are important for obtaining reliable solutions. Overall, they offered no silver bullet solution, apart from sensor fusion, though (looking at their conclusions as a whole) *method fusion* appears to be rather more important. Amongst the worst challenges, they found were those of “all hours—all weather” operation. In particular, bad illumination (especially at night) and the results of rain and snow will affect many well-known algorithms for vehicle detection, including those based on shadows. While in principle, vehicle lights should provide an easy way of detecting vehicles, in the dark, they can prove confusing, especially when rain-soaked roads cause reflections. Sun et al. therefore “believe that these cues have limited employability.” However, there are bound to be conditions under which some methods will not work well, but by using method fusion in a dynamic way, giving different methods different weights in different conditions, viable solutions should in the end be obtainable. Whereas humans could be confused in dark situations where no information at all is available, it is difficult to imagine them not being able to solve vehicle detection problems because of rain, snow, or random reflections, and certainly not simply because no shadows are visible.

While the difficulties of dealing with the problems of driving at speed on a motorway can be hugely complicated, with vehicles overtaking on either side and sometimes cutting in, the solution is often to drive more slowly thereby minimizing risks and lowering the data rate to manageable levels. However, the problems of dealing with pedestrians are considerably more complicated. This is because, in contrast to the case of vehicles which travel at more or less constant speeds in constant directions for considerable periods of time—and also have a fair amount of free space immediately around them—pedestrians are unpredictable, sometimes running to get across roads between vehicles, sometimes jay-walking, and sometimes moving in groups having even more unpredictable behavior. A basic problem is that it is unknown when a stationary pedestrian might suddenly move into the roadway and with a temporary acceleration that exceeds that of most vehicles. Hence, a great many workers have been and are producing algorithms for pedestrian detection and tracking.

### 23.11.2 DEVELOPMENTS IN PEDESTRIAN DETECTION

Geronimo et al. (2010) have recently reviewed pedestrian detection systems for ADASs. As this is very thorough and contains 146 references, the reader is recommended to work carefully through it. Nevertheless, some useful points can be made here. They emphasize that pedestrians exhibit high variability in size, pose, clothing, objects carried, and so on; they appear in cluttered scenes, can be partially occluded, and may be in poor contrast regions; they have to be identified in dynamically varying scenes when both they and the camera are moving; they often appear radically different when viewed from different directions. Geronimo et al. note that silhouette matching, e.g., using the chamfer-matching technique, is widely used for detection, yet it needs to be augmented by an additional appearance-based step. (This is not an argument against silhouette matching, but one for using it as a cue, in accordance with the idea expressed above that method fusion is required—i.e., method redundancy is needed to cope robustly with *real* scenes containing substantial clutter.) Geronimo et al. (2010) underline the need for verification and refinement. Interestingly, they note that the Kalman filter is (still) by far the most heavily used tracking algorithm—a surprising fact considering that pedestrian motions along pavements, in precincts or crossing the road exhibit far from steady motion (in fact, their motions tend to be jerky and indecisive, as they find their way around obstacles and other people). Finally, Geronimo et al. emphasize the need for all hours—all weathers performance; here, they note that NIR (near infra-red) imaging gives pictures not dissimilar to visible light images, so similar algorithms can be used for analysis. This is less true for thermal (far infrared or FIR) images, which are commonly called “night vision.” In any case, the latter respond to relative temperature, which is useful for distinguishing hot targets, including pedestrians for vehicles, but inappropriate for examining most of the background, or objects such as road signs. Thus, thermal cameras need to be backed up with visible light cameras in the day or NIR cameras in the night and so would generally constitute an unnecessary expense.

Gavrila and Munder (2007) describe a multicue pedestrian detection system: after extensive field tests in difficult urban traffic conditions, they reasonably claim it to be at the (2007) leading edge. The four main detection modules are sparse stereo-based ROI (region of interest) generation, shape-based detection, texture-based classification, and verification using dense stereo, these being complemented by a tracking module. In fact, the paper builds on earlier work (Gavrila et al., 2004), and its main contributions are the method of integration into a multicue system for pedestrian detection and a systematic ROC-based (receiver—operator characteristic based) procedure for parameter setting and system optimization. In part, the success of the system is due to the use of a novel mixture-of-experts architecture for shape and texture-based classification: here, the idea is to take the known shape information and to use texture to partition the feature space into regions of reduced variability—a process that matches well the types of clothing worn by humans. Importantly, the approach using a texture-

based mixture-of-experts weighted by the outcome of shape matching was found to outperform an approach based on single texture classifiers. Also notable is the (continued) use of chamfer matching for shape detection, prominent in much of Gavrilu's earlier work.

It was remarked earlier that stereo adds considerable complication to a vision system, which may not be justified for an in-vehicle system when most of the objects being viewed will be many meters away. This makes it no surprise that the review article by Enzweiler and Gavrilu (2009) concentrates on monocular pedestrian detection. The paper also included descriptions of a number of experimental comparisons of methods for pedestrian detection. Apart from temporal integration and tracking, methods that were tested included the following: (1) Haar wavelet-based cascades, (2) neural networks using local receptive fields, (3) histograms of orientated gradients (HOGs) together with linear SVM (support vector machine) classifiers, and (4) combined shape and texture-based approaches. The fourth of these was subsequently disregarded as its main advantage was processing speed, which was not considered relevant to the comparison. The investigation found that the HOG approach outperformed the wavelet and neural network approaches (Section 22.16 contains a brief outline of the HOG approach and also explains why it outperforms the wavelet approach in this type of application: see also Section 6.7.8). In particular, at a sensitivity of 70%, the respective false positive rates were 0.045, 0.38, and 0.86, representing huge reduction factors for false positives. [This assumes that the term "detection rate" used by the authors actually means "sensitivity" (or "recall"): see Chapter 14, Machine Learning: Probabilistic Methods.] Similarly, at a sensitivity of 60%, the precision rates were vastly improved for the HOG approach, particularly relative to the neural network approach. It should be emphasized that these results apply for intermediate resolutions with pedestrian images  $\sim 48 \times 96$  pixels, while earlier low resolution work with pedestrian images  $\sim 18 \times 36$  pixels led to Haar wavelets being the most viable option. Overall, there seemed to be slight doubt about what the critical factors actually are: in particular, the authors state "perhaps it is the data that matters most, after all," meaning that increased performance may be at least partly due to increases in the size of the training set. In addition, quite a bit depends on the processing constraints that are applied, and for tighter constraints, the Haar wavelet approach comes back into its own. However, as ever, it is difficult to standardize or specify image data, or a fortiori, image sequence data, so this paper is not able to tell the whole story. Finally, it should be noted that at this point in time, shape-based detection, and in particular, the chamfer-matching approach, has dropped out of sight because its main advantage was that of speed, and here recognition accuracy measures were the main performance criteria. In this paragraph, note that sensitivity gives a reverse measure of false negative rate,  $1 - FN / (TP + FN)$ , whereas precision gives a reverse measure of false positive rate,  $1 - FP / (TP + FP)$ .

Looking back to the work of Curio et al. (2000)—who use Hausdorff distance rather than chamfer matching for template matching—the attention is very much on analyzing limb movements, modeling human walking and observing human

gait patterns. However, they note that the upper body shows a high degree of variation in its appearance, so it is better to restrict pedestrian detection to the lower body: in fact, this strategy is both more reliable and more computationally efficient. They also point out that exact modeling is more complicated for women wearing skirts. (A similar situation must apply for men wearing robes or mackintoshes.) Overall, just as the driver is aware of motion and gait as well as the body models of pedestrians, these need to be incorporated into practical pedestrian detection algorithms in order to provide maximum reliability and robustness.

Zhang et al. (2007) performed tests on pedestrian detection in “IR (infra-red) images” (these were actually thermal images taken with a camera operating in the spectral range 7–14  $\mu\text{m}$ ). Their motivation was to make a system that was capable of working at night time, though they also noted that many undesirable activities occur at night or in relative darkness, so the methodology should be useful in other applications as well. They found that IR images are by no means dissimilar to visible light images, so similar algorithms can be used for analyzing them: i.e., there is no need to invent radically different methods for the IR domain. In particular, they found that edgelet and HOG methods (see Dalal and Triggs, 2005) could be adapted to work with IR images, and similarly for boosting and SVM cascade classification methods (Viola and Jones, 2001). Hence, they achieved detection performance for IR images comparable to state-of-the-art results for visible light. The underlying reason for this seemed to be that IR and visible light lead to similar silhouettes.

### 23.11.3 DEVELOPMENTS IN ROAD AND LANE DETECTION

Zhou et al. (2006) developed a lane detection and tracking system using a monocular monochromatic camera. They used a deformable template model to initially locate the lane markings, with tabu search for optimal location; then they used a particle filter for tracking the markings. Their experimental results showed that the resulting system was robust against broken lane markings, curved lanes, shadows, distracting edges and occlusions. Kim (2008) also used a particle filter for tracking lane markings but employed RANSAC for initial detection. Similarly, Mastorakis and Davies (2011) used RANSAC for detection but modified it for increased reliability, as described in [Sections 10.4](#) and [23.3](#): see also Borkar et al. (2009). Finally, Marzotto et al. (2010) showed how a RANSAC-based system could be implemented in real time using an FPGA (field programmable gate array) platform.

While the above approaches are suitable for urban roads, which normally have well-defined lane markings, many roads, especially in rural regions, are unstructured and lacking in markings—and the road boundaries may be overgrown with vegetation. Cheng et al. (2010) devised a system with the ability to handle both structured and unstructured types of road using a monocular camera. To achieve this, they devised a hierarchical lane detection strategy which was able to achieve high accuracy using quite simple algorithms. First, environment classification of

pixels was carried out with high dimensional feature vectors using eigenvalue decomposition regularized discriminant analysis. For unstructured roads, mean-shift segmentation was used, and then road boundary candidates were selected from the region boundaries: Bayes rule was used to select the most probable of these as actual boundaries. When the vehicle moved from one type of road to another, the environment classifier indicated that a different algorithm should be used so that accuracy could be maintained.

There is one way in which road and lane mapping schemes are restricted—namely, by the view available from the chosen camera. Typically, this will give an overall viewing angle of up to  $\sim 45^\circ$ . In fact, ideally, a vehicle-borne camera should have a full  $360^\circ$  viewing angle, so that overtaking vehicles and pedestrians about to approach from the side can be seen clearly. Omnidirectional (catadioptric) cameras may be the best answer to this problem, and many workers are actively pursuing this possibility. Cheng and Trivedi (2007) tested a system which used an omnidirectional camera for the dual tasks of lane detection and monitoring the head pose of the driver (the reason for monitoring head pose is to check that the driver is aware of the situation on the road). Their tests showed that accuracy of lane detection is reduced by a factor of (only) 2–3 because of the reduced resolution available with this sort of camera. Thus, it should prove possible to make savings in the numbers of sensors employed in practical implementations.

#### 23.11.4 DEVELOPMENTS IN ROAD SIGN DETECTION

It is a sign of the seriousness with which ADASs are nowadays being taken that a good many papers describing research into the detection and recognition of road signs have been published since the turn of the millennium. Fang et al. (2003) describe a system that uses neural networks for detecting and tracking road signs by their color and shape. The shapes considered are circles, triangles, octagons, diamonds, and rectangles. Initial detection takes place at some distance, where the road signs appear small and relatively undistorted, and tracking is carried out by a Kalman filter. At each distance, due account is taken of changes in size and shape due to increasing projective distortions, and when a potential sign has become large enough the system verifies that it is a road sign or discards it. Actual recognition is not discussed in the paper, but detection and tracking are said to be accurate and robust: although speed was slow on a single PC (personal computer), the neural networks could conveniently be run in parallel on other processors. A related paper by Fang et al. (2004) describes the types of neural network used in this sort of application. Kuo and Lin (2007) describe a similar system, again involving use of neural networks. The latter paper makes use of greater amounts of structural analysis of the images at the detection stage, e.g., using corner detection, HTs and morphology. De la Escalera et al. (2003) describe a system which starts the analysis using color classification, uses genetic

algorithms for narrowing down the search, and employs neural networks for sign classification.

McLoughlin et al. (2008) describe practically orientated work on road sign detection and also on the detection of “cat’s eyes.” Their aim is to assess the road signage quality rather than to use it, and to this end, they relate the signs to GPS information. They focus particularly on reflectivity aspects of the signs and are able to detect defective road studs and road signs. Their system is fully autonomous and thus the methodology is largely transferrable to ADASs.

Prieto and Allen (2009) describe a vision-based system for detecting and classifying traffic signs using self-organizing maps (SOM)—a type of neural network. A two-stage detection process is adopted—of first detecting potential road signs by analyzing the distribution of red pixels within the image, and then identifying the road signs from the distribution of dark pixels in their central pictograms. The HT approach and other structural analysis approaches were eschewed because they were felt to operate too slowly for (efficient) real-time operation, so the SOM approach was adopted. To achieve recognition of the pictogram, it was divided into 16 blocks arranged in the form of a triangle (or whatever shape the particular sign was found to possess). It was found necessary to normalize brightness over the region of the sign. The hardware of the embedded machine vision used for this application was a hybrid consisting of an FPGA together with a digital implementation of a SOM. Experiments showed that the system had good performance, being able to tolerate substantial changes in position, scale, orientation and partial occlusion of the road signs, and also being trainable, at least to within the model of colored surround and black on white pictograms. For further details of the SOM and the hybrid implementation, see the original paper and the references mentioned therein.

Ruta et al. (2010) have developed a system not based on neural networks (as for many of the above) but on color distance transforms, coupled with a nearest neighbor recognition system. The color distance transform is actually a set of three distance transforms, one for each color (RGB). If a particular color is absent during testing, it is accorded a maximum distance value of 10 pixels to avoid confusing the system. The color distance transform was tested for dependence on a variety of conditions, such as strong incident light, reflections, and deep shade, and was found to be robust to substantial illumination changes. Perhaps more important, it was found to be reasonably invariant to the effects of affine transformations, which a moving camera would be subject to. This is almost certainly because chamfer matching is subject to graceful degradation as distortions occur, so the distances at any template (edge) locations will *gradually* increase with the changing levels of distortion. When compared with other methods, the method performed well, the percentages of correct classifications being 22.3 for HOG/PCA, 62.6 for Haar/AdaBoost, 74.5 for HOG/AdaBoost, and 74.4 for the new method using the color distance transform. The main competitor to the new method, HOG/AdaBoost, offers an elegant solution but is much more complex than the new method and did not outperform it in any real sense. Hence, the new method seemed well adapted to the task it was set.

### 23.11.5 DEVELOPMENTS IN PATH PLANNING, NAVIGATION, AND EGOMOTION

The subjects of vehicle guidance and egomotion date from as long ago as 1992 (Brady and Wang, 1992; Dickmanns and Mysliwetz, 1992), whereas automatic visual guidance in convoys dates from a similar period (Schneiderman et al., 1995; Stella et al., 1995). Mobile robots and the need for path planning were discussed by Kanesalingam et al. (1998) and by Kortenkamp et al. (1998), and later a survey was carried out by DeSouza and Kak (2002): see also Davison and Murray (2002). Guidance of outdoor vehicles, particularly on roads, has undergone increasingly rapid development: see for example Bertozzi and Broggi (1998), Guiducci (1999), Kang and Jung (2003), and Kastrinaki et al. (2003). Zhou et al. (2003) considered the situation for elderly pedestrians—though clearly such work could also be relevant for blind people or wheelchair users. Hofmann et al. (2003) showed that vision and radar can profitably be used together to combine the excellent spatial resolution of vision with the accurate range resolution of radar.

In spite of the evident successes, there is still only a limited number of fully automated visual vehicle guidance systems in everyday use. The main problem would appear to be *potential* lack of the robustness and reliability required to trust the system in “all hours—all weathers” situations—though there are also legal implications for a system that is to be used for control rather than merely for vehicle monitoring.

---

## 23.12 PROBLEM

1. Check that the path through the maze shown in Fig. 23.14C is optimal, (1) by a hand calculation, and (2) by a computer calculation. Confirm that several other paths are also optimal. Obtain a more accurate result by taking the horizontal and vertical neighbors of any pixel as being 2 units away, and taking diagonal neighbors as being 3 units away.



This page intentionally left blank

# Epilogue—Perspectives in vision

# 24

## 24.1 INTRODUCTION

The preceding chapters have covered many topics relating to vision—how images may be processed to remove noise, how features may be detected, and how objects may be located from their features; they have also given insights into how to set up lighting and how to select rapid hardware systems, e.g., for automated visual inspection. The subject is one that has developed over a period of more than 40 years and has come a long way. However, it has developed piecemeal rather than systematically. Often, development is motivated by the particular interests of small groups of workers and is relatively ad hoc. Coupled with this is the fact that algorithms, processes, and techniques are all limited by the creativity of the various researchers: the process of design tends to be intuitive rather than systematic, and so again some arbitrariness tends to creep in from time to time. As a result, sometimes no means has yet been devised for achieving particular aims, but more usually a number of imperfect methods are available, and there is limited scientific basis for choosing between them.

All this poses the problem of how the subject may be placed on a firmer foundation. Time may help but time can also have the effect of making things more difficult as more methods and results arise which have to be considered; in any case, there is no shortcut to intellectual analysis of the state of the art. This book has aimed to carry out a degree of analysis at every stage; but in this last chapter, it is worth trying to tie it all together, to make some general statements on methodology and to indicate the direction that might be taken in the future.

Computer vision is an engineering discipline and, like all such disciplines, it has to be based on science and understanding of fundamental processes. However, as an engineering discipline, it should involve specification-based design. Once the specifications for a vision system have been laid down, it can be seen how they match up against the constraints provided by nature and

technology. In what follows, we consider first the parameters of relevance for the specification of vision systems; then we consider constraints and their origins. This leads to some clues as to how the subject could be developed further.

However, there is an important caveat to the way of thinking expressed above: by the end of the chapter, it will become clear that a major disruption has actually been introduced by the advent of a series of impressive, powerful deep learning architectures—thereby warranting a radical rethink of the way computer vision should go in the future.

---

## 24.2 PARAMETERS OF IMPORTANCE IN MACHINE VISION

The first thing that can be demanded of any engineering design is that it should work! This applies as much to vision systems as to other parts of engineering. Clearly, there is no use in devising edge detectors that do not find edges, corner detectors that do not find corners, thinning algorithms that do not thin, 3-D object detection schemes that do not find objects, and so on. But in what way could such schemes fail? Even if we ignore the possibility of noise or artifacts preventing algorithms from operating properly, there remains the possibility that at any stage important fundamental factors have not been taken into account.

For example, a boundary tracking algorithm can go wrong because it encounters a part of the boundary that is one pixel wide and crosses over instead of continuing. A thinning algorithm can go wrong because every possible local pattern has not been taken into account in the design and hence it disconnects a skeleton. A 3-D object detection scheme can go wrong because proper checks have not been made to confirm that a set of observed features is not coplanar. Of course, these types of problem may arise very rarely (i.e., only with highly specific types of input data), which is why the design error may not be noticed for a time. Often, mathematics or enumeration of possibilities can help to eliminate such errors, so problems can be removed systematically. However, being absolutely sure no error has been made is difficult—and it must not be forgotten that transcription errors in computer programs can contribute to the problems. These factors mean that algorithms should be put to extensive tests with large data sets in order to ensure that they are correct or at least contain adequate levels of robustness. There is no substitute for subjecting algorithms to variegated tests of this type to check out ideas that are “evidently” correct. This obvious fact is still worth stating, as silly errors continually arise in practice.

At this stage, imagine that we have a range of algorithms that all achieve the same results on ideal data, and that they really work. The next problem is to compare them critically and, in particular, to find how they react to *real* data and the nasty realities such as noise that accompany it. These nasty realities may be summed up as follows:

1. noise
2. background clutter
3. occlusions

4. object defects and breakages
5. optical and perspective distortions
6. nonuniform lighting and its consequences
7. effects of stray light, shadows, and glints.

In general, algorithms need to be sufficiently robust to overcome these problems. However, things are not so simple in practice. For example, HT and many other algorithms are capable of operating properly and detecting objects or features despite considerable degrees of occlusion. But how much occlusion is permissible? Or how much distortion, noise, or how much of any other of the nasty realities can be tolerated? In each specific case we could state some figures that would cover the possibilities. For example, we may be able to state that a line detection algorithm must be able to tolerate 50% occlusion, and so, a particular HT implementation is (or is not) able to achieve this. However, at this stage, we end with a lot of numbers that may mean very little on their own: in particular, they seem different and incompatible. In fact, this latter problem can largely be eliminated: each of the defects can be imagined to obliterate a definite proportion of the object (in the case of impulse noise, this is obvious; with Gaussian noise, the equivalence is not so clear but we suppose here that an equivalence can at least in principle be computed). Hence, we end up by establishing that artifacts in a particular dataset eliminate a certain proportion of the area and perimeter of all objects, or a certain proportion of all small objects. Clearly, certain of the nasty realities (such as optical distortions) tend to act in such a way as to cut down accuracy, but we concentrate here on robustness of object detection. Taking account of all these remarks, we are now in a position to proceed to the next stage of analysis.

To go further, it is necessary to set up a complete specification for the design of a particular vision algorithm. The specification can be listed as follows (but generality is maintained by not stating any particular algorithmic function):

1. the algorithm must work on ideal data
2. the algorithm must work on data that is  $x\%$  corrupted by artifacts
3. the algorithm must work to  $p$  pixels accuracy
4. the algorithm must operate within  $s$  seconds
5. the algorithm must be trainable
6. the algorithm must be implemented with failure rate less than 1 per  $d$  days
7. the hardware needed to implement the algorithm must cost less than  $\pounds L$ .

(The failure rate referred to in specification 6 can often be taken as arising mainly from hardware problems and will be ignored in what follows.)

The set of specifications listed above may at any stage of technological (especially hardware) development be unachievable; this is because they are phrased in a particular way, so they are not compromisable. However, if a given specification is getting near to its limit of achievability, a switch to an alternative

algorithm might be possible—but note that several, or all, relevant algorithms may be subject to almost identical limitations, because of underlying technological or natural constraints; alternatively, an internal parameter might be adjusted which keeps that specification within range, whereas pushing another specification closer to the limits of its range. In general, there will be some hard (nonnegotiable) specifications and others for which a degree of compromise is acceptable. As has been seen in various chapters of the book, this leads to the possibility of tradeoffs—a topic which is reviewed in the next section.

---

## 24.3 TRADEOFFS

Tradeoffs form one of the most important features of algorithms, as they permit a degree of flexibility subject only to what is possible in the nature of things. Ideally, the tradeoffs that are enunciated by theory provide absolute statements about what is possible, so that if an algorithm approaches these limits it is then probably as “good” as it can possibly be.

Next, there is the problem about where on a tradeoff curve, an algorithm should be made to operate. In many cases, the tradeoff curve (or surface) is bounded by hard limits. However, once it has been established that the optimum working point is somewhere within these limits, in a continuum, then it is appropriate to select a criterion function, whereby an optimum can be located uniquely. Details will vary from case to case but the crucial point is that an optimum must exist on a tradeoff curve, and that it can be found systematically once the curve is known. Clearly, all this implies that the science of the situation has been studied sufficiently so that relevant tradeoffs have been determined. We further illustrate this in the following subsections, which may be bypassed on a first reading.

### 24.3.1 SOME IMPORTANT TRADEOFFS

Earlier chapters of this book have revealed some quite important tradeoffs that are more than just arbitrary relations between relevant parameters. Here, a few examples will have to suffice by way of summary.

First, in [Chapter 5](#), Edge Detection, the DG edge operators were found to have only one underlying design parameter—that of operator radius  $r$ . Ignoring here, the important matter of the effect of a discrete lattice in giving preferred values of  $r$ , it was found that

1. signal-to-noise ratio varies linearly with  $r$ , because of underlying signal and noise averaging effects;
2. resolution varies inversely with  $r$ , as relevant linear features in the image are averaged over the active area of the neighborhood: The scale at which edge positions are measured is given by the resolution;

3. the accuracy with which edge position (at the current scale) may be measured depends on the square root of the number of pixels in the neighborhood and hence varies as  $r$ ;
4. computational load, and associated hardware cost, is typically proportional to the number of pixels in the neighborhood and hence varies as  $r^2$ .

Thus, operator radius carries with it four properties which are intimately related—signal-to-noise ratio, resolution (or scale), accuracy, and hardware/computational cost.

Another important problem was that of fast location of circle centers (Chapter 10: Line, Circle, and Ellipse Detection); in this case, robustness was seen to be measurable as the amount of noise or signal distortion that can be tolerated. For HT-based schemes, noise, occlusions, distortions, etc. all reduce the peak height in parameter space, thereby reducing the signal-to-noise ratio and impairing accuracy. Furthermore, if a fraction  $\beta$  of the original signal is removed, leaving a fraction  $\gamma = 1 - \beta$ , either by such distortions or occlusions or else by deliberate sampling procedures, then the number of independent measurements of the center location drops to a fraction  $\gamma$  of the optimum. This means that the accuracy of estimation of the center location drops to a fraction around  $\sqrt{\gamma}$  of the optimum.

What is important is that the effect of sampling is substantially the same as that of signal distortion, so that the more distortion that must be tolerated, the higher  $\alpha$ , the fraction of the total signal sampled, has to be. This means that as the level of distortion increases, the capability for withstanding sampling decreases, and therefore the gains in speed achievable from sampling are reduced—that is, for fixed signal-to-noise ratio and accuracy, a definite robustness—speed tradeoff exists. Alternatively, the situation can be viewed as a three-way relation between accuracy, robustness, and speed of processing. This provides an interesting insight into how the edge operator tradeoff considered earlier might be generalized.

To underline the value of studying such tradeoffs, note that any given algorithm will have a particular set of adjustable parameters which are found to control—and hence lead to tradeoffs between—the important quantities such as speed of processing, signal-to-noise ratio, and attainable accuracy already mentioned. Ultimately, such *practically* realizable tradeoffs (i.e., arising from the given algorithm) should be considered against those that may be deduced on purely theoretical grounds. Such considerations would then indicate whether a better algorithm might exist than the one currently being examined.

### 24.3.2 TRADEOFFS FOR TWO-STAGE TEMPLATE MATCHING

Two-stage template matching has been mentioned a number of times in this book as a means whereby the normally slow and computationally intensive process of template matching may be speeded up. In general, it involves looking for easily

distinguishable subfeatures, so that locating the features that are ultimately being sought involves only the minor problem of eliminating false alarms. The reason this strategy is useful is that the first stage eliminates the bulk of the raw image data, so that only a relatively trivial testing process remains. This latter process can then be made as rigorous as necessary. In contrast, the first “skimming” stage can be relatively crude, the main criterion being that it must not eliminate any of the desired features: false positives are permitted but not false negatives. However, the efficiency of the overall two-stage process is naturally limited by the number of false alarms thrown up by the first stage. (Note that similar principles arise with the boosting techniques described in [Section 21.4](#): see also [Fig. 21.5](#).)

Suppose that the first stage is subject to a threshold  $h_1$  and the second stage to a threshold  $h_2$ . If  $h_1$  is set very low, then the process reverts to the normal template matching situation, as the first stage does not eliminate any part of the image. In fact, setting  $h_1 = 0$  initially is useful so that  $h_2$  may be adjusted to its normal working value. Then,  $h_1$  can be increased to improve efficiency (reduce overall computation); a natural limit arises when false negatives start to occur—that is, some of the desired features are not being located. Further increases in  $h_1$  now have the effect of cutting down available signal, although speed continues to increase. This clearly gives a tradeoff between signal-to-noise ratio and hence accuracy of location and speed.

In a particular application in which objects were being located by the HT, the numbers of edge points located were reduced as  $h_1$  increased, so accuracy of object location was reduced (Davies, 1988f). A criterion function approach was then used to determine an optimum working condition. A suitable criterion function turned out to be  $C = T/A$ , where  $T$  is the total execution time and  $A$  the achievable accuracy. Although this approach gave a useful optimum, the optimum can be improved further if a mix of normal two-stage template matching and random sampling is used. This turns the problem into a 2-D optimization problem with adjustable parameters  $h_1$  and  $u$  (the random sampling coefficient, equal to  $1/\alpha$ ). However, in reality these types of problem are even more complex than indicated so far: in general, this is a 3-D optimization problem, the relevant parameters being  $h_1$ ,  $h_2$ , and  $u$ , although in fact a good approximation to the global optimum may be obtained by the procedure of adjusting  $h_2$  first, and then optimizing  $h_1$  and  $u$  together—or even of adjusting  $h_1$  first, then  $h_2$  and then  $u$  (Davies, 1988f). Further details are beyond the scope of the present discussion.

---

## 24.4 MOORE’S LAW IN ACTION

It has been indicated once or twice that the constraints and tradeoffs limiting algorithms are sometimes not accidental but rather the result of underlying technological or natural constraints. If so, it is important to determine this in as many

cases as possible; otherwise, workers may spend much time on algorithm development only to find their efforts repeatedly being thwarted. Usually, this is more easily said than done, but it underlines the necessity for scientific analysis of fundamentals.

The well-known law due to Moore (Noyce, 1977) relating to computer hardware states that the number of components that can be incorporated onto a single-integrated circuit increases by a factor of about two per year. Certainly, this was so for the 20 years following 1959, although the rate subsequently decreased somewhat (not enough, however, to prevent the growth from remaining approximately exponential). It is not the purpose of this chapter to speculate on the accuracy of Moore's law. However, it is useful to suppose that computer memory and power will grow by a factor approaching two per year in the foreseeable future. Similarly, computer speeds may also grow at roughly this rate in the foreseeable future. When then of vision?

Unfortunately, many vision processes such as search are inherently NP-complete and hence demand computation that grows exponentially with some internal parameter such as the number of nodes in a match graph. This means that the advance of technology is able to give only a roughly linear improvement in this internal parameter (e.g., something like one extra node in a match graph every 2 years): It is therefore not solving the major search and other problems but only easing them.

NP-completeness apart, we can often take an optimistic view that the relentless advance of computer power described by Moore's Law is leading to an era when conventional PCs will be able to cope with a fair proportion of vision tasks. Certainly, when combined with specially designed algorithms, it should prove possible to implement many of the simpler tasks in this way, leading to a much less strenuous life for the vision systems designer.

---

## 24.5 HARDWARE, ALGORITHMS, AND PROCESSES

The previous section raised the hope that improvements in hardware systems will provide the key to the development of impressive vision capabilities. However, it seems likely that breakthroughs in vision algorithms will also be required before this can come about. My belief is that until robots can play with objects and materials in the way that tiny children do they will not be able to build up sufficient information and the necessary databases for handling the complexities of real vision. The real world is too complex for all the rules to be written down overtly: these rules have to be internalized by training each brain individually. In some ways this approach is better, as it is more flexible and adaptable and at the same time more likely to be able to correct for the errors that would arise in direct transference of huge databases or programs. Nor should it be forgotten that it is the underlying processes of vision and intelligence that are important: Hardware



merely provides a means of implementation. If an idea is devised for a hardware solution to a visual problem, it reflects an underlying algorithmic process that either is or is not effective. Once it is known to be effective, then the hardware implementation can be analyzed to confirm its utility. However, we must not segregate algorithms too much from hardware design: In the end, it is necessary to optimize the whole system, which means considering both together. Ideally at least, the underlying processes should be considered first, before a hardware solution is frozen in. Hardware should not be the driving force as there is a danger that some type of hardware implementation (especially one that is temporarily new and promising) will take over and make workers blind to underlying processes. And many readily designed hardware architectures (from serial pipelines to SIMD (single instruction stream, multiple data stream), VLSI (very large scale integration), and ASIC (application specific integrated circuit) to FPGA (field programmable gate array)—and nowadays very frequently, GPU (graphics processing unit) are restricted and embody low-level vision capability rather than high-level functionality. Hardware should not be the tail that wags the vision dog.

---

## 24.6 THE IMPORTANCE OF CHOICE OF REPRESENTATION

This book has progressed steadily from low-level ideas, through intermediate-level methods to high-level processing, covering 3-D image analysis, the necessary technology, etc.—admittedly with its own type of detailed examples and emphasis. Many ideas have been covered and many strategies described. But where have we got to, and to what extent have we solved the problems of vision referred to in [Chapter 1](#), Vision, The Challenge?

Among the worst of all the problems of vision is that of minimizing the amount of processing required to achieve particular image recognition and measurement tasks. Not only do images contain huge amounts of data but often they also need to be interpreted in frighteningly small amounts of time, and the underlying search and other tasks tend to be subject to combinatorial explosions. Yet, in retrospect, we seem to have remarkably few *general* tools for coping with these problems. Indeed, the truly general tools available—ignoring high-level processing methods such as AI (artificial intelligence) tree-search—appear to be

1. reducing high-dimensional problems to lower dimensional problems that can be solved in turn;
2. the Hough transform and other indexing techniques;
3. location of features that are in some sense sparse, and which can hence help to reduce redundancy quickly (obvious examples of such features are edges and corners);
4. two-stage and multistage template matching; and
5. random sampling.

These are said to be general tools as they appear in one guise or another in a number of situations, with totally different data. However, it is pertinent to ask to what extent these are genuine tools rather than almost accidental means (or tricks) by which computation may be reduced. Further analysis yields interesting answers to this question, as will now be seen.

First, consider the Hough transform, which takes a variety of forms—the normal parametrization of a line in an abstract parameter space, the GHT which is parametrized in a space congruent to image space, the adaptive thresholding transform ([Chapter 4: The Role of Thresholding](#)) which is parametrized in an abstract 2-D parameter space, and so on. What is common about these forms is *the choice of a representation in which the data peak naturally at various points*, so that analysis can proceed with improved efficiency. The relation with item 3 above now becomes clear, making it less likely that either of these procedures is purely accidental in nature.

Next, item 1 appears in many guises—see e.g., the approaches used to locate ellipses ([Chapter 10: Line, Circle, and Ellipse Detection](#)). Thus, item 1 has much in common with item 4. Note also that item 5 can be considered a special case of item 4 (random sampling is a form of two-stage template matching with a “null” first stage, capable of eliminating large numbers of input patterns with particularly high efficiency: see Davies, 1988f). Finally, note that the example of so-called two-stage template matching covered in [Section 24.3.2](#) was actually part of a larger problem which was really multistage: the edge detector was two-stage, but this was incorporated in an HT which was itself two-stage, making the whole problem at least four-stage. It can now be seen that items 1–5 are all forms of multistage matching (or sequential pattern recognition) which are potentially more powerful and efficient than a single-stage approach. Similar conclusions are arrived at in [Appendix A](#), which deals with robust statistics and their application to machine vision.

The above discussion clearly raises the question of how complex tasks are to be broken down into the most appropriate multistage processes, and equivalently what the most suitable representation has to be for sparse feature location. At the same time, when looking at representations for vision algorithms, we need to be aware that *all representations impose their own order on a system*: for a time, this may be a good imposition, but in the end, it may turn into a dire restriction that is past its sell-by date. (This is what happened to the old chain code representation for boundary coding and also what happened to the centroidal profile approach to shape analysis.)

---

## 24.7 PAST, PRESENT, AND FUTURE

In some sense, the contents of a book such as this have to be concentrated on subject matter that is definite: Indeed, it is the duty of an author to provide

information on the definite rather than the ephemeral, so there has to be some concentration on the past. Yet, a book must also concentrate on fundamental principles, and these necessarily continue from the past to the present and the future. The difference is that principles that will only become known in the future cannot possibly be included, and here, a sound framework together with the current difficulties and unsolved problems can at least provide readers with a readiness for any principles that are to come. In fact, this book has solved some of the problems it set itself—starting with low-level processing, concentrating on strategies, limitations, and optimizations of intermediate-level processing, going some way with higher level tasks, and attempting to create an awareness of the underlying processes of vision. At the same time, there are many interesting current developments that will prove even more interesting in the future. For the subject has passed the stage of overconcentration on hardware and absolute efficiency and has focused on the important need to extend effectiveness and capability. In addition, the developments of the past decade or so have taken the subject out of the era of the ad hoc into that of mathematical precision and probabilistic formulation, so that whatever vision is expected to achieve is written down in terms of estimators that are mathematically defined and turned into rigorous implementations. Nowhere is this clearer than for the new invariant feature detectors with their massive descriptors that arguably make 3-D interpretation and motion tracking almost trivial to implement. All this means that exotic yet direly needed applications such as vision-based driver assistance systems are able to come into being—and it is possible to predict that they will be with us in the cars of the immediate future, if only we and the legal system will allow this.

Only a fool would make rash predictions (and many predictions within AI have remained elusive for more than 40 years), but it is different if the principles are clear: and they are evident to many vision workers nowadays; in fact, there is an air of euphoria over the rapidly growing maturity of the latest vision algorithms and the capability of the newest computers to implement them, so the very momentum is starting to make it straightforward to estimate when various developments will happen—a situation that is advancing all types of video analytics, in areas ranging from transport to crime detection and prevention, not to mention face recognition, biometrics, and robotics. It is hoped that the present volume will be able to communicate some of the excitement underlying these present and future developments and also some means for understanding their basis.

---

## 24.8 THE DEEP LEARNING EXPLOSION

Earlier sections of this chapter have dwelt strongly on a conventional view of the development path of computer vision, in which creativity, design, and scientific optimization need to go hand in hand. However, in 2011–2012, deep learning exploded onto the computer vision scene with staggering performance levels,

showing just how much further the subject could be pressed to go if only we gave up thinking of pure scientific analysis for a while. Effectively, this stimulus brought with it a cogent existence theorem showing things that could not be ignored—however, much we as scientists might have misgivings about them (because we don't know what is *really* going on in a neural system that is learning for itself rather than being guided by a “proper” algorithm). Nevertheless, it is well known that science advances in phases—first a practical advance, then a theoretical one, then a practical one, then a phenomenological model, and so on. Just because we have not reached an ideal theoretical stage at this point in time is not necessarily a bad thing: The required theory will emerge in very few years when its time has come. In fact, what is needed is a substantial amount more experimental data from a variety of application areas, so that we will be in a position to generalize over what is possible and arrive at sound scientific conclusions about the real capabilities and proper roles of deep networks in computer vision.

*Although some of the concentration of this chapter has been on tradeoffs and optimization, deeper issues are involved, such as finding out how to make valid specifications for image data, what representations are needed within vision algorithms and how the latter break down the overall process into viable subprocesses. There are also questions about the way in which vision algorithms are set up to rigorously estimate key parameters—a factor that relates directly to reliability, robustness, and fitness for purpose. Added to this are the exciting new applications of this rapidly maturing subject.*

*However, the new deep learning networks seem to change all this. They are now extremely impressive at the performance level. The ultimate question is whether they can be made to adequately embody the scientific approach that is necessary to allow us to be confident that their internal workings are completely reliable, and indeed that these hidden workings do not prevent us from getting a rigorous enough view of how any **overall** vision algorithm should ideally be constructed.*

---

## 24.9 BIBLIOGRAPHICAL AND HISTORICAL NOTES

Much of this chapter has summarized the work of earlier chapters and attempted to give it some perspective. In particular, two-stage template matching has been highlighted in the current chapter: the earliest work on this topic was carried out by Rosenfeld and VanderBrug (1977) and VanderBrug and Rosenfeld (1977), whereas the ideas of [Section 24.3.2](#) were developed by Davies (1988f). Two-stage template matching harks back to the spatial matched filtering concept discussed in [Chapter 11](#), The Generalized Hough Transform and elsewhere. Ultimately, this concept is limited by the variability of the objects to be detected. However, it has been shown that some account can be taken of this problem, e.g., in the design of filter masks (see Davies, 1992d). It ought also to be stated that this topic is highly formative, and though it is here developed in the context of

template matching, it is possible to see shadows and reflections of it right through the whole subject: one has only to ask how any new algorithm breaks down visual analysis into an efficient set of subprocesses and what representations they are operating in, in order to see the ramifications of this concept.

# Robust statistics



At an early stage, science students learn that averaging is an effective way of eliminating noise and improving accuracy. However, [Chapter 3, Image Filtering and Morphology](#), demonstrated unequivocally that median filtering of images is far better than mean filtering, both in retaining the form of the underlying signal and in suppressing impulse noise. Robust statistics is the subject of systematically eliminating outliers from visual or other data. This appendix aims to give useful insights into this important subject.

*Look out for:*

- the concepts “breakdown point” and “relative efficiency”
- M-, R-, and L-estimators
- the idea of an influence function
- the least median of squares (LMedS) approach
- the RANSAC approach
- the ways these methods can be applied in machine vision.

Although robust statistics is a relatively young discipline, dating largely from the 1980s, it has acquired a considerable following in machine vision and is crucial for example in the development of robust 3-D vision algorithms. A basic problem to be tackled is the impossibility of knowing how much of the input data are in the form of outliers.

## A.1 INTRODUCTION

We have found many times in this volume that noise can interfere with image signals and result in inaccurate measurements—for example, of object shapes, sizes, and positions. Perhaps more important, however, is the fact that signals other than the particular one being focused upon can lead to gross shape distortions and can thus prevent an object from being recognized or even being discerned at all. In many cases, this will render some obvious interpretation algorithm useless, though algorithms with intrinsic “intelligence” may be able to save the day. For this reason, the Hough transform has achieved some prominence: Indeed, this approach to image interpretation has frequently been described as “robust,” though no rigorous definition of robustness has been ventured so far in this volume. This appendix aims to throw further light on the problem.

Research into robustness did not originate in machine vision but evolved as the specialist area of statistics now known as robust statistics. Perhaps, the paradigm problem in this area is that of fitting a straight line to a set of points. In the physics laboratory, least squares analysis is commonly used to tackle the task. Fig. A.1A shows a straightforward situation where all the data points can be fitted with a reasonably uniform degree of exactness, in the sense that the residual errors approximate to the expected Gaussian distribution. (The residual errors or “residuals” are the deviations between the observed values and the theoretical predictions of the current model or current iteration of that model.) Fig. A.1B shows a less straightforward case, where a particular data point seems not to fall within a Gaussian distribution. Intuition indicates that this particular point represents data which have become corrupted in some way, e.g., by misreading an instrument or through a transcription error. Although the wings of a Gaussian distribution stretch out to infinity, the probability that a point will be more than five standard deviations from the center of the distribution is very small, and indeed,  $\pm 3\sigma$  limits are commonly taken as demarcating practical limits of correctness: It is taken as reasonable to disregard data points lying outside this range.

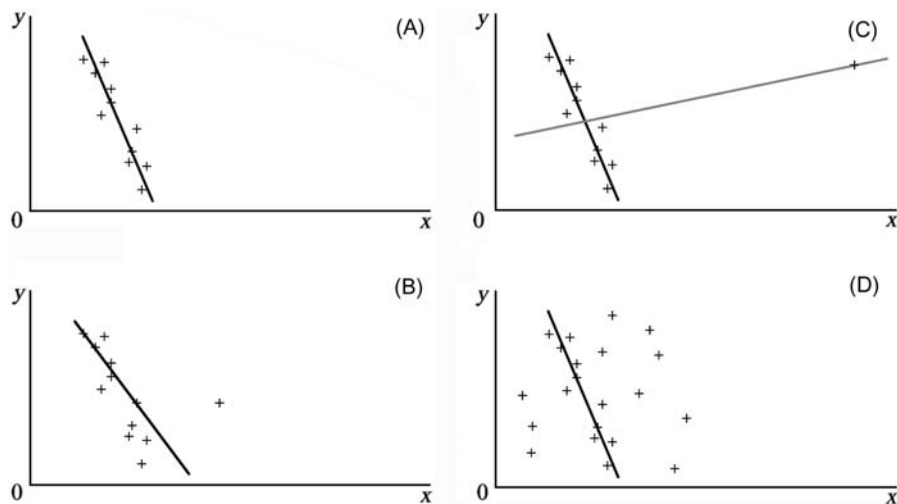


**FIGURE A.1**

Fitting of data points to straight lines. Part (A) shows a straightforward situation where all the data points can be fitted with reasonable precision; (B) shows a less straightforward case, where a particular data point seems not to fall within a Gaussian distribution; (C) shows a situation where the correct solution has been ignored by the numerical analysis procedure; (D) shows a situation where there are many rogue points, and it is not clear which points lie on the straight line and which do not: in such cases, it may not be known whether there are several, or any, lines to be fitted.

Unfortunately, the situation can be much worse than this simple example suggests. Suppose that there is a rogue data point which is a very long way off. In least squares analysis, it will have such a large leverage that the correct solution may not be found. And if the correct solution is not found, there will be no basis for excluding the rogue data point. This situation is illustrated in Fig. A.1C, where the obviously correct solution has been ignored by the numerical analysis procedure.

A worse case of line fitting occurs when there are many rogue points, and it is not clear which points lie on the straight line and which do not (Fig. A.1D). In fact, it may not be known whether there are several lines to be fitted, or whether there are *any* lines to be fitted. Whereas this circumstance would appear not to occur while data points are being plotted in physics experiments, it can arise when high energy particles are being tracked; it also occurs frequently in images of indoor and outdoor scenes where a myriad of straight lines of various lengths can appear in a great many orientations and positions. Thus, it is a real problem for which answers are required. An attempt at a full statement for this type of problem might be: devise a means for finding all the straight lines—of whatever length—in a generalized image (i.e., an image which might correspond to off-camera images, or to situations such as data points being plotted on a graph), so as to obtain the best overall fit to the dataset. Unfortunately, there are likely to be many solutions to any line-fitting task, particularly if the data points are not especially accurate (if they are highly accurate then the number of solutions will be small, and it should be easy to decide intuitively or automatically what the best solution is). In fact, a rigorous answer to the question of which solution provides the best fit requires the definition of a criterion function which in some way takes account of the number of lines and the a priori length distribution. We shall not pursue this line of attack here, as the purpose of this appendix is to give a basic account of the subject of robust statistics, not one that is tied to a particular task. Hence, we shall return below to the simpler case where there is only one line present in the generalized image, and there are a substantial number of rogue data points or “outliers” present.

---

## A.2 PRELIMINARY DEFINITIONS AND ANALYSIS

In the previous section we saw that robustness is an important factor in deciding on a scheme for fitting experimental data to numerical models. It is clearly important to have an exact measure of robustness, and the concept of a “breakdown point” long ago emerged as such a measure. The breakdown point  $\varepsilon$  of a regression scheme is defined as the smallest proportion of outlier contamination which may force the value of the estimate to exceed an arbitrary range. As we have seen, even a single outlier in a set of plots can cause least squares regression to give completely erroneous results. However, a much simpler example is to hand, namely a 1-D distribution for which the mean is computed: here again, a single outlier can cause the mean to exceed any stated bound. This means that the



breakdown point for the mean must be zero. On the other hand, the median of a distribution is well known to be highly robust to outliers, and remains unchanged if nearly half the data is corrupted. To clarify the discussion, we employ the “floor” (rounding down) operation  $\lfloor \cdot \rfloor$ , which indicates the largest integer less than or equal to the enclosed value. For a set of  $n$  data points we find that  $\lfloor n/2 \rfloor \leq n/2 \leq \lfloor n/2 \rfloor + 1$ . We now see that, for a set of  $n$  data points, the median will remain unchanged if the lowest  $\lfloor n/2 \rfloor$  points are moved to arbitrary lower values, or the highest  $\lfloor n/2 \rfloor$  points are moved to arbitrary higher values, but in either case the median value will be changed to an arbitrary value if  $\lfloor n/2 \rfloor + 1$  points are so moved. By definition (see above), this means that the breakdown point of the median is  $(\lfloor n/2 \rfloor + 1)/n$ ; this value should be compared with the value  $1/n$  for the mean. In the case of the median the breakdown point approaches 0.5 as  $n$  tends to infinity (see Table A.1). Thus the median attains the apparently maximum achievable breakdown point of 0.5, and is therefore optimal—at least in the 1-D case described in this paragraph.

In fact, the breakdown point is not the only relevant parameter for characterizing regression schemes. For example, the “relative efficiency” is also important and is defined as the ratio between the lowest achievable variance and the actual variance achieved by the regression method. In fact, the relative efficiency depends on the particular noise distribution that the data are subject to. It can be shown that the mean is optimal for elimination of Gaussian noise, having a relative efficiency of unity, while the median has a relative efficiency of  $2/\pi = 0.637$ . However, when dealing with impulse noise, the median has a higher relative efficiency than the mean, the exact values depending on the nature of the noise. This point will be discussed in more detail below.

Time complexity is a further parameter which is needed for characterizing regression methods. We shall not pursue this aspect further here, beyond making the observation that the time complexity of the mean is  $O(n)$ , while that for the median varies with the method of computation (e.g.,  $O(n)$  for the histogram approach of Section 3.3 and  $O(n^2)$  when using a bubble sort): In any case, the absolute time for computing a median normally far exceeds that for the mean.

**Table A.1** Breakdown Points for Means and Medians

$n$	Mean	Median
1	1	1
3	1/3	2/3
5	1/5	3/5
11	1/11	6/11
$\infty$	0	0.5

*This table shows how the respective breakdown points for the mean and median approach 0 and 0.5 as  $n$  tends to infinity, in the case of 1-D data.*

Of the parameters referred to above, the breakdown point has been at the forefront of workers' minds when devising new regression schemes. While it might appear that the median already provides an optimal approach for robust regression, its breakdown value of 0.5 only applies to 1-D data. It is therefore worth considering what breakdown point could be achieved for tasks such as line fitting, bearing in mind the poor performance of least squares regression. Let us take the method of Theil (1950) in which the slope of each pair of a set of  $n$  data points is computed, and the median of the resulting set of  ${}^n C_2 = \frac{1}{2}n(n-1)$  values is taken as the final slope; in fact, the intercept can be determined more simply because the problem has at that stage been reduced to one dimension. As the median is used in this procedure, at least half the slopes have to be correct in order to obtain a correct estimate of the actual slope. In what follows, we shall regard the dataset as being composed of "inliers" and "outliers", the inliers being normal valid data points. If we assume that the proportion of outliers in the data is  $\eta$ , the proportion of inliers will be  $1 - \eta$ , and the proportion of correct slopes will be  $(1 - \eta)^2$ , and this has to be at least 0.5. This means that  $\eta$  has to lie in the range:

$$\eta \leq 1 - 1/\sqrt{2} = 1 - 0.707 = 0.293 \quad (\text{A.1})$$

Thus, the breakdown point for this approach to linear regression is less than 0.3. In a 3-D data space where a best-fit plane has to be found, the best breakdown point will be even smaller, with a value  $1 - 2^{-1/3} \approx 0.2$ . The general formula for  $p$  dimensions is

$$\eta_p \leq 1 - 2^{-1/p} \quad (\text{A.2})$$

Clearly, there is a need for more robust regression schemes which becomes more urgent for larger values of  $p$ .

The development of robust multidimensional regression schemes took place relatively recently, in the 1970s. The basic estimators which were developed at that time, and classified by Huber in 1981, were the M-, R-, and L-estimators. The M-estimator is by far the most widely used and appears in a variety of forms which encompass median and mean estimators and least squares regression: We shall study this type of estimator in more detail below. The L-estimators employ linear combinations of order statistics and include the alpha-trimmed mean, with the median and mean as special cases. However, it will be easier to consider the median and the mean under the heading of M-estimators, and in what follows, we concentrate on this approach.

---

### A.3 THE M-ESTIMATOR (INFLUENCE FUNCTION) APPROACH

M-estimators operate by minimizing the sum of a suitable function  $\rho$  of the residuals  $r_i$ . Normally,  $\rho$  is taken to be a positive definite function, and for least squares ( $L_2$ ) regression, it is the square of the residuals:

$$\rho(r_i) = r_i^2 \quad (\text{A.3})$$

In general, it is necessary to perform the M-estimation minimization operation iteratively until a stable solution is obtained (at each iteration, the new set of offsets has to be added to the previous set of parameter values).

To improve upon the poor robustness of  $L_2$  regression, reflected by its zero breakdown point, an improved function  $\rho$  must be obtained which is well adapted to the particular noise and outlier content of the data. At this point we digress to consider the concept of noise more fully: “noise” tends to originate from electronic processes in the image source, and typically leads to a Gaussian distribution in the pixel intensity values. By the time positions of objects are being measured, it is strictly speaking errors rather than noise that are being considered, and the error distribution is not necessarily identical to the noise distribution that gave rise to it. However, in the later sections of this appendix, we usually refer to noise and noise distributions: the term noise will be taken to refer either to the original noise source or to the derived errors, as appropriate to the discussion. We now proceed to analyze the situation for 1-D datasets and to consider the influence of each data point. We represent the influence of a data point by an influence function  $\psi(r_i)$ , where:

$$\psi(r_i) = \frac{d\rho(r_i)}{d(r_i)} \quad (\text{A.4})$$

Notice that minimizing  $\sum_{i=0}^n \rho(r_i)$  is equivalent to reducing  $\sum_{i=0}^n \psi(r_i)$  to zero, and in the case of  $L_2$  regression:

$$\psi(r_i) = 2r_i \quad (\text{A.5})$$

In one dimension, this equation has a simple interpretation—moving the origin of coordinates to a position where  $\sum_{i=0}^n r_i = 0$ , i.e., to the position of the mean. Now that we have shown the equivalence of  $L_2$  regression to simple averaging, the source of the lack of robustness becomes all too clear—however, far away from the mean a data point is, it still retains a weight proportional to its residual value  $r_i$ . Accordingly, a wide range of possible alternative influence functions has been devised to limit the problem by cutting down the weights of distant points which are potential outliers.

An obvious approach is to limit the influence of a distant point to some maximum value: Another is to eliminate its influence altogether once its residual error exceeds a certain limiting value (Fig. A.2). We could achieve this by a variety of schemes, either cutting off the influence suddenly at this limiting distance (as in the case of the  $\pm 3\sigma$  points), or letting it approach zero according to a linear profile, or opting for a more mathematically ideal functional form with a smoother profile. In fact, there are other considerations, such as the amount of computation involved in dealing with large numbers of data points taken over a fair number of iterations. Thus, it is not surprising that a variety of piecewise linear profiles approximating to the smoother ideal profiles have been devised. In general, however, influence functions are linear near the origin, zero at large distances from the origin, and possess a region of over which they give significant weight to the data points (Fig. A.2).

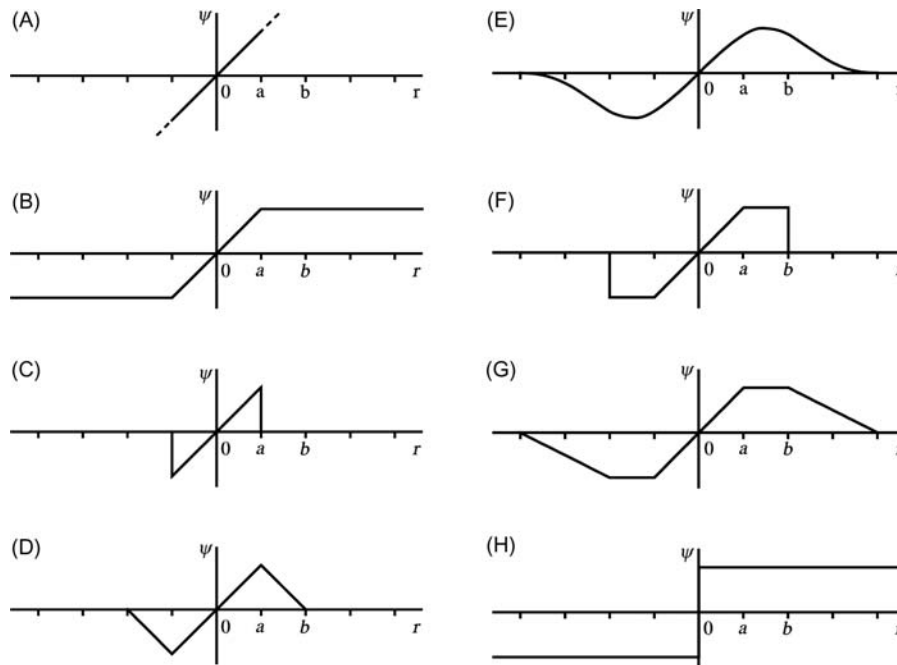


**FIGURE A.2**

Influence functions which limit the effects of outliers. Part (A) shows the case where no limit is placed on the influence of distant points; (B) shows how the influence is limited to some maximum value; (C) shows how the influence is eliminated altogether once the residual exceeds a certain maximum value; (D) shows a piecewise linear profile which gives a less abrupt variation; (E) shows a mathematically more well-behaved influence function; (F) shows another possible piecewise linear case, and (G) shows a Hampel 3-part redescending M-estimator which approximates the mathematically ideal case (E) with reasonable accuracy; (H) shows the situation for a median estimator.

Prominent among these possibilities are the Hampel 3-part redescending M-estimator, whose influence function is composed simply of convenient linear components, and the Tukey biweight estimator (Beaton and Tukey, 1974) which takes a form similar to that shown in Fig. A.2E:

$$\begin{aligned} \psi(r_i) &= r_i(\gamma^2 - r_i^2)^2 & |r_i| \leq \gamma \\ &= 0 & |r_i| > \gamma \end{aligned} \tag{A.6}$$

It was remarked above that the median operation is a special case of the M-estimator: Here, all data points on one side of the origin have a unit positive weight, and all data points on the other side of the origin have unit negative weight:

$$\psi(r_i) = \text{sign}(r_i) \tag{A.7}$$

Thus, if more data points are on one side than the other, the solution will be pulled in that direction, iteration proceeding until the median is at the origin.

It is important to appreciate that while the median has exceptionally useful outlier suppression characteristics, it actually gives outliers significant weight: In fact, the median clearly ignores how far away an outlier is, but it still counts up how many outliers there are on either side of the current origin. As a result, the median is liable to produce a biased estimate. This is good reason for considering other types of influence function for analyzing data. Finally, note that the median influence function leads to the value of  $\rho$  for  $L_1$  regression:

$$\rho(r_i) = |r_i| \quad (\text{A.8})$$

When selecting an influence function, it is important not only that the function must be appropriate but also that its scale must match that of the data. If the width of the influence function is too great, too few outliers will be rejected; if the width is too small, the estimator may be surrounded by a rather homogeneous sea of data points with no guarantee that it will do more than find a locally optimal fit to the data. These factors mean that preliminary measurements must be made to determine the optimal form of the influence function for any application.

It is now clear that we need a more scientific approach which would permit the influence function to be calculated from the noise characteristics. Hence, if the expected noise distribution is given by  $f(r_i)$ , the optimal form of the influence function (Huber, 1964) has to be

$$\psi(r_i) = -\frac{f'(r_i)}{f(r_i)} = -\frac{d}{dr_i} \ln[f(r_i)] \quad (\text{A.9})$$

The logarithmic form of this solution is interesting and helpful, as it simplifies the situation for exponential-based noise distributions such as the Gaussian and double exponential functions. For the former,  $\exp(-r_i^2/2\sigma^2)$ , we find:

$$\psi(r_i) = r_i/\sigma^2 \quad (\text{A.10})$$

and for the latter,  $\exp(-|r_i|/s)$ :

$$\psi(r_i) = \text{sign}(r_i)/s \quad (\text{A.11})$$

Since the constant multipliers may be ignored, we conclude that the mean and median are optimal estimators for signals in Gaussian and double exponential noise, respectively.

Gaussian noise may be expected to arise in many situations (most particularly because of the effects of the central limit theorem), demonstrating the intrinsic value of employing the mean or  $L_2$  regression. On the other hand, the double exponential distribution has no obvious justification in practical situations. However, it represents situations where the wings of the noise distribution stretch out rather widely, and it is good to see under what conditions, the widely used median would be optimal. Nevertheless, our purpose in wanting an explicit

mathematical form for the influence function was to optimize the detection of signals in arbitrary noise conditions and specifically those where outliers may be present.

Let us suppose that the noise is basically Gaussian, but that outliers may also be present and that these would be drawn approximately from a uniform distribution: There might for example be a uniform (but low-level) distribution of outlier values over a limited range. An overall distribution of this type is shown in Fig. A.3. Near  $r_i = 0$ , the uniform distribution of outliers will have relatively little effect and  $\psi(r_i)$  will approximate to  $r_i$ . For large  $|r_i|$ , the value of  $f'$  will be due mainly to the Gaussian noise contribution, whereas the value of  $f$  will arise mainly from the uniform distribution  $f_u$ , and the result will be

$$\psi(r_i) \approx \frac{r_i}{s^2 f_u} \exp(-r_i^2 / 2\sigma^2) \quad (\text{A.12})$$

a function which peaks at an intermediate value of  $r_i$ . This essentially proves that the form shown in Fig. A.2E is reasonable. However, there is a severe problem in that outliers are by definition unusual and rare, so it is almost impossible in most cases to be able to produce an optimum form of  $\psi(r_i)$  as suggested above. Unfortunately, the situation is even worse than this discussion might indicate. Redescending M-estimators are even more limited in that they are sensitive to local densities of data points and are therefore prone to finding false solutions—unique solutions are *not* guaranteed. Nonredescending M-estimators are guaranteed to arrive at unique solutions, though the accuracy of the latter depends on the accuracy of the preliminary scale estimate. In addition, the quality of the initial approximation tends to be of very great importance for M-estimators, particularly for redescending M-estimators.

Finally, we should point out that the above analysis has concentrated on optimization of accuracy and is ultimately based on maximum likelihood strategies (Huber, 1964). It is really concerned with maximizing relative efficiency on the assumption that the underlying distribution is known. Robustness measured according to the breakdown point criterion is not optimized, and this factor will be of vital importance in any situation where the outliers form part of a totally unexpected distribution or do not form part of a predictable distribution. (It is



**FIGURE A.3**

Distribution resulting from Gaussian noise and outliers. Here, the usual Gaussian noise contribution is augmented by a distribution of outliers which is nearly uniform over a limited range.

perhaps a philosophical question whether an outlier distribution does not exist, cannot exist, or cannot be determined by any known experimental means, e.g., because of rarity.) Clearly, methods must be engineered which are intrinsically highly robust according to the breakdown point criterion. This is what motivated the development of the LMedS approach to regression during the 1980s.

---

## A.4 THE LEAST MEDIAN OF SQUARES APPROACH TO REGRESSION

Above we have seen that a variety of estimators exist which can be used to suppress noise from numerical data and to optimize the robustness and accuracy of the final result. The M-estimator (or influence function) approach is extremely widely used and is successful in eliminating the main problems associated with the use of least squares regression (including, in 1-D, use of the mean). However, it does not in general achieve the ideal breakdown value of 0.5 and requires careful setting up to give optimal matching to the scale of the variation in the data. Accordingly, much attention has been devoted to a newer approach—LMedS regression.

The aim of LMedS regression is to capitalize on the known robustness of the median in a totally different way—by replacing the mean of the least (mean) squares averaging technique by the far more robust median. The effect of this is to ignore errors from the distant parts of the distribution and also from the central parts where the peak is often noisy and ill-defined and to focus on the parts about half-way up and on either side of the distribution. Minimization then balances the contributions from the two sides of the distribution, thereby sensitively estimating the mode position, though clearly this is achieved rather indirectly. Perhaps, the simplest view of the technique is that it determines the location of the narrowest width region which includes half the population of the distribution. In a 2-D straight-line location application, this interpretation amounts to locating the narrowest parallel-sided strip which includes half the population of the distribution (Fig. A.4). In principle, in such cases, the method operates just as effectively if the distribution is sparsely populated—as happens where the best-fit straight line for a set of experimental plots has to be determined.

The LMedS technique involves minimizing the median of the squares of the residuals  $r_j$  for all possible positions in the distribution which are potentially mode positions, i.e., it is the position  $x_i$  which minimizes  $M = \text{med}_j(r_j^2)$ . While it might be thought that  $M$  is also equal to  $M = \text{med}_j(|r_j|)$ , this is not so if there are two adjacent central positions giving equal responses (as in Fig. A.5A–C); however, the form of  $M$  guarantees that a position mid-way between these two will give an appropriate minimum. For clarity, we shall temporarily ignore this technicality and concentrate on  $M$ : The reason for doing this is to take advantage of piecewise linear responses which considerably simplify theoretical analysis.

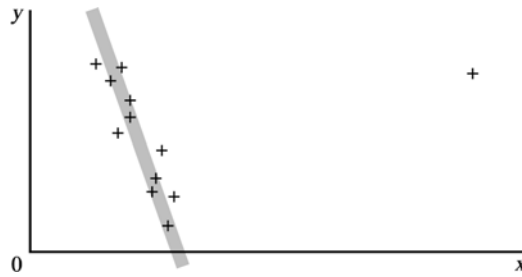


**FIGURE A.4**

Application of the least median of squares technique. Here, the narrowest parallel-sided strip is found which includes half the population of the distribution, in an attempt to determine the best-fit line. Notice the effortless superiority in performance when compared with the situation in Fig. A.1C.

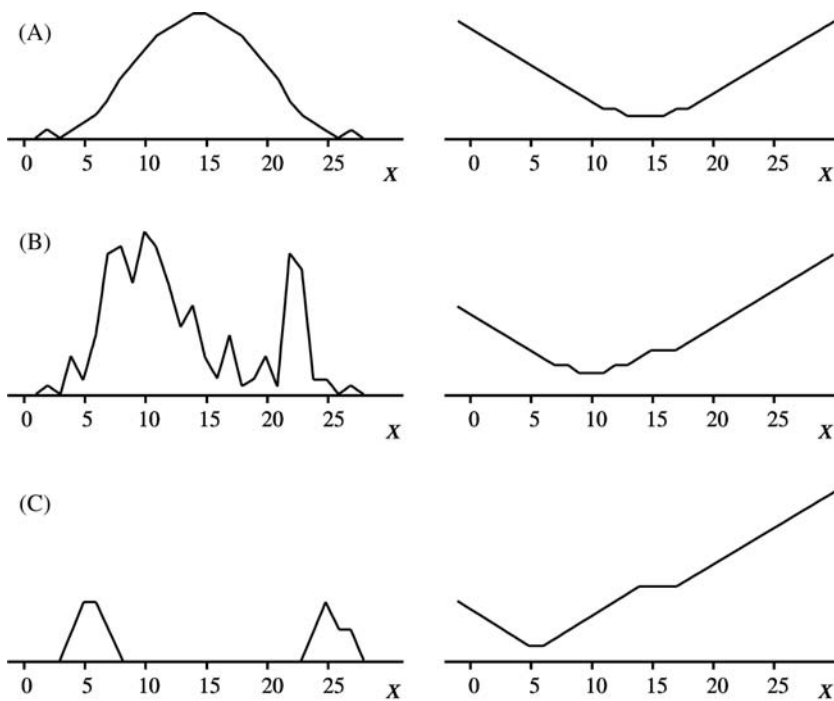


**FIGURE A.5**

Minimizing  $M$  for various distributions. This figure shows (left) the original distributions and (right) the resulting response functions  $M$ , in the following cases: (A) an approximately Gaussian distribution, (B) an “untidy” distribution, (C) a distribution with two peaks.



Fig. A.5A shows the response  $M$  when the original distribution is approximately Gaussian. There is a clear minimum of  $M$  at the mode position, and the method works perfectly. Fig. A.5B shows a case where there is a very untidy distribution, and there is a minimum of  $M$  at an appropriate position. Fig. A.5C shows a more extreme situation in which there are two peaks, and again the response  $M$  is appropriate, except that it is now clear that the technique can only focus on one peak at a time. Nevertheless, it gets an appropriate and robust answer for the case it is focusing on. If the two peaks are identical the method will still work but will clearly not give a unique solution.

The LMedS approach to regression (Rousseeuw, 1984) has acquired considerable support, since it has the maximum possible breakdown point of 0.5. In particular, it has been used for pattern recognition and image analysis applications (see, e.g., Kim et al., 1989). In these areas, the method is useful for (1) location of straight lines in digital images, (2) location of Hough transform peaks in parameter space, and (3) location of clusters of points in feature space.

Unfortunately, the LMedS approach is liable to give a biased estimate of the modes if two distributions overlap and, in any case, focuses on the main mode of a multimodal distribution. Thus, the LMedS technique has to be applied several times, alternating with necessary truncation processes, to find all the cluster centers, while weighted least squares fitting is required to optimize accuracy. The result is a procedure of some complexity and considerable computational load. Indeed, the load is in general so large that it is normally approximated by taking subsets of the data points, though this aspect cannot be examined in detail here (see, e.g., Kim et al., 1989). Once this has been carried out, the method can give quite impressive results.

Ultimately, the value of the LMedS approach lies in its increased breakdown point in situations of multidimensional data. If we have  $n$  data points in  $p$  dimensions, the LMedS breakdown point is

$$\varepsilon_{\text{LMedS}} = (\lfloor n/2 \rfloor - p + 2)/n \quad (\text{A.13})$$

which tends to 0.5 as  $n$  approaches infinity (Rousseeuw, 1984). This value must be compared with a maximum of

$$\varepsilon = 1/(p + 1) \quad (\text{A.14})$$

for standard methods of robust regression such as the M-, R-, and L-estimators discussed earlier (Kim et al., 1989). (Eq. (A.2) represents the suboptimal solution achieved by the Theil approach to line estimation.) Thus, in these latter cases, 0.33 is the best breakdown point that can be achieved for  $p = 2$ , while the LMedS approach offers 0.5. However, the relative efficiency of LMedS is relatively low (ultimately because it is a median-based estimator); as stated above, this means that it has to be used with the weighted least squares technique. We should also point out that the LMedS technique is intrinsically 1-D, so it has to be used in a “projection pursuit” manner (Huber, 1985), concentrating on one dimension at a time. For implementation details, the reader is referred to the literature (see Section A.8).

## A.5 OVERVIEW OF THE ROBUSTNESS PROBLEM

For greatest success in solving the robustness and accuracy problems—represented respectively by the breakdown point and relative efficiency criteria—it has been found in the foregoing sections that the LMedS technique should be used for finding signals (whether peaks, clusters, lines or hyperplanes, etc.), and weighted least squares regression should be used for refining accuracy, the whole process being iterated until satisfactory results are achieved. This is a complex and computation intensive process but reflects an overall strategy which has been outlined several times in earlier chapters—namely, search for an approximate solution, and then refinement to optimize location accuracy. The major question to be considered at this stage is: What is the best method for performing an efficient and effective initial search? In fact, there is a further question which is of especial relevance: Is there any means of achieving a breakdown point of greater than 0.5?

We now consider the extent to which the Hough transform tackles and solves these problems. First, it is a highly effective search procedure, though in some contexts, its computational efficiency has been called into question (however, in the present context, it must be remembered that the LMedS technique is especially computation intensive). Second, it seems able to yield breakdown points far higher than 0.5 and even approaching unity. Consider a parameter space where there are many peaks and also a considerable number of randomly placed votes. Then, any individual peak includes perhaps only a small fraction of the votes, and the peak location proceeds without difficulty in spite of the presence of 90%–99% contamination by outliers (the latter arising from noise and clutter). Thus, the strategy of searching for peaks appears to offer significant success at avoiding outliers. Yet, this does not mean that the LMedS technique is valueless, since subsequent application of LMedS is essentially able to *verify* the identification of a peak, to locate it more accurately via its greater relative efficiency, and thus to feed reliable information to a subsequent least squares regression stage. Overall, we can see that a staged progression is taking place from a high breakdown point, low relative efficiency procedure, to a procedure of intermediate breakdown point and moderate relative efficiency, and finally to a procedure of low breakdown point and high relative efficiency. We summarize the progression by giving possible figures for the relevant quantities in [Table A.2](#).

**Table A.2** Breakdown Points and Efficiency Values for Peak Finding

	HT	LMedS	LS	Overall
$\varepsilon$	0.98	0.50	0.2	0.98
$\eta$	0.2	0.4	0.95	0.95

*This table gives possible breakdown points  $\varepsilon$  and relative efficiency values  $\eta$  for peak finding. A Hough transform is used to perform an initial search for peaks; then, the LMedS technique is employed for validating the peaks and eliminating outliers; finally, least squares regression is used to optimize location accuracy. The result is far higher overall effectiveness than that obtainable by any of the techniques applied alone; however, computational load is not taken into account and is likely to be a major consideration.*

---

## A.6 THE RANSAC APPROACH

Over a good many years, RANSAC has become one of the most widely used outlier rejection and data-fitting tools: It has achieved particular value in 3-D vision. RANSAC is an acronym for *RANdom SAMple Consensus* and involves repeatedly trying to obtain a consensus (set of inliers) from the data until the degree of fit exceeds a given criterion.

To understand the process, let us first return to the LMedS approach, which is useful both in providing a graphic presentation of what it achieves and in requiring no parameters to be set in order to make it work. In fact, this latter feature is in many ways its undoing, because if the proportion of outliers in the data exceeds 50%, the resulting fit is liable to be heavily biased. A simple modification of the method is to require a smaller number of inliers—indeed, whatever proportion would be expected in the incoming data. Thus, we may go for 20% inliers, 80% outliers if this seems appropriate. This naturally leads to problems, as ideally, we will have to estimate the proportion of inliers in advance, or as part of the fitting process, and then apply the resulting value as part of the technique.

Once the “cleanness” of the LMedS method is lost, a variety of alternative solutions become possible. In fact, the RANSAC method involves not taking the proportion of inliers as fixed and finding how the residual distance (e.g., from a best-fit straight line) varies, but rather specifying a threshold residual distance  $t$  and finding how the proportion of inliers varies. Here, the word “inlier” is not a good term to use, as it implies we already know that these data are acceptable points: Instead, they should be called consensus points—at least until the end of the process. In summary, we set a threshold residual distance  $t$  and ask how much consensus this gives. Note that in principle at least,  $t$  has to be iterated as part of the whole process of finding the best fit. However, it is possible to work on the basis that the experimental uncertainty is known in advance, and if for example  $t$  is made equal to three standard deviations, this should not lead to too much error in the final fit obtained.

Another aspect of RANSAC that must be brought out is the random extraction of  $n$  data points to specify each initial potential fit, following which the hypothesized solution is tested to find how much consensus there is; then out of  $k$  trials, the best solution is the one with the greatest consensus, and at this final stage, we can interpret the consensus as the set of inliers.

Finally, the number of data points  $n$  needed to specify a potential fit is made equal to the number of degrees of freedom of the data—two for a straight line in a plane, three for a circle, four for a sphere, and so on (Fig. A.6). All that remains to be specified is the number of iterations  $k$  of sets of  $n$  data points in order to reach the final best-fit solution. One way of estimating  $k$  is to calculate the risk that all the  $k$  sets of  $n$  data points chosen will contain only outliers, so that no good data will be examined. Clearly,  $k$  must be sufficiently large to reduce the risk of this eventuality to a low enough level. Formulae to estimate  $k$  on this basis appear in several sources, e.g., Hartley and Zisserman (2000).

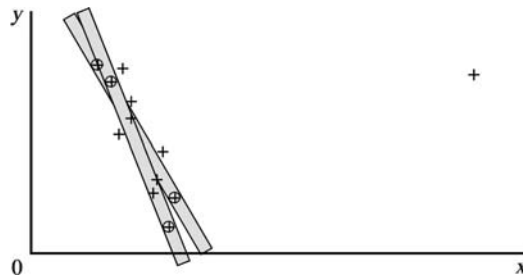


**FIGURE A.6**

The RANSAC technique. Here the + signs indicate data points to be fitted, and two instances of pairs of data points (indicated by  $\oplus$  signs) leading to hypothesized lines are also shown. Each hypothesized line has a region of influence of tolerance  $\pm t$  within which the support of maximal numbers of data points is sought. The line with the most support indicates the best fit (though weighted least squares analysis may subsequently be applied to improve it further).

Finally, note that, as happens with many other outlier identification processes, improved fits can be obtained by a final stage in which normal or weighted least squares analysis is applied to the remaining (inlier) data.

## A.7 CONCLUDING REMARKS

This appendix has aimed to place the discussion of robustness on a sounder basis than might have been thought possible in the earlier chapters of the book, where a more intuitive approach was presented. It has been necessary to delve quite deeply into the maturing and highly mathematical subject of robust statistics, and there are certain important lessons to be learnt. In particular, three relevant parameters have been found to form the basis for study in this area. The first is the breakdown point of an estimator, which shows the latter's resistance to outliers and provides the core meaning of robustness. The second is the relative efficiency of an estimator, which provides a measure of how efficiently it will use the inlier data at its disposal to arrive at accurate estimates. The third is the time complexity of the estimator when it is implemented as a computer algorithm. While this last parameter is a vital consideration in practical situations, available space has not permitted it to be covered in any depth here, though it is clear that the most robust techniques (especially LMedS) tend to be highly computation intensive. It is also found that there is a definite tradeoff between the other two parameters—techniques which have high breakdown points have low relative efficiencies and vice versa. (The reason for this may be summarized as the aim of achieving high robustness requiring considerable potentially outlier data to be discarded, even when this could be accurate data which would contribute to the overall accuracy

of the estimate.) These factors make it reasonable, and desirable, to use several techniques in sequence, or iteratively in cycle, in order to obtain the best overall performance. Thus, LMedS is frequently used in conjunction with least squares regression (see, e.g., Kim et al., 1989).

Finally, it is worth pointing out that the basis of robust statistics is that of statistical analysis of the available data: There is thus a tendency to presume that outliers are rare events due typically to erroneous readings or transcriptions. Yet in vision, the most difficult problems tend to arise from the clutter of irrelevant objects in the background, and only a tiny fraction of the incoming data may constitute the relevant inlier portion. This makes the problem of robustness all the more serious, and in principle *could* mean that until a whole image has been interpreted satisfactorily no single object can finally be identified and its position and orientation measured accurately. However, it is rare that we need to take such an extreme view in practical applications of vision.

*Robust statistics is at the core of any practical vision system. This appendix has aimed to cover the intricacies of the subject in an accessible way, dealing with important concepts such as “breakdown point” and measurement “efficiency.” What is really in question is **how** robust statistics will be incorporated into any practical vision system, not whether it needs to be.*

---

## A.8 BIBLIOGRAPHICAL AND HISTORICAL NOTES

This appendix has given a basic introduction to the rapidly maturing subject of robust statistics which has made a substantial impact on machine vision over the past 25 years or so. The most popular and successful approach to robust statistics must still be seen as the M-estimator (influence function) approach (which is broad enough to include least squares regression and median filtering), though in high-dimensional spaces, its robustness is called to question, and it is here that the newer LMedS approach has gathered a firm following. More recently, the value of using a sequence of estimators which can optimize the overall breakdown point and relative efficiency has been pointed out (Kim et al., 1989): In particular, the right combination of Hough transform (or other relevant technique), LMedS, and weighted least squares regression would seem especially powerful.

Robust statistics has been applied in a number of areas of machine vision, including robust window operators (Besl et al., 1989), pose estimation (Haralick and Joo, 1988), motion studies (Bober and Kittler, 1993), camera location and calibration (Kumar and Hanson, 1989), and surface defect inspection (Koivo and Kim, 1989), to name but a few.

The original papers by Huber (1964) and Rousseeuw (1984) are still worth reading, and the books by Huber (1981), Hampel et al. (1986), and Rousseeuw and Leroy (1987) are valuable references, containing much insight and useful material. On the application of the LMedS technique, and for more reviews of robust regression in machine vision, see Meer et al. (1990, 1991).

Note that the RANSAC technique (Fischler and Bolles, 1981) was introduced before LMedS and presaged its possibilities: thus, RANSAC was of great historical importance. The work of Siegel (1982) was also important historically in providing the background from which LMedS could take off, while the work of Steele and Steiger (1986) showed how LMedS might be implemented with attainable levels of computation.

While much of the work on robust statistics dates from the 1980s, one has only to look at the book by Hartley and Zisserman (2003) to see how deeply embedded it is in the current methodology and thinking on machine vision. An example of its application to 3-D correspondence matching is provided by Hasler et al. (2003): they consider exactly where the outlier data originates and model the whole process. Unexpected motion, occlusion of points in some views, and also viewing of convex boundaries from different positions, all lead to mismatches and outliers; they arrive at a new way of calculating outliers in image pairs, which helps to put the subject area on a more secure footing.

### A.8.1 MORE RECENT DEVELOPMENTS

In many applications RANSAC requires an overly large number of hypotheses to be made before converging to an acceptable solution: this applies especially when searching in high-dimensional spaces. Many attempts have been made to overcome this problem. Myatt et al. (2002) tackled it by noting that in general inliers tend to be closer to one another than to outliers. Their algorithm, called NAPSAC, samples sets of adjacent points in a hypersphere: thereby the probability of selecting an inlying set is significantly increased—as demonstrated using wide baseline stereo-matching data. Torr and Davidson (2003) also produced an improved version of RANSAC, which they called IMPSAC (IMPortance SAMpling Consensus). It works in a hierarchical manner and is initialized at the coarsest level by RANSAC, but then goes on to sample at a finer level to refine relevant a posteriori estimates. While IMPSAC has been applied to 3-D matching tasks, it embodies statistical techniques that can be applied to a wide variety of statistical problems to eliminate outlier corrupted data.

Chum and Matas (2005) developed another idea for improving RANSAC. Instead of using randomly chosen hypotheses, they start by testing the most promising hypotheses and gradually revert to uniform sampling as diminishing returns set in. Their method, called PROSAC, achieves large computational savings and can be as much as 100 times faster than RANSAC, e.g., with wide baseline stereo data. Effectively, PROSAC gains by ordering the hypotheses in an appropriate way. The worst case performance essentially equals that of RANSAC, though no proof exists of this. Ni et al. (2009) developed another variant of RANSAC called GroupSAC. This relies on the assumption that there exists a grouping of the data in which some of the groups have a high inlier ratio, while the others contain mostly outliers. When tested on wide baseline stereo data, GroupSAC was found to be much faster than PROSAC “most of the time,” and RANSAC was always

slower than either. Méler et al. (2010) devised yet another variant of RANSAC called BetaSAC. This was formulated as a general framework for including any relevant information for improving performance. BetaSAC offers a conditional sampling which is able to generate more suitable samples than pure random during the initial iterations. The only hypothesis required is that suitable samples can be built by successive data point selections. In the case of random ranking of samples, the method reverts to the same performance as RANSAC. When used for homography estimation, the method is always faster than RANSAC and typically 10–40 times faster than PROSAC.

---

## A.9 PROBLEMS

1. What is meant by the *breakdown point* of a data analysis method? Show how it is related to the concept of robustness. Consider also how accuracy of measurement is affected by the proportion of data points that are fully utilized by the data analysis method. Discuss the situation in relation to (1) the mean, (2) the median, and (3) the result of applying a Hampel three-part redescending M-estimator.
2. A method for locating straight lines in digital images involves taking every pair of edge points and finding where a line through both points of a pair intercepts the  $x$  and  $y$  axes. Then, medians for all such intercepts are found and the positions of any straight lines are deduced. Show that the effect of taking pairs is to reduce the breakdown point from 50% to around 30% and give an exact answer for the breakdown point. (*Hint:* start by assuming that the fraction of outliers in the original set of edge points is  $\varepsilon$  and work out the probability of half the intercept values being correct.)

# The sampling theorem

# B

In vision, everything depends on image acquisition. In the modern age, image acquisition invariably involves sampling the underlying analog signals to convert them to digital form. Ultimately, sampling is subject to the mathematical rules that are embodied in the sampling theorem. These are vitally important if we are to obtain digital signals that accurately reflect the original analog ones. It is the purpose of this appendix to remind the reader about this fundamental process.

## B.1 THE SAMPLING THEOREM

The Nyquist sampling theorem underlies all situations where continuous signals are sampled and is especially important where patterns are to be digitized and analyzed by computers. This makes it highly relevant both with visual patterns and with acoustic waveforms: hence it is described briefly in this section.

Consider the sampling theorem first in respect of a 1-D time-varying waveform. The theorem states that a sequence of samples (Fig. B.1) of such a waveform contains all the original information and can be used to regenerate the original waveform exactly, but only if (1) the bandwidth  $W$  of the original waveform is restricted and (2) the rate of sampling  $f$  is at least twice the bandwidth of the original waveform—i.e.,  $f \geq 2W$ . Assuming that samples are taken every  $T$  seconds, this means that  $1/T \geq 2W$ .

At first, it may be somewhat surprising that the original waveform can be reconstructed exactly from a set of discrete samples. However, the two conditions for achieving this are very stringent. What they are demanding in effect is that the signal must not be permitted to change unpredictably (i.e., at too fast a rate) or else accurate interpolation between the samples will not prove possible (the errors that arise from this source are called “aliasing” errors).

Unfortunately, the first condition is virtually unrealizable, since it is close to impossible to devise a low-pass filter with a perfect cutoff. Recall from Chapter 3, Image Filtering and Morphology that a low-pass filter with a perfect cutoff will have infinite extent in the time domain, so any attempt at achieving



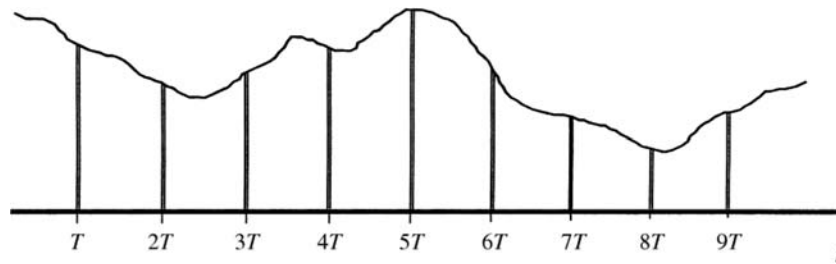


FIGURE B.1

The process of sampling a time-varying signal: a continuous time-varying 1-D signal is sampled by narrow sampling pulses at a regular rate  $f_r = 1/T$  which must be at least twice the bandwidth of the signal.

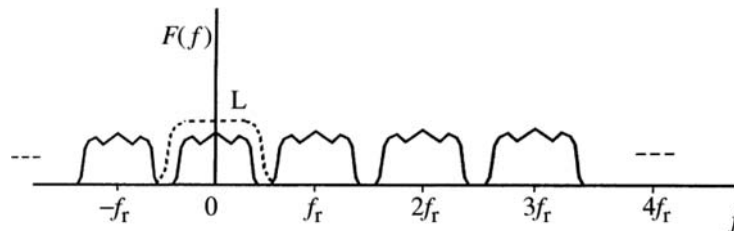
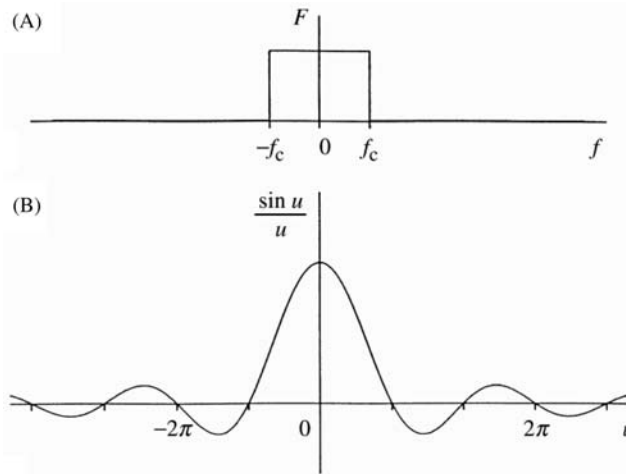


FIGURE B.2

Effect of low-pass filtering to eliminate repeated spectra in the frequency domain ( $f_r$ , sampling rate; L, low-pass filter characteristic). This diagram shows the repeated spectra of the frequency transform  $F(f)$  of the original sampled waveform. It also demonstrates how a low-pass filter can be expected to eliminate the repeated spectra to recover the original waveform.

the same effect by time domain operations must be doomed to failure. However, acceptable approximations can be achieved by allowing a “guard-band” between the desired and actual cutoff frequencies. This means that the sampling rate must be higher than the Nyquist rate (in telecommunications, satisfactory operation can generally be achieved at sampling rates around 20% above the Nyquist rate—see Brown and Glazier, 1974).

One way of recovering the original waveform is by applying a low-pass filter. This approach is intuitively correct, since it acts in such a way as to broaden the narrow discrete samples until they coalesce and sum to give a continuous waveform. Indeed, this method acts in such a way as to eliminate the “repeated” spectra in the transform of the original sampled waveform (Fig. B.2): this in itself shows why the original waveform has to be narrow-banded before sampling—so that the repeated and basic spectra of the waveform do not cross over each other and become impossible to separate with a low-pass filter. The idea may be taken further because the Fourier transform of a square cutoff filter is the sinc ( $\sin u/u$ )

**FIGURE B.3**

The sinc ( $\sin u/u$ ) function shown in (B) is the Fourier transform of a square pulse (A) corresponding to an ideal low-pass filter. In this case,  $u = 2\pi f_c t$ ,  $f_c$  being the cutoff frequency.

function (Fig. B.3). Hence, the original waveform may be recovered by convolving the samples with the sinc function (which in this case means replacing them by sinc functions of corresponding amplitudes). This has the effect of broadening out the samples as required, until the original waveform is recovered.

So far we have considered the situation only for 1-D time-varying signals. However, recalling that there is an exact mathematical correspondence between time and frequency domain signals on the one hand and spatial and spatial frequency signals on the other, the above ideas may all be applied immediately to each dimension of an image (although the condition for accurate sampling now becomes  $1/X \geq 2W_X$ , where  $X$  is the spatial sampling period and  $W_X$  is the spatial bandwidth). Here we accept this correspondence without further discussion and proceed to apply the sampling theorem to image acquisition.

Consider next how the signal from a camera may be sampled rigorously according to the sampling theorem. First, note that this has to be achieved both horizontally and vertically. Perhaps the most obvious solution to this problem is to perform the process optically, perhaps by defocussing the lens; however, the optical transform function for this case is frequently (i.e., for extreme cases of defocussing) very odd, going negative for some spatial frequencies and causing contrast reversals; hence this solution is far from ideal (Pratt, 2001). Alternatively, we could use a diffraction-limited optical system or perhaps pass the focused beam through some sort of patterned or frosted glass to reduce the spatial bandwidth artificially. None of these techniques will be particularly easy to apply nor (apart possibly from the second) will it give accurate solutions. However, this problem is not as serious

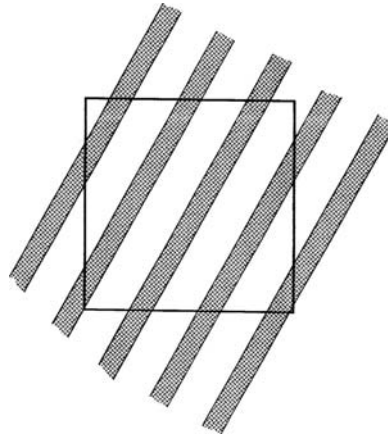


**FIGURE B.4**

Low-pass filtering carried out by averaging over the pixel region: an image with local high-frequency banding is to be averaged over the whole pixel region by the action of the sensing device.

as might be imagined. If the sensing region of the camera (per pixel) is reasonably large, and close to the size of a pixel, then the averaging inherent in obtaining the pixel intensities will in fact perform the necessary narrow-banding (Fig. B.4). To analyze the situation in more detail, note that a pixel is essentially square with a sharp cutoff at its borders: thus its spatial frequency pattern is a 2-D sinc function, which (taking the central positive peak) approximates to a low-pass spatial frequency filter: This approximation improves somewhat as the border between pixels becomes more fuzzy.

The point here is that the worst case from the point of view of the sampling theorem is that of extremely narrow discrete samples, but clearly this worst case is most unlikely to occur with most cameras. However, this does not mean that sampling is automatically ideal—and indeed it is not, since the spatial frequency pattern for a sharply defined pixel shape has (in principle) infinite extent in the spatial frequency domain. The review by Pratt (2001) clarifies the situation and shows that there is a tradeoff between aliasing and resolution error. Overall, quality of sampling will be one of the limiting factors if the greatest precision in image measurement is aimed for: if the bandwidth of the presampling filter is too low, resolution will be lost; if it is too high, aliasing distortions will creep in; and if its spatial frequency response curve is not suitably smooth, a guard band will have to be included and performance will again suffer.

The sampling theorem is well-covered in very many books on signal processing (see for example, Rosie, 1966), though details of how band-limiting should be carried out prior to sampling are not so readily available. See Pratt (2001) for further information and references about sampling in the imaging context.

# The representation of color

# C

Color input for computer vision is normally in RGB (red, green, blue) format, with typically one byte of data for each of the three input channels. However, just as the eye perceives color images subjectively as color, so it is convenient to match this using a suitable computer representation, such as HSI (hue, saturation, intensity). In HSI, the color is represented entirely by the hue channel; the brightness is represented by the intensity channel; and the saturation channel represents the *degree of coloration* present in the original RGB signal—i.e., the extent to which the color is diluted by white light.

*Look out for:*

- formulae defining the  $H$ ,  $S$ ,  $I$  parameters
- the periodic nature of the hue parameter and the complications it leads to
- the problems of achieving color constancy
- applications for which color-based segmentation is particularly beneficial.

It often happens that images have varying intensity because of random changes in illumination or because of shadows across the field of view. In such cases it can be useful to ignore the intensity and to rely on the hue parameter. More generally, it is desirable to utilize the whole HSI color space so that maximum information is available for color-based object segmentation.

## C.1 INTRODUCTION

In the early days of computer vision, digitizers usually inputted gray-scale images and thus processing was restricted to the analysis of gray-scale images. However, over the past two decades, color input has become almost universal and processing capabilities have evolved to match this requirement. Color input is normally in RGB format, with typically one byte of data for each of the three input channels. However, just as the eye perceives color images subjectively as color, so it is convenient to match this via a suitable computer representation. In fact, a great variety of color representations can be used for the purpose, depending on the requirements and whether, for example, the results are to be presented to a computer image analyzer, a display or a printer. Here we consider only computer analysis, and choose the HSI representation, which is well adapted to the task. In particular, when converting from RGB to HSI, the actual color is represented entirely by the hue channel; the brightness is represented by the intensity channel;

this leaves the saturation channel to represent the *degree of coloration* present in the original RGB signal: i.e., the saturation channel shows the extent to which the color is diluted by white light.

It often happens that images have varying intensity because of random changes in illumination or because of shadows across the field of view. In such cases it can be useful to ignore the intensity information and to provide an interpretation based on color alone: in that case it can be more reliable to base an interpretation on the data issuing from the hue channel alone. This is the strategy that is normally adopted in applications such as inspection, surveillance, and face recognition when undesired intensity variations are to be expected.

However, more sophisticated solutions are possible and in principle necessary. This is because variations in the color of the ambient light can themselves lead to different apparent colors in the light reflected from objects. In spite of this, the human eye exhibits the property of *color constancy*, reflected light *not* appearing to change as a result of variations in the color of the ambient light. Though arduous, it is possible to achieve this by computer processing, but we shall not explore this possibility further here.

---

## C.2 DETAILS OF THE HSI COLOR REPRESENTATION

As indicated above, it is common practice to concentrate on the hue parameter when the intensity parameter varies significantly because of random changes in illumination or because of shadows that may move across the field of view. Essentially, the hue parameter is independent of the intensity parameter as it varies in a plane in color space orthogonal to the intensity vector, so it holds the most undistorted and therefore the most meaningful information.

However, more generally, it is desirable to employ the whole HSI color space, so that the maximum information is available for image interpretation and in particular for color-based object segmentation. For example, we might wish to locate road signs by their colors, tomatoes by their red skins, or human faces using skin color recognition.

To carry out such tasks, we must first convert the incoming data from RGB to HSI format. First, we need to define the three HSI parameters, which we do using the formulae presented below. The most straightforward definition is that of intensity  $I$ : this is the mean light intensity, which is given by

$$I = \frac{1}{3}(R + G + B) \quad (\text{C.1})$$

Hue  $H$  is a measure of the underlying color, and saturation  $S$  is a measure of the degree to which the color is *not* diluted by white light ( $S$  is zero for white light and is unity for *least* dilution of the colors).  $S$  is given by the following formula:

$$S = 1 - \frac{\min(R, G, B)}{I} = 1 - \frac{3 \min(R, G, B)}{R + G + B} \quad (\text{C.2})$$

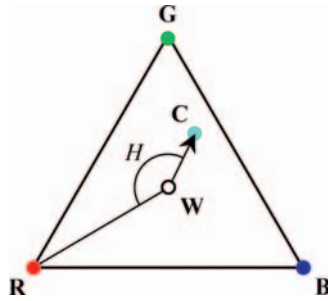


FIGURE C.1

View of the color triangle **RGB**. This contains all possible colors in all possible dilutions with white light. It is suspended between its three corners, which are points on the three color axes, indicated here by the colored dots marked as vectors **R**, **G**, **B**. White light is indicated by the vector **W** at the center of the color triangle. An arbitrary color **C** is located by hue angle  $H$  relative to the vector **R**–**W**. The diagram is 2-D and is spanned by the hue angle  $H$  and by the saturation level  $S$  (see text). Intensity  $I$  does not appear in the diagram as the latter is drawn for a constant intensity: in fact, intensity variation takes place along an axis orthogonal to the color triangle, passing through the white spot **W** at the center of the color triangle. Note that the whole side of the triangle opposite to the red dot has  $R = 0$ , and similarly for the sides opposite to the green and blue dots.

which makes it unity along the sides of the color triangle (i.e., where  $R = 0$  or  $G = 0$  or  $B = 0$ ), and zero for white light ( $R = G = B = I$ ). Note how the equation for  $S$  favors none of the  $R, G, B$  components. We emphasize that  $S$  does not express color itself but is a measure of the *proportion* of color relative to pure white. Fig. C.1 depicts the color triangle: its three corners are the points where the  $(R, G, B)$  axes (in RGB color space) cross a given constant  $I$  color plane.

Hue is defined as an angle  $H$  of rotation about the central white point **W** in the color triangle: it is the angle between the pure red direction (defined by the vector **R**–**W**) and the direction of the color **C** in question (defined by the vector **C**–**W**). The derivation of a formula for  $H$  is fairly complex and will not be attempted here. Suffice it to say that it may be determined by calculating  $\cos H$ , which depends on the dot product  $(\mathbf{C}-\mathbf{W}) \times (\mathbf{R}-\mathbf{W})$ . The final result is

$$H = \cos^{-1} \left( \frac{\frac{1}{2}[(R - G) + (R - B)]}{[(R - G)^2 + (R - B)(G - B)]^{1/2}} \right) \quad (\text{C.3})$$

or  $2\pi$  minus this value if  $B > G$  (Gonzalez and Woods, 1992).

The above discussion shows that hue is a 1-D parameter. In fact, it is a *periodic* parameter as hue is an angle with a period of  $2\pi$ . While this might appear to be only a marginal factor, it has the effect of complicating a number of image analysis computations. First, if the hue variable is to be smoothed using a 1-D moving average filter, care will have to be taken at the ends of the range 0 to  $2\pi$ . Second, if the smoothing is to be done using a 1-D median filter, the operation

cannot properly be defined because the hue values are double-valued at  $0^\circ$ . (This means that there is no unique ordering of the hue values by which to define a median value.)

Finally, the ranges of values of  $R$ ,  $G$ ,  $B$ , and  $I$  are given by the particular digitization used: we here assume that there is one byte of data for each of the RGB color parameters—in which case we have  $0 \leq R, G, B, I \leq 255$ .

---

### C.3 A TYPICAL EXAMPLE OF THE USE OF COLOR

There is one area where color has a large part to play: that is in the automatic picking, inspection, and sorting of fruit. In particular, color is very important in the determination of apple quality. Not only is it a prime indicator of ripeness, but also it contributes greatly to physical attractiveness—not least with regard to readiness for eating. Clearly, for the computer to emulate human performance in assessing the appearance of fruit, it is useful to convert the RGB representation to the HSI domain before making any judgments about color.

In the work of Heinemann et al. (1995), discriminant analysis of color based on this approach gave complete agreement between human inspectors and the computer following training on 80 samples and testing on another 66 samples. However, a warning was given about maintaining lighting intensity levels identical to those used for training: in any such pattern recognition system, it is crucial that the training set be fully representative of the eventual test set.

When checking the color of apples, the hue is the important parameter. A rigorous check on the color can be achieved by constructing the hue distribution and comparing it with that for a suitable training set. The most straightforward way to carry out the comparison is to compute the mean and standard deviation of the two distributions to be compared and to perform discriminant analysis assuming Gaussian distribution functions. The standard theory for maximum likelihood thresholding (Section 4.5.3, Eqs. (4.19)–(4.22)) then leads to an optimum hue decision threshold.

Finally, note that full color discrimination would require an optimal decision surface to be ascertained in the overall 3-D color space. In general, such decision surfaces are hyperellipses and have to be determined using the Mahalanobis distance measure (see, e.g., Webb, 2002). However, in the special case of Gaussian distributions with equal covariance matrices, or more simply with equal isotropic variances, the decision surfaces become hyperplanes.

---

### C.4 BIBLIOGRAPHICAL AND HISTORICAL NOTES

Space prevents a detailed study of the question of color: the reader is referred to more specialized texts for detailed information (e.g., Gonzalez and Woods, 1992; Sangwine and Horne, 1998). Examples of work on color inspection include food (Heinemann et al., 1995) and pharmaceutical products (Derganc et al., 2003). For early work on color constancy, see Forsyth (1990) and Finlayson et al. (2001).

# Sampling from distributions

# D

Sampling from uniform distributions can readily be achieved by using pseudo-random numbers generated by standard library functions. It is less obvious how this can be applied to more general distributions such as Gaussians. However, if the cumulative distribution function (CDF) is calculated, the overall process immediately becomes clear. At that stage the real problem is that it is not possible to deal with the general case analytically, so it is necessary to resort to numerical methods, which tend to be slow. This means that for widely used distributions such as the Gaussian, special methods have to be devised: the Box–Muller method and its polar variant have proved highly useful in this situation.

*Look out for:*

- the CDF approach
- the problems that occur when even the simple Gaussian distribution is to be used
- how these are tackled by the Box–Muller approach
- the gain achieved using the polar variant of the Box–Muller method.

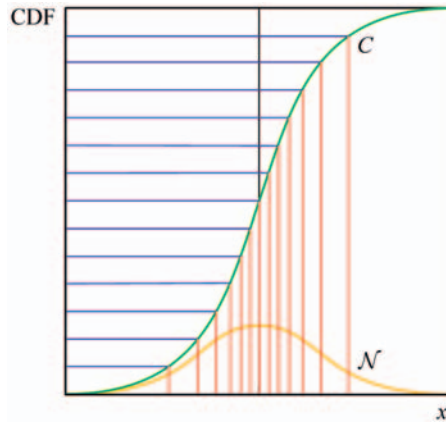
Sampling from distributions is used in [Chapter 14, Machine Learning: Probabilistic Methods](#) for quickly generating 2-D datasets; [Chapter 22, Surveillance](#) outlines how it is used as part of the particle filter approach to object tracking.

## D.1 INTRODUCTION

In many areas of statistics including machine learning, it is useful to be able to represent probability distributions by samples taken from them. Modeling distributions in this way have the effect of greatly simplifying subsequent calculations and vastly reducing computational load. In particular, the Gaussian distribution crops up very frequently in practical situations, and it is often necessary to sample it. However, even for such a simple, well-defined function, it is not altogether obvious how to draw a suitable set of samples. Indeed, the only immediately obvious case is that of the uniform distribution, which is readily sampled using pseudo-random numbers generated by standard library functions (e.g., “rand”).

Fortunately, it is not a big step to proceed from the uniform distribution to the Gaussian distribution. All we need to do is to imagine the  $M$  original measurements that would have composed the discrete histogram  $f(x)$  of the distribution, place all  $M$  of them in numerical order—thereby obtaining a continuous uniform



**FIGURE D.1**

Formation of the cumulative distribution function (CDF). The CDF of the approximately Gaussian distribution function  $\mathcal{N}$  (orange, near the bottom of the figure) is shown higher up in green. Regular, uniformly generated sample positions are selected (blue, on the left ordinate axis): these are carried across to the CDF curve  $C$  and sample locations are marked in red on the original (orange) distribution. High CDF gradient points give high densities of samples along the  $x$ -axis: these are at positions where the original distribution probabilities are greatest.

distribution—and take samples from them using a suitable process. By examining the corresponding values of the original distribution, we obtain the desired set of sample values. All this may be seen from Fig. D.1, which shows the original distribution  $\mathcal{N}$  and its CDF. The ordinate on the left is the continuous uniform distribution forming the set of all possible samples taken from the CDF, and Fig. D.1 shows these being sampled at regular intervals. Intuitively, it is clear that the samples lead to densities (of sample values) along the  $x$ -axis that are proportional to the gradient of the CDF curve; this would also be so for random samples, though in that case the sample locations would have to be smoothed out to get accurate density values. Note that the case of sampling at regular intervals has been used for clarity, but it is usual in statistical and machine learning applications to apply random sampling.

To understand the process more fully, we define the CDF according to the formula:

$$C(x) = \int_{-\infty}^x f(x)dx \quad (\text{D.1})$$

Differentiating immediately leads to the result:

$$f(x) = \frac{dC(x)}{dx} \quad (\text{D.2})$$

This proves our earlier intuitive result—that the density of sampling along  $x$  is proportional to the gradient  $\frac{dC(x)}{dx}$ .

Finally, we should normalize the starting histogram  $f$  to obtain a true probability distribution  $p$ : in that case the CDF will range from 0 to 1, and will take the form:

$$c(x) = \int_{-\infty}^x p(x)dx \quad (\text{D.3})$$

We then have

$$p(x) = \frac{dc(x)}{dx} \quad (\text{D.4})$$

---

## D.2 THE BOX–MULLER AND RELATED METHODS

While the CDF procedure seems sound, it is seldom easy to apply, because of the need to obtain and invert the CDF. In fact, only a limited number of possible probability functions lead to closed form solutions—e.g., the exponential distribution and the Cauchy distribution: in most other cases solutions need to be determined numerically, by methods such as piecewise-linear or polynomial approximation. However, the Gaussian distribution is needed for so many applications that special methods have been devised for sampling it. One such method is to calculate it in 2-D using polar coordinates. To carry this out, we define the Gaussian distribution over a suitable range, such as  $-1$  to  $+1$  in each of the  $x$  and  $y$  directions—though we also restrict it to a distance 0 to 1 radially. Thus we will be sampling within the unit circle:  $0 \leq r \leq 1$ ,  $0 \leq \theta \leq 2\pi$ . The  $r$  samples can be obtained from the uniform distribution Unif(0, 1) and the theta samples from Unif(0,  $2\pi$ ). Finally,  $x$  and  $y$  values can be obtained from the formulae

$$x = r \cos \theta \quad (\text{D.5})$$

$$y = r \sin \theta \quad (\text{D.6})$$

In fact, this approach is useful but excessively computation intensive. However, the method known as the Box–Muller transform overcomes this problem. This first expresses the distribution as

$$\begin{aligned} p(x, y) &= p(x)p(y) \\ &= \frac{1}{(2\pi)^{1/2}} \exp\left(-\frac{x^2}{2}\right) \times \frac{1}{(2\pi)^{1/2}} \exp\left(-\frac{y^2}{2}\right) \\ &= \frac{1}{2\pi} \exp\left(-\frac{x^2 + y^2}{2}\right) \\ &= \frac{1}{2\pi} \exp\left(-\frac{r^2}{2}\right) \end{aligned} \quad (\text{D.7})$$

Note that this equation has converted from Cartesians to polar coordinates, though no variation arises from the  $\theta$  coordinate: this means that the  $\theta$  distribution is subject to a uniform distribution over angles. The Box–Muller distribution takes one further step, using two independent standard uniform random variables  $u_1$  and  $u_2$ , it produces independent standard  $x$  and  $y$  distributions using the following formulae:

$$R^2 = -2 \ln u_1 \tag{D.8}$$

$$\theta = 2\pi u_2 \tag{D.9}$$

This works because  $R^2$  is the square of the norm of the standard 2-D Gaussian variable  $(x, y)$  and has the chi-squared distribution with two degrees of freedom, which means that it is identical to the Gaussian distribution. Using Eqs. (D.8) and (D.9) now permits the values of  $x$  and  $y$  to be deduced using the standard polar coordinate Eqs. (D.5) and (D.6). Note that the method produces two independent Gaussian distributions, of which one can be ignored if only a 1-D solution is required: it is of course useful for sampling from 2-D Gaussian distributions. Refer to the original paper by Box and Muller (1958) and also Pike (1965) for the subtleties of the method and proofs of its validity.

Finally, note that a separate “polar” form of the Box–Muller method is commonly used to eliminate the need to calculate the cos and sine functions, thereby speeding up the algorithm by a further significant factor: this version of the algorithm was developed by Knop (1969) and is perhaps the most widely used as it was included in Press et al. *Numerical Recipes in C* (1997).

In this book, sampling from distributions is implemented in [Chapter 14, Machine Learning: Probabilistic Methods](#), where it is used to generate the starting data in [Fig. 14.3](#) from multiple 2-D Gaussians. It is also relevant for the particle filter calculation presented in [Section 22.4](#): see especially the top parts of [Fig. 22.8](#).

---

### D.3 BIBLIOGRAPHICAL AND HISTORICAL NOTES

Space prevents a more detailed study of sampling from distributions. Bishop (2006) provides useful theory, leading up to the Box–Muller method. For further work it is useful to refer to the original paper by Box and Muller (1958), to Pike (1965), and the quite recent paper by Martino et al. (2012); and for the polar form of the method to Knop (1969) and Press et al. (1997). Rubinstein and Kroese (2007) cover more complex—and often approximate—cases that apply for empirically obtained distributions.

# References

- Abdou, I.E., Pratt, W.K., 1979. Quantitative design and evaluation of enhancement/thresholding edge detectors. *Proc. IEEE* 67, 753–763.
- Abolghasemi, V., Ahmadyfard, A., 2009. An edge-based color-aided method for license plate detection. *Image Vision Comput.* 27, 1134–1142.
- Abutaleb, A.S., 1989. Automatic thresholding of gray-level pictures using two-dimensional entropy. *Comput. Vision Graph. Image Process* 47, 22–32.
- Ade, F., 1983. Characterization of texture by “eigenfilters”. *Signal Process.* 5 (5), 451–457.
- Aggarwal, J.K., Cai, Q., 1999. Human motion analysis: a review. *Comput. Vision Image Understanding* 73 (3), 428–440.
- Agin, G.J., Binford, T.O., 1973. Computer description of curved objects. In: *Proc. Third Int. Joint Conf. on Artif. Intell.*, Stanford, California, pp. 629–640.
- Agin, G.J., Binford, T.O., 1976. Computer description of curved objects. *IEEE Trans. Comput.* 25, 439–449.
- Aguado, A.S., Montiel, M.E., Nixon, M.S., 2000. On the intimate relationship between the principle of duality and the Hough transform. *Proc. Royal Soc. London, Ser. A* 456 (1995), 503–526.
- Aguilar, W., Frauel, Y., Escolano, F., Martinez-Perez, M.E., Espinosa-Romero, A., Lozano, M.A., 2009. A robust Graph Transformation Matching for non-rigid registration. *Image Vision Comput.* 27, 897–910.
- Aleksander, I., Thomas, W.V., Bowden, P.A., 1984. WISARD: a radical step forward in image recognition. *Sens. Rev.* 4, 120–124.
- Ali, S.M., Burge, R.E., 1988. A new algorithm for extracting the interior of bounded regions based on chain coding. *Comput. Vision Graph. Image Process* 43, 256–264.
- Almansa, A., Desolneux, A., Vamech, S., 2003. Vanishing point detection without any a priori information. *IEEE Trans. Pattern Anal. Mach. Intell.* 25 (4), 502–507.
- Alter, T.D., 1994. 3-D pose from 3 points using weak-perspective. *IEEE Trans. Pattern Anal. Mach. Intell.* 16 (8), 802–808.
- Ambler, A.P., Barrow, H.G., Brown, C.M., Burstall, R.M., Popplestone, R.J., 1975. A versatile system for computer-controlled assembly. *Artif. Intell.* 6, 129–156.
- Amit, Y., 2002. *2D Object Detection and Recognition: Models, Algorithms and Networks*. MIT Press, Cambridge, MA.
- An, G., Wu, J., Ruan, Q., 2010. An illumination normalization model for face recognition under varied lighting conditions. *Pattern Recognit. Lett.* 31 (9), 1056–1067.
- Ansar, A., Daniilidis, K., 2003. Linear pose estimation from points or lines. *IEEE Trans. Pattern Anal. Mach. Intell.* 25 (5), 578–589.
- Aragon-Camarasa, G., Siebert, J.P., 2010. Unsupervised clustering in Hough space for recognition of multiple instances of the same object in a cluttered scene. *Pattern Recognit. Lett.* 31, 1274–1284.
- Arcelli, C., di Baja, G.S., 1985. A width-independent fast-thinning algorithm. *IEEE Trans. Pattern Anal. Mach. Intell.* 7, 463–474.
- Arcelli, C., Ramella, G., 1995. Finding grey-skeletons by iterated pixel removal. *Image Vision Comput.* 13 (3), 159–167.

- Arcelli, C., Cordella, L.P., Levialdi, S., 1975. Parallel thinning of binary pictures. *Electron. Lett.* 11, 148–149.
- Arcelli, C., Cordella, L.P., Levialdi, S., 1981. From local maxima to connected skeletons. *IEEE Trans. Pattern Anal. Mach. Intell.* 3, 134–143.
- Arnold, R.D., 1978. Local context in matching edges for stereo vision. *Proc. Image Understanding Workshop*, Cambridge, Massachusetts. 65–72.
- Arulampalam, M.S., Maskell, S., Gordon, N., Clapp, T., 2002. A tutorial on particle filters for online nonlinear/non-Gaussian Bayesian tracking. *IEEE Trans. Signal Process.* 50 (2), 174–188.
- Assheton, P., Hunter, A., 2011. A shape-based voting algorithm for pedestrian detection and tracking. *Pattern Recognit.* 44, 1106–1120.
- Åström, K., 1995. Fundamental limitations on projective invariants of planar curves. *IEEE Trans. Pattern Anal. Mach. Intell.* 17 (1), 77–81.
- Atherton, T.J., Kerbyson, D.J., 1999. Size invariant circle detection. *Image Vision Comput.* 17 (11), 795–803.
- Atiqzaman, M., Akhtar, M.W., 1994. Complete line segment description using the Hough transform. *Image Vision Comput.* 12 (5), 267–273.
- Babaud, J., Witkin, A.P., Baudin, M., Duda, R.O., 1986. Uniqueness of the Gaussian kernel for scale-space filtering. *IEEE Trans. Pattern Anal. Mach. Intell.* 8, 26–33.
- Badrinarayanan, V., Kendall, A., Cipolla, R., 2015. SegNet: A Deep Convolutional Encoder-Decoder Architecture for Image Segmentation. *arXiv:1511.00561v2 [cs.CV]* 8 Dec.
- Bai, X., Latecki, L.J., 2008. Path similarity skeleton graph matching. *IEEE Trans. Pattern Anal. Mach. Intell.* 30 (7), 1282–1292.
- Bai, X.Z., Zhou, F.G., 2010. Top-hat selection transformation for infrared dim small target enhancement. *Imag. Sci.* 58 (2), 112–117.
- Bai, Y., Ma, W., Li, Y., Cao, L., Guo, W., Yang, L., 2016. Multi-scale fully convolutional network for fast face detection. In: *Proc. British Machine Vision Association Conference*. 19–22 September, York. <http://www.bmva.org/bmvc/2016/papers/paper051/paper051.pdf>.
- Bailey, D.G., 2011. *Design for Embedded Image processing on FPGAs*. Wiley IEEE Press, Singapore.
- Bajcsy, R., 1973. Computer identification of visual surface. *Comput. Graph. Image Process.* 2, 118–130.
- Bajcsy, R., Liebermann, L., 1976. Texture gradient as a depth cue. *Comput. Graph. Image Process.* 5 (1), 52–67.
- Baker, S., Sim, T., Kanade, T., 2003. When is the shape of a scene unique given its light-field: a fundamental theorem of 3D vision? *IEEE Trans. Pattern Anal. Mach. Intell.* 25 (1), 100–109.
- Ball, G.H. and Hall, D.J., 1966. ISODATA, an iterative method of multivariate data analysis and pattern classification. In: *IEEE Int. Communications Conf., Philadelphia, Digest of Techn. Papers II*, pp. 116–117.
- Ballard, D.H., 1981. Generalizing the Hough transform to detect arbitrary shapes. *Pattern Recognit.* 13, 111–122.
- Ballard, D.H., Brown, C.M., 1982. *Computer Vision*. Prentice-Hall, Englewood Cliffs, NJ.
- Ballard, D.H., Sabbah, D., 1983. Viewer independent shape recognition. *IEEE Trans. Pattern Anal. Mach. Intell.* 5, 653–660.

- Bangham, J.A., Marshall, S., 1998. Image and signal processing with mathematical morphology. *IEE Electron. Commun. Eng. J.* 10 (3), 117–128.
- Barnard, S., 1983. Interpreting perspective images. *Artif. Intell.* 21, 435–462.
- Barnard, S.T., Thompson, W.B., 1980. Disparity analysis of images. *IEEE Trans. Pattern Anal. Mach. Intell.* 2 (4), 333–340.
- Barnea, D.I., Silverman, H.F., 1972. A class of algorithms for fast digital image registration. *IEEE Trans. Comput.* 21, 179–186.
- Barrett, E.B., Payton, P.M., Haag, N.N., Brill, M.H., 1991. General methods for determining projective invariants in imagery. *Comput. Vision Graph. Image Process* 53 (1), 46–65.
- Barrow, H.G., Poplestone, R.J., 1971. Relational descriptions in picture processing. In: Meltzer, B., Michie, D. (Eds.), *Machine Intelligence 6*. Edinburgh University Press, Edinburgh, pp. 377–396.
- Barrow, H.G., Tenenbaum, J.M., 1981. Computational vision. *Proc. IEEE* 69, 572–595.
- Barrow, H.G., Ambler, A.P., Burstall, R.M., 1972. Some techniques for recognising structures in pictures. In: Watanabe, S. (Ed.), *Frontiers of Pattern Recognition*. Academic Press, New York, pp. 1–29.
- Barsky, S., Petrou, M., 2003. The 4-source photometric stereo technique for three-dimensional surfaces in the presence of highlights and shadows. *IEEE Trans. Pattern Anal. Mach. Intell.* 25 (10), 1239–1252.
- Bartoli, A., Sturm, P., 2004. Nonlinear estimation of the fundamental matrix with minimal parameters. *IEEE Trans. Pattern Anal. Mach. Intell.* 26 (3), 426–432.
- Bartz, M.R., 1968. The IBM 1975 optical page reader. *IBM J. Res. Dev.* 12, 354–363.
- Bascle, B., Bouthemy, P., Deriche, R. and Meyer, F., 1994. Tracking complex primitives in an image sequence. In: *Proc. 12th Int. Conf. on Pattern Recognition*. 9–13 Oct., Jerusalem, Israel, Vol. A, pp. 426–431.
- Batchelor, B.G., 1979. Using concavity trees for shape description. *Comput. Digital Tech.* 2, 157–165.
- Battle, J., Marti, J., Ridao, P., Amat, J., 2002. A new FPGA/DSP-based parallel architecture for real-time image processing. *Real-Time Imaging* 8 (5), 345–356.
- Bay, H., Ess, A., Tuytelaars, T., Van Gool, L., 2008. Speeded-up robust features (SURF). *Comput. Vision Image Understanding* 110 (3), 346–359.
- Bay, H., Tuytelaars, T. and Van Gool, L., 2006. SURF: speeded up robust features. In: *Proc. Ninth European Conf. on Computer Vision (ECCV)*. Springer LNCS Vol. 3951, part 1, pp. 404–417.
- Beaton, A.E., Tukey, J.W., 1974. The fitting of power series, meaning polynomials, illustrated on band-spectroscopic data. *Technometrics* 16 (2), 147–185.
- Beaudet, P.R., 1978. Rotationally invariant image operators. In: *Proc. Fourth Int. Conf. on Pattern Recognition*. Kyoto, pp. 579–583.
- Beckers, A.L.D., Smeulders, A.W.M., 1989. A comment on “a note on ‘distance transformations in digital images’”. *Comput. Vision Graph. Image Process* 47, 89–91.
- Beiden, S.V., Maloof, M.A., Wagner, R.F., 2003. A general model for finite-sample effects in training and testing of competing classifiers. *IEEE Trans. Pattern Anal. Mach. Intell.* 25 (12), 1561–1569.
- Bejiga, M.B., Zeggada, A., Nouffidj, A., Melgani, F., 2017. A convolutional neural network approach for assisting avalanche search and rescue operations with UAV imagery. *Remote Sens.* 9 (100), 1–22.

- Belhumeur, P.N., Hespanha, J.P., Kriegman, D.J., 1997. Eigenfaces vs. Fisherfaces: recognition using class specific linear projection. *IEEE Trans. Pattern Anal. Mach. Intell.* 19 (7), 711–720.
- Belhumeur, P.N., Jacobs, D.W., Kriegman, D., and Kumar, N., 2011. Localizing parts of faces using a consensus of exemplars. In: *Proc. IEEE Conf. on Computer Vision and Pattern Recognition*. 20–25 June, Colorado Springs, CO, pp. 545–552.
- Bergholm, F., 1986. Edge focusing. In: *Proc. Eighth Int. Conf. on Pattern Recognition*. 27–31 October, Paris, pp. 597–600.
- Berman, S., Parikh, P., Lee, C.S.G., 1985. Computer recognition of two overlapping parts using a single camera. *IEEE Computer* 18 (3), 70–80.
- Bertozzi, M., Broggi, A., 1998. GOLD: a parallel real-time stereo vision system for generic obstacle and lane detection. *IEEE Trans. Image Process.* 7 (1), 62–81.
- Besl, P.J., Birch, J.B., Watson, L.T., 1989. Robust window operators. *Mach. Vision Appl.* 2, 179–191.
- Beun, M., 1973. A flexible method for automatic reading of handwritten numerals. *Philips Tech. Rev.* 33, 89–101; 130–137.
- Billingsley, J., Schoenfish, M., 1995. Vision-guidance of agricultural vehicles. *Auton. Robots* 2 (1), 65–76.
- Birchfield, S., 1998. Elliptical head tracking using intensity gradients and color histograms. In: *Proc. IEEE Conf. on Computer Vision and Pattern Recognition*. Santa Barbara, CA, pp. 232–237.
- Bishop, C., 1995. *Neural Networks for Pattern Recognition*. Oxford University Press, Oxford, UK.
- Bishop, C.M., 2006. *Pattern Recognition and Machine Learning*. Springer-Verlag, Berlin, Heidelberg.
- Blake, A., Zisserman, A., Knowles, G., 1985. Surface descriptions from stereo and shading. *Image Vision Comput.* 3, 183–191.
- Blanz, V., Vetter, T., 2003. Face recognition based on fitting a 3D morphable model. *IEEE Trans. Pattern Anal. Mach. Intell.* 25 (9), 1063–1073.
- Bledsoe, W.W., Browning, I., 1959. Pattern recognition and reading by machine. *Proc. East. Joint Comput. Conf.* 225–232.
- Blum, H., 1967. A transformation for extracting new descriptors of shape. In: Wathen-Dunn, W. (Ed.), *Models for the Perception of Speech and Visual Form*. MIT Press, Cambridge, MA, pp. 362–380.
- Blum, H., Nagel, R.N., 1978. Shape description using weighted symmetric axis features. *Pattern Recognit.* 10, 167–180.
- Bober, M. and Kittler, J., 1993. Estimation of complex multimodal motion: an approach based on robust statistics and Hough transform. In: *Proc. Fourth British Machine Vision Assoc. Conf.*, Univ. of Surrey. 21–23 Sept., Vol. 1, pp. 239–248.
- Bolles, R.C., 1979. Robust feature matching via maximal cliques. In: *SPIE*, 182. *Proc. Technical Symposium on Imaging Applications for Automated Industrial Inspection and Assembly*. April, Washington D.C., pp. 140–149.
- Bolles, R.C., Cain, R.A., 1982. Recognizing and locating partially visible objects: the local-feature-focus method. *Int. J. Robot. Res.* 1 (3), 57–82.
- Bolles, R.C., Horaud, R., 1986. 3DPO: a three-dimensional part orientation system. *Int. J. Robot. Res.* 5 (3), 3–26.
- Borkar, A., Hayes, M. and Smith, M.T., 2009. Robust lane detection and tracking with RANSAC and Kalman filter. In: *IEEE Int. Conf. on Image Processing*. 7–10 November, Cairo, Egypt, pp. 3261–3264.

- Bors, A.G., Hancock, E.R., Wilson, R.C., 2003. Terrain analysis using Radar shape-from-shading. *IEEE Trans. Pattern Anal. Mach. Intell.* 25 (8), 974–992.
- Boufama, B., Mohr, R., Morin, L., 1998. Using geometric properties for automatic object positioning. *Image Vision Comput.* 16 (1), 27–33.
- Bovik, A.C., Huang, T.S., Munson, D.C., 1983. A generalization of median filtering using linear combinations of order statistics. *IEEE Trans. Acoust. Speech Signal Process.* 31 (6), 1342–1349.
- Bovik, A.C., Huang, T.S., Munson, D.C., 1987. The effect of median filtering on edge estimation and detection. *IEEE Trans. Pattern Anal. Mach. Intell.* 9, 181–194.
- Box, G.E.P., Muller, M.E., 1958. A note on the generation of random normal deviates. *Ann. Math. Stat.* 29 (2), 610–611.
- Boykov, Y., Funka-Lea, G., 2006. Graph cuts and efficient N-D image segmentation. *Int. J. Comput. Vision* 70 (2), 109–131.
- Boykov, Y. and Jolly, M.-P., 2001. Interactive graph cuts for optimal boundary and region segmentation of objects in N-D images. In: *Proc. Int. Conf. on Computer Vision*. July, Vol. I, pp. 105–112.
- Boykov, Y., Kolmogorov, V., 2004. An experimental comparison of min-cut/max-flow algorithms for energy minimization in vision. *IEEE Trans. Pattern Anal. Mach. Intell.* 26 (9), 1124–1137.
- Brady, J.M., Wang, H., 1992. Vision for mobile robots. *Philos. Trans. Royal Soc. London, Ser. B* 337, 341–350.
- Brady, J.M., Yuille, A., 1984. An extremum principle for shape from contour. *IEEE Trans. Pattern Anal. Mach. Intell.* 6, 288–301.
- Brady, M., 1982. Computational approaches to image understanding. *Comput. Surv.* 14, 3–71.
- Breiman, L., 1996. Bagging predictors. *Mach. Learn.* 24 (2), 123–140.
- Bretsch, J., 1981. *Automated Inspection Systems for Industry*. IFS Publications Ltd, Bedford, UK.
- Brink, A.D., 1992. Thresholding of digital images using two-dimensional entropies. *Pattern Recognit.* 25, 803–808.
- Brivot, R., Marchant, J.A., 1996. Segmentation of plants and weeds for a precision crop protection robot using infrared images. *IEE Proc. Vision Image Signal Process.* 143 (2), 118–124.
- Broggi, A., Bertozzi, M., Fascioli, A., 2000. Architectural issues on vision-based automatic vehicle guidance: the experience of the ARGO project. *Real-Time Imaging* 6 (4), 313–324.
- Bron, C., Kerbosch, J., 1973. Algorithm 457: finding all cliques in an undirected graph [H]. *Commun. ACM* 16, 575–577.
- Brooks, M.J., 1976. *Locating Intensity Changes in Digitised Visual Scenes*. Computer Science Memo-15 (from MSc Thesis), University of Essex, Colchester, Essex, UK.
- Brooks, M.J., 1978. Rationalising edge detectors. *Comput. Graph. Image Process.* 8, 277–285.
- Brostow, G., Fauqueur, J., Cipolla, R., 2009. Semantic object classes in video: a high-definition ground truth database. *Pattern Recognit. Lett.* 30 (2), 88–97.
- Brown, C.M., 1984. Peak-finding with limited hierarchical memory. In: *Proc. Seventh Int. Conf. on Pattern Recognition*. 30 July–2 August, Montreal, pp. 246–249.
- Brown, J., Glazier, E.V.D., 1974. *Telecommunications*, second ed. Chapman and Hall, London.



- Brown, M.Z., Burschka, D., Hager, G.D., 2003. Advances in computational stereo. *IEEE Trans. Pattern Anal. Mach. Intell.* 25 (8), 993–1008.
- Bruckstein, A.M., 1988. On shape from shading. *Comput. Vision Graph. Image Process* 44, 139–154.
- Buch, N., Orwell, J., Velastin, S.A., 2010. Urban road user detection and classification using 3D wire frame models. *IET Comput. Vision* 4 (2), 105–116.
- Bunke, H., 1999. Error correcting graph matching: on the influence of the underlying cost function. *IEEE Trans. Pattern Anal. Mach. Intell.* 21 (9), 917–922.
- Bunke, H., Shearer, K., 1998. A graph distance metric based on the maximal common sub-graph. *Pattern Recognit. Lett.* 19, 255–259.
- Burr, D.J. and Chien, R.T., 1977. A system for stereo computer vision with geometric models. In: *Proc. Fifth Int. Joint Conf. on Artif. Intell.* Boston, p. 583.
- Cai, H., Mikolajczyk, K., Matas, J., 2011. Learning linear discriminant projections for dimensionality reduction of image descriptors. *IEEE Trans. Pattern Anal. Mach. Intell.* 33 (2), 338–352.
- Calderara, S., Prati, A., Cucchiara, R., 2008. HECOL: homography and epipolar-based consistent labeling for outdoor park surveillance. *Comput. Vision Image Understanding* 111 (1), 21–42.
- Califano, A., Mohan, R., 1994. Multidimensional indexing for recognizing visual shapes. *IEEE Trans. Pattern Anal. Mach. Intell.* 16 (4), 373–392.
- Canny, J., 1986. A computational approach to edge detection. *IEEE Trans. Pattern Anal. Mach. Intell.* 8, 679–698.
- Cao, Q., Ying, Y., and Li, P., 2013. Similarity metric learning for face recognition. In: *Proc. IEEE Int. Conf. on Computer Vision.* 1–8 December, Darling Harbour, Sydney, pp. 2408–2415.
- Cao, X., Wei, Y., Wen, F., and Sun, J., 2012. Face alignment by explicit shape regression. In: *Proc. IEEE Conf. on Computer Vision and Pattern Recognition.* 16–21 June, Providence, RI.
- Caselles, V., Kimmel, R., Sapiro, G., 1997. Geodesic active contours. *Int. J. Comput. Vision* 21 (1), 61–79.
- Cauchie, J., Fiolet, V., Villers, D., 2008. Optimization of an Hough transform algorithm for the search of a center. *Pattern Recognit.* 41, 567–574.
- Celebi, M.E., 2009. Real-time implementation of order-statistics-based directional filters. *IET Image Process.* 3 (1), 1–9.
- Chakravarty, I., Freeman, H., 1982. Characteristic views as a basis for three-dimensional object recognition. *Proc. Soc. Photo-opt. Instrum. Eng. Conf. Robot Vision* 336, 37–45.
- Chakravarty, V.S., Kompella, B., 2003. The shape of handwritten characters. *Pattern Recognit. Lett.* 24 (12), 1901–1913.
- Chandra, B., Kothari, R., Paul, P., 2010. A new node splitting measure for decision tree construction. *Pattern Recognit.* 43, 2725–2731.
- Chang, I.-C., Lin, S.-Y., 2010. 3D human motion tracking based on a progressive particle filter. *Pattern Recognit.* 43, 3621–3635.
- Chang, S.-L., Chen, L.-S., Chung, Y.-C., Chen, S.-W., 2004. Automatic license plate recognition. *IEEE Trans. Intell. Transp. Syst.* 5 (1), 42–53.
- Charles, D. and Davies, E.R., 2003a. Properties of the mode filter when applied to colour images. In: *Proc. IEE Int. Conf. on Visual Information Engineering, VIE 2003.* 7–9 July, Surrey, IEE Conference Publication 495, pp. 101–104.

- Charles, D. and Davies, E.R., 2003b. Distance-weighted median filters and their application to colour images. In: Proc. IEE Int. Conf. on Visual Information Engineering, VIE 2003. 7–9 July, Surrey, IEE Conference Publication 495, pp. 117–120.
- Charles, D., Davies, E.R., 2004. Mode filters and their effectiveness for processing colour images. *Imag. Sci.* 52 (1), 3–25.
- Chasles, M., 1855. Question no. 296. *Nouv. Ann. Math.* 14, 50.
- Chauduri, B.B., 1994. Dynamic clustering for time incremental data. *Pattern Recognit. Lett.* 15 (1), 27–34.
- Chen, S., Yang, X., Cao, G., 2009. Impulse noise suppression with an augmentation of ordered difference noise detector and an adaptive variational method. *Pattern Recognit. Lett.* 30 (4), 460–467.
- Chen, W., Zhang, M.-J., Xiong, Z.-H., 2011. Fast semi-global stereo matching via extracting disparity candidates from region boundaries. *IET Comput. Vision* 5 (2), 143–150.
- Chen, Y., Adjouadi, M., Han, C., Wang, J., Barreto, A., Rishe, N., Andrian, J., 2010. A highly accurate and computationally efficient approach for unconstrained iris segmentation. *Image Vision Comput.* 28, 261–269.
- Cheng, H.-Y., Yu, C.-C., Tseng, C.-C., Fan, K.-C., Hwang, J.-N., Jeng, B.-S., 2010. Environment classification and hierarchical lane detection for structured and unstructured roads. *IET Comput. Vision* 4 (1), 37–49.
- Cheng, S.Y., Trivedi, M.M., 2007. Lane tracking with omnidirectional cameras: algorithms and evaluation. *EURASIP J. Embedded Syst.* 2007, Article 46972, 1–8.
- Cherng, S., Fang, C.Y., Chen, C.P., Chen, S.W., 2009. Critical motion detection of nearby moving vehicles in a vision-based driver-assistance system. *IEEE Trans. Intell. Transp. Syst.* 10 (1), 70–82.
- Chiang, Y.P. and Fu, K.-S., 1983. Matching parallel algorithm and architecture. In: *Proceedings of the International Conference on Parallel Processing*. Computer Society Press, Columbus, Ohio, USA, pp. 374–380.
- Chittineni, C.B., 1980. Efficient feature subset selection with probabilistic distance criteria. *Inf. Sci.* 22, 19–35.
- Chiverton, J., Mirmehdi, M. and Xie, X., 2008. Variational logistic maximum a posteriori model similarity and dissimilarity matching. In: *Proc. Int. Conf. on Pattern Recognition*. 8–11 December, Tampa, FL.
- Chojnacki, W., Brooks, M.J., van den Hengel, A., Gawley, D., 2003. Revisiting Hartley's normalized eight-point algorithm. *IEEE Trans. Pattern Anal. Mach. Intell.* 25 (9), 1172–1177.
- Choudhary, R., Paliwal, J., Jayas, D.S., 2008. Classification of cereal grains using wavelet, morphological, colour, and textural features of non-touching kernel images. *Biosyst. Eng.* 99, 330–337.
- Chow, C.K., Kaneko, T., 1972. Automatic boundary detection of the left ventricle from cineangiograms. *Comput. Biomed. Res.* 5, 388–410.
- Choy, S.S.O., Choy, C.S.-T., Siu, W.-C., 1995. New single-pass algorithm for parallel thinning. *Comput. Vision Image Understanding* 62 (1), 69–77.
- Chum, O., Matas, J., 2005. Matching with PROSAC – progressive sample consensus. *Proc. IEEE Conf. Comput. Vision Pattern Recognit.* Vol. 1, 220–226.
- Chung, C.-H., Cheng, S.-C., Chang, C.-C., 2010. Adaptive image segmentation for region-based object retrieval using generalized Hough transform. *Pattern Recognit.* 43, 3219–3232.

- Chung, K.-L., Lin, Z.-W., Huang, S.-T., Huang, Y.-H., Liao, H.-Y.M., 2010. New orientation-based elimination approach for accurate line-detection. *Pattern Recognit. Lett.* 31 (1), 11–19.
- Clarifai, 2013. Average of multiple models on original training data. 0.11743. ImageNet Large Scale Visual Recognition Challenge 2013 (ILSVRC2013), Results of ILSVRC2013, <http://www.image-net.org/challenges/LSVRC/2013/results.php>.
- Clark, P. and Mirmehdi, M., 2002. On the recovery of oriented documents from single images. In: *Proc. Advanced Concepts for Intelligent Vision Systems (ACIVS)*. 9–11 Sept., Ghent, Belgium, 190–197.
- Clark, P., Mirmehdi, M., 2003. Rectifying perspective views of text in 3D scenes using vanishing points. *Pattern Recognit.* 36, 2673–2686.
- Clarke, J.C., Carlsson, S. and Zisserman, A., 1996. Detecting and tracking linear features efficiently. In: *Proc. British Machine Vision Assoc. Conf.*
- Clerc, M., Mallat, S., 2002. The texture gradient equation for recovering shape from texture. *IEEE Trans. Pattern Anal. Mach. Intell.* 24 (4), 536–549.
- Coeurjolly, D., Klette, R., 2004. A comparative evaluation of length estimators of digital curves. *IEEE Trans. Pattern Anal. Mach. Intell.* 26 (2), 252–258.
- Coifman, B., Beymer, D., McLauchlan, P., Malik, J., 1998. A real-time computer vision system for vehicle tracking and traffic surveillance. *Transp. Res.*, 6 (C), 271–288.
- Coleman, G.B., Andrews, H.C., 1979. Image segmentation by clustering. *Proc. IEEE* 67, 773–785.
- Collins, R.T., Lipton, A.J. and Kanade, T. (eds.), 2000. Special section on video surveillance. In: *IEEE Trans. Pattern Anal. Machine Intell.* Vol. 22, no. 8.
- Comaniciu, D., Meer, P., 2002. Mean shift: a robust approach toward feature space analysis. *IEEE Trans. Pattern Anal. Mach. Intell.* 24 (5), 603–619.
- Comaniciu, D., Ramesh, V., Meer, P., 2003. Kernel-based object tracking. *IEEE Trans. Pattern Anal. Mach. Intell.* 25 (5), 564–577.
- Connors, R.W., Harlow, C.A., 1980a. A theoretical comparison of texture algorithms. *IEEE Trans. Pattern Anal. Mach. Intell.* 2 (3), 204–222.
- Connors, R.W., Harlow, C.A., 1980b. Toward a structural textural analyzer based on statistical methods. *Comput. Graph. Image Process.* 12, 224–256.
- Connolly, C., 2009. Driver assistance systems aim to halve traffic accidents. *Sens. Rev.* 29 (1), 13–19.
- Cook, R.L., Torrance, K.E., 1982. A reflectance model for computer graphics. *ACM Trans. Graphics* 1, 7–24.
- Cootes, T.F., Taylor, C.J., 1996. Data driven refinement of active shape model search. In: Fisher, R.B., Trucco, E. (Eds.), *Proc. British Machine Vision Conference*. BMVA Press, pp. 383–392.
- Cootes, T.F. and Taylor, C.J., 2001. Statistical models of appearance for medical image analysis and computer vision. In: Sonka, M., and Hanson, K.M. (Eds.), *Proc. SPIE, Int. Soc. Opt. Eng. USA*, Vol. 4322, pp. 236–248.
- Cootes, T.F., Taylor, C.J., Cooper, D.H. and Graham, J., 1992. Training models of shape from sets of examples. In: *Proc. Third British Machine Vision Assoc. Conf.* 22–24 Sept., Leeds, pp. 9–18.
- Cootes, T.F., Edwards, G.J., Taylor, C.J., 2001. Active Appearance Models. *IEEE Trans. Pattern Anal. Mach. Intell.* 23 (6), 681–685.
- Corneil, D.G., Gottlieb, C.C., 1970. An efficient algorithm for graph isomorphism. *J. ACM* 17, 51–64.

- Cosío, F.A., Flores, J.A.M., Castañeda, M.A.P., 2010. Use of simplex search in active shape models for improved boundary segmentation. *Pattern Recognit. Lett.* 31 (9), 806–817.
- Costa, LdaF., Cesar, R.M., 2000. *Shape Analysis and Classification: Theory and Practice*. CRC Press, Boca Raton.
- Coudray, N., Buessler, J.-L., Urban, J.-P., 2010. Robust threshold estimation for images with unimodal histograms. *Pattern Recognit. Lett.* 31 (9), 1010–1019.
- Cowan, G., 1998. *Statistical Data Analysis*. Oxford University Press, Oxford.
- Cremers, D., Rousson, M., Deriche, R., 2007. A review of statistical approaches to level set segmentation: integrating color, texture, motion and shape. *Int. J. Comput. Vision* 72 (2), 195–215.
- Crimmins, T.R., Brown, W.R., 1985. Image algebra and automatic shape recognition. *IEEE Trans. Aerosp. Electron. Syst.* 21, 60–69.
- Cristianini, N., Shawe-Taylor, J., 2000. *An Introduction to Support Vector Machines*. Cambridge University Press, Cambridge, UK.
- Cross, A.D.J., Wilson, R.C., Hancock, E.R., 1997. Inexact graph matching with genetic search. *Pattern Recognit.* 30 (6), 953–970.
- Crowley, J.L., Bobet, P., Schmid, C., 1993. Auto-calibration by direct observation of objects. *Image Vision Comput.* 11 (2), 67–81.
- Cumani, A., Guiducci, A., 1995. Geometric camera calibration: the virtual camera approach. *Mach. Vision Appl.* 8 (6), 375–384.
- Curio, C., Edelbrunner, J., Kalinke, T., Tzomakas, C., von Seelen, W., 2000. Walking pedestrian recognition. *IEEE Trans. Intell. Transp. Syst.* 1 (3), 155–163.
- Cybenko, G., 1988. Continuous valued neural networks with two hidden layers are sufficient. *Techn. Report*, Dept. of Comput. Sci., Tufts Univ., Medford, MA.
- Cybenko, G., 1989. Approximation by superpositions of a sigmoidal function. *Math. Control, Signals Syst.* 2 (4), 303–314.
- da Gama Leitão, H.C., Stolfi, J., 2002. A multiscale method for the reassembly of two-dimensional fragmented objects. *IEEE Trans. Pattern Anal. Mach. Intell.* 24 (9), 1239–1251.
- Dalal, N. and Triggs, B., 2005. Histograms of oriented gradients for human detection. In: *Proc. Conf. on Computer Vision and Pattern Recognition*. San Diego, California, USA, pp. 886–893.
- Dalal, N., Triggs, B., Schmid, C., 2006. Human detection using oriented histograms of flow and appearance. In: Leonardis, A., Bischof, H., Prinz, A. (Eds.), *Proc. European Conf. on Computer Vision*. Springer-Verlag, Berlin, Heidelberg, pp. 428–441. Part II, LNCS 3952.
- Dance, C., Willamowski, J., Fan, L., Bray, C. and Csurka, G., 2004. Visual categorization with bags of keypoints. In: *Proc. ECCV International Workshop on Statistical Learning in Computer Vision*. Prague.
- Danielsson, P.-E., 1981. Getting the median faster. *Comput. Graph. Image Process.* 17, 71–78.
- Daugman, J.G., 1993. High confidence visual recognition of persons by a test of statistical independence. *IEEE Trans. Pattern Anal. Mach. Intell.* 15, 1148–1161.
- Daugman, J.G., 2003. Demodulation by complex-valued wavelets for stochastic pattern recognition. *Int. J. Wavelets Multiresolution Inf. Process.* 1 (1), 1–17.
- Davies, E.R., 1984a. The median filter: an appraisal and a new truncated version. In: *Proc. Seventh Int. Conf. on Pattern Recognition*. 30 July–2 August, Montreal, pp. 590–592.

- Davies, E.R., 1984b. Circularity – a new principle underlying the design of accurate edge orientation operators. *Image Vision Comput.* 2, 134–142.
- Davies, E.R., 1984c. Design of cost-effective systems for the inspection of certain food products during manufacture. In: Pugh, A. (Ed.), *Proceedings of the Fourth International Conference on Robot Vision and Sensory Controls*, London (9–11 October). IFS (Publications) Ltd, Bedford and North-Holland, Amsterdam, pp. 437–446.
- Davies, E.R., 1986. Image space transforms for detecting straight edges in industrial images. *Pattern Recognit. Lett.* 4, 185–192.
- Davies, E.R., 1987a. A new framework for analysing the properties of the generalised Hough transform. *Pattern Recognit. Lett.* 6, 1–7.
- Davies, E.R., 1987b. Design of optimal Gaussian operators in small neighbourhoods. *Image Vision Comput.* 5, 199–205.
- Davies, E.R., 1987c. The effect of noise on edge orientation computations. *Pattern Recognit. Lett.* 6, 315–322.
- Davies, E.R., 1987d. A high speed algorithm for circular object location. *Pattern Recognit. Lett.* 6, 323–333.
- Davies, E.R., 1988a. Application of the generalised Hough transform to corner detection. *IEE Proc. E* 135, 49–54.
- Davies, E.R., 1988b. A modified Hough scheme for general circle location. *Pattern Recognit. Lett.* 7, 37–43.
- Davies, E.R., 1988c. On the noise suppression and image enhancement characteristics of the median, truncated median and mode filters. *Pattern Recognit. Lett.* 7, 87–97.
- Davies, E.R., 1988d. Median-based methods of corner detection. In: Kittler, J. (Ed.), *Proceedings of the Fourth BPRA International Conference on Pattern Recognition*, Cambridge (28–30 March). *Lecture Notes in Computer Science*, Vol. 301. Springer-Verlag, Heidelberg, pp. 360–369.
- Davies, E.R., 1988e. Training sets and *a priori* probabilities with the nearest neighbour method of pattern recognition. *Pattern Recognit. Lett.* 8, 11–13.
- Davies, E.R., 1988f. Tradeoffs between speed and accuracy in two-stage template matching. *Signal Process.* 15, 351–363.
- Davies, E.R., 1989a. Finding ellipses using the generalised Hough transform. *Pattern Recognit. Lett.* 9, 87–96.
- Davies, E.R., 1989b. Edge location shifts produced by median filters: theoretical bounds and experimental results. *Signal Process.* 16, 83–96.
- Davies, E.R., 1991a. The minimal match graph and its use to speed identification of maximal cliques. *Signal Process.* 22 (3), 329–343.
- Davies, E.R., 1991b. Median and mean filters produce similar shifts on curved boundaries. *Electron. Lett.* 27 (10), 826–828.
- Davies, E.R., 1991c. Insight into operation of Kulpa boundary distance measure. *Electron. Lett.* 27 (13), 1178–1180.
- Davies, E.R., 1992a. Simple fast median filtering algorithm, with application to corner detection. *Electron. Lett.* 28 (2), 199–201.
- Davies, E.R., 1992b. Modelling peak shapes obtained by Hough transform. *IEE Proc. E* 139 (1), 9–12.
- Davies, E.R., 1992c. Locating objects from their point features using an optimised Hough-like accumulation technique. *Pattern Recognit. Lett.* 13 (2), 113–121.
- Davies, E.R., 1992d. Procedure for generating template masks for detecting variable signals. *Image Vision Comput.* 10 (4), 241–249.

- Davies, E.R., 1992e. Accurate filter for removing impulse noise from one- or two-dimensional signals. *IEE Proc. E* 139 (2), 111–116.
- Davies, E.R., 1992f. Simple two-stage method for the accurate location of Hough transform peaks. *IEE Proc. E* 139 (3), 242–248.
- Davies, E.R., 1992g. A framework for designing optimal Hough transform implementations. In: *Proc. 11th IAPR Int. Conf. on Pattern Recognition*. 30 Aug.–3 Sept., The Hague, Vol. III, pp. 509–512.
- Davies, E.R., 1999a. Chord bisection strategy for fast ellipse location. *Electron. Lett.* 35 (9), 703–705.
- Davies, E.R., 1999b. Algorithms for ultra-fast location of ellipses in digital images. In: *Proc. Seventh IEE Int. Conf. on Image Processing and its Applications*. 13–15 July, Manchester, IEE Conf. Publication no. 465, pp. 542–546.
- Davies, E.R., 1999c. Image distortions produced by mean, median and mode filters. *IEE Proc. Vision Image Signal Process.* 146 (5), 279–285.
- Davies, E.R., 2000a. Resolution of problem with use of closing for texture segmentation. *Electron. Lett.* 36 (20), 1694–1696.
- Davies, E.R., 2000b. Accuracy of multichannel median filter. *Electron. Lett.* 36 (25), 2068–2069.
- Davies, E.R., 2000c. A generalized model of the geometric distortions produced by rank-order filters. *Imag. Sci.* 48 (3), 121–130.
- Davies, E.R., 2003a. Formulation of an accurate discrete theory of median shifts. *Signal Process.* 83, 531–544.
- Davies, E.R., 2003b. Design of real-time algorithms for food and cereals inspection. *Imag. Sci.* 51 (2), 63–78.
- Davies, E.R., 2003c. An analysis of the geometric distortions produced by median and related image processing filters. *Adv. Imaging Electron Phys.* 126, 93–193.
- Davies, E.R., 2005. Using an edge-based model of the Plessey operator to determine localisation properties. *Proc. IET Int. Conf. on Visual Information Engineering*. University of Glasgow, Glasgow, pp. 385–391. (4–6 April).
- Davies, E.R., 2007a. Efficient transformation for identifying global valley locations in 1D data. *Electron. Lett.* 43 (6), 332–333.
- Davies, E.R., 2007b. Fast implementation of generalised median filter. *Electron. Lett.* 43 (9), 505–507.
- Davies, E.R., 2008. Stable bi-level and multi-level thresholding of images using a new global transformation. In: *Valestin, S. (Ed.), IET Computer Vision 2*, no. 2, Special Issue on Visual Information Engineering, pp. 60–74.
- Davies, E.R., Celano, D., 1993. Analysis of skeleton junctions in  $3 \times 3$  windows. *Electron. Lett.* 29 (16), 1440–1441.
- Davies, E.R., Plummer, A.P.N., 1981. Thinning algorithms: a critique and a new methodology. *Pattern Recognit.* 14, 53–63.
- Davies, E.R., Bateman, M., Chambers, J. and Ridgway, C., 1998. Hybrid non-linear filters for locating speckled contaminants in grain. In: *IEE Digest no. 1998/284, Colloquium on Non-Linear Signal and Image Processing*. 22 May, IEE, pp. 12/1–5.
- Davies, E.R., Ridgway, C. and Chambers, J., 2003. NIR detection of grain weevils inside wheat kernels. In: *Proc. IEE Int. Conf. on Visual Information Engineering, VIE 2003*. 7–9 July, Surrey, IEE Conference Publication 495, pp. 173–176.
- Davis, J.W., Sharma, V., 2007. Background-subtraction using contour-based fusion of thermal and visible imagery. *Comput. Vision Image Understanding* 106 (2–3), 162–182.

- Davison, A.J., Murray, D.W., 2002. Simultaneous localization and map-building using active vision. *IEEE Trans. Pattern Anal. Mach. Intell.* 24 (7), 865–880.
- de la Escalera, A., Armingol, J.Ma, Mata, M., 2003. Traffic sign recognition and analysis for intelligent vehicles. *Image Vision Comput.* 21 (3), 247–258.
- Deans, S.R., 1981. Hough transform from the Radon transform. *IEEE Trans. Pattern Anal. Mach. Intell.* 3, 185–188.
- Delagnes, P., Benois, J., Barba, D., 1995. Active contours approach to object tracking in image sequences with complex background. *Pattern Recognit. Lett.* 16 (2), 171–178.
- Dempster, A.P., Laird, N.M., Rubin, D.B., 1977. Maximum likelihood from incomplete data via the EM algorithm. *J. R. Stat. Soc.* 39 (1), 1–38.
- DeSouza, G.N., Kak, A.C., 2002. Vision for mobile robot navigation: a survey. *IEEE Trans. Pattern Anal. Mach. Intell.* 24 (2), 237–267.
- Devijver, P.A. and Kittler, J., 1980. On the edited nearest neighbour rule. In: *Proc. Fifth Int. Conf. on Pattern Recognition*. Miami Beach, Florida (IEEE Computer Soc.), pp. 72–80.
- Devijver, P.A., Kittler, J., 1982. *Pattern Recognition: a Statistical Approach*. Prentice-Hall, Englewood Cliffs, NJ.
- Dewaele, P., Van Gool, L., Wambacq, P. and Oosterlinck, A., 1988. Texture inspection with self-adaptive convolution filters. In: *Proc. Ninth Int. Conf. on Pattern Recognition*. pp. 56–60.
- Dickinson, S., Pelillo, M. and Zabih, R. (Eds.), 2001. Special Section on Graph Algorithms and Computer Vision. *IEEE Trans. Pattern Anal. Mach. Intell.* Vol. 23, no. 10, pp. 1049–1151.
- Dickmanns, E.D., Myśliwetz, B.D., 1992. Recursive 3-D road and relative ego-state recognition. *IEEE Trans. Pattern Anal. Mach. Intell.* 14 (2), 199–213.
- Dinic, E.A., 1970. Algorithm for solution of a problem of maximum flow in networks with power estimation. *Sov. Math. Dokl.* 11, 1277–1280.
- Dockstader, S.L., Tekalp, A.M., 2001. On the tracking of articulated and occluded video object motion. *Real-Time Imaging* 7 (5), 415–432.
- Dockstader, S.L. and Tekalp, A.M., 2002. A kinematic model for human motion and gait analysis. In: *Proc. Workshop on Statistical Methods in Video Processing (ECCV)*. 1–2 June, Copenhagen, Denmark, pp. 49–54. <http://dx.doi.org/10.1049/el.2012.2816>.
- Dorst, L., Smeulders, A.W.M., 1987. Length estimators for digitized contours. *Comput. Vision Graph. Image Process* 40, 311–333.
- Doucet, A., Johansen, A.M., 2011. A tutorial on particle filtering and smoothing: fifteen years later. In: Crisan, D., Rozovsky, B. (Eds.), *Oxford Handbook of Nonlinear Filtering*. Oxford University Press, Oxford, UK.
- Dougherty, E.R., Giardina, C.R., 1988. Morphology on umbra matrices. *Int. J. Pattern Recognit. Artif. Intell.* 2, 367–385.
- Dougherty, E.R., Sinha, D., 1995a. Computational gray-scale mathematical morphology on lattices (a comparator-based image algebra) Part I: architecture. *Real-Time Imaging* 1 (1), 69–85.
- Dougherty, E.R., Sinha, D., 1995b. Computational gray-scale mathematical morphology on lattices (a comparator-based image algebra) Part II: image operators. *Real-Time Imaging* 1 (4), 283–295.
- Doyle, W., 1962. Operations useful for similarity-invariant pattern recognition. *J. ACM* 9, 259–267.

- Dreschler, L., Nagel, H.-H., 1981. Volumetric model and 3D-trajectory of a moving car derived from monocular TV-frame sequences of a street scene. *Proc. Int. Joint Conf. Artif. Intell.* 692–697.
- Du Buf, J.M.H., Kardan, M., Spann, M., 1990. Texture feature performance for image segmentation. *Pattern Recognit.* 23, 291–309.
- Duda, R.O., Hart, P.E., 1972. Use of the Hough transformation to detect lines and curves in pictures. *Commun. ACM* 15, 11–15.
- Duda, R.O., Hart, P.E., 1973. *Pattern Classification and Scene Analysis*. Wiley, New York.
- Duda, R.O., Hart, P.E., Stork, D.G., 2001. *Pattern Classification*. Wiley, New York.
- Dudani, S.A., Luk, A.L., 1978. Locating straight-line edge segments on outdoor scenes. *Pattern Recognit.* 10, 145–157.
- Dudani, S.A., Breeding, K.J., McGhee, R.B., 1977. Aircraft identification by moment invariants. *IEEE Trans. Comput.* 26, 39–46.
- Duin, R.P.W., 2002. The combining classifier: to train or not to train? In: *Proc. 16th Int. Conf. on Pattern Recognition*. 11–15 Aug., Québec, Canada, Vol. II, pp. 765–770.
- Duin, R.P.W., Haringa, H., Zeelen, R., 1986. Fast percentile filtering. *Pattern Recognit. Lett.* 4, 269–272.
- Ehsan, S., Kanwal, N., Clark, A.F., McDonald-Maier, K.D., 2010. Improved repeatability measures for evaluating performance of feature detectors. *Electron. Lett.* 46 (14), 998–1000.
- Ehsan, S., Kanwal, N., Clark, A.F. and McDonald-Maier, K.D., 2011. Measuring the coverage of interest point detectors. In: *Proc. Eighth Int. Conf. on Image Analysis and Recognition (ICIAR)*. 22–24 June, British Columbia, Canada, Vol. 6753, pp. 253–261.
- Elgammal, A., Harwood, D., Davis, L., 2000. Non-parametric model for background subtraction. *Proc. Eur. Conf. Comput. Vision LNCS Vol. 1843*, 751–767.
- Ellis, T.J., Abbood, A., Brillault, B., 1992. Ellipse detection and matching with uncertainty. *Image Vision Comput.* 10 (5), 271–276.
- Eng, H.-L., Ma, K.-K., 2001. Noise adaptive soft-switching median filter. *IEEE Trans. Image Process.* 10 (2), 242–251.
- Enzweiler, M., Gavrilu, D.M., 2009. Monocular pedestrian detection: survey and experiments. *IEEE Trans. Pattern Anal. Mach. Intell.* 31 (12), 2179–2195.
- Eshel, R. and Moses, Y., 2008. Homography based multiple camera detection and tracking of people in a dense crowd. In: *Proc. IEEE Conf. on Computer Vision and Pattern Recognition*. 23–28 June, pp. 1–8.
- Eshel, R., Moses, Y., 2010. Tracking in a Dense Crowd Using Multiple Cameras. *Int. J. Comput. Vision* 88 (1), 129–143.
- Evans, A.N., Nixon, M.S., 1995. Mode filtering to reduce ultrasound speckle for feature extraction. *IEE Pro.—Vision Image Signal Process.* 142 (2), 87–94.
- Everingham, M., Van Gool, L., Williams, C.K.I., Winn, J., and Zisserman, A., 2007. The PASCAL Visual Object Classes Challenge 2007. (VOC2007) Results. <http://www.pascalnetwork.org/challenges/VOC/voc2007/>.
- Everingham, M., Zisserman, A., Williams, C.K.I., and Van Gool, L., 2006. The PASCAL Visual Object Classes Challenge 2006. (VOC2006) Results. <http://www.pascalnetwork.org/challenges/VOC/voc2006/>.
- Everingham, M., Van Gool, L., Williams, C.K.I., Winn, J., and Zisserman, A., 2008. The PASCAL Visual Object Classes Challenge 2008. (VOC2008) Results. <http://www.pascalnetwork.org/challenges/VOC/voc2008/>.



- Fang, C.Y., Chen, S.W., Fuh, C.S., 2003. Road-sign detection and tracking. *IEEE Trans. Veh. Technol.* 52 (5), 1329–1341.
- Fang, C.Y., Fuh, C.S., Yen, P.S., Cherng, S., Chen, S.W., 2004. An automatic road sign recognition system based on a computational model of human recognition processing. *Comput. Vision Image Understanding* 96, 237–268.
- Fang, X., Luo, B., Zhao, H., Tang, J., Zhai, S., 2010. New multi-resolution image stitching with local and global alignment. *IET Comput. Vision* 4 (4), 231–246.
- Fasel, B., 2002. Robust face analysis using convolutional neural networks. In: *Proc. 16th Int. Conf. on Pattern Recognition*, 11–15 Aug., Québec, Canada, Vol. II, pp. 40–43.
- Fathy, M., Siyal, M.Y., 1995. Real-time image processing approach to measure traffic queue parameters. *IEE Proc. Vision Image Signal Process.* 142 (5), 297–303.
- Fathy, M.E., Hussein, A.S., Tolba, M.F., 2011. Fundamental matrix estimation: a study of error criteria. *Pattern Recognit. Lett.* 32 (2), 383–391.
- Faugeras, O., 1992. What can be seen in three dimensions with an uncalibrated stereo rig? *Proc. Second European Conf. on Computer Vision*. In: Sandini, G. (Ed.), *Lecture Notes in Computer Science*, vol. 588. Springer-Verlag, Berlin Heidelberg, pp. 563–578.
- Faugeras, O., 1993. *Three-Dimensional Computer Vision – a Geometric Viewpoint*. MIT Press, Cambridge, MA.
- Faugeras, O., Luong, Q.-T., 2001. *The Geometry of Multiple Images*. The MIT press, Cambridge, Mass.
- Faugeras, O., Luong, Q.-T., Maybank, S.J., 1992. Camera self-calibration: theory and experiments. *Proc. Second European Conf. on Computer Vision*. In: Sandini, G. (Ed.), *Lecture Notes in Computer Science*, vol. 588. Springer-Verlag, Berlin Heidelberg, pp. 321–334.
- Faugeras, O., Quan, L., Sturm, P., 2000. Self-calibration of a 1D projective camera and its application to the self-calibration of a 2D projective camera. *IEEE Trans. Pattern Anal. Mach. Intell.* 22 (10), 1179–1185.
- Faugeras, O.D., 1978. Texture analysis and classification using a human visual model. In: *Proc. Fourth Int. Joint Conf. on Pattern Recognition*. 7–10 Nov., Kyoto, pp. 549–552.
- Faugeras, O.D. and Hebert, M., 1983. A 3-D recognition and positioning algorithm using geometrical matching between primitive surfaces. In: *Proc. Eighth Int. Joint Conf. on Artif. Intell.* pp. 996–1002.
- Fawcett, T., 2006. An introduction to ROC analysis. *Pattern Recognit. Lett.* 27, 861–874.
- Fei-Fei, L., Fergus, R., Perona, P., 2003. A Bayesian approach to unsupervised one-shot learning of object categories. In: *Proc. Ninth IEEE Int. Conf. on Computer Vision*. 14–17 October, Nice, France, Vol. 2, pp. 1134–1141.
- Felzenszwalb, P.F., Girshick, R.B., McAllester, D., Ramanan, D., 2010. Object detection with discriminatively trained part based models. *IEEE Trans. Pattern Anal. Mach. Intell.* 32 (9), 1627–1645.
- Ferrie, F.P., Levine, M.D., 1989. Where and why local shading analysis works. *IEEE Trans. Pattern Anal. Mach. Intell.* 11, 198–206.
- Fesenkov, V.P., 1929. Photometric investigations of the lunar surface. *Astronomichesk. Zh* 5, 219–234.
- Fieguth, P., Terzopoulos, D., 1997. Color-based tracking of heads and other mobile objects at video frame rates. *Proc. IEEE Conf. Comput. Vision Pattern Recognit*, San Juan, PR, USA, 17–19 June, pp. 21–27.

- Finlayson, G.D., Hordley, S.D., Hubel, P.M., 2001. Color by correlation: a simple, unifying framework for color constancy. *IEEE Trans. Pattern Anal. Mach. Intell.* 23 (11), 1209–1221.
- Fischer, B., Buhmann, J.M., 2003. Bagging for path-based clustering. *IEEE Trans. Pattern Anal. Mach. Intell.* 25 (11), 1411–1415.
- Fischler, M.A., Bolles, R.C., 1981. Random sample consensus: a paradigm for model fitting with applications to image analysis and automated cartography. *Commun. ACM* 24 (6), 381–395.
- Fitch, J.P., Coyle, E.J., Gallagher, N.C., 1985. Root properties and convergence rates of median filters. *IEEE Trans. Acoust. Speech Signal Process* 33, 230–239.
- Föglein, J., 1983. On edge gradient approximations. *Pattern Recognit. Lett.* 1, 429–434.
- Ford, L., Fulkerson, D., 1962. *Flows in Networks*. Princeton University Press, Princeton, NJ, USA.
- Forgy, E.W., 1965. Cluster analysis of multivariate data: efficiency versus interpretability of classification. *Biometrics* 21, 768–769.
- Förstner, W., Dickscheid, T. and Schindler, F., 2009. Detecting interpretable and accurate scale-invariant keypoints. In: *Proc. Int. Conf. on Computer Vision (ICCV)*. Kyoto, Japan, pp. 2256–2263.
- Forsyth, D.A., 1990. A novel algorithm for colour constancy. *Int. J. Comput. Vision* 5 (1), 5–36.
- Forsyth, D.A., Ponce, J., 2003. *Computer Vision: A Modern Approach*. Pearson Education International, Upper Saddle River, NJ.
- Forsyth, D.A., Mundy, J.L., Zisserman, A., Coelho, C., Heller, A., Rothwell, C.A., 1991. Invariant descriptors for 3-D object recognition and pose. *IEEE Trans. Pattern Anal. Mach. Intell.* 13 (10), 971–991.
- Foster, J.P., Nixon, M.S. and Prugel-Bennett, A., 2001. New area based metrics for automatic gait recognition. In: *Proc. British Machine Vision Assoc. Conf.* pp. 233–242.
- Frankot, R.T., Chellappa, R., 1990. Estimation of surface topography from SAR imagery using shape from shading techniques. *Artif. Intell.* 43, 271–310.
- Freeman, H., 1961. On the encoding of arbitrary geometric configurations. *IEEE Trans. Electron. Comput.* 10, 260–268.
- Freeman, H., 1974. Computer processing of line drawing images. *Comput. Surv.* 6, 57–97.
- Freeman, H., 1978. Shape description via the use of critical points. *Pattern Recognit.* 10, 159–166.
- Frei, W., Chen, C.-C., 1977. Fast boundary detection: a generalization and a new algorithm. *IEEE Trans. Comput.* 26, 988–998.
- Freund, Y. and Schapire, R., 1996. Experiments with a new boosting algorithm. In: *Proc. 13th Int. Conf. on Machine Learning*, pp. 148–156.
- Friedman, J., Hastie, T., Tibshirani, R., 2000. Special invited paper – additive logistic regression: a statistical view of boosting. *Ann. Stat.* 28 (2), 337–407.
- Fu, K.-S., Mui, J.K., 1981. A survey on image segmentation. *Pattern Recognit.* 13, 3–16.
- Fumera, G., Fabio, R., Alessandra, S., 2008. A theoretical analysis of bagging as a linear combination of classifiers. *IEEE Trans. Pattern Anal. Mach. Intell.* 30 (7), 1293–1299.
- Gallagher, N.C., Wise, G.L., 1981. A theoretical analysis of the properties of median filters. *IEEE Trans. Acoust. Speech Signal Process* 29, 1136–1141.
- Gallo, O., Manduchi, R., Rafii, A., 2011. CC-RANSAC: fitting planes in the presence of multiple surfaces in range data. *Pattern Recognit. Lett.* 32 (3), 403–410.

- Gao, C., Sang, N., Tang, Q., 2010. On selection and combination of weak learners in AdaBoost. *Pattern Recognit. Lett.* 31 (9), 991–1001.
- Garcia, C. and Delakis, M., 2002. A neural architecture for fast and robust face detection. In: *Proc. 16th Int. Conf. on Pattern Recognition*. 11–15 Aug., Québec, Canada, Vol. II, pp. 44–47.
- Gavrila, D., 1999. The visual analysis of human movement: a survey. *Comput. Vision Image Understanding* 73 (1), 82–98.
- Gavrila, D., 2000. Pedestrian detection from a moving vehicle. In: Vernon, D. (Ed.), *Proc. European Conf. on Computer Vision*. June, Dublin, Ireland, pp. 37–49.
- Gavrila, D.M., 1998. Multi-feature hierarchical template matching using distance transforms. In: *Proc. IEEE Int. Conf. on Pattern Recognition*. Brisbane, Australia.
- Gavrila, D.M., Groen, F.C.A., 1992. 3D object recognition from 2D images using geometric hashing. *Pattern Recognit. Lett.* 13 (4), 263–278.
- Gavrila, D.M., Munder, S., 2007. Multi-cue pedestrian detection and tracking from a moving vehicle. *Int. J. Comput. Vision* 73 (1), 41–59.
- Gavrila, D.M., Giebel, J., and Munder, S., 2004. Vision-based pedestrian detection: the PROTECTOR + system. In: *Proc. IEEE Intelligent Vehicle Symposium*. Parma, Italy.
- Geiger, D., Liu, T.-L., Kohn, R.V., 2003. Representation and self-similarity of shapes. *IEEE Trans. Pattern Anal. Mach. Intell.* 25 (1), 86–99.
- Gerig, G. and Klein, F., 1986. Fast contour identification through efficient Hough transform and simplified interpretation strategy. In: *Proc. Eighth Int. Conf. on Pattern Recognition*. 27–31 October, Paris, pp. 498–500.
- Geronimo, D., Lopez, A.M., Sappa, A.D., Graf, T., 2010. Survey of pedestrian detection for advanced driver assistance systems. *IEEE Trans. Pattern Anal. Mach. Intell.* 32 (7), 1239–1258.
- Ghosh, A., Petkov, N., 2005. Robustness of shape descriptors to incomplete contour representations. *IEEE Trans. Pattern Anal. Mach. Intell.* 27 (11), 1793–1804.
- Gibbons, A., 1985. *Algorithmic Graph Theory*. Cambridge University Press, Cambridge.
- Giblin, P.J., Kimia, B.B., 2003. On the intrinsic reconstruction of shape from its symmetries. *IEEE Trans. Pattern Anal. Mach. Intell.* 25 (7), 895–911.
- Gibson, J.J., 1950. *The Perception of the Visual World*. Houghton Mifflin, Boston, MA.
- Girshick, R., Donahue, J., Darrell, T., and Malik, J., 2014. Rich feature hierarchies for accurate object detection and semantic segmentation. In: *Proc. IEEE Conf. on Computer Vision and Pattern Recognition*. 23–28 June, Columbus, OH, pp. 580–587. See also arXiv:1311.2524v5 [cs.CV] 22 Oct.
- Girshick, R.B., 2015. Fast R-CNN. In: *Proc. IEEE Int. Conf. on Computer Vision*. 13–16 Dec, Santiago, Chile, pp. 1440–1448.
- Goetlicherian, V., 1980. From binary to grey tone image processing using fuzzy logic concepts. *Pattern Recognit.* 12, 7–15.
- Goldberg, A.V., Tarjan, R.E., 1988. A new approach to the maximum-flow problem. *J. Assoc. Comput. Mach.* 35 (4), 921–940.
- Goldman, D.B., Curless, B., Hertzmann, A., Seitz, S.M., 2010. Shape and spatially-varying BRDFs from photometric stereo. *IEEE Trans. Pattern Anal. Mach. Intell.* 32 (6), 1060–1071.
- Golightly, I., Jones, D., 2003. Corner detection and matching for visual tracking during power line inspection. *Image Vision Comput.* 21 (9), 827–840.
- Golub, G.H., van Loan, C.F., 1983. *Matrix Computations*. North Oxford, Oxford, UK.

- Gong, S., McKenna, S., Psarrou, A., 2000. *Dynamic Vision: From Images to Face Recognition*. Imperial College Press, London, UK.
- Gonnet, G.H., 1984. *Handbook of Algorithms and Data Structures*. Addison-Wesley, London.
- Gonzalez, R.C., Woods, R.E., 1992. *Digital Image Processing*. Addison Wesley, Reading, MA.
- Gonzalez, R.C., Woods, R.E., 2008. *Digital Image Processing*, third ed. Prentice Hall, Upper Saddle River, NJ.
- Gope, C., Kehtarnavaz, N., 2007. Affine invariant comparison of point-sets using convex hulls and Hausdorff distances. *Pattern Recognit.* 40, 309–320.
- Granlund, G.H., 1980. Description of texture using the general operator approach. In: Proc. Fifth Int. Conf. on Pattern Recognition. 1–4 Dec., Miami Beach, Florida, pp. 776–779.
- Greenhill, D. and Davies, E.R., 1993. Texture analysis using neural networks and mode filters. In: Proc. Fourth British Machine Vision Assoc. Conf., Univ. of Surrey, Guildford, Surrey, UK. 21–23 Sept., Vol. 2, pp. 509–518.
- Greenhill, D., Davies, E.R., 1994. Relative effectiveness of neural networks for image noise suppression. In: Gelsema, E.S., Kanal, L.N. (Eds.), *Pattern Recognition in Practice IV*. Elsevier Science B.V, pp. 367–378.
- Gregory, R.L., 1971. *The Intelligent Eye*. Weidenfeld and Nicolson, London.
- Gregory, R.L., 1972. *Eye and Brain*, second ed. Weidenfeld and Nicolson, London.
- Griffin, G., Holub, A., and Perona, P., 2006. The Caltech-256. Caltech Technical Report.
- Griffin, L.D., 2000. Mean, median and mode filtering of images. *Proc. Royal Soc. London, Ser. A* 456 (2004), 2995–3004.
- Grimson, W.E.L., Huttenlocher, D.P., 1990. On the sensitivity of the Hough transform for object recognition. *IEEE Trans. Pattern Anal. Mach. Intell.* 12 (3), 255–274.
- Grimson, W.E.L., Lozano-Perez, T., 1984. Model-based recognition and localisation from sparse range or tactile data. *Int. J. Robot. Res.* 3 (3), 3–35.
- Gross, R., Matthews, I., Baker, S., 2004. Appearance-based face recognition and light-fields. *IEEE Trans. Pattern Anal. Mach. Intell.* 26 (4), 449–465.
- Gruen, A., Huang, T.S. (Eds.), 2001. *Calibration and Orientation of Cameras in Computer Vision*. Springer-Verlag, Berlin Heidelberg.
- Guan, Y.-P., 2010. Spatio-temporal motion-based foreground segmentation and shadow suppression. *IET Comput. Vision* 4 (1), 50–60.
- Guiducci, A., 1999. Parametric model of the perspective projection of a road with applications to lane keeping and 3d road reconstruction. *Comput. Vision Image Understanding* 73, 414–427.
- Guo, S., Pridmore, T., Kong, Y., Zhang, X., 2009. An improved Hough transform voting scheme utilizing surround suppression. *Pattern Recognit. Lett.* 30 (13), 1241–1252.
- Guru, D.S., Shekar, B.H., Nagabhushan, P., 2004. A simple and robust line detection algorithm based on small eigenvalue analysis. *Pattern Recognit. Lett.* 25 (1), 1–13.
- Hall, E.L., 1979. *Computer Image Processing and Recognition*. Academic Press, New York.
- Hall, E.L., Tio, J.B.K., McPherson, C.A., Sadjadi, F.A., 1982. Measuring curved surfaces for robot vision. *IEEE Comput.* 15 (12), 42–54.
- Hampel, F.R., Ronchetti, E.M., Rousseeuw, P.J., Stahel, W.A., 1986. *Robust Statistics, The Approach Based on Influence Functions*. Wiley, New York.

- Hannah, I., Patel, D., Davies, E.R., 1995. The use of variance and entropic thresholding methods for image segmentation. *Pattern Recognit.* 28 (8), 1135–1143.
- Hansen, D.W., Ji, Q., 2010. In the eye of the beholder: a survey of models for eyes and gaze. *IEEE Trans. Pattern Anal. Mach. Intell.* 32 (3), 478–500.
- Hansen, F.R., Elliott, H., 1982. Image segmentation using simple Markov field models. *Comput. Graph. Image Process.* 20, 101–132.
- Haralick, R.M., 1979. Statistical and structural approaches to texture. *Proc. IEEE* 67 (5), 786–804.
- Haralick, R.M., 1980. Edge and region analysis for digital image data. *Comput. Graph. Image Process.* 12, 60–73.
- Haralick, R.M., 1984. Digital step edges from zero crossing of second directional derivatives. *IEEE Trans. Pattern Anal. Mach. Intell.* 6, 58–68.
- Haralick, R.M., 1989. Determining camera parameters from the perspective projection of a rectangle. *Pattern Recognit.* 22, 225–230.
- Haralick, R.M., Chu, Y.H., 1984. Solving camera parameters from the perspective projection of a parameterized curve. *Pattern Recognit.* 17 (6), 637–645.
- Haralick, R.M. and Joo, H., 1988. 2D-3D pose estimation. In: *Proc. Ninth Int. Conf. on Pattern Recognition*. 14–17 Nov., Rome, Italy, pp. 385–391.
- Haralick, R.M., Shapiro, L.G., 1985. Image segmentation techniques. *Comput. Vision Graph. Image Process* 29, 100–132.
- Haralick, R.M., Shapiro, L.G., 1992. *Computer and Robot Vision, Volume I*. Addison Wesley, Reading, MA.
- Haralick, R.M., Shapiro, L.G., 1993. *Computer and Robot Vision, Volume II*. Addison Wesley, Reading, MA.
- Haralick, R.M., Shanmugam, K., Dinstein, I., 1973. Textural features for image classification. *IEEE Trans. Syst. Man Cybern.* 3 (6), 610–621.
- Haralick, R.M., Chu, Y.H., Watson, L.T., Shapiro, L.G., 1984. Matching wire frame objects from their two dimensional perspective projections. *Pattern Recognit.* 17 (6), 607–619.
- Haralick, R.M., Sternberg, S.R., Zhuang, X., 1987. Image analysis using mathematical morphology. *IEEE Trans. Pattern Anal. Mach. Intell.* 9 (4), 532–550.
- Haritaoglu, I., Harwood, D., Davis, L.S., 2000. W<sup>4</sup>: real-time surveillance of people and their activities. In *Special Section on Video Surveillance*. *IEEE Trans. Pattern Anal. Mach. Intell.* 22 (8), 809–830.
- Harris, C. and Stephens, M., 1988. A combined corner and edge detector. In: *Proc. Fourth Alvey Vision Conf.* pp. 147–151.
- Hart, P.E., 1968. The condensed nearest neighbour rule. *IEEE Trans. Inf. Theory* 14, 515–516.
- Hartley, R., Zisserman, A., 2000. *Multiple View Geometry in Computer Vision*. Cambridge University Press, Cambridge, UK.
- Hartley, R., Zisserman, A., 2003. *Multiple View Geometry in Computer Vision*, second ed. Cambridge University Press, Cambridge, UK.
- Hartley, R.I., 1992. Estimation of relative camera positions for uncalibrated cameras. *Proc. Second European Conf. on Computer Vision*. In: Sandini, G. (Ed.), *Lecture Notes in Computer Science*, vol. 588. Springer-Verlag, Berlin Heidelberg, pp. 579–587.
- Hartley, R.I., 1995A linear method for reconstruction from lines and points. In: *Proc. Int. Conf. on Computer Vision*, pp. 882–887.

- Hartley, R.I., 1997. In defense of the eight-point algorithm. *IEEE Trans. Pattern Anal. Mach. Intell.* 19 (6), 580–593.
- Harvey, N.R. and Marshall, S., 1994. Using genetic algorithms in the design of morphological filters. In: *IEE Colloquium on Genetic Algorithms in Image Processing and Vision*, IEE, 20 Oct., IEE Digest no. 1994/193, pp. 6/1–5.
- Harvey, N.R. and Marshall, S., 1995. Rank-order morphological filters: a new class of filters. In: *Proc. IEEE Workshop on Nonlinear Signal and Image Processing*. June, Halkidiki, Greece, pp. 975–978.
- Harwood, D., Subbarao, M., Davis, L.S., 1985. Texture classification by local rank correlation. *Comput. Vision Graph. Image Process* 32, 404–411.
- Hasler, D., Sbaiz, L., Süssstrunk, S., Vetterli, M., 2003. Outlier modelling in image matching. *IEEE Trans. Pattern Anal. Mach. Intell.* 25 (3), 301–315.
- Hassner, T., Harel, S., Paz, E., Enbar, R., 2015. Effective face frontalization in unconstrained images. In: *Proc. IEEE Conf. on Computer Vision and Pattern Recognition*. 7–12 June, Boston, MA, pp. 4295–4304.
- Haykin, S., 1999. *Neural Networks: A Comprehensive Introduction*. Prentice-Hall, New Jersey, USA.
- Heijmans, H., 1991. Theoretical aspects of gray-level morphology. *IEEE Trans. Pattern Anal. Mach. Intell.* 13, 568–582.
- Heikkilä, J., 2000. Geometric camera calibration using circular control points. *IEEE Trans. Pattern Anal. Mach. Intell.* 22 (10), 1066–1076.
- Heikkonen, J., 1995. Recovering 3-D motion parameters from optical flow field using randomized Hough transform. *Pattern Recognit. Lett.* 16 (9), 971–978.
- Heinemann, P.H., Varghese, Z.A., Morrow, C.T., Sommer III, H.J., Crassweller, R.M., 1995. Machine vision inspection of “Golden Delicious” apples. *Appl. Eng. Agric* 11 (6), 901–906.
- Heinonen, P., Neuvo, Y., 1987. FIR-median hybrid filters. *IEEE Trans. Acoust. Speech Signal Process* 35, 832–838.
- Herault, L., Horaud, R., Veillon, F., Niez, J.J., 1990. Symbolic image matching by simulated annealing. *Proc. Br. Mach. Vision Assoc. Conf.* 319–324.
- Hernandez, C., Vogiatzis, G., Cipolla, R., 2011. Overcoming shadows in 3-source photometric stereo. *IEEE Trans. Pattern Anal. Mach. Intell.* 33 (2), 419–426.
- Hilario, C., Collado, J.M., Armingol, J.M. and de la Escalera, A., 2006. Visual perception and tracking of vehicles for driver assistance systems. In: *Proc. Intelligent Vehicles Symposium*. June 13–15, Tokyo, Japan, pp. 94–99.
- Hildreth, E.C., 1984. *Measurement of Visual Motion*. MIT Press, Cambridge, MA.
- Hinton, G.E., 2002. Training products of experts by minimizing contrastive divergence. *Neural Comput.* 14 (8), 1771–1800.
- Hinton, G.E., Srivastava, N., Krizhevsky, A., Sutskever, I., and Salakhutdinov, R.R., 2012. Improving Neural Networks by Preventing Co-adaptation of Feature Detectors. *arXiv:1207.0580v1 [cs.NE]* 3 Jul.
- Hlaoui, A. and Wang, S., 2002. A new algorithm for inexact graph matching. In: *Proc. 16th Int. Conf. on Pattern Recognition*. 11–15 Aug., Québec, Canada, Vol. IV, pp. 180–183.
- Ho, T.K., Hull, J.J., Srihari, S.N., 1994. Decision combination in multiple classifier systems. *IEEE Trans. Pattern Anal. Mach. Intell.* 16 (1), 66–75.
- Hochreiter, S., Schmidhuber, J., 1997. Long short-term memory. *Neural Comput.* 9 (8), 1735–1780.

- Hodgson, R.M., Bailey, D.G., Naylor, M.J., Ng, A.L.M., McNeil, S.J., 1985. Properties, implementations, and applications of rank filters. *Image Vision Comput.* 3, 4–14.
- Hofmann, U., Rieder, A., Dickmanns, E.D., 2003. Radar and vision data fusion for hybrid adaptive cruise control on highways. *Mach. Vision Appl.* 14 (1), 42–49.
- Hogg, D., 1983. Model-based vision: a program to see a walking person. *Image Vision Comput.* 1 (1), 5–20.
- Horaud, R., 1987. New methods for matching 3-D objects with single perspective views. *IEEE Trans. Pattern Anal. Mach. Intell.* 9, 401–412.
- Horaud, R., Brady, M., 1988. On the geometric interpretation of image contours. *Artif. Intell.* 37, 333–353.
- Horaud, R., Sossa, H., 1995. Polyhedral object recognition by indexing. *Pattern Recognit.* 28 (12), 1855–1870.
- Horaud, R., Conio, B., Leboulleux, O., Lacolle, B., 1989. An analytic solution for the perspective 4-point problem. *Comput. Vision Graph. Image Process* 47, 33–44.
- Horn, B.K.P., 1975. Obtaining shape from shading information. In: Winston, P.H. (Ed.), *The Psychology of Computer Vision*. McGraw-Hill, New York, pp. 115–155.
- Horn, B.K.P., 1977. Understanding image intensities. *Artif. Intell.* 8, 201–231.
- Horn, B.K.P., 1986. *Robot Vision*. MIT Press, Cambridge, MA.
- Horn, B.K.P., Brooks, M.J., 1986. The variational approach to shape from shading. *Comput. Vision Graph. Image Process* 33, 174–208.
- Horn, B.K.P., Brooks, M.J. (Eds.), 1989. *Shape from Shading*. MIT Press, Cambridge, MA.
- Horn, B.K.P., Schunck, B.G., 1981. Determining optical flow. *Artif. Intell.* 17 (1–3), 185–203.
- Horng, J.-H., 2003. An adaptive smoothing approach for fitting digital planar curves with line segments and circular arcs. *Pattern Recognit. Lett.* 24 (1–3), 565–577.
- Hornik, K., Stinchcombe, M., White, H., 1989. Multilayer feedforward networks are universal approximators. *Neural Networks* 2, 359–366.
- Horowitz, S.L. and Pavlidis, T., 1974. Picture segmentation by a directed split-and-merge procedure. In: *Proc. Second Int. Joint Conf. on Pattern Recognition*. pp. 424–433.
- Hough, P.V.C., 1962. Method and Means for Recognising Complex Patterns. US Patent 3069654.
- Hsiao, J.Y., Sawchuk, A.A., 1989. Supervised textured image segmentation using feature smoothing and probabilistic relaxation techniques. *IEEE Trans. Pattern Anal. Mach. Intell.* 11 (12), 1279–1292.
- Hsiao, J.Y., Sawchuk, A.A., 1990. Unsupervised textured image segmentation using feature smoothing and probabilistic relaxation techniques. *Comput. Vision Graph. Image Process* 48, 1–21.
- Hu, M.K., 1961. Pattern recognition by moment invariants. *Proc. IEEE* 49, 1428.
- Hu, M.K., 1962. Visual pattern recognition by moment invariants. *IRE Trans. Inf. Theory* 8, 179–187.
- Huang, C.T., Mitchell, O.R., 1994. A Euclidean distance transform using greyscale morphology decomposition. *IEEE Trans. Pattern Anal. Mach. Intell.* 16 (4), 443–448.
- Huang, G.B., and Learned-Miller, E., 2014. Labeled Faces in the Wild: Updates and New Reporting Procedures. University of Massachusetts, Amherst Technical Report UM-CS-2014-003.
- Huang, G.B., Jain, V., and Learned-Miller, E., 2007. Unsupervised joint alignment of complex images. In: *Proc. 11th IEEE Int. Conf. on Computer Vision*. 14–20 October, Rio de Janeiro, Brazil.

- Huang, L., Yang, Y., Deng, Y., and Yu, Y., 2015. DenseBox: Unifying Landmark Localization with End to End Object Detection. arXiv:1509.04874v3 [cs.CV] 19 Sep.
- Huang, T.S. (Ed.), 1983. Image Sequence Processing and Dynamic Scene Analysis. Springer-Verlag, New York.
- Huang, T.S., Yang, G.J., Tang, G.Y., 1979. A fast two-dimensional median filtering algorithm. *IEEE Trans. Acoust. Speech Signal Process* 27, 13–18.
- Huang, T.S., Bruckstein, A.M., Holt, R.J., Netravali, A.N., 1995. Uniqueness of 3D pose under weak perspective: a geometrical proof. *IEEE Trans. Pattern Anal. Mach. Intell.* 17 (12), 1220–1221.
- Hubel, D.H., 1995. Eye, Brain and Vision. Scientific American Library, New York.
- Huber, P.J., 1964. Robust estimation of a location parameter. *Ann. Math. Stat.* 35, 73–101.
- Huber, P.J., 1981. Robust Statistics. Wiley, New York.
- Huber, P.J., 1985. Projection pursuit. *Ann. Stat* 13 (2), 435–475.
- Hughes, G.F., 1968. On the mean accuracy of statistical pattern recognisers. *IEEE Trans. Inf. Theory* 14, 55–63.
- Huttenlocher, D.P., Klanderman, G.A., Rucklidge, W.J., 1993. Comparing images using the Hausdorff distance. *IEEE Trans. Pattern Anal. Mach. Intell.* 15 (9), 850–863.
- Ikeuchi, K., Horn, B.K.P., 1981. Numerical shape from shading and occluding boundaries. *Artif. Intell.* 17, 141–184.
- Isard, M., Blake, A., 1996. Contour tracking by stochastic propagation of conditional density. *Proc. Eur. Conf. Comput. Vision* 1, 343–356.
- Isard, M. and Blake, A., 1998. Icondensation: unifying low-level and high-level tracking in a stochastic framework. In: *Proc. European Conf. on Computer Vision*. Freiburg, Germany, Vol. I, pp. 893–908.
- Ito, M., Ishii, A., 1986. Three-view stereo analysis. *IEEE Trans. Pattern Anal. Mach. Intell.* 8 (4), 524–532.
- Jacinto, C.N., Arnaldo, J.A., George, S.M., 2003. Using middle level features for robust shape tracking. *Pattern Recognit. Lett.* 24, 295–307.
- Jackway, P.T., Deriche, M., 1996. Scale-space properties of the multiscale morphological dilation-erosion. *IEEE Trans. Pattern Anal. Mach. Intell.* 18 (1), 38–51.
- Jain, A.K., 2010. Data clustering: 50 years beyond  $k$ -means. *Pattern Recognit. Lett.* 31 (8), 651–666.
- Jain, A.K., Dubes, R.C., 1988. Algorithms for Clustering Data. Prentice-Hall, Englewood Cliffs, NJ.
- Jain, A.K., Duin, R.P.W., Mao, J., 2000. Statistical pattern recognition. *IEEE Trans. Pattern Anal. Mach. Intell.* 22 (1), 4–37.
- Jain, R., 1983. Direct computation of the focus of expansion. *IEEE Trans. Pattern Anal. Mach. Intell.* 5, 58–63.
- Jain, V., Learned-Miller, E., 2010. FDDB: A Benchmark for Face Detection in Unconstrained Settings. University of Massachusetts Technical Report UM-CS-2010-009.
- Jang, Y.K., Kang, B.J., Park, K.R., 2008. A study on eyelid localization considering image focus for iris recognition. *Pattern Recognit. Lett.* 29, 1698–1704.
- Janney, P., Geers, G., 2010. Texture classification using invariant features of local textures. *IET Image Process.* 4 (3), 158–171.
- Jiang, J.-A., Chuang, C.-L., Lu, Y.-L., Fahn, C.-S., 2007. Mathematical-morphology-based edge detectors for detection of thin edges in low-contrast regions. *IET Image Process.* 1 (3), 269–277.



- Jolion, J.-M., Rosenfeld, A., 1989. Cluster detection in background noise. *Pattern Recognit. Lett.* 22 (5), 603–607.
- Jones, M.J., Rehg, J.M., 2002. Statistical color models with application to skin detection. *Int. J. Comput. Vision* 46 (1), 81–96.
- Juan, A., Vidal, E., 1994. Fast  $K$ -means-like clustering in metric spaces. *Pattern Recognit. Lett.* 15 (1), 19–25.
- Kadir, T., Brady, M., 2001. Scale, saliency and image description. *Int. J. Comput. Vision* 45 (2), 83–105.
- Kadir, T., Brady, M. and Zisserman, A., 2004. An affine invariant method for selecting salient regions in images. In: *Proc. Eighth European Conf. on Computer Vision (ECCV)*. pp. 345–457.
- Kadyrov, A., Petrou, M., 2001. The trace transform and its applications. *IEEE Trans. Pattern Anal. Mach. Intell.* 23, 811–828.
- Kadyrov, A. and Petrou, M., 2002. Affine parameter estimation from the trace transform. In: *Proc. 16th Int. Conf. on Pattern Recognition*. 11–15 Aug., Québec, Canada, Vol. II, pp. 798–801.
- Kaizer, H., 1955. A Quantification of Textures on Aerial Photographs. Ms Thesis, Boston Univ., Boston, MA, USA.
- Kamat-Sadekar, V. and Ganesan, S., 1998. Complete description of multiple line segments using the Hough transform. In Davies, E.R. and Atiquzzaman, M. (eds.), *Special Issue on Projection-Based Transforms, Image Vision Computing*. Vol. 16, nos. 9–10, pp. 597–614.
- Kamel, M.S., Shen, H.C., Wong, A.K.C., Hong, T.M., Campeanu, R.I., 1994. Face recognition using perspective invariant features. *Pattern Recognit. Lett.* 15 (9), 877–883.
- Kanatani, K., Sugaya, Y. and Niitsuma, H., 2008. Triangulation from two views revisited: Hartley-Sturm vs. optimal correction. In: *Proc. British Machine Vision Assoc. Conf.*
- Kanesalingam, C., Smith, M.C.B., and Dodds, S.A., 1998. An efficient algorithm for environmental mapping and path planning for an autonomous mobile robot. In: *Proc. 29th Int. Symp. on Robotics*. Birmingham, pp. 133–136.
- Kang, D.-J., Jung, M.-H., 2003. Road lane segmentation using dynamic programming for active safety vehicles. *Pattern Recognit. Lett.* 24, 3177–3185.
- Kapur, J.N., Sahoo, P.K., Wong, A.K.C., 1985. A new method for gray-level picture thresholding using the entropy of the histogram. *Comput. Vision Graph. Image Process* 29, 273–285.
- Kasif, S., Kitchen, L., Rosenfeld, A., 1983. A Hough transform technique for subgraph isomorphism. *Pattern Recognit. Lett.* 2, 83–88.
- Kass, M., Witkin, A., 1987. Analyzing oriented patterns. *Comput. Vision Graph. Image Process* 37 (3), 362–385.
- Kass, M., Witkin, A., Terzopoulos, D., 1988. Snakes: active contour models. *Int. J. Comput. Vision* 1, 321–331.
- Kastrinaki, V., Zervakis, M., Kalaitzakis, K., 2003. A survey of video processing techniques for traffic applications. *Image Vision Comput.* 21 (4), 359–381.
- Keagy, P.M., Parvin, B., Schatzki, T.F., 1995. Machine recognition of navel orange worm damage in x-ray images of pistachio nuts. *Opt. Agric., For. Biol., SPIE* 2345, 192–203.
- Keagy, P.M., Parvin, B., Schatzki, T.F., 1996. Machine recognition of navel orange worm damage in X-ray images of pistachio nuts. *Lebensm. Wiss. Technol.* 29, 140–145.

- Kégl, B., Krzyżak, A., 2002. Piecewise linear skeletonization using principal curves. *IEEE Trans. Pattern Anal. Mach. Intell.* 24 (1), 59–74.
- Kehtarnavaz, N., Mohan, S., 1989. A framework for estimation of motion parameters from range images. *Comput. Vision Graph. Image Process* 45, 88–105.
- Kelly, P., Beardsley, P., Cooke, E., O'Connor, N., Smeaton, A., 2005. Detecting shadows and low-lying objects in indoor and outdoor scenes using homographies. *Proc. IET Conf. Visual Inf. Eng. Glasgow*, 4–6 April, 393–400.
- Kender, J.R., 1980. Shape from Texture. Carnegie-Mellon University, Comput. Sci. Techn. Rep. CMU-CS-81-102.
- Kender, J.R., 1983. Shape from Texture. Carnegie-Mellon Univ. Techn. Report CMU-CS-81-102.
- Kenney, C.S., Manjunath, B.S., Zuliani, M., Hower, G.A., van Nevel, A., 2003. A condition number for point matching with application to registration and postregistration error estimation. *IEEE Trans. Pattern Anal. Mach. Intell.* 25 (11), 1437–1454.
- Kesidis, A.L., Papamarkos, N., 2000. On the grayscale inverse Hough transform. *Image Vision Comput.* 18 (8), 607–618.
- Kessal, L., Abel, N., Demigny, D., 2003. Real-time image processing with dynamically reconfigurable architecture. *Real-Time Imaging* 9 (5), 297–313.
- Khan, S. and Shah, M., 2000. Tracking people in presence of occlusion. In: *Proc. Asian Conf. on Computer Vision*.
- Khan, S., Shah, M., 2003. Consistent labeling of tracked objects in multiple cameras with overlapping fields of view. *IEEE Trans. Pattern Anal. Mach. Intell.* 25 (10), 1355–1360.
- Khan, S., Shah, M., 2009. Tracking multiple occluding people by localizing on multiple scene planes. *IEEE Trans. Pattern Anal. Mach. Intell.* 31 (3), 505–519.
- Kim, D., Kim, D., Paik, J., 2010. Gait recognition using active shape model and motion prediction. *IET Comput. Vision* 4 (1), 25–36.
- Kim, D.-S., Lee, W.-H., Kweon, I.-S., 2004. Automatic edge detection using  $3 \times 3$  ideal binary pixel patterns and fuzzy-based edge thresholding. *Pattern Recognit. Lett.* 25 (1), 101–106.
- Kim, D.Y., Kim, J.J., Meer, P., Mintz, D. and Rosenfeld, A., 1989. Robust computer vision: a least median of squares based approach. In: *Proc. DARPA Image Understanding Workshop*, 23–26 May, Palo Alto, CA, pp. 1117–1134.
- Kim, Z.-W., 2008. Robust lane detection and tracking in challenging scenarios. *IEEE Trans. Intell. Transp. Syst.* 9 (1), 16–26.
- Kimme, C., Ballard, D., Sklansky, J., 1975. Finding circles by an array of accumulators. *Commun. ACM* 18, 120–122.
- Kimura, A. and Watanabe, T., 2002. An extension of the generalized Hough transform to realize affine-invariant two-dimensional (2D) shape detection. In: *Proc. 16th Int. Conf. on Pattern Recognition*, 11–15 Aug., Québec, Canada, Vol. I, pp. 65–69.
- Kirsch, R.A., 1971. Computer determination of the constituent structure of biological images. *Comput. Biomed. Res.* 4, 315–328.
- Kiryati, N., Bruckstein, A.M., 1991. Antialiasing the Hough transform. *Comput. Vision Graph. Image Process: Graph. Models Image Process* 53 (3), 213–222.
- Kitchen, L., Rosenfeld, A., 1979. Discrete relaxation for matching relational structures. *IEEE Trans. Syst. Man Cybern* 9, 869–874.

- Kitchen, L., Rosenfeld, A., 1982. Gray-level corner detection. *Pattern Recognit. Lett.* 1, 95–102.
- Kittler, J., 1983. On the accuracy of the Sobel edge detector. *Image Vision Comput.* 1, 37–42.
- Kittler, J., Illingworth, J., Föglein, J., 1985. Threshold selection based on a simple image statistic. *Comput. Vision Graph. Image Process* 30, 125–147.
- Klassen, E., Srivistava, A., Mio, W., Joshi, S.H., 2004. Analysis of planar shapes using geodesic paths on shape spaces. *IEEE Trans. Pattern Anal. Mach. Intell.* 26 (3), 372–383.
- Knop, R., 1969. Remark on Algorithm 334 [g5]: normal random deviates. *Commun. ACM* 12 (5), 281.
- Koenderink, J.J., van Doorn, A.J., 1979. The internal representation of solid shape with respect to vision. *Biol. Cybern.* 32, 211–216.
- Koivo, A.J., Kim, C.W., 1989. Robust image modelling for classification of surface defects on wood boards. *IEEE Trans. Syst. Man Cybern.* 19 (6), 1659–1666.
- Köktas, N.S., Yalabik, N., Yavuzer, G., Duin, R.P.W., 2010. A multi-classifier for grading knee osteoarthritis using gait analysis. *Pattern Recognit. Lett.* 31 (9), 898–904.
- Koller, D., Weber, J., Huang, T., Malik, J., Ogasawara, G., Rao, B. and Russell, S., 1994. Towards robust automatic traffic scene analysis in real-time. In: *Proc. 12th Int. Conf. on Pattern Recognition*. 9–13 Oct., Jerusalem, Israel, pp. 126–131.
- Koplowitz, J., Bruckstein, A.M., 1989. Design of perimeter estimators for digitized planar shapes. *IEEE Trans. Pattern Anal. Mach. Intell.* 11, 611–622.
- Kortenkamp, D., Bonasso, R.P., Murphy, R. (Eds.), 1998. *Artificial Intelligence and Mobile Robots*. AAAI Press/The MIT Press, Menlo Park, California; Cambridge, Massachusetts; London, England.
- Krizhevsky, A., Sutskever, I., and Hinton, G.E., 2012. ImageNet classification with deep convolutional neural networks. In: *Proc. 26th Annual Conf. on Neural Information Processing Systems*. 3–8 December, Lake Tahoe, Nevada.
- Kroon, D.-J., 2011. Segmentation of the Mandibular Canal in Cone-beam CT Data. PhD Thesis, University of Twente, The Netherlands.
- Kuehnle, A., 1991. Symmetry-based recognition of vehicle rears. *Pattern Recognit. Lett.* 12, 249–258.
- Kulpa, Z., 1977. Area and perimeter measurement of blobs in discrete binary pictures. *Comput. Graph. Image Process.* 6, 434–451.
- Kumar, R. and Hanson, A.R., 1989. Robust estimation of camera location and orientation from noisy data having outliers. In: *Proc. Workshop on Interpretation of 3D Scenes*. 27–29 Nov., Austin, TX, pp. 52–60.
- Kuo, P., Makris, D., Nebel, J.-C., 2011. Integration of bottom-up/top-down approaches for 2D pose estimation using probabilistic Gaussian modelling. *Comput. Vision Image Understanding* 115 (2), 242–255.
- Kuo, W.-J. and Lin, C.-C., 2007. Two-stage road sign detection and recognition. In: *Proc. IEEE Int. Conf. on Multimedia and Expo*. 2–5 July, Beijing, pp. 1427–1430.
- Kuo, Y.-C., Pai, N.-S., Li, Y.-F., 2011. Vision-based vehicle detection for a driver assistance system. *Comput. Math. Appl.* 61, 2096–2100.
- Kwok, P.C.K., 1989. Customising thinning algorithms. In: *Proceedings of the Third International Conference on Image Processing and its Applications*. 18–20 July, Warwick, IEE Conf. Publ. 307, 633–637.

- Lacroix, V., 1988. A three-module strategy for edge detection. *IEEE Trans. Pattern Anal. Mach. Intell.* 10, 803–810.
- Lamdan, Y. and Wolfson, H.J., 1988. Geometric hashing: a general and efficient model-based recognition scheme. In: *Proc. IEEE Second Int. Conf. on Computer Vision*, Tampa, FL (Dec.), pp. 238–249.
- Lane, R.A., Thacker, N.A., Seed, N.L., 1994. Stretch-correlation as a real-time alternative to feature-based stereo matching algorithms. *Image Vision Comput.* 12 (4), 203–212.
- Laurentini, A., 1994. The visual hull concept for silhouette-based image understanding. *IEEE Trans. Pattern Anal. Mach. Intell.* 16 (2), 150–162.
- Laws, K.I., 1979. Texture energy measures. *Proc. Image Understanding Workshop*, Nov 47–51.
- Laws, K.I., 1980a. Rapid texture identification. In: *Proc. SPIE Conf. on Image Processing for Missile Guidance*. 28 July – 1 Aug, San Diego, Calif., Vol. 238, pp. 376–380.
- Laws, K.I., 1980b. *Textured Image Segmentation*. PhD Thesis, Univ. of Southern California, Los Angeles.
- Lazarevic-McManus, N., Renno, J.R., Makris, D., Jones, G.A., 2008. An object-based comparative methodology for motion detection based on the F-Measure. *Comput. Vision Image Understanding* 111 (1), 74–85.
- Leavers, V.F., 1993. Which Hough transform? *Comput. Vision Graph. Image Process.: Image Understanding* 58 (2), 250–264.
- Leavers, V.F., Boyce, J.F., 1987. The Radon transform and its application to shape parametrization in machine vision. *Image Vision Comput.* 5, 161–166.
- Lebègue, X., Aggarwal, J.K., 1993. Significant line segments for an indoor mobile robot. *IEEE Trans. Rob. Autom.* 9 (6), 801–815.
- LeCun, Y., Boser, B., Denker, J.S., Henderson, D., Howard, R.E., Hubbard, W., Jackel, L. D., 1989. Backpropagation applied to handwritten zip code recognition. *Neural Comput.* 1 (4), 541–551.
- LeCun, Y., Bottou, L., Bengio, Y., Haffner, P., 1998. Gradient-based learning applied to document recognition. *Proc. IEEE* 86, 2278–2324.
- Lee, D.H. and Park, Y.T., 2006. Robust vehicle detection based on shadow classification. In: *Proc. 18th Int. Conf. Pattern Recognition*, Vol. 3, pp. 1167–1170.
- Lee, M.-S., Medioni, G., Mordohai, P., 2002. Inference of segmented overlapping surfaces from binocular stereo. *IEEE Trans. Pattern Anal. Mach. Intell.* 24 (6), 824–837.
- Lei, Y., Wong, K.C., 1999. Ellipse detection based on symmetry. *Pattern Recognit. Lett.* 20 (1), 41–47.
- Leibe, B., Seemann, E. and Schiele, B., 2005. Pedestrian detection in crowded scenes. In: *Proc. Conf. on Computer Vision and Pattern Recognition*.
- Lenc, K., and Vedaldi, A., 2015. R-CNN Minus R. arXiv:1506.06981 [cs.CV] 23 Jun.
- Lepetit, V., Moreno-Noguer, F., Fua, P., 2008. EPnP: An accurate O(n) solution to the PnP problem. *Int. J. Comput. Vision* 81 (2), 155–166.
- Lev, A., Zucker, S.W., Rosenfeld, A., 1977. Iterative enhancement of noisy images. *IEEE Trans. Syst. Man Cybern.* 7, 435–442.
- Levine, M.D., 1985. *Vision in Man and Machine*. McGraw-Hill, New York.
- Lézoray, O., Charrier, C., 2009. Color image segmentation using morphological clustering and fusion with automatic scale selection. *Pattern Recognit. Lett.* 30 (4), 397–406.
- Li, H. and Lavin, M.A., 1986. Fast Hough transform based on bintree data structure. In: *Proc. Conf. Comput. Vision and Pattern Recognition*. Miami Beach, Florida, pp. 640–642.

- Li, H., Lavin, M.A. and LeMaster, R.J., 1985. Fast Hough transform. In: Proc. Third Workshop on Comput. Vision: Representation and Control. Bellair, pp. 75–83.
- Li, L., Tan, C.L., 2010. Recognizing planar symbols with severe perspective deformation. *IEEE Trans. Pattern Anal. Mach. Intell.* 32 (4), 755–762.
- Li, P., Liu, X., Xiao, L., Song, Q., 2010. Robust and accurate iris segmentation in very noisy iris images. *Image Vision Comput.* 28, 246–253.
- Li, S.Z., Zhang, Z.Q., 2004. FloatBoost learning and statistical face detection. *IEEE Trans. Pattern Anal. Mach. Intell.* 26 (9), 1112–1123.
- Li, Z., Yang, J., Liu, G., Cheng, Y., Liu, C., 2011. Unsupervised range-constrained thresholding. *Pattern Recognit. Lett.* 32 (2), 392–402.
- Lian, G., Lai, J., Zheng, W.-S., 2011. Spatial–temporal consistent labeling of tracked pedestrians across non-overlapping camera views. *Pattern Recognit.* 44, 1121–1136.
- Liao, P.-S., Chen, T.-S., Chung, P.-C., 2001. A fast algorithm for multilevel thresholding. *J. Inf. Sci. Eng.* 17, 713–727.
- Lin, C.C., Chellappa, R., 1987. Classification of partial 2-D shapes using Fourier descriptors. *IEEE Trans. Pattern Anal. Mach. Intell.* 9, 686–690.
- Lindeberg, T., 1998. Feature detection with automatic scale selection. *Int. J. Comput. Vision* 30 (2), 79–116.
- Lippmann, R.P., 1987. An introduction to computing with neural nets. *IEEE Acoust., Speech, Signal Process. Mag.* 4 (2), 4–22.
- Liu, L., Sclaroff, S., 2004. Deformable model-guided region split and merge of image regions. *Image Vision Comput.* 22 (4), 343–354.
- Liu, M.L., Wong, K.H., 1999. Pose estimation using four corresponding points. *Pattern Recognit. Lett.* 20 (1), 69–74.
- Liu, W., Wen, X.-Z., Duan, B., Yuan, H., and Wang, N., 2007. Rear vehicle detection and tracking for lane change assist. In: Proc. IEEE Intelligent Vehicles Symposium. 13–15 June, pp. 252–257.
- Lladós, J., Martí, E., Villanueva, J.J., 2001. Symbol recognition by error-tolerant subgraph matching between region adjacency graphs. *IEEE Trans. Pattern Anal. Mach. Intell.* 23 (10), 1137–1143.
- Lockton, R. and Fitzgibbon, A., 2002. Real-time gesture recognition using deterministic boosting. In: Proc. British Machine Vision Assoc. Conf. 2–5 Sept., Cardiff, UK, pp. 817–826.
- Long, J., Shelhamer, E., and Darrell, T., 2015. Fully convolutional networks for semantic segmentation. In: Proc. IEEE Conf. on Computer Vision and Pattern Recognition. 7–12 June, Boston, MA, pp. 3431–3440.
- Longuet-Higgins, H.C., 1981. A computer algorithm for reconstructing a scene from two projections. *Nature* 293, 133–135.
- Longuet-Higgins, H.C., 1984. The visual ambiguity of a moving plane. *Proc. Royal Soc. London, Ser. B* 233, 165–175.
- Longuet-Higgins, H.C., Prazdny, K., 1980. The interpretation of a moving retinal image. *Proc. Royal Soc. London, Ser. B* 208, 385–397.
- Lowe, D., 2004. Distinctive image features from scale-invariant keypoints. *Int. J. Comput. Vision* 60, 91–110.
- Lowe, D.G., 1999. Object recognition from local scale-invariant features. In: Proc. Seventh Int. Conf. on Computer Vision (ICCV). Corfu, Greece, pp. 1150–1157.

- Lüdtke, N., Luo, B., Hancock, E. and Wilson, R.C., 2002. Corner detection using a mixture model of edge orientation. In: Proc. 16th Int. Conf. on Pattern Recognition. 11–15 Aug., Québec, Canada, Vol. II, pp. 574–577.
- Lukac, R., 2003. Adaptive vector median filtering. *Pattern Recognit. Lett.* 24 (12), 1889–1899.
- Luo, B., Hancock, E.R., 2001. Structural graph matching using the EM algorithm and singular value decomposition. *IEEE Trans. Pattern Anal. Mach. Intell.* 23 (10), 1120–1136.
- Luong, Q.-T., Faugeras, O., 1997. Self-calibration of a moving camera from point correspondences and fundamental matrices. *Int. J. Comput. Vision* 22 (3), 261–289.
- Lutton, E., Maître, H., Lopez-Krahe, J., 1994. Contribution to the determination of vanishing points using Hough transform. *IEEE Trans. Pattern Anal. Mach. Intell.* 16 (4), 430–438.
- Lyvers, E.R., Mitchell, O.R., 1988. Precision edge contrast and orientation estimation. *IEEE Trans. Pattern Anal. Mach. Intell.* 10, 927–937.
- Ma, L., Tan, T., Wang, Y., Zhang, D., 2003. Personal identification based on iris texture analysis. *IEEE Trans. Pattern Anal. Mach. Intell.* 25 (12), 1519–1533.
- Ma, Y., Derksen, H., Hong, W., Wright, J., 2007. Segmentation of multivariate mixed data via lossy data coding and compression. *IEEE Trans. Pattern Anal. Mach. Intell.* 29 (9), 1546–1562.
- Mackeown, W.P.J., Greenway, P., Thomas, B.T., Wright, W.A., 1994. Contextual image labelling with a neural network. *IEE Proc. Vision Image Signal Process.* 141 (4), 238–244.
- MacQueen, J.B., 1967. Some methods for classification and analysis of multivariate observations. In: Proc. Fifth Berkeley Symp. on Math. Stat. and Prob. Vol. I, pp. 281–297.
- Magee, D.R., 2004. Tracking multiple vehicles using foreground, background and motion models. *Image Vision Comput.* 22, 143–155.
- Magee, M.J., Aggarwal, J.K., 1984. Determining vanishing points from perspective images. *Comput. Vision Graph. Image Process.* 26 (2), 256–267.
- Makris, D., Ellis, T. and Black, J., 2004. Bridging the Gaps between Cameras. In: Proc. IEEE Conf. on Computer Vision and Pattern Recognition. Washington DC, USA, pp. 205–210.
- Manthalkar, R., Biswas, P.K., Chatterji, B.N., 2003. Rotation invariant texture classification using even symmetric Gabor filters. *Pattern Recognit. Lett.* 24 (12), 2061–2068.
- Marchant, J.A., 1996. Tracking of row structure in three crops using image analysis. *Comput. Electron. Agric.* 15, 161–179.
- Marchant, J.A., Brivot, R., 1995. Real-time tracking of plant rows using a Hough transform. *Real-Time Imaging* 1 (5), 363–371.
- Marchant, J.A., Onyango, C.M., 1995. Fitting grey level point distribution models to animals in scenes. *Image Vision Comput.* 13 (1), 3–12.
- Marchant, J.A., Tillett, R.D., Brivot, R., 1998. Real-time segmentation of plants and weeds. *Real-Time Imaging* 4, 243–253.
- Marr, D., 1976. Early processing of visual information. *Philos. Trans. Royal Soc. London, Ser. B* 275, 483–524.
- Marr, D., Hildreth, E., 1980. Theory of edge detection. *Proc. Royal Soc. London, Ser. B* 207, 187–217.

- Marr, D., Poggio, T., 1979. A computational theory of human stereo vision. *Proc. Royal Soc. London, Ser. B* 204, 301–328.
- Marshall, S., 2004. New direct design method for weighted order statistic filters. *IEE Proc. Vision Image Signal Process.* 151 (1), 1–8.
- Marshall, S., Harvey, N., Shah, D. (Eds.), 1998. *Proc. Noblesse Workshop on Non-linear Model Based Image Analysis*. Glasgow (1–3 July). Springer-Verlag, London.
- Marslin, R.F., Sullivan, G.D. and Baker, K.D., 1991. Kalman filters in constrained model based tracking. In: *Proc. Second British Machine Vision Assoc. Conf.* 23–26 Sept., Glasgow, pp. 371–374.
- Martino, L., Luengo, D., Míguez, J., 2012. Efficient sampling from truncated bivariate Gaussians via Box–Muller transformation. *Electron. Lett.* 48 (24), 1533–1534.
- Mastorakis, G., Davies, E.R., 2011. Improved line detection algorithm for locating road lane markings. *Electron. Lett.* 47 (3), 183–184.
- Matas, J., Chum, O., Urban, M., Pajdla, T., 2002. Robust wide baseline stereo from maximally stable extremal regions. *Proc. British Machine Vision Conf. (BMVC)*. Cardiff University, UK, pp. 384–393.
- Mathias, M., Benenson, R., Pedersoli, M., and Van Gool, L., 2014. Face detection without bells and whistles. In: *Proc. 13th European Conf. on Computer Vision*. 8–11 September, Zurich, Switzerland.
- Maybank, S., 1992. *Theory of Reconstruction from Image Motion*. Springer-Verlag, Berlin, Heidelberg.
- Maybank, S. and Tan, T. (Eds.) (2004). Special issue: Visual Surveillance. *Image Vision Comput.* 22 (7), 515–582.
- Maybank, S.J., 1986. Algorithm for analysing optical flow based on the least squares method. *Image Vision Comput.* 4, 38–42.
- Maybank, S.J., 1996. Stochastic properties of the cross ratio. *Pattern Recognit. Lett.* 17 (3), 211–217.
- Maybank, S.J., Faugeras, O., 1992. A theory of self-calibration of a moving camera. *Int. J. Comput. Vision* 8 (2), 123–151.
- Maybeck, P.S., 1979. *Stochastic Models, Estimation, and Control, Volume 1*. Academic Press, New York and London.
- McFarlane, N.J.B., Schofield, C.P., 1995. Segmentation and tracking of piglets in images. *Mach. Vision Appl.* 8 (3), 187–193.
- McGunnigle, G., Chantler, M., 2003. Resolving handwriting from background printing using photometric stereo. *Pattern Recognit.* 36, 1869–1879.
- McGunnigle, G., Dong, J., 2011. Augmenting photometric stereo with coaxial illumination. *IET Comput. Vision* 5 (1), 33–49.
- McLoughlin, S., Deegan, C., Mulvihill, C., Fitzgerald, C., Markham, C., 2008. Mobile mapping for the automated analysis of road signage and delineation. *IET Intel. Transport Syst.* 2 (1), 61–73.
- Medina-Carnicer, R., Muñoz-Salinas, R., Carmona-Poyato, A., Madrid-Cuevas, F.J., 2011. A novel histogram transformation to improve the performance of thresholding methods in edge detection. *Pattern Recognit. Lett.* 32 (5), 676–693.
- Meer, P., Georgescu, B., 2001. Edge detection with embedded confidence. *IEEE Trans. Pattern Anal. Mach. Intell.* 23 (12), 1351–1365.
- Meer, P., Mintz, D. and Rosenfeld, A., 1990. Least median of squares based robust analysis of image structure. In: *Proc. DARPA Image Understanding Workshop*. 11–13 Sept., Pittsburgh, Pennsylvania, pp. 231–254.

- Meer, P., Mintz, D., Rosenfeld, A., Kim, D.Y., 1991. Robust regression methods for computer vision: a review. *Int. J. Comput. Vision* 6 (1), 59–70.
- Méler, A., Decrouez, M. and Crowley, J., 2010. BetaSAC: a new conditional sampling for RANSAC. In: *Proc. British Machine Vision Assoc. Conf.*
- Merlin, P.M., Farber, D.J., 1975. A parallel mechanism for detecting curves in pictures. *IEEE Trans. Comput.* 28, 96–98.
- Mikolajczyk, K., 2002. Interest Point Detection Invariant to Affine Transformations. PhD Thesis. Institut National Polytechnique de Grenoble (INPG), France.
- Mikolajczyk, K. and Schmid, C., 2002. An affine invariant interest point detector. In: *Proc. European Conf. on Computer Vision (ECCV)*. Copenhagen, Denmark, pp. 128–142.
- Mikolajczyk, K., Schmid, C., 2004. Scale and affine invariant interest point detectors. *Int. J. Comput. Vision* 60 (1), 63–86.
- Mikolajczyk, K., Schmid, C., 2005. A performance evaluation of local descriptors. *IEEE Trans. Pattern Anal. Mach. Intell.* 27 (10), 1615–1630.
- Mikolajczyk, K., Tuytelaars, T., Schmid, C., Zisserman, A., Matas, J., Schaffalitzky, F., et al., 2005. A comparison of affine region detectors. *Int. J. Comput. Vision* 65, 43–72.
- Mikolov, T., Chen, K., Corrado, G., Dean, J., 2013. Efficient Estimation of Word Representations in Vector Space. arXiv:1301.3781v3 [cs.CL] 7 Sep.
- Min, T.-H., Park, R.-H., 2009. Eyelid and eyelash detection method in the normalized iris image using the parabolic Hough model and Otsu's thresholding method. *Pattern Recognit. Lett.* 30, 1138–1143.
- Minsky, M.L., Papert, S.A., 1969. *Perceptrons*. MIT Press, Cambridge.
- Mirmehdi, M., Petrou, M., 2000. Segmentation of colour textures. *IEEE Trans. Pattern Anal. Mach. Intell.* 22 (2), 142–159.
- Mirmehdi, M., Xie, X., Suri, J. (Eds.), 2008. *Handbook of Texture Analysis*. Imperial College Press, London.
- Mishra, A.K., Fieguth, P.W., Clausi, D.A., 2011. Decoupled active contour (DAC) for boundary detection. *IEEE Trans. Pattern Anal. Mach. Intell.* 33 (2), 310–324.
- Mohr, R. and Wu, C. (Eds.), 1998. In: *Special Issue on Geometric Modelling and Invariants for Computer Vision, Image Vision Computing*. 16, 1.
- Mokhtarian, F., Bober, M., 2003. *Curvature Scale Space Representation: Theory, Applications and MPEG-7 Standardisation*. Kluwer Academic Publishers, Dordrecht.
- Mokhtarian, F., Abbasi, S., Kittler, J., 1996. Efficient and robust shape retrieval by shape content through curvature scale space. In: *Proc. 1st Int. Conf. Image Database and Multi-Search*, pp. 35–42.
- Montiel, E., Aguado, A.S., Nixon, M.S., 2001. Improving the Hough transform gathering process for affine transformations. *Pattern Recognit. Lett.* 22 (9), 959–969.
- Moravec, H.P., 1977. Towards automatic visual obstacle avoidance. In: *Proc. Fifth Int. Joint. Conf. on Artificial Intelligence*. 22–25 August, Cambridge, MA, pp. 584.
- Moravec, H.P., 1980. Obstacle avoidance and navigation in the real world by a seeing robot rover. *Stanford Artif. Intell. Lab. Memo AIM-340*.
- Mori, G., Belongie, S., Malik, J., 2005. Efficient shape matching using shape contexts. *IEEE Trans. Pattern Anal. Mach. Intell.* 27 (11), 1832–1837.
- Mundy, J.L. and Zisserman, A. (Eds.), 1992a. *Geometric Invariance Computer Vision*. MIT Press, Cambridge, MA.
- Mundy, J.L. and Zisserman, A., 1992b. Appendix—Projective Geometry for Machine Vision. In Mundy, J.L. and Zisserman, A. (Eds.) (1992a), op. cit., pp. 463–519.



- Myatt, D.R., Torr, P.H.S., Nasuto, S.J., Bishop, J.M., Craddock, R., 2002. Napsac: high noise, high dimensional robust estimation – it's in the bag. *Proc. British Machine Vision Assoc. Conf.* 458–467.
- Nagao, M., Matsuyama, T., 1979. Edge preserving smoothing. *Comput. Graph. Image Process.* 9, 394–407.
- Nagel, H.-H., 1983. Displacement vectors derived from second-order intensity variations in image sequences. *Comput. Vision Graph. Image Process.* 21, 85–117.
- Nagel, H.-H., 1986. Image sequences – ten (octal) years—from phenomenology towards a theoretical foundation. In: *Proc. Eighth Int. Conf. on Pattern Recognition*. 27–31 October, Paris, pp. 1174–1185.
- Nagel, R.N., Rosenfeld, A., 1972. Ordered search techniques in template matching. *Proc. IEEE* 60, 242–244.
- Nait-Charif, H. and McKenna, S.J., 2004. Tracking poorly modelled motion using particle filters with iterated likelihood weighting. In: *Proc. Asian Conf. on Computer Vision*. Jeju Island, Korea, pp. 156–161.
- Nait-Charif, H., McKenna, S.J., 2006. Tracking the activity of participants in a meeting. *Mach. Vision Appl.* 17 (2), 83–93.
- Nakagawa, Y., Rosenfeld, A., 1979. Some experiments on variable thresholding. *Pattern Recognit.* 11, 191–204.
- Narendra, P.M., 1978. A separable median filter for image noise smoothing. In: *Proc. IEEE Computer Soc. Conf. on Pattern Recognition and Image Process.* 31 May–2 June, Chicago, pp. 137–141.
- Ng, H.-F., 2006. Automatic thresholding for defect detection. *Pattern Recognit. Lett.* 27 (14), 1644–1649.
- Ni, K., Jin, H. and Dellaert, F., 2009. GroupSAC: Efficient consensus in the presence of groupings. In: *Proc. Int. Conf. on Computer Vision*. October, Kyoto, Japan.
- Niblack, W., 1985. *An Introduction to Digital Image Processing*. Strandberg, Birkerød, Denmark.
- Nieminen, A., Heinonen, P., Neuvo, Y., 1987. A new class of detail-preserving filters for image processing. *IEEE Trans. Pattern Anal. Mach. Intell.* 9, 74–90.
- Nilsson, N.J., 1965. *Learning Machines—Foundations of Trainable Pattern-Classifying Systems*. McGraw-Hill, New York.
- Nitzan, D., Brain, A.E., Duda, R.O., 1977. The measurement and use of registered reflectance and range data in scene analysis. *Proc. IEEE* 65, 206–220.
- Nixon, M., 1985. Application of the Hough transform to correct for linear variation of background illumination in images. *Pattern Recognit. Lett.* 3, 191–194.
- Nixon, M., Aguado, A., 2008. *Feature Extraction and Image Processing*, second ed. Academic Press, Oxford, UK.
- Nixon, M.S., Tan, T.N., Chellappa, R., 2006. *Human Identification Based on Gait*. Springer, New York.
- Noble, J.A., 1988. Finding corners. *Image Vision Comput.* 6, 121–128.
- Noh, H., Hong, S., Han, B., 2015. Learning deconvolution network for semantic segmentation. In: *Proc. IEEE Int. Conf. on Computer Vision*. 13–16 December, Santiago, Chile, pp. 1520–1528. See also arXiv:1505.04366v1 [cs.CV] 17 May.
- North, D.O., 1943. An analysis of the factors which determine signal/noise discrimination in pulsed-carrier systems. In: *Rep. PTR-6C*; Reprinted in *Proc. IEEE* 51, 1963, RCA Lab., Princeton, NJ, pp. 1016–1027.

- Noyce, R.N., 1977. Microelectronics. *Sci. Am.* 237 (September), 62–69.
- Nummiaro, K., Koller-Meier, E., Van Gool, L., 2003. An adaptive color-based particle filter. *Image Vision Comput.* 21 (1), 99–110.
- O’Gorman, F., 1978. Edge detection using Walsh functions. *Artif. Intell.* 10, 215–223.
- O’Gorman, F., Clowes, M.B., 1976. Finding picture edges through collinearity of feature points. *IEEE Trans. Comput.* 25, 449–456.
- Ohanian, P.P., Dubes, R.C., 1992. Performance evaluation for four classes of textural features. *Pattern Recognit.* 25, 819–833.
- Ohta, Y., Maenobu, K. and Sakai, T., 1981. Obtaining surface orientation from texels under perspective projection. In: *Proc. Seventh Int. Joint Conf. on Artif. Intell. Vancouver*, pp. 746–751.
- Oja, E., 1982. A simplified neuron model as a principal component analyzer. *Int. J. Neural. Syst.* 1, 61–68.
- Ojala, T., Pietikäinen, M., Mäenpää, T., 2002. Multiresolution gray-scale and rotation-invariant texture classification with local binary patterns. *IEEE Trans. Pattern Anal. Mach. Intell.* 24 (7), 971–987.
- Olague, G. and Hernández, B., 2002. Flexible model-based multi-corner detector for accurate measurements and recognition. In: *Proc. 16th Int. Conf. on Pattern Recognition. 11–15 Aug., Québec, Canada, Vol. II*, pp. 578–583.
- Olson, C.F., 1998. Improving the generalized Hough transform through imperfect grouping. In Davies, E.R. and Atiquzzaman, M. (Eds.), *Special Issue on Projection-Based Transforms, Image Vision Computing*. 16 (9–10), 627–634.
- Olson, C.F., 1999. Constrained Hough transforms for curve detection. *Comput. Vision Image Understanding* 73 (3), 329–345.
- Onyango, C.M., Marchant, J.A., 1996. Modelling grey level surfaces using three-dimensional point distribution models. *Image Vision Comput.* 14, 733–739.
- Ooms, D., Palm, R., Leemans, V., Destain, M.-F., 2010. A sorting optimization curve with quality and yield requirements. *Pattern Recognit. Lett.* 31 (9), 983–990.
- Osteen, R.E., Tou, J.T., 1973. A clique-detection algorithm based on neighbourhoods in graphs. *Int. J. Comput. Inf. Sci.* 2, 257–268.
- Otsu, N., 1979. A threshold selection method from gray-level histograms. *IEEE Trans. Syst. Man Cybern.* 9 (1), 62–66.
- Pal, N.R., Pal, S.K., 1989. Object-background segmentation using new definitions of entropy. *IEE Proc. E* 136 (4), 284–295.
- Paler, K., Kittler, J., 1983. Greylevel edge thinning: a new method. *Pattern Recognit. Lett.* 1, 409–416.
- Paler, K., Föglein, J., Illingworth, J., Kittler, J., 1984. Local ordered grey levels as an aid to corner detection. *Pattern Recognit.* 17, 535–543.
- Pan, X.-B., Brady, M., Bowman, A.K., Crowther, C., Tomlin, R.S.O., 2004. Enhancement and feature extraction for images of incised and ink texts. *Image Vision Comput.* 22 (6), 443–451.
- Pan, X.D., Ellis, T.J. and Clarke, T.A., 1995. Robust tracking of circular features. In: *Proc. Sixth British Machine Vision Assoc. Conf.* 11–14 Sept., Birmingham, pp. 553–562.
- Panda, D.P., Rosenfeld, A., 1978. Image segmentation by pixel classification in (gray level, edge value) space. *IEEE Trans. Comput.* 27, 875–879.
- Papadakis, N., Bugeau, A., 2011. Tracking with occlusions via graph cuts. *IEEE Trans. Pattern Anal. Mach. Intell.* 33 (1), 144–157.

- Paragios, N., Deriche, R., 2000. Geodesic active contours and level sets for the detection and tracking of moving objects. *IEEE Trans. Pattern Anal. Mach. Intell.* 22 (3), 266–280.
- Parker, D.B., 1985. Learning-logic: casting the cortex of the human brain in silicon. Technical Report TR-47, Center for Comput. Res. in Economics and Management Sci., MIT, Cambridge, MA.
- Parker, J.R., 1994. *Practical Computer Vision Using C*. Wiley, New York.
- Patel, D., Hannah, I. and Davies, E.R., 1994. Texture analysis for foreign object detection using a single layer neural network. In: *Proc. IEEE Int. Conf. on Neural Networks*. 28 June–2 July, Florida, Vol. VII, pp. 4265–4268.
- Pavlidis, T., 1980. Algorithms for shape analysis of contours and waveforms. *IEEE Trans. Pattern Anal. Mach. Intell.* 2, 301–312.
- Pearl, J., 1988. *Probabilistic Reasoning in Intelligent Systems: Networks of Plausible Inference*. Morgan Kaufmann, San Mateo, CA.
- Pearson, K., 1901. On lines and planes of closest fit to systems of points in space. *Philos. Mag.* 2, 559–572.
- Pelillo, M., 1999. Replicator equations, maximal cliques and graph isomorphism. *Neural Comput.* 11 (8), 1933–1955.
- Pentland, A.P., 1984. Fractal-based description of natural scenes. *IEEE Trans. Pattern Anal. Mach. Intell.* 6 (6), 661–674.
- Perdoch, M., Matas, J. and Obdrzalek, S., 2007. Stable affine frames on isophotes. In: *Proc. Int. Conf. on Computer Vision (ICCV)*.
- Persoon, E., Fu, K.-S., 1977. Shape discrimination using Fourier descriptors. *IEEE Trans. Syst. Man Cybern.* 7, 170–179.
- Petrou, M. and Kittler, J., 1988. On the optimal edge detector. In: *Proc. Fourth Alvey Vision Conf.* 31 August–2 September, Manchester, pp. 191–196.
- Petrou, M., Petrou, C., 2010. *Image Processing: The Fundamentals*, second ed. John Wiley and Sons, Ltd, Chichester, UK.
- Petrou, M., Sevilla, P.G., 2006. *Image Processing: Dealing With Texture*. Wiley, Chichester, UK.
- Pfaltz, J.L., Rosenfeld, A., 1967. Computer representation of planar regions by their skeletons. *Commun. ACM* 10, 119–125.
- Pflugfelder, R. and Bischof, H., 2008. Tracking across non-overlapping views via geometry. In: *Proc. IEEE Int. Conf. on Pattern Recognition*.
- Pflugfelder, R., Bischof, H., 2010. Localization and trajectory reconstruction in surveillance cameras with nonoverlapping views. *IEEE Trans. Pattern Anal. Mach. Intell.* 32 (4), 709–721.
- Phong, B.-T., 1975. Illumination for computer-generated pictures. *Commun. ACM* 18, 311–317.
- Pietikäinen, M., Rosenfeld, A., Davis, L.S., 1983. Experiments with texture classification using averages of local pattern matches. *IEEE Trans. Syst. Man Cybern.* 13 (3), 421–426.
- Pike, M.C., 1965. Algorithm 267: random normal deviate [g5]. *Commun. ACM* 8 (10), 606..
- Pitt, M.K., Shephard, N., 1999. Filtering via simulation: auxiliary particle filters. *J. Am. Stat. Assoc.* 94 (446), 590–599.
- Plummer, A.P.N., Dale, F., 1984. *The Picture Processing Language Compiler Manual*. National Physical Laboratory, Teddington.

- Pollard, S.B., Porrill, J., Mayhew, J.E.W., Frisby, J.P., 1987. Matching geometrical descriptions in three-space. *Image Vision Comput.* 5 (2), 73–78.
- Postaire, J.G., Touzani, A., 1989. Mode boundary detection by relaxation for cluster analysis. *Pattern Recognit.* 22 (5), 477–489.
- Prati, A., Mikić, I., Trivedi, M.M., Cucchiara, R., 2003. Detecting moving shadows: algorithms and evaluation. *IEEE Trans. Pattern Anal. Mach. Intell.* 25 (7), 918–923.
- Pratt, W.K., 2001. *Digital Image Processing*, second ed. Wiley-Interscience, New York, USA.
- Press, W.H., Teukolsky, S.A., Vetterling, W.T., Flannery, B.P., 1992. *Numerical Recipes in C. The Art of Scientific Computing*, second ed. Cambridge Univ. Press, Cambridge.
- Press, W.H., Teukolsky, S.A., Vetterling, W.T., Flannery, B.P., 1997. *Numerical Recipes in C*, second ed. Cambridge University Press, Cambridge.
- Prewitt, J.M.S., 1970. Object enhancement and extraction. In: Lipkin, B.S., Rosenfeld, A. (Eds.), *Picture Processing and Psychopictorics*. Academic Press, New York, pp. 75–149.
- Prieto, M.S., Allen, A.R., 2003. A similarity metric for edge images. *IEEE Trans. Pattern Anal. Mach. Intell.* 25 (10), 1265–1273.
- Prieto, M.S., Allen, A.R., 2009. Using self-organising maps in the detection and recognition of road signs. *Image Vision Comput.* 27, 673–683.
- Princen, J., Illingworth, J. and Kittler, J., 1989a. A hierarchical approach to line extraction. In: *Proc. IEEE Computer Vision and Pattern Recognition Conf.* San Diego, pp. 92–97.
- Princen, J., Yuen, H.K., Illingworth, J. and Kittler, J., 1989b. Properties of the adaptive Hough transform. In: *Proc. Sixth Scand. Conf. on Image Analysis*. 19–22 June, Oulu, Finland, pp. 613–620.
- Princen, J., Illingworth, J., Kittler, J., 1994. Hypothesis testing: a framework for analyzing and optimizing Hough transform performance. *IEEE Trans. Pattern Anal. Mach. Intell.* 16 (4), 329–341.
- Pringle, K.K., 1969. Visual perception by a computer. In: Grasselli, A. (Ed.), *Automatic Interpretation and Classification of Images*. Academic Press, New York, pp. 277–284.
- Pritchard, D., Heidrich, W., 2003. Cloth motion capture. *Comput. Graphics Forum (Eurographics 2003)* 22 (3), 263–271.
- Pun, C.-M., Lee, M.-C., 2003. Log-polar wavelet energy signatures for rotation and scale invariant texture classification. *IEEE Trans. Pattern Anal. Mach. Intell.* 25 (5), 590–603.
- Pun, T., 1980. A new method for grey-level picture thresholding using the entropy of the histogram. *Signal Process.* 2, 223–237.
- Pun, T., 1981. Entropic thresholding, a new approach. *Comput. Graph. Image Process.* 16, 210–239.
- Rabbani, H., Gazor, S., 2010. Image denoising employing local mixture models in sparse domains. *IET Image Process.* 4 (5), 413–428.
- Rajashekhara, Chaudhuri, S., Namboodiri, V.P., 2007. Retrieval of images of man-made structures based on projective invariance. *Pattern Recognit.* 40, 296–308.
- Ramanan, D., 2006. Learning to parse images of articulated bodies. In: *Proc. Neural Information Processing Systems Conf.* pp. 1129–1136.
- Rätsch, G., Mika, S., Schölkopf, B., Müller, K.-R., 2002. Constructing boosting algorithms from SVMs: an application to one-class classification. *IEEE Trans. Pattern Anal. Mach. Intell.* 24 (9), 1184–1199.

- Ravanbakhsh, M., Mousavi, H., Rastegari, M., Murino, V., and Davis, L.S., 2015. Action Recognition with Image Based CNN Features. arXiv:1512.03980v1 [cs.CV] 13 Dec.
- Redmon, J., Farhadi, A., 2016. YOLO9000: Better, Faster, Stronger. arXiv:1612.08242v1 [cs.CV] 25 Dec.
- Redmon, J., Divvala, S., Girshick, R., and Farhadi, A., 2015. You Only Look Once: Unified, Real-time Object Detection. arXiv:1506.02640 [cs.CV] 8 Jun.
- Reed, T.R., Du Buf, J.M.H., 1993. A review of recent texture segmentation and feature extraction techniques. *Comput. Vision Graph. Image Process.: Image Understanding* 57, 359–372.
- Reeves, A.P., Akey, M.L. and Mitchell, O.R., 1983. A moment-based two-dimensional edge operator. In: *Proc. IEEE Computer Soc. Conf. on Comput. Vision and Pattern Recognition*. 19–23 June, pp. 312–317.
- Ren, J., Jiang, J., Wang, D., Ipson, S.S., 2010. Fusion of intensity and inter-component chromatic difference for effective and robust colour edge detection. *IET Image Process.* 4 (4), 294–301.
- Ren, S., He, K., Girshick, R., and Sun, J., 2015. Faster R-CNN: towards Real-time Object Detection with Region Proposal Networks. arXiv:1506.01497 [cs.CV] 4 Jun.
- Rindfleisch, T., 1966. Photometric method for lunar topography. *Photogramm. Eng.* 32, 262–276.
- Ringer, M. and Lazenby, J., 2000. Modelling and tracking articulated motion from multiple camera views. In: *Proc. 11th British Machine Vision Assoc. Conf.* 11–14 Sept., Bristol, UK, pp. 172–181.
- Rish, I., 2001. An empirical study of the naive Bayes classifier. In: *Proc. IJCAI-01 Workshop on Empirical Methods in AI, Int. Jt. Conf. on Artificial Intelligence*. pp. 41–46.
- Robert, L., 1996. Camera calibration without feature extraction. *Comput. Vision Image Understanding* 63 (2), 314–325.
- Roberts, L.G., 1965. Machine perception of three-dimensional solids. In: Tippet, J., et al., (Eds.), *Optical and Electro-optical Information Processing*. MIT Press, Cambridge, MA, pp. 159–197.
- Robinson, G.S., 1977. Edge detection by compass gradient masks. *Comput. Graph. Image Process.* 6, 492–501.
- Robles-Kelly, A. and Hancock, E.R., 2002. A graph-spectral approach to correspondence matching. In: *Proc. 16th Int. Conf. on Pattern Recognition*. 11–15 Aug., Québec, Canada, Vol. IV, pp. 176–179.
- Rocket, P.I., 2003. Performance assessment of feature detection algorithms: a methodology and case study of corner detectors. *IEEE Trans. Image Process.* 12 (12), 1668–1676.
- Rodríguez, J.J., García-Osorio, C., Maudes, J., 2010. Forests of nested dichotomies. *Pattern Recognit. Lett.* 31, 125–132.
- Rogers, D.F., 1985. *Procedural Elements for Computer Graphics*. McGraw-Hill, New York.
- Rosenblatt, F., 1958. The perceptron: a probabilistic model for information storage and organisation in the brain. *Psychol. Rev.* 65, 386–408.
- Rosenblatt, F., 1962. *Principles of Neurodynamics*. Spartan, New York.
- Rosenfeld, A., 1969. *Picture Processing by Computer*. Academic Press, New York.
- Rosenfeld, A., 1970. Connectivity in digital pictures. *J. ACM* 17, 146–160.
- Rosenfeld, A., Pfaltz, J.L., 1966. Sequential operations in digital picture processing. *J. ACM* 13, 471–494.

- Rosenfeld, A., Pfaltz, J.L., 1968. Distance functions on digital pictures. *Pattern Recognit.* 1, 33–61.
- Rosenfeld, A., Troy, E.B., 1970a. Visual texture analysis. Computer Science Center, Univ. of Maryland Techn. Report TR-116.
- Rosenfeld, A. and Troy, E.B., 1970b. Visual texture analysis. In: *Conf. Record for Symposium on Feature Extraction and Selection in Pattern Recognition*. Oct., Argonne, Ill, IEEE Publication 70C-51C, pp. 115–124.
- Rosenfeld, A., VanderBrug, G.J., 1977. Coarse-fine template matching. *IEEE Trans. Syst. Man Cybern.* 7, 104–107.
- Rosenfeld, A., de la Torre, P., 1983. Histogram concavity analysis as an aid in threshold selection. *IEEE Trans. Syst. Man Cybern.* 13 (3), 231–235.
- Rosenfeld, A., Hummel, R.A., Zucker, S.W., 1976. Scene labelling by relaxation operations. *IEEE Trans. Syst. Man Cybern.* 6, 420–433.
- Rosie, A.M., 1966. *Information and Communication Theory*. Blackie, London.
- Rosin, P., 2000. Fitting superellipses. *IEEE Trans. Pattern Anal. Mach. Intell.* 22 (7), 726–732.
- Rosin, P.L., 2001. Unimodal thresholding. *Pattern Recognit.* 34 (11), 2083–2096.
- Rosin, P.L., West, G.A.W., 1995. Curve segmentation and representation by superellipses. *IEE Proc. Vision Image Signal Process.* 142 (5), 280–288.
- Rosten, E., Porter, R., Drummond, T., 2010. Faster and better: a machine learning approach to corner detection. *IEEE Trans. Pattern Anal. Mach. Intell.* 32 (1), 105–119.
- Roth, G. and Whitehead, A., 2002. Some improvements on two autocalibration algorithms based on the fundamental matrix. In: *Proc. 16th Int. Conf. on Pattern Recognition*. 11–15 Aug., Québec, Canada, Vol. II, pp. 312–315.
- Rother, C. and Carlsson, S., 2001. Linear multi view reconstruction and camera recovery. In: *Proc. Eighth IEEE Int. Conf. on Computer Vision*, Vancouver.
- Rothwell, C.A., 1995. *Object Recognition through Invariant Indexing*. Oxford University Press, Oxford.
- Rothwell, C.A., Zisserman, A., Forsyth, D.A. and Mundy, J.L., 1992a. Canonical frames for planar object recognition. In: *Proc Second European Conf. on Computer Vision*, Santa Margherita Ligure. 19–22 May, Italy, pp. 757–772.
- Rothwell, C.A., Zisserman, A., Marinos, C.I., Forsyth, D.A., Mundy, J.L., 1992b. Relative motion and pose from arbitrary plane curves. *Image Vision Comput.* 10 (4), 250–262.
- Rousseeuw, P.J., 1984. Least median of squares regression. *J. Am. Stat. Assoc.* 79 (388), 871–880.
- Rousseeuw, P.J., Leroy, A.M., 1987. *Robust Regression and Outlier Detection*. Wiley, New York.
- Rowley, H., Baluja, S., Kanade, T., 1998. Neural network-based face detection. *IEEE Trans. Pattern Anal. Mach. Intell.* 20 (1), 23–38.
- Roy, P.P., Pal, U., Lladós, J., 2011. Document seal detection using GHT and character proximity graphs. *Pattern Recognit.* 44, 1282–1295.
- Rubinstein, R.Y., Kroese, D.P., 2007. *Simulation and the Monte Carlo Method*, second ed. Wiley, Hoboken, NJ, USA.
- Rumelhart, D.E., Hinton, G.E., Williams, R.J., 1986. Learning internal representations by error propagation. In: Rumelhart, D.E., McClelland, J.L. (Eds.), *Parallel Distributed Processing: Explorations in the Microstructure of Cognition*. The MIT Press, Cambridge, Mass, pp. 318–362.
- Rummel, P., Beutel, W., 1984. Workpiece recognition and inspection by a model-based scene analysis system. *Pattern Recognit.* 17, 141–148.

- Ruta, A., Li, Y., Liu, X., 2010. Real-time traffic sign recognition from video by class-specific discriminative features. *Pattern Recognit.* 43, 416–430.
- Rutovitz, D., 1970. Centromere finding: some shape descriptors for small chromosome outlines. In: Meltzer, B., Michie, D. (Eds.), *Machine Intelligence 5*. Edinburgh University Press, Edinburgh, pp. 435–462.
- Sagonas, C., Panagakis, Y., Zafeiriou, S., Pantic, M., 2015. Face Frontalization for Alignment and Recognition. arXiv:1502.00852v1 [cs.CV] 3 Feb.
- Sagonas, C., Panagakis, Y., Zafeiriou, S., Pantic, M., 2016. Robust statistical frontalization of human and animal faces. *Int. J. Computer Vision*. Springer, <http://dx.doi.org/10.1007/s11263-016-0920-7>, published online 20 July 2016.
- Sahoo, P.K., Soltani, S., Wong, A.K.C., Chen, Y.C., 1988. A survey of thresholding techniques. *Comput. Vision Graph. Image Process* 41, 233–260.
- Sakarya, U., Erkmén, I., 2003. An improved method of photometric stereo using local shape from shading. *Image Vision Comput.* 21 (11), 941–954.
- Sanchiz, J.M., Pla, F., Marchant, J.A., Brivot, R., 1996. Structure from motion techniques applied to crop field mapping. *Image Vision Comput.* 14, 353–363.
- Sanfeliu, A., Fu, K.S., 1983. A distance measure between attributed relational graphs for pattern recognition. *IEEE Trans. Syst. Man Cybern.* 13 (3), 353–362.
- Sangwine, S.J., Horne, R.E.N. (Eds.), 1998. *The Colour Image Processing Handbook*. Chapman and Hall, London.
- Schaffalitsky, F., Zisserman, A., 2000. Planar grouping for automatic detection of vanishing lines and points. *Image Vision Comput.* 18 (9), 647–658.
- Schapire, R.E., 1990. The strength of weak learnability. *Mach. Learn.* 5 (2), 197–227.
- Schildt, H., 1995. *C++, the Complete Reference*, third ed. McGraw-Hill, Osborne.
- Schmid, C., Mohr, R., Bauckhage, C., 2000. Evaluation of interest point detectors. *Int. J. Comput. Vision* 37 (2), 151–172.
- Schmidt, J., Fritsch, J. and Kwolek, B., 2006. Kernel particle filter for real-time 3D body tracking in monocular color images. In: *Proc. IEEE Int. Conf. on Automatic Face and Gesture Recognition*. Southampton, UK, pp. 567–572.
- Schneiderman, H., Nashman, M., Wavering, A.J., Lumia, R., 1995. Vision-based robotic convoy driving. *Mach. Vision Appl.* 8 (6), 359–364.
- Schölkopf, B., Smola, A., Müller, K.R., 1997. Kernel principal component analysis. *Int. Conf. Artif. Neural Networks* 583–588.
- Scott, G.L., 1988. *Local and Global Interpretation of Moving Images*. Pitman/Morgan Kaufmann, London/San Mateo, CA.
- Sebe, N., Lew, M.S., 2003. Comparing salient point detectors. *Pattern Recognit. Lett.* 24 (1–3), 89–96.
- Sebe, N., Tian, Q., Loupas, E., Lew, M.S., Huang, T.S., 2003. Evaluation of salient point techniques. *Image Vision Comput.* 21 (13–14), 1087–1095.
- Semple, J.G., Kneebone, G.T., 1952. *Algebraic Projective Geometry*. Oxford University Press, Oxford.
- Ser, P.-K., Siu, W.-C., 1995. Novel detection of conics using 2-D Hough planes. *IEE Proc. Vision Image Signal Process.* 142 (5), 262–270.
- Serra, J., 1982. *Image Analysis and Mathematical Morphology*. Academic Press, New York.
- Sewisy, A.A., Leberl, F., 2001. Detection ellipses by finding lines of symmetry in the images via an hough transform applied to straight lines. *Image Vision Comput.* 19 (12), 857–866.

- Sezgin, M., Sankur, B., 2004. Survey over image thresholding techniques and quantitative performance evaluation. *J. Electron. Imaging* 13 (1), 146–168.
- Sfikas, G., Nikou, C., and Galatsanos, N., 2007. Robust image segmentation with mixtures of Student's t-distributions. In: *Proc. IEEE Int. Conf. on Image Processing*. Vol. I, pp. 273–276.
- Shah, M.A., Jain, R., 1984. Detecting time-varying corners. *Comput. Vision Graph. Image Process* 28, 345–355.
- Shakespeare, W., 1599. *The Tragedy of Julius Caesar*.
- Shapiro, L.G., Haralick, R.M., 1985. A metric for comparing relational descriptions. *IEEE Trans. Pattern Anal. Mach. Intell.* 7 (1), 90–94.
- Shen, F., Wang, H., 2002. Corner detection based on modified Hough transform. *Pattern Recognit. Lett.* 23 (8), 1039–1049.
- Shen, X., Hogg, D., 1995. 3D shape recovery using a deformable model. *Image Vision Comput.* 13 (5), 377–383.
- Shima, T., Saito, S., Nakajima, M., 2010. Design and evaluation of more accurate gradient operators on hexagonal lattices. *IEEE Trans. Pattern Anal. Mach. Intell.* 32 (6), 961–973.
- Shiroyama, T., Uddin, M.S., 2004. Detection of pedestrian crossings with projective invariants from image data. *Meas. Sci. Technol.* 15, 2400–2405.
- Shirai, Y., 1972. Recognition of polyhedra with a range finder. *Pattern Recognit.* 4, 243–250.
- Shirai, Y., 1987. *Three-dimensional Computer Vision*. Springer-Verlag, Berlin.
- Shufelt, J.A., 1999. Performance evaluation and analysis of vanishing point detection techniques. *IEEE Trans. Pattern Anal. Mach. Intell.* 21 (3), 282–288.
- Shuster, R., Ansari, N., Bani-Hashemi, A., 1993. Steering a robot with vanishing points. *IEEE Trans. Rob. Autom.* 9 (4), 491–498.
- Siebel, N.T. and Maybank, S.J., 2002. Fusion of multiple tracking algorithms for robust people tracking. In: Heyden, A., Sparr, G., Nielsen, M. and Johansen, P. (Eds.), *Proc. Seventh European Conf. on Computer Vision (ECCV)*. Vol. IV, pp. 373–387.
- Siegel, A.F., 1982. Robust regression using repeated medians. *Biometrika* 69 (1), 242–244.
- Silberberg, T.M., Davies, L., Harwood, D., 1984. An iterative Hough procedure for three-dimensional object recognition. *Pattern Recognit.* 17, 621–629.
- Silletti, A., Abate, A., Axelrod, J.D., Tomlin, C.J., 2011. Versatile spectral methods for point set matching. *Pattern Recognit. Lett.* 32 (5), 731–739.
- Simard, P., Bottou, L., Haffner, P., LeCun, Y., 1999. Boxlets: a fast convolution algorithm for neural networks and signal processing, *Advances in Neural Information Processing Systems*, 11. MIT Press, Cambridge, MA, USA.
- Simonyan K., and Zisserman, A., 2015. Very Deep Convolutional Networks for Large-scale Image Recognition. arXiv:1409.1556v6 10 Apr.
- Simonyan, K., Vedaldi, A., Zisserman, A., 2014. Deep Inside Convolutional Networks: Visualising Image Classification Models and Saliency Maps. arXiv:1312.6034v2 [cs.CV] 19 Apr.
- Sirovich, L., Kirby, M., 1987. A two-dimensional procedure for the characterization of human faces. *J. Opt. Soc. Am.* 4 (3), 519–524.
- Sjöberg, F., Bergholm, F., 1988. Extraction of diffuse edges by edge focussing. *Pattern Recognit. Lett.* 7, 181–190.
- Sklansky, J., 1970. Recognition of convex blobs. *Pattern Recognit.* 2, 3–10.



- Sklansky, J., 1978. On the Hough technique for curve detection. *IEEE Trans. Comput.* 27, 923–926.
- Sklansky, J., Cordella, L.P., Leviardi, S., 1976. Parallel detection of concavities in cellular blobs. *IEEE Trans. Comput.* 25, 187–196.
- Slama, C.C. (Ed.), 1980. *Manual of Photogrammetry*, fourth ed. Amer. Soc. of Photogrammetry, Falls Church, VA.
- Smith, S., Brady, J.M., 1997. Susan – a new approach to low level image processing. *Int. J. Comput. Vision* 23 (1), 45–78.
- Smolka, B., 2010. Peer group switching filter for impulse noise reduction in color images. *Pattern Recognit. Lett.* 31 (6), 484–495.
- Soille, P., 2003. *Morphological Image Analysis: Principles and Applications*, second ed. Springer-Verlag, Heidelberg.
- Soille, P., Vogt, P., 2009. Morphological segmentation of binary patterns. *Pattern Recognit. Lett.* 30 (4), 456–459.
- Song, J., Cai, M., Lyu, M. and Cai, S., 2002. A new approach for line recognition in large-size images using Hough transform. In: *Proc. 16th Int. Conf. on Pattern Recognition*. 11–15 Aug., Québec, Canada, Vol. I, pp. 33–36.
- Sonka, M., Hlavac, V., Boyle, R., 2007. *Image Processing, Analysis, and Machine Vision*, third ed. Thomson Engineering, Toronto, Canada.
- Spence, A., Robb, M., Timmins, M., Chantler, M., 2004. Real-time per-pixel rendering of textiles for virtual textile catalogues. *Int. J. Clothing Sci. Technol.* 16 (1/2).
- Startchik, S., Milanese, R., Pun, T., 1998. Projective and illumination invariant representation of disjoint shapes. *Image Vision Comput.* 16 (9–10), 713–723.
- Stauffer, C., and Grimson, W.E.L., 1999. Adaptive background mixture models for real-time tracking. In: *Proc. IEEE Conf. on Computer Vision and Pattern Recognition*. 23–25 June, Ft. Collins, CO, pp. 246–252.
- Steele, J.M., Steiger, W.L., 1986. Algorithms and complexity for least median of squares regression. *Discrete Appl. Math.* 14, 93–100.
- Stella, E., Lovergine, F.P., D’Orazio, T., Distanti, A., 1995. A visual tracking technique suitable for control of convoys. *Pattern Recognit. Lett.* 16 (9), 925–932.
- Stephens, R.S., 1991. Probabilistic approach to the Hough transform. *Image Vision Comput.* 9 (1), 66–71.
- Stevens, K., 1980. Surface perception from local analysis of texture and contour. MIT Artif. Intell. Lab. Memo AI-TR-512.
- Stockman, G.C., Agrawala, A.K., 1977. Equivalence of Hough curve detection to template matching. *Commun. ACM* 20, 820–822.
- Straforini, M., Coelho, C., Campani, M., 1993. Extraction of vanishing points from images of indoor and outdoor scenes. *Image Vision Comput.* 11 (2), 91–99.
- Stroustrup, B., 1997. *The C++ Programming Language*, third ed. Addison-Wesley, Reading, MA, USA.
- Sturm, P., 2000. A case against Kruppa’s equations for camera self-calibration. *IEEE Trans. Pattern Anal. Mach. Intell.* 22 (10), 1199–1204.
- Sugrue, M., Davies, E.R., 2007. Motion signals provide rapid discernment of pedestrians and pedestrian behaviour. *Electron. Lett.* 43 (23), 1267–1269.
- Sugrue, M. and Davies, E.R., 2008. Motion detection and tracking by mimicking neurological dorsal/ventral pathways. In: Chapter 9 in Bharath, A. and Petrou, M. (Eds.) *Reverse Engineering the Human Vision System: Next Generation Artificial Vision Systems*. pp. 217–247.

- Sullivan, G.D., 1992. Visual interpretation of known objects in constrained scenes. *Philos. Trans. Royal Soc. London, Ser. B* 337, 361–370.
- Sun, Y., Wang, X., and Tang, X., 2013. Hybrid deep learning for face verification. In: *Proc. IEEE Int. Conf. on Computer Vision*. 1–8 December, Darling Harbour, Sydney, pp. 1489–1496.
- Sun, Y., Wang, X., and Tang, X., 2014a. Deep Learning Face Representation by Joint Identification-Verification. *arXiv:1406.4773v1 [cs.CV]* 18 Jun.
- Sun, Y., Wang, X., and Tang, X., 2014b. Deep learning face representation from predicting 10,000 classes. In: *Proc. IEEE Conf. on Computer Vision and Pattern Recognition*. 24–27 June, Columbus, Ohio, pp. 1891–1898.
- Sun, Z., Bebis, G. and Miller, R., 2004. On-road vehicle detection using optical sensors: a review. In: *IEEE Int. Conf. on Intelligent Transportation Systems*, pp. 585–590.
- Sun, Z., Bebis, G., Miller, R., 2006. On-road vehicle detection: a review. *IEEE Trans. Pattern Anal. Mach. Intell.* 28 (5), 694–711.
- Suzuki, K., Horiba, I., Sugie, N., 2003. Neural edge enhancer for supervised edge enhancement from noisy images. *IEEE Trans. Pattern Anal. Mach. Intell.* 25 (12), 1582–1596.
- Swain, M.J., Ballard, D.H., 1991. Color indexing. *Int. J. Comput. Vision* 7 (1), 11–32.
- Szegedy, C., Liu, W., Jia, Y., Sermanet, P., Reed, S., Anguelov, D., et al., 2014. Going Deeper with Convolutions. *arXiv:1409.4842v1 [cs.CV]* 17 Sep.
- Tabandeh, A.S. and Fallside, F., 1986. Artificial intelligence techniques and concepts for the integration of robot vision and 3D solid modellers. In: *Proc. Int. Conf. on Intell. Autonomous Systems*. 18–11 December, Amsterdam.
- Taigman, Y., Yang, M., Ranzato, M.'A., and Wolf, L., 2014. DeepFace: closing the gap to human-level performance in face verification. In: *Proc. IEEE Conf. on Computer Vision and Pattern Recognition*. 24–27 June, Columbus, OH, pp. 1701–1708.
- Tan, T.N., 1995. Structure, pose and motion of bilateral symmetric objects. In: *Proc. Seventh British Machine Vision Assoc. Conf.* 11–14 Sept., Birmingham, pp. 473–482.
- Tan, T.N., Sullivan, G.D., Baker, K.D., 1994. Recognizing objects on the ground-plane. *Image Vision Comput.* 12 (3), 164–172.
- Tang, Y.Y., You, X., 2003. Skeletonization of ribbon-like shapes based on a new wavelet function. *IEEE Trans. Pattern Anal. Mach. Intell.* 25 (9), 1118–1133.
- Tao, W.-B., Tian, J.-W., Liu, J., 2003. Image segmentation by three-level thresholding based on maximum fuzzy entropy and genetic algorithm. *Pattern Recognit. Lett.* 24 (16), 3069–3078.
- Teixeira, L.F., Corte-Real, L., 2009. Video object matching across multiple independent views using local descriptors and adaptive learning. *Pattern Recognit. Lett.* 30 (2), 157–167.
- Theil, H., 1950. A rank-invariant method of linear and polynomial regression analysis (parts 1–3). *Nederlandsche Akad. Wetenschappen Proc.* A53, 386–392, 521–525 and 1397–1412.
- Theodoridis, S., Koutroumbas, K., 1999. *Pattern Recognition*. Academic Press, London.
- Tighe, J., Lazebnik, S., 2013. Finding things: Image parsing with regions and per-exemplar detectors. In: *Proc. IEEE Conf. on Computer Vision and Pattern Recognition*. 23–28 June, Portland, Oregon, pp. 3001–3008.
- Tillett, R.D., Onyango, C.M., Marchant, J.A., 1997. Using model-based image processing to track animal movements. *Comput. Electron. Agric.* 17, 249–261.
- Tipping, M.E., Bishop, C.M., 1999. Mixtures of probabilistic principal component analyzers. *Neural Comput.* 11 (2), 443–482.

- Tissainayagam, P., Suter, D., 2004. Assessing the performance of corner detectors for point feature tracking applications. *Image Vision Comput.* 22 (8), 663–679.
- Toennies, K., Behrens, F. and Aurnhammer, M., 2002. Feasibility of Hough-transform-based iris localisation for real-time application. In: *Proc. 16th Int. Conf. on Pattern Recognition*. 11–15 Aug., Québec, Canada, Vol. II, pp. 1053–1056.
- Torr, P.H.S., Davidson, C., 2003. IMPSAC: synthesis of importance sampling and random sample consensus. *IEEE Trans. Pattern Anal. Mach. Intell.* 25 (3), 354–364.
- Torr, P.H.S. and Fitzgibbon, A.W., 2003. Invariant fitting of two view geometry or In defiance of the 8 point algorithm. In: *Proc. British Machine Vision Assoc. Conf.* 9–11 Sept., Norwich, UK, pp. 83–92.
- Torr, P.H.S., Fitzgibbon, A.W., 2004. Invariant fitting of two view geometry. *IEEE Trans. Pattern Anal. Mach. Intell.* 26 (5), 648–650.
- Torreão, J.R.A., 2001. A Green's function approach to shape from shading. *Pattern Recognit.* 34 (12), 2367–2382.
- Torreão, J.R.A., 2003. Geometric–photometric approach to monocular shape estimation. *Image Vision Comput.* 21 (12), 1045–1062.
- Toulson, D.L., Boyce, J.F., 1992. Segmentation of MR images using neural nets. *Image Vision Comput.* 10 (5), 324–328.
- Tsai, D.-M., 1995. A fast thresholding selection procedure for multimodal and unimodal histograms. *Pattern Recognit. Lett.* 16 (6), 653–666.
- Tsai, F.C.D., 1996. A probabilistic approach to geometric hashing using line features. *Comput. Vision Image Understanding* 63 (1), 182–195.
- Tsai, R.Y., 1986. An efficient and accurate camera calibration technique for 3D machine vision. In: *Proc. Conf. on Comput. Vision Pattern Recognition*. Miami, FL, pp. 364–374.
- Tsai, R.Y., Huang, T.S., 1984. Uniqueness and estimation of three-dimensional motion parameters of rigid objects with curved surfaces. *IEEE Trans. Pattern Anal. Mach. Intell.* 6, 13–27.
- Tsuji, S., Matsumoto, F., 1978. Detection of ellipses by a modified Hough transform. *IEEE Trans. Comput.* 27, 777–781.
- Tsukune, H. and Goto, K., 1983. Extracting elliptical figures from an edge vector field. In: *Proc. IEEE Conf. on Computer Vision and Pattern Recognition*. Washington, pp. 138–141.
- Turin, G.L., 1960. An introduction to matched filters. *IRE Trans. Inf. Theory* 6, 311–329.
- Turk, M.A., Pentland, A.P., 1991. Eigenfaces for recognition. *J. Cogn. Neurosci.* 3 (1), 71–86.
- Turney, J.L., Mudge, T.N., Volz, R.A., 1985. Recognizing partially occluded parts. *IEEE Trans. Pattern Anal. Mach. Intell.* 7, 410–421.
- Tuytelaars, T., Mikolajczyk, K., 2008. Local invariant feature detectors: a survey. *Found. Trends Comput. Graphics Vision* 3 (3), 177–280.
- Tuytelaars, T. and Van Gool, L., 2000. Wide baseline stereo matching based on local, affinely invariant regions. In: *Proc. British Machine Vision Conf. (BMVC)*, Bristol University, UK, pp. 412–422.
- Tuytelaars, T., Van Gool, L., 2004. Matching widely separated views based on affine invariant regions. *Int. J. Comput. Vision* 1 (59), 61–85.
- Tuytelaars, T., Turina, A., van Gool, L., 2003. Noncombinatorial detection of regular repetitions under perspective skew. *IEEE Trans. Pattern Anal. Mach. Intell.* 25 (4), 418–432.

- Tzomakas, C. and von Seelen, W., 1998. Vehicle Detection in Traffic Scenes Using Shadows. Internal Report 98–06. Ruhr-Universität Bochum.
- Ullman, S., 1979. *The Interpretation of Visual Motion*. MIT Press, Cambridge, MA.
- Ullmann, J.R., 1969. Experiments with the  $n$ -tuple method of pattern recognition. *IEEE Trans. Comput.* 18, 1135–1137.
- Ullmann, J.R., 1973. *Pattern Recognition Techniques*. Butterworth, London.
- Ullmann, J.R., 1974. Binarisation using associative addressing. *Pattern Recognit.* 6, 127–135.
- Ullmann, J.R., 1976. An algorithm for subgraph isomorphism. *J. ACM* 23, 31–42.
- Ulusoy, I., Yuruk, H., 2011. New method for the fusion of complementary information from infrared and visual images for object detection. *IET Image Process.* 5 (1), 36–48.
- Umeyama, S., 1988. An eigen decomposition approach to weighted graph matching problems. *IEEE Trans. Pattern Anal. Mach. Intell.* 10 (5), 695–703.
- Unser, M., 1986. Local linear transforms for texture measurements. *Signal Process.* 11, 61–79.
- Unser, M., Eden, M., 1989. Multiresolution feature extraction and selection for texture segmentation. *IEEE Trans. Pattern Anal. Mach. Intell.* 11 (7), 717–728.
- Unser, M., Eden, M., 1990. Nonlinear operators for improving texture segmentation based on features extracted by spatial filtering. *IEEE Trans. Syst. Man Cybern.* 20 (4), 804–815.
- Vaillant, R., Monroccq, C., Le Cun, Y., 1994. Original approach for the localisation of objects in images. *IEE Proc. Vision Image Signal Process.* 141 (4), 245–250.
- Valero, S., Chanussot, J., Benediktsson, J.A., Talbot, H., Waske, B., 2010. Advanced directional mathematical morphology for the detection of the road network in very high resolution remote sensing images. *Pattern Recognit. Lett.* 31 (10), 1120–1127.
- van de Sande, K.E.A., Gevers, T., Snoek, C.G.M., 2010. Evaluating color descriptors for object and scene recognition. *IEEE Trans. Pattern Anal. Mach. Intell.* 32 (9), 1582–1596.
- van de Sande, K.E.A., Uijlings, J., Snoek, C., and Smeulders, A., 2012. Hybrid coding for selective search. *PASCAL Visual Object Classes (VOC) Classification Challenge Workshop*, in conjunction with the European Conf. on Computer Vision. 12 October, Florence, Italy.
- van der Merwe, R., Doucet, A., De Freitas, N., Wan, E., 2000. The unscented particle filter. *Proc. Neural Inf. Process. Syst.* 584–590.
- van Digellen, J., 1951. Photometric investigations of the slopes and heights of the ranges of hills in the Maria of the moon. *Bull. Astron. Inst. Netherlands* 11, 283–289.
- van Dijck, H., van der Heijden, F., 2003. Object recognition with stereo vision and geometric hashing. *Pattern Recognit. Lett.* 24 (1–3), 137–146.
- van Ginneken, B., Frangi, A.F., Staal, J.J., ter Haar Romeny, B.M., Viergever, M.A., 2002. Active shape model segmentation with optimal features. *IEEE Trans. Med. Imaging* 21 (8), 924–933.
- Van Gool, L., Dewaele, P., Oosterlinck, A., 1985. Survey: Texture analysis anno 1983. *Comput. Vision Graph. Image Process* 29, 336–357.
- Van Gool, L., Proesmans, M. and Zisserman, A., 1998. Planar homologies as a basis for grouping and recognition. In *Special Issue on Geometric Modelling and Invariants for Computer Vision*, *Image Vision Comput.* 16 (1), 21–26.
- van Wyk, M.A., Durrani, T.S., van Wyk, B.J., 2002. A RKHS interpolator-based graph matching algorithm. *IEEE Trans. Pattern Anal. Mach. Intell.* 24 (7), 988–995.

- VanderBrug, G.J., Rosenfeld, A., 1977. Two-stage template matching. *IEEE Trans. Comput.* 26, 384–393.
- Vapnik, V.N., 1998. *Statistical Learning Theory*. Wiley, New York.
- Vega, I.R., Sarkar, S., 2003. Statistical motion model based on the change of feature relationships: human gait-based recognition. *IEEE Trans. Pattern Anal. Mach. Intell.* 25 (10), 1323–1328.
- Vetrov, D.P., Kropotov, D.A., Osokin, A.A., 2010. Automatic determination of the number of components in the EM algorithm of restoration of a mixture of normal distributions. *Comput. Math. Math. Phys.* 50 (4), 733–746.
- Vezzani, R. and Cucchiara, R., 2008. Ad-hoc: appearance driven human tracking with occlusion handling. In: *Proc. First Int. Workshop on Tracking Humans for Evaluation of Motion in Image Sequences (THEMIS)*. Leeds, UK, pp. 9–18.
- Vezzani, R., Grana, C., Cucchiara, R., 2011. Probabilistic people tracking with appearance models and occlusion classification: the AD-HOC system. *Pattern Recognit. Lett.* 32, 867–877.
- Vincze, M., 2001. Robust tracking of ellipses at frame rate. *Pattern Recognit.* 34 (2), 487–498.
- Vinyals, O., Toshev, A., Bengio, S., and Erhan, D., 2015. Show and tell: a neural image caption generator. In: *Proc. IEEE Conf. on Computer Vision and Pattern Recognition*. 7–12 June, Boston, MA, pp. 3156–3164. See also: arXiv:1411.4555v2 [cs.CV] 20 Apr.
- Viola, P. and Jones, M., 2001. Rapid object detection using a boosted cascade of simple features. In: *Proc. IEEE Conf. on Computer Vision and Pattern Recognition*. 8–14 December, Kauai, Hawaii, Vol. 1, pp. 511–518.
- Viola, P., Jones, M.J., 2004. Robust real-time face detection. *Int. J. Comput. Vision* 57 (2), 137–154.
- Vistnes, R., 1989. Texture models and image measures for texture discrimination. *Int. J. Comput. Vision* 3, 313–336.
- Vondrick, C., Pirsivash, H., Torralba, A., 2016. Anticipating visual representations from unlabeled video. In: *Proc. IEEE Conf. on Computer Vision and Pattern Recognition*. 26 June–1 July, Las Vegas, pp. 98–106. See also arXiv:1504.08023v2 [cs.CV] 30 Nov.
- Wang, C., Sun, H., Yada, S., Rosenfeld, A., 1983. Some experiments in relaxation image matching using corner features. *Pattern Recognit.* 16, 167.
- Wang, J., Bebis, G. and Miller, R., 2005. Overtaking vehicle detection using dynamic and quasi-static background modeling. In: *Proc. IEEE Workshop on Machine Vision for Intelligent Vehicles*. 21 June, San Diego, CA.
- Wang, J.-G., Sung, E., 2001. Gaze determination via images of irises. *Image Vision Comput.* 19 (12), 891–911.
- Wang, J.-G., Sung, E. and Venkateswarlu, R., 2003. Determining pose of a human face from a single monocular image. In: *Proc. British Machine Vision Assoc. Conf.* 9–11 Sept., Norwich, UK, pp. 103–112.
- Wang, L., Bai, J., 2003. Threshold selection by clustering gray levels of boundary. *Pattern Recognit. Lett.* 24 (12), 1983–1999.
- Wang, S., Siskind, J.M., 2003. Image segmentation with ratio cut. *IEEE Trans. Pattern Anal. Mach. Intell.* 25 (6), 675–690.
- Ward, A.D., Hamarneh, G., 2010. The groupwise medial axis transform for fuzzy skeletonization and pruning. *IEEE Trans. Pattern Anal. Mach. Intell.* 32 (6), 1084–1096.

- Webb, A., 2002. *Statistical Pattern Recognition*. Wiley, Chichester, UK.
- Weiman, C.F.R., 1976. Highly parallel digitised geometric transformations without matrix multiplication. In: Proc. Int. Joint Conf. on Parallel Processing, pp. 1–10.
- Werbos, P.J., 1974. *Beyond Regression: New Tools for Prediction and Analysis in the Behavioral Sciences*, PhD Thesis. Harvard Univ., Cambridge, MA.
- Wermser, D. and Liedtke, C.-E., 1982. Texture analysis using a model of the visual system. In: Proc. Sixth Int. Conf. on Pattern Recognition. 19–22 Oct., Munich, pp. 1078–1081.
- Wermser, D., Haussmann, G., Liedtke, C.-E., 1984. Segmentation of blood smears by hierarchical thresholding. *Comput. Vision Graph. Image Process* 25, 151–168.
- Weska, J.S., 1978. A survey of threshold selection techniques. *Comput. Graph. Image Process.* 7, 259–265.
- Weska, J.S., Rosenfeld, A., 1976. An application of texture analysis to materials inspection. *Pattern Recognit.* 8, 195–199.
- Weska, J.S., Nagel, R.N., Rosenfeld, A., 1974. A threshold selection technique. *IEEE Trans. Comput.* 23, 1322–1326.
- Weszka, J.S., Dyer, C.R., Rosenfeld, A., 1976. A comparative study of texture measures for terrain classification. *IEEE Trans. Syst. Man Cybern.* 6 (4), 269–285.
- Whelan, P.F., Molloy, D., 2001. *Machine Vision Algorithms in Java*. Springer, London.
- White, J.M., Rohrer, G.D., 1983. Image thresholding for optical character recognition and other applications requiring character image extraction. *IBM J. Res. Dev.* 27, 400–411.
- Wiejak, J.S., Buxton, H., Buxton, B.F., 1985. Convolution with separable masks for early image processing. *Comput. Vision Graph. Image Process.* 32, 279–290.
- Will, P.M., Pennington, K.S., 1971. Grid coding: a preprocessing technique for robot and machine vision. *Artif. Intell.* 2, 319–329.
- Wilson, H.R., Giese, S.C., 1977. Threshold visibility of frequency gradient patterns. *Vision Res.* 17, 1177–1190.
- Witkin, A.P., 1981. Recovering surface shape and orientation from texture. *Artif. Intell.* 17, 17–45.
- Witkin, A.P., 1983. Scale-space filtering. In: Proc. Fourth Int. Joint. Conf. on Artif. Intell. Tbilisi, Georgi, USSR, pp. 1019–1022.
- Wolf, L., Hassner, T., and Taigman, Y., 2009. Similarity scores based on background samples. In: Proc. Asian Conf. on Computer Vision.
- Wolfson, H.J., 1991. Generalizing the generalized Hough transform. *Pattern Recognit. Lett.* 12 (9), 565–573.
- Wong, R.Y., Hall, E.L., 1978. Scene matching with invariant moments. *Comput. Graph. Image Process.* 8, 16–24.
- Woodham, R.J., 1978. Reflectance map techniques for analysing surface defects in metal castings. MIT Artif. Intell. Lab. Memo AI-TR-457.
- Woodham, R.J., 1980. Photometric method for determining surface orientation from multiple images. *Opt. Eng.* 19, 139–144.
- Woodham, R.J., 1981. Analysing images of curved surfaces. *Artif. Intell.* 17, 117–140.
- Wu, A.Y., Hong, T.-H., Rosenfeld, A., 1982. Threshold selection using quadtrees. *IEEE Trans. Pattern Anal. Mach. Intell.* 4, 90–94.
- Wu, H., Yoshikawa, G., Shioyama, T., Lao, S. and Kawade, M., 2002. Glasses frame detection with 3D Hough transform. In: Proc. 16th Int. Conf. on Pattern Recognition. 11–15 Aug., Québec, Canada, Vol. II, pp. 346–349.

- Wu, T.-P., Tang, C.-K., 2010. Photometric stereo via expectation maximization. *IEEE Trans. Pattern Anal. Mach. Intell.* 32 (3), 546–560.
- Xie, Y. and Ji, Q., 2002. A new efficient ellipse detection method. In: Proc. 16th Int. Conf. on Pattern Recognition. 11–15 Aug., Québec, Canada, Vol. II, pp. 957–960.
- Xu, D., Li, Y.F., Tan, M., 2008. A general recursive linear method and unique solution pattern design for the perspective-n-point problem. *Image Vision Comput.* 26, 740–750.
- Xu, L., Oja, E., 1993. Randomized Hough transform (RHT): basic mechanisms, algorithms, and computational complexities. *Comput. Vision Graph. Image Process.: Image Understanding* 57 (2), 131–154.
- Xu, L.-Q., Landabaso, J.L. and Pardàs, M., 2005. Shadow removal with blob-based morphological reconstruction for error correction. In: Proc. Int. Conf. on Acoustics, Speech, Signal Process.
- Xu, M., Ellis, T.J., Godsill, S.J., Jones, G.A., 2011. Visual tracking of partially observable targets with suboptimal filtering. *IET Comput. Vision* 5 (1), 1–13.
- Yan, C., Sang, N., Zhang, T., 2003. Local entropy-based transition region extraction and thresholding. *Pattern Recognit. Lett.* 24 (16), 2935–2941.
- Yan, J., Zhang, X., Lei, Z., Li, S.Z., 2014. Face detection by structural models. *Image Vision Comput.* 32 (10), 790–799.
- Yan, S., Xu, D., Yang, Q., Zhang, L., 2007. Multilinear discriminant analysis for face recognition. *IEEE Trans. Image Process.* 16 (1), 212–220.
- Yang, S., Luo, P., Loy, C.C., and Tang, X., 2015a. From facial parts responses to face detection: a deep learning approach. In: Proc. IEEE Int. Conf. on Computer Vision. 13–16 December, Santiago, Chile, pp. 3676–3684.
- Yang, S., Luo, P., Loy, C.C., Tang, X., 2015b. From Facial Parts Responses to Face Detection: A Deep Learning Approach. arXiv:1509.06451v1 [cs.CV] 22 Sep.
- Yang, S., Luo, P., Loy, C.C., and Tang, X., 2017. Faceness-Net: Face Detection through Deep Facial Part Responses. arXiv:1701.08393v1 [cs.CV] 29 Jan.
- Yang, Y., Li, Z., Zhang, L., Murphy, C., Ver Hoeve, J., and Jiang, H., 2012. Local label descriptor for example based semantic image labelling. In: Proc. 12th European Conf. on Computer Vision. 7–13 October, Florence, Italy, pp. 361–375.
- Yitzhaky, Y., Peli, E., 2003. A method for objective edge detection evaluation and detector parameter selection. *IEEE Trans. Pattern Anal. Mach. Intell.* 25 (8), 1027–1033.
- Youn, E., Jeong, M.K., 2009. Class dependent feature scaling method using naive Bayes classifier for text datamining. *Pattern Recognit. Lett.* 30 (5), 477–485.
- Yu, T., Zhang, C., Cohen, M., Rui, Y. and Wu, Y., 2007. Monocular video foreground/background segmentation by tracking spatial-color Gaussian mixture models. In: Proc. IEEE Workshop on Motion and Video Computing, Austin, TA.
- Yuen, H.K., Illingworth, J. and Kittler, J., 1988. Ellipse detection using the Hough transform. In: Proc. Fourth Alvey Vision Conf. 31 August–2 September, Manchester, pp. 265–271.
- Yuen, H.K., Princen, J., Illingworth, J. and Kittler, J., 1989. A comparative study of Hough transform methods for circle finding. In: Proc. Fifth Alvey Vision Conf. 31 August–2 September, Manchester, pp. 169–174.
- Yuille, A., Poggio, T.A., 1986. Scaling theorems for zero crossings. *IEEE Trans. Pattern Anal. Mach. Intell.* 8, 15–25.
- Zahn, C.T., Roskies, R.Z., 1972. Fourier descriptors for plane closed curves. *IEEE Trans. Comput.* 21, 269–281.
- Zeiler, M., Krishnan, D., Taylor, G., and Fergus, R., 2010. Deconvolutional networks. In: Proc. IEEE Conf. on Computer Vision and Pattern Recognition. 13–18 June, San Francisco, CA, pp. 2528–2535.

- Zeiler M.D., and Fergus, R., 2014. Visualizing and understanding convolutional networks. In: Proc. 13th European Conf. on Computer Vision. 8–11 September, Zurich, Switzerland.
- Zhang, B., Tian, W., Jin, Z., 2006. Head tracking based on the integration of two different particle filters. *Meas. Sci. Technol.* 17 (11), 2877–2883.
- Zhang, G., Wei, Z., 2003. A position-distortion model of ellipse centre for perspective projection. *Meas. Sci. Technol.* 14, 1420–1426.
- Zhang, J., Modestino, J.W., 1990. A model-fitting approach to cluster validation with application to stochastic model-based image segmentation. *IEEE Trans. Pattern Anal. Mach. Intell.* 12 (10), 1009–1017.
- Zhang, L., Wu, B. and Nevatia, R., 2007. Pedestrian detection in infrared images based on local shape features. In: Proc. Third Joint IEEE Int. Workshop on Object Tracking and Classification in and Beyond the Visible Spectrum.
- Zhang, Z., 1995. Motion and structure of four points from one motion of a stereo rig with unknown extrinsic parameters. *IEEE Trans. Pattern Anal. Mach. Intell.* 17 (12), 1222–1227.
- Zheng, D., Zhao, Y., Wang, J., 2005. An efficient method of license plate location. *Pattern Recognit. Lett.* 26, 2431–2438.
- Zhou, H., Wallace, A.M., Green, P.R., 2003. A multistage filtering technique to detect hazards on the ground plane. *Pattern Recognit. Lett.* 24, 1453–1461.
- Zhou, J., Fu, Z., Robles-Kelly, A., 2011. Structured learning approach to image descriptor combination. *IET Comput. Vision* 5 (2), 134–142.
- Zhou, Y., Xu, R., Hu, X., Ye, Q., 2006. A robust lane detection and tracking method based on computer vision. *Meas. Sci. Technol.* 17 (4), 736–745.
- Zhu, X., and Ramanan, D., 2012. Face detection, pose estimation, and landmark localization in the wild. In: Proc. IEEE Conf. on Computer Vision and Pattern Recognition. 16–21 June, Providence, RI, pp. 2879–2886.
- Zhu, Y., Comaniciu, D., Pellkofer, M. and Koehler, T., 2004. Passing vehicle detection from dynamic background using robust information fusion. In: Proc. Conf. on IEEE Intelligent Transportation Systems.
- Zhuang, X., Haralick, R.M., 1986. Morphological structuring element decomposition. *Comput. Vision, Graph, Image Process.* 35, 370–382.
- Zielke, T., Braukermann, M., von Seelen, W., 1993. Intensity and edge-based symmetry detection with an application to car-following. *Comput. Vision Graph. Image Process.: Image Understanding* 58 (2), 177–190.
- Zisserman, A., Marinos, C., Forsyth, D.A., Mundy, J.L. and Rothwell, C.A., 1990. Relative motion and pose from invariants. In: Proc. 1st British Machine Vision Assoc. Conf. 24–27 Sept., Oxford, pp. 7–12.
- Zucker, S.W., 1976a. Toward a model of texture. *Comput. Graph. Image Process.* 5, 190–202.
- Zucker, S.W., 1976b. Region growing: childhood and adolescence. *Comput. Graph. Image Process.* 5, 382–399.
- Zuniga, O.A. and Haralick, R.M., 1983. Corner detection using the facet model. In: Proc. IEEE Conf. on Computer Vision and Pattern Recognition, pp. 30–37.
- Zuniga, O.A., Haralick, R.M., 1987. Integrated directional derivative gradient operator. *IEEE Trans. Pattern Anal. Mach. Intell.* 17, 508–517.



This page intentionally left blank

# Index

Note: Page numbers followed by “f” and “t” refer to figures and tables, respectively.

## A

Abstract pattern matching. *See* Pattern matching  
Accuracy, defined, 447  
Active contour models, 342–344, 345f. *See also*  
Segmentation  
practical results obtained using, 344–346  
Active shape model (ASM) approach, 351–352,  
360–361  
Active vision, 1  
AdaBoost algorithm, 425–426, 427f, 429–430,  
431t, 437–438, 440–441  
Advanced driver assistance system (ADAS).  
*See* In-vehicle vision systems  
Affine invariant detectors, 169–171  
Agglomerative algorithms, 379–380  
Agriculture example, egomotion and,  
739–742  
AlexNet architecture, 468–474  
connections and trainable parameters, 470t  
schematic of, 469f  
Algorithm design criteria, 86  
accuracy, 252–253  
tradeoffs, 327  
“Aliasing” errors, 789  
Animal tracking, 713–716  
Articulated objects, 748  
Artificial neural networks (ANNs), 383–387, 453  
self-organizing map (SOM), 756  
spatiotemporal attention (STA), 750–751  
Association graph, 315  
Automated visual inspection, 10–12  
applications, 10–11  
Autonomous mobile robots. *See* Robots,  
autonomous mobile

## B

Back-propagation algorithm, 387–391. *See also*  
Artificial neural networks (ANNs)  
Backpropagation through time (BPTT) algorithm,  
489  
Badrinarayanan *et al.*’s SegNet architecture,  
484–487  
Bagging, 449  
Bayes’ classifier, 423  
Naïve Bayes’ classifier, 371–372  
Bayes’ decision theory, 369–372  
Bayes theorem, 404

Beta [distribution] sampling consensus (BetaSAC),  
787–788  
Between-class variance method (BCVM),  
112–113, 114f  
Binary images, basic operations on, 29–33, 30f  
Binary images and shape analysis, 203  
boundary tracking procedures, 230–231  
circularity, 203  
compactness, 227  
complexity, 227  
concavity trees, 228–230  
connectedness in, 204–205  
convex deficiency, 228–230  
convex hull, 228–230  
distance functions, 214–217  
image processing operations on, 231–232  
measures for shape recognition, 227  
metric properties, 212  
modified crossing number  $\chi_{\text{skel}}$ , 226  
moment approximations, 228  
object labeling and counting, 205–211  
size filtering, 212–213  
skeletons and thinning, 218–227  
Binocular images, 502–503  
Blob size filtering, 745  
Boosting, 449  
approach, 425–428  
effectiveness of, 438  
loss functions for, 431–434  
with multiple classes, 438–443  
Boundary pattern analysis, 239  
accuracy of length measures, 252–253  
centroidal profiles, 242–247  
chain code, 254  
Fourier descriptor method, 249  
occlusion problems, 239  
( $r, \theta$ ) plot, 245f, 247  
( $s, \kappa$ ) plot, 245f  
( $s, \psi$ ) plot, 247–249  
Boundary tracking procedures, 230–231, 242  
Box–Muller method, 799–800  
Breadth–first search, 327, 332  
Brightness normalization, 472  
Bubble sort, 46, 90

## C

C++ notation, 25, 26t  
Canny edge detector, application of, 140f, 141f

- Canny operator, 136–139
    - pixel interpolation in, 138*f*
    - use of hysteresis thresholding, 137–139
  - Centroidal profile. *See* Boundary pattern analysis
  - Chord–tangent method. *See* Ellipse detection
  - Circle detection, 279–281
    - applications, 260–261
    - Hough transform and, 273–278
    - speed problem, overcoming, 279–283
    - unknown radius problem, 278–279
  - Circles, egomotion and centers of, 568–569
  - Circular operators, 126–127
    - detailed implementation of, 127–130
  - Classification concepts, 365
    - artificial neural networks (ANN), 383–387
      - back-propagation algorithm, 388–391
      - Bayes’ decision theory, 369–372
        - Naïve Bayes’ classifier, 371–372
      - bibliographical and historical notes, 396–398
        - recent developments, 398
      - classification errors, reducing, 371*f*
      - cluster analysis, 379–381
      - cost functions, 376–377
      - error–reject tradeoff, 376–377
      - multilayer perceptron (MLP) architectures, 391–392
      - nearest neighbor (NN) algorithm, 367–369
      - optimum number of features, 375–376
      - overfitting to the training data, 392–395
      - relation of the NN and Bayes’ approaches, 372–375
        - importance of NN algorithm, 374–375
        - mathematical statement of the problem, 372–374
      - supervised and unsupervised learning, 377–378
      - support vector machine (SVM), 381–383
    - Cluster analysis, 379–381. *See also* Statistical pattern recognition (SPR)
      - Forgy’s algorithm for, 380–381, 380*t*
  - Color, 21, 793
    - channel, 23–24, 54*f*, 68, 674
    - gray-tone (gray-scale) images *versus*., 21–24
    - HSI (hue, saturation, intensity) color representation, 794–796
    - subtle shades of, 24*f*
    - typical example of the use of color, 796
  - Color filtering, 54*f*, 55*f*, 68, 88
  - Color processing, 39
    - color bleeding, 54*f*, 69
    - distance-weighted median filter, 88
    - image filtering, 68–69
    - value of, 21–23, 22*f*, 23*f*
    - vector median filter, 69, 89
  - Computational load, calculating, 306–307
    - generalized Hough transform, 300–301, 301*f*
  - Computer vision, 13
  - Conditional risk, 376
  - Connectedness, in binary images, 204–205
  - Consensus point, 784
  - Contrast stretching, 27, 28*f*
  - Convolutional neural networks (CNNs), 453, 456–459
    - parameters for defining, 459–462
    - visualizing depth in, 462*f*
    - Zeiler and Fergus work on, 474–477
  - Convolutions, 33–34
  - Co-occurrence matrices, 190–191, 190*f*
  - Corner detection, 147. *See also* Feature, invariant
    - Beaudet operators, 149–150
    - DET operator, 150
    - determining orientation, 164–165
    - Dreschler–Nagel (DN) operator, 151
    - Harris operator, 156–164
    - Hough transform approach to, 329*f*
    - Kitchen–Rosenfeld (KR) operator, 150–151
    - median-based operator, 151–156
    - Plessey operator, 163
    - second-order derivative schemes, 149–151
    - SUSAN operator, 180
    - template matching, 148
    - Zuniga–Haralick (ZH) operator, 151
  - Corner properties, 148
    - bluntness, 148–149
    - contrast, 152
    - location, 164
    - orientation, 164–165
    - pointedness, 148–149
    - sharpness, 148–149
  - Counting, object, 205–211
  - Credit assignment problem, 388–389
  - Cross ratio, 551–555
    - Chasles’ theorem, 560–561
    - cross ratio functions, symmetric, 564–565
    - cross ratio spectra, 582
    - 5-point configuration, 558–559
    - ratio of ratios, 551–555
  - Crossing number  $\chi$ , 219–221
- ## D
- DeconvNet architecture, 481–484
  - Deconvolution network, 482*f*
  - Deep learning, 13–14
  - Deep learning explosion, 768–769
  - DeepID face representation system, 649–653, 652*f*
  - Deep-learning networks, 453
    - AlexNet architecture, 468–474

- connections and trainable parameters, 470*t*
    - schematic of, 469*f*
  - classification system, 454*f*
  - convolutional neural networks (CNNs), 453, 456–459
    - parameters for defining, 459–462
    - visualizing depth in, 462*f*
    - Zeiler and Fergus' work on, 474–477
  - DeconvNet architecture, 481–484
  - LeNet architecture, 463–468
  - recurrent neural networks, 487–490
  - SegNet architecture, 484–487
  - VGGNet architecture, 479–481
    - parameters, 481*t*
    - visualization experiments, 477–478
  - Deformable contours. *See* Active contour models
  - Deformable parts models (DPM), 654
  - Depth—first search, 327, 332
  - Detection, 17. *See also* Circle detection; Corner Detection; Edge detection; Ellipse detection; Eye detection; Facial feature detection; In-vehicle vision systems; Iris detection; Line detection; Surveillance crack, 99–100
    - defect, 76, 117
    - interest point, 147
    - laparoscopic tool, 272–273
    - line segment, 292
    - optimal, 328
    - parabola, 294, 725–726
    - people, 750–751
    - polygon, 302
    - vanishing point, 565–567
  - Diameter bisection method. *See* Ellipse detection
  - Difference of Gaussians (DoG), 139, 171–172
  - Differential edge operators, systematic design of, 130
  - Differential gradient (DG), 125–126
  - Differential invariants, 561–564
  - Dilation, 69
    - cancellation effects, 69–70
    - duality between erosion and, 72–73
    - operator, 70
    - properties of operators, 73–76
  - Discrete model
    - of median shifts, 60–61
    - of rank order filters, 53
  - Discriminability, defined, 446–447
  - Distance functions, 214–217
    - local maxima of, 216–217
  - Distinct class-based splitting measure (DCSM), 449–450
  - Distortion
    - barrel, 595
    - edge shift, 88
    - foreshortening, 576
    - optical, 761
    - pin cushion, 595
    - radial, 595–597
  - Distributions, sampling from, 797
    - Box–Muller and related methods, 799–800
  - Divisive algorithms, 379–380
  - Driver assistance system. *See* In-vehicle vision systems
  - Dropout, 472
- ## E
- Edge, 119
    - planar, 120, 121*f*
    - roof, 121*f*
    - step, 120, 121*f*
  - Edge detection, 119
    - advantages of, 120
    - alternative schemes, 130–134
    - basic theory of, 120–122
    - Canny operator, 136–143, 140*f*, 141*f*
    - difference of Gaussians (DoG), 171–172
    - differential gradient (DG), 125–126
    - integrated directional derivative (IDD), 132–133
    - Kirsch operator, 119
    - Laplacian of Gaussian (LoG), 169–170
    - Laplacian operator, 139–143
    - Marr–Hildreth operator, 133, 144
    - non-maximum suppression, 151, 155*f*, 156
    - orientation, 119, 121
    - Prewitt operator, 125–126, 131
    - Reeves moment-based operator, 131
    - Roberts operator, 125
    - Robinson five-level operator, 123
    - Robinson three-level operator, 123
    - Sobel operator, 125–128, 136–137, 142*f*
    - template matching (TM), 123–124
    - Yuille–Poggio operator, 144
  - Egomotion, 739–742. *See also* In-vehicle vision systems; Robots, autonomous mobile
  - Eigenface approach to face recognition, 640–643
  - Eigenfaces, 641
  - “Eigenfilters” masks, 195–196
  - Ellipse detection, 259, 284–289
    - chord–tangent method, 286–287
    - comparison of methods, 312–314
    - determining parameters, 287–289
    - diameter bisection method, 284–286
    - generalized Hough transform method, 308–312
      - reducing computational load for, 312–313, 323–326
    - superellipse, 285–286, 293–294

- Ellipses, perspective and centers of, 568–569
  - Embedding function, 346–347
  - Energy minimization process, 341–342, 344
  - Entropy-based thresholding, 103–105
  - Epipolar lines, 504–505
  - generalized epipolar geometry, 598
  - Erosion, 69
    - cancellation effects, 69–70
    - duality between dilation and, 72–73
    - operator, 70
    - properties of operators, 73–76
  - Error rates, performance measures relating to, 446–447
  - Error–reject tradeoff, 376–377
  - Essential matrix, 599–601
  - Euclidean metric, 218
  - Expectation maximization (EM) algorithm, 400–402, 404–410, 407*t*, 408*f*, 413*f*, 414*f*
  - Extrinsic camera parameters, 592–595
  - Eye detection, 582, 635*f*, 636*f*
- F**
- Face detection, 631
    - DeepID face representation system, 649–653
    - difficulties of, 643–645
    - eigenface approach to, 640–643
    - eye region, 635*f*, 636*f*
    - facial feature detection, 634–635
    - fast face detection, 654–657
      - powerful object detection schemes, 656–657
    - frontalization, 645–649
      - occlusion problem, 647*f*
    - simple approach, 632–634
    - simple sampling approach, 633*f*
    - 3-D analysis of, 658*f*
    - 3-D object, face as part of, 657–659
    - Viola–Jones approach, 636–639, 639*f*
  - “Face frontalization for Alignment and Recognition” (FAR) technique, 646–648
  - Face recognition, 582
  - Faceness-Net detector, 655*f*, 656
  - Facial feature detection, 289–290, 634–635, 728–731
  - False alarm rate, defined, 447
  - False negative error, 443–446
  - False positive error, 443–446, 450
  - Fast face detection, 654–657
    - powerful object detection schemes, 656–657
  - Fast Fourier transform (FFT), 40
  - “Fast-marching” method, 347
  - Feature, invariant, 166–179
    - affine invariant, 169–171
    - geometric transformations and feature normalization, 167–168
    - gradient location and orientation histogram (GLOH), 175
    - Harris-based, 169–171
    - Hessian scale and affine invariant detectors and descriptors, 171
    - Hessian-based, 169–171
    - histograms of oriented gradients (HOG) approach, 177–179
    - intensity extrema-based region detector (IBR), 175
    - maximally stable extremal region (MSER), 174–175
    - scale invariant, 176
    - scale invariant feature transform (SIFT), 171–172, 178, 182
    - scale-invariant feature operator (SFOP), 175, 177
    - speeded-up robust features (SURF), 172–174
    - use for wide baseline matching, 625–626
  - Feature detection
    - corner, 147
    - edge, 120–122
    - interest point, 147
  - Feature location. *See* Feature detection
  - Filters, 39
    - applications, 66–67
    - color, 68–69
    - color bleeding and, 68–69
    - distance-weighted median, 88
    - Gaussian, 42
    - Kalman, 623–625
    - limit, 44
    - low-pass, 40–42, 40*f*, 44
    - matched, 302–303
    - maximum, 53
    - median, 44–46
      - corner detector, based on, 91
    - minimum, 53
    - mode, 46–52
    - noise suppression by Gaussian smoothing, 42–44
    - particle. *See* Tracking moving objects
    - rank order, 53
    - sharp–unsharp masking, 54–55, 56*f*
    - shifts introduced by
      - median filters, 56–61
  - discrete model of, 60–61
    - rank order filters, 61–65
    - spatial, 302–303
    - spatial frequency, 42
    - switched, 89

truncated median, 48–50, 50*f*, 52*f*  
 vector median, 54*f*, 69

Fixed increment rule, 383–385, 385*t*

*F*-measure, defined, 447

Focus of contraction, 615

Focus of expansion (FoE), 615, 616*f*, 617–618, 627

Foot-of-normal method, 265–267

Forgy's algorithm for cluster analysis, 380–381, 380*t*

Fourier methods, 348

Frame store, 25, 36

Frontalization, 645–649  
 occlusion problem, 647*f*

Full perspective projection, 526, 538, 544–545, 544*f*, 569

Fully convolutional network (FCN), 484

Fundamental matrix, 601–602

**G**

Gaussian distribution, 49*f*, 105, 271–272, 400–404, 434, 771–772, 776, 797, 799–800

Gaussian filters. *See* Filters

Gaussian mixture distributions, 412*f*

Gaussian noise, 774, 778–779

Gaussian noise contribution, 779

Gaussian smoothing, 42–44

Gaussian sphere, vanishing point detection and, 566–567

Gaussians, mixtures of, 402–408  
 expectation maximization algorithm, 405–408

Generalization to grayscale images, 58–60

Generalized Hough transform (GHT), 299–302  
 basic, 300–302  
 for ellipse detection, 308–312  
 for feature collation, 323–326  
 gradient *versus* uniform weighting, 304–308  
 line detection and, 261–265  
 perimeter template, 303*f*, 306, 306*f*  
 polygon detection and, 302  
 search, 327  
 sensitivity and computational load, calculating, 306–307  
 spatial matched filtering, 302–303

Genetic algorithms (GAs), 117

Global valley algorithm, 112*t*

Global valley method (GVM), 106–108  
 practical results obtained using, 108–113

Gradient location and orientation histogram (GLOH), 175

Gradient weighting *versus* uniform weighting, 304–308

Graph matching, 299–300, 326, 328–329, 331–333

“Graph transformation matching” algorithm, 333–334

Gray-level appearance model, 355

Grayscale images  
 basic operations on, 25–29  
 morphology in, 84–86

Gray-tone (gray-scale) images, 20–21  
*versus* color, 21–24  
 discrete model of median shifts, 60–61  
 generalized morphology, 58–60  
 image processing operations on, 24–33

Group sampling consensus (GroupSAC), 787–788

## H

Haar filters, 637*f*

Hamming distance, 7

Hardware, 11

Harris interest point detector, 156–164, 165*f*  
 corner signals and shifts for various geometric configurations, 159–160  
 different forms of Harris operator, 163–164  
 performance with crossing points and T-junctions, 160–163

“HeadHunter” detector, 654

Histogram concavity analysis, 113–114

Histograms of oriented gradients (HOG) approach, 177–179

Homogeneous coordinates, 585, 587–588

Homography, 572–573, 582, 602, 694, 697, 701–702

Hough transform (HT), 259. *See also* Generalized Hough transform (GHT)  
 agriculture application, 744  
 nature of, 299–308  
 uses, 260–261  
 circle detection, 273–278, 291  
 corner detection, 164–165  
 ellipse detection, 284–286, 291  
 line detection, 261–265  
 superellipse detection, 293–294  
 vanishing point detection, 565–567  
*xy*-grouping, 264–265

HSI (hue, saturation, intensity) color representation, 794–796

Hughes effect, 438

Human gait analysis, 711–713

Hysteresis thresholding, 134–136

**I**

Image acquisition  
 sampling theorem, 789–792

- Image differencing, 612, 627
  - Image filters (filtering). *See* Filters
  - Image “preprocessing” task, 6
  - Image processing, 6, 14, 17
    - applying convolutions, 33–34
    - applying logical operations, 263
    - on binary images, 40
    - brightening, 19
    - clearing, 25
    - displaying, 25
    - expanding, 31
    - on gray-scale images, 40
    - inverting, 27, 29
    - sequential *versus* parallel operations, 35–36
    - shifting, 19
    - shrinking, 29–30
    - size filtering, 212–213
    - suppressing noise, 40
  - Image segmentation. *See* Segmentation
  - ImageNet Challenge, 468
  - ImageNet Large-Scale Visual Recognition Object Challenge (ILSVRC), 468
  - Image-Restricted, Label-Free Outside Data (IRLFOD) protocol, 649
  - Imaging modalities
    - infra-red (NIR), 719–720, 752
    - thermal, 719–720, 752, 754
    - visible, 505
  - Industrial parts, location of, 523–525
  - Inspection. *See* Automated visual inspection
  - Intensity extrema-based region detector (IBR), 175
  - Intrinsic camera parameters, 592–595
  - Invariant feature. *See* Feature, invariant
  - Invariants, 549. *See also* Feature, invariant
    - cross ratio, 551–555
    - 5-point configuration, 740*t*
    - functions, symmetric, 564–565
    - spectra, 582
    - defined, 550–551
    - differential and semidifferential, 561–564
    - for noncollinear points, 555–559
    - for points on conics, 558–559
    - reasons for using, 549
  - In-vehicle vision systems, 721. *See also* Robots,
    - autonomous mobile; Surveillance; Tracking moving objects
    - advanced driver assistance system (ADAS), 749–750
    - all hours—all weathers, 752
    - catadioptric cameras, 755
    - convoy, 723
    - global positioning system (GPS), 723, 756
    - ground plane, location and use of, 739
    - licence plate location, 731–734
    - omnidirectional cameras, 755
    - pedestrian location, 734–739
      - chamfer matching, 735*f*
      - skin color, 736
    - road lane marking location, 725–726
      - RANSAC, 725–726
    - road sign, location, 726–728
      - chamfer matching, 729*f*
      - matched filter, 727–728
    - roadway location, 723–725
    - use of vanishing points (VPs), 568–569
    - vehicle location, 728–731
      - under-vehicle shadow, 728–729
  - Inverse graphics, 9–10
  - Iris detection, 199, 289–290, 295, 729–731
    - use to estimate eye Gaze direction, 289
  - ISODATA algorithm, 380–381
  - Iterative algorithms, 381
- ## J
- Jensen’s inequality, 400
  - Junction orientation technique, 519–523
- ## K
- Kalman filter. *See* Tracking moving objects
  - K*-means algorithm, 381*t*, 397–400, 410, 413–415, 416*f*, 417*f*
  - “*k*-NN” method, 374–375
  - Krizhevsky *et al.*’s AlexNet architecture, 468–474
    - connections and trainable parameters, 470*t*
    - schematic of, 469*f*
  - Kullback–Leibler (KL) divergence function, 400, 409–410
- ## L
- “Labeled faces in the wild” (LFW) datasets, 632–634
  - Labeling, 205–211
    - object, 205–211
  - Lambertian surfaces, reflectance maps for, 509*f*
  - Landmark points, 348–350, 353–355
  - Laparoscopic tools, 272–273
    - location of tips, 273*f*
    - location using RANSAC, 272
    - orientation parameters for, 274*f*
  - Laplacian operator, 139–143
  - Laws’ texture energy approach, 193–195
  - Learning. *See* Artificial neural networks (ANNs)
    - Statistical pattern recognition (SPR)
  - Least median of squares, 780–782
  - Least squares analysis, 771–773
  - LeCun *et al.*’s LeNet architecture, 463–468

LeNet architecture, 463–468  
 Level-set approach to object segmentation, 346–347  
 LFPW (labeled face parts in the wild), 651  
 Light striping, 504  
 Line detection, 259
 

- foot-of-normal method, 265–267
- generalized Hough transform and, 261–265
- Hough transform and, 261–265
- longitudinal localization, 264–265
- RANSAC, 267–272
- slope–intercept equation, 262

 Local maximum operation, 268  
 Local–feature–focus (LFF) method, 322, 331  
 Logistic sigmoid function, 434, 435*f*  
 Logit function, 434  
 LogitBoost algorithm, 433, 435–438, 436*t*, 440–442  
 “Log-loss” function, 431  
 Longitudinal line localization, 264–265  
 Loss functions for boosting, 431–434  
 Lowe’s scale invariant feature transform, 171–172

## M

Machine learning, 13–14, 365  
 Machine vision, 12. *See also* Automated visual inspection
 

- applications, 764
- defined, 760–762
- future for, 760–762
- importance of, 760–762
- tradeoffs, 762–764

 MacQueen’s *K*-means algorithm, 381*t*  
 Mahalanobis distance, 355–357, 356*f*, 796  
 Marr–Hildreth operator, 133  
 Match graph, 315  
 Mathematical morphology, 41, 70–79
 

- closing, 76–78
- connectivity-based analysis, 78–79
- dilation
  - generalized, 70–72
- duality between dilation and erosion, 72–73
- erosion
  - generalized, 72
- grayscale imaging, 56–61
- morphological analysis, 674–676, 674*f*, 703–704, 749, 755–756, 767–768
- opening, 76–78
- residue function, 76
- top hat operator, 76
  - black, 76
  - white, 76

Matrix (matrices), 602
 

- essential, 599–602
- fundamental, 601–602
- gray-level co-occurrence, 190–193

 Maximal clique, 315–318, 321*t*, 323–326, 330  
 Maximally stable extremal region (MSER), 174–175  
 Maximum likelihood thresholding, 105–106  
 Max-pooling indices, 484–485  
 Mean filters. *See* Filters  
 Median filters, 44–46. *See also* Filters
 

- edge smoothing property of, 62*f*
- shifts introduced by, 56–61
  - continuum model of median shifts, 57–58
  - discrete model of median shifts, 60–61
  - generalization to grayscale images, 58–60

 Metric properties, in digital images, 500  
 Mobile robots. *See* Robots, autonomous mobile  
 Mode filters, 46–52, 51*f*. *See also* Filters  
 Model constraints, 342  
 Modeling AdaBoost, 428–431
 

- real AdaBoost, 430–431

 Moment approximations, 228  
 Moore’s law, 764–765  
 Morphological grouping, 79–84  
 Morphology. *See* Mathematical morphology  
 Motion, 610. *See also* Surveillance; Tracking
 

- moving objects
  - aperture problem, 612
  - focus of expansion (FOE), 617–618
  - human gait analysis, 711–713
  - Kalman filters, 623–625
  - optical flow, 611–615
  - snakes, 718
  - stereo from, 621–623
  - time-to-adjacency analysis, 618–619
  - traffic flow monitoring, 698–702

 Multilayer perceptron (MLP) architectures, 387, 388*f*, 391–392, 449–450
 

- cross-validation, 394–395, 394*f*
- learning curve for, 392*f*
- overfitting of data, 392–395, 393*f*
- training, 392–395

 Multiple classes, boosting with, 438–443  
 Multiple classifiers, 422–425  
 Multiple-view vision, 597–598

## N

Naïve Bayes’ classifier, 371–372  
 “Narrow band” method, 347  
 Nasty realities, 760–761
 

- clutter, 760
- glint, 761



- Nasty realities (*Continued*)
    - noise, 760
      - Gaussian, 761
      - impulse, 761
      - white, 302
    - occlusion, 707
  - Navigation, robots. *See* Robots, autonomous mobile
  - Nearest neighbor (NN) algorithm, 367–369
    - importance of, 374–375
    - training patterns, 367
  - Newton’s method of approximation, 400
  - Noh *et al.*’s DeconvNet architecture, 481–484
  - Noise, 40–41
    - spike, 44
    - white, 302
  - Noise removal operations, 32*f*
  - Noise suppression, 35*f*, 36–37, 40–41
    - Gaussian smoothing, 42–44
    - median filters, 44–46
    - mode filters, 46–52, 51*f*
    - rank order filters, 53
  - Noncollinear points invariants for, 555–559
  - Non-Lambertian surface, reflectance map for, 511*f*
  - Nyquist sampling theorem, 789
- O**
- Object labeling and counting, 205–211
  - Object location. *See* Detection
  - Object recognition schemes
    - 3-D, 518–519
  - Object segmentation, level-set approach to, 346–347
  - Objects location using shape models, 353–358
  - Occlusion, 687–688
    - apparent, 705
    - dynamic, 705
    - problems, 249–252, 647*f*, 700
    - reasoning, 699–700
    - scene, 705
  - “One-versus-the-rest” (OVR) classifier, 438–439
  - Optical character recognition (OCR), 95–96, 365–366
  - Optical flow, 611–615
    - interpretation of, 615–617
    - problems with, 620–621
  - Overlapping pooling, 471, 472*f*
- P**
- Parallel image processing operations, 35–36
  - Parallel thinning, 223
  - Particle filter. *See* Tracking moving objects
  - Pattern matching
    - similarity measures
      - Bhattacharyya coefficient, 688–689
  - Pattern recognition (PR), 365. *See also* Statistical pattern recognition (SPR)
  - People tracking, 664
    - applications, 664
    - basic techniques, 705
    - from vehicles, 706–707
  - Perceptron, 383, 384*f*
    - fixed increment algorithm, 385*t*
  - Performance measures, 176, 177*t*, 182
    - receiver operating characteristic (ROC), 144–145, 752–753
  - Performance measures relating to error rates, 446–447
  - Perspective, 572
    - in art, 572–578
    - vanishing point, 565–567
  - Perspective inversion, 534–535, 534*f*, 535*f*
  - Perspective *n*-point (PnP) problem, 545–546
  - Perspective projection, 500
    - full, 538, 540–541
    - symmetric trapezia problem, 543
    - 3-point problem, 542–543
    - weak, 534–538, 540*f*
  - Phong model, 510–511
  - Photometric stereo, 499, 511–514
  - Pixel–pixel operations, 37
  - Pixels, 20–21
  - Plan view of ground plane, 740*r*
    - constructing, 741
  - Point pattern matching. *See* Graph matching/Pattern matching
  - Point spread function (PSF), 33–34, 308
    - to detect elliptical objects, 312*f*
    - to detect tilted circles, 311*f*
    - typical PSF shapes for detection of ellipses with various eccentricities, 311*f*
  - Point-line duality, 261
  - Pooling and unpooling operation, 456–458
  - Positive predictive value, defined, 447
  - Precision, defined, 446–447
  - Prewitt operator, 125–126, 131
  - Principal components analysis (PCA), 347–348, 353–354, 357*f*, 419–422, 420*f*, 448–449, 640–641
    - fitting hand picture to, 355*f*
    - intensity profile approach, 358*f*
    - producing boundary features for, 349*f*
    - using improved intensity profiles, 357*f*
  - Principal point, 592–593
  - Priori probability, 373
  - Probabilistic methods, machine learning, 399
    - boosting approach, 425–428

boosting with multiple classes, 438–443  
 effectiveness of boosting, 438  
 expectation maximization (EM) algorithm,  
   general view of, 408–410  
 Gaussians, mixtures of, 402–408  
   expectation maximization algorithm,  
     405–408  
 LogitBoost algorithm, 435–438  
 loss functions for boosting, 431–434  
 modeling AdaBoost, 428–431  
   real AdaBoost, 430–431  
   multiple classifiers, 422–425  
   practical examples, 411–419  
   principal components analysis, 419–422  
 receiver operating characteristic (ROC),  
   443–447  
   performance measures relating to error rates,  
     446–447  
 Probabilistic optimization, 399–400, 413–415  
 Progressive sample consensus (PROSAC),  
   787–788  
 Projection schemes  
   3-D, 500–505  
 Propagation, 205–206

## R

( $r$ ,  $\theta$ ) plot. *See* Boundary pattern analysis  
 Radial distortions, 585–586, 601  
   correcting, 595–597  
 Rank order filters, 53  
   shifts introduced by, 61–65  
     rectangular neighborhoods, shifts in, 62–65  
 RANSAC (random sample consensus) approach,  
   261*t*, 267–272, 271*f*, 294–295, 725–726,  
   754, 784–785  
 Raw pixel measurements, 601  
 Rayleigh noise, 400–402  
 Real AdaBoost, 430–431  
 Real-time operation, 686–687, 756  
 Recall, defined, 446–447  
 Receiver operating characteristic (ROC), 443–447  
   performance measures relating to error rates,  
     446–447  
 Recognition. *See* Statistical pattern recognition  
   (SPR)  
 Recurrent neural networks, 487–490, 488*f*  
 Region of interest (RoI), 289  
 Region-growing methods, 94–95. *See also*  
   Segmentation  
 “Regions with CNN features” (R-CNN) method,  
   656–657  
 Relative efficiency, 774  
 Reproducible kernel Hilbert space (RKHS), 333

Residue operator, 89–90  
 Road, 723–725, 754–755  
   lane markings, 723–725, 726*f*, 727*f*  
   location, 725–726  
   signs, 726–728  
 Roberts operator, 125  
 Robots, autonomous mobile, 739  
   active vision, 1  
   agriculture application example, 742  
   centers of circles and ellipses, 568–569  
   cross ratios, 581  
   navigation for, 585–586  
   plan view of ground plane, constructing, 741  
   safety issues, 664  
   vanishing point detection, 581–582  
   vehicle guidance, 742–747  
 Robust estimator. *See* Robust statistics  
 Robust statistics, 771  
   beta [distribution] sampling consensus  
     (BetaSAC), 787–788  
   breakdown point, 773–776, 774*t*  
   features from accelerated segment test (FAST),  
     175  
   group sampling consensus (GroupSAC),  
     787–788  
   Hough transform and, 771  
   importance sampling consensus (IMPSAC), 787  
   influence function, 775–780  
   inlier, 775, 784  
   least median of squares (LMedS), 780–782  
   least squares regression, 775, 780, 783  
   L-estimator, 775, 782  
   M-estimator, 775, 777–778, 782  
   N adjacent points sample consensus (NAPSAC),  
     787  
   outlier, 775–776, 777*f*, 778, 785–787  
   progressive sample consensus (PROSAC),  
     787–788  
   random sample consensus (RANSAC),  
     784–785  
   relative efficiency, 774  
   R-estimator, 775, 782  
 Robustness, 176–177, 783  
 R-table, 301

## S

( $s$ ,  $\kappa$ ) plot. *See* Boundary pattern analysis  
 ( $s$ ,  $\psi$ ) plot. *See* Boundary pattern analysis  
 “Salt and pepper” noise, 32, 32*f*  
 Sampling theorem, 789–792  
 Sampling theorem, Nyquist, 789  
 Scale invariant feature transform (SIFT),  
   171–172, 178, 182

- Scaled orthographic projection, 534–536, 544–545
- Scale-invariant feature operator (SFOP), 175, 177
- Scene analysis, 9
- Schmitt trigger, 134
- Search space, 242, 279
- Segmentation, 93. *See also* Thresholding (threshold)
  - graph cuts, 529
  - region-growing, 94–95
  - snake, 698
- SegNet architecture, 484–487
- Self-similarity analysis, 255
- Semantic segmentation network, 481–483, 491–492
- Semidifferential invariants, 561–564
- Sensitivity, defined, 446–447
- Sequential image processing operations, 35–36
- Sequential labeling, 209
- Sequential thinning, 222*t*
- Shading, shape from, 506–511
- Shadows, 581
- Shape models, 348–358
  - locating objects using, 353–358
- Shape recognition. *See also* Binary images and shape analysis
  - from angle, 519
  - moment approximations, 228
  - from shading, 506–511
  - simple measures for, 203
  - skeletons and, 227
  - from texture, 515–516
- Sharp–unsharp masking, 54–55, 56*f*
- Signal-detection theory, 446
- Simonyan and Zisserman’s VGGNet architecture, 479–481
  - parameters, 481*t*
- Simplex algorithm, 714–715
- Single-layer perceptron, 386–387, 387*f*
- Singular value decomposition (SVD), 603
- Skeletons and thinning, 218–227
  - defined, 218
  - guided, 224
  - modified crossing number  $\chi_{\text{skel}}$ , 226
  - nature of skeleton, 224–225
  - node analysis, 225–226
  - shape analysis using, 226
  - thinning implementations, 221–224
- Snake energy, 341–343
- Snakes. *See* Active contour models
- Sobel operator, 125–128
- Sorting optimization curve (SOC), 450
- Spatial matched filtering, 302–303
- Specificity, defined, 446–447
- Speeded-up robust features (SURF), 172–174
- Statistical pattern recognition (SPR). *See also* Artificial neural networks (ANNs); Performance measures
  - bag-of-words, 626
- Statistical PR (SPR), 365–366, 381–383, 396
- Stereo from motion, 621–623
- Stitching photographs, 549, 551, 576–578, 582
- Straight edge detection, 264–265
- Stretching image contrast, 121–122, 154–155
- Stride and zero padding, 461*f*
- Structured lighting, 516–518
- Student’s *t*-distribution, 400–402
- Subgraph–subgraph isomorphism, 314–315, 331
- Sudden step-edge response, 120, 121*f*
- Supervised learning, 377–378
- Support vector machine (SVM), 381–383
  - principle of, 382*f*
- Surveillance, 10–12, 663. *See also* In-vehicle vision systems; Tracking moving objects
  - articulated bodies, analyzing motions of, 719
  - iterative parsing, 719
  - background modeling, 669–675
    - expectation maximization (EM) algorithm, 670–671
    - fluttering vegetation, 670, 671*f*, 673*f*
    - Gaussian mixture model (GMM), 671–674
    - non-parametric model, 678
    - parametric model, 675–677
  - field of view (FoV), 667–668, 691
  - foreground detection, 669–678
  - ghost, 671*f*, 675, 717
  - ground plane, location and use of, 694, 694*f*
  - in-plane rotation, 684–685
  - licence plate location, 702–704
  - monitoring traffic flow, 698–702
  - motion distillation, 708
    - rigidity parameter, 708–709
  - multiple cameras, 693–698
    - non-overlapping fields of view, 697–698
    - overlapping fields of view, 697–698
    - transition probability, 679
  - occlusion reasoning, 691–693, 705–707
  - out-of-plane rotation, 685
  - pedestrian location, 734–739, 748
    - chamfer matching, 691–693
    - histogram of orientated gradients (HOG), 753
    - human gait analysis, 711–713
    - minimum description length (MDL) approach, 691
    - people location, 697
    - shadow suppression, 674
    - stationary background problem, 675
    - traffic flow monitoring, 698

- Bascle method, 698–700
  - Koller method, 700–702
  - transient background problem, 675
  - use of color, 684
    - chromaticity coordinates, 677
    - chrominance parameters, 686
    - color histograms, 684–688
    - color indexing, 684
    - vehicle location, 728–731
  - Symmetric cross-ratio functions, 564–565
  - Symmetric trapezia problem, 543
    - full perspective projection, 544*f*
  - Symmetry, 123, 286–287
    - mirror symmetry, 331
    - reflection symmetry, 729–731
    - symmetry detection, 729–731
  - System design, 560, 723
- T**
- Template matching (TM), 7–8, 7*f*, 120, 123
    - boundary pattern analysis and, 242
    - coarse–fine, 246–247
    - corner detection and, 148–149
    - edge detection and, 123–124
    - multistage, 767
    - 2-stage, 763–764, 767
    - tradeoffs, 762–764
  - Texture, 185, 187*f*
    - defined, 185–186
    - descriptors, 188
    - fractal-based measures of, 198
    - Markov random field models of, 198
    - segmentation, 188–189, 199
    - shape from, 199
    - texel, 186–188
  - Texture analysis, 79
    - Ade’s eigenfilter approach, 195–197
    - autocorrelation approach, 189, 189*f*
    - gray-level co-occurrence matrices, 190–193
    - Laws’ texture energy approach, 193–195
    - spatial gray-level dependence matrix (SGLDM) approach, 190
    - structural approaches to, 197–198
  - Thinning, 218–227
    - guided, 224
    - implementations, 221–224
    - modified crossing number  $\chi_{\text{skel}}$ , 226
  - $3 \times 3$  template operators, theory of, 123–124
  - Three-dimensional (3-D) analysis, 497
    - ambiguity, 498
    - Ballard–Sabbah method, 527–528
    - camera calibration, 526, 590–592
    - eight-point algorithm, 603–604
    - essential matrix, 599–601
    - fundamental matrix, 601–602
    - generalized epipolar geometry, 598
    - homogeneous coordinates, 587–589
    - homography, 695
    - Horaud’s junction orientation technique, 519–523
    - image reconstruction, 605–608
    - image rectification, 604–605
    - image transformations, 585–586
    - industrial parts, location of, 523–525
    - intrinsic and extrinsic camera parameters, 592–595
    - multiple-view vision, 597–598
    - object recognition schemes, 518–519
    - perspective  $n$ -point (PnP) problem, 294–295, 545–546
    - photometric stereo, 511–514
    - pose estimation, 546, 786
      - use of coplanarity, 599
    - projection schemes, 500–505
    - radial distortions, correcting, 595–597
    - shape from angle, 519
    - shape from shading, 499, 506–511
      - bidirectional reflectance distribution function (BRDF), 528–529
      - smoothness, surface, 514–515
    - shape from texture, 515–516
    - Silberberg method, 527–528
    - structure from motion, 619, 627
    - structured lighting, 516–518
    - surface smoothness, 514–515
    - transformation parameters, 590
    - triangulation, 605–606
  - Three-dimensional (3-D) objects
    - inspection of, 518–519
  - Thresholding (threshold), 28, 93, 95–97. *See also*
    - Segmentation
      - adaptive, 97–101
      - between-class variance method (BCVM), 103, 112–113
      - bias when selecting, 97
      - entropy-based, 103–105
      - finding a suitable, 95–97
      - global valley method (GVM), 106–108
      - hysteresis, 101, 134–136
      - images, 93–94
      - local, 98–101
      - maximum likelihood, 105–106
      - in unimodal distributions
        - concavity analysis, 113–114
        - variance-based, 101–103
  - Time-to-adjacency analysis, 618–619
  - Top-hat operator, 76

- “Top-hat” selection transformation, 89–90
  - Tracking moving objects, 623. *See also* Surveillance
    - animal tracking, 713–716
    - Kalman filter, 623–625
    - mean shift algorithm, 683
    - monitoring traffic flow, 663
    - particle filter, 678–684
      - auxiliary particle filter (APF), 683
      - Condensation, 682
      - cumulative distribution function (CDF), 680*f*
      - iCondensation, 682–683
      - iterated likelihood weighting (ILW), 683
      - kernel particle filter, 683
    - Epanechnikov kernel, 683
    - sample impoverishment, 682
    - sampling importance resampling (SIR), 682
    - sequential importance sampling (SIS), 679–680
    - people tracking, 664
      - Leeds people tracker, 664
      - Siebel–Maybank tracker, 718
      - from vehicles, 664–665
  - Traffic flow monitoring. *See* Surveillance
  - Transform (Transformation). *See also* Hough transform (HT)
    - affine, 603–604
    - degrees of freedom (DoF), 499–500, 518–519
      - Euclidean, 561–562
      - Fourier, 40
      - Radon, 292
      - similarity, 167–168
      - trace, 330
    - Fourier, 790–791, 791*f*
  - Truncated median filter (TMF), 48–50, 50*f*, 52*f*
    - detection, 565–567
    - use to find circle and ellipse centers, 568–569
  - Variance-based thresholding, 101–103
  - Vector median filter (VMF), 69
  - Vehicle guidance. *See* In-vehicle vision systems
    - Robots, autonomous mobile
  - VGGNet architecture, 479–481
    - parameters, 481*f*
  - Video analytics. *See* Surveillance
  - Viola–Jones approach, for face recognition, 636–639, 639*f*
  - Vision, 1. *See also* Automated visual inspection; Machine vision
    - active, 2
      - human, 1–2, 749
      - multiple-view, 597–598
  - Vision, nature of, 2–10
    - inverse graphics, 9–10
    - object location, 6–8
    - recognition, 2–6
    - scene analysis, 9
  - Visualization experiments, 477–478
- W**
- Weak classifiers, 426–428, 427*f*, 437*f*, 449
  - Weak perspective projection, 535–538
  - White noise, 302
  - Wide baseline, 625
    - matching, 625
      - use of invariant feature detector, 627
    - views, 625
  - Widrow–Hoff delta rule, 385
  - Window operation, 27, 36, 39, 80*f*, 145
- Y**
- YOLO approach, 656–657
- Z**
- Zeiler and Fergus’s visualization experiments, 477–478
  - Zeiler and Fergus’s work on CNN architectures, 474–477
- U**
- Unit step edge function (USEF) concept, 180–181
  - Unpooling layer, 477–478
  - Unsupervised learning, 377–378
- V**
- Validation set, 393–395
  - Vanishing point, 568–569. *See also* In-vehicle vision systems

Fifth Edition

# COMPUTER VISION

## Principles, Algorithms, Applications, Learning

*Computer Vision: Principles, Algorithms, Applications, Learning* (previously entitled *Computer and Machine Vision*) clearly and systematically presents the basic methodology of computer vision, covering the essential elements of the theory while emphasizing algorithmic and practical design constraints. This fully revised fifth edition has brought in more of the concepts and applications of computer vision, making it a very comprehensive and up-to-date text suitable for undergraduate and graduate students, researchers and R&D engineers working in this vibrant subject.

### KEY FEATURES

- Three new chapters on Machine Learning emphasise the way the subject has been developing:
  - Two chapters cover Basic Classification Concepts and Probabilistic Models.
  - The third covers the principles of Deep Learning Networks and shows their impact on computer vision, reflected in a new chapter Face Detection and Recognition.
- A new chapter on Object Segmentation and Shape Models reflects the methodology of machine learning and gives practical demonstrations of its application.
- In-depth discussions have been included on geometric transformations, the EM algorithm, boosting, semantic segmentation, face frontalisation, RNNs and other key topics.
- Examples and applications—including the location of biscuits, foreign bodies, faces, eyes, road lanes, surveillance, vehicles and pedestrians—give the 'ins and outs' of developing real-world vision systems, showing the realities of practical implementation.
- Necessary mathematics and essential theory are made approachable by careful explanations and well-illustrated examples.
- The 'recent developments' sections included in each chapter aim to bring students and practitioners up to date with this fast-moving subject.
- Tailored programming examples—code, methods, illustrations, tasks, hints and solutions (mainly involving MATLAB and C++).



ACADEMIC PRESS

An imprint of Elsevier  
[elsevier.com/books-and-journals](http://elsevier.com/books-and-journals)

*Images courtesy of istockphoto.com*

Computer Vision

ISBN 978-0-12-809284-2



9 780128 092842